Microfluidics

www.ebook3000.com

Microfluidics

Fundamentals, Devices and Applications

Edited by Yujun Song, Daojian Cheng, and Liang Zhao

WILEY-VCH

Editors

Professor Yujun Song
University of Science and Technology Beijing
School of Mathematics and Physics
Beijing Key Laboratory of Magnetic Optoelectronic Composites and Interface Science
30 Xueyuan Road
Haidian District
100083 Beijing
PR China

Professor Daojian Cheng
Beijing University of Chemical Technology
State Key Laboratory of Organic-Inorganic Composites
15 Beisanhuan East Road
Chaoyang District
Beijing 100029
PR China

Dr. Liang Zhao
University of Science and Technology Beijing
School of Chemistry and Biochemistry
30 Xueyuan Road
100083 Beijing
PR China

Cover
The material used on the cover was kindly provided by the editors

All books published by **Wiley-VCH** are carefully produced. Nevertheless, authors, editors, and publisher do not warrant the information contained in these books, including this book, to be free of errors. Readers are advised to keep in mind that statements, data, illustrations, procedural details or other items may inadvertently be inaccurate.

Library of Congress Card No.: applied for

British Library Cataloguing-in-Publication Data
A catalogue record for this book is available from the British Library.

Bibliographic information published by the Deutsche Nationalbibliothek
The Deutsche Nationalbibliothek lists this publication in the Deutsche Nationalbibliografie; detailed bibliographic data are available on the Internet at <http://dnb.d-nb.de>.

© 2018 Wiley-VCH Verlag GmbH & Co. KGaA, Boschstr. 12, 69469 Weinheim, Germany

All rights reserved (including those of translation into other languages). No part of this book may be reproduced in any form – by photoprinting, microfilm, or any other means – nor transmitted or translated into a machine language without written permission from the publishers. Registered names, trademarks, etc. used in this book, even when not specifically marked as such, are not to be considered unprotected by law.

Print ISBN: 978-3-527-34106-1
ePDF ISBN: 978-3-527-80062-9
ePub ISBN: 978-3-527-80065-0
Mobi ISBN: 978-3-527-80066-7
oBook ISBN: 978-3-527-80064-3

Cover Design Adam-Design, Weinheim, Germany
Typesetting SPi Global, Chennai, India
Printing and Binding

Printed on acid-free paper

www.ebook3000.com

Contents

Preface *xiii*
Acknowledgments *xv*
Abbreviations *xvii*

1 Introduction: The Origin, Current Status, and Future of Microfluidics *1*
Kin Fong Lei
1.1 Introduction *1*
1.2 Development of Microfluidic Components *3*
1.3 Development of Complex Microfluidic Systems *4*
1.4 Development of Application-Oriented Microfluidic Systems *6*
1.4.1 Applications of DNA Assays *6*
1.4.2 Applications of Immunoassays *9*
1.4.3 Applications of Cell-Based Assays *11*
1.5 Perspective *14*
References *14*

2 Fundamental Concepts and Physics in Microfluidics *19*
Yujun Song, Xiaoxiong Zhao, Qingkun Tian, and Hongxia Liang
2.1 Introduction *19*
2.2 Basic Concepts of Liquids and Gases *21*
2.2.1 Mean Free Path (λ) in Fluids among Molecular Collisions *21*
2.2.2 Viscosity (μ) of Fluids *22*
2.2.3 Mass Diffusivity (D) *29*
2.2.4 Heat (Thermal) Capacity *34*
2.3 Mass and Heat Transfer Principles for Fluid *41*
2.3.1 Basic Fluidic Concepts and Law for Mass and Heat Transfer *42*
2.3.1.1 Pascal's Law and Laplace's Law *42*
2.3.1.2 Mass Conservation Principle (Continuity Equation) *44*
2.3.1.3 Energy Conservation (Bernoulli's Equation) *44*
2.3.1.4 Poiseuille's Law *45*
2.3.1.5 Velocity Profile of Laminar Flow in a Circular Tube *46*
2.3.2 Important Dimensionless Numbers in Fluid Physics *47*
2.3.3 Other Dimensionless Numbers in Fluids *50*
2.3.4 Diffusion Laws *56*

2.3.5 Conversion Equation Based on Navier–Stokes Equations *59*
2.3.5.1 Conservation of Mass Equation *60*
2.3.5.2 Conservation of Momentum Equation (Navier–Stokes Equation) *61*
2.3.5.3 Conservation of Energy Equation *62*
2.4 Surfaces and Interfaces in Microfluidics *62*
2.4.1 Surface/Interface and Surface Tension *62*
2.4.2 Surface-/Interface-Induced Bubble Formation *66*
2.4.3 Effect of Surfactants on the Surface/Interface Energy for Wetting *68*
2.4.4 Features of Surface and Interface in Microfluidics *69*
2.4.5 Capillary Effects in Microfluidic Devices *70*
2.4.6 Droplet Formation in Microfluidics *71*
2.5 Development of Driving Forces for Microfluidic Processes *74*
2.5.1 Fundamental in Electrokinetic Methods for Microfluidics *76*
2.5.2 Basic Principles of Magnetic Field-Coupled Microfluidic Process *81*
2.5.3 Basic Principles in Optofluidic Processes for Microfluidics *83*
2.6 Construction Materials Considerations *94*
Acknowledgments *100*
References *100*

3 Microfluidics Devices: Fabrication and Surface Modification *113*
Zhenfeng Wang and Tao Zhang
3.1 Introduction *113*
3.2 Microfluidics Device Fabrication *113*
3.2.1 Silicon and Glass Fabrication Process *114*
3.2.1.1 Photolithography *117*
3.2.1.2 Etching *117*
3.2.1.3 Metallization *117*
3.2.1.4 Bonding *117*
3.2.2 Polymer Fabrication Process *119*
3.2.2.1 Patterning *119*
3.2.2.2 Bonding *125*
3.2.2.3 Metallization *128*
3.2.2.4 3D Printing *128*
3.2.2.5 Surface Treatment *129*
3.2.3 Fabrication for Emerging Microfluidics Devices *129*
3.3 Surface Modification in Microfluidics Fabrication *129*
3.3.1 Plasma Treatment *132*
3.3.2 Surface Modification Using Surfactant *134*
3.3.3 Surface Modification with Grafting Polymers *135*
3.3.3.1 Surface Photo-Grafting Polymerization *135*
3.3.3.2 Surface-Initiated Atom Transfer Radical Polymerization (SI-ATRP) *137*
3.3.3.3 Grafting-to Technique *142*
3.3.4 Nanomaterials for Bulk Modification of Polymers *142*
3.4 Conclusions and Outlook *143*
References *144*

www.ebook3000.com

4 Numerical Simulation in Microfluidics and the Introduction of the Related Software *147*
Zheng Zhao, Adrian Fisher, and Daojian Cheng
4.1 Introduction *147*
4.2 Numerical Simulation Models in Microfluidics *148*
4.2.1 Molecular Dynamics (MD) *148*
4.2.2 The Direct Simulation Monte Carlo (DSMC) Method *151*
4.2.3 The Dissipative Particle Dynamics (DPD) *153*
4.2.4 Continuum Method (CM) *155*
4.2.5 The Lattice Boltzmann Method (LBM) *158*
4.2.6 Computational Fluid Dynamics (CFD) *160*
4.3 Numerical Simulation Software in Microfluidics *161*
4.3.1 CFD-ACE+ Software: Microfluidics Applications *162*
4.3.2 CFX Software: Microfluidics Applications *162*
4.3.3 FLOW-3D Software: Microfluidics Applications *164*
4.3.4 Other Software: Microfluidics Applications *166*
4.4 Conclusions *166*
Acknowledgments *167*
References *168*

5 Digital Microfluidic Systems: Fundamentals, Configurations, Techniques, and Applications *175*
Mohamed Yafia, Bara J. Emran, and Homayoun Najjaran
5.1 Introduction to Microfluidic Systems *175*
5.2 Types of Digital Microfluidic Systems *177*
5.3 DMF Chip Fabrication Techniques *179*
5.4 Different Electrode Configurations in DMF Systems *181*
5.5 Digital Microfluidic Working Principle *183*
5.5.1 Electromechanical and Energy-Based Models *183*
5.5.2 Numerical Models *184*
5.5.3 Analytical Models *184*
5.6 Electrical Signals Used and Their Effect on the DMF Operations *185*
5.6.1 Types of the Signals Used in Actuation *185*
5.6.2 The Effect of Changing the Frequency *187*
5.7 Droplet Metering and Dispensing Techniques in DMF Systems *188*
5.8 The Effect of the Gap Height between the Top Plate and the Bottom Plate in DMF Systems *189*
5.9 Modeling and Controlling Droplet Operations in DMF Systems *192*
5.9.1 Feedback Control in DMF Systems *192*
5.9.2 Droplet Sensing Techniques in DMF Systems *195*
5.9.3 Droplet Routing in DMF Systems *195*
5.9.4 Controlling and Addressing the Signals in DMF Systems *197*
5.10 Prospects of Portability in DMF Platforms *199*
5.11 Examples for Chemical and Biological Applications Performed on the DMF Platform *199*
References *203*

6 Microfluidics for Chemical Analysis *211*
Peng Song, Adrian C. Fisher, Luwen Meng, and Hoang V. Nguyen
6.1 Introduction *211*
6.2 Microfluidics for Electrochemical Analysis *212*
6.2.1 Voltammetric Analysis *212*
6.2.2 Amperometric Protocol *216*
6.2.3 Potentiometric Protocol *219*
6.2.4 Conductivity Protocol *221*
6.3 Advanced Microfluidic Methodologies for Electrochemical Analysis *223*
6.3.1 The Rotating Microdroplet *223*
6.3.2 The Microjet Electrode *224*
6.3.3 Channel Multiplex *225*
6.4 Numerical Modeling of Electrochemical Microfluidic Technologies *226*
References *229*

7 Microfluidic Devices for the Isolation of Circulating Tumor Cells (CTCs) *237*
Caroline C. Ahrens, Ziye Dong, and Wei Li
7.1 Introduction *237*
7.2 Affinity-Based Enrichment of CTCs *241*
7.2.1 CTC-Chip *243*
7.2.2 Geometrically Enhanced Differential Immunocapture (GEDI) *243*
7.2.3 Herringbone (HB)-Chip *244*
7.2.4 CTC-iChip *244*
7.2.5 High-Throughput Microsampling Unit (HTMSU) *245*
7.2.6 OncoBean Chip *246*
7.2.7 NanoVelcro Rare Cell Assays *246*
7.2.8 GO Chip *246*
7.2.9 CTC Subpopulation Sorting *247*
7.3 Nonaffinity-Based Enrichment of CTCs *247*
7.3.1 Microfluidic Filtration *249*
7.3.2 Inertial Methods *250*
7.3.2.1 Deterministic Lateral Displacement (DLD) *250*
7.3.2.2 Microfluidic Spiral Separation *250*
7.3.2.3 Vortex Platform *251*
7.3.2.4 Multiorifice Flow Fractionation (MOFF) *251*
7.3.3 Dielectrophoresis and Acoustophoresis *251*
7.4 Conclusions and Outlook *252*
References *254*

8 Microfluidics for Disease Diagnosis *261*
Jun-Tao Cao
8.1 Introduction *261*
8.2 Protein Analysis *261*
8.2.1 Secreted Proteins in Biological Fluids *261*

www.ebook3000.com

8.2.2 Membrane Protein *264*
8.3 Nucleic Acid Analysis *267*
8.4 Cell Detection *269*
8.5 Other Species *272*
8.6 Summary and Overlook *275*
References *275*

9 Gene Expression Analysis on Microfluidic Device *279*
Liang Zhao
9.1 Introduction *279*
9.2 Analysis Cell Population Gene Expression on Chip *281*
9.2.1 Nucleic Acid Analysis *281*
9.2.2 Protein Level Analysis of Gene Expression *283*
9.3 Single-Cell Gene Expression Profiling *288*
9.3.1 Imaging-Based Single-Cell Analysis on Microfluidics *289*
9.3.2 Microfluidic Methods to Single-Cell Nucleic Acid Analysis *292*
9.3.3 Next-Generation Sequencing Platforms Based on Miniaturized Systems *301*
9.4 Conclusion *305*
Acknowledgment *306*
References *306*

10 Computational Microfluidics Applied to Drug Delivery in Pulmonary and Arterial Systems *311*
Clement Kleinstreuer and Zelin Xu
10.1 Introduction *311*
10.2 Modeling Methods *312*
10.2.1 Governing Equations *312*
10.2.2 Model Closure *312*
10.2.3 Turbulence Modeling *313*
10.2.4 Fluid–Particle Dynamics Modeling *313*
10.2.5 Ferrofluid Dynamics *315*
10.2.6 Nonspherical Particle Dynamics *316*
10.2.7 Flow through Porous Media *316*
10.2.8 Fluid–Structure Interaction *317*
10.3 Pulmonary Drug Delivery *318*
10.3.1 Inhalers and Drug–Aerosol Transport *319*
10.3.2 Drug–Aerosol Dynamics *322*
10.3.3 Methodologies and Design Aspects for Direct Drug Delivery *323*
10.3.3.1 Smart Inhaler System Methodology *325*
10.3.3.2 Enhanced Deeper Lung Delivery of Drug Aerosols via Condensational Growth *326*
10.3.3.3 Shape Engineering for Novel Drug Carriers *326*
10.3.3.4 Multifunctional Nanoparticles *327*
10.3.3.5 Particle Absorption and Translocation *328*
10.4 Intravascular Drug Delivery *328*
10.4.1 Nanoparticle-Based Targeted Drug Delivery *329*

10.4.2 Catheter-Based Intravascular Drug Delivery *330*
10.4.2.1 Particle Hemodynamics *331*
10.4.2.2 Tissue Heat and Mass Transfer *332*
10.4.3 Magnetic Drug Delivery *333*
10.4.4 Direct Drug Delivery *335*
10.5 Conclusions and Future Work *338*
References *339*

11 Microfluidic Synthesis of Organics *351*
Hongxia Liang and Yujun Song
11.1 Introduction *351*
11.2 Microfluidic Nebulator for Organic Synthesis *355*
11.3 Coiled Tubing Microreactor for Organic Synthesis *356*
11.4 Chip-Based Microfluidic Reactor for Organic Synthesis *360*
11.5 Packed-Bed Microreactors for Organic Synthesis *363*
11.6 Ring-Shaped (Tube-in-Tube) Microfluidic Reactor for Organic Synthesis *365*
11.7 Summary and Outlook *368*
Acknowledgments *369*
References *369*

12 Microfluidic Approaches for Designing Multifunctional Polymeric Microparticles from Simple Emulsions to Complex Particles *375*
Jongmin Kim and Chang-Soo Lee
12.1 Introduction *375*
12.2 Flow Regimes in Microfluidics: Dripping, Jetting, and Coflowing *376*
12.2.1 Dimensionless Numbers *377*
12.2.2 T-Junction Microfluidics *377*
12.2.3 Flow-Focusing Microfluidics *378*
12.2.4 Coflowing Microfluidics *379*
12.3 Design of Multifunctional Microparticles from Emulsions *380*
12.3.1 Microfluidic Approaches with Control of the Hydrodynamic Parameters *380*
12.3.2 Microfluidic Approaches with Phase Separation *393*
12.3.3 Microfluidic Approaches with Spreading Coefficients *397*
12.4 Conclusions and Outlooks *398*
References *399*

13 Synthesis of Magnetic Nanomaterials *405*
Ali Abou-Hassan
13.1 Introduction *405*
13.2 Synthesis of Magnetic Nanomaterials Using Microreactors *406*
13.2.1 Magnetic Iron Oxide-Based Nanomaterials *406*
13.2.2 Synthesis of Metallic and Magnetic Nanomaterials *412*
13.2.3 Synthesis of Core–Shell Magnetic Nanomaterials *414*

www.ebook3000.com

13.3 Conclusion *416*
References *416*

14 Microfluidic Synthesis of Metallic Nanomaterials *419*
Jugang Ma and Yujun Song
14.1 Introduction *419*
14.2 Microfluidic Processes for Metallic Nanomaterial Synthesis *421*
14.3 Crystal Structure-Controlled Synthesis of Metallic Nanocrystals *422*
14.4 Size- and Shape-Controlled Synthesis of Metallic Nanocrystals *426*
14.5 Multi-Hierarchical Microstructure- and Composition-Controlled Synthesis of Metallic Nanocrystals *434*
14.6 Summary and Outlook *437*
Acknowledgments *439*
References *439*

15 Microfluidic Synthesis of Composites *445*
Junmei Wang and Yujun Song
15.1 Introduction *445*
15.2 Microfluidic Synthesis Systems and the Design Principles *447*
15.3 The Formation Mechanism of Composites *451*
15.4 Microfluidic Synthesis of Composites *452*
15.4.1 Composites Composed of Nonmetal Inorganics *452*
15.4.1.1 Microfluidic Synthesis of Oxide-Coated Multifunctional Composites *453*
15.4.1.2 Microfluidic Synthesis of Semiconductor–Semiconductor Composites *455*
15.4.2 Composites Composed of Metal and Nonmetal Inorganics *457*
15.4.2.1 Microfluidic Synthesis of Dielectric–Plasmonic Composites *457*
15.4.2.2 Microfluidic Synthesis of Plasmonic–Semiconductor Composites *459*
15.4.2.3 Microfluidic Synthesis of Carbon-Supported Composites *461*
15.4.3 Composites Composed of Polymers and Metals *464*
15.4.4 Composites Composed of Metal or Metal Alloy Materials *464*
15.4.5 Composites Composed of Polymer and Organic Molecular *466*
15.4.6 Composites Composed of Two or More Polymers *469*
15.4.7 Microfluidic Synthesis of Metal–Organic Frameworks (MOFs) *470*
15.5 Summary and Perspectives *471*
Acknowledgments *472*
References *472*

16 Microfluidic Synthesis of MOFs and MOF-Based Membranes *479*
Fernando Cacho-Bailo, Carlos Téllez, and Joaquin Coronas
16.1 Microfluidic Synthesis of Metal–Organic Frameworks (MOFs) *479*
16.1.1 Zeolite Background *479*
16.1.2 Microfluidic MOF Synthesis *480*
16.2 Microfluidic Synthesis of MOF-Based Membranes *488*

16.2.1 Context *488*
16.2.2 MOF Membranes by Microfluidics *489*
16.2.3 Inorganic versus Polymeric Supports: Intensification of Processes *501*
16.2.4 Support Influence on MOF Synthesis Method *504*
16.2.5 Advantages of Inner MOF Growth *506*
16.3 Conclusions and Outlook *507*
Acknowledgments *508*
References *508*

17 Perspective for Microfluidics *517*
Yujun Song and Daojian Cheng
17.1 Design, Fabrication, and Assemble of Microfluidic Systems *518*
17.2 Precise Control of Critical Device Features for Chemical Analysis and Biomedical Engineering *521*
17.3 Control of Critical Kinetic Parameters for Chemical and Materials Synthesis *522*
17.4 Development of Fundamental Theory at Micro-/Nanoscale and Fluid Mechanism at Nanoliter–Picoliter for Microfluidic Systems *525*
Acknowledgments *529*
References *529*

Index *541*

www.ebook3000.com

Preface

Confucius stated, "Learning without thought is labor lost, thought without learning is perilous." During the past decades, microfluidics has quickly become an important tool in several fields including new technologies and basic research. As both thinker and practitioner for Engineers and Scientists, it is time to summarize and build up the fundamental fluid mechanics, physics, and chemistry in microfluidics and the relationship with their amazing successful applications in consideration of the future development of this field.

Microfluidics deals with small volumes of fluids from 10^{-9} to 10^{-18} l using channels with dimensions from several to hundreds of micrometers, which can be expanded even to millimeters. Microfluidics is an intrinsically multidisciplinary field of science that embraces research in physics, chemistry, medicine, engineering, materials science, and biology (2–6). Since the first applications of microfluidic technologies in analysis appearing as capilliary format succeeded in 1992, great progresses in their applications have been achieved in chemical analysis, biomolecule detection, cell treatment, pharmaceutical screening, robust and portable point-of-care devices, controlled synthesis of materials, precise reaction control, and so on, due to their opportunities for the spatial and temporal control of matter and heat transfer. Lots of academic and industrial materials on microfluidics have been accumulated, including construction of microfluidic devices according to their unique application areas, fundamental theory in microfluidics, and success in academic or industrial applications. Now, microfluidics has been paved into one of the main stream of new technologies, which is important not just for this field but also for lots of multidisciplinary technologies struggling to be made great in time.

The purpose of this book is mainly to summarize and build up the fundamental fluid mechanics, physics, and chemistry in microfluidics and the relationship with their amazing successful applications. This book will then provide prospective insights for the blooming of microfluidics to open a new and smart era in analysis, sensing, probing, synthesis, and screening of matter. It will provide not only a fundamental tool for the current researchers and commercial users of microfluidics to find the related physics and chemistry theory and a manual for their future fantastic applications but also a useful and powerful reference for the newcomer to add their knowledge and enlighten their own strategies in the development of a new theory and application of microfluidics.

From Chapter 1 to Chapter 4, the basic principles related to microfluidics will be discussed, including the history and current status of microfluidics, the fundamental physics of fluidic mechanism, the design/fabrication/materials of microfluidic devices, the related surface and interface effect in microfluidics unique from bulk reactors, and the fluidic simulation in microfluidics. In Chapter 5, the recently developed microfluidic devices, including smart microfluidic devices (e.g., digital microfluidics) and the robust and portable point-of-care microfluidic devices and their potential applications will be discussed. Then the rapidly developed applications of microfluidics in chemical/biological analysis (i.e., Micro Total Analysis Systems (μ-TAS)) and biological medical engineering (e.g., gene express, high-throughput disease diagnosis) will be summarized in Chapters 6–10 to analyze their advantages and marvelous progress by considering their unique features. And then the related materials synthesis via varieties of microfluidic devices including lab-on-chip and microtubing-based systems will be elucidated in Chapters 11–16 to show their potentials that sometimes cannot be successful in bulk reactors, including the synthesis of organics, polymers, metals, inorganics, composites, or hybrids. Finally, we will discuss the most recent progress (e.g., opto-microfluidics and other field coupled microfluidics and their future amazing applications) and some issues in microfluidics in Chapter 17, giving the readers a full and wide vision of this attractive technology.

We hope that this book will contribute to the research and teaching of this field and also attract more readers to pay attention. We also know that it is impossible to include all progresses and aspects of this rapidly blooming and exciting field. Therefore, we will feel gratified if only this book can give readers some clues on this interesting field and promote its scientific and technological development.

Finally, I dedicated this book to my lovely daughter: Xinran Song, who is full of curious about details of tiny things and creatures and dreaming to be a famous Biologist.

Beiing, China
July 16, 2017

Yujun Song

www.ebook3000.com

Acknowledgments

This work was supported by National S&T Major Project (pre-approved No. SQ2018ZX100301), NSFC (Grant No. 51371018 & 81372425) and the Fundamental Research Funds for the Central University of China (FRF-BR-14-001B).

Abbreviations

$\vec{J}_i$	flux of component i
$\partial T/\partial x$	temperature gradient along x-direction, K/m
$\overline{B}$	magnetic field strength
$^{\partial u}/_{\partial y}$	local shear velocity
$\sim\lambda_{\mathrm{D}}$	ionic screening cloud of width
$\times$	cross product
∇	vector differential operator
a	speed of sound
A	cross-section area of the flow
A_1	cross-section areas A_1
A_2	cross-section areas A_2
AIP	American Institute of Physics
Ar	Archimedes number
At	Atwood number
Bi	Biot number
B_o	Bond number
Br	Brinkman number
c	total molar concentration (equation (2.19))
C	concentration of the species (equation (2.9))
c	light speed (equation (2.97))
Ca	capillary number
C_e	centrifuge number
Cfr	friction coefficient
c_i	molar concentration of component i
C_P	constant pressure heat capacity
C_V	constant volume heat capacity
d	collision diameter of molecules
D	diffusion coefficient (cm^2/s) (equation (2.14))
D	diffusion coefficient of the species (equation (2.92))
$\mathrm{D_{AB}}$	diffusivity of A in B
D_e	diffusion coefficient in gas or liquid filling the pore (equation (2.16))
D_e	Dean number
$\mathrm{D_h}$	hydraulic diameter

www.ebook3000.com

D_i	diffusivity of the ions
D_{ij}	Maxwell–Stefan diffusivity
DRIE	deep reactive ion etching
$\bar{E} = -\nabla\phi e$	local applied electrical filed strength
$E_{//}$	local electric strength
E	bulk modulus elasticity (N/m^2 (Pa))
$\bar{E}$	electric field
E	spacing distance (x) dependent electric field strength (equation (2.82))
Ec	Eckert number
EDL	electrical double-layer
Ek	Ekman number
E_o	Eötvös number
Eu	Euler number
F	magnitude of this force
FEP	fluorinated ethylene propylene
F_{mix}	extent efficiency of mixing two fluids next to each other accomplished only through diffusion
Fo	Fourier number
Fr	Froude number
Fr_R	rotating Froude number
Fs	shear force
g	acceleration of gravity
Ga	Galileo number
Gr	Grashof number
Gz	Graetz number
h	fluid depth (equation (2.30))
h(r)	displacement of the interface
h	height
Hg	Hagen number
I	beam intensity
I_0	intensity of the incident light
ICEK	induced-charge electrokinetic
ICEO	induced-charge electro-osmosis
IOP	Institute of Physics
J_0	zero-th order Bessel function
Ja	Jakob number
Jx	net flux
k	wavenumber of the laser beam
Kn	Knudsen number
k_rCL/D	Damköhler number
L	characteristic length
L	separation between electrodes (equation (2.94))
La	Laplace number
LC	liquid crystal
Le	Lewis number
LLCP	linear liquid crystal polymer

m	mass of molecule
M	molecular weight (equation (2.8))
M	molar mass (g/mol) (equation (2.14))
Ma	Marangoni number
M_B	molar mass of solvent B
Mo	Morton number
n	the number of components
N	Avogardro number
ñ	outward unit normal on surface
n_0	bulk concentration of ions
n1	refractive index
Nu	Nusselt number
P	static pressure (equation (2.32))
P	difference in pressure inside (P_i) and outside (P_o) of the bubble (equation (2.68))
p	pressure (atm)
∇_P	pressure gradient
P↑	beam power threshold
Pe	Péclet Number
PEEK	polyaryl etheretherketone
Pr	Prandtl number
Q	volumetric flow rate
$q"_x$	heat density along x-direction, W/m^2
R	gas constant (equation (2.1))
R and T	normal incidence for weak deformations with linearized curvatures (equation (2.99))
$R(\theta_2, \theta_1)$	classical reflection
r	internal radius (equation (2.33))
r	average distance of the liquid (equation (2.79))
r	distance from the center to the laser beam
Ra	Rayleigh number
Re	Reynolds number
Ri	Richardson number
R_o	Rossby number
R_x and R_y	radii of curvature in all axes parallel to the surface
Sc	Schmidt number
Sh	Sherwood number
SH	source or a sink of heat
St	Strouhal number
Sta	Stanton number
Ste	Stefan number
Stk	Stokes number
$T(\theta_2, \theta_1)$ $= 1 - R(\theta_2, \theta_1)$	transmission Fresnel coefficients in electromagnetic energy
T	absolute temperature
T_0	reference temperature (K)
T_1	absolute temperature

www.ebook3000.com

T_2	absolute temperature
Ta	Taylor Number
TMAs	tubular microactuators
u/y	rate of shear deformation or shear velocity
ū	average molecule velocity
ū	velocity vector
u_1	effective velocity of the fluid flow through and A_1 (equation (2.31))
u_2	effective velocity of the fluid flow through and A_2.
$\bar{u}_{ep}$	electrophoretic velocity of the species
U_{th}	largest interfacial tension
V_A	molecular volume of solute A under the boiling point, cm^3/mol.
w	half width of the light beam
We	Weber Number
W_{SLV}	work to form a kind of contact
x	heat transfer direction (equation (2.27))
x	distance from the channel wall (equation (2.90))
α	activity (equation (2.19))
α	thermal diffusivity (equation (2.28))
α	Womersley number
β	volumetric thermal expansion coefficient
β_T	isothermal compressibility
γ	relative magnitude of surface tension
γ_{SL}, γ_{LV} and γ_{SV}	interfacial tensions between solid and liquid, liquid and vapor, and solid and vapor, respectively
δ	constrictivity
Δp	characteristic pressure difference of flow
ΔP	pressure jump (equation (2.72))
ΔP	Laplace pressure (equation (2.67))
ΔT	characteristic temperature difference
ε	coefficient of thermal expansion
ε_t	porosity available for transport (dimensionless)
ε_w	dielectric constant
$\zeta_i \approx E_{0r}$	potential drop of field
ζ_i	local induced zeta potential
θ	contact angle
θ_1 and θ_2	transmission angles
κ	heat conductivity
λ	mean free path
λ_D	screening lengths
$\Lambda_{o,i}$	thermal conductivities (the subscripts i, o denote the fluids inside and outside)
μ	dynamic viscosity (equation (2.3))
μ	viscosity of liquid (equation (2.89))
$\mu\nabla^2 h$	laplace force
μ_0	reference viscosity

μ_a	pure viscosity of component a
μ_b	pure viscosity of component b
μ_{i}	chemical potential
μ_{l}	dynamic viscosity of liquid (Pa·s)
$\mu_{\mathrm{o,i}}$	shear viscosity
μ_{r}	relative viscosity (dimensionless)
μ_{s}	dynamic viscosity of slurry
μ_{T1}	dynamic viscosity of solvent at T_1
μ_{T2}	dynamic viscosity of solvent at T_2
ν	ratio of inertial forces to viscous forces
$\Pi_{\mathrm{Rad(r)}}$	balance between radiation pressure
Π_{Rad}	light pressure
ρ	density of liquid
$\rho 1$	density
ρC_P	volumetric heat capacity (J/(m^3·K))
$\rho \mathrm{gh}$	gravity
ρ_{q}	local net charge density
ρ_{tot}	sum of two densities
σ	excess free energy of a drop on a solid surface (equation (2.69))
σ	surface tension (N/m)
$\sigma_{\mathrm{A,B}} = (\sigma_1 + \sigma_2)/2$	average collision diameter (Å)
σ_d	interfacial free energy of highest energy level
σ_f	interfacial free energy of final status
$-\sigma\hat{\mathrm{H}}\,(\mathrm{r})$	laplace pressure
σ_i	interfacial free energy of initial status
τ	shear stress
$\overline{v}$	particle's velocity
$\overline{v}i$ "	diffusion velocity of the component
Φ	associated parameter of the solvent
χ	mole fraction
χ_a	mole fraction of component a
n	mole fraction of component b
Ω	temperature-dependent collision integral (usually of order 1)(dimensionless).
ω^*	characteristic frequency of interfacial wave
ω	circular frequency
ω	angular velocity of disc (equation (2.79))
ω_{i}	angular velocity of inner cylinder

www.ebook3000.com

1

Introduction: The Origin, Current Status, and Future of Microfluidics

Kin Fong Lei

Chang Gung University, Graduate Institute of Medical Mechatronics and Department of Mechanical Engineering, 259 Wen-Hua 1st Road, Kweishan, Taoyuan, Taiwan
Linkou Chang Gung Memorial Hospital, Department of Radiation Oncology, 5 Fu-Hsing Street, Kweishan, Taoyuan, Taiwan

1.1 Introduction

Microfluidic device/system is generally defined as a component that handles a small quantity (micro- or nanoliter) of fluids (liquid or gas). Because most of the applications required for handling fluids relate to biomedical and chemical analyses, microfluidics has been currently realized as miniaturized analytical technology for biomedical and chemical applications. Conventional macroscopic equipment processing in wet laboratory can be miniaturized into microscopic devices. One of the objectives of the development of microfluidic systems is to provide a total solution from the sample application to the display of analytical results. Hence, microfluidic system is also called lab-on-chip (LOC), biochip, or micro-total analysis system (μTAS). Because of the miniaturization, a number of advantages can be achieved including less sample/reagent consumption, reduction of contamination risk, less cost per analysis, reduction of tedious operations, enhancement of sensitivity and specificity, and increase of reliability.

In the beginning of the development of microfluidic technology, fabrication of microfluidic devices was based on the microelectronic manufacturing infrastructure and microelectromechanical systems (MEMS) technology. Microfluidics was realized as a branch of MEMS technology specializing in handling fluids. Silicon was the major material for the substrate of these microfluidic devices. The typical microelectronic fabrication processes include photolithography, thin-film deposition, and etching. These processes are called surface-micromachining processes that can treat silicon surface of 1–2 μm in thickness at most. However, microfluidic devices require to fabricate high-aspect-ratio microstructures and bond multi-substrates. Bulk micromachining processes and substrate bonding techniques originally

Microfluidics: Fundamentals, Devices and Applications, First Edition.
Edited by Yujun Song, Daojian Cheng, and Liang Zhao.
© 2018 Wiley-VCH Verlag GmbH & Co. KGaA. Published 2018 by Wiley-VCH Verlag GmbH & Co. KGaA.

developed for MEMS were used to construct closed-volume microfluidic devices. An example of classical silicon-based microfluidic devices is ink-jet printer head. It has a large number of high-precision microscopic nozzles that eject ink onto paper. Generally, these nozzles are 10 μm in diameter and are fabricated by silicon material. However, silicon substrate is relatively expensive and is not optically transparent. It may limit the applications of optical detection, especially for biomedical and chemical analyses. Therefore, glass and polymer materials were introduced, and microfluidic technology became a specific research area in the 2000s [1–4]. Compared with silicon substrate, glass and polymer materials are less expensive and optically transparent. Polymer materials such as polymethylmethacrylate (PMMA), polystyrene (PS), polycarbonate (PC), and polydimethylsiloxane (PDMS) were used to demonstrate the fabrication of microfluidic devices [1–7]. Among these, PDMS is one of the most commonly used materials for fabricating microfluidic devices in current research laboratories. The advantages of using PDMS material include easy replication, optical transparency, biocompatibility, and low cost. To fabricate PDMS layers with microstructures, it is generally based on soft lithography, which is a nonphotolithographic strategy of replica molding [2]. Typically, microfluidic devices can be constructed by binding glass substrates and PDMS layers [3, 4]. Glass-/PDMS-based microfluidic devices were widely demonstrated on various biomedical applications such as DNA analysis [8–15], immunoassays [16–19], and cell-based assays [20, 21]. Recently, paper substrate has been proposed to be an alternative material used for fabricating microfluidic devices [22]. The use of a paper substrate has a number of advantages including being inexpensive, thin, light in weight, and disposable. Aqueous solution can be transported by wicking and a passive pumping is realized. Paper substrate is biocompatible with various biological samples and can be modified by a wide range of functional groups that can be covalently bound to proteins, DNA, or small molecules. The original idea of paper-based microfluidics was to suggest a new class of point-of-care diagnostic device for developing countries and remote environments [23]. Since then, various diagnostic applications were demonstrated [24–31], for example, paper-based enzyme-linked immunosorbent assay (ELISA) was shown to be completed within an hour, whereas conventional ELISA requires at least 6 h [30, 31]. Moreover, biological cells were also reported to be cultured on paper substrates for more advanced analyses [32–36].

The above discussions briefly introduce different materials used for the fabrication of microfluidic devices including silicon, glass/polymer, and even paper substrates. It is noticed that the design and material used by microfluidic devices are flexible and unlimited. In this chapter, the development from the origin and current status to the future prospect in microfluidics is discussed, including: (i) development of microfluidic components; (ii) development of complex microfluidic systems; and (iii) development of application-oriented microfluidic systems. An updated and systematic in-depth discussion is provided in this chapter.

www.ebook3000.com

1.2 Development of Microfluidic Components

The development of microfluidics originated from MEMS technology, which was defined as a microscopic system integrating with electronic and mechanical components. Its objective is to miniaturize conventional macroscopic devices for measuring physical quantities into microscopic devices. Because of strong capital promotions from both government and industry, development of MEMS technology was rapid and that made the sensing components small and inexpensive. A typical example of MEMS is accelerometer, which currently is embedded in nearly every cell phone to sense gravity for identifying the orientation of the cell phone. Along with this concept, conventional macroscopic equipment processing in wet laboratory could be miniaturized into microscopic devices. These microscopic devices were designed to handle sub-milliliter fluids, so they were called microfluidic devices. In the beginning, most of the developments were focused on miniaturization of fluidic components such as pumps [37–39], mixers [40–42], and valves [43, 44]. These individual components were the fundamental elements of fluidic systems. The objective of the development was to demonstrate the capability of fluidic manipulation, but not for specific biomedical applications. For example, a silicon-based bidirectional micropump was reported and its schematic drawing is shown in Figure 1.1 [38]. The micropump was actuated by electrostatic diaphragm and two passive check valves. It was constructed by multisilicon substrates and fabricated by bulk micromachining technology. The maximum pump rate could be 850 $\mu l\,min^{-1}$ and back pressure was 31 000 Pa. Alternatively, microfluidic mixing in a continuous flow was demonstrated by ultrasonic vibration [41]. Illustration of the design of the micromixer is shown in Figure 1.2. It was constructed with a glass substrate and a silicon substrate. The glass substrate was etched and anodically bonded with the silicon substrate to form the flow channel. The silicon substrate was etched from the backside to form the oscillating diaphragm. A piezoelectric disk was then attached to the oscillating diaphragm. Laminar flows were mixed

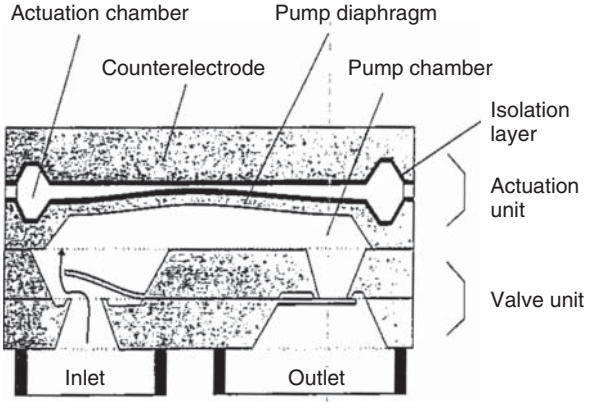


Figure 1.1 Silicon-based electrostatically driven diaphragm pump. (Zengerle *et al*. 1995 [38]. Reproduced with permission of Elsevier.)

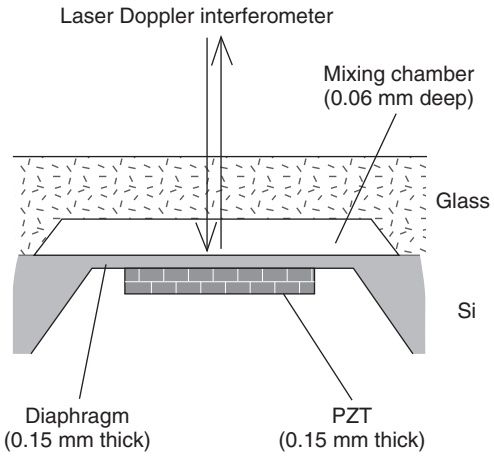


Figure 1.2 Schematic drawing of the cross-section of the micromixer. (Reprinted with permission from Ref. [41]. Copyright (2001) Elsevier.)

continuously and effectively by the ultrasonic vibration from the diaphragm actuated by the piezoelectric disk.

The above examples showed the focus of the early development of microfluidic technology in the 1990s. Fluidic manipulation and handling in microenvironment was the key issue to be solved at that moment. Because of limited substrate materials, that is, silicon and glass, microfluidic components were mainly fabricated by bulk micromachining technology. However, silicon substrate is relatively expensive and is not optically transparent. It may limit the applications of using optical detection, especially for biomedical and chemical analyses.

1.3 Development of Complex Microfluidic Systems

In the 2000s, polymer materials were introduced to construct microfluidic devices/systems [1–4]. Currently, PDMS is one of the most commonly used materials for fabricating microfluidic devices/systems in research laboratories. Because of the advantage of easy replication, complicated microfluidic systems were successfully fabricated by integrating many fluidic components [3, 4]. A pioneer work was demonstrated constructing a microfluidic system integrating with on–off valves, switching valves, and pumps [3]. The system was entirely consisted of elastomer based on multilayer soft lithography. Another developed latching microfluidic valve structures controlled independently by using an on-chip pneumatic demultiplexer [45]. A microfluidic system was constructed by a four-bit demultiplexer for routing pressure and vacuum pulses from a single input connection to each of the 16 latching valves as shown in Figure 1.3. Because these valve assemblies can form the standard logic gates, it was expected to develop complex pneumatic microprocessors for handling fluids. Besides microfluidic operations in a continuous flow, manipulation of discrete microdroplets was introduced and called digital microfluidics [46–48]. Electrolytic droplets were actuated by direct electrical control of the surface tension through a pair of opposing planar electrodes that was based on electrowetting-on-dielectric

www.ebook3000.com

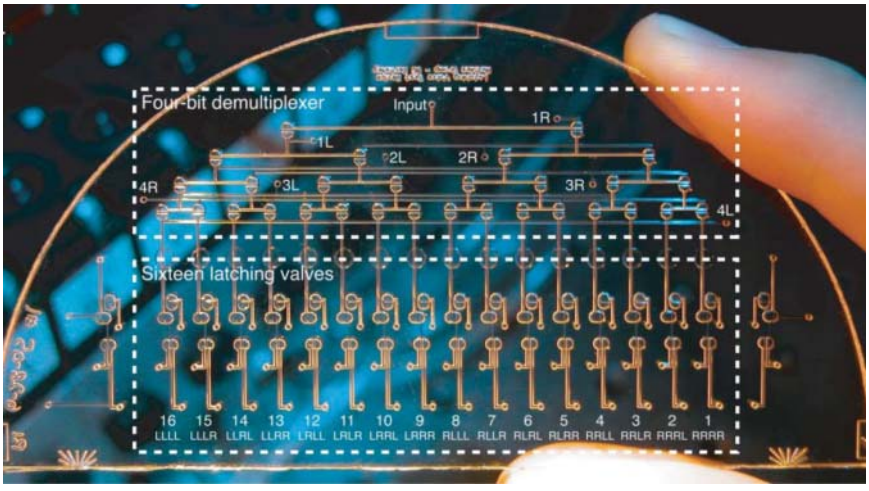


Figure 1.3 Photograph of the multiplexed latching valve system with a 4-bit demultiplexer and 16 latching valves. (Grover *et al*. 2006 [45]. Reproduced with permission of Royal Society of Chemistry.)

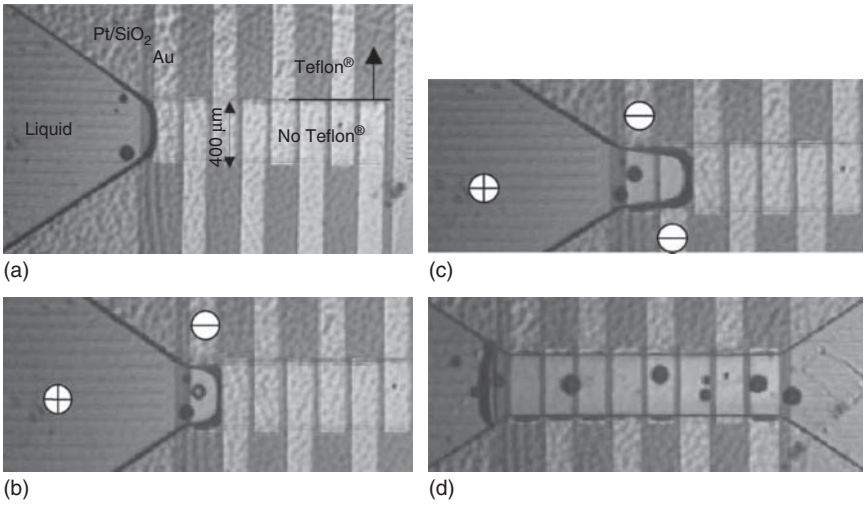


Figure 1.4 Manipulation of discrete microdroplets by digital microfluidics. (a) Liquid introduced, (b) first electrode biased, (c) first and second electrodes biased, and (d) all the electrodes biased. (Lee *et al*. 2002 [47]. Reproduced with permission of Elsevier.)

(EWOD) principle. By applying electrical potentials to sequential electrodes, a droplet can be dispensed from a reservoir, transported to any position on the array, merged with other droplets to perform reactions, and split into two droplets. An example of the manipulation of microdroplets is shown in Figure 1.4. Digital microfluidics was proposed to have several advantages over traditional counterparts, such as elimination of dead volume, enhancement

of mixing ratio, precision on the control of the volume, and encapsulation of biomolecules for monitoring. In the early 2000s, demonstrations of fabricating complex microfluidic systems have been extensively reported. These developments provided a solid foundation for the investigations of microfluidic systems in the applications of various biomedical and chemical analyses.

1.4 Development of Application-Oriented Microfluidic Systems

By the mature development of microfluidic technology, a broad spectrum of applications has been demonstrated by the microfluidic systems. Because of the characteristics of microfluidics such as miniaturization and automation, conventional biomedical and chemical analyses could be precisely and effectively operated in a single microfluidic system. A number of advantages are obtained including less sample/reagent consumption, reduction of contamination risk, less cost per analysis, reduction of tedious operations, enhancement of sensitivity and specificity, and increase of reliability.

1.4.1 Applications of DNA Assays

Microfluidic systems have been demonstrated on DNA assays [8–15]; a pioneer work was published in 1998 [12]. Microchannels, heaters, temperature sensors, and fluorescent detectors were integrated into a single silicon-/glass-based microfluidic system. Operations such as capturing DNA, mixing reagents, and amplification, separation, and detection of DNA products were automatically

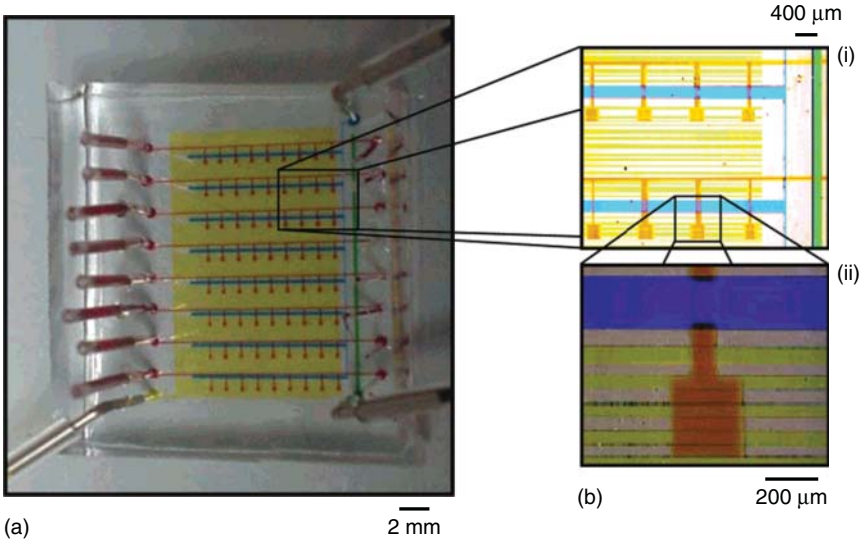


Figure 1.5 Microfluidic RT-PCR system. (a) Photograph of the system loaded with food dye. (b) Optical micrographs of eight reaction chambers (i) and one reaction chamber (ii). (Marcus *et al*. 2006 [13]. Reproduced with permission of American Chemical Society.)

www.ebook3000.com

manipulated by electroosmotic pumping. Detection of specific target DNA strand was successfully demonstrated, showing an integrated and automatic microfluidic device and providing a foundation of microfluidic DNA analysis. Another example was reported for performing reverse transcriptase polymerase chain reaction (RT-PCR) in microfluidic system [13]. It was shown to detect less than 50 β-actin transcripts from a total RNA template. A photograph of the microfluidic system is shown in Figure 1.5. The system was composed of three layers of PDMS bonded to a glass cover slip to construct valves and reactors. This work showed the capability of enabling highly parallel single-cell gene expression analysis. Moreover, DNA hybridization was showed to be accelerated by microfluidic technology [14]. Dynamic hybridization was achieved by local microfluidic vortexes generated by electrokinetic forces on a concentric circular microelectrode, shown in Figure 1.6a. The vortexes increased collision efficiency between target DNA strands suspended in solution and probe DNA strands

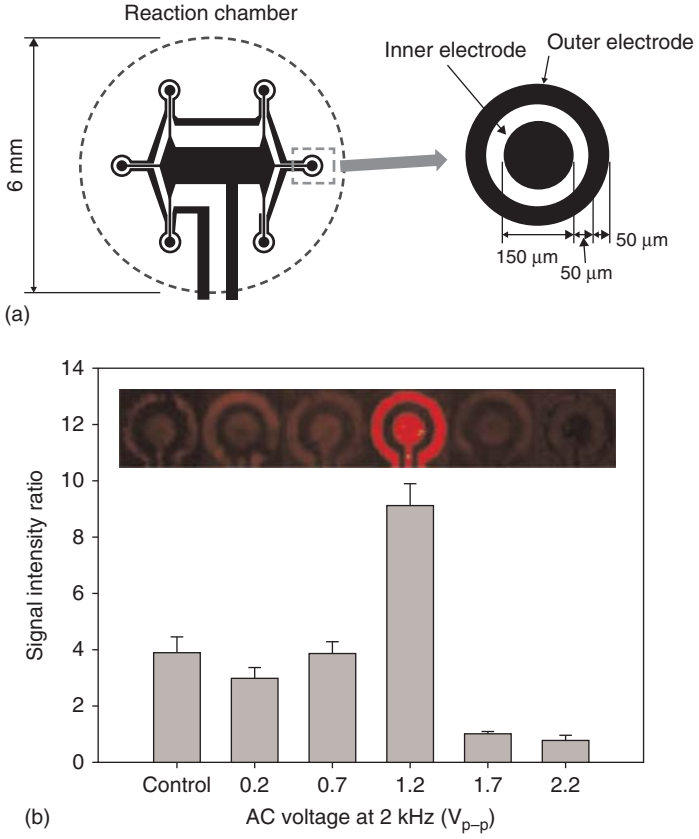


Figure 1.6 Electrokinetic acceleration of DNA hybridization. (a) Illustration of the concentric circular microelectrode for generating electrokinetic forces to achieve dynamic hybridization. (b) Results of 5-min dynamic hybridization represented by signal intensity ratio under the AC voltages at 2 kHz and different actuating voltages of 0.2, 0.7, 1.2, and 2.2 V_{p-p}. Control was 1-h static hybridization, that is, without applying electric signal. (Lei *et al*. 2015 [14]. Reproduced with permission of American Chemical Society.)

immobilized on the electrode surface. Results revealed that 5-min dynamic hybridization significantly increased the signal intensity ratio to over 1-h static hybridization, shown in Figure 1.6b. This study provided a strategy to accelerate DNA hybridization for practical rapid genetic diagnostic device.

Alternatively, digital microfluidics has been applied to the polymerase chain reaction (PCR) for potential point-of-care applications [49]. PCR in the droplets showed amplification efficiencies with no evaporation loss. The optimal hold time was found to be 9 and 30 s for denaturation and annealing/extension in thermal cycling, respectively. Droplet-based PCR can be monitored in real time and provides amplification with a cycle threshold of ~10 cycles earlier than benchtop instruments. Moreover, a digital microfluidic platform was developed for multiplexed real-time PCR [50], as shown in Figure 1.7. This system was demonstrated on the detection of DNA levels of methicillin-resistant *Staphylococcus aureus*, *Mycoplasma pneumoniae*, and *Candida albicans*. Recently, detection of Deoxyribonuclease I (DNase I) has been demonstrated by paper-based substrate using gold nanoparticle colorimetric probes [24]. In this

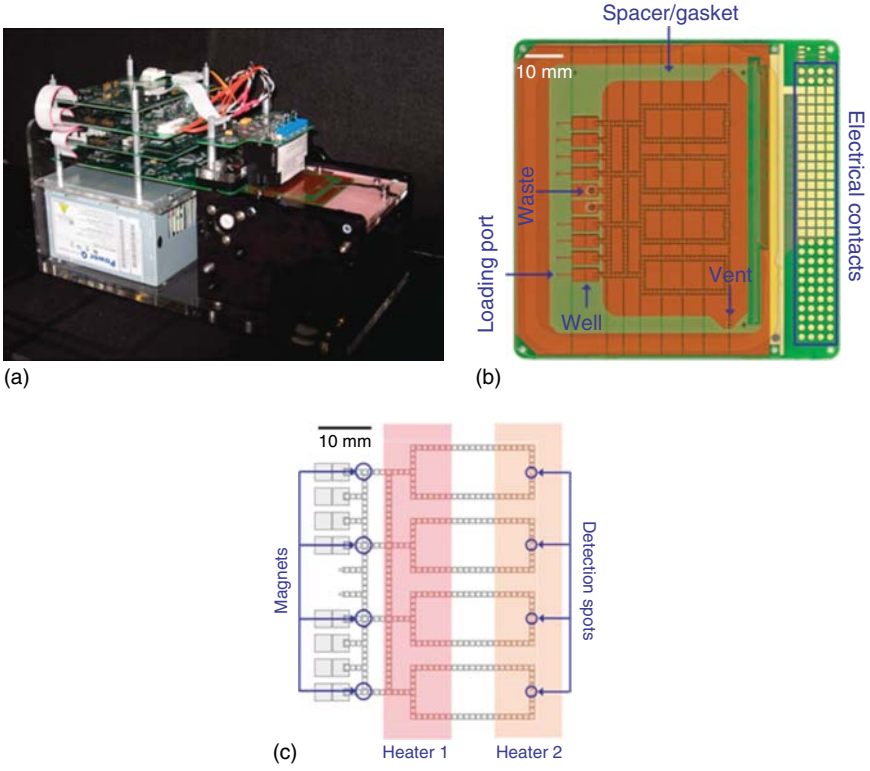


Figure 1.7 Self-contained digital microfluidic PCR system. (a) The instrument including power supply, control electronics, fluorometer module, heaters, and cartridge deck (shown with cartridge loaded). (b) Photograph of an assembled microfluidic cartridge comprising a printed circuit board chip, polymer spacer/gasket, and glass-top plate with drilled holes. (c) Schematic of the PCR chip showing electrode positions relative to heaters, magnets, and detectors. (Hua *et al*. 2010 [50]. Reproduced with permission of American Chemical Society.)

www.ebook3000.com

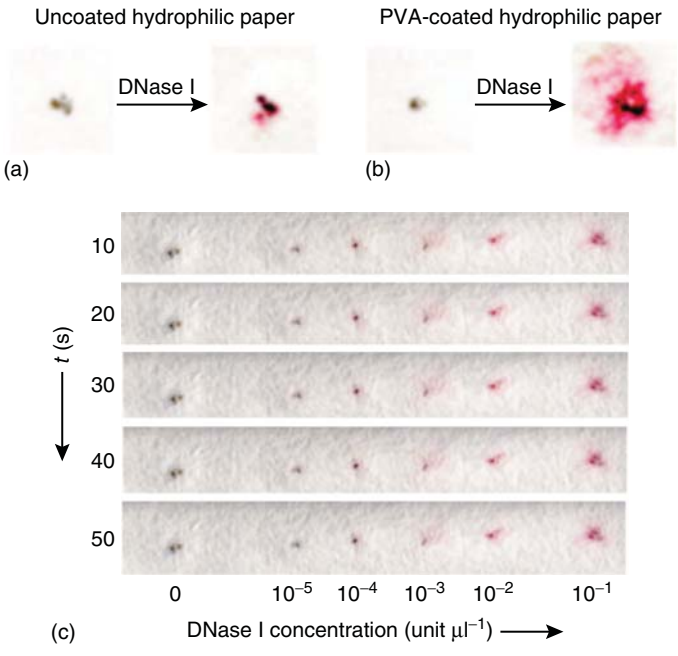


Figure 1.8 DNase I assay on (a) uncoated hydrophilic paper and (b) PVA-coated hydrophilic paper. One microliter of DNase I solution was applied in (a) and (b). Images were obtained at 20 s after adding DNase I solution. (c) DNase I assay on PVA-coated hydrophilic paper as functions of assay time and DNase I concentration. (Zhao *et al*. 2008 [24]. Reproduced with permission of American Chemical Society.)

work, colored and DNA-cross-linked gold nanoparticles aggregates were spotted on paper substrates. The addition of target DNase I solution dissociated the gold aggregates into dispersed gold nanoparticles, which generated an intense red color on paper within 1 min. Both hydrophobic and poly(vinyl alcohol) (PVA)-coated hydrophilic paper substrates were suitable for this biosensing platform and their results are shown in Figure 1.8. It was expected that it can provide a simple and practical bioassay platform for disease diagnostics, pathogen detection, and quality monitoring of food and water.

1.4.2 Applications of Immunoassays

Microfluidic immunoassays have also been intensively demonstrated on various disease detections [51–54]. Immunoassay is a bioanalytical technique for measuring the presence and concentration of antigen in biological liquid. It is widely used in clinical, pharmaceutical, and scientific research laboratories for diagnostics. Operation of immunoassay involves repeated steps of incubation and washing. Making conventional immunoassay using multi-well microplate is time-consuming and labor intensive. By introducing microfluidic technology, immunoassay can be automatically performed by sequentially pumping samples and reagents to the reaction chamber based on various microfluidic manipulation mechanisms in the microfluidic device. For example, pneumatic

micropumps were integrated in a microfluidic device to manipulate reagents for the detection of hepatitis C virus (HCV) and syphilis from serum samples [55]. Fluid manipulation was based on peristaltic effect driven by time-phased deflection of PDMS membranes along the fluidic channel. The detection process was automatic, and it began with bonding screening antigens, that is, HCV and syphilis, to the detection chambers. Then, sample, washing buffer, horseradish peroxidase (HRP)-labeled secondary antibody, developing buffer, and stopping buffer in individual reservoirs were sequentially pumped to the detection chambers by the "spider web" pneumatic micropumps. Immunoassay results were detected by the measurement of absorbance. This work showed a highly integrated microfluidic device and the immunoassay could be performed automatically. Alternatively, centrifugal force was utilized to demonstrate sequential manipulation of reagents in a compact disk (CD)-based microfluidic device [56, 57]. The CD-based microfluidic device for ELISA is shown in Figure 1.9. Because of the mature developments of precision rotation control and optical reading in CD technology, CD-based microfluidics was expected to have great commercial potential. Immunoassay was showed to be performed by controlling the rotational speed of the disk. Different solutions involved in the immunoassay process were sequentially and automatically manipulated by centrifugal force, demonstrating the analysis of rat IgG from a hybridoma cell culture. By using the CD-based microfluidics, less reagent consumption and shorter assay time were realized over the conventional method. Alternatively, ELISA has been demonstrated using paper substrate [30, 31]. Subtyping of influenza A (H1N1) and (H3N2) viruses was reported, and the detection limits of 2.7×10^3 and 2.7×10^4 pfu/assay for H1 and H3 detection could be achieved, respectively [31]. The use of paper for the development of diagnostic devices has the advantages of being lightweight, ease-to-use, and low cost, and paper-based immunoassay is appropriate to be applied for rapid screening in point-of-care applications.

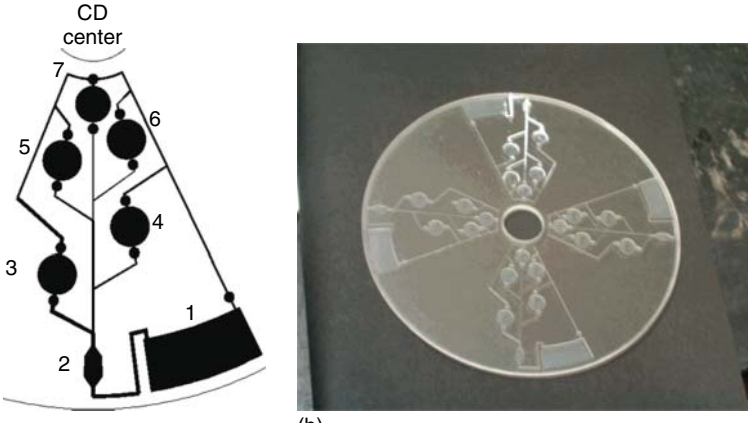


Figure 1.9 CD-based microfluidic device for the application of ELISA. (a) Schematic of five-step sequencing CD. (b) A computer numerical control-machined CD. (Lai *et al*. 2004 [56]. Reproduced with permission of American Chemical Society.)

www.ebook3000.com

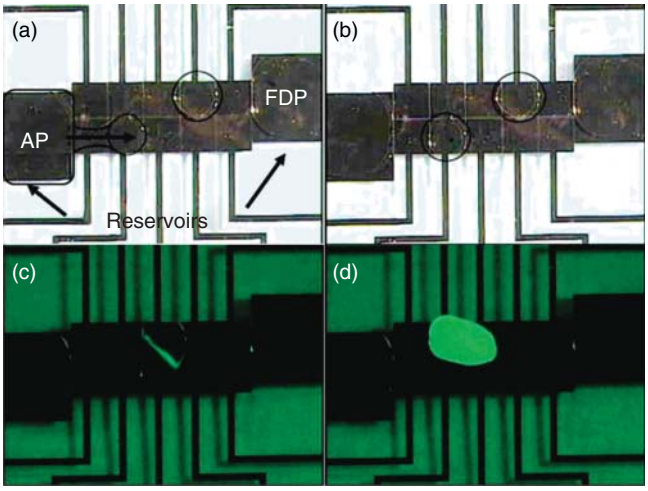


Figure 1.10 Fluorescent enzymatic assay on a digital microfluidic device. (a) A droplet containing fluorescein diphosphate (FDP) was dispensed from the reservoir on the right, while (b) a droplet of alkaline phosphatase (AP) was dispensed from the reservoir on the left. (c) When the droplets were merged under fluorescent illumination, the product was observed at the interface of the droplets. (d) After active mixing, the reaction proceeded to completion. (Miller and Wheeler 2008 [58]. Reproduced with permission of American Chemical Society.)

Furthermore, a microfluidic device based on electrowetting manipulation has been developed to perform multiplexed enzyme analysis [58]. Samples and reagents in the form of discrete droplets were manipulated on the device, as shown in Figure 1.10. Droplets of alkaline phosphatase and fluorescein diphosphate were merged and mixed on the device, and then the fluorescent product was detected by fluorescence plate reader. The detection limit achieved was $\sim 7.0 \times 10^{-20}$ M. Also, heterogeneous immunoassays have been demonstrated by efficient handling of magnetic microbeads using electrowetting manipulation [59]. A sample droplet and a reagent droplet containing magnetic beads conjugated to primary antibodies, blocking proteins, and secondary antibodies were dispensed on the system. These two droplets were then merged, mixed, and incubated by electrowetting manipulation. A permanent magnet was applied to immobilize the sandwiched microbead complexes, followed by the washing of the unbound components. Finally, a reagent droplet was applied for the chemiluminescent detection. Sandwich heterogeneous immunoassays on human insulin and interleukin-6 (IL-6) were demonstrated with a total time of 7 min to result for each assay.

1.4.3 Applications of Cell-Based Assays

Cell culture is a fundamental biological technique for various investigations such as study of physiology and chemistry of cells [60, 61] and cellular response under the exploration of tested substances [62, 63]. In conventional cell culture practice, cells are cultured in culture vessels, that is, Petri dish or multi-well microplate. During the culture course, culture medium is supplied manually and replaced

regularly. Although this operation is standardized and widely used today, it limits the throughput and possibility of automation. Because of the development of microfluidic technology, microfluidic cell culture devices have been developed and constructed a miniaturized cell culture environment [64–66]. An example of a microfluidic cell culture device composed of a 10×10 culture chamber array to demonstrate a high-throughput cell-based screening was shown [66]. Photographs of the microfluidic device are shown in Figure 1.11a. Mammalian HeLa cells were cultured in the well and grown nearly to confluency after 7.5 days, as shown in Figure 1.11b. A miniaturized perfusion cell culture environment was demonstrated, showing a promising evidence of microfluidic cell culture model. By using microfluidic technology for cell culture, there are several advantages such as providing a closed environment without the need of an incubator, monitoring cellular responses in a real-time manner, minimizing reagent consumption, and reducing the number of seeding cells.

The above discussions are based on a two-dimensional (2D) culture model where cells spread on a flat surface on a monolayer format. However, recent

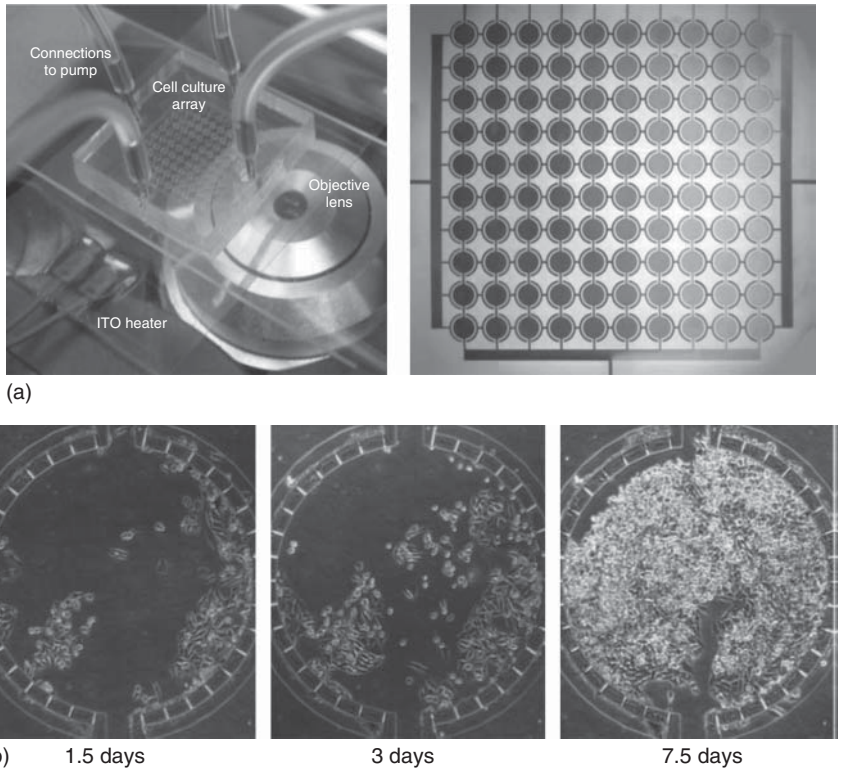


Figure 1.11 Microfluidic cell culture system. (a) A 10×10 culture chamber array on a microfluidic chip mounted on an optical microscope. (b) Cell growth inside a microfluidic cell culture chamber. Mammalian HeLa cells were cultured in the well and grown nearly to confluency at day 7.5. (Reprinted with permission from Ref. [66]. Copyright (2004) Royal Society of Chemistry.)

www.ebook3000.com

studies reported 2D culture models cannot well mimic the native cellular microenvironment because animal cells inhabit three-dimensional (3D) environment [67, 68]. Hence, 3D cell culture model in which cells are encapsulated and cultured in a 3D polymeric scaffold material was proposed [67, 68]. It is regarded as realizing a better approximation of *in vivo* conditions than 2D surfaces and providing a more physiologically meaningful culture condition for cell-based assays. Recently, impedimetric measurement of 3D cell culture was demonstrated by gelling a spot of cells–hydrogel mixture (1 μl) on planar electrodes [69]. On the other hand, a perfusion 3D cell culture microfluidic chip was developed to construct a precise, stable, and well-defined culture environment for 3D cell-based assays [70]. The microfluidic chip consisted of six 3D culture chambers, as shown in Figure 1.12a. A pair of vertical parallel electrodes located at the opposite sidewalls of the culture chamber was embedded for the on-site

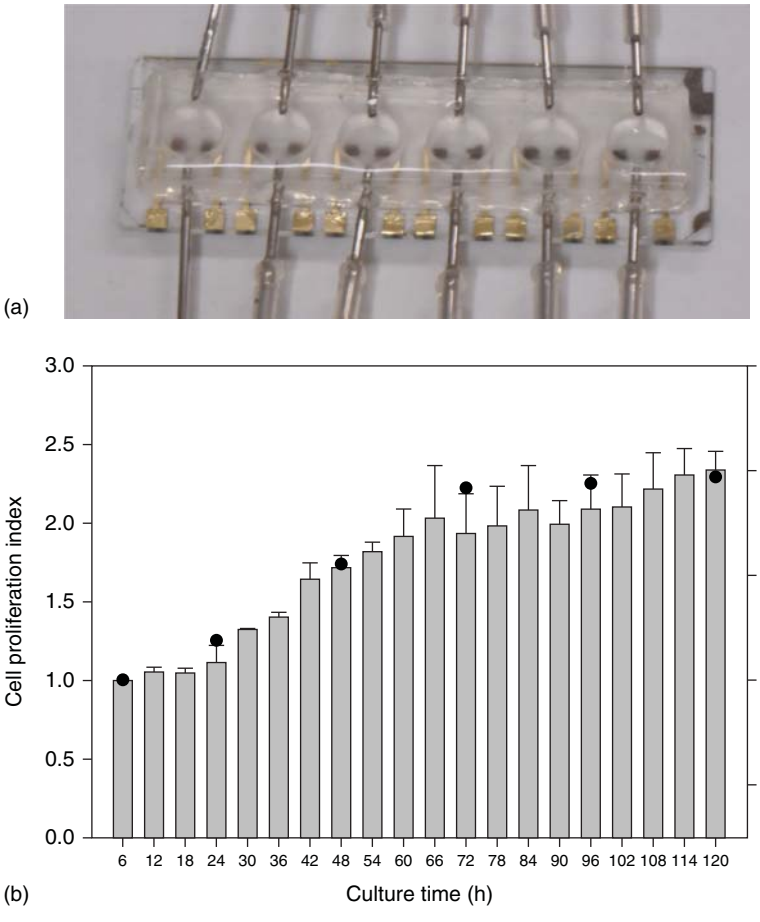


Figure 1.12 Real-time impedimetric monitoring of cell proliferation in a perfusion 3D cell culture microfluidic chip. (a) Photograph of the microfluidic chip. (b) Quantification of cell proliferation in 3D culture environment under medium perfusion for up to 5 days. (Lei *et al*. 2014 [70]. Reproduced with permission of Elsevier.)

impedance measurement. Cells encapsulated in the hydrogel were loaded into the chamber and could receive uniform electric field during the measurement. Real-time and noninvasive impedimetric monitoring of cell proliferation were demonstrated and is shown in Figure 1.12b. Quantification of cell proliferation could be realized in 3D culture environment. This microfluidic device has a high potential to develop an automatic and high-throughput platform for drug screening applications.

1.5 Perspective

The current development of microfluidic systems has been discussed and these systems have been demonstrated on various biomedical and chemical applications. These excellent works showed the mature development of microfluidic technology in research laboratories. Moreover, some of the research projects have been turned into commercial products. For example, a portable and user-friendly blood diagnostic equipment called Abbott i-STAT analyzer has been launched for clinical diagnostics. Only a few drops of blood are required for the blood analysis, and results are automatically uploaded to the patient's chart within minutes. Moreover, a commercial platform, that is, Advanced Liquid Logic, based on the technology of digital microfluidics was developed for gene and protein analysis. It is designed for life science research and provides cost-effective automation solutions for complex bioassay workflows. For microfluidic cell-based assays, benchtop equipment for real-time quantitative monitoring of cellular response has been commercialized for high-throughput drug screening applications. The equipment is named xCELLigence system, and its major advantage is to provide quantitative indexes to describe cellular responses during the culture course. However, these excellent products have not made great impact on the market. Most of the assays in clinical and research laboratories still rely on conventional equipment. It may be because these newly developed microfluidic products need to take time to compete with the existing equipment that have been perfected over the decades. But it is expected that more commercial microfluidic products will be launched in the near future.

References

1 Xia, Y., Kim, E., Zhao, X.M. *et al.* (1996) Complex optical surfaces formed by replica molding against elastomeric masters. *Science*, **273**, 347–349.
2 Xia, Y. and Whitesides, G.M. (1998) Soft lithography. *Annu. Rev. Mater. Sci.*, **28**, 153–184.
3 Unger, M.A., Chou, H.P., Thorsen, T. *et al.* (2000) Monolithic microfabricated valves and pumps by multilayer soft lithography. *Science*, **288**, 113–116.
4 Wu, H., Odom, T.W., Chiu, D.T. *et al.* (2003) Fabrication of complex three-dimensional microchannel systems in PDMS. *J. Am. Chem. Soc.*, **125**, 554–559.

www.ebook3000.com

5 Klank, H., Kutter, J.P., and Geschke, O. (2002) CO_2-laser micromachining and back-end processing for rapid production of PMMA-based microfluidic systems. *Lab Chip*, **4**, 242–246.

6 Chen, C.S., Breslauer, D.N., Luna, J.I. *et al.* (2008) Shrinky-dink microfluidics: 3D polystyrene chips. *Lab Chip*, **8**, 622–624.

7 Wabuyele, M.B., Ford, S.M., Stryjewski, W. *et al.* (2001) Single molecule detection of double-stranded DNA in poly(methylmethacrylate) and polycarbonate microfluidic devices. *Electrophoresis*, **22**, 3939–3948.

8 Erickson, D., Liu, X., Krull, U. *et al.* (2004) Electrokinetically controlled DNA hybridization microfluidic chip enabling rapid target analysis. *Anal. Chem.*, **76**, 7269–7277.

9 Zhang, Y. and Jiang, H.R. (2016) A review on continuous-flow microfluidic PCR in droplets: advances, challenges and future. *Anal. Chim. Acta*, **914**, 7–16.

10 Zhang, Y. and Ozdemir, P. (2009) Microfluidic DNA amplification – a review. *Anal. Chim. Acta*, **638**, 115–125.

11 Park, S., Zhang, Y., Lin, S. *et al.* (2011) Advances in microfluidic PCR for point-of-care infectious disease diagnostics. *Biotechnol. Adv.*, **29**, 830–839.

12 Burns, M.A., Johnson, B.N., Brahmasandra, S.N. *et al.* (1998) An integrated nanoliter DNA analysis device. *Science*, **282**, 484–487.

13 Marcus, J.S., Anderson, W.F., and Quake, S.R. (2006) Parallel picoliter RT-PCR assays using microfluidics. *Anal. Chem.*, **78**, 956–958.

14 Lei, K.F., Wang, Y.H., Chen, H.Y. *et al.* (2015) Electrokinetic acceleration of DNA hybridization in microsystems. *Talanta*, **138**, 149–154.

15 He, Y., Tsutsui, M., Fan, C. *et al.* (2011) Gate manipulation of DNA capture into nanopores. *ACS Nano*, **5**, 8391–8397.

16 Diercks, A.H., Ozinsky, A., Hansen, C.L. *et al.* (2009) A microfluidic device for multiplexed protein detection in nano-liter volumes. *Anal. Biochem.*, **386**, 30–35.

17 Herr, A.E., Hatch, A.V., Throckmorton, D.J. *et al.* (2007) Microfluidic immunoassays as rapid saliva-based clinical diagnostics. *Proc. Natl. Acad. Sci. U.S.A.*, **104**, 5268–5273.

18 Bhattacharyya, A. and Klapperich, C.M. (2007) Design and testing of a disposable microfluidic chemiluminescent immunoassay for disease biomarkers in human serum samples. *Biomed. Microdevices*, **9**, 245–251.

19 Yang, D., Niu, X., Lin, Y. *et al.* (2008) Electrospun nanofibrous membranes: a novel solid substrate for microfluidic immunoassays for HIV. *Adv Mater.*, **20**, 4770–4775.

20 van den Brink, F.T.G., Gool, E., Frimat, J.P. *et al.* (2011) Parallel single-cell analysis microfluidic platform. *Electrophoresis*, **32**, 3094–3100.

21 Lei, K.F., Wu, Z.M., and Huang, C.H. (2015) Impedimetric quantification of the formation process and the chemosensitivity of cancer cell colonies suspended in 3D environment. *Biosens. Bioelectron.*, **74**, 878–885.

22 Ballerini, D.R., Li, X., and Shen, W. (2012) Patterned paper and alternative materials as substrates for low-cost microfluidic diagnostics. *Microfluid. Nanofluid.*, **13**, 769–787.

23 Martinez, A.W., Phillips, S.T., and Whitesides, G.M. (2010) Diagnostics for the developing world: microfluidic paper-based analytical devices. *Anal. Chem.*, **82**, 3–10.

24 Zhao, W., All, M.M., Aguirre, S.D. *et al.* (2008) Paper-based bioassays using gold nanoparticle colorimetric probes. *Anal. Chem.*, **80**, 8431–8437.

25 Ellerbee, A.K., Phillips, S.T., Siegel, A.C. *et al.* (2009) Quantifying colorimetric assays in paper-based microfluidic devices by measuring the transmission of light through paper. *Anal. Chem.*, **81**, 8447–8452.

26 Dungchai, W., Chailapakul, O., and Henry, C.S. (2009) Electrochemical detection for paper-based microfluidics. *Anal. Chem.*, **81**, 5821–5826.

27 Zang, D., Ge, L., Yan, M. *et al.* (2012) Electrochemical immunoassay on a 3D microfluidic paper-based device. *Chem. Commun.*, **48**, 4683–4685.

28 Nie, Z., Nijhuis, C.A., Gong, J. *et al.* (2009) Electrochemical sensing in paper-based microfluidic devices. *Lab Chip*, **10**, 477–483.

29 Lei, K.F., Yang, S.I., Tsai, S.W. *et al.* (2015) Paper-based microfluidic sensing device for label-free immunoassay demonstrated by biotin-avidin binding interaction. *Talanta*, **134**, 264–270.

30 Cheng, C.M., Martinez, A.W., Gong, J. *et al.* (2010) Paper-based ELISA. *Angew. Chem. Int. Ed.*, **49**, 4771–4774.

31 Lei, K.F., Huang, C.H., Kuo, R.L. *et al.* (2015) Paper-based enzyme-free immunoassay for rapid detection and subtyping of influenza A H1N1 and H3N2 viruses. *Anal. Chim. Acta*, **883**, 37–44.

32 Derda, R., Laromaine, A., Mammoto, A. *et al.* (2009) Paper-supported 3D cell culture for tissue-based bioassays. *Proc. Natl. Acad. Sci. U.S.A.*, **106**, 18457–18462.

33 Deiss, F., Mazzeo, A., Hong, E. *et al.* (2013) Platform for high-throughput testing of the effect of soluble compounds on 3D cell cultures. *Anal. Chem.*, **85**, 8085–8094.

34 Simon, K.A., Park, K.M., Mosadegh, B. *et al.* (2014) Polymer-based mesh as supports for multi-layered 3D cell culture and assays. *Biomaterials*, **35**, 259–268.

35 Lei, K.F. and Huang, C.H. (2014) Paper-based microreactor integrating cell culture and subsequent immunoassay for the investigation of cellular phosphorylation. *ACS Appl. Mater. Interfaces*, **6**, 22423–22429.

36 Huang, C.H., Lei, K.F., and Tsang, N.M. (2016) Paper-based microreactor array for rapid screening of cell signaling cascades. *Lab Chip*, **16**, 2911–2920.

37 Amirouche, F., Zhou, Y., and Johnson, T. (2009) Current micropump technologies and their biomedical applications. *Microsyst. Technol.*, **15**, 647–666.

38 Zengerle, R., Ulrich, J., Kluge, S. *et al.* (1995) A bidirectional silicon micropump. *Sens. Actuators, A*, **20**, 81–86.

39 Jang, L.S. and Kan, W.H. (2007) Peristaltic piezoelectric micropump system for biomedical applications. *Biomed. Microdevices*, **9**, 619–626.

40 Jeong, G.S., Chung, S., Kim, C.B. *et al.* (2010) Applications of micromixing technology. *Analyst*, **135**, 460–473.

www.ebook3000.com

41 Yang, Z., Matsumoto, S., Goto, H. *et al.* (2001) Ultrasonic micromixer for microfluidic systems. *Sens. Actuators, A*, **93**, 266–272.
42 Lei, K.F. and Li, W.J. (2008) A novel in-plane microfluidic mixer using vortex pumps for fluidic discretization. *JALA*, **13**, 227–236.
43 Oh, K.W. and Ahn, C.H. (2006) A review of microvalves. *J. Micromech. Microeng.*, **16**, R13–R39.
44 Zeng, S., Li, B., Su, X. *et al.* (2009) Microvalve-actuated precise control of individual droplets in microfluidic devices. *Lab Chip*, **9**, 1340–1343.
45 Grover, W.H., Ivester, R.H.C., Jensen, E.C. *et al.* (2006) Development and multiplexed control of latching pneumatic valves using microfluidic logical structures. *Lab Chip*, **6**, 623–631.
46 Pollack, M.G. and Fair, R.B. (2000) Electrowetting-based actuation of liquid droplets for microfluidic applications. *Appl. Phys. Lett.*, **77**, 1725–1726.
47 Lee, J., Moon, H., Fowler, J. *et al.* (2002) Electrowetting and electrowetting-on-dielectric for microscale liquid handling. *Sens. Actuators, A*, **95**, 259–268.
48 Urbanski, J.P., Thies, W., Rhodes, C. *et al.* (2006) Digital microfluidics using soft lithography. *Lab Chip*, **6**, 96–104.
49 Wang, F. and Burns, M.A. (2009) Performance of nanoliter-sized droplet-based microfluidic PCR. *Biomed. Microdevices*, **11**, 1071–1080.
50 Hua, Z., Rouse, J.L., Eckhardt, A.E. *et al.* (2010) Multiplexed real-time polymerase chain reaction on a digital microfluidic platform. *Anal. Chem.*, **82**, 2310–2316.
51 Lei, K.F. (2012) Microfluidic systems for diagnostic applications: a review. *JALA*, **17**, 330–347.
52 Han, K.N., Li, C.A., and Seong, G.H. (2013) Microfluidic chips for immunoassays. *Annu. Rev. Anal. Chem.*, **6**, 119–141.
53 Lafleur, L., Stevens, D., McKenzie, K. *et al.* (2012) Progress toward multiplexed sample-to-result detection in low resource setting using microfluidic immunoassay cards. *Lab Chip*, **12**, 1119–1127.
54 Zheng, C., Wang, J., Pang, Y. *et al.* (2012) High-throughput immunoassay through in-channel microfluidic patterning. *Lab Chip*, **12**, 2487–2490.
55 Wang, C.H. and Lee, G.B. (2005) Automatic bio-sampling chips integrated with micro-pumps and micro-valves for disease detection. *Biosens. Bioelectron.*, **21**, 419–425.
56 Lai, S., Wang, S., Luo, J. *et al.* (2004) Design of a compact disk-like microfluidic platform for enzyme-linked immunosorbent assay. *Anal. Chem.*, **76**, 1832–1837.
57 Madou, M., Zoval, J., Jia, G. *et al.* (2006) Lab on a CD. *Annu. Rev. Biomed. Eng.*, **8**, 601–628.
58 Miller, E.M. and Wheeler, A.R. (2008) A digital microfluidic approach to homogeneous enzyme assays. *Anal. Chem.*, **80**, 1614–1619.
59 Sista, R.S., Eckhardt, A.E., Srinivasan, V. *et al.* (2008) Heterogeneous immunoassays using magnetic beads on a digital microfluidic platform. *Lab Chip*, **8**, 2188–2196.

60 Metallo, C.M. and Heiden, M.G.V. (2013) Understanding metabolic regulation and its influence on cell physiology. *Mol. Cell*, **49**, 388–398.
61 Samavedi, S., Whittington, A.R., and Goldstein, A.S. (2013) Calcium phosphate ceramics in bone tissue engineering: a review of properties and their influence on cell behavior. *Acta Biomater.*, **9**, 8037–8045.
62 Azmi, A.S., Bao, B., and Sarkar, F.H. (2013) Exosomes in cancer development, metastasis, and drug resistance: a comprehensive review. *Cancer Metast. Rev.*, **32**, 623–642.
63 Ko, H.C. and Gelb, B.D. (2014) Concise review: drug discovery in the age of the induced pluripotent stem cell. *Stem Cell Transl. Med.*, **3**, 500–509.
64 Lei, K.F. (2014) Review on impedance detection of cellular responses in micro/nano environment. *Micromachines*, **5**, 1–12.
65 Lecault, V., White, A.K., Singhal, A. *et al* (2012) Microfluidic single cell analysis: from promise to practice. *Curr. Opin. Chem. Biol.*, **16**, 381–390.
66 Hung, P.J., Lee, P.J., Sabounchi, P. *et al.* (2005) A novel high aspect ratio microfluidic design to provide a stable and uniform microenvironment for cell growth in a high throughput mammalian cell culture array. *Lab Chip*, **5**, 44–48.
67 Cukierman, E., Pankov, R., Stevens, D.R. *et al.* (2001) Taking cell-matrix adhesions to the third dimension. *Science*, **294**, 1708–1712.
68 Abbot, A. (2003) Cell culture: biology's new dimension. *Nature*, **424**, 870–872.
69 Jeong, S.H., Lee, D.W., Kim, S. *et al.* (2012) A study of electrochemical biosensor for analysis of three-dimensional (3D) cell culture. *Biosens. Bioelectron.*, **35**, 128–133.
70 Lei, K.F., Wu, M.H., Hsu, C.W. *et al.* (2014) Real-time and non-invasive impedimetric monitoring of cell proliferation and chemosensitivity in a perfusion 3D cell culture microfluidic chip. *Biosens. Bioelectron.*, **51**, 16–21.

www.ebook3000.com

2

Fundamental Concepts and Physics in Microfluidics

Yujun Song, Xiaoxiong Zhao, Qingkun Tian, and Hongxia Liang

University of Science and Technology Beijing, Centre for Modern Physics Technology, Applied Physics Department, Beijing Key Laboratory for Magneto-Photoelectric Composite and Interface Science, 30 Xueyuan Road, Haidian District, Beijing 100083, PR China

2.1 Introduction

Manipulating small amounts of fluids (gases and/or liquids) to perform reactions, analysis, or fundamental investigations in materials, energy, environment, medicine, biology, physics, and chemistry is of great interest in both scientific research and industrial applications [1–10]. Microfluidics is the science and technology that process or manipulate small amounts of fluids from 10^{-6} to 10^{-12} l (or even 10^{-15} l) in the structures or channels that have at least one dimension in micrometer scale or less, or from 1 μm to 1 mm [5, 6, 11–13]. This field is primarily driven by technological applications whose aims are to develop entire laboratories inside chips. There are two main kinds of microfluidic systems, termed as lab-on-a-chip (LC) and micro total analysis systems (μ-TAS) [13–15]. Although the two terms are often used interchangeably, LC is usually used to describe devices that integrate several laboratory processes on a single chip, whereas μ-TAS are often considered to integrate all laboratory processes required for analysis on a single chip [13]. For both cases, fluid flows in one or more channel networks, fabricated into or from a solid substrate, are the essential element of the analytical or preparative function of the devices. Microfluidics have quickly become important tools in several fields including new synthesis technologies as well as basic researches for sensing, which now are not limited to the two kinds of microfluidic device systems according to the current progress in this field [6–10, 14–18]. Many micro-tubing and spray-drying nebulator-based microfluidic systems particularly for controlled materials and chemical synthesis have been intensively developed and become one new majority type [7–9, 16–18].

One reason for their fast development is based on the predictability of the flows at such scale and the exquisite control of interfaces in microchannels. Nowadays microfluidics have been used in many scientific and industrial fields. More often they are treated as tools for the development of various topics related to chemistry, materials, biology, or physics.

Microfluidics: Fundamentals, Devices and Applications, First Edition.
Edited by Yujun Song, Daojian Cheng, and Liang Zhao.
© 2018 Wiley-VCH Verlag GmbH & Co. KGaA. Published 2018 by Wiley-VCH Verlag GmbH & Co. KGaA.

In this chapter we focus on the physical foundations on which this discipline relies on. The space feature scale in microfluidics is micrometer, between macroscale and nanoscale, which endows a duality in fluid flow behavior. However, microscale is far longer than the mean free path (λ) of molecule motion. Therefore, the fluid in the microscale space obeys the law of continuous medium, which can be treated by the continuity equation [13, 14]. Generally, most of the basic fluid mechanisms with the governing equation for a bulk fluid in motion can also be used in microfluidics, such as Pascal's law, Laplace's law, Bernoulli's and Poiseuille's laws, and Navier–Stokes–Fourier fluid dynamic models, which will be elucidated briefly in this chapter. However, as the scale is reduced, the viscous force effect becomes dominant in microfluidics, different from that in macroscale wherein the inertial force effect dominates the flow behavior, leading to small Reynolds number and laminar flow becomes dominant. Therefore, the dominant mass transport type changes from convection to diffusion. Surface and edge effects from viscous force and surface tension on the thermal transmission become dominated due to enhanced surface-to-volume ratios [13]. In addition, electrodialysis and electrophoretic mobility are independent in scale, leading to unique flow features in microfluidics related to electric fields [15, 19, 20]. The unique diffusion transport and capillary effects as well as the related viscosity, surface tension, and surface and interface effects, which are dominant in microfluidic systems and also affected by external field (e.g., electric, optical, magnetic, gravity, thermal fields), will be discussed in this chapter [13–15, 19, 21].

Mixing fluids (liquids and/or gases) is critical to develop microfluidic processes, including the driving power and the control system. Currently, the fluid driving forces for microfluidic processes can be categorized mainly into five kinds of methods: (i) mechanical methods by mechanical pumps (e.g., syringe pump, self-priming pumps, piezoelectric actuator), (ii) gravity field driving methods, (iii) electrokinetic methods by electric fields, (iv) magnetic field driving methods, and (v) electromagnetic field actuation methods (e.g., optical fields or opto-thermocapillary effects) [3, 5, 13–15, 19, 21, 22].

Due to the high aspect ratio (surface/volume) and size effects in microstructures and fluids ranging from microliters to picoliters or even femtoliters, there are some unique mesoscopic features in microfluidic scopes besides those fluids that follow the principles based on the continuity medium as the device size or the system scale is more than the typical phase coherence scale [13–15, 23]. Below the typical phase coherence scale (the critical size), the quantum dynamical principles will dominate the system thermodynamic status [24, 25]. Between the critical size (e.g., the atomic or molecular scale) and the macroscale, which is usually called mesoscale range (e.g., the small dimension of microchannels to change the fluid friction and Reynolds number, the phonon mean free path for the thermal transport, the mean free path of molecule motion for mixing and chemical reaction) [14, 24–27], there are lots of new phenomena that cannot be explained only by the continuity equation or much difficult to be simulated by the quantum dynamical mechanism. Quantum theory can be only used to quantitatively predict some thermodynamic parameters (e.g., specific heat capacity) of simple systems. New theory and calculation methods have to be developed for mesoscale

www.ebook3000.com

physical systems, which are particularly critical for mass and thermal transport in the multiphase mixing and reaction [23, 28]. In the following, we will first demonstrate the basic fluid mechanism from the law of continuous medium and some unique mesoscopic features in microchannels. Then, the development in electric field driving fluids and light actuating fluids will be further summarized. Finally, construction materials of microfluidic devices for special application fields will be summarized for readers' benefit in the selectivity of suitable types of microfluidic devices.

2.2 Basic Concepts of Liquids and Gases

Fluids, whether liquids or gases, different from solids, will reshape as long as force is applied and determined by the surrounding interface and/or solid boundary. As shown in Figure 2.1 [13], fluid motion is controlled by the interaction and internal shear among fluid layers and/or interfaces with the solid surrounding. Gases can be expanded and compressed more easily than liquids due to the lower density and larger spacing between molecules. At the molecular scale (~nanometer), the interaction between layers involves collisions of many molecules [13, 14]. At the macroscale (>100 μm), the physical properties of a fluid resulted from the statistical average of such molecular interactions [25, 26]. The effects of individual molecular collisions can be ignored and the liquids can be dealt as the bulk, or continuum, properties. Of course, both of them can be mixed together to form gas bubbles embedded in liquids or liquid drop suspension in gas mixtures, which still preserves the continuum properties.

2.2.1 Mean Free Path (λ) in Fluids among Molecular Collisions

Gases in microchannels can be generally treated as the ideal gas, following Eq. (2.1) [13]:

$$PV = nRT \tag{2.1}$$

where P is the pressure, V the volume, n the amount (mol) of substance of gas molecules, and T the absolute temperature. In this equation R is the gas constant, given by $R = k_B N_A$, where k_B is Boltzmann's constant (1.38×10^{-23} J K^{-1}) and N_A

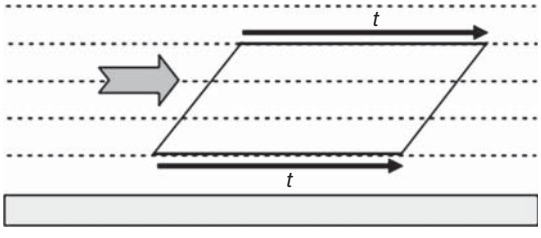


Figure 2.1 Fluids deform under the action of a shearing force (*t*). The fluid can be considered as laminas parallel to a surface. Each fluid lamina applies a shear force *t* to the next one and is in turn sheared by those it touches [13]. (Reproduced with permission from Ref. [13] Copyright 2013 John Wiley & Sons, Ltd, UK.)

is Avogadro's constant (6.022×10^{23} mol^{-1}). It means that equal volumes of gases at the same temperature and pressure contain the same number of molecules.

Although on average the molecules in gases are widely spaced apart, they are in constant motion and often collide with each other. The mean free path (λ) between molecular collisions in gas phases can be calculated by Eq. (2.2) if we treat each molecule as a hard sphere with the diameter of d [13, 24]:

$$\lambda_{\text{mfp}} = \frac{k_{\text{B}} T}{\sqrt{2}\pi P d^2} \tag{2.2}$$

Clearly, the mean free path (λ) between molecular collisions in gas phases increases with the temperature increase and decreases with the pressure increase. The average distance between collisions of molecules in gas phases at normal condition (room temperature and one atmospheric pressure) is hundreds of times (~500–600 times) more than their molecular radius (~0.1–0.3 nm) and some tens of times longer than their average molecular separation distance (several nanometers) [13, 24].

This means that gas molecules can travel over significant distances at the molecular scale before they collide with each other. Therefore, gases are usually compressive under pressure. The molecules in liquids are much closer together than those in gases, whose distances are about the addition of their radii of molecules, about 0.1 nm if there is no too much pressure. They are usually forming molecule clusters by cohesive forces such as those arising from intermolecular van der Waals interactions (including hydrogen bonds).

2.2.2 Viscosity (μ) of Fluids

Different from the solid status where molecules are usually vibrating in the fixed positions, molecules in liquids are free to move and only limited by the cohesive forces that give rise to viscous effects, which are affected mainly by temperature and slightly by pressure. Therefore, like solids, liquids are usually treated as non-compressive. Thus, viscosity (μ) is much important for liquid molecules, particularly in the mass and heat transport analysis of liquid–liquid and gas–liquid interphases.

Viscosity (μ) or the dynamic viscosity of a fluid is a measure of its resistance to the gradual deformation by the shear stress or the tensile stress that is often discussed in terms of *Couette* flow [29–31]. As shown in Figure 2.2, a fluid is contained between two parallel boundary plates: one stationary plate and one moving plate, moving at a constant horizontal speed u [32, 33]. Most of fluids have nonzero viscosity. A fluid that has no resistance to shear stress is known as an ideal or inviscid fluid. Zero viscosity is observed only at a very low temperature in superfluids, such as two isotopes of helium, helium-3 and helium-4, as they are liquefied by cooling to cryogenic temperatures [34, 35].

The magnitude of this force F is found to be proportional to the speed u and the area A of each plate and inversely proportional to their separation y:

$$F = \mu A \frac{u}{y} \tag{2.3}$$

www.ebook3000.com

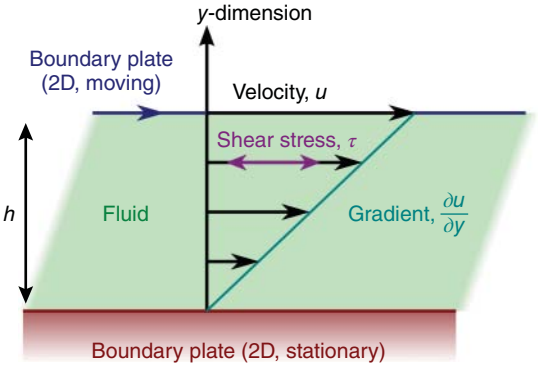


Figure 2.2 Laminar shear of fluid between two plates. Friction between the fluid and the moving boundaries causes the fluid to shear due to the shear stress (τ) caused by the velocity gradient ($^{\partial u}/_{\partial y}$) at the relative fluid velocity (u). The force required for this action is a measure of the fluid's viscosity.

The proportionality factor μ in this formula is the viscosity (specifically, the dynamic viscosity) of the fluid. In a macroscale Couette flow device, the fluid velocity immediately next to a surface will equal to the velocity of that surface. This is referred to as zero slip. If the fluid is a *Newtonian* fluid, such as water, the fluid velocity will change smoothly from zero at the stationary surface to the velocity of the moving surface, or the spatial gradient of the fluid velocity $\mathrm{d}u/\mathrm{d}y$ is a constant. In a general parallel flow (such as could occur in a straight pipe), the shear stress is proportional to the gradient of the velocity, such as in the rectangular cross section-shaped microfluidic channels.

The ratio u/y is called the rate of shear deformation or shear velocity and is the derivative of the fluid speed in the direction perpendicular to the plates. Isaac Newton expressed the viscous forces by the differential equation (2.4):

$$\tau = \mu \frac{\partial u}{\partial y} \tag{2.4}$$

where $\tau = F/A$ and $^{\partial u}/_{\partial y}$ is the local shear velocity. This formula assumes that the flow is moving along parallel lines and the y-axis, perpendicular to the flow, points in the direction of maximum shear velocity. This equation can be used where the velocity does not vary linearly with y, such as in fluid flowing through a round tube or pipe (Figure 2.3), which is much suitable for the flow type in round-shaped microfluidic channels; it can be expressed as Eq. (2.4) due to the gradient shear stress.

In industries or engineering, the kinematic viscosity is commonly used, termed as the ratio of the dynamic viscosity μ to the density of the fluid ρ ($\nu = \mu/\rho$). It is widely used in the petroleum industry, such as in the measurement of mobility of jet fuel, diesel oil, lubricating oil, crude oil, and other petroleum products and dark petroleum products. The kinematic viscosity is sometimes referred to as diffusivity of momentum (called "momentum diffusivity") because it is analogous to heat diffusivity and mass diffusivity. The SI unit of μ is Pa s (or $\mathrm{N\,s\,m^{-2}}$, $\mathrm{kg\,m^{-1}\,s^{-1}}$ and that of ν is $\mathrm{m^2\,s^{-1}}$. The reciprocal of viscosity ($1/\mu$) is termed as fluidity, which is convenient to estimate the viscosity of mixtures, as shown in Eq. (2.5):

$$\mu \approx \frac{1}{{}^{\chi_a}/_{\mu_a} + {}^{\chi_b}/_{\mu_b}} \tag{2.5}$$

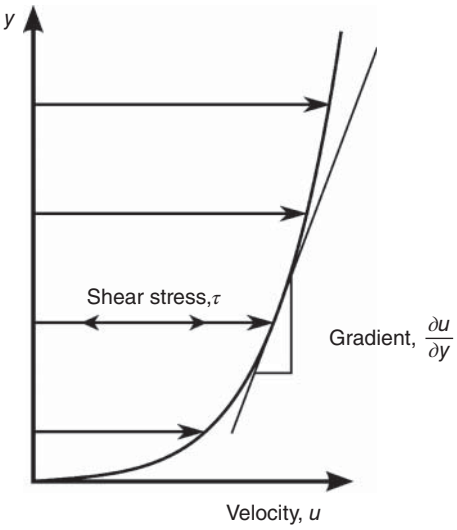


Figure 2.3 A general parallel flow (e.g., the flow type in a straight round-shaped tube). The shear stress (τ) is proportional to the gradient $^{\partial u}/_{\partial y}$ of the velocity (u).

where χ_a and χ_b are the mole fractions of components a and b, respectively, and μ_a and μ_b are the pure viscosities of components a and b, respectively.

It is a convenient concept when analyzing the Reynolds number (the key parameters to determine the flow types, laminar or turbulent) using ν, which expresses the ratio of the inertial forces to the viscous forces:

$$Re = \frac{\rho u L}{\mu} = \frac{uL}{\nu} \tag{2.6}$$

where L is a typical length scale in the fluid system.

Viscosity in gases arises principally from the molecular diffusion that transports momentum between layers of flow. The kinetic theory of gases allows accurate prediction of the behavior of gaseous viscosity. The relationship between the mean free path (λ) of gas molecules and that of diffusing particles can be derived according to the simple assumption that the velocity of molecules depends linearly on the distance they are coming from, as shown in Eq. (2.7):

$$\mu = \rho \bar{u} \lambda \quad \text{or} \quad \nu = \bar{u} \lambda \tag{2.7}$$

where ρ is the density of the fluid and ū is the average molecular velocity ($\bar{u} = \sqrt{\langle u^2 \rangle}$). Within the regime where the theory is applicable, viscosity is independent of pressure and increases as temperature increases due to the increased λ and ū assuming the constant whole volume of fluids.

More precisely, the theoretical prediction of gas viscosity can be obtained by Eq. (2.8) according to the hard-sphere molecules with fixed diameters [36, 37]:

$$\mu = \frac{1}{3} n m \bar{v} \lambda = \frac{2(MRT)^{\frac{1}{2}}}{3\pi^{\frac{3}{2}} N_A d^2} = C \times \frac{(MT)^{\frac{1}{2}}}{d^2} \tag{2.8}$$

where $n(\rho)$ is the number of molecules per cubic centimeter, m the mass of molecule, ū the mean molecular speed, M the molecular weight, R the gas constant, T the absolute temperature, d the collision diameter of molecules, and

www.ebook3000.com

N_A the Avogadro's constant. According to this equation, the viscosity of gases is proportional to the square root of temperature.

However, it is known that the effective collision diameters of real molecules depend on their relative velocities. Thus viscosity deviates significantly sometimes from the simple $T^{1/2}$ behavior.

These deviations of viscosity have been used in the more detailed study to investigate the nature of molecule forces. According to the previous theoretical model and this deviation, scientists have found a relatively simple expression of the viscosity of an ideal gas experimentally, or Sutherland's formula, as shown in Eq. (2.9):

$$\mu = \mu_0 \frac{T_0 + C}{T + C}\left(\frac{T}{T_0}\right)^{3/2} = \xi \frac{T^{3/2}}{T + C}, \qquad \xi = \frac{\mu_0 (T_0 + C)}{T_0^{3/2}}: \text{ a constant} \quad (2.9)$$

where μ_0 is the reference viscosity (in the same units as μ) at reference temperature T_0, T the input temperature (K), T_0 the reference temperature (K), and C the Sutherland's constant for the gas. Note that this equation is valid for temperatures between $0 < T < 555$ K with an error due to pressure less than 10% below 3.45 MPa. Table 2.1 shows the summary of parameters of some common gases in Sutherland's formula.

For further simplification, the viscosity of some conventionally used carrier gases can be approximately calculated by Eq. (2.10) [37]:

$$\mu/\mu_0 = (T/T_0)^x \text{ or } \mu = cT^x \quad (2.10)$$

where x depends on the gas types and temperatures, usually about 0.7. As for air, x can be $8/\rho$ at temperature between 90 and 300 K and ρ is the air density. As for the common carrier gases, such as N_2, H_2, and He, x is 0.699, 0.659, and 0.629, respectively, measured by gas chromatography and is 0.697, 0.659, and 0.649, respectively, by theoretical predication. Table 2.2 gives some gases at 273 and 300 K.

Table 2.3 lists the viscosities of some typical liquids. Clearly, the dynamic viscosity of liquids is typically several orders of magnitude higher than the dynamic viscosity of gases. Since the additional forces between molecules

Table 2.1 Sutherland's constant, reference values, and ξ values for some gases.

Gas	C (K)	T_0 (K)	μ_0 (μPa s)	ξ (μPa s K$^{-1/2}$)
Air	120	291.15	18.27	1.512041288
N_2	111	300.55	17.81	1.406732195
O_2	127	292.25	20.18	1.693411300
CO_2	240	293.15	14.8	1.572085931
CO	118	288.15	17.2	1.428193225
H_2	72	293.85	8.76	0.636236562
NH_3	370	293.15	9.82	1.297443379
SO_2	416	293.65	12.54	1.768466086

Table 2.2 Viscosities of selected gases of 273 and 300 K at 100 kPa (μPa s) [38].

Gas	At 0 °C (273 K)	At 27 °C (300 K)
Air	17.4	18.6
H_2	8.4	9.0
He	—	20.0
Ar	—	22.9
Xe	21.2	23.2
CO_2	—	15.0
CH_4	—	11.2
C_2H_6	—	9.5

Table 2.3 Viscosities of some typical liquids (at 25 °C unless specified).

Liquid	Viscosity (Pa s)
Acetone [38]	3.06×10^{-4}
Benzene [38]	6.04×10^{-4}
Castor oil [38]	0.985
Corn syrup [38]	1.3806
Ethanol [38]	1.074×10^{-3}
Ethylene glycol	1.61×10^{-2}
Glycerol (at 20 °C) [39]	1.2
HFO-380	2.022
Mercury [38]	1.526×10^{-3}
Methanol [38]	5.44×10^{-4}
Motor oil SAE 10 (20 °C) [40]	0.065
Motor oil SAE 40 (20 °C) [40]	0.319
Nitrobenzene [38]	1.863×10^{-3}
Liquid nitrogen at 77 K	1.58×10^{-4}
Propanol [38]	1.945×10^{-3}
Olive oil	0.081
Pitch	2.3×10^{8}
Sulfuric acid [38]	2.42×10^{-2}
Water	8.94×10^{-4}

become important, this leads to an additional contribution to the shear stress though the exact mechanics are still controversial. The viscosity of gas increases with the temperature, which is contrary for liquids. With increase of temperature, the molecular kinetic energy will increase, which will reduce these cohesive forces and hence the viscosity. An increase of molecular kinetic energy will also

www.ebook3000.com

facilitate an increased molecular interchange between the fluid layers and hence their viscosity. However, the increase of molecular kinetic energy produces a relatively smaller effect when compared with reduction of the cohesive forces. Thus, the net result is that liquids show a reduction in viscosity with temperature increase. Water has a higher viscosity than liquids such as benzene because of the cohesive hydrogen bonds (Eq. (2.11)):

$$\mu = 0.01779/[1 + 0.03368(T - 273.15) + 0.0002210(T - 273.15)^2] \quad (2.11)$$

With increasing pressure (very high pressure for liquids), the energy required for the relative movement of molecules in both gases and liquids is increased, and therefore the viscosity is increased.

The viscosity of a Newtonian fluid depends only on temperature and concentration (if diluted with another miscible fluid). For some fluids, particularly molten polymers or biological liquids such as blood, their viscosity depends also on the internal stress. These are classed as non-Newtonian fluids. Their viscosity decreases with an increase of the rate of the applied shear stress $\mathrm{d}\tau/\mathrm{d}t$ applied to a fluid flowing between two parallel surfaces, one moving at a constant velocity and the other one stationary, and is defined by

$$\mathrm{d}\tau/\mathrm{d}t = u/h \quad (2.12)$$

where u is the velocity of the moving surface and h is the distance between the two parallel surfaces.

Non-Newtonian fluids exhibit viscoelastic behavior (or shear thinning), and some of them require an initial shear stress before they start to move – such as blood. Viscoelastic fluids exhibit a relaxation time, typically ranging from milliseconds to seconds, given by the reciprocal of the critical shear rate. The critical shear rate corresponds to the shear threshold at which the viscosity starts to change or, for the case of molten polymers, where the polymer chains make the transition from a coiled to a stretched configuration. Figure 2.4 gives the relationship between the rate of shearing strain and the shearing stress of four typical fluids often encountered in the fluid flow research, including Newtonian fluid and non-Newton fluids (Bingham plastic fluid, shear thinning fluid, and shear thickening fluid).

Newton's law of viscosity is a constitutive equation (like Hooke's law, Fick's law, Ohm's law) that is not a fundamental law of nature but an approximation holding in some materials and failing in others. A fluid that behaves according to Newton's law, with a viscosity μ that is independent of stress, is said to be Newtonian. Gases, water, and many common liquids can be considered Newtonian in ordinary conditions. There are many non-Newtonian fluids that significantly deviate from that law in some way or the other, for example, (i) shear thickening liquids, whose viscosity increases with the rate of shear strain; (ii) shear thinning liquids, whose viscosity decreases with the rate of shear strain; (iii) thixotropic liquids, which become less viscous over time when shaken, agitated, or otherwise stressed; (iv) rheopectic liquids, which become more viscous over time when shaken, agitated, or otherwise stressed; and (v) Bingham plastics, which behave as a solid at low stresses but flow as a viscous fluid at high stresses. Shear thinning liquids are very commonly, but misleadingly, often described as thixotropic.

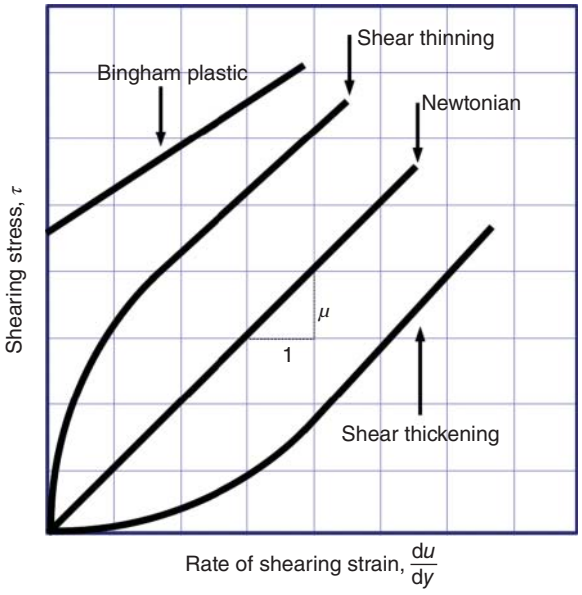


Figure 2.4 Relation between the shear strain rate and the shear stress of four types of fluids.

Even for a Newtonian fluid, viscosity usually depends on its composition and temperature. For gases and other compressible fluids, it depends on the temperature and varies very slowly with pressure. The viscosity of some fluids may depend on other parameters. A magnetorheological fluid, for example, becomes thicker when subjected to a magnetic field, possibly behaving like a solid.

Fluids mixed with particles (i.e., slurry) are also common cases in microfluidic processes, particularly in the synthesis of micro- or nanoparticles and polymers or the sensing systems using functional particles as probes. Therefore, it is important to analyze the viscosity of the slurry. The term slurry describes mixtures of liquid and solid particles that retain some fluidity. The viscosity of slurry can be described as relative to the viscosity of the liquid phase (Eq. (2.13)):

$$\mu_s = \mu_r \cdot \mu_l \tag{2.13}$$

where μ_s and μ_l are the dynamic viscosities of the slurry and liquid (Pa s), respectively, and μ_r is the relative viscosity (dimensionless).

Depending on the size and concentration of the solid particles, several models describe the relative viscosity as a function of volume fraction Φ of solid particles. Currently, there are four empirical correlations to calculate the relative viscosity (μ_r) of slurry, as shown in Figure 2.5. In the case of extremely low concentrations of fine particles, Einstein's equation seems reasonable, giving $\mu_r = 1 + 2.5\Phi$ [41]. In the case of higher concentrations, a modified equation matches the real slurry very well by taking into account the interaction among solid particles, giving $\mu_r = 1 + 2.5\Phi + 14.1\Phi^2$, proposed by Guth and Simha [42]. Further modification of this equation was proposed by Thomas from the fitting of the empirical data, giving $\mu_r = 1 + 2.5\Phi + 10.05\Phi^2 + Ae^{B\Phi}$, where $A = 0.00273$ and $B = 16.6$ [43].

www.ebook3000.com

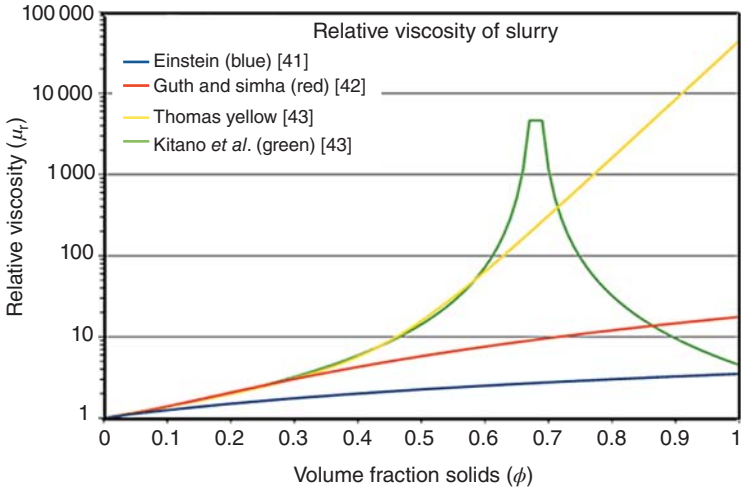


Figure 2.5 Solid fraction-dependent relative viscosity (μ_r) of slurry calculated from Einstein [41], Guth and Simha [42], Thomas [43], and Kitano *et al*. [44].

In the case of high shear stress (above 1 kPa), another empirical equation was proposed by Kitano *et al*. for polymer melts as $\mu_r = (1 - \phi/A)^{-2}$, where $A = 0.68$ for smooth spherical particles [44].

In order to obtain rapid mixing for uniform reaction, turbulent flow is usually favored in mixing. However, the vortices or eddies often occur in turbulence, leading to the eddy viscosity. In the study of turbulence in fluids, a common practical strategy for calculation is to ignore the small-scale vortices (or eddies) in the motion and to calculate a large-scale motion with an eddy viscosity that characterizes the transport and dissipation of energy in the small-scale flow. Values of eddy viscosity used in modeling ocean circulation may be from 5×10^4 to 10^6 Pa s depending upon the resolution of the numerical grid.

2.2.3 Mass Diffusivity (*D*)

The mixing in fluids depends not only on the viscosity of fluids but also on the mass diffusion coefficient or the mass diffusivity (D), which is the basic physical parameter of fluids used in Fick's laws and varieties of equations in fluid mechanism to describe the flow mixing and diffusion status of fluids [45]. Diffusivity represents the speed of the mass migration due to the thermal motion of molecules, atoms, or ions without bulk mass motion, which can occur by one or more objects motion among different phases. It is a proportionality constant between the molar flux due to molecular/atom/ion diffusion and the gradient in the concentration of the species in fluids (or the driving force for diffusion). The higher the diffusivities of substances, the faster they can diffuse into each other. The SI unit of diffusivity is $m^2\ s^{-1}$, the same as the kinematic viscosity.

D is very important in the analysis and calculation of the mass transfer, absorption, desorption, and catalysis process. The diffusivities of substances depend on

the temperature, the pressure, and the media morphologies. As for two kinds of gases, temperature-dependent diffusivity can be described as Eq. (2.14), advanced by Chapman–Enskog theory (with error of 8%) [45–47]:

$$D = \frac{1.858 \times 10^{-3} T^{3/2} \sqrt{1/M_A + 1/M_B}}{p\sigma_{A,B}^2 \Omega} \tag{2.14}$$

where D is the diffusion coefficient ($cm^2\ s^{-1}$) [46, 47], A and B index the two kinds of molecules present in the gaseous mixture, T is the absolute temperature (K), M is the molar mass ($g\ mol^{-1}$), p is the pressure (atm), $\sigma_{A,B} = (\sigma_1 + \sigma_2)/2$ is the average collision diameter (Å) [48], and Ω is a temperature-dependent collision integral (usually of order 1) (dimensionless) [48].

In the case of liquids, temperature-dependent diffusivity can be calculated by Stokes–Einstein equation (2.15) [45, 46]:

$$\frac{D_{T_1}}{D_{T_2}} = \frac{T_1 \mu_{T_2}}{T_2 \mu_{T_1}} \tag{2.15}$$

where D is the diffusion coefficient, T_1 and T_2 are the corresponding absolute temperatures, and μ_{T_1} and μ_{T_2} are the dynamic viscosities of the solvent at T_1 and T_2, respectively. Therefore, the diffusivity of fluids is proportional to temperature and inversely proportional to the viscosity that reduces with the temperature increase.

The effective diffusion coefficient describes diffusion through the pore space of porous media [49]. It is macroscopic in nature, because it is not the individual pores but the entire pore space that should be considered. The effective diffusion coefficient for transport through the pores, D_e, is estimated as follows [49]:

$$D_e = \frac{D\varepsilon_t \delta}{\tau} \tag{2.16}$$

where D_e is the diffusion coefficient in gas or liquid filling the pores, ε_t is the porosity available for transport (dimensionless), δ is the constrictivity, and τ is the tortuosity. Constrictivity is a dimensionless parameter used to describe transport processes (often molecular diffusion) in porous media, which depends on the ratio of the diameter of the diffusing particle to the pore diameter. The value of constrictivity is always less than 1. The constrictivity is not defined for a single pore, but as the parameter of the entire pore space considered, a macro parameter. Tortuosity is a property of curve being tortuous (twisted and having many turns), which can be estimated by the arc–chord ratio (the ratio of the length of the curve (L) to the direct distance between the ends of curves). This is commonly used to describe diffusion in porous media. Another method used for quantifying tortuosity in three-dimensional (3D) has been applied in 3D reconstructions of solid oxide fuel cell cathodes where the Euclidean distance sums of the centroids of a pore are divided by the length of the pore [50].

As for very diluted nonelectrolyte solutions (solute A in solvent B), their diffusivity can be estimated using the Wilke–Chang formula (Eq. (2.17)) [51–53]:

$$D_{AB} = 7.4 \times 10^{-15} \frac{(\phi M_B)^T T}{\mu V_A^{0.6}} \tag{2.17}$$

www.ebook3000.com

where D_{AB} is the diffusivity of A in B (i.e., infinite diluted diffusivity, $m^2\ s^{-1}$; T is the temperature of solution, K; μ is the viscosity of solvent, Pa s; M_B is the molar mass of solvent B, kg $kmol^{-1}$; ϕ is the associated parameter of solvent, which is 2.6, 1.9, 1.5, 1.0, and 1.0 for water, methanol, ethanol, benzene, and ether, respectively; V_A is the molecular volume of solute A under the boiling point, $cm^3\ mol^{-1}$.

V_A can be determined by the density of liquid under boiling point or can be estimated by the Tyn–Calus equation: $V_A = 0.285 V_c^{1.048}$ (V_c is the critical volume of liquid, $cm^3\ mol^{-1}$; see values of some gases and organics in Table 2.4). Clearly, we have to pay attention that D_{AB} is different from D_{BA} in solution according to Eq. (2.17), which is different from the diffusivity of gases.

The gas–gas diffusivity is in the range of $10^{-5}\ m^2\ s^{-1}$. The gas diffusivity in liquids is in the range of 10^{-9}–$10^{-10}\ m^2\ s^{-1}$. Table 2.5 gives the diffusivity of some common binary gas system at certain temperature and atmosphere. Table 2.6 gives the diffusivity of some typical gases in solvents and solutes in solvents.

As for the case of the biomass diffusivity in water, Eq. (2.17) can be used to estimate if their molar mass is less than 1000 g mol^{-1} or molecular volume is less than 500 $cm^3\ mol^{-1}$. Otherwise, Eq. (2.18) has to be used (the Polson method):

$$D_{AB} = \frac{9.40 \times 10^{-15} T}{\mu (M_A)^{1/3}} \tag{2.18}$$

where μ is the viscosity of solvent, Pa s; and M_A is the molar mass of biomass. Table 2.7 gives some diffusivity of some typical biomass.

The multicomponent fluid system can be described by the Maxwell–Stefan diffusion (or Stefan–Maxwell diffusion) model (Eq. (2.19)). The equation assumes

Table 2.4 V_C of some gases and solvents.

Matter	V_C ($cm^3\ mol^{-1}$)	Matter	V_C ($cm^3\ mol^{-1}$)	Matter	V_C ($cm^3\ mol^{-1}$)
Methane	99.2	Chloroform	238.9	Ammonia	72.5
Ethane	148.3	Methanol	118	Nitrogen	89.8
Propane	203	Ethanol	167.1	Nitrogen monoxide	57.7
n-Butane	255	*n*-Propanol	219	Nitrogen dioxide	167.8
n-Hexane	370	Isopropanol	220	Nitrous oxide	97.4
Ethylene	130.4	Acetone	209	Sulfur dioxide	122.2
Propylene	181	Methyl ethyl ketone	267	Sulfur trioxide	127.3
Vinyl chloride	169	Acetic acid	171	Hydrogen chloride	80.9
Acetylene	112.7	Ethyl acetate	286	Hydrogen	65.1
Benzene	259	Chlorine	123.8	Hydrogen sulfide	98.6
Toluene	316	Bromide	127.2	Carbon monoxide	93.2
Chlorobenzene	308	Iodine	155	Carbon dioxide	93.9
Cyclohexane	308	Oxygen	73.4	Carbon disulfide	160
Carbon tetrachloride	275.9	Ozone	88.9	Water	57.1

Table 2.5 Diffusivity of some binary gas system at 1 atm, 1.013×10^5 Pa.

Gas system	T (K)	D (10^{-5} m^2 s^{-1})	Gas system	T (K)	D (10^{-5} m^2 s^{-1})
H_2–air	273	6.11	Methanol–air	273	1.32
He–air	317	7.56	Ethanol–air	273	1.02
O_2–air	273	1.78	1-Butanol–air	273	0.703
Cl_2–air	273	1.24	Benzene–air	298	0.962
H_2O–air	273	2.20	Methanol–air	298	0.844
	298	2.56	H_2–CO	273	6.51
	332	3.05	H_2–CO_2	273	5.50
NH_3–air	273	1.98	H_2–N_2	273	6.89
CO_2–air	273	1.38		294	7.63
	298	1.64	H_2–NH_3	298	7.83
SO_2–air	293	1.22	He–Ar	298	7.29

Table 2.6 Diffusivity of solutes in some solvents with very low concentration.

Solute	Solvent	T (K)	D (10^{-9} m^2 s^{-1})	Solute	Solvent	T (K)	D (10^{-9} m^2/s)
NH_3	H_2O	285	1.64	Acetic acid	H_2O	298	1.26
		288	1.77	Propionate	H_2O	298	1.01
O_2	H_2O	291	1.98	HCl (9 kmol m^{-3})	H_2O	283	3.30
		298	2.41	(2.5 kmol m^{-3})		283	2.50
CO_2	H_2O	298	2.00	Benzoic acid	H_2O	298	1.21
H_2	H_2O	298	4.80	Acetone	H_2O	298	1.28
Methanol	H_2O	288	1.26	Acetic acid	Benzene	298	2.09
Ethanol	H_2O	283	0.84	Urea	Ethanol	285	0.54
		298	1.24	H_2O	Ethanol	298	1.13
1-Propanol	H_2O	288	0.87	KCl	H_2O	298	1.87
Formic acid	H_2O	298	1.52	KCl	1,2-Glycol	298	0.119
Acetic acid	H_2O	283	0.769				

steady state, or the absence of velocity gradients. The basic assumption of the theory is that a deviation from equilibrium between the molecular friction and thermodynamic interactions leads to diffusion flux [54]. The molecular friction between two components is proportional to their difference in speed and their mole fractions. In the simplest case, the gradient of chemical potential is the driving force of diffusion. For complex systems, such as electrolytic solutions, and other drivers, such as a pressure gradient, the equation must be expanded to

www.ebook3000.com

Table 2.7 Diffusivity of some biomass in water.

Solute	T (K)	D (10^{-9} m^2 s^{-1})	Mole mass (kg kmol^{-1})
Urea	293	1.20	60.1
	25	1.348×10^{-9}	—
Glycerin	20	0.825×10^{-9}	92.1
Glycine	25	1.055×10^{-9}	75.1
Octylic acid sodium	25	8.75×10^{-10}	166.2
Bovine serum albumin	25	6.81×10^{-11}	67 500
Urease	25	4.01×10^{-11}	482 700
	20	3.46×10^{-11}	
Soy protein	20	2.91×10^{-11}	361 800
Fat oxygenase	20	5.29×10^{-11}	97 400
Human blood fibrinogen	20	1.98×10^{-11}	339 700
Human serum albumin	20	5.93×10^{-11}	72 300
Gamma globulin (human)	20	4.00×10^{-11}	153 100
Creatinine	37	1.08×10^{-9}	113.1
Sucrose	37	0.697×10^{-9}	342.3
	20	0.460×10^{-9}	

include additional terms for interactions [55]:

$$\frac{\nabla \mu_i}{RT} = \nabla \ln \alpha_i = \sum_{\substack{j=1 \\ j \neq i}}^{n} \frac{\chi_i \chi_j}{D_{ij}} (\vec{v}_j - \vec{v}_i) = \sum_{\substack{j=1 \\ j \neq i}}^{n} \frac{c_i c_j}{c^2 D_{ij}} \left(\frac{\vec{J}_j}{c_j} - \frac{\vec{J}_i}{c_i} \right) \tag{2.19}$$

where ∇ is the vector differential operator, χ is the mole fraction, μ is the chemical potential, α is the activity, i and j are indexes for component i and j, n is the number of components, D_{ij} is the Maxwell–Stefan diffusivity, $\vec{v}_i$ is the diffusion velocity of component i, c_i is the molar concentration of component i, c is the total molar concentration, and $\vec{J}_i$ is the flux of component i.

The diffusivity of A in the gas mixture can be estimated by Eq. (2.20) for multicomponent gas system advanced by Wilke and coworker [56] according to the Maxwell–Stefan diffusion model:

$$D'_{\mathrm{A}} = \frac{1 - y_{\mathrm{A}}}{\dfrac{y_{\mathrm{B}}}{D_{\mathrm{AB}}} + \dfrac{y_{\mathrm{C}}}{D_{\mathrm{AC}}} + \dfrac{y_{\mathrm{D}}}{D_{\mathrm{AD}}} + \cdots} \tag{2.20}$$

where $y_{\mathrm{A}}, y_{\mathrm{B}}, y_{\mathrm{C}}, y_{\mathrm{D}}$, etc. are the mole fractions of components A, B, C, D, etc. and D_{AB}, D_{AC}, D_{AD}, etc. are the respective binary diffusivity of component A with respect to each component of the mixture, which can be estimated by binary diffusivity (Eqs. (2.14)–(2.18)).

As for multicomponent liquids, the diffusivity of i in the liquid mixture can be also estimated according to the Maxwell–Stefan diffusion model; see details in Ref. [57].

2.2.4 Heat (Thermal) Capacity

In microfluidic devices, the mass is also very important in heat transfer, which is mainly performed at a microscale, and the flow type is usually laminar. Mixing procedures are thus limited to diffusion and/or secondary flows. First, we have to learn some basic concepts of thermal transfer, such as the heat (thermal) capacity (e.g., constant volume heat capacity, C_V; constant pressure heat capacity, C_P) of materials and the corresponding intrinsic characteristics to control.

Heat capacity or thermal capacity is a measurable physical quantity equal to the ratio of the heat (Q) added to (or removed from) an object to the resulting temperature change (ΔT), which is an extensive property of matter or is proportional to the size of the system [58]. The SI unit of heat capacity is $\mathrm{J\,K^{-1}}$ or $\mathrm{kg\,m^2\,(K\,s^2)^{-1}}$. When expressing the same phenomenon as an intensive property, the heat capacity is divided by the amount of substance, mass or volume; thus the quantity is independent of the size or extent of the sample, termed as specific heat capacity, which is the amount of heat needed to raise the temperature of 1 kg of mass ($C_{P,m}$, $C_{V,m}$, $\mathrm{J\,(kg\,K)^{-1}}$) or $1\ \mathrm{m^3}$ of volume ($C_{P,V}$, $C_{V,V}$, $\mathrm{J\,(m^3\,K)^{-1}}$) by 1 K. In engineering, the volumetric heat capacity is often used, which is used almost exclusively for liquids and solids since for gases it may be confused with specific heat capacity at constant volume. In chemistry, the molar heat capacity (C_{mol}, $\mathrm{J\,(mol\,K)^{-1}}$), specified relative to 1 mol amount of substance, is often used.

Heat capacity can be experimentally calculated by the general equation (2.21) because heat capacity does depend upon temperature:

$$C(T) = \frac{\delta Q}{\mathrm{d}T} \tag{2.21}$$

where the symbol δ is used to imply that heat is a path function, meaning that its change depends on how the thermodynamic system changes from the initial state to the final state.

The relationship between heat capacity and the thermodynamic energy state function and the system parameters can be elucidated as follows [59].

The internal energy of a closed system changes either by adding heat to the system or by the system performing work, which can be written mathematically as in Eq. (2.22):

$$\Delta E = E_{in} - E_{out} \quad \text{or} \quad \mathrm{d}U = \delta Q - \delta W \tag{2.22}$$

As a result of an increase of the system volume, it can be written as $\mathrm{d}U = \delta Q - P\,\mathrm{d}V$.

If heat is added at constant volume (isobaric volume), the second term of this relation vanishes and one can readily obtain

$$C_V = \left(\frac{\partial U}{\partial T}\right)_V = \left(\frac{\partial Q}{\partial T}\right)_V \tag{2.23}$$

www.ebook3000.com

Equation (2.23) defines the heat capacity at constant volume, C_V. Clearly, it is related to changes in internal energy. Further, heat capacity at constant pressure (Isobaric), C_P, refers to the change in the enthalpy ($H = U + PV$; $dH = \delta Q + V\,dP$) of the system, which can be defined as

$$C_P = \left(\frac{\partial H}{\partial T}\right)_P = \left(\frac{\partial Q}{\partial T}\right)_P \tag{2.24}$$

Equations (2.23) and (2.24) are property relations and are therefore independent of the type of process. In other words, they are valid for any substance going through any process. Both the internal energy and enthalpy of a substance can change with the transfer of energy in many forms, that is, heat or work [59].

The relation of the two heat capacities can be obtained by the fundamental thermodynamic relation, as shown in Eq. (2.25):

$$C_P - C_V = T\left(\frac{\partial P}{\partial T}\right)_{V,n}\left(\frac{\partial V}{\partial T}\right)_{P,n} \tag{2.25}$$

where the partial derivatives are taken at constant volume and constant number of particles, and constant pressure and constant number of particles, respectively. This equation can also be rewritten as

$$C_P - C_V = VT\frac{\varepsilon^2}{\beta_T} \tag{2.26}$$

where ε is the coefficient of thermal expansion and β_T is the isothermal compressibility.

There are lots of factors affecting the heat capacity besides temperature. Temperature reflects the average randomized kinetic energy of constituent particles of matter (e.g., atoms or molecules) relative to the center of mass of the system, while heat is the transfer of energy across a system boundary into the body other than by work or mass transfer. Translation, rotation, and vibration of atoms represent the degrees of freedom of motion that classically contribute to the heat capacity of fluids (i.e., gas), while only vibrations are needed to describe the heat capacities of most solids according to the Dulong–Petit law [59, 60]. Other contributions can come from magnetic [61] and electronic [60] degrees of freedom in solids, but these rarely make substantial contributions.

For quantum mechanical reasons, at any given temperature, some of these freedom degrees may be unavailable, or only partially available, to store thermal energy. In such cases, the specific heat capacity is a fraction of the maximum. As the temperature approaches absolute zero, the specific capacity of a system approaches zero due to loss of available degrees of freedom. Quantum theory can be used to quantitatively predict the specific heat capacity of simple systems. These thermal data can be directly calculated from the first principles, such as the path integral Monte Carlo method based on the quantum dynamical principles.

A general theory of the heat capacity of liquids has not yet been achieved and is still an active area of research. It was long thought that phonon theory is not able to explain the heat capacity of liquids, since liquids only sustain longitudinal phonons, but not transverse phonons, which in solids are responsible for 2/3 of

the heat capacity. However, Brillouin scattering experiments with neutrons and with X-rays confirm that transverse phonons do exist in liquids, albeit restricted to frequencies above a threshold called the Frenkel frequency [62]. Since most energy is contained in these high-frequency modes, a simple modification of the Debye model is sufficient to yield a good approximation to experimental heat capacities of simple liquids [63].

Hydrogen-containing polar molecules (e.g., water, ethanol, tetrahydrofuran, ammonia, *N*-methylpyrrolidone, glycerin) have powerful intermolecular hydrogen bonds in their liquid phase. These bonds provide additional positions where heat can be stored as potential energy of vibration, even at very low temperatures. Hydrogen bonds account for the fact that liquid water stores nearly the theoretical limit of $3R$ per mole of atoms, even at relatively low temperatures (i.e., near the freezing point of water). Table 2.8 gives the specific heat capacity of some typical materials.

In physics, thermal conductivity (κ) is the property of a material to conduct heat. It is evaluated primarily in terms of Fourier's law for heat conduction as in Eq. (2.27):

$$\kappa_x = \frac{q''_x}{\partial T/\partial x} \tag{2.27}$$

where x is the heat transfer direction; q''_x is the heat density along x-direction, $\mathrm{W\,m^{-2}}$; and $\partial T/\partial x$ is the temperature gradient along x-direction, $\mathrm{K\,m^{-1}}$. The SI unit of thermal conductivity is $\mathrm{W\,(m\,K)^{-1}}$. For scientific use, thermal conductance is often used, which is the quantity of heat that passes in unit time through a plate of particular area and thickness when its opposite faces differ in temperature by 1 K.

Thermal conductivity is the intrinsic physical properties of materials related to their electron transportation or phonon (lattice vibrations) status. There are several factors affecting this parameter, such as temperatures, phases and phase change routes, crystal orientation, electronic conductivity, microstructure and density (e.g., porous), magnetic fields, and flow types (e.g., convection, radiation).

The effect of temperature on thermal conductivity is different for metals and nonmetals. In metals, thermal conductivity is primarily due to free electrons. Following the Wiedemann–Franz law, thermal conductivity of metals is approximately proportional to the absolute temperature (in kelvin) times electrical conductivity. In pure metals the electrical conductivity decreases with increasing temperature and thus the product of the two, the thermal conductivity, stays approximately constant. In alloys the change in electrical conductivity is usually smaller, and thus thermal conductivity increases with temperature, often proportional to temperature. However, thermal conductivity in nonmetals is mainly due to lattice vibrations (phonons). Except for high-quality crystals at low temperatures, the phonon mean free path is not reduced significantly at higher temperatures. Thus, thermal conductivity of nonmetals is approximately constant at high temperatures. At low temperatures well below the Debye temperature, thermal conductivity decreases, as does the heat capacity. When a material undergoes a phase change from solid to liquid or from liquid to gas, the thermal conductivity may change. An example

www.ebook3000.com

Table 2.8 Specific heat capacities at 25 °C (298 K) unless otherwise noted.

Substance	Phase	Isobaric mass heat capacity C_P (J g^{-1} K^{-1})	Isobaric molar heat capacity $C_{P,m}$ (J mol^{-1} K^{-1})	Isochoric molar heat capacity $C_{V,m}$ (J mol^{-1} K^{-1})	Isobaric volumetric heat capacity $C_{P,v}$ (J cm^{-3} K^{-1})	Isochoric atom-molar heat capacity in units of R $C_{V,am}$ (atom-mol^{-1})
Air (sea level, dry, 273.15 K)	Gas	1.0035	29.07	20.7643	0.001297	~1.25 R
Air (typical room condition[a])	Gas	1.012	29.19	20.85	0.00121	~1.25 R
Nitrogen	Gas	1.040	29.12	20.8	—	1.25 R
Neon	Gas	1.0301	20.7862	12.4717	—	1.50 R
Oxygen	Gas	0.918	29.38	21.0	—	1.26 R
Argon	Gas	0.5203	20.7862	12.4717	—	1.50 R
CO_2 [64]	Gas	0.839*	36.94	28.46	—	1.14 R
Hydrogen	Gas	14.30	28.82	—	—	1.23 R
Helium	Gas	5.1932	20.7862	12.4717	—	1.50 R
Methane, 2 °C	Gas	2.191	35.69	—	—	0.85 R
Hydrogen sulfide H_2S [64]	Gas	1.015*	34.60	—	—	1.05 R
Steam at 100 °C	Gas	2.080	37.47	28.03	—	1.12 R
Methanol	Liquid	2.14	68.62	—	—	1.38 R
Ethanol	Liquid	2.44	112	—	1.925	1.50 R
Ethylene glycol	Liquid	2.2	—	—	—	—
Gasoline (octane)	Liquid	2.22	228	—	1.64	1.05 R
Ammonia	Liquid	4.700	80.08	—	3.263	3.21 R
Water at 25 °C	Liquid	4.1813	75.327	74.53	4.1796	3.02 R
Water at 100 °C	Liquid	4.1813	75.327	74.53	4.2160	3.02 R
Water at −10 °C (ice)	Solid	2.05	38.09	—	1.938	1.53 R
Glass	Solid	0.84	—	—	2.1	—
Silica (fused)	Solid	0.703	42.2	—	1.547	1.69 R
Granite	Solid	0.790	—	—	2.17	—
Graphite	Solid	0.710	8.53	—	1.534	1.03 R
Diamond	Solid	0.5091	6.115	—	1.782	0.74 R

(Continued)

Table 2.8 (Continued)

Substance	Phase	Isobaric mass heat capacity C_P (J g^{-1} K^{-1})	Isobaric molar heat capacity $C_{P,m}$ (J mol^{-1} K^{-1})	Isochoric molar heat capacity $C_{V,m}$ (J mol^{-1} K^{-1})	Isobaric volumetric heat capacity $C_{P,v}$ (J cm^{-3} K^{-1})	Isochoric atom-molar heat capacity in units of R $C_{V,am}$ (atom-mol^{-1})
Aluminum	Solid	0.897	24.2	—	2.422	2.91 R
Steel	Solid	0.466	—	—	3.756	—
Tin	Solid	0.227	27.112	—	1.659	3.26 R
Titanium	Solid	0.523	26.060	—	2.6384	3.13 R
Zinc	Solid	0.387	25.2	—	2.76	3.03 R
Chromium	Solid	0.449	23.35	—	—	2.81 R
Nickel	Solid	0.440	—	—	—	—
Copper	Solid	0.385	24.47	—	3.45	2.94 R
Brass	Solid	0.380	—	—	—	—
Silver	Solid	0.233	24.9	—	2.44	2.99 R
Gold	Solid	0.129	25.42	—	2.492	3.05 R
Paraffin wax $C_{25}H_{52}$	Solid	2.5 (ave)	900	—	2.325	1.41 R
Polyethylene	Solid	2.3027	—	—	—	—

a) Assuming an altitude of 194 m above mean sea level (the worldwide median altitude of human habitation), an indoor temperature of 23 °C, a dewpoint of 9 °C (40.85% relative humidity), and 760 mmHg sea level-corrected barometric pressure (molar water vapor content = 1.16%).

of this would be the change in thermal conductivity that occurs when ice (thermal conductivity of 2.18 W (m K)$^{-1}$ at 0 °C) melts to form liquid water (thermal conductivity of 0.56 W (m K)$^{-1}$ at 0 °C) [65]. Some substances, such as non-cubic crystals, can exhibit different thermal conductivities along different crystal orientation, due to differences in phonon coupling along a given crystal orientation. Sapphire is a notable example of variable thermal conductivity based on orientation and temperature, with 35 W (m K)$^{-1}$ along the *a*-axis and 32 W (m K)$^{-1}$ along the *ca*-axis [66, 67]. Wood generally conducts better along the grain than across it. When anisotropy is present, the direction of heat flow may not be exactly the same as the direction of the thermal gradient. In metals, thermal conductivity approximately tracks electrical conductivity according to the Wiedemann–Franz law, as freely moving valence electrons transfer not only electric current but also heat energy. However, the general correlation between electrical and thermal conductance does not hold for other materials (e.g., nonmetals) due to the increased importance of phonon carriers for heat in nonmetals. Highly electrically conductive silver is less thermally conductive than diamond, which is an electrical insulator, but it is conductive of heat via phonons due to its ordered array of atoms. The influence of magnetic fields on thermal conductivity is known as the Righi–Leduc effect, or the thermal analog of the Hall effect.

www.ebook3000.com

Ceramic coatings with low thermal conductivities are used on exhaust systems to prevent heat from reaching sensitive components (e.g., thermal barrier coatings for aeroengine). Air and other gases are generally good insulators, in the absence of convection. Therefore, many insulating materials function simply by having a large number of gas-filled pockets, which prevent large-scale convection. Examples of these include expanded and extruded polystyrene (popularly referred to as "styrofoam") and silica aerogel, as well as warm clothes. Natural, biological insulators such as fur and feathers achieve similar effects by

Table 2.9 Thermal conductivity (κ) of some materials.

Materials	T (°C)	κ (W m^{-1} K^{-1})	Materials	T (°C)	κ (W m^{-1} K^{-1})
Aluminum	300	230	Asbestos sheet	50	0.17
Steel (1% C)	18	45	ABS resin	—	0.25
Stainless steel	20	16	PDMS	25	0.134–0.159
Copper	100	377	SU-8 (epoxy resin)	25	0.2–2.2
Bronze	25	189	PMMA	25	0.14–0.2
Nickel	100	57	PP	25	0.21–0.26
Silver	100	412	PC	25	0.2
Gold	25	317	LDPE	25	0.33
Graphite	0	151	HDPE	25	0.5
Graphene [68, 69]	25	3080–5300	50% acetic acid	20	0.35
Carbon nanotube [70]	25	~1500–2900	Acetone	30	0.17
Diamond	25	2300	Aniline	0–20	0.17
Glass	30	1.09	Benzene	30	0.16
Mica	50	0.43	80% ethanol	20	0.24
Silica	25	7.6	60% glycerin	20	0.38
Fused quartz	25	1.4–2	40% glycerin	20	0.45
Quartz *a*-axis	25	0.7	Heptane	30	0.14
Quartz *c*-axis	25	11.7	Mercury	28	8.36
Silica, 10 nm	25	0.2	Water	30	0.62
Silica, 100 nm	25	0.9	Steam (H_2O)	100	0.023
Silica, 200 nm	25	1.3	Hydrogen	0	0.17
Silica, aerogel	25	0.13	Carbon dioxide	0	0.015
Silicon	25	150	Air	0	0.024
Glass wool	—	0.041	Air	100	0.031
85% MgO	—	0.070	Methane	0	0.029
Al_2O_3 sapphire	25	45	Oxygen	0	0.024
AlN	25	150	Nitrogen	0	0.024
SiC	—	490	Ethylene	0	0.017
Porcelain	25	1.5	Ethane	0	0.018
PTFE	25	0.25	Argon	25	0.016
Polyurethane foam	25	0.02	Neon (gas)	25	0.046

Table 2.10 Thermal diffusivity of some materials and substances.

Material	Thermal diffusivity ($m^2\ s^{-1}$)	Material	Thermal diffusivity ($m^2\ s^{-1}$)
Water at 25 °C [73]	1.43×10^{-7}	PDMS [74]	$1.1–1.5 \times 10^{-7}$
Alcohol [75]	7×10^{-8}	PMMA at 18 °C [76]	1.15×10^{-7}
Water vapor (1 atm, 400 K)	2.338×10^{-5}	Polycarbonate (PC) at 18 °C [76]	1.6×10^{-7}
Air (27 °C) [75]	1.9×10^{-5}	Polypropylene (PP) at 25 °C [73]	0.096×10^{-6}
Oil, engine (saturated liquid, 100 °C)	7.38×10^{-8}	Polyvinyl chloride (PVC) [75]	8×10^{-8}
Argon (300 K, 1 atm) [77, 78]	2.2×10^{-5}	Polytetrafluorethylene (PTFE) at 25 °C [79]	0.124×10^{-6}
Helium (300 K, 1 atm) [77, 78]	1.9×10^{-4}	Aluminum [75]	9.7×10^{-5}
Hydrogen (300 K, 1 atm) [77, 78]	1.6×10^{-4}	Aluminum 6061-T6 alloy [75]	6.4×10^{-5}
Nitrogen (300 K, 1 atm) [77, 78]	2.2×10^{-5}	Iron [75]	2.3×10^{-5}
Silicon [75]	8.8×10^{-5}	Copper at 25 °C [80]	1.11×10^{-4}
Quartz (highly crystalline SiO_2) [75]	1.4×10^{-6}	Silver, pure (99.9%)	1.6563×10^{-4}
Silicon dioxide (polycrystalline) [75]	8.3×10^{-7}	Gold [75]	1.27×10^{-4}
Glass, window	3.4×10^{-7}	Tin [75]	4.0×10^{-5}
Si_3N_4 with CNTs 26 °C [81]	9.142×10^{-6}	Molybdenum (99.95%) at 25 °C [82]	54.3×10^{-6}
Si_3N_4 without CNTs 26 °C [81]	8.605×10^{-6}	Al–10Si–Mn–Mg at 20 °C [83]	74.2×10^{-6}
Pyrolytic graphite, normal to layers	3.6×10^{-6}	Al–5Mg–2Si–Mn at 20 °C [84]	44.0×10^{-6}
Carbon/carbon composite at 25 °C [80]	2.165×10^{-4}	Steel, AISI 1010 (0.1% carbon) [85]	1.88×10^{-5}
Aluminum oxide (polycrystalline)	1.20×10^{-5}	Steel, 1% carbon [85]	1.172×10^{-5}
Paraffin at 25 °C [73]	0.081×10^{-6}	Steel stainless 304A at 27 × °C [75]	4.2×10^{-6}
Rubber [86]	$0.89–1.3 \times 10^{-7}$	Inconel 600 at 25 °C [87]	3.428×10^{-6}
SU-8 [88]	1.1×10^{-7}	Wood (yellow pine)	8.2×10^{-8}

www.ebook3000.com

dramatically inhibiting convection of air or water near an animal'\s skin. Light gases, such as hydrogen and helium, typically have high thermal conductivity. Dense gases such as xenon and dichlorodifluoromethane have low thermal conductivity. An exception, sulfur hexafluoride, a dense gas, has a relatively high thermal conductivity due to its high heat capacity. Argon, a gas denser than air, is often used in insulated glazing (double-paned windows) to improve their insulation characteristics (Table 2.9).

Usually, materials with very low thermal conductivity are called as thermal insulators (e.g., $\kappa < 0.12\,\mathrm{W\,(m\,K)^{-1}}$ at 350 °C). Those materials with $\kappa < 0.05\,\mathrm{W\,(m\,K)^{-1}}$ can be called as high efficient thermal insulators.

As the specific heat capacity and thermal conductivity of materials is determined, the thermal diffusivity (α) can be used in the heat transfer analysis, which is defined as the thermal conductivity divided by density and specific heat capacity at constant pressure (Eq. (2.28)) [38]:

$$\alpha = \frac{\kappa}{\rho C_\mathrm{P}} \tag{2.28}$$

where κ is the thermal conductivity ($\mathrm{W\,(m\,K)^{-1}}$), ρ is the density ($\mathrm{kg\,m^{-3}}$), and C_P is the specific heat capacity ($\mathrm{J\,(kg\,K)^{-1}}$). Thus, ρC_P can be considered as the volumetric heat capacity ($\mathrm{J\,(m^3\,K)^{-1}}$).

The heat transfer equation can be defined as [71, 72]

$$\frac{\partial T}{\partial t} = \alpha \nabla^2 T \tag{2.29}$$

Therefore, thermal diffusivity is the ratio of the time derivative of temperature to its curvature, quantifying the rate at which temperature concavity is "smoothed out" [72]. In a substance with high thermal diffusivity, heat moves rapidly through it because the substance conducts heat quickly relative to its volumetric heat capacity. Table 2.10 gives the thermal diffusivity of some typical materials, and some of them are often used in microfluids and nanofluids or microfluidic device construction (see also Ref. [89]).

2.3 Mass and Heat Transfer Principles for Fluid

The space feature scale in microfluidics is micrometer, which is far longer than the mean free path (λ) of molecule motion. Therefore, the bulk single-phase fluid in the micrometer scale should obey the law of continuous medium, which can be treated by the continuity equation. Thus, the properties of a fluid such as density, pressure, and velocity remain constant at any defined point, and changes in these properties due to molecular motions are taken to be negligible. The physical properties of fluids can be defined as continuous functions of time and space. The basic equations in fluid mechanism are applicable for microfluidics. The following are some basic equations related to mass and heat transfer, which may be modified according to the detailed microfluidic feature (particular the surface tension of walls of microchannels and interface properties of different fluid phases) in the applications. Since the reactions of different systems in microfluidics are very

different, we will not discuss in this chapter the related mass and heat transfer caused by the reaction.

2.3.1 Basic Fluidic Concepts and Law for Mass and Heat Transfer

The basic fluid mechanism includes three basic conversion principles, which are mass conversion, energy conversion, and momentum conversion, and the corresponding equation, or continuity equation, dynamic energy equation (Bernoulli's Equation) and momentum equation, respectively. Their basic concepts are from Pascal's law and Laplace's law.

2.3.1.1 Pascal's Law and Laplace's Law

Usually, pressure difference is the driving force of the fluid motion, whose unit is measured in units of pascal (Pa, $\mathrm{N\,m^{-2}}$). **Blaise Pascal** is a famous philosopher and mathematician from France who summarized the famous *Pascal's law* in channels: *the pressure exerted anywhere in an enclosed, incompressible, static fluid is transmitted equally in all directions throughout the fluid*. The pressure exerted by a static fluid is called as s*tatic fluid pressure*, which arises from the weight of that fluid and so depends only upon the fluid depth h, its density ρ, and the acceleration of gravity g:

$$P_{\text{static fluid}} = \rho g h \tag{2.30}$$

Pascal's law can be interpreted to indicate that any *change* in pressure applied at any given point of the fluid is transmitted *undiminished* throughout the fluid. As shown in Figure 2.6 this makes a large multiplication of force possible and forms the basis for the operation of a hydraulic press that provides the means to lift a heavy weight with a small force, or "**micro**" can be transmitted to "**giant**" using the fluidic lever.

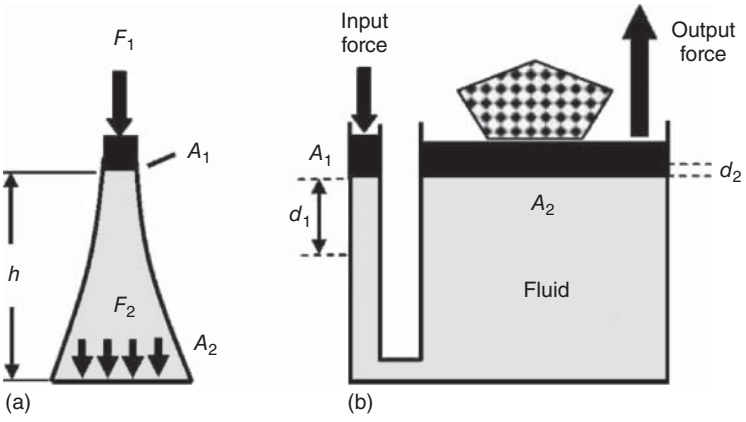


Figure 2.6 Demonstrations of Pascal's law. (a) The pressure in a vessel is transmitted equally throughout a fluid, or $F_1A_1 = F_2A_2$. (b) The operation of a hydraulic press relies on the fact that any change in pressure applied at any given point of a fluid is transmitted undiminished throughout the fluid. (Pethig and Smith 2013 [13]. Reproduced with permission of John Wiley & Sons.)

www.ebook3000.com

The relationship between the fluid pressure and the wall tension of vessels of different shapes and sizes can be described by ***Laplace's law*** (Pierre-Simon Laplace was an influential French scholar whose work was important in the development of mathematics, statistics, physics, and astronomy. He also developed the idea of the scalar potential and applied it in the velocity potential of a fluid). Laplace's law states that ***the tension on the wall of a cylindrical chamber is the product of the pressure times the radius of the cylinder*** (***or half that value for a spherical chamber***). Thus, a vessel of large radius will require a larger wall tension than one of smaller radius to withstand a given internal fluid pressure. Also, for a given vessel radius and internal pressure, a spherical vessel will have half the wall tension of a cylindrical vessel, as shown in Figure 2.7. As explained in Figure 2.8, if the fluid pressure remains constant, the inward component ($\tau \sin\theta$) of the wall tension must remain the same. As the wall curvature ($\sin\theta$) is less, the total wall tension must increase in order to obtain the same inward component of tension.

Therefore, the spherical reactors have more material-efficient shape than the cylindrical reactors even though they are usually difficult to realize in microscale. The flow of blood in arteries and veins (treated as microchannel) is a good example of Laplace's law in action. The larger arteries of the body are subject to higher wall tensions than the smaller arteries having comparable blood pressures. Arteries are reinforced by fibrous bands to strengthen them against the risks of an aneurysm (capillaries with their very thin walls rely on their small radii). If an artery wall develops a weak spot and expands as a result, the expansion subjects the weakened wall to even more tension. The weakened vessel may continue to expand in what is called an aneurysm and lead to rupture

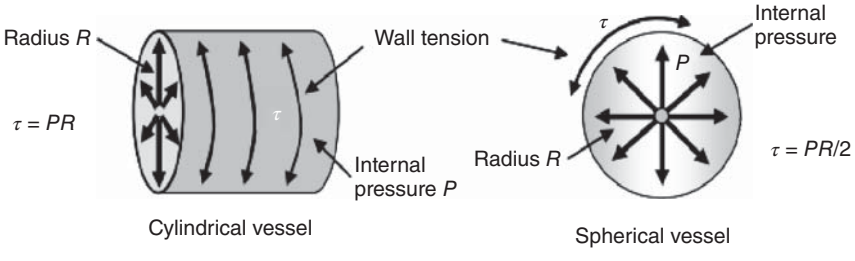


Figure 2.7 Laplace's law indicates that the tension on the wall of a cylindrical vessel is twice that of a spherical vessel of the same radius and internal pressure. (Pethig and Smith 2013 [13]. Reproduced with permission of John Wiley & Sons.)

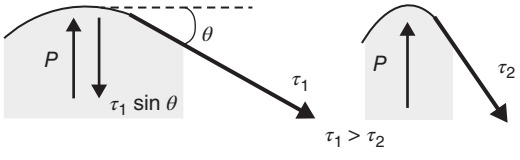


Figure 2.8 Wall tension τ increases with vessel radius because for a fixed internal pressure P, the counter component of the wall tension $\tau \sin\theta$ must equal P. (Pethig and Smith 2013 [13]. Reproduced with permission of John Wiley & Sons.)

of the vessel. This is why aneurysms require prompt medical attention. This issue is also often met in microchannel design. Therefore, the defect-free fabrication is very important in microchannel.

Now we can consider the flow of fluids in channels and the forces that act on them or some principles related to address the mass transfer.

2.3.1.2 Mass Conservation Principle (Continuity Equation)

It can be assumed that all of the fluid mass steadily pass through the tube at any cross-sectional area (e.g., A_1 and A_2), which are treated as the same flow measured as Q in units of kg s^{-1}, or the mass of fluid crossing each section of the pipe per unit time must be the same. The mass conversion can be expressed as Eq. (2.31) as the fluid enters through the tube at two positions (1 and 2) with the cross-sectional areas of A_1 and A_2 (Figure 2.9):

$$A_1\rho_1 u_1 = A_2\rho_2 u_2 \tag{2.31}$$

where ρ_1 and ρ_2 are the density of the fluid flowing through A_1 and A_2 and u_1 and u_2 are the effective velocity of the fluid flow through A_1 and A_2.

2.3.1.3 Energy Conservation (Bernoulli's Equation)

Bernoulli's principle states that, for viscous free fluid flow, an increase of the fluid velocity occurs simultaneously with a decrease in fluid pressure (ΔP) or a decrease in the fluid's potential energy, as shown in Figure 2.10. This principle can be applied to various types of fluid flow and quantified using various forms of what is known as Bernoulli's equation. A simple form of this equation is valid for incompressible fluids and for compressible gases moving at speeds well below the velocity of sound in a particular gas. This equation can be derived from the principle of conservation of energy, which states that in a steady fluid flow, the sum of all forms of mechanical energy remains constant along a flow line. The fluid possesses kinetic energy due to its motion, and because of its location in the Earth's gravitational field, it also possesses potential energy. Work is also being done on the fluid due to the static pressure acting on it. If there are no frictional losses, we can apply the law of conservation of energy and write Bernoulli's equation as

$$P + \rho gh + {}^1\!/_2\rho u^2 = \text{constant} \tag{2.32}$$

where P is the static pressure, h the height above some reference level, u the velocity, ρ the density, and g the acceleration due to gravity at any chosen elemental

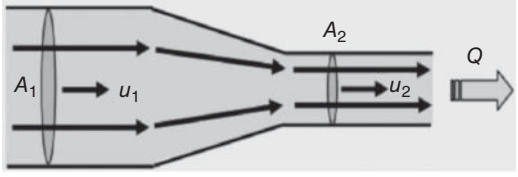


Figure 2.9 Fluid flow through a tube whose cross-sectional areas are A_1 and A_2 at two positions (A_1 and A_2). The flow rate Q can be determined as either volumetric flow ($m^3\ s^{-1}$) or mass flow (kg s^{-1}). (Pethig and Smith 2013 [13]. Reproduced with permission of John Wiley & Sons.)

www.ebook3000.com

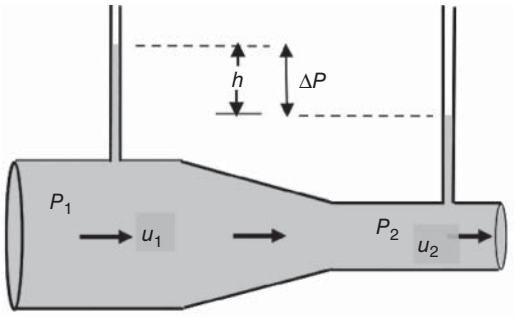


Figure 2.10 Fluid flowing through a constriction, leading to a pressure drop $\Delta P = P_1 - P_2$, with $P_1 > P_2$ because $u_1 < u_2$. (Pethig and Smith 2013 [13]. Reproduced with permission of John Wiley & Sons.)

volume in the fluid flow line. The term ($^1/_2\rho u^2$) is known as the dynamic pressure, and the total pressure is the sum of the static pressure P and this dynamic pressure. The sum of the elevation h and static pressure head ($P/\rho g$) is known as the hydraulic head.

2.3.1.4 Poiseuille's Law

Bernoulli's principle assumes the fluid flow is not influenced by viscous forces. In fact, for the case of smooth, turbulence-free fluid flow, viscous shearing forces shown in Figure 2.1 will determine the fluid velocity profile across a channel. There will be zero fluid slip at the surfaces of the channel walls and the flow velocity will increase toward the center line of the channel. The consequence of this is that in order to pump a viscous fluid along a channel a pressure difference, ΔP must be applied between its inlet and outlet, irrespective of any changes of the channel diameter. In the 1840s, Poiseuille experimentally and then theoretically derived the following relationship (2.33) for fluid flow in pipes of circular cross section assuming the smooth channel and laminar flow:

$$\Delta P = \frac{8\mu LQ}{\pi r^4} \tag{2.33}$$

where L is the length of the tube, r is its internal radius, and μ is the dynamic viscosity of the fluid. This is also known as the *Hagen–Poiseuille* relationship in recognition of the contributions made by Hagen.

In practice, microfluidic channels of either a rectangular or semicircular cross section are easier to fabricate than those of circular cross section (e.g., by placing a flat plate on top of a rectangular or rounded trench), particularly for LC devices. The fluidic pressure difference ΔP of a rectangular channel with a high aspect ratio (i.e., width $w \gg$ height h) can be calculated using the following formula assuming the laminar flow type:

$$\Delta P = \frac{12\mu LQ}{wh^3} \tag{2.34}$$

For a channel of semicircular cross section defined by a radius of curvature r, the pressure drop will be calculated as

$$\Delta P = \frac{64\mu LQ}{3r^4} \tag{2.35}$$

Therefore, for any specified channel geometry, the flow pressure drop is directly proportional to the viscosity of the fluid. If the walls are not perfectly smooth

and sufficiently rough to induce 3D components of fluid flow near the wall surfaces, the pressure drop will tend to be greater than that predicted by the above equations and the fluid pressure drop will be larger. If the friction coefficient (C_{fr}) and the hydraulic diameter (D_h) are introduced into the calculation, the pressure drop can be rewritten as the following equation [90–92]:

$$\Delta P = C_{fr}\frac{\mu LQ}{2AD_h^2} \tag{2.36}$$

where C_{fr} are 64 and 96 for the circular cross section and for rectangular cross section, respectively, and A is the cross-sectional area of the flow.

2.3.1.5 Velocity Profile of Laminar Flow in a Circular Tube

As depicted in Figure 2.11, the laminar flow in a tube of circular cross section takes the form of concentric thin-walled tubes of fluids, and its velocity increases from zero at the tube wall to a maximum at the center line of the tube. The flow is directed along the tube's axis and there are no pressure gradients across the tube diameter. A shear stress τ exists between each tube and increases by $d\tau$ for each tube. A pressure drop between the ends of the fluid tube is required to overcome the shear stress τ. It is normally assumed that the pressure declines uniformly with distance down the fluid stream, so the pressure gradient $\Delta P/\Delta L$ is assumed to be constant.

Consider the elemental fluid tube shown in Figure 2.11: for fluids in ΔL with radius r and thickness dr, if τ is the shear stress per unit area acting on the surface of this tube, the shear force F_s is given as

$$F_s = 2\pi r\Delta L\tau \tag{2.37}$$

From Equation $\tau = \mu\, du/dx = -\tau\, du/dr$ $(x = R - r)$, it can be given that

$$F_s = -2\pi r\Delta L\mu\, du/dr \tag{2.38}$$

At equilibrium this shear force will balance the force acting on the ends of the fluid tube as a result of the pressure difference ΔP, giving

$$\Delta P\pi r^2 = -\frac{2\pi r\Delta L\mu\ du}{dr} \tag{2.39}$$

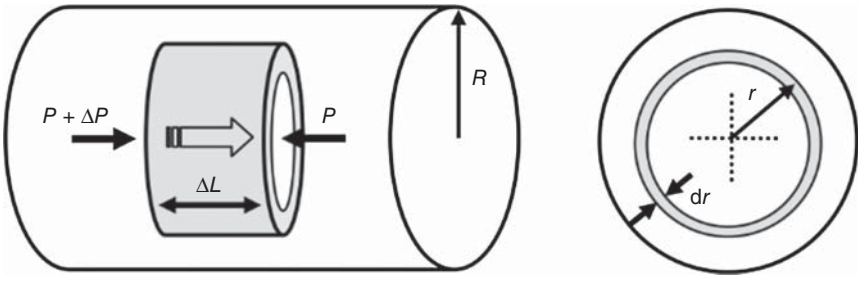


Figure 2.11 Laminar flow in a cylindrical tube can be depicted as a series of concentric "stream tubes" of length ΔL whose velocities increase as a function of the distance (R–r) from the pipe wall toward the center axis of the tube. (Pethig and Smith 2013 [13]. Reproduced with permission of John Wiley & Sons.)

www.ebook3000.com

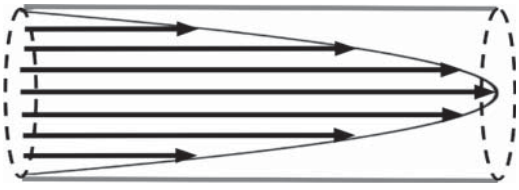


Figure 2.12 Laminar flow exhibits a parabolic fluid velocity profile, as described by Eq. (2.41). The velocity is zero at the channel wall and reaches a maximum at the center line of the channel. (Pethig and Smith 2013 [13]. Reproduced with permission of John Wiley & Sons.)

Then we can get the velocity change:

$$\mathrm{d}u = -\frac{\Delta P}{2\mu\Delta L} r \, \mathrm{d}r \tag{2.40}$$

The velocity u of a fluid tube at any radius r can be found by integrating between the limits $u = 0$ at $r = R$ and $u = u$ at $r = r$ (Eq. (2.41)):

$$\int_0^u \mathrm{d}u = -\frac{\Delta P}{2\mu\Delta L} \int_R^r r \, \mathrm{d}r \tag{2.41}$$

From Eq. (2.41), the velocity profile can be obtained along the radius of the tube (2.42):

$$u(r) = -\frac{\Delta P}{2\eta\Delta L}(r^2 - R^2) = \frac{\Delta P}{2\eta\Delta L}(R^2 - r^2) \tag{2.42}$$

The fluid velocity profile across the pipe is clearly parabolic, as shown in Figure 2.12, with zero velocity at the pipe walls and a maximum velocity along the central axis (at $r = 0$).

The maximum velocity is given as

$$u = \frac{\Delta p P^2}{4\eta\Delta L} \tag{2.43}$$

The mean velocity $\langle u \rangle$ in the cross section can be obtained as

$$\langle u \rangle = \frac{1}{\pi R^2} \int_0^R v(r) 2\pi r \, \mathrm{d}r = \frac{\Delta p P^2}{8\eta\Delta L} \tag{2.44}$$

which corresponds to half the maximum value. The volumetric flow rate Q is given by the product of the mean velocity and the cross-sectional area (2.45), corresponding to the Hagen–Poiseuille relationship of Eq. (2.33):

$$Q = \frac{\Delta p P^2 \pi R^2}{8\mu\Delta L} = \frac{\pi R^4 \Delta p}{8\mu\Delta L} \tag{2.45}$$

2.3.2 Important Dimensionless Numbers in Fluid Physics

The nondimensionalization of the governing equations of fluid flows is important for both theoretical and computational reasons. Nondimensional scaling provides a method for developing dimensionless groups that can provide physical insight into the importance of various terms in the system of governing

equations. Computationally, dimensionless forms have the added benefit of providing numerical scaling of the system discrete equations, thus providing a physically linked technique for improving the ill conditioning of the system of equations. They can be used in the mechanism and theory development of microfluidic physics. Moreover, dimensionless forms also allow us to present the solution in a compact way. Some of the important dimensionless numbers used in fluid mechanics and heat transfer are given as follows.

Reynolds Number (*Re*)

$$Re = \frac{\rho u L}{M} = \frac{\text{inertial force}}{\text{viscous force}}$$

As the characteristic length in microfluidic devices is decreased, inertial forces (which are dominant in macroscale systems) decrease significantly compared with viscous forces. Since inertial terms are the cause for creating turbulence, flow regimes tend toward laminar flow at small dimensions. The Reynolds number (*Re*) compares the relative magnitudes of inertial force ($\rho u^2/L$) and viscous force ($\mu u/L^2$). In microfluidics, *Re* is typically less than 1 and the flow is still in laminar regime as *Re* less than 1500. For $Re = 1$, nonlinear terms (such as convective acceleration) can be neglected, such that fluid flow switches to the Stokes regime.

Knudsen Number (*Kn*)

$$Kn = \frac{\lambda}{L} = \frac{\text{length of mean free path}}{\text{characteristic dimension}}$$

The validity of continuum model is normally assessed using the measure of free path length λ, as embodied by the *Kn*, which is the ratio of the mean free path length to the characteristic dimension (L). The assumption of continuum model is valid as long as the *Kn* is small ($Kn \ll 1$). On the basis of various magnitudes of Knudsen numbers, flow regimes change from continuous flow to slip flow, and finally free molecule flow regime as *Kn* increases to 1 [93].

Schmidt Number (*Sc*)

$$Sc = Le\ Pr = \frac{N}{D_{\text{AB}}} = \frac{\text{momentum diffusivity}}{\text{mass diffusivity}}$$

where ν is the kinematic viscosity of fluid and D_{AB} is the diffusivity coefficient. *Sc* is used to characterize fluid flows in which there are simultaneous momentum and mass diffusion convection processes [30].

Prandtl Number (*Pr*)

$$Pr = \frac{\nu}{\alpha} \frac{\text{momentum diffusivity}}{\text{thermal diffusivity}}$$

Small values of the Prandtl number, $Pr \ll 1$, means the thermal diffusivity dominates, whereas with large values, $Pr \gg 1$, the momentum diffusivity dominates the behavior. In heat transfer problems, the Prandtl number controls the relative thickness of the momentum and thermal boundary layers. When *Pr* is small, it means that the heat diffuses quickly compared with the velocity (momentum). This means that for liquid metals the thickness of the thermal boundary layer is

www.ebook3000.com

much bigger than the velocity boundary layer. *Pr* is about 7 for water at 20 °C and around 0.7–0.8 for air and many other gases.

Péclet Number (*Pe*)

The Péclet number is defined as

$$Pe = \frac{\text{advective transport rate}}{\text{diffusive transport rate}}$$

In the context of species or mass transfer, the **Péclet** number is the product of the **Reynolds** number and the **Schmidt** number. In the context of the thermal fluids, the thermal **Péclet** number is equivalent to the product of the **Reynolds** number and the Prandtl number.

For mass transfer, it is defined as

$$Pe = Re_{\mathrm{L}} Sc = \frac{uL}{D} \frac{\text{inertia (convection)}}{\text{mass diffusion}}$$

where L is the characteristic length, u the local flow velocity, and D the mass diffusivity (diffusion coefficient). When Reynolds number is small (which is generally the case in microfluidic systems), flow is not turbulent, and hence fluid mixing by convection is not significant. In such cases, mixing through diffusion becomes important. To define a measure of diffusive versus convective transport, the Péclet number (uL/D) is defined as the ratio of convective transport (uL) to diffusive transport (D) [14].

For heat transfer, the Péclet number is defined as

$$Pe = Re_{\mathrm{L}} Pr = \frac{uL}{\alpha} \frac{\text{inertia (convection)}}{\text{thermal diffusion}}$$

where L is the characteristic length, u the local flow velocity, and α the thermal diffusivity.

A flow will often have different Péclet numbers for heat and mass transportation. This can lead to the phenomenon of double diffusive convection. In the context of particulate motion, the Péclet number has also been called the **Brenner number**, with symbol *Br*, in honor of Howard Brenner.

Damköhler Number (*Da*)

$$Da = \frac{k_{\mathrm{r}} CL}{D} = \frac{\text{reaction speed}}{\text{mass diffusion}}$$

where k_{r} is the surface reaction constant. Extensive development of microfluidic applications has led to the incorporation of chemical reactions on surfaces. For instance, in immunoassay diagnostic devices, functionalized surface of the microchannel serves as a reacting surface, and the relative speed of reaction versus diffusion is one of the key factors in determining efficiency of the assay. The Damköhler number ($k_{\mathrm{r}} CL/D$) compares the relative speed of diffusive transport (D) and surface reaction ($k_{\mathrm{r}} CL$).

Weber Number (*We*)

$$We = \frac{\rho u^2 L}{\sigma} = \frac{\text{inertial force}}{\text{surface tension force}}$$

where ρ is the density of the fluid (kg m^{-3}); u is its velocity (m s^{-1}); L is the characteristic length of the fluid, typically the droplet diameter (m); and σ is the surface

tension ($N\,m^{-1}$). The **Weber number** (*We*) is a dimensionless number in fluid mechanics that is often useful in analyzing fluid flows where there is an interface between two different fluids, especially for multiphase flows with strongly curved surfaces [94]. It can be thought of as a measure of the relative importance of the fluid's inertia compared with its surface tension. The quantity is useful in analyzing thin film flows and the formation of droplets and bubbles.

Capillary Number (*Ca*)

$$Ca = \frac{We}{Re} = \frac{u \times \mu}{\gamma}$$

In microfluidic devices, surface effects are extremely important due to the high surface area-to-volume ratio. Thus, surface tension plays a significant role in many microfluidic applications, including droplet formation. The relative magnitude of surface tension (γ) with respect to viscous effects (μu) is compared by defining the dimensionless capillary number ($\mu u/\gamma$). One use of *Ca* is to make droplets with different dimensions (by choosing appropriate capillary numbers) to study chemical reaction kinetics [95].

Mach Number (*Ma*)

$$Ma = \frac{U}{(E/\rho)^{1/2}} = \frac{\text{inertial force}}{\text{elastic (compressibility) force}}$$

where ρ is the density of fluid ($kg\,m^{-3}$) and E is the bulk modulus elasticity ($N\,m^{-2}$ (Pa)). The Mach number is defined as the ratio of flow velocity to the velocity of sound in that medium; this number serves as a measure of fluid compressibility. For *Ma* less than 0.3, the fluid can be considered incompressible.

2.3.3 Other Dimensionless Numbers in Fluids

Froude Number

$$Fr = \frac{u}{(gL)^{1/2}} = \frac{\text{inertial force}}{\text{gravitational force}}$$

The Froude number is based on the speed–length ratio. It has some analogy with the Mach number. In theoretical fluid dynamics, it is not frequently considered since usually the equations are considered in the high Froude limit of negligible external field, leading to homogeneous equations that preserve mathematical aspects. For example, homogeneous Euler equations are conservation equations. However, in naval architecture the Froude number is a very significant figure used to determine the resistance of a partially submerged object moving through water. Dynamics of vessels that have the same Froude number are easily compared as they produce a similar wake, even if their size or geometry is otherwise different.

Archimedes Number

$$Ar = \frac{Re^2}{Fr} = \frac{gL^3\rho(\rho_s - \rho)}{\mu^2}$$

It is a dimensionless number defined as the ratio of external forces to internal viscous forces. When analyzing potentially mixed heat convection of a liquid,

www.ebook3000.com

the Archimedes number parametrizes the relative strength of free and forced convection. When $Ar \gg 1$, natural convection dominates, that is, less dense bodies rise and denser bodies sink, and when $Ar \ll 1$, forced convection dominates.

Atwood Number

$$At = \frac{(\rho_1 - \rho_2)}{(\rho_1 + \rho_2)}$$

Note: Used in the study of density stratified flows.

Bond Number or Eötvös Number

$$Eo = Bo = \frac{We}{Fr} = \frac{\rho g L^2}{\sigma}$$

It is a dimensionless number measuring the importance of surface tension forces compared with body forces and is used (together with **Morton number**) to characterize the shape of bubbles or drops moving in a surrounding fluid. A high value of the Eötvös or Bond number indicates that the system is relatively unaffected by surface tension effects; a low value (typically less than one) indicates that surface tension dominates. Intermediate numbers indicate a nontrivial balance between the two effects. It may be derived in a number of ways, such as scaling the pressure of a drop of liquid on a solid surface. It is usually important, however, to find the right length scale specific to a problem by doing a ground-up scale analysis.

Morton Number

$$Mo = \frac{We^3}{FrRe^4} = \frac{g\mu}{\Delta\rho\sigma^3}$$

In fluid dynamics, the **Morton number** (*Mo*) is a dimensionless number used together with the Eötvös number or Bond number to characterize the shape of bubbles or drops moving in a surrounding fluid or continuous phase.

Rossby Number

$$Ro = \frac{U}{\Omega L} = \frac{\text{inertial force}}{\text{Coriolis force}}$$

A small Rossby number signifies a system that is strongly affected by Coriolis forces, and a large Rossby number signifies a system in which inertial and centrifugal forces dominate. For example, in tornadoes, the Rossby number is large ($\approx 10^3$), in low-pressure systems it is low (≈ 0.1–1), and in oceanic systems it is of the order of unity, but depending on the phenomena can range over several orders of magnitude ($\approx 10^{-2}$–10^2).

Centrifuge Number

$$Ce = \frac{We}{Ro^2} = \frac{\rho\Omega^2 L^3}{\sigma}$$

Dean Number

$$De = \frac{Re}{(R/h)^{1/2}}$$

The Dean number deals with the stability of two-dimensional (2D) flows in a curved channel with mean radius R and width $2h$.

Deborah Number

$$De = \frac{\tau}{t_p} = \frac{\text{relaxation time}}{\text{characteristic time scale}}$$

Note: Commonly used in rheology to characterize how "fluid" a material is. The smaller the *De*, the more the fluid the material appears.

Ekman Number

$$Ek = \frac{\mu}{\rho\sigma L^2} = \frac{\text{viscous force}}{\text{Coriolis force}}$$

It is the ratio of viscous forces in a fluid to the fictitious forces arising from planetary rotation. More generally, in any rotating flow, the Ekman number is the ratio of viscous forces to Coriolis forces. When the Ekman number is small, disturbances are able to propagate before decaying owing to frictional effects. It describes the order of magnitude for the thickness of an Ekman layer, a boundary layer in which viscous diffusion is balanced by Coriolis effects rather than the usual convective inertia.

Euler Number

$$Eu = \frac{\Delta p}{\rho u^2} = \frac{\text{pressure force}}{\text{inertial force}}$$

It expresses the relationship between a local pressure drop, for example, over a restriction and the kinetic energy per volume and is used to characterize losses in the flow, where a perfect frictionless flow corresponds to an Euler number of 0.

Galileo Number

$$Ga = \frac{Re^2}{Fr} = \frac{\rho^2 g L^3}{\mu^2}$$

Galileo number is proportional to (*Re*·gravity force)/(viscous force) and is used in momentum and heat transfer in general and viscous flow and thermal expansion calculations in particular.

Graetz Number

$$Gz = \frac{d_i Pe}{L} = \frac{u d_i}{\nu}$$

It characterizes laminar flow in a conduit [96]. This number is useful in determining the thermally developing flow entrance length in ducts. A Graetz number of approximately 1000 or less is the point at which flow would be considered thermally fully developed [97].

Grashof Number

$$Gr = \frac{g\beta(T_{hot} - T_{ref})L^3}{\nu^2} = \frac{\text{buoyancy force}}{\text{viscous force}}$$

The **Grashof number** (*Gr*) is a dimensionless number in fluid dynamics and heat transfer that approximates the ratio of the buoyancy to viscous force acting on a fluid. It frequently arises in the study of situations involving natural convection. The transition to turbulent flow occurs in the range $10^8 < Gr < 10^9$ for natural convection from vertical flat plates. At higher Grashof numbers, the boundary layer is turbulent; at lower Grashof numbers, the boundary layer is laminar.

www.ebook3000.com

Hagen Number

$$Hg = \frac{\mathrm{d}p\rho L^3}{\mathrm{d}x\mu^2}$$

It is the forced flow equivalent of the Grashof number.

Laplace Number

$$La = \frac{Re^2}{We} = \frac{\rho\sigma L}{\mu^2}$$

La is used in the characterization of free surface fluid dynamics. It represents a ratio of surface tension to the momentum transport (especially dissipation) inside a fluid.

Ohnesorge Number

$$Oh = \frac{We^{1/2}}{Re} = \frac{\mu}{(\rho\sigma L)^{1/2}}$$

It is related to the viscous forces to inertial and surface tension forces, which is often used to relate to free surface fluid dynamics such as dispersion of liquids in gases and in spray technology [98, 99].

Richardson Number

$$Ri = \frac{Gr}{Re^2} = \frac{-g\beta(T_{\mathrm{hot}} - T_{\mathrm{ref}})L}{u^2} = \frac{\text{buoyancy force}}{\text{flow shear force}}$$

It expresses the ratio of the buoyancy term to the flow shear term. If the Richardson number is much less than unity, buoyancy is unimportant in the flow. If it is much greater than unity, buoyancy is dominant (in the sense that there is insufficient kinetic energy to homogenize the fluids). If the Richardson number is of order unity, then the flow is likely to be buoyancy driven: the energy of the flow derives from the potential energy in the system originally. In thermal convection problems, the Richardson number represents the importance of natural convection relative to the forced convection. Typically, the natural convection is negligible when $Ri < 0.1$, forced convection is negligible when $Ri > 10$, and neither is negligible when $0.1 < Ri < 10$. It may be noted that usually the forced convection is large relative to natural convection except in the case of extremely low forced flow velocities.

Rotating Froude Number

$$Fr_R = \frac{Fr}{Ro^2} = \frac{\Omega^2 L}{g}$$

Sherwood Number

$$Sh = \frac{h_{\mathrm{m}}L}{D_{\mathrm{AB}}}$$

The Sherwood number represents the dimensionless concentration gradient at the solid surface.

Stokes Number

$$Stk = \frac{\tau u_{\mathrm{o}}}{d_{\mathrm{c}}} = \frac{\text{stopping distance of a particle}}{\text{characteristic dimension of the obstacle}}$$

Commonly *Stk* is used in particles suspended in fluid. For $Stk \ll 1$, the particle negotiates the obstacle. For $Stk \gg 1$, the particle travels in straight line and eventually collides with obstacle.

Strouhal Number (*for Oscillatory Flow*)

$$St = \frac{L}{ut_{\text{ret}}} = \frac{\text{inertia (local)}}{\text{inertia (convection)}}$$

If t_{ref} is taken as the reciprocal of the circular frequency ω of the system, then

$$St = \frac{\omega L}{u}$$

Taylor Number

$$Ta = \frac{\rho^2 \Omega_{\text{i}}^2 L^4}{\mu^2}$$

where $L = [r_{\text{i}}(r_{\text{o}} - r_{\text{i}})^3]^{1/4}$. *Ta* characterizes the importance of centrifugal "forces" or so-called inertial forces due to rotation of a fluid about an axis, relative to viscous forces. The typical context of the Taylor number is in characterization of the Couette flow between rotating colinear cylinders and rotating concentric spheres. In the case of a system that is not rotating uniformly, such as the case of cylindrical Couette flow, where the outer cylinder is stationary and the inner cylinder is rotating, inertial forces will often tend to destabilize a system, whereas viscous forces tend to stabilize a system and damp out perturbations and turbulence.

Biot Number

$$Bi = \frac{hL}{K_{\text{s}}} = \frac{\text{conductive resistance in solid}}{\text{convective resistance in thermal boundary layer}}$$

Bi gives a simple index of the ratio of the heat transfer resistances inside of and at the surface of a body. This ratio determines whether or not the temperatures inside a body will vary significantly in space, while the body heats or cools over time, from a thermal gradient applied to its surface. In general, problems involving small Biot numbers (much smaller than 1) are thermally simple, due to uniform temperature fields inside the body. Biot numbers much larger than 1 signal more difficult problems due to nonuniformity of temperature fields within the object. It should not be confused with the Nusselt number, which employs the thermal conductivity of the fluid and hence is a comparative measure of conduction and convection, both in the fluids. The Biot number has a variety of applications, including transient heat transfer and use in extended surface heat transfer calculations. The physical significance of Biot number can be understood by imagining the heat flow from a small hot metal sphere suddenly immersed in a pool to the surrounding fluid. The heat flow experiences two resistances: the first within the solid metal (which is influenced by both the size and composition of the sphere) and the second at the surface of the sphere. If the thermal resistance of the fluid/sphere interface exceeds that thermal resistance offered by the interior of the metal sphere, the Biot number will be less than one. For systems where it is much less than one, the interior of the sphere may be presumed always to have the same temperature, although this temperature may be changing, as heat

www.ebook3000.com

passes into the sphere from the surface. The equation to describe this change in (relatively uniform) temperature inside the object is simple exponential one described in Newton's law of cooling.

Brinkman Number

$$Br = \frac{\mu u^2}{K(T_w - T_o)}$$

Brinkman number is related to heat conduction from a wall to a flowing viscous fluid. It is commonly used in polymer processing.

Eckert Number

$$Ec = \frac{u^2}{C_p \Delta T}$$

Eckert number represents the kinetic energy of the flow relative to the boundary layer enthalpy difference. *Ec* plays an important role in high speed flows for which viscous dissipation is significant.

Fourier Number

$$Fo = \frac{\alpha t}{L^2} = \frac{\text{rate of heat conduction}}{\text{rate of thermal energy stored}}$$

Fourier number represents the dimensionless time. It may be interpreted as the ratio of current time to time to reach steady state.

Jakob Number

$$Ja = \frac{c_p(T_w - T_{sat})}{h_{fg}}$$

The Jakob number represents the ratio of sensible heat to latent heat absorbed (or released) during the phase change process.

Womersley Number

$$\alpha = (\pi Re\, St)^{1/2} = L\frac{(\rho\omega)^{1/2}}{\mu^{1/2}}$$

The Womersley number is used in biofluid mechanics. It is a dimensionless expression of the pulsatile flow frequency in relation to the viscous effects.

Lewis Number

$$Le = \frac{\alpha}{D_{AB}} = \frac{\text{thermal diffusivity}}{\text{mass diffusivity}}$$

The Lewis number (*Le*) is a dimensionless number defined as the ratio of thermal diffusivity to mass diffusivity. It is used to characterize fluid flows where there is simultaneous heat and mass transfer by convection.

Marangoni Number

$$Ma = -\frac{d\sigma}{dT}\frac{L\Delta T}{\mu\alpha}$$

The Marangoni number is the ratio of thermal surface tension force to the viscous force.

Nusselt Number

$$Nu = \frac{hL}{K_f}$$

The Nusselt number represents the dimensionless temperature gradient at the solid surface.

Rayleigh Number

$$Ra = Gr\,Pr = \frac{g\beta(T_{hat} - T_{ref})L^3}{\nu\alpha} = \frac{\text{buoyancy}}{\text{viscous} \times \text{rate of heat diffusion}}$$

In fluid mechanics, the **Rayleigh number** (*Ra*) for a fluid is a dimensionless number associated with buoyancy-driven flow, also known as free convection or natural convection. When the Rayleigh number is below a critical value for that fluid, heat transfer is primarily in the form of conduction; when it exceeds the critical value, heat transfer is primarily in the form of convection.

Stanton Number

$$Sta = \frac{Nu}{Re\,Pr} = \frac{h}{\rho U c_n}$$

The Stanton number is the modified Nusselt number. It is used in analogy between heat transfer and viscous transport in boundary layers.

Stefan Number

$$Ste = \frac{C_p\,dT}{L_m} = \frac{\text{specific heat}}{\text{latent heat}}$$

The Stefan number is useful in the study of heat transfer during phase change.

Table 2.11 summarizes these dimensionless numbers and the related nomenclature and symbols in these numbers.

2.3.4 Diffusion Laws

This mass diffusion process can be described by Fick's first equation (2.46) [13]:

$$J_x = -D\frac{\partial C}{\partial x} \tag{2.46}$$

This equation states that the net flux J_x (mol $(m^2\,s)^{-1}$) of diffusing molecules or particles is proportional to the concentration gradient and diffusion constant of the molecule/particle (the negative sign indicates that the molecules diffuse down to the concentration gradient). Unless the concentration gradient is artificially maintained (e.g., with a continuous source and sink of the molecules or particles), the factor $\partial C/\partial x$ will change as a function of time. This leads to Fick's second equation (2.47):

$$\frac{\partial C}{\partial t} = D\frac{\partial^2 C}{\partial x^2} \tag{2.47}$$

This equation can be used (with the appropriate boundary conditions) to determine how a nonuniform distribution of molecules or particles will redistribute themselves as a function of time. Diffusion along a microfluidic channel

www.ebook3000.com

Table 2.11 Nomenclature for dimensionless numbers.

a	speed of sound
C_p	specific heat capacity at constant pressure
D_{AB}	mass diffusivity coefficient
$\mathrm{d}T$	temperature difference between phases
d_{c}	characteristic dimension of the obstacle
d_{i}	hydraulic diameter of the duct
g	gravitational acceleration
h	heat transfer coefficient
h_{fg}	latent heat of condensation
h_{m}	mass transfer coefficient
K	bulk modulus of elasticity
K_{f}	thermal conductivity of fluid
K_{s}	thermal conductivity of solid
L	characteristic length scale
L_{m}	latent heat of melting
R	radius of the channel
r_{i}	radius of the inner cylinder
r_{o}	radius of the outer cylinder
T_{hot}	temperature of the hot wall
T_{ref}	reference temperature
T_{o}	bulk fluid temperature
T_{sat}	saturation temperature
T_{w}	wall temperature
T_{∞}	quiescent temperature of the fluid
t	Time
t_{ref}	reference time
t_{p}	characteristic time scale
U	characteristic velocity scale
U_{o}	fluid velocity far away from the object
$\mathrm{d}P/\mathrm{d}x$	pressure gradient
$\mathrm{d}\sigma/\mathrm{d}T$	rate of change of surface tension with temperature
α	thermal diffusivity of fluid
β	volumetric thermal expansion coefficient
Δp	characteristic pressure difference of flow
ΔT	characteristic temperature difference
$\Delta\rho$	difference in density of the two phases
λ	length of mean free path

(Continued)

Table 2.11 (Continued)

μ	viscosity of fluid
ν	kinematic viscosity of fluid
ρ	density of fluid
ρ_1	density of heavier fluid
ρ_2	density of lighter fluid
ρ_s	density of solid
γ	surface tension
τ	relaxation time
Ω	angular velocity
ω	circular frequency
ω_i	angular velocity of inner cylinder

is effectively a one-dimensional problem. In this case the solutions of Fick's second equation are

$$\frac{\partial C}{\partial x} = \frac{C_0}{(4\pi Dt)^{1/2}} e^{-x^2/4Dt} \quad \text{and} \quad \frac{\partial C}{\partial t} = -\frac{x}{2t}\frac{\partial C}{\partial x} \tag{2.48}$$

Mixing several fluids in chambers of micron scale is not as easy as it seems to be since the Reynolds number for these geometries is usually rather small, and therefore flow status is usually laminar flow and no turbulent flow. Thus, liquid streamlines do not interfere with each other, resulting in zero mixing.

In Figure 2.13, a fluidic Y-junction is used to flow together two liquids into a third channel of diameter 100 mm. Two practical questions are: (i) how long the third channel should be to achieve complete mixing of the two liquids, and (ii) to what extent mixing is influenced by the rate of fluid flow? In the absence of mechanical stirring, the only way for the merging liquid streams to mix is through the diffusion of their constituent molecules across the interface between

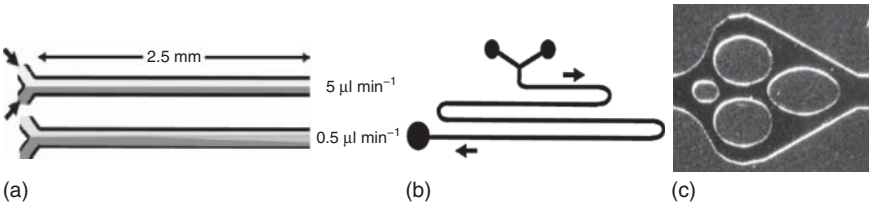


Figure 2.13 (a) Modeling of liquid streams flowing together via a Y-junction into a channel of radius 100 mm. Mixing of the fluids is evident for a fluid flow rate of 0.5 ml min^{-1}, but not at 5 ml min^{-1}. (b) A serpentine geometry is often used in lab-on-a-chip devices to accommodate the long channel lengths required for the mixing of laminar fluid streams. ((a, b) Pethig and Smith 2013 [13]. Reproduced with permission of John Wiley & Sons.) (c) Micropole arrays for mixing enhancement [91]. (Reproduced with permission from Ref. [91] Copyright 2004 IOP Publishing.)

www.ebook3000.com

the traveling liquids. The profile of this interface will broaden and dissipate with time along the channel. If a flow rate of 5.0 µl min^{-1} is chosen, then, as shown in Figure 2.13, no discernable mixing of the two fluid streams occurs after a distance of 2.5 mm along the third channel. A 10-fold reduction of the flow rate to 0.5 µl min^{-1} does result in some mixing of the two fluid streams, but it is clear that the channel length will need to extend much further before complete mixing occurs. The long channel lengths required for the thorough mixing of laminar flow streams can be accommodated in LC designs using the serpentine geometry shown in Figure 2.13b or using some special design (e.g., Figure 2.13c micropole arrays [91] or sudden narrowed channels [100] as in Figure 14.2).

The extent efficiency of mixing two fluids next to each other accomplished only through diffusion can be given by F_{mix} (2.49) [92]:

$$F_{mix} = \frac{Dt}{l^2} \tag{2.49}$$

where t is the stream contact time allowed for mixing, l is the system dimension perpendicular to the flow direction, and D is the reactant diffusion constant (10^{-9} m^2 s^{-1} for water). In general, the mixing process ranges from substantial up to almost complete for F_{mix} values in the range of 0.1–1. For instance, as one lateral mixer with one capillary length of $L = 2.4$ mm, the central distance between two streamlines of $l = 85$ µm and depth of $d = 5$ µm depth, the mixing time can be calculated to $t = 1.01$ s for $F_{mix} = 0.14$ and water-based liquids. Thus, the flow rate through a $w = 2.21$ mm wide mixer is $Q = Lwd/t = 1.707$ µl min^{-1} [92]. In addition, we have to pay attention that flow status, mixer geometry, and channel shape design are very crucial parameters for high efficient mixing at microscale.

2.3.5 Conversion Equation Based on Navier–Stokes Equations

The Navier–Stokes equations are widely used to describe the behavior of fluids in terms of continuous functions of space and time. They include mass, energy, and momentum conservation laws and are considered in terms of flux rather than changes of their instantaneous values. In mathematical terms this is represented as partial derivatives of the dependent fluid variables.

The calculation of fluid velocities and pressures at the macroscopic scale is based on the assumption that the fluid can be treated as a continuum. Apart from fluid velocity u and pressure P, for the most general situation that includes compressible and incompressible fluids, we also require knowledge of the density ρ, viscosity μ, specific heat C_p, and temperature T of the fluid. Pressure and temperature characterize the energy state and number of molecules present in a given volume of fluid. If the pressure and temperature do not vary too greatly within this volume element, analytical functions can be derived that relate the density, viscosity, and specific heat to the pressure and temperature. In a 3D system five unknowns are therefore left, namely, P, T, v_x, v_y, and v_z. These five unknowns are related by a system of equations of the conservation of mass, the conservation of momentum, and the conservation of energy.

The equations describing these three conservation laws are often referred to the Navier–Stokes equations, but it is more correct to reserve this description to the equations that describe conservation of momentum. Conservation of energy usually concerns heat flow in fluid systems in which a temperature gradient is created by an energy source or sink associated with chemical reactions or heating and cooling devices. For most microfluidic flows in LC devices, the temperature is constant, in which case the conservation of energy equation is redundant. The derivations of the conservation of mass and conservation of momentum equations are thus focused on.

2.3.5.1 Conservation of Mass Equation

To simplify the situation, as depicted in Figure 2.14, a 2D element $(\Delta x, \Delta y)$ Cartesian coordinate is considered, with fluid velocities u and v in the x- and y-directions, respectively. It can be then generalized to the 3D case.

For the system of fluid flow shown in Figure 2.14, the conservation of mass is given by

$$\frac{\partial(\rho\Delta x\Delta y)}{\partial t} = \rho u\Delta y + \rho u\Delta x - \left[\rho u + \frac{\partial(pu)\Delta x}{\partial x}\right]\Delta y - \left[\rho v + \frac{\partial(pv)\Delta y}{\partial y}\right]\Delta x \tag{2.50}$$

Equation (2.50) can be written as after divided by $\Delta x\Delta y$

$$\frac{\partial\rho}{\partial t} + \frac{u\partial\rho}{\partial x} + \frac{\partial\rho}{\partial y} + \rho\left[\frac{\partial u}{\partial x} + \frac{\partial v}{\partial y}\right] = 0 \tag{2.51}$$

Defining the operator D/Dt in 3D Cartesian coordinates as, Eq. (2.51) can be rewritten in the vector form (Eq. (2.52)): tg

$$\frac{\mathrm{D}\rho}{\mathrm{D}t} + \rho\nabla\cdot\vec{V} = 0 \tag{2.52}$$

where $\vec{V}$ is the velocity vector (u, v, w). Here incompressible liquids are mainly concerned, in which case terms such as $\frac{\partial\rho}{\partial t}$, $\frac{\partial\rho}{\partial x}$, and $\mathrm{D}\rho/\mathrm{D}t$ are zero, and density ρ remains constant.

Equations (2.51) and (2.52) thus reduce, for the 3D case, to

$$\frac{\partial u}{\partial x} + \frac{\partial v}{\partial y} + \frac{\partial w}{\partial z} = 0 \tag{2.53}$$

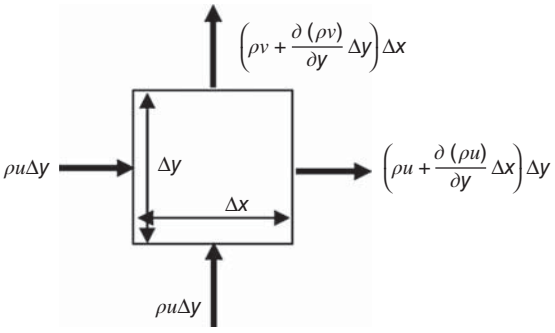


Figure 2.14 Conservation of fluid mass for a volume element $\Delta x\,\Delta y$. (Pethig and Smith 2013 [13]. Reproduced with permission of John Wiley & Sons.)

www.ebook3000.com

And then the mass conversion will be

$$\nabla \cdot \vec{V} = 0 \tag{2.54}$$

2.3.5.2 Conservation of Momentum Equation (Navier–Stokes Equation)

The change of momentum in a fluid element is given by the balance between the inlet and outlet fluid momentum and the tangential and normal stresses acting on that element. These are considered separately in Figures 2.15 and 2.16 for the 2D case.

For Newtonian fluids the tangential stress t and normal stress s are given as

$$\tau_{xy} = \eta \left(\frac{\partial v}{\partial x} + \frac{\partial u}{\partial y} \right) \tag{2.55}$$

and

$$\sigma_x = P - 2\eta \frac{\partial u}{\partial x} \left(\frac{\partial u}{\partial x} + \frac{\partial v}{\partial y} \right) \tag{2.56}$$

Summing the forces shown in Figure 2.16 in the x-direction and using the mass conservation in Eq. (2.57),

$$\rho \frac{\mathrm{D}u}{\mathrm{D}t} = -\frac{\partial \sigma_x}{\partial_x} + \frac{\partial \tau_{xy}}{\partial y} + F_x \tag{2.57}$$

Combining this result with Eq. (2.54) gives the Navier–Stokes equation (2.58)

$$\rho \left(\frac{\partial u}{\partial t} + u \frac{\partial u}{\partial x} + v \frac{\partial u}{\partial y} + w \frac{\partial u}{\partial z} \right) = -\frac{\partial P}{\partial x} + \mu \left(\frac{\partial^2 u}{\partial x^2} + \frac{\partial^2 u}{\partial y^2} + \frac{\partial^2 u}{\partial z^2} \right) + F_x \tag{2.58}$$

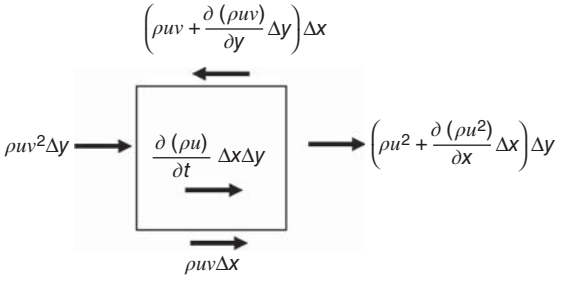


Figure 2.15 Inlet and outlet fluid momentum for a fluid element in the x-direction. (Pethig and Smith 2013 [13]. Reproduced with permission of John Wiley & Sons.)

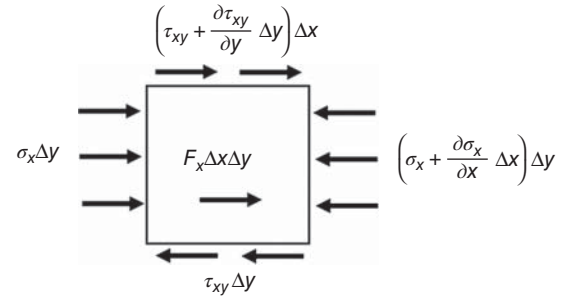


Figure 2.16 The normal and tangential stresses acting on the volume element shown in Figure 2.15. (Pethig and Smith 2013 [13]. Reproduced with permission of John Wiley & Sons.)

Extending this to three-dimensional, the following equations can be obtained:

$$\rho\left(\frac{\partial v}{\partial t}+u\frac{\partial v}{\partial x}+v\frac{\partial v}{\partial y}+w\frac{\partial v}{\partial z}\right)=-\frac{\partial P}{\partial y}+\mu\left(\frac{\partial^2 v}{\partial x^2}+\frac{\partial^2 v}{\partial y^2}+\frac{\partial^2 v}{\partial z^2}\right)+F_y \tag{2.59}$$

$$\rho\left(\frac{\partial u}{\partial t}+u\frac{\partial u}{\partial x}+v\frac{\partial u}{\partial y}+w\frac{\partial u}{\partial z}\right)=-\frac{\partial P}{\partial z}+\mu\left(\frac{\partial^2 w}{\partial x^2}+\frac{\partial^2 w}{\partial y^2}+\frac{\partial^2 w}{\partial z^2}\right)+F_z \tag{2.60}$$

And then the momentum conversion in vector form will be

$$\rho\frac{\mathrm{D}\vec{V}}{\mathrm{D}t}=-\nabla P+\mu\Delta\vec{V}+\vec{F} \tag{2.61}$$

where $\vec{V}$ is the velocity vector (u, v, w) and $\vec{F}$ is the force per unit volume acting on the element $(\Delta x, \Delta y, \Delta z)$.

2.3.5.3 Conservation of Energy Equation

To derive this equation we identify either a source or a sink of heat (SH) and specify the specific heat capacity C_p and heat conductivity κ of the liquid. The specific heat is defined as the amount of heat Q per unit mass required to raise the temperature of a material by 1 °C:

$$Q=C_pM\Delta T \tag{2.62}$$

The thermal conductivity of a substance is defined in terms of the quantity of heat Q conducted per unit time Δt down a unit temperature gradient ΔT in a direction normal to a surface of unit area ΔA. The heat conduction must arise only from the temperature gradient, and not from a secondary heat source or chemical reaction, for example:

$$k=Q\Delta T/\Delta t\Delta A=-Q/(\partial T\partial n) \tag{2.63}$$

The specific heat of water is $4.186\,\mathrm{J\,(g\,K)^{-1}}$, and its thermal conductivity is $\sim 0.6\,\mathrm{W\,(m\,K)^{-1}}$. In 3D Cartesian coordinates, the conservation of energy equation will be

$$\rho C_{\mathrm{p}}\left(\frac{\partial T}{\partial t}+u\frac{\partial T}{\partial x}+v\frac{\partial T}{\partial y}+w\frac{\partial T}{\partial z}\right)=\frac{\partial}{\partial x}\left(k\frac{\partial T}{\partial x}\right)+\frac{\partial}{\partial y}\left(k\frac{\partial T}{\partial y}\right)+\frac{\partial}{\partial z}\left(k\frac{\partial T}{\partial z}\right)+S_{\mathrm{H}} \tag{2.64}$$

Currently, the theoretical analysis and numerical calculation methods for the fluid mechanism are molecular dynamics method (e.g., Fourier law for the diffusion model) and the phonon Boltzmann equations. Some progress of their current applications in microfluidic process calculation will be discussed in Chapter 4 in details.

2.4 Surfaces and Interfaces in Microfluidics

2.4.1 Surface/Interface and Surface Tension

A surface is the shell of a macroscopic object in contact with its environment (Figure 2.17a), and an interface is the boundary between two phases (usually two

www.ebook3000.com

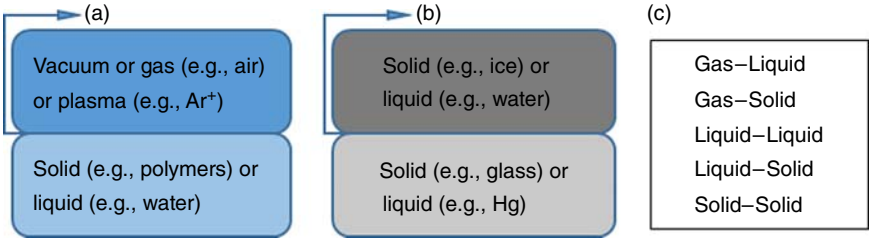


Figure 2.17 Types of interface and surface. (a) Surface; (b) interface; and (c) types of interfaces.

immiscible or partial immiscible condensed phases; Figure 2.17b). In a broad sense, surface is a special type of interface. Energy is needed to create a surface or push two phases contact close enough to create an interface. Work (W) to create a unit surface (A) is defined as the free surface energy ($\gamma = \mathrm{d}W/\mathrm{d}A$), or surface tension or interfacial tension, with the unit of $\mathrm{J\,m^{-2}}$ or $\mathrm{N\,m^{-1}}$. Thermodynamically, every system wants to decrease its surface energy.

There are several types of interfaces as shown in Figure 2.17c. In microfluidics, there are commonly gas–liquid interface, gas–solid interface, and liquid–solid interface. The liquid–solid interface is the most common one, where the wetting is one often encountered phenomenon. Wetting is the ability of a liquid to maintain contact with a solid surface resulting from intermolecular interactions when the two are brought together. The degree of wetting (wettability) is determined by a force balance between adhesive and cohesive forces [101]. Wetting is important in the bonding or adherence of two materials. Wetting and the surface forces that control wetting are also responsible for other related effects, including so-called capillary effects. The contact angle (θ), as seen in Figure 2.18a, is the angle at which the liquid–vapor interface meets the solid–liquid interface. It is determined by the resultant between adhesive and cohesive forces. The tendency of a drop to spread out over a flat solid surface increases as the contact angle decreases. Thus, it also provides an inverse measure of wettability [102] and is formed by a liquid (L)/vapor (V) interface meeting the solid surface (S) (Figure 2.18a), which follows Young's equation (2.65) [103]. Some typical wetting phenomena according to the contact angle are schemed in Figure 2.18b:

$$\gamma_{\mathrm{SV}} = \gamma_{\mathrm{SL}} + \gamma_{\mathrm{LV}} \cos\theta \quad \text{or} \quad \cos\theta = \frac{\gamma_{\mathrm{SV}} - \gamma_{\mathrm{SL}}}{\gamma_{\mathrm{LV}}} \tag{2.65}$$

where γ_{SL}, γ_{LV}, and γ_{SV} are the interfacial tensions between the solid and the liquid, the liquid and the vapor, and the solid and the vapor, respectively. Alternatively, in combination with the definition of work of adhesion, we can obtain the Young and Dupre equation (2.66). W_{SLV} is the work to form this kind of contact:

$$W_{\mathrm{SLV}} = \gamma_{\mathrm{LV}}(1 + \cos\theta) \tag{2.66}$$

Table 2.12 describes varying contact angles and their corresponding solid–liquid and liquid–liquid interactions. Regardless of the amount of wetting, the shape of a liquid drop on a rigid surface is roughly a truncated sphere. For water, a wetting surface may also be termed as hydrophilic, and a non-wetting surface as hydrophobic. Table 2.13 gives the contact angle of water on different solid surface (water is $72\,\mathrm{mN\,m^{-1}}$) [101]. Superhydrophobic surfaces have contact angles

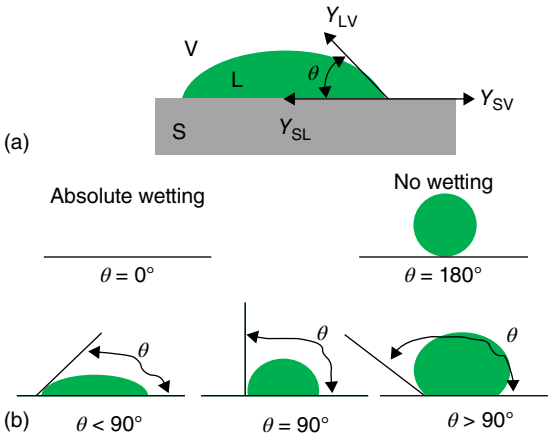


Figure 2.18 (a) The defined contact angle in the liquid–solid wetting and (b) the types of wetting and the corresponding contact angle.

Table 2.12 Contact angles and their corresponding solid–liquid and liquid–liquid interactions.

Contact angle	Degree of wetting	Strength of	
		S–L interactions	L–L interactions
$\theta = 0$	Perfect wetting	Strong	Weak
$0 < \theta < 90°$	High wettability	Strong	Strong
		Weak	Weak
$90° \leq \theta < 180°$	Low wettability	Weak	Strong
$\theta = 180°$	Perfectly non-wetting	Weak	Strong

Source: Eustathopoulos *et al*. 1999 [103]. Reproduced with permission of Elsevier.

Table 2.13 Contact angle of water on different solid surface (20–25 °C).

Solid	θ (°)	Solid	θ (°)	Solid	θ (°)
Paraffin	110	PMMA	59.3	Naphthalene	103
PTFE	108	Polypropylene	108	Graphite	86
FEP	108	Human skin	90.8	Graphon	82
PET	79.1	Talc	78.3	Stearic acid	80
Butyl rubber	110.8	Polyethylene	103	Sulfur	78
Platinum	40	Silver iodide	17	Glass	~0

greater than 150°, showing almost no contact between the liquid drop and the surface, which is often referred to as the "lotus effect."

Two major examples of the Cassie–Baxter model are the "petal effect" and "lotus effect," as schemed in Figure 2.19 [104, 105]. The intrinsic hydrophobicity of a surface can be enhanced by being textured with different length scales of roughness. The red rose takes advantage of this by using a hierarchy of

www.ebook3000.com

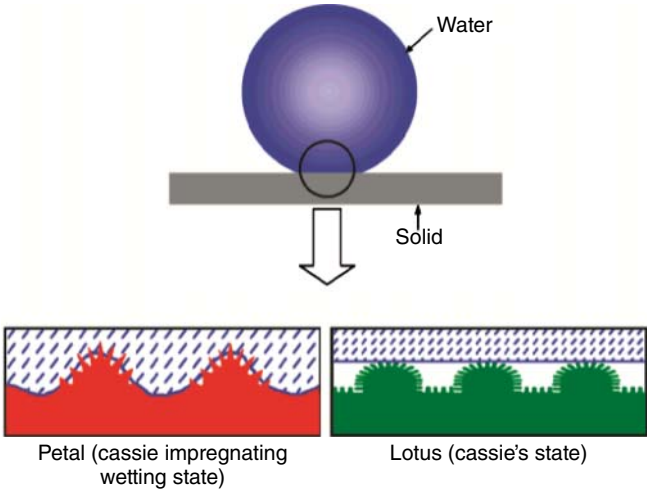


Figure 2.19 "Petal effect" and "Lotus effect." (Lin *et al*. 2008 [104]. Reproduced with permission of American Chemical Society.)

micro- and nanostructures on each petal to provide sufficient roughness for superhydrophobicity. More specifically, each rose petal has a collection of micropapillae on the surface, and each papilla, in turn, has many nanofolds. The term "petal effect" describes the fact that a water droplet on the surface of a rose petal is spherical in shape, but cannot roll off even if the petal is turned upside down. The water drops maintain their spherical shape due to the superhydrophobicity of the petal (the contact angle is about 152.4°), but do not roll off because the petal surface has a high adhesive force with water.

When comparing the "petal effect" with the "lotus effect," it is important to note some striking differences. The surface structure of the lotus petal and the rose petal, as seen in Figure 2.19, can be used to explain the two different effects. The ever familiar lotus petal has a randomly rough surface and low contact angle hysteresis, which means that the water droplet is not able to wet the microstructure spaces between the spikes. This allows air to remain inside the texture, causing a heterogeneous surface composed of both air and solid. As a result, the adhesive force between the water and the solid surface is extremely low, allowing the water to roll off easily (i.e., "self-cleaning" phenomena).

On the other hand, the rose petal's micro- and nanostructures are larger in scale than the lotus leaf, which allows the liquid film to impregnate the texture. However, as seen in the bottom schemes of Figure 2.20, the liquid can enter into the larger-scale grooves (left scheme), but it cannot enter into the smaller grooves (right scheme). This is known as the Cassie impregnating wetting regime. Since the liquid can wet the larger-scale grooves, the adhesive force between the water and solid is very high. This explains why the water droplet will not fall off even if the petal is tilted at an angle or turned upside down. However, this effect will fail if the droplet has a volume larger than 10 μl because the balance between weight and surface tension is surpassed.

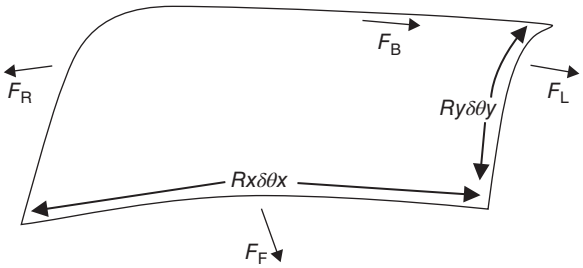


Figure 2.20 Surface tension forces acting on a tiny (differential) patch of surface. $\delta\theta x$ and $\delta\theta y$ indicate the amount of bend over the dimensions of the patch.

In addition, the energy associated with surface tension can be used to drive liquids through microfluidic devices, or called capillary phenomena. By treating the surfaces of microchannels to be hydrophilic, water will be driven through microchannels (typical of LC devices) without any applied pressure. This flow is driven by the attractive energy between the water and the channel wall surface.

2.4.2 Surface-/Interface-Induced Bubble Formation

If no force acts normal to a stretched surface, the surface must remain flat. However, if the pressure on one side of the surface differs from the pressure on the other side, the pressure difference times surface area results in a normal force. In order for the surface tension forces to cancel the force due to pressure, the surface must be curved. Figure 2.20 shows how surface curvature of a tiny patch of surface leads to a net component of surface tension forces acting normal to the center of the patch.

When all the forces are balanced, the resulting equation is known as the Young–Laplace equation [106]:

$$\Delta P = \gamma(1/R_x + 1/R_y) \tag{2.67}$$

where ΔP is the pressure difference, known as the Laplace pressure [107]; γ is surface tension; and R_x and R_y are radii of curvature in each of the axes that are parallel to the surface.

The quantity in parentheses on the right-hand side is in fact twice the mean curvature of the surface (depending on normalization). Solutions to this equation determine the shape of water drops, puddles, menisci, soap bubbles, and all other shapes determined by surface tension (such as the shape of the impressions that a water strider's feet make on the surface of a pond). Table 2.14 shows how the internal pressure of a water droplet increases with decreasing radius. For not very small drops, the effect is subtle, but the pressure difference becomes enormous when the drop sizes approach the molecular size. For a single molecule this concept becomes meaningless.

The pressure inside an ideal (one surface) soap bubble can be derived from thermodynamic free energy considerations. At constant temperature and particle number, the differential Helmholtz energy is given by $\mathrm{d}F = -\Delta P\,\mathrm{d}V + \mathrm{d}W = -P\,\mathrm{d}V + \gamma\,\mathrm{d}A$, $\Delta P = (P_\mathrm{i} - P_\mathrm{o})$ that is the pressure difference inside (P_i) and outside (P_o) of the bubble, and γ is the surface tension (Eq. (2.68)). In equilibrium, $\mathrm{d}F = 0$, and so $\Delta P\,\mathrm{d}V = \gamma\,\mathrm{d}A$. For a spherical bubble with radius

www.ebook3000.com

Table 2.14 ΔP of water drops of different radii at standard pressure and temperature.

Droplet radius	1 mm	100 µm	1 µm	10 nm
ΔP ($\times 10^5$ Pa)	0.00142	0.01459	1.4550	145.50

of r and neglected thickness, the volume and surface area are given simply by $V = 4/3\pi r^3$ and $A = 4\pi r^2$. Thus, $\mathrm{d}V = 4\pi r^2\,\mathrm{d}r$ and $\mathrm{d}A = 8\pi r\,\mathrm{d}r$.

Clearly, $\Delta P = (P_\mathrm{i} - P_\mathrm{o})$ is equivalent to the Young–Laplace equation when $R_x = R_y$, such as an air bubble in a liquid or a fluid droplet in air that has just one (outer) surface to take into account. For real soap bubbles, the pressure is doubled due to the presence of two interfaces, one inside and one outside (Eq. (2.68)):

$$\Delta P = (P_\mathrm{i} - P_\mathrm{o}) = 4\gamma/r \tag{2.68}$$

The $1/r$ relationship in this equation indicates that it is more difficult to inflate a small balloon than a larger one. This is of anatomical relevance. Oxygen exchange in the lungs takes place across the membranes of small balloon-like structures called alveoli. Their surface tension is lowered nearly 15-fold by a surfactant coating so that a very small pressure difference is sufficient to inflate them with air. Elastic recoil of the alveoli assists with their deflation (exhalation).

Air bubbles pose a big problem in microfluidic devices because their small radius of curvature r will require a large pressure to remove them from a fluidic channel. In the initial wetting of a hydrophilic device, air can become trapped where a wide channel narrows down to a smaller one. Air bubbles can also form after the device is wet, if air spontaneously comes out of solution.

Surface tension values for some common fluid–air interfaces are given in Table 2.15. Clearly, water has a significantly larger surface tension, about three times higher than other solvents, like alcohol, soap solutions, and oils, reflecting not only the relatively small size of the water molecule but also the cohesive energy supplied by hydrogen bonds in water. Fluorides have the lowest surface tension. Liquid metals (e.g., mercury) exhibit the highest surface tension values.

Table 2.15 Surface tensions of some liquids in air at 20 °C.

Liquids	γ (mN m^{-1})	**Liquids**	γ (mN m^{-1})	**Liquids**	γ (mN m^{-1})
Water	72.8	*n*-Hexane	18.43	Nitrobenzene	43.9
Ethanol	22.3	Perfluorohexane	11.91	Acetic acid	27.6
Methanol	22.6	Tetrahydrofuran	26.4	Oleic acid	32.50
Propanol, 25 °C	23.7	Benzene	28.9	Oleylamine	31.4
Soap solution	25.0	Toluene	28.4	Glycerine	63.1
Olive oil	32.0	*m*-Xylene	28.9	*N*-Methyl-2-pyrrolidone	40.8
Acetone	23.7	Bromobenzene	36.5	Mercury	465

A strategy to reduce air bubbles is to initially wet the device with a liquid, such as alcohol, that has a lower surface tension. Then water can be fed in behind the other liquid without exposing any air/water interface. This reduces the force by a factor of around 3 due to surface tension that must be overcome to push air bubbles through a constriction. Therefore, the initial pressure to push the fluid flowing in microchannels is usually a little bit higher than the normal operation pressure if there exist lots of air bubbles in microdevices.

Because surface tension action is confined to the interface, it does not appear in the Navier–Stokes equations, which deal with pressure gradients within a bulk fluid. A total force $\gamma\, \mathrm{d}l$ will act on a surface line element $\mathrm{d}l$. If the surface line element is a closed loop and the surface tension is uniform, the net surface tension force acting on the loop is zero. If surface tension gradients are present, a net force on the surface element may distort it through an induced flow of surface liquid. Surface tension gradients can be increased from the presence of a surfactant.

2.4.3 Effect of Surfactants on the Surface/Interface Energy for Wetting

Surface/interface tension is a significant and useful force in microfluidic devices. A molecule in the bulk fluid experiences mutually attractive forces with neighboring molecules. Van der Waals forces are usually the most dominant, and for aqueous solutions hydrogen-bond forces are also significant. A molecule at the surface is attracted by a reduced number of neighbors. Therefore, it is in an energetically unfavorable state. The creation of a new surface is thus energetically costly, and fluids will act to minimize their surface area. This is the driving force for small volumes of fluids to form a spherical shape, as, for example, trickles of water or other continuous fluids breaking up into spherical drops by minimizing the total surface area. If U is the total cohesive energy per molecule in the bulk fluid, a halved value of $U/2$ for a molecule will be located at a flat surface. The surface tension created per unit area of surface is directly related to this cohesive energy reduction. Therefore, reducing the cohesive energy of a fluid favors to obtain smaller drops or bubbles since the surface tension is proportional to the curvature ratio (or $1/r$, r is the radius of sphere drops). This is the fundamental for the droplet microfluidic reactors.

Chemical compounds that can reduce the surface tension of a liquid are known as surfactants. Detergents, soaps, fatty acids, and fatty alcohols are common examples. They can be used to stabilize mixtures of oil and water, for example, by reducing the surface tension at the interface between the oil and water molecules. Their molecular structures often consist of a hydrophilic head and a hydrophobic tail group. Thus, their location at a free liquid surface can be energetically favorable. Gradients in surfactant concentration will result in surface tension gradients.

Like many technological processes, microfluidic processes also require control of liquid spreading over solid surfaces. By reducing the surface tension with surfactants, non-wetting materials can be made to become partially or completely wetting. The excess free energy (σ) of a drop on a solid surface is [108]

$$\sigma = \gamma S + \pi r^2 \gamma_{\mathrm{SL}} - \gamma_{\mathrm{SV}} \tag{2.69}$$

www.ebook3000.com

where γ is the liquid–vapor interfacial tension, γ_{SL} is the solid–liquid interfacial tension, γ_{SV} is the solid–vapor interfacial tension, S is the area of liquid–vapor interface, P is the excess pressure inside liquid, and r is the radius of droplet base.

Based on this equation, the excess free energy is minimized when γ decreases, γ_{SL} decreases, or γ_{SV} increases. Surfactants are absorbed onto the liquid–vapor, solid–liquid, and solid–vapor interfaces, which modify the wetting behavior of hydrophobic materials to reduce the interface free energy. When surfactants are absorbed onto a hydrophobic surface, the polar head groups face into the solution with the tail pointing outward. In more hydrophobic surfaces, surfactants may form a bilayer on the solid, causing it to become more hydrophilic. The dynamic drop radius can be characterized as the drop starts to spread. Therefore, the contact angle changes based on the following equation [108]:

$$\cos\theta(t) = \cos\theta_0 + (\cos\theta_\infty - \cos\theta_0)\left(1 - e^{\frac{-t}{\tau}}\right) \tag{2.70}$$

where θ_0 is initial contact angle, θ_∞ is final contact angle, and τ is the surfactant transfer time scale. As the surfactants are absorbed, the solid–vapor surface tension increases and the edges of the drop become hydrophilic, resulting in spreading of the drop.

2.4.4 Features of Surface and Interface in Microfluidics

The microstructures (e.g., microchannels, microcells) are the places for the mass and thermal exchange in the microdevices. Since specific surface areas of microstructures lie between 10 000 and 50 000 $m^2\ m^{-3}$, much higher than those of traditional reactors that are generally about 100 $m^2\ m^{-3}$ and in rare cases reach 1000 $m^2\ m^{-3}$, the effects of electrokinetic effect in microchannel (e.g., enhanced electric double layer on channel walls), wall slip and wall roughness, and other surface and interface effects on the fluid motion and the thermal transportation will be dominant in microfluidics [109–113]. The fluid mechanism in microfluidics may have some unique features related to the surface and interface. As the scale of space for materials is reduced to micrometer, there exist microscale mass and thermal transfer effects due to the surface- and interface-dependent flow status, which leads to reduced thermal conductivity with the film thickness decrease (e.g., the case of silica thin films in Table 2.9), and thermal conductors can become thermal insulators. As the ultrafast thermal exchange occurs, the micro effects will appear, leading to the temporal separation of temperature gradients and thermal vectors [28].

It is very important in the design and optimizes the structure of microdevices to realize their desired functions by deeply understanding the flow and thermal transfer characteristics in microchannels. In microfluidic reactors, mass transfer is mainly performed at microscale, and flow type is usually laminar flow. Mixing procedures are thus limited to diffusion and/or secondary flows. Increasing the interfacial contact between phases directly influences the overall mass transport coefficient, and the interfacial mass transport coefficient observed in a microreactor can range from 0.05 to 15 s^{-1} as compared with 0.001–0.02 s^{-1} in standard laboratory-scale bottle-batched reactors [114, 115]. Mixing times in microfluidic reactors can be down to several milliseconds that are generally smaller than

those in bulk reactors due to the small dimensions for mass diffusion. A nearly complete mixture can be achieved within a few seconds and often as little as a few milliseconds because chemical molecules have short paths to move.

Similarly, high heat-exchanging efficiency can be created in microfluidic reactors [116] due to their higher surface-to-volume ratio (specific surface areas) than in the bulk reactor [109–113]. Specific surface areas of microstructures lie between 10 000 and 50 000 $m^2\ m^{-3}$, while those of traditional reactors are generally about 100 $m^2\ m^{-3}$ and in rare cases reach 1000 $m^2\ m^{-3}$ [12, 109–113]. Since the heat transfer coefficient is inversely proportional to the channel diameter, the heat transfer coefficient in microdevices is significantly higher than that for traditional heat exchangers [116–118]. The high heat-exchanging efficiency allows for fast heating and cooling of reaction mixtures within the microstructures. Thus, heat can be applied and removed, creating a safe experiment environment at high temperature, improving the reactor efficiency at high temperature, which is not realized easily in bulk batch reactors.

Therefore, surface/interface features of the microstructures can significantly affect the mass and thermal diffusion and exchange among the continuous fluids, the formation of droplets, and the gas-separated segment flows.

2.4.5 Capillary Effects in Microfluidic Devices

In a sufficiently narrow capillary of circular cross section (radius: a), the interface between fluids and the capillary surface forms a meniscus that is a portion of the surface of a sphere and has radius r given by

$$r = a/\cos\theta \tag{2.71}$$

This geometrical relationship is shown in Figure 2.21. The contact angle θ depends on the free surface energies of the fluid and the capillary surface in contact.

The pressure jump ΔP across this surface is

$$\Delta P = 2\gamma/r \tag{2.72}$$

Since $r = a/\cos\theta$, the pressure difference can thus be given by Eq. (2.73):

$$\Delta P = 2\gamma\cos\theta/a \tag{2.73}$$

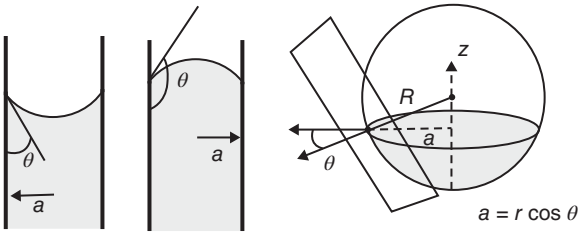


Figure 2.21 The contact angle θ between a sphere and a tangent plane is the angle between the normal to the sphere at the point of tangency and to the plane perpendicular to the z-axis. (Pethig and Smith 2013 [13]. Reproduced with permission of John Wiley & Sons.)

www.ebook3000.com

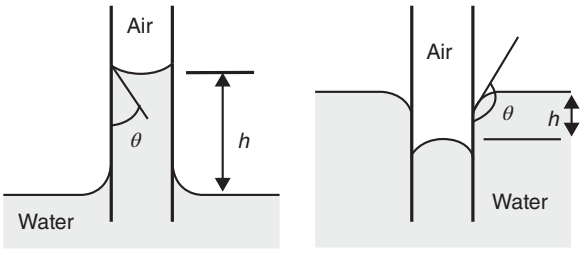


Figure 2.22 To maintain hydrostatic equilibrium, the capillary pressure is balanced by the height h of a fluid in a capillary. The height change depends on the magnitude of the contact angle. (a) The hydrophilic capillary wall; (b) the hydrophobic capillary wall. θ: the contact angle between the air phase and the water phase. (Pethig and Smith 2013 [13]. Reproduced with permission of John Wiley & Sons.)

To maintain hydrostatic equilibrium, the induced capillary pressure is balanced by a change in height (h) of the fluid. As shown in Figure 2.22, this height change can be positive or negative, depending on whether the contact angle is less or greater than 90°. At equilibrium we have the condition

$$2\gamma \cos\theta / a = h\rho g \tag{2.74}$$

where ρ is the density of the liquid in the capillary and g is the gravitational acceleration constant. From Eq. (2.74), we obtain the capillary height h as

$$h = 2\gamma \cos\theta / \rho g a \tag{2.75}$$

2.4.6 Droplet Formation in Microfluidics

In microfluidic process, the important and interesting phenomena as an entire consequence of the surface tension effect are the breakup of streams into drops, the so-called Plateau–Rayleigh instability, and particularly the droplet formation between immiscible fluids, where the surface/interface tension significantly affects the dynamics of the free surface and interface [14, 106].

Since the droplet generation technique is the heart of droplet-based microfluidics, the fundamental surface/interface kinetics and thermodynamics will be discussed for the overview of different droplet generation techniques based on the capillary interface action in microdevices. The interfacial instabilities underlying microfluidic droplet production will be analyzed with respect to the specific device geometries. The scaling of droplet sizes with respect to hydrodynamic models will be further discussed.

Kinetically, the explanation of this instability starts with the existence of tiny perturbations in the stream. These are always present, no matter how smooth the stream is. If the perturbations are resolved into sinusoidal components, some components grow with time, while others decay with time. Among those that grow with time, some grow at faster rates than others. Whether a component decays or grows and how fast it grows is entirely a function of its wave number

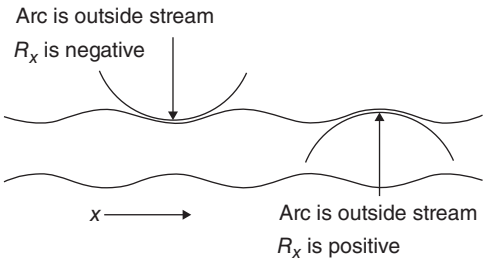


Figure 2.23 Intermediate stage of a jet breaking into drops. Radii of curvature in the axial direction are shown. Equation for the radius of the stream is $r(x) = r_0 + A_k \cos(kx)$, where r_0 is the radius of the unperturbed stream, A_k is the amplitude of the perturbation, x is distance along the axis of the stream, and k is the wave number.

(a measure of how many peaks and troughs per centimeter) and the radii of the original cylindrical stream, as shown in Figure 2.23 [106].

As the flow rate is suddenly increased to enhance the perturbation by the special design of the channel, as, for example, narrow the filament of the dispersed liquid down until pinch-off takes place (flow focusing), as shown in Figure 2.24, for the frequently used droplet generation device (the cylindrical jet). As the surface tension cannot keep the sinusoidal components continuously with the external energy entering into the continuous fluid, separated drops will be formed [119]. Clearly, surface tension plays an important role in microfluidic flows when immiscible free interfaces are present.

By injecting the first fluid (e.g., water) into a stream of the second immiscible fluid (e. g, oil) at the orifice of the cylindrical jet, droplets can be generated in the two-phase flows. Competing stresses drive the interface/surface tension to reduce the interfacial area, and viscous stresses act to extend and drag the interface downstream to cause the pinch-off effect. These stresses destabilize the interface to form droplets of radius (r) after the cylindrical jet.

Generally, there are three major steps involved in the droplet generation process, as outlined in Figure 2.24b. First of all, an interface must be created between the two immiscible liquids fed into the system. Initially, this is an interface between two single connected regions. It must therefore be considerably deformed in order to reach the final state, where the dispersed phase liquid fills many disconnected regions. Since the final state will be reached by decay from a deformed interface, there must be an intermediate state within the device with higher interfacial free energy than the final state, which spontaneously decays into the latter.

Clearly, considerable amounts of energy have been injected into the dispersion system as shown in Figure 2.24c to overcome the excess free energy of the interfaces for separating the dispersed phase from the continuous phase in the emulsion to form drops, which can be provided from the pumping. The energy change is sketched schematically in Figure 2.24c, where σ_i and σ_f correspond to the initial state and the final state, respectively. There will be an intermediate state with a higher energy level (σ_d) involved somewhere within the device. The solid thick arrow represents the energy fed from the system into the liquid interface, while the thin arrow represents the spontaneous decay into the dispersed state. The intermediate energy level (σ_d) corresponds to a saddle point in the total interfacial energy of the system (the dashed circle in Figure 2.24a and the dashed arrow in imagec).

These free energies may be defined by assigning to each "final" droplet with the total volume of V_1 surrounded in the suitable region of continuous phase

www.ebook3000.com

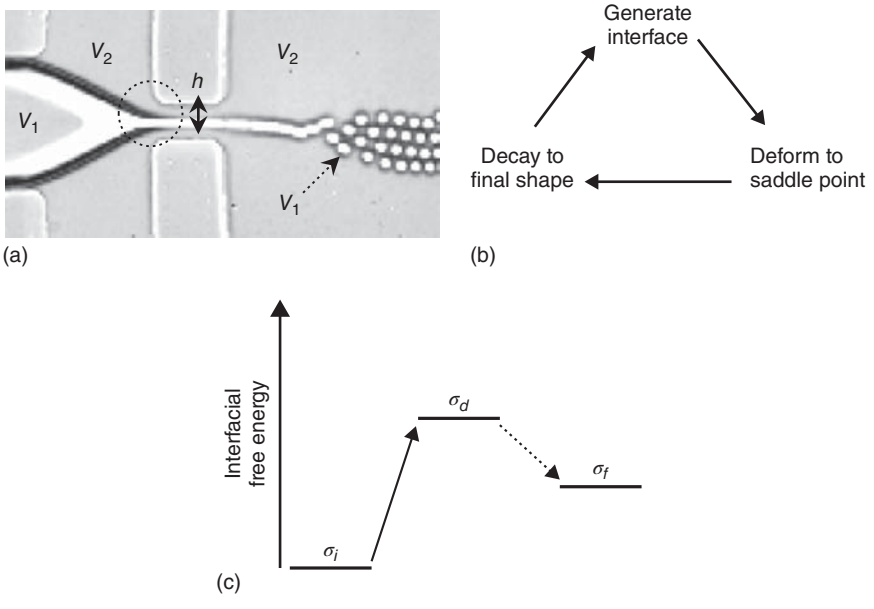


Figure 2.24 (a) Capillary instabilities in a microfluidic two-phase flow (V_1, phase 1 for drops; V_2, phase 2 as continuous supporting phase for drops, and h: the width of the injector). A stream of water flows in streams of oil and is geometrically focused into a narrow cylindrical jet. The jet is destabilized by the Rayleigh–Plateau instability forming small, monodisperse droplets. (Reprinted with permission from Ref. [119] Copyright 2003 AIP Publishing.) (b) Three-stage principle to generate a series of droplets of a liquid within a second (immiscible) liquid counter phase [15]. (c) The interfacial free energy change during the droplet formation from the initial status (σ_i) to the intermediate status with the highest energy level (σ_d) and to the final status with the energy (σ_f) between σ_i and σ_d [15]. ((b, c) Reprinted with permission from Ref. [15] Copyright 2012 IOP Publishing.)

with volume V_2, such that the total liquid in the channel on the right-hand side can be viewed as composed of many liquid elementary cells as indicated by the white dots. We define the interfacial free energies with respect to a state where all channels are filled with the liquid representing the continuous phase. According to the analysis of Seemann *et al*. [15], the free energy of a final state consisting of spherical droplets with radius r can be obtained as Eq. (2.76):

$$\sigma_f = 4\pi r 2\gamma = \gamma(4\pi)^{1/3}(3V_1)^{2/3} \tag{2.76}$$

where γ is the interfacial tension between the two liquids. For calculating the energy of the initial state, σ_i, the continuous phase liquid (V_2) has to be replaced with the dispersed phase liquid (V_1) in the corresponding channel on the left-hand side. The corresponding change in interfacial free energy is proportional to $(\gamma_1 - \gamma_2)$, where γ_i is the interfacial tension the liquid with index i makes with the channel wall. We then obtain for the initial energy, using Young's equation [103],

$$\sigma_i \gamma \cos\theta S_1 V_1 / A_1 \tag{2.77}$$

where θ is the contact angle the continuous phase makes at the channel wall of the injecting orifice in the presence of the dispersed phase. If there is no preference

of the walls for one or the other liquid, we have $\theta = \pi/2$ and thus $\sigma_i = 0$. S_1 and A_1 are the surface area and the volume, respectively, of the feed channel of the dispersed phase liquid. The ratio A/S of a channel is a length characterizing its size. For a circular tube as well as for a square channel, for example, it is equal to 1/4 of the channel width. The expression $S_1 V_1/A_1$ simply represents the interface that the volume V_1 forms with the wall of the inlet channel.

An estimate for the size of the droplets can be simply obtained by balancing the two stresses on the interface [120]. Capillary stresses of magnitude γ/r balance viscous stresses $\mu u/h$, resulting into a characteristic droplet size about r (Eq. (2.78)):

$$r = h\gamma/\mu u = h/Ca \tag{2.78}$$

Here the capillary number $Ca = \mu u/\gamma$ is used, a dimensionless parameter found whenever interfacial stresses compete with viscous stresses. An advantage of this strategy is that one can produce monodisperse droplets due to the deterministic nature of microfluidic flows.

Notably, the dynamics of flow-focusing bubble-forming systems is largely independent of *Ca* for both low-*Re* [121] and high-*Re* flows [122]. Geometric techniques have been used to create droplets of varieties of sizes and size distributions [123, 124]. This strategy has been used to study chemical reaction kinetics on millisecond time scales by injecting reactive chemicals together to form droplets [95, 124–126] and to develop a platform for protein crystallization [127]. Droplets are advantageous for this sort of study because reagents are not dispersed beyond the boundary of the drop. Detailed work on droplet-forming devices including studies of the rich variety of droplet patterns that are formed in channels can be referred to Refs [15, 119] and also Chapter 5 of this book.

2.5 Development of Driving Forces for Microfluidic Processes

Driving forces from external environments are the first key parameter to promote the function of mass and heat exchange in microfluidic devices besides the reaction potentials. There are several forces to drive fluids flowing through microchannels: body forces, surface tension forces, thermal fluctuation forces, electric field forces, photoinduced forces [3, 5, 22], magnetic forces [128, 129], acoustic induced forces [130, 131], and so on [14].

The body forces include centrifugal forces [132, 133], gravity forces [134, 135], and electrostatic forces [14, 136], which have been used in the microfluidic devices, described as follows. The centrifugal force can be equipped into the microfluidic devices simply by the disks controlled by a computer CD driver. The device design is shown in Figure 2.25. The centrifugal forces are expressed as

$$F_{\text{volume},\omega} = \rho\omega^2 r \tag{2.79}$$

where ω is the angular velocity of the disk, ρ is the density of the fluid, ř is the average distance of the liquid plug in the channel from the center of rotation, and

www.ebook3000.com

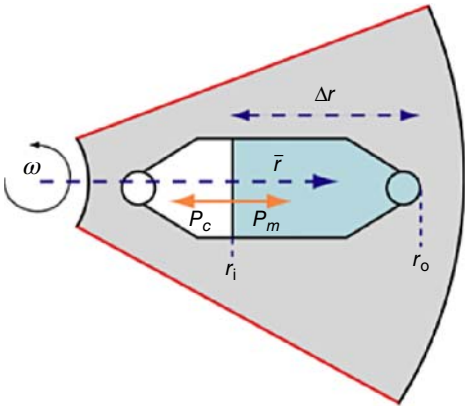


Figure 2.25 Schematic diagram of the forces acting on the microfluidic channel during rotation of the disk. The centrifugal pressure counterbalances the capillary pressure and two of them push the liquid in the opposite direction. (Adapted from Garcia-Cordero *et al*. 2010 [132]. Reproduced with permission of John Wiley & Sons.)

Δr is the radial length of the liquid plug. The apparent hydrostatic pressure in this microfluidic device created by the centripetal force at the start of the liquid plug is

$$P_{\mathrm{m}} = \rho\omega^2 \check{r}\Delta r \tag{2.80}$$

Δr and ř are defined as $\Delta r = r_0 - r_{\mathrm{i}}$, and $\check{r} = (r_0 + r_{\mathrm{i}})/2$.

The gravity force is expressed as

$$F_{\mathrm{volume},g} = \rho g \tag{2.81}$$

The gravity force can be equipped into the microfluidic devices just by the altitude of the fluid or the liquid height in the microfluidic devices.

The electrostatic forces are related to the electric field ($E(x)$) in the microdevices, which is one type of electric field forces. They can be expressed as

$$F_{\mathrm{volume},q} = \rho_q(x)E(x) \tag{2.82}$$

where ρ_q is the charge density and E is the spacing distance (x)-dependent electric field strength.

Electric field forces and photoinduced forces are the two main streams in the development of the driving forces, which will be discussed in detail in the following sections. Here we will focus on the surface/interface tension driving effects and some fluctuation forces used in microfluidics.

Several strategies for the manipulation of microfluidics using solid–liquid interface energy have been reviewed by Bain [137] and Squires and Quake [14]. Figure 2.26 gives one of the simplest examples: a long droplet of length L in a channel of radius r with an inhomogeneous surface – hydrophobic (with ${\gamma_{\mathrm{SL}}}^{\mathrm{L}}$) for $z < 0$ and hydrophilic (${\gamma_{\mathrm{SL}}}^{\mathrm{R}} > {\gamma_{\mathrm{SL}}}^{\mathrm{L}}$) for $z < 0$ [14, 138]. Thermodynamically, the droplet wants to move onto the hydrophilic surface to get the lowest potential, and moving with velocity u decreases the stored interfacial energy at a rate $\sim\Delta\gamma ru$, where $\Delta\gamma = {\gamma_{\mathrm{SL}}}^{\mathrm{L}} - {\gamma_{\mathrm{SL}}}^{\mathrm{R}}$. This energy is lost to viscous dissipation, which consumes a power $\sim\mu uL$ (μ: viscosity) when dissipation is dominated by the viscous shear in the bulk. Assuming the capillary energy released to be balanced by viscous dissipation, it gives $\mu u/\Delta\gamma = Ca = r/L$. Again, the capillary number

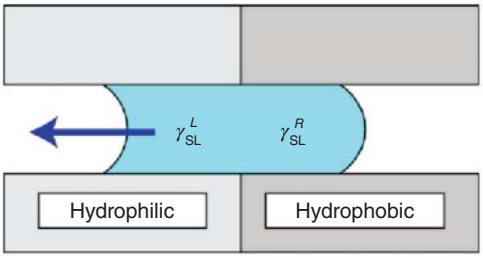


Figure 2.26 Droplet motion due to a gradient in solid–liquid interfacial energy. A droplet straddling hydrophobic and hydrophilic surfaces can release stored interfacial energy by moving further into the hydrophilic region [14, 138]. (Reproduced with permission from Ref. [14] Copyright 2005 American Physical Society.)

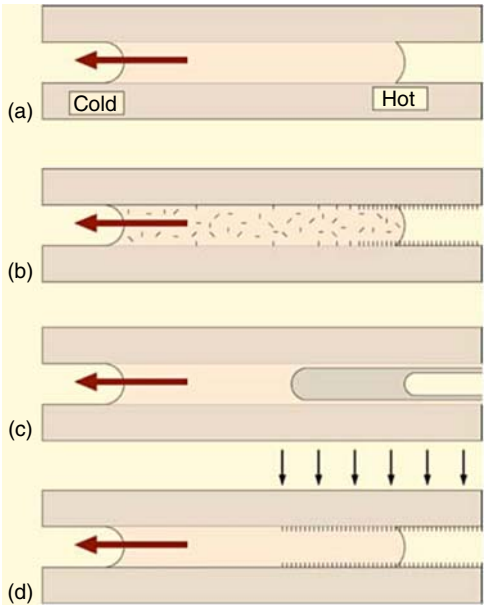


Figure 2.27 Driving droplet motion with gradients in solid–liquid interfacial energy driven by (a) thermal gradients, (b) droplets that contain a chemical that reacts to reduce surface wettability, (c) liquid bi-slugs that leave a coating film that lowers the overall surface energy, and (d) light-induced reactions that create wettability gradients. (Reproduced with permission from Ref. [14] Copyright 2005 American Physical Society.)

arises naturally because capillary stresses are balanced by viscous stresses. In this case, the droplet moves at a velocity $u \sim \Delta\gamma r/\mu L$.

In addition, Squires and Quake also summarize other driving forces in microfluidics produced by field fluctuation forces caused by thermal gradients, chemical reaction gradients, liquid bi-slugs, and light-induced reactions, as illustrated in Figure 2.27 [14].

2.5.1 Fundamental in Electrokinetic Methods for Microfluidics

Electrokinetic methods play an important role as driving forces in microfluidic processes, particularly in fluids with charged solutes for pumping, mixing, gradient generation, separation, sorting, and analysis on LC microdevices. These methods utilize electric fields as driving forces, including electroosmosis, electrophoresis, and dielectrophoresis.

Electrokinetically driven flows in microchannels are generally laminar because of the slow velocity and small characteristic length scale and thus small Reynolds number ($Re \ll 1$), which is problematic for situations requiring rapid mixing of different solutions in microchannels. In addition, electroosmosis flows are

www.ebook3000.com

not robust since they depend sensitively on the physicochemical properties of the solution (e.g., solution pH, ionic strength) and the channel walls (e.g., surface charge density and distribution, adsorption of solutes). Inhomogeneities in surface charge density will increase the pressure gradients of the flow and require large operation voltage. Electrochemical reactions at electrodes have to be suppressed by some methods to modify the electrode surface to avoid metallic ion injection, water electrolysis and the associated bubbles, and the introduction of pH or solute gradients. However, they have some significant advantages over conventional pressure-driven flow, such as pluglike velocity profile, ease of control and switch flow, and no mechanical moving parts. If the above issues can be addressed or not affects the goal of the microfluidic processes. Therefore, numerous endeavors have been introduced to overcome the slow mixing issue based on a variety of technologies such as piezoelectrics [139, 140], pneumatics [141], acoustic radiation [142], multiple voltage arrangements [143], and induced-charge electroosmosis (ICEO) as well as some electrokinetic mixing-based microstructure design (e.g., T-shaped mixers) [144, 145]. These electrokinetic-based mixing methods usually rely on the complex channel design, surface modification, and external voltage control to adjust the interaction of electric fields and the electric double layers or the charged solutes [20].

Aqueous solutions are electrically conductive due to the ubiquitous presence of dissolved ions (e.g., from dissolved salts, ionic groups on surfaces, or dissociated water molecules). Solid–liquid interfaces tend to develop surface charge, which attracts oppositely charged counterions and repels similarly charged co-ions. The resulting ionic double layer screens the surface charge over a characteristic Debye length λ_D (i.e., the screening length or the thickness of the electric double layer). With the exception of these charged double layers, the fluid is charge neutral.

The diffuse part of the double layer (Figure 2.28) is established when diffusive transport tending to smooth ion gradients balances electrostatic transport driving counterions toward the interface [146]. Ions in the solution with the number density ($n_{\pm}$) and the charge ($\pm q$) set up an electrostatic field ϕ obeying Poisson's equation (2.83) [14]:

$$\nabla^2\phi = -\frac{\rho_q}{\varepsilon_w} = -\frac{q(n_+ - n_-)}{\varepsilon_w} \tag{2.83}$$

where ε_w is the permittivity of the solution. Due to their small size, ions are highly mobile and respond quickly to the local electric field with potential ψ. In equilibrium, each ion is statistically distributed according to the Boltzmann distribution:

$$n_{\pm} = n_0 e^{\left(\mp\frac{q\psi}{k_B T}\right)} \tag{2.84}$$

where n_0 is the bulk concentration of ions. The fields are related by the mean-field assumption: the electrostatic potential ϕ set up by the ions (Eq. (2.83)) is assumed to be the same as the field ψ to which they respond (Eq. (2.84)). Combining Eqs (2.83) and (2.84), the nonlinear Poisson–Boltzmann equation (2.85) can be obtained:

$$\nabla^2\frac{q\phi}{k_B T} = k^2 \sinh\left(\frac{q\phi}{k_B T}\right) \tag{2.85}$$

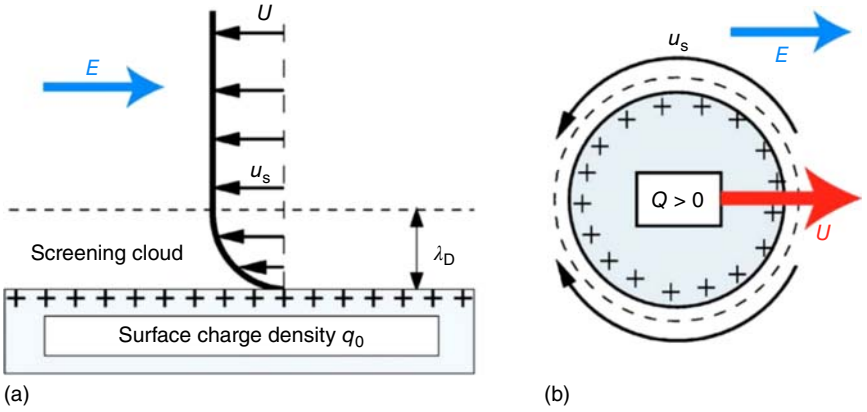


Figure 2.28 (a) An ionic screening cloud of width $\sim\lambda_D$ forms around a charged solid surface in an electrolytic solution. An external electric field forces the mobile ions in the screening cloud to result in electroosmotic flow (Eq. (2.89)). (b) Under an applied electric field, a freely suspended charged particle in an electrolyte moves via electrophoresis, with velocity equal in magnitude and opposite in direction to Eq. (2.89). (Squires and Bazant 2004 [146]. Reproduced with permission of Cambridge University.)

which can be linearized for small potentials ($\phi \ll k_B T/q \approx 26\,\text{mV}$), giving

$$\nabla^2\phi = \frac{\phi}{\lambda_D^2} \tag{2.86}$$

$$\lambda_D = \sqrt{\frac{\varepsilon_w k_B T}{2n_0 q^2}} \tag{2.87}$$

Table 2.16 gives typical screening lengths (λ_D) of water and some aqueous electrolytic solution. Water dissolves salts so well because its small polar molecules form hydration shells around ions that enforce this separation; nonpolar solvents do not and thus have much lower conductivities [147]. Notably, even pure water (pH = 7) has only a 1.0 µm screening length. Typical aqueous screening lengths are ~1 nm, much smaller than typical device dimensions.

In addition, the applied electrical potential in the liquid ϕ_e is also governed by Laplace's equation in the equilibrium states [20], where $\nabla^2\phi_e = 0$ with the

Table 2.16 Ion densities and the screening lengths (λ_D) for water and aqueous electrolytic solutions of varying salt concentration at 20 °C.

Concentration	Ion density (ions nm^{-3})	λ_D (nm)
0.1 µM (pure, pH 7)	6×10^{-8}	1000
1 mM	6×10^{-4}	10
100 mM	0.06	1.0
1000 mM	0.6	0.3

Source: Squires and Quake 2005 [14]. Reproduced with permission of Reviews of Modern Physics.

www.ebook3000.com

boundary conditions: $n\nabla\phi = 0$ at channel wall, $\phi = \phi_0$ at inlet, and $\phi = 0$ at outlet [148].

The equations governing incompressive liquid flow are the Navier–Stokes equation and the continuity equation given as

$$\rho\left[\frac{\partial\overline{u}}{\partial t} + \overline{u}\nabla\overline{u}\right] = -\nabla P + \mu\nabla^2\overline{u} + \overline{E}\rho_q \tag{2.88}$$

where ū is the velocity vector, ∇P is the pressure gradient, μ is the viscosity, ρ is the density of the fluid, ρ_q is the local net charge density, and $\bar{\mathrm{E}} = -\nabla\phi_\mathrm{e}$ is the local applied electrical filed strength. Since the local net charge density is not zero only in the electric double layer (EDL), the driving force for electroosmotic flow (EOF), $\bar{\mathrm{E}}\rho_q$, exists only in EDL.

The standard electrokinetic flow involves the interaction between an external-operated electric field and the electric double layer near a nonconducting surface with fixed electric charge either from solutes or from channel walls. It is usually to form dipole-induced double layers in the liquid. The nonzero charge density in the diffuse layer gives rise to an electric body force (Eq. (2.82)) tangent to the surface. The resultant electrokinetic flow appears to slip outside the screening layer and the slip flow velocity varies proportionally to the local tangential electric field $E_{\|}$ given by the Helmholtz–Smoluchowski formula in the one-dimensional model [149]:

$$u = -\frac{\varepsilon_\mathrm{w}\xi_\mathrm{i}}{\mu}E_{||} \tag{2.89}$$

where ε_w and μ are the dielectric constant and the viscosity of the liquid. This equation means that when channel walls comprise the solid–fluid interface, EOF is driven with a velocity that varies linearly with the applied field.

If there exists an induced-charge electrokinetic flow, the velocity is not dependent on the electric field linearly because of the dependence of the local induced zeta potential ζ_i on the local electric strength $E_{\|}$, as shown in Eq. (2.90). In the conventional case, the Helmholtz–Smoluchowski formula will be changed back to Eq. (2.89) according to the Stokes equations [14]:

$$u = -\frac{\varepsilon_\mathrm{w}\xi_\mathrm{i}}{\mu}E_{||}(1 - e^{-x/\lambda_\mathrm{D}}) \tag{2.90}$$

where x is the distance from the channel wall. This equation represents a fluid velocity that exponentially approaches Smoluchowski's constant slip velocity outside of the diffuse layer.

When the charged solid–fluid interface is a freely suspended particle, electroosmotic slip causes the particle itself to move electrophoretically (Figure 2.28b) with velocity as follows:

$$u = -\frac{\varepsilon_\mathrm{w}\xi_\mathrm{i}}{\mu}E_{||} = \mu_\mathrm{E}E_{||} \tag{2.91}$$

Several rather surprising results hold in the limit where the double layer λ_D becomes thinner compared with the particle size. The electrophoretic mobility μ_E for an object with fixed ζ is independent of particle size, shape, or number.

Multiple particles of the same zeta potential (but possibly different shape and size) experience identically zero interaction, and the fluid flow is parallel everywhere to electric field lines [150, 151]. Finally, the electrophoretic mobility of a particle is independent of its dielectric constant [152].

The concentration field of electrolytes or other chemical components in such as an EOF can be described by Eq. (2.92):

$$\frac{\partial C}{\partial t} + (\overline{u} + \overline{u}_{\mathrm{ep}})\overline{\nabla} C = D\nabla^2 C \tag{2.92}$$

where C is the concentration of the species, D is the diffusion coefficient of the species, and $\bar{u}_{\mathrm{ep}}$ is the electrophoretic velocity of the species. In most microfluidic applications, electroosmotic velocity is on the order of $1\,\mathrm{mm\,s^{-1}}$, and the diffusion coefficient of most simple electrolytes is approximately $1.0 \times 10^{-10}\,\mathrm{m^2\,s^{-1}}$. It can be found that the order of magnitude of the convection term in Eq. (2.92) is approximately 1000 times that of the diffusion term. Therefore, the flow field should give a good indication of the concentration field, consequently a basic understanding of the mixing effectiveness. Generally, the stronger the local flow circulation is, the better the mixing is. Thus, it can be expected that the flow circulation resulted from the induced nonuniform zeta potential on the conducting hurdle surfaces can greatly enhance the species mixing.

The previous discussion gives us the classic electrokinetic description, in which homogeneous surfaces possess a constant surface charge–zeta potential. Interesting and useful phenomena can arise in some actual systems with inhomogeneous zeta potentials. Currently, there are three main inhomogeneous systems designed for efficient mixing in microfluidics: (i) systems with patterned surface charge, (ii) systems whose surface charge can be actively controlled, and (iii) systems with nonlinear induced-charge electrokinetic (ICEK) flows that occur when applied fields act on the charge clouds that are induced around polarizable surfaces. There should be some variations of the previous equations on this theme as treating these actual flows, such as one ICEK flow system where the electric field that is suddenly applied across an electrolytic solution containing a conducting post initially intersects the post at right angle to satisfy the equipotential condition. In the steady state of the ICEK system, the induced zeta potential is dipolar, with magnitude $\zeta_{\mathrm{i}} \approx E_0 r$ representing the potential drop of the field E_0 over the post size r. Using Eq. (2.89), an ICEO slip velocity is established with magnitude $U_{\mathrm{ICEO}} \approx \varepsilon_{\mathrm{w}} {E_0}^2 r/\mu$.

Time scale is also an important parameter to screen the mixing using electrokinetic forces. One main key advantage in ICEK systems is that the alternating current (AC) fields can be established without electrochemical reactions, so long as the frequency is low enough that induced-charge clouds have time to form, but fast enough that electrodes and the fields they establish are not screened. The time scale required for an induced-charge cloud to form around a conducting body is given by Eq. (2.93):

$$\tau_{\mathrm{c}} \approx \lambda_{\mathrm{D}} r / D_{\mathrm{i}} \tag{2.93}$$

where D_{i} is the diffusivity of the ions. This represents the resistor/capacitor (RC) time for an equivalent circuit (similar as the charge/discharge time of RC circuits)

www.ebook3000.com

consisting of a charge cloud capacitor and a bulk resistor [146, 153–155]. Similarly, the time scale over which the electrodes themselves are screened is given by

$$\tau_c \approx \lambda_D r / D_i \tag{2.94}$$

where L is the separation between electrodes [156–159]. Thus, ICEK applications allow closely spaced electrodes to be used, so that higher fields can be established using low applied voltages.

The previous equations and the matching boundary conditions for flow and concentration fields can be currently solved numerically using the nonlinear finite element solver of COMSOL Multiphysics, FLUENT, MATLAB, or other fluid mechanics simulation software (e.g., FIDAP, CFX, FLOW-3D, STAR-CD, PHOENICS, ADINA).

2.5.2 Basic Principles of Magnetic Field-Coupled Microfluidic Process

Since the solutes (ions, molecules, or charged and magnetic particles) in the fluids usually are charged or are themselves magnetic ions, their motion in microchannels is definitely affected by external magnetic fields. Similar to fluids in microchannels actuated by homogeneous or inhomogeneous electric field, magnetic fields can be coupled with the microfluidic devices either in the field-controlled synthesis [160], rapid mixing [161], or sorting of droplets containing magnetic particles for chemical or biological analysis [128, 129] under applied external magnetic fields. Placing some magnetic particles in fluids (e.g., ferrofluids) or droplets (e.g., magnetic bubbles) allow us to manipulate fluids or droplets on demand as the fluids or droplets follow the included magnetic fields, either in synthesis or in the analysis. The following is some fundamental consideration on the magnetic field-controlled microfluidic processes.

Magnetic field is the magnetic effect of electric currents and magnetic materials and at any given point is specified by both a *direction* and a *magnitude* (or strength). Clearly, it is a vector field [162]. The term is used for two distinct but closely related fields denoted by the symbols $\overline{B}$ and $\overline{H}$, where $\overline{H}$ is measured in units of amperes per meter (symbol: A m^{-1} or A/m) in the SI. $\overline{B}$ is measured in teslas (symbol: T; note that although the symbol is capital T, "tesla" is written in lower case in the SI system) and newtons per meter per ampere (symbol: N m^{-1} A^{-1} or N/(m·A)) in the SI. It is most commonly defined in terms of the Lorentz force that exerts on moving electric charges. Magnetic fields can be produced either by moving electric charges or by the intrinsic magnetic moments of elementary particles associated with a fundamental quantum property or their spins [162].

The magnetic field is defined by the force it exerts on a moving charged particle. It is well known that a particle of charge q in an electric field $\bar{E}$ experiences a force $\overline{F} = q\overline{E}$ and when a charged particle moves in the vicinity of a current-carrying wire, the force depends on the velocity of that particle. The velocity-dependent portion can be separated out such that the force on the particle satisfies the *Lorentz force law*:

$$\overline{F} = q(\overline{E} + \overline{v} \times \overline{B}) \tag{2.95}$$

where $\overline{v}$ is the particle's velocity and "×" denotes the cross product. The vector $\overline{B}$ is termed the magnetic field, and it is *defined* as the vector field necessary to make the Lorentz force law correctly describe the motion of a charged particle.

A charged particle moving in a $\overline{B}$ field experiences a sideways force that is proportional to the strength of the magnetic field, the component of the velocity that is perpendicular to the magnetic field, and the charge of the particle. This force is known as the Lorentz force and is given by Eq. (2.96):

$$\overline{F} = q\overline{v} \times \overline{B}) \tag{2.96}$$

The Lorentz force is always perpendicular to both the velocity of the charged particle and the magnetic field that creates it. When a charged particle moves in a static magnetic field, it traces a helical path in which the helix axis is parallel to the magnetic field and in which the speed of the particle remains constant. Because the magnetic force is always perpendicular to the motion, the magnetic field cannot do work on an isolated charge. It can only do work indirectly, via the electric field generated by changing magnetic field.

Up to now, the magnetic field-controlled microfluidic synthesis process is still under development while some progresses has been achieved in the active mixing [163] and the sorting of droplets containing magnetic particles [128, 129]. Stabilized suspensions of superparamagnetic colloidal particles in a liquid carrier phase exhibit a high magnetic permeability [128]. In the presence of an inhomogeneous magnetic field, such a ferrofluid will flow into the direction of increasing magnetic field strength. Similar to dielectrophoresis, the ferrofluid droplets can be directed into a desired direction by applying an inhomogeneous magnetic field whose field strength can be varied [129, 163, 164]. A ferrofluid can also be used as the continuous phase. In this case, the droplet manipulation is indirect as the continuous phase will locally form a barrier in a microfluidic channel at the position of highest magnetic field strength and the droplets will react to the local variation in the channel geometry [165]. In the example shown in Figure 2.29, the ferrofluid forms a geometric barrier for the arriving droplets and forces them to move into one of the channels of a Y-junction [15, 165].

Our recent results indicate that the magnetic and optical properties of nanoparticles can be significantly tuned by the external magnetic field (<150 Oe) during their formation, such as the redshift and enhanced intensity for the FeZnSe nanocrystals and the enhanced saturation and anisotropy in the FeZn nanocrystals [160]. The devices for this field controlled are described in Figure 2.30.

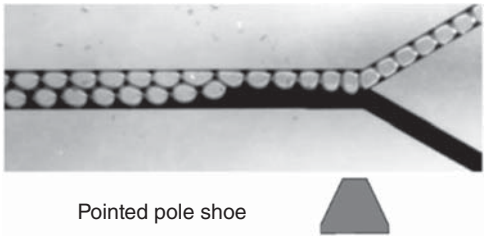


Figure 2.29 Droplet redirected by clogging one channel of a Y-junction with a plug formed by the continuous ferrofluid by externally applying an inhomogeneous magnetic field [15, 165]. (Reproduced with permission from Ref. [165], Copyright 2008 Royal Society of Chemistry.)

www.ebook3000.com

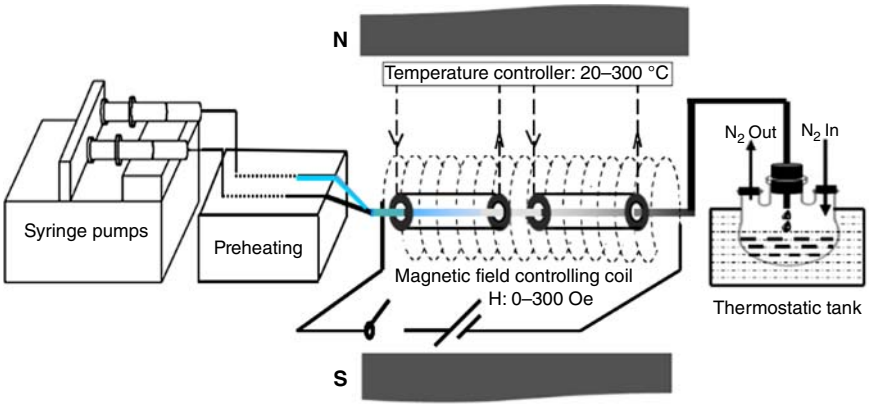


Figure 2.30 Magnetic field-coupled microfluidic process for materials synthesis with two orthogonal magnetic fields with strength tunable from 0 to 300 Oe [160] (N: the north pole of the magnetic field; S: the south pole of the magnetic field).

2.5.3 Basic Principles in Optofluidic Processes for Microfluidics

Conversion of light energy to liquid motion has proven to be a new arena for the actuation of microfluidic systems by using optical forces (through radiation pressure and optical tweezers) [3, 166, 167]. Optical force driving microactuation is featured by their contactless spatial (micrometric focusing spots) and temporal (ultrafast, depending on the light time) control, dynamical reconfiguration, and unnecessary dedicated microfabrication [22]. Contrary to classical total microanalysis systems, which are generally constrained to perform predesigned tasks, these optical processes proved to be very powerful in manipulating suspensions in a single fluid phase via optical forces, including pumping [168–170], sorting [171, 172], conveying [173], and propelling [174]. Moreover, this combination of optics and microfluidics, called optofluidics [166], has become an emergent research field offering an unprecedented level of integration for building a new generation of optically actuated microdevices, merging optical reconfigurability, the softness of fluid, smoothness of fluid interfaces, and compactness [22, 175–178]. Besides the optical forces, light modulation of electrical actuation (optoelectrowetting and photocontrol of EOF) and light-induced capillary forces have been developed in the manipulation of very small amount of liquids in recent years [3, 22].

It is still in the infant stage toward the "total optical lab-on-a-chip" and contactless digital microfluidics even though lots of achievements in the optical manipulation devices have been obtained for these purposes, such as optical switching [179] and splitting [167], adaptive lensing [166, 180], interferometry [181] and lasing [11, 182], and combination of acoustic and optical manipulation of fluids [183].

In microfluidics, this technique is usually aimed at extending the concept to the optical manipulation of fluids or digital microfluidics (e.g., droplet microfluidics). It is indeed appealing to investigate how far light can (or cannot) be used to build

channels, induce flows, drive droplet formation, and finally actuate droplets in channels. First, some earlier theoretical developments on optical pressure have to be considered [184]: the first motivation of Ashkin and Dziedzic was to determine in which direction the bending or deformation of a fluid interface separating two dielectric liquids with different refractive indices occurs [185]. The light propagating through the liquid–liquid interface or air–liquid interface causes a small deformation of the interface, which is brought about by the discontinuity of the light momentum between them. From this theory, the laser light wave can couple to a liquid interface and drive its bending or deformation that can become unstable and even trigger a liquid jet emitting microdroplets periodically as the deformation is large enough or forming light-induced jetting [22].

As shown in Figure 2.31a, light with the beam intensity I per unit area is assumed traveling from one medium with refractive index (n_1) and density (ρ_1) to another medium with n_2 and ρ_2, separated by an interface that has been deformed by the general force effects from the light pressure, gravity (g), and interface tension (σ) [186]. The light momentum is proportional to the refractive index of the medium, and the discontinuity at the interface generates the light pressure Π_{Rad}, which can deform the interface. Since the momentum carried by the incident propagating light depends on the refractive index, it is not conserved when the beam travels from one to the other dielectric medium, and the resulting discontinuity produces a radiation pressure applied to the interface, as locally schemed in Figure 2.31b. Considering the Minkowski formalism [187], its expression can be given as

$$\Pi_{\text{Rad}} = n_2 \cos^2\theta_2 \left[1 + R(\theta_2, \theta_1) - \frac{\tan\theta_2}{\tan\theta_1} T(\theta_2, \theta_1)\right] \frac{I}{c} \tilde{n} \tag{2.97}$$

where I is the beam intensity, ñ is the outward unit normal on the surface, c is the light speed, and $R(\theta_2, \theta_1)$ and $T(\theta_2, \theta_1) = 1 - R(\theta_2, \theta_1)$ are the classical reflection and transmission Fresnel coefficients in electromagnetic energy, respectively.

Consequently, Π_{Rad} is always normal to the interface. Moreover, by considering the expressions of the reflection and transmission coefficients $R(\theta_2, \theta_1)$ and $T(\theta_2, \theta_1)$ [188], it can be easily deduced that the optical radiation force Π_{Rad} is always directed toward the dielectric medium of the lowest index of refraction (n_1). This means that interface bending does not depend on beam propagation, and the main reason for that is that a photon gains momentum when passing from a low to a large refractive index medium.

Considering that the radiation pressure can be balanced with the gravity and the Laplace force of the curved interface (Figure 2.32a), the displacement of the interface $h(r)$ is given by [186]

$$\Pi_{\text{Rad}}(r) = (\rho_1 - \rho_2) g h(r) - \sigma \nabla^2 h(r) \tag{2.98}$$

where $\nabla^2 h(r) = \hat{\text{H}}(r)$, or the interface double mean curvature in cylindrical coordinates [190]. Equation (2.98) shows that the height of the deformation results from the balance between radiation pressure $\Pi_{\text{Rad}}(r)$ (Eq. (2.97)) and both buoyancy $(\rho_1 - \rho_2) g h(r)$ and Laplace pressure $-\sigma \hat{\text{H}}(r)$. Then Eq. (2.99) can

www.ebook3000.com

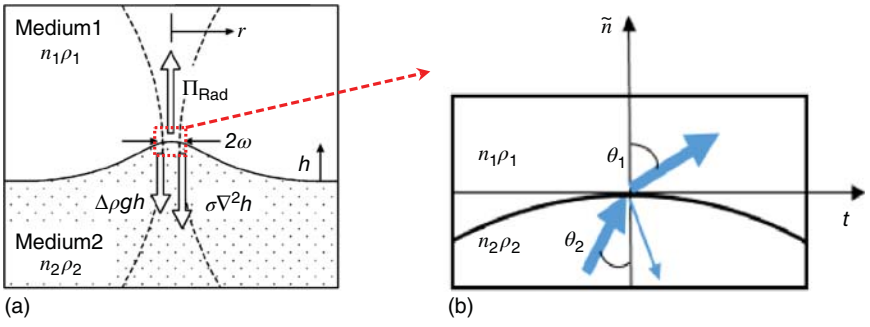


Figure 2.31 (a) Three kinds of force at the interface between two liquids with different refractive indexes and densities; Π_{Rad} is the light pressure, $\mu\nabla^2 h$ is the Laplace force, and ρgh is the gravity force. The density of the medium 1 is less than that of the medium 2, or $\rho_1 < \rho_2$. (Reproduced with permission from Ref. [186], Copyright 2004 Royal Society of Chemistry.) (b) Schematic representation used for the calculation of the radiation pressure exerted by a laser beam on an interface separating two dielectric fluids characterized by the indices of refraction n_2 and n_1. The angles of incidence and transmission are, respectively, (θ_2) and (θ_1), where t and n are the tangent and the normal directions at the location where the beam impinges the interface [22].

be obtained:

$$(\rho_1 - \rho_2)gh(r) - \frac{\sigma}{r}\frac{\mathrm{d}}{\mathrm{d}r}\left(\frac{r\hat{H}(r)}{\sqrt{1+\hat{H}(r)^2}}\right) = \frac{n_2 I(r)}{c}\cos^2\theta_2\left(1 + R - \frac{\tan\theta_2}{\tan\theta_1}T\right) \tag{2.99}$$

The incidence and transmission angles θ_1 and θ_2 can be related to the shape of the deformation. Using the expression of R and T at normal incidence for weak deformations with linearized curvatures, as shown in Figure 2.32b, Eq. (2.99) reduces to

$$\Pi_{\mathrm{Rad}}(r) = (\rho_1 - \rho_2)gh(r) - \sigma\Delta_{\mathrm{r}}h(r) = \frac{2n_1 I(r)}{c}\left(\frac{n_1 - n_2}{n_1 + n_2}\right) \tag{2.100}$$

where

$$I(r) = \frac{2I_0}{\pi w^2}\exp\left(-\frac{2r^2}{w^2}\right) \tag{2.101}$$

where I_0 is the intensity of the incident light, w is the half width of the light beam at the relevant interface, and r is the distance from the center to the laser beam.

For the axially symmetric configuration, an arbitrary function can be expanded as the sum of the zeroth-order Bessel function. In this case, the interface is deformed symmetrically on the interface plane, and the displacement $h(r)$ is written as

$$h(r) = \Pi_0\int_0^\infty \frac{kJ_0\exp(-w^2k^2/8)}{\sigma k^2 + g\Delta\rho}\mathrm{d}k \tag{2.102}$$

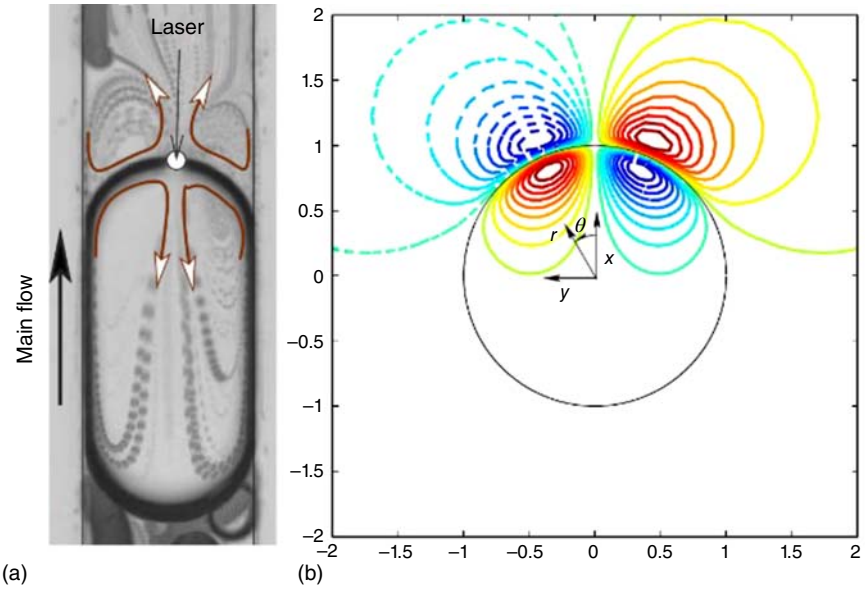


Figure 2.32 (a) Overlay of 100 images from a video sequence showing the motion of seeding particles near the hot spot. Note that the motion along the interface is directed toward the hot spot. (b) Stream function contours obtained from the depth-averaged model. Dashed and continuous contours indicate counterclockwise and clockwise flows, respectively. (Baroud *et al*. 2007 [189]. Reproduced with permission of American Physical Society.)

where J_0 is the zeroth-order Bessel function, k is the wave number of the laser beam, and $\Delta\rho = \rho_1 - \rho_2$, Π_0 can be calculated as

$$\Pi_0 = \frac{I_0}{c\pi} \times \frac{n_1 - n_2}{n_1 + n_2} \tag{2.103}$$

Equations (2.102) and (2.103) suggest that the displacement of the liquid interface is proportional to the laser intensity and is, approximately, inversely proportional to the interfacial tension. The precise measurement of the interface deformation gives information on the properties of the liquid interface, such as the interfacial tension or the viscosity near the interface. The typical form of $h(r)$ calculated with the actual experimental parameters for the pure water surface is raised up by ~10 nm, and the curvature at the area of laser beam irradiation is convex under a pump laser with the wavelength of 532 nm, w of 30 μm, and I_0 of 500 mW.

While for a beam from the liquid with a small refractivity n_1 to the liquid with a large refractivity n_2, a continuous transition from a bell to a nipple-like shape of increasing pedestal can be observed, as shown in Figure 2.32b. The morphology is totally different when the beam propagates in the reversed direction, from the large to the small refractive index fluid [191]. The deformation height deviates from the linear regime (shown by the dashed line) for increasing incident beam power and diverges at some well-defined beam power threshold $P_{\uparrow}$. Above this instability threshold, a beam-centered stationary liquid jet forms, which emits

www.ebook3000.com

droplets at its tip. Once the jet is formed, droplets are continuously shed at the tip. Since the index of refraction of the droplet is larger than that of the surrounding fluid, the beam automatically traps them. This brings directionality in the emission and transport of droplets that can be actuated by tilting the beam.

Thus, the liquid jets can be produced and stabilized by light pressure that can control the surface and interface tension. However, this surface or interface force always applies normally to interfaces and thus is unable to explain the fluid flow inside the structure at the origin of the droplet shedding at the jet tip or the fluid accumulation at the bottom of liquid channels. A bulk effect is required in the absence of tangential forcing. Radiation pressure is nonetheless known to push suspended particles, as demonstrated by optical levitation [192], because light momentum changes direction when it is elastically scattered by the particles. This momentum change results in a scattering force applied to the particle. As a macroscopic consequence, the photon momentum lost during the beam propagation in a suspension of nanoparticles is transferred to the fluid by momentum conservation. Light is therefore able to drive bulk flows in liquid suspensions and emulsions.

If the laser intensity is modulated at the frequency ω, the displacement of the interface varies in time and excites the interfacial waves with various wave numbers. The radiation pressure of the modulated laser is given by

$$\Pi_{\mathrm{Rad}}(r,t) = \frac{4\Pi_0}{w^2}\exp\left(-\frac{2r^2}{w^2}\right)\exp(i\omega t) \tag{2.104}$$

The displacement of the interface around $r=0$ is represented as a function of time (t) as

$$h(r,t) = \frac{\Pi_0}{\rho}\int_0^\infty \frac{k^2 J_0 \exp(-w^2k^2/8)\exp(i\omega t)}{\omega^{*2}-\omega^2}\mathrm{d}k \tag{2.105}$$

where ω^* is the characteristic frequency of the interfacial wave and given by the following dispersion relation with the wave number k:

$$(i\rho_{\mathrm{tot}}\omega^* + 2\mu k^2) + \rho_{\mathrm{tot}}(\sigma k^3 + \Delta\rho g k) = 4\mu^2 k^4\left(1+\frac{i\rho_{\mathrm{tot}}\omega^*}{\mu k^2}\right)^{1/2} \tag{2.106}$$

where ρ_{tot} is the sum of the two densities and μ is that of the viscosity [193, 194].

Within a "total optical lab-on-a-chip" framework, the radiation pressure of a laser wave is able to drive large-scale flows with flow rates of several hundreds of cubic micrometer per second using scattering forces. Such light-induced flows should exist whenever fluids have spatial variation in the refractive index, such as in nanocolloidal suspensions [186].

The deformation of the interface, however, is very weak on classical interfaces since the bulk and surface optical forces are usually too weak to counteract hydrodynamic forces acting on fast moving droplets, usually in the pN range calculated by Eq. (2.97), leading to a very low flow rate that is not enough for practical applications [22, 190, 195]. An optical alternative is based on the production of localized thermocapillary stresses, known as the Marangoni effect, on the drop interface [196]. In the presence of a surfactant, the thermocapillary forces can be in the μN range [189].

Thermocapillary forcing is usually associated with the temperature-dependent interfacial tension $\sigma(T)$ between two immiscible fluids. The highly focused laser spot with a resolution about several micrometers square or less can produce a thermal gradient in the droplets in a carrying fluid within a channel. This thermal gradient will produce an interfacial tension gradient ($\partial\sigma/\partial T > 0$) due to the temperature gradient, which will consequently induce a viscous stress in both fluids [22, 189]. It results in an interfacial flow, directed toward the area of the largest interfacial tension both inside and outside the drop (U_{Th}). Considering mechanical momentum conservation, the droplet will move in the opposite direction ($\tilde{U}_0$). In an unbounded fluid, the thermocapillary migration of a droplet is given by the following expression (Eq. (2.107)) [196]:

$$U_{\mathrm{Th}} = -\frac{2}{2\mu_{\mathrm{o}} + 3\mu_{\mathrm{i}}} \left(\frac{\partial\sigma}{\partial T}\right) \frac{r}{2 + \Lambda_{\mathrm{i}}\Lambda_{\mathrm{o}}} \nabla T \tag{2.107}$$

where r is the droplet radius, $\mu_{\mathrm{o,i}}$ and $\Lambda_{\mathrm{o,i}}$ are shear viscosities and thermal conductivities, and the subscripts i, o denote the fluids inside and outside the drop. Equation (2.107) shows that U_{Th} depends on the thermal gradient and not the temperature directly. Then, even weak, an overheating may drive efficiently thermocapillary flows if the thermal gradient is large, as usually happens with laser light. Moreover, since thermocapillary flows have an interfacial origin, they are particularly suitable to drive flows at small scales where surface effects dominate bulk behaviors, as in microchannels. Such a thermal gradient can be induced by laser, when light is partially absorbed by one of the two fluids.

Laser heating can not only produce thermocapillary effects for fluid actuation but also produce active and precisely localized mixing in ultrasmall areas (several micrometer squares or less) [189]. In addition, this optical method does not need complex microstructure packaging and use complicated external power sources as in the conventional fluid actuation methods, such as heat convection differential pressure, ultrasonic actuation, magnetic actuation, or electrokinetic pressure [197]. Laser heating has shown a new insight in the precise spatial and temporary resolved active mixing. It has the following four advantages [198]: (i) laser waves can easily be focused over spatial scales in the typical range of microchannels; (ii) laser heating is contactless and thus does not need any complex packaging or patterning of heating elements; (iii) laser heating is totally reconfigurable in terms of input energy (beam power), spatial extension (beam waist), duration (chopping), and positioning within the channel in a very fast way (compared with hydrodynamic time scales); and finally (iv) multi-actuation is also easy to implement using spatial light modulators and/or galvanometric mirrors.

Baroud *et al.* have shown us the first step toward thermocapillary mixing in microchannels (local heating by a continuous argon-ion laser with wavelength in vacuum $\lambda_{Ar+} = 514$ nm, in the TEM00 mode, focused inside the channel through $a \times 5$ or $\times 10$ microscope objective to a beam waist $\omega_0 = 5.2$ or 2.6 µm, respectively), as illustrated in Figure 2.32a. A water drop flowing in a 140 µm wide channel at a few millimeters per second is blocked by the laser due to thermocapillary stresses. For pure liquids, the direction of the Marangoni flow along the interface is directed from the hot (low surface tension to the cold) high surface tension regions. However, the flows in their experiments point toward the laser along the

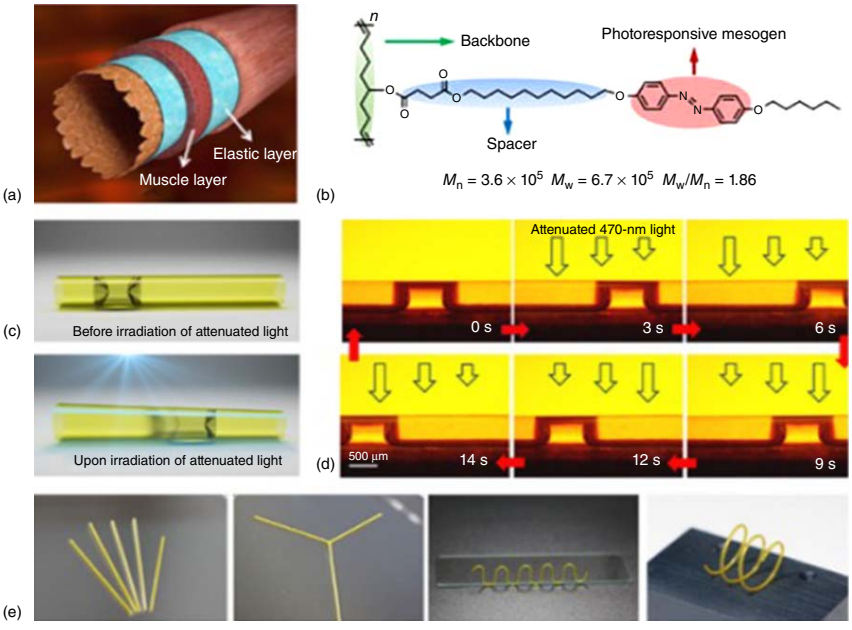
www.ebook3000.com

interface, indicating an increase of surface tension with temperature. Consistent with previous studies, their experiments also suggest a linear increase of surface tension with temperature in the presence of surfactants. Using tracer particles in both fluids, convection rolls inside and outside drop can be clearly observed due to the presence of the laser beam. The tracer velocity at the beam location can reach 11 mm s^{-1}. The presence of rolls inside and outside the drop illustrates the procedure to perform thermocapillary mixing in both fluids. Indeed, a single set of vortices is obviously not sufficient, but chaotic mixing should emerge by using three independent beams, each producing its set of vortices to enhance efficient rapid mixing. A typical predicted flow field simulated through depth-averaged Stokes equations is shown in Figure 2.32b, in which the four recirculation regions are clearly visible [189]. The velocity gradients display a separation of scales in the normal and tangential directions, as observed from the distance between the streamlines in the two directions. If the laser spot position is not center in the drop or using two laser spots, the mixing pattern can be changed significantly for oriented mixing [177].

So far, there are three main types of direct light-driven manipulation of liquids: using optical forces (through radiation pressure and optical tweezers) [199, 200], light modulation of electrical actuation (optoelectrowetting and photocontrol of EOF) [201–204], and light-induced capillary forces [22, 175–178]. The last of these actuation approaches has advantages over the first two in that it requires neither special optical setups nor complex microfabrication steps, but uses capillary forces generated from a light-induced wettability gradient and Marangoni effects [205]. Therefore, it has become of particular interest because light can provide contactless spatial and temporal control especially when triggered by light-induced capillary forces [175, 205].

However, existing light-driven technologies suffer from an inherent limitation in that liquid motion is strongly resisted by the effect of contact-line pinning [3]. For example, the capillary force arising from a wettability gradient is too small to overcome the effect of contact-line pinning, so the motion is limited to specific liquids over a relatively short distance, in simple linear trajectories, and at low speed (10–50 µm s^{-1}) [22, 178]. And use of the light-induced Marangoni effect requires either local heating or the addition of surfactants to liquids, which is undesirable for biomedical applications and undoubtedly produces sample contamination [11, 175, 176, 206, 207].

In order to overcome these shortcomings in the light-driven manipulation of liquid, recently, a novel strategy was advanced by Yu *et al*. by manipulating fluid slugs by photoinduced asymmetric deformation of tubular microactuators (TMAs), which induces capillary forces for liquid propulsion [3]. Enlightened by the layered structures of robust artery walls (Figure 2.33a), Yu *et al*. designed a new linear liquid crystal polymer (LLCP; Figure 2.33b) and synthesized a high-molecular-weight polyolefin as LLCP with narrow polydispersity via the ring-opening metathesis polymerization (a kind of living polymerization) [3]. This kind of LLCP is a strong and tough material, due to their ordered lamellar structure and high molecular weight. Moreover, the absence of a chemical network means that broken samples can be reshaped; a "healed" fiber with a cross-sectional area of 0.02 mm^2 can still sustain a large load, up to ~52 g, about



www.ebook3000.com

Figure 2.33 (a) Schematic illustration of the structure of artery walls. The middle coat of an artery, called the tunica media, consists of alternating muscle layers and elastic layers, which are responsible for stimuli-responsive deformation and mechanical robustness, respectively. (b) Molecular structure of a novel linear liquid crystal polymer (LLCP). M_n, number average molecular weight; M_w, weight average molecular weight. (c) Schematics showing the motion of a slug of fully wetting liquid confined in a tubular microactuator (TMA) driven by photodeformation. The light is incident perpendicular to the long axis of the TMA and has a gradient of incident intensity (produced by attenuation), decreasing from left to right. Shape transformation of the TMA from cylindrical to conical is induced by this gradient of light intensity. As a result, the slug advances to the narrower end of the TMA. (d) Lateral photographs of the light-induced motion of a silicone oil slug in a TMA fixed on a substrate that was taken through an optical filter to remove light with wavelengths below 530 nm. On irradiation by 470 nm light whose intensity (represented by open arrows) is attenuated increasingly from left to right (top row), the silicone oil slug is self-propelled toward the right; when the direction of attenuation is reversed (bottom row), the direction of movement of the slug is also reversed. (e) Photographs showing left to right a batch of freestanding straight, serpentine, and helical TMAs. The serpentine TMA is leaning against the edge of a glass slide. The inner diameter of the straight TMAs is 0.5 mm, and that of both serpentine and helical TMAs is 0.6 mm. The wall thickness of all the TMAs is ~8 μm. (Lv *et al*. 2016 [3]. Reproduced with permission of Nature Publishing Group.)

100 times of the traditional cross-linking liquid crystal polymers. Thanks to rational structure design and the robust mechanical properties of the LLCP, structurally defined and robust TMAs can be conveniently fabricated via a solution or melting processing. Most importantly, this kind of LLCP is a new generation of light-induced shape deformation materials. The asymmetric geometry change can be produced upon irradiation by 470 nm light with an intensity gradient along the TMA (Figure 2.33c), leading to axis-oriented capillary driving forces. The capillary forces can overcome viscous forces to drive the inner liquid flowing into the narrow side of TMAs under the Laplace pressure difference. Thus, such irradiated TMAs can thus successfully manipulate liquid motion by light (Figure 2.33d). Based on the robust mechanical properties of this kind of LLCP and their excellent solution or melting processing ability, TMAs with arbitrary geometries, such as "Y"-shaped, serpentine, and helical, can be further prepared from the mechanically robust LLCP by the same method (Figure 2.33e).

This is a novel optofluidic technology realized by the light-induced asymmetric shape deformation of LLCP, which can transfer optical energy to mechanical energy and then to the capillary forces to drive polar, nonpolar, or complex liquids (including emulsion, petrol, silicon oil, or even biomedical fluids) flowing in microchannels. By adjusting the irradiation conditions, this new technology can precisely regulate the flow direction and speed (up to 5.9 mm s^{-1}) and can realized long-distance motion (up to 53 mm motion of a microfluid in a TMA). These microactuators are able to exert photocontrol of a wide diversity of liquids over a long distance with controllable velocity and direction and hence to mix multiphase liquids, to merge liquids, and even to drive liquids to run uphill by overcoming the gravity force. It is also the first time to realize the S-shaped and spiral motion in the closed tube, satisfying the requirement of the manipulation of small amounts of fluids.

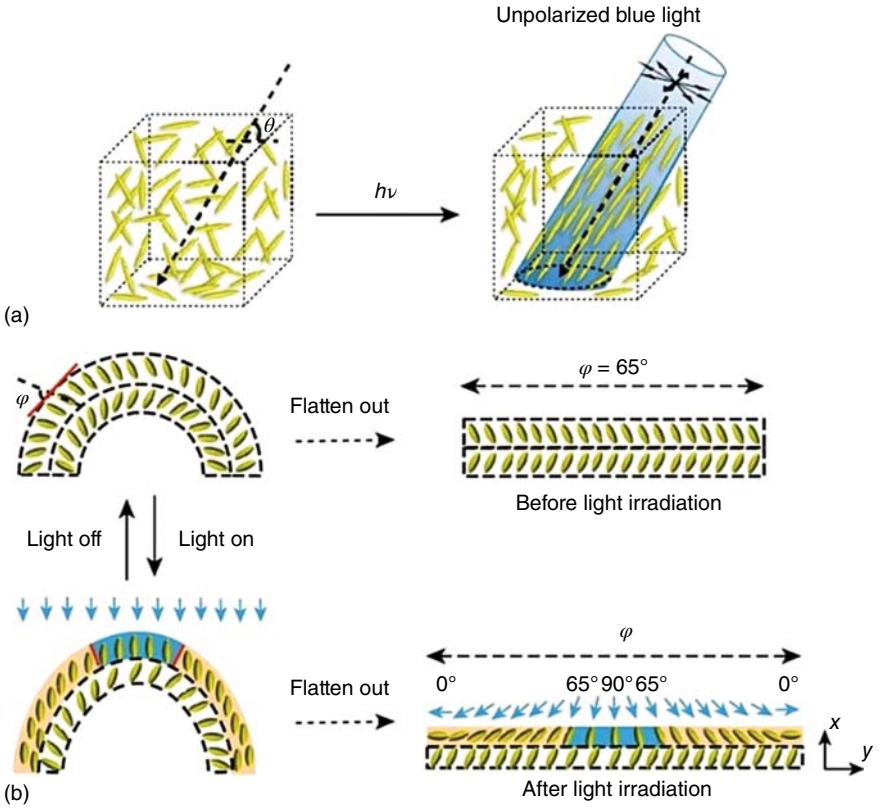


Figure 2.34 Mechanism of photodeformation of the tubular microactuators (TMA) and velocity of light-induced liquid motion. (a) Schematics showing reorientation of mesogens in azobenzene-containing LC systems with non-polarized blue light that is incident at angle θ. Double arrows show the polarization direction of the light. (b) Schematics illustrating the reorientation of mesogens in the cross-sectional area of the TMA before and after irradiation by unpolarized 470 nm light. To facilitate understanding the photo-reorientation, the wall is flattened out into a plane. The normal direction of the lamellae is along the *x*-direction in the scheme. Before irradiation by the light, ϕ of all the liquid crystal (LC) mesogens is 65° (top). On light irradiation, the LC mesogens in the exposed surface of the TMA are realigned to the direction of the actinic light, which results in the change of ϕ in the exposed area (bottom). The orange and blue parts of the cross-sectional area, respectively, expand and contract along the *y*-axis on light irradiation. This photoinduced reorientation leads to the decrease in thickness of the TMA wall (along the *x*-axis) and the elongation of the perimeter of the TMA (along the *y*-axis), which contributes to the increase of cross-sectional area. (c) Left, plot showing the area of six different cross sections before (red line) and after (black line) irradiation by attenuated 470 nm light. Error bars, s.d. ($n = 3$). *z* represents the distance between one end of the TMA and the cross section. Length of blue arrows denotes the intensity of 470-nm light, produced by varying its attenuation. (Lv *et al*. 2016 [3]. Reproduced with permission of Nature Publishing Group.)

www.ebook3000.com

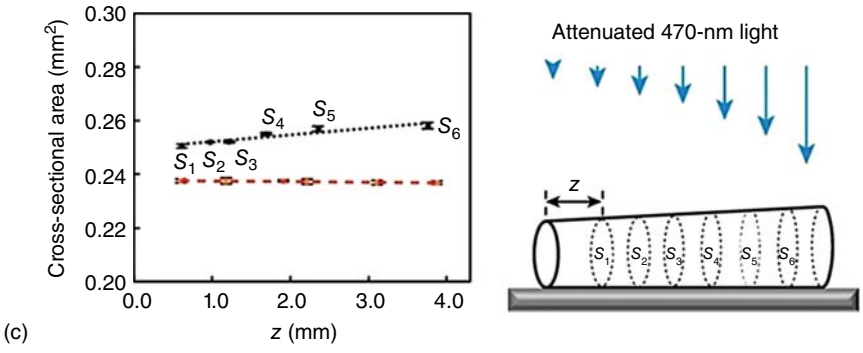


Figure 2.34 (*Continued*)

Figure 2.34 gives the mechanism to manipulation of liquid by the photodeformation of the liquid crystal polymer microstructures [3]. Their liquid handling abilities arise from asymmetric photodeformation of the TMAs in response to attenuated 470 nm blue light, a novel principle for inducing capillary force. In the case of unpolarized light, only the propagation direction is perpendicular to the polarized direction of the unpolarized light; thus the azobenzene mesogens orient along the propagation direction of the actinic unpolarized light (Figure 2.34a). When the TMAs are exposed to unpolarized 470 nm light whose actinic direction is perpendicular to the long axis of the TMAs, the azobenzene mesogens are reoriented along the propagation direction (Figure 2.34b). Therefore, the tilt angles ϕ of azobenzene mesogens in the different exposed areas are different because the lamellae of the LLCP are arranged coaxially in the TMA wall. In order to facilitate understanding of this photo-reorientation, the wall of the TMA is flattened out into a plane, as shown in Figure 2.34b. According to the tilt angle of azobenzene mesogens, the azobenzene mesogens in ~70% of the exposed area are reoriented to exhibit $\phi \leq 65^\circ$, which means this area expands along the y-axis. The rest of the azobenzene mesogens are tilted with $65^\circ < \phi \leq 90^\circ$, leading to contraction along the y-axis. In other words, the expansion of the light-exposed area is far larger than the contraction of that area. This photoinduced reorientation results in a decrease of the thickness of the TMA wall (along the x-axis in Figure 2.34b) and an elongation of the perimeter of the TMA (along the y-axis in Figure 2.34b), which together cause an increase of the cross-sectional area of the TMA. Moreover, the higher the light intensity, the larger the increase in cross-sectional area. Figure 2.34c shows that the cross-sectional areas of the photodeformed TMA at different positions increase with the increase of the light intensity upon irradiation by attenuated 470 nm light, whereas the cross-sectional areas at different positions without irradiation are almost the same. Therefore, the TMA deforms to an asymmetric cone-like geometry, which generates adjustable capillary force to propel liquids in the direction of light attenuation.

This kind of TMAs preserves the dual functions as the fluid tube and the driving pumping, which can simplify the whole microfluidic system for further integration and miniaturization. Therefore, the TMAs shall have great applications in the chemical and biological analysis, microfluidic synthesis, and LC.

2.6 Construction Materials Considerations

Mechanical performances, fluid mechanism (mass diffusion and thermal diffusion), and physicochemical properties (optical, corrosion resistance to solvents or harsh environment, such as moist, acid, base, ultralow or very high operation temperature, or reaction) of materials have to be considered comprehensively in the design and fabrication of microfluidic devices. The mass diffusion and thermal diffusion of some materials can be referred to Sections 2.2.3 and 2.3.4, 2.3.2 and 2.4.4, respectively and Tables 2.1–2.8.

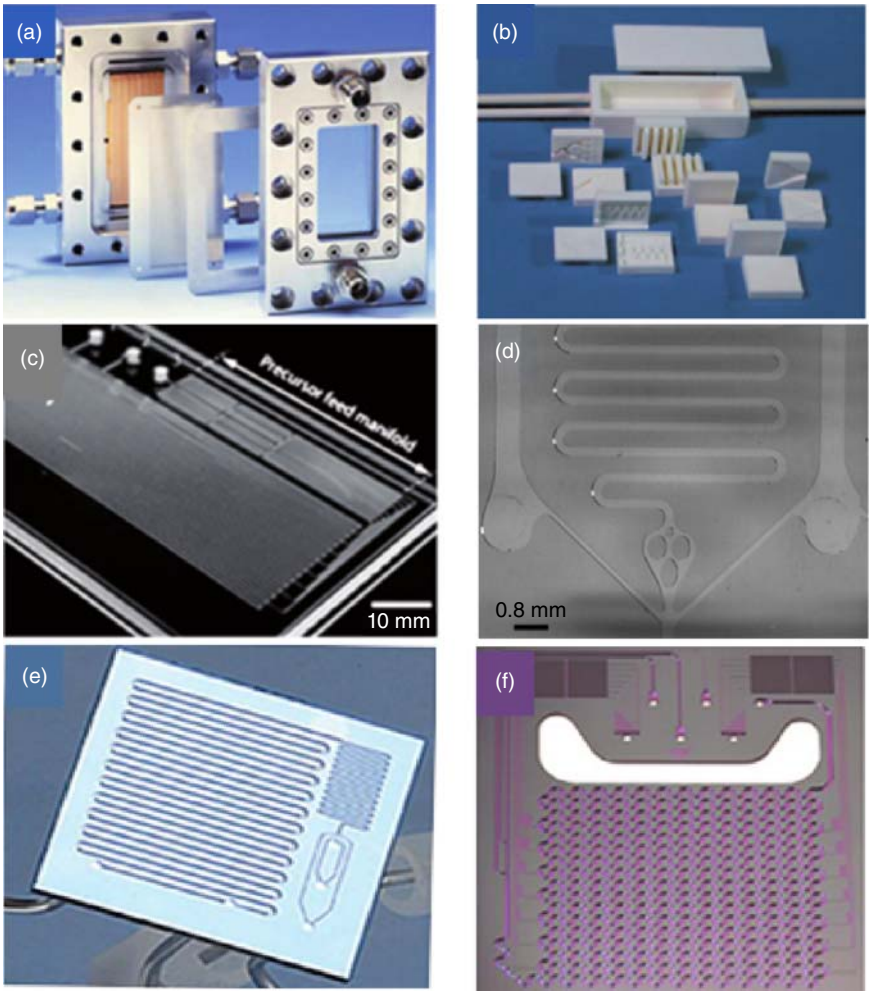


Figure 2.35 Examples of microreactors fabricated from (a) metal. (Jahnisch *et al*. 2004 [208]. Reproduced with permission of John Wiley & Sons.) (b) Ceramic. (Geyer *et al*. 2006 [209]. Reproduced with permission of John Wiley & Sons. (c) Polymers (e.g., PDMS). (Copyright Lab on a chip, reproduced with permission [210–212].) (d) SU-8 on PMMA or PEEK substrates. (Copyright from Refs [91, 212].) (e, f) Silicon- or glass-based microfluidic reactors. (Jensen 2006 [213]. Reproduced with permission of Cambridge University Press.)

www.ebook3000.com

Microfluidic devices made of metals (e.g., stainless steel, copper; Figure 2.35a) can endure high temperatures and pressures, but at the cost of corrosion under strong acid condition; ceramic microfluidic reactors (Figure 2.35b) are very stable in acidic environments even at high temperature reactor conditions; however, the process of microfabrication is very complicated [208]. Polymer-based device (Figure 2.35c, PDMS; Figure 2.35d, SU-8 on polyaryletheretherketone) (PEEK) or PMMA) can be fast fabricated at the cost of easy expansion or dissolution in organic solvents [91, 210–212]. Injection-molding, hot-embossing, or phase-separation-micromolding techniques are used to prepare polymer-based reactors. Recently, there has been a fluoropolymer device (e.g., fluorinated ethylene propylene (FEP) or PEEK) that is applied to PDMS microfluidic reactor due to chemically inert properties [210–212]. Glass or ceramic is often the material of choice for chemists, but the isotropic nature of hydrogen fluoride etching makes it difficult to create deep channels in glass [214, 215]. Silicon-based or fused glass-based microfluidic reactor (Figure 2.35e,f) can be prepared by photolithography or deep reactive ion etching (DRIE) techniques. 3D silicon structures are able to withstand high temperature and pressure.

When oxidized, silicon behaves very similar to glass and is chemically inert to most reagents and solvents. Simultaneously, due to the high heat transfer coefficient of silicon material, silicon has found widespread use in the construction of microfluidic reactors; however, cost and device failure may be its potential limitations [112, 214]. Other types of microfluidic devices fabricated by varieties of materials will not be introduced here one by one, which can be referred to Chapter 3, Chapter 11, and other related chapters of this book if you are interested. To date, it is still essential to improve the fabrication processes, identification and utilization of appropriate material of construction and, most importantly, integration of microprocessing components related to the microfluidic reactor system (such as micro-pumps or electroosmosis parts, micro-heaters, and micro-separators).

Acronyms

AIP	American Institute of Physics
DRIE	deep reactive ion etching
EDL	electric double layer
FEP	fluorinated ethylene propylene
ICEK	induced-charge electrokinetic
ICEO	induced-charge electroosmosis
IOP	Institute of Physics
LC	liquid crystal
LLCP	linear liquid crystal polymer
PEEK	polyaryletheretherketone
SH	source or sink of heat
TMAs	tubular microactuators
h in Dean number equation	half width of micro-channel
R in Dean number equation	mean radius of a curved micro-channel

Nomenclatures

$\vec{J}_i$	flux of component i
$\partial T/\partial x$	temperature gradient along x-direction, K m^{-1}
$\overline{B}$	magnetic field
$^{\partial u}/_{\partial y}$	local shear velocity
$\sim\lambda_{\mathrm{D}}$	ionic screening cloud of width
$\times$	cross product
∇	vector differential operator
a	speed of sound
A	cross-sectional area of the flow
A_1	cross-sectional area A_1
A_2	cross-sectional area A_2
Ar	Archimedes number
At	Atwood number
Bi	Biot number
Bo	Bond number
Br	Brinkman number
c	total molar concentration (Eq. (2.19))
C	concentration of the species (Eq. (2.9))
c	light speed (Eq. (2.97))
Ca	capillary number
Ce	centrifuge number
C_{fr}	friction coefficient
c_i	molar concentration of component i
C_{P}	constant pressure heat capacity
C_{V}	constant volume heat capacity
d	collision diameter of molecules
D	diffusion coefficient (cm^2 s^{-1}) (Eq. (2.14))
D	diffusion coefficient of the species (Eq. (2.92))
D_{AB}	diffusivity of A in B
D_{e}	diffusion coefficient in gas or liquid filling the pore (Eq. (2.16))
De	Dean number
D_{h}	hydraulic diameter
D_{i}	diffusivity of the ions
D_{ij}	Maxwell–Stefan diffusivity
$\bar{\mathrm{E}} = -\nabla\phi e$	local applied electrical filed strength
$E_{\parallel}$	local electric strength
E	bulk modulus elasticity (N m^{-2} (Pa)$^{-1}$)
$\bar{\mathrm{E}}$	electric field
E	spacing distance (x)-dependent electric field strength (Eq. (2.82))
Ec	Eckert number
Ek	Ekman number
Eo	Eötvös number
Eu	Euler number

www.ebook3000.com

F	magnitude of this force
F_{mix}	extent efficiency of mixing two fluids next to each other accomplished only through diffusion
Fo	Fourier number
Fr	Froude number
Fr_R	rotating Froude number
F_s	shear force
g	acceleration of gravity
Ga	Galileo number
Gr	Grashof number
Gz	Graetz number
h	fluid depth (Eq. (2.30))
$h(r)$	displacement of the interface
h	height
Hg	Hagen number
I	beam intensity
I_0	intensity of the incident light
J_0	zeroth-order Bessel function
Ja	Jakob number
J_x	net flux
K	wave number of the laser beam
Kn	Knudsen number
k_rCL/D	Damköhler number
L	characteristic length
L	separation between electrodes (Eq. (2.94))
La	Laplace number
Le	Lewis number
m	mass of molecule
M	molecular weight (Eq. (2.8))
M	molar mass ($g\,mol^{-1}$) (Eq. (2.14))
Ma	Marangoni number
M_B	molar mass of solvent B
Mo	Morton number
n	number of components
N_A	Avogadro's number
ñ	outward unit normal on the surface
n_0	bulk concentration of ions
n_1	refractive index
Nu	Nusselt number
P	static pressure (Eq. (2.32))
P	difference in pressure inside (P_i) and outside (P_o) of the bubble (Eq. (2.68))
p	pressure (atm)
∇_P	pressure gradient
$P\uparrow$	beam power threshold
Pe	Péclet number
Pr	Prandtl number

Q	volumetric flow rate
q''_x	heat density along x-direction, W m^{-2}
R	gas constant (Eq. (2.1))
R and T	normal incidence for weak deformations with linearized curvatures (Eq. (2.99))
$R(\theta_2, \theta_1)$	classical reflection
r	internal radius (Eq. (2.33))
r	average distance of the liquid (Eq. (2.79))
r	distance from the center to the laser beam
Ra	Rayleigh number
Re	Reynolds number
Ri	Richardson number
Ro	Rossby number
R_x and R_y	radii of curvature in each of the axes that are parallel to the surface
Sc	Schmidt number
Sh	Sherwood number
Sr	Strouhal number
Sta	Stanton number
Ste	Stefan number
Stk	Stokes number
$T(\theta_2, \theta_1) = 1 - R(\theta_2, \theta_1)$	transmission Fresnel coefficients in electromagnetic energy
T	absolute temperature
T_0	reference temperature (K)
T_1	absolute temperatures
T_2	absolute temperatures
Ta	Taylor number
u/y	rate of shear deformation or shear velocity
$\bar{u}$	average molecule velocity
$\bar{u}$	velocity vector
u_1	effective velocity of the fluid flow through A_1 (Eq. (2.31))
u_2	effective velocity of the fluid flow through A_2
$\bar{u}_{ep}$	electrophoretic velocity of the species
U_{Th}	largest interfacial tension
V_A	molecular volume of solute A under boiling point, cm^3 mol^{-1}
w	half width of the light beam
We	Weber number
Wo	Womersley number
W_{SLV}	work to form a kind of contact
x	heat transfer direction (Eq. (2.27))
x	distance from the channel wall (Eq. (2.90))
α	activity (Eq. (2.19))
α	thermal diffusivity (Eq. (2.28))
α	Womersley number
β	volumetric thermal expansion coefficient

www.ebook3000.com

β_T	isothermal compressibility
γ	relative magnitude of surface tension
γ_{SL}, γ_{LV}, and γ_{SV}	interfacial tensions between the solid and the liquid, the liquid and the vapor, and the solid and the vapor, respectively
δ	constrictivity
Δp	characteristic pressure difference of flow
ΔP	pressure jump (Eq. (2.72))
ΔP	Laplace pressure (Eq. (2.67))
ΔT	characteristic temperature difference
ε	coefficient of thermal expansion
ε_t	porosity available for the transport (dimensionless)
ε_w	dielectric constant
$\zeta_i \approx E_{0r}$	potential drop of the field
ζ_i	local induced zeta potential
θ	contact angle
θ_1 and θ_2	transmission angles
κ	heat conductivity
λ	mean free path
λ_D	screening lengths
$\Lambda_{o,i}$	thermal conductivities (the subscripts i, o denote the fluids inside and outside)
μ	dynamic viscosity (Eq. (2.3))
μ	viscosity of the liquid (Eq. (2.89))
$\mu\nabla^2 h$	Laplace force
μ_0	reference viscosity
μ_a	pure viscosity of the component a
μ_b	pure viscosity of the component b
μ_i	chemical potential
μ_l	dynamic viscosity of the liquid (Pa s)
$\mu_{o,i}$	shear viscosities
μ_r	relative viscosity (dimensionless)
μ_s	dynamic viscosity of the slurry
μ_{T_1}	dynamic viscosity of the solvent at T_1
μ_{T_2}	dynamic viscosity of the solvent at T_2
ν	ratio of the inertial forces to the viscous forces
$\Pi_{Rad(r)}$	balance between radiation pressure
Π_{Rad}	light pressure
ρ	density of the liquid
ρ_1	density
ρC_P	volumetric heat capacity ($J\,m^{-3}\,K^{-1}$)
$\rho g h$	gravity
ρ_q	local net charge density
ρ_{tot}	sum of the two densities
σ	excess free energy of a drop on a solid surface (Eq. (2.69))
σ	surface tension ($N\,m^{-1}$)
$\sigma_{A,B} = (\sigma_1 + \sigma_2)/2$	average collision diameter (Å)

σ_d	*interfacial free energy of the* highest energy level
σ_f	*interfacial free energy of the* final status
$-\sigma\hat{H}(r)$	Laplace pressure
σ_i	*interfacial free energy of the initial status*
τ	shear stress
$\vec{v}$	particle's velocity
$\vec{v}_i$	diffusion velocity of component
ϕ	associated parameter of solvent
χ	mole fraction
χ_a	mole fraction of the component a
χ_b	mole fraction of the component b
Ω	temperature-dependent collision integral (usually of order 1) (dimensionless)
ω^*	characteristic frequency of the interfacial wave
ω	circular frequency
ω	angular velocity of the disk (Eq. (2.79))
ω_i	angular velocity of inner cylinder

Acknowledgments

This work was supported by National S&T Major Project (pre-approved No. SQ2018ZX100301), NSFC (Grant No. 51371018 & 81372425) and the Fundamental Research Funds for the Central University of China (FRF-BR-14-001B).

References

1 deMello, A.J. (2006) Control and detection of chemical reactions in microfluidic systems. *Nature*, **442**, 394–402.
2 Nightingale, A.M. *et al.* (2013) Large-scale synthesis of nanocrystals in a multichannel droplet reactor. *J. Mater. Chem. A*, **1**, 4067–4076.
3 Lv, J.-a. *et al* (2016) Photocontrol of fluid slugs in liquid crystal polymer microactuators. *Nature*, **537**, 179–185.
4 Whitesides, G.M. (2006) The origins and the future of microfluidics. *Nature*, **442**, 368–373.
5 Psaltis, D., Quake, S.R., and Yang, C. (2006) Developing optofluidic technology through the fusion of microfluidics and optics. *Nature*, **442**, 381–386.
6 Craighead, H. (2006) Future lab-on-a-chip technologies for interrogating individual molecules. *Nature*, **442**, 387–393.
7 Amstad, E. *et al.* (2015) Production of amorphous nanoparticles by supersonic spray-drying with a microfluidic nebulator. *Science*, **349**, 956–960.
8 Adamo, A. *et al.* (2016) On-demand continuous-flow production of pharmaceuticals in a compact, reconfigurable system. *Science*, **352**, 61–67. doi: 10.1126/science.aaf1337

www.ebook3000.com

9 Park, J.I., Saffari, A., Kumar, S., Gunther, A., and Kumacheva, E. (2010) Microfluidic synthesis of polymer and inorganic particulate materials. *Annu. Rev. Mater. Res.*, **40**, 415–443.

10 Kim, H. *et al.* (2016) Submillisecond organic synthesis: Outpacing Fries rearrangement through microfluidic rapid mixing. *Science*, **352**, 691–694. doi: 10.1126/science.aaf1389

11 Fan, X. and Yun, S.-H. (2014) Optofluidic bio-lasers: concept and applications. *Nat. Methods*, **11**, 141–147.

12 Ren, K., Zhou, J., and Wu, H. (2013) Materials for microfluidic chip fabrication. *Acc. Chem. Res.*, **46**, 2396–2406.

13 Pethig, R.R. and Smith, S. (2013) *Introductory Bioelectronics: For Engineers and Physical Scientists*, John Wiley & Sons, Inc., p. 462.

14 Squires, T.M. and Quake, S.R. (2005) Microfluidics: fluid physics at the nanoliter scale. *Rev. Mod. Phys.*, **77**, 977–1026.

15 Seemann, R., Brinkmann, M., Pfohl, T., and Herminghaus, S. (2012) Droplet based microfluidics. *Rep. Prog. Phys.*, **75**, 016601.

16 Sebastian, V., Arruebo, M., and Santamaria, J. (2014) Reaction engineering strategies for the production of inorganic nanomaterials. *Small*, **10**, 835–853.

17 Wang, R. *et al.* (2015) A general strategy for nanohybrids synthesis via coupled competitive reactions controlled in a hybrid process. *Sci. Rep.*, **5**, 9189.

18 Wang, J., Wang, Z., Li, S., Wang, R., and Song, Y. (2017) Surface and interface engineering of FePt/C nanocatalysts for electro-catalytic methanol oxidation: enhanced activity and durability. *Nanoscale*, **9**, 4066–4075.

19 Harnett, C.K., Templeton, J., Dunphy-Guzman, K.A., Senousy, Y.M., and Kanouff, M.P. (2008) Model based design of a microfluidic mixer driven by induced charge electroosmosis. *Lab Chip*, **8**, 565–572.

20 Wu, Z. and Li, D. (2008) Micromixing using induced-charge electrokinetic flow. *Electrochim. Acta*, **53**, 5827–5835.

21 Utz, M. and Landers, J. (2010) Magnetic resonance and microfluidics. *Science*, **330**, 1056–1058.

22 Delville, J.-P. *et al.* (2009) Laser microfluidics: fluid actuation by light. *J. Opt. A: Pure Appl. Opt.*, **11**, 034015.

23 Noorian, H., Toghraie, D., and Azimian, A.R. (2014) The effects of surface roughness geometry of flow undergoing Poiseuille flow by molecular dynamics simulation. *Heat Mass Transfer*, **50**, 95–104.

24 Yoseph, I. (2008) *Introduction to Mesoscopic Physics*, 2nd edn, Oxford University Press, p. 252.

25 Ma, Z. (2007) Fundamentals and recent progress of mesoscopic physics. *Physics*, **36**, 98–129(in Chinese).

26 Jiang, J., Hao, Y., and SHi, M. (2006) Experimental study on flow and heat transfer characteristics in rectangular microchannel. *J. Therm. Sci. Technol.*, **5**, 189–194in Chinese.

27 Guo, Z. (2000) Frontier of heat transfer-microscale heat transfer. *Adv. Mech.*, **30**, 1–6in Chinese.

28 Tien, C.L., Majumdar, A., and Gemer, F.M. (1998) *Microscale Energy Transport*, 1st edn, CRC Press, Taylor & Francis, p. 400.

29 Streeter, V.L., Wylie, E.B., and Bedford, K.W. (1998) *Fluid Mechanics*, McGraw-Hill.
30 Incropera, F.P. and DeWitt, D.P. (2007) *Fundamentals of Heat and Mass Transfer*, John Wiley & Sons, Inc..
31 Holman, J.P. (2002) *Heat Transfer*, McGraw-Hill.
32 Lide, D.R.E. (1992) *CRC Handbook of Chemistry and Physics*, 73rd edn, CRC Press Inc..
33 Wikipedia contributors, "Viscosity," Wikipedia, The Free Encyclopedia https://en.wikipedia.org/w/index.php?title=Viscosity&oldid=787847922 (accessed July 16, 2017).
34 Grimm, R. (2005) Low-temperature physics: a quantum revolution. *Nature*, **435**, 1035–1036.
35 Burnett, K. (2007) Atomic physics: cold gases venture into flatland. *Nat. Phys.*, **3**, 589.
36 Laidler, K.J. (1993) *The World of Physical Chemistry*, Oxford University Press, pp. 150–154.
37 Sommers, T.S. and Nahir, T.M. (2005) Temperature dependence of viscosities of common carrier gases. *J. Chem. Educ.*, **82**, 1089–1090.
38 Lide, D.R. (2006) *CRC Handbook of Chemistry and Physics*, 87th edn, CRC Press, p. 2592.
39 Viscosity of Liquids and Gases, http://hyperphysics.phy-astr.gsu.edu. (accessed 20 Jun 2017)
40 Glenn, E. (1988) *The Physics Hypertextbook – Viscosity*.
41 Einstein, A. (1906) Eine neue Bestimmung der Moleküldimensionen (A new determination of molecular dimensions). *Ann. Phys.*, **19**, 289–306.
42 Guth, E. and Simha, R. (1936) Untersuchungen über die Viskosität von Suspensionen und Lösungen. 3. Über die Viskosität von Kugelsuspensionen. *Kolloid Z.*, **74**, 266.
43 Thomas, D.G. (1965) Transport characteristics of suspension: VIII. A note on the viscosity of Newtonian suspensions of uniform spherical particles. *J. Colloid Sci.*, **20**, 267–277.
44 Kitano, T., Kataoka, T., and Shirota, T. (1981) An empirical equation of the relative viscosity of polymer melts filled with various inorganic fillers. *Rheol. Acta*, **20**, 207–209.
45 Haynes, W.M. (2012) *CRC Handbook of Chemistry and Physics*, 93rd edn, CRC Press.
46 Cussler, E. and Diffusion, L. (1997) *Mass Transfer in Fluid Systems*, 2nd edn, Cambridge University Press.
47 Welty, J.R., Wicks, C.E., Wilson, R.E., and Rorrer, G. (2001) *Fundamentals of Momentum, Heat, and Mass Transfer*, John Wiley & Sons, Inc..
48 Hirschfelder, J., Curtiss, C.F., and Bird, R.B. (1954) *Molecular Theory of Gases and Liquids*, John Wiley & Sons, Inc.
49 Grathwohl, P. (1998) *Diffusion in Natural Porous Media: Contaminant Transport, Sorption/Desorption and Dissolution Kinetics*, Kluwer Academic.
50 Gostovic, D., Smith, J.R., Kundinger, D., Jones, K., and Wachsman, E. (2007) Three-dimensional reconstruction of porous LSCF cathodes. *Electrochem. Solid-State Lett.*, **10**, B214–B217.

www.ebook3000.com

51 Olander, D.R. (1961) The diffusivity of water in organic solvents. *AIChE J.*, **7**, 175–176.
52 Miyabe, K. and Isogaib, R. (2011) Estimation of molecular diffusivity in liquid phase systems by the Wilke–Chang equation. *J. Chromatogr. A*, **1218**, 6639–6645.
53 Wilke, C.R. and Chang, P. (1955) Correlation of diffusion coefficients in dilute solutions. *AIChE J.*, **1**, 264–270.
54 Rehfeldt, S. and Stichlmair, J. (2007) Measurement and calculation of multicomponent diffusion coefficients in liquids. *Fluid Phase Equilib.*, **256**, 99–104.
55 Bird, R.B., Stewart, W.E., and Lightfoot, E.N. (2007) *Transport Phenomena*, 2nd edn, John Wiley & Sons, Inc..
56 Fairbanks, D.F. and Wilke, C.R. (1950) Diffusion coefficients in multicomponent gas mixtures. *Ind. Eng. Chem.*, **42**, 471–475.
57 Kooijman, H.A. and Taylor, R. (1991) Estimation of diffusion coefficients in multicomponent liquid systems. *Ind. Eng. Chem. Res.*, **30**, 1217–1222.
58 Halliday, D., Resnick, R., and Walker, J. (2013) *Fundamentals of Physics Extended*, 10th edn, John Wiley & Sons, Inc., p. 1448.
59 Cengel, Y.A. and Boles, M.A. (2010) *Thermodynamics: An Engineering Approach*, 7th edn, McGraw-Hill.
60 Kittel, C. (2005) *Introduction to Solid State Physics*, 8th edn, John Wiley & Sons, Inc., p. 141.
61 Blundell, S. (2001) *Magnetism in Condensed Matter. Oxford Master Series in Condensed Matter Physics*, 1st edn, Oxford University Press, p. 27.
62 Braun, O.M. (2004) *The Frenkel-Kontorova Model: Concepts, Methods and Applications*, Springer.
63 Bolmatov, D., Brazhkin, V.V., and Trachenko, K. (2012) The phonon theory of liquid thermodynamics. *Sci. Rep.*, **2**, 421.
64 Young, G. (2008) *Young and Geller College Physics*, 8th edn, Pearson Education.
65 Technology, N. N. I. o. S. a.
66 Xu, C.-H., Du, S.-Y., Meng, S.H., Han, J.C., and Wang, G.G. (2007) Effect of sapphire thermal performance anisotropy on crystal growth by SAPMAC method. *J. Synth. Cryst.*, **36**, 1261–1265.
67 Byvik, C.E., Inge, A.T., Buoncristiani, A.M., and Roberts, L. (1986) Conference on Lasers and Electro-Optics paper THB2 (OSA Technical Digest (Optical Society of America, 1986), San Francisco, CA, 1986).
68 Balandin, A.A. *et al.* (2008) Superior thermal conductivity of single-layer graphene. *Nano Lett.*, **8**, 902–907.
69 Balandin, A.A. (2011) Thermal properties of graphene and nanostructured carbon materials. *Nat. Mater.*, **10**, 569–581.
70 Fujii, M. *et al.* (2005) Measuring thermal conductivity of a single carbon nanotube. *Phys. Rev. Lett.*, **95**, 065502.
71 Carslaw, H.S. and Jaeger, J.C. (1959) *Conduction of Heat in Solids*, 2nd edn, Oxford University Press, p. 520.
72 Bergman, T.L., Lavine, A.S., Incropera, F.P., and DeWitt, D.P. (2011) *Fundamentals of Heat and Mass Transfer*, 7th edn, John Wiley & Sons, Inc., p. 1072.

73 Blumm, J. and Lindemann, A. (2003) Characterization of the thermophysical properties of molten polymers and liquids using the flash technique. *High Temp. High Pressures*, **35/36**, 627–632. doi: 10.1068/htjr144

74 Borca-Tasciuc, T. *et al.* (2007) Anisotropic thermal diffusivity characterization of aligned carbon nanotube-polymer composites. *J. Nanosci. Nanotechnol.*, **7**, 1581–1588.

75 Wilson, J. (2007) *Design, Materials, Compounds, Adhesives, Substrates*, vol. **13** Test & Measurement.

76 Agari, Y., Ueda, A., Omura, Y., and Nagai, S. (1997) Thermal diffusivity and conductivity of PMMA/PC blends. *Polymer*, **38**, 2649–2655.

77 Baierlein, R. (1999) *Thermal Physics*, Cambridge University Press, p. 372.

78 Lide, D.R. (2009) *CRC Handbook of Chemistry and Physics*, 90th edn, CRC Press.

79 Blumm, J., Lindemann, A., Meyer, M., and Strasser, C. (2010) Characterization of PTFE using advanced thermal analysis techniques. *Int. J. Thermophys.*, **31**, 1919–1927. doi: 10.1007/s10765-008-0512-z

80 Casalegno, V. *et al.* (2010) Measurement of thermal properties of a ceramic/metal joint by laser flash method. *J. Nucl. Mater.*, **407**, 83–87. doi: 10.1016/j.jnucmat.2010.09.032

81 Koszor, O., Lindemann, A., Davin, F., and Balázsi, C. (2009) Observation of thermophysical and tribological properties of CNT reinforced Si_3N_4. *Key Eng. Mater.*, **409**, 354–357. doi: 10.4028/www.scientific.net/KEM.409.354

82 Paradis, P.-F., Ishikawa, T., and Yoda, S. (2002) Noncontact measurements of thermophysical properties of molybdenum at high temperatures. *Int. J. Thermophys.*, **23**, 555–569.

83 Hofer, P. and Kaschnitz, E. (2011) Thermal diffusivity of the aluminium alloy Al-10Si-Mn-Mg (Silafont 36) in the solid and liquid states. *High Temp. High Pressures*, **40**, 311–322.

84 Kaschnitz, E. and Küblböck, M. (2008) Thermal diffusivity of the aluminium alloy Al-5Mg-2Si-Mn (Magsimal-59) in the solid and liquid states. *High Temp. High Pressures*, **37**, 221–230.

85 Lienhard, J.H. (2006) *A Heat Transfer Textbook*, 3rd edn, Phlogiston Press, p. 698.

86 Unsworth, J. and Duarte, F.J. (1979) Heat diffusion in a solid sphere and Fourier Theory. *Am. J. Phys*, **47**, 891–893. doi: 10.1119/1.11601

87 Blumm, J., Lindemann, A., and Niedrig, B. (2003) Measurement of the thermophysical properties of an NPL thermal conductivity standard Inconel 600. *High Temp. High Pressures*, **35/36**, 621–626. doi: 10.1068/htjr145

88 Sangermano, M. *et al.* (2015) Enhancement of electrical and thermal conductivity of Su-8 photocrosslinked coatings containing graphene. *Prog. Org. Coat.*, **86**, 143–146.

89 Eckert, E.R.G. and Drake, R.M. (1985) *Heat and Mass Transfer*, 2nd edn, McGraw-Hill Inc., New York.

90 Gravesen, P., Branebjerg, J., and Jensen, O.S. (1993) Microfluidics-a review. *J. Micromech. Microeng.*, **3**, 168–182.

www.ebook3000.com

91 Song, Y., Kumar, C.S.S.R., and Hormes, J. (2004) Fabrication of SU-8 based microfluidic reactor on a PEEK substrate sealed by a 'flexible semi-solid transfer'(FST) process. *J. Micromech. Microeng.*, **14**, 932–940.

92 Koch, M., Chatelain, D., Evans, A.G.R., and Brunnschweiler, A. (1998) Two simple micromixers based on silicon. *J. Micromech. Microeng.*, **8**, 123–126.

93 Gad-el-Hak, M. (2006) *The MEMS Handbook*, CRC Press.

94 Arnold, F. and Norbert, R. (2000) *Dynamics of Droplets*, vol. **15**, Springer Science & Business Media.

95 Song, H. and Ismagilov, R.F. (2003) Millisecond kinetics on a microfluidic chip using nanoliters of reagents. *J. Am. Chem. Soc.*, **125**, 14613–14619.

96 Nellis, G. and Klein, S. (2009) *Heat Transfer*, Cambridge, p. 663.

97 Shah, R.K. and Sekulic, D.P. (2003) *Fundamentals of Heat Exchanger Design*, John Wiley & Sons, Inc., p. 503.

98 Lefebvre, A.H. (1989) *Atomization and Sprays*, Hemisphere Publishing Corp..

99 Ohnesorge, W. (1936) Formation of drops by nozzles and the breakup of liquid jets. *J. Appl. Math. Mech.*, **16**, 355–358.

100 Song, Y., Li, R., Sun, Q., and Jin, P. (2011) Controlled growth of Cu nanoparticles by a tubular microfluidic reactor. *Chem. Eng. J.*, **168**, 477–484.

101 Adamson, A.W. and Gast, A.P. (1997) *Physical Chemistry of Surfaces*, 6th edn, Wiley-Interscience.

102 Sharfrin, E. (1960) Constitutive relations in the wetting of low energy surfaces and the theory of the retraction method of preparing monolayers. *J. Phys. Chem.*, **64**, 519–524. doi: 10.1021/j100834a002

103 Eustathopoulos, N., Nicholas, M.G., and Drevet, B. (1999) *Wettability at High Temperatures*, Oxford.

104 Lin, F. *et al* (2008) Petal effect: a superhydrophobic state with high adhesive force. *Langmuir*, **24**, 4114–4119.

105 Giacomello, A., Chinappi, M., Meloni, S., and Casciola, C.M. (2012) Metastable wetting on superhydrophobic surfaces: continuum and atomistic views of the Cassie–Baxter–Wenzel transition. *Phys. Rev. Lett.*, **109**, 765–781.

106 de Gennes, P.-G., Brochard-Wyart, F., and Quéré, D. (2002) *Capillary and Wetting Phenomena-Drops, Bubbles, Pearls, Waves*, Springer.

107 Butt, H.-J., Graf, K., and Kappl, M. (2006) *Physics and Chemistry of Interfaces*, Wiley-VCH Verlag GmbH & Co. KGaA.

108 Lee, K.S. (2008) Kinetics of wetting and spreading by aqueous surfactant solutions. *Adv. Colloid Interface Sci.*, **144**, 54–65. doi: 10.1016/j.cis.2008.08.005

109 Gutmann, B., Cantillo, D., and Kappe, C.O. (2015) Continuous-flow technology—a tool for the safe manufacturing of active pharmaceutical ingredients. *Angew. Chem. Int. Ed.*, **54**, 6688–6728. doi: 10.1002/anie.201409318

110 Hartman, R.L., McMullen, J.P., and Jensen, K.F. (2011) Deciding whether to go with the flow: evaluating the merits of flow reactors for synthesis. *Angew. Chem. Int. Ed.*, **50**, 7502–7519. doi: 10.1002/anie.201004637

111 Wakami, H. and Yoshida, J. (2005) Grignard exchange reaction using a microflow system: from bench to pilot plant. *Org. Process Res. Dev.*, **9**, 787–791. doi: 10.1021/op0501500

112 Hartman, R.L. and Jensen, K.F. (2009) Microchemical systems for continuous-flow synthesis. *Lab Chip*, **9**, 2495–2507. doi: 10.1039/b906343a

113 Song, Y.J., Sun, Q.Q., Zhang, T., Jin, P.Y., and Han, L. (2010) Synthesis of boron nitride nanotubes by an oxide-assisted chemical method. *J. Nanopart. Res.*, **12**, 2689–2697. doi: 10.1007/s11051-010-0012-5

114 Losey, M.W., Schmidt, M.A., and Jensen, K.F. (2001) Microfabricated multiphase packed-bed reactors: characterization of mass transfer and reactions. *Ind. Eng. Chem. Res.*, **40**, 2555–2562. doi: 10.1021/ie000523f

115 Kreutzer, M.T., Gunther, A., and Jensen, K.F. (2008) Sample dispersion for segmented flow in microchannels with rectangular cross section. *Anal. Chem.*, **80**, 1558–1567. doi: 10.1021/ac702143r

116 Schubert, K. *et al.* (2001) Microstructure devices for applications in thermal and chemical process engineering. *Microscale Thermophys. Eng.*, **5**, 17–39.

117 Mason, B.P., Price, K.E., Steinbacher, J.L., Bogdan, A.R., and McQuade, D.T. (2007) Greener approaches to organic synthesis using microreactor technology. *Chem. Rev.*, **107**, 2300–2318. doi: 10.1021/cr050944c

118 Carter, C.F., Baxendale, I.R., O'Brien, M., Pavey, J.B.J., and Ley, S.V. (2009) Synthesis of acetal protected building blocks using flow chemistry with flow IR analysis: preparation of butane-2,3-diacetal tartrates. *Org. Biomol. Chem.*, **7**, 4594–4597. doi: 10.1039/b917289k

119 Anna, S.L., Bontoux, N., and Stone, H.A. (2003) Formation of dispersions using "flow-focusing" in microchannels. *Appl. Phys. Lett.*, **82**, 364–366.

120 Taylor, G.I. (1934) The formation of emulsions in definable fields of flow. *Proc. R. Soc. London, Ser. A*, **146**, 501–523.

121 Garstecki, P. *et al.* (2004) Formation of monodisperse bubbles in a microfluidic flow-focusing device. *Appl. Phys. Lett.*, **85**, 2649–2651.

122 Gordillo, J.M., Gañáncalvo, A.M., and Pérezsaborid, M. (2001) Monodisperse microbubbling: absolute instabilities in coflowing gas–liquid jets. *Phys. Fluids*, **13**, 3839–3842.

123 Link, D.R., Anna, S.L., Weitz, D.A., and Stone, H.A. (2004) Geometrically mediated breakup of drops in microfluidic devices. *Phys. Rev. Lett.*, **92**, 054503.

124 Song, H., Bringer, M.R., Tice, J.D., Gerdts, C.J., and Ismagilov, R.F. (2003) Experimental test chaotic advection droplets moving through microfluidic channels. *Appl. Phys. Lett.*, **83**, 4664–4666.

125 Tice, J.D., Song, H., Lyon, A.D., and Ismagilov, R.F. (2003) Formation of droplets and mixing in multiphase microfluidics at low values of the Reynolds and the Capillary numbers. *Langmuir*, **19**, 9127–9133.

126 Lucchetta, E.M., Lee, J.H., Fu, L.A., Patel, N.H., and Ismagilov, R.F. (2005) Dynamics of Drosophila embryonic patterning network perturbed in space and time using microfluidics. *Nature*, **434**, 1134–1138.

127 Zheng, B., Roach, L.S., and Ismagilov, R.F. (2003) Screening of protein crystallization conditions on a microfluidic chip using nanoliter-size droplet. *J. Am. Chem. Soc.*, **125**, 11170–11171.

www.ebook3000.com

128 Shikida, M., Takayanagi, K.K.I., Honda, H., and Sato, K. (2006) Using wettability and interfacial tension to handle droplets of magnetic beads in a micro-chemical-analysis system. *Sens. Actuators, B*, **113**, 563–569.

129 Zhang, K. *et al* (2009) On-chip manipulation of continuous picoliter-volume superparamagnetic droplets using a magnetic force. *Lab Chip*, **9**, 2992–2999.

130 Batchelor, G.K. (2001) *An Introduction to Fluid Mechanics*, Cambridge University Press.

131 Riley, N. (2001) Steady streaming. *Annu. Rev. Fluid Mech.*, **33**, 43–65.

132 Garcia-Cordero, J.L., Basabe-Desmonts, L., Ducrée, J., and Ricco, A.J. (2010) Liquid recirculation in microfluidic channels by the interplay of capillary and centrifugal forces. *Microfluid. Nanofluid.*, **9** (4–5).

133 Ibrahim, F., Nozari, A.A., Jahanshahi, P., and Soin, N. (2010) Analysis and experiment of centrifugal force for microfluidic ELISA CD platform. 2010 IEEE EMBS Conference on Biomedical Engineering & Sciences, 466-470.

134 Lee, K. *et al.* (2012) Gravity-oriented microfluidic device for cell spheroid formation. *Biomicrofluidics*, **6**, 14114–141147.

135 Yamada, H. *et al.* (2008) Fabrication of gravity-driven microfluidic device. *Rev. Sci. Instrum.*, **79**, 124301.

136 Yao, B. *et al.* (2004) A microfluidic device based on gravity and electric force driving for flow cytometry and fluorescence activated cell sorting. *Lab Chip*, **4**, 603–607.

137 Bain, C.D. (2001) Motions of liquids on surfaces. *ChemPhysChem*, **2**, 580–582.

138 Weislogel, M.M. (1997) Steady spontaneous capillary flow in partially coated tubes. *AIChE J.*, **43**, 645–654.

139 Yang, Z., Goto, H., Matsumoto, M., and Maeda, R. (2000) Active micromixer for microfluidic systems using lead-zirconate-titanate(PZT)-generated ultrasonic vibration. *Electrophoresis*, **21**, 116–119.

140 Woias, P., Hauser, K., and Yacoub-George, E. (2000) *Micro Total Analysis Systems*, Kluwer Academic Publishers, p. 277.

141 Hosokawa, K., Fujii, T., and Endo, I. (2000) *Micro Total Analysis Systems*, Kluwer Academic Publishers, p. 481.

142 Yasuda, K. (2000) Non-destructive, non-contact handling method for biomaterials in micro-chamber by ultrasound. *Sens. Actuators, B*, **64**, 128–135.

143 Johnson, T.J., Ross, D., Gaitan, M., and Locascio, L.E. (2001) Laser modification of preformed polymer microchannels: application to reduce band broadening around turns subject to electrokinetic flow. *Anal. Chem.*, **73**, 3656–3661.

144 Harrison, D.J. *et al.* (1993) Micromachining a miniaturized capillary electrophoresis based chemical analysis system on a chip. *Science*, **261**, 895–897.

145 Fu, L.-M. and Lin, C.-H. (2007) A rapid DNA digestion system. *Biomed. Microdevices*, **9**, 277–286.

146 Squires, T.M. and Bazant, M.Z. (2004) Induced-charge electro-osmosis. *J. Fluid Mech.*, **509**, 217–252.

147 Morrison, I.D. (1993) Electrical charges in nonaqueous media. *Colloids Surf., A*, **71**, 1–37.

148 Keh, H.J. and Anderson, J.L. (1985) Boundary effects on electrophoretic motion of colloidal spheres. *J. Fluid Mech.*, **153**, 417–439.
149 Hunter, R.J. (1981) *Zeta Potential in Colloid Science: Principals and Applications*, Academic Press, p. 364.
150 Anderson, J.L. (1989) Colloid transport by interfacial forces. *Annu. Rev. Fluid Mech.*, **21**, 61–99.
151 Morrison, F.A. (1970) Electrophoresis of a particle of arbitrary shape. *J. Colloid Interface Sci.*, **34**, 210–214.
152 O'Brien, R.W. and White, L.R. (1978) Electrophoretic mobility of a spherical colloidal particle. *J. Chem. Soc., Faraday Trans. 2*, **2**, 1607–1626.
153 MaCdonald, J.R. (1970) Double layer capacitance and relaxation in electrolytes and solids. *Trans. Faraday Soc.*, **1970**, 943–958.
154 Bazant, M.Z. and Squires, T.M. (2004) Induced-charge electrokinetic phenomena: theory and microfluidic applications. *Phys. Rev. Lett.*, **92**, 066101.
155 Simonov, I.N. and Shilov, V.N. (1977) Theory of low-frequency dielectric-dispersion of a suspension of ideally polarizable spherical-particles. *Colloid J. USSR*, **39**, 775–780.
156 Ajdari, A. (2000) Pumping liquids using asymmetric electrode arrays. *Phys. Rev. E*, **61**, R45.
157 Gonzalez, A., Ramos, A., Green, N.G., Castellanos, A., and Morgan, H. (2000) Fluid flow induced by nonuniform AC electric fields in electrolytes on microelectrodes II, a linear double-layer analysis. *Phys. Rev. E*, **61**, 4019–4028.
158 Hollingsworth, A.D. and Saville, D.A. (2004) Dielectric spectroscopy and electrophoretic mobility measurements interpreted with the standard electrokinetic model. *J. Colloid Interface Sci.*, **272**, 235–245.
159 Bazant, M.Z., Thornton, K., and Ajdari, A. (2004) Diffuse charge dynamics in electrochemical systems. *Phys. Rev. E*, **70**, 021506.
160 Liang, H., Junmei, W., and Song, Y. (2017) Magnetic control microfluidic synthesis of FeZn, ZnSe and the doped nanomaterials and their magnetic and optical properties. Thesis for Master Degree of Science.
161 Wen, C.Y., Liang, K.P., Chen, H., and Fu, L.M. (2011) Numerical analysis of a rapid magnetic microfluidic mixer. *Electrophoresis*, **32**, 3268–3276.
162 Jiles, D.C. (1998) *Introduction to Magnetism and Magnetic Materials*, 2nd edn, CRC Press.
163 Owen, D. (2016) Mixing and sampling in a microfluidic channel using rotating magnetic microbeads. PhD thesis. Georgia Institute of Technology.
164 Cao, Q., Han, X., and Li, L. (2015) An active microfluidic mixer utilizing a hybrid gradient magnetic field. *Int. J. Appl. Electromagnet Mech*, **47**, 583–592.
165 Surenjav, E., Priest, C., Herminghaus, S., and Seemann, R. (2009) Manipulation of gel emulsions by variable microchannel geometry. *Lab Chip*, **9**, 325–330.
166 Nguyen, N.-T. (2010) Micro-optofluidic Lenses: a review. *Biomicrofluidics*, **4**, 031501.

www.ebook3000.com

167 Nguyen, N.-T., Kong, T.-F., Goh, J.-H., and Low, C.L.-N. (2007) A micro optofluidic splitter and switch based on hydrodynamic spreading. *J. Micromech. Microeng.*, **17**, 2169–2174.

168 Galajda, P. and Ormos, P. (2001) Complex micromachines produced and driven by light. *Appl. Phys. Lett.*, **78**, 249–251.

169 Neale, S., Macdonald, M., Dholakia, K., and Krauss, T. (2005) All-optical control of microfluidic components using form birefringence. *Nat. Mater.*, **4**, 530–533.

170 Leach, J., Mushfique, H., di Leonardo, R., Padgett, M., and Cooper, J. (2006) An optically driven pump for microfluidics. *Lab Chip*, **6**, 735–739.

171 Terray, A., Oakey, J.S., and Marr, D.W.M. (2002) Microfluidic control using colloidal devices. *Science*, **296**, 1841–1844.

172 Applegate, R.W. *et al.* (2006) Microfluidic sorting system based on optical waveguide integration and diode laser bar trapping. *Lab Chip*, **6**, 422–426.

173 Grujic, K., Helleso, O.G., Hole, J.P., and Wilkinson, J.S. (2005) Sorting of polystyrene microspheres using a Y-branched optical waveguide. *Opt. Express*, **13**, 1–7.

174 Hart, S.J., Terray, A., Arnold, J., and Leski, T.A. (2007) Sample concentration using optical chromatography. *Opt. Express*, **15**, 2724–2731.

175 Diguet, A. *et al.* (2009) Photomanipulation of a droplet by the chromocapillary effect. *Angew. Chem. Int. Ed.*, **48**, 9281–9284.

176 Kotz, K.T., Noble, K.A., and Faris, G.W. (2004) Optical microfluidics. *Appl. Phys. Lett.*, **85**, 2658–2660.

177 Cordero, M.L. *et al.* (2009) Mixing via thermocapillary generation of flow patterns inside a microfluidic drop. *New J. Phys.*, **11**, 075033.

178 Ichimura, K., Oh, S.-K., and Nakagawa, M. (2000) Light-driven motion of liquids on a photoresponsive surface. *Science*, **288**, 1624–1626.

179 Campbell, K. *et al.* (2004) A microfluidic 2×2 optical switch. *Appl. Phys. Lett.*, **85**, 6119–6121.

180 Zhang, D.-Y., Justis, N., and Lo, Y.-H. (2004) Fluidic adaptive lens of transformable lens type. *Appl. Phys. Lett.*, **84**, 4194.

181 Grillet, C. *et al.* (2004) Compact tunable microfluidic interferometer. *Opt. Express*, **12**, 5440–5447.

182 Li, Z., Zhang, Z., Emery, T., Scherer, A., and Psaltis, D. (2006) Single mode optofluidic distributed feedback dye laser. *Opt. Express*, **14**, 696–701.

183 Huang, P.-H. *et al.* (2012) A single-layer, planar, optofluidic switch powered by acoustically driven, oscillating microbubbles. *Appl. Phys. Lett.*, **101**, 141101.

184 Kats, A.V. and Kontorovich, V.M. (1969) Bending of surface and self-focusing of a laser beam in a linear medium. *ZhETF Pisma Redaktsiiu*, **9**, 192.

185 Kats, A.V. and Kontorovich, V.M. (1975) Lens effect due to the pressure of light on the surface of a transparent dielectric. *Sov. Phys. JETP*, **41**, 346–351.

186 Mitani, S. and Sakai, K. (2005) Observation of interfacial tension minima in oil-water-surfactant systems with laser manipulation technique. *Faraday Discuss.*, **129**, 141–153.

187 Gordon, J.P. (1973) Radiation forces and momenta in dielectric media. *Phys. Rev. A*, **8**, 14–21.
188 Born, M. and Wolf, E. (1999) *Principles of Optics*, Cambridge University Press.
189 Baroud, C.N., Delville, J.P., Gallaire, F., and Wunenburger, R. (2007) Thermocapillary valve for droplet production and sorting. *Phys. Rev. E*, **75**, 046302.
190 Casner, A. and Delville, J.-P. (2001) Giant deformations of a liquid–liquid interface induced by the optical radiation pressure. *Phys. Rev. Lett.*, **87**, 054503.
191 Casner, A., Delville, J.P., and Brevik, I. (2003) Asymmetric optical radiation pressure effects on liquid interfaces under intense illumination. *J. Opt. Soc. Am. B*, **20**, 2355–2362.
192 Ashkin, A. (1997) Optical trapping and manipulation of neutral particles using lasers. *Proc. Natl. Acad. Sci. U.S.A.*, **94**, 4853–4860.
193 Levich, V.G. (1962) *Physicochemical Hydrodynamics*, Prentice-Hall, p. 700.
194 Probstein, R.F. (2005) *Physicochemical Hydrodynamics: An Introduction*, John Wiley & Sons, Inc..
195 Sapuppo, F., Anandan, P., and Bucolo, M. (2011) IEEE International Conference on Automation Science and Engineering Vol. ThC4.2 (IEEE, Trieste, Italy, 2011) 381-386.
196 Barton, K.D. and Subramanian, R.S. (1989) The migration of liquid drop in a vertical temperature gradient. *J. Colloid Interface Sci.*, **133**, 211–221.
197 Nguyen, N.T. and Wu, Z. (2005) Micromixers-a review. *J. Micromech. Microeng.*, **15**.
198 Grigoriev, R.O. (2005) Chaotic mixing in spherical microdroplets. *Phys. Fluids*, **17**, 033601.
199 Ashkin, A., Dziedzic, J.M., Bjorkholm, J.E., and Chu, S. (1986) Observation of single beam gradient force optical trap for dielectric particles Opt. *Lett.*, **11**, 288–290.
200 Ashkin, A. and Dziedzic, J.M. (1973) Radiation pressure on a free liquid surface. *Phys. Rev. Lett.*, **30**, 139–142.
201 Chiou, P.Y., Moon, H., Toshiyoshi, H., Kim, C.-J., and Wu, M.C. (2003) Light actuation of liquid by optoelectrowetting. *Sens. Actuators, A*, **104**, 222–228.
202 Park, S.-Y., Teitell, M.A., and Chiou, E.P.Y. (2010) Single-sided continuous optoelectrowetting (SCOEW) for droplet manipulation with light patterns. *Lab Chip*, **10**, 1655–1661.
203 Moorthy, J., Khoury, C., Moore, J.S., and Beebe, D.J. (2001) Active control of electroosmotic flow in microchannels using light. *Sens. Actuators, B*, **75**, 223–229.
204 Oroszi, L., Dér, A., Kirei, H., Ormos, P., and Rakovics, V. (2006) Control of electro-osmotic flow by light. *Appl. Phys. Lett.*, **89**, 263508.
205 Baigl, D. (2012) Photo-actuation of liquids for light-driven microfluidics: state of the art and perspectives. *Lab Chip*, **12**, 3637–3653.
206 Kotz, K.T., Gu, Y., and Faris, G.W. (2005) Optically addressed droplet-based protein assay. *J. Am. Chem. Soc.*, **127**, 5736–5737.

www.ebook3000.com

207 Venancio-Marques, A. and Baigl, D. (2014) Digital optofluidics: LED-gated transport and fusion of microliter-sized organic droplets for chemical synthesis. *Langmuir*, **30**, 4207–4212.

208 Jahnisch, K., Hessel, V., Lowe, H., and Baerns, M. (2004) Chemistry in microstructured reactors. *Angew. Chem. Int. Ed.*, **43**, 406–446. doi: 10.1002/anie.200300577

209 Geyer, K., Codee, J.D.C., and Seeberger, P.H. (2006) Microreactors as tools for synthetic chemists – The chemists' round-bottomed flask of the 21st century? *Chem. Eur. J.*, **12**, 8434–8442.

210 Lee, J.N., Park, C., and Whitesides, G.M. (2003) Solvent compatibility of poly(dimethylsiloxane)-based microfluidic devices. *Anal. Chem.*, **75**, 6544–6554. doi: 10.1021/ac0346712

211 Willis, P.A. *et al.* (2007) Monolithic Teflon (R) membrane valves and pumps for harsh chemical and low-temperature use. *Lab Chip*, **7**, 1469–1474. doi: 10.1039/b707892g

212 Song, Y. and Henry, L.L. (2009) Nearly monodispersion CoSm nanoparticles synthesized by a microfluidic reactor. *Nanoscale Res. Lett.*, **4**, 1130–1134.

213 Jensen, K.F. (2006) Silicon-based microchemical systems: characteristics and applications. *MRS Bull.*, **31**, 101–107.

214 Song, Y.J. *et al.* (2011) Synthesis of well-dispersed aqueous-phase magnetite nanoparticles and their metabolism as an MRI contrast agent for the reticuloendothelial system. *Eur. J. Inorg. Chem.*, 3303–3313. doi: 10.1002/ejic.201100017

215 Fletcher, P.D.I. *et al.* (2002) Micro reactors: principles and applications in organic synthesis. *Tetrahedron*, **58**, 4735–4757. doi: 10.1016/s0040-4020(02)00432-5

3

Microfluidics Devices: Fabrication and Surface Modification

Zhenfeng Wang and Tao Zhang

Singapore Institute of Manufacturing Technology, 2 Fusionopolis Way, #08-04, Innovis, Singapore 138634

3.1 Introduction

The benefits of microfluidics technology could only be realized through device fabrication. However, it has never been straightforward in selecting the proper materials and fabrication techniques that meet the application and market requirements. In this chapter, a variety of process technologies for prototyping and producing microfluidic devices, especially the polymer-based devices, will be introduced. On the other hand, in the microscale, the surface property could be largely amplified, which becomes the leading factor of the device function. Surface properties such as wettability and adhesion may determine the characteristics of microfluidic devices in many applications. In the late part of this chapter, some surface modification techniques for tailoring the surface property of microfluidic channels and cavities will be explained.

3.2 Microfluidics Device Fabrication

Microfluidics started from inorganic materials such as silicon and glass. The fabrication process techniques largely evolved from semiconductor integrated circuits (ICs) or microelectromechanical systems (MEMS) fabrication. Accurate dimensional control in fabrication, excellent solvent resistance, and perfect surface property in electrophoresis applications are some of the major drivers for silicon- and glass-based microfluidics. Polymer-based microfluidics came much later, but gained dramatic growth either in prototyping and mass production. Thanks to the simple but high-quality replication of microfluidics and its very complicated features using poly(dimethylsiloxane) (PDMS), one kind of elastomer, prototyping of microfluidic device became extremely easy. For the mass production, there are mature manufacturing methods such as injection molding and plastic welding ready for adoption in making low-cost disposable devices. The recent adoption of three-dimensional (3D) printing technology

Microfluidics: Fundamentals, Devices and Applications, First Edition.
Edited by Yujun Song, Daojian Cheng, and Liang Zhao.
© 2018 Wiley-VCH Verlag GmbH & Co. KGaA. Published 2018 by Wiley-VCH Verlag GmbH & Co. KGaA.

www.ebook3000.com

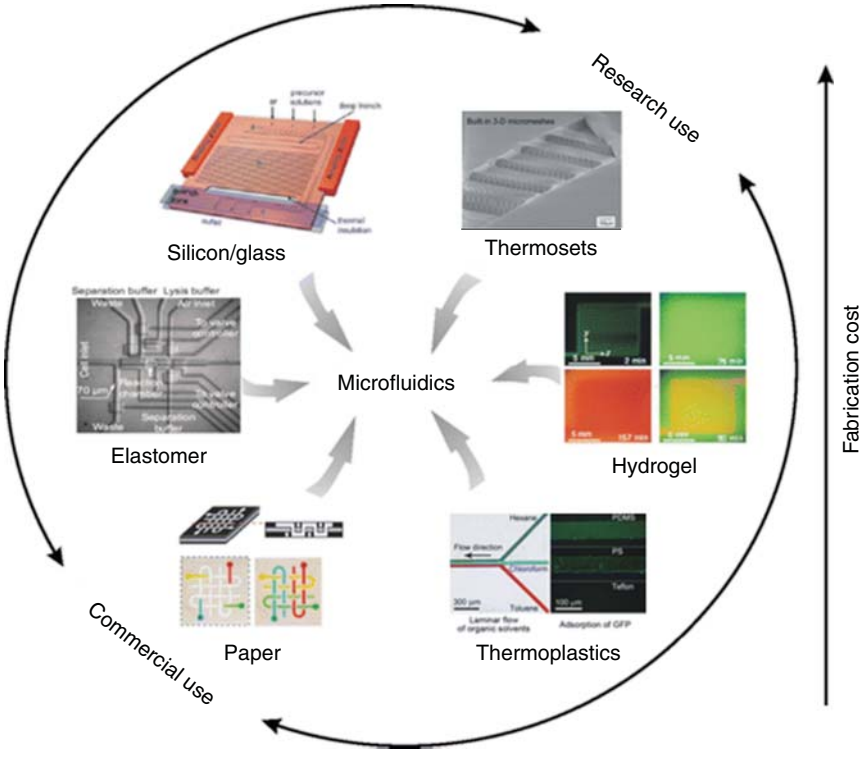


Figure 3.1 Illustration of different materials used in microfluidics device fabrication. (Ren *et al*. 2013 [1]. Reproduced with permission of American Chemical Society.)

in microfluidics introduced thermoset materials in device prototyping. Paper microfluidics has demonstrated their potentials in extremely low-cost fabrication, while hydrogel device have been used in cell culture applications. Figure 3.1 illustrated the different materials used in microfluidics fabrication and the simplified comparison between their major applications and cost [1]. Some characteristics and properties of these materials have been summarized in Table 3.1. Understanding the material property could be crucial in selecting proper device materials and fabrication techniques for specific microfluidic applications. For example, the high-density micro-pillar array used as capillary pump could only be easily fabricated through silicon dry etching process [2], but would be very tough for injection molding of thermoplastics.

3.2.1 Silicon and Glass Fabrication Process

A microfluidic device generally consists of embedded channels and cavities, as well as opening holes as fluidic interface. Generally the micro-features (channel and cavity) are created on one piece of planar plate and subsequently sealed by another piece of planar plate. In some cases the electrical connections are needed so as to integrate active components such as sensors or heaters. Table 3.2 summarized the selection guidelines about the device fabrication processes.

Table 3.1 Overview of materials for microfluidic device fabrication.

Property	Silicon/glass[a)]	Elastomers	Thermoset	Thermoplastics	Hydrogel	Paper
Young's (tensile) modulus (GPa)	130–180/ 50–90	~0.0005	2.0–2.7	1.4–4.1	Low	0.0003–0.0025
Common technique for microfabrication[b)]	Photolitho-graphy	Casting	Casting, photopolymer-ization	Thermo-molding	Casting, photopolymer-ization	Photolithography, printing
Smallest channel dimension	<100 nm	<1 μm	<100 nm	~100 nm	~10 μm	~200 μm
Channel profile	Limited 3D	3D	Arbitrary 3D	3D	3D	2D
Multilayer channels	Hard	Easy	Easy	Easy	Medium to high	Easy
Thermostability	Very high	Medium	High	Medium to high	Low	Medium
Resistance to oxidizer	Excellent	Moderate	Good	Moderate to good[c)]	Low	Low
Solvent compatibility	Very high	Low	High	Medium to high	Low	Medium
Hydrophobicity	Hydrophilic	Hydrophobic	Hydrophobic	Hydrophobic	Hydrophilic	Amphiphilic
Surface charge	Very stable	Not stable	Stable	Stable	N/A	N/A
Permeability to oxygen (Barrer[d)])	<0.01	~500	0.03–1	0.05–5	>1	>1
Optical transparency	No/high	High	High	Medium to high	Low to medium	Low

a) Photosensitive glass can be considered as thermoset.
b) Most of the materials can be fabricated by laser ablation, but compared with those obtained with lithographic or molding methods, the ablated features usually have a rougher surface and are often misshaped.
c) Excellent for Teflon.
d) 1 Barrer = 10^{-10} [cm^3 O_2(STD)] cm cm^{-2} s^{-1} $cmHg^{-1}$.

Source: Ren *et al*. 2013 [1]. Reproduced with permission of Royal Society of Chemistry.

www.ebook3000.com

Table 3.2 Selection of the glass and silicon fabrication process according to the requirements of the application (optical, geometrical, electrical, and thermal).

				Possible processing routes and criteria for their selection (preferred process options are shown in bold)	
Step	**Selection to be made**			**Route A**	**Route B**
1	Materials involved in the microfabrication process			• **Glass/glass** (take this route if the application requires optical transparency of the device)	• **Glass/silicon** (a more common and well-established route)
2	Patterning method	Microchannels		• **Wet etching in HF/HCl** • Dry etching (recommended only if vertical walls or high aspect ratio structures are required)	**Dry etching of the silicon** For complex microfluidic devices requiring multiple channel layers, the silicon wafer can be patterned on both sides and via holes etched through the wafer to connect them; alternatively, the glass can be patterned (by wet etching) as well as the silicon
		Through holes for fluidic ports		• **Wet etching** • **Sand-blasting** • Drilling	• **Dry etching** • Laser-drilling • Sand-blasting
3	Bonding method	No electrical connection	The device operates above ~200 °C	• **Fusion bonding** • Anodic bonding with metallic or a:Si layer	• **Anodic bonding**
			The device operates at or below ~200 °C	• **Adhesive bonding** • Anodic bonding with metallic or a:Si layer • Fusion bonding	• **Anodic bonding** • Adhesive bonding
		With electrical connection	The device operates above ~200 °C	• **Anodic** bonding (the thickness of the metallic layer can be critical) • Bonding using an intermediate layer	• **Anodic bonding** (the thickness of the metallic layer can be critical)
			The device operates at or below ~200 °C	• **Adhesive bonding** • Anodic bonding (the thickness of the metallic layer can be critical)	• **Adhesive bonding** • Anodic bonding (the thickness of the metallic layer can be critical)
4	Fluid connections			• Permanent: push-fit tubing into polymer ports (optionally fix with glue or PDMS) • Permanently attached ferrule with removable capillary tubing (e.g., Nanoport) • Temporary: push-fit capillary tubing into PDMS device (permanent if PDMS is plasma treated) • Mechanically clamped chip holder	

Source: Iliescu *et al.* 2012 [3] Copyright 2012 AIP Publishing LLC.

3.2.1.1 Photolithography

The shapes and dimensions of the features (channel, cavity, electrode, etc.) are usually defined through photolithography process. On the substrate (glass or silicon) surface, a layer of photosensitive polymer (photoresist) is coated through spin coating or dry film lamination, before it's exposed to intense light at selective areas that are defined by photomask. Alternatively, the photoresist layer can be exposed through direct laser or e-beam scanning without using a photomask. The exposed areas could be dissolved and washed away by special solution (developer). The remaining photoresist will harden under baking, which became a protection layer in further etching process.

3.2.1.2 Etching

After photolithography, the substrate surface is covered by protection layers on selective areas following the design. Etching is to selectively remove material from the substrate and form a microstructure. A widely used method is wet etching, which is to immerse the substrate into reactive chemical solution and get the material in the exposed area removed. For silicon substrate, the wet etching could be anisotropic, where the etching rate depends on the silicon crystallographic orientation and varies in different directions. Whereas for glass, the wet etching generally is isotropic, achieving the identical etching rate at all directions. Another etching method is dry etching, for example, the deep reactive ion etching (RIE). Extremely high aspect ratio structures such as deep holes with straight vertical side wall could be realized on silicon and glass substrates using dry etching.

3.2.1.3 Metallization

The microelectrodes on the substrate need to be deposited and patterned according to the design and passivated under the insulated layer. Figure 3.2 summarizes the techniques available for patterning the microelectrodes through lift-off process and depositing/patterning the passivation layer [4]. The metallic material consists of a 20 nm Ti (for adhesion) and 200 nm Pt, deposited through e-beam evaporation. Prior to the metal deposition, the substrate surface has been covered with a patterned layer of photoresist. The pattern of microelectrodes is formed by stripping the underneath photoresist. SiO_2 is a commonly used passivation material in MEMS microfabrication, which can be deposited through sputtering and patterned by standard photolithography. Parylene is another commonly used passivation material due to its superior mechanical and electrical properties. It can be patterned through standard photolithography and stripped through O_2 RIE. SU-8 is a photoresist widely used in MEMS microfabrication, which generates high aspect ratio structures through standard photolithography. On the other hand, dry film, a photoresist film used in printed circuit board manufacturing, can be applied on the surface using simple lamination tools. The patterns can be generated under UV exposure. Although dry-film passivation is easy and low cost to apply, the resolution is not as good as other passivation methods.

3.2.1.4 Bonding

During the bonding process, two or more pieces of silicon and/or glass substrate join together and form a stack. The bonding process could be direct (without

www.ebook3000.com

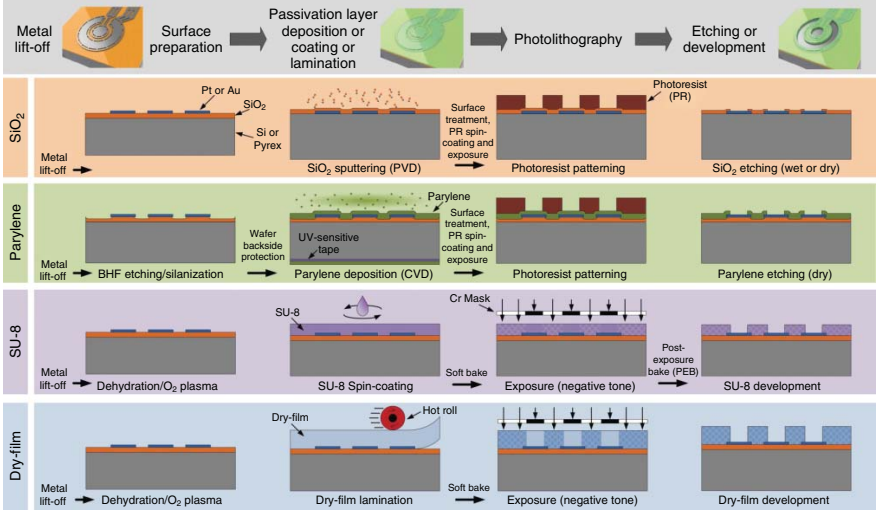


Figure 3.2 Summary of the process flows for sputtered SiO_2, Parylene deposition, SU-8 spin coating, and dry-film lamination. (Temiz *et al*. 2012 [4]. Reproduced with permission of Royal Society of Chemistry.)

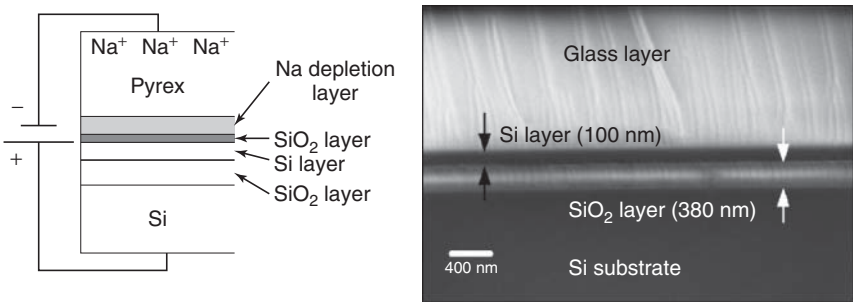


Figure 3.3 (a) Schematic representation of the layer sequence. (b) Cross-sectional scanning electron microscope image of wafer-bonded silicon on insulator (SOI) to glass. ([5] Copyright 2004 AIP Publishing LLC.)

intermediate material) or indirect (with intermediate layer, such as adhesive). In order to achieve strong bonding, the substrates need to be extremely flat, smooth, clean, and free of void. A popular silicon–glass bonding process is anodic bonding, where the pair of substrate experience electrical field and elevated temperature, as shown in Figure 3.3 [5]. Borosilicate glass such as Pyrex 7740 has high concentration of Na^+, which are driven away from the interface under high negative voltage. The depletion of Na^+ will establish a high electrical field between the glass–silicon interfaces, transport the oxygen from glass to the surface, and combine it with silicon to form SiO_2, which creates strong bonding. The elevated temperature will increase the mobility of ions and assist the bonding process.

3.2.2 Polymer Fabrication Process

There are many process techniques available for fabricating polymer microfluidic devices. Some techniques have been well established in manufacturing industry such as injection molding and ultrasonic welding, but still face new challenges in fulfilling the requirement of microfluidic devices. Some are emerging techniques such as 3D printing and roll-to-roll micro-embossing, which give the design and fabrication of polymer microfluidic devices more flexibility. Three types of polymer materials are involved in the microfluidics fabrication [6]. One type is thermoset, whose T_g is very high and close to the decomposition temperature (T_D). Thermoset materials including polyimide, photoresists like SU-8, and photocurable resins for stereolithography (SLA) cannot be reshaped after cured. Another type is thermoplastic materials, such as poly(methyl methacrylate) (PMMA), polycarbonate (PC), and cyclic olefin copolymer (COC). Thermoplastics soften with low T_g, which is far lower than TD, resulting in a large process window of reshaping. The third type is elastomer like PDMS. The process techniques we discuss under this section are mainly focusing on the fabrication of thermoplastics.

3.2.2.1 Patterning

Polymer patterning could be done with a mold (injection molding, embossing) or without a mold (micro-milling, 3D printing). Figure 3.4 compares the process

www.ebook3000.com

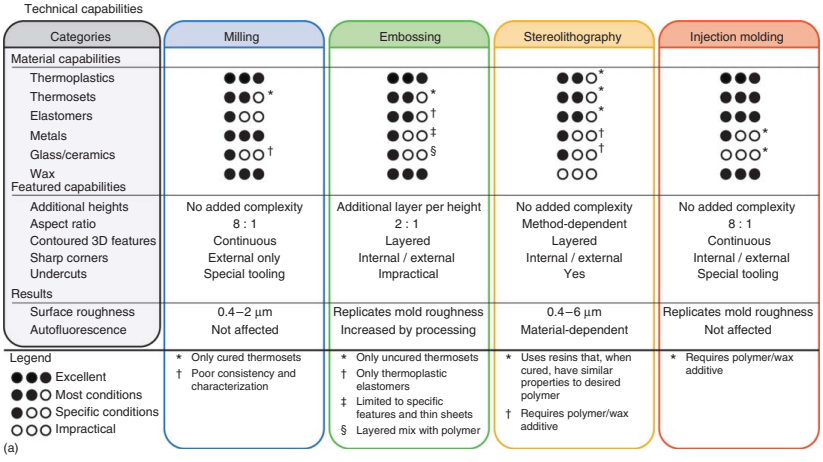
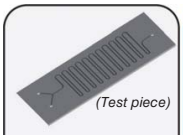


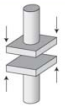
Figure 3.4 A comparison between milling and other microfabrication methods for plastics, in terms of (a) material compatibility, feature capability, and quality, and (b) cost. In (a), three filled circles = "excellent," while three open circles = "impractical" or "inadequate"; see legend (bottom left of a). In (b), for process times, "Time" represents the time of fabrication for one device for both on site and outsourced devices. "Cost" (in USD) is an estimate, where on-site fabrication is calculated based on the cost of goods used (not including labor; estimated from the labs of other authors), and outsourced fabrication is based on the lowest-quoted price we obtained for the different quantities. N/A = not applicable. (Guckenberger *et al.* 2015 [7]. Reproduced with permission of Royal Society of Chemistry.)

Cost comparison





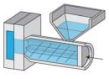
Milling



Embossing



Stereolithography



Injection molding

	Milling				Embossing		Stereolithography		Injection molding	
Setup costs	*(On-site)*		*(Outsourced)*		*(On-site)*		*(Outsourced)*		*(Outsourced)*	
Equipment	$15k <		N/A		$15k <		N/A		N/A	
Tooling / supplies	$500		N/A		$50		N/A		N/A	
Process times and costs										
Outsourced expenses	Time	Cost	Time	Cost	Time	Cost	Time	Cost	Time	Cost
Mold / tooling	N/A	N/A	N/A	N/A	4–15 d	$55–321	N/A	N/A	N/A	$2255
Device fabrication	N/A	N/A	11–15 d	$137	N/A	N/A	4–6 d	$33	11–15 d	$2
On-site expenses										
Machine setup	10 m	N/A	N/A	N/A	5 m	N/A	N/A	N/A	N/A	N/A
Material setup	<5 m	$1	N/A	N/A	< 5 m	$1	N/A	N/A	N/A	N/A
Device fabrication	10 m	N/A	N/A	N/A	30 m	N/A	N/A	N/A	N/A	N/A
Subtotal:	25 m	$1	N/A	N/A	40 m	$1	N/A	N/A	N/A	N/A
Expenses (per device)										
1 Devices	<1 h	$1	11–15 d	$137	4–15 d	$56–322	4–6 d	$33	11–15 d	$2257
25 Devices	1 d	$1	11–15 d	$137	6–17 d	$3–14	4–6 d	$33	11–15 d	$92
50 Devices	3 d	$1	11–15 d	$137	8–19 d	$2–7	4–6 d	$33	11–15 d	$47

(b)

Figure 3.4 (*Continued*)

www.ebook3000.com

capabilities and cost of four major polymer patterning techniques, for example, micro-milling, hot embossing, SLA, and injection molding [7]. Micro-milling and SLA could provide a wide range of feature capabilities and achieve complex features, while hot embossing and injection molding could deliver a very high quality of finished parts in terms of surface roughness and dimensional accuracy. In cost comparison, injection molding needs the highest investment on infrastructure, equipment, and technical know-how. If high-volume production is required, injection molding and hot embossing become more cost-effective per part. In contrast, the cost per part for micro-milling and SLA could be more constant, independent to the amount of produced parts. Generally, micro-milling is most suitable for rapid prototyping due to its low start-up cost, high resolution, and versatility regarding feature geometries and material choices. On the other hand, injection molding remains the most suitable patterning process for large-volume production due to the high fidelity of replication and low cost per part.

PDMS Casting PDMS is the most-employed material used in labs for prototyping microfluidic devices through casting. A mixture of liquid PDMS and cross-linking agent is poured on the surface of a mold, where the micro-features have been created through micromachining or MEMS process and heating. After the PDMS is hardened, it could be peeled off from the mold surface, while the micro-features (liquid channels, cavities) have been replicated in high fidelity. This piece of PDMS replica can be reversibly bonded with a glass slide by simple stacking and form the complete microfluidic prototype.

Mold Fabrication Replication process such as injection molding and hot embossing needs mold in the process, which largely determines the quality of the patterned polymer parts. The mold for polymer microfluidics devices needs to be mirror finished for achieving optically transparent and extremely flat polymer surface due to the polymer bonding requirement. Tool steel is conventionally used as the mold material and its features are machined through milling. However, fine features (50 μm or less) are very common in microfluidic device design, which are extremely difficult for conventional micromachining techniques such as micro-milling and micro-electrical discharge machining(EDM). Electroformed nickel and bulk metallic glass (BMG) appear to be the appropriate mold materials; the fabrication process is illustrated in Figure 3.5 [8]. A silicon master is first fabricated through standard UV lithography process and deep RIE, which forms the microstructures with high aspect ratio. In the case of nickel mold, after coating a thin layer of Ti/Ni, the silicon master is put in a nickel bath for electroplating. Once the nickel layer reaches the target thickness, the piece is put in KOH bath and gets the silicon material dissolved. The remained nickel piece needs to be further polished and milled to the desired overall outer dimension. For the BMG case, the silicon master is used as a mold to hot-emboss a piece of blank BMG, transferring the features to the BMG. The silicon is then dissolved in KOH solution and the BMG mold is fabricated.

Injection Molding During the injection molding process, the thermoplastic granules are transferred from the hopper to the heated barrels. The molten polymer

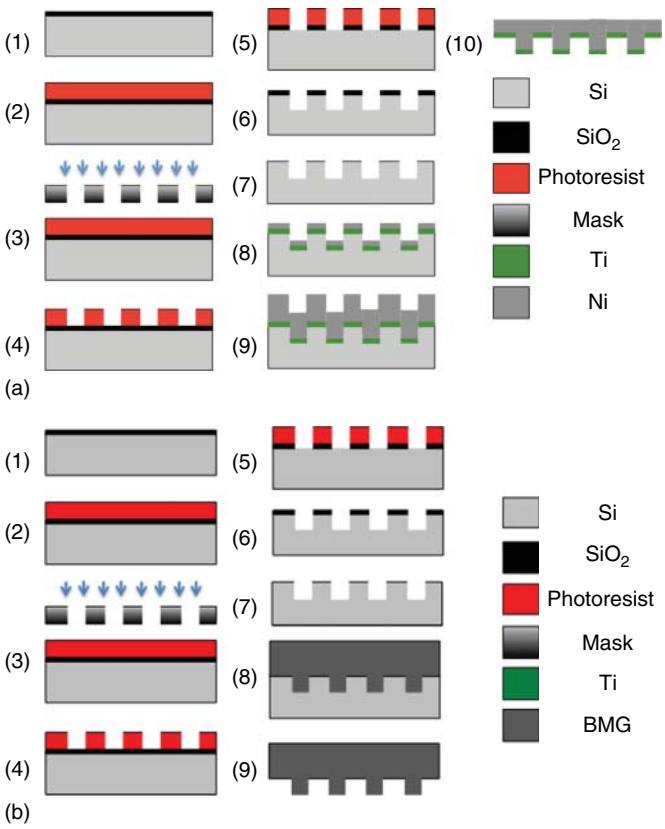


Figure 3.5 Process chains for manufacturing of Ni and BMG tool inserts: (a) UV-LIGA process: (1) Si oxidation, (2) spin coating photoresist, (3) UV lithography, (4) development, (5) etching SiO_2 and removing photoresist, (6) RIE etching of Si, (7) PVD coating Ti and Ni, (8) electroplating, (9) Si dissolving, and (10) Ni wafer dicing and polishing; (b) thermoplastic forming process: (1)–(7) are the same as with the UV-LIGA process, (8) BMG thermoplastic forming into Si master, (9) Si dissolving in KOH solution. (Zhang *et al*. 2016 [8]. Reproduced with permission of Elsevier.)

material is forced into the mold cavity under pressure and held for a certain time before the mold is cooled down. The polymer part gets solidified after the mold temperature is reduced below the glass-transition temperature of the polymer and ejected to complete the molding cycle. Common processing parameters usually include melt temperature, mold temperature, injection speed, injection pressure, holding pressure, and so on. The part quality can be measured in terms of complete filling, dimension stability, residual stress, and mechanical properties. Particularly for the high precision molding for microfluidic devices, shrinkage and shape stability could be a concern due to the thermal history of the molding process [9]. Increasing the holding pressure, or extending the cooling time, could help to alleviate the shrinkage but with the cost of long cycle time. On the other hand, "hesitation effect" needs to be considered when the design consists of high aspect ratio microstructures because the molten polymer tends to flow

www.ebook3000.com

more easily into cavities with relatively lower flow resistance areas, that is, areas with larger cross section, before entering the finer channels, which may result in premature freezing and cause incomplete polymer filling.

Hot Embossing Despite of the low throughput, hot embossing is still an attractive replication method for fabricating polymer microfluidic devices due to its simple setup. By stacking a mold (steel, silicon, PDMS, etc.) with desired features on top of the polymer substrate, thus putting the assembly under a hot presser, the features can be transferred to the polymer surface at elevated temperature (above the glass transition temperature of polymer) and pressure. The polymer part is then separated from the mold once the assembly is cooled down.

The process throughput of hot embossing is generally low due to the single-part operation. However, it has a high-throughput variant, the roller embossing, which is a continuous process [10]. As shown in Figure 3.6, the replication of features is between two rollers rather than two plates. The mold is a flexible copper film, whose features are formed through UV lithography and transferred to COC substrate through roller embossing. All the process of mold fabrication, polymer replication, and bonding can be implemented on a roll-to-roll manufacturing platform.

Laser Ablation Different from PDMS casting, thermoplastic injection molding, and hot embossing process, direct patterning process like laser ablation and micro-milling does not require mold. CO_2 laser has been used very often in creating microchannels on PMMA substrate as a rapid prototyping method.

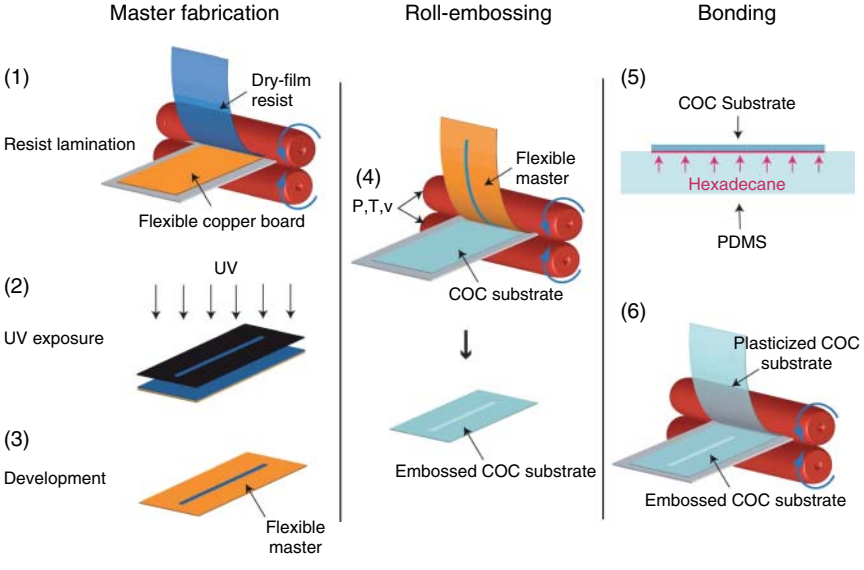


Figure 3.6 Schematic representation of the lamination-based processes: (1) lamination of the dry film resist on the substrate, (2, 3) photolithography steps, (4) replication by roll-embossing, (5, 6) bonding steps. (Miserere *et al*. 2012 [10]. Reproduced with permission of Royal Society of Chemistry.)

When CO_2 laser shines on PMMA surface, it raises up the localized temperature, where the polymer material melts and evaporates away, leaving a channel. The as-machined surface is usually quite rough, but can be smoothen through thermal annealing [11] or solvent polishing [12]. On the other hand, UV lasers, which have high photon energy, have been applied in fabricating high-quality microstructures on more polymer materials. When the energy is greater than the molecular bond strength, the UV photon breaks the bond directly and this results in a "cold" photoablation [13].

Micro-milling Micro-milling is a way to produce microchannels and other complex microscale features on polymer surface by directly removing the material through the high speed movement of cutting tools. The resolution is closely related to the machine setting and the selection of cutting tool, which usually defines the minimal feature of the final parts. Apart from surface roughness, the presence of bur could be another concern, which could be diminished by optimizing the toolpath [7].

3.2.2.2 Bonding

Polymer bonding is to encapsulate the open channels and cavities on the polymer substrate using another piece of polymer plate or film. Good optical transparency and strong bonding strength under elevated flow pressure are generally required for the post-bonding part.

Thermal Bonding Thermal bonding is to join thermoplastic plates with flat and smooth surface together under heat and pressure. At least one of the plates needs to be heated to the temperature close to or higher than its T_g, which enables the sufficient interdiffusion of polymer chains together with the applied force on the interface. The three key parameters in this process are temperature, pressure, and bonding time, which influence the effective bonding area and bonding strength, as shown in Figure 3.7 [14]. Besides the bonding area and strength, the deformation of the features caused by the bonding process is another important quality indicator. Surface treatment could increase the surface energy, lower down the bonding time, and reduce the feature deformation. In some cases, part warpage may occur during the process due to the releasing of residual stress, which could be introduced during patterning process such as injection molding.

When applying proper solvent solution, the surface of thermoplastic parts can be dissolved and solidified once the solvent solution is evaporated. This surface is ready to bond with another polymer part by forming new chemical bonds along the interface. This solvent bonding method can join the thermoplastic parts under much lower temperature compared with that in thermal bonding, which alleviates the risk of deformation caused by heating. The similar bonding scheme can be applied to plasticizer, which could reduce the cohesive intermolecular forces along the polymer chains and therefore lower the glass transition temperature [15]. Figure 3.8 shows the bonding of PMMA plate using 5% (w/v) dibutyl phthalate (DBP) solution in isopropanol under 90 °C, which is much lower than the glass transition temperature of PMMA. In solvent or plasticizer bonding, particular precaution should be taken to avoid the microchannel damage or clogging caused by the undesirable exposure to the bonding reagents.

www.ebook3000.com

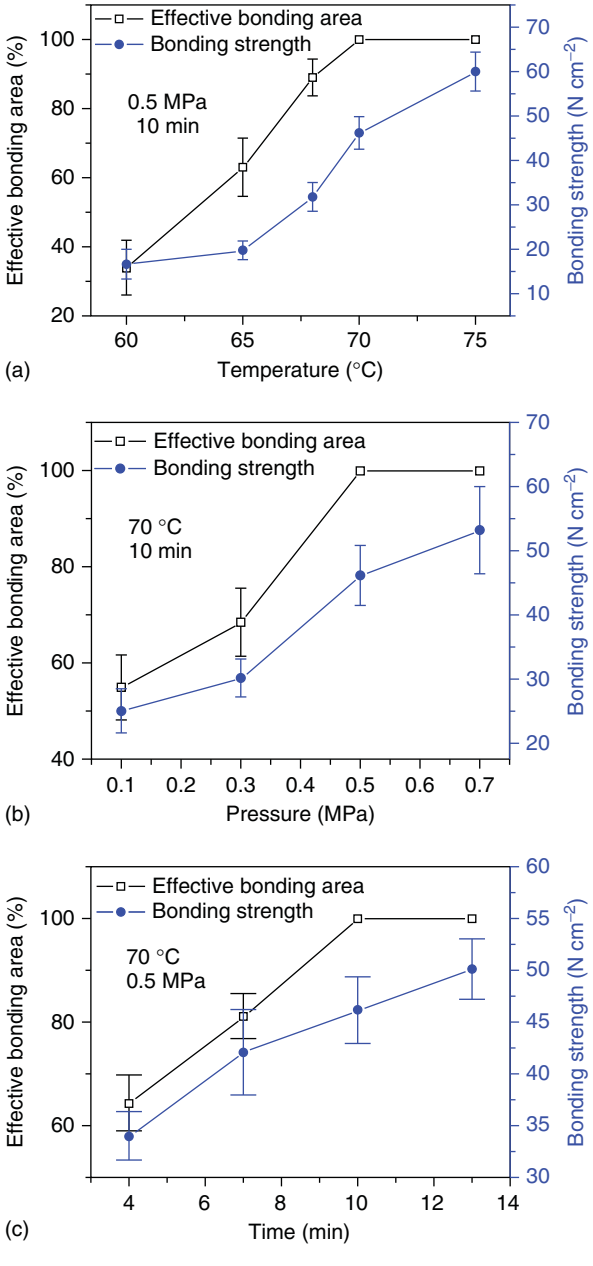
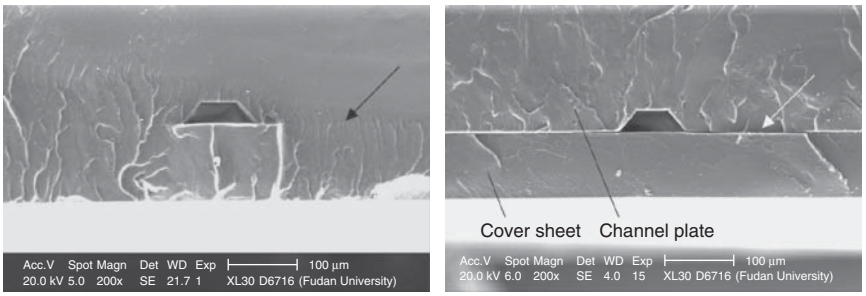


Figure 3.7 Process study of thermal bonding. Effect of temperature (a), pressure (b), and time (c) on the effective bonding area and bonding. ([14] Copyright 2014 Springer.)

Laser Bonding Thermoplastic plates can be bonded by laser as well. When stacking a laser-transparent polymer (the cover) with a laser-absorbent material (the bottom), a high-density laser light can pass through the cover and heat up the bottom. The material at the interface will be molten and create a hermetic bond. This mechanism has been applied in bonding PMMA plates with infrared (IR)



(a) (b)

Figure 3.8 Scanning electron microscopy (SEM) images illustrating the cross section of channel in PMMA microchips that were bonded with (a) and without (b) the assistance of DBP at 90 °C. Accelerating voltage: 20 kV and magnification: 200×. (Duan *et al*. 2010 [15]. Reproduced with permission of Elsevier.)

laser [16], where the cover is transparent and the bottom is opaque. In order to bond two pieces of transparent plate, a thin layer of IR-absorbent material needs to be applied between the bonding interfaces, which absorb the laser energy and generate localized heating, joining the two plates at designated areas. As a localized welding technique, the throughput of laser bonding relates to the scanning speed and power of laser.

Ultrasonic Bonding Similar to laser bonding, ultrasonic bonding joins the polymer parts through localized heating process, which results from vibrational friction between the bonding interface. Energy director structures define the region of thermal fusion. The typical bonding time is very short compared with that in thermal bonding and solvent bonding, while the major process parameters include the transducer amplitude, welding time, pressure, and energy. Figure 3.9 illustrates the design of two joining types [17]. In design (A), the energy director is a butt joint welding with the opposite plate that had no additional joint structure. In this case, only one plate is needed to make an energy director to enable the bonding, while no alignment is needed between the two parts. On the other hand, the molten polymer from the energy director may generate a gap and increase the channel depth. For the design (B), which uses tongue-and-groove joint, additional structures need to be created on both bonding plates and the alignment needs to be done prior to the bonding. This design eliminates the change of channel depth caused by the bonding process.

Adhesive Bonding UV-curable liquid adhesive can be used to bond polymer microfluidic devices. The way of applying adhesive has to be carefully chosen in order to prevent the clogging of microchannels after adhesive curing [18]. Another method of adhesive bonding is to use lamination films, such as pressure- and thermal-sensitive films. The film lamination process could have a high throughput in a roll-to-roll manner. The release liner of the lamination film could be directly used as the cover layer of microfluidic devices when the material compatibility is not an issue.

www.ebook3000.com

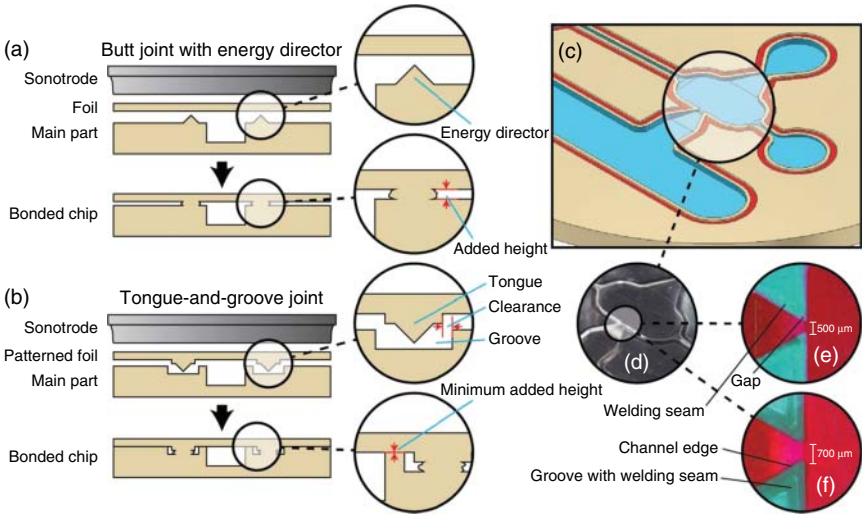


Figure 3.9 Sketches of two joint types for ultrasonic welding and presentation of chip systems with like joints. (a) Sketch of butt joint energy director pre- and post-welding. The energy director material results in an added channel height. (b) Sketch of a tongue-and-groove joint pre- and post-welding. The energy director material is contained within the groove, resulting in no added height. (c) Sketch of the microfluidic main part showing the channel system (blue) and the groove (red). (d) Photograph of ultrasonically welded chip with the same channel system featuring a butt joint. The width of the capillary microvalve is 500 µm. Parts (e) and (f) show micrographs of capillary microvalves, filled with a 1.3% (v/v) sarkosyl Rhodamine B fluorescent dye solution. For the butt joint, the liquid extends outside the channel because of the added height between the chip and foil (e), whereas no liquid is observed outside the channel for the tongue-and-groove joint (f). Contrast and color were adjusted for clarity. The darker tint of turquoise is a welding phenomenon known as flash that changes the refractive properties of the polymer. (Kistrup *et al*. 2015 [17]. Reproduced with permission of Royal Society of Chemistry.)

3.2.2.3 Metallization

Creating conductive patterns on polymer surface generates additional values to the microfluidic devices as microelectrodes of sensors and actuators, electrical interconnects, antenna, heaters, and so on. Thin layers (typically less than 300 µm) of metallic material can be deposited through MEMS process such as sputtering and evaporation. A shadow mask stacking on the substrate will define the shape of the patterns. The resolution will be limited by the shadow mask fabrication. For thicker electrodes, conventional screen printing technique could be applied, while the material choices are limited by the availability of printing pastes, which contain the conductive particles. The adhesion between the conductive layer and polymer substrate could be a concern especially under the condition of temperature changing due to the unmatched coefficient of thermal expansion.

3.2.2.4 3D Printing

In recent years, 3D printing is quickly becoming an important prototyping method, which has shown good potential in producing polymer microfluidic

devices. Various 3D printing techniques such as SLA, multi-jet modeling (MJM), photopolymer inkjet printing, fused deposition modeling (FDM), and thermoplastic extrusion have demonstrated their capabilities in directly forming the embedded channels in polymer block without the need of bonding process [19]. 3D printing provides alternative choices of fabrication method in prototyping or low-volume production of polymer microfluidic devices and eliminates the need of lamination (bonding) process. Currently some factors including the resolution, material properties (biocompatibility, optical transparency), and throughput limit the usage of 3D printing in microfluidics. In Table 3.3, available 3D printing technologies are summarized and the advantages/disadvantages for fabricating microfluidic devices are compared.

3.2.2.5 Surface Treatment

The polymer surface can be modified into being hydrophilic or hydrophobic according to the need of microfluidic applications, such as liquid sample loading or flow stop. Such modification can be realized through chemical coating and other methods, whose details will be revealed in Section 3.3.

3.2.3 Fabrication for Emerging Microfluidics Devices

Some trends could be observed about the development of fabrication technologies for microfluidic devices. The level of integration and the complexity of the design would be increased, which enhances the functions of the microfluidics system. More components, such as valves, filters, sensors, and heaters, need to be integrated within one microfluidic device. On the other hand, some nanoscale structures would be required, which relate to the study of nanofluidics, the study and application of fluid flow in channels/pores with at least one characteristic dimension below 100 nm. Such nanostructures provide ultrahigh surface-to-volume ratio and approach to the size of important biomolecules such as DNA and protein. Figure 3.10 shows the typical channel width/channel height (depth) that can be reached by the main fabrication approaches summarized in the review [21], which is helpful to guide corresponding fabrication process design. The nanolithography-based techniques include electron beam lithography (EBL), focused ion beam (FIB), nanoimprint lithography (NIL), interferometric lithography (IL), and sphere lithography (SL). MEMS-based nanofabrication approaches include sacrificial layer releasing, etching and bonding, etching, bonding and deposition, edge lithography, and space techniques. Nanomaterial-based techniques include nanowire, nanotube, block copolymer, tracked etching nanopores, anodized aluminum oxide (AAO), and ion-selective materials.

3.3 Surface Modification in Microfluidics Fabrication

Surface properties such as wettability play a very important role in microfluidic devices. There are two ways to control the wettability of solid surfaces: chemical composition and geometrical structures of the surfaces. Generally, surface

www.ebook3000.com

Table 3.3 The different types of 3D printing technologies currently used for making chips, their energy source (referring to the energy that is required to join the material), materials that are compatible with the machines, advantages and disadvantages of the machines, and applications in the fields of microfluidics and biology.

3D printing	Energy source	Materials	Advantages	Disadvantages	Application
Stereolithography (SLA)	Laser/UV	Photocurable resin/polymer – acrylonitrile butadiene styrene (ABS)-like, and so on	High resolution, good surface finish	Requires post curing and removal of support structures	• Making of master mold • Microfluidic chips with active features • Microfluidics interface (MFI) • Pathogen detection • Biological assay (cell observations)
Digital micro-mirror device-based projection printing (DMD-PP)	UV	Photocurable resin/polymer	Good resolution, fast build time compared with SLA	Limited build volume, peeling of parts from the tray may damage the chip	• Making of master mold • Cancer assay (studies on cell migration)
Two-photon polymerization (2PP)	Femto-second laser	Photocurable resin/polymer	Very high resolution with small features	Slow build time	• Biology observation on cell mobility
Fused deposition modeling (FDM)	Thermal	Thermoplastics such as ABS, polycarbonate, and poly-phenylsulfone; elastomers	Cheap materials, ease of support removal	Slow build time, restricted accuracy Not many transparent materials available	• Pathogen detection of bacteria • Pathogen detection of viruses
Inkjet	UV	Photocurable resin/polymer	Fast build speed Multi material printing	Removal of support materials from the channels is tedious	• Making of master mold • Versatile chips for different types of electrodes for gas detection • Toxicity assay • Biological assay (cell observations)
Bioprinting	Laser/UV	Hydrogels, viscous materials, photocurable resin	Multiple materials, cells can be printed as well	Low build rate, extrudes as filament only, viscous solution may clog system	• Making of vascular channels

Source: Ho *et al*. 2015 [20] Copyright 2015 Royal Society of Chemistry.

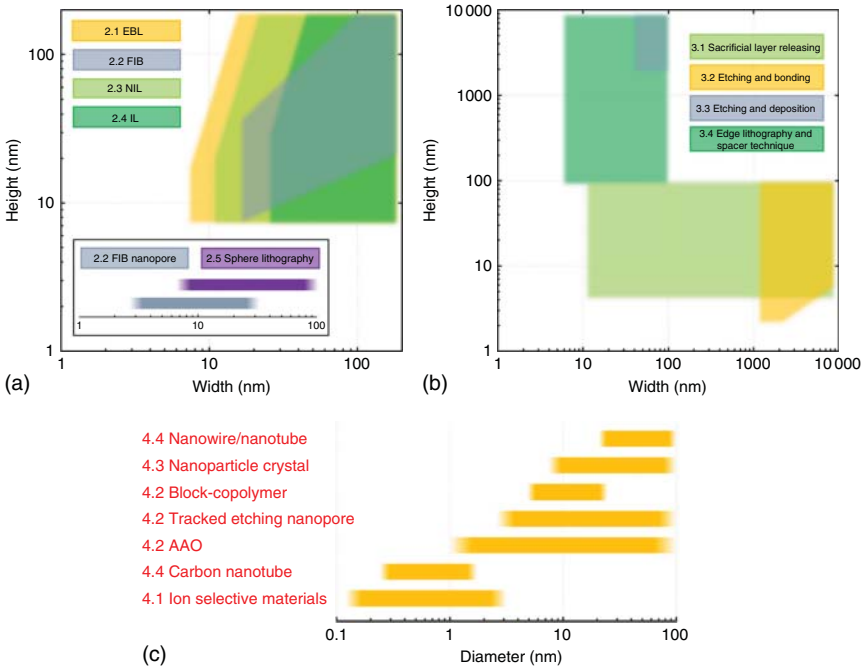


Figure 3.10 Achievable geometries and feature sizes of nanofluidic devices using current nanofabrication approaches. (a) Nanolithography-based techniques; (b) MEMS-based techniques; and (c) nanomaterials-based techniques. ([21] Copyright 2013 AIP Publishing LLC.)

roughness can enhance the effect, especially by fractal structures. In widely used materials for microfluidic device, glass and oxidized silicon have intrinsic hydrophilic surface, which produces low flow friction of water in fine channels. Recently, polymer-based microfluidic devices become more popular because of their outstanding properties such as low cost and easily generated channels. However, most polymeric materials have pristine surfaces with low surface energies and are hydrophobic rather than hydrophilic, which leads to problems such as high flow resistance that even bubbles in thin channels, high operation pressure, and high device complexity.

Surface modification methods that have been published to date can be categorized into chemical and physical methods. Chemical modification immobilizes functional molecules to create the desired surface properties so that the surfaces become passivated or activated with attached chemicals. On the other hand, physical modification may change the surface roughness, grain size, and grain boundaries by exposure to laser, plasma, heat, or polishing. Figure 3.11 illustrates normally employed surface modification methods for microfluidic materials [22]. Surfaces of microfluidic devices can be modified by these illustrated methods to overcome or reduce their inherent shortages or disadvantages. This section covers the recent advances in plasma treatment and surface grafting for the surface modification of microfluidic device substrates.

www.ebook3000.com

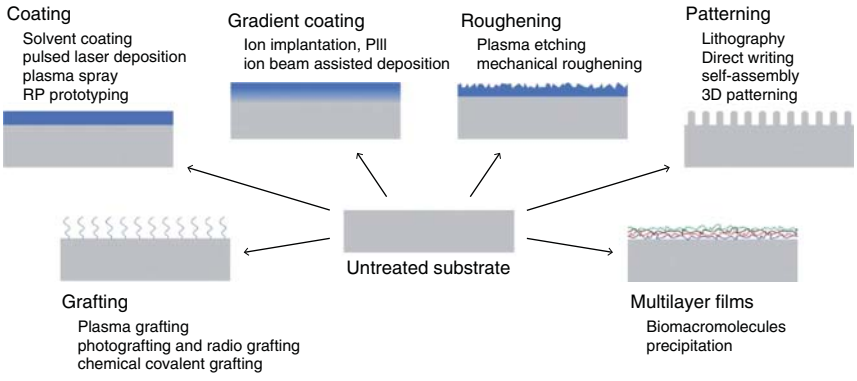


Figure 3.11 Schematic diagrams of surface modification techniques. (Qiu *et al*. 2014 [22] https://academic.oup.com/rb/article/1/1/67/2909403/Advances-in-the-surface-modification-techniques-of. Used under CC BY 4.0 https://creativecommons.org/licenses/by/4.0/.)

3.3.1 Plasma Treatment

Plasma is a state of matter that is partially or fully ionized and contains charged particles of free ions, electrons, radicals, and neutral particles of atoms and molecules. Plasma treatment is a technique that relies on the use of an ionized gas to functionalize the outer surface. Its key benefits are the short treatment times and easy operation, which make it one of the most efficient ways to modify surfaces such as silicon, glass, or polymers. Plasma could be divided into thermal (also called high temperature, hot, or equilibrium) and nonthermal (also called low temperature, cold, or nonequilibrium). The thermal plasma is nearly fully ionized, where electrons and heavy particles have the same temperature. The temperature required to generate thermal plasma is typically ranging from 4000 to 20 000 K [23]. Such high temperature is destructive for polymers. For nonthermal plasma, only a small fraction of the gas molecules are ionized, where ions and neutrals are at a much lower temperature (maybe as low as room temperature), although the temperature of electrons could reach several thousand degrees Celsius. The plasma used for the surface modification of polymer-based microfluidic device is nonthermal, which can be generated by different sources, including corona discharges, dielectric barrier discharges, radio frequency discharges, and so on [24].

A practical challenge with plasma oxidation of polymer-based microfluidic device is the hydrophobic recovery, which could be caused by the creeping movement of polymer chains from the bulk to the surface and the rearrangement of highly mobile polymer chains at room temperature to minimize the surface energy. These effects are acerbated by the low glass transition temperature of PDMS, which is in the order of −120 °C. More recently, Priest *et al*. [25] reported an entirely new approach to the selective plasma oxidization of a PDMS surface within a microchannel. In this work molten gallium electrode pads were placed inside bulk PDMS along a bonded microchannel in order to create patterned electrodes for plasma production, as shown in Figure 3.12. The use of patterned electrodes not only localized the plasma spatially by tuning the applied voltage

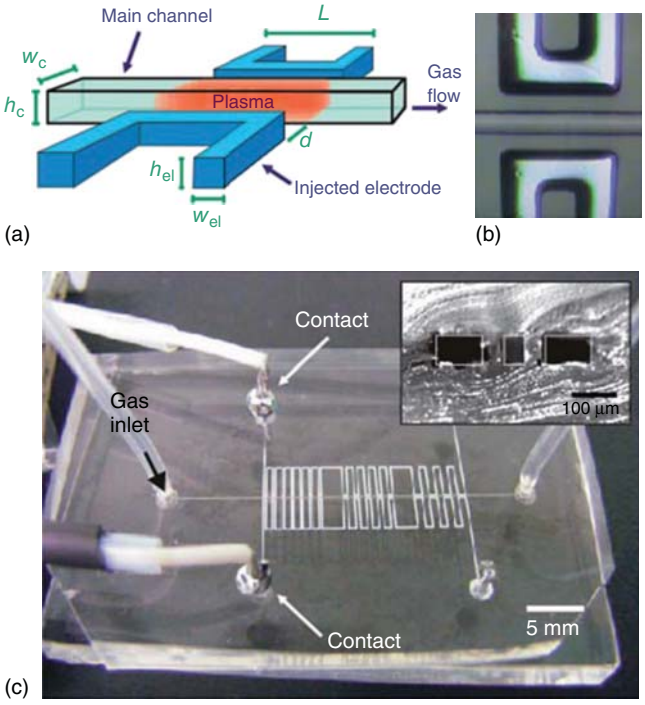


Figure 3.12 PDMS microchip with injected electrode pads for generating localized plasma in main channel. (a) Chip design, showing the injected electrodes, the main channel, and the localized plasma. (b) Injected gallium electrodes adjacent to main channel. (c) PDMS microchip with patterned gallium electrodes adjacent to main channel. Cross section of main channel and gallium electrodes is shown in the inset. (Priest *et al*. 2011 [25]. Reproduced with permission of Royal Society of Chemistry.)

and frequency but also reduced the treatment time. This local plasma activation differed from previous approaches where typically an entire microchannel is exposed to a plasma [26] or plasma microjet [27].

Another plasma treatment method is plasma polymerization. Plasma polymerization is a process that ionizes monomer gas into plasma state and induces radical polymerization to create polymer coating on a substrate, so as to change the surface property of the pristine surfaces (Figure 3.13). This technology has been widely used on microfluidic devices especially for biomedical applications. For example, Liu *et al*. [28] employed plasma polymerization to modify surfaces via generating different functional groups (amine, carboxyl, methyl, and hydroxyl) and found that the plasma polymerization of allylamine on the surface promoted osteogenic differentiation of human adipose-derived stem cells.

Plasma treated with O_2 plasma or other gases generates surface silanol groups, which can further react with alkoxy- or chlorosilanes. These silanes can be tuned with certain functional head groups, which introduce a desired surface chemical functionality. For example, O_2 plasma-pretreated PDMS has been used to covalently attach four different aminonaphthol silanes via silanization [29]. The results showed that the water contact angle (WCA) values of two

www.ebook3000.com

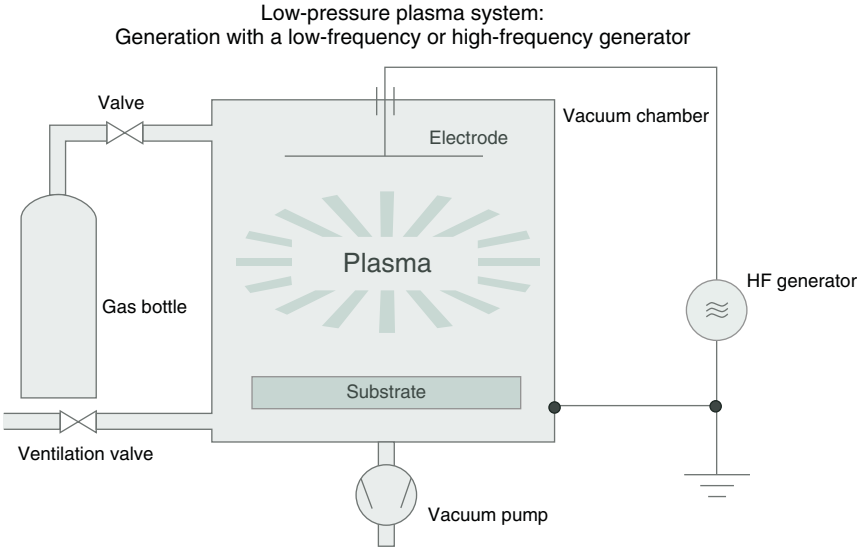


Figure 3.13 Sketch of a plasma polymerization system. The monomer in gas bottle can be plasmarized by the HF generator and polymerized on substrate to form a polymer coating. (Copyright 2011 Diener Electronic LLC.)

surfaces modified with two different aminonaphthols decreased from 109° of native PDMS to 83° and 79°, respectively, while those modified with fluorinated aminonaphthols increased from 109° to 116° and 122°, respectively. Sofla and Martin [30] have reported an interesting surface modification technique using tridecafluoro-1,1,2,2-tetrahydrooctyl trichlorosilane vapor on non-pretreated PDMS and glass surfaces for permanent or nonpermanent bonding between PDMS and glass, depending on the vapor deposition time. They found that all the samples were permanently bonded using a deposition time of 24 h, while no permanent bonding was obtained using deposition time of 3 h or less.

3.3.2 Surface Modification Using Surfactant

Surfactants are widely used to pretreat microchannels and often added to the running buffer of analytical microfluidic separations to render the surface hydrophilic *in situ*. Various surfactants have been used for dynamic surface modification, which are summarized in Ref. [31]. Wu and Hjort [32] have added a nonionic surfactant Pluronic F127 (polyethylene oxide)$_{100}$(polypropylene oxide)$_{65}$(polyethylene oxide)$_{100}$ ((PEO)$_{100}$(PPO)$_{65}$(PEO)$_{100}$) into PDMS prepolymer before curing. Figure 3.14 shows that the Pluronic F127 molecules embedded in the PDMS migrate toward the water/PDMS interface to minimize surface energy when the microchannel was filled with water. This results in the hydrophobic interaction between the polypropylene oxide (PPO) segments and PDMS, causing the hydrophilic polyethylene oxide (PEO) to extend outward from the surface. The WCA of the Pluronic F127-modified PDMS surface changed from 99° to 63° after immersing the sample in water for 24 h, as

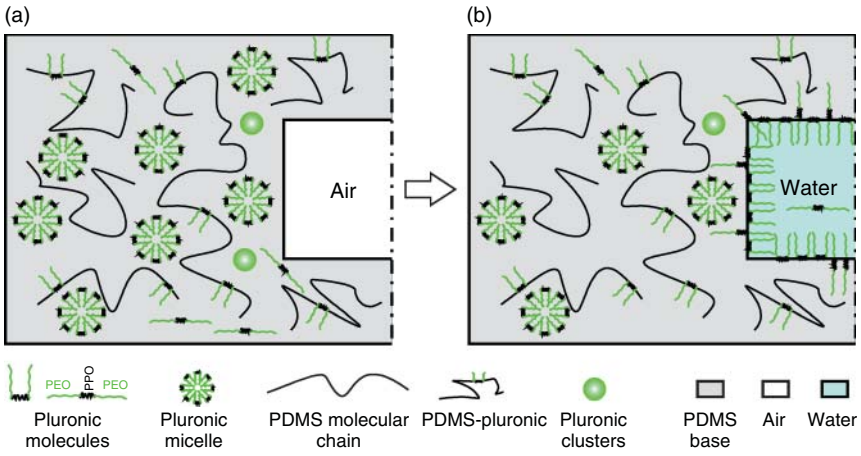


Figure 3.14 Schematics of the process of surface modification of PDMS with Pluronic F127. (a) The microchannel based on Pluronic F127 embedded PDMS and (b) when the microchannel based on Pluronic F127 embedded PDMS was filled with water, Pluronic F127 molecules migrated to the water interface with hydrophilic PEO toward water and hydrophobic PPO toward PDMS. (Wu and Hjort 2009 [32]. Reproduced with permission of Royal Society of Chemistry.)

compared with a WCA of 104° for native PDMS. Furthermore, this Pluronic F127-modified PDMS was shown to significantly suppress the nonspecific adsorption of a fluorescein isothiocyanate (FITC)-labeled IgG antibody due to the improved hydrophilicity, compared with native PDMS.

3.3.3 Surface Modification with Grafting Polymers

Most of those coatings mentioned above are physically bound to the substrate, and the binding strength is limited. On the other hand, graft polymer coating is widely used for tailoring the surface chemistry and wettability of microfluidic devices or introducing surface functional groups for further modification. Graft polymer coating can be divided into two main categories: grafting-onto and grafting-from. The first approach, termed graft-onto, consists of the adsorption to surfaces of pre-synthesized polymer chains end-functionalized with a chemical anchoring group (Figure 3.15, left). Alternatively, graft-from approaches, in which a polymer is grown *in situ* from the surface via a surface-adsorbed initiation group, are generally capable of producing denser polymer layers (Figure 3.15, right).

3.3.3.1 Surface Photo-Grafting Polymerization

Compared with other modification methods, surface graft polymerizations induced by UV irradiation exhibit some advantages, for example, fast reaction rate, low cost of processing, simple equipment, and easy industrialization. Moreover, the distribution of grafted chains is limited within a shallow region near the surface. Surface photo-grafting polymerization thus offers the unique ability to tune and manipulate surface properties without damaging the bulk material.

www.ebook3000.com

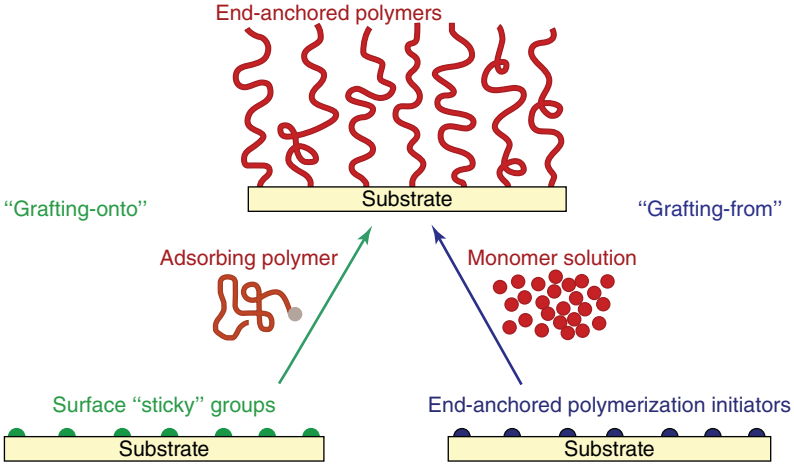


Figure 3.15 Sketch of surface polymer grafting approaches: *graft-onto* (left) and *graft-from* (right).

UV light is extensively used to carry out surface graft polymerization, often in the presence of a photoinitiator or photosensitizer. Compared with Norrish type I photoinitiators [33], Norrish type II photoinitiators were more frequently used, predominantly because the latter results in higher grafting efficiency, while the former leads to lower grafting efficiency even with higher polymerization yield and higher polymerization rate [34]. Among the existing Norrish type II photoinitiators, probably the most widely selected have been benzophenone (BP) [35] and its derivatives [36], showing effectively initiating or co-initiating a number of radical-induced surface photo-grafting polymerizations. In principle, when UV irradiated, BP or BP-based molecules are excited to a singlet state and then jump to a triplet state by intersystem crossing (ISC) (Figure 3.16). Investigations have demonstrated that BP and its derivatives in a triplet state undergo

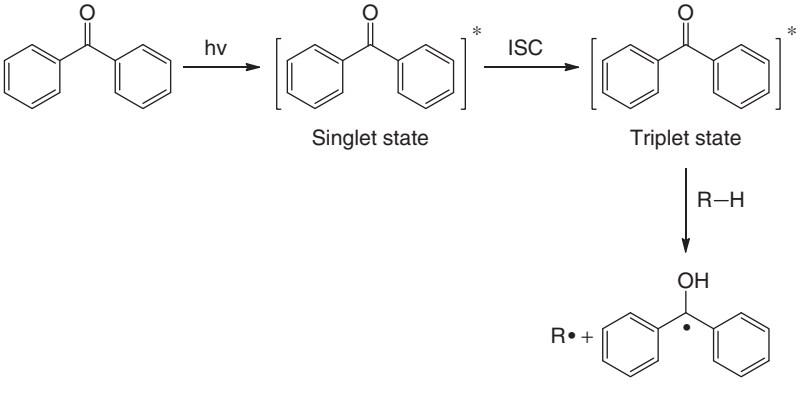


Figure 3.16 Photo-grafting polymerization initiated by BP. (Dworjanyn and Garnett 1988 [34]. Reproduced with permission of John Wiley & Sons.)

hydrogen-abstracting reactions from substrates, consequently providing surface radicals (R•) capable of initiating surface graft polymerization.

Su and Liao [37] and Lin *et al*. [38] have hydrophilized a PDMS surface via a one-step UV exposure with a mixture of BP and monomer solutions (acrylic acid copolymer (AAc) and acrylamide (AAm), respectively). The resulting hydrogel-modified PDMS microchannel could be employed to generate both water-in-oil-in-oil (W/O/O) and water-in-oil-in-water (W/O/W) emulsions. Patterned poly (acrylamide)-modified PDMS microchannel was obtained through a photomask and then successfully patterned with trypsin using ethyl-3-(3-dimethylamino-propyl) carbodiimide/*N*-hydroxysuccinimide (EDC/NHS) coupling to produce proteolytic surface patches [39].

Wang and Yang [40] opened up an alternative strategy to achieve surface photo-grafting polymerization and 3D construction on the surface, that is, firstly coated methyl methacrylate/1,2-divinylbenzene (MMA/DVB) microemulsion on casting polypropylene (CPP) films, and then conducted photo-grafting with BP as photoinitiator. Atomic force microscopy (AFM) images demonstrated that the grafted layer was built up by nanoparticles about 30–50 nm in diameter. These particles were linked together and further covalently tethered onto the CPP surface. The possible mechanism for the formation of the above topography was schematically illustrated in Figure 3.17.

As introduced above, monolayer of nanoparticles on a substrate was produced facilely [41], as presented in Figure 3.18. When the inverse microemulsion of *N*-vinyl pyrrolidone/*N*,*N*-methylenebisacrylamide (NVP/MBAA) was used instead of the MMA/DVB emulsion mentioned above, superhydrophilic surfaces were attained [41].

3.3.3.2 Surface-Initiated Atom Transfer Radical Polymerization (SI-ATRP)

Surface-initiated atom transfer radical polymerization (SI-ATRP) is another popular choice for grafting-from. ATRP normally offers the possibility to select the most convenient and appropriate initiator for the monomer in question. However, in grafting by ATRP from a polymer surface, there is one restriction and complication that initiating sites need to be generated at the original surface. In

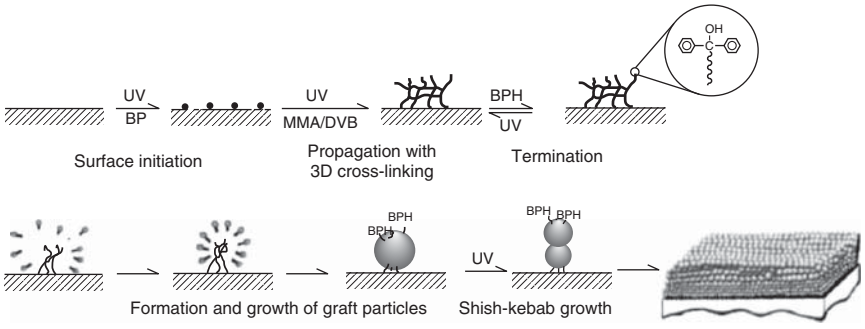


Figure 3.17 Chemical formation of the graft chains and the growing mechanism of the graft particles. (Wang and Yang 2004 [40]. Reproduced with permission of American Chemical Society.)

www.ebook3000.com

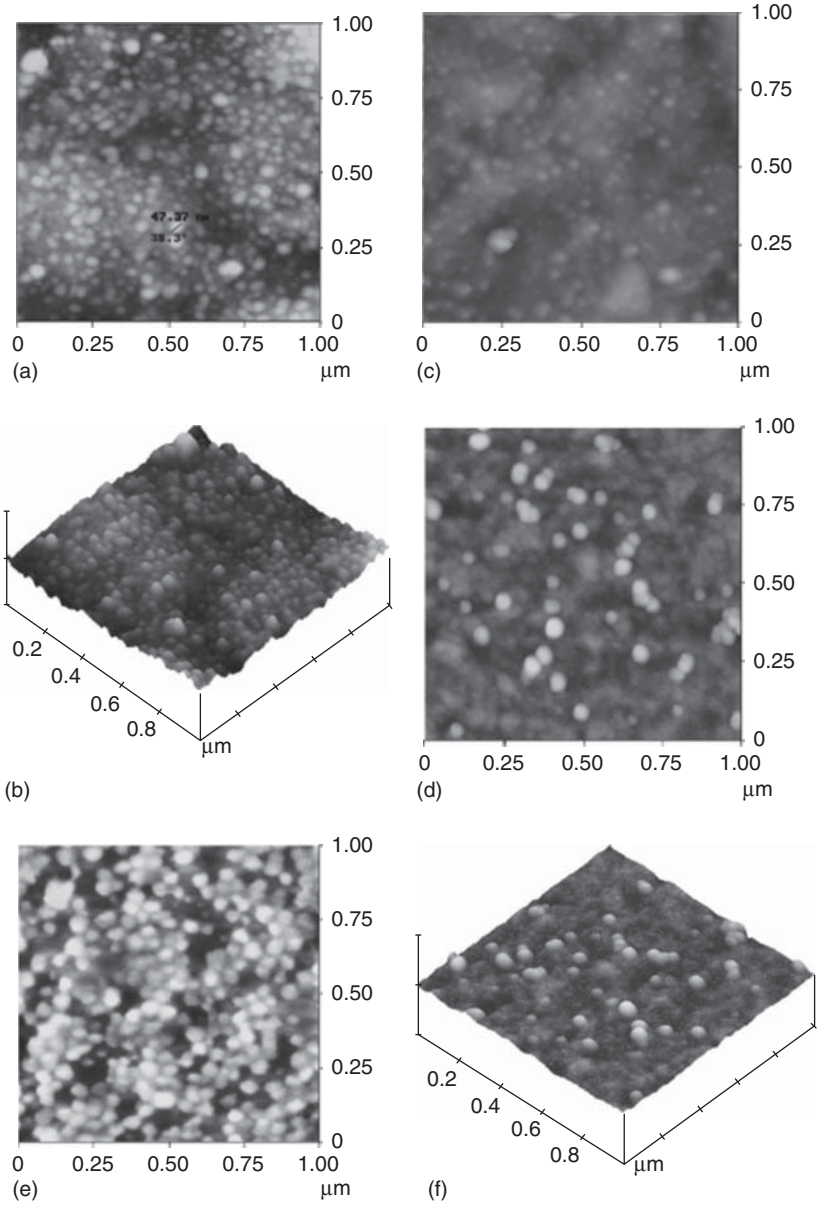


Figure 3.18 AFM images of film topography after surface photo-grafting microemulsion by the one-step method (MMA concentration 6 wt% in (a) and (b)) and two-step method (MMA concentration 20 wt% in (c, d, and f)); 30 wt% in (e): (a) height image of the film after 2 min UV irradiation; GY 0.679 wt%; (b) three-dimensional (3D) effect of the height image in (a); (c) height image of the film after 2 min UV irradiation; GY 0.070 wt%; (d) height image of the film after 4 min UV irradiation; GY 0.095 wt%; (e) height image of the film after 6 min UV irradiation; GY 0.188 wt%; and (f) 3D effect of the height image (d). (Wang and Yang 2004 [40]. Reproduced with permission of American Chemical Society.)

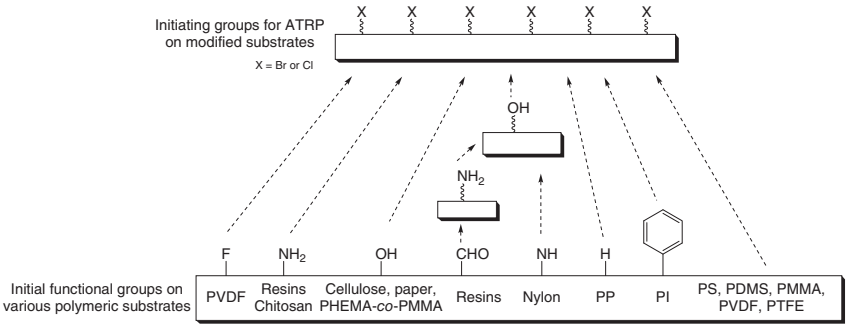


Figure 3.19 Sketch of preparation of initiating groups for ATRP on organic/polymeric substrates.

www.ebook3000.com

principle, the concept of grafting from a polymer also allows an initiator gradient, enabling a variation in the grafting density. The grafted polymer layer can then be designed to vary from mushrooms or isolated chains to brushes or high grafting density, which has been shown to have large implications for some biofunctionalities in microfluidic applications [42].

Fabrication of the Initiator for SI-ATRP In Figure 3.19, the polymeric substrates and their original functional groups are summarized. These functional groups are transformed into initiating groups for SI-ATRP as explained below. Amino groups are seldom formed on surfaces (although examples do exist, e.g., in chitosan), but many natural materials are endowed with hydroxyl groups. Cellulose membranes, paper, or NH_2–glass slides were, for example, reacted with 2-bromoisobutyrylbromide (Br-*i*-BuBr) and triethylamine (TEA) to form the bromoester or bromoamide initiator.

Normally, a UV/ozone or oxygen plasma surface pretreatment step is required for ATRP on commonly used polymer materials for microfluidic devices. Li *et al*. [43] successfully employed oxygen plasma to generate hydroxyl groups on PP film. Then the PP–OH surface produced a stable initiator layer via the C—O—Si bonds. The procedure followed for the immobilization of ATRP initiator on the PP film is shown in Figure 3.20.

Biofunctional Coatings Various monomers have been used for SI-ATRP to prepare polymer coatings that can be applied within the field of biotechnology for microfluidic devices. The term *biofunctionality* is used to emphasize that the polymer coating not only is of interest in biological applications but also has been

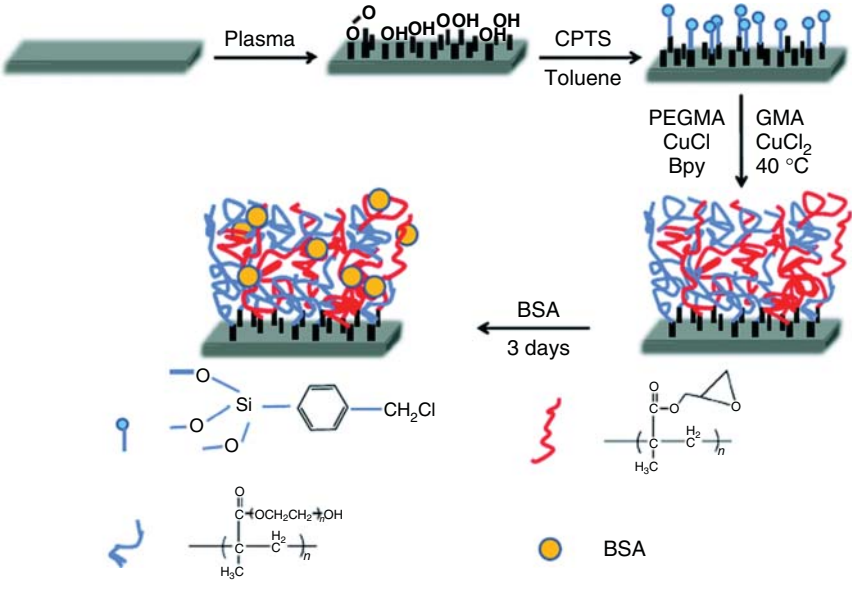


Figure 3.20 Schematic diagram illustrating the processes of BSA immobilization onto PP surface. (Li *et al*. 2014 [43]. Reproduced with permission of Royal Society of Chemistry.)

tested within these applications. In this chapter, we gave one example in this area: inhibition of nonspecific fouling.

Inhibition of nonspecific fouling, non-fouling, antifouling, and resistance against biofouling are terms to describe surfaces that reduce both protein adsorption and cell adhesion, which is important in polymer-based microfluidic devices such as protein sensor, real-time PCR, and cell sorting devices. Interactions between the proteins or cells and the surface determine the tendency to nonspecific fouling. Hydrophobic and electrostatic interactions are considered to be the major driving forces for fouling, but the importance of these interactions depends on the protein structure and the surface properties. For instance, nonspecific fouling depends on the surface wettability, specific chemical groups on the surface, surface charge, balance between hydrophobic and hydrophilic groups, and mobility of the polymer brushes. Figure 3.21 listed monomers

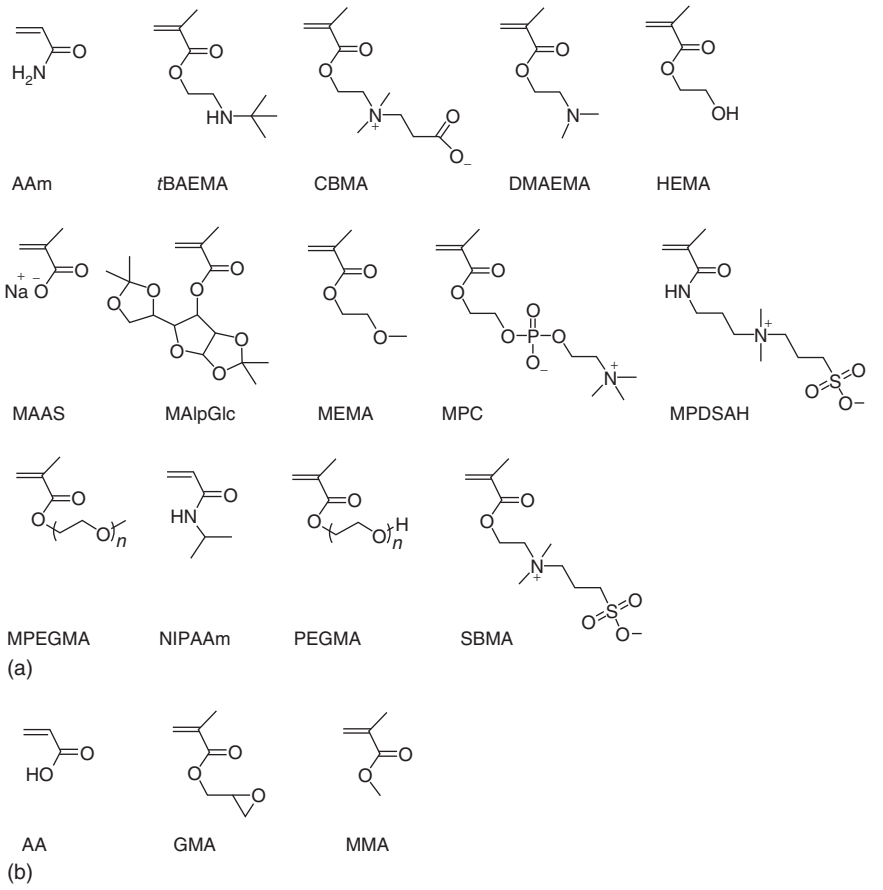


Figure 3.21 (a) Polymer grafts on surfaces made from the monomers inhibit nonspecific fouling and (b) the monomers result in antifouling coatings when incorporated in copolymer structures. (Fristrup *et al*. 2009 [44]. Reproduced with permission of Royal Society of Chemistry.)

www.ebook3000.com

employed in publications for antifouling purpose via SI-ATRP approach [44]. Experiments with poly(ethylene glycol) methacrylate (PEGMA) polymerized from silicon or glass have shown that the stability of the poly(PEGMA) was enhanced from 1 day to more than 7 days without any reduction in the antifouling properties when a solution with only ATRP initiator modified by trimethoxysilane was replaced by a mixture of 60 mol% ATRP initiator modified by trimethoxysilane and 40 mol% inert trimethoxysilane [45].

3.3.3.3 Grafting-to Technique

In contrast to "grafting-from," pre-polymerized polymers have been grafted onto reactive sites on a surface via a "grafting-to" approach. Lillehoj *et al*. [46] have attached poly(ethylene glycol) (PEG) onto air plasma-pretreated PDMS surfaces via a "grafting-to" approach, which resulted in ether bond formation. The PEG-modified PDMS surface showed long-term stability maintaining a WCA ≤ 22 for 47 days at room temperature under atmospheric conditions. In another "grafting-to" approach, Geissler *et al*. [47] first treated PDMS with a maleic anhydride (MA) plasma and then hydrolyzed the MA film by immersing it in water. This was then followed by EDC/NHS coupling with NH_2-functional PEG. A more recent example of "grafting-to" approach is reported in the previous work [48], which grafted allylhydridopolycarbosilane (AHPCS) onto a plasma-pretreated PDMS surface, and the resulting AHPCS film was converted into a silica film via hydrolysis in NaOH solution. The WCA after hydrolysis was shown to decrease to 35°.

3.3.4 Nanomaterials for Bulk Modification of Polymers

There are two main types of nanomaterials that have been incorporated into polymers, namely, carbon nanotubes (CNTs) and nanoparticles. Each of them possesses advanced properties such as superior thermal and electrical conductivity and mechanical strength, which make them ideally suited to polymer microfluidic device technologies. It is envisaged that the integration and structuring of nanocomposite materials into microfluidic devices will lead to higher performance of microfluidic components such as active microvalves, heaters, sorters, pumps, electrochemical, and pressure sensors [49, 50]. Patterned assembly of nanocomposites on a microchannel surface will also afford predetermined properties with respect to cell and protein adhesion, immobilization of biomolecules, and generation of conductive zones.

In particular, the rapid development of point-of-care test based on microfluidic devices has necessitated the integration of simple electronics with external microelectronic circuits. Here, the first challenge is the fabrication of flexible conductive materials suitable for use in soft lithographic techniques. An easy solution to this problem may come from the integration of a conductive material into polymer such as metal nanoparticles, carbon black, or CNTs [51, 52].

To date, the most widely used approach to produce conductive polymer composites is by simple mixing of polymer with suspensions of single-walled CNTs or multiwalled CNTs [53, 54]. Despite the simplicity of this approach, the properties of polymer/CNT composites are limited due to a decrease in

electrical conductivity of the CNTs after embedment into polymer, a result of the inherent insulating nature of polymer. This reduced conductivity has significant implications on composites planned for eventual use as electrodes or conduits in microfluidic devices [55, 56].

3.4 Conclusions and Outlook

The fabrication of silicon- and glass-based microfluidic devices could be straightforward by making use of the well-established MEMS technology, such as deep reactive-ion etching (DRIE), anodic bonding, and thin-film metallization. On the other hand, to address the increasing demand of disposable applications such as *in vitro* diagnostic (IVD) devices and health screening kits, polymer microfabrication technologies need to be developed specifically to meet the requirements of microfluidic devices. For example, the geometrical accuracy of the features could be critical to the device functions such as concentration measurement, which implies a lot of challenges to the polymer fabrication process including mold insert fabrication, process control of injection molding, and lamination. In general, there is a lot of room to improve the polymer microfluidic device fabrication, especially the component and material integration and accurate dimensional control after lamination (bonding). Nontraditional fabrication platforms, for example, the roll-to-roll manufacturing, may find that their 3D printing technologies bring an alternative for microfluidics device prototyping and low-volume production, which would play more significant roles in the future along with the improvement of material properties and tools.

Surface properties of microfluidics devices especially polymer-based materials are critical to certain applications such as point-of-care devices. Plasma treatment provided a simple and fast method to generate hydrophilic surfaces at relatively low cost. However, the short duration of hydrophilic effect is the major drawback of this approach. On the other hand, physical coating systems such as using surfactant to treat polymer channels are easy to carry out but suffer from poor durability. Surface grafting methods including photo-initiated surface grafting polymerization and SI-ATRP provide chemical bonding between coating layer and substrates, which can offer almost permanent hydrophilic and hydrophobic effects and biofunctionalities. For mass production, surface grafting techniques still need more research in order to decrease the cost and reduce process complexity.

Abbreviations

COC	cyclic olefin copolymer
FITC	fluorescein isothiocyanate
MEMS	microelectromechanical systems
PDMS	poly(dimethylsiloxane)
PEG	poly(ethylene glycol)
PEGMA	poly(ethylene glycol)methacrylate
PMMA	poly(methyl methacrylate)

www.ebook3000.com

RIE	reactive ion etching
T_g	glass transition temperature
SI-ATRP	surface-initiated atom transfer radical polymerization

References

1 Ren, K., Zhou, J., and Wu, H. (2013) *Acc. Chem. Res.*, **46**, 2396.
2 Gervais, L. and Delamarche, E. (2009) *Lab Chip*, **9**, 3330–3337.
3 Iliescu, C., Taylor, H., Avram, M., Miao, J., and Franssila, S. (2012) *Biomicrofluidics*, **6**, 016505.
4 Temiz, Y., Ferretti, A., Leblebicib, Y., and Guiducci, C. (2012) *Lab Chip*, **12**, 4920.
5 Kim, H.S., Blick, R.H., Kim, D.M., and Eom, C.B. (2004) *Appl. Phys. Lett.*, **85**, 2370.
6 Becker, H. and Gärtner, C. (2008) *Anal. Bioanal. Chem.*, **390**, 89.
7 Guckenberger, D.J., de Groot, T.E., Wan, A.M.D., Beebea, D.J., and Young, E.W.K. (2015) *Lab Chip*, **15**, 2364.
8 Zhang, N., Srivastava, A.P., Browne, D.J., and Gilchrist, M.D. (2016) *J. Mater. Process. Technol.*, **231**, 288.
9 Attia, U.M., Marsona, S., and Alcockb, J.R. (2009) *Microfluid. Nanofluid.*, **7**, 1.
10 Miserere, S., Mottet, G., Taniga, V., Descroix, S., Viovya, J.L., and Malaquin, L. (2012) *Lab Chip*, **12**, 1849.
11 Cheng, J.Y., Wei, C.W., Hsua, K.H., and Young, T.H. (2004) *Sens. Actuators, B*, **99**, 186.
12 Wang, Z.K., Zheng, H.Y., Lim, R.Y.H., Wang, Z.F., and Lam, Y.C. (2011) *J. Micromech. Microeng.*, **21**, 095008.
13 Knowles, M.R.H., Rutterford, G., Karnakis, D., and Ferguson, A. (2007) *Int. J. Adv. Manuf. Technol.*, **33**, 95.
14 Cheng, E., Yin, Z., Zou, H., and Chen, L. (2015) *Microfluid. Nanofluid.*, **18**, 527.
15 Duan, H., Zhang, L., and Chen, G. (2010) *J. Chromatogr. A*, **1217**, 160.
16 Kim, J. and Xu, X. (2003) *J. Laser Appl.*, **15**, 255.
17 Kistrup, K., Poulsen, C.E., Hansen, M.F., and Wolff, A. (2015) *Lab Chip*, **15**, 1998.
18 Tsao, C.W. and DeVoe, D.L. (2009) *Microfluid. Nanofluid.*, **6**, 1.
19 Bhattacharjee, N., Urrios, A., Kang, S., and Folch, A. (2016) *Lab Chip*, **16**, 1720.
20 Ho, C.M.B., Ng, S.H., Lia, K.H.H., and Yoon, Y.J. (2015) *Lab Chip*, **15**, 3627.
21 Duan, C., Wang, W., and Xie, Q. (2013) *Biomicrofluidics*, **7**, 026501.
22 Qiu, Z., Chen, C., and Lee, I. (2014) *Regener. Biomater.*, 67.
23 Bogaerts, A., Neyts, E., and Gijbels, R. (2002) *Spectrochim. Acta, Part B*, **57**, 609.
24 Desmet, T., Morent, R., and Geyter, N.D. (2009) *Biomacromolecules*, **10**, 2351.
25 Priest, C., Gruner, P.J., Szili, E.J., Al-Bataineh, S.A., Bradley, J.W., Ralston, J., Steele, D.A., and Short, R.D. (2011) *Lab Chip*, **11**, 541.

26 Martin, I.T., Dressen, B., Boggs, M., Liu, Y., Henry, C.S., and Fisher, E.R. (2007) *Plasma Processes Polym.*, **4**, 414.
27 Tan, H.M.L., Fukuda, H., Akagi, T., and Ichiki, T. (2007) *Thin Solid Films*, **515**, 5172.
28 Liu, X., Feng, Q., and Bachhuka, A. (2014) *ACS Appl. Mater. Interfaces*, **6**, 9733.
29 Cortese, G., Martina, F., Vasapollo, G., Cingolani, R., Gigli, G., and Ciccarella, G. (2010) *J. Fluorine Chem.*, **131**, 357.
30 Sofla, A.Y.N. and Martin, C. (2010) *Lab Chip*, **10**, 250.
31 Zhou, J.W., Ellis, A.V., and Voelcker, N.H. (2010) *Electrophoresis*, **31**, 2.
32 Wu, Z. and Hjort, K. (2009) *Lab Chip*, **9**, 1500.
33 Ang, C.H., Garnett, J.L., and Levotetal, R. (1980) *J. Polym. Sci.: Polym. Lett. Ed*, **18**, 471.
34 Dworjanyn, P.A. and Garnett, J.L. (1988) *J. Polym. Sci., Part C: Polym. Lett.*, **26**, 135.
35 Jiang, W., Awasum, J.N., and Irgum, K. (2003) *Anal. Chem.*, **75**, 2768.
36 Deng, J.P., Yang, W.T., and Rånby, B. (2000) *J. Appl. Polym. Sci.*, **77**, 1513.
37 Liao, C.Y. and Su, Y.C. (2010) *Biomed. Microdevices*, **12**, 125.
38 Lin, H.H., Chang, S.C., and Su, Y.C. (2010) *Microfluid. Nanofluid.*, **9**, 1091.
39 Ma, D., Chen, H.W., Li, Z.M., and He, Q.H. (2010) *Biomicrofluidics*, **4**, 044107.
40 Wang, Y.X. and Yang, W.T. (2004) *Langmuir*, **20**, 6225.
41 Wang, Y.X., Zhong, W.B., Jiang, N., and Yang, W.T. (2005) *Macromol. Rapid Commun.*, **26**, 87.
42 Mei, Y., Wu, T., Xu, C., Langenbach, K.G., Elliott, J.T., Vogt, B.D., Beers, K.L., Amis, E.J., and Washburn, N.R. (2005) *Langmuir*, **21**, 12309.
43 Li, C., Jin, J., and Yin, J. (2014) *RSC Adv.*, **4**, 24842.
44 Fristrup, C.J., Jankova, K., and Hvilsted, S. (2009) *Soft Matter*, **5**, 4623.
45 Tugulu, S. and Klok, H.A. (2008) *Biomacromolecules*, **9**, 906.
46 Lillehoj, P.B., Wei, F., and Ho, C.M. (2010) *Lab Chip*, **10**, 2265.
47 Geissler, A., Vallat, M.F., Fioux, P., Thomann, J.S., Frisch, B., Voegel, J.C., Hemmerle, J., Schaaf, P., and Roucoules, V. (2010) *Plasma Process.* , **7**, 64.
48 Yeh, P.Y., Rossi, N.A.A., Kizhakkedathu, J.N., and Mu, C.A. (2010) *Microfluid. Nanofluid.*, **9**, 199.
49 Jeong, O.C. and Konishi, S. (2008) *Sens. Actuat. A*, **143**, 97.
50 Casals-Terré, J., Duch, M., Plaza, J.A., Esteve, J., Pérez-Castillejos, R., Vallés, E., and Gómez, E. (2008) *Sens. Actuators, A*, **147**, 600.
51 Vlandas, A., Kurkina, T., Ahmad, A., Kern, K., and Balasubramanian, K. (2010) *Anal. Chem.*, **82**, 6090.
52 Kim, B.S., Lee, S.W., Yoon, H., Strano, M.S., Shao-Horn, Y., and Hammond, P.T. (2010) *Chem. Mater.*, **22**, 4791.
53 Liu, C.X. and Choi, J.W. (2009) *J. Micromech. Microeng.*, **19**, 7.
54 Khosla, A. and Gray, B.L. (2009) *Mater. Lett.*, **63**, 1203.
55 Kohlmeyer, R.R., Javadi, A., Pradhan, B., Pilla, S., Setyowati, K., Chen, J., and Gong, S.Q. (2009) *J. Phys. Chem. C*, **113**, 17626.
56 Chua, T.P., Mariatti, M., Azizan, A., and Rashid, A.A. (2010) *Compos. Sci. Technol.*, **70**, 671.

www.ebook3000.com

4

Numerical Simulation in Microfluidics and the Introduction of the Related Software

Zheng Zhao[1,2], Adrian Fisher[2], and Daojian Cheng[1]

[1] Beijing University of Chemical Technology, College of Chemical Engineering, State Key Laboratory of Organic-Inorganic Composites, No. 15 Beisanhuan East Road, Chaoyang District, Beijing 100029, PR China
[2] Beijing University of Chemical Technology, International Research Center for Soft Matter, No. 15 Beisanhuan East Road, Chaoyang District, Beijing 100029, PR China

4.1 Introduction

Over the last decade microfluidics has become a very important area of research due to its wide-ranging applications including microelectromechanical systems (MEMS) [1, 2], fuel cells [3], oil recovery [4], chemical and biology analysis [5], and biomedical devices [6]. Generally, microfluidics studies the behavior of small volumes of fluids, typically in the order of microliters, nanoliters, or even picoliters. Moreover, microfluidics has been used to answer fundamental questions in physics including the behavior of single molecule or particle in fluid flow or the validity of the no-slip boundary condition [7, 8]. Recently, a wide variety of microfluidic systems including microreactors [9], microheat exchangers [10], and lab-on-a-chip modules [11] have been developed with at least one of the dimensions of the microfluidic system below a few millimeters in size. It is well recognized that as fluidic systems are reduced in size, phenomena such as viscosity, diffusion, surface tension, and contact lines become ever more different and may, at the microscale, dominate over gravitational and inertial effects that are often dominant in microfluidics. For example, the diminutive scale of the flow channels in microfluidic systems increases the surface-to-volume ratio, causing surface effects such as wettability or surface charges to be more important than in macroscopic systems [12]. However, Reynolds numbers in microfluidic systems are usually small (i.e., usually below 0.1), and hence diffusive species mixing plays an important role but is an inherently slow process [13].

With recent technical advances, experimental investigations of a wide range of different fluid behaviors in microfluidic systems have become possible. However, theoretical and numerical analyses are critical to reveal underlying mechanisms, to examine various effects, to provide design guidelines for practical applications, and even to interpret the phenomena observed in the experiment. Theoretical analysis is certainly limited to very simple situations, and therefore, numerical simulations are often employed to obtained detailed and in-depth information,

Microfluidics: Fundamentals, Devices and Applications, First Edition.
Edited by Yujun Song, Daojian Cheng, and Liang Zhao.
© 2018 Wiley-VCH Verlag GmbH & Co. KGaA. Published 2018 by Wiley-VCH Verlag GmbH & Co. KGaA.

especially for that which is not available from direct experiments [14]. This chapter addresses the growing use of numerical simulations for microfluidics with the aim of supporting readers who wish to understand or exploit numerical methods as part of their research activities. Despite the large number of papers [15, 16] and reviews [17, 18] in the area of microfluidics, the majority of the work has focused on introducing the commonly used numerical simulation models and the related software.

This chapter is structured as follows. Section 4.2 gives the different numerical simulation models that are available for simulation of microfluidics, focusing on the general conservation laws that govern the transport of microfluidics. In particular modeling approaches such as molecular dynamics (MD), direct simulation Monte Carlo (DSMC) method, the dissipative particle dynamics (DPD), continuum method (CM), lattice Boltzmann method (LBM), and computational fluid dynamics (CFD) are reviewed. In Section 4.3, a broad assessment of software commonly used in the numerical simulation of microfluidics is presented, providing perspectives on different applied arrangement of computational microfluidics. The chapter ends with conclusions and perspective overview in Section 4.4.

4.2 Numerical Simulation Models in Microfluidics

Numerical simulation models in microfluidics can play an important role in both (i) establishing design rules to optimize the performance of a given microfluidic device and (ii) allowing estimation of the theoretical and practical limits of the performance of the microfluidic devices given a set of constraints (e.g., time and cost). During the past few years, the numerical simulation models adopted for microfluidic investigations have led to a more clear understanding of both the physical and chemical characteristics of the system. The modeling approaches address the properties of microfluidic systems from atomistic to continuum level. Atomistic-level numerical simulation models typically use statistical mechanics to address molecular-level interactions. At the mesoscale, numerical simulation models work with small ensembles of matter with a characteristic size or particle number. The continuum-level numerical simulation models use the well-known macroscopic laws, although they may use outputs from mesoscale or atomistic calculations for boundary conditions. In this chapter, we will briefly cover commonly used methods such as MD and DSMC, but we will also focus on CM, LBM, and CFD based on the Navier–Stokes (NS) equations.

4.2.1 Molecular Dynamics (MD)

At the atomistic level of description, matter is composed of atoms or molecules and obeys statistical mechanics. The equations of statistical mechanics can be solved numerically by the MD method, where individual particles are considered to move under their own intermolecular forces and follow Newton's second law. Therefore, the MD method is frequently used to study microfluidic behavior by the evolution of individual molecules interacting with each other through an appropriate intermolecular potential [19]. Here the microscopic molecular

www.ebook3000.com

structures and interactions are well represented. However, the MD method is computationally expensive, and the computational effort increases linearly with the number of particles and the physical time scale simulated, even with the most advanced supercomputers. It has been found that there are strong motivations for studying microfluidics by the MD method although computationally expensive. For example, in the investigation of nano-jets [20], significant differences are found from the results by traditional CFD calculation methods and MD methods. In particular, fluctuations were found to be important in the breakup and stability of such jets [21]. Fluctuations, such as those that stem from molecular disorder and collisions, arise in a natural manner in MD method but are usually lacking in CFD descriptions. This is particularly important for problems that physically lead to instability or small fluctuations, which tend to occur at interfaces.

The MD method has been used to study a broad range of physical properties of microfluidic systems. For example, the stationary hydrodynamic problems in microfluidics have been investigated by the MD method and successfully compared with continuum-based simulations [22, 23]. More challenging nonstationary microfluidics such as the Rayleigh–Taylor (RT) [24] and Kelvin–Helmholtz instabilities [25] have been simulated by the MD method and used to describe the full complexity of the mixing process. In addition, MD has been applied to study a number of other problems in dynamic calculations of microfluidics, for example, shock-driven turbulence [26] and swimming by microorganisms [27] (Figure 4.1).

In the MD method, in a fluid, N interacting atoms or molecules (here referred to generically as "particles") have positions and velocities x_j and v_j, respectively, where $1 \leq j \leq N$. The most fundamental level at a fluid (or any other material) can

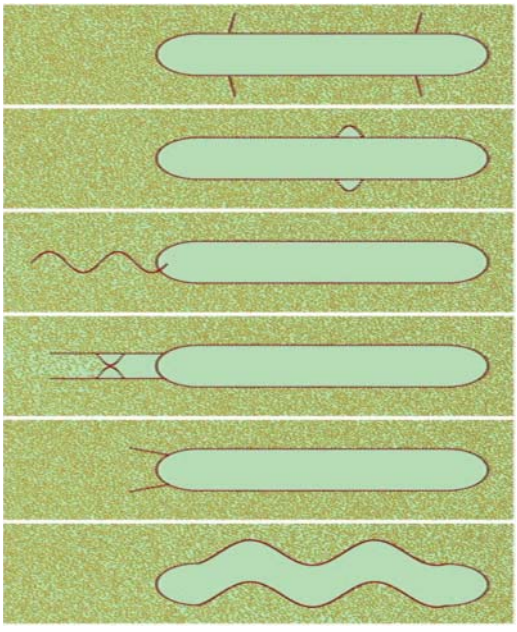


Figure 4.1 A selection of 2D swimmer designs in microfluidics: *biflaps*, *cigar*, *flagellum*, *jet*, *legs*, and *snake*; fluid atoms near the swimmer are shown and the swimming direction is to the right. (Rapaport 2008 [27]. Reproduced with permission of Elsevier.)

be described by the time-dependent Schrödinger equation (TDSE) [28]:

$$i\hbar\partial_t\psi(x_1\ldots x_N,t) = -\sum_{j=1}^{N}\frac{\hbar^2}{2m_j}\Delta x_j\psi(x_1\ldots x_N,t) + V(x_1\ldots x_N)\psi(x_1\ldots x_N,t) \tag{4.1}$$

Here, $j(x_1\ldots x_N,t)$ is the wave function for the N particles, $V(x_1\ldots x_N,t)$ is the interaction potential, m_j is the mass of the jth particle, and $\hbar$ is Planck's constant. In many cases, the size of the quantum-mechanical wave packet representing each particle is reasonably small compared with the average distance between particles. This condition can be characterized by a dimensionless number equal to the ratio of the de Broglie thermal wavelength of a particle to the average distance between particles [29]:

$$B \equiv n^{1/3}\left(\frac{2\pi\hbar^2}{mk_{\mathrm{B}}T}\right)^{1/2} \tag{4.2}$$

Here, n is the number density of particles, T is the temperature, and k_{B} is Boltzmann's constant. When B is reasonably small, as in the case of water, although not for hydrogen, we can neglect quantum effects in describing the atomic nuclei and pass to the classical limit, in which the variables (x_i, v_j) – nominally random quantities under the TDSE – are replaced by their mean values to yield the familiar Newtonian equations of motion for MD:

$$\left.\begin{aligned}\frac{\mathrm{d}}{\mathrm{d}t}x_j &= v_j,\\ \frac{\mathrm{d}}{\mathrm{d}t}v_j &= -\frac{1}{m_j}\nabla_{x_j}V(x_1\ldots x_N),\end{aligned}\right\}\quad 1\le j\le N \tag{4.3}$$

Since this is a system of ordinary differential equations rather than a many-dimensional partial differential equation as in Eq. (4.1), Eq. (4.2) is comparatively straightforward to integrate numerically. It is for this reason that MD has become such a useful and popular material simulation method in many different microfluidics applications. MD can also consider the probability density function $f(\{x_j\},\{v_j\},t)$ of the positions and velocities of the N particles. We define the continuum mass density and velocity fields of the fluid as

$$\rho(x,t) \equiv \sum_{k=1}^{N} m_k \int \mathrm{d}x_1\ldots\mathrm{d}x_N\mathrm{d}v_1\ldots\mathrm{d}v_N\delta(x-x_k)f(\{x_j\},\{v_j\},t) \tag{4.4}$$

$$u(x,t) \equiv \frac{1}{\rho(x,t)}\sum_{k=1}^{N} m_k \int \mathrm{d}x_1\ldots\mathrm{d}x_N\mathrm{d}v_1\ldots\mathrm{d}v_N\delta(x-x_k)f(\{x_j\},\{v_j\},t) \tag{4.5}$$

Note that these fields are related to averages of the microscopic densities of various quantities. According to the previous equation, the behavior of microfluidics can be further investigated by MD simulation.

www.ebook3000.com

4.2.2 The Direct Simulation Monte Carlo (DSMC) Method

DSMC [30] is a method similar to MD, except that the interparticle interactions are modeled stochastically via random collisions in which momentum and kinetic energy are exchanged. Due to the simplified nature of the interactions, DSMC is generally 10–100 times faster than MD, depending on the fluid density. The main drawback of DSMC is the fact that it is restricted to the description of fluids with an ideal gas equation of state. DSMC has traditionally been used for the description of rarefied gases in aerospace and industrial applications. More recently, however, it has been applied to more diverse problems in microfluidic dynamics. For example, Kadau *et al.* studied the RT instability by DSMC simulation [20, 31], which has been compared with experiments and continuum simulations as shown in Figure 4.2 and Table 4.1. Moreover, it was found that the DSMC simulation started with an almost perfectly flat interface, perturbed only on the length scale of an interatomic distance. Furthermore, thermal fluctuations will excite all possible interfacial modes in a random fashion, and they will subsequently grow (on average) according to the continuum linear-stability prediction [32]. In addition to RT instability, DSMC simulations were also used to study the Richtmyer–Meshkov instability [33], vortex shedding [34], and astrophysical problems [35]. Since DSMC is nominally derived from the Boltzmann equation, its region of validity straddles the boundary between MD and CM.

In the set of rules describing DSMC, however, no such physical scaling is immediately apparent or rigorously derivable. Therefore, it is of great utility and interest to empirically check whether the dynamics of DSMC displays the same scaling as that described in the NS equation as follows:

$$\rho\{\partial_t u + (u \cdot \nabla)u\} = -\nabla p + \mu \Delta u - \rho g \hat{e}_z \tag{4.6}$$

Here, ρ is the mass density, $u = u(x, t; g)$ is the velocity field of the fluid, $p = p(x, t; g)$ is the pressure field, μ is the shear viscosity, and g is the acceleration due to gravity. To check whether the dynamics of DSMC displays the same scaling as that described in the NS equation, Kadau *et al.* have performed an empirical check in the context of DSMC simulation of the RT instability [36]. The results from such a simulation can be rendered dimensionless through the use of two quantities: λ_{max}, the wavelength of maximum linear instability for perturbations

Table 4.1 Measured droplet diameter (d_{meas}) and theoretically calculated diameter (d_{stokes}) obtained by experiment, DSMC, and MD.

	d_{meas}	d_{meas}/λ_{max}	d_{stokes}/λ_{max}	d_{meas}/d_{stokes}	w_{system}/λ_{max}
Experiment	0.60 cm	0.73	0.11	6.5	8.5
2D DSMC	231 nm	1.64	0.35	4.6	39.7
2D DSMC	122 nm	1.35	0.36	3.7	30.9
2D MD	67.5 nm	0.88	0.23	3.8	7.3
3D DSMC	80.4 nm	1.31	0.36	3.6	17.2

Source: Kadau *et al.* 2007 [31]. Copyright 2007, National Academy of Sciences, U.S.A. Reproduced with permission.

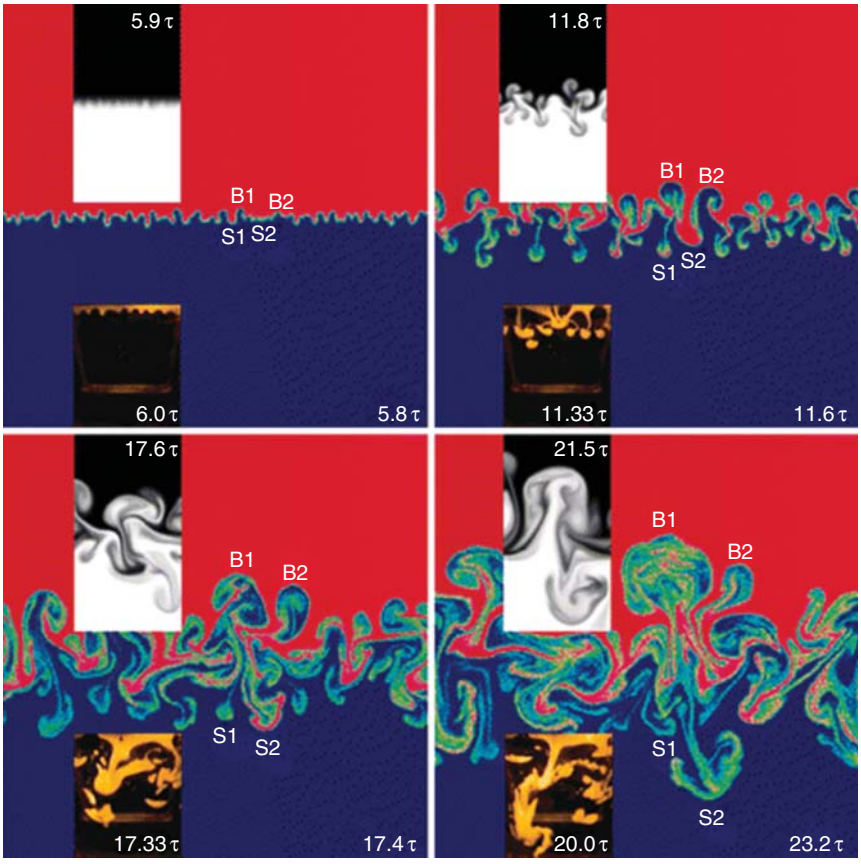


Figure 4.2 Time evolution of an RT instability. DSMC simulation of a 2D RT instability employing 570 million particles, where the heavy fluid (red) is on top of the light fluid (blue) and the gravitational field points downward ($A = 0.67$). The initially flat interface roughens due to thermal fluctuations, and modes near the most unstable mode develop first. Later, merger processes become dominant. At even later times, breakups occur that reduce the overall growth of the mixing layer. The position of individual spikes (S1, S2) and bubbles (B1, B2) shows the variation of movement and development of individual spikes and bubbles. (Kadau *et al*. 2007 [31]. Copyright 2007, National Academy of Sciences, U.S.A. Reproduced with permission.)

on the interface, and τ, the exponential growth time of that most unstable mode, which can be defined as follows [36]:

$$\lambda_{\max} = f_1(A, V)\left(\frac{\overline{\mu}^2}{g(\rho_h - \rho_l)^2}\right)^{1/3} \tag{4.7}$$

and

$$\tau = f_2(A, V)\left(\frac{\overline{\mu}}{g^2(\rho_h - \rho_l)}\right)^{1/3} \tag{4.8}$$

www.ebook3000.com

where $\overline{\mu} = 1/2(\mu_h + \mu_l)$ is the averaged shear viscosity and f_1 and f_2 are the unknown dimensionless functions of the Atwood number A and the viscosity ratio $V = \mu_h/\mu_l$. The nature of this dependence on g is such that any two systems obeying the above physical scaling should become equivalent when nondimensionalized in this way. The results show that DSMC simulations considering the fractal dimension of the interface for each gravity and within fluctuations are approximately the same as described in the NS equation. Therefore, the dynamics of DSMC can display the same scaling as that described in the NS equation.

4.2.3 The Dissipative Particle Dynamics (DPD)

The DPD [37, 38] method is a potentially very powerful and simple microfluidics approach [39], which facilitates the simulation of the statics and dynamics of complex fluids and soft matter systems at physically interesting length and time scales. From a technical point of view, DPD differs from MD method in two respects [40]. First, the conservative pairwise forces between DPD particles (which represent clusters of microscopic particles) are soft repulsive, which makes it possible to extend the simulations to longer time scales. Second, a special "DPD thermostat" for the canonical ensemble is implemented in terms of dissipative as well as random pairwise forces such that the momentum is locally conserved, which results in the emergence of hydrodynamic flow effects on the macroscopic scale. In DPD, microfluidics are modeled by pairwise interacting particles (which we shall in general refer to as fluid particles (FP)), the dynamics of which follows Newton's second law:

$$F_i = m_i r_i \tag{4.9}$$

with the mass m_i of particle i and its spatial coordinate r_i in the laboratory-fixed frame. F_i is the total force acting on it. In the simplest form, F_i is the sum of pairwise conservative, dissipative, and random forces:

$$F_i = \sum_j (F_{ij}^{C} + F_{ij}^{D} + F_{ij}^{R}) + F_i^{ext} \tag{4.10}$$

F_i^{ext} is an external force such as gravity. The conservative force in standard DPD is a soft central repulsion acting between particle i and j [41]:

$$F_{ij}^{C} = \begin{cases} A_{ij} w^{C}(r_{ij}) e_{ij} & r_{ij} < 1 \\ 0 & r_{ij} \geq 1 \end{cases} \tag{4.11}$$

where $\boldsymbol{r}_{ij} = \boldsymbol{r}_i - \boldsymbol{r}_j$, $r_{ij} = |\boldsymbol{r}_{ij}|$, and $e_{ij} = r_{ij}/\boldsymbol{r}_{ij}$. The weight function $w^{C}(r) = (1 - r/r_c)$ vanishes for an interparticle distance r larger than a cutoff radius r_c (see Figure 4.3a). And then the dissipative force F_{ij}^{D} can be defined as [42]

$$F_{ij}^{D} = \begin{cases} -\gamma \omega^{D}(r_{ij})(\boldsymbol{v}_{ij} \cdot \boldsymbol{e}_{ij})\boldsymbol{e}_{ij} & r_{ij} < 1 \\ 0 & r_{ij} \geq 1 \end{cases} \tag{4.12}$$

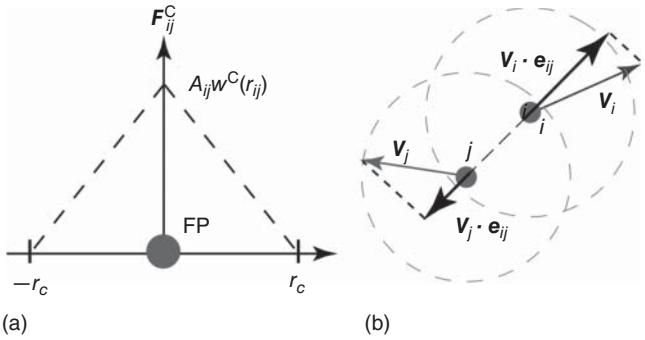


Figure 4.3 (a) Pair-force of a fluid particle. (b) Calculation of the relative velocity v_{ij} between two particles. (Steiner *et al*. 2009 [41]. Reproduced with permission of Springer.)

with contributions from the random force F_{ij}^{R} [43]:

$$F_{ij}^{R} = \begin{cases} \sigma w^{R}(r_{ij})\xi_{ij}\boldsymbol{r}_{ij}(\Delta t)^{\frac{1}{2}} & r_{ij} < 1 \\ 0 & r_{ij} \geq 1 \end{cases} \tag{4.13}$$

where σ is the amplitude of the random variable ξ_{ij}. The dissipative force is proportional to the relative velocity $\boldsymbol{v}_{ij} = \boldsymbol{v}_i - \boldsymbol{v}_j$ of two FPs, as illustrated in Figure 4.3b. Note the dependence of F^{R} on the square root of the integration time step Δt: F_{ij}^{D} and F_{ij}^{R} obey a fluctuation–dissipation theorem where σ and γ are related by $\sigma^2 = 2\gamma k_B T$ and $w_{ij}^{R}(r)^2 = w_{ij}^{D}(r)$ and k_B is Boltzmann's constant. Moreover, the forces model used in DPD is central and implies a conservation of linear and angular momentum. Then, the NS equation can be further calculated in DPD method based on the forces model introduced earlier.

In the past decades, the DPD method was improved by various authors [44, 45] and has frequently been applied in microfluidic systems. For example, Steiner *et al.* explore the DPD approach to study a realistic engineering problem involving the design process of a special type of microfluidic chamber serving as a bead-based immunoassay [41]. As shown in Figure 4.4, Steiner *et al.* built the periodic boundary conditions in the DPD simulation (Figure 4.4b) based on the experimental situation (Figure 4.4a). In addition, Li *et al.* studied the motions of red blood cells in Y-shaped bifurcating microfluidic channels based on the DPD simulation technique [46]. Using standard projection operator techniques, Espanol and Warren obtained the DPD macroscopic hydrodynamic equations [37]. Hoogerbrugge and Koelman simulated the microscopic hydrodynamic phenomena with DPD [38]. Keaveny *et al.* used the DPD method to simulate simple and complex geometry macroscopic flows [47]. Although lots of work using the DPD method to simulate macroscopic flows have been reported, many aspects that are important for carrying out studies for specific microfluidic systems by DPD method are still not yet well developed.

www.ebook3000.com

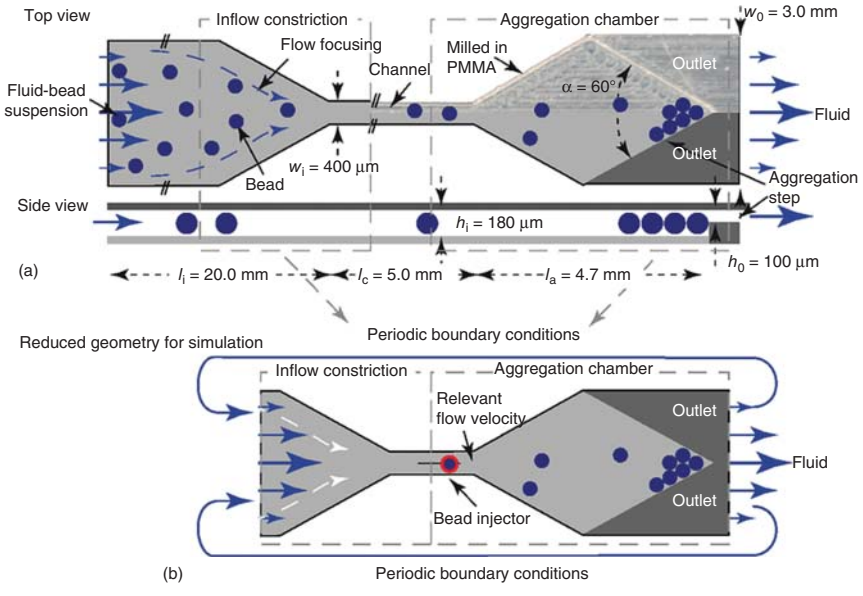


Figure 4.4 Diamond-shaped microfluidic aggregation chamber with inlet at the left and outlet at the right side. Suspended polystyrene beads of diameter dB = 150 lm enter the inlet during the experiments at the left. (a) Geometry of experiments: the inflow constriction, channel, and aggregation chamber are h_i = 180 lm in height, while the outlet height is set to h_o = 100 lm. (b) Reduced simulation model: flow boundary conditions are realized with periodic boundary conditions in DPD. (Steiner *et al*. 2009 [41]. Reproduced with permission of Springer.)

4.2.4 Continuum Method (CM)

CM is commonly used to compute microfluidic flows based on macroscopic conservation laws for mass, momentum, and energy. They rely on the coupling of a method for description of the phase evolution (which often expresses the conservation of phase specific mass) with a solver for the momentum equation (e.g., the NS equation) and the energy equation. There are various methods used to describe the interface evolution in the CM and then consider the coupling of these algorithms with equations describing the transport of momentum, species mass, and energy. Detailed information about these balance equations can be found in various textbooks; see, for example, Bird *et al.* [48]. Generally, CM can be classified in approaches where the interface thickness is zero (sharp interface) or finite (diffusive interface). In sharp interface methods, the physical interface is a functional interface of zero thickness, and physical quantities such as density and viscosity are discontinuous at the interface. Mathematically, such an interface is a $(D-1)$ dimensional object in a D-dimensional space. In diffuse interface methods, the interface has a finite thickness, and physical quantities vary continuously across the interface. It is important to note that numerical interface thickness in

diffuse interface methods is usually much larger than the actual physical thickness (e.g., liquid–fluid interfaces typically a few nanometers [49]). In the following, we first briefly describe methods with formally zero interface thickness and then methods where the interface thickness is finite, either for numerical or physical (modeling) reasons.

The methods with formally zero interface thickness mainly include the moving mesh (MM) method, front-tracking (FT) method, level set (LS) method, and the interface reconstruction volume-of-fluid (IR-VOF) method. The MM method [50, 51] can be performed for both the interior and the interface elements to maintain good mesh quality, to achieve enough mesh resolution, to capture the changing curvature, and to obtain computational efficiency. In the FT method [52, 53], interfacial locations are tracked by a set of Lagrangian marker points. A marker point lying on the interface at position x_p is adverted by the flow according to

$$\frac{\mathrm{d}x_\mathrm{p}}{\mathrm{d}t} = \boldsymbol{u}_\mathrm{p} \tag{4.14}$$

The velocity $\boldsymbol{u}_\mathrm{p}$ at position x_p is determined from the velocity field on the Eulerian grid by interpolation. The LS method was introduced by Osher and Sethian [54] as a general technique to capture a moving interface. It has subsequently been applied to two-phase microfluidic [55, 56] system. For example, Liu *et al.* investigated the motion of water droplets immersed in an oil flow through an array of microfluidic ratchets by an LS method [57, 58] (see Figure 4.5) and found that the droplet moved faster in the diffuser direction than in the nozzle direction (in agreement with experiments).

In IR-VOF methods, the convective term can be written in conservative form and integrated over the volume v_mc of a mesh cell with boundary ∂v_mc. Application of the Gauss divergence theorem and division by v_mc yields

$$\frac{\partial f_+}{\partial t} + \frac{1}{V_\mathrm{mc}} \oiint_{\partial V_\mathrm{mc}} (\hat{n}_{\partial V_\mathrm{mc}} \cdot \boldsymbol{u}) X_+ \ \mathrm{d}S = 0 \tag{4.15}$$

Here

$$f_+ \equiv \frac{1}{V_\mathrm{mc}} \iiint_{V_\mathrm{mc}} X_+ \ \mathrm{d}V \quad \text{with } 0 \le f_+ \le 1 \tag{4.16}$$

f_+ is the volume fraction of phase (+) in the mesh cell and $\hat{n}_{\partial V_\mathrm{mc}}$ is the unit normal vector on ∂V_mc (pointing outward of the mesh cell). For a hexahedral mesh cell, the closed surface integral over ∂V_mc consists of six contributions, one for each face of the mesh cell. Moreover, the inherent volume (and mass) conservation property is the main advantage of IR-VOF methods.

The methods with formally finite interface thickness mainly include the color function volume-of-fluid (CF-VOF) method, conservative level set (C-LS) method, and phase-field (PF) method. A noted disadvantage of IR-VOF methods is the complexity of the interface reconstruction, especially in three-dimensional (3D). For a simplified computational treatment, VOF methods without interface reconstruction have been developed. Therefore, the CF-VOF method introduces

www.ebook3000.com

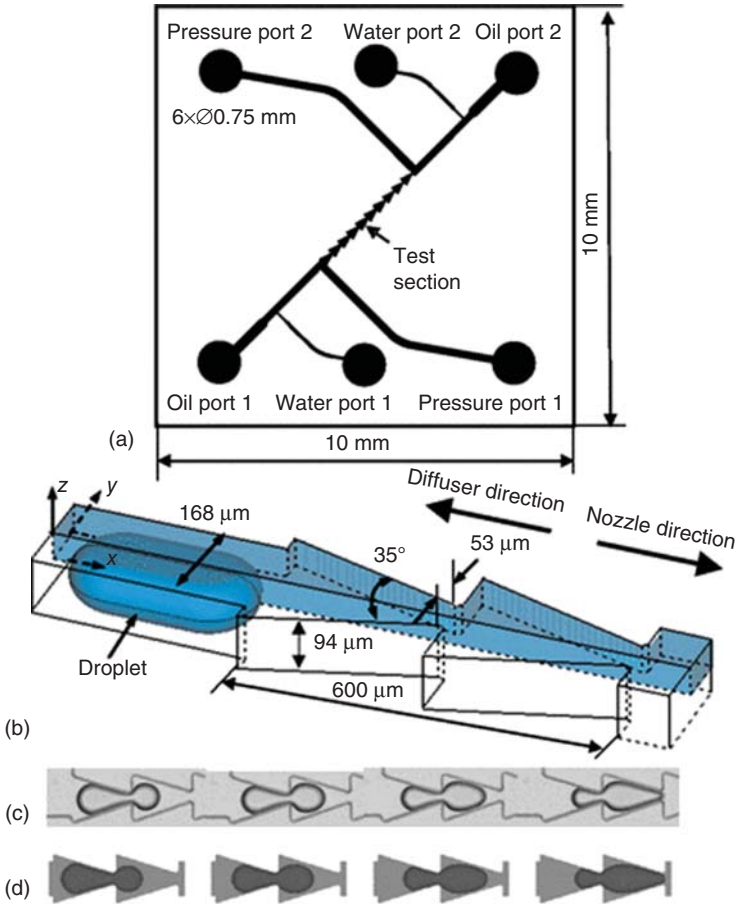
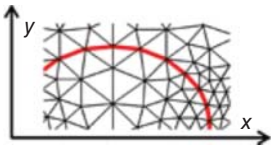
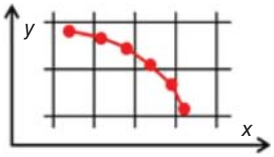
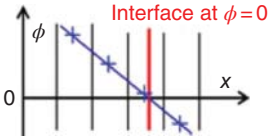
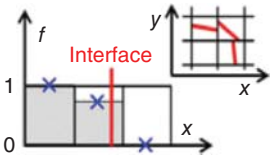
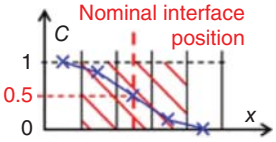
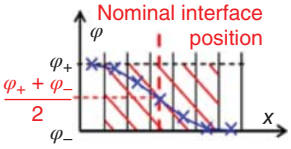


Figure 4.5 Numerical simulation of the motion of a droplet through microfluidic ratchets by a LS method. (a) Device schematic for investigation of microdroplets in diffuser/nozzle structures. The test section contains 10 diffuser/nozzle structures; (b) numerical model and dimensions of the ratchet; (c) deformation of a droplet passing through the ratchet; (d) simulated deformation of a droplet under the same conditions as of the experiment shown in (c). (Liu *et al*. 2009 [58]. Reproduced with permission of American Physical Society.)

a (smooth) color function C that can be considered as an approximation for the volume fraction function in the classical IR-VOF method. The C-LS method [59] was developed by combining elements from the CF-VOF and LS method. Instead of the signed distance function usually used to define the interface, the C-LS method uses a regularized indicator function C. Using this approach, the PF method can be considered as a particular type of diffuse interface model that is based on fluid free energy. Therefore, the PF methods have been commonly used to study the flow of two incompressible and immiscible microfluidic phases with different densities [60, 61]. For clarity, Wörner has illustrated the main features (shown as Table 4.2) of the various methods including zero interface thickness methods and the finite interface thickness methods [62].

Table 4.2 Illustration of the different features for different continuum methods.

Type	Thickness	Method	Interface representation	Interface evolution
Lagrangian type	Zero interface thickness	Moving mesh		Lagrangian movement of interface (unstructured grid)
		Front-tracking		Lagrangian movement of interface marker point within structured grid
Eulerian type		Level set		Advection equation for signed distance function φ
		IR-VOF		Geometric evaluation of phase fluxes across mesh cell faces
	Finite interface thickness	CF-VOF and C-LS		Advection for color function C (in C-LS followed by a compression step)
		Phase-field		Cahn–Hilliard for order parameter ϕ

Source: Wörner 2012 [62]. Reproduced with permission of Springer.

4.2.5 The Lattice Boltzmann Method (LBM)

The LBM has experienced tremendous advances and has been well accepted as a useful method to simulate various fluid behaviors [62]. For computational microfluidics, LBM has been developed to solve microfluidics-related processes and phenomena, such as heat transfer, electric/magnetic field, and

www.ebook3000.com

diffusion [14]. According to Verhaeghe's work [63], the LBM is a simple explicit algorithm that can be derived from the linearized Boltzmann equation and is often associated with a square (in 2D) or cubic (in 3D) lattice on which the discretized particle distribution function $f_i(\boldsymbol{r}_j, t_n) \equiv f(\boldsymbol{r}_j, \boldsymbol{c}_i, t_n)$ evolves. The particle velocity space is discretized into a symmetric discrete velocity set $\{\boldsymbol{c}_i\} = -\{\boldsymbol{c}_i\}$. The grid size and the time step are chosen in such a way that in discrete time $t_n \equiv \delta_t \mathbb{N}_0 = \delta_t\{0, 1, 2, \dots\}$, fictitious particles represented by f_i move synchronously from one grid point $\boldsymbol{r}_j$ to one of its neighbors $\boldsymbol{r}_j + \boldsymbol{c}_i\delta_t$ according to their discrete velocities. In the most general form, the lattice Boltzmann equation can be written as

$$f(\boldsymbol{r}_j + \boldsymbol{c}\delta_t, t + \delta_t) \equiv f(\boldsymbol{r}_j, t) + \boldsymbol{\Omega}[f(\boldsymbol{r}_j, t)] + \mathbf{F}(\boldsymbol{r}_j, t) \tag{4.17}$$

where $\boldsymbol{\Omega}$ is the collision term and $\mathbf{F}$ is the external forcing and boldface symbols denote $(Q+1)$-tuple vectors for a model of $(Q+1)$ discrete velocities, for example,

$$f(\boldsymbol{r}_j + \boldsymbol{c}\delta_t, t + \delta_t) \equiv (f_0(\boldsymbol{r}_j, t_n + \delta_t), \dots, +f_Q(\boldsymbol{r}_j + \boldsymbol{c}_Q\delta_t, t_n + \delta_t))^T \tag{4.18}$$

where T denotes the transpose operator. In LBM, commonly used lattices in two and three dimensions are the D2Q7 ($D=2$, $Q=7$), D2Q9, D2Q13, D3Q15, D3Q19, and D3Q27 models, respectively. As shown in Figure 4.6, here we give the D2Q9 and D3Q19 models as an example [14]. Details for other models are similar and readily available in the literature [64].

LBM has several advantages over conventional CFD methods. For example, mesh refinement or boundary-fitted grid is usually necessary for arbitrary boundaries in CFD simulations [65]. However, LBM can relatively easily implement such complex boundaries by imposing, for example, the bounce-back or modified bounce-back schemes to the microfluidic particle distributions, as demonstrated

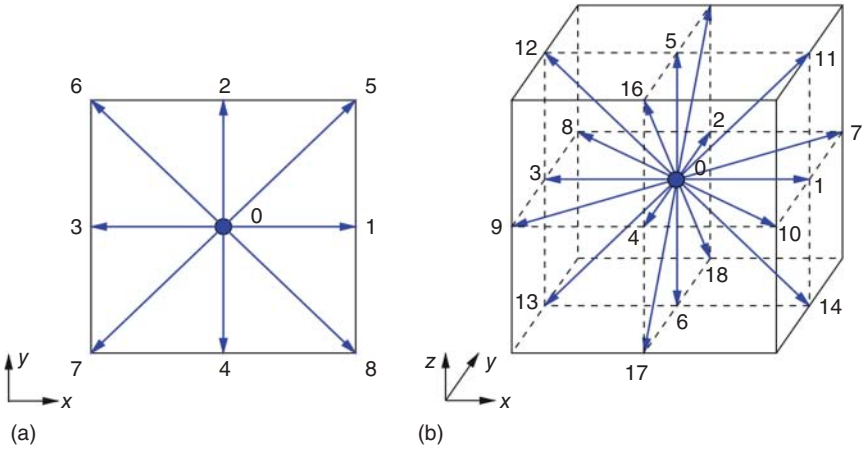


Figure 4.6 Schematics of the D2Q9 (a) and D3Q19 (b) lattice models. The edge length of both the D2Q9 square and the D3Q19 cube is 2 $\Delta x/\Delta t$, and dashed lines show the midplanes of the D3Q19 cube. The lattice velocities are indicated by arrows starting from the square/cube center. Note there is a zero lattice velocity $\boldsymbol{c}_o = 0$ in both models. (Zhang 2011 [14]. Reproduced with permission of Springer.)

in simulations of porous flows [66, 67] and particulate suspension flows [68, 69]. It also exhibits some attractiveness for incorporating microscopic interactions and implementing parallel computation [70]. Therefore, as in other fluid-related areas, it has been extensively applied to study various transport phenomena and processes in microfluidic systems. For example, researchers studied the microscopic gaseous flow behavior in MEMS by LBM [63, 71]. Moreover, LBM provides an efficient method to simulate droplet formation by considering important factors such as flow rate, surface tension, and wettability [72, 73]. For example, Van der Graaf *et al.* studied the droplet formation process at a T junction in a microchannel by LBM and compared the simulation results with experiment (Figure 4.7) [74]. Another major application of LBM models is to simulate droplet dynamics in microfluidic devices for their practical importance in biochemical and biomedical analyses [75, 76].

4.2.6 Computational Fluid Dynamics (CFD)

CFD method is an invaluable tool that has been commonly applied in the area of microfluidic devices and the particularities associated with it [77] and that enables a better understanding of the role of environment factors such as temperature and pressure that modulate it. In microdimensions, for example, surface forces dominate over body forces requiring special attention for problems involving two-phase flows with free surfaces that are often driven by capillary forces. Typical flow situations are capillary wicking or formation of droplets that are characterized by low Weber and Reynolds numbers [78, 79]. To model free surface flows including surface tension effects, among others, the so-called volume-of-fluid (VOF) method has been established [80] and is still being refined [81, 82]. Another particularity in microfluidics is the increased importance of diffusion for mixing phenomena. Since in microfluidic flow problems the Reynolds numbers are typically very small, turbulence is hardly ever observed and mixing is driven by diffusion only at low Peclet numbers [83]. Considering the previous factors and limitation of experiment, CFD has

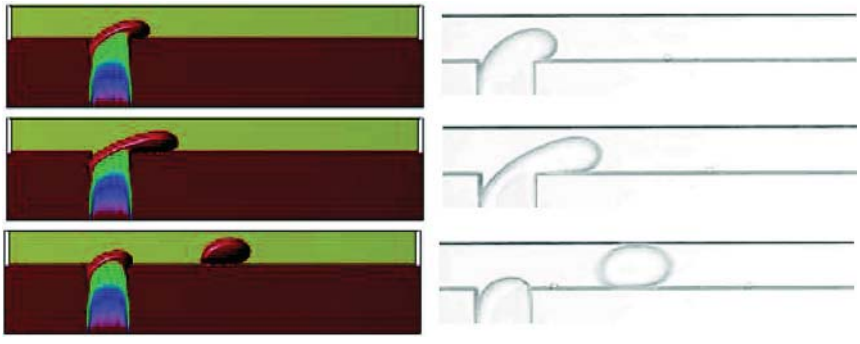


Figure 4.7 Snapshots of LBM simulation (a) and experiment (b) of droplet formation at a T junction. Note that the simulation and experimental pictures were displayed with different time intervals. (Van der Graaf *et al*. 2006 [74]. Reproduced with permission of American Chemical Society.)

www.ebook3000.com

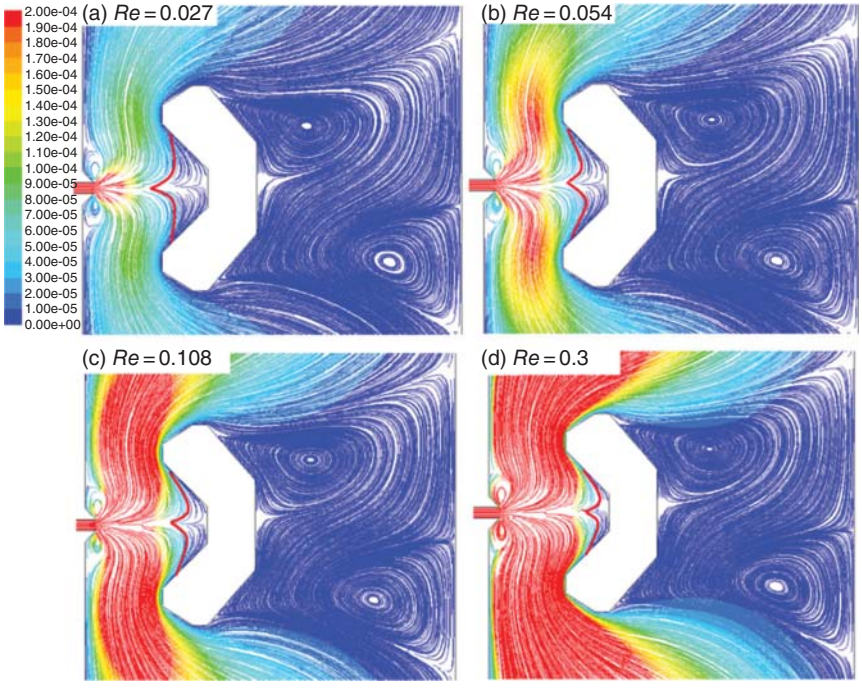


Figure 4.8 Streamline patterns at different inlet Reynolds numbers (*Re*s) from the microfluidic flow based on CFD simulation (colored by velocity magnitude (m s^{-1})). (Reprinted with permission from Van der Graaf *et al*. [74].)

been frequently applied to microfluidic system and enable us to understand the implications of microfluidic and investigate important insights into the design and optimization of microfluidic devices [84, 85]. For example, Shen *et al.* studied the flow behavior of single-cell manipulation and shear stress reduction in microfluidic chips using CFD as shown in Figure 4.8 [86]. CFD methods start from the continuum equations and solve them numerically by appropriate schemes [14]. However, CFD has difficulties to incorporate the microscopic interactions, which are crucial in many microfluidic circumstances, for example, the dynamics of wetting and interfacial slip [14]. CFD methods used in microfluidic were well described in previous papers [85, 87], and we direct interested readers to these reviews for further information.

4.3 Numerical Simulation Software in Microfluidics

With the growing availability of more powerful computing platforms, large-scale and accurate computer simulations of microfluidics are becoming increasingly popular. In particular, the growth in recent years in the area of large-memory parallel multi-computers has allowed numerical simulation to be performed in three dimensions with system sizes that are approaching experimentally relevant regimes, namely, the micrometer scale. Simulations at this length scale promise eventually to bridge the gap between the microscopic (atomistic) description and

the macroscopic (continuum mechanics) description of microfluidics. Therefore, many researchers have been working on developing numerical simulation software that would allow us to run calculation on microfluidic systems with millions of atoms since the 1990s. Among these numerical simulation software, CFD software is more widely and successfully used in standard design processes for microfluidic systems compared with other software. Thus, in this chapter, we will mainly cover commonly used CFD software such as CFD-ACE+, CFX, and FLOW-3D, but we will also briefly introduce other software such as Scalable Parallel Short-Range Molecular Dynamics (SPaSM), DL_POLY, and Large-scale Atomic/Molecular Massively Parallel Simulator (LAMMPS).

4.3.1 CFD-ACE+ Software: Microfluidics Applications

Version 2004.0.25 of CFD-ACE+ (ESI-CFD, Inc., Huntsville, AL) is claimed to be an integrated software package for multi-physic computational analysis [88]. The program consists of three main parts: CFD-GEOM for geometry and grid generation, CFD-GUI for setting boundary and initial conditions, and CFD-VIEW as an interactive visualization program. CFD-GEOM is built in geometry and grid generation system with a large set of CAD functions to create and manipulate whole geometries with a subsequent meshing. After setting up the geometry, the appropriate solver settings can be chosen in CFD-GUI where the solvers for different physical problems are divided into so-called modules specifying the kind of physical problem that can be switched on and off separately. Most of the modules can be combined with others, giving the opportunity to simulate different physical domains at the same time, for example, microfluidics problems in combination with chemical reactions, free surfaces, and so on. Moreover, the VOF method in CFD-ACE+ offers some additional features like an algorithm to remove the so-called flotsam and jetsam [87]. According to the features of CFD-ACE+ mentioned earlier, there are lots of applications of CFD-ACE+ in microfluidics. For example, Lee *et al.* used CFD-ACE+ to design and analyze the microfluidic circuit of three types of microfluidic gradient generators as shown in Figure 4.9 [89]. Makhijani *et al.* simulated the flow in structurally programmable microfluidic channels by CFD-ACE+ [90]. The CFD-ACE+ was also used to study the flow of the microstructures in the microfluidic device used for capturing physically single cells [91]. Przekwas *et al.* applied CFD-ACE+ in analyzing the hybridization and electrophoretic separation process in microfluidic networks [92].

4.3.2 CFX Software: Microfluidics Applications

CFX is a commonly used CFD software and lots of versions have been developed such as version 5.7.1 [93]. For the task of grid generation, there are two tools available: ANSYS DesignSpace in combination with AI*Environment and ICEM CFD [94]. To define physical properties such as material properties and boundary conditions as well as solver settings, the preprocessor CFX-Pre is provided with the CFX package. Both CFX-Pre and the postprocessor CFX-Post can be either controlled with the CFX Expression Language (CEL) or with Perl scripting. The CFX-Solver can handle multiphase flows of any number of different fluids, where fluids can be gases or liquids, and all material properties can either be constant

www.ebook3000.com

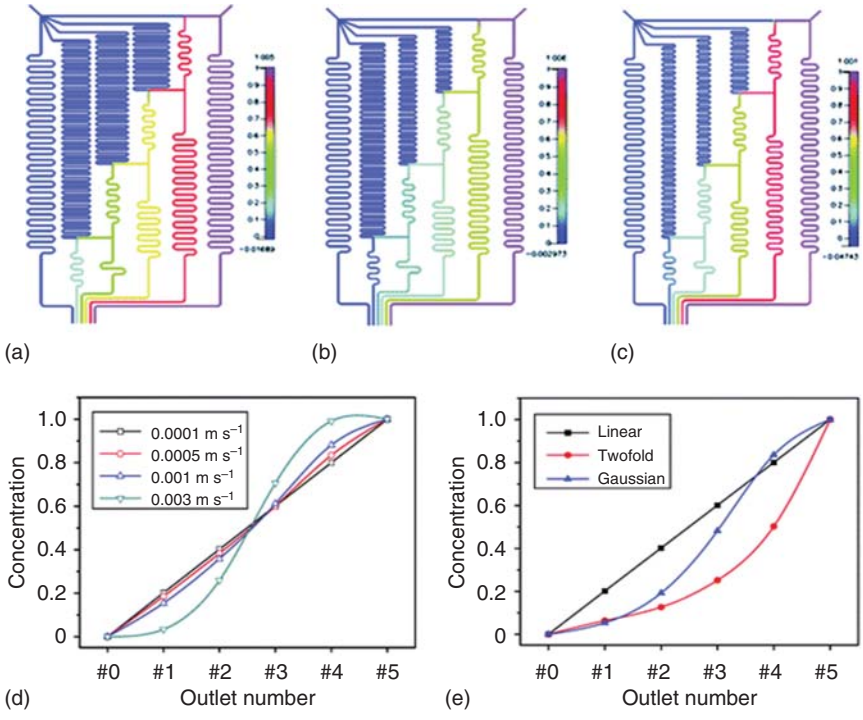


Figure 4.9 CFD-ACE simulation results for three types of microfluidic gradient generators: (a) linear, (b) twofold logarithmic, and (c) Gaussian distribution. (d) Concentration profiles of the linear type of devices as a function of flow rate. (e) Concentration profiles of three types of devices in the flow rate of 0.0001 m s^{-1}. (Lee *et al*. 2009 [89]. Reproduced with permission of Royal Society of Chemistry.)

or dependent on any variable in the simulation. All problems can be calculated on structured and unstructured meshes. Like most CFD tools, CFX also uses the finite-volume method for spatial discretization. However, the VOF method for free surfaces is implemented in a different way. No surface reconstruction is applied, but the volume fraction is computed based on solving an artificially stabilized ("compressive scheme") advection equation [95]. Surface tension can also be accounted for, and it is computed based on the local gradient of the VOF variable. In contrast to the other tools, CFX does not use a segregated solver for flow speed and pressure, but a fully coupled solver. CFX can perform all types of simulations on multiple processors.

As mentioned before, CFX is often used to handle multiphase flow behavior of any number of different microfluidics problems. For example, CFX has been used for analyzing fluid performance of a microfluidic reactor for FDG radiopharmaceutical synthesis [96]. Bui *et al.* used CFX to model the separation of metal ions in a microfluidic chip [97]. Sauli *et al.* performed numerical simulations using CFX software to study the WSS investigation in a microfluidic forward-facing step (FFS) channel at *Re* 500 [98]. The microfluidic distribution of vertical cross-sectional views was investigated numerically by CFX software [99].

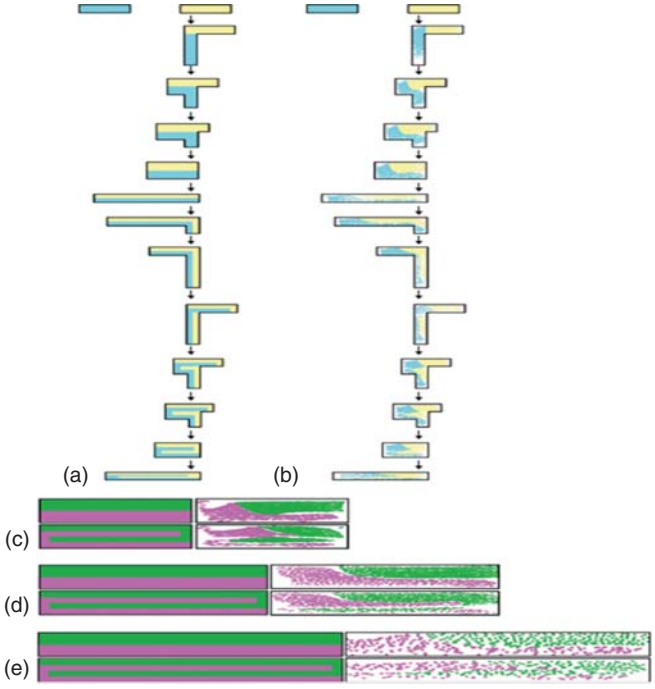


Figure 4.10 Schematics of (a) mixing process of MBT device, (b) microfluidic distributions derived from CFX simulations for the MBT device, and (c)–(e) ideal mixing process and microfluidic distributions derived from CFX simulations in aspect ratios of (c) 4, (d) 6, and (e) 8. Each image shows the cross sections in the most stretched channel. One MBT process was performed from the top views to bottom ones. (Yasui *et al*. 2011 [99]. Reproduced with permission of Royal Society of Chemistry.)

The numerical simulation results (CFX) are displayed as cross-sectional views in the flow direction in Figure 4.10. Chen *et al.* reported the design and validation of a two-layered microfluidic device platform for single-cell capture using CFX software [100]. Moreover, CFX was used to model and simulate the temperature, pressure, and velocity in polymerase chain reaction microfluidics [101]. Therefore, CFX software is an important tool to study the characteristics of microfluidics in different applications.

4.3.3 FLOW-3D Software: Microfluidics Applications

The FLOW-3D package [102] consists of a graphical user interface (GUI) and a separate tool called FLOW-VU for meshing and handling external STL files of 3D geometries. The pre- and postprocessing as well as the study of the simulation results is done by FLOW-VU. The multiprocessor capable solver can handle different physical regimes such as compressible and incompressible flow situations and one- or two-fluid problems with a free surface. The meshing procedure in FLOW-3D is based on a multiple block meshing. Therefore, the main advantage of FLOW-3D is the possibility to refine a mesh dependent on the required spatial accuracy and independent of the geometry, which is an interesting feature

www.ebook3000.com

in microfluidics applications with large aspect ratios. A disadvantage is that only structured grids can be handled, and furthermore these multiple block meshes are not compatible for exchange with most other solvers [87].

In FLOW-3D, free surface problems can be solved using the implemented VOF method [80] including surface tension and applying standard VOF solution methods as well as a new semi-Lagrangian VOF advection method. Generally, FLOW-3D simulation consists of three basic steps: the approximation of the fluid interface in a cell with a planar surface, the movement of the fluid volume according to the local velocity field, and the computation of the new fluid fraction values in the computational cells using an overlay procedure. For this algorithm, FLOW-3D only supports automatic time steps and no fixed time steps. This makes it difficult to compare FLOW-3D with the other tools concerning computation time. A further remarkable fact is that all problems have to be calculated time dependent because FLOW-3D does not provide the possibility of steady-state simulations.

FLOW-3D simulations have been validated for microfluidics applications. For example, Bhattacharjee used FLOW-3D to study the symmetric and asymmetric splitting of droplets in an electrowetting-based digital microfluidic system [103]. As shown in Figure 4.11, Howell and Li discussed droplet translocation in microfluidics and provides a technique for modeling and simulating a microfluidic device by using the FLOW-3D software [104]. In addition, Chandorkar and Palit simulated the droplet dynamics and mixing behavior in microfluidic devices using a FLOW-3D software [105]. In Bahadur's study, FLOW-3D was used to

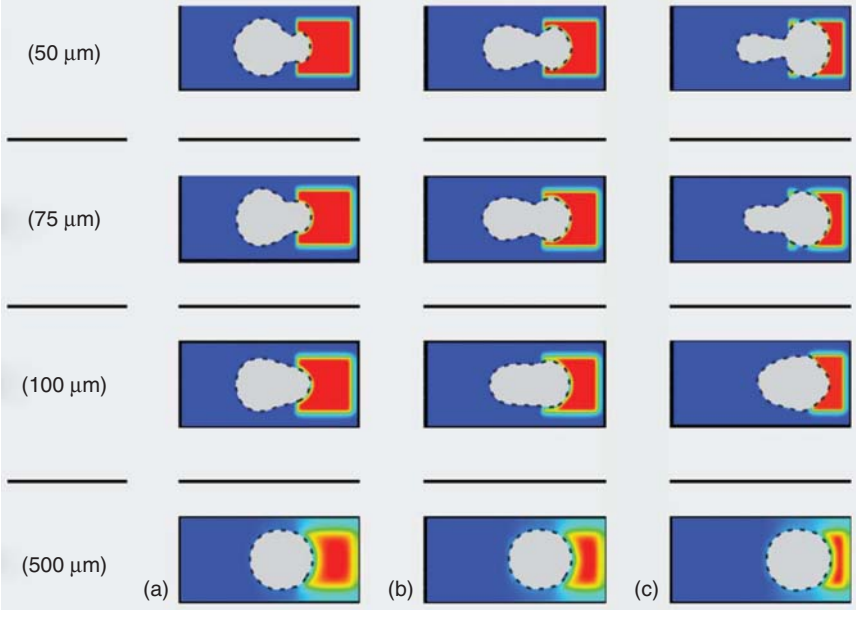


Figure 4.11 FLOW-3D simulation results for droplet motion at different gap heights when the droplet leading edge reaches (a) 0.5, (b) 1, and (c) 1.5 mm at 50, 75, 100, and 500 μm. (Howell and Li 2010 [104]. Reproduced with permission of Springer.)

investigate the dynamic behavior of the cells undergoing different flow patterns and vibration within microfluidic channels [106].

4.3.4 Other Software: Microfluidics Applications

Atomistic methods such as MD, DCMC, and LBM represent a framework for describing microfluidics at an atomic level of detail. Therefore, different software according to different atomistic methods have been developed to fit into the descriptions of microfluidics, each requiring its own set of approximations and having its own range of applicability. Therefore, besides the commonly used CFD software, it is also instructive to review other atomistic simulation software by which the dynamics of a microfluidics may be detail characterized.

As computational power is more than doubling every 18 months, larger-scale atomistic simulations software can be performed. For example, large-scale SPaSM dynamics software is a commonly used atomistic dynamics code. With this SPaSM software, we wanted to honor the father of the SPaSM code [107, 108], Peter S. Lomdahl, who together with his student Dave Beazley first initiated and spearheaded SPaSM in the early 1990s and who recently performed the first trillion atom simulation on the Blue Gene/L system [109] and simulated the RT instability with microfluidic system sizes up to 7 billion atoms [31]. LAMMPS software [110] is another open-source classical atomistic simulation code. LAMMPS is parallelized with MPI by spatially decomposing the simulation domain. The code is designed in a modular fashion to facilitate extension, making it an ideal candidate for use in a hybrid model [111]. There are lots of reports applying LAMMPS in microfluidic system. For example, Pereira *et al.* investigated the role of interfacial and wetting properties to the microfluidics displacement in hydrophilic pore network models (PNMs) based on LAMMPS [112]. Hu *et al.* used LAMMPS to study the flow boundary conditions for the interface between two immiscible microfluidics [113]. Li *et al.* used LAMMPS to explore the spreading behavior of the water-based nanofluid droplet on a solid substrate [114]. Recently, LAMMPS was also applied to study the biology microfluidic system. For instance, the blood–plasma separation in Y-shaped bifurcating microfluidic channels is performed using LAMMPS [46] as shown in Figure 4.12, in which the time integration of the motion equations is computed through a modified velocity Verlet algorithm. It takes 5.0×10^7 time steps for a typical simulation performed in the current study. In terms of computing time, on average, it takes about 1.3 million CPU core hours for a typical simulation on the Blue Gene/P system at the Argonne Leadership Computing Facility (ALCF).

4.4 Conclusions

We have summarized different numerical simulation models (MD, DSMC, DPD, CM, LBM, and CFD) and related software (CFD-ACE+, CFX, FLOW-3D, and other commonly used software) for microfluidics. Typical strategies of force implementation, interaction potential, and boundary condition in numerical simulation models have been introduced. These simulations demonstrate that numerical simulation is an efficient and useful approach for computational

www.ebook3000.com

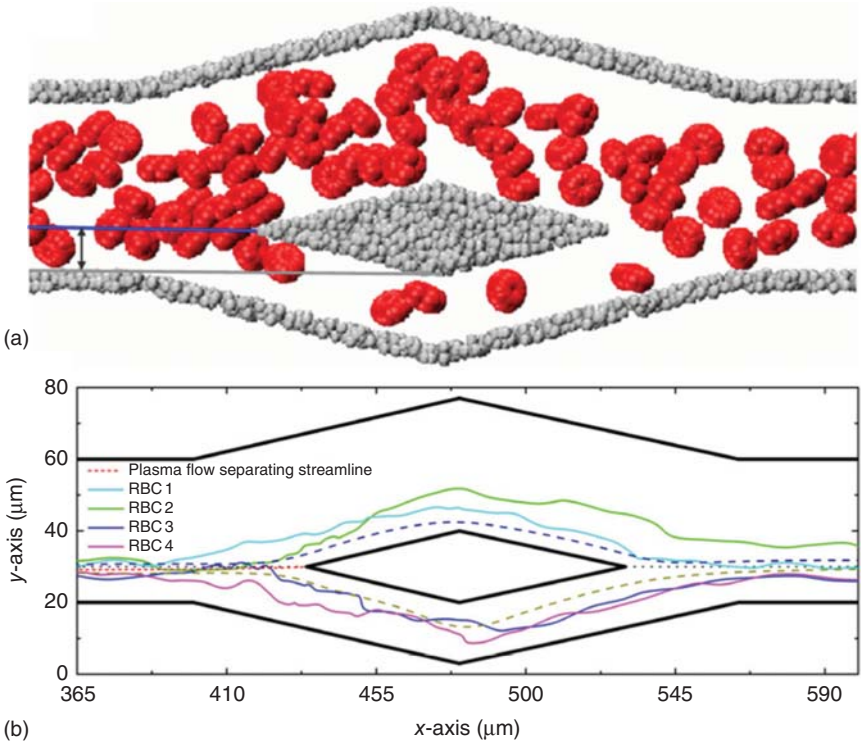


Figure 4.12 (a) LAMMPS simulation of the Y-shaped bifurcating microfluidic channel wall. (b) Path displacement of individual RBCs flowing in bifurcating microfluidic channels for *wd* = 3.0. (Wu *et al*. 2012 [46]. Reproduced with permission of American Chemical Society.)

microfluidics for its physical representation of microscopic interactions and convenience in modeling complex boundaries. Although about 114 publications have been referred in this review, the coverage is definitely not complete due to the large amount of literature and diverse interests in numerical simulation of microfluidics. However, this chapter was composed from a practical point of view for researchers in computational microfluidics, and the theoretical aspects were not addressed in detail. Nevertheless, knowledge of these involved theories might be necessary to better understand the strength and limit of numerical simulation in studying microfluidic systems, and interested readers can refer to the other relevant literature or text. We hope that this chapter can serve as a guide to apply numerical simulation models in microfluidic systems for achieving the performance desired for applications in diagnostics or high-throughput screening.

Acknowledgments

This work is supported by the National Natural Science Foundation of China (21576008, 91634116, 91334203), BUCT Fund for Disciplines Construction and Development (Project No. XK1501), and "Chemical Grid Project" of BUCT.

References

1 Beskok, A., Karniadakis, G.E., and Trimmer, W. (1996) Rarefaction and compressibility effects in gas microflows. *J. Fluids Eng.*, **118** (3), 448–456.
2 Gad-el-Hak, M. (1999) The fluid mechanics of microdevices – the Freeman scholar lecture. *J. Fluids Eng.*, **121** (1), 5–33.
3 De Jong, J., Lammertink, R., and Wessling, M. (2006) Membranes and microfluidics: a review. *Lab Chip*, **6** (9), 1125–1139.
4 Upreti, S., Lohi, A., Kapadia, R., and El-Haj, R. (2007) Vapor extraction of heavy oil and bitumen: a review. *Energy Fuels*, **21** (3), 1562–1574.
5 Li, D. (2004) *Electrokinetics in Microfluidics*, vol. **2**, Academic Press.
6 Nisar, A., Afzulpurkar, N., Mahaisavariya, B., and Tuantranont, A. (2008) MEMS-based micropumps in drug delivery and biomedical applications. *Sens. Actuators, B*, **130** (2), 917–942.
7 Tabeling, P. (2005) *Introduction to Microfluidics*, Oxford University Press on Demand.
8 Lauga, E., Brenner, M., and Stone, H. (2005) Microfluidics: the no-slip boundary condition, in *Handbook of Experimental Fluid Dynamics* (eds C. Tropea, J. Foss, and A. Yarin), Springer-Verlag, New York.
9 Ehrfeld, W., Hessel, V., and Löwe, H. (2000) *Microreactors: New Technology for Modern Chemistry*, Wiley-VCH Verlag GmbH & Co. KGaA, Weinheim, p. 2005.
10 Schubert, K., Brandner, J., Fichtner, M., Linder, G., Schygulla, U., and Wenka, A. (2001) Microstructure devices for applications in thermal and chemical process engineering. *Microscale Thermophys. Eng.*, **5** (1), 17–39.
11 Geschke, O., Klank, H., and Telleman, P. (2008) *Microsystem Engineering of Lab-on-a-chip Devices*, vol. **100**, John Wiley & Sons, Inc.
12 Harting, J., Kunert, C., and Hyväluoma, J. (2010) Lattice Boltzmann simulations in microfluidics: probing the no-slip boundary condition in hydrophobic, rough, and surface nanobubble laden microchannels. *Microfluid. Nanofluid.*, **8** (1), 1–10.
13 Lee, C.-Y., Chang, C.-L., Wang, Y.-N., and Fu, L.-M. (2011) Microfluidic mixing: a review. *Int. J. Mol. Sci.*, **12** (5), 3263–3287.
14 Zhang, J. (2011) Lattice Boltzmann method for microfluidics: models and applications. *Microfluid. Nanofluid.*, **10** (1), 1–28.
15 Bashir, S., Rees, J.M., and Zimmerman, W.B. (2011) Simulations of microfluidic droplet formation using the two-phase level set method. *Chem. Eng. Sci.*, **66** (20), 4733–4741.
16 Joensson, H.N. and Andersson Svahn, H. (2012) Droplet microfluidics – a tool for single-cell analysis. *Angew. Chem. Int. Ed.*, **51** (49), 12176–12192.
17 Garstecki, P., Fuerstman, M.J., Stone, H.A., and Whitesides, G.M. (2006) Formation of droplets and bubbles in a microfluidic T-junction – scaling and mechanism of break-up. *Lab Chip*, **6** (3), 437–446.
18 Squires, T.M. and Quake, S.R. (2005) Microfluidics: fluid physics at the nanoliter scale. *Rev. Mod. Phys.*, **77** (3), 977.

www.ebook3000.com

19 Kim, B.H., Beskok, A., and Cagin, T. (2008) Thermal interactions in nanoscale fluid flow: molecular dynamics simulations with solid–liquid interfaces. *Microfluid. Nanofluid.*, **5** (4), 551–559.
20 Kadau, K., Barber, J.L., Germann, T.C., Holian, B.L., and Alder, B.J. (1916) Atomistic methods in fluid simulation. *Philos. Trans. R. Soc. London, Ser. A*, **2010** (368), 1547–1560.
21 Moseler, M. and Landman, U. (2000) Formation, stability, and breakup of nanojets. *Science*, **289** (5482), 1165–1169.
22 Rapaport, D. (2006) Hexagonal convection patterns in atomistically simulated fluids. *Phys. Rev. E*, **73** (2), 025301.
23 Hirshfeld, D. and Rapaport, D. (2000) Growth of Taylor vortices: a molecular dynamics study. *Phys. Rev. E*, **61** (1), R21.
24 Kadau, K., Germann, T.C., Hadjiconstantinou, N.G., Lomdahl, P.S., Dimonte, G., Holian, B.L., and Alder, B.J. (2004) Nanohydrodynamics simulations: an atomistic view of the Rayleigh–Taylor instability. *Proc. Natl. Acad. Sci. U.S.A.*, **101** (16), 5851–5855.
25 Glosli, J.N., Richards, D.F., Caspersen, K., Rudd, R.E., Gunnels, J.A., and Streitz, F. H. (2007) Extending stability beyond CPU millennium: a micron-scale atomistic simulation of Kelvin–Helmholtz instability. Proceedings of the 2007 ACM/IEEE Conference on Supercomputing, ACM, p 58.
26 Root, S., Hardy, R.J., and Swanson, D.R. (2003) Continuum predictions from molecular dynamics simulations: shock waves. *J. Chem. Phys.*, **118** (7), 3161–3165.
27 Rapaport, D. (2008) Molecular dynamics studies of swimming at the microscopic scale. *Comput. Phys. Commun.*, **179** (1), 155–158.
28 Öhrn, Y. and Deumens, E. (1999) Toward an ab initio treatment of the time-dependent Schrödinger equation of molecular systems. *J. Phys. Chem. A*, **103** (47), 9545–9551.
29 Hansen, J.-P. and McDonald, I.R. (1990) *Theory of Simple Liquids*, Elsevier.
30 Bird, G.A. (1994) *Molecular Gas Dynamics and the Direct Simulation of Gas Flows*, Clarendon Press.
31 Kadau, K., Rosenblatt, C., Barber, J.L., Germann, T.C., Huang, Z., Carlès, P., and Alder, B.J. (2007) The importance of fluctuations in fluid mixing. *Proc. Natl. Acad. Sci. U.S.A.*, **104** (19), 7741–7745.
32 Barber, J., Kadau, K., Germann, T., and Alder, B. (2008) Initial growth of the Rayleigh–Taylor instability via molecular dynamics. *Eur. Phys. J. B*, **64** (2), 271–276.
33 Barber, J.L., Kadau, K., Germann, T.C., and Alder, B.J. (2007) Simulation of fluid instabilities using atomistic methods, shock compression of condensed matter – 2007. Proceedings of the Conference of the American Physical Society Topical Group on Shock Compression of Condensed Matter, AIP Publishing pp. 301–304.
34 Usami, M., Kamiya, T., Maeda, H., and Furukawa, Y. (2008) DSMC calculation of Karman vortex flow and Taylor vortex flow by an improved new collision scheme (U–system 3), rarefied gas dynamics. Proceedings of the

26th International Symposium on Rarefied Gas Dynamics, AIP Publishing, pp. 365–370.
35 Zhang, J., Goldstein, D., Varghese, P., Gimelshein, N., Gimelshein, S., Levin, D., and Trafton, L. (2003) DSMC Modeling of gas dynamics, radiation, and fine particulates in ionian volcanic jets, AIP conference. Proceedings, IOP Institute of Physics Publishing Ltd, pp. 704-711.
36 Kadau, K., Barber, J.L., Germann, T.C., and Alder, B.J. (2008) Scaling of atomistic fluid dynamics simulations. *Phys. Rev. E*, **78** (4), 045301.
37 Espanol, P. and Warren, P. (1995) Statistical mechanics of dissipative particle dynamics. *Europhys. Lett.*, **30** (4), 191.
38 Hoogerbrugge, P. and Koelman, J. (1992) Simulating microscopic hydrodynamic phenomena with dissipative particle dynamics. *Europhys. Lett.*, **19** (3), 155.
39 Moeendarbary, E., Ng, T., and Zangeneh, M. (2009) Dissipative particle dynamics: introduction, methodology and complex fluid applications – a review. *Int. J. Appl. Mech.*, **1** (04), 737–763.
40 Besold, G., Vattulainen, I., Karttunen, M., and Polson, J.M. (2000) Towards better integrators for dissipative particle dynamics simulations. *Phys. Rev. E*, **62** (6), R7611.
41 Steiner, T., Cupelli, C., Zengerle, R., and Santer, M. (2009) Simulation of advanced microfluidic systems with dissipative particle dynamics. *Microfluid. Nanofluid.*, **7** (3), 307–323.
42 Groot, R.D. and Warren, P.B. (1997) Dissipative particle dynamics: bridging the gap between atomistic and mesoscopic simulation. *J. Chem. Phys.*, **107** (11), 4423.
43 Marsh, C., Backx, G., and Ernst, M. (1997) Static and dynamic properties of dissipative particle dynamics. *Phys. Rev. E*, **56** (2), 1676.
44 Trofimov, S., Nies, E., and Michels, M. (2002) Thermodynamic consistency in dissipative particle dynamics simulations of strongly nonideal liquids and liquid mixtures. *J. Chem. Phys.*, **117** (20), 9383–9394.
45 Lowe, C. (1999) An alternative approach to dissipative particle dynamics. *Europhys. Lett.*, **47** (2), 145.
46 Wu, Y., Cai, S., Wang, D., He, W., and Li, Y. (2012) Syntheses of water-soluble octahedral, truncated octahedral, and cubic Pt–Ni nanocrystals and their structure–activity study in model hydrogenation reactions. *J. Am. Chem. Soc.*, **134** (21), 8975–8981.
47 Keaveny, E.E., Pivkin, I.V., Maxey, M., and Karniadakis, G.E. (2005) A comparative study between dissipative particle dynamics and molecular dynamics for simple-and complex-geometry flows. *J. Chem. Phys.*, **123** (10), 104107.
48 Bird, R., Stewart, W., and Lightfoot, E. (2007) *Transport Phenomena*, 2nd rev. edn, John Wiley & Sons, Inc., New York.
49 Yang, C. and Li, D. (1996) A method of determining the thickness of liquid–liquid interfaces. *Colloids Surf., A*, **113** (1), 51–59.
50 Welch, S.W. (1995) Local simulation of two-phase flows including interface tracking with mass transfer. *J. Comput. Phys.*, **121** (1), 142–154.

www.ebook3000.com

51 Ganesan, S. and Tobiska, L. (2008) An accurate finite element scheme with moving meshes for computing 3D-axisymmetric interface flows. *Int. J. Numer. Methods Fluids*, **57** (2), 119–138.

52 Unverdi, S.O. and Tryggvason, G. (1992) A front-tracking method for viscous, incompressible, multi-fluid flows. *J. Comput. Phys.*, **100** (1), 25–37.

53 Tryggvason, G., Bunner, B., Esmaeeli, A., Juric, D., Al-Rawahi, N., Tauber, W., Han, J., Nas, S., and Jan, Y.-J. (2001) A front-tracking method for the computations of multiphase flow. *J. Comput. Phys.*, **169** (2), 708–759.

54 Osher, S. and Sethian, J.A. (1988) Fronts propagating with curvature-dependent speed: algorithms based on Hamilton-Jacobi formulations. *J. Comput. Phys.*, **79** (1), 12–49.

55 Sussman, M., Smereka, P., and Osher, S. (1994) A level set approach for computing solutions to incompressible two-phase flow. *J. Comput. Phys.*, **114** (1), 146–159.

56 Sethian, J. and Smereka, P. (2003) Level set methods for fluid interfaces. *Annu. Rev. Fluid Mech.*, **35** (1), 341–372.

57 Liu, J., Yap, Y.F., and Nguyen, N.-T. (2009) Behavior of microdroplets in diffuser/nozzle structures. *Microfluid. Nanofluid.*, **6** (6), 835–846.

58 Liu, J., Yap, Y.F., and Nguyen, N.-T. (2009) Motion of a droplet through microfluidic ratchets. *Phys. Rev. E*, **80** (4), 046319.

59 Olsson, E. and Kreiss, G. (2005) A conservative level set method for two phase flow. *J. Comput. Phys.*, **210** (1), 225–246.

60 Yue, P., Feng, J.J., Liu, C., and Shen, J. (2004) A diffuse-interface method for simulating two-phase flows of complex fluids. *J. Fluid Mech.*, **515**, 293–317.

61 Takada, N., Misawa, M., and Tomiyama, A. (2006) A phase-field method for interface-tracking simulation of two-phase flows. *Math. Comput. Simul*, **72** (2), 220–226.

62 Wörner, M. (2012) Numerical modeling of multiphase flows in microfluidics and micro process engineering: a review of methods and applications. *Microfluid. Nanofluid.*, **12** (6), 841–886.

63 Verhaeghe, F., Luo, L.-S., and Blanpain, B. (2009) Lattice Boltzmann modeling of microchannel flow in slip flow regime. *J. Comput. Phys.*, **228** (1), 147–157.

64 Wolf-Gladrow, D.A. (2000) *Lattice-gas cellular automata and Lattice Boltzmann models: an introduction*, Springer Science & Business Media.

65 Tu, J., Yeoh, G.H., and Liu, C. (2012) *Computational fluid dynamics: a practical approach*, Butterworth-Heinemann.

66 Martys, N.S. and Chen, H. (1996) Simulation of multicomponent fluids in complex three-dimensional geometries by the Lattice Boltzmann method. *Phys. Rev. E*, **53** (1), 743.

67 Koido, T., Furusawa, T., and Moriyama, K. (2008) An approach to modeling two-phase transport in the gas diffusion layer of a proton exchange membrane fuel cell. *J. Power Sources*, **175** (1), 127–136.

68 Heemels, M., Hagen, M., and Lowe, C. (2000) Simulating solid colloidal particles using the Lattice-Boltzmann method. *J. Comput. Phys.*, **164** (1), 48–61.

69 Joshi, A.S. and Sun, Y. (2009) Multiphase Lattice Boltzmann method for particle suspensions. *Phys. Rev. E*, **79** (6), 066703.

70 Succi, S. (2001) *The Lattice Boltzmann Equation: for Fluid Dynamics and Beyond*, Oxford University Press.

71 Guo, Z. and Zheng, C. (2008) Analysis of Lattice Boltzmann equation for microscale gas flows: relaxation times, boundary conditions and the Knudsen layer. *Int. J. Comput. Fluid Dyn.*, **22** (7), 465–473.

72 Liu, H. and Zhang, Y. (2009) Droplet formation in a T-shaped microfluidic junction. *J. Appl. Phys.*, **106** (3), 034906.

73 Gupta, A., Murshed, S.S., and Kumar, R. (2009) Droplet formation and stability of flows in a microfluidic T-junction. *Appl. Phys. Lett.*, **94** (16), 164107.

74 Van der Graaf, S., Nisisako, T., Schroen, C., Van Der Sman, R., and Boom, R. (2006) Lattice Boltzmann simulations of droplet formation in a T-shaped microchannel. *Langmuir*, **22** (9), 4144–4152.

75 Lin, Y.-H., Lee, C.-H., and Lee, G.-B. (2008) Droplet formation utilizing controllable moving-wall structures for double-emulsion applications. *J. Microelectromech. Syst.*, **17** (3), 573–581.

76 Fair, R.B., Khlystov, A., Tailor, T.D., Ivanov, V., Evans, R.D., Srinivasan, V., Pamula, V.K., Pollack, M.G., Griffin, P.B., and Zhou, J. (2007) Chemical and biological applications of digital-microfluidic devices. *IEEE Des. Test Comput.*, **24** (1), 10–24.

77 Erickson, D. (2005) Towards numerical prototyping of labs-on-chip: modeling for integrated microfluidic devices. *Microfluid. Nanofluid.*, **1** (4), 301–318.

78 Frohn, A. and Roth, N. (2000) *Dynamics of Droplets*, Springer Science & Business Media.

79 Tarnogrodzki, A. (1993) Theoretical prediction of the critical Weber number. *Int. J. Multiphase Flow*, **19** (2), 329–336.

80 Hirt, C.W. and Nichols, B.D. (1981) Volume of fluid (VOF) method for the dynamics of free boundaries. *J. Comput. Phys.*, **39** (1), 201–225.

81 van Sint Annaland, M., Deen, N., and Kuipers, J. (2005) Numerical simulation of gas bubbles behaviour using a three-dimensional volume of fluid method. *Chem. Eng. Sci.*, **60** (11), 2999–3011.

82 Brackbill, J., Kothe, D.B., and Zemach, C. (1992) A continuum method for modeling surface tension. *J. Comput. Phys.*, **100** (2), 335–354.

83 Nguyen, N.-T. and Wu, Z. (2004) Micromixers – a review. *J. Micromech. Microeng.*, **15** (2), R1.

84 Huang, M., Fan, S., Xing, W., and Liu, C. (2010) Microfluidic cell culture system studies and computational fluid dynamics. *Math. Comput. Modell.*, **52** (11), 2036–2042.

85 Weber, M.W. and Shandas, R. (2007) Computational fluid dynamics analysis of microbubble formation in microfluidic flow-focusing devices. *Microfluid. Nanofluid.*, **3** (2), 195–206.

86 Shen, F., Li, X., and Li, P.C. (2014) Study of flow behaviors on single-cell manipulation and shear stress reduction in microfluidic chips using computational fluid dynamics simulations. *Biomicrofluidics*, **8** (1), 014109.

www.ebook3000.com

87 Glatzel, T., Litterst, C., Cupelli, C., Lindemann, T., Moosmann, C., Niekrawietz, R., Streule, W., Zengerle, R., and Koltay, P. (2008) Computational fluid dynamics (CFD) software tools for microfluidic applications – a case study. *Comput. Fluids*, **37** (3), 218–235.

88 Stout, P.J., Yang, H., Dionne, P., Leonard, A., Tan, Z., Przekwas, A.J., and Krishnan, A. (1999) CFD-ACE+: A CAD system for simulation and modeling of MEMS. Design, Test, and Microfabrication of MEMS/MOEMS, International Society for Optics and Photonics, pp. 328–339.

89 Lee, K., Kim, C., Ahn, B., Panchapakesan, R., Full, A.R., Nordee, L., Kang, J.Y., and Oh, K.W. (2009) Generalized serial dilution module for monotonic and arbitrary microfluidic gradient generators. *Lab Chip*, **9** (5), 709–717.

90 Makhijani, V., Reich, A., Puntambekar, A., Hong, C., and Ahn, C. (2001) Simulation of flow in structurally programmable microfluidic channels. Technical Proceedings of the 2001 International Conference on Modeling and Simulation of Microsystems.

91 Jang, L.-S. and Wang, M.-H. (2007) Microfluidic device for cell capture and impedance measurement. *Biomed. Microdevices*, **9** (5), 737–743.

92 Przekwas, A., Makhijani, V., Athavale, M., Klein, A., and Bartsch, P. (2000) Computational simulation of bio-microfluidic processes in integrated DNA biochips. Micro Total Analysis Systems 2000, Springer, pp. 561–564.

93 Ansys, I. (2004) *ANSYS users manual*, vol. **275**, ANSYS Inc., Southpointe, p. 18.

94 Ansys, I., CFD (2005) *ICEM CFD Theory Guide*, Ansys Inc.

95 Zwart, P., Scheuerer, M., and Bogner, M. (2003) Free surface flow modelling of an impinging jet. ASTAR International Workshop on Advanced Numerical Methods for Multidimensional Simulation of Two-Phase Flow, pp. 15–16.

96 Oh, J., Lee, B., Nam, K., Attla, G., Lee, K., and Cjai, J. (2011) Design features of microfluidic reactor for [18F] FDG radiopharmaceutical synthesis. Application of Accelerators in Research and Industry: 21st International Conference, AIP Publishing, pp. 426–429.

97 Bui, A., Zhu, Y., and Petkovic-Duran, K. (2006) Modeling of separation of metal ions in a microfluidic chip. *Mobilities*, **100**, 1.

98 Sauli, Z., Retnasamy, V., Taniselass, S., Nadzri, N.S., Mei, T.H., Anwar, K., and Abdullah, N. (2014) WSS investigation in microfluidic FFS channel at Re 500. *Appl. Mech. Mater.*, **487**, 294–297.

99 Yasui, T., Omoto, Y., Osato, K., Kaji, N., Suzuki, N., Naito, T., Watanabe, M., Okamoto, Y., Tokeshi, M., and Shamoto, E. (2011) Microfluidic baker's transformation device for three-dimensional rapid mixing. *Lab Chip*, **11** (19), 3356–3360.

100 Chen, H., Sun, J., Wolvetang, E., and Cooper-White, J. (2015) High-throughput, deterministic single cell trapping and long-term clonal cell culture in microfluidic devices. *Lab Chip*, **15** (4), 1072–1083.

101 Mohammed, A., Adeniyi, A.A., and Hassan, A.B. (2012) Modelling of serpentine continuous flow polymerase chain reaction microfluidics. *IJEST*, **4**, 1183–1189.

102 Barkhudarov, M.R. (2004) *Lagrangian VOF Advection method for FLOW-3D*, Flow Science Inc, pp. 1–10.

103 Bhattacharjee, B. (2012) *Study of droplet splitting in an electrowetting based digital microfluidic system*, University of British Columbia.

104 Howell, N. and Li, W. (2010) Modeling and simulation of droplet translocation and fission by electrowetting-on-dielectrics (EWOD). *Front. Mech. Eng. Chin.*, **5** (4), 376–388.

105 Chandorkar, A. and Palit, S. (2009) Simulation of droplet dynamics and mixing in microfluidic devices using a VOF-based method. *Sens. Trans.*, **7**, 136.

106 Bahadur, I.M. and Mills, J.K. (2011) Fluidic vacuum-based biological cell holding device with piezoelectrically induced vibration. 2011 IEEE/ICME International Conference on Complex Medical Engineering (CME), IEEE, pp. 85–90.

107 Beazley, D.M. and Lomdahl, P.S. (1994) Message-passing multi-cell molecular dynamics on the Connection Machine 5. *Parallel Comput.*, **20** (2), 173–195.

108 Beazley, D.M. and Lomdahl, P.S. (1997) Controlling the data glut in large-scale molecular-dynamics simulations. *Comput. Phys.*, **11** (3), 230–238.

109 Germann, T.C. and Kadau, K. (2008) Trillion-atom molecular dynamics becomes a reality. *Int. J. Mod. Phys. C*, **19** (09), 1315–1319.

110 Plimpton, S. (1995) Fast parallel algorithms for short-range molecular dynamics. *J. Comput. Phys.*, **117** (1), 1–19.

111 Cosden, I.A. and Lukes, J.R. (2013) A hybrid atomistic–continuum model for fluid flow using LAMMPS and OpenFOAM. *Comput. Phys. Commun.*, **184** (8), 1958–1965.

112 Pereira, A.O., Lara, L.S., and Miranda, C.R. (2016) Combining molecular dynamics and Lattice Boltzmann simulations: a hierarchical computational protocol for microfluidics. *Microfluid. Nanofluid.*, **20** (2), 1–15.

113 Hu, Y., Zhang, X., and Wang, W. (2010) Boundary conditions at the liquid–liquid Interface in the Presence of Surfactants. *Langmuir*, **26** (13), 10693–10702.

114 Li, Y., Wang, F., Liu, H., and Wu, H. (2015) Nanoparticle-tuned spreading behavior of nanofluid droplets on the solid substrate. *Microfluid. Nanofluid.*, **18** (1), 111–120.

www.ebook3000.com

5

Digital Microfluidic Systems: Fundamentals, Configurations, Techniques, and Applications

Mohamed Yafia, Bara J. Emran, and Homayoun Najjaran

The University of British Columbia, School of Engineering, 3333 University Way, Kelowna, BC V1V 1V7, Canada

5.1 Introduction to Microfluidic Systems

Microfluidics is the science of studying the behavior of the microliter droplets manipulated in the micrometer range. In fact, microfluidic devices can replace benchtop equipment and perform advanced and complex processes saving valuable time and space. Microfluidic chips are usually used for their great advantages such as reduction of the analysis time, saving of samples and reagents, miniaturization, portability, and cost reduction. In brief, Table 5.1 shows a concise comparison that illustrates the advantages of using microfluidic systems to similar fully automated benchtop systems. When the term microfluidics is used, the first thing that comes to our mind is the shape of the long and connected microchannels engraved in glass, silicon, or polydimethylsiloxane (PDMS) substrates. Known as the continuous microfluidic channels, they allow different fluids to flow at predefined paths at the same time. Different flow streams can then be merged to perform advanced microfluidic operations where mixing can occur between different liquids as demonstrated in Figure 5.1a. However, the flow path through each channel is fixed once these channels are fabricated. This means that the continuous microchannels have to be designed for a specific operation as the chip cannot be reconfigured later if any modifications to the operation are needed.

As a result, the need for another system that can handle microfluidic operations in a reconfigurable manner has emerged to allow for the current more advanced and sophisticated microfluidic applications. Digital microfluidic (DMF) system is one of the promising microfluidic platforms that has been introduced to manipulate microliter droplets on discrete electrodes using electrical signals. This system can handle several droplets and run several processes independently at the same time. Unlike the continuous microchannel systems, a DMF system has no predesigned channels or fixed inlet and outlet ports. Hence, the droplets are not restricted to a certain flow path. The droplet path can be reconfigured easily as different paths can be programmed to control the droplet motion. In addition, complex routing algorithms can be applied based on the requirements of the intended operation. The simplicity of operating the DMF system is another

Microfluidics: Fundamentals, Devices and Applications, First Edition.
Edited by Yujun Song, Daojian Cheng, and Liang Zhao.
© 2018 Wiley-VCH Verlag GmbH & Co. KGaA. Published 2018 by Wiley-VCH Verlag GmbH & Co. KGaA.

Table 5.1 Comparison between the processes using traditional automation methods versus microfluidics systems.

	Robot	Microfluidic drops
Total reactions	5×10^7	5×10^7
Reaction volume	100 µl	6 pl
Total volume	5 000 l	150 µl
Reactions/day	73 000	1×10^8
Total time	~2 years	~7 h
Number of plates/devices	260 000	2
Cost of plates/devices	$520 000	$1.00
Cost of tips	$10 million	$0.30
Amortized cost of instruments	$280 000	$1.70
Substrate	$4.75 million	$0.25
Total cost	$15.81 million	$2.50

Source: Reprinted with permission from Ref. [1]. Copyright 2010 PNAS.

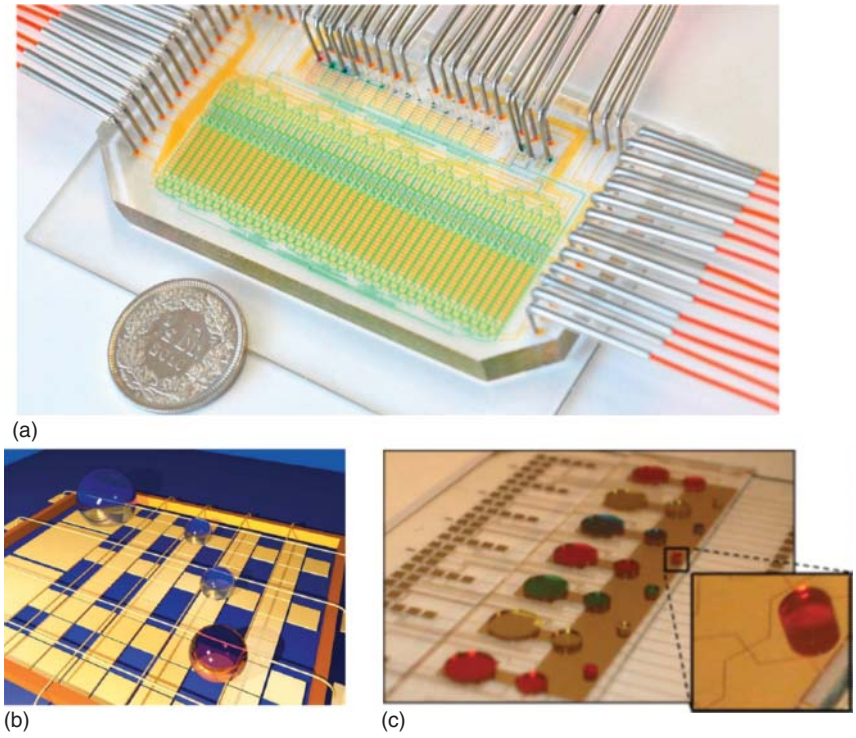


Figure 5.1 (a) Continuous microchannels with fixed flow paths. (Junkin *et al*. 2016 [2]. Reproduced with permission of Elsevier.) The two main types of the digital microfluidics system with reconfigurable droplet path: (b) open DMF system (Fouillet and Achard 2004 [3]. Reproduced with permission of Elsevier.) and (c) closed DMF system. (Barbulovic-Nad *et al*. 2010 [4]. Reproduced with permission of Royal Society of Chemistry.)

www.ebook3000.com

big advantage that happens by eliminating any mechanical moving parts such as microvalves or pumps. Specifically, moving the droplets can be achieved using just electrical signals with very small power consumption.

5.2 Types of Digital Microfluidic Systems

There are two main types of DMF systems. The first type is the open DMF system where droplets are located on a single plate where the activated electrodes are arranged. The second type is the closed DMF system in which droplets are sandwiched between top and bottom plates. In the latter, the electrodes are again arranged on one of the plates and the other plate provides a conductive surface. The grounding of the open DMF system can be a wire passing through the droplets or a grounding electrode sitting beside the activated high voltage electrode. In contrast, the grounding of the closed DMF system is always the top plate. With this in mind, a layer of transparent metal is used in order to facilitate the visualization of the droplets and the DMF processes. The transparent metal that is usually used for the grounding top plate is indium tin oxide (ITO). Figure 5.1 demonstrates the difference between these two DMF systems and Figure 5.2 illustrates a schematic that shows the multiple layers that form the DMF chips and how they are constructed.

Several DMF operations can be performed on the droplets inside the DMF system. Specifically, droplet transport, merging, mixing, splitting, and dispensing are the typical operations that can be performed in DMF systems. Droplet transport from one electrode to another occurs when a high voltage signal is conveyed to the activated electrode. In a similar manner, droplet merging between two droplets occurs when the middle electrode becomes activated. In contrast, splitting a droplet needs two electrodes to be activated on both sides of the main droplet at the same time to cut the droplet. Likewise, dispensing requires two or more electrodes to be activated simultaneously to complete the cutting process of the droplet. One of these electrodes is a large reservoir electrode holding a relatively bigger droplet. The other smaller electrodes are activated in a sequence to dispense and cut a smaller droplet out of the reservoir droplet. In particular, all these operations can be performed successfully in closed DMF systems. On the other hand, splitting and dispensing cannot be performed in open DMF systems since the hydrodynamic forces generated in an open system are not capable to split or cut the droplet in this configuration. We will now discuss the advantages and disadvantages of the open and closed DMF systems.

Open DMF systems are characterized by having open access to the droplet from the top as there is no top plate required. Notably, this direct access can facilitate the delivery of the droplets to the system. As a result, any step required at the detection stage can be much easier when the top plate is not used. On the positive side, eliminating the top plate can also reduce the friction and consequently high droplet velocities can be achieved. The coplanar arrangement of the electrodes, without a need for any wires, allowed very high droplet speeds of up to 260 mm s^{-1} [5].

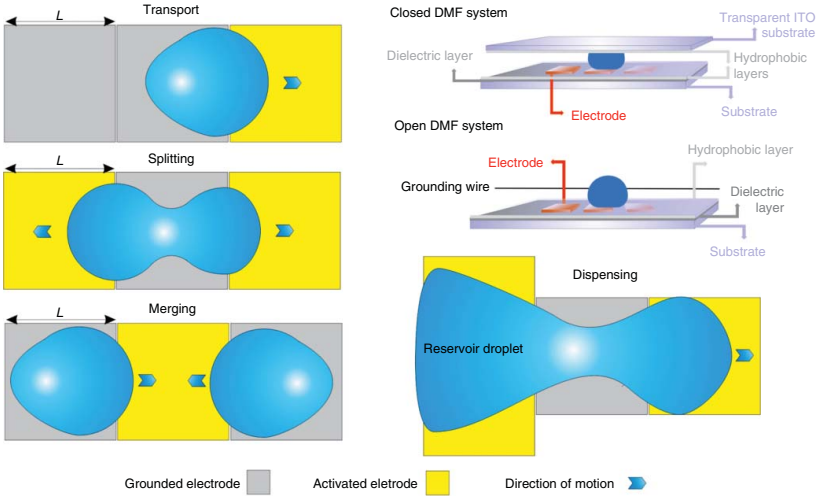


Figure 5.2 The four main DMF operations and the constructing layers of an open and a closed DMF system. The bottom plate has the same construction in the two DMF systems. The top plate acts as ground in the closed system and a wire passing through the droplet acts as ground in the open system.

www.ebook3000.com

On the negative side, it is important to realize that the excessive evaporation that occurs to the droplet is one of the main limitations of the open DMF system. Closed DMF systems can solve this issue by allowing to add a filler medium, usually silicon oil, to protect droplet from evaporation in sensitive applications. Another key point is the ability of the closed DMF system to split and cut the droplets easily. Further, lowering the required actuation voltage can be achieved using a combination of multiple dielectric layers [6].

5.3 DMF Chip Fabrication Techniques

Photolithography is the most commonly used technique to fabricate DMF chips [7]. This method requires multiple fabrication steps performed in a clean room environment to obtain a very detailed resolution in the micron range. The fabrication starts with sputtering a conductive material on glass substrates and then patterning the electrodes according to the designed mask. Next, spin coating is used to deposit the photoresist layer. Eventually, baking and wet etching take place to form the required electrodes. Further, several dielectric electric layers can be added on top of the electrodes to isolate them from the droplets. Parylene C deposited with chemical vapor deposition system is the most commonly used dielectric layer in DMF systems. At last, a hydrophobic layer is added later on top to increase the contact angle and decrease the friction between the droplet and the surface. Teflon AF 1600 and CYTOP are the most commonly used hydrophobic layers.

Researchers are working these days on rapid prototyping techniques to facilitate the fabrication process of DMF chips. The main target of these techniques is to use simple fabrication methods by avoiding using expensive materials and highly equipped facilities. Hence, several fabrication techniques were tried on flexible and rigid substrate materials using different conductive metals or inks to generate the electrodes and the connection tracks. To reduce the cost of the substrates and the electrodes, DMF chips were fabricated from copper printed circuit board (PCB) substrates [8, 9] as shown in Figure 5.3i. To reduce the fabrication time and cost, inkjet printing can be used as a mask for the etchant instead of using photoresist in the photolithography process. Although this method facilitates some fabrication procedures, it still requires the wet etching process that involves using chemicals. Instead of using rigid silicon and glass chips, fabricating on flexible substrates was also introduced to reduce the cost of the material and perform new operations on bent surfaces. Given these points, copper on polyethylene terephthalate (PET) substrates was used to fabricate a completely functional DMF chip as shown in Figure 5.3j [12]. This substrate provided the ability to move the droplet on bent surfaces and in all the 3D directions. Different researchers tried later to fabricate the DMF chip on paper substrates. Printing on paper substrates using inkjet printing can produce functional DMF electrodes as shown in Figure 5.3a–d [10, 13]. In addition, screen printing can also generate DMF chips from different inks on various types of substrates [14]. Silver- and carbon-based inks can be screen printed on glass, paper, and wax paper substrates using this method. Another simple

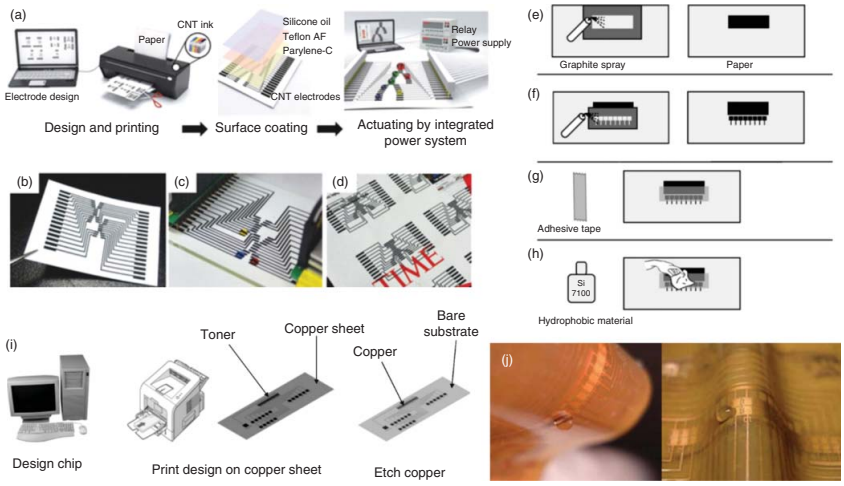


Figure 5.3 Rapid prototyping techniques for fabricating DMF chips. Figure (a–d) show the process of ink jet printing of conductive ink on paper substrate. (Ko *et al*. 2014 [10]. Reproduced with permission of John Wiley & Sons.) Figure (e–h) show the process of spraying graphite through a mask on paper substrate. (Abadian and Jafarabadi-Ashtiani 2014 [11]. Reproduced with permission of Springer.) (i) Printing toner on PCB and then etching the copper substrate. (Abdelgawad and Wheeler 2007 [8]. Reproduced with permission of John Wiley & Sons.) (j) All terrain droplet actuation. (Abdelgawad *et al*. 2008 [12]. Reproduced with permission of Royal Society of Chemistry.)

www.ebook3000.com

and low cost method was introduced by spraying graphite on paper through a template to generate conductive DMF electrodes as shown in Figure 5.3e–h [11]. However, the output resolution was limited compared with the other fabrication techniques, and the produced chip can operate with a range of droplet volume that starts from 15 µl. To decrease the fabrication cost and make the whole process very simple, they applied a clear tape as a dielectric layer. Moreover, they replaced the expensive hydrophobic coating with a rain repellant Rain-X® or a silicon additive hydrophobic layer. Although the later techniques cannot achieve high printing resolutions, the chips produced were able to successfully perform the DMF processes in closed and open system configurations.

5.4 Different Electrode Configurations in DMF Systems

The electrode design plays an important role in controlling the forces acting on the droplet in open and closed systems. In closed DMF systems, the top plate is always acting as a grounding plate. In this case, there is no specific configuration in the top plate design since the top plate is just a conductive and usually transparent ITO plate coated with a hydrophobic layer. Hence, the appropriate electrode configuration is designed on the bottom plate. The actuation force generated depends immensely on how the electrode shape affects the pattern of the electric fields and the charges generated around the droplet. A comparison between a square, an interdigitated, and a crescent electrode designs has been performed to assess the effect of electrode shape on the droplet dynamics (see Figure 5.4a–c) [15]. Their experimental and numerical results illustrated that the crescent shape has superior performance compared with the flat electrode as the velocity is almost doubled at the same voltage level. Sometimes a hydrophilic spot is generated for trapping a droplet [18] or for acting as a detection site [19]. To manipulate different sizes of droplets on the same electrode design, Chen *et al*. [16] proposed using extended interdigitated fingers between the electrodes. Unlike the normal electrode designs, their extended finger design allowed various droplet sizes to be manipulated using the electrode design shown in Figure 5.4d. On the other hand, Figure 5.4e shows that the open system has more design reconfigurations. In open systems, the grounding can be just a wire passing in the middle of the droplet [3], engraved and exposed metal line between the activated electrodes [20, 21], or grounding electrodes that are completely covered beneath the dielectric layer and the hydrophobic layer [12, 22]. In the grounding wire configurations, the droplet motion is impeded by both the hydrophobic surface and friction from the contact line touching the grounding wire. However, in the grounding electrode configurations, the droplet motion is only impeded by the hydrophobic surface covering the bottom plate.

In open DMF systems, the grounding configuration can change the actuating forces significantly. A comparison between all the electrodes and grounding reconfigurations in open DMF systems was performed using Comsol Multiphysics to calculate the forces generated from each design [17]. In the last three grounding configurations in Figure 5.4e, another array of electrodes arranged beside the high voltage electrodes is acting as the grounding electrodes. The main

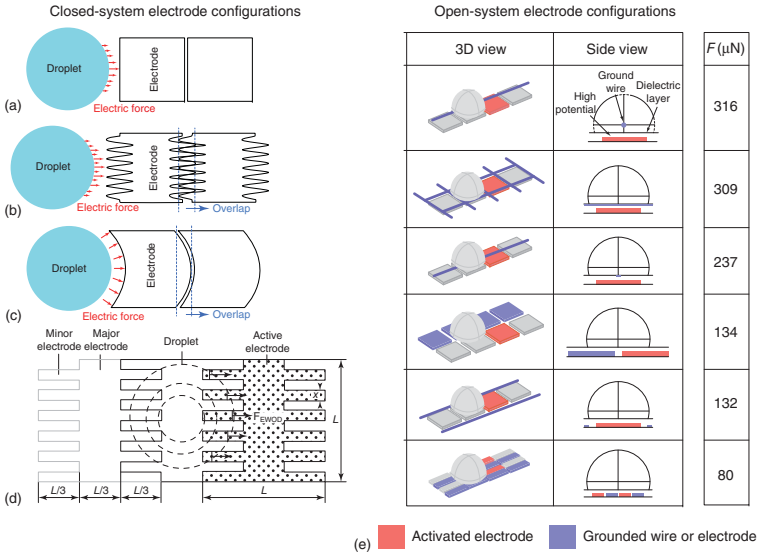


Figure 5.4 (a) Square, (b) interdigitated, and (c) crescent electrodes in closed DMF systems where the highest driving force comes from the crescent shape. ((a–c) Rajabi and Dolatabadi 2010 [15]. Reproduced with permission of Elsevier.) (d) Interdigitated electrode shape with extended fingers for actuating different droplet volumes. (Reprinted with permission from Ref. [16]. Copyright 2012 AIP Publishing LLC.) (e) Several configurations of electrodes and grounding systems in open DMF chips where the driving force is decreasing from the top to the bottom. (Reprinted with permission from Ref. [17]. Copyright 2009 AIP Publishing LLC.)

www.ebook3000.com

difference in these last three configurations is that there is no direct contact with the droplet and the ground as the dielectric layer and the hydrophobic layer are covering the grounding electrodes.

5.5 Digital Microfluidic Working Principle

Many studies were introduced to differentiate between the forces involved in the droplet actuation process in DMF systems. The driving force acting on the droplet is due to electrowetting on dielectric (EWOD) for conductive droplets and dielectrophoresis (DEP) for nonconductive droplets [23]. The electrowetting phenomena have been used in numerous applications such as electrowetting microlenses [24], electrowetting microvalves [25, 26], and point-of-care devices [27]. In EWOD, charge accumulation occurs on the surface due to the high voltage applied beneath the dielectric layer. This charge accumulation draws the droplet toward the activated electrode, and the magnitude of the force depends on several parameters such as the applied voltage level and the thickness of the dielectric layer. For instance, a prototype device that used EWOD as a method of actuation was fabricated and tested in the reference [28]. This prototype was managed to demonstrate an average velocity of 30 mm s^{-1} and switching rates of up to 20 Hz, which increased the transport of droplets many folds over the previous methods. In EWOD, the electric field does not penetrate the droplet.

On the other hand, DEP acts on insulating droplets where the electric field starts to penetrate the droplet and the nonuniformity of the electric field forces the droplet to move toward the activated electrode under the influence of the ponderomotive force. An electrowetting test is usually performed to evaluate the ability of the fabricated DMF system to change the contact angle of the droplet sitting on the hydrophobic surface. A phenomenon called contact angle saturation occurs when the voltage increases and the contact angle remains the same without any change beyond a certain voltage limit. Several theories are proposed to explain the contact angle saturation effect such as the corona discharge that may occur at the edge of the droplet and the instability that happens when a large number of small droplets are ejected at the surface [29]. Electrowetting on inclined surfaces has been studied by Datta *et al*. [30] where a similar model to Bahadur and Garimella [31] was used to study the effect of the inclination angle on the threshold voltage required for moving the droplet and the forces generated at different angles.

Several models were introduced to analyze the droplet behavior and calculate the forces acting on the droplets when the voltage is applied. These models can be numerical models or analytical models. Electrohydrodynamic is involved as the system is influenced by electrical signals and fluid mechanics.

5.5.1 Electromechanical and Energy-Based Models

An electromechanical model was interpreted for the electrowetting phenomenon by Jones [32] who described the forces generated using Maxwell stress tensor or capacitance models. He showed that the electrical force generated does not depend on the contact angle as he emphasized that the forces generated are

not related to the changes in the contact angle. An energy-based analysis that depends on energy minimization was introduced by Bahadur and Garimella [31]. They categorized the actuating forces and the opposing forces according to the following arrangement: the shear force generated from the two plates scrutinizing the droplet, the opposing viscous force from the filler medium, air or oil, and the contact line friction. The actuating force was distributed among the three regions according to a network of capacitance arrangement between the dielectric layer and the droplet where they found that the result matches the result from the electromechanical model. A similar model was developed for the dielectric droplets and experimentally validated using a transformer oil droplet between two plates [33].

5.5.2 Numerical Models

Numerical models are used to demonstrate the effect of every single parameter on the droplet dynamics during motion. In some numerical models, an electrohydrodynamic approach can be used to calculate the driving force on the droplet and determine how the maximum switching frequency can be affected by droplet size, the spacing between the electrodes, and the gap height between the top and the bottom plates [34, 35]. A lattice Boltzmann numerical model can also be used to simulate the contact line dynamics, hysteresis, and contact angle changes where Navier–Stokes equation alone is not sufficient to identify these changes [36]. Ignoring the dynamic behavior of the triple contact generated errors in modeling the contact angle and the droplet velocity. Therefore, modeling the dynamic contact angle during motion introduced more accurate results [37]. A volume-of-fluid technique can be employed to characterize the parameters that affect actuation. The typical parameters include actuation voltage, electrode size, and droplet velocity [38]. A commercially available computational fluid dynamic (CFD) software called flow-3D can also demonstrate what happens to the droplet motion under extreme conditions such as the severe necking and elongation that happens to the droplet during motion at low gap heights [39]. Berthier *et al*. [40] used another software called Evolver to demonstrate the droplet transport, splitting, and dispensing processes.

5.5.3 Analytical Models

Analytical models can be also used to study the droplet dynamics during motion as a function of the droplet interface properties [41]. The main advantage of using analytical models is to eliminate the time-consuming calculations required in the numerical and CFD simulations. A scaling model has been introduced to study the dimensionless parameters that affect the actuation in DMF systems [42]. This model predicts the threshold voltage required for transport dispensing and splitting in terms of dimensionless parameters that involve the electrode length, gap height, dielectric layer constant, and dielectric layer thickness. Scaling down the experiments to the picoliter scale was performed to demonstrate the effectiveness of these models on a wide range of droplet volumes.

www.ebook3000.com

5.6 Electrical Signals Used and Their Effect on the DMF Operations

5.6.1 Types of the Signals Used in Actuation

High voltages are usually required for performing DMF operations in closed and open systems with different electrode configurations as shown in Figure 5.5a–d. Alternating current (AC) and DC signals are the commonly used signals in DMF applications. While choosing the signal type, there are some advantages and disadvantages that have to be taken into consideration. The DC signal has a lower threshold actuation voltage compared with that of the AC signal. When DC signal is used, hysteresis occurs due to the polarization of the dielectric layer. On the contrary, using AC signals prevent the dipole from having a fixed alignment and prevent the charge trapping on the dielectric layer. Notably, the effectiveness and the repeatability of the DMF chips decrease when the dielectric layer becomes charged and electrolysis also occurs more frequently while using DC signals. This effect will increase the voltage threshold limit during repetitive actuation to reproduce the same electrowetting effect.

Some variations were performed on the shape of the DC signal to manipulate the droplets more effectively by discretizing the DC signal to separate pulses as shown in Figure 5.5e, f [44]. The droplet transport dynamics was greatly affected by changing the duty cycle of the DC pulse train, whose usage greatly enhanced the droplet motion process by controlling the droplet velocity and minimizing the droplet overshoot, deformation, and fragmentation. In addition, using a natural discharge after pulse is another modification that can be introduced to DC signals in order to enhance the droplet motion [45]. This technique is characterized by introducing several DC pulses followed by several natural discharge cycles. The DC signal has one high peak with relatively larger width at the beginning of the signal compared with the consecutive several high peaks that have the same low base voltage level. The shape of this signal is shown in Figure 5.5g. This actuation technique enabled higher velocities and prolonged lifetime for the chips by decreasing the actuation voltage required. A comparison between the fixed DC signal and the DC signal with natural discharge showed the superiority of the latter technique in every aspect. However, they found that AC signals are still considered the safest to use when they compared with all the techniques in terms of the electrode lifetime.

The droplet can be transported at lower voltage levels using a pre-charging technique [46]. A pre-charging voltage with an opposite polarity to the driving voltage is applied and can remain for 2 min where the droplet actuation can be performed at 12 V. The charges stored inside the droplet reduce the actuation voltages by utilizing both electrostatic forces and dielectrophoretic forces in moving the droplets. A similar charging technique was introduced to move discrete droplets submerged in silicone oil using discrete electrode pins where several droplet operations were performed successfully such as droplet translation and coalescence [47, 48].

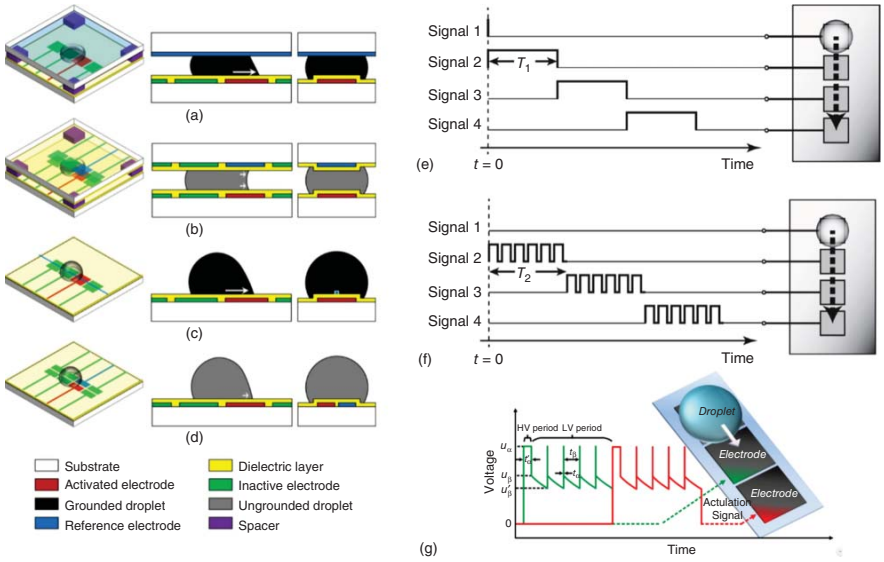


Figure 5.5 The arrangement of the electrodes used in DMF actuation in closed systems (parts a and b) and open system (parts c and d). ((a–d) Chang and Pak 2011 [43]. Reproduced with permission of Elsevier.) The timing sequence of the electrical signals used (e) when DC signals are used and (f) when DC pulse train signal is used. (Reprinted with permission from Ref. [44]. Copyright 2012 AIP Publishing LLC.) (g) DC pulses with natural discharge. (Dong *et al*. 2015 [45]. Reproduced with permission of Springer.)

www.ebook3000.com

5.6.2 The Effect of Changing the Frequency

The effect of the frequency on the droplet actuation can be explained by using Maxwell stress tensor and RC circuit models [49]. The model predicts that at low frequencies, where the frequency is less than the critical frequency, the droplet acts as a conductor, and the voltage drop occurs mainly inside the dielectric layer. In this case, the force generated is due to the electric field acting on the droplet/air interface. As the frequency increases, the ponderomotive force effect also increases, the electric field starts to penetrate the liquid surface, and the droplet becomes insulating where the voltage drop becomes distributed between the dielectric layer and the droplet itself.

The effect of frequency on the shape of the electric field acting on the droplet was studied by Lee *et al*. [50]. When DC voltages are applied, the droplet becomes charged and the charges accumulate at the surface. In this case, no current will pass through the droplet. The electric field does not penetrate the droplet, and it becomes concentrated at the droplet edge as shown in Figure 5.6. On the other hand, when AC frequencies are applied, the droplet does not have enough time to be completely charged so some current will start passing through it, and the electric field starts to penetrate the droplet. The extent of the penetration of the electric field depends on the frequency until the critical frequency is reached and the droplet becomes saturated. The critical frequency is 85 kHz in Figure 5.6. Remarkably, the actuation voltage threshold required for initiating the DMF operations increases when the frequency of the AC signals increases.

A comparison between the behavior of the conductive and insulating droplets has been introduced experimentally by Chatterjee *et al*. [51] where they discussed

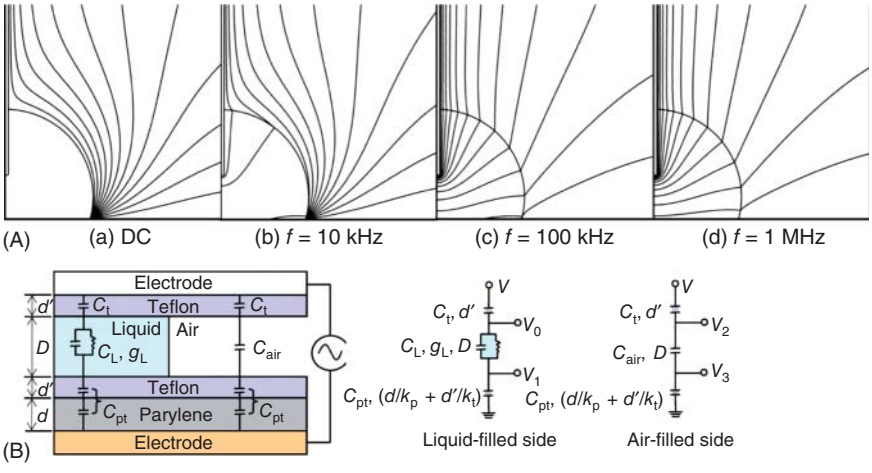


Figure 5.6 (A) The effect of the frequency on the shape of the electric field surrounding the droplet that shows that the penetration of the electric field increases by increasing the frequency. (Reprinted with permission from Ref. [50]. Copyright 2009 AIP Publishing LLC.) (B) RC circuit model used to describe the DMF system. (Chatterjee *et al*. 2009 [51]. Reproduced with permission of Royal Society of Chemistry.)

an electromechanical model to calculate the forces acting on different droplets at different frequencies. They found that the droplets act as a pure conducting medium when the frequency used is less than the critical frequency. The capacitance models used take into account the dielectric layers, the hydrophobic layers, and the droplet to calculate the effective capacitance in the RC circuit. When insulating droplet is used, the effective capacitance depends on the droplet and the dielectric layer capacitance for both AC and DC signals [52]. This effective capacitance depends on the dielectric layer only when DC is used to actuate a conductive droplet. On the other hand, the effective capacitance depends on several variables when AC signal is used to actuate conductive droplets. In this case, the effective capacitance depends on the droplet, the dielectric layer, and the frequency-dependent droplet conductivity. Several attempts were performed to manipulate conductive and polar droplets via electrowetting and nonpolar insulating droplets via DEP on the same chip [53]. Transport, mixing, and splitting were performed on water and silicon oil droplets although their actuation mechanisms are completely different. They applied different voltage types, AC for electrowetting and DC for DEP, to manipulate these two different droplets effectively at the same time where V_{DEP} and V_{EWOD} were not the same. To minimize the difference between the generated actuation forces, they recommended using low gap heights that, however, can increase the possibility of the dielectric layer breakdown. Moreover, they used frequencies above 1 kHz because, at low frequencies, the voltage is dissipated inside the dielectric layer that tends more to increase the electrowetting effect.

To sum up, EWOD occurs at low frequencies and high conductivity where the origin of the force is the charge trapping and the polarization that occur near the meniscus of the droplet. In EWOD, no electric field passes through the droplet. Conversely, DEP effect increases at high frequencies and low droplet conductivity where the origin of the force is the ponderomotive force that acts on the dielectric material between the two plates, which is the droplet in DMF systems. In DEP, the electric field starts to penetrate the droplet. It can be explained by using Maxwell stress tensor and energy methods. Capacitive and resistive circuits can be used to study the effect of changing the frequency. Finally, AC signals are the most commonly used signals for actuation in the DMF systems as the AC signals outperform the other signals in many aspects.

5.7 Droplet Metering and Dispensing Techniques in DMF Systems

Lab-on-a-chip applications require accurate volume metering and dispensing specially for point-of-care devices. As DMF can play an important role in portable applications [54, 55], many researchers studied how to control the volume of the dispensed droplets in a repeatable manner with decreased droplet volume variability. Micro- and nanoliter droplet dispensing on DMF systems was performed by Pollack *et al.* [56]. This dispensing was based on cutting

www.ebook3000.com

a smaller droplet from a larger on-chip reservoir located on a big electrode. The reservoir droplet is dragged to the smaller actuating electrodes. Then, to terminate the cutting process between the reservoir droplet and the end of the extended liquid column, one has to deactivate the middle electrodes to separate the dispensed droplet from the reservoir droplet. A control system has been added to this rudimentary setup to accurately dispense the required volumes where the droplet dispensing mechanism has been integrated with a capacitance feedback signal [57, 58]. They were able to demonstrate that the droplet volume can be controlled when the dispensing is performed from an on-chip reservoir and an off-chip reservoir. Many efforts were introduced to improve the resolution of the dispensed droplets to reach the picoliter scale [59]. The repeatability of the whole process is crucial to decrease the droplet volume variability in sensitive chemical and biological applications. Therefore, a long-term assessment study was performed to better understand the reliability and repeatability of the dispensing process [60]. They found that decreasing the gap height between the top and the bottom plates is better to improve the repeatability of the process. They also found that the reservoir electrode size should match the size of the neighboring dispensing electrodes to enhance the droplet dispensing quality. Dispensing of volatile liquids in air, instead of using silicon oil as filler medium, has also been introduced to DMF systems [61]. It was found that controlling the volume during dispensing volatile liquids is harder since one has to compensate for the evaporation. All the previous methods were using active dispensing where two electrodes or more are activated at the same time. Passive dispensing from a bigger droplet can be performed using virtual micro-wells where only one electrode is activated and another electrode has a hydrophilic spot [18], which is patterned on the top ITO plate using a lift-off process. The dielectric and the hydrophobic layers on the lower plate remain intact. The passive dispensing was characterized by lower dispensed droplet volume variability when compared with the active dispensing process. Another dispensing using DEP and a special electrode design to isolate the dispensed droplet was introduced to dispense nanoliter droplets [62]. For performing further DMF operations, an optimal dispensing algorithm for parallel DMF processes has been developed to minimize the time required for moving the droplet from the dispensing site to the testing site using integer linear programming [63].

5.8 The Effect of the Gap Height between the Top Plate and the Bottom Plate in DMF Systems

The effect of the gap height on the droplet motion was investigated in several studies. Chen *et al.* [64] studied the effect of the gap height on the threshold actuation voltage at high frequencies in DEP and at low frequencies in EWOD. They found that the minimum actuation voltage increases when the gap height increases. Moreover, they found that the minimum actuation voltage increases

with less conductive liquids at a fixed gap height and fixed frequency. In addition, increasing the frequency will increase the minimum actuation voltage required at a fixed gap height and fixed conductivity. Yafia and Najjaran [65] demonstrated a high precision actuation mechanism for changing the gap height in real time while performing different DMF processes. Moreover, they showed that all the principle DMF operations can be enhanced using the optimum gap height for each operation. Changing the gap height can have a great effect on all of the parameters and forces acting on the droplet during motion. The driving force significantly increases when the gap height decreases. They showed that the optimum gap height for moving the droplet exists when the droplet footprint matches the electrode size. Changing the gap height can be useful during splitting or dispensing since a minimum gap height is required to achieve successful cutting process. In addition, dispensing variable droplet volumes can be performed with the same electrode size using different gap heights. Therefore, the variable gap height actuation mechanism is capable of optimizing all the principal DMF processes. The following example demonstrates how the gap height can enhance a sequence of DMF processes that includes transport, splitting, and dispensing. First, the gap height can be adjusted to dispense the required droplet volume. Second, the gap height is optimized for the droplet motion according to the droplet footprint and the electrode size. Third, since a droplet splitting process is required in the following step, therefore the gap height should be reduced for having successful splitting process. After the droplet splitting process happens, the smaller droplets may not be able to move as their footprint becomes smaller than the electrode size. Then, the gap height should be decreased further to facilitate their motion. If merging is required, the droplet footprint will increase significantly compared to the electrode size and the droplet motion will become impeded. Consequently, the gap height has to be increased again to optimize the droplet motion at this bigger volume. The previous steps are summarized in Figure 5.7a–g.

Changing the gap height can also induce changes in the droplet morphology during transport in DMF systems [39, 67]. The droplet retains its circular shape during motion at higher gap heights that is above 150 μm with electrode size of 2 mm. The droplet starts to deform and elongate during motion when the gap height decreases. At extremely low gap heights, the droplet shows extreme necking and the droplet velocity profile changes significantly. At this low gap height, the droplet leading edge motion slows down in a creeping motion regime without any acceleration or deceleration till the end of the motion compared to the normal motion stages at higher gap heights. This shows that the numerical models that assume that the droplet retains its circular shape during motion are invalid at extremely low gap heights. A piezoelectric control system has been added by to the DMF system by Li *et al*. [66] to change the position of the top plate and change the gap height (see Figure 5.7h). This solution has several advantages over the electromagnetic stages used by Yafia and Najjaran [65] as it uses small piezoactuators, which utilize low power when actuation and whose compact size makes them compatible with portable DMF systems.

www.ebook3000.com

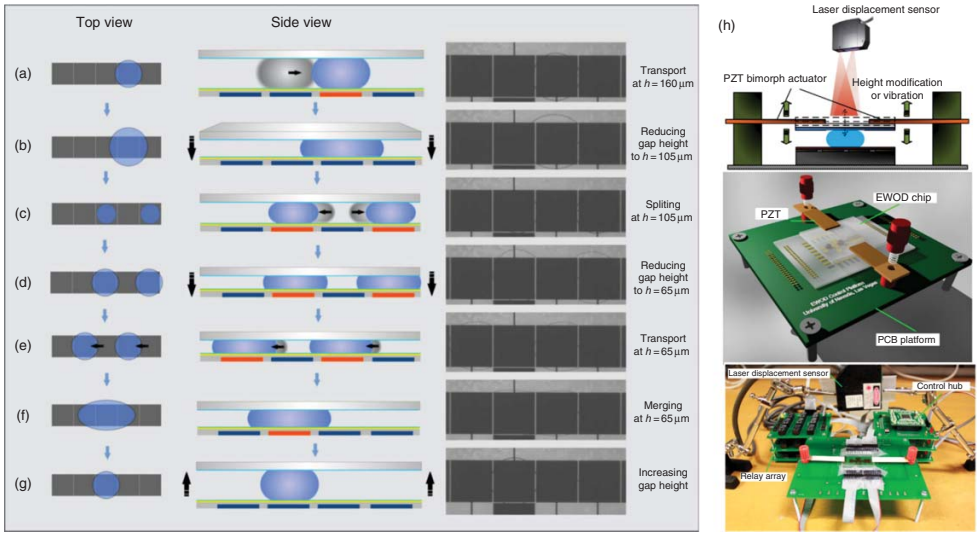


Figure 5.7 Adjusting the optimum gap height for each DMF operation from (a–g). (Yafia and Najjaran 2013 [65]. Reproduced with permission of Elsevier.) (h) The piezoactuator used to change the gap height in DMF systems. (Li *et al*. 2016 [66]. Reproduced with permission of Elsevier.)

5.9 Modeling and Controlling Droplet Operations in DMF Systems

For dynamic systems, modeling and controlling are the main keys to enhance the system performance. Having an accurate dynamic model that resembles the DMF system behavior improves our understanding of the platform and helps in designing a suitable control system. With the appropriate control system, one could enhance the system's response to reach the desired performance [68]. In the last decade, the area of control of the DMF systems has drawn a lot of interest. However, the research on the control of individual droplets is still immature and needs more attention and improvement. In DMF, the size, position, and other characteristics of the droplet are manipulated via controlling an electric field to modulate the surface tension. The main challenges on controlling droplets in DMF systems lie in moving droplets faster and more precisely while avoiding system uncertainties including model uncertainties, external disturbances, and measurement noise. Dynamic systems are exposed to disturbances that, in a relative sense, can become even more pronounced in microsystems. Thus, moving droplets while compensating system disturbances to achieve a robust controller becomes very important. The reliability and robustness of the control system become even more critical for DMF applications which manipulate different chemicals, such as in DMF based micro-reactors. In certain applications in DMF systems, time is critical and one needs to move droplets for a long distance. Accordingly, there are interests in designing control systems that are able to achieve faster motion for an individual droplet in precise and reliable fashion. In other applications, such as in droplet creation applications, controlling the droplet volume and amount is very crucial. As a result, some researchers have worked in improving the control systems in order to achieve precise control operations. In this section, we have addressed these main obstacles that challenge the DMF system and review their recent solutions.

5.9.1 Feedback Control in DMF Systems

DMF systems are exposed to different uncertainties and disturbances, such as adsorption and aging of the insulation, that need to be considered while designing the control system. For instance, system failure might occur when a sample of a droplet fails to reach its desired destination due to surface damages. Thus, researchers have worked on developing various feedback control system to ensure that the droplet motion has been performed successfully. For instance, in continuous microfluidic channels, a precise flow rate control using flow sensor was presented in the reference [69]. The method uses feedback control to monitor and control an on-chip pump used in integrated microfluidic genetic analysis devices. A real-time feedback control scheme for fluid guidance through capillary networks has been applied successfully in the previous work [70]. The fluid switching is dynamically controlled through simple external pressure and

www.ebook3000.com

membrane deflection using robust digital control techniques. The approach has demonstrated its capability to precisely control flows of complex fluids such as blood. However, it has only focused on the single cell level. Controlling DMF systems is less complex since it is carried out by directly manipulating the actuation voltage applied to the electrodes. More precisely, it does not require the use of microvalves and pumps compared with continuous microfluidic channels. In Ref. [71], the authors have developed a feedback control system for DMF systems to monitor the movement of droplets. The control system will increase the driving voltages until movement occurs, and the applied voltage remains high until the droplet reaches its target position. This control system uses a fixed detection threshold that works fine in detecting droplets of only one chemical composition. However, it is unsuitable of manipulating droplets of various chemical compositions that frequently occur in many applications in DMF systems. To address this problem, researchers in previous work [72] have proposed a fuzzy-based control system. The intelligent system approach for control has the ability to manage droplet routing and fault tolerance operation autonomously. The prototype holds high potential; however, it is still not well established. The control system relies on a field-programmable gate array (FPGA) and a large number of switches that increase its complexity and initial cost.

For quantitative applications, it is essential to have a real-time control to generate and monitor droplet volume. For instance, a method for controlling on-chip droplet dispensing by EWOD actuation was successfully presented in the reference [57]. The method measures the intrinsic capacitance value of an electrolyte droplet to meter the droplet volume. The limitation of the method lies in the size of the coupling needle since its size cannot be scaled proportionally with the electrode size. One possible solution for the scalability is to use a better fluidic coupler. Another solution is to combine droplet volume calibration with any droplet dispensing methods such as the one presented in [73]. Gong and Kim proposed a method to eliminate the side-connecting lines using a control of droplet volume with through-substrate electrical connections [74]. Then they suggested a feedback control of the driving voltage to improve the robustness and overcome the uncertainty [75]. Furthermore in Ref. [76], the authors designed an all-electronic feedback control of on-chip droplet generation in real time. The electronic board contains the combination of a capacitance sensing, a fast voltage modulation, and a discrete-time PID controller. Although the proposed scheme showed a significant improvement compared with the other control schemes, such as open-loop control, still, the controller need a human intervention to calibrate its parameters for different devices. A solution may lie around using more sophisticated and advanced feedback control algorithms, such as an adaptive controller or a neural network.

Bhattacharjee and Najjaran introduced the basics of the feedback control analysis of a DMF system under the influence of external driving forces [77]. Various simulation tests have been carried out to demonstrate the performance of the DMF system, including the transient and steady-state responses,

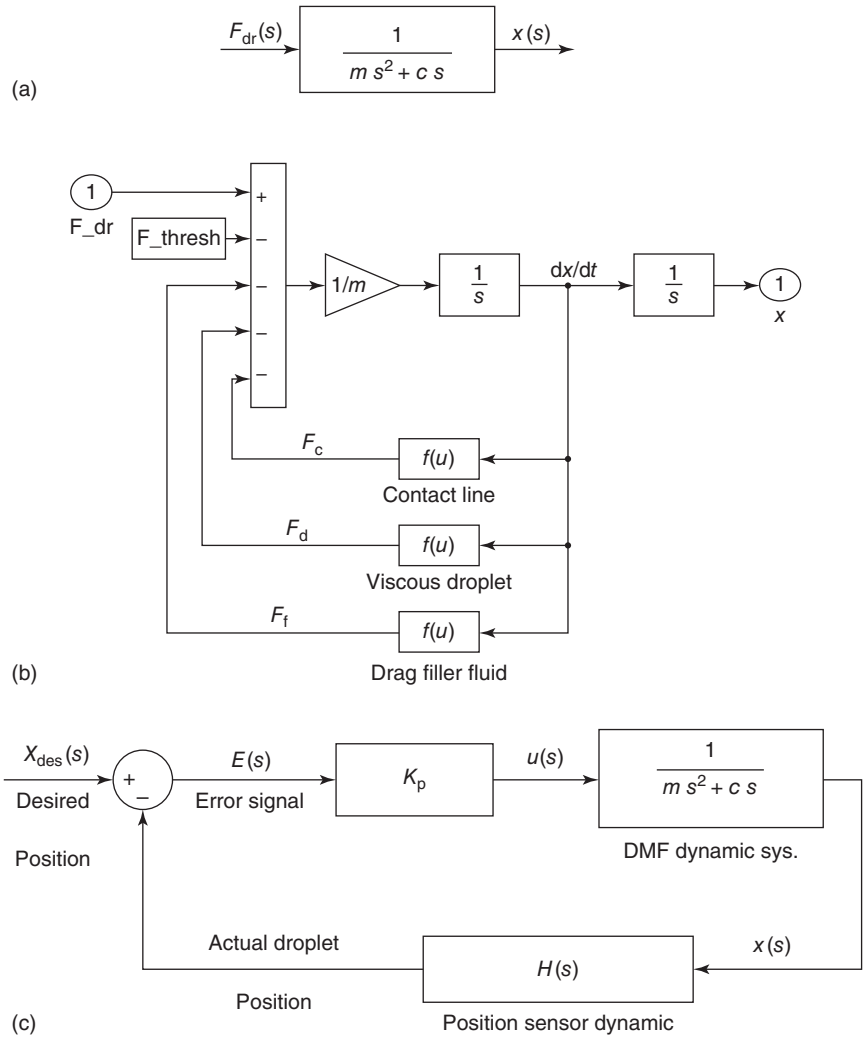


Figure 5.8 An open-loop system model in linear form is shown in part (a) and in nonlinear form in part (b). An example of simple feedback control shown in part (c).

under different control parameters. Figure 5.8 shows an example of a simple proportional feedback control system derived from the error signal between the desired and the actual positions of the droplet. The system uses a position sensor with a unity feedback and a simplified dynamic model to simulate the droplet motion in a planar array of cells. Figure 5.8 shows different model simulations of droplet dynamics. Parts (a) and (b) represent the open-loop dynamic model of the droplet movements in linear and nonlinear forms, respectively. Part (c) is an example of a simple feedback control system, where m and c are plant parameters representing the mass and the damping coefficients, respectively. K_p is the proportional control gain, and $H(s)$ represents the dynamic of the position sensor. Thus, the error signal is defined as $E(s) = X_{des}(s) - x(s)$.

www.ebook3000.com

Different tools can be used to improve system robustness and reliability, for instance, an open-source platform, DropBot, designed by the previous work [78] for end users in order to assist in optimizing device design and controlling DMF devices. The platform is able to precisely control the applied electrostatic and measure instantaneous droplet velocity.

5.9.2 Droplet Sensing Techniques in DMF Systems

Determining the droplet position is crucial for decision making during different DMF operations and sending a feedback signal for the control system. Optical detection of the droplets can be performed in DMF systems. The droplet visibility DMF can be readily provided since there is no covering plate in open systems and the top grounding plate can be transparent in closed systems. Therefore, machine vision can be utilized for automation in DMF systems and measuring the kinetics of biomolecular interactions [79]. However, this method requires optical lenses and digital cameras to detect and recognize the droplet presence. Also, image processing is computationally expensive, and fast response feedback systems require high performance computers. Other methods were introduced to simplify the process of detecting the droplet position without using optical systems. Capacitive sensing can be implemented easily to DMF systems as the droplet can act as a capacitor and the dielectric layer helps in trapping the charges even when a conductive droplet is used. In open and closed systems, a droplet can be detected by the coplanar electrodes lying on the bottom plate [80]. This method utilizes the electric field passing between the coplanar electrodes and detects the droplet position accurately as shown in Figure 5.9. Another method was introduced to detect the droplet position only in closed systems since it uses the top and the bottom plates in detecting the droplet capacitance [81].

5.9.3 Droplet Routing in DMF Systems

Droplet routing algorithms are very important for DMF applications when large number of droplets need to be handled. In droplet routing, the control system needs to generate a path in order to transport each droplet without any unwanted droplets mixing while maximizing fault tolerance and minimizing timing process. Multiple attempts have been carried out by researchers to design routing algorithms for DMF systems. For instance, a high performance droplet routing algorithm was proposed in Ref. [82] to enhance timing and fault tolerance. The proposed algorithm has demonstrated better results compared with the commonly used routing algorithms, such as the two-stage and A* algorithms. However, their performance is not significantly better than the widely used network-flow-based algorithm. In addition, an optimal strategy based on integer linear programming was developed in the previous work [83] mainly for large-scale problems. The latter has introduced two different heuristic techniques and compared them based on their efficiency and completion time.

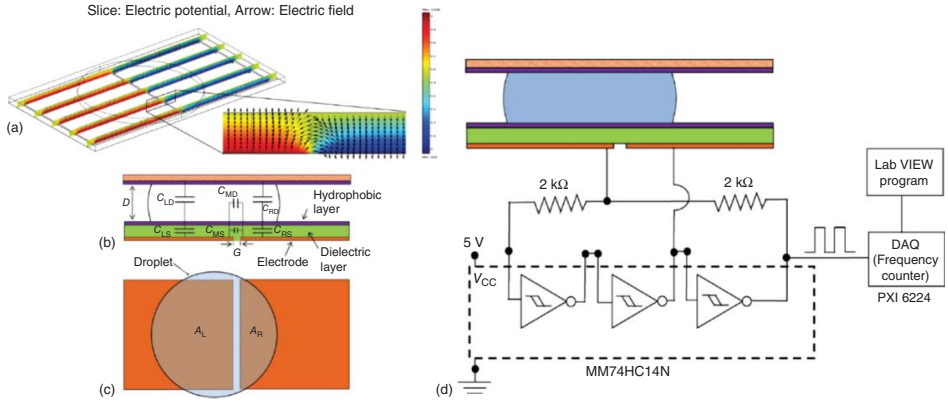


Figure 5.9 (a) The simulation of the electric field penetrating the droplet during capacitance measurement. (b) Schematic of the capacitance model to detect the droplet position shown in (c). (d) The circuit used for capacitance measurement. (Bhattacharjee and Najjaran 2012 [80]. Reproduced with permission of Royal Society of Chemistry.)

www.ebook3000.com

5.9.4 Controlling and Addressing the Signals in DMF Systems

Addressing large number of DMF electrodes is not a simple task during the design and the microfabrication process as it requires a large number of connection lines and a certain path to be designed for each line. Accordingly, minimizing the number of electrodes, connection lines, and connection pads is preferred. A simple array of two rows of electrodes is favored whenever possible in order to address each row of electrodes from one side without having any problem in the connection line arrangement. For designing more than two rows of electrodes, small extra spacing have to be considered between the outside electrodes to connect very thin connection lines to the middle electrodes that are lying inside. Different solutions were introduced to address a larger number of middle electrodes and generally handle a larger number of electrodes at the same time. Multiple PCB layers can also be used to address a large number of electrodes simultaneously to solve the problem of adding extra spacing between the electrodes for the additional connection lines [84]. Post-processing fabrication processes were performed to enhance the surface roughness that arises during the PCB fabrication process. These surface enhancements eventually helped in decreasing the actuation voltage required.

Addressing a specific electrode enclosed in an array of $m \times n$ electrodes can be troublesome when the number of electrodes increases. The first problem arises from routing the connection lines to the inner electrodes in the array. The second problem comes from the large number of connection pads required to address each electrode (which equals to $m \times n$). To solve these problems, thin-film transistor arrays are used to reduce the connection pads required to $m + n$ as shown in Figure 5.10b, c [86]. Once this problem was solved, another approach to utilize these capabilities was introduced by decreasing the electrode size and increasing the number of the electrodes [85] where the electrode size has been decreased to 200 µm and the number of the electrodes has been increased to an array of 64×64 electrodes. This approach also used thin-film transistor (TFT) to enable the activation of large number of electrodes at the same time. In addition, they were able to perform all the DMF operations on any droplet size by combining the small electrodes to accommodate each droplet volume and shape as shown in Figure 5.10a.

Multiplexing technique was also introduced to decrease the number of connections required and address a large number of electrodes with fewer connection pads [87, 88]. This technique depends on horizontal and vertical long electrodes fabricated on the top and the bottom plates separately. Aligning two electrodes perpendicular to each other and addressing them at the same time will activate a certain spot in the array where the droplet will start to move. Figure 5.10d demonstrates two scenarios where one of the droplets will move in the multiplexed system and the other droplet will not move.

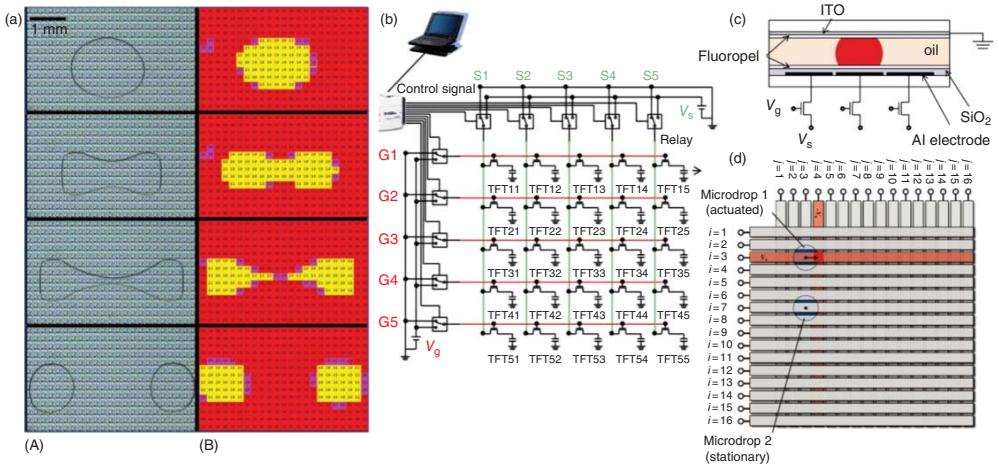


Figure 5.10 (a) Activating large number of small electrodes according to the required droplet pattern. (Hadwen *et al*. 2012 [85]. Reproduced with permission of Royal Society of Chemistry.) (b) Using thin-film transistors to reduce the number of connection pads required in a large array of electrodes. (Noh *et al*. 2012 [86]. Reproduced with permission of Royal Society of Chemistry.) (c) The method of connecting the transistor to the electrode. (d) Multiplexer array shows how one droplet will move, while another one will not be affected when two long electrodes are activated. ((c, d) Collier *et al*. [87] http://www.mdpi.com/2072-666X/2/4/369/htm. Used under CC BY 3.0 https://creativecommons.org/licenses/by/3.0/.)

www.ebook3000.com

5.10 Prospects of Portability in DMF Platforms

Technical difficulties arise when researchers try to implement microfluidics into a portable system such as a point-of-care testing device. Specifically in DMFs, AC signals are preferable and all operations require high voltages. High voltage switches and high level controllers are also required to organize the sequence of the droplet motion. In addition, a portable droplet analysis and detection method needs to be added to the system. A method of communication is also required for sending and receiving the commands from the system. Some solutions were introduced to enable the portability of the DMF system by adding commercial components such as DC to DC converters [54]. Urban [89] discussed the electronic options that can be integrated in portable microfluidic devices to control the process. He found that most applications utilize the popular off-the-shelf Arduino microcontrollers. Yafia *et al*. [55] tried to integrate all modules required in a DMF system into a portable device that can be battery powered. The casing of this system was designed to enable attaching a smartphone on top of the device. This position allows the smartphone camera to directly capture the droplet motion, color, and position using a microlens that can be easily attached to the phone camera. All operations can be controlled directly from the phone using a Bluetooth connection. Choosing small rechargeable 3.7 V lithium ion batteries as a power supply for the portable DMF system made it more convenient to use and can be easily recharged (Figure 5.11).

5.11 Examples for Chemical and Biological Applications Performed on the DMF Platform

The real value of the DMF platform is realized when it is used in performing chemical and biological assays. DMF is one of the promising microfluidic platforms since numerous applications have successfully been implemented into it and more applications are introduced at an increasing rate. Droplets of several human physiological fluids were manipulated on a DMF platform to perform enzymatic glucose assay [90]. Applications for newborn screening such as dried blood spot analysis have been performed on the DMF platform [91]. Figure 5.12A demonstrates a sequence for the steps of this test. This was coupled to mass spectrometry for analyzing blood samples (shown in Figure 5.12C, D) [93]. Moreover, DNA sequencing of *Candida parapsilosis* was implemented on a PCB DMF chip with an optimized protocol to increase the signal over background [92]. The device and the PCB chip used in this process can be seen in Figure 5.12B. Moreover, hormones tests are important as they can be frequently required in clinical samples. Hence, estrogen assays were performed to quantify the estrogen hormone in breast tissue and blood on a DMF chip [95]. At last, advanced detection techniques can be integrated to the DMF platform such as surface plasmon resonance imaging (Figure 5.12E) where the output signal can be enhanced by 200% [94].

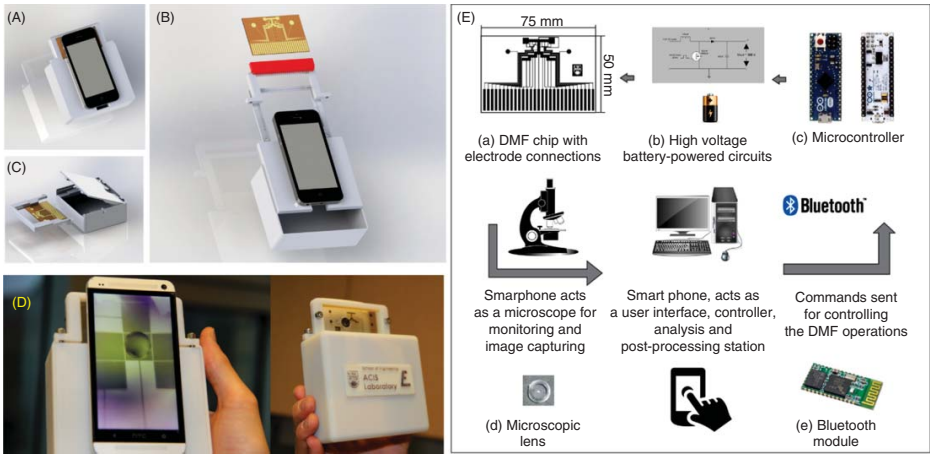
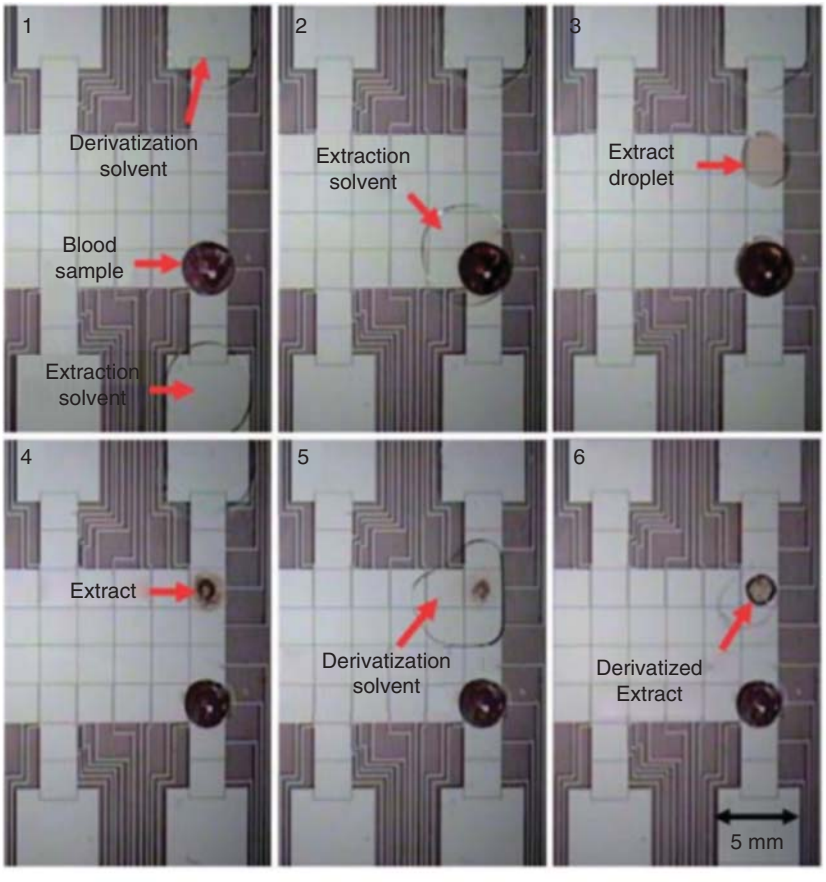
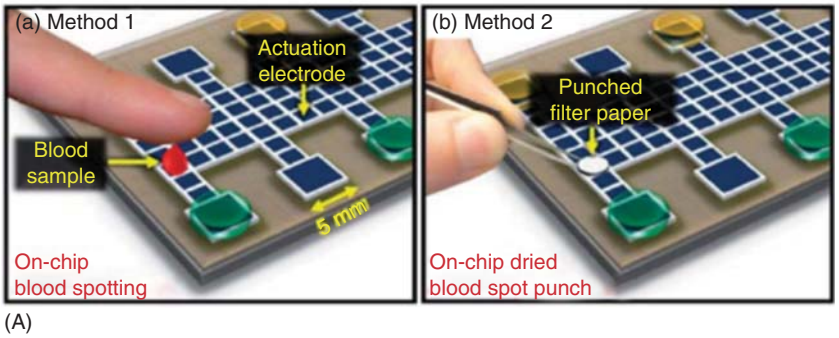


Figure 5.11 A portable DMF platform that can be controlled and operated by a smartphone. The 3D design of the platform is shown in (A–C). (D) The 3D printed platform with the smartphone attached to it. (E) A schematic that shows the different components that are combined in this portable platform. (Yafia *et al*. [55] http://www.mdpi.com/2072-666X/6/9/1289/htm. Used under CC BY 4.0 https://creativecommons.org/licenses/by/4.0/.)

www.ebook3000.com





(A)

Figure 5.12 (A) Sequence of the dried blood spot analysis. (Jebrail *et al*. 2011 [91]. Reproduced with permission of Royal Society of Chemistry.) (B) Automated DNA sequencing device with a PCB chip showing the position of samples and reagents. (Boles *et al*. 2011 [92]. Reproduced with permission of American Chemical Society.) (C, D) Coupling the DMF system with ionization mass spectrometry. (Shih *et al*. 2012 [93]. Reproduced with permission of American Chemical Society.) (E) Surface plasmon resonance imaging on a droplet enclosed in a closed DMF system. (Malic *et al*. 2011 [94]. Reproduced with permission of Elsevier.)

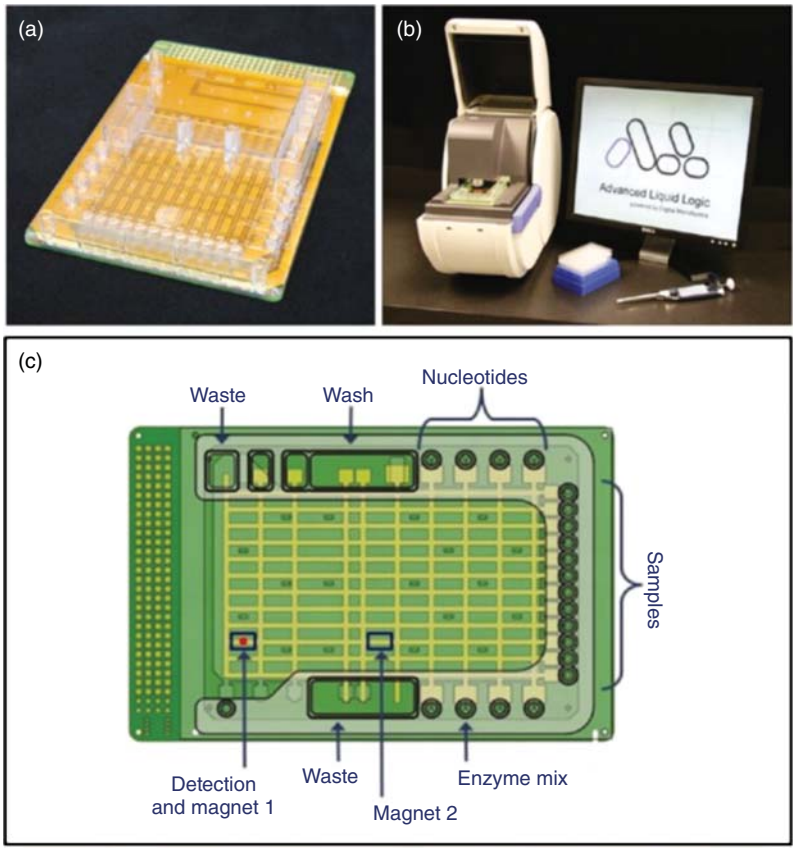
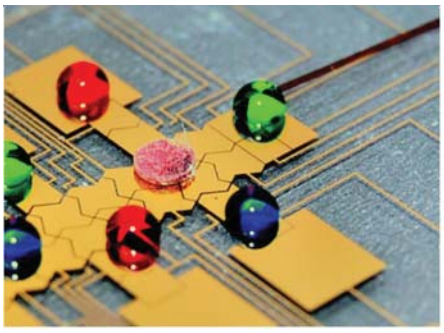
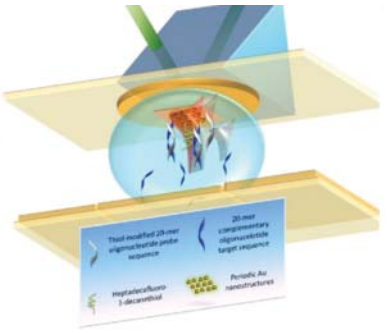


Figure 5.12 (*Continued*)

www.ebook3000.com



(D)



(E)

Figure 5.12 (*Continued*)

References

1 Agresti, J.J., Antipov, E., Abate, A.R., Ahn, K., Rowat, A.C., Baret, J.-C., Marquez, M., Klibanov, A.M., Griffiths, A.D., and Weitz, D.A. (2010) Ultrahigh-throughput screening in drop-based microfluidics for directed evolution. *Proc. Natl. Acad. Sci. U.S.A.*, **107** (9), 4004–4009.

2 Junkin, M., Kaestli, A.J., Cheng, Z., Jordi, C., Albayrak, C., Hoffmann, A., and Tay, S. (2016) High-content quantification of single-cell immune dynamics. *Cell Rep.*, **15** (2), 411–422.

3 Fouillet, Y. and Achard, J.-L. (2004) Microfluidique discrète et biotechnologie. *C. R. Phys.*, **5** (5), 577–588.

4 Barbulovic-Nad, I., Au, S.H., and Wheeler, A.R. (2010) A microfluidic platform for complete mammalian cell culture. *Lab Chip*, **10** (12), 1536–1542.

5 Banerjee, A.N., Qian, S., and Joo, S.W. (2011) High-speed droplet actuation on single-plate electrode arrays. *J. Colloid Interface Sci.*, **362** (2), 567–574.

6 Samad, M.F., Kouzani, A.Z., Hossain, M.F., Mohammed, M.I., and Alam, M.N.H. (2017) Reducing electrowetting-on-dielectric actuation voltage using a novel electrode shape and a multi-layer dielectric coating. *Microsyst. Technol.*, **23** (7), 3005–3013.

7 Pollack, M., Shenderov, A., and Fair, R. (2002) Electrowetting-based actuation of droplets for integrated microfluidics. *Lab Chip*, **2** (2), 96–101.

8 Abdelgawad, M. and Wheeler, A.R. (2007) Rapid prototyping in copper substrates for digital microfluidics. *Adv. Mater.*, **19** (1), 133–137.

9 Abdelgawad, M. and Wheeler, A.R. (2007) Low-cost, rapid-prototyping of digital microfluidics devices. *Microfluid. Nanofluid.*, **4** (4), 349–355.

10 Ko, H., Lee, J., Kim, Y., Lee, B., and Jung, C.-H. (2014) Active digital microfluidic paper chips with inkjet printed patterned electrodes. *Adv. Mater.*, **26**, 2335–2340.

11 Abadian, A. and Jafarabadi-Ashtiani, S. (2014) Paper-based digital microfluidics. *Microfluid. Nanofluid.*, **16** (5), 989–995.

12 Abdelgawad, M., Freire, S.L.S., Yang, H., and Wheeler, A.R. (2008) All-terrain droplet actuation. *Lab Chip*, **8** (5), 672–677.

13 Fobel, R., Kirby, A.E., Ng, A.H.C., Farnood, R.R., and Wheeler, A.R. (2014) Paper microfluidics goes digital. *Adv. Mater.*, **26** (18), 2838–2843.

14 Yafia, M., Shukla, S., and Najjaran, H. (2015) Fabrication of digital microfluidic devices on flexible paper-based and rigid substrates via screen printing. *J. Micromech. Microeng.*, **25**, 57001.
15 Rajabi, N. and Dolatabadi, A. (2010) A novel electrode shape for electrowetting-based microfluidics. *Colloids Surf., A*, **365** (1–3), 230–236.
16 Chen, J., Yu, Y., Li, J., Lai, Y., and Zhou, J. (2012) Size-variable droplet actuation by interdigitated electrowetting electrode. *Appl. Phys. Lett.*, **101** (23), 234102.
17 Abdelgawad, M., Park, P., and Wheeler, A.R. (2009) Optimization of device geometry in single-plate digital microfluidics. *J. Appl. Phys.*, **105** (9), 094506.
18 Eydelnant, I.A., Uddayasankar, U., Bingyu, L., Liao, M., and Wheeler, A.R. (2012) Virtual microwells for digital microfluidic reagent dispensing and cell culture. *Lab Chip*, **12** (4), 750–757.
19 Samiei, E., Luka, G.S., Najjaran, H., and Hoorfar, M. (2016) Integration of biosensors into digital microfluidics: Impact of hydrophilic surface of biosensors on droplet manipulation. *Biosens. Bioelectron.*, **81**, 480–486.
20 Cooney, C.G., Chen, C.-Y., Emerling, M.R., Nadim, A., and Sterling, J.D. (2006) Electrowetting droplet microfluidics on a single planar surface. *Microfluid. Nanofluid.*, **2** (5), 435–446.
21 Paik, P.Y., Pamula, V.K., and Chakrabarty, K. (2008) Adaptive cooling of integrated circuits using digital microfluidics. *IEEE Trans. Very Large Scale Integr. VLSI Syst.*, **16** (4), 432–443.
22 Yi, U.-C. and Kim, C.-J. (2006) Characterization of electrowetting actuation on addressable single-side coplanar electrodes. *J. Micromech. Microeng.*, **16** (10), 2053–2059.
23 Young, P.M. and Mohseni, K. (2008) Calculation of DEP and EWOD forces for application in digital microfluidics. *J. Fluids Eng.*, **130** (8), 81603.
24 Li, C. and Jiang, H. (2012) Electrowetting-driven variable-focus microlens on flexible surfaces. *Appl. Phys. Lett.*, **100** (23), 231105–2311054.
25 Satoh, W., Yokomaku, H., Hosono, H., Ohnishi, N., and Suzuki, H. (2008) Electrowetting-based valve for the control of the capillary flow. *J. Appl. Phys.*, **103** (3), 34903.
26 Mérian, T., He, F., Yan, H., Chu, D., Talbert, J.N., Goddard, J.M., and Nugen, S.R. (2012) Development and surface characterization of an electrowetting valve for capillary-driven microfluidics. *Colloids Surf., A*, **414**, 251–258.
27 Sista, R., Hua, Z., Thwar, P., Sudarsan, A., Srinivasan, V., Eckhardt, A., Pollack, M., and Pamula, V. (2008) Development of a digital microfluidic platform for point of care testing. *Lab Chip*, **8** (12), 2091–2104.
28 Pollack, M.G., Fair, R.B., and Shenderov, A.D. (2000) Electrowetting-based actuation of liquid droplets for microfluidic applications. *Appl. Phys. Lett.*, **77** (11), 1725.
29 Vallet, M., Vallade, M., and Berge, B. (1999) Limiting phenomena for the spreading of water on polymer films by electrowetting. *Eur. Phys. J. B*, **11** (4), 583–591.

www.ebook3000.com

30 Datta, S., Das, A.K., and Das, P.K. (2016) Unravelling electrostatic actuation on inclined and humped surfaces: effect of substrate contact angle. *Ind. Eng. Chem. Res.*, **55** (14), 3949–3959.

31 Bahadur, V. and Garimella, S.V. (2006) An energy-based model for electrowetting-induced droplet actuation. *J. Micromech. Microeng.*, **16** (8), 1494–1503.

32 Jones, T.B. (2005) An electromechanical interpretation of electrowetting. *J. Micromech. Microeng.*, **15** (6), 1184–1187.

33 Kumari, N., Bahadur, V., and Garimella, S.V. (2008) Electrical actuation of dielectric droplets. *J. Micromech. Microeng.*, **18** (8), 85018.

34 Ahmadi, A., Devlin, K.D., and Hoorfar, M. (2012) Numerical study of the microdroplet actuation switching frequency in digital microfluidic biochips. *Microfluid. Nanofluid.*, **12** (1–4), 295–305.

35 Ahmadi, A., Najjaran, H., Holzman, J.F., and Hoorfar, M. (2009) Two-dimensional flow dynamics in digital microfluidic systems. *J. Micromech. Microeng.*, **19** (6), 65003.

36 Clime, L., Brassard, D., and Veres, T. (2010) Numerical modeling of electrowetting transport processes for digital microfluidics. *Microfluid. Nanofluid.*, **8** (5), 599–608.

37 Keshavarz-Motamed, Z., Kadem, L., and Dolatabadi, A. (2010) Effects of dynamic contact angle on numerical modeling of electrowetting in parallel plate microchannels. *Microfluid. Nanofluid.*, **8** (1), 47–56.

38 Mohseni, K., Arzpeyma, A., and Dolatabadi, A. (2008) Behaviour of a moving droplet under electrowetting actuation: numerical simulation. *Can. J. Chem. Eng.*, **84** (1), 17–21.

39 Yafia, M. and Najjaran, H. (2015) Droplet necking and morphology variations induced by changing the gap height during transport in digital microfluidic systems. *J. Microelectromech. Syst.*, **24** (5), 1647–1658.

40 Berthier, J., Clementz, P., Raccurt, O., Jary, D., Claustre, P., Peponnet, C., and Fouillet, Y. (2006) Computer aided design of an EWOD microdevice. *Sens. Actuators, A*, **127** (2), 283–294.

41 Schertzer, M.J., Gubarenko, S.I., Ben-Mrad, R., and Sullivan, P.E. (2010) An empirically validated analytical model of droplet dynamics in electrowetting on dielectric devices. *Langmuir*, **26** (24), 19230–19238.

42 Song, J.H., Evans, R., Lin, Y.-Y., Hsu, B.-N., and Fair, R.B. (2008) A scaling model for electrowetting-on-dielectric microfluidic actuators. *Microfluid. Nanofluid.*, **7** (1), 75–89.

43 Chang, J. and Pak, J.J. (2011) Twin-plate electrowetting for efficient digital microfluidics. *Sens. Actuators, B*, **160** (1), 1581–1585.

44 Murran, M.A. and Najjaran, H. (2012) Direct current pulse train actuation to enhance droplet control in digital microfluidics. *Appl. Phys. Lett.*, **101** (14), 144102.

45 Dong, C., Chen, T., Gao, J., Jia, Y., Mak, P.I., Vai, M.I., and Martins, R.P. (2015) On the droplet velocity and electrode lifetime of digital microfluidics: voltage actuation techniques and comparison. *Microfluid. Nanofluid.*, **18** (4), 673–683.

46 Choi, K., Im, M., Choi, J.-M., and Choi, Y.-K. (2011) Droplet transportation using a pre-charging method for digital microfluidics. *Microfluid. Nanofluid.*, **12** (5), 821–827.

47 Im, D.J., Yoo, B.S., Ahn, M.M., Moon, D., and Kang, I.S. (2013) Digital electrophoresis of charged droplets. *Anal. Chem.*, **85** (8), 4038–4044.

48 Jung, Y.-M. and Kang, I.S. (2009) A novel actuation method of transporting droplets by using electrical charging of droplet in a dielectric fluid. *Biomicrofluidics*, **3**, 022402.

49 Jones, T.B., Fowler, J.D., Chang, Y.S., and Kim, C.J. (2003) Frequency-based relationship of electrowetting and dielectrophoretic liquid microactuation. *Langmuir*, **19** (18), 7646–7651.

50 Lee, H., Yun, S., Ko, S.H., and Kang, K.H. (2009) An electrohydrodynamic flow in ac electrowetting. *Biomicrofluidics*, **3** (4), 44113.

51 Chatterjee, D., Shepherd, H., and Garrell, R.L. (2009) Electromechanical model for actuating liquids in a two-plate droplet microfluidic device. *Lab Chip*, **9** (9), 1219–1229.

52 Kumari, N., Bahadur, V., and Garimella, S.V. (2008) Electrical actuation of electrically conducting and insulating droplets using ac and dc voltages. *J. Micromech. Microeng.*, **18** (10), 105015.

53 Fan, S.-K., Hsieh, T.-H., and Lin, D.-Y. (2009) General digital microfluidic platform manipulating dielectric and conductive droplets by dielectrophoresis and electrowetting. *Lab Chip*, **9** (9), 1236–1242.

54 Gong, J., Fan, S., and Kim, C.J. (2004) Portable digital microfluidics platform with active but disposable lab-on-chip. 17th IEEE International Conference on Micro Electro Mechanical Systems, vol. 3, pp. 355–358.

55 Yafia, M., Ahmadi, A., Hoorfar, M., and Najjaran, H. (2015) Ultra-portable smartphone controlled integrated digital microfluidic system in a 3D-printed modular assembly. *Micromachines*, **6** (9), 1289–1305.

56 Ren, H., Fair, R.B., Pollack, M.G., and Shaughnessy, E.J. (2002) Dynamics of electro-wetting droplet transport. *Sens. Actuators, B*, **87** (1), 201–206.

57 Ren, H., Fair, R.B., and Pollack, M.G. (2004) Automated on-chip droplet dispensing with volume control by electro-wetting actuation and capacitance metering. *Sens. Actuators, B*, **98** (2–3), 319–327.

58 Ren, H. and Fair, R. (2002) Micro/nano liter droplet formation and dispensing by capacitance metering and electrowetting actuation. Proceedings of the IEEE-NANO, pp. 369–372.

59 Izadian, A. and Garrell, R. (2010) Pico-droplet dispensing control in digital microfluidic systems. IEEE Conference on Decision and Control (CDC), vol. 49, pp. 4583–4586.

60 Elvira, K., Leatherbarrow, R., Edel, J., and DeMello, A. (2012) Droplet dispensing in digital microfluidic devices: assessment of long-term reproducibility. *Biomicrofluidics*, **6** (2), 22003–2200310.

61 Ding, H., Sadeghi, S., Shah, G.J., Chen, S., Keng, P.Y., Kim, C.-J.C., and van Dam, R.M. (2012) Accurate dispensing of volatile reagents on demand for chemical reactions in EWOD chips. *Lab Chip*, **12** (18), 3331–3340.

62 Wang, K.-L., Jones, T.B., and Raisanen, A. (2009) DEP actuated nanoliter droplet dispensing using feedback control. *Lab Chip*, **9** (7), 901–909.

www.ebook3000.com

63 Zhang, L. and Kuang, J. (2014) Optimal test droplets dispensing for parallel testing for digital microfluidic biochip. *J. Inst. Eng: Ser. B*, **95** (3), 203–211.

64 Chen, C.-H., Tsai, S.-L., Chen, M.-K., and Jang, L.-S. (2011) Effects of gap height, applied frequency, and fluid conductivity on minimum actuation voltage of electrowetting-on-dielectric and liquid dielectrophoresis. *Sens. Actuators, B*, **159** (1), 321–327.

65 Yafia, M. and Najjaran, H. (2013) High precision control of gap height for enhancing principal digital microfluidics operations. *Sens. Actuators, B*, **186**, 343–352.

66 Li, Y., Baker, R.J., and Raad, D. (2016) Improving the performance of electrowetting on dielectric microfluidics using piezoelectric top plate control. *Sens. Actuators, B*, **229**, 63–74.

67 Yafia, M. and Najjaran, H. (2014) The effect of changing the gap height on droplet deformation during transport in digital microfluidics systems. International Conference on Nanochannels, Microchannels, and Minichannels, Chicago, IL.

68 Ferreira, A. and Aphale, S.S. (2011) A survey of modeling and control techniques for micro- and nanoelectromechanical systems. *IEEE Trans. Syst. Man Cybern. Part C Appl. Rev.*, **41** (3), 350–364.

69 Easley, C.J., Karlinsey, J.M., Bienvenue, J.M., Legendre, L.A., Roper, M.G., Feldman, S.H., Hughes, M.A., Hewlett, E.L., Merkel, T.J., Ferrance, J.P., and Landers, J.P. (2006) A fully integrated microfluidic genetic analysis system with sample-in-answer-out capability. *Proc. Natl. Acad. Sci. U.S.A.*, **103** (51), 19272–19277.

70 Vestad, T., Marr, D.W.M., and Oakey, J. (2004) Flow control for capillary-pumped microfluidic systems. *J. Micromech. Microeng.*, **14** (11), 1503–1506.

71 Shih, S.C.C., Fobel, R., Kumar, P., and Wheeler, A.R. (2011) A feedback control system for high-fidelity digital microfluidics. *Lab Chip*, **11** (3), 535–540.

72 Gao, J., Liu, X., Chen, T., Mak, P.-I., Du, Y., Vai, M.-I., Lin, B., and Martins, R.P. (2013) An intelligent digital microfluidic system with fuzzy-enhanced feedback for multi-droplet manipulation. *Lab Chip*, **13** (3), 443–451.

73 Cho, S.K., Moon, H., and Kim, C. (2003) Creating, transporting, cutting, and merging liquid droplets by electrowetting-based actuation for digital microfluidic circuits. *J. Microelectromech. Syst.*, **12** (1), 70–80.

74 Gong, J. and Kim, C.-J. (2005) Two dimensional digital microfluidic system by multi-layer printed circuit board. 18th IEEE International Conference on MEMS, pp. 726–729.

75 Gong, J. and Kim, C.-J. (2006) Real-time feedback control of droplet generation for EWOD digitial microfluidics. Micro Total Analysis Systems – Proceedings of MicroTAS 2006 Conference: 10th International Conference on Miniaturized Systems for Chemistry and Life Sciences, 2006, pp. 1046–1048.

76 Gong, J. and Kim, C.J. (2008) All-electronic droplet generation on-chip with real-time feedback control for EWOD digital microfluidics. *Lab Chip*, **8** (6), 898–906.

77 Bhattacharjee, B. and Najjaran, H. (2010) Droplet position control in digital microfluidic systems. *Biomed. Microdevices*, **12** (1), 115–124.
78 Fobel, R., Fobel, C., and Wheeler, A.R. (2013) DropBot: an open-source digital microfluidic control system with precise control of electrostatic driving force and instantaneous drop velocity measurement. *Appl. Phys. Lett.*, **102** (19), 193513.
79 Shin, Y.-J. and Lee, J.-B. (2010) Machine vision for digital microfluidics. *Rev. Sci. Instrum.*, **81** (1), 14302.
80 Bhattacharjee, B. and Najjaran, H. (2012) Droplet sensing by measuring the capacitance between coplanar electrodes in a digital microfluidic system. *Lab Chip*, **12** (21), 4416–4423.
81 Murran, M.A. and Najjaran, H. (2012) Capacitance-based droplet position estimator for digital microfluidic devices. *Lab Chip*, **12** (11), 2053–2059.
82 Cho, M., Pan, D.Z., and Member, S. (2008) A high-performance droplet routing algorithm for digital microfluidic biochips. *IEEE Trans. Comput. Des. Integr. Circuits Syst.*, **27** (10), 1714–1724.
83 Su, F. and Chakrabarty, K. (2008) High-level synthesis of digital microfluidic biochips. *ACM J. Emerging Technol. Comput. Syst.*, **3** (4), 1–32.
84 Gong, J. and Kim, C.J. (2008) Direct-referencing two-dimensional-array digital microfluidics using multilayer printed circuit board. *J. Microelectromechanical Syst.*, **17** (2), 257–264.
85 Hadwen, B., Broder, G.R., Morganti, D., Jacobs, A., Brown, C., Hector, J.R., Kubota, Y., and Morgan, H. (2012) Programmable large area digital microfluidic array with integrated droplet sensing for bioassays. *Lab Chip*, **12** (18), 3305–3313.
86 Noh, J.H., Noh, J., Kreit, E., Heikenfeld, J., and Rack, P.D. (2012) Toward active-matrix lab-on-a-chip: programmable electrofluidic control enabled by arrayed oxide thin film transistors. *Lab Chip*, **12** (2), 353–360.
87 Collier, C.M., Wiltshire, M., Nichols, J., Born, B., Landry, E.L., and Holzman, J.F. (2011) Nonlinear dual-phase multiplexing in digital microfluidic architectures. *Micromachines*, **2** (4), 369–384.
88 Nichols, J., Ahmadi, A., Hoorfar, M., Najjaran, H., and Holzman, J.F. (2008) Micro drop actuation using multiplexer structures. ASME 2008 6th International Conference on Nanochannels, Microchannels, and Minichannels, Darmstadt, June 23–25, 2008, pp. 1085–1092.
89 Urban, P.L. (2015) Universal electronics for miniature and automated chemical assays. *Analyst*, **140** (4), 963–975.
90 Srinivasan, V., Pamula, V.K., and Fair, R.B. (2004) An integrated digital microfluidic lab-on-a-chip for clinical diagnostics on human physiological fluids. *Lab Chip*, **4** (4), 310–315.
91 Jebrail, M.J., Yang, H., Mudrik, J.M., Lafrenière, N.M., McRoberts, C., Al-Dirbashi, O.Y., Fisher, L., Chakraborty, P., and Wheeler, A.R. (2011) A digital microfluidic method for dried blood spot analysis. *Lab Chip*, **11** (19), 3218–3224.
92 Boles, D.J., Benton, J.L., Siew, G.J., Levy, M.H., Thwar, P.K., Sandahl, M.A., Rouse, J.L., Perkins, L.C., Sudarsan, A.P., Jalili, R., Pamula, V.K., Srinivasan, V., Fair, R.B., Griffin, P.B., Eckhardt, A.E., and Pollack, M.G. (2011) Droplet-based pyrosequencing using digital microfluidics. *Anal. Chem.*, **83** (22), 8439–8447.

www.ebook3000.com

93 Shih, S.C.C., Yang, H., Jebrail, M.J., Fobel, R., McIntosh, N., Al-Dirbashi, O.Y., Chakraborty, P., and Wheeler, A.R. (2012) Dried blood spot analysis by digital microfluidics coupled to nanoelectrospray ionization mass spectrometry. *Anal. Chem.*, **84** (8), 3731–3738.

94 Malic, L., Veres, T., and Tabrizian, M. (2011) Nanostructured digital microfluidics for enhanced surface plasmon resonance imaging. *Biosens. Bioelectron.*, **26** (5), 2053–2059.

95 Mousa, N.A., Jebrail, M.J., Yang, H., Abdelgawad, M., Metalnikov, P., Chen, J., Wheeler, A.R., and Casper, R.F. (2009) Droplet-scale estrogen assays in breast tissue, blood, and serum. *Sci. Transl. Med.*, **1** (1), 1ra2.

6

Microfluidics for Chemical Analysis

Peng Song[1,3], Adrian C. Fisher[2,3], Luwen Meng[2], and Hoang V. Nguyen[2]

[1] *Beijing University of Technology, College of Environmental and Energy Engineering, Department of Chemistry and Chemical Engineering, Beijing Key Laboratory for Green Catalysis and Separation, No. 100 Pingleyuan, Beijing 100124, PR China*
[2] *University of Cambridge, School of Technology, Department of Chemical Engineering and Biotechnology, New Museums Site, Pembroke Street, Cambridge CB2 3RA, UK*
[3] *Beijing University of Chemical Technology, International Research Center for Soft Matter, No. 15 Beisanhuan East Road, Beijing 100029, PR China*

6.1 Introduction

Recent rapid developments in the field of microfluidics have led to a vast array of novel technologies available for chemical analysis. In this chapter, we focus on how electrochemical methods have been successfully adopted and developed in conjunction with microfluidics.

The ability to manufacture precise electrode geometries and the ease of integration with the methodologies used for the fabrication of microfluidic devices have also led to vast researches and commercial interests in the field.

In the area of electrochemical analysis, there has been a long and successful history of uniting electrochemical measurements with hydrodynamic strategies. In particular techniques such as the rotating disk and ring disk [1, 2], tube [3], wall tube [4], wall jet [5], channel flow cell [6], and confluence reactor [7] have been utilized to explore a plethora of coupled competing processes typically involved in electrolysis reactions, for example, mass transport via diffusion, convection and migration, heterogeneous and/or homogeneous chemical reactions, adsorption/desorption, electron transfer, ion pairing, and so on. A key aspect of the flexibility of these approaches has been the quantitative nature of the analysis that can be undertaken by application of appropriate analytical theory [8] or numerical analysis [6]. In particular the use of numerical modeling such as finite difference (FD) [6], finite element (FE) [7, 9–13], and boundary element methods [14–17] have been proved to be highly successful.

These larger-scale electrochemical hydrodynamic techniques are often operated with flows associated with low Reynolds numbers; it is therefore not surprising that many workers have sought to develop microfluidic alternatives to the more traditional macroscopic hydrodynamic electrodes. In this chapter, we review a segment of electrochemical techniques used in combination with

Microfluidics: Fundamentals, Devices and Applications, First Edition.
Edited by Yujun Song, Daojian Cheng, and Liang Zhao.
© 2018 Wiley-VCH Verlag GmbH & Co. KGaA. Published 2018 by Wiley-VCH Verlag GmbH & Co. KGaA.

www.ebook3000.com

microfluidics, with a section dedicated to techniques and numerical approaches that can provide quantitative measurements for chemical and mechanistic analysis.

The chapter is structured as follows: the first section explores different electrochemical protocols used within microfluidic devices, including voltammetry, amperometry, potentiometry, and conductivity. In the next section, a series of novel electrochemical microfluidic technologies are reviewed, and the chapter concludes with a short review of electrochemical simulation methods that can be employed to explore the quantification of the current–voltage characteristics of the electrochemical analysis carried out using microengineered electrodes and reactors.

6.2 Microfluidics for Electrochemical Analysis

In this section, the protocols typically adopted for electrochemical analysis within microfluidic environments are discussed and reviewed. A microengineering approach for electrochemical analysis offers considerable potential advantages in the flexibility of design and manufacturing of microfluidic devices, with factors such as process costs, time, accuracy, reliability, material choice, and access to an array of high precision engineering tools, all benefits of the approach. The precise manipulation of fluids enables an extremely accurate handling of samples for electrochemical analysis and all other specific purposes such as mixing, heating exchange, and droplet delivery [18].

In the field of electrochemical analysis using microfluidics, a vast academic literature has now been reported for a variety of electrochemical protocols, including voltammetry, amperometry, potentiometry, and conductometry. In the following sections, the applications of these electrochemical protocols are introduced, and illustrative examples are used from the literature to highlight areas of current research activity. For simplicity, in the protocol sections, the microfluidic chip for applications using simple single microfluidic channels for incorporation of the electrode devices below details the different experimental strategies applied for each of these protocols along with a series of examples taken from literature.

6.2.1 Voltammetric Analysis

Voltammetry plays a central role in electrochemical analysis, with either a steady or time-variant potential applied to an electrochemical cell. The corresponding current flow as a function of time is then recorded typically as a function of the fluid delivery rate to the electrode [19]. In a typical voltammetric measurement, the resulting current consists of two components, faradaic and non-faradaic current. The faradaic current is produced by a charge transfer process resulting directly from any redox chemistry. The non-faradaic current arises from the charging and discharging characteristics of the cell [20].

Early quantitative electrochemical studies exploiting voltammetry in microfluidic environments have been reported [21–23]. A series of rectangular microchannel structures were used in conjunction with microelectrodes embedded within one wall of the cell. Hydrodynamic voltammetry measurements in

combination with numerical modeling were able to reveal the quantitative variation of the current as a function of mass transport rate to the electrode. Linear sweep measurements were carried out by using test solutions containing the redox active compound *N,N,N′,N′* tetramethyl-1,4-phenylene diamine to explore the relationship between transport-limited current and the volumetric flow rate. This approach was extended by Fisher *et al*. who studied the properties of single and dual electrode (generator–collector) configurations [24] within microengineered rectangular ducts.

Dryden *et al*. reported a digital microfluidics (DMF) approach with integrated electroanalysis for chemical sensing applications [25]. DMF was reported as a novel technique that enabled the manipulation of small volumes of solutions as well as the automated handling of discrete samples. The reported device was used for the detection of acetaminophen with a limit of detection (LOD) of 76 μm and good precision with minimal human intervention.

Microfluidic applications for environmental applications are also widespread, and many exploit voltammetric stripping approaches for analysis. In a recent study a microfluidic approach has been used to sample and analyze the concentration of lead in river water [26]. In this approach, individual bespoke modules include microfabricated piezoelectrically actuated pumps, with the microelectrochemical cells integrated within one platform. The device provided a low cost and rapid detection method for the monitoring of toxic metals in environmental water.

The detection of trace explosives or other harmful agents is also an area of active research for microfluidic sensors. In one report the investigation of trace levels of 2,4,6-trinitrotoluene (TNT) was explored. A detection limit of 2×10^{-12} mol of TNT was reported with the consumption of 47 nl of analysis sample [27]. The work was also extended to explore the voltammetric response of catechol (CA), hydrazine, and nickel as test species. The advantages of the voltammetric analysis devices include enhanced detection limit, minimal sample consumption, high efficiency, and liquid handling ability.

The above studies employed voltammetric methods using a steady or linearly varying voltage waveform to explore the current characteristics of the system. However, alternating current (AC) voltammetry is also a highly popular tool for electrochemical analysis and has also been adopted for measurements in microfluidic environments [28]. In this approach, a sinusoidally varying voltage input is applied to the microengineered electrochemical cell, and the current response is monitored typically as a function of applied frequency (Figure 6.1).

The resulting output current can be analyzed in both phase and magnitude using a frequency response analyzer or using a Fourier transform (FT) algorithm [29]. Compared with traditional linear sweep voltammetric methods, AC voltammetry can be more sensitive and provide information about the complex phase relationships within the electrochemical cell.

Using a large amplitude AC voltammetry approach, Bond *et al*. have reported microfluidic electrochemical measurements using fast Fourier transform (FFT) analysis to investigate the higher harmonic characteristics of the system [30]. AC measurements were used to investigate the redox properties of ferrocenemethanol in an aqueous solution containing 0.1 M KNO_3 as electrolyte. Figure 6.2 reveals the power of the large amplitude AC approach, with the

www.ebook3000.com

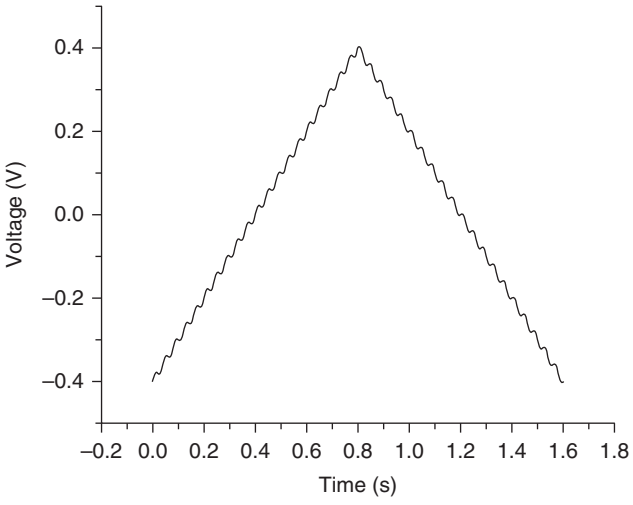


Figure 6.1 Potential waveform of AC voltammetry.

low applied frequencies (<15 Hz) and the lower order harmonics showing a strong dependence on the microfluidics of the system. While at higher applied frequencies (>90 Hz), all voltammetric harmonics are found independent of the microfluidic volumetric flow rates. It is therefore possible in a single measurement to explore microfluidics-, capacitance-, and diffusion-dominated regimes of the electrochemical analyzer. This unique and currently underexploited approach is used for the quantitative analysis of microfluidic electrochemical systems.

More traditional AC voltammetry measurements using a small amplitude voltage waveform and monitor only the first harmonic response have been successfully utilized for microfluidic electrochemical DNA sensor applications. Ferguson *et al*. succeeded in detecting varying trace levels of Salmonella [31]. Samples were pumped into a microchannel, and analysis was performed under stationary conditions as shown in Figure 6.3.

Hebert *et al*. have reported the detection of different native carbohydrates with AC voltammetry using a microfluidic chip [32]. The approach used copper electrodes with a nichrome adhesion layer and a polydimethylsiloxane (PDMS) microchannel. Figure 6.4 shows the fundamental harmonic response of the carbohydrates in the frequency domain information. The authors reported an increase in both sensitivity and selectivity compared to traditional DC voltammetric measurements.

In an extension to this strategy, the method was shown to achieve selectivity between two analyses that are not separated chromatographically. Figure 6.5 shows that there is no signal of dopamine (DA) shown in the even harmonic response of the system [33] by selecting the appropriate applied potential window (which in this case was centered at 134 mV vs Ag/AgCl – the formal potential of DA).

Voltammetric measurements for enzyme immunoassays are also of major interest in the pharmaceutical industry. The potential to combine fast on-chip

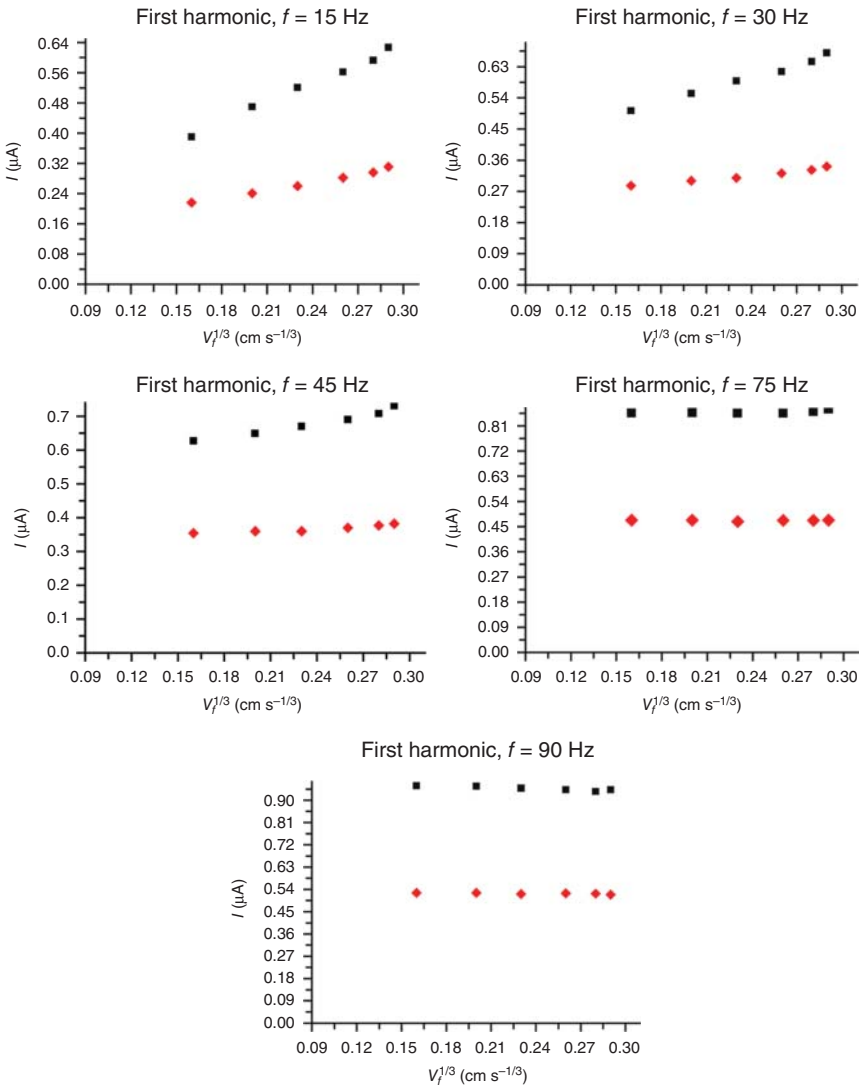


Figure 6.2 Dependence of peak current at designated frequencies ($\Delta E = 80$ mV) for the fundamental AC harmonic component on the cube root of the volume flow rate for the oxidation of 1.0 (■) and 0.5 mM (red ♦) ferrocenemethanol in 0.1 or 0.05 M aqueous KNO_3, respectively. (Matthews *et al*. 2012 [30]. Reproduced with permission of American Chemical Society.)

electrochemical analysis with a high-throughput platform offers the possibility to rapidly screen large libraries of drug candidates and chemical compounds. Díaz-González *et al*. has reviewed the different detection methods with AC voltammetry found to be highly successful in analyzing osteocalcin and pneumolysin detection with carbon paste electrodes (CPEs) [34].

www.ebook3000.com

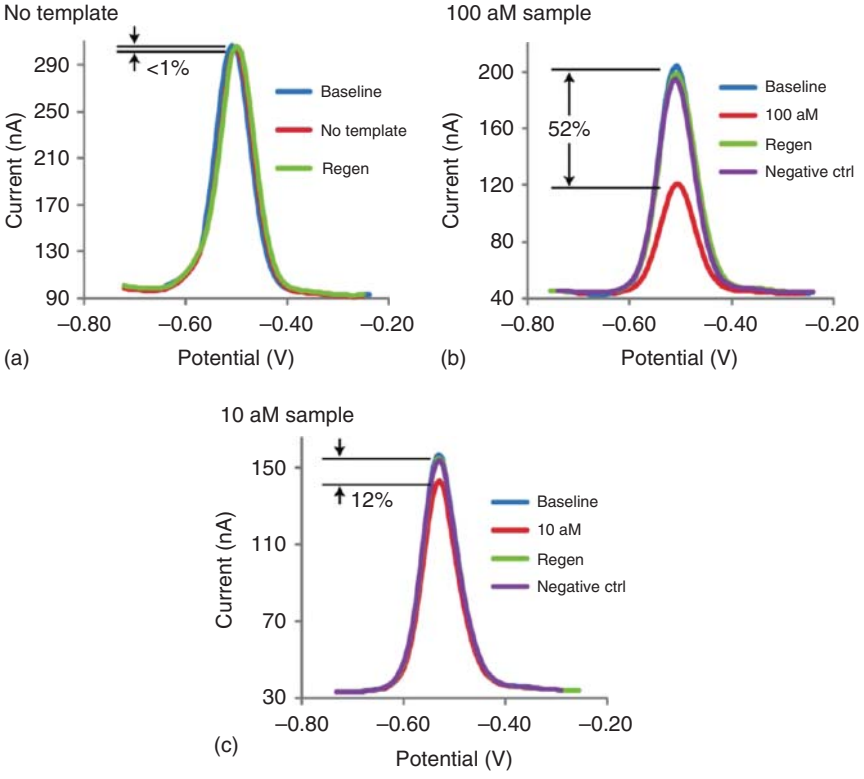


Figure 6.3 Limits of integrated microfluidic electrochemical DNA (IMED) detection with Salmonella genomic DNA. (a) The zero-template negative control yielded <1% change in the faradaic current (red) compared with the baseline (blue). Probe regeneration with guanidine hydrochloride resets the sensor to within 98% of its initial state (green). (b) The 100 aM sample produced a 52% signal change. (c) The 10 aM sample produced a 12% signal change, with respect to the baseline (red, blue). Each detection was validated with sensor regeneration, which returned the probe current to >96% of the baseline (green). Signals in panels (b and c) were also compared against externally prepared zero-template negative controls, which resulted in drops of 1% and 0%, respectively (purple). (Ferguson *et al*. 2009 [31]. Reproduced with permission of American Chemical Society.)

6.2.2 Amperometric Protocol

In amperometric measurements, typically a DC current is measured at a fixed potential. These methods have proved popular for a number of sensor applications including a wide range of biological systems.

Amperometric detection has been widely reported for applications in electrophoretic separations [35, 36]. In one report a simple glass-based microfluidic chip was fabricated with a 30 μm-carbon fiber microdisk electrode, platinum counter electrode (CE), and Ag/AgCl reference electrode (RE). The approach was used to analyze DNA restriction fragments and polymerase chain reaction (PCR) product size and monitor DA and CA in a capillary electrophoresis system [37]. Under optimized conditions, the amperometric responses of DA and CA showed

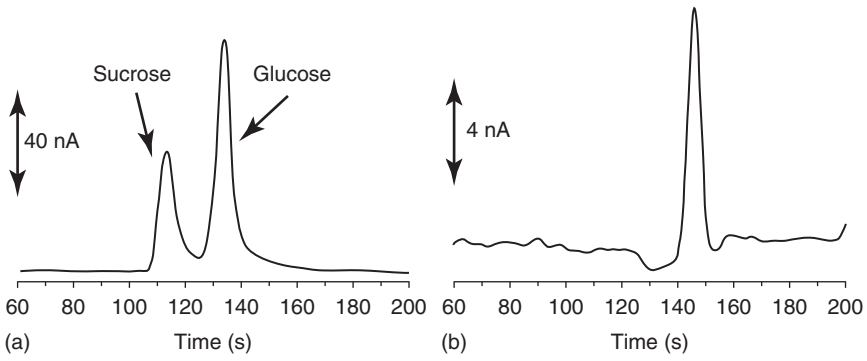


Figure 6.4 Separation and detection of carbohydrates utilizing a 50 μm-wide copper electrode. Separation conditions: 0.1 M NaOH running electrolyte; applied voltage, +500 V to B with +275 V pull-back voltages applied to S and SW; injection, +1 kV to S for 5 s with SW grounded and B and BW floating; SV was accomplished by applying a 9 Hz sine wave from 0 to 600 mV versus Ag/AgCl. (a) Electropherogram of 6 mM sucrose and 8 mM glucose shown at the first harmonic (9 Hz). (b) Electropherogram of 10 mM maltose shown at the third harmonic (27 Hz). (Hebert *et al*. 2002 [32]. Reproduced with permission of John Wiley & Sons.)

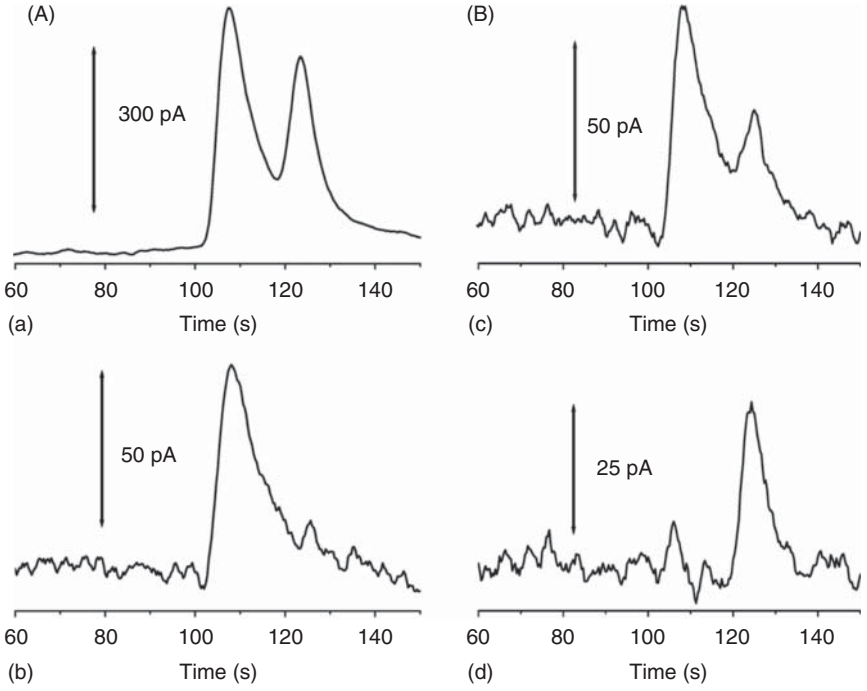


Figure 6.5 Manipulation of the applied potential window to enhance selectivity. Separation of 5 μM DA and 5 μM isoproterenol. All electrophoresis conditions were identical to those in Figure 6.4. SV detection was accomplished by applying a 3-Hz sine wave with a 500-mV amplitude with a variable offset. (A) Excitation offset centered on the half-wave potential of isoproterenol (180 mV (vs Ag/AgCl)). First harmonic (3 Hz) time course (a) and fourth harmonic (12 Hz) time course (b). (B) Excitation offset centered on the half-wave potential of DA (134 mV (vs Ag/AgCl)). Third harmonic (9 Hz) time course (c) and second harmonic (6 Hz) time course (d). The resolution between dopamine and isoproterenol is 0.9. (Reprinted with permission from Ref. [33].)

www.ebook3000.com

a linear fit from 5 to 200 and 20 to 800 µm, respectively, with a detection limit of DA and CA of 0.51 and 2.9 µm, respectively.

The rapid detection of cholesterol has been reported using a PDMS microchip for capillary electrophoresis [38]. In this study, direct amperometric detection of cholesterol was successfully applied with a detection concentration between 38.7 µg dl^{-1} and 270.6 mg dl^{-1}; the detection limit was found to be 38.7 ng dl^{-1}. The microfluidic characteristics of the system were exploited to allow up to 60 samples h^{-1} to be processed. Similar strategies have been reported for glucose [39], nitroaromatic compounds [40], sulfonamides [41], nitric oxide [42, 43], and cancer makers carcinoembryonic antigen (CEA) and cancer antigen 15-3 (CA15-3) [44].

In an advanced amperometric detection approach, the use of a centrifugal microfluidic platform [45] has been reported. In this microfluidic approach, the detection for the C-reactive protein (CRP) with the LOD of 4.9 pg ml^{-1} was achieved. It was reported that the LOD demonstrated a 17-fold improvement when compared with quantification by optical density. The throughput of this novel automated device was comparatively high (<20 min) as shown in Figure 6.6.

Centrifugal microfluidic devices were also used for the determination of glucose to control human serum [46]. The approach reported consisted of a PDMS reservoir coupled to a mixing chamber, a spiral channel, and a waste reservoir. A CPE was used as the working electrode (WE) for glucose detection. A graphene–polyaniline (G-PANI) nanocomposite solution was introduced onto the WE for hydrogen peroxide detection. (The hydrogen peroxide was produced via the glucose oxidase solution in separated reservoirs.) After extensive investigation, optimal conditions were reported and a linear calibration between 1 and 10 mM with an LOD of 0.29 mM was achieved as illustrated in Figure 6.7.

Amperometric measurements have also been reported coupled with high performance liquid chromatography (HPLC) to allow dual absorbance and electrochemical detection [47]. The electrochemical device was constructed from

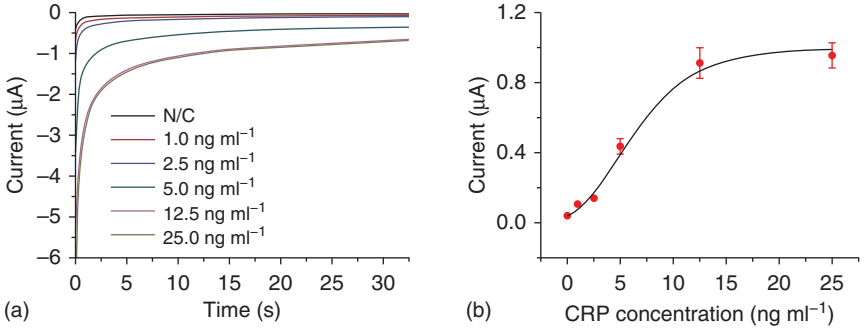


Figure 6.6 (a) Amperometric plots obtained on disk for the range of CRP concentrations tested. (b) A calibration curve for stagnant electrochemical measurements taken on disk for the CRP biomarker. Measurements were taken by applying a 20.2 V bias to the working electrode with respect to the on-chip pseudo-reference gold electrode. Note: Error bars represent the standard deviation. (Kim *et al*. 2013 [45]. Reproduced with permission of Royal Society of Chemistry.)

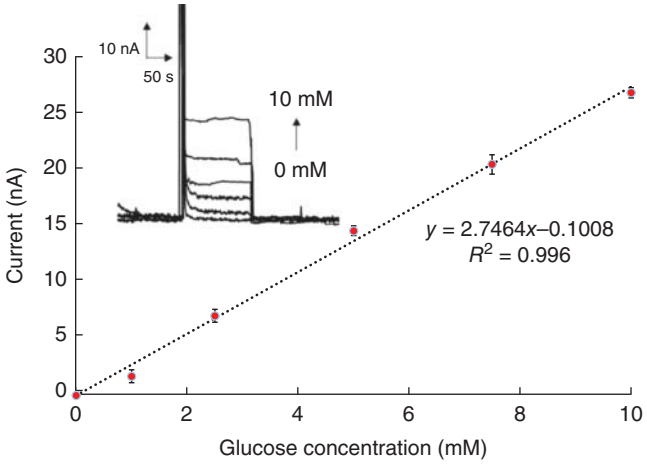


Figure 6.7 Calibration curve and amperogram (inset) for glucose assay using e-CD system based on a G-PANI/CoPc-CPE at applied potential of +0.4 V versus CPE. (Rattanarat *et al*. 2015 [46]. Reproduced with permission of John Wiley & Sons.)

PDMS and CPEs. Chemicals including 2,5-dihydroxybenzoic acid, 2,3-dihydroxybenzoic acid, and CA were quantitatively analyzed, and percentage recoveries of the order more than 97%, 92%, and 95% were reported for 2,5-dihydroxybenzoic acid, 2,3-dihydroxybenzoic acid, and CA, respectively.

6.2.3 Potentiometric Protocol

In the case of potentiometric measurements, the electrode or electrochemical cell is now designed to monitor the potential of the system as a function of time. Typically the electrode is designed to be selective in its electrochemical response to a specific analyte. These so-called ion-selective electrodes (ISEs) have been intensively used in potentiometric detection with microfluidic devices.

A major area of ISE research is in the field of pH sensing; in one report, a novel pH-sensitive single-walled carbon nanotube (SWCNT) material was developed for incorporation within microfluidic environments [48]. The variation in pH value was measured from the electronic structure changes in the semiconducting SWCNTs as a potentiometric measurement. A microfluidic chip was built with an SWCNT pH-sensing WE and Ag/AgCl RE as shown in Figure 6.8. Using calibration, an ideal Nernstian response of 59.71 mV pH^{-1} was observed between pH values of 3 and 11.

Potentiometric methods have also been developed for applications using droplet-generating microfluidic devices. In one report the binding kinetics between RNA and Mg^{2+}were investigated [49]. The combined use of potentiometric analysis with a microdroplet device led to a short time response (0.06 s) and utilization of very small quantities of RNA sample (<20 µl) as shown in Figure 6.9.

The simplicity of potentiometric microanalyzers also allows their application in remote or isolated environments. ISEs have already been employed in

www.ebook3000.com

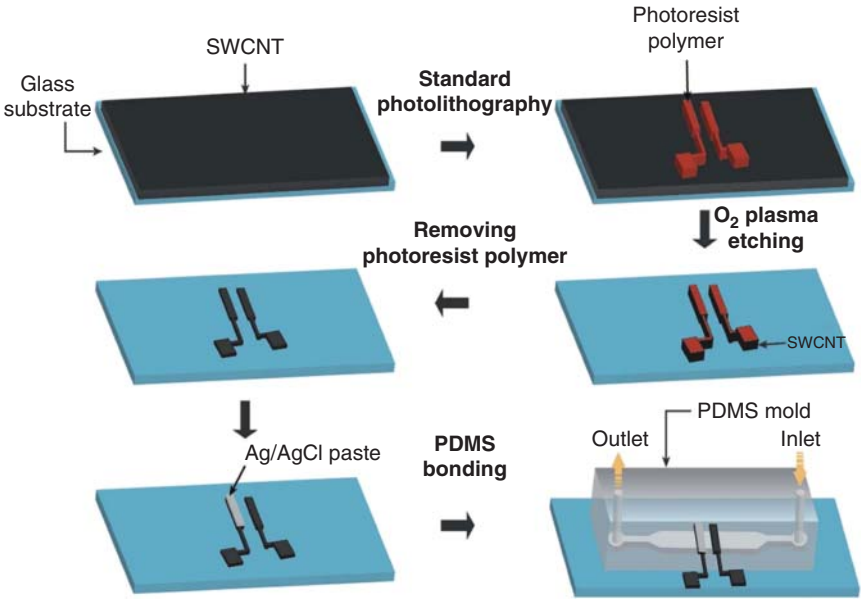


Figure 6.8 Schematic fabrication process of the microfluidic pH-sensing chip. (Li *et al*. 2014 [48]. Reproduced with permission of Royal Society of Chemistry.)

NASA space programmers to monitor potassium and nitrate ions levels from a water-recycling process [50]. The device was fabricated with a low temperature co-fired ceramic (LTCC), and the reported biparametric device used two ISEs with a screen-printed Ag/AgCl RE. The all-solid nitrate polymeric membranes demonstrated a linear fit between electrochemical response and ion concentration ranging from 10 to 1000 mg l^{-1} with a detection limit of 9.56 mg l^{-1}. The all-solid potassium polymeric membranes gave a detection range from 1.9 to 155 mg l^{-1} with a detection limit of 0.81 mg l^{-1}. Furthermore, a similar device employing cyclic olefin copolymer (COC) was developed to monitor the presence of ammonium ion for future manned space missions [51].

Potentiometric measurements can operate with very low cost components, and several studies have reported electrochemical sensors integrated with paper-based and textile-based microfluidic devices [52–54]. In one report, potentiometric measurements were utilized with ion-sensing electrochemical paper-based analytical devices (EPADs) employing a miniaturized paper RE and a small ion-selective paper electrode (ISPE) [52]. A printed wax barrier was applied to define the sample area and reference zone for the sensing of chloride ions using a Ag/AgCl RE. In addition to electrolytes including potassium, sodium, and calcium ions, a PVC-based ion-selective membrane was introduced to separate the sample zone from a paper indicator electrode. The ion-sensing EPADs demonstrated a linear response over three orders of magnitude of electrolyte concentration with a slope of $59.2/z$ mV, which is close to the expected theoretical value. Further paper-based microfluidic chip studies have been reported for cadmium and palladium ions and pH value [53].

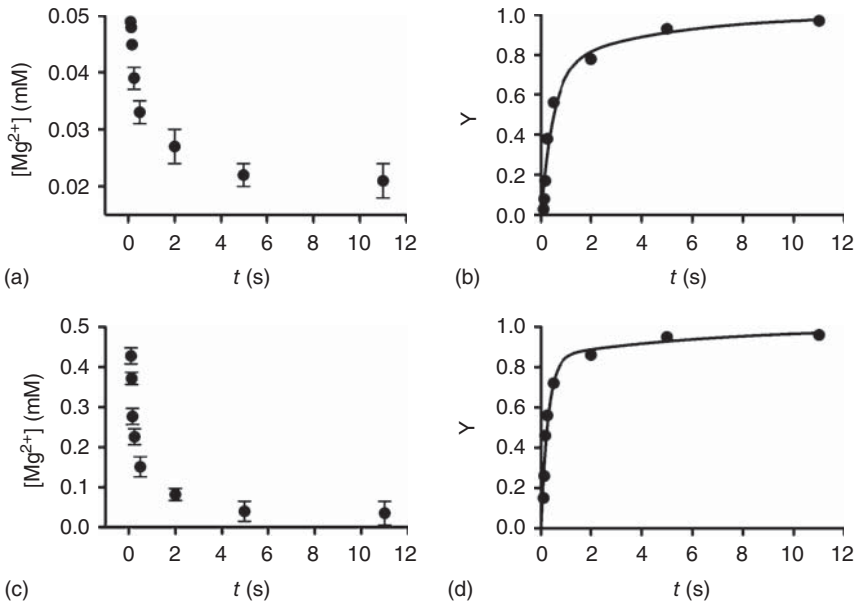


Figure 6.9 (a, c) The change of free Mg^{2+} concentration during the RNA and Mg^{2+} binding process. The initial concentrations are (a) 0.050 mM Mg^{2+} and 0.019 mM RNA and (c) 0.50 mM Mg^{2+} and 0.23 mM RNA. (b, d) The temporal change of the fraction of RNA–Mg^{2+} binding reactions Y. $Y = ([Mg^{2+}] - [Mg^{2+}]_f)/([Mg^{2+}]_i - [Mg^{2+}]_f)$, where $[Mg^{2+}]_f$ and $[Mg^{2+}]_i$ are the final and initial Mg^{2+} concentrations in the droplets, respectively. The data points in (b) and (d) are calculated from the data presented in (a) and (c), respectively. The curves are the fitting result of a two-exponential model. (Han *et al*. 2012 [49]. Reproduced with permission of Royal Society of Chemistry.)

6.2.4 Conductivity Protocol

Conductivity detection is perhaps the simplest of the electrochemical analysis protocols employed within microfluidic devices. However, this low cost technology can provide useful insights and is typically adopted by using a pair of facing Pt electrodes separated by a small and well-defined distance.

A polymethylmethacrylate (PMMA) chip and a pair of Pt wires with an end-to-end space of approximately 20 μm conductivity measurements have been used to monitor the solution concentration of amino acids, peptides, proteins, and oligonucleotides [55]. It has been reported that in order to record the solution conductivity accurately, a bipolar-pulse conductivity detection method was developed. Concentration monitoring of the amino acid and alanine was successfully achieved in the range 10–100 nM with an LOD of 8.0 nM via calibration.

A multichannel microfluidic chip integrated with a contact conductivity sensor array has been reported for the chip analysis of amino acids, peptides, proteins, and oligonucleotides [56]. A lithographically patterned gold electrode array was assembled on a microfluidic chip using a thermal bonding approach. A pair of gold microelectrodes with a width of 60 μm and a spacing of 5 μm operated as the conductivity detectors in a 16-channel device. Using high-speed,

www.ebook3000.com

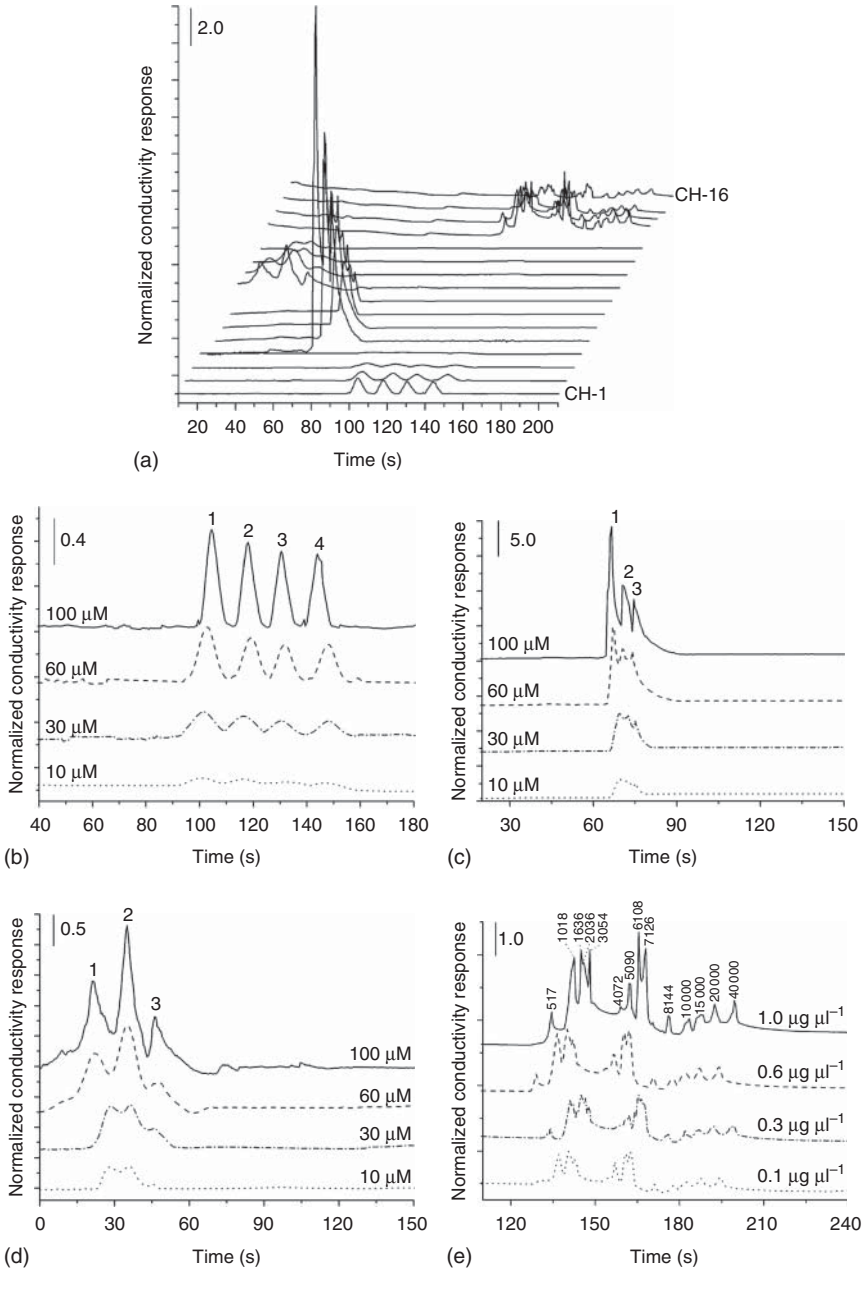

2.0
Normalized conductivity response
CH-16
CH-1
20 40 60 80 100 120 140 160 180 200
Time (s)
(a)
0.4
1
2
3
4
100 μM
60 μM
30 μM
10 μM
40 60 80 100 120 140 160 180
Time (s)
(b)
5.0
1
2
3
100 μM
60 μM
30 μM
10 μM
30 60 90 120 150
Time (s)
(c)
0.5
1
2
3
100 μM
60 μM
30 μM
10 μM
0 30 60 90 120 150
Time (s)
(d)
1.0
1018
1636
2036
3054
6108
7126
517
5090
4072
8144
10000
15000
20000
40000
1.0 μg μl−1
0.6 μg μl−1
0.3 μg μl−1
0.1 μg μl−1
120 150 180 210 240
Time (s)
(e)

Figure 6.10 (a) Sixteen-channel microchip electrophoresis of different samples using the PC microchip and setup. Channels 1–4, μ-CZE of amino acids; channels 5–8, μ-CZE of peptides; channels 9–12, μ-CZE of proteins; channels 13–16, μ-CEC of oligonucleotides. The electrophoresis was performed at 90 V cm^{-1} with bipolar pulse amplitude of ±0.6 V and a bipolar frequency of 6.0 kHz. Details on the separation buffers used for each sample can be found in the experimental section. (b) An expanded view of the electrophoretic trace for the μ-CZE analysis of amino acids, which consisted of (1) alanine; (2) valine; (3) glutamine; and (4) tryptophan. (c) An expanded view of the μ-CZE analysis of peptides, which contained (1) leucine enkephalin; (2) methionine enkephalin; and (3) oxytocin. (d) Expanded view of the electrophoretic trace for the μ-CZE analysis of proteins consisting of (1) chymotrypsinogen A; (2) cytochrome C; and (3) bovine serum albumin. (e) Expanded view for the μ-CEC analysis of a 1 kbp oligonucleotide ladder comprised of 517, 1018, 1636, 2036, 3054, 4072, 5090, 6108, 7126, 8144, 10 000, 15 000, 20 000, and 40 000 bp fragments. All concentrations used for the analyses are shown in the figure. Figures (b)–(e) were reconstructed from the data shown in (a). (Shadpour *et al*. 2007 [56]. Reproduced with permission of American Chemical Society.)

parallel microchip capillary zone electrophoresis (μ-CZE) and capillary electrochromatography (μ-CEC) and a bipolar-pulse voltage waveform with a pulse amplitude of 0.6 V and a frequency of 6.0 kHz allowed an LOD of 7.1 μM for alanine to be achieved as demonstrated in Figure 6.10.

Conductivity measurements have also been used for medical studies of dehydration. In one report, a conductometric sensor was developed for dehydration detection for athletes and soldiers [57]. The sensor was constructed with a PDMS microfluidic channel using a lithographic process. An AC voltage signal at a frequency of 10 kHz was used as the source voltage and the results reported a sensitivity to sodium solution.

6.3 Advanced Microfluidic Methodologies for Electrochemical Analysis

In Section 6.2, the application of different electrochemical analysis protocols has been reviewed, and the majority of the studies used simple single- or multiple-channel structures as the microfluidic structure. However, the flexibility of the microfluidic approach has allowed the development of many unique fluid handling platforms. In this section, we focus briefly on several more advanced architectures that have been developed for electrochemical applications.

6.3.1 The Rotating Microdroplet

Centrifugal microfluidic platforms take advantage of the forces acting on liquids in rotating chips, and these systems have been reported to offer several benefits in design and operation [58, 59]. The first is the simplicity of the actuation compared with those more traditional platforms driven by syringe pumps, gravity pumps, and peristaltic pumps. The second relates to sample handling, where in the centrifugal approach, a fluid can be sealed or contained within a controlled (often disk) structure. This is particularly important when handling potentially infectious samples. Technologically the centrifugal platforms have also been shown to achieve a wide range of flow rates and have less sensitivity to

www.ebook3000.com

physiochemical liquid properties such as viscosity, pH, or wetting behavior. This feature enables the handling of a wide range of solutions in sample analysis and disease diagnostics [60].

In more advanced studies, it has been reported that this technique can be integrated with microdroplet formation [61]. In one application of this, electrochemical velocimetry was introduced to study the flow in real time on rotating fluidic devices as shown in Figure 6.11.

6.3.2 The Microjet Electrode

Microjet devices generate fluid and concentration gradients by pneumatically ejecting a fluid out of a nozzle [62] with the jet impinging onto an electrode (Figure 6.12) or using two arrays sitting opposite to each other with the fluid impinging into a cell culture area [63]. The fluid-dynamic properties and gradient formation have been investigated optically by using time-lapse confocal fluorescence micrographs and fluorescently labeled dextrans as models of biological molecules [64].

There are several distinct benefits of microjet devices [64]. In single nozzle microjet measurements reported by Unwin *et al*., the flow field develops a highly

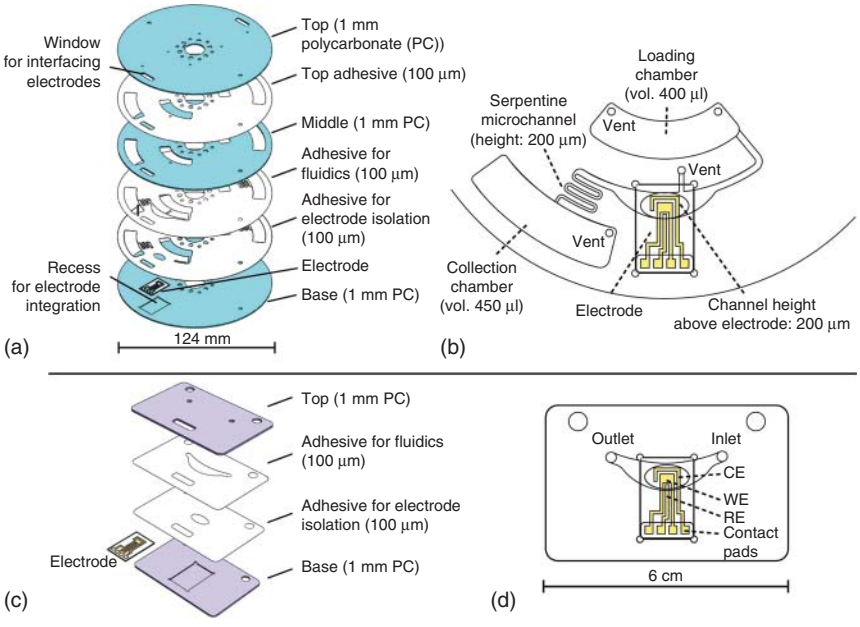


Figure 6.11 (a) Exploded view of a microfluidic disk with embedded electrodes for electrochemical velocimetry. Teal blue layers represent the 1 mm-thick polycarbonate layers, and white layers represent 100 mm-thick double-sided adhesive layers. (b) Details of the microfluidic disk design. (c) Exploded view of a stationary microfluidic device containing the same electrodes and a portion of the microfluidic design found in the disk. (d) Top view of the assembled stationary microfluidic device. Embedded within both the microfluidic disk and the stationary microfluidic chip is a set of miniaturized gold working (WE), reference (RE), and counter (CE) electrodes patterned onto a glass substrate. (Abi-Samra *et al*. 2013 [61]. Reproduced with permission of Royal Society of Chemistry.)

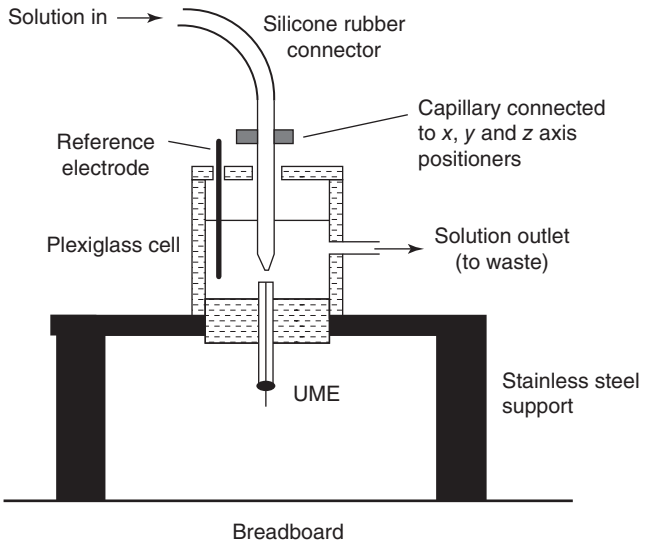


Figure 6.12 Schematic drawing (not to scale) of the microjet electrode. (Reprinted with permission from Ref. [62].)

nonuniformly accessible electrode, leading to a more mechanistically resolving approach for quantitative mechanistic analysis of redox reactions. In the dual array approach, the high-flow resistance enables steady-state gradients to be established for biological cell monitoring applications, without exposing cells to confounding. In addition, the gradients could be controlled dynamically and independently via the microjet devices.

6.3.3 Channel Multiplex

The development of multiplexed microchannels has also reported predominately for biological analysis applications. A low cost microfluidic platform has been reported for simultaneous electrochemical detection of multiplexed assays of different antibiotics [65]. The device employed dry film photoresist technology for microfabrication, which enabled a robust and convenient biosensor chip as shown in Figure 6.13. Different enzyme-linked assays were successfully accomplished via electrochemical evaluations. With a further modification, the detection limits of 6.33 and 9.22 ng ml^{-1} were obtained for tetracycline and pristinamycin, respectively.

In further developments, a multiplex electrochemical microreactor was designed to offer a point-of-care personalized device for qualitative detection of SjAb in human serum [66]. Screen-printed electrodes were employed to achieve low cost and reproductive devices. The antigens were immobilized on the interface of screen-printed carbon electrode array to capture SjAb. Furthermore, Munge *et al*. gave a detailed introduction on multiplex immunosensor arrays for cancer biomarker proteins employing electrochemical method [67]. Various nanomaterial-based methods were introduced to get sensitive and quick results for early-stage cancer diagnostics. They pointed out major challenges associated with reagent additions and washing steps for microchannels.

www.ebook3000.com

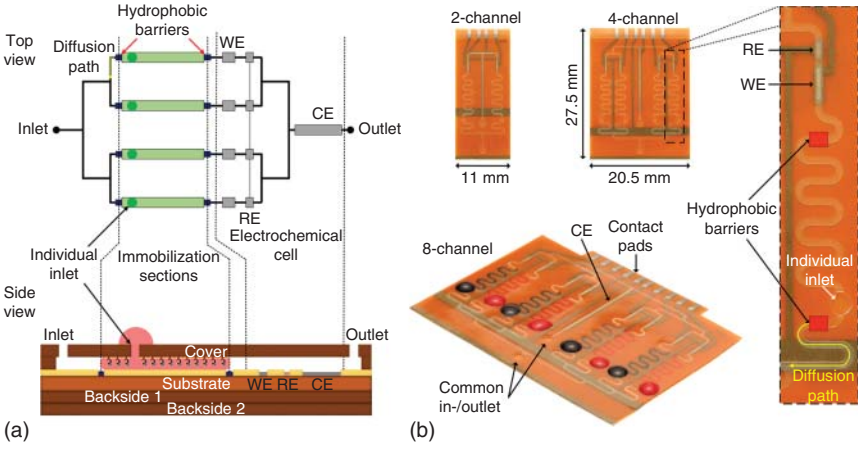


Figure 6.13 (a) Schematic top and side views of the microfluidic multiplexed platform. Different immobilization sections (green) in combination with a single electrochemical cell including multiple working electrodes (WEs), counter electrode (CE), and reference electrodes (RE) are arranged in a microfluidic network. Assay reagents (red) are loaded via the individual inlets by capillary force. (b) Photographs of the microfluidic biosensors comprising either two, four, or eight immobilization sections. Each immobilization section (of the 8-channel chip) is loaded with another assay reagent (red or black), passively metered by the hydrophobic barriers. A diffusion path is introduced to prevent any cross-talk between neighboring channels during the simultaneous readout. (Kling *et al*. 2016 [65]. Reproduced with permission of American Chemical Society.)

6.4 Numerical Modeling of Electrochemical Microfluidic Technologies

The previous sections have detailed the experimental development and applications of microfluidic devices using electrochemical analysis strategies. In many cases, quantitative kinetic and mechanistic information can be extracted from the measurements by application of appropriate numerical models of both the microelectrode and microfluidic properties of the devices. In this section, we will briefly review some of the key continuum methods implemented for electrochemical analysis of microengineered electrochemical reactors.

Numerical methods have long been applied in the field of electrochemistry, as a tool both to design or predict *a priori* experiments and to support analysis of experimental data. Though detailed methodologies differ, all of numerical procedures share these underlying steps:

1) Proposing physical model and corresponding (conservative) equations.
2) Discretization of the problem leads to finite number degree of freedoms.
3) Solving the equation systems.
4) Post-process results and derive desired values.

In FD approach, the modeled domain is divided into points or nodes (Figure 6.14). From conservation equations (mass, energy, or momentum), one desires to solve for the corresponding field variables (concentration,

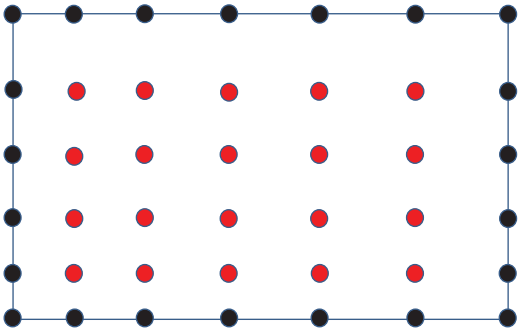


Figure 6.14 Solution approach in FD by breaking down the interested region into discrete points. Boundary nodes are colored black and interior ones are red.

temperature, velocity, etc.) at these nodes. Using Taylor expansions, these equations are discretized and can be used to relate the field values of a node to its neighborhood [68]. To close the problem, boundary conditions, being either Dirichlet (fixed boundary value) or Neumann (fixed boundary flux), are also discretized, finally leading to a system of equations. Routine solution methods (e.g., linear or nonlinear solvers) are then applied (step 3 above), and the process is repeated until convergence is achieved or other conditions are satisfied.

As FD can be simple in terms of both concept and implementation, it has been the method of choice for many practitioners both in electrochemistry and other areas such as biology [69]. A fast and reliable simulation method has been used for macroelectrode [70–72], microelectrode [73–75], and coupled chemical reaction problems in electrochemistry. A wide range of procedures are available for solution of the discretized model, with the alternating direction implicit (ADI) FD method popular for microelectrode applications [76, 77]. Recent reports also consider the effects of low supporting electrolytes, critically, these models evaluate the zero-field approximation used in simulations and numerically estimate the amount of supporting salts [78] that can produce diffusion-like cyclic voltammograms for a given redox system.

More complex structures have also been modeled, and it has been reported that approximate porous electrode structures can be approximated by constructing stacked layers of homogenous spherical electrodes on top of each other [79].

FD does however present some limitations in applicability especially when complex geometries are involved; in these cases often the FE is adopted to address these challenges. The FE approach employs a formulation that, instead of dividing a domain into a series of discrete points, divides the region into a set of smaller elements. The final solution is then approximated as polynomial combination of the field values at elements' nodes and shape functions. The FE approach involves integration across the elements and regions as opposed to local approximation seen in FD. Furthermore, boundary conditions are naturally accounted for during integration process.

Thanks to improvements in mathematical formulation and computer power, FE has become a standard analysis tool in many areas, for example, structural mechanics, fluid mechanics, heat transport, and soil mechanics. Its strength lies in flexibility to generate any mesh shape and adaptability to problems at hand.

www.ebook3000.com

In electrochemistry, FE is still less popular due to the higher complexity in code implementations.

In microengineering applications, the simulations of two-dimensional inlaid electrodes have been explored [80, 81]. Studies on stagnant [82] and flow environments have been reported [83] to numerically investigate the effects of protrusion heights and recession depths on current response (Figure 6.15).

Adaptive mesh refinement has been considered by many authors [84]. The underlying principle is straightforward: if errors in some elements exceed certain tolerance, then these elements are locally refined to achieve better solutions.

The increase in the development of microfluidic devices has also led to a greater activity in electrochemical modeling applications. The combination of microscale electrodes and microfluidic environments leads to more complex numerical solutions to the convection–diffusion equations. FE simulations [84] were employed to aid in the design and construction of devices used for electrochemical measurements as shown in Figure 6.16. Experimental studies were carried out with voltammetric measurements using organic and aqueous solutions containing ferrocene and potassium ferrocyanide, respectively, as a function of various flow rates. The numerical data demonstrated 3D fluid dynamics, and this fluid structure was used to quantify the current density on the working a microband electrode as a function of mass transport. Theoretical and experimental results were consistent, and a relationship between mass transport-limited current and volume flow rate was given.

Electrochemical applications using hydrodynamic modulation within microfluidic environments have also been modeled. FE studies were used to quantitatively explore the hydrodynamic modulation effects, notably modulations of the inlet pressure and harmonic oscillations of electrode disk, taking into account the time-variant nature of the fluid flow.

In addition to FD and FE approaches, other numerical methods have been reported to solve the system partial differential equations including finite volume [85] and lattice-Boltzmann approaches [86].

Nowadays there is a wide selection of numerical implementations for the above methods in many programming languages. Because of its mathematical simplicity, most of FD codes can be implemented in-house. For FE or FV, implementations are considerably more complex, and although in-house codes are

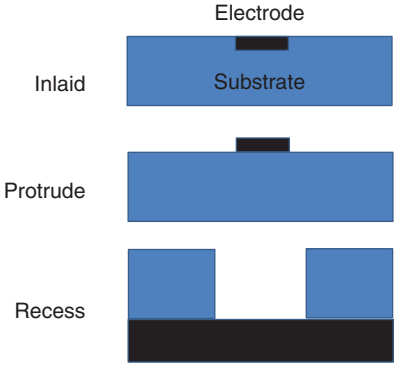


Figure 6.15 Due to fabrication process, the resulted electrode can be one of the three types: inlaid, protrude, or recess.

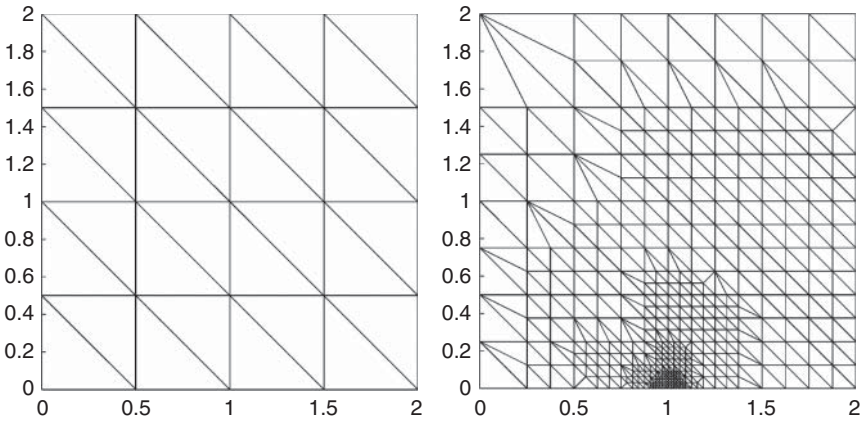


Figure 6.16 An example of adaptive mesh refinement for an inlaid disk. The starting mesh (top) is locally refined around the singular point 1 until tolerance is achieved (bottom). (Feldberg and Goldstein 1995 [85]. Reproduced with permission of Elsevier.)

still present, a significant focus has shifted to commercial software. Open-source codes (such as FreeFEM++) or proprietary packages such as COMSOL Multiphysics or Ansys offer automatic generation of geometry, meshing, solutions, and post-processing as well as visual graphics.

In addition, they are able to couple and solve multiphysics problems (e.g., mass diffusion under reactions and heat generations, fluid and solid structure interactions), thanks to extensive and well-developed libraries.

With commercial codes, the user concentrates on physical understanding of the problem and solution prototype rather than mathematical details. Thus, it tends to require less time and labor to solve a problem. However, the software cannot completely substitute the user's role. Since these methods are very general, good solutions are still required to certain inputs from users, especially the mesh refinement step to faithfully represent the problem in physics.

References

1 Riddiford, A.C. (1966) The rotating disk system, in *Advances in Electrochemistry and Electrochemical Engineering*, vol. **4** (ed. P. Delahay), Interscience, New York, London, pp. 47–116.
2 Albery, W.J., Hitchman, M.L., and Albery, W.J. (1971) *Ring-Disc Electrodes*, Clarendon Press, Oxford, pp. 17–28.
3 Albery, W.J. and Bruckenstein, S. (1966) Ring-disc electrodes. Part 2–Theoretical and experimental collection efficiencies. *Trans. Faraday Soc.*, **62**, 1920–1931.
4 Albery, W.J. and Brett, C.M. (1983) The wall-jet ring-disc electrode: Part I. Theory. *J. Electroanal. Chem. Interfacial Electrochem.*, **148** (2), 201–210.
5 Chin, D.T. and Tsang, C.H. (1978) Mass transfer to an impinging jet electrode. *J. Electrochem. Soc.*, **125** (9), 1461–1470.

www.ebook3000.com

6 Compton, R.G., Pilkington, M.B., and Stearn, G.M. (1988) Mass transport in channel electrodes. The application of the backwards implicit method to electrode reactions (EC, ECE and DISP) involving coupled homogeneous kinetics. *J. Chem. Soc., Faraday Trans. 1 F*, **84** (6), 2155–2171.

7 Fulian, Q., Stevens, N.P., and Fisher, A.C. (1998) Computer-aided design and experimental application of a novel electrochemical cell: the confluence reactor. *J. Phys. Chem. B*, **102** (19), 3779–3783.

8 Matsuda, H. (1967) Theory of the steady-state current potentials curves of redox electrodes reactions in hydrodynamic voltammetry. II Laminar pipe- and channel-flows. *J. Electroanal. Chem.*, **15**, 325–336.

9 Stevens, N.P., Gooch, K.A., and Fisher, A.C. (2000) Computational electrochemistry. Simulations of homogeneous chemical reactions in the confluence reactor and channel flow cell. *J. Phys. Chem. B*, **104** (6), 1241–1248.

10 Fulian, Q., Gooch, K.A., Fisher, A.C., Stevens, N.P., and Compton, R.G. (2000) Computer-aided design and experimental investigation of a hydrodynamic device: the microwire electrode. *Anal. Chem.*, **72** (15), 3480–3485.

11 Stevens, N.P. and Fisher, A.C. (1998) Transient voltammetry under hydrodynamic conditions. *Electroanalysis*, **10** (1), 16–20.

12 Stevens, N.P., Hickey, S.J., and Fisher, A.C. (1997) Finite element simulations in electrochemistry, in *Anales de química*, vol. **93**(4), , Springer-Verlag, pp. 225–232.

13 Stevens, N.P. and Fisher, A.C. (1997) Finite element simulations in electrochemistry. 2. Hydrodynamic voltammetry. *J. Phys. Chem. B*, **101** (41), 8259–8263.

14 Fulian, Q., Williams, N.A., and Fisher, A.C. (1999) Computational electrochemistry: three-dimensional boundary element simulations of double electrode geometries. *Electrochem. Commun.*, **1** (3), 124–127.

15 Fulian, Q., Fisher, A.C., and Denuault, G. (1999) Applications of the boundary element method in electrochemistry: scanning electrochemical microscopy. *J. Phys. Chem. B*, **103** (21), 4387–4392.

16 Fulian, Q., Fisher, A.C., and Denuault, G. (1999) Applications of the boundary element method in electrochemistry: scanning electrochemical microscopy, Part 2. *J. Phys. Chem. B*, **103** (21), 4393–4398.

17 Fulian, Q. and Fisher, A.C. (1998) Computational electrochemistry: the boundary element method. *J. Phys. Chem. B*, **102** (48), 9647–9652.

18 Whitesides, G.M. (2006) The origins and the future of microfluidics. *Nature*, **442** (7101), 368–373.

19 Compton, R.G. and Banks, C.E. (2007) *Understanding Voltammetry*, World Scientific, Singapore.

20 Grahame, D.C. (1952) Fiftieth anniversary: mathematical theory of the faradaic admittance pseudocapacity and polarization resistance. *J. Electrochem. Soc.*, **99**, 370C–385C.

21 Yunus, K. and Fisher, A.C. (2003) Voltammetry under microfluidic control, a flow cell approach. *Electroanalysis*, **15** (22), 1782–1786.

22 Henley, I.E., Yunus, K., and Fisher, A.C. (2003) Voltammetry under microfluidic control: computer-aided design development and application of novel microelectrochemical reactors. *J. Phys. Chem. B*, **107** (16), 3878–3884.

23 Sullivan, S.P., Johns, M.L., Matthews, S.M., and Fisher, A.C. (2005) Lattice Boltzmann simulations of electrolysis reactions: microfluidic voltammetry. *Electrochem. Commun.*, **7** (12), 1323–1328.

24 Fisher, A.C., Gooch, K.A., Henley, I.E., and Yunus, K. (2002) Voltammetry under microfluidic control. *Anal. Sci./Suppl.*, **17**, i371–i374.

25 Dryden, M.D., Rackus, D.D., Shamsi, M.H., and Wheeler, A.R. (2013) Integrated digital microfluidic platform for voltammetric analysis. *Anal. Chem.*, **85** (18), 8809–8816.

26 Lin, Y., Zhao, R., Thrall, K.D., Timchalk, C.A., Bennett, W.D., and Matson, D.W. (1999) Integration of microfluidics/electrochemical system for trace metal analysis by stripping voltammetry, in *Symposium on Micromachining and Microfabrication*, International Society for Optics and Photonics, pp. 248–256.

27 Wang, J., Polsky, R., Tian, B., and Chatrathi, M.P. (2000) Voltammetry on microfluidic chip platforms. *Anal. Chem.*, **72** (21), 5285–5289.

28 Bond, A.M. (1980) *Modern Polarographic Methods in Analytical Chemistry*, CRC Press.

29 Zoski, C.G. (2007) *Handbook of Electrochemistry*, Elsevier.

30 Matthews, S.M., Shiddiky, M.J., Yunus, K., Elton, D.M., Duffy, N.W., Gu, Y., Fisher, A.C., and Bond, A.M. (2012) Attributes of direct current aperiodic and alternating current harmonic components derived from large amplitude Fourier transformed voltammetry under microfluidic control in a channel electrode. *Anal. Chem.*, **84** (15), 6686–6692.

31 Ferguson, B.S., Buchsbaum, S.F., Swensen, J.S., Hsieh, K., Lou, X., and Soh, H.T. (2009) Integrated microfluidic electrochemical DNA sensor. *Anal. Chem.*, **81** (15), 6503–6508.

32 Hebert, N.E., Kuhr, W.G., and Brazill, S.A. (2002) Microchip capillary electrophoresis coupled to sinusoidal voltammetry for the detection of native carbohydrates. *Electrophoresis*, **23** (21), 3750–3759.

33 Hebert, N.E., Snyder, B., McCreery, R.L., Kuhr, W.G., and Brazill, S.A. (2003) Performance of pyrolyzed photoresist carbon films in a microchip capillary electrophoresis device with sinusoidal voltammetric detection. *Anal. Chem.*, **75** (16), 4265–4271.

34 Díaz-González, M., González-García, M.B., and Costa-García, A. (2005) Recent advances in electrochemical enzyme immunoassays. *Electroanalysis*, **17** (21), 1901–1918.

35 Woolley, A.T., Lao, K., Glazer, A.N., and Mathies, R.A. (1998) Capillary electrophoresis chips with integrated electrochemical detection. *Anal. Chem.*, **70** (4), 684–688.

36 Rackus, D.G., Shamsi, M.H., and Wheeler, A.R. (2015) Electrochemistry, biosensors and microfluidics: a convergence of fields. *Chem. Soc. Rev.*, **44** (15), 5320–5340.

37 Wu, Y., Lin, J.M., Su, R., Qu, F., and Cai, Z. (2004) An end-channel amperometric detector for microchip capillary electrophoresis. *Talanta*, **64** (2), 338–344.

38 Ruecha, N., Siangproh, W., and Chailapakul, O. (2011) A fast and highly sensitive detection of cholesterol using polymer microfluidic devices and amperometric system. *Talanta*, **84** (5), 1323–1328.

www.ebook3000.com

39 Joo, S., Park, S., Chung, T.D., and Kim, H.C. (2007) Integration of a nanoporous platinum thin film into a microfluidic system for non-enzymatic electrochemical glucose sensing. *Anal. Sci.*, **23** (3), 277–281.

40 Nie, D., Li, P., Zhang, D., Zhou, T., Liang, Y., and Shi, G. (2010) Simultaneous determination of nitroaromatic compounds in water using capillary electrophoresis with amperometric detection on an electrode modified with a mesoporous nano-structured carbon material. *Electrophoresis*, **31** (17), 2981–2988.

41 Won, S.Y., Chandra, P., Hee, T.S., and Shim, Y.B. (2013) Simultaneous detection of antibacterial sulfonamides in a microfluidic device with amperometry. *Biosens. Bioelectron.*, **39** (1), 204–209.

42 Hunter, R.A., Privett, B.J., Henley, W.H., Breed, E.R., Liang, Z., Mittal, R., Yoseph, B.P., McDunn, J.E., Burd, E.M., Coopersmith, C.M., Ramsey, J.M., and Schoenfisch, M.H. (2013) Microfluidic amperometric sensor for analysis of nitric oxide in whole blood. *Anal. Chem.*, **85** (12), 6066–6072.

43 Hunter, R.A. and Schoenfisch, M.H. (2015) S-nitrosothiol analysis via photolysis and amperometric nitric oxide detection in a microfluidic device. *Anal. Chem.*, **87** (6), 3171–3176.

44 Kellner, C., Botero, M.L., Latta, D., Drese, K., Fragoso, A., and O'Sullivan, C.K. (2011) Automated microsystem for electrochemical detection of cancer markers. *Electrophoresis*, **32** (8), 926–930.

45 Kim, T.H., Abi-Samra, K., Sunkara, V., Park, D.K., Amasia, M., Kim, N., Kim, J., Kim, H., Madou, M., and Cho, Y.K. (2013) Flow-enhanced electrochemical immunosensors on centrifugal microfluidic platforms. *Lab Chip*, **13** (18), 3747–3754.

46 Rattanarat, P., Teengam, P., Siangproh, W., Ishimatsu, R., Nakano, K., Chailapakul, O., and Imato, T. (2015) An electrochemical compact disk-type microfluidics platform for use as an enzymatic biosensor. *Electroanalysis*, **27** (3), 703–712.

47 Pluangklang, T., Wydallis, J.B., Cate, D.M., Nacapricha, D., and Henry, C.S. (2014) A simple microfluidic electrochemical HPLC detector for quantifying Fenton reactivity from welding fumes. *Anal. Methods*, **6** (20), 8180–8186.

48 Li, C.A., Han, K.N., Pham, X.H., and Seong, G.H. (2014) A single-walled carbon nanotube thin film-based pH-sensing microfluidic chip. *Analyst*, **139** (8), 2011–2015.

49 Han, Z., Chang, Y.Y., Au, S.W.N., and Zheng, B. (2012) Measuring rapid kinetics by a potentiometric method in droplet-based microfluidic devices. *Chem. Commun.*, **48** (10), 1601–1603.

50 Calvo-López, A., Arasa-Puig, E., Puyol, M., Casalta, J.M., and Alonso-Chamarro, J. (2013) Biparametric potentiometric analytical microsystem for nitrate and potassium monitoring in water recycling processes for manned space missions. *Anal. Chim. Acta*, **804**, 190–196.

51 Calvo-López, A., Ymbern, O., Puyol, M., Casalta, J.M., and Alonso-Chamarro, J. (2015) Potentiometric analytical microsystem based on the integration of a gas-diffusion step for on-line ammonium determination in water recycling processes in manned space missions. *Anal. Chim. Acta*, **874**, 26–32.

52 Lan, W.J., Zou, X.U., Hamedi, M.M., Hu, J., Parolo, C., Maxwell, E.J., Bühlmann, P., and Whitesides, G.M. (2014) Paper-based potentiometric ion sensing. *Anal. Chem.*, **86** (19), 9548–9553.

53 Lisak, G., Cui, J., and Bobacka, J. (2015) Paper-based microfluidic sampling for potentiometric determination of ions. *Sens. Actuators, B*, **207**, 933–939.

54 Lisak, G., Arnebrant, T., Ruzgas, T., and Bobacka, J. (2015) Textile-based sampling for potentiometric determination of ions. *Anal. Chim. Acta*, **877**, 71–79.

55 Galloway, M., Stryjewski, W., Henry, A., Ford, S.M., Llopis, S., McCarley, R.L., and Soper, S.A. (2002) Contact conductivity detection in poly(methyl methacrylate)-based microfluidic devices for analysis of mono- and polyanionic molecules. *Anal. Chem.*, **74** (10), 2407–2415.

56 Shadpour, H., Hupert, M.L., Patterson, D., Liu, C., Galloway, M., Stryjewski, W., Goettert, J., and Soper, S.A. (2007) Multichannel microchip electrophoresis device fabricated in polycarbonate with an integrated contact conductivity sensor array. *Anal. Chem.*, **79** (3), 870–878.

57 Liu, G., Smith, K., and Kaya, T. (2014) Implementation of a microfluidic conductivity sensor–a potential sweat electrolyte sensing system for dehydration detection. 36th Annual International Conference of the IEEE Engineering in Medicine and Biology Society, IEEE, pp. 1678–1681.

58 Burger, R., Amato, L., and Boisen, A. (2016) Detection methods for centrifugal microfluidic platforms. *Biosens. Bioelectron.*, **76**, 54–67.

59 Strohmeier, O., Keller, M., Schwemmer, F., Zehnle, S., Mark, D., von Stetten, F., Zengerle, R., and Paust, N. (2015) Centrifugal microfluidic platforms: advanced unit operations and applications. *Chem. Soc. Rev.*, **44** (17), 6187–6229.

60 Burger, R., Kirby, D., Glynn, M., Nwankire, C., O'Sullivan, M., Siegrist, J., Kinahan, D., Aguirre, G., Kijanka, G., Gorkin, R.A., and Ducrée, J. (2012) Centrifugal microfluidics for cell analysis. *Curr. Opin. Chem. Biol.*, **16** (3), 409–414.

61 Abi-Samra, K., Kim, T.H., Park, D.K., Kim, N., Kim, J., Kim, H., Cho, Y.-K., and Madou, M. (2013) Electrochemical velocimetry on centrifugal microfluidic platforms. *Lab Chip*, **13** (16), 3253–3260.

62 Macpherson, J.V., Marcar, S., and Unwin, P.R. (1994) Microjet electrode: a hydrodynamic ultramicroelectrode with high mass-transfer rates. *Anal. Chem.*, **66** (13), 2175–2179.

63 Keenan, T.M. and Folch, A. (2008) Biomolecular gradients in cell culture systems. *Lab Chip*, **8** (1), 34–57.

64 Keenan, T.M., Hsu, C.H., and Folch, A. (2006) Microfluidic "jets" for generating steady-state gradients of soluble molecules on open surfaces. *Appl. Phys. Lett.*, **89** (11), 114103.

65 Kling, A., Chatelle, C., Armbrecht, L., Qelibari, E., Kieninger, J., Dincer, C., Weber, W., and Urban, G. (2016) Multianalyte antibiotic detection on an electrochemical microfluidic platform. *Anal. Chem.*, **88** (20), 10036–10043.

66 Deng, W., Xu, B., Hu, H., Li, J., Hu, W., Song, S., Feng, Z., and Fan, C. (2013) Diagnosis of schistosomiasis japonica with interfacial co-assembly-based multi-channel electrochemical immunosensor arrays. *Sci. Rep.*, 3. doi: 10.1038/srep01789

www.ebook3000.com

67 Munge, B.S., Stracensky, T., Gamez, K., DiBiase, D., and Rusling, J.F. (2016) Multiplex immunosensor arrays for electrochemical detection of cancer biomarker proteins. *Electroanalysis*, **28** (11), 2644–2658.

68 Smith, G.D. (1985) *Numerical Solution of Partial Differential Equations: Finite Difference Methods*, Oxford University Press.

69 Obaid, H.A., Ouifki, R., and Patidar, K.C. (2013) An unconditionally stable nonstandard finite difference method applied to a mathematical model of HIV infection. *Int. J. Appl. Math. Comput. Sci.*, **23** (2), 357–372.

70 Rudolph, M. (1991) A fast implicit finite difference algorithm for the digital simulation of electrochemical processes. *J. Electroanal. Chem. Interfacial Electrochem.*, **314** (1), 13–22.

71 Rudolph, M. (1992) Digital simulations with the fast implicit finite difference (FIFD) algorithm: Part II. An improved treatment of electrochemical mechanisms with second-order reactions. *J. Electroanal. Chem.*, **338** (1), 85–98.

72 Feldberg, S.W. (1990) A fast quasi-explicit finite difference method for simulating electrochemical phenomena: Part I. Application to cyclic voltammetric problems. *J. Electroanal. Chem. Interfacial Electrochem.*, **290** (1), 49–65.

73 Aoki, K., Tokuda, K., and Matsuda, H. (1987) Theory of chronoamperometric curves at microband electrodes. *J. Electroanal. Chem. Interfacial Electrochem.*, **225** (1), 19–32.

74 Aoki, K., Akimoto, K., Tokuda, K., Matsuda, H., and Osteryoung, J. (1984) Linear sweep voltammetry at very small stationary disk electrodes. *J. Electroanal. Chem. Interfacial Electrochem.*, **171** (1), 219–230.

75 Heinze, J. (1981) Diffusion processes at finite (micro) disk electrodes solved by digital simulation. *J. Electroanal. Chem. Interfacial Electrochem.*, **124** (1–2), 73–86.

76 Gavaghan, D.J. (1998) An exponentially expanding mesh ideally suited to the fast and efficient simulation of diffusion processes at microdisc electrodes. 2. Application to chronoamperometry. *J. Electroanal. Chem.*, **456** (1), 13–23.

77 Gavaghan, D.J. (1998) An exponentially expanding mesh ideally suited to the fast and efficient simulation of diffusion processes at microdisc electrodes. 3. Application to voltammetry. *J. Electroanal. Chem.*, **456** (1), 25–35.

78 Dickinson, E.J., Limon-Petersen, J.G., Rees, N.V., and Compton, R.G. (2009) How much supporting electrolyte is required to make a cyclic voltammetry experiment quantitatively "diffusional"? A theoretical and experimental investigation. *J. Phys. Chem. C*, **113** (25), 11157–11171.

79 Barnes, E.O., Chen, X., Li, P., and Compton, R.G. (2014) Voltammetry at porous electrodes: A theoretical study. *J. Electroanal. Chem.*, **720**, 92–100.

80 Galceran, J., Cecı´ lia, J., Salvador, J., Monné, J., Torrent, M., Companys, E., Puy, J., Garcés, J.L., and Mas, F. (1999) Voltammetric currents for any ligand-to-metal concentration ratio in fully labile metal-macromolecular complexation. Easy computations, analytical properties of the currents and a graphical method to estimate the stability constant. *J. Electroanal. Chem.*, **472** (1), 42–52.

81 Penczek, M. and Stojek, Z. (1987) Current distribution at a submicrodisc electrode. *J. Electroanal. Chem. Interfacial Electrochem.*, **227** (1), 271–274.

82 Ferrigno, R., Brevet, P.F., and Girault, H.H. (1997) Finite element simulation of the chronoamperometric response of recessed and protruding microdisc electrodes. *Electrochim. Acta*, **42** (12), 1895–1903.
83 Ferrigno, R., Brevet, P.F., and Girault, H.H. (1997) Finite element simulation of the amperometric response of recessed and protruding microband electrodes in flow channels. *J. Electroanal. Chem.*, **430** (1), 235–242.
84 Gavaghan, D.J., Gillow, K., and Süli, E. (2006) Adaptive finite element methods in electrochemistry. *Langmuir*, **22** (25), 10666–10682.
85 Feldberg, S.W. and Goldstein, C.I. (1995) Examination of the behavior of the fully implicit finite-difference algorithm with the Richtmyer modification: behavior with an exponentially expanding time grid. *J. Electroanal. Chem.*, **397** (1), 1–10.
86 Du, G., Matthews, S.M., Johns, M.L., and Fisher, A.C. (2007) Computational electrochemistry: Lattice Boltzmann simulations of voltammetry at microelectrodes. *Electrochem. Commun.*, **9** (10), 2519–2524.

www.ebook3000.com

7

Microfluidic Devices for the Isolation of Circulating Tumor Cells (CTCs)

Caroline C. Ahrens, Ziye Dong, and Wei Li

Texas Tech University, Department of Chemical Engineering, 807 Canton Avenue, Lubbock, TX 79409, United States

7.1 Introduction

Cancer is well recognized as a major public health challenge throughout the world. In the United States specifically, cancer is expected to surpass heart disease as the leading cause of death in the next few years [1], and greater than one in three individuals is expected to develop invasive cancer during his or her lifetime [1]. These invasive or metastatic cancers are often deadly as they frequently are not amenable to surgical resection [2]. Cancer metastasizes when cancer cells leave the primary tumor site and travel to distant secondary or metastatic sites [3]. Circulating tumor cells (CTCs) are those specific cells that have left the primary or even metastatic tumors and entered into the peripheral blood. The most common immunohistologic characterization of a CTC is a nucleated EpCAM+/CK+/CD45− cell, although, as discussed in the following, such definitions continue to evolve as researchers better characterize the complex role of CTCs in disease. As CTCs are hypothesized to be precursors to metastasis [4], isolating CTCs has been a promising approach to better characterize both primary tumors and their metastases. CTCs have been identified as part of so-called liquid biopsies [5] in the blood of cancer patients, where quantifying the presence and character of these cells promises to be useful both for cancer detection and to direct cancer treatment [3, 6, 7].

Capturing these clinically relevant CTCs poses significant fundamental and engineering challenges because these cells are extremely rare compared with other cells in the blood and are not conclusively differentiated with a unique surface marker [8]. The number of CTCs detected in cancer patient blood is often as low as a few cells per milliliter [9], corresponding to tens of cancer cells among billions of blood cells. The first and only FDA-approved device for CTC detection is the CellSearch platform (currently licensed by Janssen Diagnostics) [10], which achieved FDA approval in 2004. This test isolates cells having the surface marker epithelial cell adhesion molecule (EpCAM). Patient whole blood is incubated with anti-EpCAM antibodies conjugated to magnetic beads and then isolated via magnetic separation. While the CellSearch platform

Microfluidics: Fundamentals, Devices and Applications, First Edition.
Edited by Yujun Song, Daojian Cheng, and Liang Zhao.
© 2018 Wiley-VCH Verlag GmbH & Co. KGaA. Published 2018 by Wiley-VCH Verlag GmbH & Co. KGaA.

has shown the prognostic utility of CTC detection in breast [11], colon [2], and prostate cancers [12], it is limited in its ability to detect only the subpopulation of EpCAM presenting CTCs [13, 14] and involves destructive postprocessing, thereby precluding additional assays that require viable cells. These limitations have motivated the development of numerous follow-on approaches both to capture a more complete and comprehensive panel of patient CTCs and to better characterize this clinically useful cell population.

The application of microfluidics to CTC capture and detection has been an especially promising approach to improve established benchtop methods of CTC isolation and characterization. Compared with the CellSearch platform 10 and isolation by size of epithelial tumor cells (ISET) (Rarecells) [15], an early now-commercialized benchtop technology, microfluidic systems, offers the potential for many advantages including high throughput, low reagent volumes, high sensitivity, a small footprint, a length scale similar to that of cellular systems, and ready automatic operation allowing integrated loading, separation, and analysis. The extreme flow control coupled with high surface-to-volume ratios enhances the techniques dependent on surface capture. Further, the small length scales allow microscale phenomenon governed by low Reynolds number and the dominant role of laminar flow and viscous forces [16]. While various materials have been used to fabricate microfluidic devices for CTC studies, polydimethylsiloxane (PDMS) has been especially useful in prototyping technologies and advancing the applications of microfluidics in this field due to its cost efficiency, optical properties, biological compatibility, and ease of manufacture [17]. Despite such promise, significant technical hurdles remain including the slow processing speed inherent to microflow, nonspecific binding, and significant processing variability [18].

In comparing the many microfluidic and benchtop platforms put forward to characterize cancer cells in patient blood [19], a growing consensus is that a single technology may not be optimal for every end application [20]. CTC screening for early cancer detection might prioritize different device performance criteria than applications targeting patient-specific drug screening on isolated CTCs. However, we suggest that each technology might generally be evaluated as optimizing performance by balancing the following parameters:

- Efficient CTC capture (high yield): Especially for screening purposes, a technology should capture CTCs from a wide variety of cancers across all stages of disease progression. For applications intended to monitor and direct treatment, efficient capture is essential to ensure that the recovered CTCs are representative of the CTC population within a patient's blood and to allow sufficient cancer material for subsequent genomic, proteomic, or phenotypic analyses. Whereas established approaches have targeted efficient capture of the full population of CTCs, future work is expected to target a specific subpopulation of CTCs identified as especially clinically relevant.
- High isolation specificity or purity: CTC counting and characterization both require sufficient removal of the large number of normal blood cells. Purity is especially important when captured cells are analyzed in bulk without additional purification.
- High throughput: Due to the small number of CTCs within the blood and the limited stability of CTCs within the blood microenvironment, clinically

www.ebook3000.com

applicable CTC capture technologies should quickly process large sample volumes.

- Nondestructive cell capture and culture: Significant interest has developed in the expansion and culture of captured cells most notably directed toward patient-specific drug screening [21]. These more intricate phenotypic analyses require the isolation of viable cancer cells that maintain *in vivo*-like cell responsiveness.

Looking forward, engineers must continue to collaborate with scientists and clinicians to define evaluating metrics for specific devices, as complete CTC capture might not be the only engineering objective. Together two recent studies showcase the opportunity to extend detection beyond CTC count. First, the Southwest Oncology Group (SWOG) S0500 clinical trial found that for the specific cohort of metastatic breast cancer patients, patient survival was not enhanced by CTC enumeration-directed treatment [22]. Second, a trial directed by the company Epic Sciences identified a treatment-specific marker in CTCs as directing drug therapies for castration-resistant prostate cancer patients [23]. These studies suggest that specific applications may dictate isolation and characterization of a targeted subset of what are now considered CTCs and highlight the rapid development in the clinical applications of CTC capture technologies.

This chapter outlines the application of microfluidic devices to CTC capture with a focus on those that have been validated in a clinical setting with CTC capture from patient blood (Table 7.1). We detail nine specific detection strategies

Table 7.1 Microfluidic devices for isolation of circulating tumor cells (CTCs).

Microfluidic devices	Capture approach	Key attributes	Clinical validation	References
CTC-Chip	Antibody-coated microposts	Micropost array allows optimal antibody cell contact; flow rates of 1–2 ml h^{-1}	Breast, colon, lung, pancreatic, prostate	[24]
Geometrically enhanced differential immunocapture (GEDI)	Antibody-coated microposts integrated with size-based separation	Integrates numerous detection antibodies; enhanced purity with size-based preseparation	Breast, gastric, pancreatic, prostate	[25–28]
OncoBean Chip	Antibody-coated microposts in radial flow	Radial flow allows rapid flow rate (10 ml h^{-1}) and capture along a gradient of shear stress	Breast, lung, pancreatic	[29]
HB-Chip	Antibody-coated surface with structural micromixing	Herringbone structure increases mixing, enzymatic and thermal release of captured cells	Breast, lung, prostate	[30]
High-throughput microsampling unit (HTMSU)	Antibody-coated surface of sinusoidal channels	Integrates capture, electrochemical detection, and mRNA analysis; commercialized by BioFluidica	Multiple myeloma, pancreatic (PDX model)	[31–33]

(Continued)

Table 7.1 (Continued)

Microfluidic devices	Capture approach	Key attributes	Clinical validation	References
NanoVelcro Rare Cell Assays	Antibody/aptamer-coated nanostructured surface	Multiple generations of devices optimized for specific clinical application including *ex vivo* expansion and single-cell assays	Lung, melanoma, pancreatic, prostate	[34]
GO Chip	Antibody-coated graphene oxide surface	Nanostructure increases effective capture area; cells can be cultured on device (1–3 ml h^{-1})	Breast, lung, pancreatic	[35]
CTC subpopulation sorting chip	Antibody-based magnetic-activated cell sorting through varied velocity chambers	Profiles CTC surface marker heterogeneity	Prostate	[36]
CTC-iChip	Hydrodynamic sorting, inertial focusing, and magnetically activated cell antibody sorting	Operates through positive capture or negative depletion; 10 ml h^{-1}; licensed by Janssen	Breast, colorectal, lung, pancreatic, prostate	[37, 38]
SB membrane	CTC capture between 40 µm focusing pore and 8 µm capture pores	Low shear stress allows recovery of viable cells	Tested in mouse model	[39]
CTC cluster chip	Clusters trapped in bifurcating traps under low shear flow	CTC clusters identified in 30–40% of a variety of tumors, some 2 cell clusters	Breast, melanoma, prostate	[40]
Multiplex spiral device	Larger cells (CTCs) pushed outward in spiral flow through Dean flow fractionation	Rapid processing; trapezoidal channel is commercialized by Clearbridge BioMedics as the ClearCell FX	Breast, lung	[41–44]
Vortex	Larger cells (CTCs) captured in microvortices and released by decreasing flow	Captures viable cells, no preprocessing; clusters observed	Breast, lung	[45, 46]
Multiorifice flow fractionation (MOFF)	Larger cells are moved to channel center through series of expansion and contraction	Multiple processing increases capture efficiency; high purity	Breast	[47, 48]
ApoStream	Dielectrophoresis with inertial separation	Continuous-flow, label-free capture; commercialized and used in many clinical trials	Bladder, breast, hepatocellular, lung, prostate	[49]
taSSAW	Tilted-angle standing surface acoustic waves (taSSAWs)	Label-free, 1.2 ml h^{-1} blood equivalent; developing technology	Lung	[50]

www.ebook3000.com

employing aspects of affinity-based CTC detection (e.g., the isolation of cancer cells using specific surface makers) and also introduce an overview to the field of nonaffinity-based detection (e.g., filtration, hydrodynamic, and dielectrophoresis (DEP) methods to isolate cancer cells based on physical properties such as cell size and deformability and dielectric properties). These approaches, integrated into a microfluidic device either independently or in combination, offer great potential to expand the application of CTCs to improve patient health.

7.2 Affinity-Based Enrichment of CTCs

In traditional affinity-based CTC enrichment (Figure 7.1), an antigen or marker on the outer cell membrane of a tumor cell is bound to a corresponding affinity capture unit tethered to a solid surface. An example is the CellSearch device discussed previously where the EpCAM protein on a cancer cell surface is captured by anti-EpCAM antibodies conjugated to magnetic beads, thereby magnetically labeling only EpCAM-expressing cells [10]. A magnetic field can be applied to isolate labeled cells from the bulk blood. Subsequent affinity capture devices have explored alternative geometries and choices of capture ligands.

The majority of established microfluidic affinity-based CTC capture techniques operate through a related general technique, specifically the selective arrest of flowing cells by stationary antibody-coated solid surfaces or microstructures. These surfaces are designed to encourage maximum contact between the flowing cells and capture surfaces with minimum processing time. While most early devices targeted cells derived from epithelial cancers expressing EpCAM, the limitations of using this single marker for universal cancer detection have been broadly recognized [14, 51]. Cancers derived from stromal cells would never be expected to have epithelial markers, and even CTCs from primary tumors of epithelial origin may lose their epithelial markers prior to entering circulation during an epithelial-to-mesenchymal transition (EMT) [52]. New technologies have employed a growing number of alternative markers including prostate-specific membrane antigen (PSMA) [25, 53] that is conserved during EMT [54], mesenchymal markers including cell surface vimentin [55], and panels of antibodies targeting cancer-specific antigens such as human epidermal growth factor receptor 2 (HER2) and epidermal growth factor receptor (EGFR) [56]. An alternative to positive selection of the CTCs is the so-called negative selection or the removal of blood cells through positive selection with a white blood cell (WBC)-specific marker such as CD45 or CD15 [37, 57–59]. Finally, technologies have also expanded beyond antibody capture, most notably to aptamer-based CTC target recognition. These synthetic DNA or RNA oligonucleotide ligands can be optimized to specifically recognize target molecules with affinities comparable with that of antibody–antigen interactions [60]. As outlined in the recent review [60], aptamers have seen growing applications in CTC capture and identification and represent a promising alternative to antibodies for developing a universal capture strategy.

Recent technologies have extended affinity-based techniques beyond optimizing only for efficient capture to the so-called next generation of capture

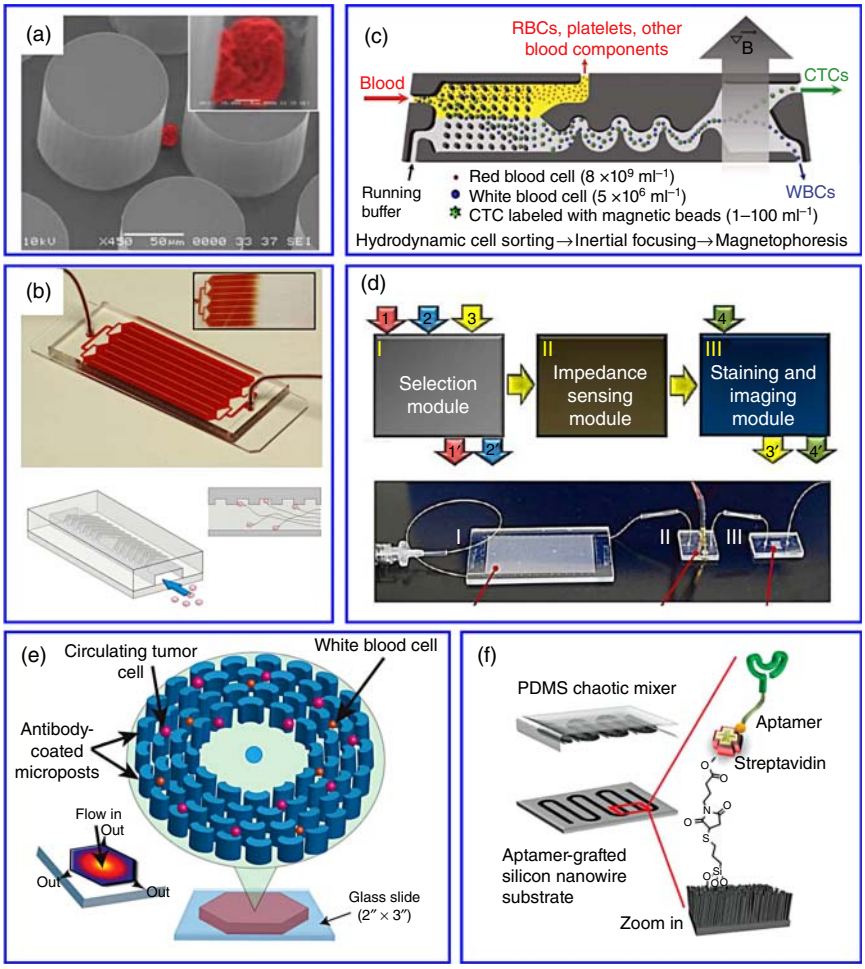


Figure 7.1 Affinity-based enrichment of CTCs. (a) CTC-Chip: scanning electron microscope image of a captured NCI-H1650 lung cancer cell spiked into the blood (pseudo-colored red). The inset shows a high magnification view of the cell. (Nagrath *et al*. 2007 [24]. Reproduced with permission of John Wiley & Sons.) (b) The HB-Chip consists of a microfluidic array of channels with a single inlet and exit. Inset illustrates the uniform blood flow through the device. (Stott *et al*. 2010 [30]. Copyright 2010. Reproduced with permission from United States National Academy of Sciences.) (c) Schematic of three microfluidic components of the CTC-iChip. (Ozkumur *et al*. 2013 [38]. Copyright 2013. Reproduced with permission from United States National Academy of Sciences.) (d) Schematic representation of the modular HTMSU microfluidic system for CTC analysis and a picture of the assembled systems. (Kamande *et al*. 2013 [31]. Reproduced with permission of American Chemical Society.) (e) Schematic representation of the OncoBean Chip. (Murlidhar *et al*. 2014 [29]. Reproduced with permission of John Wiley & Sons.) (f) Schematic representation of aptamer cocktail-based CTC assay in a version of the NanoVelcro Rare Cell Assay. (Zhao *et al*. 2016 [34]. Reproduced with permission of John Wiley & Sons.)

www.ebook3000.com

technologies [20]. New affinity-based devices integrate both selective capture and triggered release of CTCs. Differential affinity capture strategies have allowed high-throughput characterization of patient CTC heterogeneities [36] by integrating capture strategies that inherently differentiate and identify CTC subpopulations. Capture cells can be released and recovered from the device by incorporating various release mechanisms including those enzymatically [31, 61] or thermally [56, 62] triggered. Finally, the field is rapidly developing techniques for the capture of viable cells appropriate for on-chip culture and expansion [35] as well as methods for incorporating on-chip phenotypic assays [63].

The following section introduces nine prominent approaches to affinity-based CTC capture in microfluidic devices.

7.2.1 CTC-Chip

The CTC-Chip (Figure 7.1a) was the first technology to extend established immunomagnetic capture to capture through a microfluidic device in which cells flowing through the device are arrested by tethered antibodies [24]. It consists of an etched silicon chip containing 78 000 high aspect ratio posts designed both to promote optimized flow and to allow maximum interior surface area for anti-EpCAM antibody conjugation and cancer cell capture. It was also shown to have capture efficiencies greater than 65% when isolating cancer cell lines spiked into whole human blood flowing at a rate of $2\,\mathrm{ml\,h^{-1}}$. Capturing cells directly from whole blood represented a significant improvement over previously developed processes that required blood preprocessing, such as red blood cell (RBC) lysis. These preprocessing steps increased the processing time and potentially reduced CTC retention. Capture purity, which is defined as the ratio of captured cancer cells to captured contaminating WBCs, was reported around 9%. The CTC-Chip was used to isolate CTCs in 115 of 116 cancer patients, where CTCs were defined as cells identified by immunostaining as being negative for CD45 and positive for cytokeratin (CK). However, the device presented several practical challenges. The relatively tall device introduced difficulties in imaging captured cells in various z planes. Further, the CTC-Chip showed limited throughput, as capture efficiency dramatically decreased at flow rates higher than $2.5\,\mathrm{ml\,h^{-1}}$ likely due to insufficient time for the cells to contact the device walls. In 2008, the same group demonstrated the utility of the CTC-Chip for patient treatment by using DNA recovered from the CTC-Chip to identify EGFR mutations in captured CTCs [6].

7.2.2 Geometrically Enhanced Differential Immunocapture (GEDI)

In the geometrically enhanced differential immunocapture (GEDI) microfluidic device, staggered octagonal microposts generate optimized flow trajectories that direct larger CTCs toward capturing antibody-coated posts, thereby enhancing the overall device capture efficiency and selectivity [26]. GEDI-based capture is particularly noteworthy due to its extensive computational optimization and its early integration of diverse antibody-based capture strategies. In the first generation of the GEDI device, arrest of prostate cancer cells was mediated not by EpCAM but rather by PSMA, a cell surface marker thought to be preserved

during EMT [54]. The device showed 85% capture efficiency for LnCAP cancer cells spiked into whole blood at a flow rate of 1 ml h^{-1}. Moreover, GEDI devices successfully detected CTCs in 90% of human patients with castrate-resistant prostate cancer with greater than 60% purity, where a CTC was defined as a PSMA+/CD45− cell [26]. Isolated cells were further characterized by cDNA sequencing and immunostaining to identify cells containing mutated androgen receptors. This technology was later computationally optimized and extended to allow anti-HER2-based CTC capture in the blood from breast and gastric cancer patients [27]. Most recently, pancreatic cells were isolated using a combination of anti-EpCAM and cancer-specific mucin 1 (MUC1) antibodies [28].

7.2.3 Herringbone (HB)-Chip

The principles for microfluidic affinity capture through disrupted laminar flow pioneered with micropost affinity capture strategies were extended to design the HB-Chip (Figure 7.1b), a patterned planar capture device [30]. Rather than relying on microposts, Stott *et al.* fabricated a PDMS device in a herringbone pattern, a design that had been previously established as promoting microvortices and turbulent flow [30]. The so-called HB-Chip integrated repeating herringbone patterns onto the top surface of the microchannels and coated the entire device interior with anti-EpCAM antibodies through a series of chemical conjugations. Compared with capture through microposts, surface capture as demonstrated with the HB-Chip is more amenable to large-scale production and allows fabrication through a wider variety of transparent materials, thereby integrating more straightforward imaging of captured cells. Compared with the CTC-Chip, devices that integrate the microvortex-generating herringbone pattern maintained high capture efficiency and purity even at higher flow rates. The HB-Chip demonstrated a capture efficiency of 92% and purity of about 14% when isolating cancer cell lines spiked into whole blood flowing at a rate of 1.2 ml h^{-1} and, significantly, maintained a capture efficiency of greater than 40% when flow rate was increased to 4.8 ml h^{-1}. In patient samples, it captured CTCs in the whole blood of 14 of 15 metastatic prostate cancer patients. Fluorescence *in situ* hybridization (FISH) was successfully performed on the device, and downstream processing recovered the RNA appropriate for RT-PCR. In addition to isolating single cells, the gentle processing was shown to also isolate intact CTC clusters [30], where clusters of CTCs have been identified as significant contributor to CTC-mediated metastasis [65]. Subsequent extensions of the original HB-Chip have tethered affinity antibodies through a sacrificial polymer layer. Bulk enzymatic degradation [61] or localized heating [56] in these degradable systems maintains high capture efficiencies while allowing triggered release of viable cells appropriate for downstream culture and functional assays [21].

7.2.4 CTC-iChip

The CTC-iChip (Figure 7.1c) is the newest-generation microfluidic device developed by the Toner research group and combines affinity-based separation techniques with inertial techniques [38]. In inertial-based preseparation, RBCs and platelets are removed from whole blood in a technique known

www.ebook3000.com

as deterministic lateral displacement (DLD), as discussed in more detail in the following section. The remaining WBCs and CTCs are incubated with antibody-conjugated magnetic particles. For so-called positive selection, cells are incubated with microparticles coated with anti-EpCAM antibody targeting CTCs, while for negative selection cells are exposed to CD45 and CD15 antibodies targeting WBCs. The cells are then passed through an asymmetric inertial focusing channel that aligns the cells before they are being subjected to magnetic defection. In positive mode, the labeled CTCs are deflected and isolated, whereas in negative mode the labeled WBCs are removed, leaving a population enriched in CTCs. Both positive and negative selection enabled greater than 75% recovery of several cancer cell lines spiked into whole blood, with recovery of SKBR3 breast cancer cells being greater than 98%. The CTC-iChip used in the negative mode successfully recovered CTCs from the blood of patients having cancer types not readily isolated through EpCAM-based capture. In particular, the negative depletion method was used to identify CTCs in patients with melanoma and triple-negative breast cancer, for which CTCs typically display primarily mesenchymal markers and are not captured by most positive isolation techniques. A final significant improvement in the CTC-iChip compared with previous technologies is its rapid blood processing, with throughput up to $10\,\mathrm{ml\,h^{-1}}$ processing whole blood. This technology continues to develop. A recent publication introduces improved negative depletion through beads conjugated to a combination of anti-CD66b, anti-CD45, and a granulocyte marker [37]. Such continuing studies demonstrate the versatility of the CTC-iChip for capturing a wide variety of CTC subpopulations.

7.2.5 High-Throughput Microsampling Unit (HTMSU)

In an initial design, the high-throughput microsampling unit (HTMSU affinity-based CTC enrichment) (Figure 7.1d) promoted antibody-based CTC arrest to the surface of 51 parallel serpentine microchannels coated with anti-EpCAM [32]. Fabrication through hot embossing of plastic, rather than the more common soft lithography, enables this efficient capture to sinusoidal surfaces that have a high aspect ratio and thereby large antibody-functionalized surfaces. Importantly, in subsequent modules, an integrated platinum conductivity sensor allows immediate label-free counting based on distinct cancer cell conductivity compared with that of WBCs. Cancer cells spiked into whole blood were captured with up to 97% efficiency. The captured cells could be released with exposure to trypsin, a relatively nonspecific proteolytic enzyme frequently used in cell culture, and immediately characterized using an integrated conductivity sensor. The device was extended to increase throughput and fully integrate an impedance sensor within a three-module device achieving (i) capture, (ii) rapid label-less CTC counting through impedance spectroscopy, and (iii) assembly of released CTCs onto a 2D grid for cell staining and imaging [31]. This device successfully detected a mean of 53 CTCs $\mathrm{ml^{-1}}$ from patients with metastatic pancreatic ductal adenocarcinoma (PDAC) and 11 CTCs $\mathrm{ml^{-1}}$ from patients with local PDAC [31]. As an additional proof of clinical utility, in 2014, HTMSU detection was applied to quantifying CTC burden in a patient-derived xenograft (PDX) mouse model of

PDAC. EpCAM-functionalized HTMSU devices were used to track CTC number as a biomarker of response to treatment [33]. The study showed that mice with the targeted therapy had significantly reduced CTC burden compared with those receiving vehicle controls.

7.2.6 OncoBean Chip

The OncoBean Chip (Figure 7.1e) was designed for ultrahigh-throughput affinity-based CTC isolation through integrating radial flow, in contrast to the linear flow common to other microfluidic separation techniques [29]. Since velocities decrease with increased cross-sectional area, capture across a range of shear rates decreasing radially from the center is introduced. Capture antibodies uniformly coat the surface of an array of bean-shaped posts. It is hypothesized that the constant affinity capture coupled with the varied shear rates allows a cell to be captured at its optimal radial position as determined by its surface antigen expression. Cancer cell lines were isolated from whole blood with greater than 80% efficiency and greater than 93% viability at the rapid flow rate of 10 ml h^{-1}. Clinical applicability was demonstrated through isolation of cancer cells from breast, pancreatic, and lung cancer patient blood [29].

7.2.7 NanoVelcro Rare Cell Assays

Integrating nanoscale engineering into microfluidic CTC capture devices offers opportunities to increase device performance as demonstrated through the so-called NanoVelcro device. In an early generation of the NanoVelcro microfluidic chip, a silicon nanopillar (SiNP) array grafted with targeted capture antibodies was assembled into a microfluidic device integrated with a chaotic micromixer [66]. MCF-7 breast cancer cell lines were captured from culture medium with 45–65% efficiency and high captured cell viability. Improved capture efficiency compared to a non-patterned surface is attributed to the high surface area of these nanopillars and optimized mixing strategies. This original geometry has been additionally iterated to incorporate improved nanostructures, capture strategies, and post-capture processing techniques. Extending the technology and demonstrating compatibility with patient samples, CTCs purified from lung cancer patients were effectively captured and released, where release was triggered by cooling the microfluidic device from 37 to 4 °C [67]. This rapid and gentle release enabled ready genomic analysis of capture CTCs and serial monitoring [62]. More recently, the NanoVelcro platform successfully achieved sensitive and differentiated capture of CTCs from non-small cell lung carcinoma (NSCLC) patients using aptamer-based capture (Figure 7.1f) [34]. The evolution of the NanoVelcro platform and its diverse clinical applications is outlined in a recent review [68].

7.2.8 GO Chip

The GO Chip has achieved highly sensitive and selective capture of CTCs to antibodies tethered to a graphene oxide (GO) surface [35]. Similar to the principles enabling capture through NanoVelcro, the high surface area-to-volume

www.ebook3000.com

ratio inherent in the GO nanomaterial dramatically increases both sensitivity and selectivity of cancer cell capture compared with pure 2D capture while maintaining an effectively 2D surface. GO nanosheets were first assembled onto 58 957 flower-shaped patterned gold surfaces and then chemically functionalized with EpCAM antibodies. The GO Chip successfully isolated cancer cell lines spiked into donor blood with high sensitivity of greater than 94% and high purity with a flow rate of 1 ml h^{-1}. In a demonstration of clinical utility, it was used to isolate CTCs from early-stage lung cancer, metastatic prostate cancer, and metastatic breast cancer patients. All cancer patients had at least 2 CTCs captured per milliliter of blood, with as many as 23 CTCs ml^{-1} from one patient sample. No CTCs were identified in healthy controls. Finally, captured spiked MCF-7 cells were cultured on the capture surface for 6 days, which suggests the future potential for *in situ* culture and phenotypic characterization of captured patient cells.

7.2.9 CTC Subpopulation Sorting

Whereas microfluidic affinity-based technologies presented previously rely on capture to a solid surface, most conventional benchtop CTC affinity-based detection methods, such as the CellSearch platform, isolate targeted cells through magnetic-activated cell sorting (MACS). Both benchtop and microfluidic applications of MACS first label targeted cells with antibody-conjugated magnetic beads and then capture labeled particles through local magnetic fields. Several devices integrating microfluidics and MACS have been highlighted in a recent review [69, 70]. Here we highlight one specific device, a CTC subpopulation sorting chip, that extends micro-MACS to both capture and characterize CTCs. The CTC subpopulation sorting chip processes samples by first incubating whole blood containing CTCs with anti-EpCAM-conjugated nanoparticles before flowing blood into a microfluidic device incorporating capture regions that each experience a magnetic field [36]. Each subsequent cell capture zone has decreasing overall velocity and incorporates microscale X-shaped obstacles introducing localized regions of low flow appropriate for magnetically mediated cell arrest. Magnetically labeled CTCs are trapped in specific zones as dictated by their surface EpCAM expression levels, where, for example, only highly magnetically labeled cells having high concentrations of surface EpCAM are arrested from the rapid flow in the first zone. The device was successful in profiling heterogeneous EpCAM expression levels in cells isolated from prostate cancer patient blood.

7.3 Nonaffinity-Based Enrichment of CTCs

An alternative to affinity-based CTC enrichment relies on label-free CTC separation dictated by distinct physical properties of CTCs and blood cells (Figure 7.2). As highlighted in a recent review, the size of cancer cells and WBCs measured in area or diameter varies widely based on the measurement method and the individual sample characteristics. Nonetheless, CTCs were determined to have

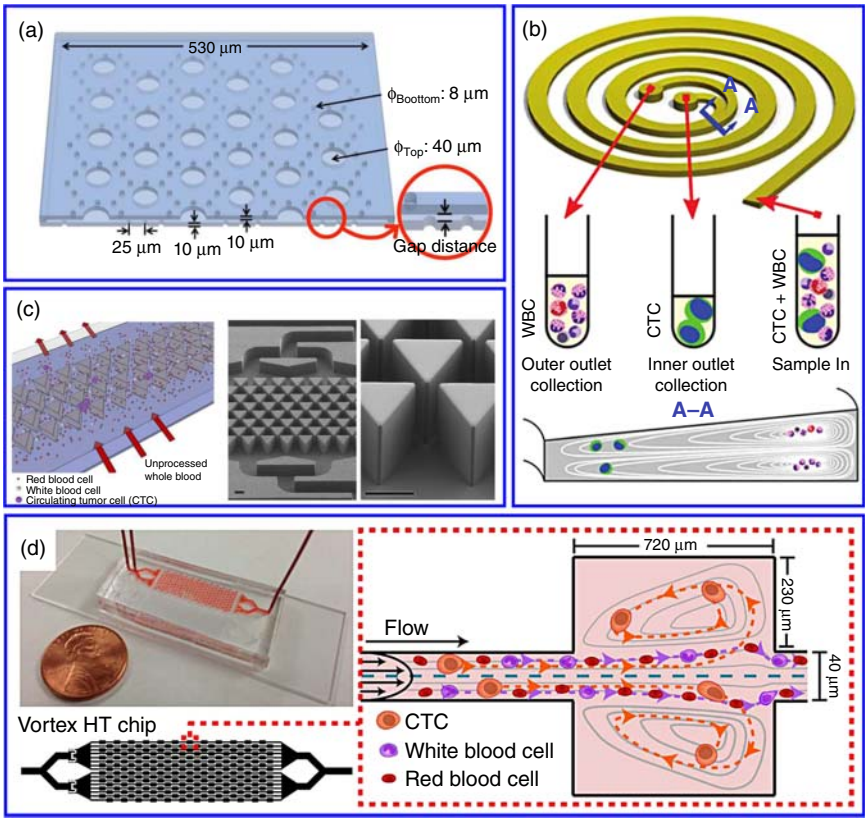


Figure 7.2 Nonaffinity-based enrichment of CTCs. (a) A 3D view of an elemental unit model of the separable bilayer (SB) filter with key geometrical parameters labeled, including the gap distance in the inset. (Zhou *et al*. 2014 [39]. Reproduced with permission of Nature Publishing Group.) (b) Operating principle of CTC enrichment by a spiral channel with a trapezoidal cross section (80/130 μm: inner/outer channel height). (Warkiani *et al*. 2014 [41] http://pubs.rsc.org/-/content/articlehtml/2014/lc/c3lc50617g. Used under CC BY 3.0 https://creativecommons.org/licenses/by-nc/3.0/.) (c) Schematics and SEM micrographs of the cluster chip that captures CTC clusters from unprocessed whole blood; scale bars, 60 μm. (Sarioglu *et al*. 2015 [40]. Reproduced with permission of Nature Publishing Group.) (d) Digital photo and schematic of High Throughput Vortex Chip (Vortex HT). (Che *et al*. 2016 [45] https://www.ncbi.nlm.nih.gov/pmc/articles/PMC4914319/. Used under CC BY 3.0 https://creativecommons.org/licenses/by/3.0/.)

diameters ranging from 12 to 25 μm, and WBCs range from 8 to 14 μm [71]. Therefore, at least a subset of a patient's CTCs is expected to be bigger than blood cells and have distinct deformation properties [9]. These differences allow CTCs to be isolated from bulk blood without relying on surface markers and instead use various filtration and inertial separation strategies [7]. ISET (Rarecells Diagnostics) is a commercially available benchtop technology that demonstrated early on the utility of size-based capture. The device captured and characterized those epithelial-derived cells unable to pass through a polycarbonate membrane filter with 8 μm pores [15]. In comparison studies, many of these cells were not

www.ebook3000.com

identified as CTCs by the affinity-based CellSearch approach [72]. However, the largest WBCs are usually larger than the smallest CTCs, making both high yield and high purity CTC isolation challenging using only nonaffinity techniques [9].

The rapidly innovating field of label-free CTC enrichment has extended initial bulk filtration methods both to integrate microfluidic filtration techniques and to introduce inertial-based cell separation. The impressive innovation in the field has been recently reviewed [73]. Here we highlight a subset of these approaches with demonstrated clinical utility. We also introduce a second area of nonaffinity-based CTC enrichment relying on external fields including DEP and acoustophoresis. These methods allow the separation of CTCs without targeting or even knowing specific surface markers, thereby recovering what is expected to be a more physically homogeneous but phenotypically diverse population of CTCs.

7.3.1 Microfluidic Filtration

Microfluidic device-mediated sized-based CTC isolation has been developed either by integrating membranes similar to those used in benchtop devices into microfluidic devices or by using more traditional microfluidic micro-molding techniques to produce alternative filtration systems. Here we highlight several select clinically validated approaches that extend macroscale dead-end membrane filtration to microfluidic devices.

In 2010, Lin *et al.* used a parylene membrane microfilter to identify CTCs in 51 out of 57 patients having various cancer types compared with only 26 patients identified with the CellSearch method [13]. In a similar strategy Lim *et al.* isolated CTCs at a flow rate of 1 ml min^{-1} using a densely arrayed porous silicon microsieve [74]. High flow in these dead-end filtration techniques requires high shear stresses at the membrane surface, which greatly limits captured cell viability. An alternative filter design incorporates a separable bilayer (SB) that limits stress to cells captured at the membrane surface by integrating a stacked 2-membrane sieving structure (Figure 7.2a) [39]. The first of the two porous parylene filters contains an array of 40 μm pores, which are aligned over an array of 8 μm pores in the second layer. Viable CTCs can be recovered from the gap between the membranes, allowing the potential for functional analysis and on-chip expansion of captured CTCs. This technology is being commercialized as the FactChecker CTC capture system (Circulogix).

Finally, a recent publication by the Toner group introduces a microchip technology designed specifically for CTC cluster filtration (Figure 7.2c) [40]. This device incorporates multiple rows of shifted triangular pillars forming consecutive cluster traps that allow low shear stress capture that does not exceed the shear stresses in human capillaries. The CTC cluster chip detected CTC clusters in 30–40% of patients with metastatic breast or prostate cancer or with melanoma [40]. The gentle capture allowed additional exploration of heterogeneity within the tumor and cluster populations as well as characterization of cluster-adherent leukocytes.

Together these filtration-based technologies and others support high-throughput CTC capture independent of specific surface markers. However,

filtration technologies are still limited to detecting only a subpopulation of large CTCs, and throughput is often hindered by clogging within the membrane or device.

7.3.2 Inertial Methods

The high level of fluid control delivered by microfluidic devices enables inertial methods as an alternative approach for size-dependent separation of cancer and blood cells in flow. Similar to filtration techniques, inertial methods rely primarily on size differences between tumor cells and blood cells to separate cell populations [75]. Compared with affinity techniques, flow-based isolation approaches allow comparably high throughput and do not require complex high-resolution features or modified surface chemistries, making them particularly appropriate for low-cost mass production. Further, by removing physical barriers, such approaches limit the significant challenges inherent to membrane and affinity techniques of recovering highly viable cells appropriate for downstream analysis. Various complementary approaches have been integrated into microfluidic devices to differentiate cell flow and isolate target cell populations.

The following introduces certain advances in inertial-based separation techniques, again emphasizing those that have shown CTC capture in patient samples. For a more in-depth discussion, the reader is referred to a recent review outlining the fundamental principles of inertial-based microfluidics [75] and others detailing the specific applications of these principles to CTC capture [73, 76].

7.3.2.1 Deterministic Lateral Displacement (DLD)

DLD is a microfluidic-based separation technique in which fluid under laminar flow regimes is passed through asymmetric microarrays of obstacles. Depending on the size of the particles and character of the array, a given particle of a given size will follow a distinct and predetermined flow pattern [77]. Applying this particle separation approach to CTCs has allowed high flow rate (10 ml min^{-1}), efficient (>85%) size-based recovery of breast cancer cells spiked into whole blood [78]. DLD has also been used for preseparation or debulking of whole blood as an initial step in CTC isolation. As introduced earlier, the CTC-iChip uses DLD generated by an array of microposts to separate CTCs and WBCs from RBCs [38].

7.3.2.2 Microfluidic Spiral Separation

An alternative approach for inertial CTC separation uses centrifugal forces through a principle known as Dean flow fractionation (DFF) [41–44]. Fluids flowing through a curved channel develop a secondary lateral flow. A particle or cell traveling through the channel can migrate across the direction of flow due to differences in the inertial lift force and the Dean drag force experienced by that object. Devices having various spiral geometries have been fabricated to promote the focusing of larger CTCs by inertial lift forces to the inner wall at the device outlet and the focusing of smaller blood cells by Dean vortices to the outer wall. Hou *et al.* demonstrated the successful application of DFF to isolate CTCs in lung cancer patient blood [43]. For spiked cancer cells in blood,

www.ebook3000.com

the device demonstrated a recovery rate of greater than 85% at a flow rate of 3 ml h^{-1} blood [43]. Khoo *et al.* expanded device throughput and reported an ultrahigh-throughput spiral device. The device contained three stacked spiral microfluidic channels with forked inlets and outlets. The group processed 7.5 ml of patient blood in less than 5 min and detected CTCs in all 56 tested breast and lung cancer patients [42]. A commercial version of the DFF is being developed by Clearbridge BioMedics as the ClearCell FX, which integrates a trapezoidal cross section (Figure 7.2b) designed to improve separation by positioning the larger CTCs along the shorter inner wall [41].

7.3.2.3 Vortex Platform

The Vortex platform uses differences in shear gradient lift force and wall effect lift force to trap large particles in vortices flanking the main channel flow. Vortex devices align cells by inertial focusing in straight channels before flowing them into a series of multiple expansion contraction reservoirs that develop microvortices in the wider rectangular reservoirs that trap larger cells [46]. They successfully isolated CTCs from breast and lung cancer patient blood without requiring RBC lysis [46]. Concentrated CTCs were captured with rapid processing times (20 min for 7.5 ml of whole blood) and limited leukocyte contamination (purity 57–94%) [46]. The High Throughput Vortex Chip (Vortex HT) (Figure 7.2d) demonstrates even higher throughput and tunable capture efficiency by reflowing the sample waste through the device [45].

7.3.2.4 Multiorifice Flow Fractionation (MOFF)

Multiorifice flow fractionation (MOFF) uses regions of microchannel expansion and contraction to initiate inertial forces that again separate larger CTCs from smaller blood cells. Hyun *et al.* showed CTC isolation from 24 breast cancer patients using the parallel multiorifice flow fractionation (p-MOFF) device [47]. A second multistage multiorifice flow fractionation (MS-MOFF) allows secondary separation, further isolating cells that escaped from the first isolation and achieving 98.9% isolation efficiencies of MCF-7 cells spiked into blood [48].

7.3.3 Dielectrophoresis and Acoustophoresis

With so-called DEP and acoustophoresis, electrical and acoustic forces, respectively, have been integrated into microfluidic devices to direct label-free cell separation. In the following, we briefly introduce both technologies and example devices but refer the reader to a recent review addressing both DEP and acoustophoresis for more detailed discussions [19].

In DEP-mediated CTC isolation, separation is based on intrinsic differences in the dielectric forces acting on cancer cells and blood cells in the presence of an external nonuniform electric field. The relative force intensities depend on a variety of factors including extrinsic properties such as the medium and the electric field gradient, as well as properties intrinsic to a cell such as the cell's size, shape, and electrical properties as determined by its unique cell membrane character and overall cellular composition. In 1995, Becker *et al.* demonstrated a preliminary application of DEP to CTC isolation, reporting the

static DEP-mediated isolation of breast cancer cells spiked into the blood [79]. More recently, integration of DEP within microfluidic devices has allowed facile techniques for patterning microelectrode arrays in various geometries along microchannels to form nonuniform electric fields and often integrated nonlinear flow profiles. High-throughput processing of clinical samples was demonstrated using the continuous-flow DEP field-flow fractionation (DEPFFF) device that separates CTCs based on an optimized balance between DEP and sedimentation forces [80]. ApoStream (ApoCell) has commercialized this approach using DEP and optimized the flow for CTC capture. In validation of this technology with spiked cancer cells, the ApoStream device showed greater than 70% recovery of viable cells. Notably, ApoStream was been shown to process cells from 7.5 ml centrifugation-processed blood in 1 h, a significantly higher throughput than most previous DEP techniques [49]. This commercialized product has been utilized in a variety of clinical applications including enriching CTCs in a variety of epithelial cancers to monitor the expression of folate receptor alpha [81].

Acoustophoretic-based CTC isolation relies on the generation of ultrasonic resonances in microfluidic channels. As comprehensively reviewed elsewhere [82], differences in particle or cell size, density, mass, and compressibility can lead to differential acoustophoretic mobility and cell separation. Whereas the principles of ultrasonic separation have been known for decades, a device having sufficient throughput to identify CTCs in clinical samples was only demonstrated in 2015 [50]. In addition to extensive validation in spiked samples, this device used tilted-angle standing surface acoustic waves (taSSAWs) to isolate CTCs from three patients with metastatic breast cancer. After RBC lysis, the remaining WBCs and CTCs were run through the taSSAW device at a flow rate of 1.2 ml whole blood equivalent per hour.

7.4 Conclusions and Outlook

Microfluidic approaches to CTC capture continue to integrate new materials, geometries, and forces to improve device performance. Each new approach differentially addresses the demands of capture efficiency, sample purity, throughput, and integration of nondestructive processing.

Considering the many devices presented in this chapter for CTC affinity and nonaffinity-based capture suggests several generalizations concerning the overall capabilities of these technologies. The gentle capture most often achieved through affinity-based devices is minimally influenced by physical properties such as cell size, which allows capture both of small CTCs often missed by many physical isolation techniques and of large CTC clusters often disrupted in more aggressive processing. Compared with nonaffinity techniques, those that integrate affinity capture generally achieve high selectivity of CTCs without requiring labor-intensive and potentially destructive preprocessing such as RBC lysis. Affinity capture technologies further offer the potential to identify and differentiate subpopulations of cancer cells based on differences in cell surface marker expression [36]. Further, the traditional challenges that have limited affinity capture including low throughput and difficulty releasing cells have been

www.ebook3000.com

partially addressed. Two techniques integrating affinity capture, the CTC-iChip and the OncoBean, have demonstrated efficient capture at 10 ml h^{-1} processing speeds. New release technologies have allowed viable cells to be removed from the capture substrate, thereby enabling downstream processing not applicable to cells remaining in the device [20].

However, a major limitation for affinity-based CTC capture remains integrated with the complex biology of CTCs. All known positive affinity capture ligands support incomplete capture of a cell population biased to the chosen capture ligands, as universal capture ligands expressed on the surface of all cancer cells have yet to be identified. Capture through nonaffinity-based techniques is sometimes preferred as complete capture would not require universal capture ligands. Nonaffinity-based techniques are also attractive as they often integrate comparably straightforward and scalable approaches to device manufacture. However, established techniques relying only on physical separation must choose between high efficiency and high purity because of the overlapping physical properties within the populations of CTCs and WBCs.

Limitations in both affinity and nonaffinity capture suggest that the most promising approaches for complete CTC detection will continue to be integrated devices, such as the CTC-iChip, that multiplex complementary isolation strategies. We expect future innovation in microfluidic CTC capture to focus on technologies balancing the practical merits of simplicity, reproducibility, and cost effectiveness. Existing and future microfluidic devices for CTC characterization are expected to support fundamental characterization of disease progression and to help direct patient diagnosis and treatment.

Abbreviations

CD15	3-fucosyl-*N*-acetyl-lactosamine, a cluster of differentiation antigen
CD45	protein tyrosine phosphatase, receptor type, C
CK	cytokeratin
DEP	dielectrophoresis
DLD	deterministic lateral displacement
EGFR	epidermal growth factor receptor
EMT	epithelial-to-mesenchymal transition
EpCAM	epithelial cell adhesion molecule
FISH	fluorescence *in situ* hybridization
GEDI	geometrically enhanced differential immunocapture
GO	graphene oxide
HER2	human epidermal growth factor receptor 2
HTMSU	high-throughput microsampling unit
ISET	isolation by size of epithelial tumor cells
LnCAP	lymph node carcinoma of the prostate
MACS	magnetic-activated cell sorting
MCF-7	Michigan Cancer Foundation-7
MOFF	multiorifice flow fractionation
MUC1	mucin 1, cell surface associated

NSCLC	non-small cell lung carcinoma
PDAC	pancreatic ductal adenocarcinoma
PDMS	polydimethylsiloxane
PDX	patient-derived xenograft
PSMA	prostate-specific membrane antigen
SWOG	Southwest Oncology Group
taSSAW	tilted-angle standing surface acoustic waves

References

1 Siegel, R.L., Miller, K.D., and Jemal, A. (2015) Cancer statistics, 2015. *CA Cancer J. Clin.*, (65), 5–29.

2 Cohen, S.J., Punt, C.J., Iannotti, N., Saidman, B.H., Sabbath, K.D., Gabrail, N.Y., Picus, J., Morse, M., Mitchell, E., and Miller, M.C. (2008) Relationship of circulating tumor cells to tumor response, progression-free survival, and overall survival in patients with metastatic colorectal cancer. *J. Clin. Oncol.*, **26**, 3213–3221.

3 Pantel, K. and Speicher, M.R. (2016) The biology of circulating tumor cells. *Oncogene*, **35**, 1216–1224.

4 Baccelli, I., Schneeweiss, A., Riethdorf, S., Stenzinger, A., Schillert, A., Vogel, V., Klein, C., Saini, M., Bauerle, T., Wallwiener, M., Holland-Letz, T., Hofner, T., Sprick, M., Scharpff, M., Marme, F., Sinn, H.P., Pantel, K., Weichert, W., and Trumpp, A. (2013) Identification of a population of blood circulating tumor cells from breast cancer patients that initiates metastasis in a xenograft assay. *Nat. Biotechnol.*, **31**, 539–544.

5 Maheswaran, S. and Haber, D.A. (2010) Circulating tumor cells: a window into cancer biology and metastasis. *Curr. Opin. Genet. Dev.*, **20**, 96–99.

6 Maheswaran, S., Sequist, L.V., Nagrath, S., Ulkus, L., Brannigan, B., Collura, C.V., Inserra, E., Diederichs, S., Iafrate, A.J., and Bell, D.W. (2008) Detection of mutations in EGFR in circulating lung-cancer cells. *N. Engl. J. Med.*, **359**, 366–377.

7 Yu, M., Stott, S., Toner, M., Maheswaran, S., and Haber, D.A. (2011) Circulating tumor cells: approaches to isolation and characterization. *J. Cell Biol.*, **192**, 373–382.

8 Willipinski-Stapelfeldt, B., Riethdorf, S., Assmann, V., Woelfle, U., Rau, T., Sauter, G., Heukeshoven, J., and Pantel, K. (2005) Changes in cytoskeletal protein composition indicative of an epithelial-mesenchymal transition in human micrometastatic and primary breast carcinoma cells. *Clin. Cancer Res.*, **11**, 8006–8014.

9 Phillips, K.G., Kuhn, P., and McCarty, O.J. (2014) Physical biology in cancer. 2. The physical biology of circulating tumor cells. *Am. J. Physiol. Cell Physiol.*, **306**, C80–C88.

10 Allard, W.J., Matera, J., Miller, M.C., Repollet, M., Connelly, M.C., Rao, C., Tibbe, A.G., Uhr, J.W., and Terstappen, L.W. (2004) Tumor cells circulate in the peripheral blood of all major carcinomas but not in healthy subjects or patients with nonmalignant diseases. *Clin. Cancer Res.*, **10**, 6897–6904.

www.ebook3000.com

11 Cristofanilli, M., Budd, G.T., Ellis, M.J., Stopeck, A., Matera, J., Miller, M.C., Reuben, J.M., Doyle, G.V., Allard, W.J., and Terstappen, L.W. (2004) Circulating tumor cells, disease progression, and survival in metastatic breast cancer. *N. Engl. J. Med.*, **351**, 781–791.

12 de Bono, J.S., Scher, H.I., Montgomery, R.B., Parker, C., Miller, M.C., Tissing, H., Doyle, G.V., Terstappen, L.W., Pienta, K.J., and Raghavan, D. (2008) Circulating tumor cells predict survival benefit from treatment in metastatic castration-resistant prostate cancer. *Clin. Cancer Res.*, **14**, 6302–6309.

13 Lin, H.K., Zheng, S., Williams, A.J., Balic, M., Groshen, S., Scher, H.I., Fleisher, M., Stadler, W., Datar, R.H., Tai, Y.C., and Cote, R.J. (2010) Portable filter-based microdevice for detection and characterization of circulating tumor cells. *Clin. Cancer Res.*, **16**, 5011–5018.

14 van der Toom, E.E., Verdone, J.E., Gorin, M.A., and Pienta, K.J. (2016) Technical challenges in the isolation and analysis of circulating tumor cells. *Oncotarget*, **7**, 62754–62766.

15 Vona, G., Sabile, A., Louha, M., Sitruk, V., Romana, S., Schütze, K., Capron, F., Franco, D., Pazzagli, M., Vekemans, M., Lacour, B., Bréchot, C., and Paterlini-Bréchot, P. (2000) Isolation by size of epithelial tumor cells: a new method for the immunomorphological and molecular. *Am. J. Pathol.*, **156**, 57–63.

16 Beebe, D.J., Mensing, G.A., and Walker, G.M. (2002) Physics and applications of microfluidics in biology. *Annu. Rev. Biomed. Eng.*, **4**, 261–286.

17 Whitesides, Y.X.G. (1998) Soft lithography. *Annu. Rev. Mater. Sci.*, **28**, 153–184.

18 Chin, C.D., Linder, V., and Sia, S.K. (2012) Commercialization of microfluidic point-of-care diagnostic devices. *Lab Chip*, **12**, 2118–2134.

19 Qian, W., Zhang, Y., and Chen, W. (2015) Capturing cancer: emerging microfluidic technologies for the capture and characterization of circulating tumor cells. *Small*, **11**, 3850–3872.

20 Green, B.J., Saberi Safaei, T., Mepham, A., Labib, M., Mohamadi, R.M., and Kelley, S.O. (2016) Beyond the capture of circulating tumor cells: next-generation devices and materials. *Angew. Chem. Int. Ed.*, **55**, 1252–1265.

21 Pantel, K. and Alix-Panabieres, C. (2016) Functional studies on viable circulating tumor cells. *Clin. Chem.*, **62**, 328–334.

22 Smerage, J.B., Barlow, W.E., Hortobagyi, G.N., Winer, E.P., Leyland-Jones, B., Srkalovic, G., Tejwani, S., Schott, A.F., O'Rourke, M.A., and Lew, D.L. (2014) Circulating tumor cells and response to chemotherapy in metastatic breast cancer: SWOG S0500. *J. Clin. Oncol.*, **32**, 3483–3489.

23 Scher, H.I., Lu, D., Schreiber, N.A., Louw, J., Graf, R.P., Vargas, H.A., Johnson, A., Jendrisak, A., Bambury, R., and Danila, D. (2016) Association of AR-V7 on circulating tumor cells as a treatment-specific biomarker with outcomes and survival in castration-resistant prostate cancer. *JAMA Oncol.*, **2**, 1441–1449.

24 Nagrath, S., Sequist, L.V., Maheswaran, S., Bell, D.W., Irimia, D., Ulkus, L., Smith, M.R., Kwak, E.L., Digumarthy, S., Muzikansky, A., Ryan, P., Balis, U.J., Tompkins, R.G., Haber, D.A., and Toner, M. (2007) Isolation of rare circulating tumour cells in cancer patients by microchip technology. *Nature*, **450**, 1235–1239.

25 Santana, S.M., Liu, H., Bander, N.H., Gleghorn, J.P., and Kirby, B.J. (2012) Immunocapture of prostate cancer cells by use of anti-PSMA antibodies in microdevices. *Biomed. Microdevices*, **14**, 401–407.
26 Gleghorn, J.P., Pratt, E.D., Denning, D., Liu, H., Bander, N.H., Tagawa, S.T., Nanus, D.M., Giannakakou, P.A., and Kirby, B.J. (2010) Capture of circulating tumor cells from whole blood of prostate cancer patients using geometrically enhanced differential immunocapture (GEDI) and a prostate-specific antibody. *Lab Chip*, **10**, 27–29.
27 Galletti, G., Sung, M.S., Vahdat, L.T., Shah, M.A., Santana, S.M., Altavilla, G., Kirby, B.J., and Giannakakou, P. (2014) Isolation of breast cancer and gastric cancer circulating tumor cells by use of an anti HER2-based microfluidic device. *Lab Chip*, **14**, 147–156.
28 Thege, F.I., Lannin, T.B., Saha, T.N., Tsai, S., Kochman, M.L., Hollingsworth, M.A., Rhim, A.D., and Kirby, B.J. (2014) Microfluidic immunocapture of circulating pancreatic cells using parallel EpCAM and MUC1 capture: characterization, optimization and downstream analysis. *Lab Chip*, **14**, 1775–1784.
29 Murlidhar, V., Zeinali, M., Grabauskiene, S., Ghannad-Rezaie, M., Wicha, M.S., Simeone, D.M., Ramnath, N., Reddy, R.M., and Nagrath, S. (2014) A radial flow microfluidic device for ultra-high-throughput affinity-based isolation of circulating tumor cells. *Small*, **10**, 4895–4904.
30 Stott, S.L., Hsu, C.H., Tsukrov, D.I., Yu, M., Miyamoto, D.T., Waltman, B.A., Rothenberg, S.M., Shah, A.M., Smas, M.E., Korir, G.K., Floyd, F.P. Jr., Gilman, A.J., Lord, J.B., Winokur, D., Springer, S., Irimia, D., Nagrath, S., Sequist, L.V., Lee, R.J., Isselbacher, K.J., Maheswaran, S., Haber, D.A., and Toner, M. (2010) Isolation of circulating tumor cells using a microvortex-generating herringbone-chip. *Proc. Natl. Acad. Sci. U.S.A.*, **107**, 18392–18397.
31 Kamande, J.W., Hupert, M.L., Witek, M.A., Wang, H., Torphy, R.J., Dharmasiri, U., Njoroge, S.K., Jackson, J.M., Aufforth, R.D., Snavely, A., Yeh, J.J., and Soper, S.A. (2013) Modular microsystem for the isolation, enumeration, and phenotyping of circulating tumor cells in patients with pancreatic cancer. *Anal. Chem.*, **85**, 9092–9100.
32 Adams, A.A., Okagbare, P.I., Feng, J., Hupert, M.L., Patterson, D., Göttert, J., McCarley, R.L., Nikitopoulos, D., Murphy, M.C., and Soper, S.A. (2008) Highly efficient circulating tumor cell isolation from whole blood and label-free enumeration using polymer-based microfluidics with an integrated conductivity sensor. *J. Am. Chem. Soc.*, **130**, 8633–8641.
33 Torphy, R.J., Tignanelli, C.J., Kamande, J.W., Moffitt, R.A., Herrera Loeza, S.G., Soper, S.A., and Yeh, J.J. (2014) Circulating tumor cells as a biomarker of response to treatment in patient-derived xenograft mouse models of pancreatic adenocarcinoma. *PLoS ONE*, **9**, e89474.
34 Zhao, L., Tang, C., Xu, L., Zhang, Z., Li, X., Hu, H., Cheng, S., Zhou, W., Huang, M., Fong, A., Liu, B., Tseng, H.R., Gao, H., Liu, Y., and Fang, X. (2016) Enhanced and differential capture of circulating tumor cells from lung cancer patients by microfluidic assays using aptamer cocktail. *Small*, **12**, 1072–1081.
35 Yoon, H.J., Kim, T.H., Zhang, Z., Azizi, E., Pham, T.M., Paoletti, C., Lin, J., Ramnath, N., Wicha, M.S., Hayes, D.F., Simeone, D.M., and Nagrath, S. (2013)

www.ebook3000.com

Sensitive capture of circulating tumour cells by functionalized graphene oxide nanosheets. *Nat. Nanotechnol.*, **8**, 735–741.

36 Mohamadi, R.M., Besant, J.D., Mepham, A., Green, B., Mahmoudian, L., Gibbs, T., Ivanov, I., Malvea, A., Stojcic, J., Allan, A.L., Lowes, L.E., Sargent, E.H., Nam, R.K., and Kelley, S.O. (2015) Nanoparticle-mediated binning and profiling of heterogeneous circulating tumor cell subpopulations. *Angew. Chem. Int. Ed.*, **54**, 139–143.

37 Karabacak, N.M., Spuhler, P.S., Fachin, F., Lim, E.J., Pai, V., Ozkumur, E., Martel, J.M., Kojic, N., Smith, K., Chen, P.I., Yang, J., Hwang, H., Morgan, B., Trautwein, J., Barber, T.A., Stott, S.L., Maheswaran, S., Kapur, R., Haber, D.A., and Toner, M. (2014) Microfluidic, marker-free isolation of circulating tumor cells from blood samples. *Nat. Protoc.*, **9**, 694–710.

38 Ozkumur, E., Shah, A.M., Ciciliano, J.C., Emmink, B.L., Miyamoto, D.T., Brachtel, E., Yu, M., Chen, P.-I., Morgan, B., Trautwein, J., and Toner, M. (2013) Inertial focusing for tumor antigen–dependent and–independent sorting of rare circulating tumor cells. *Sci. Transl. Med.*, **5**, 179ra47.

39 Zhou, M.D., Hao, S., Williams, A.J., Harouaka, R.A., Schrand, B., Rawal, S., Ao, Z., Brenneman, R., Gilboa, E., Lu, B., Wang, S., Zhu, J., Datar, R., Cote, R., Tai, Y.C., and Zheng, S.Y. (2014) Separable bilayer microfiltration device for viable label-free enrichment of circulating tumour cells. *Sci. Rep.*, **4**, 7392.

40 Sarioglu, A.F., Aceto, N., Kojic, N., Donaldson, M.C., Zeinali, M., Hamza, B., Engstrom, A., Zhu, H., Sundaresan, T.K., Miyamoto, D.T., Luo, X., Bardia, A., Wittner, B.S., Ramaswamy, S., Shioda, T., Ting, D.T., Stott, S.L., Kapur, R., Maheswaran, S., Haber, D.A., and Toner, M. (2015) A microfluidic device for label-free, physical capture of circulating tumor cell clusters. *Nat. Methods*, **12**, 685–691.

41 Warkiani, M.E., Guan, G., Luan, K.B., Lee, W.C., Bhagat, A.A.S., Chaudhuri, P.K., Tan, D.S.-W., Lim, W.T., Lee, S.C., and Chen, P.C. (2014) Slanted spiral microfluidics for the ultra-fast, label-free isolation of circulating tumor cells. *Lab Chip*, **14**, 128–137.

42 Khoo, B.L., Warkiani, M.E., Tan, D.S., Bhagat, A.A., Irwin, D., Lau, D.P., Lim, A.S., Lim, K.H., Krisna, S.S., Lim, W.T., Yap, Y.S., Lee, S.C., Soo, R.A., Han, J., and Lim, C.T. (2014) Clinical validation of an ultra high-throughput spiral microfluidics for the detection and enrichment of viable circulating tumor cells. *PLoS One*, **9**, e99409.

43 Hou, H.W., Warkiani, M.E., Khoo, B.L., Li, Z.R., Soo, R.A., Tan, D.S., Lim, W.T., Han, J., Bhagat, A.A., and Lim, C.T. (2013) Isolation and retrieval of circulating tumor cells using centrifugal forces. *Sci. Rep.*, **3**, 1259. doi: 10.1038/srep01259

44 Warkiani, M.E., Khoo, B.L., Wu, L., Tay, A.K., Bhagat, A.A., Han, J., and Lim, C.T. (2016) Ultra-fast, label-free isolation of circulating tumor cells from blood using spiral microfluidics. *Nat. Protoc.*, **11**, 134–148.

45 Che, J., Yu, V., Dhar, M., Renier, C., Matsumoto, M., Heirich, K., Garon, E.B., Goldman, J., Rao, J., Sledge, G.W., and Di Carlo, D. (2016) Classification of large circulating tumor cells isolated with ultra-high throughput microfluidic Vortex technology. *Oncotarget*, **7**, 12748–12760.

46 Hur, S.C., Mach, A.J., and Di Carlo, D. (2011) High-throughput size-based rare cell enrichment using microscale vortices. *Biomicrofluidics*, **5**, 22206.

47 Hyun, K.A., Kwon, K., Han, H., Kim, S.I., and Jung, H.I. (2013) Microfluidic flow fractionation device for label-free isolation of circulating tumor cells (CTCs) from breast cancer patients. *Biosens. Bioelectron.*, **40**, 206–212.

48 Moon, H.S., Kwon, K., Hyun, K.A., Seok Sim, T., Chan Park, J., Lee, J.G., and Jung, H.I. (2013) Continual collection and re-separation of circulating tumor cells from blood using multi-stage multi-orifice flow fractionation. *Biomicrofluidics*, **7**, 014105.

49 Gupta, V., Jafferji, I., Garza, M., Melnikova, V.O., Hasegawa, D.K., Pethig, R., and Davis, D.W. (2012) ApoStream, a new dielectrophoretic device for antibody independent isolation and recovery of viable cancer cells from blood. *Biomicrofluidics*, **6**, 024133.

50 Li, P., Mao, Z., Peng, Z., Zhou, L., Chen, Y., Huang, P.-H., Truica, C.I., Drabick, J.J., El-Deiry, W.S., and Dao, M. (2015) Acoustic separation of circulating tumor cells. *Proc. Natl. Acad. Sci. U.S.A.*, **112**, 4970–4975.

51 Grover, P.K., Cummins, A.G., Price, T.J., Roberts-Thomson, I.C., and Hardingham, J.E. (2014) Circulating tumour cells: the evolving concept and the inadequacy of their enrichment by EpCAM-based methodology for basic and clinical cancer research. *Ann. Oncol.*, **25**, 1506–1516.

52 Kalluri, R. and Weinberg, R.A. (2009) The basics of epithelial-mesenchymal transition. *J. Clin. Invest.*, **119**, 1420–1428.

53 Moul, J.W., Merseburger, A.S., and Srivastava, S. (2002) Molecular markers in prostate cancer: the role in preoperative staging. *Clin. Prostate Cancer*, **1**, 42–50.

54 Diamond, E., Lee, G.Y., Akhtar, N.H., Kirby, B.J., Giannakakou, P., Tagawa, S.T., and Nanus, D.M. (2012) Isolation and characterization of circulating tumor cells in prostate cancer. *Front. Oncol.*, **2**, 131. doi: 10.3389/fonc.2012.00131

55 Satelli, A., Brownlee, Z., Mitra, A., Meng, Q.H., and Li, S. (2015) Circulating tumor cell enumeration with a combination of epithelial cell adhesion molecule–and cell-surface vimentin–based methods for monitoring breast cancer therapeutic response. *Clin. Chem.*, **61**, 259–266.

56 Reategui, E., Aceto, N., Lim, E.J., Sullivan, J.P., Jensen, A.E., Zeinali, M., Martel, J.M., Aranyosi, A.J., Li, W., Castleberry, S., Bardia, A., Sequist, L.V., Haber, D.A., Maheswaran, S., Hammond, P.T., Toner, M., and Stott, S.L. (2015) Tunable nanostructured coating for the capture and selective release of viable circulating tumor cells. *Adv. Mater.*, **27**, 1593–1599.

57 Stelzer, G.T., Shults, K.E., and Loken, M.R. (1993) CD45 gating for routine flow cytometric analysis of human bone marrow specimens. *Ann. N.Y. Acad. Sci.*, **677**, 265–280.

58 Yang, L., Lang, J.C., Balasubramanian, P., Jatana, K.R., Schuller, D., Agrawal, A., Zborowski, M., and Chalmers, J.J. (2009) Optimization of an enrichment process for circulating tumor cells from the blood of head and neck cancer patients through depletion of normal cells. *Biotechnol. Bioeng.*, **102**, 521–534.

www.ebook3000.com

59 Hyun, K.A., Lee, T.Y., and Jung, H.I. (2013) Negative enrichment of circulating tumor cells using a geometrically activated surface interaction chip. *Anal. Chem.*, **85**, 4439–4445.

60 Dickey, D.D. and Giangrande, P.H. (2016) Oligonucleotide aptamers: a next-generation technology for the capture and detection of circulating tumor cells. *Methods*, **97**, 94–103.

61 Li, W., Reategui, E., Park, M.H., Castleberry, S., Deng, J.Z., Hsu, B., Mayner, S., Jensen, A.E., Sequist, L.V., Maheswaran, S., Haber, D.A., Toner, M., Stott, S.L., and Hammond, P.T. (2015) Biodegradable nano-films for capture and non-invasive release of circulating tumor cells. *Biomaterials*, **65**, 93–102.

62 Ke, Z., Lin, M., Chen, J.-F., Choi, J.-S., Zhang, Y., Fong, A., Liang, A.-J., Chen, S.-F., Li, Q., and Fang, W. (2014) Programming thermoresponsiveness of NanoVelcro substrates enables effective purification of circulating tumor cells in lung cancer patients. *ACS Nano*, **9**, 62–70.

63 Zhang, Y., Zhang, W., and Qin, L. (2014) Mesenchymal-mode migration assay and antimetastatic drug screening with high-throughput microfluidic channel networks. *Angew. Chem. Int. Ed.*, **53**, 2344–2348.

64 Stroock, A.D., Dertinger, S.K., Ajdari, A., Mezić, I., Stone, H.A., and Whitesides, G.M. (2002) Chaotic mixer for microchannels. *Science*, **295**, 647–651.

65 Aceto, N., Bardia, A., Miyamoto, D.T., Donaldson, M.C., Wittner, B.S., Spencer, J.A., Yu, M., Pely, A., Engstrom, A., Zhu, H., Brannigan, B.W., Kapur, R., Stott, S.L., Shioda, T., Ramaswamy, S., Ting, D.T., Lin, C.P., Toner, M., Haber, D.A., and Maheswaran, S. (2014) Circulating tumor cell clusters are oligoclonal precursors of breast cancer metastasis. *Cell*, **158**, 1110–1122.

66 Wang, S., Liu, K., Liu, J., Yu, Z.T., Xu, X., Zhao, L., Lee, T., Lee, E.K., Reiss, J., Lee, Y.K., Chung, L.W., Huang, J., Rettig, M., Seligson, D., Duraiswamy, K.N., Shen, C.K., and Tseng, H.R. (2011) Highly efficient capture of circulating tumor cells by using nanostructured silicon substrates with integrated chaotic micromixers. *Angew. Chem. Int. Ed.*, **50**, 3084–3088.

67 Hou, S., Zhao, H., Zhao, L., Shen, Q., Wei, K.S., Suh, D.Y., Nakao, A., Garcia, M.A., Song, M., Lee, T., Xiong, B., Luo, S.C., Tseng, H.R., and Yu, H.H. (2013) Capture and stimulated release of circulating tumor cells on polymer-grafted silicon nanostructures. *Adv. Mater.*, **25**, 1547–1551.

68 Chen, J.F., Zhu, Y., Lu, Y.T., Hodara, E., Hou, S., Agopian, V.G., Tomlinson, J.S., Posadas, E.M., and Tseng, H.R. (2016) Clinical applications of Nanovelcro rare-cell assays for detection and characterization of circulating tumor cells. *Theranostics*, **6**, 1425–1439.

69 Myung, J.H. and Hong, S. (2015) Microfluidic devices to enrich and isolate circulating tumor cells. *Lab Chip*, **15**, 4500–4511.

70 Ferreira, M.M., Ramani, V.C., and Jeffrey, S.S. (2016) Circulating tumor cell technologies. *Mol. Oncol.*, **10**, 374–394.

71 Harouaka, R.A., Nisic, M., and Zheng, S.-Y. (2013) Circulating tumor cell enrichment based on physical properties. *J. Lab. Autom.*, **18**, 455–468.

72 Paterlini-Brechot, P. (2014) Circulating tumor cells: who is the killer? *Cancer Microenviron.*, **7**, 161–176.

73 Patil, P., Madhuprasad, M., Kumeria, T., Losic, D., and Kurkuri, M. (2015) Isolation of circulating tumour cells by physical means in a microfluidic device: a review. *RSC Adv.*, **5**, 89745–89762.

74 Lim, L.S., Hu, M., Huang, M.C., Cheong, W.C., Gan, A.T., Looi, X.L., Leong, S.M., Koay, E.S., and Li, M.H. (2012) Microsieve lab-chip device for rapid enumeration and fluorescence *in situ* hybridization of circulating tumor cells. *Lab Chip*, **12**, 4388–4396.

75 Zhang, J., Yan, S., Yuan, D., Alici, G., Nguyen, N.T., Ebrahimi Warkiani, M., and Li, W. (2016) Fundamentals and applications of inertial microfluidics: a review. *Lab Chip*, **16**, 10–34.

76 Jin, C., McFaul, S.M., Duffy, S.P., Deng, X., Tavassoli, P., Black, P.C., and Ma, H. (2014) Technologies for label-free separation of circulating tumor cells: from historical foundations to recent developments. *Lab Chip*, **14**, 32–44.

77 Huang, L.R., Cox, E.C., Austin, R.H., and Sturm, J.C. (2004) Continuous particle separation through deterministic lateral displacement. *Science*, **304**, 987–990.

78 Loutherback, K., D'Silva, J., Liu, L., Wu, A., Austin, R.H., and Sturm, J.C. (2012) Deterministic separation of cancer cells from blood at 10 mL/min. *AIP Adv.*, **2**, 42107.

79 Becker, F.F., Wang, X.-B., Huang, Y., Pethig, R., Vykoukal, J., and Gascoyne, P. (1995) Separation of human breast cancer cells from blood by differential dielectric affinity. *Proc. Natl. Acad. Sci. U.S.A.*, **92**, 860–864.

80 Shim, S., Stemke-Hale, K., Tsimberidou, A.M., Noshari, J., Anderson, T.E., and Gascoyne, P.R. (2013) Antibody-independent isolation of circulating tumor cells by continuous-flow dielectrophoresis. *Biomicrofluidics*, **7**, 11807.

81 O'Shannessy, D.J., Davis, D.W., Anderes, K., and Somers, E.B. (2016) Isolation of circulating tumor cells from multiple epithelial cancers with ApoStream® for detecting (or monitoring) the expression of folate receptor alpha. *Biomark Insights*, **11**, 7.

82 Destgeer, G. and Sung, H.J. (2015) Recent advances in microfluidic actuation and micro-object manipulation via surface acoustic waves. *Lab Chip*, **15**, 2722–2738.

www.ebook3000.com

8

Microfluidics for Disease Diagnosis

Jun-Tao Cao

Xinyang Normal University, College of Chemistry and Chemical Engineering, 237# Nanhu Road, Xinyang 464000, PR China

8.1 Introduction

Possessing unique characteristics such as high throughput, low-reagent consumption, rapid analysis, and its portability, microfluidic system has demonstrated its great promise in early disease diagnosis. Based on the microfluidic platform, the disease-related biomarkers (DNA, RNA, and proteins) in body fluids such as blood, urine, and other body fluids or low-abundant marker on tumor cell surfaces could be determined with high efficiency and sensitivity [1]. This chapter summarizes the recent advances of microfluidic system in the assay of proteins, nucleic acids, and cells in complex samples.

8.2 Protein Analysis

Measurement of biomarker proteins holds great promise for early disease diagnosis, for guidance, for personalized therapy, and for drug development. With the unique features of miniaturization, high integration, and low cost, microfluidics is emerging as a powerful tool for protein assay. The microfluidic-based protein quantitation has great potential for integration of sample preparation, separation, and detection in the same microplatform. Up to now, various microfluidic-based methods have been developed for disease-related protein analysis.

8.2.1 Secreted Proteins in Biological Fluids

The proteins secreted by the cells are a rich source of disease-related biomarkers. For research and diagnosis purposes, the ability to determine low levels of proteins in a cost- and time-effective manner is important. However, the detection of low-abundance proteins is still challenging in biological fluids. Herrmann *et al.* [2] designed a dual-network microfluidic enzyme-linked immunosorbent assay (ELISA) platform for the TNF-α detection in serum with a limit of detection (LOD) of 2.6 pM. Koh *et al.* [3] presented an innovative centrifugal

Microfluidics: Fundamentals, Devices and Applications, First Edition.
Edited by Yujun Song, Daojian Cheng, and Liang Zhao.
© 2018 Wiley-VCH Verlag GmbH & Co. KGaA. Published 2018 by Wiley-VCH Verlag GmbH & Co. KGaA.

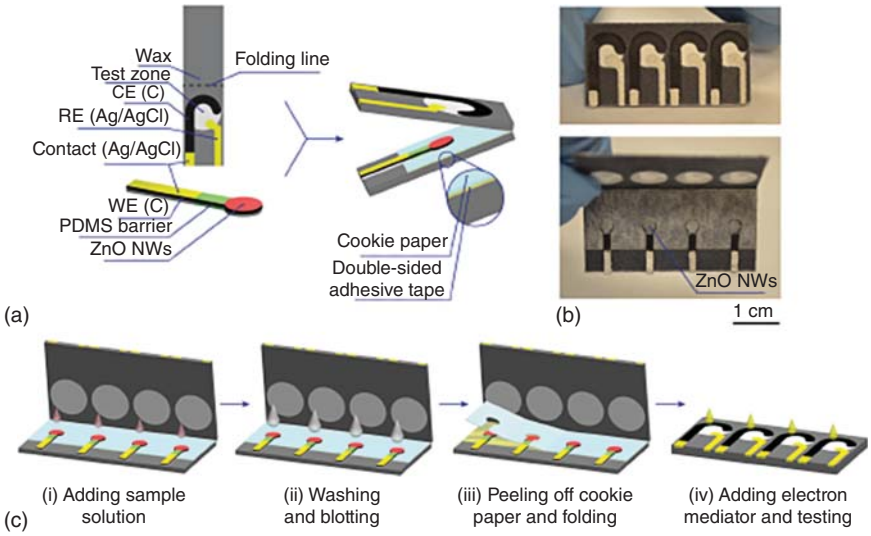


Figure 8.1 Device design and assay operation procedure. (a) Schematic of the components (left) and the assembly (right) of origami μPAD. (b) Photographs of an origami μPAD showing the top view and inside view (before origami). (c) Schematic of the assay operations of the origami μPAD. (Adapted from Li and Liu 2016 [4]. Reproduced with permission of John Wiley & Sons.)

microfluidic platform for ultrasensitive point-of-care (POC)/incident detection of botulinum toxin, achieving total sample-to-answer time of <30 min with a 2 μl required volume of the unprocessed sample. Microfluidic paper-based analytical devices (μPADs) represent a promising platform for POC diagnosis. Integrating zinc oxide nanowires and electrochemical impedance spectroscopy biosensing mechanism, Li and Liu [4] reported the first microfluidic paper-based origami nanobiosensor for label-free, ultrasensitive immunoassays. The device design and assay procedure are illustrated in Figure 8.1. The strategy could achieve an ultralow LOD of 60 fg ml^{-1} for rabbit IgG in phosphate-buffered saline and a low LOD of 300 fg ml^{-1} for human immunodeficiency virus p24 antigen in human serum. Undoubtedly, the μPAD-based designs possess significant potential for low cost and rapid molecular diagnosis of early-stage diseases.

Compared with the single biomarker analysis, multiplexed biomarker protein tests provide more reliable diagnostics than single biomarkers [5]. By integration of surface-enhanced Raman scattering (SERS) microspectroscopy using glass-coated, highly purified SERS nanoparticle clusters as labels, with a microfluidic device comprising multiple channels, Wang *et al.* [6] constructed a robust platform for the sensitive duplex detection of pathogen antigens. Using nanoyeast single-chain variable fragments (NYscFv) as an attractive alternative to monoclonal antibodies, the platform for individual detection of *Entamoeba histolytica* antigens EHI_115350 and EHI_182030 was achieved with LODs of 1 and 10 pg ml^{-1}, respectively. Malhotra *et al.* [7] used a nanostructured microfluidic array to measure a four-protein panel of biomarker proteins, and the protein panel was validated for accurate oral cancer diagnostics. The method exhibits ultralow detection into the 5–50 fg ml^{-1} range for simultaneous

www.ebook3000.com

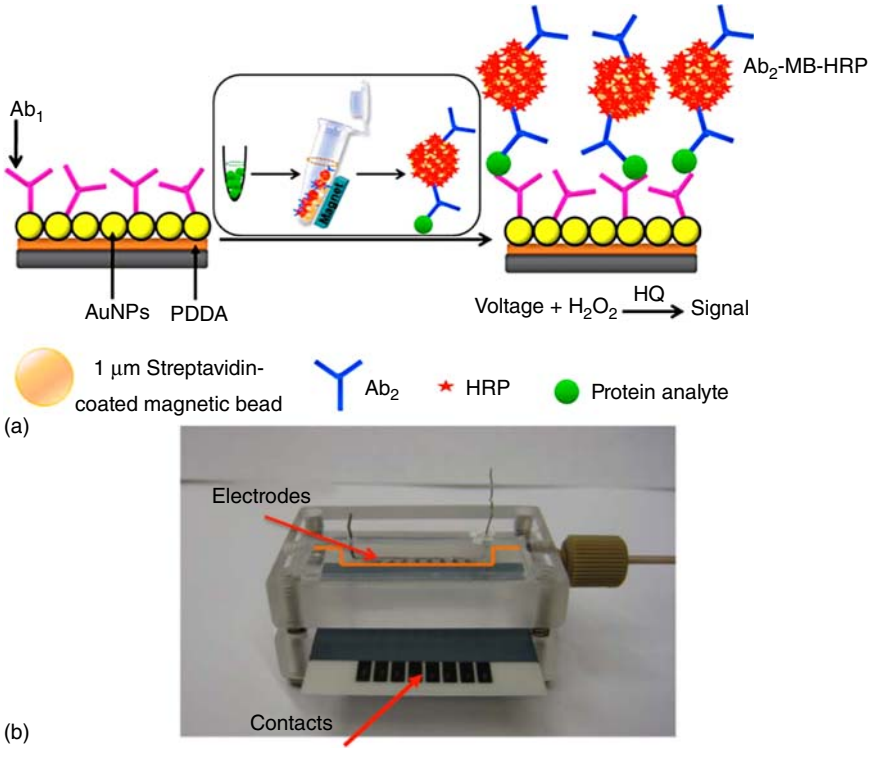


Figure 8.2 Strategy for ultrasensitive amperometric detection by microfluidic immunoarray. (a) A single sensor in the array with capture antibodies. Protein analytes are captured offline (inside box) on Ab2-magnetic beads (MB)-herseradish peroxidise (HRP) bioconjugates with ~4 00 000 HRP labels and ~1 00 000 Ab2. On the right in panel A, a single sensor is depicted after subsequent Ab2-MB-HRP magnetically separation and injection into (b) the eight-sensor immunoarray, which is connected to a pump and injector valve (not shown). Amperometric signals are developed at −0.3 V versus Ag/AgCl by injecting a mixture of H_2O_2 and hydroquinone and measuring the eight currents. (Adapted from Malhotra *et al*. 2012 [7]. Reproduced with permission of American Chemical Society.)

measurement of proteins interleukin 6 (IL-6), IL-8, vascular endothelial growth factor (VEGF), and VEGF-C in diluted serum. The strategy for ultrasensitive amperometric detection by microfluidic immunoarray is shown in Figure 8.2.

Tang *et al.* [8] developed a high-throughput electrochemical array featuring 32 individually addressable microelectrodes that is further multiplexed with an 8-port manifold to provide 256 sensors. The technique can execute 256 measurements within 1 h, and the system was used to determine prostate cancer biomarker proteins prostate-specific antigen (PSA), prostate-specific membrane antigen (PSMA), IL-6, and platelet factor-4 (PF-4) in serum. Piraino *et al.* [9] engineered a multiplexed digital–analog microfluidic platform, which integrated 16 independent and isolated microfluidic unit cells for the highly sensitive detection of 3–4 biomarkers in quadruplicate requiring only a 5 μl sample.

Although immunoassay is one of the most important techniques for protein detection in clinical diagnosis and biochemical analysis, the antibody adopted in the immunoassay is always temperature sensitive and irreversibly denatured and

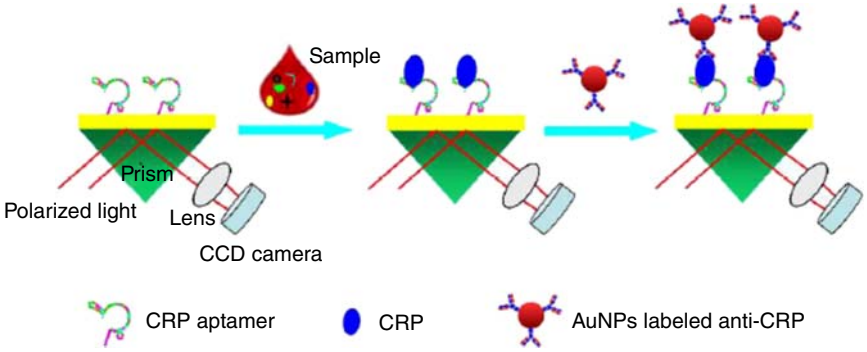


Figure 8.3 Schematic illustration of the AuNPs-enhanced SPR biosensor with an aptamer–antibody sandwich assay. (Adapted from Wu 2016 [14]. Reproduced with permission of Royal Society of Chemistry.)

has a limited shelf life. Aptamers with merits of high specificity, affinity, good stability, and relatively easy preparation [10] have been considered as desirable candidates for high-throughput methods for protein analysis. Nowadays, they have been quickly developed to detect a variety of targets such as proteins, peptides, drugs, small molecules, metal ions, and even whole cells. Recently, to achieve fast detection with simplicity, specificity, and economy, methods of coupling aptamers and microfluidics have attracted increasing attentions [11–14]. For example, an aptamer-based impedimetric bioassay for thrombin as target protein was developed using the microfluidic system and magnetic separation [13]. Wu *et al.* combined the microfluidic with an Au nanoparticle-enhanced surface plasmon resonance biosensor to detect the C-reactive protein using an aptamer–antibody sandwich assay (shown in Figure 8.3) [14].

8.2.2 Membrane Protein

Protein expression plays a crucial role in biology, pathology, and biomedical studies. The type and abundance of protein expressions on cell surface could provide important information for disease diagnosis, monitoring, and clinical therapeutics. Recently, the membrane protein has been considered as candidate biomarkers for cancer. Currently, conventional analytical technology including ELISA, Western blotting, and flow cytometry have been widely used for membrane proteins analysis [15]. Microfluidics as an effective alternative technique has also been used for membrane protein detection. Epithelial cellular adhesion molecule (EpCAM) is a cell surface protein and is overexpressed by epithelial carcinomas such as lung, colorectal, breast, head, neck, and hepatic origin. Fernández-Baldo *et al.* [16] reported a microfluidic immunosensor with a nanostructured platform in zinc oxide nanoparticles covered by polyvinyl alcohol (ZnONPs-PVA) coupled with laser-induced fluorescence (LIF) for detection of epithelial cell adhesion molecule with an LOD of 1.2 pg ml^{-1}. The modification process is shown in Figure 8.4. Although the microfluidic immunosensor offers a truthful and useful analytical tool in the diagnosis and prognosis of epithelial cancer, the information obtained is the average outcome from a population of cells and thus associated with cellular heterogeneity loss.

www.ebook3000.com

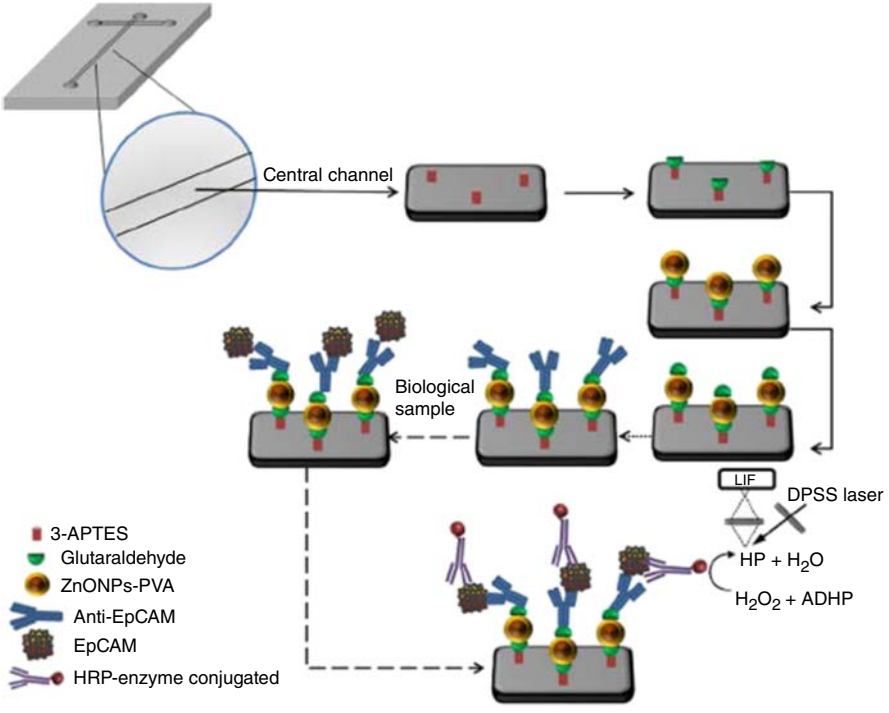


Figure 8.4 Schematic representation of the glass microfluidic surface modification and the immunological reaction. Anti-EpCAM antibodies were covalently bounded onto ZnONPs covered by polyvinyl alcohol (ZnONPs-PVA), which were covalently attached over the 3-aminopropyl triethoxysilane (3-APTES)-modified glass microfluidic surface. EpCAM present in the sample reacted immunologically with anti-EpCAM immobilized on a ZnONPs-PVA–3-APTES-modified glass microfluidic sensor. The bound EpCAM was quantified by HRP-conjugated anti-EpCAM antibody using acetyl-3,7-dihydroxyphenoxazine (ADHP) as an enzymatic mediator. The highly fluorescent resorufin (HP) generated was measured by LIF using excitation at 561 nm and emission at 585 nm. (Adapted from Fernández-Baldo *et al*. 2016 [16]. Reproduced with permission of Elsevier.)

To address this problem, microfluidic-chip-based high-throughput single-cell analysis has the potential to analyze a large quantity of individual cells to determine a distribution of response. Oh *et al.* [17] demonstrated the first cell-based protein detection in a microsystem, wherein *Escherichia coli* cells are genetically engineered to express the desired capture proteins on the membrane surface and are spatially arrayed as sensing elements in a microfluidic device. Tang's group [18] reported a highly sensitive and homogeneous detection of membrane protein on single living cells by aptamer and nicking enzyme-assisted fluorescence signal amplification in microfluidic droplets (shown in Figure 8.5). Based on the system, rapid, highly sensitive, and high-throughput single-cell analysis of the low-abundance biomarker, cell membrane protein tyrosine kinase-7, has been achieved.

In addition, the microfluidic protocol using a single antibody type was also developed to measure the difference in antigen expression between two different cell lines [19].

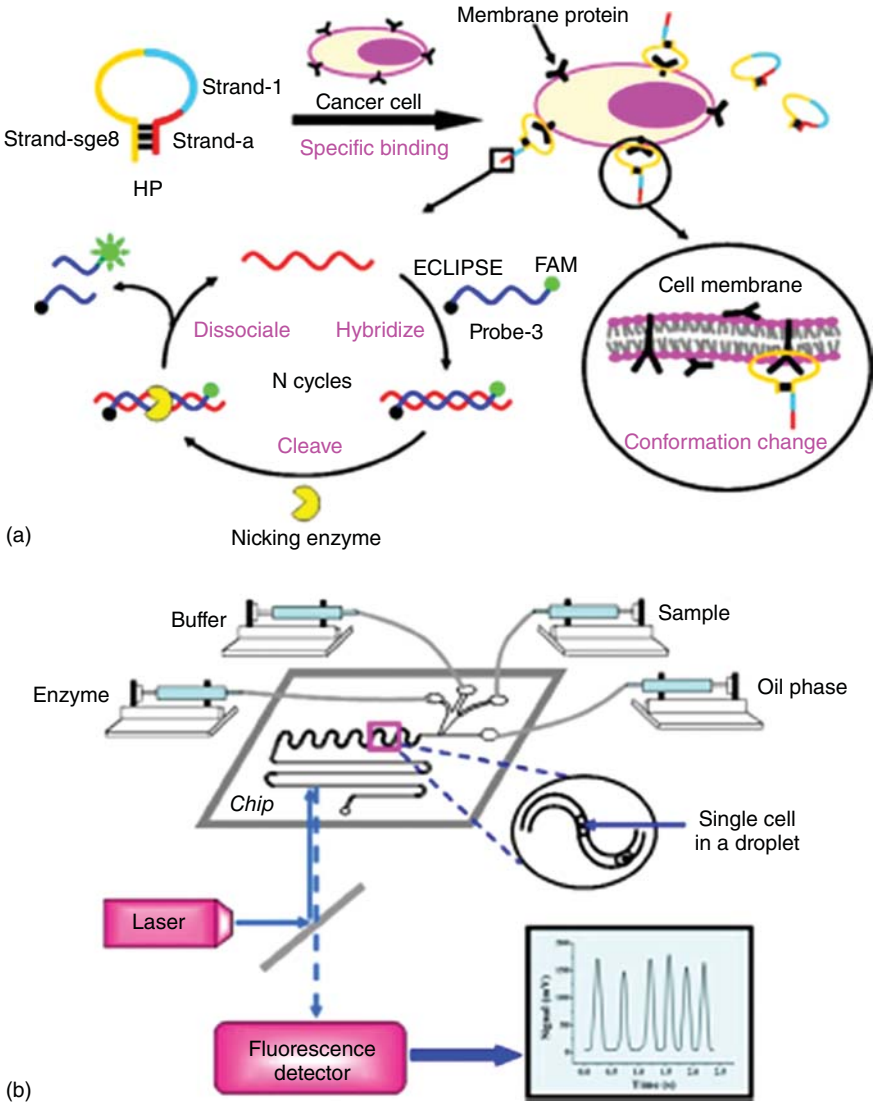


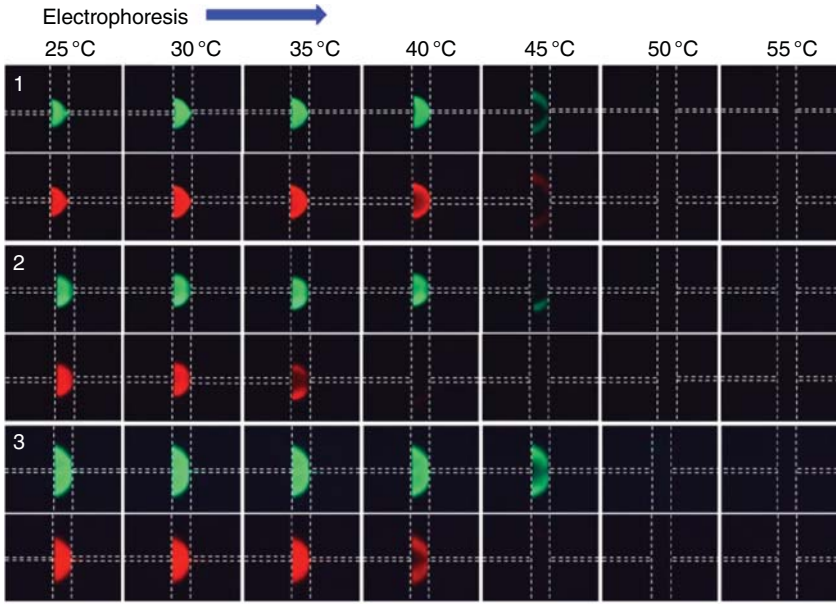
Figure 8.5 Schematic representation of the aptamer and nicking enzyme-assisted signal amplification assay for membrane protein on single living cells and (b) basic principle of microfluidic droplet system. (a) The fluidic channel network consists of four inlets and one outlet. Three of the inlets are used to deliver aqueous solutions (enzyme, buffer, and sample) and the fourth inlet delivers the water immiscible oil phase. The volumetric flows are controlled using the precision syringe pump containing four channels. A laser-induced fluorescence optical setup is used to focus the laser on the channel of the microfluidic system and collect the fluorescence arising from the cells in the droplets. (Adapted from Li *et al*. 2014 [18]. Reproduced with permission of American Chemical Society.)

www.ebook3000.com

8.3 Nucleic Acid Analysis

The analysis of nucleic acids (DNA or RNA) is of great importance for diagnosis and therapy since the abnormal expression of the nucleic acids is always associated with tumorigenesis, metastasis, and cancer progression. Microfluidic system possessed inherent superiority to overcome the challenges including difficulties in handling small sample volumes and high variability in measurements in the traditional biological nucleic acid assay [20].

Mousavi *et al.* [21] employed a capped gold nano-slit surface plasmonic resonance (SPR) sensor and a microfluidic chip for the determination of urinary miRNA-16-5p in the urine of acute kidney injury patients. Wang *et al*. [22] integrated a microfluidic chip with personal glucose meter to develop a quantitative approach for the detection of DNA using personal glucose meters. Jung *et al.* [23] developed a polydimethylsiloxane (PDMS)-based microfluidic linear hydrogel array for multiplexed single nucleotide polymorphism detection with ~1000 times more sensitive than planar microarrays. The analytical results were shown in Figure 8.6. By immobilization of the antibodies (for protein detection)



(a)

Figure 8.6 (a) Fluorescence images and (b) dissociation curves of carboxyfluorescein (FAM)-labeled matched and Texas Red-labeled one base mismatched targets captured in each capture gel containing 20 μM K12-probe-1 (1), the M13mp18 probe (2), and K12-probe-2 DNAs (3) at the indicated temperature. The experimentally determined dissociation temperature (T_d) for perfectly matched and mismatched target oligonucleotides were T_d (B-1, match) = 42.3 ± 0.3 °C, T_d (B-1, mismatch) = 39.9 ± 0.2 °C, T_d (B-2, match) = 42.2 ± 0.3 °C, T_d (B-1, mismatch) = 34.1 ± 0.8 °C, T_d (B-3, match) = 43.1 ± 0.2 °C, T_d (B-3, mismatch) = 38.5 ± 0.5 °C. (Adapted from Jung *et al*. 2012 [23]. Reproduced with permission of American Chemical Society.)

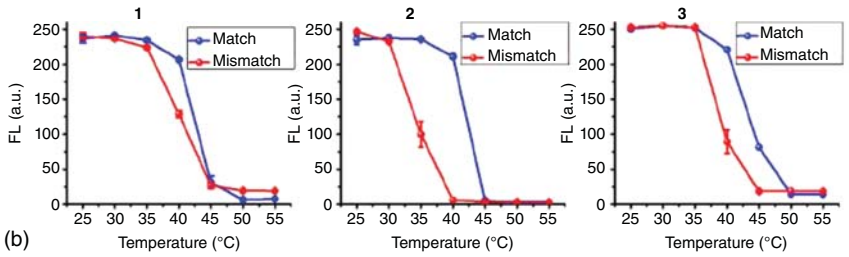


Figure 8.6 (*Continued*)

or hybridization probe (nucleic acids) in the parallel, serpentine microchannels, the identification of multiple targets could be accomplished in multiple samples simultaneously [24]. Prado *et al.* [25] reported the detection of unlabeled model-purified oligonucleotides RNA polyadenosine (5′-AAAAAAAAAA-3′) and polycytosine (5′-CCCCCCCCCC-3′) by SERS combining silver nanoparticles as enhancing surfaces on microfluidic platforms, appearing a highly promising for probing unlabeled nucleotides.

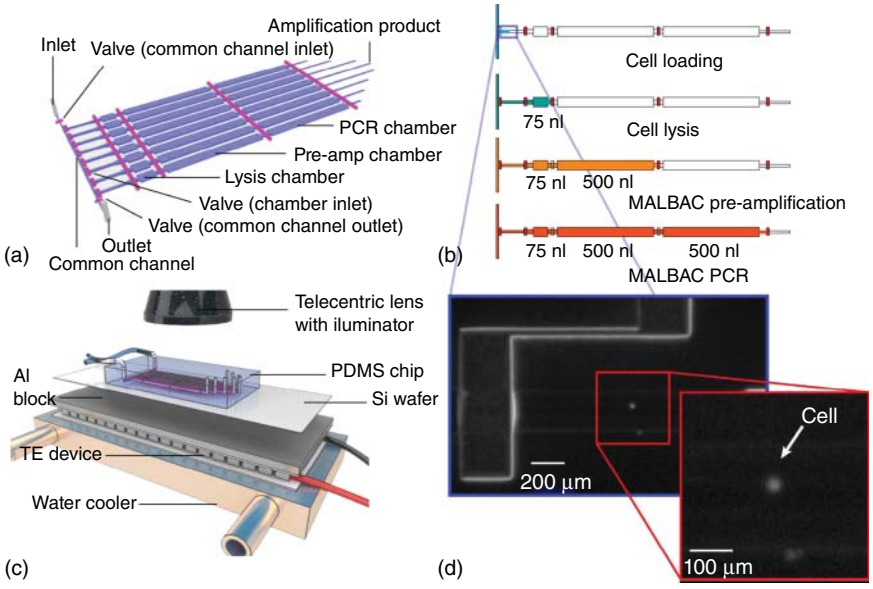


Figure 8.7 An integrated microfluidic device designed for single-cell MALBAC reactions. (a) Schematics of the device showing the fluidic channels (purple) and the control channels (magenta). (b) The operation of MALBAC reactions on a chip. Cells are suspended in phosphate buffered saline (PBS), and single cells are loaded manually by controlling the corresponding valves. Then, the cells are lysed and a two-step MALBAC reaction is performed. (c) Thermocycler and imaging system for the MALBAC reaction device. The PDMS chip is bonded to a Si wafer and placed on a Peltier device, which is attached to a water cooler. (d) Scattering of a single cell on-chip. (Adapted from Yu *et al*. 2014 [27]. Reproduced with permission of American Chemical Society.)

www.ebook3000.com

The quantification of mRNA or DNA at single-cell level could provide direct insight into how intercellular heterogeneity plays a role in disease progression and outcomes. Thompson *et al.* [26] developed the absolute quantification of single-cell mRNA transcripts by digital, one-step reverse transcription PCR in a simple microfluidic array device called the self-digitization (SD) chip. Yu *et al.* [27] developed a microfluidic device to perform multiplex single-cell whole-genome amplification (WGA) using multiple annealing and looping-based amplification cycles (MALBACs, shown in Figure 8.7). The device provided an easy-to-operate approach to perform single-cell sequencing library preparation with minimum hands-on time. This method reduces the requirement of manual expertise as well as the risk of contamination, demonstrating great promise in future applications especially the medical diagnosis.

Besides the abovementioned approaches, the droplet microfluidics have also been used for detection, quantification, and sequence analysis of the nucleic acids at the single-molecule level, and the related works have been reviewed in the previous report [28].

8.4 Cell Detection

The collection and identification of cells from body fluids is of great importance for early diagnosis of disease and evaluation of the patient response to therapy. For personalizing antibiotic treatment of urinary tract infections (UTIs), a method for rapid identification and susceptibility testing of uropathogenic microbes has been developed via immunosorbent ATP bioluminescence assay on a microfluidic simulator [29]. Typical process of microfluidic simulator use in UTI case is shown in Figure 8.8. Dou *et al.* [30] reported a versatile and cost-effective PDMS/paper hybrid microfluidic device integrated with loop-mediated isothermal amplification (LAMP) for the rapid, sensitive, and instrument-free detection of the main meningitis-causing bacteria, *Neisseria meningitidis*.

Circulating tumor cells (CTCs), a new type of biomarker, shed in peripheral blood at advanced metastatic stages of solid cancers, have gained increasing attention. However, the rarity of CTCs in the bloodstream makes the detection inaccessible. Lee *et al.* [31] proposed a centrifugal force-based size-selective CTC isolation platform that can isolate and enumerate CTCs from whole blood within 30 s with high purity, greatly improving downstream molecular analyses of captured CTCs. Nonetheless, the variation in size, morphology, expression profile, and antigen exposure may influence the reliable detection and evaluation of CTCs. Augustsson *et al.* [32] developed a noncontact, label-free microfluidic acoustophoresis method to separate prostate cancer cells from white blood cells (WBCs) through forces generated by ultrasonic resonances in microfluidic channels. Overview of the acoustophoresis microfluidic chip and system is shown in Figure 8.9. The feasibility of this method has been validated by discriminating tumor cells from WBCs using erythrocyte-lysed blood from healthy volunteers

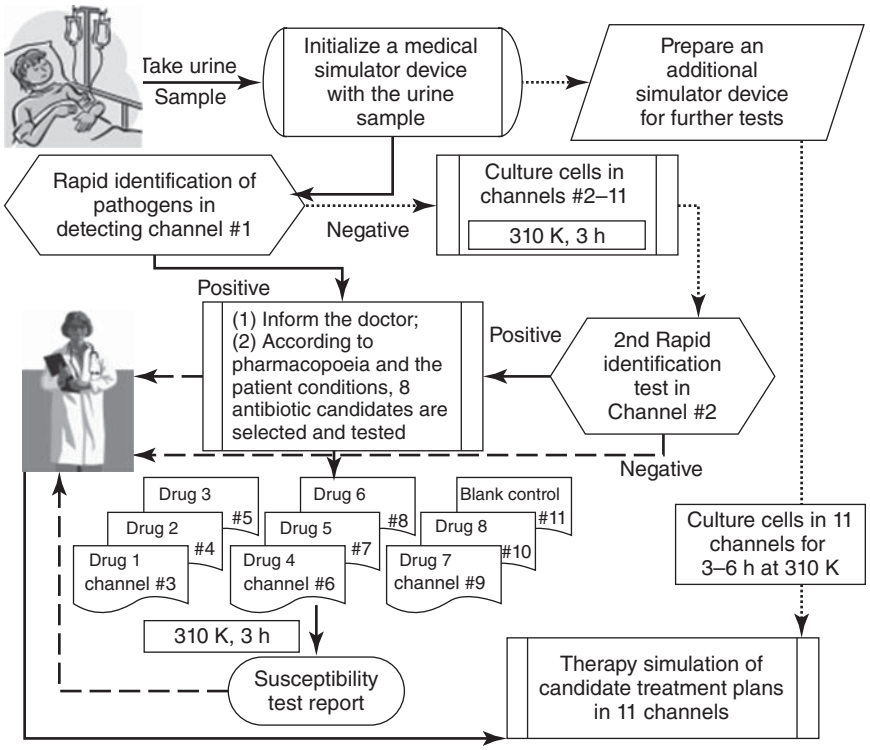


Figure 8.8 Typical process of microfluidic simulator use in a UTI case. After the urine sample of a patient is taken, a microfluidic simulator is loaded and prepared for the rapid identification of pathogens, whereas another simulator is also initialized to start cell proliferation. When the rapid immunosorbent ATP-bioluminescence assay (IATP-BLA) test shows a positive result, the doctor is informed in a timely manner, and, at most, eight antibiotic candidates are tested in the left channels. The results of the on-chip antimicrobial susceptibility testing (AST) are promptly reported to the doctor 3 h later. If the first IATP-BLA test returns a negative result, the second test double checks the result after 3 h of cell proliferation. The susceptibility report promptly delivers results to the doctor to permit the selection of appropriate antibiotics for optimal treatment of the individual patient. At last, the doctor can verify the antibiotic regimen options on the backup simulator before the real treatment is given to the patient, especially for chronic UTI cases. (Adapted from Dong and Zhao 2015 [29]. Reproduced with permission of American Chemical Society.)

spiked with tumor cells from three prostate cancer cell lines (DU145, PC3, LNCaP). Their technology showed a cancer cell recovery ranges from 93.6% to 97.9% with purity ranging from 97.4% to 98.4%. By combining microfluidics with SERS, a novel detection platform was constructed for the identification of individual mammalian cells continuously flowing in a microfluidic channel. The results were obtained for all of the cell mixture containing cancerous and noncancerous prostate cells, the lowest being 1 in 100 cells [33].

www.ebook3000.com

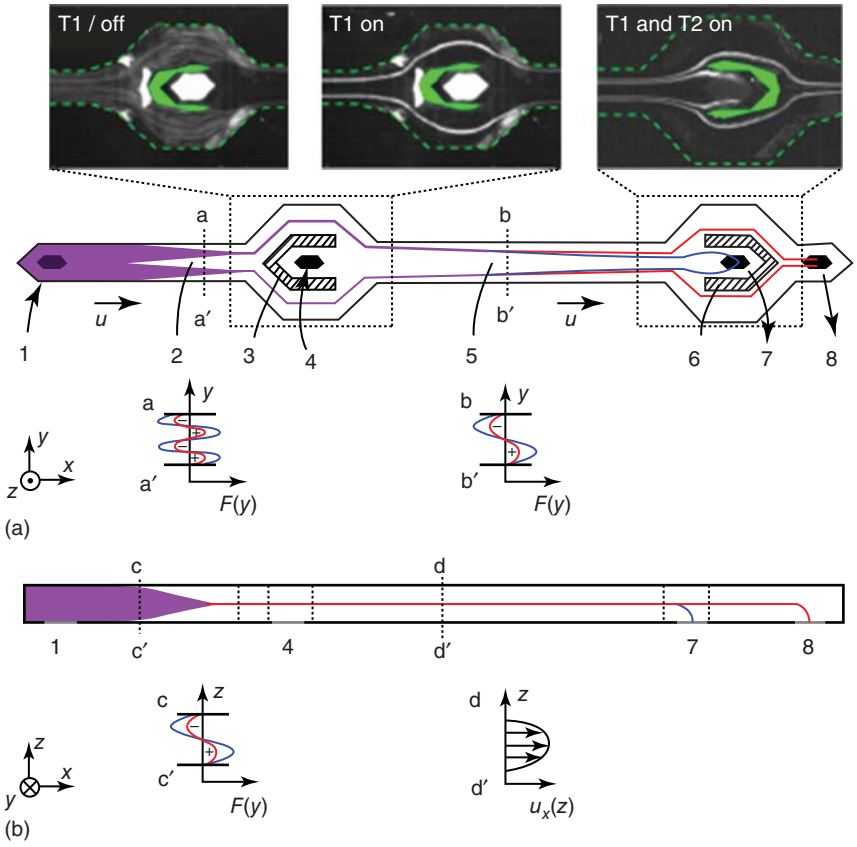
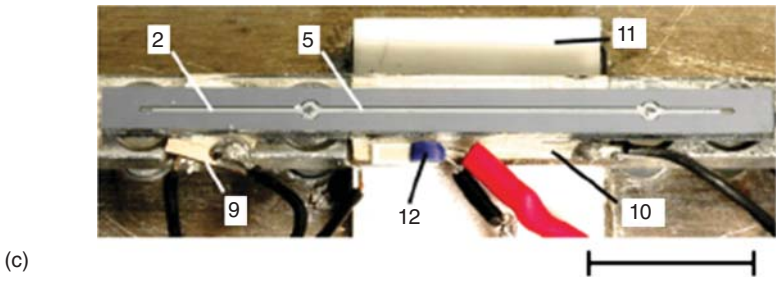
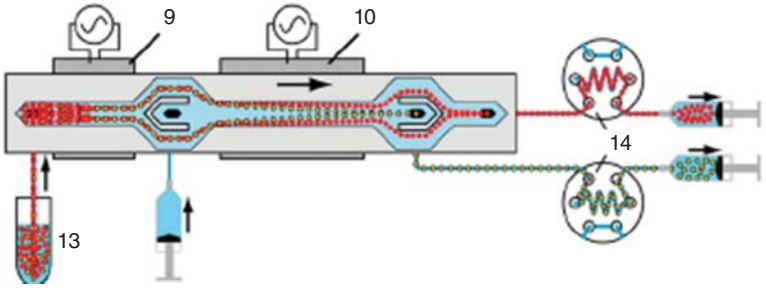


Figure 8.9 Overview of the acoustophoresis microfluidic chip and system. (a) Top view schematic. A suspension of cells/particles enters the system through the inlet (1) after which cells are prealigned in an acoustophoresis channel (2) by means of an acoustic field (a–a′) in the *yz*-plane. The two bands of cells are bifurcated (3) to two sides of a central inlet fluid flow (4) and the prealigned cells are thereafter flow laminated to proximity of the walls of a separation channel (5), where the trajectories of individual cells are deflected in an acoustic field (b–b′) according to their intrinsic acoustic properties and morphology. At the trifurcation outlet (6), a subgroup of cells can be selectively guided to the central outlet of the chip (7) by tuning the intensity of the second acoustic field, while cells of low acoustophoretic mobility will be guided to the side outlet (8). Insets show prealigned (T1 on) and nonprealigned (T1 off) microbeads at the end of the prealignment channel, with 5 and 7 μm beads separated at the central outlet (T1 and T2 on). (b) Side view schematic. Cells/particles are prealigned in the vertical direction by means of an acoustic force (c–c′) to minimize the influence of the parabolic flow profile (d–d′) in the channel, which may otherwise affect the trajectories of the cells. (c) A photo showing the positions of the piezoceramic transducers (9 and 10), the Peltier element that regulates the temperature (11), and the temperature sensor (12). Scale bar = 10 mm. (d) A schematic of the flow configuration for the acoustophoresis cell separation experiments. Syringe pumps drive the flow in the outlets and in the central fluid inlet. Cell suspension is drawn from the bottom of a test tube (13) by suction. The outlets are sampled via two sample loops (14), each with a volume of 100 μl. (Adapted from Augustsson *et al*. 2012 [32]. Reproduced with permission of American Chemical Society.)



(c)



(d)

Figure 8.9 (*Continued*)

8.5 Other Species

Besides the protein, nucleic acid, and cell analysis, the levels of small molecules such as glucose, amino acids, and dopamine in body fluids are also closely related with human health. As for glucose detection, a portable microplasma generation device (MGD) operated in ambient air is introduced for making a μPAD that serves as a primary healthcare platform [34]. The μPAD coupled with colorimetric assay for glucose and nitrite was performed and the low-cost, miniaturized, and portable platform is suitable for infield diagnostic tests. In the other work, a robust 3D-printed microfluidic analysis system integrated with Food and Drug Administration (FDA)-approved clinical microdialysis probes was constructed for monitoring real-time glucose and lactate levels [35]. However, the traditional personal glucose meters (PGMs) are fabricated to monitor only blood glucose levels [36]. To broad the applicability of the PGMs, various protocols have been proposed for the non-glucose analytes detection by selective linking of non-glucose targets with aptamers, DNAzymes, or antibodies, through the conjugation of these recognizing elements with enzymes, which could catalyze the conversion of non-glucose analytes to glucose [37–41]. The multistep target binding and enzymatic reactions in these methods make the detection less user-friendly for POC applications. To overcome this limitation, Zhang *et al.* [42] developed a simple and general quantitative POC diagnostic system by integration target recognition using DNA aptamer or biotin–streptavidin (STV) with a lateral flow device for sample processing and PGM for signal readout. The detection mechanism and analytical results are shown in Figure 8.10. The competitive assays in a single step for detection of both a small molecule as well as a large protein have been achieved.

www.ebook3000.com

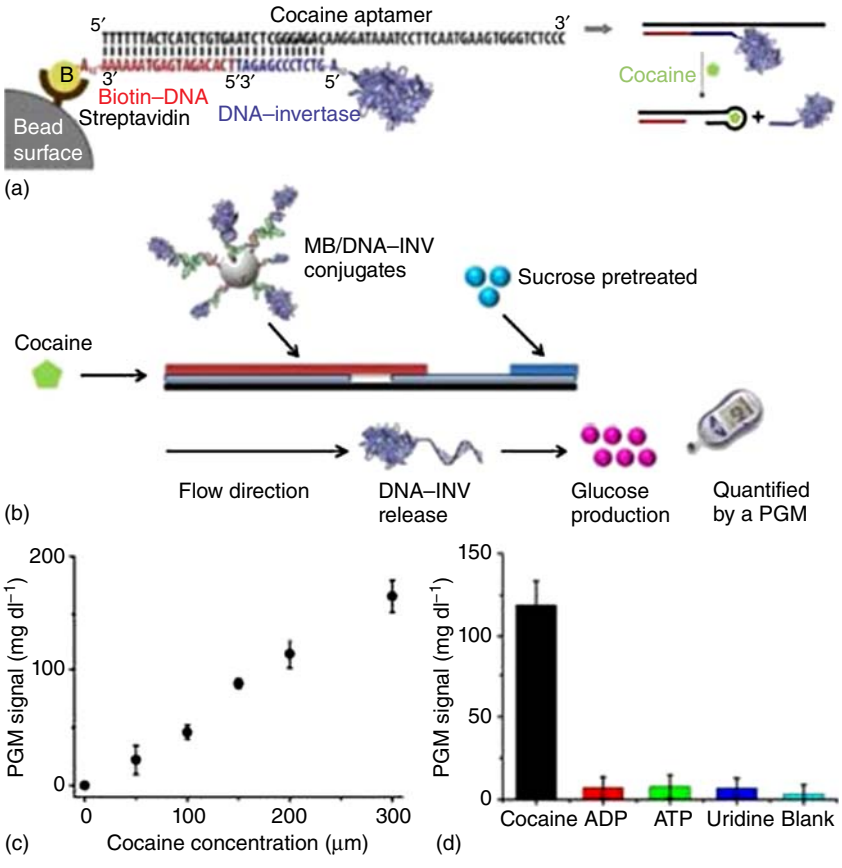


Figure 8.10 (a) Cocaine-induced release of immobilized DNA–invertase conjugates from DNA–invertase conjugate functionalized magnetic beads (MBs). DNA–invertase conjugates are immobilized onto MBs by DNA hybridization with a cocaine aptamer and biotin–DNA. (b) Proof-of-concept competitive assay for the detection of cocaine by DNA–invertase conjugate functionalized MBs using a PGM integrated with a lateral flow dipstick. (c) Relationship between PGM signals and cocaine concentrations in the samples. (d) Selectivity of the proposed PGM-LFDs system for cocaine detection. The concentrations of analytes were 200 μM. (Adapted from Zhang *et al*. 2016 [42]. Reproduced with permission of American Chemical Society.)

Islets of Langerhans could regulate the *in vivo* blood glucose levels through the secretion of endocrine hormones. To better understand the autocrine and paracrine roles that amino acids play in islet physiology, a device containing an islet chamber with the ability to perfuse stimulants coupled with an amino acid measurement system using online derivatization and electrophoretic separation integrated on a single microchip has been fabricated (shown in Figure 8.11). The device was used to perform online monitoring of the secretion profiles of amino acids from 2 to 5 islets [43].

The D-amino acids, d-methionine (d-Met), and d-leucine (d-Leu) are biomarkers involved in relevant diseases caused by *Vibrio cholerae*. Batalla *et al.* [44]

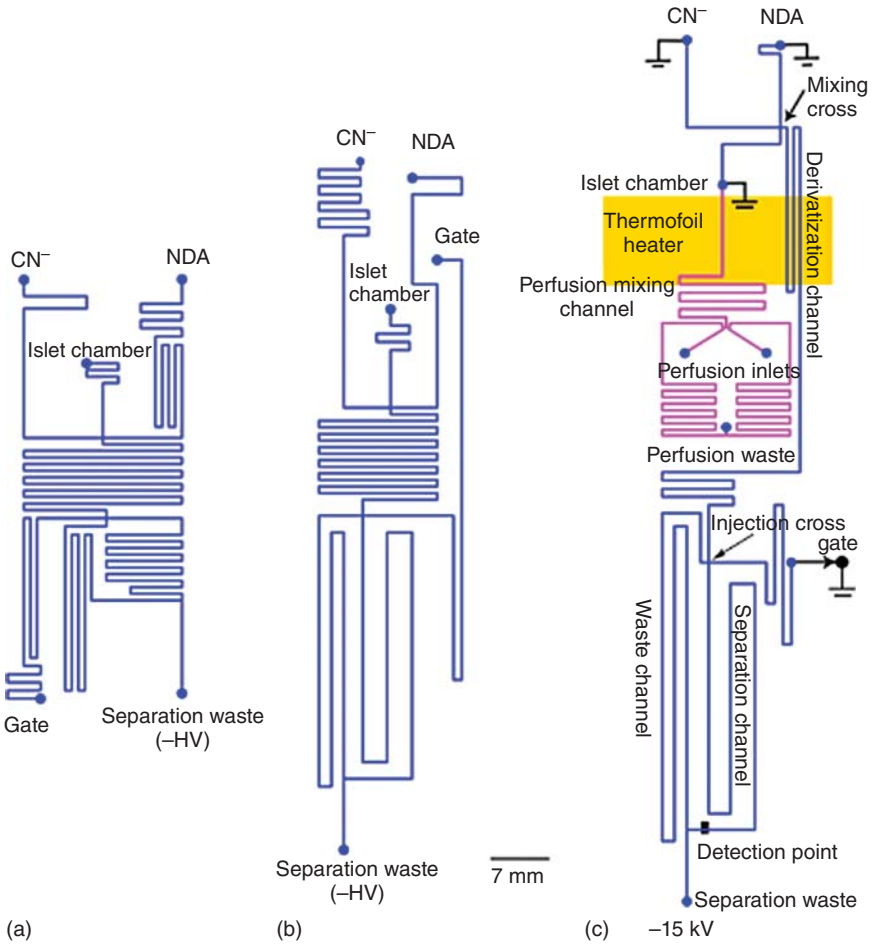


Figure 8.11 Microfluidic device designs. All designs tested had three grounded sample reservoirs (islet, CN^-, and NDA), a separation waste reservoir where –HV was applied, and a gate reservoir where the voltage was alternated between ground and float. (a) The initial chip design was 6.5 × 3 cm, and the distance between the gate and separation waste was 1.5 cm. (b) The second iteration of the device design used an enlarged chip with a dimension of 10 × 2.5 cm. The distance between the gate and the grounded islet chamber was 1 cm. (c) The final channel design had an overall dimension of 12.5 × 2.5 cm. The distances between the gate and separation waste reservoir and between the gate and islet chamber were 4 and 3.5 cm, respectively. The perfusion channels (magenta) were etched ~30 μm deep and ~100 μm wide on the bottom layer. The electroosmotic flow (EOF) (blue) channels were etched on the top layer and were ~5 × 20 μm (depth × width). A thermofoil heater (yellow region) was placed underneath the device with the edge next to the islet chamber to maintain the temperature of the chamber at 37 °C. (Adapted from Wang *et al*. 2016 [43]. Reproduced with permission of American Chemical Society.)

www.ebook3000.com

designed an enzyme-based microfluidic chip coupled to graphene electrodes for the separation and enantiomeric detection of d-Met and d-Leu, manifesting a promising principle for the development of POC devices for *in situ* screening of *V. cholerae*-related diseases. In addition, the simultaneous quantification of multiple small molecules in primary liver cells at single-cell levels was also proposed based on multicolor fluorescence-based microfluidic device [45].

8.6 Summary and Overlook

Due to the capability of being portability, high throughput, quantitative measurements, microfluidics has become a promising platform that allows fast and effective analysis of disease-associated biomarkers, such as proteins, nucleic acids, and even cells from tumor site. However, most of the developed systems are proof-of-concept prototypes and require external bulk instruments. μPADs with low cost and suitable for large-scale production are expected to become an equipment-free method for disease diagnosis. In addition, with the advancement of the nanomaterials and nanotechnology, the integration of nanomaterials within the microfluidic devices would bring advances to their sensitivity, stability, and robustness. We envision that microfluidic technique will continue to evolve, and advanced microfluidic devices will certainly offer facile, powerful, and user-friendly tools enabling rapid, specific, and sensitive detection for disease diagnosis.

References

1 Nahavandi, S., Baratchi, S., Soffe, R., Tang, S.-Y., Nahavandi, S., Mitchell, A., and Khashayar, K. (2014) Microfluidic platforms for biomarker analysis. *Lab Chip*, **14** (9), 1496–1514.

2 Herrmann, M., Veres, T., and Tabrizian, M. (2008) Quantification of low-picomolar concentrations of TNF-α in serum using the dual-network microfluidic ELISA platform. *Anal. Chem.*, **80** (13), 5160–5167.

3 Koh, C.-Y., Schaff, U.Y., Piccini, M.E., Stanker, L.H., Cheng, L.W., Ravichandran, E., Singh, B.-R., Sommer, G.J., and Singh, A.K. (2015) Centrifugal microfluidic platform for ultrasensitive detection of botulinum toxin. *Anal. Chem.*, **87** (2), 922–928.

4 Li, X. and Liu, X. (2016) A microfluidic paper-based origami nanobiosensor for label-free, ultrasensitive immunoassays. *Adv. Healthc. Mater.*, **5** (11), 1326–1335.

5 Kwon, S., Cho, C.H., Lee, E.S., and Park, J.-K. (2015) Automated measurement of multiple cancer biomarkers using quantum-dot-based microfluidic immunohistochemistry. *Anal. Chem.*, **87** (8), 4177–4183.

6 Wang, Y., Rauf, S., Grewal, Y.S., Spadafora, L.J., Shiddiky, M.J.A., Cangelosi, G.A., Schlücker, S., and Trau, M. (2014) Duplex microfluidic SERS detection of pathogen antigens with nanoyeast single-chain variable fragments. *Anal. Chem.*, **86** (19), 9930–9938.

7 Malhotra, R., Patel, V., Chikkaveeraiah, B.V., Munge, B.S., Cheong, S.C., Zain, R.B., Abraham, M.T., Dey, D.K., Gutkind, J.S., and Rusling, J.F. (2012) Ultrasensitive detection of cancer biomarkers in the clinic by use of a nanostructured microfluidic array. *Anal. Chem.*, **84** (14), 6249–6255.

8 Tang, C.K., Vaze, A., Shen, M., and Rusling, J.F. (2016) High-throughput electrochemical microfluidic immunoarray for multiplexed detection of cancer biomarker proteins. *ACS Sens.*, **1** (8), 1036–1043.

9 Piraino, F., Volpetti, F., Watson, C., and Maerkl, S.J. (2016) A digital–analog microfluidic platform for patient-centric multiplexed biomarker diagnostics of ultralow volume samples. *ACS Nano*, **10** (1), 1699–1710.

10 Ellington, A.D. and Szostak, J.W. (1990) In vitro selection RNA molecules that bind specific ligands. *Nature*, **346** (6287), 818–822.

11 Wang, Q., Liu, W., Xing, Y., Yang, X., Wang, K., Jiang, R., Wang, P., and Zhao, Q. (2014) Screening of DNA aptamers against myoglobin using a positive and negative selection units integrated microfluidic chip and its biosensing application. *Anal. Chem.*, **86** (13), 6572–6579.

12 Du, Y., Chen, C., Zhou, M., Dong, S., and Wang, E. (2011) Microfluidic electrochemical aptameric assay integrated on-chip: a potentially convenient sensing platform for the amplified and multiplex analysis of small molecules. *Anal. Chem.*, **83** (5), 1523–1529.

13 Wang, Y., Ye, Z., Ping, J., Jing, S., and Ying, Y. (2014) Development of an aptamer-based impedimetric bioassay using microfluidic system and magnetic separation for protein detection. *Biosens. Bioelectron.*, **59**, 106–111.

14 Wu, B., Jiang, R., Wang, Q., Huang, J., Yang, X., Wang, K., Li, W., Chen, N., and Li, Q. (2016) Detection of C-reactive protein using nanoparticle-enhanced surface plasmon resonance using an aptamer–antibody sandwich assay. *Chem. Commun.*, **52** (17), 3568–3571.

15 Altschuler, S.J. and Wu, L.F. (2010) Cellular heterogeneity: do differences make a difference? *Cell*, **141** (4), 559–563.

16 Fernández-Baldo, M.A., Ortega, F.G., Pereira, S.V., Bertolino, F.A., Serrano, M.J., Lorente, J.A., Raba, J., and Messina, G.A. (2016) Nanostructured platform integrated into a microfluidic immunosensor coupled to laser-induced fluorescence for the epithelial cancer biomarker determination. *Microchem. J.*, **128**, 18–25.

17 Oh, S.H., Lee, S.-H., Kenrick, S.A., Daugherty, P.S., and Soh, H.T. (2006) Microfluidic protein detection through genetically engineered bacterial cells. *J. Proteome Res.*, **5** (12), 3433–3437.

18 Li, L., Wang, Q., Feng, J., Tong, L.L., and Tang, B. (2014) Highly sensitive and homogeneous detection of membrane protein on a single living cell by aptamer and nicking enzyme assisted signal amplification based on microfluidic droplets. *Anal. Chem.*, **86** (12), 5101–5107.

19 Zhang, Y. and Pappas, D. (2016) Microfluidic cell surface antigen expression analysis using a single antibody type. *Analyst*, **141** (4), 1440–1447.

20 Ansari, M.I.H., Hassan, S., Qurashi, A., and Khanday, F.A. (2016) Microfluidic-integrated DNA nanobiosensors. *Biosens. Bioelectron.*, **85**, 247–260.

www.ebook3000.com

21 Mousavi, M.Z., Chen, H.-Y., Lee, K.-L., Lin, H., Chen, H.-H., Lin, Y.-F., Wong, C.-S., Li, H.F., Wei, P.-K., and Cheng, J.-Y. (2015) Urinary micro-RNA biomarker detection using capped gold nano-slit SPR in a microfluidic chip. *Analyst*, **140** (13), 4097–4104.

22 Wang, Q., Wang, H., Yang, X., Wang, K., Liu, F., Zhao, Q., Liu, P., and Liu, R. (2014) Multiplex detection of nucleic acids using a low cost microfluidic chip and a personal glucose meter at the point-of-care. *Chem. Commun.*, **50** (29), 3824–3826.

23 Jung, Y.K., Kim, J., and Mathies, R.A. (2015) Microfluidic linear hydrogel array for multiplexed single nucleotide polymorphism (SNP) detection. *Anal. Chem.*, **87** (6), 3165–3170.

24 He, S., Zhang, Y., Wang, P., Xu, X.i., Zhu, K., Pan, W., Liu, W., Cai, K., Sun, J., Zhang, W., and Jiang, X. (2015) Multiplexed microfluidic blotting of proteins and nucleic acids by parallel, serpentine microchannels. *Lab Chip*, **15** (1), 105–112.

25 Prado, E., Colin, A., Servant, L., and Lecomte, S. (2014) SERS spectra of oligonucleotides as fingerprints to detect label-free RNA in microfluidic devices. *J. Phys. Chem. C*, **118** (25), 13965–13971.

26 Thompson, A.M., Gansen, A., Paguirigan, A.L., Kreutz, J.E., Radich, J.P., and Chiu, D.T. (2014) Self-digitization microfluidic chip for absolute quantification of mRNA in single cells. *Anal. Chem.*, **86** (24), 12308–12314.

27 Yu, Z., Lu, S., and Huang, Y. (2014) Microfluidic whole genome amplification device for single cell sequencing. *Anal. Chem.*, **86** (19), 9386–9390.

28 Kang, D.-K., Ali, M.M., Zhang, K., Pone, E.J., and Zhao, W. (2014) Droplet microfluidics for single-molecule and single-cell analysis in cancer research, diagnosis and therapy. *TrAC, Trends Anal. Chem.*, **58**, 145–153.

29 Dong, T. and Zhao, X. (2015) Rapid identification and susceptibility testing of uropathogenic microbes via immunosorbent ATP-bioluminescence assay on a microfluidic simulator for antibiotic therapy. *Anal. Chem.*, **87** (4), 2410–2418.

30 Dou, M., Dominguez, D.C., Li, X., Sanchez, J., and Scott, G. (2014) A versatile PDMS/paper hybrid microfluidic platform for sensitive infectious disease diagnosis. *Anal. Chem.*, **86** (15), 7978–7986.

31 Lee, A., Park, J., Lim, M., Sunkara, V., Kim, S.Y., Kim, G.H., Kim, M.H., and Cho, Y.-K. (2014) All-in-one centrifugal microfluidic device for size-selective circulating tumor cell isolation with high purity. *Anal. Chem.*, **86** (22), 11349–11356.

32 Augustsson, P., Magnusson, C., Nordin, M., Lilja, H., and Laurell, T. (2012) Microfluidic, label-free enrichment of prostate cancer cells in blood based on acoustophoresis. *Anal. Chem.*, **84** (18), 7954–7962.

33 Pallaoro, A., Hoonejani, M.R., Braun, G.B., Meinhart, C.D., and Moskovits, M. (2015) Rapid identification by surface-enhanced Raman spectroscopy of cancer cells at low concentrations flowing in a microfluidic channel. *ACS Nano*, **9** (4), 4328–4336.

34 Kao, P.-K. and Hsu, C.-C. (2014) Battery-operated, portable, and flexible air microplasma generation device for fabrication of microfluidic paper-based analytical devices on demand. *Anal. Chem.*, **86** (17), 8757–8762.

35 Gowers, S.A.N., Curto, V.F., Seneci, C.A., Wang, C., Anastasova, S., Vadgama, P., Yang, G.-Z., and Boutelle, M.G. (2015) 3D printed microfluidic device with integrated biosensors for online analysis of subcutaneous human microdialysate. *Anal. Chem.*, **87** (15), 7763–7770.

36 Clarke, S.F. and Foster, J.R. (2012) A history of blood glucose meters and their role in self-monitoring of diabetes mellitus. *Br. J. Biomed. Sci.*, **69** (2), 83–93.

37 Xiang, Y. and Lu, Y. (2011) Using personal glucose meters and functional DNA sensors to quantify a variety of analytical targets. *Nat. Chem.*, **3** (9), 697–703.

38 Yan, L., Zhu, Z., Zou, Y., Huang, Y., Liu, D., Jia, S., Xu, D., Wu, M., Zhou, Y., Zhou, S., and Yang, C.J. (2013) Target-responsive "sweet" hydrogel with glucometer readout for portable and quantitative detection of non-glucose targets. *J. Am. Chem. Soc.*, **135** (10), 3748–3751.

39 Ma, X., Chen, Z., Zhou, J., Weng, W., Zheng, O., Lin, Z., Guo, L., Qiu, B., and Chen, G. (2014) Aptamer-based portable biosensor for platelet-derived growth factor-BB (PDGF-BB) with personal glucose meter readout. *Biosens. Bioelectron.*, **55**, 412–416.

40 Wang, W.J., Huang, S., Li, J.J., Rui, K., Zhang, J.R., and Zhu, J.J. (2016) Coupling a DNA-based machine with glucometer readouts for amplified detection of telomerase activity in cancer cells. *Sci. Rep.*, **6**, 23504.

41 Du, Y., Hughes, R.A., Bhadra, S., Jiang, Y.S., Ellington, A.D., and Li, B. (2015) A sweet spot for molecular diagnostics: Coupling isothermal amplification and strand exchange circuits to glucometers. *Sci. Rep.*, **5**, 11039.

42 Zhang, J.-J., Shen, Z., Xiang, Y., and Lu, Y. (2016) Integration of solution-based assays onto lateral flow device for one-step quantitative point-of-care diagnostics using personal glucose meter. *ACS Sens.*, **1** (9), 1091–1096.

43 Wang, X., Yi, L., and Roper, M.G. (2016) Microfluidic device for the measurement of amino acid secretion dynamics from murine and human islets of Langerhans. *Anal. Chem.*, **88** (6), 3369–3375.

44 Batalla, P., Martín, A., López, M.Á., González, M.C., and Escarpa, A. (2015) Enzyme-based microfluidic chip coupled to graphene electrodes for the detection of D-Amino acid enantiomer-biomarkers. *Anal. Chem.*, **87** (10), 5074–5078.

45 Li, Q., Chen, P., Fan, Y., Wang, X., Xu, K., Li, L., and Tang, B. (2016) Multi-color fluorescence detection-based microfluidic device for single-cell metabolomics: simultaneous quantitation of multiple small molecules in primary liver cells. *Anal. Chem.*, **88** (17), 8610–8616.

www.ebook3000.com

9

Gene Expression Analysis on Microfluidic Device

Liang Zhao

University of Science and Technology Beijing, Research Center for Bioengineering and Sensing Technology, School of Chemistry and Biological Engineering, 30 Xueyuan Road, Beijing 100083, PR China
University of Science and Technology Beijing, School of Chemistry and Bioengineering, Beijing 100083, PR China
University of Science and Technology Beijing, Beijing Key Laboratory for Bioengineering and Sensing Technology, Beijing 100083, PR China

9.1 Introduction

Nowadays, biological science has entered the era of systematic investigation ranging from genomic informative analysis for hereditary interpretations, to single-cell epigenetic exploration, to integrative proteomic study. Quantitative measurements of the key parameters are fundamental issues in life science research. Among these parameters, gene expression level within cells stands out at the central stage and plays a pivotal role in the study of molecular or cell biology. In a sense, modern life science tightly relies on the reliable analysis of gene expression. Thus, profiling the gene expression and its regulation with dependable precision are therefore of great importance. According to the central dogma, gene expression originates from DNA molecules from which the genetic information is transcribed to mRNA and then translated to proteins, indicating that at least three molecular levels have been involved in this process. Firstly, in a cell, the genome represented as individual DNA molecules encoded all the information from which the regulation of gene expression originates. Nevertheless, the copy number of mRNA is also low due to the short life span, which is conservatively regulated by different RNAse in living cells. At last, some particular proteins, such as transcription factors, which regulate the gene expression, are relatively less abundant. Moreover, along with this, cellular heterogeneity is in fact an inherent feature of life and has been recognized as significant in the studies of embryo development, immunology, bacterial survival strategy, and even tumor initiation. The average analysis of gene expression results in median answers and from which some of the detailed and important information could be obscured. These fundamental issues asked the profiling of gene expression to be more delicate, more sensitive, and, more importantly, quantitatively enough to probe single cells.

To meet the hurried demands for quantitatively probing the gene expression at different levels, new technologies such as quantitative real time polymerase

Microfluidics: Fundamentals, Devices and Applications, First Edition.
Edited by Yujun Song, Daojian Cheng, and Liang Zhao.
© 2018 Wiley-VCH Verlag GmbH & Co. KGaA. Published 2018 by Wiley-VCH Verlag GmbH & Co. KGaA.

chain reaction (PCR) assay, DNA microarray, flow cytometry-based detection, immunofluorescence, Western blotting, and even sophisticated mass spectrometry have been expeditiously invented for dissecting the nucleic acids and proteins in cells. However, these approaches often require not only large amounts of starting materials such as extracted DNA, RNA, or proteins from more than 5000 cells but also relatively complex procedures that are not directly coupled with cell isolation, genetic material purification, and phenotype investigation. Recently, although new protocols appropriate to dissect single cell based on these tools have been developed, there are still a number of limitations such as multiple steps of dilutions of single-cell materials after lysis, which consequently hit the roof of the sensitivity.

Microfluidic circuits, a technology that manipulates the tiny amount of liquid from picoliters to nanoliters within the structure of micrometer dimensions, are ideally suitable to address these problems by providing limited scalability associated with temporal and spatial controlling, reduced reagent consumption, inherited capability coupled with microscopy, and ease of parallelization and automation. Over a decade of rapid evolution and interdisciplinary interaction, stretching fields of chemistry, advanced engineering, cellular biology, imaging processing, and molecular biological techniques have now enabled microfluidic genetic and protein analyses to access the detailed information that is previously hard to glean through conventional methods. Recent developments in microfluidics have further expanded the investigation of gene expression by enabling the realization of different level of biochemical experiments on a single chip, ranging from automatic cell culture and single-cell imaging to digital PCR analysis of rare DNA sample.

This chapter provides an overview of recently developed microfluidic approaches for analyzing gene expression both on small cell populations and on individual cell levels. We are especially interested on how the microfluidic techniques were used to make the studies different from the conventional assays that are routinely adopted in biological laboratory and how these new devices help to address the existing issues within traditional methods. Instead of making an attempt to be comprehensive, we choose the most exciting works on this field, specifically those discussing the applications of microfluidic devices to single-cell level analysis, which may pave a way to transform the scenario of quantitative system biology combined with miniaturized formats, and highlighting the next-generation sequencing technologies. Accordingly, three realms have been discussed in this chapter:

1) The studies of gene expression in cell population associated studies with a microfluidic method. This will include the genetic analysis of nucleic acids and protein imaging dissecting normally founded on fluorescent protein constructing within the genome of cells.
2) Recent works on microfluidics related to single-cell genetic profiling or gene expression. Both imaging process like fluorescent protein facilitated imaging and RNA fluorescent *in situ* hybridization (FISH) and the nucleic acid amplification-based technology have been studied at single-cell level within a microfluidic device.

www.ebook3000.com

3) We will check out some of the most recent commercial progresses employing microfluidic methods as a promising tool for conducting biochemical assays on chip in an integrative way.

9.2 Analysis Cell Population Gene Expression on Chip

9.2.1 Nucleic Acid Analysis

As a platform of controlling of fluidic behavior in micrometer channels and structures, microfluidic approaches offer a rapid, cost-reducing, and easy operation for genetic probing at nucleic level. One of the original virtues of microfluidic platform is the possibility of being integrated with multiple functions. Burns presented a pioneer work for analysis of DNA on chip [1], a system where DNA and reagent solutions can be consequently introduced, mixed, amplified or digested, and finally separated and detected in a glass–silicon chip by photolithographic fabrication. Target DNA fragment has been successfully amplified and detected by integrated thermal cycler and a photodiode underneath the gel channel. With a similar device, they accomplished a test of genetic analysis of influenza viral strain (A/LA/1/87 and A/Sydney/5/97) subtyping that distinguished the polymorphism in the hemagglutinin coding region [2]. This system is consisted of some key components (phase change valves, thermal cycler reaction chambers, and pulsed drop motion) that allow two steps of biochemical reactions (PCR amplification of HA1 gene and HapI endonuclease digestion) serially taking place on a single chip. Other than detecting DNA by gel electrophoresis, Lagally from Mathies' group developed the first portable microsystem combined with microchamber PCR with capillary electrophoresis separation and laser-excited fluorescence detection [3]. This device was used to identify the pathogenic variants of *Escherichia coli* (O55:H7 and O157:H7) producing shiga toxin from commensal background *E. coli* K12 cells via primer-selective amplification during PCR. Not only PCR but also other methods of nucleic acid amplification have been utilized in microchip capillary electrophoresis (CE) system for the detection of specific gene. Mahmoudian *et al.* [4] developed an integrated platform for rolling circle amplification (RCA) and circle-to-circle amplification (C2CA) of circular probe (padlock probe) and subsequent electrophoretic detection DNA fragments from bacterial pathogen *Vibrio cholerae* poly(methyl methacrylate) microchip. The RCA reaction was carried out in the sample reservoir of chip at a temperature of 37 °C, and the whole process of identification of bacterial genomic DNA took less than 65 min (including amplification reaction and electrophoresis) by this system. Fang *et al.* [5] coupled loop-mediated isothermal amplification (LAMP) method with a microchannel chip to detect pseudorabies virus (PRV) gene in sample by the naked eye or via an optic sensor. This platform is suitable to be used as a point-of-care pathogen testing device because of extreme accessibility of operation, reaction condition (hot water bath), and readout (naked eye). Similarly, Stedtfeld *et al.* [6] reported a portable battery contained genetic testing device termed "Gene-Z" that consists four-arrayed channels of 15 reaction chambers and within which dehydrated primers have been previously dispensed. Specific pathogens *E. coli*

(eaeA and stx2 genes) and *Staphylococcus aureus* (mecA and vicK genes) were detected in real time during LAMP amplification by integration of light-emitting diodes (LEDs) and photodiodes beneath the reaction chambers on this platform. Moreover, the coupling of nucleic acids extraction or purification has been adopted as an essential part in microfluidic circuit. To address this issue, still with LAMP amplification method, either magnetic beads conjugated with specific oligonucleotides [7, 8] or microfabricated glass pillar structures [9] have been applied in the microchip for capturing target RNA or DNA. By using an immune magnetic target binding strategy, Ferguson *et al.* developed a point-of-care system that integrates sample treatments including capture, concentration and purification, reverse transcription and PCR amplification, and sequence-dependent electrochemical detection on a single chip [10] (Figure 9.1a). They demonstrated that this system is capable of sensing H1N1 influenza virus from

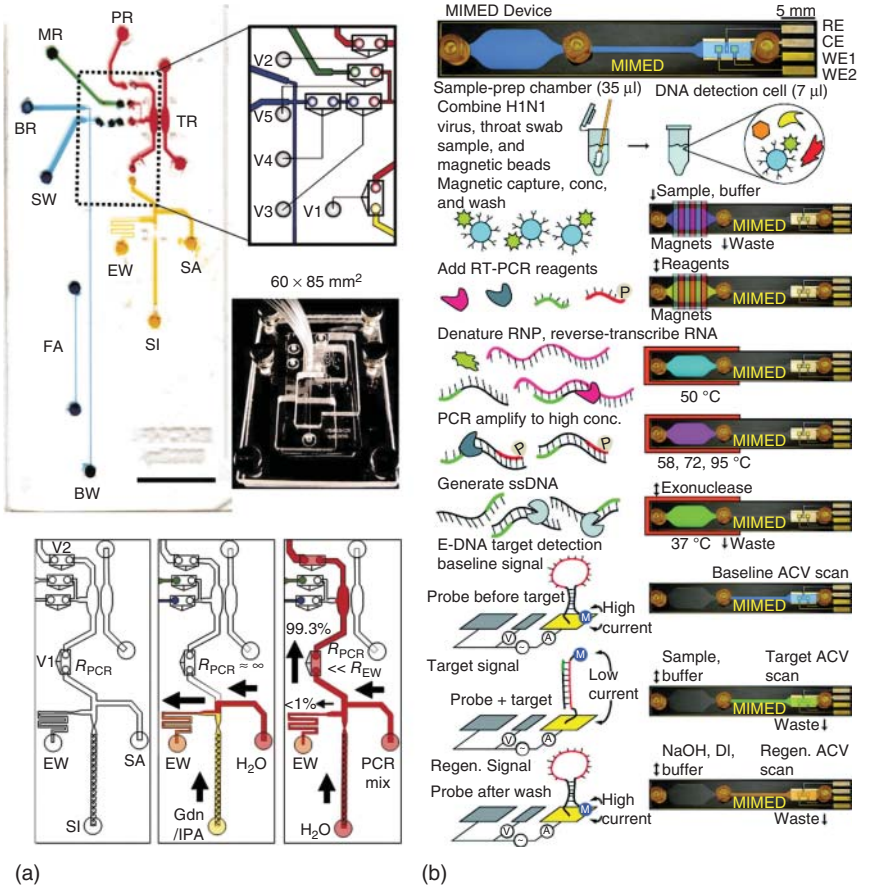


Figure 9.1 (a) A microfluidic system integrates sample treatments, reverse transcription and PCR amplification, and sequence-dependent electrochemical detection on a single chip. (Ferguson *et al*. 2011 [10]. Reproduced with permission of American Chemical Society.) (b) A sample-in-answer-out system that contains extraction of nucleic acids from the whole blood, amplification, and electrophoresis readout [11].

www.ebook3000.com

swab samples directly within ~3.5 h and a limit of detection (LOD) approximately four orders magnitude below those in clinical trials. Silica microstructure [12] is another promising material for binding and eluting of nucleic acids. Shaw *et al.* constructed a silica monolith in a self-contained microfluidic format where direct DNA extraction and PCR amplification have been conducted in channel. Recently, they extended this protocol to RNA extraction and reverse transcription for semiquantitative expression analysis of cytochrome P450 gene, which encodes enzymes involving in metabolism of pharmaceutical agents [13]. Notably, their device, where the PCR reagents have been pre-stored inside the channel for at least 8 weeks at 4 °C without loss of activity, can refer itself as a "ready-to-use" apparatus offering potentials for clinical detection. Irimia *et al.* [14] designed a microfluidic system for the purification of total cellular RNA and incorporated it in a whole transcriptome amplification protocol to identify the biological pathway spanning over 312 genes from stimulated and unstimulated cells. Two silica columns served as a key component to accumulate total RNA in this system where as small as 150 cells have been lysed directly. Compared with the microarray data analysis from bulk isolation control (0.3 ng RNA), the microfluidic purification (150 cells) microarray gene heatmap shows a good consistence with bulk analysis result.

A lot of works have presented the feasibility of genetic detection in microfluidic device by employing of multiplexed pretreatments on chip including DNA or RNA extraction and purification, followed by amplification and detection of the target gene online. The full integration of gene analysis on microfluidic device, more importantly, from raw samples such as whole blood is still an attractive, cost-effective, time-saving goal for scientist. Easley of Landers' group described a sample-in-answer-out microfluidic genetic analysis system capable of accepting whole blood samples with extraction of nucleic acids, PCR specific amplification, and electrophoresis separation for reading out [11]. They validated this device by performing online detection of *Bacillus anthracis* (anthrax) gene in 750 nl of whole blood from living infected mice and of *Bordetella pertussis* gene in 1 μl of nasal aspirate from a patient (Figure 9.1b). Interestingly, to realize complex processing during the treatment of raw samples without cross contamination, some unique advances of microfluidics, such as differential flow resistances, elastomeric valves, laminar flow, and electrophoresis, have been implemented within the device. Sethu and Toner demonstrated a method for the depletion of erythrocytes in whole blood, enabling amplification and transcriptome microarray analysis after concentration of leukocytes on chip. This technique can circumvent unwanted stressing on cells that altered gene expression during the selective bulk lysis in conventional processing.

9.2.2 Protein Level Analysis of Gene Expression

Gene expression is actually not linearly patterned in cells. The regulation of gene expression is highly conservative and controlled: for example, at genomic level, triggering and silencing are mediated by transcription factor and histone protein modification that are related to acetylation and methylation. Chromatin immunoprecipitation (ChIP) is a useful method to investigate DNA–protein

interactions. Traditional assay for ChIP requires a skillful person to perform, involves complex and tedious manual steps, and usually needs a large population of cells as a starting material. Wu *et al*. [15] developed an Auto ChIP platform to implement ChIP analysis from 2000 cells in a rapid, automated way. Taking advantage of valve integration on chip for mixing and controlling of minimal aqueous sample and solid beads, they significantly shortened the key incubation step in ChIP from overnight to 2 h because of the enhanced immunoprecipitation efficiency in scaled volume, therefore cutting the length of the assay to less than a day compared with 2–7 days with conventional method. Furthermore, they increased the ChIP throughput to 14 ChIP and two control measurements at one assay on a microfluidic device [16]. Aside from being lengthy and tricky, the traditional ChIP is also hampered by unsuccessful selection of suitable antibodies, which is very laborsome. To address this problem, the author demonstrated the utility of their high-throughput ChIP (HTChIP) device in antibody screening assays by simultaneously comparing multiple antibodies specificity in ChIP, enabling superiority of laborsaving. In addition, they also showed the possibility of using this platform to detect the changes in the epigenetic state induced by cytokine stimulant over time. Geng *et al.* reported an altered design of microfluidic device to perform ChIP [17]. Combining partially opened elastomeric valve with antibody-conjugated magnetic beads, the device is able to conduct multiple steps during ChIP experiment including cell lysis, MNase digestion, inactivation, and immunoprecipitation and wash the unwanted DNA fragments. They examined two genomic locations (folate receptor and β-globin) for the enrichment of acetylated histone H3 and found the sensitivity of detection can reach as few as 50 cells.

Proteins, the final products of gene expression, dominate nearly all the biological processes in living cells. Thus protein analysis is one of the key missions in the gene expression profiling. Conventional gene expression analysis techniques such as gene specific detection by electrophoresis, reverse transcription PCR, or microarray analysis often begin with a destructive way to lyse or extract materials of gene expression such as DNA, RNA, or protein. The cellular dynamic gene expression could only be collected at a given time point by reconstructing the information from separated subpopulations using these methods. Signals of protein expression pathway at the same population or the same cell are therefore inaccessible. Recent developments in imaging, specifically by using fluorescent protein technologies, are now allowing noninvasive measurements of gene expression at protein level with high temporal and spatial resolution in the same sample of cell population or even individual cell. Thompson *et al.* described a dynamic gene expression investigation in a living cell array microfluidic chip combining with a green fluorescent protein (GFP) reporter (d2EGFP) that have been preconstructed in HeLa cell line [18]. This device was used to detect the activation of a transcription factor (NF-κB) in response to cytokine tumor necrosis factor α (TNF-α) within eight different concentrations, which came from the upstream of microfluidic concentration generator (Figure 9.2a). Time-lapse imaging and quantitative analysis of fluorescent intensity obtained the gene expression dynamics of NF-κB given the cell population located in downstream culture chamber. Likewise, King *et al*. [19] reported a compact experimental platform that incorporated monoclonal live cell transcriptional

www.ebook3000.com

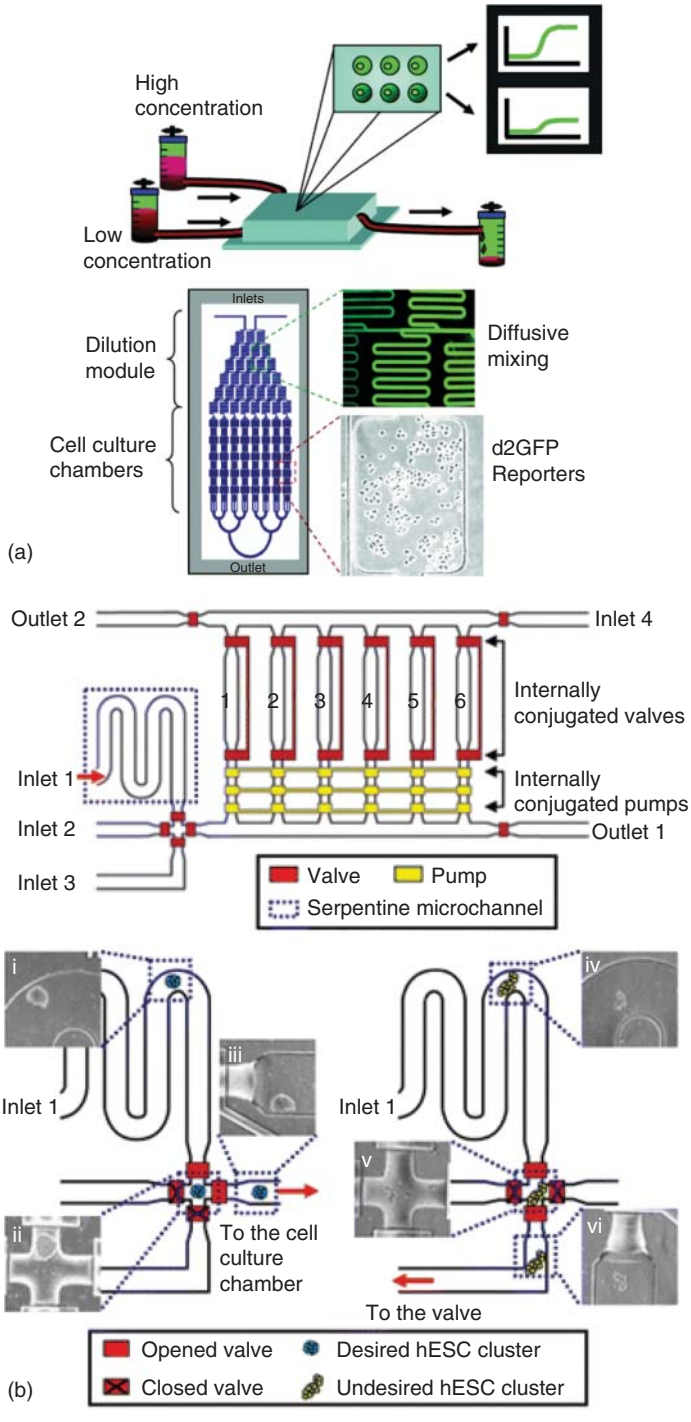


Figure 9.2 (a) Dynamic gene expression profiling in a microfluidic chip combining with a GFP reporter (d2EGFP) that have been preconstructed in HeLa cell line. (Thompson *et al*. 2004 [18]. Reproduced with permission of American Chemical Society.) (b) The hESCs-μchip for reproducible quantitative culture and multiparameter analysis of pluripotent state of hESCs in semiautomated fashion.

reporter libraries into microfluidic perfusion culture system to dissect the real-time gene expression dynamics across a broad range of stimulus–response pairs. Still using time-lapse imaging process, the researchers can collect 192 time courses, totaling up to ~5000 single time point measurements at one experiment on chip. Because of integrated elastomeric microvalves ensuring the isolation between each cell culture chambers, multiple reporter cell lines and different soluble factors are able to deliver into each chamber in an addressable manner. Analogously, in conjugation with fluorescent protein reporter in human embryonic stem cells (hESCs), Kamei *et al.* [20] demonstrated, for the first time, a microfluidic device (hESCs-μchip) for reproducible quantitative culture and multiparameter analysis of pluripotent state of hESCs in semiautomated fashion (Figure 9.2b). In order to monitor the hESC self-renewal status in real time, there are three knock-in hESC lines: HSF1-LG that expresses firefly luciferase and enhanced green fluorescent protein (EGFP) driven by ubiquitin promoter and HSF1-OCT4-EGFP and H1-OCT4-EGFP that express EGFP under the endogenous OCT4 promoter were used for image evaluating OCT4 gene expression, which plays a central role in maintaining pluripotency. On this system, hESCs clones from the bulk culture can be carefully selected and subsequently introduced into given microculture chambers by using microvalve-controlling configuration. Noteworthily, to confirm the pluripotent state of hESCs on chip, immunocytochemistry were also carried out in the same device for probing a number of pluripotency markers, like alkaline phosphatase (AP), stage-specific embryonic antigen 4 (SSEA4), OCT4, Nanog, tumor-related antigen (TRA)-1-60, and TRA-1-81.

Immunocytochemistry is another powerful tool for high sensitive and specific imaging of protein expression within cells. Although it is an end-point assay for analysis protein distribution within cells, immunofluorescence (IF) enables distinguishing of multiple biomarker proteins without genetic engineering and has been regarded as a routing technique in clinical diagnosis. Weigum *et al.* presented a cell-based lab-on-a-chip sensor to early detect oral cancer biomarker epidermal growth factor receptor (EGFR), whose overexpressing indicates early oral tumorigenesis and aggressive cancer phenotypes [21]. Using this microfluidic tool, integrated with porous membrane, which functioned as a micro-sieve capture element, EGFR immunocytofluorescence assays were completed in less than 10 min. Three oral cancer cell lines and one negative control cell line have been studied as a module cancer cells to demonstrate this diagnosis platform for oral squamous cell carcinoma (OSCC) detection. The results showed that, compared with MDA-MB-435S cells that express low levels of EGFR, three cancerous cell lines overexpressed EGFR in the order of magnitude 7–10-fold, indicating from fluorescent imaging analysis. Barkefors and coworkers established a fluidic device to generate stable gradient of multiple vessel inducing factors such as vascular endothelial growth factor A (VEGFA) and FGF2 in a 3-dimensional (3D) gel culture chamber for perturbing the angiogenic sprouting process and vessel remodeling in the embryonic mouse kidneys and embryoid bodies. This chip consisted of two components: a central chamber where the cell bodies have been previously cultured, sided by two channels for perfusion of stimuli molecule gradients after assembling on a Petri dish. The fluorescent immunoassay was conducted after 48 h of gradient-maintained

www.ebook3000.com

culture of embryonic mouse kidney. Directional angiogenesis has been clearly observed after immunostaining of CD31 protein, a known marker for endothelial cells, indicating that this method is capable of controlling complex biological processes such as angiogenesis. Conventional IF methods require a considerable amount of samples, with tedious liquid manipulations for the sample treatment. To overcome such limitations, Shen from Huang's group reported an integrative microfluidic chip to detect lysosomal storage disorders (LSDs) based on highly parallel IF experiments including optimization of parameters for staining and high-throughput analysis of different cell lines [22]. Authors demonstrated that all liquid handling processes for immunofluorescent diagnosis, like long-term cell culture, fixation, antibody incubation, and washing can be feasibly integrated on a single chip (Figure 9.3). By taking advantages of pneumatic valves and

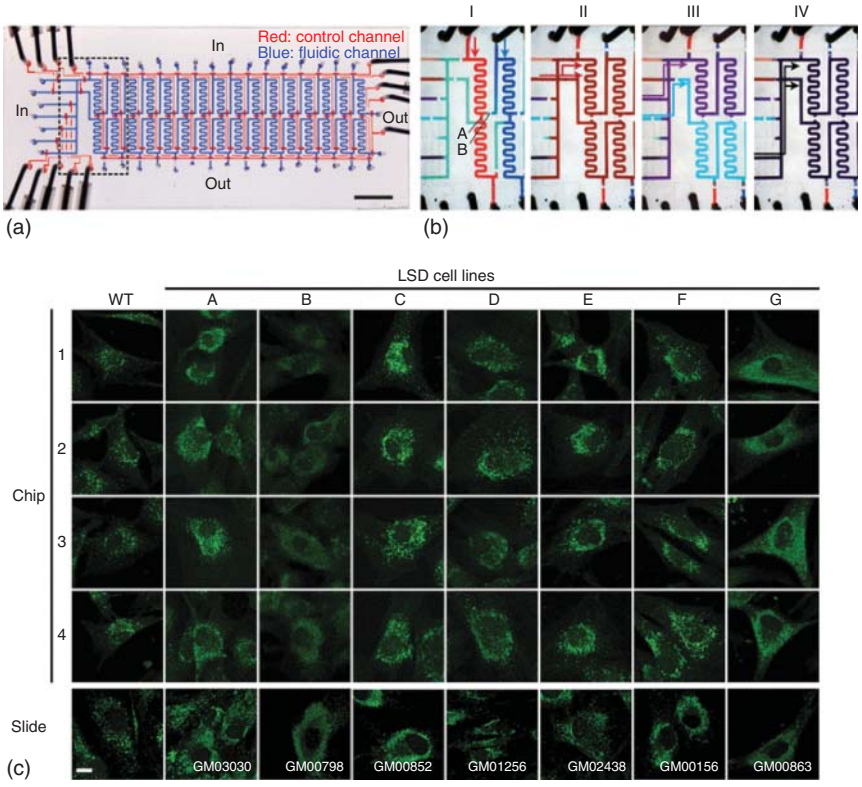


Figure 9.3 A high-throughput IF chip for analyzing LSDs in parallel. (a) A 32-section chip could handle 16 different groups of cell samples in a single experimental run. Each experimental group had a control running in parallel. The scale bar is 5 mm. (b) Liquid flow in different steps could be reconfigured by integrated valves. I: Cell loading; II: fixation and washing; III: primary antibody incubation; and IV: secondary antibody incubation and washing. Valve A was used to separate the experimental groups and their control groups; valve B was used to isolate different samples. (c) Confocal images of LAMP1 immunofluorescence for different cell lines. We picked four representative images from each cell line that had been stained on chip and compared them with the result from conventional methods on glass slides. Wild-type fibroblast cell lines were also shown in the first row as a control. Scale bar: 5 μm. (Shen *et al*. 2012 [22]. Reproduced with permission of Royal Society of Chemistry.)

automated controlling, the whole IF staining procedure can be completed in less than 3 h with antibody consumption significantly down to 0.3 µl, which is a 100-fold reduction compared with conventional assay on glass slide. Two target proteins, lysosomal-associated membrane protein 1 (LAMP1) and microtubule-associated protein 1 light chain 3 (LC3), were chosen to conduct the immunofluorescent staining. On this chip, we automatically stained 16 different cell samples (15 cell lines from human patients with different LSDs and 1 wild-type fibroblast cell line as the control) in parallel way. Thus, this microfluidic approach provides a promising way for automated high-throughput molecular imaging at cell level that can be applied for diagnostic analysis.

9.3 Single-Cell Gene Expression Profiling

The individual cell is the basic building stone of life. It is known that heterogeneity is one of the fundamental natures of living cells in organism. Understanding complex networks in biological systems such as a bacterial community, a progressing tumor, a developing embryo, or a population of cells enclosed with same environmental niche requires interpretations of quantitative data dissecting from single cells. For this reason, the previous widely adopted workflows for profiling gene expression from bulk or population biological sample have inevitably encountered their "bottleneck." To date, single-cell studies have been realized by a number of instrumentations and derivate protocols from conventional biotechnologies. For instance, microscopic imaging approaches have been used to directly visualize nucleic acid in either fixed [23] or living cell [24] by FISH. Real-time analysis of protein expression has been revolutionized by rapidly growing developments of genetically encoded fluorescent proteins, enabling detailed observation of the distribution of interested proteins within living cells. Flow cytometry and fluorescence-activated cell sorting is a powerful tool for high-throughput single-cell analysis and cataloging. At the same time, increasingly molecular techniques have been developed to unveil the nucleic information from individual cells, such as single-cell real time PCR (RT-PCR) [25, 26], single-cell DNA microarray [27], and even methods for high-fidelity amplification of DNA [28] and RNA [29] from single cells and consequently analysis using next-generation sequencing technique. However, researchers are still seeking new approaches offering rapid, accurate, highly controllable, automatable, and cost-efficient ways to dissect individual cells from populations. Over two decades of fast growth and development, microfluidics has just begun to show its power in addressing challengeable problems existing in traditional biological researches. For example, different from adding, centrifuging, and transferring samples from one PCR tube to another, microfluidic formats can manipulate complex liquid processing within a sealed device that is prone to be less contaminated than previous repeatedly opening and closing the sample tube. In this section, we try to peer-review some of the most exciting examples of microfluidic-based single-cell studies that may open a way to fulfill the tool pool for resolving the cell-to-cell viability in complex biological framework.

www.ebook3000.com

9.3.1 Imaging-Based Single-Cell Analysis on Microfluidics

Direct observation of cells under a microscope is one of the most straightforward methods to plumb single-cell biology. Advances in imaging such as automated microscopy coupled with GFP reporter have been applied to analyze gene expression and allow high content screening with resolution of single-cell or even subcellular precision. Notwithstanding, using the Petri dish or culture plates to handle cell samples lacks scalability and throughput with highly spatial and temporal controlling of extracellular environments during imaging. Addressable imaging of single cells requires sophisticated instrument such as programmable electromotive stage and lacks inner reference object inside culture device. The imaging experiments on 96-well or 384-well plate including changing culture medium or adding a stimulus are often very monotonous. The inherent scalability and ease of manipulating small volume makes microfluidics a promising tool to address these limitations.

β-Galactosidase (β-gal) has been the standard reporter for gene expression because of its robustness and high sensitivity for detecting single molecules using a enzyme catalysis reaction. However, single molecule detection is hard to be realized because the fluorescent products cannot be kept in the cell, the cell efflux pumps efficiently expel the foreign organic molecules from cytoplasm, and then fluorescent molecules will rapidly diffuse away. Cai from Xie's group implements a microfluidic device to circumvent this efflux problem [30]. They trap cells in a closed small microchamber, such that fluorescent product expelled from cytoplasm can accumulate and quickly reach an equilibrium enough to be detected due to the limited space for diffusing in tiny chambers (Figure 9.4a). The short mixing time of fluorescent molecules in chamber guarantees that the signal of fluorescence intensity outside the cells accurately reflects the enzymatic reaction in the cell. The authors characterized the *E. coli* lac-Z gene expression pattern by burst size and burst frequency and found that the average burst size indicated a good consistency with previously estimation that briefly 25–30 β-gal monomers per mRNA. They further demonstrated that this assay in microfluidic channel allows real-time observation of the stochastic expression of β-gal at single-molecule sensitivity for single prokaryotic (*E. coli*) and eukaryotic cells (yeast, mouse stem cells). Similarly, Taniguchi in Xie's group [31] measured stochastic gene expression with single-molecule sensitivity at both protein and mRNA levels simultaneously and found that at single-cell level, protein and mRNA copy numbers for any given gene are actually uncorrelated. They screened over 1000 genes via a yellow fluorescent protein (YFP) library of *E. coli*, in which each strain contains a specific gene with YFP fusion sequence. A 96-channel microfluidic array was implemented to isolate the different strains of *E. coli* cells in order to facilitate high-throughput automated imaging process (Figure 9.4b). Combined with FISH with single-molecule sensitivity, which used an atto594-labeled 20-oligmer nucleotide as a probe to tag the YFP-mRNA sequence in the cell strain, the author can assemble information of the molecule copy numbers of YFP and YFP-mRNA at the same time. They explained that the general lack of mRNA–protein correlation of the same gene at single-cell level may attribute to the different life spans between mRNA and proteins. In other

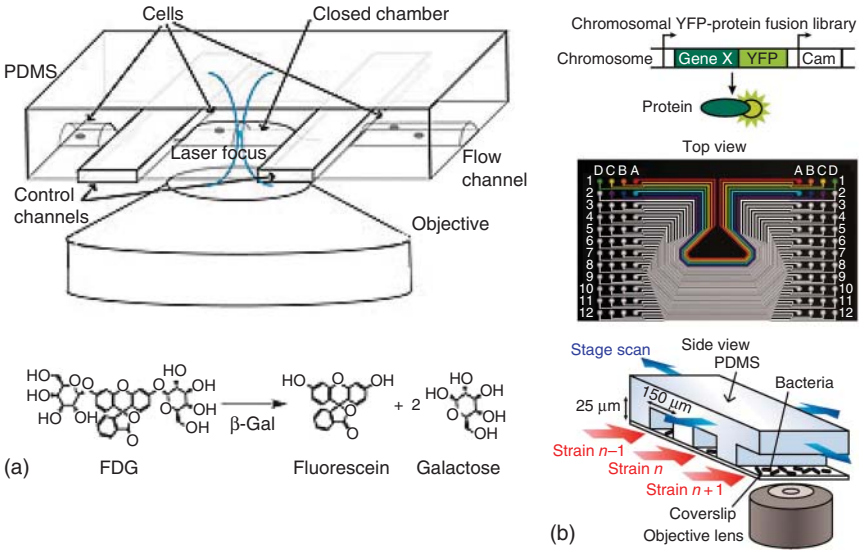


Figure 9.4 (a) Lac-Z gene expression assay in microfluidic channel allows real-time observation of the stochastic expression of β-gal at single-molecule sensitivity for single prokaryotic (*E. coli*) and eukaryotic cells (yeast, mouse stem cells). (Cai *et al*. 2006 [30]. Reproduced with permission of Nature Publishing Group.) (b) Stochastic gene expression with single-molecule sensitivity both at protein and mRNA level simultaneously and found that at single-cell level in a microfluidic device.

words, mRNA is conversely regulated and typically degraded within minutes in *E. coli*, unlike the proteins, which have a longer lifetime. Understanding how protein pathway networks respond to variable extracellular excitations is required in time-dependent analysis of gene expression with single cells. By using microfluidic techniques, scientists are able to investigate the bacterial community through trapping them within a small volume. Boedicker *et al*. [32] demonstrated that with confinement in a small droplet, *Pseudomonas aeruginosa* initiate the quorum sensing (QS) and achieve QS-dependent growth in the latter. To study the QS pathway of *P. aeruginosa*, the author constructed a fluorescent reporter gene lasB, which can activate QS in bacteria cells. The microfluidic droplet array was created by serial introduction in the biocompatible SU-8 photoresist wells within polydimethylsiloxane (PDMS) channels, which were firstly primed by bacteria-containing culture media and let the germ to settle, and then subsequent air flow was introduced over the wells to form segregation. Interestingly, different from commonly stated belief that QS responses require a large number of cells, the micro-confinement results showed that QS pathway can even be activated in a small volume that contains only a single cell.

Multiwall-based assays combined with fluorescent report gene and automated microscopy have increasingly been used to detect heterogeneity in cellular pathway [33] but, at the same time, are insufficient in scalability and temporal control of given stimuli. To resolve this issue, Taylor *et al*. designed a high-throughput microfluidic single-cell imaging platform to study yeast MAPK mating pathway with highly controllable time-varying stimulant perturbing [34]. This device is constituted of 2048 microfluidic cell-trapping chambers and allows testing 32 extracellular factor-concentration sequences for a total of 256 simultaneous

www.ebook3000.com

perfusion experiments per single run. The author demonstrated their device is capable of investigating the signal pathway by imaging the genetically encoded EGFP expression in single yeast cells that were temporally stimulated by α-factor, a mating peptide binding with membrane G protein-coupled receptor. The results showed that with cells under low dose but high frequency of stimuli, the gene expression responses are similar to the profiling of cells suffering high dose but low frequency of pheromone giving. This reading-out, therefore, is hard to gain when using the traditional method of MAPK pathway investigation. Besides specific pathway, the life span of yeast, a model for eukaryotic life, also interests researchers. To follow a single yeast cell growth, one has to remove the daughter cells from its mother by micromanipulation on agar gel. Ryley and Pereira-Smith fabricated a micrometer structure (yeast jails) array on microfluidic channel that allows imaging tracking of yeast life span by trapping single yeast cell in the "jail" site that enables feasibility of easily flushing the daughter cell away [35]. Two target genes, the RAS2 that extend yeast life span and the HSP104 relating to heat shock response, were fused with YFP and GFP, respectively, to execute the time-lapse fluorescence imaging process. The result indicates that both gene expressions vary at least twofold by interpretation of single-cell analysis data. Recently, Lee *et al*. developed a new platform to address the mother–daughter dissection problem by using PDMS micropads to allow for trapping of mother yeast, removal of daughter cells, and imaging of phenotypic changing occurring within the whole life span [36]. In addition to the acquisition of "young to death" data, the author exploited the capability to investigate heterogeneous changing in cellular and vacuolar morphologies during the complete life span of individual cells. Visualization of vacuolar was achieved by encoding VPH1, which is a subunit of the vacuolar ATPase, with GFP to observe the vacuole size and shape changing potentially associated with higher autophagy activity. In their data, a tubular morphology, a fused shape, or a fragmented structure were observed as three subsets before the death of a cell, indicating heterogeneity at the level of subcellular structures such as vacuole.

Lecault *et al.* developed a high-throughput microfluidic platform for living cell imaging studies of long-term culture of hematopoietic cells, a nonadherent cell line, with automated configuration [37]. The nonadherent cell culture with time-lapse imaging is challengeable in microfluidic cultivation mode, because it is hard to immobilize nonadherent cells during medium changing. The author addressed this problem sampling by culture cells on the bottom of a cubic culture chamber ($160 \times 160 \times 160\ \mu m^3$) that facilitates cells to settle down during medium refreshing or stimuli giving. In addition, this device shows the capabilities of long-time cultivation (5 days) by putting a large bath chamber onto culture location, essentially blocking dehydration effect that may hamper cell phenotype maintenance. Moreover, selective recovery of clone can be realized by piercing the PDMS membrane with a micropipette after peeling off the overlaying chamber layer. Immunohistochemistry on live cells was used to identify different lineages of single cells (lin+/lin−) by using three lineage markers (Gr-1, Mac-1, and B220). Using a high-throughput automated microfluidic cell culture platform previously developed by Gomez-Sjoberg *et al*. [38], Tay *et al*. [39] studied how single mammalian cells respond to different concentrations of TNF-α that interfere transcription factor NF-κB pathway. They observed that under temporal extracellular TNF-α stimulation, single-cell

level process, where NF-κB entered the nucleus from cytoplasm and backed out again in an oscillation manner, could be visualized by means of imaging fluorescent fusion proteins (p65-DsRed and H2B-GFP) in individual cells. The author found that, different from the studies on population [40] or single-cell detection but impaired by high TNF-α concentration without temporal control [41], 3T3 mouse fibroblast cells responded to low dose of TNF-α in a digital way; that is, the activation of NF-κB pathway was heterogeneous and not all cells responded to TNF-α. This method showed the value of high-throughput quantitative analysis with single-cell resolution in understanding how gene expression pathway works.

Notably, imaging-based methods, like fluorescence reporter, require the pre-constructed cell lines that contain fluorescent proteins fused with specific loci on the genome and can hardly realize quantification of multiple genes expression. To address this dilemma, we developed a microfluidic cell-patterning assay (Ip-Do assay, in-channel printing device opening assay) that enables not only patterning multiple cells on the same substrate with controllable niches but also analyzing corresponding cell pellet gene expression by standard quantitative PCR (qPCR) method (Figure 9.5). In this work [42], we validated Ip-Do assay by studying personal medical antitumor drug screening in a single chip with limited cells. To test the gene expression during apoptosis in different cell types, wild-type breast tumor cell MCF-7 and drug-resisting cell line MCF/Adr were used as models of clinical case of chemotherapy. By conducting analysis of Ip-Do assay, around 400 cells in total have been printed on the substrate and processed image analysis after drug treatment. Moreover, the gene expression pattern shows that the ABCB1, which encodes multidrug efflux pump protein P-gp, was transcriptionally awaked by high-dose drug treatment.

9.3.2 Microfluidic Methods to Single-Cell Nucleic Acid Analysis

The majority of our understanding of gene expression has been gleaned from a large population of cells or genetic materials such as extracted DNA, RNA, or abundant protein, lacking of dynamic data within individual cells. Analogous to imaging methods, microfluidic formats allow single-cell investigation with advances in precision and high throughput and are incorporable with well-established analysis method, combined with self-sealing that also reduced the possibility of being contaminated.

In microbiology, single-cell genome analysis is particularly challenging because majority of microorganisms have yet to be identified or cultured, with the remaining vast "dark mater" to be unveiled. Marcy *et al.* [43] described a microfluidic platform enabling genomic analysis of single TM7 phylum without cultivation (Figure 9.6a). The chip provides the capabilities of parallel isolation of individual bacteria, addressable sorting, lysis, and amplification of their genome by conducting multiple-strand displacement amplification (MDA) within 60-nl volume. By performing specific primer PCR amplification, the TM7 16S rRNA genes from amplified genomic DNA have been indentified obtaining from 34 of 35 captured single cells. Using the same device, individual *E. coli* were isolated and genomic DNA by MDA were amplified in this 60 nl device. In addition, by comparing

www.ebook3000.com

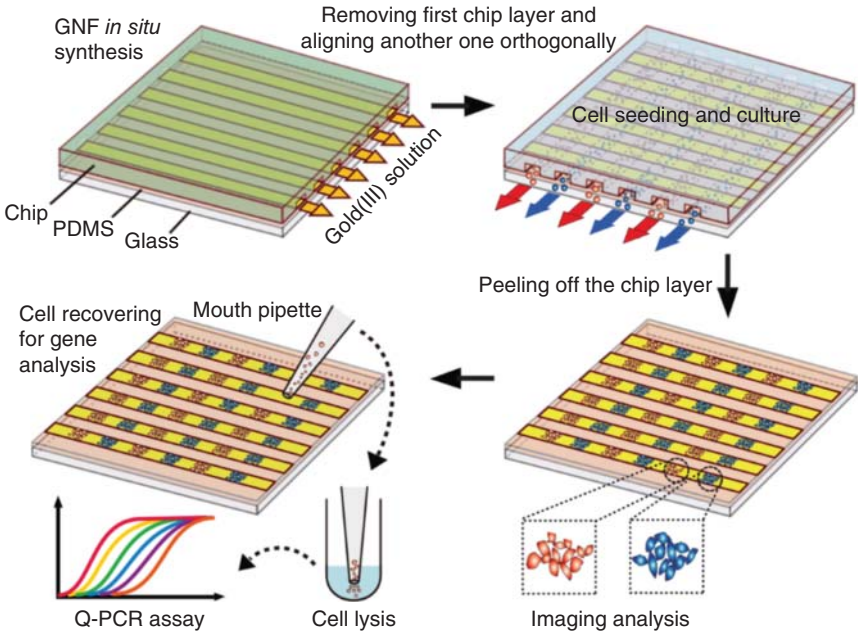


Figure 9.5 Schematic illustration for "Ip-Do assay" for cell patterning and gene analysis. The gold nanofilm on PDMS as a strip pattern, gold(III) chloride solution was introduced into the chip and incubated to perform reduction, followed by human fibronectin incubation. Cells were injected into microfluidic channels, which have been orthogonally aligned with gold strips after the removal of the previous microchip layer. Cells patterned on hFN-modified gold-islands in channels after incubation. Following imaging analysis, the desired pellets of patterned cells can be further retrieved by mouth pipette to perform consequent qPCR analysis. (Zhou *et al*. 2015 [42]. Reproduced with permission of American Chemical Society.)

with standard 50-μl reaction, it was found that the amplification bias was greatly reduced in small volume, thus enabling a more even data of all sequences. This phenomenon could be explained by reduction of competition from contaminants in physical confined reaction or template DNA damage. However, the author also claimed that the difference in amplification bias or coverage between nanoliter and microliter reactions should not be solely attributed to the small reaction volume. Zeng *et al.* [45] described a high-performance single-cell genetic analysis platform that utilizes high-throughput microfluidic emulsion generation to conduct single-cell multiplex PCR. In this method, multiplex single-cell PCR was developed to quantitatively detect both normal K12 cells and pathogenic *E. coli* O157 cells with an LOD of 1/105.

Microfluidic scalability shows great potentials on single-cell genome studies not only in microorganism but also in human genotyping. Haplotyping, analysis of combinations of alleles at resolution of loci across a single chromosome, is hard to access with the current method. Fan from Quake's group developed a microfluidic approach to parallel amplify single individual chromosomes isolated from a single cell, which is in its metaphase [46]. This device consists of different regions that allow single-cell capturing, identification, lysis, releasing,

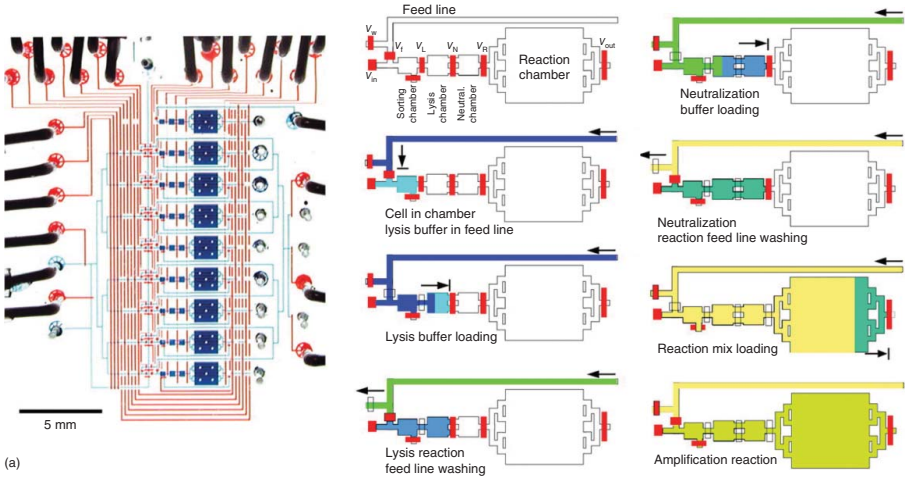
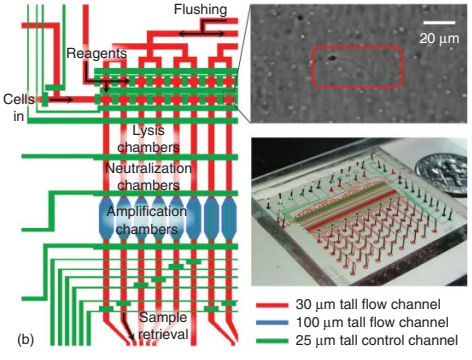


Figure 9.6 (a) A microfluidic platform enabling genomic analysis of single TM7 phylum without cultivation. The chip provides the capabilities of parallel isolation of individual bacteria, addressable sorting, lysis, and amplification of their genome by conducting multiple-strand displacement amplification (MDA) within 60-nl volume. (Marcy *et al*. 2007 [43]. Copyright 2007, National Academy of Sciences, U.S.A. Reproduced with permission.) (b) Dissecting high-resolution genome-wide personal recombination map using microfluidic device by analyzing the whole genomes of >100 single human sperm cells and 93 single sperm samples. On this device, individual sperm cells can be isolated, lysed, amplified, and retrieved from independent outlets. (Wang *et al*. 2012 [44]. Reproduced with permission of Elsevier.)

www.ebook3000.com



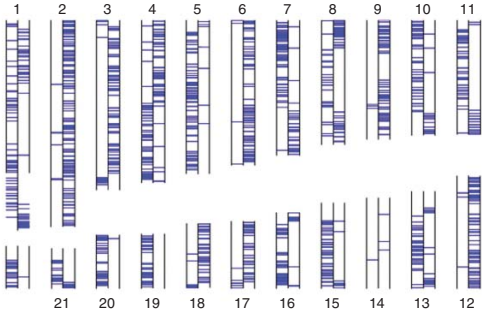


Figure 9.6 (*Continued*)

and chromosome partition, followed by single chromosome amplification by phi29 polymerase MDA. From a patient, whose genome has been sequenced and clinically annotated, they directly analyzed haplotyping of the human leukocyte antigen (HLA), which is associated with autoimmune diseases. This method enabled them to study the two alleles of each chromosome independently. Recently, Wang *et al.* in Quake's group [44], using a similar chip, finished and first reported high-resolution genome-wide personal recombination map for an individual by analyzing the whole genomes of >100 single human sperm cells, and 93 single sperm samples were used to generate the recombination map (Figure 9.6b). On this device, individual sperm cells can be isolated, lysed, amplified, and retrieved from independent outlets. By mapping the genotyping results from each sperm cell to the two somatic haplotypes obtained by direct deterministic phasing of single lymphocytes, the results showed a detection of single chromosome deletion events in two sperm cells, whereas the other 91 cells gave a total of 2075 autosomal crossover events (22.8 ± 04 SE in each sperm).

In other alternatives of amplification, digital polymerase chain reaction (digital PCR) is a promising and reliable method in screening the gene expression without bias amplification [47]. Different from traditional real-time PCR known as "relative quantification," digital PCR, known as "absolute quantification," divides the diluted sample mixture into many segmentations, making sure that most of the segmentations will contain only one or no DNA molecule. So after the thermal cycling for amplification, digital signal (on or off) appears. By calculating the percentage of the signal among all the segmentations, the concentration of the sample can be drawn. This method not only avoids the potential amplification bias and false positive phenomena that happen in real-time PCR but also provides a much easier way of handling. Ottesen *et al.* [48] used a microfluidic digital PCR to amplify and analyze a key gene of homoacetogenesis pathway encoding formyl-tetrahydrofolatesynthetase (FTHFS) that is involved in the mutualistic symbiosis between termites and their gut bacteria. They hooked up the data between 16S rRNA and FTHFS gene to interpret the complex relationships in symbiosis. In this chip, experimental sample can be partitioned into 1176 individual chambers with 6.25 nl for reaction, and each device contains 12 of such sample array, that is, over 14 000 independent chambers, that were used for digital PCR per device. Recently, Heyries *et al.* [49] have increased this throughput of digital PCR to 440 000 reaction chambers per centimeter square and over 1 000 000 chambers per device using a two phase-based partition protocol. Because of the permeability of the PDMS material of the microfluidic chip, each microreactor is a dead end of the microfluidic channel, and reaction mix could be flushed into all the reactors, the gas could be squeezed out, and then the mix could be separated by the oil through the public channels (Figure 9.7). Men *et al.* have developed an even smaller volume (36 fl per reactor) array of microreactors with a much higher throughput and easier handling [50]. The microreactors were completely sealed via the deformation of a PDMS membrane. This design has a number of advantages: avoiding potential contamination of sample, high density and efficiency, ease for experiment operators to work with, and available for samples to be compared in parallel. In a demonstration, the copy number of a certain gene can be calculated simply after a simple sample loading, a half-hour thermal cycling, and fluorescent imaging.

www.ebook3000.com

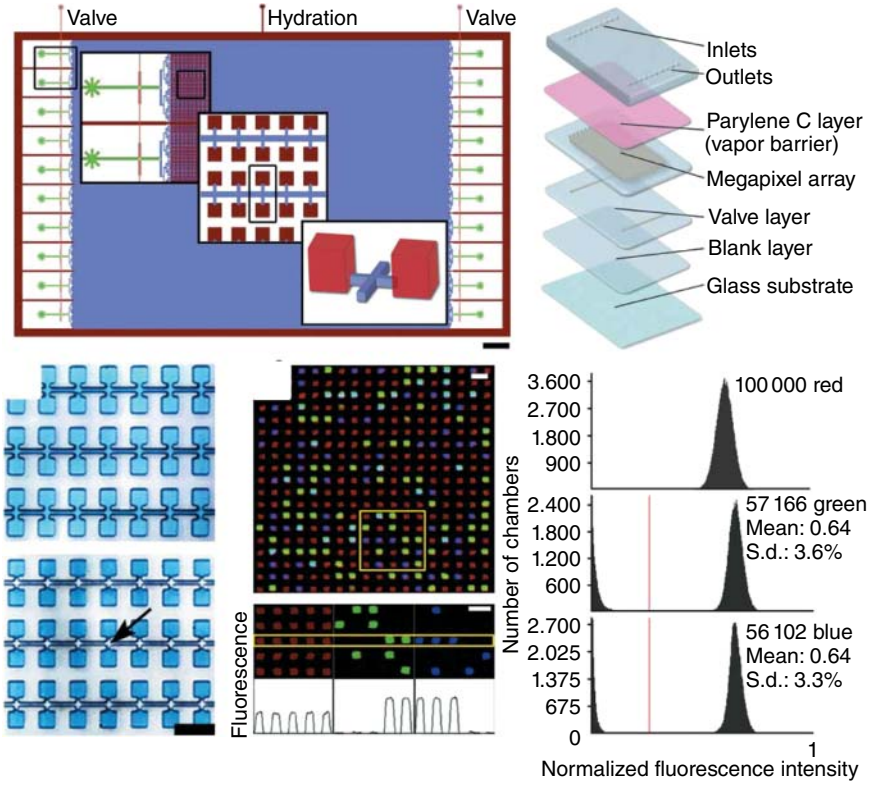


Figure 9.7 Digital qPCR with high throughput of up to 440 000 reaction chambers per centimeter square and over 1 000 000 chambers per device using a two-phase-based partition protocol. (Heyries *et al*. 2011 [49]. © 2011, Rights Managed by Nature Publishing Group.)

In spite of profiling genome, transcriptome analysis is of utmost importance because the mRNA level tethered firmly with gene expression. Recent progresses in dissecting mRNA or miRNA of single cells show the power of combinational strategy of interrogating nucleic acid amplification methods with newly developed instrumentations such as fluorescence-activated cell sorting (FACS), RT-PCR, microarray, and even sequencing technology. However, few of these applications demonstrate the direct integration of single-cell isolation from following the steps of liquid handling for amplification until finally to the reading-out of signal.

Marcus from Quake's group reported the first method for single-cell mRNA analysis by isolating single cells, together with cell lysis, mRNA purification, cDNA synthesis, and cDNA purification in one single microfluidic device [51]. Four parallel units were fabricated to perform picking up and reverse transcription in four individual cells, providing quantitative measurement on each cell. Two housekeeping genes, GAPDH and HPRT, were used to validate the utility of this system. Affinity columns of dynabeads conjugated with oligo (dT25) were constructed by sieve valves to capture mRNA with a poly A-tail from single lysed cells. Gel electrophoresis results demonstrated that the amount of cDNA from a single NIH/3T3 cell is comparable with off-chip experiment.

Zhong *et al.* [52] expanded this method to measure three gene (B2M, Nodal, and Fzd4) expressions in a single hESC. The results indicated that rather than a heterogeneous cell population, hESC colony is highly heterogeneous, and many single cells do not express all three of these genes. The improvements of converting single-cell mRNA to cDNA in microfluidic device lie in not only the low consuming of reagents but also a better mRNA-to-cDNA efficiency compared with benchtop reactions. Chen *et al.* [53] used a 32-single-cell throughputs integrated microfluidic chip to measure the housekeeping gene expression levels in HeLa and 293T cells for rapid assessment of genetic stability of a cell population. In this device, the U-shaped sieve structures [54–56] fabricated as cell trapping cup to realize fast and reproducible loading of single cells. The single-cell gene expression measurements suggested that, compared with immortalized cell line 293T cell populations, the cancer cell line HeLa has more instability than housekeeping gene β-actin.

The above methods of microfluidics show great potentials on single-cell gene expression profiling with robustness and parallel processing. Nevertheless, integration of all steps on chip, including single-cell selection, sorting, cDNA synthesis, purification, and, more importantly, direct online detection, to measure gene expression changes from single cell and is still difficult to archive. Toriello *et al.* [57] presented a microfluidic system for analysis of gene expression in single cells. This method successfully realized the integration of single-cell capture, reverse transcription, amplification, electrophoresis separation, and quantitative detection on a single device (Figure 9.8). To conduct single-cell gene analysis, Jurkat cells are firstly modified by ssDNA with which cells can be captured by affinity capture on a small gold/thiol/ssDNA pad with size defined as $25 \times 25\,\mu m^2$, ensuring individual cell docking. Additionally, they used a capture matrix to immobilize target fragments, enabling an online purification, making sure of specific detection without nonspecific interference. The author found that there are two subsets in the Jurkat cell population, which has been treated with siRNA directed at GAPDH mRNA; one subset shows a moderate (~50%) silencing effectiveness of GAPDH and another subset has been completely silenced (100%). This heterogeneity of siRNA silencing is hard to be revealed by bulk analysis on 50 cells. By using on-chip RT-qPCR data imaging acquisition, another example of full integration of single-cell mRNA probing is reported by White *et al.* [58]. This constructed a 300 parallel throughput microfluidic device to perform single-cell capture, lysis, reverse transcription, and qPCR analysis. A CCD detector for imaging analysis was mounted above a thermocycler plate where the whole device could be placed on to perform qPCR. The authors noticed that the proper dilution of starting cell lysate is important to RT-qPCR reaction, because an inhibition occurs at concentrations beyond 10 cell equivalents per 50 nl reaction, and a noise happens when starting at concentration below one copy per 100 nl. Therefore, the total volume of 60.6 nl, consisting of a 0.6 nl cell capture channel, a 10 nl reverse transcription chamber, and a 50 nl qPCR box, has been designed to carry out serial reactions on each single cell. To demonstrate the application of this platform in quantitative analysis of single-cell mRNA heterogeneity, nine different miRNAs have been tested at single-cell level in both K562 cells and CA1S cells, which are hESCs. The results illustrate

www.ebook3000.com

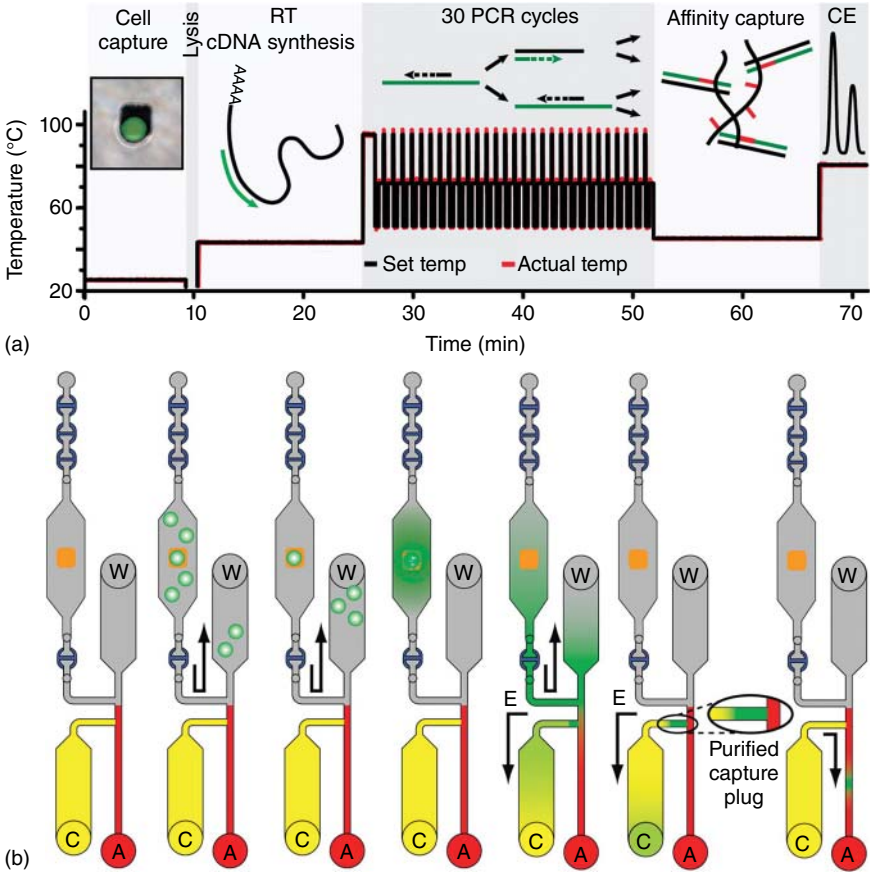


Figure 9.8 Schematic of the biochemical steps performed in the integrated gene expression microdevice. (a) The analysis is complete in <75 min. (b) Depiction of the operation of the single-cell gene expression microsystem. (Toriello *et al*. 2008 [57]. Copyright 2008, National Academy of Sciences, U.S.A. Reproduced with permission.)

the ability of assessing difference in single-cell resolution and the expression levels of miR-16 were normally expressed at each cell population, whereas miR-223 were highly variable in both cell lines and notably only 3.6% of 74 tested cells were miR-233 detected in hESC line, suggesting a role of this miRNA as a differentiation-specific miRNA. More recently, White *et al.* combined in their previous work single-cell RT-PCR [58] with megapixel digital PCR [49] to fulfill the single-cell RT-digital PCR on chip [59]. To realize single-cell RT-digital PCR analysis, they integrated all the steps from single-cell isolation, washing, lysis, reverse transcription, and digital PCR (dPCR) imaging on a single microfluidic device with a throughput of 200 cells per run. Each captured single cell was parallelly lysed and reverse transcripted, and half of the RT products were introduced into an independent dPCR arrays, containing 1020 reaction chambers. The authors validated the ability of their platform on absolute measurements of the single-cell mRNA by probing GAPDH, as a housekeeping gene;

BCR-ABL, as a low-abundance transcripts; and miR-16 miRNA, as a conserved short noncoding RNA that associated with RNA-induced silencing. Technical replicates show that the mean GAPDH expression was reproducible, ranging from 1412 to 1741 copies per cell with coefficient of variation (CV = 40%). Similar heterogeneity was also detected in BCR-ABL and miR-16. In addition, they also applied the device to assess the extent of single-nucleotide RNA editing on chr16:22296860 (hg19) in EEF2K coding region. The results showed that the on-chip single-cell measurements of EEF2K editing consist in the population average editing frequency.

At the same time, while researchers are exploring on the divergent possibilities of developing new microfluidic technologies for single-cell gene expression analysis, a commercial product based on single-cell RT-PCR has already found its way on dissecting biological questions. The Fluidigm Corp. first demonstrates a microfluidic dynamic array-based platform can be used to perform high-throughput gene expression measurements with quantitative PCR [60]. This device requires less pipetting than the conventional 96-well qPCR while allowing 2304 simultaneous qPCR reactions in a single chip. This system (Fluidigm 48.48 dynamic array systems) was used to perform quantitative analysis of miRNA expression in A549 and H1299 lung cancer cell lines [61]. Compared with traditional measurement (single-plex) on ABI 7900, microfluidic multiplex system showed a slightly greater sensitivity. By using the same qPCR system, Petriv *et al.* established 288 miRNA profiles for 27 phenotypically distinct cell populations isolated from normal adult mouse hematopoietic tissues [62]. Before introducing their cDNA to microfluidic qPCR arrays, they first performed a workflow consisting of two steps: multiplexed reverse transcription and multiplexed cDNA preamplification. The results reveal that, during hematopoietic differentiation, hierarchical relationships between different populations were clustered according to their functional properties. Single-cell measurements revealed heterogeneity between FACS-purified populations and miRNA expression is very strictly regulated within functionally homogeneous cells.

The embryonic development is one of the fundamental biological questions that need to be answered. How is an embryo derived from an individual zygote? And how does the embryo maintain its pluripotency while there are three differentiated cell types coexisted in same blastocyst [63]? Guo *et al.* [64] used a Fluidigm dynamic array chip to profile mRNA expression patterns of 48 genes in over 500 single cells from a 1-cell zygote to the 64-cell blastocyst, providing a penetration of the earliest cell fate decisions of the developing mouse embryo. Their workflow mainly involved the manual separation of single cells from single blastocyst that has been stained to distinguish the outer cells (red fluorescence) and inner cells (unstained), followed by direct cell lysis, reverse transcript, sequence-specific preamplification in a single tube, and quantitation of gene expression using Fluidigm system. The results showed the dominant hierarchical clusters of gene expression have emerged as early as ~64-cell blastocysts, indicating three cell types known to exist at this developing stage. Id2 and Sox2 as the earliest markers of outer and inner cells have been identified using this technique. The authors finally depicted a schematic model of gene expression changes in the development of the three blastocyst lineages, putting an insight into developmental decisions at cellular level. Different from mammalian

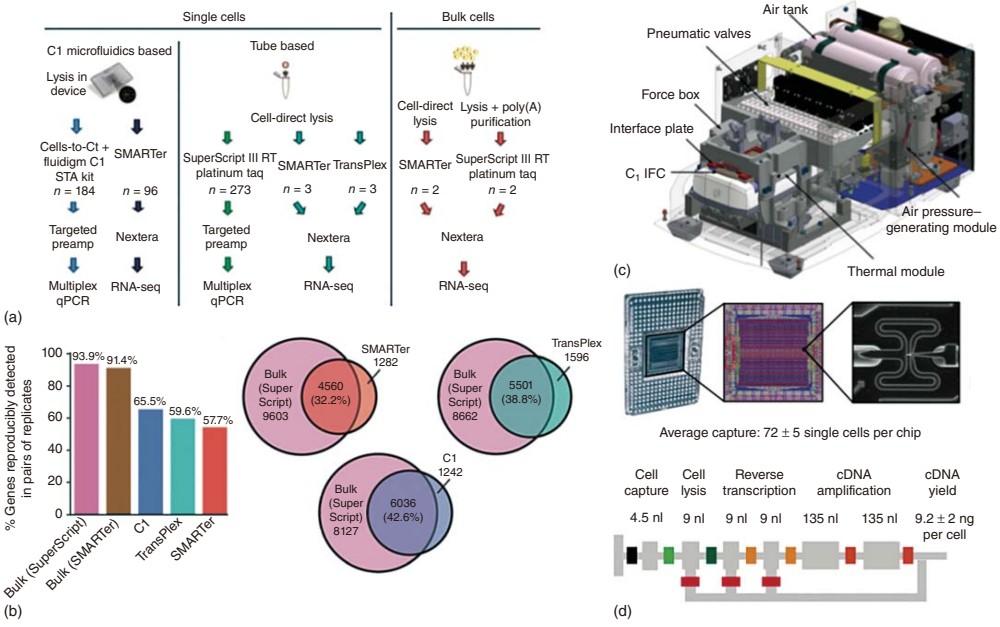
www.ebook3000.com

embryo differentiation, the technique of inducing pluripotent stem cells (iPSCs) allows reprogramming of differentiated murine cells to a pluripotent state by overexpression of Oct4, Sox2, Klf4, and c-Myc [65]. During this reprogramming process, only a fraction of cells are transferred to be iPSCs [66], and there has been little known to the sequence of molecular events that drive this process. Buganim from Jaenisch's group disclosed that there are two phases in reprogramming process: a stochastic gene expression in early reprogramming state followed by a hierarchical phase with Sox2 being the central factor in regulation [67]. The combination of Fluidigm dynamic arrays with FACS significantly facilitated their research, allowing high-throughput single-cell analysis of 48 genes in approximately 7000 single cells during reprogramming. Besides the revealing of a two-phase sequence in reprogramming, the author also found that the expression of Esrrb, Utf1, Lin28, and Dppa2 is a better predictor for successful reprogramming than the expression of the previous markers Fbxo15, Fgf4, and Oct4. In addition, they showed that the reprogramming of pluripotency can be archived by various subsets of transcription factors even without previously suggesting factors Oct4, Sox2, Nanog, c-Myc, and Klf4.

9.3.3 Next-Generation Sequencing Platforms Based on Miniaturized Systems

In recent years, next-generation sequencing (NGS) technologies have been creating a revolution in biology science by their capability of rapid sequencing of whole genomes and transcriptomes, enabling informative details that cannot be accessible by other tools [68, 69]. It is noticeable that the miniaturized controlling of enzymatic reactions fulfills the NGS, enabling massively parallel reading-out formation using microfabricated micrometer-scale reaction system. At least four commercially available platforms for NGS have widespread use at present: the Roche/454 FLX [70], the Illumina HiSeq series [71], the Applied Biosystems SOLiD™ system [72], and the recently available IonTorrent™ system [73] from Life Technologies Co. Ltd In all of these platforms, essential steps of enzyme-based reactions for sequencing benefit from microfabricated elements, either micrometer-scale reaction well arrays such as Roche 454 and Ion Torrent, recently developed fluorogenic sequencing method, or substrate microarray systems such as Illumina and SOLiD-4.

Roche 454 pyrosequencing is the first commercialized NGS technique invented by Margulies *et al*. [74]; it can be considered as the representative technology of pyrosequencing, enabled by the detection of photonic signals from each incorporation of a nucleotide by DNA polymerase, followed by the release of pyrophosphate, which initiates a series of downstream reactions coupled with luciferase reaction. They utilized an optical fiber fabricated slide containing 1 600 000 individual wells to conduct pyrosequencing and were able to sequence 25 million bases at 99% accuracy in a run. Monoclonal template DNA-conjugated on the microbeads was first amplified using emulsion PCR and then enriched. After that, enriched template-carrying beads are deposited into open picoliter-scale wells, arrayed along a $60 \times 60\,mm^2$ fibreoptic slide. Only one bead can be deposited into one well because of the size of each bead. To create a cyclical reaction system, a smaller beads that conjugated with ATP sulfurylase and luciferase necessary to generate light from free pyrophosphate



www.ebook3000.com

are also loaded into the wells, therefore generating the independent sequencing reactors. Until now, the reported max length of read using 454 systems was 800 bp in average and with throughput of 1 Mbp reads per run (454 FLX+).

The Ion Torrent system [75], an altered sequencing method without relying on optical signal, has been developed by Rothberg team in 2011. By directly detecting the protons released when nucleotides (dNTP) are incorporated into the growing DNA molecules, sequence data can be obtained on this ion-sensing platform. The authors integrated the most widely spreading complementary metal-oxide semiconductor (CMOS) with ultrahigh density microfabricated reactors to solve the sensing and addressing issues of their system. They demonstrated the performance of this system by sequencing human (*Homo sapiens*) and three bacterial genomes, *Vibrio Fisheri*, *Rhodopseudomonas Palustris*, and *E. coli*. The coverage of whole genome was 99.21% for human and 96.8%, 99.64%, and 100% for the three bacteria, respectively. To date, this system with a sensor having a density of 32 000 wells mm^{-2} is able to generate 800 Mbp per run data with average maximum reading length of 200 bp.

To circumvent the inevitable requiring of simultaneous real-time monitoring of all reactors in previous pyrosequencing technologies, Sims from Xie's group developed a "fluorogenic pyrosequencing" method combining terminal phosphate-labeled fluorogenic nucleotides (TPLFNs) and resealable PDMS microreactors [76]. This approach is scalable and highly sensitive, offering benefits of raid reaction cycle, reduced reagent consumption, and generation of native DNA. A microfluidic arrays containing 20 000 wells mm^{-2} with a diameter of 5 μm each and distance of 7.5 μm in between was used to carry out fluorogenic reaction and elastomerically trapping fluorophores in it, which can be detected at any time, avoiding the need for real-time monitoring.

Recently, Fluidigm released its benchmark microfluidic approach to perform single-cell RNA-seq on chip. This microfluidic system performs single-cell capturing, reverse transcription and cDNA amplification in nanoliter reaction volumes, which increased the efficiency of chemical reactions and may improve the accuracy of RNA sequencing. Wu from Quake's group presented quantitative RNA-seq analysis of 102 single-cell transcriptomes (Figure 9.9a,b)

Figure 9.9 Fluidigm C1 platform for single-cell RNAseq methods. (a) Schematic of the experimental strategy. (b) Reproducibility, as evaluated by the percentage of genes detected in pairs of replicate samples out of the mean total number of genes detected in this pair of samples. Sensitivity, as evaluated by the overlap between genes detected by single-cell and bulk RNA-seq measurement. Bulk values listed exclude the overlap values. Percentages are calculated as the number of genes detected in both relative to the number of genes detected in the bulk measurement. ((a, b) Wu *et al*. 2014 [77]. Reproduced with permission of Nature Publishing Group.) (c) Capturing single cells and quantifying mRNA levels using the C1 Single-Cell Auto Prep System. Key functional components of the C1 System are labeled, including the pneumatic components necessary for control of the microfluidic integrated fluidic circuit (IFC) and the thermal components necessary for preparatory chemistry. (d) Left, complete IFC with carrier; reagents and cells are loaded into dedicated carrier wells, and reaction products are exported to other dedicated carrier wells. A single cell captured in a 4.5-nl capture site; there are 96 captures sites per IFC. The average single-cell capture rate was 72 ± 5 cells (mean $\pm$ s.e.m.) per chip. ((c, d) Pollen *et al*. 2014 [78]. © 2013, Rights Managed by Nature Publishing Group.)

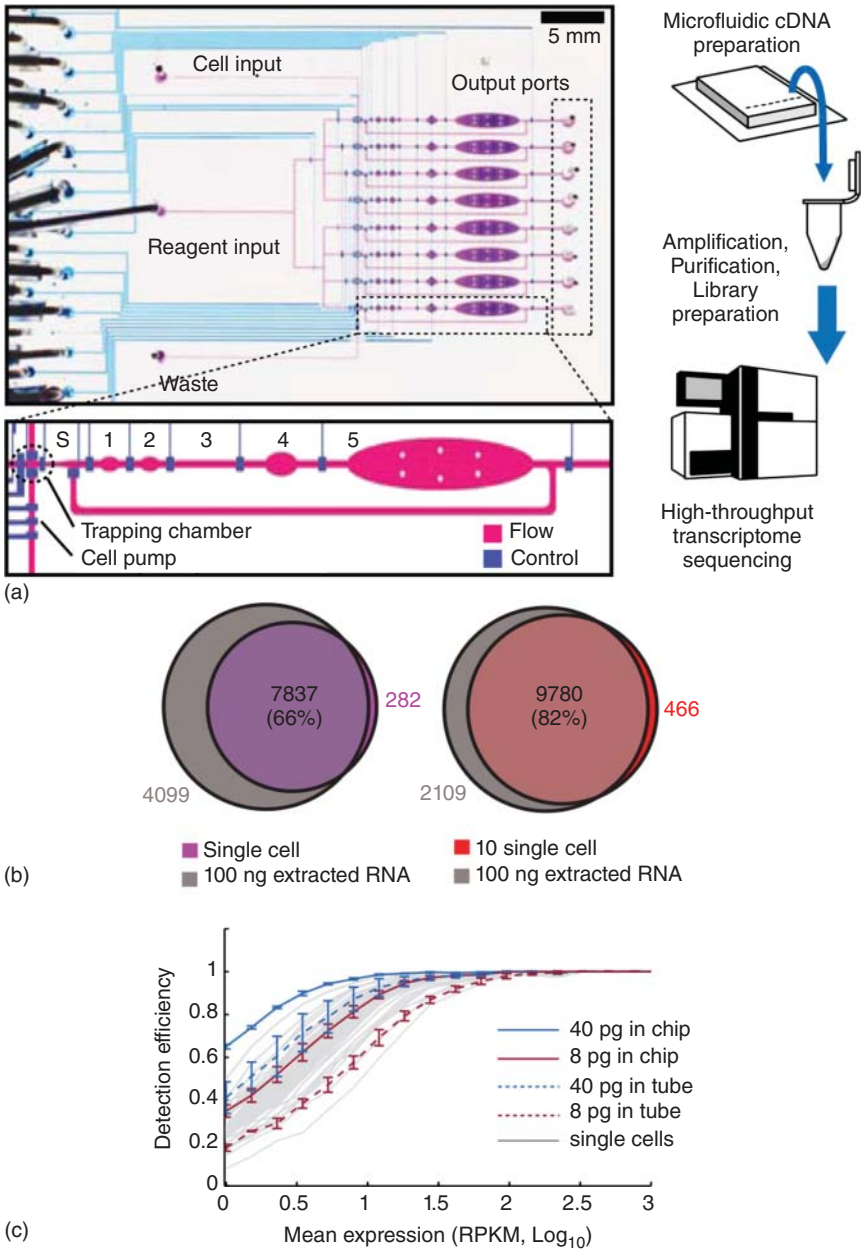


Figure 9.10 Microfluidic single-cell transcriptome sequencing. (a) Micrograph of the device. Channel stained with colored dye. Blue lines indicate the control channels, whereas purple lines are the flow channels. Double-stranded cDNA was recovered from the output ports and experimental pipeline. (b) The sensitivity of the technology demonstrated by Venn mapping. Comparison of genes detected with reads per kilobase per million (RPKM) > 1 in a typical cell with the genes detected in the 100-ng bulk sample. (c) Detection efficiency were validated by the ratio of genes detected in the single-cell libraries (gray lines) and to the genes detected in the bulk library binned by expression level [79].

www.ebook3000.com

[77]. The authors assessed the performance of Fluidigm C1 and 48.48 qPCR platforms, in both microliter and nanoliter volumes, compared their method to conventional RNA-seq of the same sample using bulk total RNA, and validated their results by independently profiling expressions of 40 genes in the same sample by multiplexed qPCR. Further, by conducting only 301 nl of total volume from single-cell capture to cDNA amplification in microfluidic chip, Pollen *et al*. demonstrated that shallow single-cell sequencing (~50 000 reads per cell) is sufficient for unbiased classifying of different cell types and biomarkers by validating 301 single cells from 11 populations on Fluidigm C1 platform (Figure 9.9c,d) [78].

In terms of low amount of starting materials in single-cell RNA-seq technologies, sensitivity and precision present some of the major obstacles. Besides Fluidigm, in 2014, we developed another microfluidic approach to perform single-cell RNA-seq library preparation with a total volume of only 140 nl, which is an over 600-fold decrease from the benchtop protocol (90 µl) [79]. We sacrificed transcript coverage for the increased mRNA detection sensitivity of oligo (dT) primers and showed that, by sequencing 10 single cells to an average of 2 00 000 reads each, this method was able to effectively reconstruct a large portion of the bulk transcriptome. In addition, by using bulk RNA sample as a technical variation control, we demonstrated the microfluidic approach is slightly more reproducible than the tube-based protocol, showing stronger correlation between replicates of both 40- and 8-pg samples (Figure 9.10).

9.4 Conclusion

To date, microfluidic formats have been used as a powerful tool that is extremely helpful on probing gene expression at multiple cellular levels, including DNA genotyping, RNA detection, and protein imaging and even for NGS. To simplify this statement, the advances in microfluidic platform could be attributed to two major characters. First, the ability to handle tiny liquid volume can facilitate experiments conducted in solutions with high throughput, massive parallelization, and multiple conditions. In this vein, microfluidics stands out from various methods by its capability to scale down biological reactions to nanoliter volume, enabling experiments on chip that have no benchtop equivalent. Several merits can be gained from small length-scale fluid physics, like high throughput, shorter diffusion time, and scalable formats, that enable hundreds of reactions to be conducted simultaneously. Those advantages give the microfluidic device capabilities to interrogate gene expression quantitatively in DNA, RNA, and protein level, by all means ranging from imaging acquiring to nucleic acid measurements. Second, the inherent feasibility of integration renders microfluidic technology an ideal tool that can be coupled with other modules like heating and detection on the same chip to perform complex and laborious solution-based experiments, such as PCR, qPCR, immunochemistry staining, and single-cell analysis. In terms of gene expression analysis, due to the compatibility of materials including PDMS and glass used to fabricate microfluidic device, different readout methods like microscopic imaging and spectroscopy can be implemented directly to figure the

signal out. In this sense, a microfluidic chip is not a research end point itself, but an experimental tool that is comparable with traditional tools, such as 96-well plate and pipette, allowing researchers to perform their routine work. Therefore, there are two basic demands that a research tool has to meet: reliability and easy to use. We believe these requirements are still the directions that microfluidic community should move to.

Noticeably, we need to point out that microfluidics is just one of the many available methods for probing gene expression; it may not be as versatile as a dreamful "golden key" that is expected to solve all the biological problems we meet. We envisioned that by interrogating with other methods especially newly developed tools, such as RNA sequencing and single-cell DNA sequencing, microfluidics may definitely pave a way for unveiling biological mysteries.

Acknowledgment

We acknowledge the funding support from the National Natural Science Foundation of China (Grant 21675011, 21305007). This work is also financially supported by the Fundamental Research Funds for the Central Universities (2302013FRF-TP-13-040A).

References

1 Burns, M.A. *et al.* (1998) An integrated nanoliter DNA analysis device. *Science*, **282** (5388), 484–487.
2 Pal, R. *et al.* (2005) An integrated microfluidic device for influenza and other genetic analyses. *Lab Chip*, **5** (10), 1024–1032.
3 Lagally, E.T. *et al.* (2004) Integrated portable genetic analysis microsystem for pathogen/infectious disease detection. *Anal. Chem.*, **76** (11), 3162–3170.
4 Mahmoudian, L., Kaji, N., Tokeshi, M., Nilsson, M., and Baba, Y. (2008) Rolling circle amplification and circle-to-circle amplification of a specific gene integrated with electrophoretic analysis on a single chip. *Anal. Chem.*, **80** (7), 2483–2490.
5 Fang, X., Liu, Y., Kong, J., and Jiang, X. (2010) Loop-mediated isothermal amplification integrated on microfluidic chips for point-of-care quantitative detection of pathogens. *Anal. Chem.*, **82** (7), 3002–3006.
6 Stedtfeld, R.D. *et al.* (2012) Gene-Z: a device for point of care genetic testing using a smartphone. *Lab Chip*, **12** (8), 1454–1462.
7 Wang, C.H., Lien, K.Y., Wang, T.Y., Chen, T.Y., and Lee, G.B. (2011) An integrated microfluidic loop-mediated-isothermal-amplification system for rapid sample pre-treatment and detection of viruses. *Biosens. Bioelectron.*, **26** (5), 2045–2052.
8 Wang, C.H., Lien, K.Y., Wu, J.J., and Lee, G.B. (2011) A magnetic bead-based assay for the rapid detection of methicillin-resistant *Staphylococcus aureus* by using a microfluidic system with integrated loop-mediated isothermal amplification. *Lab Chip*, **11** (8), 1521–1531.

www.ebook3000.com

9 Wu, Q. *et al.* (2011) Integrated glass microdevice for nucleic acid purification, loop-mediated isothermal amplification, and online detection. *Anal. Chem.*, **83** (9), 3336–3342.

10 Ferguson, B.S. *et al.* (2011) Genetic analysis of H1N1 influenza virus from throat swab samples in a microfluidic system for point-of-care diagnostics. *J. Am. Chem. Soc.*, **133** (23), 9129–9135.

11 Easley, C.J. *et al.* (2006) A fully integrated microfluidic genetic analysis system with sample-in-answer-out capability. *Proc. Natl. Acad. Sci. U.S.A.*, **103** (51), 19272–19277.

12 Nischang, I., Brueggemann, O., and Svec, F. (2010) Advances in the preparation of porous polymer monoliths in capillaries and microfluidic chips with focus on morphological aspects. *Anal. Bioanal. Chem.*, **397** (3), 953–960.

13 Shaw, K.J., Hughes, E.M., Dyer, C.E., Greenman, J., and Haswell, S.J. (2013) Integrated RNA extraction and RT-PCR for semi-quantitative gene expression studies on a microfluidic device. *Lab. Invest.*, **93**, 961–966.

14 Irimia, D. *et al.* (2009) Genome-wide transcriptome analysis of 150 cell samples. *Integr. Biol. (Camb)*, **1** (1), 99–107.

15 Wu, A.R. *et al.* (2009) Automated microfluidic chromatin immunoprecipitation from 2000 cells. *Lab Chip*, **9** (10), 1365–1370.

16 Wu, A.R. *et al.* (2012) High throughput automated chromatin immunoprecipitation as a platform for drug screening and antibody validation. *Lab Chip*, **12** (12), 2190–2198.

17 Geng, T. *et al.* (2011) Histone modification analysis by chromatin immunoprecipitation from a low number of cells on a microfluidic platform. *Lab Chip*, **22** (17), 2842–2848.

18 Thompson, D.M. *et al.* (2004) Dynamic gene expression profiling using a microfabricated living cell array. *Anal. Chem.*, **76** (14), 4098–4103.

19 King, K.R. *et al.* (2007) A high-throughput microfluidic real-time gene expression living cell array. *Lab Chip*, **7** (1), 77–85.

20 Kamei, K. *et al.* (2009) An integrated microfluidic culture device for quantitative analysis of human embryonic stem cells. *Lab Chip*, **9** (4), 555–563.

21 Weigum, S.E. *et al.* (2007) Cell-based sensor for analysis of EGFR biomarker expression in oral cancer. *Lab Chip*, **7** (8), 995–1003.

22 Shen, J. *et al.* (2012) An integrated chip for immunofluorescence and its application to analyze lysosomal storage disorders. *Lab Chip*, **12** (2), 317–324.

23 Raj, A., van den Bogaard, P., Rifkin, S.A., van Oudenaarden, A., and Tyagi, S. (2008) Imaging individual mRNA molecules using multiple singly labeled probes. *Nat. Methods*, **5** (10), 877–879.

24 Bertrand, E. *et al.* (1998) Localization of ASH1 mRNA particles in living yeast. *Mol. Cell.*, **2** (4), 437–445.

25 Heid, C.A., Stevens, J., Livak, K.J., and Williams, P.M. (1996) Real time quantitative PCR. *Genome Res.*, **6** (10), 986–994.

26 Kurimoto, K., Yabuta, Y., Ohinata, Y., and Saitou, M. (2007) Global single-cell cDNA amplification to provide a template for representative high-density oligonucleotide microarray analysis. *Nat. Protoc.*, **2** (3), 739–752.

27 Kurimoto, K. *et al.* (2006) An improved single-cell cDNA amplification method for efficient high-density oligonucleotide microarray analysis. *Nucleic Acids Res.*, **34** (5), e42.

28 Zong, C., Lu, S., Chapman, A.R., and Xie, X.S. (2012) Genome-wide detection of single-nucleotide and copy-number variations of a single human cell. *Science*, **338** (6114), 1622–1626.

29 Tang, F.C. *et al.* (2009) mRNA-Seq whole-transcriptome analysis of a single cell. *Nat. Methods*, **6** (5), U377–U386.

30 Cai, L., Friedman, N., and Xie, X.S. (2006) Stochastic protein expression in individual cells at the single molecule level. *Nature*, **440** (7082), 358–362.

31 Taniguchi, Y. *et al.* (2010) Quantifying *E. coli* proteome and transcriptome with single-molecule sensitivity in single cells. *Science*, **329** (5991), 533–538.

32 Boedicker, J.Q., Vincent, M.E., and Ismagilov, R.F. (2009) Microfluidic confinement of single cells of bacteria in small volumes initiates high-density behavior of quorum sensing and growth and reveals its variability. *Angew. Chem. Int. Ed.*, **48** (32), 5908–5911.

33 Paliwal, S. *et al.* (2007) MAPK-mediated bimodal gene expression and adaptive gradient sensing in yeast. *Nature*, **446** (7131), 46–51.

34 Taylor, R.J. *et al.* (2009) Dynamic analysis of MAPK signaling using a high-throughput microfluidic single-cell imaging platform. *Proc. Natl. Acad. Sci. U.S.A.*, **106** (10), 3758–3763.

35 Ryley, J. and Pereira-Smith, O.M. (2006) Microfluidics device for single cell gene expression analysis in Saccharomyces cerevisiae. *Yeast*, **23** (14–15), 1065–1073.

36 Lee, S.S., Avalos Vizcarra, I., Huberts, D.H., Lee, L.P., and Heinemann, M. (2012) Whole lifespan microscopic observation of budding yeast aging through a microfluidic dissection platform. *Proc. Natl. Acad. Sci. U.S.A.*, **109** (13), 4916–4920.

37 Lecault, V. *et al.* (2011) High-throughput analysis of single hematopoietic stem cell proliferation in microfluidic cell culture arrays. *Nat. Methods*, **8** (7), 581–586.

38 Gomez-Sjoberg, R., Leyrat, A.A., Pirone, D.M., Chen, C.S., and Quake, S.R. (2007) Versatile, fully automated, microfluidic cell culture system. *Anal. Chem.*, **79** (22), 8557–8563.

39 Tay, S. *et al.* (2010) Single-cell NF-kappaB dynamics reveal digital activation and analogue information processing. *Nature*, **466** (7303), 267–271.

40 Cheong, R. *et al.* (2006) Transient IkappaB kinase activity mediates temporal NF-kappaB dynamics in response to a wide range of tumor necrosis factor-alpha doses. *J. Biol. Chem.*, **281** (5), 2945–2950.

41 Cohen, A.A. *et al.* (2008) Dynamic proteomics of individual cancer cells in response to a drug. *Science*, **322** (5907), 1511–1516.

42 Zhou, H., Zhao, L., and Zhang, X. (2015) In-channel printing-device opening assay for micropatterning multiple cells and gene analysis. *Anal. Chem.*, **87** (4), 2048–2053.

43 Marcy, Y. *et al.* (2007) Dissecting biological "dark matter" with single-cell genetic analysis of rare and uncultivated TM7 microbes from the human mouth. *Proc. Natl. Acad. Sci. U.S.A.*, **104** (29), 11889–11894.

www.ebook3000.com

44 Wang, J., Fan, H.C., Behr, B., and Quake, S.R. (2012) Genome-wide single-cell analysis of recombination activity and de novo mutation rates in human sperm. *Cell*, **150** (2), 402–412.

45 Zeng, Y., Novak, R., Shuga, J., Smith, M.T., and Mathies, R.A. (2010) High-performance single cell genetic analysis using microfluidic emulsion generator arrays. *Anal. Chem.*, **82** (8), 3183–3190.

46 Fan, H.C., Wang, J., Potanina, A., and Quake, S.R. (2011) Whole-genome molecular haplotyping of single cells. *Nat. Biotechnol.*, **29** (1), 51–57.

47 Baker, M. (2012) Digital PCR hits its stride. *Nat. Methods*, **9**, 541–544.

48 Ottesen, E.A. *et al.* (2006) Microfluidic digital PCR enables multigene analysis of individual environmental bacteria. *Science*, **314**, 1464–1467.

49 Heyries, K.A. *et al.* (2011) Megapixel digital PCR. *Nat. Methods*, **8** (8), 649–651.

50 Men, Y. *et al.* (2012) Digital polymerase chain reaction in an array of femtoliter polydimethylsiloxane microreactors. *Anal. Chem.*, **84** (10), 4262–4266.

51 Marcus, J.S. *et al.* (2006) Microfluidic single-cell mRNA isolation and analysis. *Anal. Chem.*, **78** (9), 3084–3089.

52 Zhong, J.F. *et al.* (2008) A microfluidic processor for gene expression profiling of single human embryonic stem cells. *Lab Chip*, **8** (1), 68–74.

53 Chen, Y. *et al.* (2012) An automated microfluidic device for assessment of mammalian cell genetic stability. *Lab Chip*, **12** (20), 3930–3935.

54 Di Carlo, D., Aghdam, N., and Lee, L.P. (2006) Single-cell enzyme concentrations, kinetics, and inhibition analysis using high-density hydrodynamic cell isolation arrays. *Anal. Chem.*, **78** (14), 4925–4930.

55 Wang, Z., Kim, M.C., Marquez, M., and Thorsen, T. (2007) High-density microfluidic arrays for cell cytotoxicity analysis. *Lab Chip*, **7** (6), 740–745.

56 Zhao, L., Caot, J.T., Wu, Z.Q., Li, J.X., and Zhu, J.J. (2013) Lab-on-a-chip for anticancer drug screening using quantum dots probe based apoptosis assay. *J. Biomed. Nanotechnol.*, **9** (3), 348–356.

57 Toriello, N.M. *et al.* (2008) Integrated microfluidic bioprocessor for single-cell gene expression analysis. *Proc. Natl. Acad. Sci. U.S.A.*, **105** (51), 20173–20178.

58 White, A.K. *et al.* (2011) High-throughput microfluidic single-cell RT-qPCR. *Proc. Natl. Acad. Sci. U.S.A.*, **108** (34), 13999–14004.

59 White, A.K. *et al.* (2013) High-throughput microfluidic single-cell digital polymerase chain reaction. *Anal. Chem.*, **85** (15), 7182–7190.

60 Spurgeon, S.L., Jones, R.C., and Ramakrishnan, R. (2008) High throughput gene expression measurement with real time PCR in a microfluidic dynamic array. *PLoS One*, **3** (2), e1662.

61 Jang, J.S. *et al.* (2011) Quantitative miRNA expression analysis using fluidigm microfluidics dynamic arrays. *BMC Genomics*, **12**, 144.

62 Petriv, O.I. *et al.* (2010) Comprehensive microRNA expression profiling of the hematopoietic hierarchy. *Proc. Natl. Acad. Sci. U.S.A.*, **107** (35), 15443–15448.

63 Rossant, J. and Tam, P.P. (2009) Blastocyst lineage formation, early embryonic asymmetries and axis patterning in the mouse. *Development*, **136** (5), 701–713.

64 Guo, G. *et al.* (2010) Resolution of cell fate decisions revealed by single-cell gene expression analysis from zygote to blastocyst. *Dev. Cell*, **18** (4), 675–685.

65 Takahashi, K. and Yamanaka, S. (2006) Induction of pluripotent stem cells from mouse embryonic and adult fibroblast cultures by defined factors. *Cell*, **126** (4), 663–676.

66 Hanna, J. *et al.* (2009) Direct cell reprogramming is a stochastic process amenable to acceleration. *Nature*, **462** (7273), 595–601.

67 Buganim, Y. *et al.* (2012) Single-cell expression analyses during cellular reprogramming reveal an early stochastic and a late hierarchic phase. *Cell*, **150** (6), 1209–1222.

68 Mortazavi, A., Williams, B.A., McCue, K., Schaeffer, L., and Wold, B. (2008) Mapping and quantifying mammalian transcriptomes by RNA-Seq. *Nat. Methods*, **5** (7), 621–628.

69 Mardis, E.R. (2008) Next-generation DNA sequencing methods. *Annu. Rev. Genomics Hum. Genet.*, **9**, 387–402.

70 https://en.wikipedia.org/wiki/454_Life_Sciences

71 https://www.illumina.com/systems/sequencing-platforms.html

72 Valouev, A., Ichikawa, J., Tonthat, T., Stuart, J., Ranade, S., Peckham, H., Zeng, K., Malek, J.A., Costa, G., McKernan, K., Sidow, A., Fire, A., and Johnson, S.M. (2008) A high-resolution, nucleosome position map of *C. elegans* reveals a lack of universal sequence-dictated positioning. *Genome Res.*, **18**, 1051–1063.

73 Rothberg, J.M., Hinz, W., Rearick, T.M., Schultz, J., Mileski, W., Davey, M., Leamon, J.H., Johnson, K., Milgrew, M.J., Edwards, M., Hoon, J., Simons, J.F., Marran, D., Myers, J.W., Davidson, J.F., Branting, A., Nobile, J.R., Puc, B.P., Light, D., Clark, T.A., Huber, M., Branciforte, J.T., Stoner, I.B., Cawley, S.E., Lyons, M., Fu, Y., Homer, N., Sedova, M., Miao, X., Reed, B., Sabina, J., Feierstein, E., Schorn, M., Alanjary, M., Dimalanta, E., Dressman, D., Kasinskas, R., Sokolsky, T., Fidanza, J.A., Namsaraev, E., McKernan, K.J., Williams, A., Roth, G.T., and Bustillo, J. (2011) An integrated semiconductor device enabling non-optical genome sequencing. *Nature*, **475**, 348–352.

74 Margulies, M. *et al.* (2005) Genome sequencing in microfabricated high-density picolitre reactors. *Nature*, **437** (7057), 376–380.

75 Rothberg, J.M. *et al.* (2011) An integrated semiconductor device enabling non-optical genome sequencing. *Nature*, **475** (7356), 348–352.

76 Sims, P.A., Greenleaf, W.J., Duan, H., and Xie, X.S. (2011) Fluorogenic DNA sequencing in PDMS microreactors. *Nat. Methods*, **8** (7), 575–580.

77 Wu, A.R. *et al.* (2014) Quantitative assessment of single-cell RNA-sequencing methods. *Nat. Methods*, **11** (1), 41–46.

78 Pollen, A.A. *et al.* (2014) Low-coverage single-cell mRNA sequencing reveals cellular heterogeneity and activated signaling pathways in developing cerebral cortex. *Nat. Biotechnol.*, **32**, 1053–1058.

79 Streets, A.M. *et al.* (2014) Microfluidic single-cell whole transcriptome sequencing. *Proc. Natl. Acad. Sci. U.S.A.*, **111** (19), 7048–7053.

www.ebook3000.com

10

Computational Microfluidics Applied to Drug Delivery in Pulmonary and Arterial Systems

Clement Kleinstreuer[1,2] *and Zelin Xu*[1]

[1] *North Carolina State University, Department of Mechanical & Aerospace Engineering, 911 Oval Dr, Raleigh, NC 27695, USA*
[2] *North Carolina State University and University of North Carolina at Chapel Hill, Joint Department of Biomedical Engineering, 911 Oval Dr, Raleigh, NC 27695, USA*

10.1 Introduction

Microfluidics, the technique of handling fluid flow in microconduits, has found wide applications in a broad range of fields from engineering to medicine [1–3]. This was partly enabled by the rapid development of computational tools and the increase in computer power that provide fast, accurate, and detailed information of fluid–particle dynamics. Especially computational microfluidics has become an essential tool for understanding complex processes in drug delivery, assisting the development of new medical devices, and evaluating treatment efficacy and patient outcome. For instance, modeling has been considered to be among the seven key priorities for enabling the translation of nanomedicine from the laboratory to the clinic [4]. This chapter presents the fundamentals of computational microfluidics with applications in pulmonary and arterial drug delivery.

Despite numerous efforts in developing carriers and devices for pulmonary and arterial drug delivery, we still face many challenges in delivering drugs directly to the targeted sites to combat diseases without affecting healthy tissues or organs. Clearly, ideal drug delivery through intravascular methods would result in 100% drug deposition on tumors or inflamed areas, while drug delivery through pulmonary routes would avoid premature deposition and mucociliary clearance. Various methods and devices have been developed to achieve these goals, as recently reviewed by Kleinstreuer *et al*. [5, 6] and Kleinstreuer and Childress [7]. This chapter builds on these review efforts with an added emphasis on the fundamentals of computational microfluidics with updated applications.

Specifically, Section 10.2 presents the modeling methods of micro-biofluid dynamics, focusing on the general conservation laws that govern the transport of fluids, and the modeling approaches for specific aims such as two-phase flow, magnetic particle dynamics, nonspherical particle dynamics, flow in porous media, and fluid–structure interactions. It lays the foundation for the applications on pulmonary and arterial drug delivery discussed in Sections 10.3

Microfluidics: Fundamentals, Devices and Applications, First Edition.
Edited by Yujun Song, Daojian Cheng, and Liang Zhao.
© 2018 Wiley-VCH Verlag GmbH & Co. KGaA. Published 2018 by Wiley-VCH Verlag GmbH & Co. KGaA.

and 10.4, respectively. The novel topic is *direct drug delivery*, that is, from the injection/inhalation point to the diseased site. It is a patented method that enhances the efficacy of treatment by precisely targeting diseased sites with the aid of patient-specific computational models and a new set of medical devices. This chapter concludes with the challenges still faced in optimal drug delivery and provides perspectives on future directions of computational micro-biofluidics.

10.2 Modeling Methods

This section discusses the fundamentals of computational microfluidics including the governing equations, constitutive equations, and specific modeling methods for complex fluid–particle dynamics as applied to drug delivery in pulmonary and arterial systems. It provides the foundation for the discussions in the application sections.

10.2.1 Governing Equations

The governing equations describing the incompressible fluid flow in both pulmonary and arterial systems are the Navier–Stokes (N-S) equations for mass, momentum, and energy conservation:

$$\frac{\partial u_j}{\partial x_j} = 0 \tag{10.1}$$

$$\rho \frac{\mathrm{D}u_i}{\mathrm{D}t} = \frac{\partial \tau_{ij}}{\partial x_j} - \frac{\partial p}{\partial x_i} + \rho f_i \tag{10.2}$$

$$\rho c_\mathrm{p} \frac{\mathrm{D}T}{\mathrm{D}t} = \frac{\partial}{\partial x_j}\left[\left(\frac{k}{c_\mathrm{g}} + \frac{\rho \nu_\mathrm{T}}{\sigma_\mathrm{T}}\right)\frac{\partial T}{\partial x_j}\right] + \left(\frac{\partial u_i}{\partial x_j} + \frac{\partial u_j}{\partial x_i}\right)\frac{\partial u_i}{\partial x_j} \tag{10.3}$$

The quantities ρ, u_i, τ_{ij}, p, T, f_i and k are fluid density, fluid velocity vector, shear stress tensor, pressure, temperature, applicable body forces and thermal conductivity, respectively. In addition, ν_T is the turbulent eddy viscosity, σ_T is the turbulent Prandtl number, and c_g is the specific heat of the fluid.

10.2.2 Model Closure

Equation (10.2) requires additional constitutive equations for closure. For Newtonian fluids (e.g., air in respiratory airways and blood in arteries with shear rates over 100 s^{-1}), the relationship between the shear stress tensor and the shear strain is given by

$$\tau_{ij} = \mu\left(\frac{\partial u_i}{\partial x_j} + \frac{\partial u_j}{\partial x_i}\right) \tag{10.4}$$

where μ is the fluid viscosity. While blood flow is typically laminar, rapidly inhaled air may become locally turbulent. Hence, appropriate turbulence models suitable for problem-specific simulations have to be selected and solved together with the Reynolds-averaged Navier–Stokes (RANS) equations (Section 10.2.3).

www.ebook3000.com

Blood is a non-Newtonian fluid with shear-thinning viscosity at low shear rates. Several models can be used to describe the dependence of viscosity on the local shear rate, including the Carreau model and the Quemada model. Several studies have demonstrated the accuracy of a modified Quemada model [8, 9]. It reproduces the shear-thinning behavior of blood and avoids the singular behavior at very low shear rates. Specifically, the apparent viscosity of blood is expressed as

$$\mu_{\text{app}} = \max\left(\mu_0, \left[\sqrt{\mu_\infty} + \sqrt{\tau_0}/\left(\sqrt{\lambda} + \sqrt{\dot{\gamma}}\right)\right]^2\right) \tag{10.5}$$

where $\mu_0 = 0.0309$ (g cm^{-1} s^{-1}) is the minimum viscosity, $\mu_\infty = 0.02654$ (g cm^{-1} s^{-1}) is an asymptotic viscosity, $\tau_0 = 0.0436$ (g cm^{-1} s^{-1}) is the apparent yield stress, $\dot{\gamma}$ (s^{-1}) is the local shear rate, and $\lambda = 0.0181$ (s^{-1}) is the shear-rate modifier.

10.2.3 Turbulence Modeling

Based on the normal human breathing conditions, that is, 15–90 l min^{-1} ($300 < Re_{\text{inlet}} < 10^4$), the airflow in the human glottis region can be laminar–turbulent–laminar [10]. Of the several RANS models, the shear stress transport (SST) transition model is especially suitable for laminar–turbulent transitional flows as compared with the low-Reynolds-number k–omega model and the standard k–omega model [10]. It is capable of predicting mean velocity distributions and turbulence kinetic energy profiles accurately at reasonable computational cost. Tan *et al.* [11] also demonstrated that a correlation-based transitional SST model may achieve a better overall agreement with experimental data than the standard SST model for pulsatile flow in an axisymmetrically restricted tube. The SST transition model solves two additional transport equations, that is, one for the intermittency and another for the transition onset criterion in terms of momentum thickness Reynolds number. The corresponding turbulence equations may be found in Menter *et al.* [12, 13].

10.2.4 Fluid–Particle Dynamics Modeling

Depending on the particle size and concentration, different methods can be used to simulate computationally the fluid–particle dynamics of drug delivery. Modeling approaches for such two-phase flow phenomena include the two-fluid method, the Euler–Euler method, and the Euler–Lagrange method. In basic two-fluid flow modeling, both fluid and particle phases are considered as "fluids" with the two volume fractions summing up to unity. Specifically, the governing equations for phase α are as follows:

$$\frac{\partial(\varphi_\alpha \rho_\alpha)}{\partial t} + \nabla(\varphi_\alpha \rho_\alpha u_\alpha) = 0 \tag{10.6}$$

$$\frac{\partial}{\partial t}(\varphi_\alpha \rho_\alpha u_\alpha) + \nabla(\varphi_\alpha \rho_\alpha u_\alpha u_\alpha) = -\varphi_\alpha \nabla p + \nabla[\varphi_\alpha \mu_\alpha(\nabla u_\alpha + (\nabla u_\alpha)^T)] + F_\alpha \tag{10.7}$$

$$\frac{\partial(\varphi_\alpha \rho_\alpha h)}{\partial t} + \nabla[\varphi_\alpha \rho_\alpha u_\alpha h_\alpha] = \nabla(k_\alpha \nabla T_\alpha) + Q_\alpha \tag{10.8}$$

where φ is the volume fraction and F_α is the surface force due to the existence of another phase [14]. In the Euler–Euler approach, nano-sized particles are considered to be "dissolved" in the carrier fluid; that is, in addition to the N-S equations, the coupled species mass transfer equation for the particle (or species) concentration is solved [15].

The Euler–Lagrange approach is used for micron-size particles with relatively large Stokes numbers ($Stk \equiv \rho_p d_p u/9\mu D > 1$, D being the hydraulic diameter and u being the mean velocity). This method relies on the flow-field solution (Euler part) and uses Newton's second law (Lagrange part) to update the particle location in the flow field:

$$m_p \frac{\mathrm{d}u_j^p}{\mathrm{d}t} = F_j^D + F_j^p + F_j^G \tag{10.9}$$

$$\begin{aligned} F_j^D &= \frac{1}{8}\pi\rho_p d_p^2 C_d (u_j - u_j^p)|u_j - u_j^p| \\ F_j^p &= d_p^3 \frac{\pi}{6}\frac{\partial p}{\partial k_j} \\ F_j^G &= \frac{\pi}{6} d_p^3 (\rho_p - \rho) g_j \end{aligned} \tag{10.10}$$

Here, for solid spherical particles, $C_d = 24(1 + 0.15\,Re_p^{0.687})/Re_p$, and for spherical droplets,

$$C_d = \frac{3.05(783\kappa^2 + 2142\kappa + 1080)}{(60 + 29\kappa)(4 + 3\kappa)} Re_p^{-0.74}; \quad 4 < Re_p < 100 \tag{10.11}$$

where $\kappa = \mu_p/\mu$ and $Re_p = \rho|u_j - u_j^p|d_p/\mu_{app}$ is the particle Reynolds number. The quantities m_p, ρ_p, and d_p are the particle's mass, density, and diameter, respectively.

The drag force due to particle slip with respect to the fluid, F_j^D, can be simplified in the creeping flow regime, in which $Re_p < 1$:

$$F_j^D = 3\pi\mu d_p (u_j - u_j^p) \tag{10.12}$$

Other forces such as virtual mass force, lift force, and Basset history force are usually insignificant in pulmonary and arterial flow simulations [8, 16].

In many situations, forces due to particle–particle interactions are important. For example, the red blood cells in microvessels can create significant diffusional fluxes, while particle–particle and particle–wall interactions strongly influence particle transport and deposition in respiratory airways [17]. The discrete element method (DEM) may be used to explicitly model the contact and interaction between the fluid, particles, and the wall surface. Feng and Kleinstreuer [17] developed a dense discrete phase model (DDPM) coupled with DEM to model micron-particle transport, interaction, and deposition in the lung airways. In this model, DEM models particle collision, while DDPM describes fluid–particle flow. The coupling between the discrete and continuous phases was achieved via an interphase interaction term in the Navier–Stokes equation.

Recently, studies have focused on delivering nanoparticles (NPs) to pulmonary and arterial systems. For such small particles, Brownian diffusion affects particle

www.ebook3000.com

distribution and subsequent deposition. Hence, as part of the Euler–Euler approach, the convection–diffusion mass transfer equation can be used to describe the local particle concentrations. For example, for aerosol transport applied to pulmonary drug delivery, it can be expressed as

$$\frac{\partial Y}{\partial t} + \frac{\partial}{\partial x_j}(u_j Y) = \frac{\partial}{\partial x_j}\left[\left(\tilde{D} + \frac{\nu_T}{\sigma_T}\right)\frac{\partial Y}{\partial x_j}\right] \tag{10.13}$$

where $\tilde{D}$ is the aerosol diffusion coefficient and Y is the particle mass fraction.

10.2.5 Ferrofluid Dynamics

Magnetic drug delivery is a promising tumor treatment method. The magnetic force acting on a magnetized particle is proportional to its magnetic moment $\vec{m}$ (A m^2) and to the gradient of the magnetic field H (A m^{-1}):

$$\vec{F}_{\text{mag}} = \mu_0(\vec{m} \cdot \nabla)\vec{H} \tag{10.14}$$

The magnetic susceptibility of human tissue is five to seven orders of magnitude lower than that of typical ferromagnetic particles used in magnetic drug delivery [18]. Therefore, Eq. (10.14) can be rewritten as

$$\vec{F}_{\text{mag}} = \frac{\chi \forall}{2\mu_0}\nabla \vec{B}^2 \tag{10.15}$$

where $\mu_0 = 4\pi \times 10^{-7}$ (H m^{-1}) is the permeability of vacuum, $\forall$ is the particle volume, χ is the magnetic susceptibility of the particle, and $\vec{B}$ (T) is the magnetic flux density.

In addition to the magnetic force, the interparticle force due to magnetic dipole interactions may also be considered [19]. The concentration c of magnetic nanoparticles (MNPs) in the blood flow can be obtained using an enhanced advection–diffusion equation:

$$\frac{\partial c}{\partial t} = \nabla \cdot (c\vec{v}_p) + \nabla \cdot (D_{\text{tot}} \nabla c) \tag{10.16}$$

Here, the particle velocity is a result of the combined effect of hydrodynamic and magnetic forces:

$$\vec{v}_{\text{p}} = \vec{v}_{\text{f}} + \vec{v}_{\text{mag}}; \quad \vec{v}_{\text{mag}} = \frac{\vec{F}_{\text{mag}}}{6\pi\mu a} \tag{10.17}$$

While the effective diffusion coefficient D_{tot} is due to the Brownian motion and shear-induced diffusion,

$$D_{\text{tot}} = D_{\text{Br}} + D_{\text{sh}} = \kappa_{\text{B}} T/6\pi\mu a + K_{\text{sh}}(r_{\text{RBC}})^2 \dot{\gamma} \tag{10.18}$$

In the above equations, a is the hydrodynamic radius of the particle, κ_{B} is Boltzmann's constant, T is the absolute temperature, r_{RBC} is the radius of red blood cells, and K_{sh} is a dimensionless coefficient depending on the hematocrit. D_{Br} is the Brownian diffusion coefficient and D_{sh} represents the shear-induced diffusion, which is due to interactions between red blood cells that give rise to a diffusional flux. It can be important when the diffusive flux is comparable with the advective flux due to the magnetic field [20].

10.2.6 Nonspherical Particle Dynamics

At present, traditional spherical drug carriers remain dominant due to the ease of synthesis and testing. Hence, concerning computational microfluidics applied in pulmonary and arterial drug delivery, most investigations assumed drug carriers to be perfectly spherical. This assumption also holds true for a lot of situations in shear flow where nonspherical particles with low aspect ratios are considered. In these cases, a modified drag force may be used to model the fluid–particle dynamics [21].

The orientation of nonspherical particles, influenced by their rotations, is important in drug transport and deposition. To accurately describe particle rotation, equations for Eulerian rotational motion must be introduced and solved together with Newton's second law for translational motion. Feng and Kleinstreuer [22] employed this approach to simulate laminar–turbulent flow in a subject-specific lung airway with ellipsoidal particles of different aspect ratios.

10.2.7 Flow through Porous Media

Occasionally fluid flow through porous media needs to be considered in computational microfluidics. Examples include blood flow through medical devices inserted in arteries [23, 24], biofluid flow and nanodrug diffusion from blood vessels into tissues [25], and effective airflow in the lung alveoli regions. Fluid flow in porous medium is governed by Darcy's law and its extensions [1]:

$$\frac{\partial p}{\partial x_i} = -\frac{\mu}{K}u_j - \frac{C_f \rho |u_j| u_j}{\sqrt{K}} + \mu \frac{\partial^2 u_j}{\partial x_i^2} \tag{10.19}$$

Here, u_j is the superficial velocity vector, K is the permeability, and C_f is the inertia resistance factor. The second term on the right-hand side (RHS) of the equations accounts for the inertia effect. The third term accounts for the no-slip boundary conditions at internal obstructions. It is especially useful when considering interstitial flow in tissues. The permeability K and the inertia coefficient C_f are both functions of the matrix porosity, matrix composition, and matrix geometry. Several correlations have been developed to estimate permeability for biological materials, of which the Carman–Kozeny equation and its variations have found widespread use [26]:

$$K = \frac{\varepsilon^3}{G \cdot S_p^2} = \frac{\varepsilon r_h^2}{G} \tag{10.20}$$

Here, ε is the fractional void volume, G is the geometry-dependent Kozeny factor, S_p is the wetted surface area per unit volume, and r_h is the mean hydraulic radius of the pores. Table 10.1 provides typical values of tissue permeability relevant to the present topic. The data were compiled from Swartz and Fleury [25].

It is known that the matrix composite of tissues can reduce diffusivities by as much as 80% from their free solution value [27]. Therefore, to model NP diffusion in tissues, the diffusion coefficient needs to be modified to account for the porous nature of tissues. Kosto and Deen [28] provided a relationship between free solute

www.ebook3000.com

Table 10.1 Specific permeability (K) or hydraulic conductivity (K') of human tissues.

	Tissue/material	K (cm^2)	K' (cm^2 mmHg^{-1} s^{-1} × 10^{-8})
Biopolymers	Fibrin coarse to fine (3 mg ml^{-1})	10^{-8}–10^{-11}	
	Collagen gel	10^{-12}–10^{-14}	
Tumors	Human glioblastoma		65–7000
	Human soft tissue sarcoma		9.2
	Human colon adenocarcinoma		45
	Hepatoma		0.8–4.1 28 (different source)
Normal tissues	Subcutaneous plane		0.6–0.85
	Subcutaneous slice		6.0
	Blood clot unretracted/retracted	10^{-8}–10^{-10}	
	Aortic media and intima		0.4–2.0

and matrix diffusivity as

$$\frac{D_G}{D_0} = \exp(-\phi^{0.5}(1 + R_H/r_f) \tag{10.21}$$

where ϕ is the fiber volume fraction, R_H is the hydrodynamic radius of the pores, and r_f is the fiber radius.

10.2.8 Fluid–Structure Interaction

The bounding surfaces of the human lung airways and blood arteries are not rigid, especially in the deep lung region (e.g., alveoli) and in large arteries (e.g., hepatic arteries) [29]. Under pulsatile flow conditions due to either rhythmic breath or heartbeat, the periodic wall movement can be modeled using the conservation of momentum [30]:

$$\rho_{wall}\frac{\partial^2 \hat{u}_i}{\partial t^2} = \frac{\partial \sigma_{ji}}{\partial x_j} + f_i \tag{10.22}$$

In this equation, ρ_{wall} is the density of the wall tissue, $\hat{u}_i$ is the displacement vector for the wall, σ_{ji} is the mechanical stress tensor, and f_i are body force vectors.

The coupled conservation equations, that is, Eqs. (10.1) and (10.2), can be rewritten in integral form for control volume CV with control surface CS, assuming W_i to be the velocity of the CV boundary, as

$$\int_{CS}(u_j - W_j)n_j dA = 0 \tag{10.23}$$

$$\rho\frac{d}{dt}\int_{CV(t)} u_i \, dV + \rho\int_{CS}(u_j - W_j)u_i n_j \, dA = -\int_{CS}\rho n_j \, dA + \int_{CS}\mu(\dot{\gamma})\left(\frac{\partial u_i}{\partial x_j} - \frac{\partial u_j}{\partial x_i}\right)n_j \, dA \tag{10.24}$$

Often, the structure can undergo large strains due to the physiological pressures and the distensibility of the wall [30]. For example, the hepatic arteries can exhibit about a 20% increase in diameter within the physiological pressure range of 75–170 mmHg, as well as stiffening with increasing loads. The second-order Yeoh hyperelastic material model can be used to model the response of the wall:

$$\psi = \alpha(I_1 - 3) + \beta(I_1 - 3)^2 \tag{10.25}$$

where ψ is the strain energy density, I_1 is the first invariant of the left Cauchy–Green deformation tensor, and α and β are constants depending on material properties.

In some cases, the pressure–diameter data are available for arteries. Then the analytical pressure–radius relationship of a flexible, thick-walled cylinder can be used to estimate the elastic properties:

$$p_i = \int_{r_i}^{r_o} (\sigma_{\theta\theta} - \sigma_{rr}) \frac{\mathrm{d}r}{r} \tag{10.26}$$

where $\sigma_{\theta\theta}$ is the circumferential stress, σ_{rr} is the radius stress, r_i is the deformed internal radius, and r_o is the deformed outer radius. Assuming no residual stresses, $r = \sqrt{R^2 - R_i^2 + r_i^2}$, where R is the undeformed radius and R_i is the undeformed internal radius. For a second-order Yeoh material,

$$\sigma_{\theta\theta} - \sigma_{rr} = \left(2\alpha + 4\beta\left[\left(\frac{R}{r}\right)^2 + \left(\frac{r}{R}\right)^2 - 2\right]\right)\left[\left(\frac{r}{R}\right)^2 - \left(\frac{R}{r}\right)^2\right] \tag{10.27}$$

10.3 Pulmonary Drug Delivery

Pulmonary drug delivery is one of the three popular drug delivery routes. It takes advantage of the large surface area of the lung (about 100 m^2) and the thin epithelial layer (i.e., 0.2–0.7 μm) as given by Ruge *et al.* [31]. Also, it enjoys a high degree of convenience when delivering drugs just via inhalation. When used to treat lung diseases such as asthma, chronic obstructive pulmonary disease, cystic fibrosis, or lung tumors, the drug aerosols can travel directly to the target area, circumventing the systemic circulation and thus reducing clearance and side effects [6]. Pulmonary insulin delivery is also suitable in the treatment of diabetes and other systemic diseases by rapid absorption of drug aerosols from the alveolar region into the systemic circulation.

Novel drug formulations and inhaler devices have been the main concern because aerosol dynamics plays an important role in the successful pulmonary drug delivery. Specifically, the physicochemical properties of the drug carriers as well as the complex flow in drug delivery devices and the human lung ultimately determine drug transport and deposition. The drug efficacy is greatly affected by the local deposition dosage and subsequent mass transfer into systemic regions [32–34]. Hence, research on pulmonary drug delivery has focused on evaluating the aerosol dynamics to determine the optimal particle properties as well as configurations of drug delivery devices [35–37].

www.ebook3000.com

Computational fluid–particle dynamics (CF-PD) can provide detailed information on drug aerosol transport and deposition due to complex mechanisms [38, 39]. It can readily take into account the effects of interpersonal variability in the lung airway geometry, which significantly affects the drug delivery efficiency [40]. Therefore, it could serve as an effective design and optimization tool for improving pulmonary drug delivery. In this section, current devices for pulmonary drug delivery such as pressurized metered-dose inhaler (pMDI), dry powder inhaler (DPI), and nebulizer will be discussed, focusing on their delivery mechanisms, efficiencies, and challenges for future improvements. Following this, computational drug–aerosol dynamics, that is, the transport and deposition of drug carriers, will be discussed, including solid micron particles, NPs, and vapor–droplet mixtures. Key parameters that affect effective pulmonary drug delivery will be addressed. Finally, this section offers a description of the methodologies and design aspects for optimal pulmonary drug delivery.

10.3.1 Inhalers and Drug–Aerosol Transport

The three most popular types of pulmonary drug delivery devices are pMDIs, DPIs, and nebulizers. They feature distinct delivery mechanisms and offer different delivery options.

The pMDIs store drug–propellant mixtures in a canister and release accurate amounts upon human actuation, offering fast and cost-effective delivery of drug aerosols. It expels the drug aerosol driven by propellants through a nozzle at high velocities ($>30\ \mathrm{m\ s^{-1}}$) according to Newman [41]. Figure 10.1 shows the components and delivery mechanisms of a pMDI. When the canister is pressed into the actuator seating, the formulation will decompress within the metering valve, generating a metered dose of a drug-containing aerosol in the form of polydisperse droplets. The droplets evaporate after being generated from the atomization nozzle, thereby reducing the size of the aerosols. The high jet velocity of the pMDI-generated aerosols induces strong impaction in the oral cavity, making it difficult for deeper lung drug delivery. For example, one type of pMDIs only delivers approximately 10–20% of the emitted medications to the lung, while the rest deposits in the oropharynx [43]. In addition, pMDIs suffer from unsynchronized device actuation and patient inhalation. Thus, breath-actuated MDIs [44] and spacer devices have been introduced. The latter uses a one-way valve to create a holding chamber (>750 ml) after pMDI actuation, which sieves the droplets and produces a fine aerosol with smaller particle sizes to reduce the inertial effect [45].

The DPIs differ from pMDIs in the drug carrier form; that is, DPIs deliver drugs into the pulmonary system in the form of dry solid particles (see Figure 10.2). Specifically, DPIs fill a cartridge (or blister packs) with drug-carrying powders. For passive DPIs, the patient introduces air into the powder bed by breathing, which creates turbulent flow that leads to the fluidization of a powder blend. The powders then enter the patient's pulmonary system via inhalation. Nowadays, active DPIs are replacing passive ones, which use external forces to consistently deliver drugs independent of the inspiration flow [46]. DPIs contain medicine in

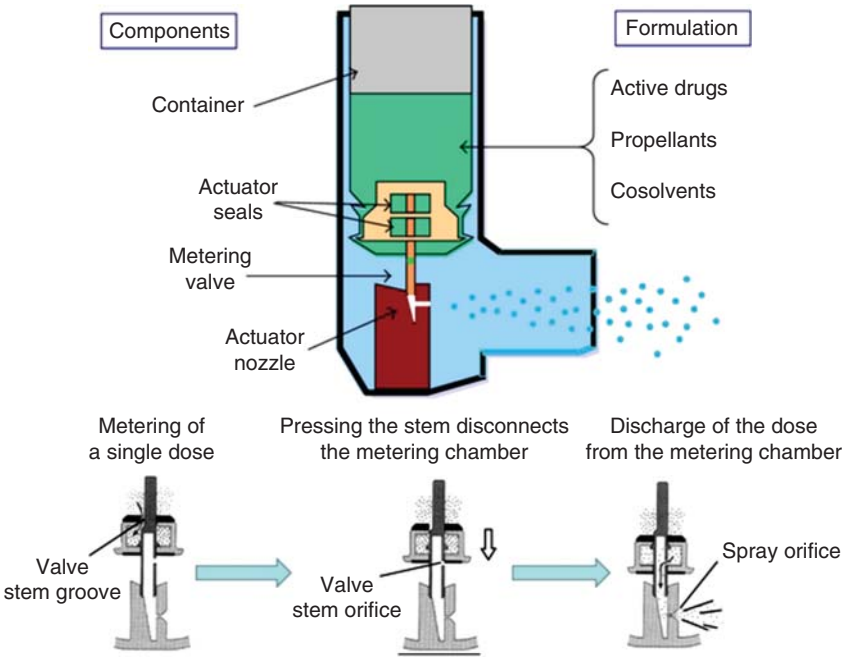


Figure 10.1 Components of a pMDI. Lower panels illustrate the process of aerosol generation. (Lavorini 2013 [42] https://www.hindawi.com/journals/isrn/2013/102418/. Used under CC BY 3.0 https://creativecommons.org/licenses/by/3.0/.)

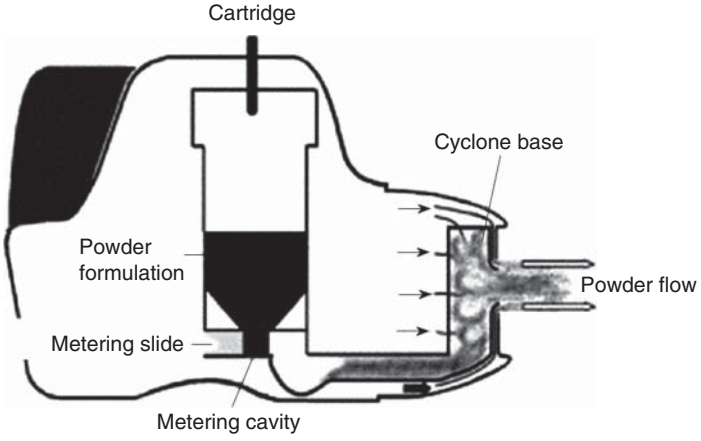


Figure 10.2 Typical structure of unit-dose dry powder inhaler. (Reprinted with permission from Kleinstreuer *et al*. [6].)

a variety of types, for example, single-dose capsule-based designs and multidose units containing drugs in bulk or individual blister packages [47, 48]. DPIs are portable and easy to use and can deliver high drug payloads. However, they may need frequent refilling and have strict storage requirements in terms of temperature and humidity to avoid drug-powder clumping.

www.ebook3000.com

Nebulizers are pulmonary drug delivery devices that generate small-scale droplets in the form of mist aerosols from a liquid solution/suspension [44]. Nebulizers offer unique delivery possibilities that deliver the drug directly to the desired site, thus limiting the side effects of certain medication, for example, steroids [6]. Figure 10.3 illustrates several conventional designs of nebulizers. Atomizers (or jet nebulizers) are the most common ones. They use compressed gas to generate high-velocity air jets across the fluid-medication suspension to create droplet aerosols inside the nebulizing chamber. Ultrasonic wave nebulizers generate aerosols via the vibration of a piezoelectric crystal at a high frequency (>1 MHz) through the drug liquid with low noise. They provide faster delivery of pharmaceuticals compared with atomizers. Smaller portable devices (vibrating mesh nebulizers) have been developed, which generate droplet drug aerosols by actuating a mesh/membrane with multiple apertures so that it vibrates at the top of a liquid reservoir (Figure 10.3c). Still, new types of nebulizers like breath-enhanced nebulizer and dosimetric nebulizer exist on the market to provide high output efficiency and avoid apparatus loss and exhaled loss [50].

Both pMDIs and DPIs are portable and fast delivering devices for low medication dosages. In addition, nebulizers are able to deliver higher drug dosages at the cost of portability and delivery efficiency. A new-generation device is the soft mist inhaler, that is, a propellant-free inhaler that avoids coordination difficulties between inhalation and actuation. It delivers accurately predetermined dosages of aerosols at a low velocity and is independent of inspiratory characteristics of the patients. The deposition fraction in the upper respiratory system can reach 40% due to lower inertial impaction [51].

Despite the continuous effort in improving the devices, current inhalers suffer from inefficiencies at delivering pharmaceutical aerosols to the lungs due to high depositional losses (25–75% for MDIs and DPIs) in the devices and extrathoracic airways as well as undesired particle size distributions [52]. Therefore, improving the delivery efficiency of medicines to the lungs will greatly reduce side effects and treatment costs.

In summary, the efficacy of drug delivery devices depends mainly on two factors: drug formulation and device design. The device configuration affects the flow path, delivery condition, and aerosol property, which significantly influence subsequent transport and deposition of the inhaled particles in the

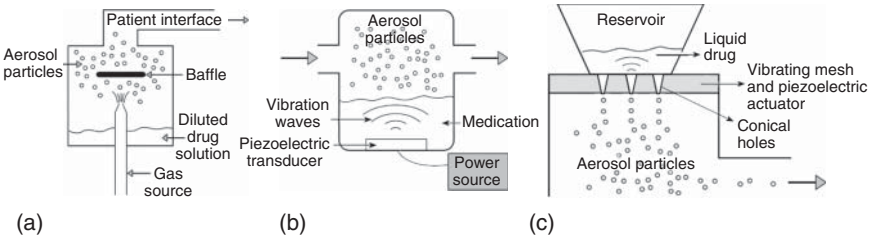


Figure 10.3 Typical structures of different nebulizer categories. (a) Atomizer (jet nebulizer); (b) ultrasonic wave nebulizer. ((a, b) Muchão and da Silva Filho [49] http://www.scielo.br/scielo.php?pid=S0021-75572010000500004&script=sci_arttext&tlng=pt. used under CC BY 4 https://creativecommons.org/licenses/by-nc-nd/4.0/deed.en.). (c) Vibrating mesh nebulizer. (Reprinted with permission from Kleinstreuer *et al*. [6].)

human respiratory system. In addition, the patient's inhalation behavior may significantly affect the drug delivery and resulted efficacy. CF-PD has found wide applications in the development and evaluation of inhalers [53, 54], capturing effects such as turbulence in the inhaler, spray momentum, and inlet jet effects, as well as best possible geometric design and operational conditions. In the following subsection, drug–aerosol dynamics as revealed by CF-PD simulations in the inhaler and in the human respiratory airway is discussed with applications to the development of novel pulmonary drug delivery devices. This will then be followed by a discussion of the methodologies and design aspects for direct pulmonary drug delivery.

10.3.2 Drug–Aerosol Dynamics

Inhalers generate and deliver drug aerosols in the form of solid particles or droplets with vapors for therapeutic purposes. The objective is to generate well-controlled drug aerosols with desired properties and deliver drugs from their releasing position to target deposition regions in the human lung for optimal medical effectiveness. Current medical care industry with more specialized treatment options desires that the drug aerosols be effectively delivered not only to a specific lung region (e.g., central or peripheral, right or left) but also to the site of disease, or even to distinct cell types via transport through biological barrier, for example, epithelial cells of the pulmonary blood or lymphatic systems [6, 31]. Apparently, the fluid–particle dynamics during drug–aerosol generation, transport, deposition, absorption, and clearance are essential for guiding the development of novel pulmonary drug delivery methods. This section provides a discussion of these aspects.

In Section 10.2 the underlying principles for CF-PD modeling of lung aerosol dynamics have been outlined. The governing equations coupled with constitutive equations and specific supplementary equations enable the modeling of laminar or turbulent airflows, spherical and nonspherical micro-/NP transport and deposition, vapor–droplet interaction via evaporation and condensation [55], and species heat and mass transfer [56]. These models take into account various deposition mechanisms, such as impaction [57], sedimentation [35, 36], and diffusion [58] under steady and transient inhalation conditions [59]. The modeling approaches can be categorized into mixture models, two-fluid models, discrete phase models (DPMs), and dense dispersed phase models, as well as the DEM. Once validated, these models provide cost-effective ways to analyze factors influencing pulmonary drug delivery. Specifically, CF-PD simulations provide detailed local deposition characteristics in the lung airways while considering patient-specific airway geometry and inhalation pattern. This knowledge is vital for evaluating drug efficacy, because it allows the prediction of localized particle dissolution, transport through the mucus, and uptake at the cellular level. It should be noted that other respiratory delivery models exist, such as the 1D whole-lung respiratory dosimetry model, which provides correlations to estimate the penetration depth of aerosols into the lungs [60]. However, those models neglect the particle flow physics in complex airway geometry and hence are not universally applicable.

www.ebook3000.com

Airflow patterns and particle dynamics have been analyzed in different inhaler devices for performance improvement [53, 54]. For example, methods to de-aggregate the drug powders in DPIs and to reduce device deposition in pMDIs and DPIs have been proposed based on computational studies [37, 61, 62]. In addition, CF-PD studies have been performed on spray inhalers. For instance, Kleinstreuer *et al*. [35, 36] numerically investigated the transport and deposition of drug aerosols from a pMDI into a human upper airway model. The effects of different inhaler configurations and propellants on deposition pattern have been determined (see Figure 10.4). Most importantly, they showed that by generating a controlled air–particle stream, a smart inhaler could provide locally targeted drug–aerosol delivery. Longest and Hindle [63] analyzed droplet transport and deposition from a soft mist inhaler into a mouth–throat geometry and found that recirculation within the inhaler mouthpiece causes about 30% deposition in the device. Hence they improved the inhaler design by reducing turbulence intensity and increasing the effective mouthpiece diameter [64]. Inthavong *et al*. [65] showed that greater penetration of micron particles in the nasal cavity can be achieved via adjusting the swirl fraction of a nasal spray device.

Most of the CF-PD studies of pulmonary drug delivery devices did not consider particle–particle interaction effects. However, this effect can be important especially for DPIs where the dynamic process of powder dispersion and de-aggregation may significantly affect the particle size distribution and hence lung deposition. Therefore, a combined computational fluid dynamics (CFD)–DEM has been used to study the breakup of powder agglomerates in a commercial Aerolizer® inhaler model [66]. The results showed that an increased airflow rate helps to break up the agglomerates; nonetheless, high flow rates will also increase device deposition, indicating an optimal operation zone. Particle–particle interaction may also be important in the human lung airways. For example, Feng and Kleinstreuer [17] showed that particle interaction is a major deposition mechanism for dense particle suspensions in human lung models. For a recent review, see Ruzycki *et al*. [67].

10.3.3 Methodologies and Design Aspects for Direct Drug Delivery

The primary goal of advanced pulmonary drug delivery is to maximize the delivery efficiency and minimize side effects, along with ease of use, good patient compliance, device reliability, and reduced cost. Current inhaler devices have poor lung delivery efficiencies of 40–60% for pMDIs and DPIs and up to 80% for soft mist inhalers due to premature deposition [39]. Still, these efficiencies only indicate post-throat deposition, that is, their pulmonary depositions are non-focused. Therefore, new methodologies are desired to enable direct drug delivery through the pulmonary route to predetermined sites/regions to treat diverse lung-related diseases including cancer. Because it is difficult to control/address patient variability in terms of lung airway geometry and breathing pattern, mainly two strategies can be employed toward achieving this goal: formulation of the drug delivery vehicles (particulate matters) with disease-specific optimal physicochemical properties and redesigning of the drug delivery devices to allow for optimal tumor targeting. The physicochemical

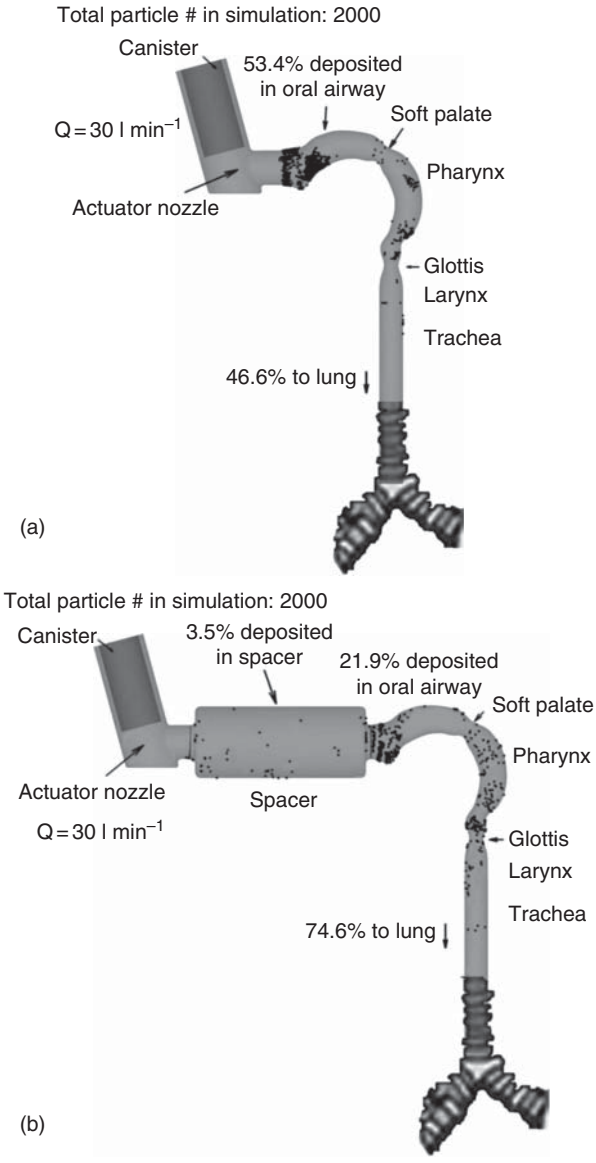


Figure 10.4 Simulation result of hydrofluoroalkane (HFA) propelled pMDI droplet deposition without (a) and with (b) spacer. (Reprinted with permission from Kleinstreuer *et al*. [35, 36].)

properties that can affect the transport and deposition of drug aerosols include initial particle size, shape, density, concentration, hygroscopicity, charge, and surfactant. Drug delivery devices can be redesigned to generate aerosols with desired particle properties; they should also accommodate optimized release position, angle, and inhalation flow rate (i.e., a patient's breathing pattern).

www.ebook3000.com

In this part, novel computational methods in pulmonary drug delivery are discussed, focusing on direct drug–aerosol delivery, enhanced deeper lung delivery of drug aerosols via condensational growth, shape engineering for novel drug carriers, multifunctional NPs for targeted drug delivery, and particle absorption and translocation. Magnetic drug delivery that was initially designed for controlled arterial delivery will be discussed in the next section, as the underlying principles are the same.

10.3.3.1 Smart Inhaler System Methodology

Targeted drug–aerosol delivery is most desirable when expensive and/or aggressive drug aerosols have to reach a specific site in the lung (e.g., to coat a tumor), a specific deep lung region (e.g., to achieve rapid drug absorption of, say, insulin), or the olfactory bulb (e.g., to bring morphine quickly past the blood–brain barrier for pain management). It has been shown that particle deposition location depends on the upstream release position [68–71]. Taking advantage of this effect, Kleinstreuer *et al*. [35, 36, 72] developed a novel, patient-specific targeted drug–aerosol delivery methodology that controls air–particle stream by using a smart inhaler system (SIS) [73]. Specifically, subject-specific CF-PD simulation will be conducted to determine control parameters such as particle properties, particle stream release position, and inhalation waveform, so as to deliver particles from the mouth to the deep lung region, passing the oropharynx, larynx, trachea, and through the major left or right lung bifurcations. Once the delivery route is determined, the SIS will adjust the adaptive nozzle to its optimal radial position and release the particle stream according to a modulated inhalation waveform. The new methodology can improve the aerosol delivery efficiency to specific lung locations up to 85%, according to validated computer experiments [35, 36, 72]. This technique will significantly reduce premature and off-target deposition, thus reducing side effects and delivery dosage, leading to lower cost. This method is demonstrated in Figure 10.5.

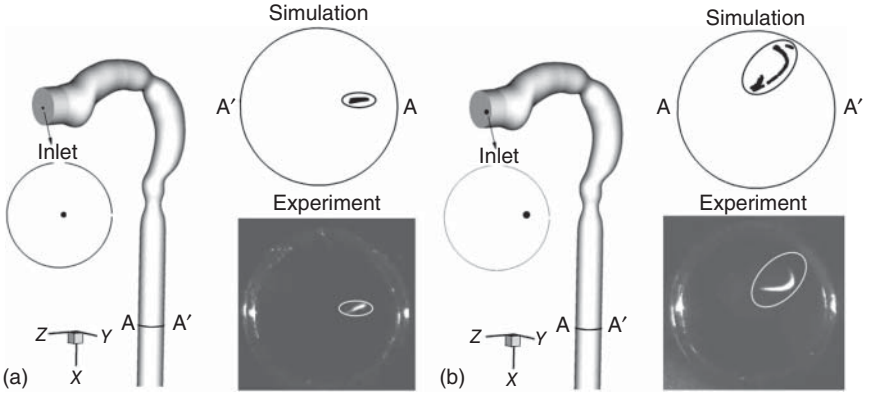


Figure 10.5 Comparisons of simulated and measured particle distributions with different inlet release positions. (Reprinted with permission from Kleinstreuer *et al*. [35, 36].)

10.3.3.2 Enhanced Deeper Lung Delivery of Drug Aerosols via Condensational Growth

Aerosol deposition due to inertia-related particle impaction can cause significant drug loss in the extrathoracic airways, especially for particles with large Stokes numbers [58, 74, 75]. Therefore, reducing particle inertia and turbulence intensity has been proposed to moderate drug–aerosol loss [76–78]. This can be achieved by mixing the particle stream with low density helium–oxygen mixtures. A novel enhanced condensational growth (ECG) aerosol delivery method has also been proposed [79]. This method takes advantage of the fact that droplet aerosols experience size change due to condensation, which influence particle deposition pattern [16, 47, 48, 80, 81]. Specifically, small particles (100–1000 nm) are delivered through nasal or oral airways with highly humidified air and above body temperature. Particles are able to penetrate through the oral or nasal cavity due to small Stokes numbers and low inertia, practically reducing deposition loss before entering the trachea. Further, particles grow in size to 2–4 μm by condensation due to high humidity and deposit in deeper lung regions [82]. A computational study has demonstrated an order-of-magnitude increase in deposition efficiency in the tracheobronchial airway to 32–46% [83]. This concept has also been validated by *in vitro* experiments. Alternatively, this method can be modified by delivering dry particles consisting of hygroscopic excipient, incurring condensational growth in the humid airway [84]. This excipient enhanced growth (EEG) method has been demonstrated to reduce mouth–throat deposition to less than 1% and achieve maximum alveolar delivery of 90% [85]. Improvement of DPIs with EEG formulation has further been numerically demonstrated [86, 87] and experimentally validated [88]. It should be noted that, compared with the direct drug–aerosol delivery method, ECG and EEG are not able to offer localized drug delivery. In addition, Zhang *et al*. [89] demonstrated that evaporating micron particles are also able to penetrate deeper into the lung.

10.3.3.3 Shape Engineering for Novel Drug Carriers

It has been well demonstrated that particle size affects the deposition pattern and subsequent dissolution, absorption, and clearance (DAC). This has been used to develop new pulmonary drug delivery methods. In addition, the shape of particles matters in drug delivery as well [90]. It has been shown that NP shape may greatly influence its bio-circulation, bio-distribution, and cellular uptake and thus affect the overall drug efficacy [90] during arterial drug delivery. For example, particles with an aspect ratio of three were shown to be internalized about four times faster than their spherical counterparts of the same volumes [91]. On the other hand, inhaled nonspherical particles, such as fibers, ellipsoids, and disks, exhibit quite different airway trajectories and hence deposition patterns in terms of local wall concentration and propensity for mass transfer and clearance [21, 92]. Compared with spherical particles, fiber-like carriers are more likely to reach the deeper lung airways by aligning with the airflow field [22, 93, 94]. In addition, thin nano-fibers experience intense Brownian excitation, which disturbs the fiber alignment with the flow and enhances deposition [95].

Because of the many advantages found in nonspherical particles for drug delivery, a lot of studies have been devoted to engineering drug carriers of

www.ebook3000.com

different shapes. This implies new challenges for accurate and realistic computer modeling of drug delivery. For example, elongated fine mannitol particles were shown to offer better aerosolization properties in a DPI [96]. Furthermore, a larger fraction can be delivered to the lower airways compared with spherical particles. It should be noted that rotational motion of fibers significantly affects their transport and deposition in human respiratory airways. Effective drag correlations [65] are not able to model fiber rotation and alignment with the flow, thus failing to provide correct deposition data.

10.3.3.4 Multifunctional Nanoparticles

As mentioned, inhaled nanometer-size particles can avoid extrathoracic deposition and travel into the deep lung regions by virtue of their small inertia, thus enhancing delivery efficiency. Another advantage of NPs is that they can be easily internalized by cells, avoiding clearance due to mucociliary movement and hence achieve rapid onset of action. More exciting possibilities are enabled by multifunctional NPs, which are surface modified to carry cell-specific ligand that readily combines with target cancer cells. For instance, targeted delivery to alveolar macrophages can help to treat diseases such as tuberculosis [97]. Additional functionality such as imaging can be realized by adding contrast agents into these NPs, thereby assisting better drug-targeting control.

NPs exhibit a quite different flow behavior from micron particles due to the strong effect of Brownian motion. Indeed, deposition of NPs takes place primarily by Brownian diffusion [98]. Thus, a thorough understanding of the NP transport and deposition characteristics in the human respiratory systems is necessary for developing novel pulmonary drug delivery methods. Zhang and Kleinstreuer [99] conducted a computational study of NP deposition in a human upper airway and found minor effects of turbulent fluctuations on NP deposition. Shi *et al*. [100] reported that the olfactory region of the nasal cavity receives <1% deposition for NPs less than 5 nm in diameter, which was later confirmed by Garcia *et al*. [101]. Moreover, for NPs >5 nm, very low deposition fraction was found in nasal airways due to low diffusivities [102]. Zhang *et al*. [103] pointed out that in a 16-generation tracheobronchial airway model, uniform NP concentrations can be assumed beyond generation G12. An effective diffusion parameter can be used to correlate deposition efficiencies at each bifurcation, providing a tool for nanodrug deposition evaluation. Zhang and Kleinstreuer [10] modeled NP deposition in a combined nasal–oral–tracheobronchial airway model and found that changing the breathing route (from nasal to oral breathing) significantly influences NP deposition in nasal and oral cavities, nasopharynx, and oropharynx. It also measurably affects depositions from pharynx to the bronchial airways but only for NPs $\leq$5 nm. Xi and Longest [104] suggested that secondary flows may significantly influence NP deposition in a nasal–laryngeal geometry, emphasizing the importance of the physical realism of airway models. However, Xi *et al*. [105] modeled NP deposition in nasal–laryngeal airways of newborn, infant, and young children and reported little effect on morphology and dimension by total deposition fraction and maximum local deposition enhancement. In light of the geometrical impact, it is also important to consider geometry changes of the airway due to diseases [106] or surgery [107] for effective drug delivery using

NPs. Still, the particle release position clearly influences the local deposition patterns of NPs [108, 109], indicating opportunities for applications of the direct drug–aerosol delivery method [35, 36].

10.3.3.5 Particle Absorption and Translocation

Particle deposition in human respiratory airways has been extensively studied to address the challenges in pulmonary drug delivery. This promotes the understanding of the dynamics of pharmaceutical aerosols from their generation in inhaler devices to the deposition point. However, to evaluate the efficacy of the drug delivery, particle fate *after* deposition also needs to be addressed. This includes particle absorption/clearance and translocation via systemic circulation. Effective drug delivery devices will be able to not only deliver pharmaceutical aerosols to the desired region of the lung but also ensure the generated particles be easily absorbed for on-time action.

CF-PD modeling is able to provide regional deposition data in complex respiratory geometries. This data can serve as input for evaluation of subsequent particle absorption and translocation into the systemic regions. For example, Rygg and Longest [110] developed a new CFD model for nasal aerosol delivery from spray formation through absorption at the respiratory ipithelial surface. Kolanjiyil and Kleinstreuer [32, 33] introduced a multi-compartmental model that combines with a CF-PD model to study insoluble NP deposition and barrier mass transfer from deposition locations in lung airways to systemic regions. This model can predict NP kinetics in the human body, that is, temporal NP accumulation in the blood and lymphatic systems and in different organs, providing quantitative information for nanodrug development and targeting. Rygg *et al*. [34] further extended the model of Rygg and Longest [110] to include compartmental pharmacokinetic modeling after drug particle absorption and provided information on pharmacokinetic plasma concentration profiles. It is thus beneficial to have these complete models that incorporate particle transport and deposition from drug delivery devices to geometrically realistic human respiratory systems, particle absorption by local epithelial cells or clearance by mucociliary movements, and translocation into blood and lymphatic system and other organs. They provide tools to evaluate the full cycle of drug delivery from a kinetic point of view.

10.4 Intravascular Drug Delivery

Chemotherapeutic agents have poor specificity and therefore exhibit dose-limiting toxicity when systemically administrated, especially in cancer treatment. So one of the key challenges in arterial drug delivery lies in reducing off-target drug deposition to lower systemic toxicity when using intra-arterial delivery methods. Depending on the disease type and treatment method, drugs are delivered using diverse carriers such as radioactive microspheres, chemo-embolic agents, and multifunctional NPs. In this section, computational microfluidics applications in current intravascular drug delivery methods and promising methods under development will be discussed, specifically

www.ebook3000.com

catheter-based intravascular drug delivery, after a brief outline of currently featured conventional "passive and active targeting" methods. This localized drug delivery method effectively reduces the side effects associated with systemic drug delivery. Finally, a novel direct tumor-targeting methodology is presented, where the injected drug-loaded microspheres and NPs are delivered directly to the target sites.

10.4.1 Nanoparticle-Based Targeted Drug Delivery

To reduce the toxicity of systemically administrated chemotherapeutic agents, recent interest has been focused on developing vehicles that can deliver particles directly to the tumor or inflammatory cells, releasing the drug at a controlled rate and maximizing the therapeutic efficacy. The development of nanotechnologies has enabled a wide spectrum of nanomedicines to be engineered and tailored for this therapeutic purpose. New possibilities in drug delivery were enabled by the small size of NPs and the possibility it offers to encapsulate poorly soluble drugs, facilitate combination regimens, protect therapeutic molecules, and modify their blood circulation and tissue distribution [111]. Generally, passive and active drug targeting has been explored, taking advantage of the unique properties of NPs (see Figure 10.6).

In passive targeting, NPs passively reach the target site following blood flow. By virtue of the enhanced permeability and retention (EPR) effect, NPs may more readily enter the tumor interstitium when passing by and linger for prolonged periods of time. The preferential distribution to the tumor is due to the leaky walls of the tumor blood vessels and the poor lymphatic drainage of tumor tissues. The accumulation of NPs at/in tumor tissues is affected by the extravasation of

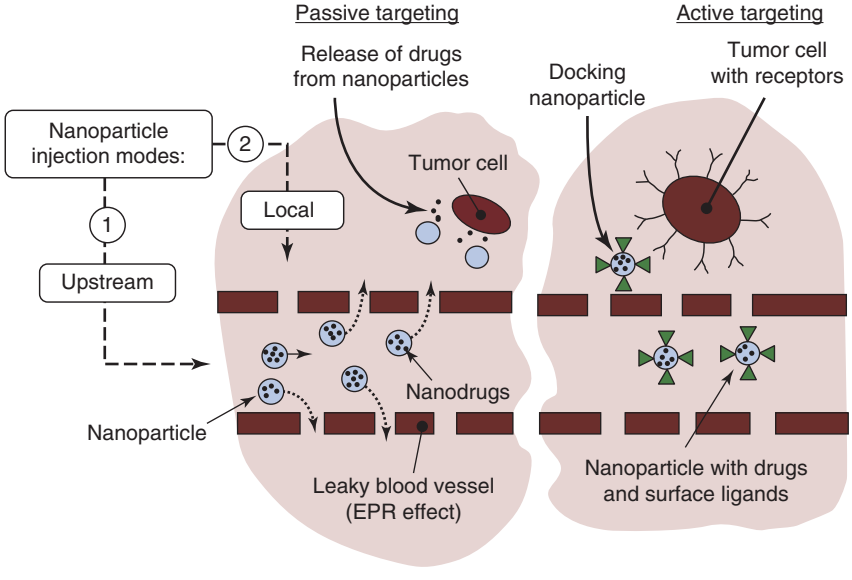


Figure 10.6 Passive targeting versus active targeting. (Reprinted from Kleinstreuer *et al*. [5] with permission from Elsevier.)

particles from the blood vessels, their diffusion through the extravascular tissue, and their interaction with tumor cells [112]. Obviously, hemodynamics and interstitial flow play important roles in the processes [113], because the kinetics of NPs is governed by physical laws [114, 115], in addition to the biological effects. Different methods have been developed to increase NP concentrations in tumor tissue, including modifying tumor biology and changing physicochemical parameters of NPs to extend their circulation time and enhance margination in microvasculature [116]. Consequently, advantageous drug deposition in tumors has been observed in animal models. However, there has been little direct evidence of EPR-induced preferential tumor accumulation of drugs in humans [117]. Since the optimal parameters to maximize drug accumulation and retention in humans can be different to those required in animal models, translating the experience from an animal model to human remains challenging, especially when considering the interpatient variability and tumor heterogeneity in humans. Moreover, even *after* EPR-facilitated NP deposition in the tumor, subsequent drug release from the NPs [118] and cellular uptake will significantly affect the therapeutic efficacy. Therefore, it is necessary to optimize drug release profiles and enhance drug affinity for cancer cells. Active targeting can help to achieve these goals.

In active targeting (or ligand-mediated targeting), the NPs are surface modified with tissue- or cell-specific ligands. Once they have reached the target site, these NPs will recognize and bind to overexpressed antigens or receptors in malignant tissues, cells, or subcellular domains. Active targeting increases the affinity of the NPs for tumor cells and increases the retention and uptake by the targeted disease cells. However, this technique requires that NPs are already in the proximity of the tumor or diseased sites for their therapeutic actions to be effective. Hence, it relies on the EPR effect to increase NP accumulation in the extravascular space of the tumor. As a result, active targeting faces the same challenge that passive targeting has, that is, to deliver NPs to the target site for EPR to take effect and to avoid systemic clearance of the NPs while circulating in the bloodstream. NP carriers designed to achieve active targeting and controlled drug release include inorganic NPs, polymeric NPs, liposomes, dendrimers, micelles, and so on [7, 119].

Computer simulation of NP transport in vasculatures and tissues is crucial for the evaluation of NP delivery efficiency [120–123]. The NP transport is usually modeled using continuum models where the convection–diffusion equations (see Eqs. (10.13) and (10.16)) are used to describe the NP concentrations. In addition, a source term may be added to represent the degradation or reaction due to ligand–receptor binding as well as cell uptake [124]. For example, the dynamic binding process can be described using a reaction equation that depicts the adhesion and detachment rates due to bonding force and drag force [125].

10.4.2 Catheter-Based Intravascular Drug Delivery

Compared with systemic administration of drugs, catheter-based intravascular drug delivery provides localized delivery of drug-carrying particles to the target organ or tissues using a catheter smartly inserted into the blood vessels. This technique can be used for chemo- or radio-embolization using microspheres. For example, in transcatheter arterial embolization or trans-arterial embolization

www.ebook3000.com

(TAE), a thin, flexible catheter can be guided to an infusion location as close to the target site as possible by virtue of real-time imaging techniques (e.g., angiography). Selective embolization of vessels feeding individual tumors is then performed, intended to reduce the blood flow or block the terminal vessels. This method helps to treat cancer by two means: to starve the cancer cells by reducing blood supply and to deliver radioactive or chemotherapeutic doses that directly kill the cancer cells. It has been proved effective for patients with diseases such as unresectable hepatocellular carcinoma (HCC) [126], uterine fibroids [127], and cirrhosis [128]. In this section, the discussion will be focused on embolization using micron particles.

10.4.2.1 Particle Hemodynamics

Catheter-based intravascular drug delivery aims to deliver drug vehicles to a local target site to minimize systemic toxicity. However, aberrant particle deposition in nontarget locations still causes severe side effects, alongside diminished efficacy [129]. This may be due to path deviation, when particles enter off-target artery branches, or reflux, when particles backflow into upstream arteries after downstream embolization. Traditionally, TAE has been performed using end-hole catheters, which are prone to off-target delivery, because they have little control over the antegrade flow and allow reflux once flow stasis is achieved. One promising method to eliminate undesired particle reflux is to use an antireflux structure during microsphere administration [130–132].

Apparently, particle hemodynamics plays a key role in the effective delivery of drug carriers to the target site. CF-PD simulations will help to elucidate the key parameters that affect the drug delivery process and provide suggestions on developing next-generation medical devices and on how to improve the procedure [133, 134]. It also helps to better understand the role of biomechanical parameters in diseases and to better manage patients via patient-specific clinical decision making [135–137].

Xu *et al*. [24] computationally studied the particle hemodynamics in a hepatic artery system following injection using an antireflux catheter. An illustration of the antireflux catheter is shown in Figure 10.7. The surefire expandable catheter tip is a porous membrane made of fibrous material with elastic frames. It will expand to the artery wall under force-free condition and be constricted when the antegrade blood flow exerts large force on it. The study used a modified Darcy's equation to describe blood flow through the porous membrane and Lagrangian method for particle tracking. The study showed that the antireflux catheter caused a significant pressure drop across the deployed tip. The pressure drop is proportional to the level of embolic saturation of the vascular bed. This information can be used to signify a quantitative infusion endpoint. Hence, the antireflux catheter could effectively eliminate particle reflux and related side effects. In addition, the results showed that the pulsatile blood flow and uneven distribution of flow rate over different downstream branches have significant effects on the particle destination. The latter is due to the geometric asymmetry of the hepatic artery system. Thus, particles will migrate preferentially to certain downstream vessels according to the injection location, artery geometry, and blood flow conditions. In order to guarantee that the target vessels feeding

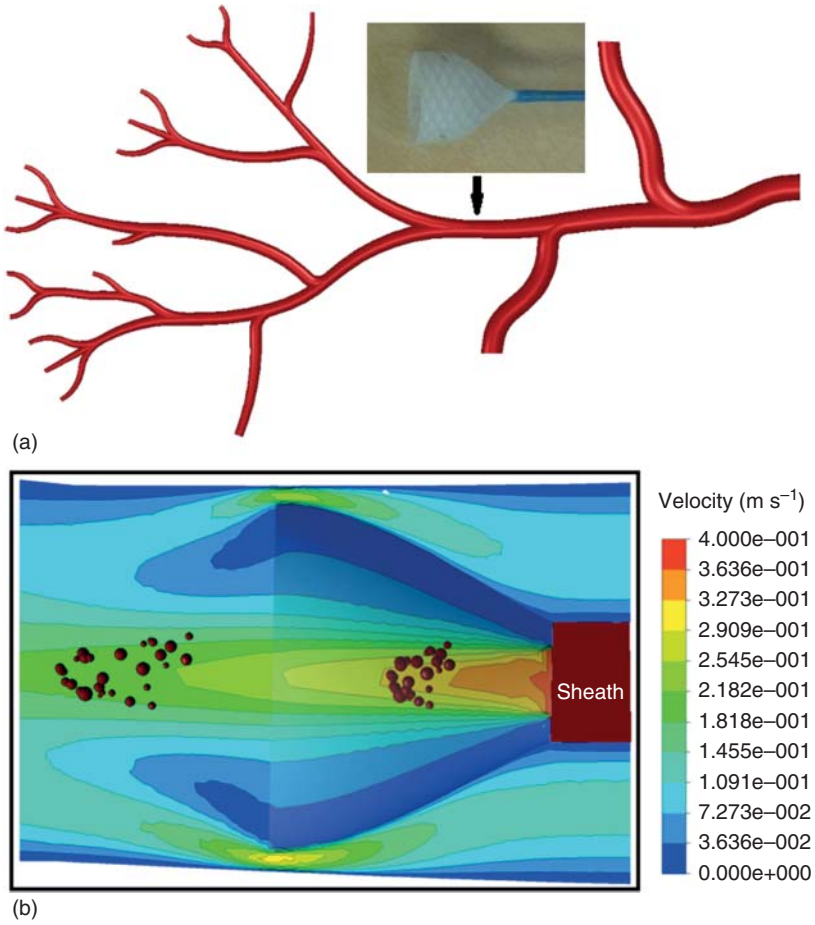


Figure 10.7 CF-PD modeling of embolotherapy using an antireflux catheter. (Xu *et al*. 2016 [24]. Reproduced with permission of Springer.)

tumor tissues are occluded, embolization should occur in all downstream vessel branches. Hence, off-target deposition will still affect healthy tissues fed by arteries downstream the injection point.

Direct tumor-targeting methodology can tackle this issue through the development of patient-specific computational models and catheter positioning technologies that enable image-guided tumor targeting. In addition, magnetic drug delivery can reduce the aberrant deposition and enhance the efficacy of TAE by attracting or steering the drug-bearing magnetic particles to the target site. These two methods are discussed in the following two subsections.

10.4.2.2 Tissue Heat and Mass Transfer

So far we showed that particle hemodynamic simulations may accurately and realistically visualize and optimize a drug delivery process. In addition, computational methods can also be used to study diffusional phenomena where

www.ebook3000.com

drugs penetrate into the cancerous and normal tissues [138, 139] as well as heat transfer processes, especially in cases of hyperthermia. While in Section 10.4.1 NP transport from blood vessels to extravascular tissues was discussed, this section presents aspects related to tissue heat transfer during drug delivery.

Hyperthermia is a thermal therapy method in cancer treatment in which the tumor is heated to elevated temperatures between 40 and 45 °C. This takes advantage of the fact that tumor cells are more sensitive to temperature increase than healthy ones. Hyperthermia is usually applied together with radiation therapy or chemotherapy to enhance their therapeutic effects. Recently, magnetic fluid hyperthermia has shown clinical effectiveness to treat prostate cancer [140] and glioblastoma multiforme [141]. In this method, MNPs are introduced to the tumor via arterial or direct injection, hoping for active targeting. Then the tumor is exposed to an alternating magnetic field, which induces local heat through particle magnetic relaxation. Similar to chemo-/radio-embolization, arterial embolization hyperthermia (AEH) uses magnetic particles to first selectively embolize tumor-feeding arteries and then generate heat to inflict fatal thermal damage to cancerous tissues. The thermal dose is determined by the temperature profile obtained in the tissues as a result of particle deposition pattern and spatial power loss under external AC magnetic field. Computer simulation can help the treatment planning by providing 3D temperature distribution due to magnetic field and particle distribution in the tissue [142–145]. The bioheat transfer in tissues can be described using Pennes' equation ([15], among others):

$$(\rho c_{\mathrm{p}})_{\mathrm{T}} \frac{\partial T}{\partial t} = k\nabla^2 T + (m c_{\mathrm{p}})_{\mathrm{B}}(T_{\mathrm{B}} - T_{\mathrm{T}}) + S_{\mathrm{m}} + S_{\mathrm{T}} \tag{10.28}$$

Here, the subscripts T and B represent tissue and blood, respectively. In addition, m is the blood perfusion, S_{m} is the energy dissipation rate due to magnetic heating, and S_{T} is the heat generation rate due to biological metabolism.

The effectiveness of hyperthermia is affected by the properties of the NPs, excitation source, and targeted tissue [143]. The behavior of different types of NPs under different degrees of excitation and the resulting heating effects on the surrounding media can be modeled using Eq. (10.28). Magnetic heating due to Néel relaxation and Brownian relaxation has been explored by Liangruksa *et al*. [144]. The effects of NP heating on biological tissues can be evaluated via the Arrhenius cell-injury model [142]. Tumor heterogeneity and nonuniform particle distribution greatly affect the outcome of hyperthermia [145]. The combined effects of hyperthermia plus chemotherapy and hyperthermia plus radiation may be even more beneficial [146].

10.4.3 Magnetic Drug Delivery

Magnetic drug targeting uses an external magnetic field to attract or steer drug-carrying MNPs, or MNP-encapsulating magnetic micro-carriers (MMC), to a targeted site after particle injection into bloodstream or inhalation into the respiratory system, thereby increasing site-specific drug accumulation. This method is promising in reducing off-target particle deposition of TAE and additional opportunities in nanodrug delivery. However, many variables can complicate the execution of this technique, including the physicochemical

properties of the drug-loaded MNPs, field strength and geometry [147, 148], depth of the target tissue [149], rate of blood flow [150], and vascular supply [151].

A lot of the research has focused on engineering the MNPs and MMCs as candidate vehicles. In addition, different magnetic drug delivery systems have been developed to target tumors at different locations [152]. For example, in addition to delivery systems based on intra-arterial administration of drug-loaded MNPs, magnetizable aerosols can be used for inhalative magnetic drug targeting within the lung (see Figure 10.8b) using commercially available nebulizers [154] or to enhance olfactory region deposition using magneto-phoretic guidance [155]. Also, MNP targeting to a magnetizable stent embedded in a blood vessel has been proposed [156].

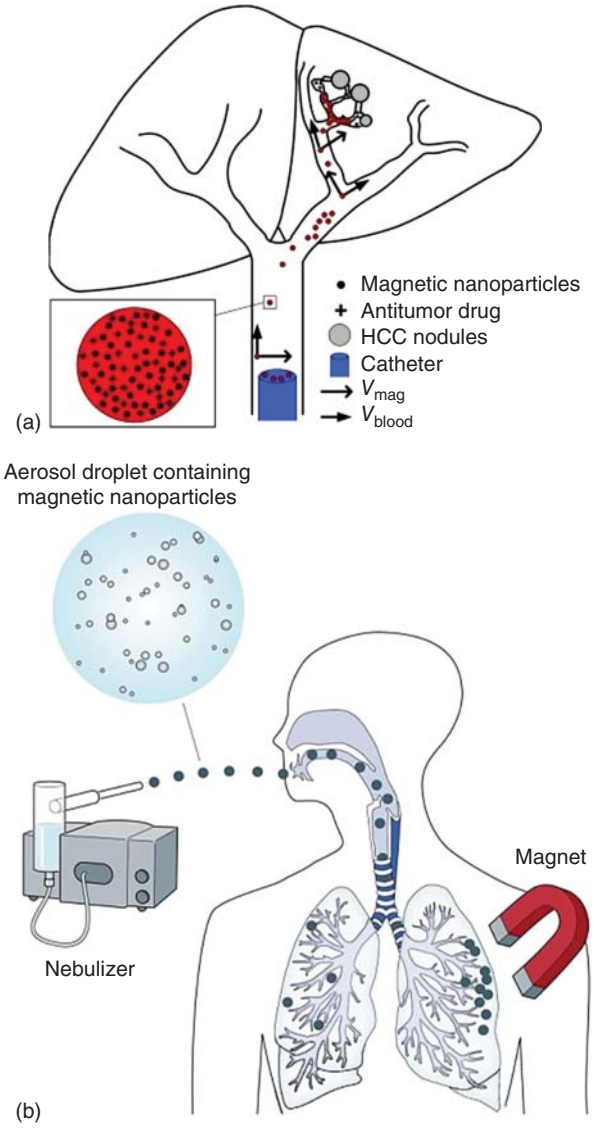


Figure 10.8 Magnetic drug delivery: (a) steering of therapeutic magnetic microparticles for liver chemoembolization. (Pouponneau *et al*. 2009 [153]. Reproduced with permission of Elsevier.) (b) Magnetic delivery of aerosol droplets for lung disease treatment. (Dolovich anf Dhand 2011 [44]. Reproduced with permission of Elsevier.)

www.ebook3000.com

The governing equations for magnetic drug delivery are provided in Section 10.2. When MMC trajectories are of interest, the Lagrangian particle tracking method can be employed [149]. This is especially important when using magnetic navigation to guide particle trajectories in order to achieve tumor targeting [157]. Figure 10.8a shows a schematic of magnetic particle steering for liver chemoembolization.

Two-dimensional modeling showed that if an external magnet is used, the magnetic force is always stronger in the region between the targeted site and the skin surface. Therefore, targeting only a specific interior region of the body is difficult [20]. Under typical human physiological conditions, the MNP delivery can be dominated by diffusion, blood convection, and magnetic force, depending on their relative importance in vessels of different sizes [18]. However, it is unclear which regime is the most relevant one in actual clinical applications. For micrometer-size MMCs, the particle dynamics is unlikely to be dominated by diffusion. Local fluid dynamics due to complex vasculature geometry plays an important role by altering the drag force and thus particle-capturing efficiency [149].

Magnetic drug delivery suffers from restrictions on the particle size and magnetic field strength. It is only applicable when the tumor is located near the body surface and the flow rate is small, because the magnetic strength decays very fast with distance [20]. This is part of the reason that scaling-up the technique from small animal models to human beings is difficult. A magnetic implant near the target site could increase the magnetic field gradient in deep tissue [158]; however, this is undesirable and often not clinically feasible. In addition, magnetic carriers will also tend to accumulate in the intervening tissue between the magnet and the target site where the fields and gradients are higher.

To address these issues, using multiple magnets may be necessary [159]. Modeling efforts have shown that instead of using a single external magnet or implanting magnets in patients, it may be possible to control the MNP trajectories by manipulating multiple external electromagnets dynamically, using feedback control algorithm, thus focusing MMCs to deep-tissue targets [160]. However, scaling up this concept into 3D vasculatures with real-time sensing and control is challenging. Mathematical modeling plays an important role in this approach through quantifying real-time magnetic forces on MNPs or MMCs and predicting particle trajectories in blood and tissue *in vivo*, subject to the interaction of magnetic force and resistance force [161, 162].

10.4.4 Direct Drug Delivery

To deliver drugs to the tumor-feeding vasculature, a novel direct tumor-targeting methodology has been proposed [163]. In this technique, the drug-loaded particles are carried by the blood flow directly to the target site. This is achieved by controlling the catheter position (i.e., radial position in the arterial particle injection plane), infusion speed, and injection timing precisely in a predetermined manner. Patient-specific CF-PD simulations, incorporating catheter geometry, nonlinear vessel compliance, and pulsatile flow characteristics, can establish the optimal release sites for selected branch targeting and provide the control parameters for infusion [8, 30, 135, 136, 164–169].

To successfully implement the direct tumor-targeting methodology, three key steps need to be accomplished: (i) evaluate patient and obtain (hepatic) artery geometry as well as flow conditions, (ii) determine patient-specific microsphere release maps using computer simulations, and (iii) precisely position the catheter remotely to enable image-guided tumor targeting. The three steps can be implemented as follows.

In the first step, patient evaluation includes classifying the tumor and determining the best treatment route. In addition, accurate geometrical models of hepatic arterial anatomy are essential to CF-PD modeling. Therefore, in this stage, MR or CT imaging will be used to obtain the geometry file of the truncated patient hepatic artery system after the tumor-feeding artery branches are identified. Injection of angiographic contrast can aid in vessel isolation from the surrounding tissues. The flow conditions will also be obtained for model input/output conditions including transient blood perfusion rates and physiological pressure waveforms.

The second step focuses on generating a computational particle release map. In this step, the geometric file obtained from the first step will be converted for meshing and subsequent CF-PD simulations on a patient-by-patient basis. Specifically, a vast amount of particles (radioactive spheres or drug-eluting beads) are randomly released over the whole cross-sectional plane of the injection point (say, the proper hepatic artery in the case of liver-tumor targeting). The particle trajectories are modeled through the system as indicated in Figure 10.9 to generate a patient-specific particle release map (PRM) that visually links particle injection regions with associated exit branches. Such PRMs can then be used to determine radial micro-catheter positions to achieve optimal targeting. For example, in the scenario given in Figure 10.9, the catheter should be placed in zone 1 of the PRM while avoiding the remaining zones to target the tumor. This step determines not only the optimal drug release position but also the best drug injection interval and speed during the cardiac cycle as well as the suitable particle properties in terms of size and density.

The final step of the methodology consists of guiding the catheter to the optimal injection point and positioning the catheter tip at the predetermined radial location of the injection plane. A smart micro-catheter (SMC) can be used to provide

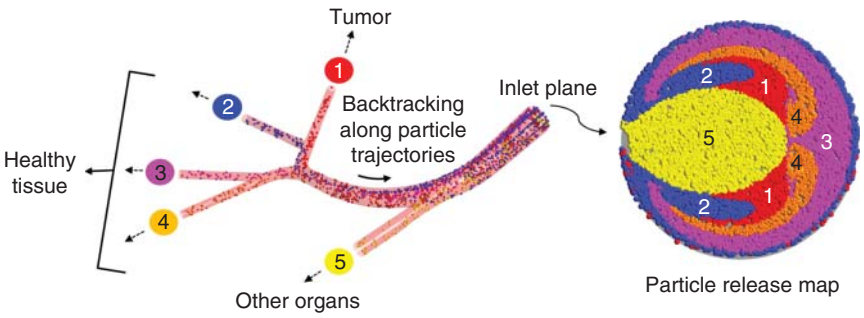


Figure 10.9 Illustration of the particle release map for direct tumor-targeting methodology. (Reprinted from [30, 165], with permission from Springer.)

www.ebook3000.com

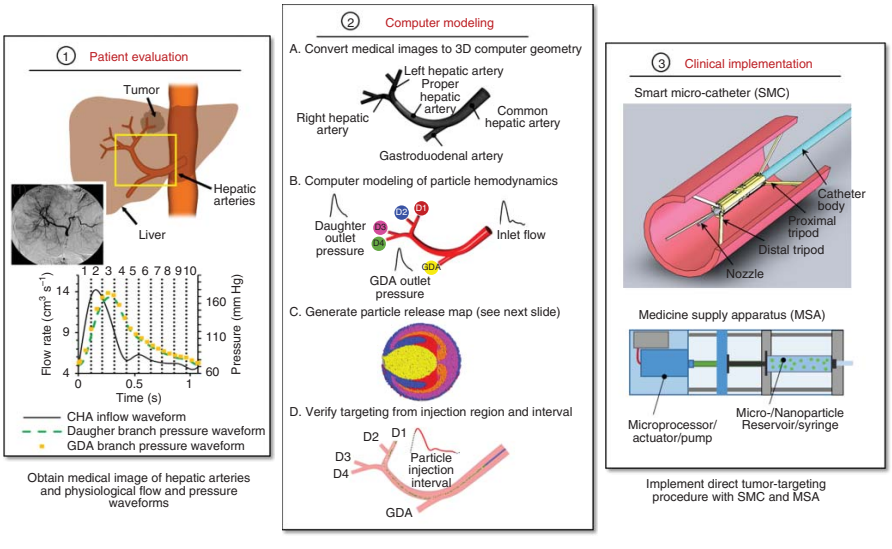


Figure 10.10 Computational medical management program. (Lewandowski *et al*. 2007 [170]. Reproduced with permission of Springer.)

the precise positioning and alignment of the catheter tip [5, 6, 163]. Once the catheter is in position, a medicine supply apparatus (MSA) can be used to control the particle release. The MSA includes a programmable syringe pump and supply lines that are able to provide precise control.

A computational medical management program has been proposed to implement the optimal tumor-targeting methodology, that is, patient-specific direct drug delivery. Figure 10.10 illustrates the three steps discussed. Examples of possible SMC and MSA designs have also been demonstrated.

This direct drug delivery method has been demonstrated in representative [8, 30, 61, 135, 136] and patient-inspired [164] hepatic artery systems and validated by *in vitro* experiments [168]. It was first designed to improve embolotherapy for liver cancers and has since been extended to study the behaviors of emboli in cerebral arteries that cause stroke [171].

10.5 Conclusions and Future Work

In this chapter the fundamentals of computational microfluidics are presented with applications to methods and devices in pulmonary and intravascular drug delivery. Clearly, computational microfluidics plays a vital role in the understanding of drug delivery processes, development of direct drug delivery methods with associated devices, and evaluation of drug delivery efficiency. It can be used to model not only aerosol dynamics in the human respiratory systems and particle hemodynamics in the human vasculatures but also tissue heat and mass transfer as well as aspects of pharmacokinetics. Such capabilities with fairly realistic and accurate results at relatively low costs make computational microfluidics a perfect tool for research and development in drug delivery.

Pulmonary and arterial drug delivery faces many challenges despite the numerous new possibilities enabled by microfluidics and nanotechnology. The prominent one is that most of the current delivery strategies assume that drugs/carriers are already somehow at the diseased site. However, how to accurately deliver drugs to these sites inside the human body while avoiding systemic clearance is still ignored or inadequately addressed. One of the most promising methodologies is the direct drug delivery approach, which targets the drugs to the diseased location via a computationally determined patient-specific drug release map. This methodology is applicable to both pulmonary and arterial drug deliveries and has been numerically simulated and experimentally validated. Nevertheless, some of the challenges that need to be addressed in future studies are discussed next.

In addition, to further optimize drug aerosol formulation, pulmonary drug delivery needs to focus on the entire chain of delivery, that is, from controlled aerosol generation in the devices, to controlled aerosol transport and deposition at desired sites, and finally to controlled aerosol translocation and uptake. Avoiding the clearance of deposited drug aerosols to promote absorption is critical to the delivery efficiency and the action of the active drug ingredients. In light of these, comprehensive computational models are needed to capture the entire life cycle of drugs in the delivery process to provide complete information on delivery efficiency.

www.ebook3000.com

The so-called passive and active drug targeting through the arterial route can benefit from preferential accumulation of drug carriers at vasculatures feeding the diseased tissues/organs. However, to get the medicine to the diseased regions, direct delivery of drugs from the infusion point to predetermined sites is necessary in order to reduce drug circulation time as well as off-target drug deposition and to provide precise dosages. In summary, the new tumor-targeting methodology (see Figure 10.10) has the potential to significantly enhance treatment efficiency, minimize side effects, and reduce cost. To achieve this goal, it is necessary to develop fast, patient-specific computer simulation models that provide optimal direct drug delivery parameters.

References

1 Kleinstreuer, C. (2014) *Microfluidics and Nanofluidics: Theory and selected Applications*, John Wiley & Sons, Inc., Hoboken, NJ.
2 Sackmann, E.K., Fulton, A.L., and Beebe, D.J. (2014) The present and future role of microfluidics in biomedical research. *Nature*, **507** (7491), 181–189.
3 Whitesides, G.M. (2006) The origins and the future of microfluidics. *Nature*, **442** (7101), 368–373.
4 Sanhai, W.R., Sakamoto, J.H., Canady, R., and Ferrari, M. (2008) Seven challenges for nanomedicine. *Nat. Nanotechnol.*, **3** (5), 242–244.
5 Kleinstreuer, C., Childress, E.M., and Kennedy, A.S. (2013) Targeted drug delivery: Multifunctional nanoparticles and direct micro-drug delivery to tumors, in *Transport in Biological Media* (eds S. Becker and A. Kuznetsov), Chapter 10., Academic Press, Amsterdam.
6 Kleinstreuer, C., Feng, Y., and Childress, E.M. (2014) Drug-targeting methodologies with applications: a review. *World J. Clin. Cases*, **2** (12), 742.
7 Kleinstreuer, C. and Childress, E.M. (2014) in *Encyclopedia of Microfluidics and Nanofluidics* (ed. D. Li), Springer Science & Business Media, New York.
8 Basciano, C.A., Kleinstreuer, C., Kennedy, A.S., Dezarn, W.A., and Childress, E.M. (2010) Computer modeling of controlled microsphere release and targeting in a representative hepatic artery system. *Ann. Biomed. Eng.*, **38** (5), 1862–1879.
9 Buchanan, J.R., Kleinstreuer, C., and Comer, J.K. (2000) Rheological effects on pulsatile hemodynamics in a stenosed tube. *Comput. Fluids*, **29** (6), 695–724.
10 Zhang, Z. and Kleinstreuer, C. (2011) Computational analysis of airflow and nanoparticle deposition in a combined nasal–oral–tracheobronchial airway model. *J. Aerosol Sci.*, **42** (3), 174–194.
11 Tan, F.P., Soloperto, G., Bashford, S., Wood, N.B., Thom, S., Hughes, A., and Xu, X.Y. (2008) Analysis of flow disturbance in a stenosed carotid artery bifurcation using two-equation transitional and turbulence models. *J. Biomech. Eng.*, **130** (6), 061008.
12 Menter, F.R., Langtry, R., and Völker, S. (2006) Transition modelling for general purpose CFD codes. *Flow, Turbul. Combust.*, **77** (1–4), 277–303.

13 Menter, F.R., Langtry, R.B., Likki, S.R., Suzen, Y.B., Huang, P.G., and Völker, S. (2006) A correlation-based transition model using local variables – Part I: model formulation. *J. Turbomach.*, **128** (3), 413–422.
14 Kleinstreuer, C. and Xu, Z. (2016) Mathematical modeling and computer simulations of nanofluid flow with applications to cooling and lubrication. *Fluids*, **1** (2), 16.
15 Kleinstreuer, C. (2006) *Biofluid Dynamics: Principles and Selected Applications*, Taylor & Francis, Boca Raton, FL.
16 Feng, Y., Kleinstreuer, C., and Rostami, A. (2015) Evaporation and condensation of multicomponent electronic cigarette droplets and conventional cigarette smoke particles in an idealized G3–G6 triple bifurcating unit. *J. Aerosol Sci.*, **80**, 58–74.
17 Feng, Y. and Kleinstreuer, C. (2014) Micron-particle transport, interactions and deposition in triple lung-airway bifurcations using a novel modeling approach. *J. Aerosol Sci.*, **71**, 1–15.
18 Nacev, A., Beni, C., Bruno, O., and Shapiro, B. (2011) The behaviors of ferromagnetic nano-particles in and around blood vessels under applied magnetic fields. *J. Magn. Magn. Mater.*, **323** (6), 651–668.
19 Cherry, E.M. and Eaton, J.K. (2014) A comprehensive model of magnetic particle motion during magnetic drug targeting. *Int. J. Multiphase Flow*, **59**, 173–185.
20 Grief, A.D. and Richardson, G. (2005) Mathematical modelling of magnetically targeted drug delivery. *J. Magn. Magn. Mater.*, **293** (1), 455–463.
21 Kleinstreuer, C. and Feng, Y. (2013) Computational analysis of non-spherical particle transport and deposition in shear flow with application to lung aerosol dynamics – A review. *J. Biomech. Eng.*, **135** (2), 021008.
22 Feng, Y. and Kleinstreuer, C. (2013) Analysis of non-spherical particle transport in complex internal shear flows. *Phys. Fluids*, **25** (9), 091904.
23 Hassan, T., Ezura, M., Timofeev, E.V., Tominaga, T., Saito, T., Takahashi, A., Takayama, K., and Yoshimoto, T. (2004) Computational simulation of therapeutic parent artery occlusion to treat giant vertebrobasilar aneurysm. *Am. J. Neuroradiol.*, **25** (1), 63–68.
24 Xu, Z., Jernigan, S., Kleinstreuer, C., and Buckner, G.D. (2016) Solid tumor embolotherapy in hepatic arteries with an anti-reflux catheter system. *Ann. Biomed. Eng.*, **44** (4), 1036–1046.
25 Swartz, M.A. and Fleury, M.E. (2007) Interstitial flow and its effects in soft tissues. *Annu. Rev. Biomed. Eng.*, **9**, 229–256.
26 Levick, J.R. (1987) Flow through interstitium and other fibrous matrices. *Q. J. Exp. Physiol.*, **72** (4), 409–437.
27 Ramanujan, S., Pluen, A., McKee, T.D., Brown, E.B., Boucher, Y., and Jain, R.K. (2002) Diffusion and convection in collagen gels: implications for transport in the tumor interstitium. *Biophys. J.*, **83** (3), 1650–1660.
28 Kosto, K.B. and Deen, W.M. (2004) Diffusivities of macromolecules in composite hydrogels. *AlChE J.*, **50** (11), 2648–2658.
29 Li, Z. and Kleinstreuer, C. (2005) Blood flow and structure interactions in a stented abdominal aortic aneurysm model. *Med. Eng. Phys.*, **27** (5), 369–382.

www.ebook3000.com

30 Childress, E.M. and Kleinstreuer, C. (2014b) Impact of fluid–structure interaction on direct tumor-targeting in a representative hepatic artery system. *Ann. Biomed. Eng.*, **42** (3), 461–474.
31 Ruge, C.A., Kirch, J., and Lehr, C.M. (2013) Pulmonary drug delivery: from generating aerosols to overcoming biological barriers—therapeutic possibilities and technological challenges. *Lancet Respir. Med.*, **1** (5), 402–413.
32 Kolanjiyil, A.V. and Kleinstreuer, C. (2013) Nanoparticle mass transfer from lung airways to systemic regions – Part I: whole-lung aerosol dynamics. *J. Biomech. Eng.*, **135** (12), 121003.
33 Kolanjiyil, A.V. and Kleinstreuer, C. (2013b) Nanoparticle mass transfer from lung airways to systemic regions – Part II: Multi-compartmental modeling. *J. Biomech. Eng.*, **135** (12), 121004.
34 Rygg, A., Hindle, M., and Longest, P.W. (2016) Linking suspension nasal spray drug deposition patterns to pharmacokinetic profiles: a proof-of-concept study using computational fluid dynamics. *J. Pharm. Sci.*, **105** (6), 1995–2004.
35 Kleinstreuer, C., Shi, H., and Zhang, Z. (2007a) Computational analyses of a pressurized metered dose inhaler and a new drug-aerosol targeting methodology. *J. Aerosol Med.*, **20** (3), 294–309.
36 Kleinstreuer, C., Zhang, Z., and Kim, C.S. (2007b) Combined inertial and gravitational deposition of micron particles in small model airways of a human respiratory system. *J. Aerosol Sci.*, **38** (10), 1047–1061.
37 Longest, P.W., Son, Y.J., Holbrook, L., and Hindle, M. (2013) Aerodynamic factors responsible for the deaggregation of carrier-free drug powders to form micrometer and submicrometer aerosols. *Pharm. Res.*, **30** (6), 1608–1627.
38 Kleinstreuer, C. and Zhang, Z. (2010) Airflow and particle transport in the human respiratory system. *Annu. Rev. Fluid Mech.*, **42**, 301–334.
39 Kleinstreuer, C., Zhang, Z., and Donohue, J.F. (2008b) Targeted drug-aerosol delivery in the human respiratory system. *Annu. Rev. Biomed. Eng.*, **10**, 195–220.
40 Li, Z., Kleinstreuer, C., and Zhang, Z. (2007) Simulation of airflow fields and micron particle deposition in realistic human lung airway models. Part II: Particle transport and deposition. *Eur. J. Mech. B. Fluids*, **26** (5), 650–668.
41 Newman, S.P. (2005) Principles of metered-dose inhaler design. *Respir. Care*, **50** (9), 1177–1190.
42 Lavorini, F. (2013) The challenge of delivering therapeutic aerosols to asthma patients. *ISRN Allergy*, **2013**, 102418.
43 Newman, S.P., Pavia, D., Morén, F., Sheahan, N.F., and Clarke, S.W. (1981) Deposition of pressurised aerosols in the human respiratory tract. *Thorax*, **36** (1), 52–55.
44 Dolovich, M.B. and Dhand, R. (2011) Aerosol drug delivery: developments in device design and clinical use. *Lancet*, **377** (9770), 1032–1045.
45 Barry, P.W. and O'Callaghan, C. (1996) Inhalational drug delivery from seven different spacer devices. *Thorax*, **51** (8), 835–840.
46 Islam, N. and Gladki, E. (2008) Dry powder inhalers (DPIs) - a review of device reliability and innovation. *Int. J. Pharm.*, **360** (1), 1–11.

47 Zhang, X., Ma, Y., Zhang, L., Zhu, J., and Jin, F. (2012a) The development of a novel dry powder inhaler. *Int. J. Pharm.*, **431** (1), 45–52.

48 Zhang, Z., Kleinstreuer, C., and Hyun, S. (2012b) Size-change and deposition of conventional and composite cigarette smoke particles during inhalation in a subject-specific airway model. *J. Aerosol Sci.*, **46**, 34–52.

49 Muchão, F.P. and da Silva Filho, L.V. (2010) Advances in inhalation therapy in pediatrics. *J. Pediatr. (Rio J)*, **86** (5), 367–376.

50 Rau, J.L. (2005) The inhalation of drugs: advantages and problems. *Respir. Care*, **50** (3), 367–382.

51 Kesser, K.C. and Geller, D.E. (2009) New aerosol delivery devices for cystic fibrosis. *Respir. Care*, **54** (6), 754–768.

52 Longest, P.W., Tian, G., Li, X., Son, Y.J., and Hindle, M. (2012) Performance of combination drug and hygroscopic excipient submicrometer particles from a soft mist inhaler in a characteristic model of the airways. *Ann. Biomed. Eng.*, **40** (12), 2596–2610.

53 Longest, P.W. and Holbrook, L.T. (2012) In silico models of aerosol delivery to the respiratory tract—development and applications. *Adv. Drug Delivery Rev.*, **64** (4), 296–311.

54 Wong, W., Fletcher, D.F., Traini, D., Chan, H.K., and Young, P.M. (2012) The use of computational approaches in inhaler development. *Adv. Drug Delivery Rev.*, **64** (4), 312–322.

55 Feng, Y., Kleinstreuer, C., Castro, N., and Rostami, A. (2016) Computational transport, phase change and deposition analysis of inhaled multicomponent droplet–vapor mixtures in an idealized human upper lung model. *J. Aerosol Sci.*, **96**, 96–123.

56 Zhang, Z. and Kleinstreuer, C. (2003) Species heat and mass transfer in a human upper airway model. *Int. J. Heat Mass Transfer*, **46** (25), 4755–4768.

57 Shi, H., Kleinstreuer, C., and Zhang, Z. (2007) Modeling of inertial particle transport and deposition in human nasal cavities with wall roughness. *J. Aerosol Sci.*, **38** (4), 398–419.

58 Zhang, Z., Kleinstreuer, C., Donohue, J.F., and Kim, C.S. (2005) Comparison of micro-and nano-size particle depositions in a human upper airway model. *J. Aerosol Sci.*, **36** (2), 211–233.

59 Zhang, Z. and Kleinstreuer, C. (2002) Transient airflow structures and particle transport in a sequentially branching lung airway model. *Phys. Fluids*, **14** (2), 862–880.

60 Finlay, W.H. and Martin, A.R. (2008) Recent advances in predictive understanding of respiratory tract deposition. *J. Aerosol Med. Pulm. Drug Deliv.*, **21** (2), 189–206.

61 Coates, M.S., Chan, H.K., Fletcher, D.F., and Chiou, H. (2007) Influence of mouthpiece geometry on the aerosol delivery performance of a dry powder inhaler. *Pharm. Res.*, **24** (8), 1450–1456.

62 Wong, W., Fletcher, D.F., Traini, D., Chan, H.K., Crapper, J., and Young, P.M. (2011) Particle aerosolisation and break-up in dry powder inhalers: Evaluation and modelling of the influence of grid structures for agglomerated systems. *J. Pharm. Sci.*, **100** (11), 4710–4721.

www.ebook3000.com

63 Longest, P.W. and Hindle, M. (2009) Evaluation of the Respimat Soft Mist inhaler using a concurrent CFD and in vitro approach. *J. Aerosol Med. Pulm. Drug Deliv.*, **22** (2), 99–112.

64 Hindle, M. and Longest, P.W. (2013) Quantitative analysis and design of a spray aerosol inhaler. Part 2: improvements in mouthpiece performance. *J. Aerosol Med. Pulm. Drug Deliv.*, **26** (5), 237–247.

65 Inthavong, K., Tian, Z.F., Tu, J.Y., Yang, W., and Xue, C. (2008) Optimizing nasal spray parameters for efficient drug delivery using computational fluid dynamics. *Comput. Biol. Med.*, **38** (6), 713–726.

66 Tong, Z., Zheng, B., Yang, R., Yu, A., and Chan, H. (2013) CFD-DEM investigation of the dispersion mechanisms in commercial dry powder inhalers. *Powder Technol.*, **240**, 19–24.

67 Ruzycki, C.A., Javaheri, E., and Finlay, W.H. (2013) The use of computational fluid dynamics in inhaler design. *Expert Opin. Drug Deliv.*, **10** (3), 307–323.

68 Kimbell, J.S., Segal, R.A., Asgharian, B., Wong, B.A., Schroeter, J.D., Southall, J.P., Dickens, C.J., Brace, G., and Miller, F.J. (2007) Characterization of deposition from nasal spray devices using a computational fluid dynamics model of the human nasal passages. *J. Aerosol Med.*, **20** (1), 59–74.

69 Kleinstreuer, C. and Zhang, Z. (2003) Targeted drug-aerosol deposition analysis for a four-generation lung airway model with hemispherical tumors. *J. Biomech. Eng.*, **125** (2), 197–206.

70 Zhang, Z. and Kleinstreuer, C. (2001) Effect of particle inlet distributions on deposition in a triple bifurcation lung airway model. *J. Aerosol Med.*, **14** (1), 13–29.

71 Zhang, Z., Kleinstreuer, C., and Kim, C.S. (2002) Aerosol deposition efficiencies and upstream release positions for different inhalation modes in an upper bronchial airway model. *Aerosol Sci. Technol.*, **36** (7), 828–844.

72 Kleinstreuer, C., Zhang, Z., Li, Z., Roberts, W.L., and Rojas, C. (2008c) A new methodology for targeting drug-aerosols in the human respiratory system. *Int. J. Heat Mass Transfer*, **51** (23), 5578–5589.

73 Kleinstreuer, C. and Seelecke, S. (2011) Inhaler system for targeted maximum drug-aerosol delivery. US Patent No. 7,900,625.

74 DeHaan, W.H. and Finlay, W.H. (2004) Predicting extrathoracic deposition from dry powder inhalers. *J. Aerosol Sci.*, **35** (3), 309–331.

75 Takano, H., Nishida, N., Itoh, M., Hyo, N., and Majima, Y. (2006) Inhaled particle deposition in unsteady-state respiratory flow at a numerically constructed model of the human larynx. *J. Aerosol Med.*, **19** (3), 314–328.

76 Gemci, T., Shortall, B., Allen, G.M., Corcoran, T.E., and Chigier, N. (2003) A CFD study of the throat during aerosol drug delivery using heliox and air. *J. Aerosol Sci.*, **34** (9), 1175–1192.

77 Longest, P.W., Hindle, M., Choudhuri, S.D., and Xi, J. (2008) Comparison of ambient and spray aerosol deposition in a standard induction port and more realistic mouth–throat geometry. *J. Aerosol Sci.*, **39** (7), 572–591.

78 Sandeau, J., Katz, I., Fodil, R., Louis, B., Apiou-Sbirlea, G., Caillibotte, G., and Isabey, D. (2010) CFD simulation of particle deposition in a reconstructed human oral extrathoracic airway for air and helium–oxygen mixtures. *J. Aerosol Sci.*, **41** (3), 281–294.

79 Longest, P.W. and Hindle, M. (2010) CFD simulations of enhanced condensational growth (ECG) applied to respiratory drug delivery with comparisons to in vitro data. *J. Aerosol Sci.*, **41** (8), 805–820.

80 Zhang, Z., Kim, C.S., and Kleinstreuer, C. (2006a) Water vapor transport and its effects on the deposition of hygroscopic droplets in a human upper airway model. *Aerosol Sci. Technol.*, **40** (1), 1–16.

81 Zhang, Z., Kleinstreuer, C., and Kim, C.S. (2006b) Isotonic and hypertonic saline droplet deposition in a human upper airway model. *J. Aerosol Med.*, **19** (2), 184–198.

82 Hindle, M. and Longest, P.W. (2010) Evaluation of enhanced condensational growth (ECG) for controlled respiratory drug delivery in a mouth-throat and upper tracheobronchial model. *Pharm. Res.*, **27** (9), 1800–1811.

83 Tian, G., Longest, P.W., Su, G., and Hindle, M. (2011) Characterization of respiratory drug delivery with enhanced condensational growth using an individual path model of the entire tracheobronchial airways. *Ann. Biomed. Eng.*, **39** (3), 1136–1153.

84 Hindle, M. and Longest, P.W. (2012) Condensational growth of combination drug-excipient submicrometer particles for targeted high-efficiency pulmonary delivery: evaluation of formulation and delivery device. *J. Pharm. Pharmacol.*, **64** (9), 1254–1263.

85 Tian, G., Longest, P.W., Li, X., and Hindle, M. (2013) Targeting aerosol deposition to and within the lung airways using excipient enhanced growth. *J. Aerosol Med. Pulm. Drug Deliv.*, **26** (5), 248–265.

86 Son, Y.J., Longest, P.W., and Hindle, M. (2013a) Aerosolization characteristics of dry powder inhaler formulations for the excipient enhanced growth (EEG) application: effect of spray drying process conditions on aerosol performance. *Int. J. Pharm.*, **443** (1), 137–145.

87 Son, Y.J., Longest, P.W., Tian, G., and Hindle, M. (2013b) Evaluation and modification of commercial dry powder inhalers for the aerosolization of a submicrometer excipient enhanced growth (EEG) formulation. *Eur. J. Pharm. Sci.*, **49** (3), 390–399.

88 Longest, P.W., Golshahi, L., Behara, S.R., Tian, G., Farkas, D.R., and Hindle, M. (2015) Efficient nose-to-lung (N2L) aerosol delivery with a dry powder inhaler. *J. Aerosol Med. Pulm. Drug Deliv.*, **28** (3), 189–201.

89 Zhang, Z., Kleinstreuer, C., Kim, C.S., and Cheng, Y.S. (2004) Vaporizing microdroplet inhalation, transport, and deposition in a human upper airway model. *Aerosol Sci. Technol.*, **38** (1), 36–49.

90 Truong, N.P., Whittaker, M.R., Mak, C.W., and Davis, T.P. (2015) The importance of nanoparticle shape in cancer drug delivery. *Expert Opin. Drug Deliv.*, **12** (1), 129–142.

91 Gratton, S.E., Ropp, P.A., Pohlhaus, P.D., Luft, J.C., Madden, V.J., Napier, M.E., and DeSimone, J.M. (2008) The effect of particle design on cellular internalization pathways. *Proc. Natl. Acad. Sci. U.S.A.*, **105** (33), 11613–11618.

92 Chen, X., Zhong, W., Tom, J., Kleinstreuer, C., Feng, Y., and He, X. (2016) Experimental-computational study of fibrous particle transport and deposition in a bifurcating lung model. *Particuology*, **28**, 102–113.

www.ebook3000.com

93 Sturm, R. and Hofmann, W. (2009) A theoretical approach to the deposition and clearance of fibers with variable size in the human respiratory tract. *J. Hazard. Mater.*, **170** (1), 210–218.

94 Tian, L. and Ahmadi, G. (2013) Fiber transport and deposition in human upper tracheobronchial airways. *J. Aerosol Sci.*, **60**, 1–20.

95 Tian, L. and Ahmadi, G. (2016) Transport and deposition of nano-fibers in human upper tracheobronchial airways. *J. Aerosol Sci.*, **91**, 22–32.

96 Kaialy, W. and Nokhodchi, A. (2013) Engineered mannitol ternary additives improve dispersion of lactose–salbutamol sulphate dry powder inhalations. *AAPS J.*, **15** (3), 728–743.

97 Sung, J.C., Pulliam, B.L., and Edwards, D.A. (2007) Nanoparticles for drug delivery to the lungs. *Trends Biotechnol.*, **25** (12), 563–570.

98 Shi, H., Kleinstreuer, C., Zhang, Z., and Kim, C.S. (2004) Nanoparticle transport and deposition in bifurcating tubes with different inlet conditions. *Phys. Fluids*, **16** (7), 2199–2213.

99 Zhang, Z. and Kleinstreuer, C. (2004) Airflow structures and nano-particle deposition in a human upper airway model. *J. Comput. Phys.*, **198** (1), 178–210.

100 Shi, H., Kleinstreuer, C., and Zhang, Z. (2006) Laminar airflow and nanoparticle or vapor deposition in a human nasal cavity model. *J. Biomech. Eng.*, **128** (5), 697–706.

101 Garcia, G.J., Schroeter, J.D., and Kimbell, J.S. (2015) Olfactory deposition of inhaled nanoparticles in humans. *Inhalation Toxicol.*, **27** (8), 394–403.

102 Shi, H., Kleinstreuer, C., and Zhang, Z. (2008) Dilute suspension flow with nanoparticle deposition in a representative nasal airway model. *Phys. Fluids*, **20** (1), 013301.

103 Zhang, Z., Kleinstreuer, C., and Kim, C.S. (2008) Airflow and nanoparticle deposition in a 16-generation tracheobronchial airway model. *Ann. Biomed. Eng.*, **36** (12), 2095–2110.

104 Xi, J. and Longest, P.W. (2009) Characterization of submicrometer aerosol deposition in extrathoracic airways during nasal exhalation. *Aerosol Sci. Technol.*, **43** (8), 808–827.

105 Xi, J., Berlinski, A., Zhou, Y., Greenberg, B., and Ou, X. (2012) Breathing resistance and ultrafine particle deposition in nasal–laryngeal airways of a newborn, an infant, a child, and an adult. *Ann. Biomed. Eng.*, **40** (12), 2579–2595.

106 Chen, X.B., Lee, H.P., Chong, V.F.H., and Wang, D.Y. (2010) A computational fluid dynamics model for drug delivery in a nasal cavity with inferior turbinate hypertrophy. *J. Aerosol Med. Pulm. Drug Deliv.*, **23** (5), 329–338.

107 Abouali, O., Keshavarzian, E., Ghalati, P.F., Faramarzi, A., Ahmadi, G., and Bagheri, M.H. (2012) Micro and nanoparticle deposition in human nasal passage pre and post virtual maxillary sinus endoscopic surgery. *Respir. Physiol. Neurobiol.*, **181** (3), 335–345.

108 Si, X.A., Xi, J., Kim, J., Zhou, Y., and Zhong, H. (2013) Modeling of release position and ventilation effects on olfactory aerosol drug delivery. *Respir. Physiol. Neurobiol.*, **186** (1), 22–32.

109 Wang, S.M., Inthavong, K., Wen, J., Tu, J.Y., and Xue, C.L. (2009) Comparison of micron-and nanoparticle deposition patterns in a realistic human nasal cavity. *Respir. Physiol. Neurobiol.*, **166** (3), 142–151.

110 Rygg, A. and Longest, P.W. (2016) Absorption and clearance of pharmaceutical aerosols in the human nose: development of a CFD model. *J. Aerosol Med. Pulm. Drug Deliv.*, **29**, 416–431.

111 Bertrand, N., Wu, J., Xu, X., Kamaly, N., and Farokhzad, O.C. (2014) Cancer nanotechnology: the impact of passive and active targeting in the era of modern cancer biology. *Adv. Drug Delivery Rev.*, **66**, 2–25.

112 Hara, T., Iriyama, S., Makino, K., Terada, H., and Ohya, M. (2010) Mathematical description of drug movement into tumor with EPR effect and estimation of its configuration for DDS. *Colloids Surf., B*, **75** (1), 42–46.

113 Florence, A.T. (2006) *Nanoparticles as Drug Carriers*, Imperial College Press, London, pp. 9–27.

114 Bao, G., Bazilevs, Y., Chung, J.H., Decuzzi, P., Espinosa, H.D., Ferrari, M., Gao, H., Hossain, S.S., Hughes, T.J., Kamm, R.D., Liu, W.K., Marsden, A., and Schrefler, B. (2014) USNCTAM perspectives on mechanics in medicine. *J. R. Soc. Interface*, **11** (97), 20140301.

115 Florence, A.T. (2012) Targeting nanoparticles: the constraints of physical laws and physical barriers. *J. Controlled Release*, **164** (2), 115–124.

116 Li, Y., Stroberg, W., Lee, T.R., Kim, H.S., Man, H., Ho, D., Decuzzi, P., and Liu, W.K. (2014) Multiscale modeling and uncertainty quantification in nanoparticle-mediated drug/gene delivery. *Comput. Mech.*, **53** (3), 511–537.

117 Nichols, J.W. and Bae, Y.H. (2014) EPR: evidence and fallacy. *J. Controlled Release*, **190**, 451–464.

118 Hossain, S.S., Hossainy, S.F., Bazilevs, Y., Calo, V.M., and Hughes, T.J. (2012) Mathematical modeling of coupled drug and drug-encapsulated nanoparticle transport in patient-specific coronary artery walls. *Comput. Mech.*, **49** (2), 213–242.

119 Faraji, A.H. and Wipf, P. (2009) Nanoparticles in cellular drug delivery. *Bioorg. Med. Chem.*, **17** (8), 2950–2962.

120 Hossain, S.S., Zhang, Y., Liang, X., Hussain, F., Ferrari, M., Hughes, T.J., and Decuzzi, P. (2013) In silico vascular modeling for personalized nanoparticle delivery. *Nanomedicine*, **8** (3), 343–357.

121 Hossain, S.S., Hughes, T.J., and Decuzzi, P. (2014) Vascular deposition patterns for nanoparticles in an inflamed patient-specific arterial tree. *Biomech. Model. Mechanobiol.*, **13** (3), 585–597.

122 Kleinstreuer, C., Li, J., and Koo, J. (2008a) Microfluidics of nano-drug delivery. *Int. J. Heat Mass Transfer*, **51** (23), 5590–5597.

123 Liu, Y., Shah, S., and Tan, J. (2012) Computational modeling of nanoparticle targeted drug delivery. *Rev. Nanosci. Nanotechnol.*, **1** (1), 66–83.

124 Welter, M. and Rieger, H. (2013) Interstitial fluid flow and drug delivery in vascularized tumors: a computational model. *PLoS One*, **8** (8), e70395.

125 Tan, J., Wang, S., Yang, J., and Liu, Y. (2013) Coupled particulate and continuum model for nanoparticle targeted delivery. *Comput. Struct.*, **122**, 128–134.

www.ebook3000.com

126 Maluccio, M.A., Covey, A.M., Porat, L.B., Schubert, J., Brody, L.A., Sofocleous, C.T., Getrajdman, G.I., Jarnagin, W., DeMatteo, R., Blumgart, L.H., and Fong, Y. (2008) Transcatheter arterial embolization with only particles for the treatment of unresectable hepatocellular carcinoma. *J. Vasc. Interv. Radiol.*, **19** (6), 862–869.

127 Goodwin, S.C., Vedantham, S., McLucas, B., Forno, A.E., and Perrella, R. (1997) Preliminary experience with uterine artery embolization for uterine fibroids. *J. Vasc. Interv. Radiol.*, **8** (4), 517–526.

128 Haan, J.M., Biffl, W., Knudson, M.M., Davis, K.A., Oka, T., Majercik, S., Dicker, R., Marder, S., Scalea, T.M., and Western Trauma Association Multi-Institutional Trials Committee (2004) Splenic embolization revisited: a multicenter review. *J. Trauma Acute Care Surg.*, **56** (3), 542–547.

129 van den Hoven, A.F., Smits, M.L., Rosenbaum, C.E., Verkooijen, H.M., van den Bosch, M.A., and Lam, M.G. (2014) The effect of intra-arterial angiotensin II on the hepatic tumor to non-tumor blood flow ratio for radioembolization: a systematic review. *PLoS One*, **9** (1), e86394.

130 Arepally, A., Chomas, J., Kraitchman, D., and Hong, K. (2013) Quantification and reduction of reflux during embolotherapy using an antireflux catheter and tantalum microspheres: ex vivo analysis. *J. Vasc. Interv. Radiol.*, **24** (4), 575–580.

131 Bannerman, D. and Wan, W. (2016) Multifunctional microbeads for drug delivery in TACE. *Expert Opin. Drug Deliv.*, **13**, 1289–1300.

132 van den Hoven, A.F., Lam, M.G., Jernigan, S., van den Bosch, M.A., and Buckner, G.D. (2015) Innovation in catheter design for intra-arterial liver cancer treatments results in favorable particle-fluid dynamics. *J. Exp. Clin. Cancer Res.*, **34** (1), 1.

133 Aramburu, J., Antón, R., Rivas, A., Ramos, J.C., Sangro, B., and Bilbao, J.I. (2017) Computational particle–haemodynamics analysis of liver radioembolization pretreatment as an actual treatment surrogate. *Int. J. Numer. Methods Biomed. Eng.*, **33**, e02791.

134 Johnson, N., Abraham, J., Helgeson, Z., and Hennessey, M. (2010) Numerical simulation of blood flow in the presence of embolizing agents. In ASME 2010 International Mechanical Engineering Congress and Exposition Vancouver, British Columbia, Canada, pp. 191–198.

135 Basciano, C.A., Kleinstreuer, C., Hyun, S., and Finol, E.A. (2011a) A relation between near-wall particle-hemodynamics and onset of thrombus formation in abdominal aortic aneurysms. *Ann. Biomed. Eng.*, **39** (7), 2010–2026.

136 Basciano, C.A., Kleinstreuer, C., and Kennedy, A.S. (2011b) Computational fluid dynamics modeling of 90Y microspheres in human hepatic tumors. *J. Nucl. Med. Radiat. Ther.*, **2** (112), 2.

137 Khodaee, F., Vahidi, B., and Fatouraee, N. (2016) Analysis of mechanical parameters on the thromboembolism using a patient-specific computational model. *Biomech. Model. Mechanobiol.*, 1–11.

138 Goh, Y.M.F., Kong, H.L., and Wang, C.H. (2001) Simulation of the delivery of doxorubicin to hepatoma. *Pharm. Res.*, **18** (6), 761–770.

139 Morrison, P.F., Chen, M.Y., Chadwick, R.S., Lonser, R.R., and Oldfield, E.H. (1999) Focal delivery during direct infusion to brain: role of flow

rate, catheter diameter, and tissue mechanics. *Am. J. Physiol.*, **277** (4), R1218–R122.

140 Johannsen, M., Gneveckow, U., Eckelt, L., Feussner, A., Waldöfner, N., Scholz, R., Deger, S., Wust, P., Loening, S.A., and Jordan, A. (2005) Clinical hyperthermia of prostate cancer using magnetic nanoparticles: presentation of a new interstitial technique. *Int. J. Hyperthermia*, **21** (7), 637–647.

141 Maier-Hauff, K., Rothe, R., Scholz, R., Gneveckow, U., Wust, P., Thiesen, B., Feussner, A., von Deimling, A., Waldoefner, N., Felix, R., and Jordan, A. (2007) Intracranial thermotherapy using magnetic nanoparticles combined with external beam radiotherapy: results of a feasibility study on patients with glioblastoma multiforme. *J. Neurooncol.*, **81** (1), 53–60.

142 Huang, H.C., Rege, K., and Heys, J.J. (2010) Spatiotemporal temperature distribution and cancer cell death in response to extracellular hyperthermia induced by gold nanorods. *ACS Nano*, **4** (5), 2892–2900.

143 Kaddi, C.D., Phan, J.H., and Wang, M.D. (2013) Computational nanomedicine: modeling of nanoparticle-mediated hyperthermal cancer therapy. *Nanomedicine*, **8** (8), 1323–1333.

144 Liangruksa, M., Ganguly, R., and Puri, I.K. (2011) Parametric investigation of heating due to magnetic fluid hyperthermia in a tumor with blood perfusion. *J. Magn. Magn. Mater.*, **323** (6), 708–716.

145 Xu, R., Yu, H., Zhang, Y., Ma, M., Chen, Z., Wang, C., Teng, G., Ma, J., Sun, X., and Gu, N. (2009) Three-dimensional model for determining inhomogeneous thermal dosage in a liver tumor during arterial embolization hyperthermia incorporating magnetic nanoparticles. *IEEE Trans. Magn.*, **45** (8), 3085–3091.

146 Purushotham, S. and Ramanujan, R.V. (2010) Modeling the performance of magnetic nanoparticles in multimodal cancer therapy. *J. Appl. Phys.*, **107** (11), 114701.

147 Cao, Q., Han, X., and Li, L. (2012) Numerical analysis of magnetic nanoparticle transport in microfluidic systems under the influence of permanent magnets. *J. Phys. D: Appl. Phys.*, **45** (46), 465001.

148 Yue, P., Lee, S., Afkhami, S., and Renardy, Y. (2012) On the motion of superparamagnetic particles in magnetic drug targeting. *Acta Mech.*, **223** (3), 505–527.

149 Haverkort, J.W., Kenjereš, S., and Kleijn, C.R. (2009) Computational simulations of magnetic particle capture in arterial flows. *Ann. Biomed. Eng.*, **37** (12), 2436–2448.

150 Kayal, S., Bandyopadhyay, D., Mandal, T.K., and Ramanujan, R.V. (2011) The flow of magnetic nanoparticles in magnetic drug targeting. *RSC Adv.*, **1** (2), 238–246.

151 Sun, C., Lee, J.S., and Zhang, M. (2008) Magnetic nanoparticles in MR imaging and drug delivery. *Adv. Drug Delivery Rev.*, **60** (11), 1252–1265.

152 Tietze, R., Zaloga, J., Unterweger, H., Lyer, S., Friedrich, R.P., Janko, C., Pöttler, M., Dürr, S., and Alexiou, C. (2015) Magnetic nanoparticle-based drug delivery for cancer therapy. *Biochem. Biophys. Res. Commun.*, **468** (3), 463–470.

www.ebook3000.com

153 Pouponneau, P., Leroux, J.C., and Martel, S. (2009) Magnetic nanoparticles encapsulated into biodegradable micron particles steered with an upgraded magnetic resonance imaging system for tumor chemoembolization. *Biomaterials*, **30** (31), 6327–6332.
154 Baumann, R., Glöckl, G., Nagel, S., and Weitschies, W. (2012) Preparation and characterization of magnetizable aerosols. *Eur. J. Pharm. Sci.*, **45** (5), 693–697.
155 Xi, J., Zhang, Z., and Si, X.A. (2015) Improving intranasal delivery of neurological nanomedicine to the olfactory region using magnetophoretic guidance of microsphere carriers. *Int. J. Nanomed.*, **10**, 1211.
156 Wang, S., Zhou, Y., Tan, J., Xu, J., Yang, J., and Liu, Y. (2014) Computational modeling of magnetic nanoparticle targeting to stent surface under high gradient field. *Comput. Mech.*, **53** (3), 403–412.
157 Pouponneau, P., Bringout, G., and Martel, S. (2014) Therapeutic magnetic microcarriers guided by magnetic resonance navigation for enhanced liver chemoembilization: a design review. *Ann. Biomed. Eng.*, **42** (5), 929–939.
158 Cregg, P.J., Murphy, K., and Mardinoglu, A. (2012) Inclusion of interactions in mathematical modelling of implant assisted magnetic drug targeting. *Appl. Math. Modell.*, **36** (1), 1–34.
159 Han, X., Cao, Q., and Li, L. (2012) Design and evaluation of three-dimensional electromagnetic guide system for magnetic drug delivery. *IEEE Trans. Appl. Supercond.*, **22** (3), 4401404.
160 Shapiro, B. (2009) Towards dynamic control of magnetic fields to focus magnetic carriers to targets deep inside the body. *J. Magn. Magn. Mater.*, **321** (10), 1594–1599.
161 Nacev, A., Komaee, A., Sarwar, A., Probst, R., Kim, S.H., Emmert-Buck, M., and Shapiro, B. (2012) Towards control of magnetic fluids in patients: directing therapeutic nanoparticles to disease locations. *IEEE Control Syst.*, **32** (3), 32–74.
162 Shapiro, B., Kulkarni, S., Nacev, A., Sarwar, A., Preciado, D., and Depireux, D.A. (2014) Shaping magnetic fields to direct therapy to ears and eyes. *Annu. Rev. Biomed. Eng.*, **16**, 455–481.
163 Kleinstreuer, C. (2015) Methods and devices for targeted injection of microspheres. US Patent 9,149,605 B2.
164 Childress, E.M., Kleinstreuer, C., and Kennedy, A.S. (2012) A new catheter for tumor-targeting with radioactive microspheres in representative hepatic artery systems—part II: solid tumor-targeting in a patient-inspired hepatic artery system. *J. Biomech. Eng.*, **134** (5), 051005.
165 Childress, E.M. and Kleinstreuer, C. (2014a) Computationally efficient particle release map determination for direct tumor-targeting in a representative hepatic artery system. *J. Biomech. Eng.*, **136** (1), 011012.
166 Kennedy, A.S., Kleinstreuer, C., Basciano, C.A., and Dezarn, W.A. (2010) Computer modeling of Yttrium-90–microsphere transport in the hepatic arterial tree to improve clinical outcomes. *Int. J. Radiat. Oncol. Biol. Phys.*, **76** (2), 631–637.
167 Kleinstreuer, C., Basciano, C.A., Childress, E.M., and Kennedy, A.S. (2012) A new catheter for tumor targeting with radioactive microspheres in

representative hepatic artery systems. Part I: impact of catheter presence on local blood flow and microsphere delivery. *J. Biomech. Eng.*, **134** (5), 051004.

168 Richards, A.L., Kleinstreuer, C., Kennedy, A.S., Childress, E.M., and Buckner, G.D. (2012) Experimental microsphere targeting in a representative hepatic artery system. *IEEE Trans. Biomed. Eng.*, **59** (1), 198–204.

169 Zhu, S.J., Poon, E.K., Ooi, A.S., and Moore, S. (2015) Enhanced targeted drug delivery through controlled release in a three-dimensional vascular tree. *J. Biomech. Eng.*, **137** (3), 031002.

170 Lewandowski, R.J., Sato, K.T., Atassi, B., Ryu, R.K., Nemcek, A.A. Jr.,, Kulik, L., Geschwind, J.F., Murthy, R., Rilling, W., Liu, D., and Bester, L. (2007) Radioembolization with ^{90}Y microspheres: angiographic and technical considerations. *Cardiovasc. Interv. Radiol.*, **30** (4), 571–592.

171 Fabbri, D., Long, Q., Das, S., and Pinelli, M. (2014) Computational modelling of emboli travel trajectories in cerebral arteries: influence of microembolic particle size and density. *Biomech. Model. Mechanobiol.*, **13** (2), 289–302.

www.ebook3000.com

11

Microfluidic Synthesis of Organics

Hongxia Liang and Yujun Song

University of Science and Technology Beijing, Centre for Modern Physics Technology, Applied Physics Department, Beijing Key Laboratory for Magneto-Photoelectric Composite and Interface Science, 30 Xueyuan Road, Beijing 100083, PR China

11.1 Introduction

Multipurpose batch or semi-batch reactors have an irreplaceable role in the fine chemical industry. Billions of bottle-batched bulk reactors in industries or glasswares in laboratories are currently used, such as autoclave reactors, jacketed vessels, reaction towers, round-bottomed flasks, distillation columns, separating funnels, and test tubes [1]. This batch technology has been little changed over the past centuries [2]. In conventional vessels, mixing of components is usually through intensive stirring, and heat transfer has to overcome the interface and wall thermal resistance, which has notorious issues in the redesign of reactor structures and the re-optimization of reaction parameters during scaling-up.

Microfluidic reactors are devices with the inner dimensions under a millimeter in scale and more specifically between several micrometers and hundreds of micrometers [3]. Due to their unique features as compared with the traditional bulk reactors (e.g., fast mass and heat transfer, scale-out feature, and stable laminar flow diffusion), microfluidic reactors have been widely used in pharmaceutical, biotechnology, and chemical industry for application such as fine chemical, diagnosis, crystallization, and high-throughput screening [4–9] since they were first developed in the early 1990s [4, 6–8, 10].

In microfluidic reactors, mass transfer is mainly performed at microscale, and flow type is usually laminar flow; mixing procedures are thus limited to diffusion and/or secondary flows. Increasing the interfacial contact between phases directly influences the overall mass transport coefficient; the interfacial mass transport coefficient observed in a microreactor can range from 0.05 to 15 s^{-1} as compared with 0.001–0.02 s^{-1} in standard laboratory-scale bottle-batched reactors [11, 12]. Mixing times in microfluidic reactors can be down to several milliseconds that are generally smaller than those in bulk reactors due to the small dimensions for the mass diffusion. A nearly complete mixture can be achieved within a few seconds and often as little as a few milliseconds because chemical molecules have short paths to move.

Microfluidics: Fundamentals, Devices and Applications, First Edition.
Edited by Yujun Song, Daojian Cheng, and Liang Zhao.
© 2018 Wiley-VCH Verlag GmbH & Co. KGaA. Published 2018 by Wiley-VCH Verlag GmbH & Co. KGaA.

Similarly, high heat-exchanging efficiency can be created in microfluidic reactors [13] due to their higher surface-to-volume ratio (specific surface areas) than in the bulk reactor [4, 6, 14–16]. Specific surface areas of microstructures lie between 10 000 and 50 000 $m^2\,m^{-3}$, while those of traditional reactors are 100 $m^2\,m^{-3}$ and in rare cases reach 1000 $m^2\,m^{-3}$. Since the heat transfer coefficient is inversely proportional to the channel diameter, the heat transfer coefficient in microdevices is significantly higher than that for traditional heat exchangers [13, 17, 18]. This high heat-exchanging efficiency allows for fast heating and cooling of reaction mixtures within the microstructures. Thus, heat can be applied and removed, creating a safe experiment environment at high temperature, improving the reactor efficiency at high temperature, which is not realized easily in bulk batch reactors.

It is also advantageous to precisely control reaction variables such as pressure, residence time, and concentrations; these factors can affect significantly the yield and quality of products [19–21]. Importantly, when the actual reaction volume is very small, the hazard potential of strongly exothermic or explosive reactions can be drastically reduced, or more technical safety can be obtained as compared to conventional reactor even at high operating pressure [4, 22]. Moreover, the fraction of gas volume in a pressurized liquid-filled system is significantly reduced, which is crucial to avoid evaporation of low-boiling reagents or formation of explosive gas mixtures [3, 23]. The principle of preserving or maximizing the efficiency and eliminating safety concerns by avoiding hazardous reaction conditions in chemistry synthesis is shown in Figure 11.1. There are four types of reactors that have been invented and made improvements, including coiled tubing reactors, chip-based reactors, packed-bed reactors, and tube-in-tube reactors, as well as a new system – microfluidic nebulator.

In addition, surface tension becomes a significant and useful force in microfluidic devices, which depends on the surface roughness geometry and gaps among roughness elements [24]. A molecule at the surface is attracted by a reduced number of neighbors and so is in an energetically unfavorable state, which is very

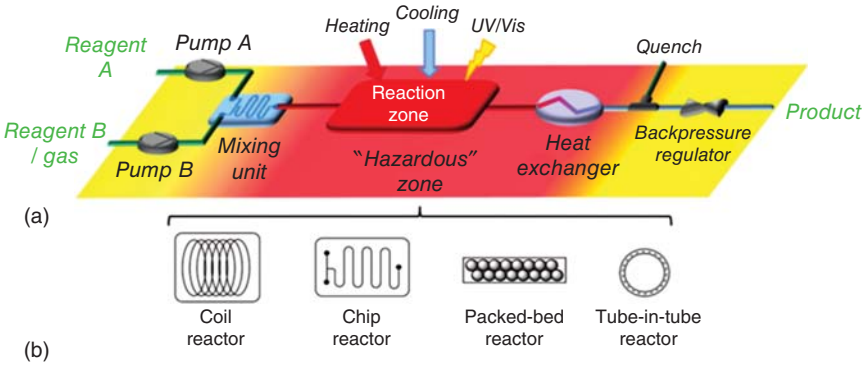


Figure 11.1 (a) General concept of flow chemistry using microfluidic reactors. Reagents can be combined at precisely specified points along the reactor (residence time), heated, cooled, and quenched. The pressure resistance and high heat exchange efficiency allows high-temperature operation in superheated solvents. (b) Graphical presentation of continuous-flow reactors used in this chapter. (Gutmann *et al*. 2015 [4]. Reproduced with permission of John Wiley & Sons.)

www.ebook3000.com

important for some catalytic reaction or oriented synthesis [25]. Therefore, the development of microfluidic reactors has paved the way for replacing the conventional organic synthesis processes and some unique chemical synthesis that is difficult in the bulk process.

The most important aspect of microfluidic reactors is the hydrodynamic flow in the microchannels. The flow types are mostly laminar, oriented, and highly symmetric. Therefore, the multiphase flows often exhibit high order among phases. These features favor to perform rational design since basic physical mechanisms or intrinsic kinetics can be directly applied in microfluidic reactors. For example, the prediction and confirmation of residence time distributions can be obtained precisely, which is crucial for the flow type and reaction control.

Due to the features mentioned previously, researchers further enable the control of reactive intermediates and facilitate highly selective reactions via microfluidic processes, which are usually difficult in conventional bulk reactors [26]. Microfluidic reactors can be used as convenient process engineering tools, particularly in the synthesis of fine chemicals and pharmaceuticals. In fine chemical and medicine synthesis, it is complex since multiple reaction and separation steps are often involved, and each step has alternate pathways and technical approaches [6, 27]. Another benefit of microfluidic technology is that the linking of individual reactions into multistep sequences is possible. One reaction to flow seamlessly into another can be realized along the microchannel, creating a rapid route to the desired complex product by combining multiple synthetic steps into one continuous operation [1, 27]. Up to now, the innovative strategies to multistep syntheses can combine multiple synthetic steps into single microfluidic reactor networks [28–30] that can include mixing, reaction, extraction, separation, and analysis processes, whose kinetic parameters (e.g., residence time, temperature, stoichiometry, reactant flow rates, etc.) can be conveniently controlled by an automatic control system, as exampled in Figure 11.2 for the synthesis of an inhibitor for casein kinase I. The kinase is considered to be important in molecular pathways that regulate the circadian rhythm in mammalian systems. A particular class of substituted imidazo[1,2-*b*]pyridazine structures has recently been reported by Sanofi-Aventis as an inhibitor of casein kinase I. The control software can also be used to predict the minimum amount of each reagent needed for the entire run based upon the reactor

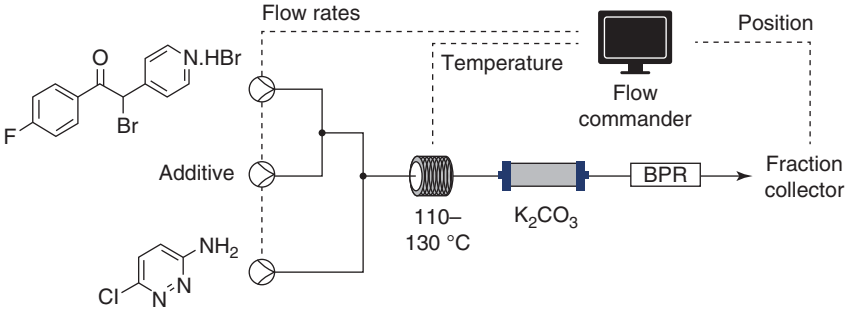


Figure 11.2 Automated system was used to trial 17 different reaction conditions during an optimization screening process. (Ley *et al*. 2015 [1]. Reproduced with permission of John Wiley & Sons.)

volume, column units, and tubing dimensions. Thus, a series of experiments (e.g., here 17 reactions) can be carried out automatically and simultaneously by varying reaction times, temperatures, and reagent concentrations to find optimal conditions for the optimal yields and high throughput, which can greatly improve isolated yields and the product purity in a short run time [31].

Generally, the applicability of microfluidic reactors depends on their structure size and the chemical and physical properties of the constructed materials. Different types of microfluidic reactors have been fabricated from a wide range of materials, including polymers [32, 33], ceramics [34], glass, metals, stainless steel, and silicon [35] as shown in Figure 11.3. Each material has its features, which can be selected according to the requirement of the desired reaction operated in the microfluidic reactor, whose advantages and disadvantages can be referred in Chapters 1 and 2. Different types of microfluidic devices occupy a very important position in organic synthesis. Fabrication of microfluidic reactors is still in its infant stage, which can be referred to Chapter 1. In this chapter, our aim is to provide chemists and engineers with useful information in deciding whether to carry out reactions in microfluidic reactors or not. By carefully selecting typical examples, features (advantages and limitations) of each type of microfluidic reactors will be analyzed and discussed to elucidate how they can be used in the organic synthesis.

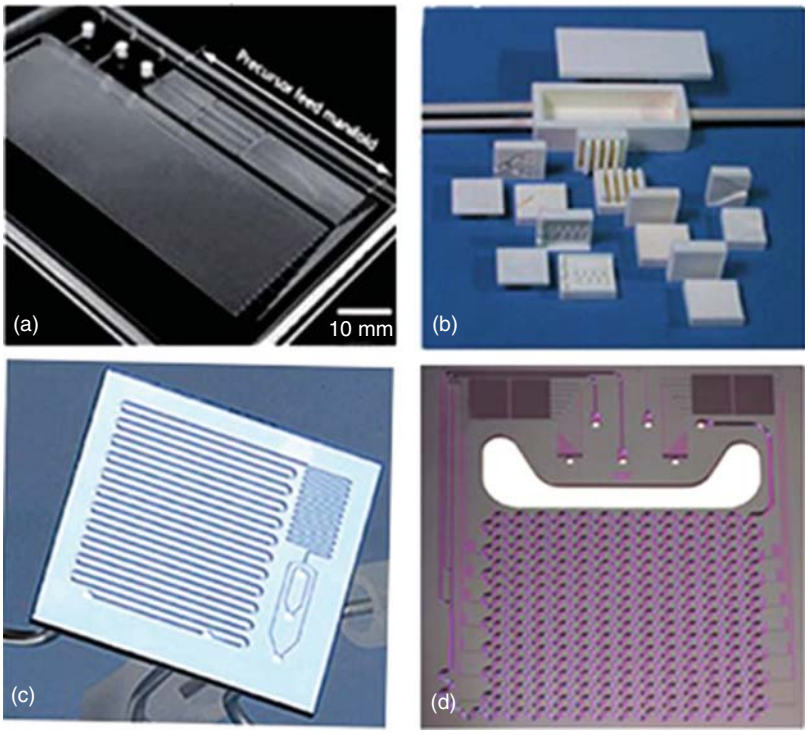


Figure 11.3 Examples of microreactors fabricated from (a) PDMS. (b) Ceramic. (Knitter *et al*. 2001 [34]. Reproduced with permission of Springer.) (c, d) Silicon. ((a, c, d) Wakami and Yoshida 2005 [14]. Reproduced with permission of American Chemical Society.)

www.ebook3000.com

11.2 Microfluidic Nebulator for Organic Synthesis

A microfluidic nebulator is a spray drier that enables supersonic air speeds to be achieved at moderate pressures. The device can produce amorphous nanoparticles (NPs) from a wide range of materials by supersonic spray drying, and the drops produced by the microfluidic nebulator are so small that they dry before crystal nuclei can form [36]. As is shown in Figure 11.4, the microfluidic nebulator is produced from poly(dimethylsiloxane) (PDMS) using soft lithography. A pair of inlets for an additional fluid intersects a main fluid-inlet channel so that two fluid streams can mix, and it also contains six air inlets. The flux of air can be controlled through the channel by tuning its pressure at the air inlets. In comparison with traditional spray drying, it is advantageous to formulate the amorphous structure, which can greatly increase the bioavailability of hydrophobic drugs, because the solubility of amorphous materials is much higher than that of the corresponding crystal [37]. With plenty of materials with a high propensity to crystallize [38], crystallization is typically much faster than termination of the precipitation reaction; however, the drop solvent produced by the microfluidic nebulator is dried so quickly that molecules have no time to arrange into a crystalline structure. Moreover, the solubility of amorphous materials can be greatly enhanced, and their stability during storage increases with decreasing particle size [36, 39], which is advantageous for hydrophobic drug. In addition, no excipient of any kind is required to prevent crystallization due to the very rapid evaporation of the solvent that prevents the formation of crystal nuclei. The microfluidic nebulator can produce amorphous NPs from both organic and inorganic materials; only the application in organic synthesis using the reactor is discussed.

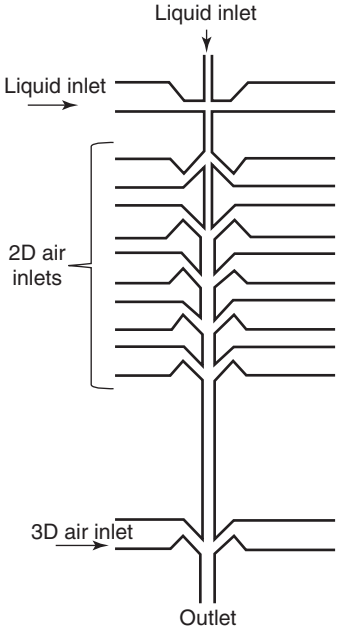


Figure 11.4 Schematic illustration of the junctions of the microfluidic nebulator. (Knitter *et al*. 2001 [34]. Reproduced with permission of Springer.)

Moreover, the hydrophobic organic drug fenofibrate has been produced with the microfluidic nebulator. Amorphous drug NPs are produced by dissolving fenofibrate in ethanol and injecting this solution into the first fluid inlet, and then air is injected into the first pair of air inlets in the opposite direction to the ethanol flow. When the droplet leaves the device, it begins to evaporate and come to dry. These NPs have characterized that their average diameter is 14 nm with an inlet pressure of 0.28 MPa. It is well known that an average diameter of drug NPs is almost 350 nm with traditional available spray-drying method. The smallest-sized fenofibrate NPs were indicated to be always amorphous. Esther Amstad *et al*. argue that amorphous NPs form is a result of this production route. Surprisingly, if they are either deposited as monolayers or coated with a polymer, fenofibrate NPs remained amorphous even when stored for 7 months at room temperature under ambient conditions, because amorphous drugs have the high propensity toward crystallization during storage.

Similarly, clotrimazole amorphous drug was also produced with the microfluidic nebulator, and then clotrimazole NPs were spray-dried into the polymer matrices [40]. Even though clotrimazole has a higher propensity to crystallize, experiment results prove that spray-dried NPs remain amorphous for at least 4 months even if stored at 65 °C. Moreover, clotrimazole NPs have excellent stability to their good dispersion and are well separated from each other. In addition, spray-dried NPs have a sufficiently high kinetic energy to penetrate into the polymer matrix, thereby enabling storage of these NPs at a higher density without risking aggregation. NPs are also produced from other hydrophobic drugs, including estradiol and danazol, with small size distributions. The nebulator to prepare polymer-coated amorphous drug NPs that are much more stable against crystallization than drug particles is produced using bulk methods or commercially available spray driers.

11.3 Coiled Tubing Microreactor for Organic Synthesis

Coiled tubing microreactor is a microfluidic device constructed of tubing coils, which are widely used in organic synthesis. The choice of the structural material depends on chemical compatibility, temperature, and pressure, as well as ease of fabrication and integration [41]. Materials of coiled tubing reactors can be constructed of stainless steel and some special thermosetting polymers (e.g., polyetheretherketone (PEEK), polytetrafluorethylene (PTFE), perfluoroalkoxy (PFA)) that are inert to many chemical solvents. A variety of reactions can be performed for the synthesis of intermediates and natural products, such as halogenation [42, 43], fluorination [44], nitration [45], and oxidation [46, 47]. A typical example using the coiled tubing microreactor is the preparation of nitriles from carboxylic acids (Figure 11.5) [48]. Nitriles are an important class of compounds in organic synthesis, having widespread application as intermediates

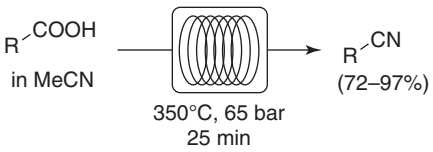


Figure 11.5 Continuous-flow high-*T*/*p* acid–nitrile exchange reaction.

www.ebook3000.com

in the preparation of several other functional groups or heterocycles, such as tetrazoles [49]. The acid–nitrile exchange reaction is a simple reaction for the direct generation of nitriles from carboxylic or sulfuric acids by heating for 4–18 h, but usually low yields and mixed products. The reaction temperature must be more than 300 °C to achieve enough transformation rates. However, it is difficult for the conventional batch reactor to operate at more than 300 °C. Microfluidic technology can overcome this problem, allowing this process to be performed at high temperatures and pressures in a safe and controllable status. As the reaction of benzoic acid in acetonitrile to generate benzonitrile was performed via batch processes, only 10% of benzoic acid was converted into benzonitrile, and the resulting products only had 1% and 7% yields of benzamide and *N*-acetylbenzamide, respectively, which is almost useless in practical application. However, the reaction can be performed very well in a stainless-steel coiled tubing microreactor because stainless-steel microreactors can be performed at enough high temperature and pressure (high-T/p). With residence times of 25 min at 350 °C and 65 bar, about 94% of benzoic acid can be converted into benzonitrile. Despite the high temperature, the microreactor displayed a very good compatibility with common functional groups, such as halogen, nitro, alcohol, and ester.

The liquid-phase continuous-flow processing in a high-T/p regime is a useful synthetic method to perform pyrolysis reactions that are typically carried out using flash vacuum pyrolysis (FVP) protocols. FVP is a special form of gas-phase thermolysis; synthetic protocols involving FVP conditions possess many undisputed advantages, for example, the avoidance of intermolecular secondary reactions in the heating zone, and FVP is also a valuable synthetic tool for the preparation of many interesting stable compound classes. However, it is difficult to translate FVP protocols from laboratory scale (milligrams or grams) to industrial scale (kilograms or tons) in a reasonable time frame if the precursor is of only modest volatility [50]. Lots of intermediates cannot be synthesized using the traditional batch method, in particular unusual hetero- or carbocyclic systems. Fortunately, coiled tubing microreactors can meet this requirement, which not only can resolve the above issues but also can reduce the reaction time from several hours to a few minutes under the high-T/p. As is shown in Figure 11.6, benzoyl Meldrum's acid can be transferred to either the 1,3-dioxin-4-one intermediate or the oxoketene dimer by precisely controlling the residence time and temperature using the coiled tubing microreactor. It can

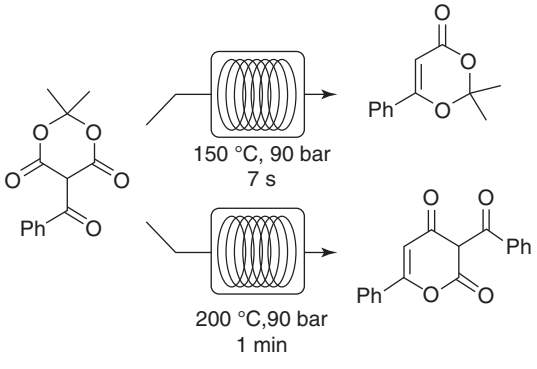
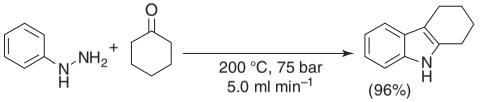
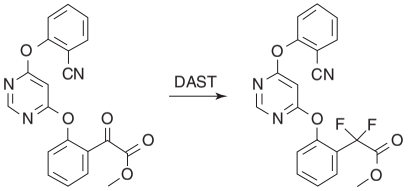
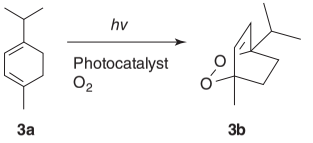
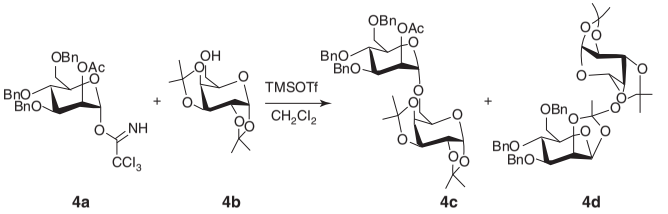


Figure 11.6 Liquid-phase high-T/p continuous-flow pyrolysis of Meldrum' s acid.

Table 11.1 A summary of nanomaterials synthesized using microfluidic reactors.

Reactor type	Organics synthesized	Reaction type	Reaction condition	Advantages and features	References
Microfluidic nebulator	—	Synthesis of fenofibrate	Flow rate of 1 ml h^{-1}; 0.28 MPa	The method can produce amorphous NPs, and their solubility is much higher	[36]
Coil reactor by stainless tube	 1a 1b	Synthesis of tetrahydrocarbazole	20 °C; 75 bar; 5.0 ml min^{-1}	96% yield in 8 min; batch reaction requires days for unactivated substrates	[51]
Coiled reactor with PEEK, PTFE, or PFA tube	 2a 2b	Electrophilic substitution of aromatics (e.g., fluorination, nitration)	80 °C; residence times of 27 min; 100 ml min^{-1}	94% yield without hazards/challenges	[44]
Lab-on-chip reactor by glass	 3a 3b	Synthesis of ascaridole (singlet oxygen)	Pure oxygen at a flow rate of 15 µl min^{-1}; solvent at a flow rate of 1 µl min^{-1}	Efficient transformation (>80% conversion) can be achieved with an irradiation (reaction) time of less than 5 s	[52]

www.ebook3000.com

Lab-on-chip reactor by silicon	 OBn OAc BnO BnO O NH CCl3 OH O O O O TMSOTf CH2Cl2 OBn OAc BnO BnO O O O O

provide the acylketene–acetone adduct a selectivity close to 90% and the dimer an almost complete selectivity (about 98%).

The synthesis of tetrahydrocarbazole can be performed by stainless-steel coiled tubing microreactors (Table 11.1). Transformations requiring high temperatures can be conveniently realized in a continuous-flow microreactor that is based on standard HPLC-type equipment. With the optimum reaction temperature of 200 °C and a pressure of 75 bar, the 96% yield of the product can be achieved at a flow rate of 5.0 ml min^{-1}, leading the generation of 25 g of indole product within 1 h. Compared with the traditional methods, the production yields can be greatly increased. Because of efficient heat transfer through the thin steel reactor coil, rapid heating and cooling of the reaction mixture can be realized easily. A series of experiments have been conducted using this microreactor, such as the Diels–Alder reaction of 2,3-dimethylbutadiene, acrylonitrile to the cyclohexene adduction, and the Claisen rearrangement of allyl phenyl ether. Optimizing the reaction conditions conveniently in the coiled tubing microreactor can increase production yields and conversion.

In addition to the synthesis of tetrahydrocarbazole, fluorinating reactions can be performed in the coiled tubing microreactor constructed with PEEK, PTFE, and PFA. Fluorinated molecules are basic chemicals for many commercially important products. A set of experiments have been reported using diethylaminosulfur trifluoride (DAST) as a commonly used reagent for the conversion of alcohols and carbonyl compounds into their corresponding fluoro derivatives. However, this reagent has many disadvantages, such as volatility and sensitivity to water, low efficiency of conversion, and the causticity of by-products in this reaction. It is difficult for traditional batch methods to resolve these issues effectively. The use of DAST in a continuous-flow microreactor constructed with polymer tubes (PEEK, PTFE, PFA) can provide a flexible and safety enhanced scale-out process. Selective fluorination with DAST undergoes a dismutation above 90 °C. Products synthesized with this microreactor not only avoid aforementioned challenges but also reach a yield of 94% [44].

11.4 Chip-Based Microfluidic Reactor for Organic Synthesis

Microfluidic reactors consisting of a network of miniaturized channels can often be embedded in a flat substrate, or the so-called lab-on-chip [35]. In recent years, a variety of lab-on-chip microfluidic reactors have been developed, and several of them are now commercially available. Injection-molding, hot-embossing, or phase-separation-micromolding techniques are used to prepare these microfluidic reactors. It is likely that the majority of microfluidic devices will eventually be constructed from polymers (rather than silicon or glass) due to the wide availability of constructed materials, commercial chip manufacturers, and highly cost-effective fabrication methods (such as injection molding, hot embossing, and 3D printing), which means that the reactors can be "printed" [56]. Figure 11.7 shows one silicon-based microfluidic reactor layout, including

www.ebook3000.com

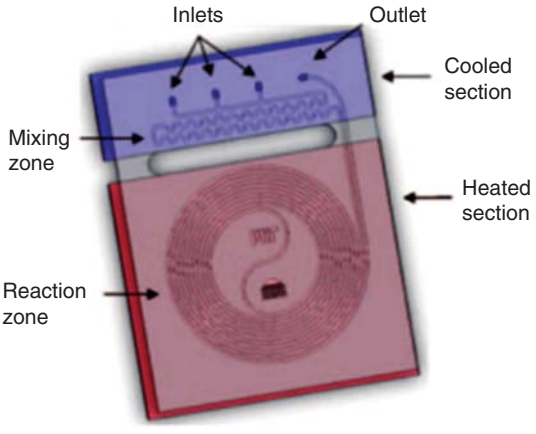


Figure 11.7 High-*T*/*p* aminolysis reactions for medicine synthesis. (Webb and Jamison 2010 [28]. Reproduced with permission of Royal Society of Chemistry.)

the reagent inlets, mixing, reaction, quench zones, and cooling of the outlet. The reaction mixture can experience two or more different temperature zones. In the mixing stage, the reactant solutions can be thoroughly mixed to form a uniform reaction solution under cooling and then react at the desired temperature in the heated zone, which is very important for rapid reaction to eliminate concentration gradients. For most organic syntheses, the small reactor scale and the high thermal conductivity of silicon ensure that the reactant solutions can be heated to the desired temperature in less than seconds [57]. Clearly, lab-on-chip microfluidic reactors constructed by chemically and physically robust materials of highly thermal conductivity enable the reaction to be conducted at well-defined conditions due to rapid thermal equilibration, which favors kinetic optimization and controlled scale-up.

Metoprolol is a special medicine for the treatment of hypertension. In conventional batch conditions, epoxide aminolysis is typically performed using multiple equivalents of isopropylamine, with reaction times ranging from 2 to 5 h. Therefore, to date, new efficient processes are eagerly desired to resolve the shortage of metoprolol. A silicon-based lab-on-chip microfluidic reactor can be used to synthesize metoprolol via aminolysis as shown in Figure 11.8 [58]. Using the silicon-chip-based microfluidic process, the amount of isopropylamine can be increased, while bis-alkylation can be decreased at 240 °C. Most amazing complete conversion can be finished at 240 °C with a residence time of only 15 s and a yield of metoprolol up to 7 g h^{-1}. Therefore, the aminolysis of epoxides

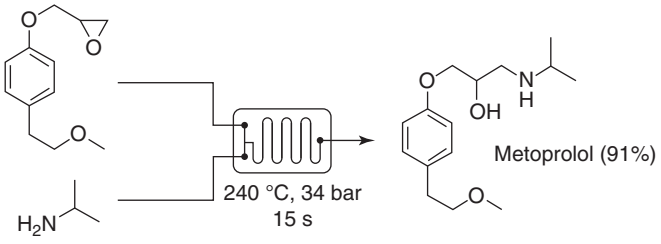


Figure 11.8 Preparation of metoprolol via one silicon-based lab-on-chip microfluidic reactor.

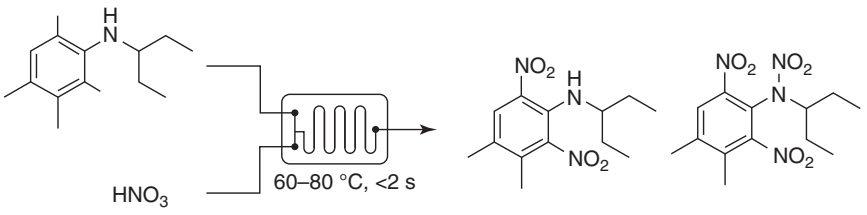


Figure 11.9 Nitration reactions under microfluid.

using the silicon-chip-based microfluidic reactor proved to be a highly efficient process. The microfluidic reactor is capable of reaching very high temperatures that are not possible in microwave batch processes.

Another advantage of using microfluidic process is that some tedious intermediate separation process and potential explosive dangers can be avoided. For example, chip-based microfluidic processes (Figure 11.9) without the need for separation of intermediates have been successfully developed in the synthesis of dinitro herbicides through the one-step dinitration approach. In conventional batch processes, synthesis of dinitro herbicides is often conducted by a two-step process that has many shortcomings, such as long reaction time, large amounts of waste solvents, low selectivity, and the higher safety risk due to the easily exploding nitration, which is extremely dangerous due to highly exothermic thermodynamics as well as possible decomposition and explosion of nitro compounds. Using lab-on-chip silicon-based microfluidic reactors, both the process safety and the product selectivity can be greatly improved due to much small local reaction volume and relatively large surface-to-volume ratio [59, 60]. Disaster from the lost control of the key nitration reactions can be efficiently avoided. With 65% nitric acid at temperatures of 60–80 °C and residence times of less than 2 s, the microfluidic reactor can be operated continuously for more than 1 h to produce 0.54 kg of products at 97% yield and the undesired by-product, and the isolation step of the intermediate can be eliminated. Microfluidic reactors definitely offer great opportunities for one-step dinitration of aniline derivatives in a continuous and selective way. However, a batch process with one-step dinitration under identical conditions would be impossible or very hazardous due to its local large reaction volume.

The chip-based microfluidic reactor technology has also been successfully used to synthesize ascaridole from *R*-terpinene safely and efficiently by eliminating the inherent dangers of large quantities of oxygenated solvents. Even though singlet oxygen produced by irradiation is used rather widely in contemporary organic synthesis, it is inherently difficult to adapt the batch process to large-scale production. Recent development has addressed some problems but still leaves the safety issue associated with large quantities of oxygenated organic solvents unsolved. The chip-based microfluidic reactors are ideal for processing these hazardous reactions. Importantly, microflow alternatives to traditional batch processes can be scaled up by simple multi-parallel strategy (or scale-out) [61]. The small cross section of the glass microchannels results in effective irradiation even using relatively low-intensity light sources. This leads to reduced sample heating and therefore reduced radical recombination. An efficient

www.ebook3000.com

transformation of >80% conversion can be achieved with a reaction time of less than 5 s. However, under the same reaction condition, this singlet oxygen reaction has to be performed for 4 h in a 100 ml flask, whose conversion is only 67%. Clearly, compared with the batch method, the chip-based microfluidic reactor has much more advantages: it avoids the major inherent dangers and allows for reliable reaction even with relatively low-intensity light sources [52, 62].

Finally, the sample glycosylation of glycosyl donor and nucleophile (acceptor) to form disaccharide and the formation of orthoester have been successfully performed using lab-on-chip silicon-based microfluidic reactors [53]. Under optimal reaction conditions, the yield of the product can be increased until maximum conversion is achieved. Most importantly, the formation of orthoester as a major side product can be formed at lower temperatures around −70 °C, which is difficult in the batch reactor. The glycosylation reaction still has several unsolved problems using conventional processes, such as the challenge in accurately predicting the reactivity of the coupling partners and precisely controlling the reaction variables. The emergence of the chip-based microreactor provides organic chemists a new tool for the optimization of the reaction conditions to achieve a particular transformation at low cost and high throughput to address these issues.

11.5 Packed-Bed Microreactors for Organic Synthesis

A continuous-flow process based on a chiral transition-metal complex in a supported ionic liquid phase (SILP) using supercritical carbon dioxide ($scCO_2$) as the mobile phase has been developed for asymmetric catalytic transformations of low-volatility organic substrates at mild reaction temperatures (Figure 11.10) [63, 64], which are also transferred in microfluidic processes. Many reactions have been successfully carried out continuously by using this kind of microfluidic

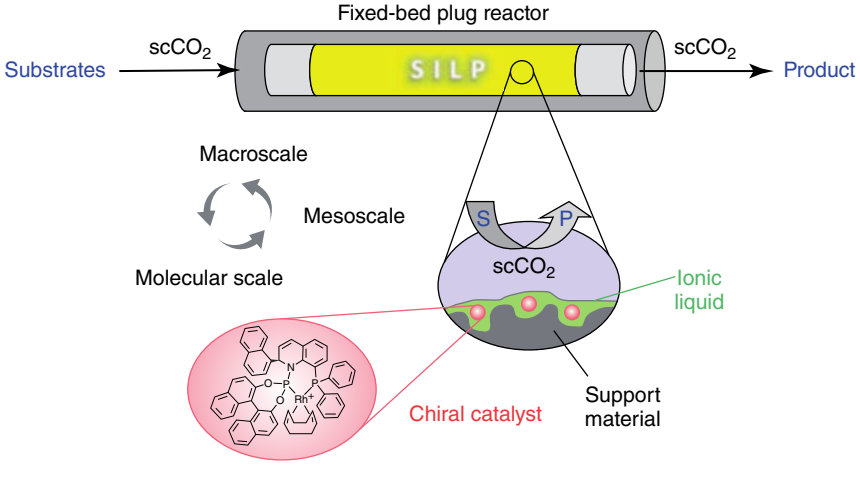


Figure 11.10 Schematic representation of the reactor setup using a water scavenger ($scCO_2$) under relatively mild conditions. (Bourne *et al*. 2009 [62]. Reproduced with permission of John Wiley & Sons.)

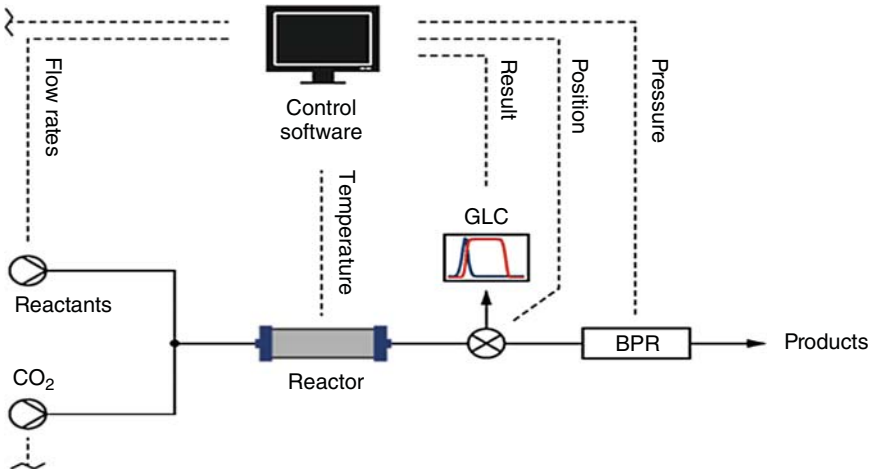


Figure 11.11 Adaptive packed-bed microfluidic process optimization for continuous methylation of alcohols in supercritical CO_2. The alcohol was mixed with CO_2 before passing through a reactor column packed with catalyst. (Ley *et al*. 2015 [1]. Reproduced with permission of John Wiley & Sons.)

packed-bed systems [65], such as hydrogenation, hydroformylation, oxidation, photooxidation, and acid-catalyzed reactions, particularly etherification.

Figure 11.11 shows an automated optimization platform of a packed-bed microfluidic reactor system for the methylation of 1-pentanol [66], where four reaction parameters (reaction temperature, pressure, CO_2 flow rate, and 1-pentanol/methylating agent ratio) can be optimized for high yield and selectivity. Traditionally, one reaction parameter is usually varied and optimized at a time, whose effect can be evaluated as other parameters are constant. However, it is difficult to reveal the synergy among parameters. Using this automation microfluidic process, it is possible to develop a self-optimizing high-throughput system to directly utilize the synergy among these four parameters for high yield automatically at low cost and less time consumption. The aforementioned four parameters can be optimized simultaneously for the etherification of 1-pentanol. With only 10 experiments, the yield can reach 90%, and the final fully optimized conditions can reach >98% yield after several more experiments using dimethyl carbonate and methanol as the methylating agents. This kind of packed-bed microfluidic processes favors to self-optimizing by incorporating online analysis, reactor control, and an evolutionary search algorithm, which obtain not only the optimized yield but also the space–time yield.

The hydrogenation of dimethyl itaconate (Figure 11.12a) with supercritical carbon can be conducted in this packed-bed microfluidic process. Superior quality products can be obtained at a space–time yield up to 0.7 kg l^{-1} h^{-1} and productivities of more than 100 kg product per gram of rhodium-based catalysts or 14 kg per gram of ligands at 40 °C [63]. This microfluidic process has also been successfully used for asymmetric hydrogenation by using a chiral transition-metal catalyst in SILP with $scCO_2$ flow. Contrary to the effect of the conventional supported liquid-phase (SLP) catalysts in a batch liquid-phase process, the morphology of

www.ebook3000.com

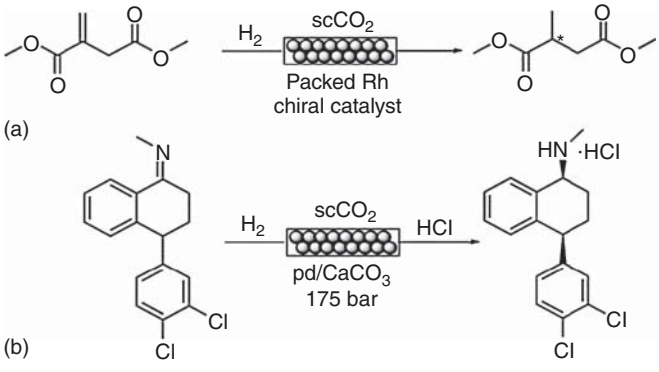


Figure 11.12 Continuous-flow hydrogenations in the packed-bed microfluidic reactors using $scCO_2$ as the mobile phase.

the support material in the SILP system has little effect on the catalyst activity using the $scCO_2$ fixed-bed microfluidic reactor.

Similarly, the hydrogenation of racemic sertraline imine in the synthesis of *cis*-(1*S*,4*S*)-sertraline hydrochloride (Figure 11.12b), which is the active ingredient of the drug for the treatment of depression and other anxiety-related disorders, has been successfully conducted in a packed-bed microfluidic reactor using $scCO_2$ as the mobile solvent. The best results can be achieved using $Pd/CaCO_3$ as catalysts at a reaction temperature of 40 °C and pressure of 175 bar. Under optimized conditions for the hydrogenation, dechlorination, and dehydrogenation, side reactions can be suppressed almost completely with a chemoselectivity of more than 99%, and racemic sertraline can be formed with excellent diastereoselectivity in a *cis*/*trans* ratio of 97 : 3 [67].

Another application for the packed-bed microfluidic reactor in organic synthesis is the gas–liquid reaction, such as the synthesis of radiolabeled amides by CO carbonylation cross-coupling [54], by which dicarboxylic acid monoamides can be synthesized by directly introducing CO gas into the packed-bed microfluidic system. The reactant solution is passing through X-Cube with 0.5 ml min^{-1} flow rate at 100 °C and 30 bar, and carbon monoxide is introduced into the X-Cube simultaneously, in which CO gas is mixed with the liquid reactant solution. The optimal reaction conditions have been shown in Table 11.1, suggesting a product of 75% purity and 96% conversion with the reaction time of less than 2 min, better than the result of the batch technique. As the same reaction was carried out in a pressurized autoclave and in a conventional flask reactor using a CO-filled balloon, the conversions are only 22% and 36% with the reaction time of 1 h, respectively. Therefore, the packed-bed microfluidic reactor preserves higher selectivity and conversion within a shorter time than the conventional batch process [68].

11.6 Ring-Shaped (Tube-in-Tube) Microfluidic Reactor for Organic Synthesis

A ring-shaped (tube-in-tube) microfluidic reactor was developed for the liquid–gas two-phase reaction, based on a gas-permeable Teflon AF-2400

membrane enclosed within a thick-walled impermeable outer tube (e.g., PTFE or stainless steel) [55, 69], as shown in left-top of Figure 11.12. Teflon AF-2400 is a copolymer of tetrafluoroethylene and perfluorodimethyldioxolane with a highly porous and amorphous structure, whose chemical resistance and mechanical strength are comparable with that of standard PTFE. Accordingly, the AF-2400 tube serves as a robust hydrophobic permeable membrane that selectively allows a wide variety of gases, but not liquids, as shown in right-top of Figure 11.12. This membrane tube plays a role as an effective, economic, and scalable tube-in-tube microfluidic reactor for both homogeneous and heterogeneous catalytic hydrogenation. This ring-shaped microfluidic reactor can be established with pressurization that required only minimal gas volume, improving the safety profile of the whole system. Most importantly, the gas-permeable membrane can be used as millions of ultra-small gas distributors for uniform reaction and can effectively remove excess unreacted hydrogen. Therefore, this kind of microfluidic reactors provides an opportunity to further assemble necessary parts (e.g., driving, sensing, collecting, separating) to a reaction system for efficient multistep and multiphase flow chemistry processing, as shown in the central integrated system of Figure 11.13.

The catalytic hydrogenation of multiple bonds has become one of the most widely used and important reactions in organic synthesis. However, there are some very serious drawbacks to the use of hydrogen that must be taken into consideration. Most hydrogenation requires high concentrations of hydrogen, which has a serious safety consideration that often requires substantial technical and additional investment to ensure safe operation. Unfortunately, despite efforts

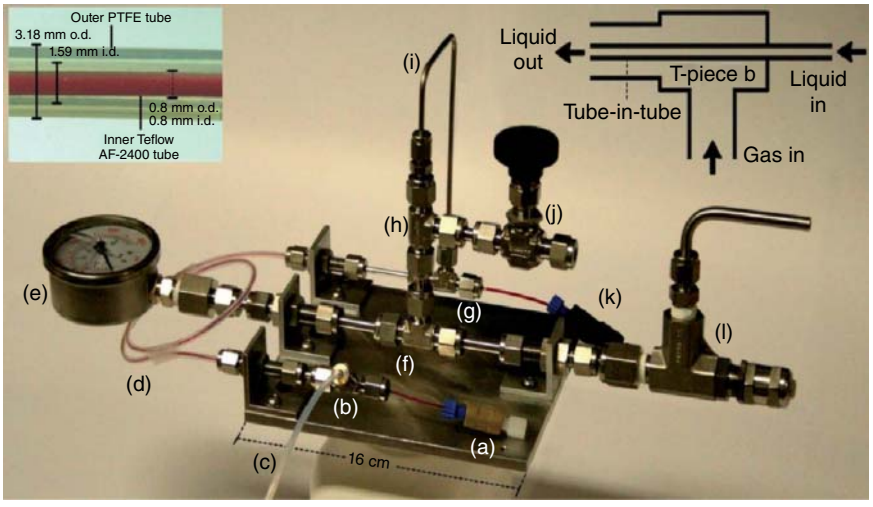


Figure 11.13 Hydrogenation reactor/injector. Key: (a) solution inlet; (b) Swagelok T-piece; (c) gas inlet (1/800 o.d. PTFE tubing); (d) tube-in-tube gas–liquid contactor (inner tube is 0.8 mm o.d. Teflon AF-2400, and outer tube is 1/800 o.d. PTFE); (e) pressure gauge; (f–h) Swagelok T-pieces; (i) 1/800 stainless-steel connector between T-pieces (g) and (h); (j) Swagelok needle valve; (k) solution outlet; (l) pressure relief valve. Left-top inset: Close-up view of the tube-in-tube configuration; solution dyed red. Right-top inset: Simplified diagrammatical view of connections at T-piece (b). (O'Brien *et al*. 2010 [69]. Reproduced with permission of American Chemical Society.)

www.ebook3000.com

to maximizing safety, there still are lots of explosions and even loss of life. The potential energy stored in a pressurized container is approximately proportional to its volume. The adoption of a continuous microfluidic strategy that uses a low local operating reaction volume would be highly safer as compared with the corresponding large volume batch process. In the ring-shaped microfluidic reactor, gas can be efficiently and rapidly delivered to the liquid reactant stream in the microchannels via permeation through the central semipermeable Teflon AF-2400 tube. Thus, hydrogenation for a series of alkene products has been conducted using the above ring-shaped microfluidic system under a hydrogen pressure up to 25 bar. To ensure complete conversion, a slightly lower combined flow rate (1.4 ml min^{-1}) for long residence time and 0.002 equiv. of catalyst were used. Therefore, all products can be isolated in quantitative yield and high purity after removal of solvent, resulting in a 100% conversion. Given that the combined residence time in the reactor/injector and residence loop is around 93 s, these reactions are still extremely rapid.

Carbon monoxide (CO) has proven to be a practical carbonyl source for the preparation of a wide variety of carbonyl compounds. However, both academic and industrial research have demonstrated a certain reluctance to study related reactions using batch method due to the difficulty in handling the odorless, toxic, and flammable CO gas. Using tube-in-tube microfluidic systems, carbonylation reactions can be successfully carried out in a safe mode [70]. This easy-to-use and safe reaction system has paved the new way for low-pressure carbonylation reactions, whereby CO gas can be delivered by decarbonylation reactions or by decomplexation from a metal carbonyl complex. This system consists of a two-chamber reactor (CO ware) with two new solid CO precursors. As shown in Figure 11.14, the inner decarbonylation chamber filled with HCOOH and H_2SO_4 is heated at 80 °C for some time (e.g., 15 min) to generate the desired CO gas, which can diffuse across the membrane and be consumed by reactants (e.g., iodobenzene with 1-octene) in the outer chamber in the presence of catalysts (e.g., palladium chloride). After that, the decarbonylation chamber will be cooled to room temperature by a water bath, and the coupling reaction will be carried out at room temperature for 24 h, leading to the desired alkynyl ketone in a high yield of 91% [71].

Ozonolysis is an extremely useful synthetic transformation and is considered to be more environmentally acceptable than alternative processes using metal species such as the toxic and volatile osmium tetroxide. Development

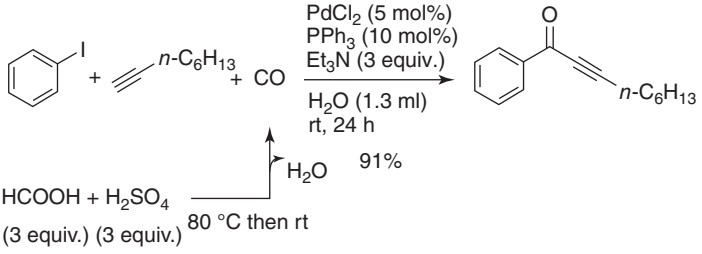


Figure 11.14 Carbonylation Sonogashira reaction with *ex situ* generated CO in a tube-in-tube reactor. (Brancour *et al*. 2013 [71]. Reproduced with permission of American Chemical Society.)

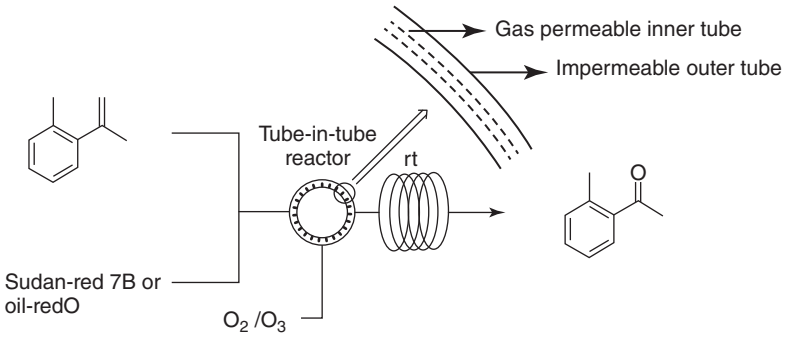


Figure 11.15 The ozonolysis of alkenes with generated O_2/O_3 in a tube-in-tube reactor.

of ozonolysis from the batch process into a continuous-flow process is highly desirable. This kind of tube-in-tube microfluidic processes has been also developed in the ozonolysis of a series of alkenes (Figure 11.15) [69, 72]. Using the length of the AF-2400 tubing connected to a syringe pump, the ozonolysis of a series of alkenes was then carried out continuously and safely. The best result can be obtained by facilitating rapid purification and simplify the analysis of products. A complete conversion of substrate with a yield of 93% can be realized with a 1 h residence time in the apparatus. The ozonolysis of alkenes represents a good example of using the tube-in-tube microfluidic process wherein such a reaction shows the potentially dangerous nature of the intermediate ozonides or a simple and convenient microfluidic device can bring about the ozonolysis of alkenes via gas-to-liquid transfer through semipermeable Teflon AF-2400 tubing.

Another advantage of the continuous-flow technique using the tube-in-tube microfluidic process is the potential to facilitate the rapid and efficient computer-assisted measurement of gas solubility in liquids. This kind of tube-in-tube microfluidic process including a permeable membrane system will be very useful in finding more applications beyond the scope that were demonstrated using other reactive gases (e.g., CO, acetylene, ethylene, SO_2, O_2, etc.) for the controllable and uniform multiphase reaction, which is usually difficult to realize in the conventional batch methods. Importantly, the gas-permeable membrane can be used to effect removal of excess unreacted gas (e.g., hydrogen), providing an opportunity for efficient multistep microflow chemistry processing.

11.7 Summary and Outlook

This chapter has been focused on selecting the appropriate microfluidic reactor for some reactions in organic or medicine synthesis. Microfluidic system comprises five types of reactors throughout this chapter, including microfluidic nebulator reactors, coiled tubing microfluidic reactors, chip-based microfluidic reactors, packed-bed microfluidic reactors, and tube-in-tube or ring-shaped microfluidic reactors. Each type has its own characteristics, which can be used to prepare organic or medicine synthesis at different reaction conditions. Due to the excellent mass transfer and heat transfer performance in small-diameter reactors

www.ebook3000.com

and the comparatively small reaction volumes, these microfluidic devices are uniquely suited for fast and exothermic reactions, which are usually difficult to be conducted safely and efficiently in the conventional batch processes. Furthermore, microfluidic reactors that are integrated with online analysis and feedback algorithms can provide reaction information more efficiently than flask-batched reactors, which can easily realize an automatic process. Kinetic investigations in microfluidic reactors with online analysis capabilities have less experimental variances than the typical batch reactors. Determining the rate constant for reactions that involve a volatile reagent in flask reactors is complicated by the uncertainty of the distribution of compounds in the liquid phase and the headspace. However, this uncertainty usually does not exist in a microfluidic reactor, and the complications can be alleviated in microfluidic reactors through the use of on-chip quench stream and incorporating online spectroscopic measurements.

Even though current pharmacy and fine chemicals are by far produced by batch processing, the development of automated microfluidic systems is very fast due to their advantages such as precisely kinetic control, high product selectivity, environmental friendliness, operation safety, and low cost in optimization of reaction conditions and scale-out features. Advances are in multistage separations, online analysis, and online kinetic control and optimization. The use of "exotic" reagents and extreme process conditions in combination with modern reactor technology offers the promise of cheap equipment and production cost, less waste and emissions, and increased safety. Therefore, it seems that in the near future, many large-scale batch processes where thousands of kilograms of potentially corrosive, toxic, or explosive chemicals have to be mixed and stirred for long period of time can be replaced by these kinds of microfluidic processes [73]. Of course, microfluidic systems also have some issues for improvement. For instance, the cost of fabricating thousands of microfluidic reactors with identical features is not trivial, and the uniform flow rate control in each channel from a single source is also a problem, including the blockage and self-cleaning of microfluidic channels during long-term operation. Therefore, direct translation of normal batch process into a microfluidic reactor process is indeed not a trivial issue [74]. Overcoming such challenges and further innovation in the required infrastructure to operate microfluidic chemical reaction system for long-term will enable application to address future synthesis problems to satisfy our societal requirements.

Acknowledgments

This work was supported by National S&T Major Project (pre-approved No. SQ2018ZX100301), NSFC (Grant No. 51371018 & 81372425) and the Fundamental Research Funds for the Central University of China (FRF-BR-14-001B).

References

1 Ley, S.V., Fitzpatrick, D.E., Ingham, R.J., and Myers, R.M. (2015) Organic synthesis: March of the machines. *Angew. Chem. Int. Ed.*, **54** (11), 3449–3464.

2 Wiles, C. and Watts, P. (2012) Continuous flow reactors: a perspective. *Green Chem.*, **14** (1), 38–54.
3 Jahnisch, K., Hessel, V., Lowe, H., and Baerns, M. (2004) Chemistry in microstructured reactors. *Angew. Chem. Int. Ed.*, **43** (4), 406–446.
4 Gutmann, B., Cantillo, D., and Kappe, C.O. (2015) Continuous-flow Technology A tool for the safe manufacturing of active pharmaceutical ingredients. *Angew. Chem. Int. Ed.*, **54** (23), 6688–6728.
5 Song, Y., Hormes, J., and Kumar, C.S. (2008) Microfluidic synthesis of nanomaterials. *Small*, **4** (6), 698–711.
6 Hartman, R.L., McMullen, J.P., and Jensen, K.F. (2011) Deciding whether to Go with the flow: evaluating the merits of flow reactors for synthesis. *Angew. Chem. Int. Ed.*, **50** (33), 7502–7519.
7 Baxendale, I.R., Brocken, L., and Mallia, C.J. (2013) Flow chemistry approaches directed at improving chemical synthesis. *Green Process. Synth.*, **2** (3), 211–230.
8 Jensen, K.F., Reizman, B.J., and Newman, S.G. (2014) Tools for chemical synthesis in microsystems. *Lab Chip*, **14** (17), 3206–3212.
9 Longstreet, A.R. and McQuade, D.T. (2013) Organic reaction systems: using microcapsules and microreactors to perform chemical synthesis. *Acc. Chem. Res.*, **46** (2), 327–338.
10 Anderson, N.G. (2012) Using continuous processes to increase production. *Org. Process Res. Dev.*, **16** (5), 852–869.
11 Losey, M.W., Schmidt, M.A., and Jensen, K.F. (2001) Microfabricated multiphase packed-bed reactors: characterization of mass transfer and reactions. *Ind. Eng. Chem. Res.*, **40** (12), 2555–2562.
12 Kreutzer, M.T., Gunther, A., and Jensen, K.F. (2008) Sample dispersion for segmented flow in microchannels with rectangular cross section. *Anal. Chem.*, **80** (5), 1558–1567.
13 Schubert, K., Brandner, J., Fichtner, M., Linder, G., Schygulla, U., and Wenka, A. (2001) Microstructure devices for applications in thermal and chemical process engineering. *Microscale Thermophys. Eng.*, **5** (1), 17–39.
14 Wakami, H. and Yoshida, J. (2005) Grignard exchange reaction using a microflow system: from bench to pilot plant. *Org. Process Res. Dev.*, **9** (6), 787–791.
15 Hartman, R.L. and Jensen, K.F. (2009) Microchemical systems for continuous-flow synthesis. *Lab Chip*, **9** (17), 2495–2507.
16 Song, Y.J., Sun, Q.Q., Zhang, T., Jin, P.Y., and Han, L. (2010) Synthesis of boron nitride nanotubes by an oxide-assisted chemical method. *J. Nanopart. Res.*, **12** (7), 2689–2697.
17 Mason, B.P., Price, K.E., Steinbacher, J.L., Bogdan, A.R., and McQuade, D.T. (2007) Greener approaches to organic synthesis using microreactor technology. *Chem. Rev.*, **107** (6), 2300–2318.
18 Carter, C.F., Baxendale, I.R., O'Brien, M., Pavey, J.B.J., and Ley, S.V. (2009) Synthesis of acetal protected building blocks using flow chemistry with flow IR analysis: preparation of butane-2,3-diacetal tartrates. *Org. Biomol. Chem.*, **7** (22), 4594–4597.

www.ebook3000.com

19 Riva, E., Gagliardi, S., Mazzoni, C., Passarella, D., Rencurosi, A., Vigo, D. *et al.* (2009) Efficient continuous flow synthesis of hydroxamic acids and suberoylanilide hydroxamic acid preparation. *J. Org. Chem.*, **74** (9), 3540–3543.

20 Green, R.A., Brown, R.C.D., and Pletcher, D. (2015) Understanding the performance of a microfluidic electrolysis cell for routine organic electrosynthesis. *J. Flow Chem.*, **5** (1), 31–36.

21 Watts, K., Baker, A., and Wirth, T. (2014) Electrochemical synthesis in microreactors. *J. Flow Chem.*, **4** (1), 2–11.

22 Veser, G. (2001) Experimental and theoretical investigation of H-2 oxidation in a high-temperature catalytic microreactor. *Chem. Eng. Sci.*, **56** (4), 1265–1273.

23 Hessel, V., Kralisch, D., Kockmann, N., Noel, T., and Wang, Q. (2013) Novel process windows for enabling, accelerating, and uplifting flow chemistry. *ChemSusChem*, **6** (5), 746–789.

24 Noorian, H., Toghraie, D., and Azimian, A.R. (2014) The effects of surface roughness geometry of flow undergoing Poiseuille flow by molecular dynamics simulation. *Heat Mass Transfer*, **50** (1), 95–104.

25 Pfahler, J.H.J., Bau, H. *et al* (1990) Liquid transport in micron and submicron channels. *Sens. Actuators, A*, **22** (1), 431–434.

26 Myers, R.M., Fitzpatrick, D.E., Turner, R.M., and Ley, S.V. (2014) Flow chemistry meets advanced functional materials. *Chem. Eur. J.*, **20** (39), 12348–12366.

27 Baxendale, I.R., Deeley, J., Griffiths-Jones, C.M., Ley, S.V., Saaby, S., and Tranmer, G.K. (2006) A flow process for the multi-step synthesis of the alkaloid natural product oxomaritidine: a new paradigm for molecular assembly. *Chem. Commun.*, **24**, 2566–2568.

28 Webb, D. and Jamison, T.F. (2010) Continuous flow multi-step organic synthesis. *Chem. Sci.*, **1** (6), 675.

29 McQuade, D.T. and Seeberger, P.H. (2013) Applying flow chemistry: methods, materials, and multistep synthesis. *J. Org. Chem.*, **78** (13), 6384–6389.

30 Ahmed-Omer, B., Barrow, D.A., and Wirth, T. (2011) Multistep reactions using microreactor chemistry. *Arkivoc*, **2011**, 26–36.

31 Venturoni, F., Nikbin, N., Ley, S.V., and Baxendale, I.R. (2010) The application of flow microreactors to the preparation of a family of casein kinase I inhibitors. *Org. Biomol. Chem.*, **8** (8), 1798–1806.

32 Rolland, J.P., Van Dam, R.M., Schorzman, D.A., Quake, S.R., and DeSimone, J.M. (2004) Solvent-resistant photocurable "liquid Teflon" for microfluidic device fabrication. *J. Am. Chem. Soc.*, **126** (8), 2322–2323.

33 Guber, A.E., Heckele, M., Herrmann, D., Muslija, A., Saile, V., Eichhorn, L. *et al.* (2004) Microfluidic lab-on-a-chip systems based on polymers – fabrication and application. *Chem. Eng. J.*, **101** (1–3), 447–453.

34 Knitter, R., Gohring, D., Risthaus, P., and Hausselt, J. (2001) Microfabrication of ceramic microreactors. *Microsyst. Technol.*, **7** (3), 85–90.

35 Geyer, K., Codee, J.D.C., and Seeberger, P.H. (2006) Microreactors as tools for synthetic chemists – The chemists' round-bottomed flask of the 21st century? *Chem. Eur. J.*, **12** (33), 8434–8442.

36 Amstad, E., Gopinadhan, M., Holtze, C., Osuji, C.O., Brenner, M.P., Spaepen, F. *et al.* (2015) Production of amorphous nanoparticles by supersonic spray-drying with a microfluidic nebulator. *Science*, **349** (6251), 956–960.

37 Laitinen, R., Lobmann, K., Strachan, C.J., Grohganz, H., and Rades, T. (2013) Emerging trends in the stabilization of amorphous drugs. *Int. J. Pharm.*, **453** (1), 65–79.

38 Kawabata, Y., Wada, K., Nakatani, M., Yamada, S., and Onoue, S. (2011) Formulation design for poorly water-soluble drugs based on biopharmaceutics classification system: basic approaches and practical applications. *Int. J. Pharm.*, **420** (1), 1–10.

39 Amstad, E., Spaepen, F., and Weitz, D.A. (2015) Crystallization of undercooled liquid fenofibrate. *Phys. Chem. Chem. Phys.*, **17** (44), 30158–30161.

40 Amstad, E., Spaepen, F., and Weitz, D.A. (2016) Stabilization of the amorphous structure of spray-dried drug nanoparticles. *J. Phys. Chem. B*, **120** (34), 9161–9165.

41 Jensen, K.F. (2006) Silicon-based microchemical systems: characteristics and applications. *MRS Bull.*, **31** (2), 101–107.

42 Breen, J.R., Sandford, G., Yufit, D.S., Howard, J.A.K., Fray, J., and Patel, B. (2011) Continuous gas/liquid–liquid/liquid flow synthesis of 4-fluoropyrazole derivatives by selective direct fluorination. *Beilstein J. Org. Chem.*, **7**, 1048–1054.

43 Sterk, D., Jukic, M., and Casar, Z. (2013) Application of flow photochemical bromination in the synthesis of a 5-bromomethylpyrimidine precursor of rosuvastatin: improvement of productivity and product purity. *Org. Process Res. Dev.*, **17** (1), 145–151.

44 Baumann, M., Baxendale, I.R., Martin, L.J., and Ley, S.V. (2009) Development of fluorination methods using continuous-flow microreactors. *Tetrahedron*, **65** (33), 6611–6625.

45 Cantillo, D., Damm, M., Dallinger, D., Bauser, M., Berger, M., and Kappe, C.O. (2014) Sequential nitration/hydrogenation protocol for the synthesis of triaminophloroglucinol: safe generation and use of an explosive intermediate under continuous-flow conditions. *Org. Process Res. Dev.*, **18** (11), 1360–1366.

46 Nieuwland, P.J., Koch, K., van Harskamp, N., Wehrens, R., van Hest, J.C., and Rutjes, F.P. (2010) Flash chemistry extensively optimized: high-temperature Swern-Moffatt oxidation in an automated microreactor platform. *Chem. Asian J.*, **5** (4), 799–805.

47 He, Z. and Jamison, T.F. (2014) Continuous-flow synthesis of functionalized phenols by aerobic oxidation of grignard reagents. *Angew. Chem. Int. Ed.*, **53** (13), 3353–3357.

48 Cantillo, D. and Kappe, C.O. (2013) Direct preparation of nitriles from carboxylic acids in continuous flow. *J. Org. Chem.*, **78** (20), 10567–10571.

49 Roh, J., Vavrova, K., and Hrabalek, A. (2012) Synthesis and functionalization of 5-substituted tetrazoles. *Eur. J. Org. Chem.*, **31**, 6101–6118.

50 Cantillo, D., Sheibani, H., and Kappe, C.O. (2012) Flash flow pyrolysis: mimicking flash vacuum pyrolysis in a high-temperature/high-pressure liquid-phase microreactor environment. *J. Org. Chem.*, **77** (5), 2463–2473.

www.ebook3000.com

51 Razzaq, T., Glasnov, T.N., and Kappe, C.O. (2009) Continuous-flow microreactor chemistry under high-temperature/pressure conditions. *Eur. J. Org. Chem.*, **2009** (9), 1321–1325.

52 Wootton, R.C.R., Fortt, R., and de Mello, A.J. (2002) A microfabricated nanoreactor for safe, continuous generation and use of singlet oxygen. *Org. Process Res. Dev.*, **6** (2), 187–189.

53 Ratner, D.M., Murphy, E.R., Jhunjhunwala, M., Snyder, D.A., Jensen, K.F., and Seeberger, P.H. (2005) Microreactor-based reaction optimization in organic chemistry glycosylation as a challenge. *Chem. Commun.*, **5**, 578–580.

54 Csajagi, C., Borcsek, B., Niesz, K., Kovacs, I., Szekelyhidi, Z., Bajko, Z. *et al.* (2008) High-efficiency aminocarbonylation by introducing CO to a pressurized continuous flow reactor. *Org. Lett.*, **10** (8), 1589–1592.

55 O'Brien, M., Taylor, N., Polyzos, A., Baxendale, I.R., and Ley, S.V. (2011) Hydrogenation in flow: Homogeneous and heterogeneous catalysis using Teflon AF-2400 to effect gas–liquid contact at elevated pressure. *Chem. Sci.*, **2** (7), 1250–1257.

56 Becker, H. and Gartner, C. (2000) Polymer microfabrication methods for microfluidic analytical applications. *Electrophoresis*, **21** (1), 12–26.

57 Wang, J., Zhao, K., Shen, X., Zhang, W., Ji, S., Song, Y. *et al.* (2015) Microfluidic synthesis of ultra-small magnetic nanohybrids for enhanced magnetic resonance imaging. *J. Mater. Chem. C*, **3** (48), 12418–12429.

58 Bedore, M.W., Zaborenko, N., Jensen, K.F., and Jamison, T.F. (2010) Aminolysis of epoxides in a microreactor system: a continuous flow approach to beta-amino alcohols. *Org. Process Res. Dev.*, **14** (2), 432–440.

59 Acke, D.R.J. and Stevens, C.V. (2007) A HCN-based reaction under microreactor conditions: industrially feasible and continuous synthesis of 3,4-diamino-1H-isochromen-1-ones. *Green Chem.*, **9** (4), 386–390.

60 Yoon, T.H., Park, S.H., Min, K.I., Zhang, X.L., Haswell, S.J., and Kim, D.P. (2008) Novel inorganic polymer derived microreactors for organic microchemistry applications. *Lab Chip*, **8** (9), 1454–1459.

61 Jensen, K.F. (2001) Microreaction engineering – is small better? *Chem. Eng. Sci.*, **56** (2), 293–303.

62 Bourne, R.A., Han, X., Poliakoff, M., and George, M.W. (2009) Cleaner continuous photo-oxidation using singlet oxygen in supercritical carbon dioxide. *Angew. Chem. Int. Ed.*, **48** (29), 5322–5325.

63 Hintermair, U., Francio, G., and Leitner, W. (2013) A fully integrated continuous-flow system for asymmetric catalysis: enantioselective hydrogenation with supported ionic liquid phase catalysts using supercritical CO(2) as the mobile phase. *Chemistry*, **19** (14), 4538–4547.

64 Jutz, F., Andanson, J.M., and Baiker, A. (2011) Ionic liquids and dense carbon dioxide: a beneficial biphasic system for catalysis. *Chem. Rev.*, **111** (2), 322–353.

65 Han, X. and Poliakoff, M. (2012) Continuous reactions in supercritical carbon dioxide: problems, solutions and possible ways forward. *Chem. Soc. Rev.*, **41** (4), 1428–1436.

66 Bourne, R.A., Skilton, R.A., Parrott, A.J., Irvine, D.J., and Poliakoff, M. (2011) Adaptive process optimization for continuous methylation of alcohols in supercritical carbon dioxide. *Org. Process Res. Dev.*, **15** (4), 932–938.
67 Clark, P., Poliakoff, M., and Wells, A. (2007) Continuous flow hydrogenation of a pharmaceutical intermediate, 4-(3,4-dichlorophenyl)-3,4-dihydro-2H-naphthalenyidene-methylamine, in supercritical carbon dioxide. *Adv. Synth. Catal.*, **349** (17–18), 2655–2659.
68 Ager, D.J., de Vries, A.H.M., and de Vries, J.G. (2012) Asymmetric homogeneous hydrogenations at scale. *Chem. Soc. Rev.*, **41** (8), 3340–3380.
69 O'Brien, M., Baxendale, I.R., and Ley, S.V. (2010) Flow ozonolysis using a semipermeable teflon AF-2400 membrane to effect gas–liquid contact. *Org. Lett.*, **12** (7), 1596–1598.
70 Hermange, P., Lindhardt, A.T., Taaning, R.H., Bjerglund, K., Lupp, D., and Skrydstrup, T. (2011) Ex situ generation of stoichiometric and substoichiometric (CO)-C-12 and (CO)-C-13 and its efficient incorporation in palladium catalyzed aminocarbonylations. *J. Am. Chem. Soc.*, **133** (15), 6061–6071.
71 Brancour, C., Fukuyama, T., Mukai, Y., Skrydstrup, T., and Ryu, I. (2013) Modernized Low pressure carbonylation methods in batch and flow employing common acids as a CO source. *Org. Lett.*, **15** (11), 2794–2797.
72 Hubner, S., Bentrup, U., Budde, U., Lovis, K., Dietrich, T., Freitag, A. *et al.* (2009) An ozonolysis-reduction sequence for the synthesis of pharmaceutical intermediates in microstructured devices. *Org. Process Res. Dev.*, **13** (5), 952–960.
73 Hartman, R.L., Sahoo, H.R., Yen, B.C., and Jensen, K.F. (2009) Distillation in microchemical systems using capillary forces and segmented flow. *Lab Chip*, **9** (13), 1843–1849.
74 Song, Y.J., Doomes, E.E., Prindle, J., Tittsworth, R., Hormes, J., and Kumar, C. (2005) Investigations into sulfobetaine-stabilized cu nanoparticle formation: toward development of a microfluidic synthesis. *J. Phys. Chem. B*, **109** (19), 9330–9338.

www.ebook3000.com

12

Microfluidic Approaches for Designing Multifunctional Polymeric Microparticles from Simple Emulsions to Complex Particles

Jongmin Kim and Chang-Soo Lee

Chungnam National University, Department of Chemical Engineering and Applied Chemistry, 99 Daehak-ro, Yuseong-gu, Daejeon 34134, Republic of Korea

12.1 Introduction

In the past century, polymeric materials have been intensively used in a wide range of fields, such as nanotechnology [1], biotechnology [2], electronics [3], and clean and reusable energy [4]. Specifically, polymeric microparticles with sizes ranging from 1 to 1000 μm have been applied in diagnoses, tissue engineering, microreactions, and analytical applications, such as column supports and beads for flow cytometry. Generally, the overall functions of polymeric microparticles are strongly affected by their physical and chemical properties. For example, controlling the uniform size and shape of polymeric microparticles is essential for achieving quantitative encapsulation and uniformly controlled release kinetics [5]. Conventionally, polymeric microparticles are synthesized by emulsion polymerization, which utilizes a mechanical agitator to provide shear stress between two immiscible fluids. The provided shear stress forms an emulsion that can be polymerized into polymeric microparticles. However, the sizes of the emulsions and their cores and shells are usually nonuniform. To overcome the drawbacks of the conventional method, various emulsification methods, such as microchannel emulsification [6], membrane extrusion [7], microthread generation [8], and viscoelastic shearing [9], have been developed to obtain highly controlled size and uniformity. For the past few decades, microfluidics has emerged as one of the most attractive technologies for producing many polymeric materials that are useful for materials engineering, food science, and biotechnology [10]. Microfluidic approaches offer finely controlled environments for producing droplets. Thus, they are considered to be the most reliable alternatives to the conventional bulk emulsification method. The droplets formed through microfluidics can be directly used as microreactors for chemical and biochemical reactions [11]. Additionally, the droplets can be applied to synthesize photonic materials [12], micro objects, consumer and personal care products [13], particle-based display technologies [14], field-responsive rheological fluids [15], therapeutics [16], tissue engineering scaffolds [17], high-performance composite filler materials [18], and

Microfluidics: Fundamentals, Devices and Applications, First Edition.
Edited by Yujun Song, Daojian Cheng, and Liang Zhao.
© 2018 Wiley-VCH Verlag GmbH & Co. KGaA. Published 2018 by Wiley-VCH Verlag GmbH & Co. KGaA.

food additives [19]. For these applications, monodispersity and uniformity are required to exhibit constant and predictable behaviors during their application. In microfluidics, there are three representative fluid regimes, such as dripping, jetting, and coflowing, that can be controlled by hydrodynamic parameters. Specifically, dripping and jetting regimes are generally used for the formation of emulsions. The resulting emulsions are used as basic templates of various polymeric materials, such as single particles, hydrogels, and responsive microcapsules, with high uniformity and desired properties. In addition, the most important feature of microfluidics is the ability to precisely manipulate fluids from microliter to picoliter volumes or less. This character offers the possibility to form multiple emulsions that can be applied to produce various polymeric capsules and anisotropic particles with a finely controlled shape [20], size [20], pore size [21], core–shell structure [22], and chemical anisotropy [23]. In this chapter, we focus on introducing microfluidic approaches for the formation of multifunctional polymeric microparticles from simple microspheres to complex microparticles. Specifically, a brief introduction to dimensionless numbers and three fluidic regimes in microfluidics that depend on hydrodynamic parameters is discussed in Section 12.2. Then, the formation of complex emulsions and functional microparticles controlled by hydrodynamic parameters, phase separation, and spreading coefficients is discussed in Section 12.3. This chapter concludes with several efficient design routes for obtaining functional particles and provides perspectives on the future development of microfluidic devices.

12.2 Flow Regimes in Microfluidics: Dripping, Jetting, and Coflowing

Generally, microfluidic devices with T-junctions, flow-focusing, and coflowing channels are the most widely used geometries to form dripping (droplet formation), jetting, and coflowing (stable jetting) flow regimes, respectively, shown in Figure 12.1. In the literature, there are several studies that have addressed the formation mechanism from dripping to jetting regime in microfluidic devices [24]. Particularly, Nunes *et al.* intensively investigated the formation of the dripping, transition, and jetting regimes and their mechanisms by summarizing numerous simulation and experimental results [25]. Thus, in this section, we

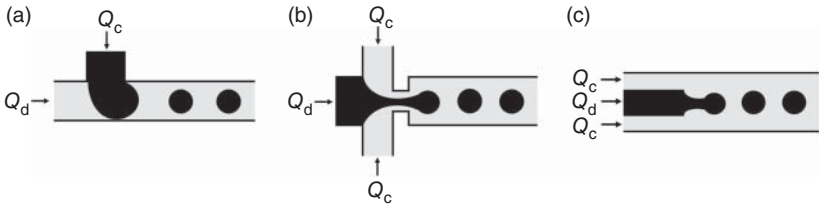


Figure 12.1 Three representative microfluidic devices: (a) T-junction microfluidic device; (b) flow-focusing microfluidic device; and (c) coflowing microfluidic device. The variables Q_d and Q_c represent the disperse phase and continuous phase, respectively.

www.ebook3000.com

focus on introducing the major dimensionless numbers with physical parameters in microfluidics. Subsequently, we discuss major parameters to control the flow status from dripping to jetting in each microfluidic device.

12.2.1 Dimensionless Numbers

The dripping and jetting regions in each microfluidic device can be controlled by several fluidic physical parameters, such as the geometries of the devices, ratio of the flow rates of the multiple fluids, densities of fluids (ρ), interfacial tension (γ), and viscosities of the fluids (μ). There are several dimensionless numbers that can be determined by the physical parameters of the fluids [24b, h, 26]. Among the many dimensionless numbers, we briefly introduce three representative numbers in microfluidics that are very useful for predicting and controlling the flow from the dripping to the jetting regimes in microfluidics. First is the Reynolds number (*Re*), which reflects the relative importance of inertial forces compared with the viscous stresses and is defined by the characteristic velocity U, where D_{H} is the hydraulic diameter of the microchannel and ρ is the density of the fluid. Typically, the *Re* is less than 1 ($Re \ll 1$) due to the small dimensions in microscale channels:

$$Re = \frac{\rho U D_H}{\mu} \tag{12.1}$$

Thus, the capillary number (*Ca*), defined by the relative importance between the interfacial tension and viscosity, is considered to be the most dominant parameter, where μ is the viscosity of the fluid, U is the characteristic velocity, and γ is the interfacial tension. The *Ca* in microfluidics generally ranges between 10^{-3} and 10:

$$Ca = \frac{\mu U}{\gamma} \tag{12.2}$$

The Weber number (*We*) is defined by the relative importance between inertia and the capillary pressure, where d is the characteristic diameter of the fluid. *We* is also considered to be a significant number when the inertial and capillary forces have dominant roles compared with the viscous stresses, such as the formation of jetting during coflowing with a high flow rate [24b, 25]:

$$We = Re \cdot Ca = \frac{\rho d U^2}{\gamma} \tag{12.3}$$

12.2.2 T-Junction Microfluidics

T-junction microfluidic devices were first introduced by Thorsen *et al.* Two immiscible fluids are injected into each inlet, and they meet at the T-junction, as shown in Figure 12.1a. In this state, three different fluidic regimes occur depending on the physical parameters of the fluids; the fluid regimes are referred to as squeezing, dripping, and jetting. Two of the major parameters to achieve each fluid regime are the capillary number (*Ca*) and the ratio of the flow rates among the fluids.

At low *Ca* ($<10^{-2}$) values, the shear forces are not sufficient to distort the disperse phase, resulting in confined fluidic environments formed by blocking the

channel through the growth of the disperse phase. In this state, the disperse phase increases its pressure, while a thin film of the continuous phase between the disperse phase and the wall of the device is generated at the T-junction. This squeezes the disperse phase, eventually breaking it up into droplets. This kind of pressure-dominated formation of droplets is known as "squeezing."

At relatively higher Ca ($>10^{-2}$) values, the continuous phase strongly shears the disperse phase without confining it at the junction, causing breakup into droplets. This shear-dominated formation of droplets is referred to as "dripping." The sizes of the droplets in these fluidic regimes can be controlled by the Ca and ratio of the flow rates between the continuous phase (Q_c) and disperse phase (Q_d) [27]. For example, Garstecki *et al.* reported that the size of drops formed at low Ca values mainly depends on the ratio of the flow rates of the disperse phase and the continuous phase (Q_d/Q_c) [27b]. The typical size of droplets formed at low Ca values is larger than that of the microchannels, while at relatively higher Ca values, the size of the droplets is affected by the local shear stress, forming smaller droplets than the size of the microchannel. At even higher Ca ($>10^{-1}$) values, jetting or coflowing occurs favorably [28]. For example, Gupta *et al.* demonstrated that jetting and stable coflowing were generated as the Ca increased from 0.1 to 0.3 within the given dimensions of the T-junction microfluidic devices [28b]. In addition, Guillot and Colin showed that stable coflowing developed as the flow rate of the disperse phase overcome that of the continuous phase, and the critical values of the flow rate were decreased by increasing the viscosity of the disperse phase [28a, 29].

12.2.3 Flow-Focusing Microfluidics

The flow-focusing microfluidic process, first introduced by Anna *et al.* [30], is also one of the most general methods for studying the flow formation from the dripping to jetting regime via controlling the physical parameters of the fluids [24c, 31]. In this microfluidic device, two immiscible fluids composed of a continuous phase and a disperse phase are injected into each inlet, and they are focused into one small orifice, as shown in Figure 12.1b. In this flow state, the symmetrical shear force driven by the continuous phase affects the disperse phase, leading to an elongated flow state. The elongation-dominated velocity field of the continuous phase consistently stretches the disperse phase into a thin jet, finally breaking up the thread into droplets. In the literature, many studies have been reported that simplify the laws or models for understanding the dominant transition mechanisms among the fluid regimes and predicting the size and distributions of the droplets [31b, f, i, 32]. Despite many contributions from researchers, the detailed dynamics still remain arguable, and further research is required. However, the Ca and ratio of the fluids (Q_d/Q_c) are typically considered to play a key role for controlling dripping and jetting [24b, c, 31b, 32d, 33]. For example, Liu and Zhang demonstrated that the transition among dripping, jetting, and stable coflowing is controlled by increasing the ratio of the fluids (Q_d/Q_c) from 0.6 to 3 at a given Ca (0.004). Humphry *et al.* showed the geometry dominant formation of stable coflowing by varying the ratio of the flow rates, and they revealed

www.ebook3000.com

that the boundary condition between stable and unstable coflowing occurred at $Q_d/Q_c \fallingdotseq 0.58$. In addition, the size of the droplets was controlled by simply varying the *Ca* and ratio of the flow rates [24c, 32a, b]. Generally, the droplet size decreased by increasing the ratio of the flow rates between the continuous phase and the disperse phase (Q_c/Q_d) [32a, b].

12.2.4 Coflowing Microfluidics

Coflowing is a simple method for forming droplets that was first utilized at the macroscale by Umbanhowar *et al.* and developed at the microscale by several pioneers [24a, d, e, 34]. Coflowing microfluidic devices are typically composed of a set of concentric capillaries: inner and outer capillaries with parallel alignment. Through each capillary, the disperse phase and continuous phase are individually injected, forming parallel flow, as shown in Figure 12.1c. In this state, the disperse phase becomes unstable due to surface tension, minimizing the interfacial area, which is known as the Rayleigh–Plateau instability [35]. This result leads to breaking the disperse phase into droplets. Specifically, there are two distinctive fluid regimes for droplet formation: dripping and jetting. For example, Utada *et al.* demonstrated that when each flow rate is low, droplets are formed at the tip of the inner capillary, which is known as dripping. When increasing the ratio of the flow rates (Q_c/Q_d), the size of the droplets decreases. When the size of the droplets is approximately similar to that of the tips, the fluids enter the jetting regime, which eventually becomes unstable due to the Rayleigh–Plateau instability. This result eventually leads the formation of droplets at the tip of the extended jet. It was reported that the transition between dripping and jetting relies on the force balance. There is a competition between the drag force, which stretches the emerging disperse phase, and the interfacial tension, which favors breaking up the disperse phase into droplets. This leads to the transition between dripping and jetting [24a]. In coflowing microfluidics, the size of the droplets decreases with the increasing ratio of the flow rates (Q_c/Q_d), while a decreasing interfacial tension leads to an increased droplet size [34b]. In addition, the sizes of the droplets generated in the dripping regime are relatively more monodisperse than those in the jetting regime because the point of the pinch-off is not consistent [34b]. Stable jetting (coflowing) is formed by controlling the *Ca*, viscosity of each fluid, and degree of confinement [24a, d, e, 34d, e]. For example, Guillot *et al.* demonstrated that a stable transition from jetting to dripping occurred by changing the *Ca*. At high *Ca* values, the fluid inertia becomes more important than the surface tension, leading to convective instability. In this state, increasing the fluid velocity is favorable, enabling the formation of stable jetting. In contrast, absolute stability is dominant at low *Ca* values, leading to disturbances in the fluid velocity. These results allowed the fluids to break into droplets [36]. In short, the formation of dripping and jetting in T-junction, flow-focusing, and coflowing microfluidics was discussed. *Ca* and the ratio of the flow rates are major parameters for controlling the dripping regime and the jetting regime. In the following sections, the formation of functional particles by using droplet microfluidic processes is discussed.

12.3 Design of Multifunctional Microparticles from Emulsions

In this section, we introduce the formation of multifunctional microparticles from emulsion templates by reviewing several studies. The parameters for controlling the formation of complex emulsions are categorized into three types. The first type includes the hydrodynamic parameters, the second includes the phase separation parameters, and the third includes parameters related to the spreading coefficient, as shown in Figure 12.2. The emulsion templates are polymerized by various methods, such as photopolymerization, redox polymerization, freezing and thawing, and ionic gelation. Several reports [37] have summarized each polymerization method and have provided examples. Therefore, we do not discuss polymerization methods in this chapter.

12.3.1 Microfluidic Approaches with Control of the Hydrodynamic Parameters

Studies to synthesize microspheres in microfluidic devices were first demonstrated by using hydrogenated fish oil, as reported by Nakajima and colleagues

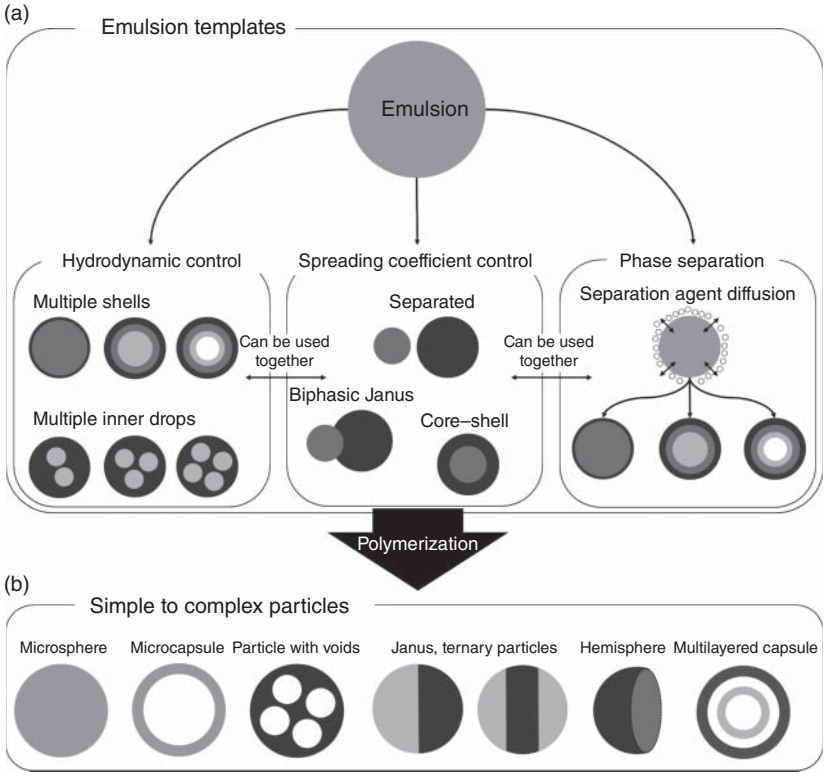
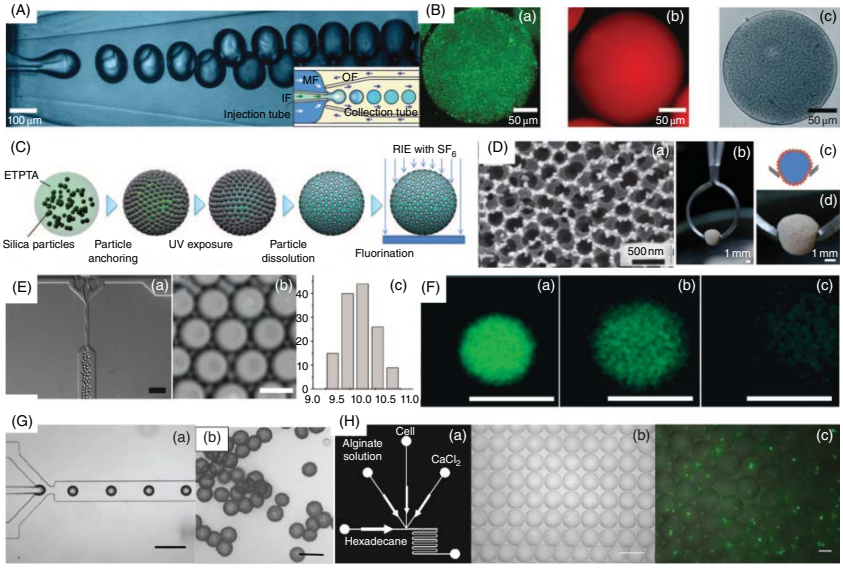


Figure 12.2 Simple and complex microparticles formed via the polymerization of emulsion templates; (a) complex emulsion templates formed by microfluidics with controlled parameters and (b) polymerized simple and complex particles.

www.ebook3000.com

[38]. A subsequent process, including an oil-in-water (O/W) emulsion formed at 70 °C and solidification by freezing and drying, produced monodisperse microspheres with a coefficient of variation (CV) of less than 5%. This result clearly showed a significant improvement compared with conventional suspension polymerization. Additionally, microfluidic processes provide unique opportunities for increasing the functionality of particles by incorporating various additives, such as dyes in a model drug, magnetic nanoparticles, quantum dots, and photonic crystals [39]. For example, Kim *et al.* showed the formation of temperature-sensitive microgels composed of poly(*N*-isopropylacrylamide) (pNIPAm) due to emulsion formation via a coflowing capillary microfluidic device and subsequent *in situ* redox polymerization, as shown in Figure 12.3A [39a]. According to their report, they simply controlled the size of the microsphere in the range of 10–1000 μm by varying the flow rates. In addition, they incorporated additives, such as polystyrene microparticles, quantum dots, and magnetic nanoparticles, in the NIPAm microspheres by physical entrapment, as shown in Figure 12.3B. Furthermore, the microspheres exhibited temperature-dependent volumetric change that could be applied in applications for novel biomaterials, such as drug delivery systems and artificial tissues [39a]. The ability to encapsulate small particles within microgels was utilized as a template to form Janus microsphere with strong water-repellent properties, as reported by Kim *et al.* [40]. Emulsions composed of photocurable resins containing silica particles were formed via coflowing capillary microfluidic devices. The formed emulsion was photopolymerized by UV irradiation, and then subsequent wet-etched silica particles were used as the templates, leading to the formation of microspheres with many cavities. Then, fluorination was applied to the microsphere with cavities, enabling the formation of Janus microspheres with superhydrophobic properties, as shown in Figure 12.3C. The superhydrophobicity of the Janus microspheres, which originated from the fluorinated cavity structures, was clearly demonstrated by handling liquid marbles composed of water droplets stabilized by the Janus microspheres, as shown in Figure 12.3D. The efficient method to form monodisperse Janus microspheres based on the microfluidics enables design routes for superhydrophobic materials with very uniform and unique properties, which are not easily created by the conventional technologies [40]. Microfluidic approaches have also been utilized to design efficient carriers for the encapsulation of drugs, peptides, proteins, and cells that can be utilized in various biomedical applications [39a, 42]. Specifically, biological, polymer-based hydrogels have been intensively studied due to their biocompatibility, low toxicity, and degradability. For example, Geest *et al.* demonstrated that biodegradable monodisperse hydrogels composed of dextran hydroxyethyl methacrylate (dex-HEMA) could be conveniently synthesized using microfluidic devices [41]. A W/O emulsion (dex-HEMA in oil) was formed in the microchannels, and then UV irradiation was subsequently used to form monodisperse dex-HEMA hydrogels (9.9 ± 0.3 μm), as shown in Figure 12.3E. The hydrogels exhibited the excellent ability to release pre-entrapped proteins fluorescein isothiocyanate labelled bovine serum albumin (FITC-BSA) within 30 s due to the spontaneous degradation of dex-HEMA, which was induced by hydrolysis in a sodium hydroxide solution, as shown in Figure 12.3F.



www.ebook3000.com

Figure 12.3 Formation of functional microspheres via microfluidic devices and their versatile applications as drug delivery systems, superhydrophobic Janus microspheres, biodegradable hydrogels, and cell encapsulants. (A) pNIPAm microspheres in a coflowing microfluidic device. (B) Composite materials that encapsulate fluorescent PS particles (a), quantum dots (b), and magnetic particles (c). ((A, B) Kim *et al*. 2007 [39a]. Reproduced with permission of John Wiley & Sons.) (C) A scheme showing the formation of superhydrophobic Janus microsphere via a coflowing microfluidic device and reactive ion etching (RIE) treatment. (D) A scanning electron microscopy (SEM) image showing the cavity structures on the superhydrophobic sites of the Janus microspheres (a) and their application by handling liquid marbles (b–d). ((C, D) Kim *et al*. 2010 [40]. Reproduced with permission of John Wiley & Sons.) (E) Biodegradable dex-HEMA hydrogels (a) and their optical images (b), indicating their size distribution uniformity (c). (F) Time sequence images showing the spontaneous release of FITC-BSAs (green) from the dex-HEMA hydrogels due to hydrolysis. ((E, F) Geest *et al*. 2005 [41]. Reproduced with permission of American Chemical Society.) (G) Spherical alginates in a microfluidic device with controlled gelation conditions (a) and their optical images showing monodisperse alginate microspheres (b). (Reproduced with permission from Ref. [42d]. Copyright 2006 American Chemical Society.) (H) A scheme showing the *in situ* encapsulation of yeast cells in alginate hydrogels via a microfluidic device (a), an optical image showing monodisperse alginate hydrogels (b), and a merged image showing *in situ* encapsulation of yeast cells (fluorescently tagged with green fluorescent protein, GFP) in the alginate hydrogels (c). (Choi *et al*. 2007 [43]. Reproduced with permission of Springer.)

Encapsulating bioactive materials in alginate beads is also an important issue [44], so many microfluidic-based approaches for the formation of alginate hydrogels have been developed [42d, j, 45]. According to Zhang *et al.*, hydrogels based on various biopolymers were formed using flow-focusing microfluidic devices. A biopolymer emulsion (W/O) was formed, and gelation occurred during the external diffusion of calcium ions from the continuous phase into the disperse phase (biopolymer phase). Specifically, spherical alginate hydrogels were formed by controlling the gelation conditions (time, cross-linking agents), as shown in Figure 12.3G [42d]. Additionally, Choi *et al.* demonstrated that the *in situ* encapsulation of cells in monodisperse alginate hydrogels could be conducted using microfluidic devices [43]. These authors utilized a microfluidic device with a specific geometry to improve the rapid emulsion formation and mixing efficiency. An alginate solution, a yeast cell suspension, and a calcium ion solution were injected into each inlet and met at the junction, leading to biased shear force-driven breakoff to form a monodisperse emulsion. Subsequently, gelation rapidly occurred due to chaotic mixing driven by the channel, allowing *in situ* encapsulation of cells in the monodisperse alginate hydrogels (coefficient value <1.1%), as shown in Figure 12.3H. It is expected that the microfluidic approach for the formation of alginate hydrogels can potentially be used for drug delivery systems, transplantation, biosensors, microreactors, and artificial cells [43].

One of the critical drawbacks of conventional methods, and even of microfluidic devices, is the difficulty of forming geometrically anisotropic particles (nonspherical particles) due to the intrinsically spherical shape of emulsion-driven processes due to surface minimization [30, 46]. To overcome these drawbacks, several pioneers have offered novel microfluidic approaches based on controlling the hydrodynamic parameters, such as the dimensions of the microfluidic channels and volume of the emulsions. These approaches have

enabled the formation of nonspherical emulsions within confined microfluidic devices, leading to the formation of geometrically anisotropic particles [39b, 47]. For example, Dendukuri *et al.* demonstrated the formation of nonspherical particles via the *in situ* UV irradiation of O/W emulsions formed using a T-junction microfluidic device [47]. The plug-shaped Norland optical adhesive (NOA) emulsion (O/W) was formed at low *Ca* values by changing the flow rates of the continuous phase (Q_c), while the disk-shaped NOA emulsion was formed by confining the droplets in shallow microchannels. The resulting emulsions were polymerized using UV irradiation, forming monodisperse plug- and disklike particles, as shown in Figure 12.4A,B. According to their report, the size of the nonspherical particles could be controlled by simply varying the flow rates of the two phases (Q_c, Q_d). Similarly, Xu *et al.* showed the formation of spherical and nonspherical particles using UV irradiation on emulsions formed with flow-focusing microfluidic devices [39b]. The shapes of the particles, such as microspheres, rods, disks, and ellipsoids, were predetermined by the emulsion within the confined microchannels, as shown in Figure 12.4C,D. According to their report, the shapes of the generated emulsion were highly dependent on the height and width of the microchannels.

Anisotropic particles with geometrical and chemical properties are intensively studied due to their unique properties and potential for various applications [37b, 48]. Specifically, Janus particles with two distinctly different properties, such as different compositions, geometries, functionalities, and electrical properties, are considered to be attractive materials for displays [23c], optical sensors [49], self-propulsive objects [50], Pickering emulsions [51], and anisotropic building blocks for self-assembly [52]. Microfluidic approaches with finely controlled hydrodynamic parameters have become promising routes for synthesizing Janus particles with highly uniform properties [23, 53]. For example, Prasad *et al.* demonstrated the formation of organic–inorganic hybrid Janus microspheres via microfluidic devices integrated with *in situ* UV polymerization. Organic and inorganic monomers, composed of functionalized perfluoropolyether (PFPE) and hydrolytic allylhydridopolycarbosilane (AHPCS), were individually injected into each inlet, and they subsequently met at a junction with a 2% sodium dodecyl sulfate (SDS) aqueous solution (continuous phase), leading to a Janus emulsion with two distinctive parts. The resultant templates were subsequently exposed to UV irradiation, forming hybrid Janus microspheres with organic–inorganic properties and high uniformity (CV < 3.5%), as shown in Figure 12.5A,B [23b]. According to their report, the sizes of the Janus microsphere were easily controlled by varying the ratio of the flow rates between the continuous phase (Q_c) and disperse phase (Q_d). Specifically, *Ca* played a key role in determining the formation of the Janus microspheres and relative size control of the organic and inorganic parts of the Janus microspheres. Symmetric Janus microspheres were only formed in a specific range of *Ca* for each organic and inorganic fluid with a constant Q_c. In addition, the size of the organic or inorganic parts could be manipulated by relatively increasing the *Ca* of the organic or inorganic fluids, allowing the formation of asymmetric Janus microspheres, as shown in Figure 12.5C. Additionally, Nisisako *et al.* demonstrated the formation of Janus microspheres with asymmetric electrical properties by using a y-shaped

www.ebook3000.com

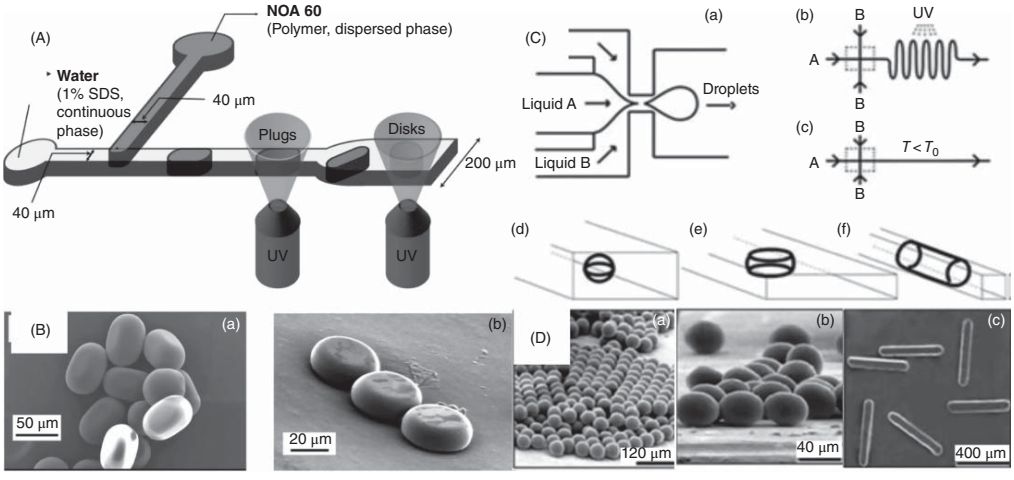


Figure 12.4 Formation of nonspherical microparticles via controlling the dimensions of the microchannels and volume of the emulsion. (A) A scheme describing the formation of plug-like and disklike microparticles in T-junction microfluidic device. (B) Scanning electron microscopy (SEM) images of the plug-like and disklike particles. (Reproduced with permission from Ref. [47]. Copyright 2005 American Chemical Society.) (C) A scheme describing the formation of microspheric, ellipsoidal, and rod-shaped microparticles in a flow-focusing microfluidic device.(D) SEM images of the spherical, ellipsoidal, and rod-shaped microparticles. (Reproduced with permission from Ref. [39b]. Copyright 2005 Wiley-VCH.)

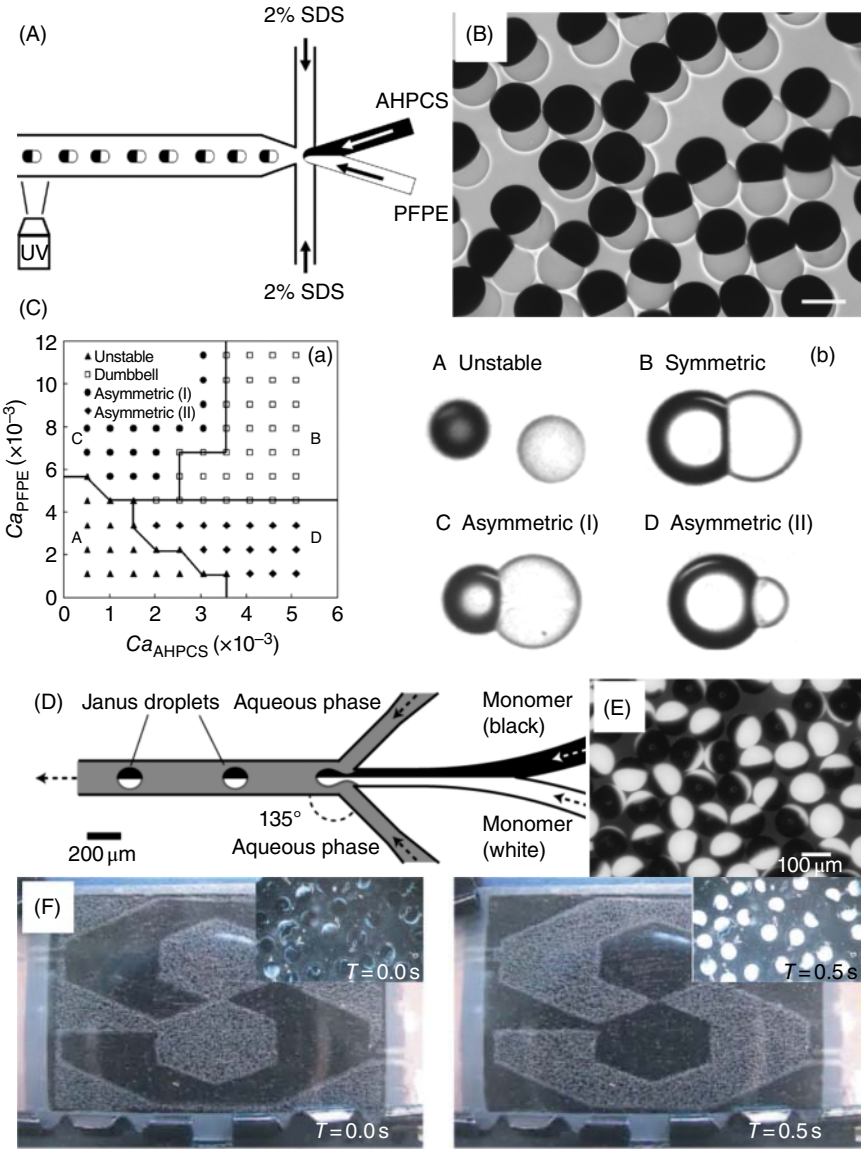


Figure 12.5 Formation of hybrid Janus microspheres via controlling the capillary number in the microfluidic device. (A) Janus microspheres with organic (PFPE) and inorganic (AHPCS) properties via microfluidic channels integrated with *in situ* UV polymerization and (B) an optical image showing monodisperse Janus microspheres with a PFPE part (white) and an AHPCS part (black). (C) A phase diagram of the Janus microspheres controlled by the capillary number (a) and four distinctive regimes (b). ((A–C) Prasad *et al*. 2009 [23b]. Reproduced with permission of John Wiley & Sons.) (D) Janus microspheres developed via a y-shaped microfluidic device. (E) An optical imaging showing monodisperse microspheres with two distinctive parts: carbon black (black) and titanium oxide (white). (F) Actuation of a display due to the color change between black and white depending on the direction of an applied electrical field; inset images show enlarged images of the Janus microspheres displaying either black or white depending on each direction. ((D–F) Nisisako *et al*. 2006 [23c]. Reproduced with permission of John Wiley & Sons.)

www.ebook3000.com

microfluidic device with a finely controlled capillary number (*Ca*) [23c]. First, carbon black and titanium oxides were dispersed in the monomers with initiators, forming black and white prepolymer solutions, respectively. Then, the two prepolymer solutions were injected into each inlet and met with an aqueous phase at the junction, leading to the formation of bicolored Janus emulsions. The resulting templates were thermally polymerized to form monodispersed Janus microsphere with two distinctive parts, as shown in Figure 12.5D,E. According to their report, the *Ca* was one of the most important parameters for consistently producing bicolored emulsions. At low *Ca* values with a constant Q_d, the stable formation of Janus emulsions occurred, while polydisperse emulsions were formed due to unstable breakage at high *Ca* values. The viscosity ratio between the two prepolymer solutions was also important; when the two prepolymer solutions flowed at the same flow rate with different viscosities, the formation of the bicolored Janus emulsion was unstable. The formed Janus microspheres with different charge properties were utilized for display technology by showing color changes between black and white, depending on the direction of an applied electric field, as shown in Figure 12.5F.

Design routes for the formation of anisotropic microparticles can be extended by using multiple emulsion templates, such as double emulsions (W/O/W or O/W/O) and triple emulsions (W/O/W/O or O/W/O/W). Moreover, the multilayered structures of such droplets are very useful for forming functional microcapsules for encapsulation that can be applied to cosmetics [54], drug delivery [55], and food applications [56]. There are numerous studies that have formed multiple emulsions within microfluidic devices that are applicable to form functional microcapsules [22, 57]. For example, Utada *et al.* demonstrated the formation of a double emulsion and microcapsules via a coflowing microfluidic device combined with flow focusing [57a]. The device was composed of two cylindrical capillaries that faced each other in a square capillary. The innermost fluid (aqueous) was injected via one cylindrical capillary, and the middle fluid (oil) was injected through between the capillary used for the innermost fluid and square capillary. The outermost fluid (aqueous) was simultaneously injected into the opposite side along the wall of the square capillary. All fluids were forced to meet at the orifice formed by the remaining cylindrical capillary, leading to the formation of highly monodisperse double emulsions. The size and number of inner droplets could be easily tuned by controlling the flow rates of all the fluids. Lorenceau *et al.* demonstrated the formation of double emulsions and polymersomes via coflowing microfluidic devices [58]. The device was composed of two cylindrical capillaries that faced each other in a square capillary. The innermost fluid (water) was injected via one cylindrical capillary, while the middle fluid (a diblock copolymer in a tetrahydrofuran (THF)-toluene cosolvent mixture) was injected between the capillary used for the innermost fluid and square capillary. The outermost fluid (glycerol/water mixture) was simultaneously injected into the opposite side along the wall of the square capillary. This caused the breakup of the coflow consisting of the inner and middle fluids due to hydrodynamic focusing, enabling the formation of highly monodisperse double emulsions, as shown in Figure 12.6A. In this state, polymersomes were formed due to self-assembled vesicle formation within the middle layer of the double emulsions, which was driven by the slow evaporation of the cosolvents,

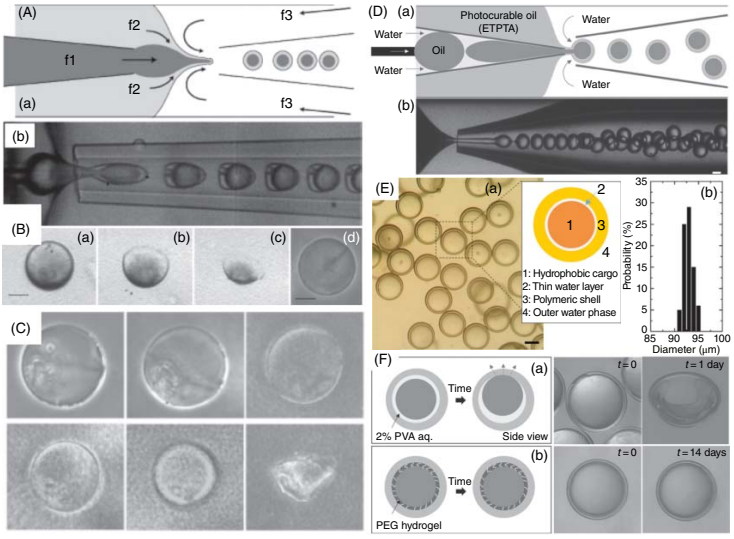


Figure 12.6 Formation of double and triple emulsions, polymersomes, and microcapsules via coflowing microfluidics. (A) A scheme (a) and an optical image (b) showing the formation of double emulsions via coflowing microfluidics. (B) A sequential image showing the formation of polymersomes from double emulsions by the evaporation of the cosolvents from the mixtures in the middle layer; as the solvents evaporated, the layers became invisible (a–c). Phase contrast images showing the polymersomes (d). (C) The shrinkage of the polymersomes driven by the osmotic pressure difference between the external and internal environments. ((A–C) Lorenceau *et al*. 2005 [58]. Reproduced with permission of American Chemical Society.) (D) Triple emulsions with an ultrathin water layer via coflowing microfluidics. (E) An optical image and quantitative analysis showing the uniformity of the monodisperse microcapsules with ultrathin water layers. (F) The buckling of the microcapsules due to leakage of the hydrophobic cargo (a) and the stable retention of the hydrophobic cargo within the microcapsules due to the hydrogel acting as a diffusion barrier (b). (Choi *et al*. 2016 [59]. Reproduced with permission of John Wiley & Sons.)

www.ebook3000.com

as shown in Figure 12.6B. The formed polymersomes exhibited the ability to controllably release the inner water fluids due to the osmotic pressure difference. When sucrose was added to the polymersome-dispersed solution, the polymersomes became shrunken due to the osmotic pressure difference between the inner and outer environments. This result causes the release of water from the polymersomes, indicating their potential application as microcapsules with stimuli-responsive releasing kinetics, as shown in Figure 12.6C. One of the emerging issues for the encapsulation of active materials is retaining a high efficiency while stably storing cargo materials. Particularly, high cost materials, for example, densely encapsulated fragrances, are challenging due to their volatility [60]. Recently, microfluidic approaches have offered an alternative way to form finely controlled microcapsules that are promising for overcoming the current technical hurdles in the industry [57d, 59]. Choi *et al.* demonstrated a high encapsulation efficiency for volatile hydrophobic cargo in polymeric microcapsules formed by the polymerization of triple emulsions including an ultrathin water layer [59]. Confined O/W biphasic fluids within a small injection capillary were subjected to coflow with an oil phase composed of a photocurable solution and subsequent formation of O/W/O double emulsions within the square capillary. The resulting O/W/O double emulsions were additionally emulsified by a continuous aqueous phase in the collection tube, leading to monodisperse triple emulsions (O/W/O/W) with an ultrathin water layer. This environment provided a high encapsulation efficiency for the hydrophobic cargo within the ultrathin water layer, as shown in Figure 12.6D,E. In addition, the triple emulsions were polymerized into monodisperse microcapsules with coefficient of variation of 2%, as shown in Figure 12.6E.Moreover, the retention of hydrophobic cargo could be enhanced via the formation of a hydrogel layer after polymerization of the hydrogel precursor in the ultrathin water layer. The hydrophobic cargo in the microcapsules without the hydrogel layer easily leaked within 1 day, showing buckling of the microcapsule. In contrast, the microcapsules with the hydrogel layer showed high retention ability for the cargo without any changes in the microcapsule until 14 days, as shown in Figure 12.6F. The unique environment for the hydrophobic cargo surrounded by the water thin layer enabled a high encapsulation efficiency and enhanced retention, which represented the capability of the microfluidics to form finely controlled functional materials with desirable properties.

Microfluidic devices also offer the capability to control the size, number, and compositions of inner droplets by varying the flow rates of various fluids and controlling the dimensions of the microchannel [20a, 22, 57a, 61]. For example, Okushima *et al.* demonstrated the formation of double emulsions and the ability to control the size of the emulsions as well as the number of encapsulated droplets by using glass-based T-junction microfluidic devices [22, 61d]. Basically, the double emulsions were formed by a two-step emulsification within the microchannels. The aqueous droplets were emulsified by the oil phase at the hydrophobic T-junction, and then the resultant W/O emulsion flowed through the hydrophilic T-junction. At this junction, the W/O emulsions were additionally emulsified by the aqueous phase, leading to the formation of monodisperse W/O/W double emulsions, as shown in Figure 12.7A. The size of the inner and outer droplets and

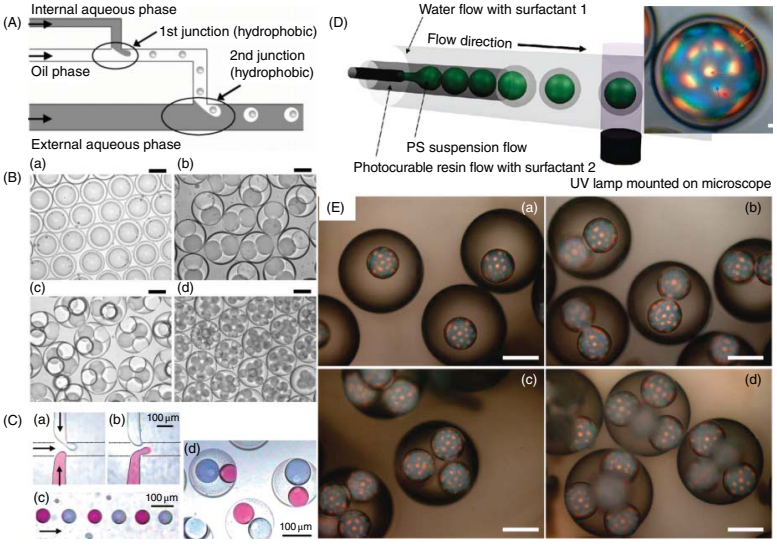


Figure 12.7 Formation of double emulsions and core–shell particles with controlled inner droplets or cores by varying the flow rates of each fluid. (A) A scheme showing double emulsions formed via a two-step emulsification in a T-junction microfluidic device. (B) Double emulsions with controlled sizes and numbers of inner droplets. (Nisisako *et al*. 2005 [61d]. Reproduced with permission of Royal Society of Chemistry.) (C) Controlling the compositions of inner droplets in double emulsions by using a cross junction. ((A, C) Okushima *et al*. 2004 [22]. Reproduced with permission of American Chemical Society.) (D) A scheme showing the encapsulation of crystalline colloidal arrays (CCAs) within microparticles after UV irradiation of double emulsions (inset: diffraction colors in the core–shell particles). (E) Core–shell particles with controlled numbers of inner cores within the CCAs. (Kim *et al*. 2008 [62]. Reproduced with permission of American Chemical Society.)

www.ebook3000.com

the number of the inner droplets could be manipulated by varying the flow rates, as shown in Figure 12.7B. In addition, the compositions of the inner droplets could be manipulated by the selective encapsulation of different core droplets at the cross junction (Figure 12.7C). It is expected that the capability to control the compositions of inner droplets within double emulsions is a promising approach for the development of droplet-based assays and multiplexed assays [63].

The ability to control the size and number of droplets within double emulsions has been utilized to encapsulate crystalline colloidal arrays (CCAs) [62]. The double-emulsion encapsulating CCAs were formed by a two-step coflowing emulsification. For example, an aqueous suspension of polystyrene nanoparticles (PS, 328 nm in diameter, 10 vol% particle loading) as inner droplets and a photocurable solution for the middle phase were subjected to coflow and break up into a W/O emulsion containing PS particles in the inner droplets. Then, the resultant W/O emulsions additionally met a continuous phase, leading to the formation of W/O/W emulsions containing PS nanoparticles. The double emulsions were polymerized by UV irradiation, forming microcapsules with CCAs, as shown in Figure 12.7D. The number of inner core-containing CCAs of the core–shell particles could be finely controlled by controlling the flow rates, as shown in Figure 12.7E. According to their report, the formed capsules exhibited unique diffraction patterns that were not achieved using conventional film-type arrays. In addition, enhanced stability of the CCAs was achieved due to the ability of the encapsulated environments to reduce the permeability of the ions and molecules that negatively affect the CCAs, as compared to the conventional technology.

Highly monodisperse complex emulsions with precisely controlled sizes, shells, and numbers of cores are expected to be applied in a wide range of applications. There are several approaches for producing complex emulsions, which have been proposed by several pioneers [20a, b, 64]. For example, Chu *et al.* demonstrated the formation of triple emulsions with precisely controlled sizes and numbers of inner droplets by using multiple coflowing microfluidic devices [20a]. First, the innermost fluids were injected into the injection capillary and emulsified by the coaxially flowing middle fluid through the transition capillary. The resulting single emulsion was additionally emulsified by the outermost fluids, leading to the formation of a triple emulsion, as shown in Figure 12.8A. The dimension of the orifice and the flow rates of all the fluids were important parameters for controlling the size of the inner, middle, and outer droplets. Depending on the parameters, hierarchical levels of multiple emulsions were formed, as shown in Figure 12.8B. The complex emulsions, W/O/W/O emulsions containing a photocurable NIPAm solution in the outer aqueous layer, were used as templates to form novel microcapsules with thermosensitivity. The formed pNIPAm particles exhibited highly controlled release properties that depended on the temperature. At low temperatures, the hydrogel shells of the microcapsules retained the oil droplet-containing water droplets, while the water droplets were released at high temperatures due to the shells shrinking and breaking, as shown in Figure 12.8C. The results demonstrated the potential of using microfluidics to design novel materials with highly engineered structures for the controlled releasing of active materials. The microfluidic approaches introduced so far with elegant control of

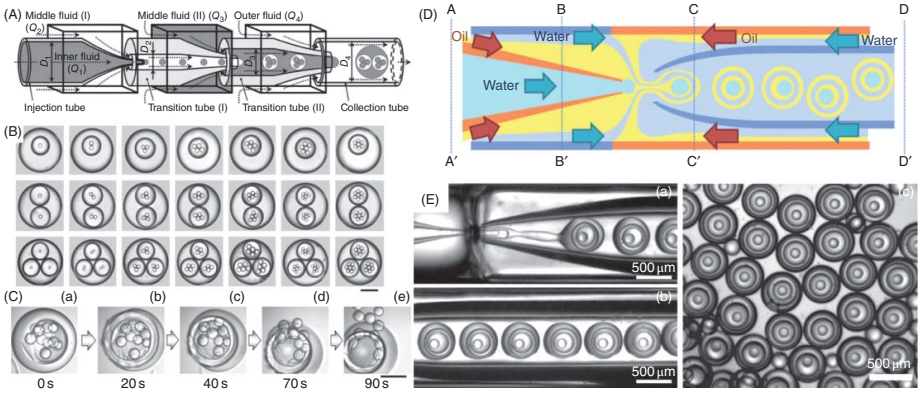


Figure 12.8 Formation of highly complex emulsions and thermoresponsive capsules via capillary microfluidic devices. (A) A scheme showing the formation of complex triple emulsions via stepwise emulsification in a coflowing microfluidic device. (B) Precisely controlling the size and number of inner droplets in the triple emulsions. (C) Sequential images showing the release of the oil and water droplets from microcapsules by increasing the temperature to 50 °C. (D) A scheme showing the one-step formation of W/O/W/O/W quadruple emulsions via a coflowing microfluidic device. (E) Optical images showing the formation of quadruple emulsions (a, b) and the high uniformity of the quadruple emulsions (c). (Adapted from Chu *et al*. 2007 [20a] and Kim and Weitz 2011 [20b].)

www.ebook3000.com

the hydrodynamic parameters enable the formation of complex emulsions with uniformly controlled properties. However, the approaches require complicated designs or serial devices composed of single-droplet generators. In addition, it is difficult to synchronize the frequency of droplet formation [20b]. An alternative route for forming highly ordered complex emulsions based on one-step emulsification in a microfluidic device was demonstrated by Kim and Weitz [20b]. To produce the complex emulsions, a square capillary and two cylindrical capillaries were used for injection and collected individually. Briefly, two biphasic fluid streams (O_1/W_1, W_2/O_4) were injected into both ends of the square capillary, forming three coaxial interfaces. In the meantime, the inner most fluid (W_3) was injected into one end, triggering the breakup of the interface. This result enabled the formation of monodisperse quadruple emulsions in a single step, as shown in Figure 12.8D,E. The results shown in this study are potentially applicable in many areas, such as novel drug carriers, displays, and microreactors due to the stability, simplicity, and controllability of the process.

12.3.2 Microfluidic Approaches with Phase Separation

Another alternative route for complex emulsions based on phase separation within a simple microfluidic device was recently introduced by Choi *et al.* [20d]. Briefly, a disperse phase composed of a monomer and a good solvent for the monomer (D-solvent) and a continuous phase composed of a separation agent (SA) and a good solvent for the SA (C-solvent) were used to form a single emulsion. The disperse phase and the continuous phase that contained the SA were injected into each inlet of a simple cross-shaped microfluidic channel, and they met at the flow-focusing regime, leading to the formation of single droplets. In this state, the SAs in the continuous phase diffused into the disperse phase via the interface, leading to the transformation of the single emulsions into complex emulsions, as shown in Figure 12.9A,B. The types of emulsions, between double, triple, and quadruple emulsions, were controlled by the rate of phase separation, as shown in Figure 12.9C. The combination of the phase separation and dewetting processes due to the changing interfacial energy further transformed the emulsions into Janus double and Janus triple emulsions, as shown in Figure 12.9D. In addition, the selective encapsulation of components could be simultaneously achieved during the formation of the complex emulsions. The encapsulation selectivity of each component to a compartment highly relied on their solubility in each phase. For example, water-soluble fluorescent dyes (red color) were selectively encapsulated into the water-rich phase of the quadruple emulsions, as shown in Figure 12.9E. Also, hydrophobic (green) and hydrophilic (red) fluorescent dyes were selectively encapsulated into water-poor and water-rich phases, respectively, during the formation of double and Janus emulsions, as shown in Figure 12.9F. The results shown in their report are promising for the facile encapsulation of drugs into selective compartments without further processing and for designing anisotropic particles from complex emulsion templates.

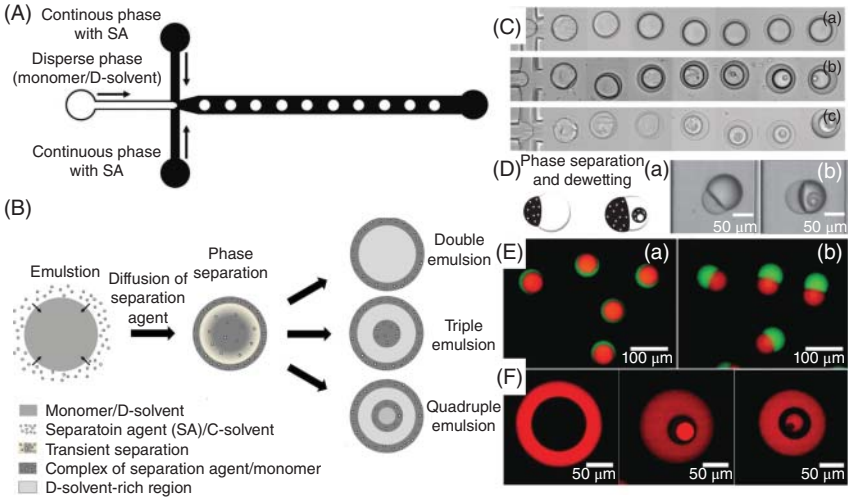


Figure 12.9 Formation of complex emulsions via phase separation and their application for selectively encapsulating cargo molecules. (A) A scheme showing the formation of complex emulsions from a single droplet within a simple microfluidic device. (B) A scheme showing the transformation of a single emulsion into a complex emulsion driven by phase separation. (C) A sequential image showing the evolution of phase separation to form a double (a), a triple (b), and a quadruple emulsion (c). (D) A scheme (a) and optical images (b) of the Janus double and Janus triple emulsions formed by combining phase separation and dewetting. (E) A fluorescent image showing that the hydrophilic (red) and hydrophobic (green) dyes were simultaneously introduced into each part of the double emulsion (a) and Janus emulsion (b). (F) Confocal images showing the selective encapsulation of hydrophobic dyes (red) into the shell regions of each multiple emulsion. (Choi *et al*. 2013 [20d]. Reproduced with permission of John Wiley & Sons.)

In addition, complex emulsions with ordered internal structures were formed due to the phase separation of a ternary mixture, as recently demonstrated by Haase and Brujic [20c]. Briefly, a disperse phase composed of an oil, a polar solvent, and water flow was injected through a capillary into a continuous phase (aqueous) to initiate dripping. During the formation of the droplets, mass transfer between the two phases occurred due to diffusion out toward the continuous phase of the oil and polar solvent with simultaneous diffusion in toward the disperse phase of the water with the surfactant. This process changed the composition within the droplets and subsequently induced spinodal decomposition or nucleation and growth under nonequilibrium conditions. Subsequently, coalescence occurred and these cycles repeated until the phase separation stopped, finally forming a complex emulsion. Depending on the initial composition of the mixtures, the number of cycles can be changed to control the final form of the complex emulsion, as shown in Figure 12.10A. The approach was utilized to form poly(methyl methacrylate) (PMMA) microcapsules with selective cargo loading capabilities and unilamellar vesicles, as shown in Figure 12.10B. Additionally, droplets with complex internal structures could be formed by using lipids and the coalesce of oil layers upon droplet contact with subsequent evaporation of the oil from the outer layer, as shown in Figure 12.10C.

www.ebook3000.com

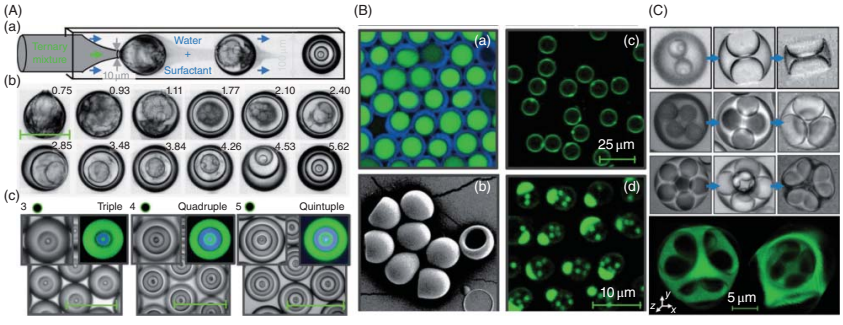
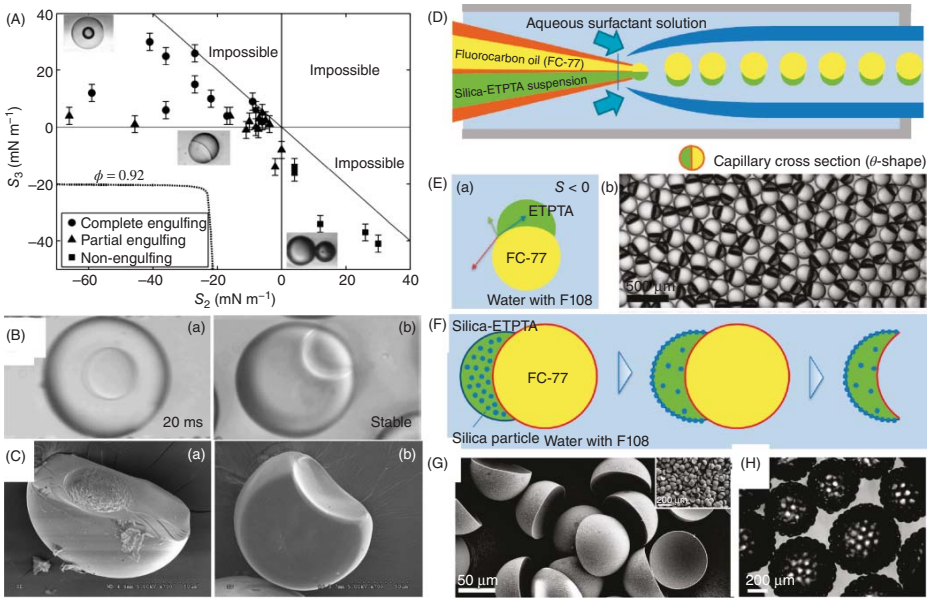


Figure 12.10 Formation of complex emulsions through phase separation in a coflowing microfluidic device and their application to form capsules, vesicles, and droplets with highly ordered internal structures. (A) A scheme showing the formation (a) and evolution (b) of complex emulsions (c), such as double, triple, quadruple, and quintuple emulsions. (B) Fluorescent images showing PMMA microcapsules with the selective encapsulation of different dyes (a), and their collapsed structures are shown in the SEM image (b). The fluorescent images show the unilamellar vesicles (c) and the vesicles encapsulating 1 μm colloids (d). (C) Shape changes of the complex emulsions with different numbers of water droplets ($N = 2$: top, $N = 4$: middle, and $N = 6$: bottom) and ordered inner structures in the final state (fluorescent image; green). (Haase and Brujic 2014 [20c]. Reproduced with permission of John Wiley & Sons.)



www.ebook3000.com

12.3.3 Microfluidic Approaches with Spreading Coefficients

In addition to controlling the hydrodynamic parameters and phase separation, spreading coefficients are also useful parameters for controlling the structures of emulsions. Normally, the structures of a three-phase system, for example, double emulsions at the equilibrium state, are determined by their minimum interfacial energy. Torza and Mason mathematically derived the spreading coefficient that is related to the interfacial tension of all three phases [65]. The spreading coefficient is defined by

$$S_i = \gamma_{jk} - (\gamma_{ij} + \gamma_{ik}) \tag{12.4}$$

where γ_{jk} is the interfacial tension between phase j and k [65a, 66]. There are three structures that are predicted by the spreading coefficient: (i) complete engulfing when $S_1 < 0$, $S_2 > 0$, and $S_3 < 0$, (ii) non-engulfing when $S_1 < 0$, $S_2 < 0$, and $S_3 > 0$, and (iii) partial engulfing when $S_1 < 0$, $S_2 < 0$, and $S_3 < 0$. Previously, it was reported that different structures of emulsions could be formed even though the same liquids were used [61a]. Pannacci *et al.* used the spreading coefficient to demonstrate the possibility of achieving structural differences in the emulsion state, such as equilibrium and nonequilibrium states [66b]. First, double emulsions were formed via a flow-focusing microfluidic device and left to reach equilibrium. The three different structures at equilibrium included complete engulfing (core–shell), partial engulfing, and separation. The results matched the predictions from the spreading coefficient well, as shown in Figure 12.11A. Then, early states of the emulsions were analyzed, which showed the evolution of the structures from complete double emulsions to partial engulfing emulsions, as shown in Figure 12.11B. The results indicated structural differences between the emulsions at equilibrium and nonequilibrium states. This characteristic was utilized to form anisotropic particles that could not be formed using conventional methods. When the double emulsions were polymerized at a nonequilibrium state, core–shell particles were formed. In contrast, Janus particles (spherical particles with dimple structures) were formed when the double emulsion was polymerized at the equilibrium state, as shown in Figure 12.11C. There are several reports that show the formation of emulsions, polymersomes, and

Figure 12.11 Formation of anisotropic microparticles from partial engulfing (paired) emulsions via microfluidic devices with controlled spreading coefficients. (A) A phase diagram showing three different structures depending on the spreading coefficient. (B) Core–shell double emulsion at a nonequilibrium state (a) and partial engulfing at the equilibrium state (b). (C) The polymerized particles with core–shell and dimple structures, shown in the SEM images. ((A–C) Pannacci *et al*. 2008 [66b]. Reproduced with permission of American Physical Society.) (D) A scheme showing the formation of paired emulsions via a coflowing microfluidic device. (E) A scheme showing the formation of paired droplets with a negative spreading coefficient for ethoxylated trimethylolpropane triacrylate (ETPTA) (a) and an image showing monodisperse paired emulsions formed via the microfluidic device (b). (F) A scheme showing the procedure of the formation of an amphiphilic microparticle from a paired droplet. (G) A SEM image showing Moiré fringe formed only on the convex surfaces of the amphiphilic particles and a SEM image with low magnification. (H) An optical image showing the stabilization of fluorocarbon oil droplets with amphiphilic microparticles. (Kim *et al*. 2011 [67b]. Reproduced with permission of American Chemical Society.)

liposomes with controlled interfacial energies or spreading coefficients. These resultant emulsions or polymersomes were used to form anisotropic particles, monodisperse capsules, and multicompartment capsules [23a, 67]. For example, Kim *et al.* utilized the spreading coefficient to form crescent moon-shaped microparticles, which could be used as particle stabilizers [67b]. Briefly, the coflowing microfluidic device contained a theta-shaped injection capillary, a collection capillary, and a square capillary. A fluorocarbon oil and photocurable solution containing silica colloids were injected into the theta injection capillary to the aqueous phase, leading to breakage and droplet formation, as shown in Figure 12.11D. The spreading coefficient of each oil–water interface was strongly negative, implying that the oil phase and photocurable solution formed paired emulsions, as shown in Figure 12.11E. Crescent moon-shaped microparticles were formed after UV irradiation of the paired emulsion comprised of a photocurable solution and fluorocarbon oil followed by the subsequent removal of the fluorocarbon oil. The crescent moon-shaped microparticles exhibited amphiphilic properties due to the different surface structures of the inner curved (concave) and outer curved (convex) regions that originated due to the selective adsorption of silica colloids at the concave surfaces, as shown in Figure 12.11F. The formed crescent moon-shaped microparticles were highly stabilize at the oil–water interface due to their structural advantages and amphiphilic properties: a concave hydrophobic surface and convex hydrophilic surface, as shown in Figure 12.11G,H. The results shown in the study demonstrated that microfluidic processes with controlled spreading coefficients are highly promising for designing anisotropic particles with uniform shapes and sizes [67b].

12.4 Conclusions and Outlooks

This chapter described the formation of complex emulsions and the synthesis of new functional particles using microfluidic technology. Precisely designed microfluidic devices with controlled hydrodynamic parameters, phase separation, and spreading coefficients allow us to produce functional microparticles with novel geometries and physicochemical properties. Specifically, we can produce precisely controlled core–shell structures with precise numbers and sizes and high uniformity. The controlled inner/external structures of the microparticles are highly unique and cannot be achieved via conventional manufacturing processes. The microfluidic technology for synthesizing functional materials is still in its early stages, and the following issues will be further considered. First, a comparative analysis between conventional technologies and microfluidic processes is required to show the strength of microfluidic processes for designing complex functional microparticles. Next, studying the relationship between the structural characteristics of microparticles and their corresponding functionalities will be required, which will be useful for the synthesis of structurally diverse functional particles. Since the productivity of individual microfluidic devices is relatively low, a scale-up process for mass production still remains a possible area of future work.

www.ebook3000.com

References

1 Grosse, C. and Delgado, A.V. (2010) *Curr. Opin. Colloid Interface Sci.*, **15**, 145–159.
2 Nagarwal, R.C., Kant, S., Singh, P.N., Maiti, P., and Pandit, J.K. (2009) *J. Controlled Release*, **136**, 2–13.
3 Wood, V., Panzer, M.J., Caruge, J.M., Halpert, J.E., Bawendi, M.G., and Bulovic, V. (2010) *Nano Lett.*, **10**, 24–29.
4 Rhodes, R., Asghar, S., Krakow, R., Horie, M., Wang, Z.J., Turner, M.L., and Saunders, B.R. (2009) *Colloids Surf., A*, **343**, 50–56.
5 De La Vega, J.C., Elischer, P., Schneider, T., and Hafeli, U.O. (2013) *Nanomedicine*, **8**, 265–285.
6 Kawakatsu, T., Kikuchi, Y., and Nakajima, M. (1997) *J. Am. Oil Chem. Soc.*, **74**, 317–321.
7 (a) Nakashima, T., Shimizu, M., and Kukizaki, M. (2000) *Adv. Drug Delivery Rev.*, **45**, 47–56; (b) Nakashima, T., Shimizu, M., and Kukizaki, M. (1992) *Key Engineering Materials*, vol. **61**, Trans Tech Publications, pp. 513–516.
8 Ganan-Calvo, A.M. (1998) *Phys. Rev. Lett.*, **80**, 285–288.
9 (a) Mason, T.G. and Bibette, J. (1997) *Langmuir*, **13**, 4600–4613; (b) Perrin, P. (1998) *Langmuir*, **14**, 5977–5979.
10 (a) Whitesides, G.M. (2006) *Nature*, **442**, 368–373; (b) Stone, H.A., Stroock, A.D., and Ajdari, A. (2004) *Annu. Rev. Fluid Mech.*, **36**, 381–411.
11 (a) Song, H., Chen, D.L., and Ismagilov, R.F. (2006) *Angew. Chem. Int. Ed.*, **45**, 7336–7356; (b) Theberge, A.B., Courtois, F., Schaerli, Y., Fischlechner, M., Abell, C., Hollfelder, F., and Huck, W.T.S. (2010) *Angew. Chem. Int. Ed.*, **49**, 5846–5868.
12 (a) Kim, S.H., Lee, S.Y., Yang, S.M., and Yi, G.R. (2011) *NPG Asia Mater.*, **3**, 25–33; (b) Sacanna, S. and Pine, D.J. (2011) *Curr. Opin. Colloid Interface Sci.*, **16**, 96–105.
13 Pardeike, J., Hommoss, A., and Muller, R.H. (2009) *Int. J. Pharm.*, **366**, 170–184.
14 (a) Comiskey, B., Albert, J.D., Yoshizawa, H., and Jacobson, J. (1998) *Nature*, **394**, 253–255; (b) Oh, S.W., Kim, C.W., Cha, H.J., Pal, U., and Kang, Y.S. (2009) *Adv. Mater.*, **21**, 4987–4991.
15 Stanway, R. (2004) *Mater. Sci. Technol.*, **20**, 931–939.
16 Velasco, D., Tumarkin, E., and Kumacheva, E. (2012) *Small*, **8**, 1633–1642.
17 Chung, B.G., Lee, K.H., Khademhosseini, A., and Lee, S.H. (2012) *Lab Chip*, **12**, 45–59.
18 Thangawng, A.L., Howell, P.B., Spillmann, C.M., Naciri, J., and Ligler, F.S. (2011) *Lab Chip*, **11**, 1157–1160.
19 Gouin, S. (2004) *Trends Food Sci. Technol.*, **15**, 330–347.
20 (a) Chu, L.Y., Utada, A.S., Shah, R.K., Kim, J.W., and Weitz, D.A. (2007) *Angew. Chem. Int. Ed.*, **46**, 8970–8974; (b) Kim, S.H. and Weitz, D.A. (2011) *Angew. Chem. Int. Ed.*, **50**, 8731–8734; (c) Haase, M.F. and Brujic, J. (2014) *Angew. Chem. Int. Ed.*, **53**, 11793–11797; (d) Choi, C.H., Weitz, D.A., and Lee, C.S. (2013) *Adv. Mater.*, **25**, 2536–2541.

21 Lee, D. and Weitz, D.A. (2009) *Small*, **5**, 1932–1935.

22 Okushima, S., Nisisako, T., Torii, T., and Higuchi, T. (2004) *Langmuir*, **20**, 9905–9908.

23 (a) Nie, Z.H., Li, W., Seo, M., Xu, S.Q., and Kumacheva, E. (2006) *J. Am. Chem. Soc.*, **128**, 9408–9412; (b) Prasad, N., Perumal, J., Choi, C.H., Lee, C.S., and Kim, D.P. (2009) *Adv. Funct. Mater.*, **19**, 1656–1662; (c) Nisisako, T., Torii, T., Takahashi, T., and Takizawa, Y. (2006) *Adv. Mater.*, **18**, 1152–1156.

24 (a) Utada, A.S., Fernandez-Nieves, A., Stone, H.A., and Weitz, D.A. (2007) *Phys. Rev. Lett.*, **99**, 094502; (b) Christopher, G.F. and Anna, S.L. (2007) *J. Phys. D: Appl. Phys.*, **40**, R319–R336; (c) Abate, A.R., Poitzsch, A., Hwang, Y., Lee, J., Czerwinska, J., and Weitz, D.A. (2009) *Phys. Rev. E*, **80**, 026310; (d) Guillot, P., Colin, A., and Ajdari, A. (2008) *Phys. Rev. E*, **78**, 016307; (e) Herrada, M.A., Ganan-Calvo, A.M., and Guillot, P. (2008) *Phys. Rev. E*, **78**, 046312; (f) Seemann, R., Brinkmann, M., Pfohl, T., and Herminghaus, S. (2012) *Rep. Prog. Phys.*, **75**, 016601; (g) Gu, H., Duits, M.H.G., and Mugele, F. (2011) *Int. J. Mol. Sci.*, **12**, 2572–2597; (h) Zhao, C.X. and Middelberg, A.P.J. (2011) *Chem. Eng. Sci.*, **66**, 1394–1411.

25 Nunes, J.K., Tsai, S.S.H., Wan, J., and Stone, H.A. (2013) *J. Phys. D: Appl. Phys.*, **46**, 114002.

26 Squires, T.M. and Quake, S.R. (2005) *Rev. Mod. Phys.*, **77**, 977–1026.

27 (a) van Steijn, V., Kleijn, C.R., and Kreutzer, M.T. (2009) *Phys. Rev. Lett.*, **103**, 214501; (b) Garstecki, P., Fuerstman, M.J., Stone, H.A., and Whitesides, G.M. (2006) *Lab Chip*, **6**, 437–446.

28 (a) Guillot, P. and Colin, A. (2005) *Phys. Rev. E*, **72**, 066301; (b) Gupta, A., Murshed, S.M.S., and Kumar, R. (2009) *Appl. Phys. Lett.*, **94**, 164107; (c) Gupta, A. and Kumar, R. (2010) *Phys. Fluids*, **22**, 122001.

29 Tice, J.D., Lyon, A.D., and Ismagilov, R.F. (2004) *Anal. Chim. Acta*, **507**, 73–77.

30 Anna, S.L., Bontoux, N., and Stone, H.A. (2003) *Appl. Phys. Lett.*, **82**, 364–366.

31 (a) Anna, S.L. and Mayer, H.C. (2006) *Phys. Fluids*, **18**, 121512; (b) Cubaud, T. and Mason, T.G. (2008) *Phys. Fluids*, **20**, 053302; (c) Yobas, L., Martens, S., Ong, W.L., and Ranganathan, N. (2006) *Lab Chip*, **6**, 1073–1079; (d) Humphry, K.J., Ajdari, A., Fernandez-Nieves, A., Stone, H.A., and Weitz, D.A. (2009) *Phys. Rev. E*, **79**, 056310; (e) Berthier, J., Le Vot, S., Tiquet, P., David, N., Lauro, D., Benhamou, P.Y., and Rivera, F. (2010) *Sens. Actuators, A*, **158**, 140–148; (f) Funfschilling, D., Debas, H., Li, H.Z., and Mason, T.G. (2009) *Phys. Rev. E*, **80**, 015301(R); (g)Lapierre, F., Wu, N., and Zhu, Y. (2011) Smart nano-micro materials and devices. International Society for Optics and Photonics, pp. 82040H-82047H; (h)Lee, W., Walker, L.M., and Anna, S.L. (2008) The XV International Congress on Rheology: The Society of Rheology 80th Annual Meeting, vol. 1027, AIP Publishing, pp. 994–996; (i) Lee, W., Walker, L.M., and Anna, S.L. (2009) *Phys. Fluids*, **21**, 032103; (j) Ong, W.L., Hua, J.S., Zhang, B.L., Teo, T.Y., Zhuo, J.L., Nguyen, N.T., Ranganathan, N., and Yobas, L. (2007) *Sens. Actuators, A*, **138**, 203–212; (k) Peng, L., Yang, M., Guo, S.S., Liu, W., and Zhao, X.Z. (2011) *Biomed. Microdevices*, **13**, 559–564.

www.ebook3000.com

32 (a) Nie, Z.H., Seo, M.S., Xu, S.Q., Lewis, P.C., Mok, M., Kumacheva, E., Whitesides, G.M., Garstecki, P., and Stone, H.A. (2008) *Microfluid. Nanofluid.*, **5**, 585–594; (b) Garstecki, P., Stone, H.A., and Whitesides, G.M. (2005) *Phys. Rev. Lett.*, **94**, 164501; (c) Dollet, B., van Hoeve, W., Raven, J.P., Marmottant, P., and Versluis, M. (2008) *Phys. Rev. Lett.*, **100**, 034504; (d) Ward, T., Faivre, M., Abkarian, M., and Stone, H.A. (2005) *Electrophoresis*, **26**, 3716–3724.

33 Seo, M., Paquet, C., Nie, Z.H., Xu, S.Q., and Kumacheva, E. (2007) *Soft Matter*, **3**, 986–992.

34 (a) Umbanhowar, P.B., Prasad, V., and Weitz, D.A. (2000) *Langmuir*, **16**, 347–351; (b) Cramer, C., Fischer, P., and Windhab, E.J. (2004) *Chem. Eng. Sci.*, **59**, 3045–3058; (c) Jeong, W.J., Kim, J.Y., Choo, J., Lee, E.K., Han, C.S., Beebe, D.J., Seong, G.H., and Lee, S.H. (2005) *Langmuir*, **21**, 3738–3741; (d) Utada, A.S., Fernandez-Nieves, A., Gordillo, J.M., and Weitz, D.A. (2008) *Phys. Rev. Lett.*, **100**, 014502; (e) Guillot, P., Colin, A., Utada, A.S., and Ajdari, A. (2007) *Phys. Rev. Lett.*, **99**, 104502; (f) Castro-Hernandez, E., Gundabala, V., Fernandez-Nieves, A., and Gordillo, J.M. (2009) *New J. Phys.*, **11**, 075021; (g) Cordero, M.L., Gallaire, F., and Baroud, C.N. (2011) *Phys. Fluids*, **23**, 094111.

35 Rayleigh, L. (1892) *Philos. Mag.*, **34**, 145–154.

36 Guillot, P., Ajdari, A., Goyon, J., Joanicot, M., and Colin, A. (2009) *C.R. Chim.*, **12**, 247–257.

37 (a) Tumarkin, E. and Kumacheva, E. (2009) *Chem. Soc. Rev.*, **38**, 2161–2168; (b) Dendukuri, D. and Doyle, P.S. (2009) *Adv. Mater.*, **21**, 4071–4086; (c) Zhang, H., Tumarkin, E., Sullan, R.M.A., Walker, G.C., and Kumacheva, E. (2007) *Macromol. Rapid Commun.*, **28**, 527–538.

38 Sugiura, S., Nakajima, M., Tong, J.H., Nabetani, H., and Seki, M. (2000) *J. Colloid Interface Sci.*, **227**, 95–103.

39 (a) Kim, J.W., Utada, A.S., Fernandez-Nieves, A., Hu, Z.B., and Weitz, D.A. (2007) *Angew. Chem. Int. Ed.*, **46**, 1819–1822; (b) Xu, S., Nie, Z., Seo, M., Lewis, P., Kumacheva, E., Stone, H.A., Garstecki, P., Weibel, D.B., Gitlin, I., and Whitesides, G.M. (2005) *Angew. Chem. Int. Ed.*, **44**, 3799; (c) Hwang, D.K., Dendukuri, D., and Doyle, P.S. (2008) *Lab Chip*, **8**, 1640–1647.

40 Kim, S.H., Lee, S.Y., and Yang, S.M. (2010) *Angew. Chem. Int. Ed.*, **49**, 2535–2538.

41 De Geest, B.G., Urbanski, J.P., Thorsen, T., Demeester, J., and De Smedt, S.C. (2005) *Langmuir*, **21**, 10275–10279.

42 (a) Ross, C.J.D., Bastedo, L., Maier, S.A., Sands, M.S., and Chang, P.L. (2000) *Human Gene Ther.*, **11**, 2117–2127; (b) Liu, Z.C. and Chang, T.M.S. (2006) *Liver Transpl.*, **12**, 566–572; (c) Cirone, P., Bourgeois, J.M., and Chang, P.L. (2003) *Hum. Gene Ther.*, **14**, 1065–1077; (d) Zhang, H., Tumarkin, E., Peerani, R., Nie, Z., Sullan, R.M.A., Walker, G.C., and Kumacheva, E. (2006) *J. Am. Chem. Soc.*, **128**, 12205–12210; (e) Chicheportiche, D. and Reach, G. (1988) *Diabetologia*, **31**, 54–57; (f) Edd, J.F., Di Carlo, D., Humphry, K.J., Koster, S., Irimia, D., Weitz, D.A., and Toner, M. (2008) *Lab Chip*, **8**, 1262–1264; (g) Dove, A. (2002) *Nat. Biotechnol.*, **20**, 339–343; (h) Breguet, W., Gugerli, R., Pernetti, M., von Stockar, U., and Marison, I.W. (2005) *Langmuir*, **21**,

9764–9772; (i) DeLong, S.A., Moon, J.J., and West, J.L. (2005) *Biomaterials*, **26**, 3227–3234; (j) Tan, W.H. and Takeuchi, S. (2007) *Adv. Mater.*, **19**, 2696–2701.

43 Choi, C.H., Jung, J.H., Rhee, Y.W., Kim, D.P., Shim, S.E., and Lee, C.S. (2007) *Biomed. Microdevices*, **9**, 855–862.

44 (a) Seifert, D.B. and Phillips, J.A. (1997) *Biotechnol. Progr.*, **13**, 562–568; (b) Gombotz, W.R. and Wee, S.F. (1998) *Adv. Drug Delivery Rev.*, **31**, 267–285.

45 (a) Nisisako, T., Torii, T., and Higuchi, T. (2004) *Chem. Eng. J.*, **101**, 23–29; (b) Sugiura, S., Oda, T., Izumida, Y., Aoyagi, Y., Satake, M., Ochiai, A., Ohkohchi, N., and Nakajima, M. (2005) *Biomaterials*, **26**, 3327–3331; (c) Liu, K., Ding, H.J., Liu, J., Chen, Y., and Zhao, X.Z. (2006) *Langmuir*, **22**, 9453–9457; (d) Wang, Q., Zhang, D., Xu, H.B., Yang, X.L., Shen, A.Q., and Yang, Y.J. (2012) *Lab Chip*, **12**, 4781–4786.

46 (a) Xia, Y.N., Gates, B., Yin, Y.D., and Lu, Y. (2000) *Adv. Mater.*, **12**, 693–713; (b) Thorsen, T., Roberts, R.W., Arnold, F.H., and Quake, S.R. (2001) *Phys. Rev. Lett.*, **86**, 4163–4166; (c) Nisisako, T., Torii, T., and Higuchi, T. (2002) *Lab Chip*, **2**, 24–26.

47 Dendukuri, D., Tsoi, K., Hatton, T.A., and Doyle, P.S. (2005) *Langmuir*, **21**, 2113–2116.

48 (a) Perro, A., Reculusa, S., Bourgeat-Lami, E., Duguet, E., and Ravaine, S. (2006) *Colloids Surf., A*, **284**, 78–83; (b) Mitragotri, S. and Lahann, J. (2009) *Nat. Mater.*, **8**, 15–23; (c) Perro, A., Reculusa, S., Ravaine, S., Bourgeat-Lami, E.B., and Duguet, E. (2005) *J. Mater. Chem.*, **15**, 3745–3760; (d) Walther, A. and Muller, A.H.E. (2008) *Soft Matter*, **4**, 663–668; (e) Wurm, F. and Kilbinger, A.F.M. (2009) *Angew. Chem. Int. Ed.*, **48**, 8412–8421; (f) Yang, S.M., Kim, S.H., Lim, J.M., and Yi, G.R. (2008) *J. Mater. Chem.*, **18**, 2177–2190; (g) Jiang, S., Chen, Q., Tripathy, M., Luijten, E., Schweizer, K.S., and Granick, S. (2010) *Adv. Mater.*, **22**, 1060–1071; (h) Pawar, A.B. and Kretzschmar, I. (2010) *Macromol. Rapid Commun.*, **31**, 150–168.

49 McConnell, M.D., Kraeutler, M.J., Yang, S., and Composto, R.J. (2010) *Nano Lett.*, **10**, 603–609.

50 Howse, J.R., Jones, R.A.L., Ryan, A.J., Gough, T., Vafabakhsh, R., and Golestanian, R. (2007) *Phys. Rev. Lett.*, **99**, 048102. doi: 10.1103/physrevlett.99.048102

51 Walther, A., Hoffmann, M., and Muller, A.H.E. (2008) *Angew. Chem. Int. Ed.*, **47**, 711–714.

52 Glotzer, S.C. and Solomon, M.J. (2007) *Nat. Mater.*, **6**, 557–562.

53 (a) Liu, S.S., Wang, C.F., Wang, X.Q., Zhang, J., Tian, Y., Yin, S.N., and Chen, S. (2014) *J. Mater. Chem. C*, **2**, 9431–9438; (b) Seiffert, S. and Weitz, D.A. (2010) *Polymer*, **51**, 5883–5889; (c) Shepherd, R.F., Conrad, J.C., Rhodes, S.K., Link, D.R., Marquez, M., Weitz, D.A., and Lewis, J.A. (2006) *Langmuir*, **22**, 8618–8622.

54 (a) Yoshida, K., Sekine, T., Matsuzaki, F., Yanaki, T., and Yamaguchi, M. (1999) *J. Am. Oil Chem. Soc.*, **76**, 195–200; (b) Lee, M.H., Oh, S.G., Moon, S.K., and Bae, S.Y. (2001) *J. Colloid Interface Sci.*, **240**, 83–89.

55 (a) Davis, S.S. and Walker, I.M. (1987) *Methods Enzymol*, **149**, 51–64; (b) Hammond, S.A., Tsonis, C., Sellins, K., Rushlow, K., Scharton-Kersten, T.,

www.ebook3000.com

Colditz, I., and Glenn, G.M. (2000) *Adv. Drug Delivery Rev.*, **43**, 45–55; (c) Vasiljevic, D., Parojcic, J., Primorac, M., and Vuleta, G. (2006) *Int. J. Pharm.*, **309**, 171–177.

56 Muschiolik, G. (2007) *Curr. Opin. Colloid Interface Sci.*, **12**, 213–220.

57 (a) Utada, A.S., Lorenceau, E., Link, D.R., Kaplan, P.D., Stone, H.A., and Weitz, D.A. (2005) *Science*, **308**, 537–541; (b) Fernandez-Nieves, A., Vitelli, V., Utada, A.S., Link, D.R., Marquez, M., Nelson, D.R., and Weitz, D.A. (2007) *Phys. Rev. Lett.*, **99**, 157801. doi: 10.1103/physrevlett.99.157801 (c) Kim, S.H., Kim, J.W., Cho, J.C., and Weitz, D.A. (2011) *Lab Chip*, **11**, 3162–3166; (d) Lee, H., Choi, C.H., Abbaspourrad, A., Wesner, C., Caggioni, M., Zhu, T., and Weitz, D.A. (2016) *ACS Appl. Mater. Interfaces*, **8**, 4007–4013; (e) Zhao, Y.J., Shum, H.C., Chen, H.S., Adams, L.L.A., Gu, Z.Z., and Weitz, D.A. (2011) *J. Am. Chem. Soc.*, **133**, 8790–8793; (f) Sun, B.J., Shum, H.C., Holtze, C., and Weitz, D.A. (2010) *ACS Appl. Mater. Interfaces*, **2**, 3411–3416; (g) Windbergs, M., Zhao, Y., Heyman, J., and Weitz, D.A. (2013) *J. Am. Chem. Soc.*, **135**, 7933–7937; (h) Amstad, E., Kim, S.H., and Weitz, D.A. (2012) *Angew. Chem. Int. Ed.*, **51**, 12499–12503; (i) Zhou, S.B., Fan, J., Datta, S.S., Guo, M., Guo, X., and Weitz, D.A. (2013) *Adv. Funct. Mater.*, **23**, 5925–5929; (j) Abbaspourrad, A., Carroll, N.J., Kim, S.H., and Weitz, D.A. (2013) *J. Am. Chem. Soc.*, **135**, 7744–7750; (k) Abbaspourrad, A., Datta, S.S., and Weitz, D.A. (2013) *Langmuir*, **29**, 12697–12702; (l) DiLauro, A.M., Abbaspourrad, A., Weitz, D.A., and Phillips, S.T. (2013) *Macromolecules*, **46**, 3309–3313; (m) Hayward, R.C., Utada, A.S., Dan, N., and Weitz, D.A. (2006) *Langmuir*, **22**, 4457–4461.

58 Lorenceau, E., Utada, A.S., Link, D.R., Cristobal, G., Joanicot, M., and Weitz, D.A. (2005) *Langmuir*, **21**, 9183–9186.

59 Choi, C.H., Lee, H., Abbaspourrad, A., Kim, J.H., Fan, J., Caggioni, M., Wesner, C., Zhu, T.T., and Weitz, D.A. (2016) *Adv. Mater.*, **28**, 3340–3344.

60 (a) Herrmann, A. (2007) *Angew. Chem. Int. Ed.*, **46**, 5836–5863; (b) Tree-udom, T., Wanichwecharungruang, S.P., Seemork, J., and Arayachukeat, S. (2011) *Carbohydr. Polym.*, **86**, 1602–1609; (c) Sansukcharearnpon, A., Wanichwecharungruang, S., Leepipatpaiboon, N., Kerdcharoen, T., and Arayachukeat, S. (2010) *Int. J. Pharm.*, **391**, 267–273; (d) Theisinger, S., Schoeller, K., Osborn, B., Sarkar, M., and Landfester, K. (2009) *Macromol. Chem. Phys.*, **210**, 411–420; (e) Sadovoy, A.V., Lomova, M.V., Antipina, M.N., Braun, N.A., Sukhorukov, G.B., and Kiryukhin, M.V. (2013) *ACS Appl. Mater. Interfaces*, **5**, 8948–8954.

61 (a) Nie, Z.H., Xu, S.Q., Seo, M., Lewis, P.C., and Kumacheva, E. (2005) *J. Am. Chem. Soc.*, **127**, 8058–8063; (b) Barbier, V., Tatoulian, M., Li, H., Arefi-Khonsari, F., Ajdari, A., and Tabeling, P. (2006) *Langmuir*, **22**, 5230–5232; (c) Wan, J., Bick, A., Sullivan, M., and Stone, H.A. (2008) *Adv. Mater.*, **20**, 3314–3318; (d) Nisisako, T., Okushima, S., and Torii, T. (2005) *Soft Matter*, **1**, 23–27.

62 Kim, S.H., Jeon, S.J., and Yang, S.M. (2008) *J. Am. Chem. Soc.*, **130**, 6040–6046.

63 (a) Nolan, J.P. and Sklar, L.A. (2002) *Trends Biotechnol.*, **20**, 9–12; (b) Zheng, B., Tice, J.D., Roach, L.S., and Ismagilov, R.F. (2004) *Angew. Chem. Int. Ed.*,

43, 2508–2511; (c) Zheng, B., Tice, J.D., and Ismagilov, R.F. (2004) *Anal. Chem.*, **76**, 4977–4982.

64 (a) Panizza, P., Engl, W., Hany, C., and Backov, R. (2008) *Colloids Surf., A*, **312**, 24–31; (b) Abate, A.R. and Weitz, D.A. (2009) *Small*, **5**, 2030–2032.

65 (a) Torza, S. and Mason, S. (1970) *J. Colloid Interface Sci.*, **33**, 67–83; (b) Torza, S. and Mason, S. (1969) *Science*, **163**, 813–814.

66 (a) Loxley, A. and Vincent, B. (1998) *J. Colloid Interface Sci.*, **208**, 49–62; (b) Pannacci, N., Bruus, H., Bartolo, D., Etchart, I., Lockhart, T., Hennequin, Y., Willaime, H., and Tabeling, P. (2008) *Phys. Rev. Lett.*, **101**, 164502. doi: 10.1103/physrevlett.101.164502

67 (a) Nisisako, T. and Hatsuzawa, T. (2010) *Microfluid. Nanofluid.*, **9**, 427–437; (b) Kim, S.H., Abbaspourrad, A., and Weitz, D.A. (2011) *J. Am. Chem. Soc.*, **133**, 5516–5524; (c) Shum, H.C., Kim, J.W., and Weitz, D.A. (2008) *J. Am. Chem. Soc.*, **130**, 9543–9549; (d) Xu, J.H., Ge, X.H., Chen, R., and Luo, G.S. (2014) *RSC Adv.*, **4**, 1900–1906; (e) Deng, N.N., Yelleswarapu, M., and Huck, W.T.S. (2016) *J. Am. Chem. Soc.*, **138**, 7584–7591; (f) Shum, H.C., Zhao, Y.J., Kim, S.H., and Weitz, D.A. (2011) *Angew. Chem. Int. Ed.*, **50**, 1648–1651; (g) Deng, N.N., Wang, W., Ju, X.J., Xie, R., Weitz, D.A., and Chu, L.Y. (2013) *Lab Chip*, **13**, 4047–4052.

www.ebook3000.com

13

Synthesis of Magnetic Nanomaterials

Ali Abou-Hassan

Sorbonne Universités, UPMC Univ Paris 06, Laboratoire PHysico-Chimie des Electrolytes et Nanosystèmes InterfaciauX (PHENIX), UMR CNRS 8234, 4 Place Jussieu, Paris 75005, France

13.1 Introduction

Microfluidics is the science and technology of systems that process or manipulate small (10^{-9}–10^{-18} l) amounts of fluids, using channels with dimensions of several to hundreds of micrometers [1, 2]. Much of the original motivation for microfluidics arose out of developments in biology, but the microfluidic systems have now been improved to the state where they are emerging as promising tools for high-throughput discovery and screening in chemistry and materials science [3, 4]. There are several benefits from using microreactors for nanomaterial synthesis [5]. In brief, because of their small dimensions, process parameters such as pressure, temperature, residence time, flow rate, and mixing can be easily controlled in small microfluidic channels (microreactors) [5, 6]. Moreover, the small reactor volumes (nanoliters to microliters) result in minimal reagent consumption and fast responses to system perturbations, permitting rapid adjustment of reactor conditions to tune the material properties in real time [7, 8].

Depending on the flow types in microfluidic devices, two categories of microreactors were reported for the elaboration of nanomaterials: single-phase continuous flow (see Figure 13.1a) and emulsion (two phase) of microdroplets/segmented flow microreactors (see Figure 13.1b, c). Continuous flow reactors have found the widest use in synthetic applications due to their simplicity and operational flexibility [8, 10]. Reagents mix and react under diffusion-based laminar flow reaction; reaction times, temperatures, mixing efficiency, and reagent concentrations are parameters to control for the synthesis of nanomaterials. A significant problem encountered in single-phase microfluidic systems is that of achieving rapid and efficient mixing of fluids while minimizing the Taylor–Aris dispersion effect caused by the parabolic (Poiseuille) velocity profile. The latter is responsible for the large distribution of residence times that may cause significant variation in the yield, efficiency, and product distribution of a reaction [6]. The confinement of reactions in nanoliter-sized droplets can serve as a method to overcome these problems [9]. In multiphase microfluidic reactors, the interfaces between immiscible phases enable to compartmentalize

Microfluidics: Fundamentals, Devices and Applications, First Edition.
Edited by Yujun Song, Daojian Cheng, and Liang Zhao.
© 2018 Wiley-VCH Verlag GmbH & Co. KGaA. Published 2018 by Wiley-VCH Verlag GmbH & Co. KGaA.

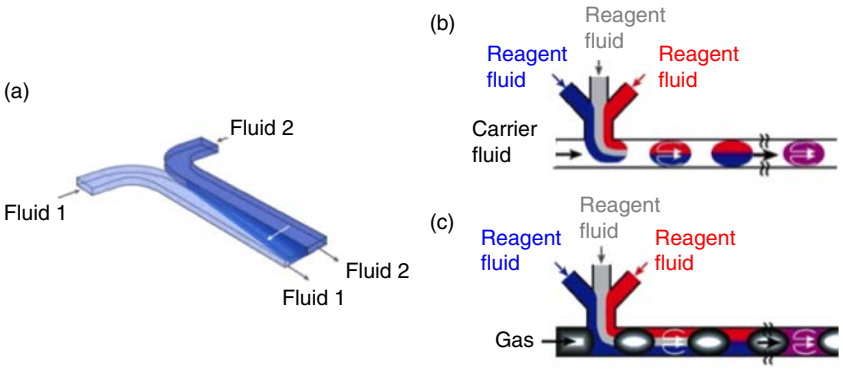


Figure 13.1 (a) Mixing of two miscible fluid streams under laminar flow conditions. The component streams mix only by diffusion, creating a dynamic diffusive interface with predictable geometry. Reactions can be studied in two types of segmented flows in microfluidic channels. (Atencia and Beebe 2005 [1]. Reproduced with permission of Nature Publishing Group.) (b) Discrete liquid plugs are encapsulated by an immiscible continuous phase (e.g., a fluorocarbon-based carrier fluid). Reactions occur within the dispersed phase (within the plugs). Owing to the surface properties of the microchannel walls, these walls are preferentially wetted by the continuous phase. (c) Aqueous slugs are separated by another immiscible phase (e.g., discrete gas bubbles). Reactions occur within the continuous phase (i.e., within the slugs). ((b, c) Song *et al*. 2006 [9]. Reproduced with permission of John Wiley & Sons.)

reactants into droplets or "plugs" effectively narrowing the residence time distribution in both phases compared to single-phase systems. The residence time distribution is narrowed, which is significant for the continuous ("wetting") phase and becomes effectively discrete for the discontinuous (droplet) phase. In one common multiphase system, oil that totally wets the walls of the microfluidic channel constitutes the continuous phase, containing droplets of the aqueous solutions of interest. To facilitate gas–liquid reactions or reactions in anhydrous solvents, gas–liquid segmented reactors have also been developed, in which the droplet phase consists of discrete bubbles of a gas within a liquid continuous phase [11]. In this chapter, the different magnetic nanomaterials that have been synthesized using microfluidic reactors are presented.

13.2 Synthesis of Magnetic Nanomaterials Using Microreactors

13.2.1 Magnetic Iron Oxide-Based Nanomaterials

There are several phases of iron oxides and hydroxides; however the magnetic ones have received great attention due to their large applications in biomedicine and nanomedicine. There are several processes for the synthesis of magnetic iron oxide nanoparticles (NPs) in bulk. The reader can refer to the following Refs [12, 13] for more details on this topic. Herein only the synthesis of magnetic iron oxides in microreactors is presented. Historically, the coprecipitation method, which consists in alkalinization of a mixture of iron(II) and iron(III) mixture

www.ebook3000.com

with a stoichiometric molar ratio of 1 : 2, has been one of the first methods to be transposed in microreactors, certainly because the reaction occurs in aqueous solution at room temperature and it also allows the use of polymer-based microreactors such as polydimethylsiloxane (PDMS) without any sophisticated chemical engineering. To avoid technical problems related to adsorption and clogging in typical 2D channels, we designed a 3D coaxial flow microreactor (Figure 13.2a) in PDMS performing the mixing of two coaxial flows of miscible fluids (one containing the iron "precursor salts," the other one a strong base) [10, 14]. It offers the opportunity to enable a precision positioning of the precursors to flow at the center of the channel in both longitudinal and lateral dimensions, and, on the other hand, it avoids adsorption of any precipitate species onto the PDMS walls as the latter are totally wetted by the alkaline outer flow.

The iron(II/III) solution of total concentration 10^{-2} mol l^{-1} was injected in the inner flow with a volumetric rate flow Q_{in} ($1 < Q_{in} < 100$ µl min^{-1}). The alkaline solution of TMAOH (0.172 mol l^{-1}) was injected in the outer flow with a volumetric rate flow Q_{out} ($100 < Q_{out} < 400$ µl min^{-1}). TMAOH was chosen prior to any other bases as the TMA^+ cations afford enhanced stability of colloidal

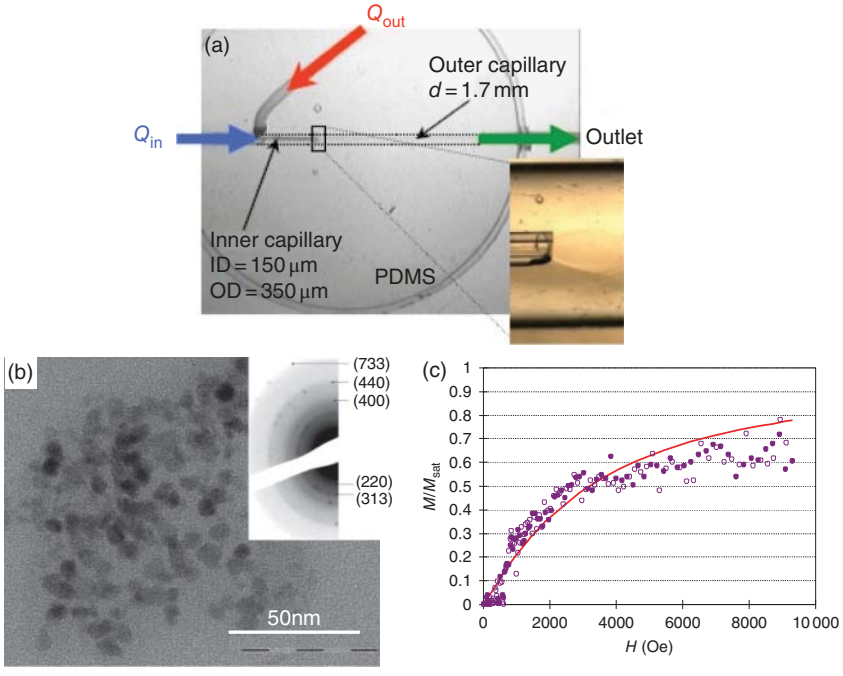


Figure 13.2 (a) Coaxial flow device operating under laminar regime. The inset image shows the outlet of the inner capillary with the solution of iron +II and iron +III flowing into the stream of TMAOH alkaline solution; (b) TEM image of nanoparticles prepared in the channel (for flow rates $Q_{in} = 100$ µl min^{-1} and $Q_{out} = 400$ µl min^{-1}). The inset shows the electron microdiffraction pattern with the Miller indices of γ-Fe_2O_3; (c) Magnetization curve of a stable suspension in water of nanoparticles produced in the millifluidic device. The inset curves represent the fitting log-normal laws for the numbers distribution (solid line) and the volume distribution (dotted line) of diameters. (Copyright© 2008, the Royal Society of Chemistry.)

oxide dispersion [15]. At the exit the reaction was "quenched" by fast solvent extraction (using didodecyl dimethyl ammonium bromide in cyclohexane) to prevent any aging of the NPs in the aqueous solution. The suspensions obtained in cyclohexane were always stable, and the NPs produced in the channel were fairly spherical with an average size around 7 nm. The evidence of their crystallinity was provided by the electron microdiffraction pattern in the inset of Figure 13.2b, which shows the presence of the maghemite phase γ-Fe_2O_3. The magnetization curve of the suspension (Figure 13.2c) followed the typical Langevin law of superparamagnetism, calculated for an assembly of NPs with a rather narrow distribution of diameters fitted by a log-normal law of parameters $d_0 = 6$ nm and $\sigma = 0.2$. The specific magnetization of the materials was also deduced, $m_s = M_{sat}/\phi = 1.4 \times 10^5$ A m^{-1}, which is much below the bulk value of maghemite γ-Fe_2O_3 (3.5×10^5 A m^{-1}), but not so far from the m_s value of about 2.6×10^5 A m^{-1} usually obtained for NPs of approximately the same sizes prepared with a standard large-scale synthesis.

An easy to scale-up and reproducible method for the production of magnetic NPs in microreactors was described by Simmons *et al.* [16]. They carried out the reaction in a commercially available glass microreactor using continuous flow of both reagent streams in order to avoid the use of two phases. The reaction was successfully run for 40 h without blockage due tailoring of flow rates and by delaying the precipitation until a serpentine channel (after the T mixer), thus facilitating the removal of the NPs simply by the flow of the mixture. The careful control of precipitation using the laminar flow technique gave NPs of similar size and polydispersity to those prepared in homemade continuous flow reactors while avoiding channel blockage. Furthermore, the phase composition of the NPs has been comprehensively analyzed, and the samples found to contain 71.8% γ-Fe_2O_3 and 28.2% Fe_3O_4 by weight. Very recently the same group [17] used a similar laminar microfluidic strategy to control the chemical stoichiometry of Zn-substituted Fe_3O_4 NPs. The linear increase of Zn content ($Zn_xFe_{3-x}O_4$ with $0 \leq x \leq 0.48$) caused a linear increase in properties such as the saturation magnetization, relative to pure Fe_3O_4.

Droplet-based microreactors have been also used for the synthesis of magnetic iron oxide nanomaterials. Frenz *et al.* [18] described the synthesis of maghemite NPs by coprecipitation of iron(II) and iron(III) by an alkaline solution of ammonium hydroxide. The microfluidic device (see Figure 13.3a) consisted of two hydrodynamically coupled nozzles. During droplet formation in one of the nozzles, the aqueous stream blocks the oil coming from the central channel, leading to increased oil flow through the second nozzle. Once the droplet is released, the oil flow switches back to the first channel, allowing droplet pairing at various flow rates.

Iron chloride solution was flushed into one arm of the nozzle and ammonium hydroxide into the second arm, which led to droplet pairs containing the two reagents. To start a reaction the droplet pairs can be coalesced by applying an electrical field between the two on-chip electrodes. Transmission electron microscopy (TEM) (Figure 13.3b) and electron microdiffraction pattern (Figure 13.3c) showed that synthesized NPs are monocrystalline and that the phase is γ-Fe_2O_3. The average particle size deduced from TEM images is smaller

www.ebook3000.com

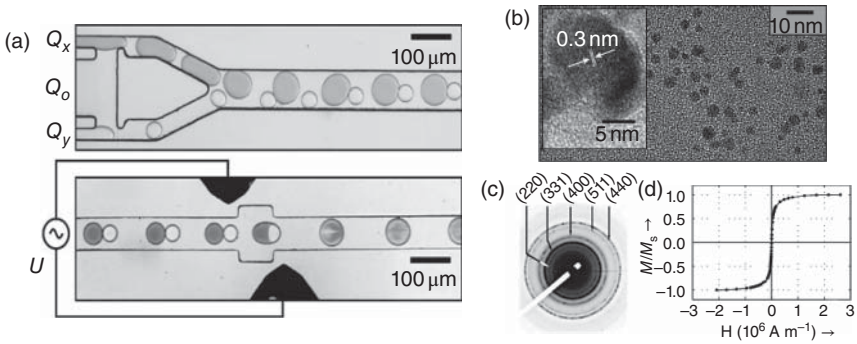


Figure 13.3 (a) Up: pairing module. Two aqueous phases are injected by the outer channels and are synchronously emulsified by the central oil channel. The flow rates are $Q_o = 800$ ml h^{-1} for the oil and $Q_x = 400$ ml h^{-1}, $Q_y = 100$ ml h^{-1} for the aqueous phases. (b) Fusion module. Paired droplets can be coalesced by applying an electrical voltage U between the two electrodes. $Q_o = 650$ ml h^{-1}, $Q_x = 100$ ml h^{-1}, $Q_y = 60$ ml h^{-1}. Characterization of the iron oxide particles is produced. (b) TEM image of the nanoparticles. Inset: HR-TEM image of a particle showing (220) spinel planes. (c) Electron diffraction pattern indicating different planes of the spinel structure. (d) Magnetization M/M_s (M_s is the saturation magnetization) as a function of the magnetic field H. (Frenz *et al.* 2008 [18]. Reproduced with permission of John Wiley & Sons.)

for the fast compound mixing (4 ± 1 nm) than for bulk mixing (9 ± 3 nm). The superparamagnetic character of the NPs is confirmed by the absence of hysteresis in the magnetization curve (Figure 13.3d). Similar strategy based on droplet microfluidics has been reported by Kumar *et al.* [19] by using a driven capillary-based droplet reactor for the aqueous preparation of dextran-coated superparamagnetic iron oxide (SPIO) NPs. The reactor yielded small, stable, highly crystalline particles with a narrow size distribution ($\sigma_d/d = 22\%$), a large saturation magnetization of 58 emu g^{-1}, and a high T_2 relaxivity of 66 mM^{-1} s^{-1}.

Very recently the group of Santamaria [20] in Spain demonstrated the potential of using gas slug microfluidics as a system of choice to synthesize a variety of high purity and custom-made crystalline iron oxide nanostructures. Depending on the gas atmosphere (see Figure 13.4a) used by the authors (inert (N_2), oxidizing (O_2), or reducing (CO, H_2)), different morphologies including octahedral or layered-shaped and crystalline structures such as magnetite Fe_3O_4 and feroxyhyte (δ-FeOOH) were synthesized in a high yield and with highly reproducible fabrication process (see Figure 13.4b–e). The authors demonstrated that not only the productivity was enhanced by strongly reducing residence times with respect to the batch process (from hours to minutes or even seconds) but also a high degree of control over the resulting product characteristics (size, shape, crystalline phase) can be obtained by simply changing the composition of the gas used to create the slugs. Moreover, their results showed that it is beneficial to segregate the mixing and reaction stages. A fast mixing is essential (since nearly all of the oxide precursors are removed from the liquid phase in less than a minute, leading to a fast nucleation process), followed by a reaction stage where the temperature and reaction atmosphere are selected depending on the desired characteristics. On the level of magnetism, the synthesized magnetite

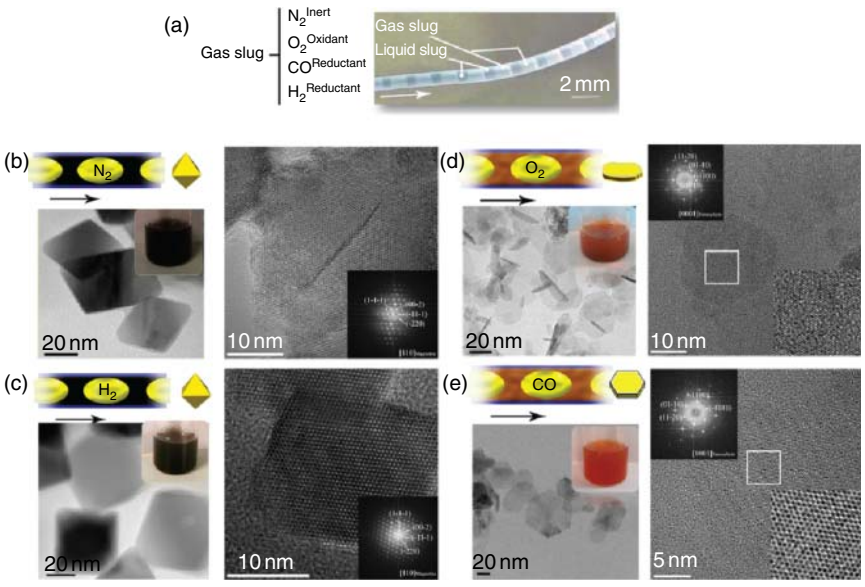


Figure 13.4 Magnetic nanomaterials produced by the liquid segmentation of reagents with different gas sources: (a) optical image of the gas–liquid slug for different gas phase compositions in the segmented flow; (b–d) TEM images of MNPs obtained under different gas atmospheres, optical images of colloids (insets), HR-TEM images, and FFT [(b) N_2, 100 °C, and 6 min; (c) H_2, 100 °C, and 1 min; (d) O_2, 100 °C, and 1 min; (e) CO, 80 °C, and 1 min]. White squares indicate the area selected for the high magnification inset. (Reprinted with permission from Ref. [20] Copyright© 2015, the American Chemical Society.)

NPs showed a magnetization that is very similar to that of the particles produced in a batch reactor where a saturation magnetization of 84 emu g^{-1}, a remanence of 15 emu g^{-1}, and a coercivity of 115 Oe were obtained at 37 °C.

Low temperature synthesis of magnetic NPs using coprecipitation method suffers unfortunately from a large polydispersity in size of the resulting NPs, which is usually due to the overlapping of the nucleation and the growth steps during synthesis [21]. Synthesis in high boiling solvents can provide an opportunity to decouple the nucleation and growth steps and lead to the formation of more monodisperse NPs [21, 22]. The transposition of such synthesis in microfluidic reactors is still in its infancy, which is probably related to the many chemical engineering requirements, including the technological ones that need to be overcome. Marre *et al.* [23] developed a chemically compatible microsystems in silicon and Pyrex that can operate across expanded process conditions such as high pressure and high temperature (supercritical conditions). Applications of such microreactors were illustrated by the synthesis of Fe_3O_4 NPs at $T = 300$ °C in toluene (which was maintained liquid by applying pressure $p = 10$ MPa) by thermal decomposition of iron oleate precursor [22] that was formed on chip. Indeed by selectively heating only the top of the microreactor, an on-chip thermal gradient could be generated, which was used to create temperature gradients along the microreactor (see Figure 13.5). In the first zone $Fe(CO)_5$ and

www.ebook3000.com

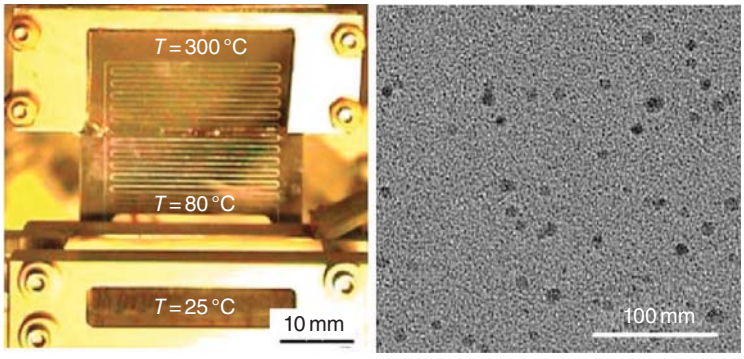


Figure 13.5 A 100 µl for the two-step on-chip synthesis of iron oxide NPs in liquid toluene under HP/HT conditions and a TEM image. (Marre *et al*. 2010 [23]. Reproduced with permission of American Chemical Society.)

oleic acid reacted to form iron oleate, which was then heated on chip at 300 °C to produce magnetic NPs with 8 nm average diameter as concluded from TEM, however without any further characterizations (see Figure 13.5).

Very recently the continuous flow synthesis of magnetic iron oxides from the same precursor, that is, iron oleate, was reported by Glasgow *et al.* [24]. The continuous flow reactor consisted of a reactor coil (length: 50 ft (15.24 m), diameter: 0.085 in. (2.16 mm) stainless steel tubing) that was submerged in a salt bath heated using a hot plate around 300 °C. The mixture composed of iron oleate, oleic acid, and trioctylamine was flashed inside the microreactor with a constant flow rate (0.175 ml min^{-1}) with an average reaction time of 86 min. The continuous flow reactor was shown as a practical method for the synthesis of uniform iron oxide particles ranging between 6 and 10 nm. Furthermore, the particles produced in the continuous flow reactor were confirmed as crystalline as demonstrated from X-ray diffraction (XRD), and it was concluded that the iron oleate/oleic acid molar ratio was the largest deciding factor in particle size.

Another interesting synthesis method that is attractive to transfer in microreactors is the well-known polyol process [25–27]. It allows the synthesis of a variety of metals and metal oxides by a simple reduction/thermal decomposition process to temperatures above 160 °C. Arndt *et al.* [28] studied the synthesis of silver NPs in a droplet microreactor composed of a Y junction and a perfluoroalkoxy tube (0.8 mm ID, $L = 3$ m) heated to 160 °C in an oven and demonstrated that it was possible to undergo also magnetite NP synthesis following the polyol process. Slugs containing the reagent mixture such as the iron precursor iron(III) acetylacetonate, oleylamine, and so on were generated using ethylene glycol or hexadecene as the continuous phase. The residence time of the liquid in the capillary was adjusted by the flow rate, leading to residence times from 30 to 150 s. Iron oxide NPs with a diameter of 20 nm were obtained from TEM when a mixture of hexadecane, oleylamine, and oleic acid was used. The authors provided no further characterizations.

In the next section, the different syntheses of metallic and magnetic NPs using microreactors are reviewed.

13.2.2 Synthesis of Metallic and Magnetic Nanomaterials

The controlled synthesis of metallic NPs with stable crystal structures and stable physical and chemical properties is a key issue for commercial applications. For these applications, the use of a microfluidic reactor process has been proven to be a flexible approach to control the fine crystal structures and the magnetic properties during the ripening and aging of the NPs. For instance, Song *et al.* [29] developed an *in situ* rapidly cooling microfluidic process (IRCMP) in which cobalt nanoparticles (CoNPs) with stable amorphous structures and magnetic properties are synthesized by using elevated reaction temperatures followed by rapid quenching of the colloids at reduced temperatures. The CoNPs were synthesized in the microfluidic reactor by reduction of $CoCl_2$ in tetrahydrofuran (THF) solution using lithium hydrotriethylborate ($Li[B(C_2H_5)_3H]$) as a reducing agent and 3-(*N,N*-dimethyldodecylammonia)-propanesulfonate (SB12) as a stabilizer. The magnetic properties and crystal structures of the amorphous CoNPs were empirically shown to be stable for at least 3 months. Later on [30], the same author described a similar microfluidic reactor process for the synthesis of wormlike Fe NPs coated with polyvinylpyrrolidone (PVP) at room temperature. The high aspect ratio-shaped Fe NPs obtained by this method could be further transformed into large ellipsoid species with refined crystal structures and increased aggregation by way of a sonication process, evidenced by their TEM images, selected area electron diffraction (SAED), XRD, X-ray absorption near K-edge structure (XANES), and extended X-ray absorption fine structure (EXAFS). Due to the compensation effects on the magnetic properties of NPs from their increased size, enhanced magnetic coupling, refined crystal structure, and the reduced aspect ratio, the sonication-treated Fe NPs show a slightly enlarged coercivity (H_c), an enhanced saturation magnetization (M_s), and a slight suppress in the increased blocking temperature (T_b).

The spatiotemporally splitting NP formation route is critical but extremely challenging in terms of methodology development for large-scale continuous production of NPs with defined sizes, structures, and properties, particularly for magnetic and/or hybrid NPs. For this purpose, Shen et *al.* [31] built a transparent chip-based simple programmed microfluidic processes (C-SPMPs, Figure 13.6a, b) and sequentially developed transparent microtubing-based simple programmed microfluidic processes (MT-SPMPs). By C-SPMPs and MT-SPMPs, four stages including mixing/reaction, nucleation, growth, and termination during NPs formation could be well-separated and observed by the changes of flow color along the microchannels for the first time using magnetic Co, Fe, Ni, CoFe (Figure 13.6c–f), and NiFe NPs as examples. A four-section mechanism was proposed and discussed for the development of these strategies by the *in situ* monitoring of the changes in the relative C=O and C—O bond content in the coordinating cyclic lactam groups in the bi-channel solvent (i.e., *N*-methy-2-pyrrolidone) and the stabilizer (i.e., PVP) and UV–Vis spectra of reaction solution using the formation of CoFe NPs as a model. These strategies are beneficial for optimizing each stage by tuning channel length, flow rate, reactant concentration, and reaction and termination temperatures for the synthesis

www.ebook3000.com

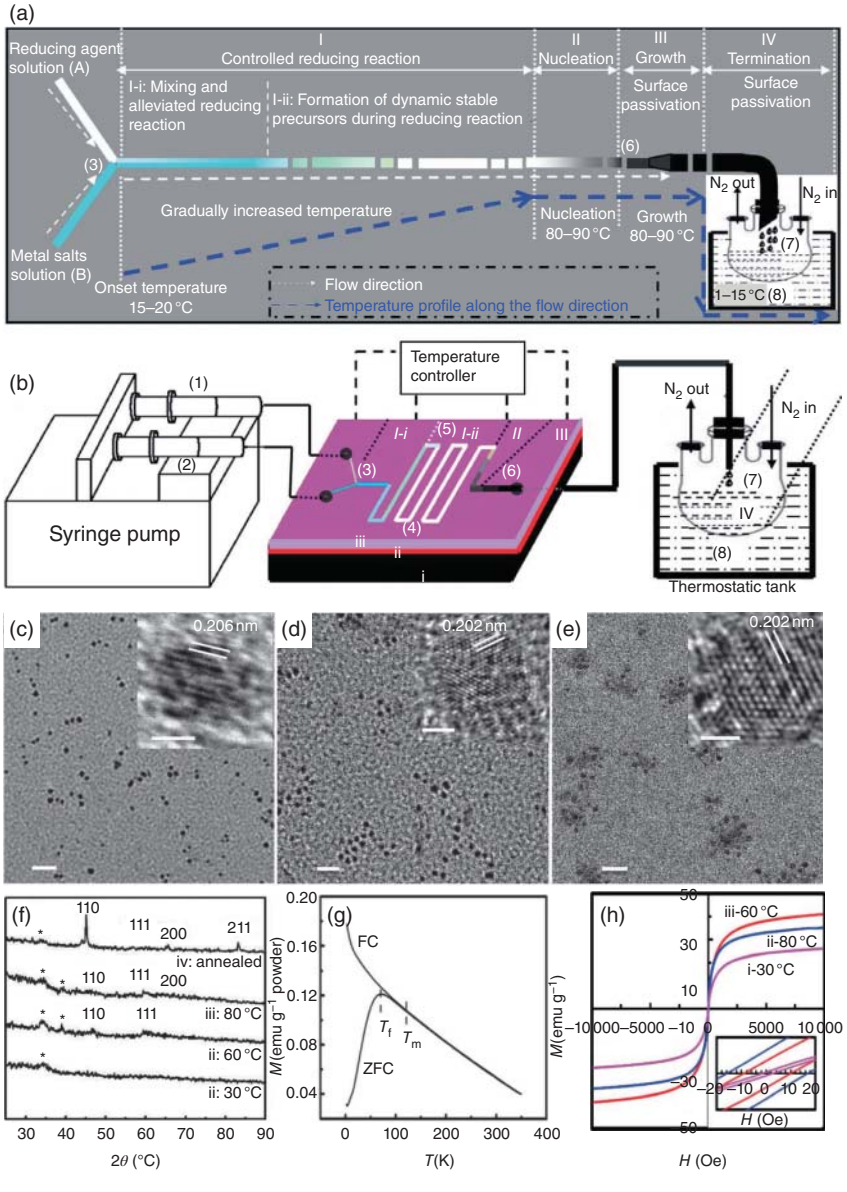


Figure 13.6 (a) Principle of the proposed four-section formation mechanism of nanoparticles via the simple programmed microfluidic process. (b) Experimental setup of the transparent chip-based simple programmed microfluidic processes (C-SPMPs). TEM images of CoFe nanoparticles synthesized at room temperature (c), at 60 °C (d), and at 80 °C (e) by C-SPMPs (insets: HR-TEM image of a typical particle). Scale bar: 10 nm; in inset images: 1 nm. (f) XRD patterns of CoFe NPs synthesized at room temperature (i), 60 °C (ii), 80 °C (iii), and one annealed sample (iv). (g) Room temperature hysteresis loop of CoFe nanoparticles synthesized at room temperature (i), at 60 °C (ii), and at 80 °C (iii). (h) Thermo-magnetism (FC–ZFC) curve of the largest CoFe NPs synthesized at 60 °C. (Shen *et al*. 2014 [31]. Reproduced with permission of Royal Socity of Chemistry.)

of NPs with uniform sizes of less than 5 nm. Their magnetic (Figure 13.6g, h) and optical properties were further evaluated, and they exhibited spin-glass-like behavior and unique ultraviolet absorbance, respectively. The developed SPMPs themselves preserve a scale-out feature with a current productivity of at least 13.0 g/(day-line) according to the Fe, Co, or Ni content.

13.2.3 Synthesis of Core–Shell Magnetic Nanomaterials

An *in situ* redox process based on microfluidic reactors (see Figure 13.7A) was described by Song et *al.* [32] for the continuous synthesis of amorphous nanostructures with metallic cores and metal oxide shells at large scale. The fabricated [Fe(B)]@Fe_xO_y NPs were formed by reduction of $FeCl_2$ by $NaBH_4$ in the presence of PVP, followed by their oxidation in water. The core–shell structures as confirmed by TEM images (see Figure 13.7B), Z contrast scanning transmission electron microscope (STEM) images (see Figure 13.7C), high-resolution transmission electron microscopy (HR-TEM) images (see Figure 13.7D), and whose shell thickness distribution and core size distribution are summarized in Figure 13.7E and F, respectively, were found to last for 4–5 months. Investigation on their long-term stabilities suggested that the described synthesis process provides a large-scale synthetic strategy for various metallic core and metal oxide shell NPs. Relationship between their structures and magnetic properties indicates that their typical permanent ferromagnetic properties can be attributed to the exchanging coupling interaction among core–shells and/or tiny crystallites in shells. Indeed their room temperature hysteresis loops (see Figure 13.7G:a–c) show monophase magnetic features. All of them exhibit typical permanent ferromagnetism with enough high remanence (M_r) and coercivity (H_c). These NPs can maintain high saturation magnetism (70 emu g^{-1}) even after exposure in air for 4–5 months. Interestingly, the fresh NPs exhibit significant exchange bias (H_e: 91 Oe) at room temperature (see Figure 13.7G:a), while those aged NPs show small exchange bias (see Figure 13.7G:b,c), possibly due to the enhanced exchange coupling by the crystallites in shells.

Using the same microfluidic channel, Wang *et al.* [33] developed a core alloying and shell gradient-doping strategy for the controlled surface modification of NPs, realized by a coupled competitive reducing nucleation and precipitation reaction. They extended this method to the surface modification of Fe and CoFe NPs by doping zinc oxide and aluminum oxide to form well-dispersed stable ultrasmall $Fe_{(1-x)}Zn_x$@$Zn_{(1-y)}Fe_y$O-$(OH)_z$ and $CoFe_{(1-x)}Al_x$@$Al_{(1-y)}(CoFe)_y$O-$(OH)_z$ nanohybrids as contrast agents for magnetic resonance imaging (MRI). They exhibit greatly enhanced $T_1$and T_2 weighted spin echo imaging effects. Particularly, $CoFe_{(1-x)}Al_x$@$Al_{(1-y)}(CoFe)_y$O-$(OH)_z$ nanohybrids give a T_1 relaxation rate (R_1) of 0.156 (μg-CoFe $ml^{-1})^{-1}$ S^{-1} and a T_2 relaxation rate (R_2) of 0.486 (μg-CoFe $ml^{-1})^{-1}$ S^{-1}, much higher than that of the commercial gadopentetate dimeglumine ($R_1 = 0.022$ (μg-Gd $ml^{-1})^{-1}$ S^{-1}; $R_2 = 0.025$ (μg-Gd $ml^{-1})^{-1}$ S^{-1}. The R_1 of $CoFe_{(1-x)}Al_x$@$Al_{(1-y)}(CoFe)_y$O-$(OH)_z$ nanohybrids is also higher than that of SPIO NPs ($R_1 = 0.121$ (μg-Fe $ml^{-1})^{-1}$ S^{-1}. SPIO NPs of 7.1 ± 1.2 nm still show an excellent negative MRI contrast agent by the highest R_2 (5.07 (μg-Fe $ml^{-1})^{-1}$ S^{-1}) and R_2/R_1 ratio (42) among these reagents.

www.ebook3000.com

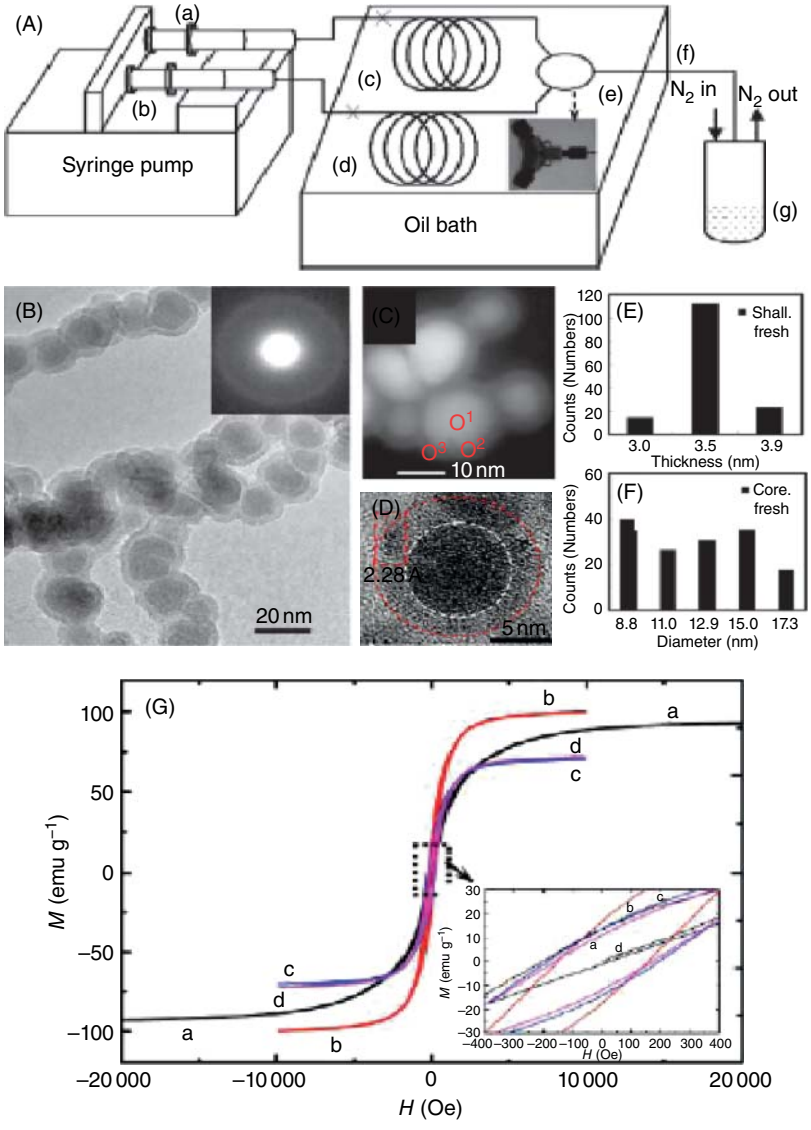


Figure 13.7 (A) Experimental setup of the integrated tubular microfluidic reactor: (a) One syringe pump for the metal salt solution; (b) one syringe pump for the reducing agent solution; (c) the preheating stainless steel spiral (inner diameter (ID) = 127 μm, length (*L*) = 15 cm) for the metal salt solution; (d) the preheating stainless steel spiral (ID = 127 μm, *L* = 15 cm) for the reducing agent solution; (e) the Y-mixer (ID = 500 μm) for the reaction of nanoparticle formation; (f) the microtubing (ID = 127 μm, *L* = 25–50 cm) for the nanoparticle growth; and (g) the product receiver. Core–shell morphology for the freshly prepared core–shell nanoparticles is demonstrated by the typical TEM image (B) and the Z contrast STEM image (C), and one HR-TEM image for a single nanoparticle (D), whose shell thickness distribution and core size distribution are summarized in (E) and (F), respectively. (G) Magnetic hysteresis loops at room temperature for the freshly prepared core–shell nanoparticles (a), the core–shell nanoparticles aged for 30–45 days in air at room temperature (b), and the core–shell nanoparticles aged for 4 (c) and 5 (d) months in air at room temperature, respectively. Inset: Magnified center range. (Song *et al*. 2013 [32]. Reproduced with permission of American Chemical Society.)

13.3 Conclusion

In this chapter we reviewed the different synthesis that have been described and transposed in microreactors for the synthesis of magnetic nanomaterials from molecular precursors. Nanomaterials ranging from metal oxides to metallic or core–shell-mixed nanostructures were described. In general the monodispersity of the resulting NPs is decreased compared to bulk synthesis as well as the time of synthesis. Although lot of attention has been brought to the synthesis of magnetic nanomaterials at room temperature, less has been done in the field of high thermal decomposition. This is probably related to the difficulty in transposing such processes in microreactors considering the different chemical engineering issues. Moreover the expectations from microreactors were many in the field of material science such as for discovering new nanomaterials and understanding the nucleation and growth mechanisms during NP formation. It appears clear that little has been achieved in this field, and mainly the investigations are restricted to systematic transposition of already known reactions and processes.

References

1 Atencia, J. and Beebe, D.J. (2005) Controlled microfluidic interfaces. *Nature*, **437** (7059), 648–655.
2 Whitesides, G.M. (2006) The origins and the future of microfluidics. *Nature*, **442** (7101), 368–373.
3 Kobayashi, J., Mori, Y., Okamoto, K., Akiyama, R., Ueno, M., Kitamori, T., and Kobayashi, S. (2004) A microfluidic device for conducting Gas–liquid–solid hydrogenation reactions. *Science*, **304** (5675), 1305–1308.
4 Hansen, C.L., Skordalakes, E., Berger, J.M., and Quake, S.R. (2002) A robust and scalable microfluidic metering method that allows protein crystal growth by free interface diffusion. *Proc. Natl. Acad. Sci. U.S.A.*, **99** (26), 16531–16536.
5 Jensen, K.F. (2001) Microreaction engineering – is small better? *Chem. Eng. Sci.*, **56** (2), 293–303.
6 deMello, A.J. (2006) Control and detection of chemical reactions in microfluidic systems. *Nature*, **442** (7101), 394–402.
7 Pennemann, H., Hessel, V., and Löwe, H. (2004) Chemical microprocess technology – from laboratory-scale to production. *Chem. Eng. Sci.*, **59** (22–23), 4789–4794.
8 Abou-Hassan, A., Sandre, O., and Cabuil, V. (2010) Microfluidics in inorganic chemistry. *Angew. Chem. Int. Ed.*, **49** (36), 6268–6286.
9 Song, H., Chen, D.L., and Ismagilov, R.F. (2006) Reactions in droplets in microfluidic channels. *Angew. Chem. Int. Ed.*, **45** (44), 7336–7356.
10 Abou-Hassan, A., Sandre, O., Neveu, S., and Cabuil, V. (2009) Synthesis of goethite by separation of the nucleation and growth processes of ferrihydrite nanoparticles using microfluidics. *Angew. Chem. Int. Ed.*, **48** (13), 2342–2345.
11 Yen, B.K.H., Günther, A., Schmidt, M.A., Jensen, K.F., and Bawendi, M.G. (2005) A microfabricated Gas–liquid segmented flow reactor for

www.ebook3000.com

high-temperature synthesis: the case of CdSe quantum Dots13. *Angew. Chem. Int. Ed.*, **44** (34), 5447–5451.

12 Cornell, R.M. and Schwertmann, U. (2004) *The Iron Oxides*, Wiley-VCH Verlag GmbH & Co. KGaA, pp. 1–7.

13 Chaneac, C., Duchateau, A., and Abou-Hassan, A. (2016) *Iron Oxides*, Wiley-VCH Verlag GmbH & Co. KGaA, pp. 225–242.

14 Abou Hassan, A., Sandre, O., Cabuil, V., and Tabeling, P. (2008) Synthesis of iron oxide nanoparticles in a microfluidic device: preliminary results in a coaxial flow millichannel. *Chem. Commun.*, **15**, 1783–1785.

15 Massart, R. (1981) Preparation of aqueous magnetic liquids in alkaline and acidic media. *IEEE Trans. Magn.*, **17** (2), 1247–1248.

16 Simmons, M., Wiles, C., Rocher, V., Francesconi, M., and Watts, P. (2013) The preparation of magnetic iron oxide nanoparticles in microreactors. *J. Flow Chem.*, **3** (1), 7–10.

17 Simmons, M.D., Jones, N., Evans, D.J., Wiles, C., Watts, P., Salamon, S., Escobar Castillo, M., Wende, H., Lupascu, D.C., and Francesconi, M.G. (2015) Doping of inorganic materials in microreactors – preparation of Zn doped Fe_3O_4 nanoparticles. *Lab Chip*, **15** (15), 3154–3162.

18 Frenz, L., El Harrak, A., Pauly, M., Bégin-Colin, S., Griffiths, A.D., and Baret, J.-C. (2008) Droplet-based microreactors for the synthesis of magnetic iron oxide nanoparticles. *Angew. Chem. Int. Ed.*, **47** (36), 6817–6820.

19 Kumar, K., Nightingale, A.M., Krishnadasan, S.H., Kamaly, N., Wylenzinska-Arridge, M., Zeissler, K., Branford, W.R., Ware, E., deMello, A.J., and deMello, J.C. (2012) Direct synthesis of dextran-coated superparamagnetic iron oxide nanoparticles in a capillary-based droplet reactor. *J. Mater. Chem.*, **22** (11), 4704–4708.

20 Larrea, A., Sebastian, V., Ibarra, A., Arruebo, M., and Santamaria, J. (2015) Gas slug microfluidics: a unique tool for ultrafast, highly controlled growth of iron oxide nanostructures. *Chem. Mater.*, **27** (12), 4254–4260.

21 Kim, S.-W., Park, J., Jang, Y., Chung, Y., Hwang, S., Hyeon, T., and Kim, Y.W. (2003) Synthesis of monodisperse palladium nanoparticles. *Nano Lett.*, **3** (9), 1289–1291.

22 Park, J., An, K., Hwang, Y., Park, J.-G., Noh, H.-J., Kim, J.-Y., Park, J.-H., Hwang, N.-M., and Hyeon, T. (2004) Ultra-large-scale syntheses of monodisperse nanocrystals. *Nat. Mater.*, **3** (12), 891–895.

23 Marre, S., Adamo, A., Basak, S., Aymonier, C., and Jensen, K.F. (2010) Design and packaging of microreactors for high pressure and high temperature applications. *Ind. Eng. Chem. Res.*, **49** (22), 11310–11320.

24 Glasgow, W., Fellows, B., Qi, B., Darroudi, T., Kitchens, C., Ye, L., Crawford, T.M., and Mefford, O.T. (2016) Continuous synthesis of iron oxide (Fe_3O_4) nanoparticles via thermal decomposition. *Particuology*, **26**, 47–53.

25 Hachani, R., Lowdell, M., Birchall, M., Hervault, A., Mertz, D., Begin-Colin, S., and Thanh, N.T.K. (2016) Polyol synthesis, functionalisation, and biocompatibility studies of superparamagnetic iron oxide nanoparticles as potential MRI contrast agents. *Nanoscale*, **8** (6), 3278–3287.

26 Fievet, F., Lagier, J.P., Blin, B., Beaudoin, B., and Figlarz, M. (1989) Homogeneous and heterogeneous nucleations in the polyol process for the

preparation of micron and submicron size metal particles. *Solid State Ionics*, **32**, 198–205.

27 Hugounenq, P., Levy, M., Alloyeau, D., Lartigue, L., Dubois, E., Cabuil, V., Ricolleau, C., Roux, S., Wilhelm, C., Gazeau, F., and Bazzi, R. (2012) Iron oxide monocrystalline nanoflowers for highly efficient magnetic hyperthermia. *J. Phys. Chem. C*, **116** (29), 15702–15712.

28 Arndt, D., Thoming, J., and Baumer, M. (2013) Improving the quality of nanoparticle production by using a new biphasic synthesis in a slug flow microreactor. *Chem. Eng. J.*, **228**, 1083–1091.

29 Song, Y.J., Henry, L.L., and Yang, W.T. (2009) Stable amorphous cobalt nanoparticles formed by an *in situ* rapidly cooling microfluidic process. *Langmuir*, **25** (17), 10209–10217.

30 Song, Y.J., Jin, P.Y., and Zhang, T. (2010) Microfluidic synthesis of Fe nanoparticles. *Mater. Lett.*, **64** (16), 1789–1792.

31 Shen, X.M., Song, Y.J., Li, S., Li, R.S., Ji, S.X., Li, Q., Duan, H.P., Xu, R.W., Yang, W.T., Zhao, K., Rong, R., and Wang, X.Y. (2014) Spatiotemporal-resolved nanoparticle synthesis via simple programmed microfluidic processes. *RSC Adv.*, **4** (64), 34179–34188.

32 Song, Y., Ji, S., Song, Y.-J., Li, R., Ding, J., Shen, X., Wang, R., Xu, R., and Gu, X. (2013) In situ redox microfluidic synthesis of core–shell nanoparticles and their long-term stability. *J. Phys. Chem. C*, **117** (33), 17274–17284.

33 Wang, J.M., Zhao, K., Shen, X.M., Zhang, W.W., Ji, S.X., Song, Y.J., Zhang, X.D., Rong, R., and Wang, X.Y. (2015) Microfluidic synthesis of ultra-small magnetic nanohybrids for enhanced magnetic resonance imaging. *J. Mater. Chem. C*, **3** (48), 12418–12429.

www.ebook3000.com

14

Microfluidic Synthesis of Metallic Nanomaterials

Jugang Ma and Yujun Song

University of Science and Technology Beijing, Beijing Key Laboratory for Magneto-Photoelectric Composite and Interface Science, Centre for Modern Physics Technology, Applied Physics Department, 30 Xueyuan Road, Haidian District, Beijing 100083, PR China

14.1 Introduction

Nanomaterials exhibit some unique physicochemical properties due to their size, shape, and microstructure (e.g., quantum size effect, small size effect, surface, interface effect, etc.). Nanomaterials have shown extensive industrial applications in new energy, catalysis, optoelectronic information, high-density magnetic recording media, sensors, biotechnology, and biomedical nanotechnology in the past decades, particularly for metallic nanomaterials [1–3]. There are many methods used to prepare metallic nanomaterials whether through physical fabrication or chemical synthesis [4–6]. The physical processes, such as grinding, evaporation condensation, ion sputtering, and laser ablation, can be featured as harsh and expensive or difficult to control their sizes, shapes, and structure levels, because of the requirement of high pressure or ultra-vacuum, high temperature, expensive equipment, and large-scale precise atom arrangement. And the functionalization of metallic nanomaterial cannot be precisely controlled even though they preserve high purity as compared with those synthesized by the chemistry methods. Synthesis of metal nanocrystals is usually through bottom-up processes, which can achieve the control of the atomic level. Chemical vapor deposition (CVD), metal salt reduction, and hydrothermal process are the most common methods to synthesize nanomaterials. Preparation of metallic nanomaterials by chemical methods makes the theoretical atomic design of nanomaterials possible. Sizes can be from a few to hundreds of nanometers; compositions can be from single elements to alloys [7–9]. However, there are still some issues in the controlled synthesis of metallic nanomaterials, such as the control in crystal structures and morphologies, hierarchical structure and composition regulation, ultrasmall sizes (sub-nano or less than 3 nm), and the corresponding physicochemical property control. It was no doubt that the regulation of the thermodynamic parameters in each stage of the nanocrystal formation is the key step to optimize their morphologies and structures and to

Microfluidics: Fundamentals, Devices and Applications, First Edition.
Edited by Yujun Song, Daojian Cheng, and Liang Zhao.
© 2018 Wiley-VCH Verlag GmbH & Co. KGaA. Published 2018 by Wiley-VCH Verlag GmbH & Co. KGaA.

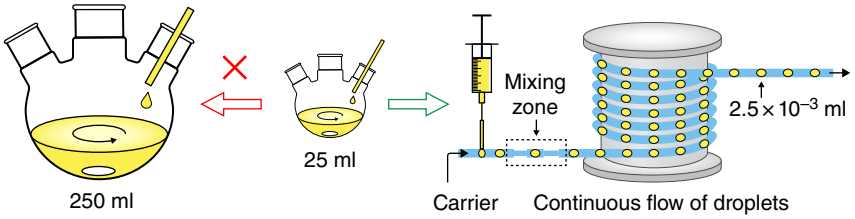


Figure 14.1 A schematic illustration of two opposite approaches to scaling up the production of noble-metal nanocrystals, which involves increase and decrease in the volume of reaction solution, respectively. (Zhang and Xia 2014 [10]. Reproduced with permission of John Wiley & Sons.)

realize their industrial application. It is not trivial for traditional methods to address all those above problems.

Compared with traditional bottle-batched synthesis methods, microfluidic processes also have unique advantages in controlled linear scale-up (i.e., scale out), and reactants can be added at desired channel positions. As shown in Figure 14.1, the first one produces a large quantity of products by increasing the volume of reactor, which has to face the torturous issue of redesigning the reactor and adjusting the corresponding reaction conditions due to the slow and nonuniform mass mixing and heat transportation in the large reaction volume. Microfluidics can be scaled out by just paralleling many copies of the same synthesis lines without losing control of reaction conditions and unit volumes along the microchannels.

Microfluidic systems have been used in the precise synthesis of many kinds of materials (e.g., organics, inorganics, polymers, and metallic materials) due to their advantages in precise reaction control, including high heat and mass transfer, temperature control, high surface-to-volume ratio, efficient mixing, low reagent consumption, and continuous production [11, 12]. One can regulate the residence times within these systems by varying the reactant flow rates and/or the structure design of the flow channel [13, 14]. Most important, it is convenient for microfluidic processes to control the spatiotemporal kinetic parameters of each stage in the formation of nanocrystals along the direction of microchannels, particularly for the process development of nanoparticle (NP) synthesis via metal salt reduction or hydrothermal and solvothermal methods. Therefore, microfluidic technology has promoted not only chemistry analysis, biomedical engineering, and disease diagnosis but also the synthesis of metallic nanomaterials [14–18]. Our series of work have shown that sizes, shapes, compositions, crystal structures, and hierarchical structures of metallic nanomaterials can be conveniently controlled by microfluidic processes due to the precise control of reaction parameters of each stage of nanocrystal formation along microfluidic channels, including mixing, reaction, nucleation, growth, aggregation, and termination [9, 19–24]. Therefore, metallic nanocrystals with controlled microstructures and unique or enhanced physicochemical properties (magnetic, optics, electricity, localized surface plasmon resonance [LSPR]) can be synthesized via microfluidic processes [25–28].

www.ebook3000.com

14.2 Microfluidic Processes for Metallic Nanomaterial Synthesis

There are two main flow types of microfluidic reactors for the synthesis of metallic nanomaterials, the segmented flow (including droplets) and the continuous (usually laminar) flow. The continuous/laminar flow can facilitate the diffusive mixing at the low Reynolds number due to the competition between shear forces and surface tension [29, 30]. In order to enhance the mixing efficiency, multipole arrays, sequence zigzag channel, or flow focusing (sudden narrowed channels) can be designed to ignite turbulent flows. As shown in Figure 14.2, two kinds of reactant fluids mixed at the orifice of the Y-mixer can run rapidly and be mixed significantly because of the suddenly much narrowed channel sizes (flow focusing). The velocity distribution shows the velocity is faster than that near the wall of the channels. The simulation results indicate that the flows are still laminar types at the increased velocity (Figure 14.2, top left). However, as the flow is pushed into the much narrowed channel from the outlet of the Y-mixer, the velocity is increased so high to form the turbulent flow, as shown in the center top and right top images in Figure 14.2, leading to a more rapid mixing in the narrow channel than that in the Y-mixer.

In the segmented flow, the interspaces can be composed of two phases (usually one gas phase formed by inlet air or gas generated in the reaction (e.g., H_2) and one liquid phase formed by oil or two immiscible liquid phases) that can further separate the continuous reaction fluids into thousands of single segments or droplets (Figure 14.3) with much smaller reaction volume than the continuous laminar flow. However, stable droplets sometimes are difficult to obtain, and the

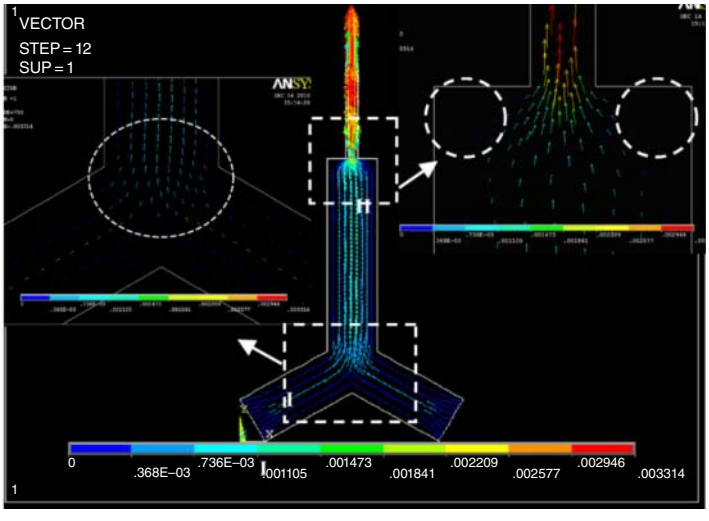


Figure 14.2 A schematic illustration of two opposite approaches to scale up the production of noble-metal nanocrystals, which involves channel diameter change-induced reaction flow types. (Song *et al*. 2011 [31]. Reproduced with permission of Elsevier.)

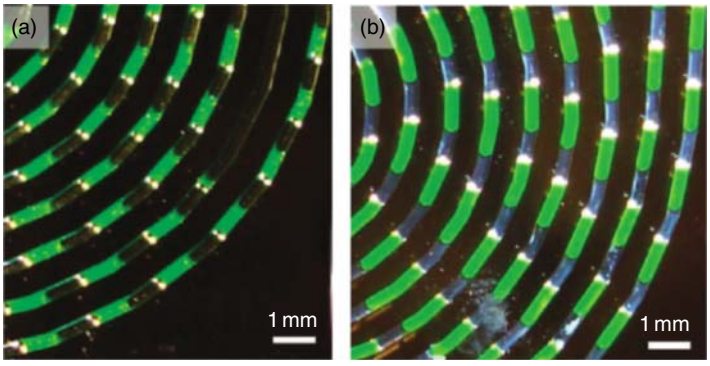


Figure 14.3 (a) Segmented slugs generated in (a) the hydrophilic microchannel (water as the carrier phase) and (b) the hydrophobic microchannel (water as the dispersed phase). Fluorescein was added to the aqueous phase to improve the optical resolution. (Cabeza *et al*. 2012 [32]. Reproduced with permission of American Chemical Society.)

flow rate cannot be increased as much as those in the continuous flow, which is usually the main obstacle for the high yield of nanocrystals.

Up to now, microfluidic processes have been widely used in the synthesis of metallic nanocrystals with well-controlled crystal structures, sizes and shapes, components, and compositions, which will be summarized and discussed in the following sections. At the same time, some special microfluidic processes will be elucidated here to show their unique features in the synthesis of specific metallic nanocrystals.

14.3 Crystal Structure-Controlled Synthesis of Metallic Nanocrystals

Face-centered cubic (fcc) and hexagonal close-packed (hcp) are two common close-packed lattices that can be stabilized in low dimensionality solids like nanodisks and nanospheres [33]. Sometimes, the small formation energy difference between two crystal phases of materials makes it difficult to tune the reaction conditions to control crystal phases by conventional bottle-batched processes. It can be conveniently realized through precisely and sensitively tuning the kinetic parameters in microfluidic processes like reaction times, flow rates, reaction temperatures, growth period, and quenching procedures.

Cobalt is a common metal material with a wealth of magnetic properties as well as the three different phases of Co NPs. The magnetization of fcc and hcp samples decreases as the temperature is increased above the blocking temperatures (T_b, the temperature below which the magnetization of the particles can spontaneously align), and the ε Co has a greater T_b more than 330 K. However, compared with buck Co, the reduced magnetic moment is attributed to both a size effect and remnants of the surfactant used in the sample preparation. The hcp phase cobalt with anisotropic high magnetic coercivity is more useful for permanent magnetic applications, while the fcc cobalt NPs have soft magnetic

www.ebook3000.com

properties. The net anisotropy of ε Co NPs is smaller than that of fcc cobalt, which is an order of magnitude smaller than that of hcp cobalt. Therefore, phase-controlled synthesis of Co nanocrystal is very important but very difficult since there is little energy difference among the three phases, particularly at nanoscale. In our prior work, three different phases of Co NPs have been synthesized successfully via precisely tuning the fluid kinetic energy (i.e., flow velocity) and growth procedures in microfluidic channels (Figure 14.4) [34].

At the flow rates of 0.9 and 0.08 ml min^{-1} together with an immediate quenching step, fcc and hcp Co crystals were formatted concomitantly, while ε-Co could be obtained without the quenching step but with an elongated Ostwald ripening (OR) period of more than 8 h. After theoretical analysis and experiment characterization, as shown in Figure 14.4, it was found that a high kinetic energy level (high flow rate) leads to mainly fcc structure (route 1), while a low kinetic energy level (low flow rate) results in mainly hcp structure (route 2). Due to the rearrangement of atoms in crystals by Ostwald ripening, the hcp-phased Co nanocrystal synthesized at a low kinetic energy level can shift to the metastable ε-phase Co nanocrystals (route 3) after being stored in the primarily produced particle solution. This is also due to the impact of the nearly isoenergetic crystal structures among the three phases of Co at nanoscale.

The above results on the crystal structure control via the flow kinetic energy level in microfluidic processes were also observed by Meital Shviro and David Zitoun in their Ni nanocrystal synthesis, where four kinds of Ni nanocrystals of different crystal phases (from fcc to hcp) are synthesized in a microfluidic device via the flow velocity control. The fcc phase Ni nanocrystals can be formed at relatively high flow rates (the high kinetic energy level, e.g., 25 µl min^{-1}), while metastable hcp-phased Ni nanocrystals are preferentially formed at relatively low flow rates (the low kinetic energy level, e.g., 100 µl min^{-1}) [33].

Although phase-controlled synthesis of Co nanocrystals can be realized by tuning the flow kinetic energy level, it is still a challenge to synthesize other metal nanocrystals with controlled crystal phases by tuning the flow kinetic energy since the energy difference between different phases in most metals are usually high enough, far over the possible flow kinetic energy. The problems are possibly overcome by controlling reaction temperatures, by utilizing oriented attachment (OA) process, by preventing aggregation and coarsening caused by Ostwald ripening, or by further annealing the resulting phase transformation during the formation stage of nanocrystals.

Thus an *in situ* rapid cooling and passivating microfluidic (IRCPM) process has been developed for the synthesis of nearly monodispersed amorphous alloy nanocrystals to realize the *in situ* spatial and temporal controls of reaction kinetics and utilize the advantages of efficient mass and heat transfer in microfluidics. Nearly all of the monodispersed amorphous CoSm alloy nanocrystals were synthesized by the IRCPM process. In comparison, the routine microfluidic process was also conducted by performing the quenching and collecting process at room temperature and without surface deactivation of nanocrystals. The results show that those nanocrystals obtained by the IRCPM process have a size deviation of about 8%, smaller than that obtained by routine microfluidic process (15%), as shown in Figure 14.5a,b. The transmission electron microscopy

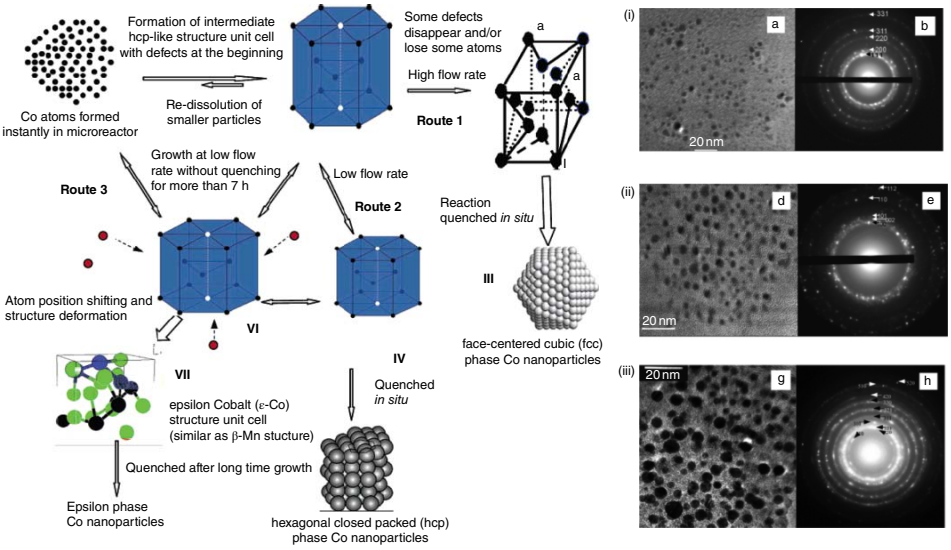


Figure 14.4 Schematic representation of the proposed formation route for the fcc, hcp, and ε-Co nanocrystals using a microfluidics process. (Liu *et al*. 2006 [34]. Reproduced with permission of Elsevier.)

www.ebook3000.com

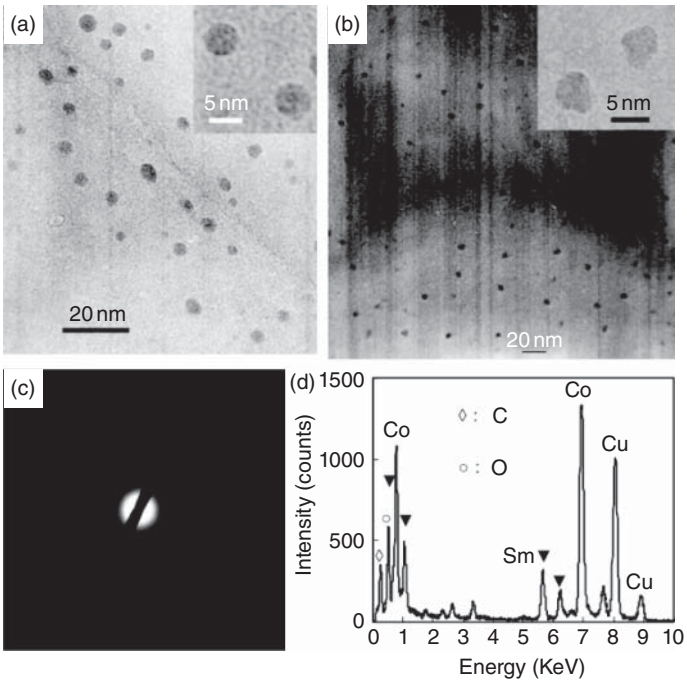


Figure 14.5 The near monodispersion CoSm alloy NPs synthesized by the microfluidic reactors. (a) The Co_5Sm nanocrystals collected under room temperature show ellipsoidal or spherical shape with broad size distribution of 5.1 ± 0.8 nm. (b) The as-synthesized Co_5Sm nanocrystals, cold quenched, mostly show nonspherical shape and uniform size of 4.8 ± 0.4 nm. (c) The selected area electron diffraction (SAED) of CoSm alloy nanocrystals shows dispersed rings, suggesting an amorphous phase. (d) The EDS spectrum of the CoSm alloy NPs indicates alloy composition reaching the intended stoichiometry (Co/Sm = 5 : 1). (Song and Henry 2009 [35]. Reproduced with permission of Springer.)

(TEM) image (Figure 14.5b) suggests that the suppression of OR can produce nanocrystals with uniform and small sizes. The broad, diffuse rings and the absence of diffraction spots indicate that the nanocrystals obtained by IRCPM process preserve amorphous phase (Figure 14.5c). The reason of the formation of the 4.8 nm Co_5Sm NPs with amorphous phase is likely due to the rapid cooling rate (1.5×10^5 K s^{-1} based on a hot ball model), which would freeze the crystal structure of nanocrystals at 50 °C and terminate the further growth and crystallization during the formation of nanocrystals. Analysis on the energy dispersive X-ray spectroscopy (EDS) spectrum (Figure 14.5d) of the CoSm alloy NPs also indicates that the alloy composition reached the intended stoichiometry atom ratio (Co/Sm = 5 : 1) and had a slight surface oxidation.

Subsequent tests revealed that these CoSm nanocrystals had a low coercivity and Tb probably due to their unique amorphous phased alloy cores and surface oxidization. The interaction among the ferromagnetic Co_5Sm cores and the antiferromagnetic oxidized surface layers endowed these nanocrystals with an H_c ranged from −300 to 150 Oe at 10 K. The amorphous CoSm nanocrystals in our study have the blocking temperature near 40 K and an average coercivity of 225 Oe at 10 K. Those CoSm NPs also exhibit high anisotropic magnetic

properties with a wasp-waist hysteresis loop and a bias coercivity shift due to the shape anisotropy and the exchange coupling between the alloy core and the thin oxidized surface layer.

More examples and details on other magnetic NP synthesis via microfluidic processes can be referred to Chapter 15.

14.4 Size- and Shape-Controlled Synthesis of Metallic Nanocrystals

Size and shape have a significant impact on the physical and chemical properties of NPs. With the decreasing of size in nanomaterials, the surface and interface become more prominent for their properties, and undesired conflicts between structures and performances appeared, particularly at nanoscale. Microfluidic approaches have achieved successes in the NP synthesis due to their reduced risk of scale-up and the precise control of thermodynamic and kinetic parameters in desired reaction stages along the microchannels for size and shape control. Except for the high surface area-to-volume ratio, tunable inner-wall properties, flow orientation, flexible structure designs, and homogeneous reaction handling at the microscale or submicroscale environment of the micromixers, the most promising advantage is the precise control of every stage (nucleation, growth, formation) in NP synthesis, which determines the size and shape of NPs. This innovative approach not only provides varieties of nanostructures for better understanding the surface enhancement and interface coupling effects but also gives a picture of the effect of size and shape on the property and performance of NPs.

Since the plasmonic properties of metal NPs intrinsically rely on their size, shape, surface morphology, crystal structure, inter-particle spacing, and the dielectric environment around them, methods to control the above structural and environmental parameters and study their effects on their plasmonic properties have become one of the most rapidly developing research fields. Microfluidic processes provide the possibility to resolve these issues and nanocrystals with sizes from nanometer to micrometer, shapes of sphere, rod, cube, or others, and controlled environments (e.g., surface ligands) can be synthesized accordingly.

Taking gold nanocrystals as examples, the combined effect of the reagent concentration and the flow rate can influence the relative growth rates of different crystal facets and induce the shape anisotropy during the growth stage. Therefore, gold nanocrystals can be shaped by changing the flow rate (Q_S: aqueous gold NP seed suspension, Q_{R1}: aqueous Au^{3+} and hexadecyl trimethyl ammonium bromide (CTAB) reagent solutions, Q_{R2}: ascorbic acid (AA)) and the concentration of Ag^+ reagent to control the growth of seed crystals (less than 5 nm) to sphere or spheroidal (Figure 14.6a-i, $Q_S/Q_{R1}/Q_{R2} = 2.5/20/2.5\ \mu l\ min^{-1}$, $[Ag^+(R1)] = 0$ mM; Figure 14.6a-ii, $Q_S/Q_{R1}/Q_{R2} = 2.6/20/2.6\ \mu l\ min^{-1}$, $[Ag^+(R1)] = 0.02$ mM) and then to rod shape (Figure 14.6b-i, $Q_S/Q_{R1}/Q_{R2} = 2.5/20/2.5\ \mu l\ min^{-1}$, $[Ag^+(R1)] = 0.05$ mM; Figure 14.6b-ii, $Q_S/Q_{R1}/Q_{R2} = 2.6/20/2.6\ \mu l\ min^{-1}$, $[Ag^+(R1)] = 0.07$ mM; Figure 14.6b-iii, $Q_S/Q_{R1}/Q_{R2} = 2.6/20/2.6\ \mu l\ min^{-1}$, $[Ag^+(R1)] = 0.1$ mM;

www.ebook3000.com

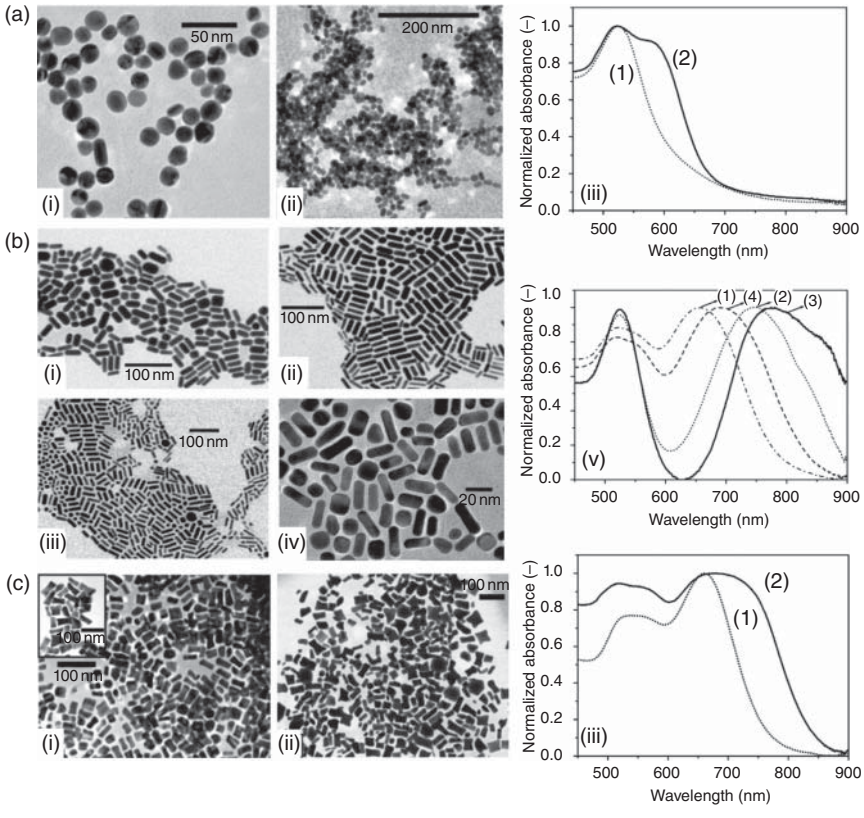


Figure 14.6 TEM images of spherical (a-i) and spheroidal (a-ii), rod shaped with the aspect ratios of 2.3 ± 0.5 (b-i), 3.2 ± 0.5 (b-ii), 4 ± 0.5 (b-iii), and 2.7 ± 0.3 (b-iv), extended and sharp-edged (c-i, c-ii) Au nanocrystals with different sizes and their corresponding UV/Vis absorbance spectra: a-iii, b-v, and c-iii, respectively, synthesized using droplet-based microfluidic processes. (Duraiswamy and Khan 2009 [36]. Reproduced with permission of John Wiley & Sons.)

Figure 14.6b-iv, $Q_S/Q_{R1}/Q_{R2} = 9/20/9\,\mu l\,min^{-1}$, $[Ag^+(R1)] = 0.1\,mM$). Sharp-edged nanocrystals like cubes, stars, tetrapods, and dog bones can also be synthesized when changing the reduce agent concentration and the feed flow rate (Figure 14.6c-i, $Q_S/Q_{R1}/Q_{R2} = 10/10/10\,\mu l\,min^{-1}$, [The reduce agent(R2)] = 40 mM; Figure 14.6c-ii, $Q_S/Q_{R1}/Q_{R2} = 2.6/8/2.6\,\mu l\,min^{-1}$, [The reduce agent(R2)] = 10 mM).

Their shape-dependent optical absorbance spectra were also shown in Figure 14.6. The spectrum difference indicates that the morphology of NPs will determine the absorbance peak position or the optical resonances.

All the optical absorbance spectra correspond to the shape of the nanocrystals. In Figure 14.6a-iii, absorbance spectrum shows spherical gold NPs exhibiting a single absorbance maximum at 520 nm and anisotropic spheroids with an additional absorbance maximum at 600 nm. Two peaks at 520 nm correspond to transverse plasmon resonance of anisotropic particles and the single surface

plasmon resonance of nearly isotropic spherical particles. Weak peak at 600 nm represents the longitudinal plasmon resonance of anisotropic gold NPs. The difference between spheres and spheroids in Figure 14.6a indicates that the morphology and aspect ratio of NPs determine the absorbance peak position. This also applies to the other absorbance spectrum in Figure 14.6b,c. As the aspect ratio (between 2 and 4) increases, optical resonances are tuning based on the size and shape of NPs and the peaks of transverse plasmon resonance and longitudinal plasmon resonance are more obvious (Figure 14.6b). Two broad peaks, peculiarly shaped NPs with acute-angled edges in Figure 14.6b, mean the good polydispersity in the particle population.

The flow rate corresponds to different flow kinetic energies, which can control the growth NPs by affecting the solute collision energy, channel wall surface shearing effects, and residue time for growth and Ostwald ripening. Temperature will directly determine the reaction rate to produce metal atoms, the nucleation and diffusion energy of formed atoms, and the competition feature of the different crystal facet formations and attachments. Therefore, the impact of temperature on the nanocrystal formation and facet attachment in microfluidic processes is even more distinct in the facet-controlled growth than the simple flow rate, leading to distinct shape-controlled growth. Sphere- and rod-shaped Sn–SnO_2 nanohybrids with different sizes have been synthesized by controlling the stabilizer types and the fluid temperatures in microchannel as shown in Figure 14.7.

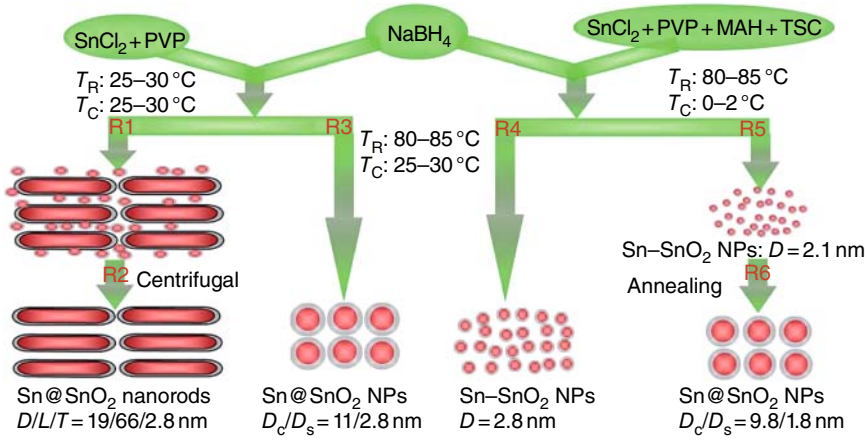


Figure 14.7 Synthesis routes and reaction conditions of microtubing-based, simple-programmed microfluidic processes (MTSPMPs) for Sn–SnO_2 nanohybrids with different morphologies and crystal structures: R1, Sn@SnO_2 nanorods mixed with some nanospheres; R2, Sn@SnO_2 nanorods with the shell thickness of 2.8 ± 0.2 nm obtained by the centrifugation of the solution from R1; R3, Sn@SnO_2 NPs (crystalline core: 11.0 ± 3.1 nm; amorphous shell: 2.8 ± 0.4 nm); R4, 2.1 nm Sn–SnO_2 NPs; R5, 2.6 nm Sn–SnO_2 NPs; R6, Sn@SnO_2 NPs (crystalline core: 9.8 ± 1.0 nm; shell: 1.8 ± 0.2 nm). T_R: reaction temperature, T_C: collection temperature. D: diameter, L: length, T: thickness, D_C: core diameter, D_S: shell thickness. (Li *et al*. 2014 [21]. Reproduced with permission of Royal Society of Chemistry.)

www.ebook3000.com

The ability of microfluidic processes in the controlled synthesis of rod- and sphere-shaped SnFe core–shell alloy NPs was further demonstrated by just tuning the reaction temperature. At a relatively lower temperature (30 °C), smooth environment gives more possibility to the nucleation and growth of NPs, and oriented growth is prioritized along the high-energy surface plane to satisfy the need of minimizing the total system energy. Thus, nanorods with the diameter of 20–30 nm and length of 50–60 nm can be synthesized (Figure 14.8a–c). At a higher temperature (90 °C), the orientated growth of NPs can be terminated at a short time, and all facets grow at the similar probability due to the high system energy, forming 14–18 nm sphere-shaped FeSn NPs (Figure 14.8d–f).

Due to the distinct core–shell structure and composition synthesized in microfluidic system at different temperatures, FeSn NPs show many unique magneto-optical properties. Superparamagnetic property of FeSn nanospheres can be observed just above 2 K (the lowest temperature during the measurement), indicating SnFe alloy cores surrounded by a Fe_2O_3 doping amorphous Sn_3O_4 layers (or tin ferrite shells) were formed. The photoluminescence spectra show a blueshift of about 58 nm in hybrid nanospheres doped with Fe and/or iron oxides compared with that of pure Sn@SnO_2 [21].

Some other methods have been coupled with microfluidic processes to control the morphologies of NPs. A pulsed mixing method is also an efficient way to mix two fluids by intermittently switching the mixing stage off and on. During the pulsed mixing process, two solutions are alternately pumped into the Y-shaped micromixer to produce pulsed layers between each solution. These pulsed layers are then introduced into the expanded microchannel, and the two

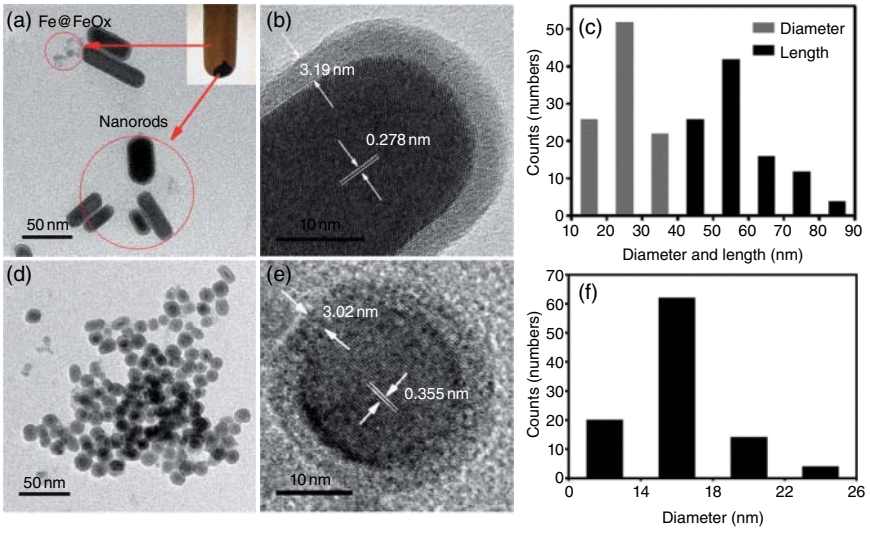
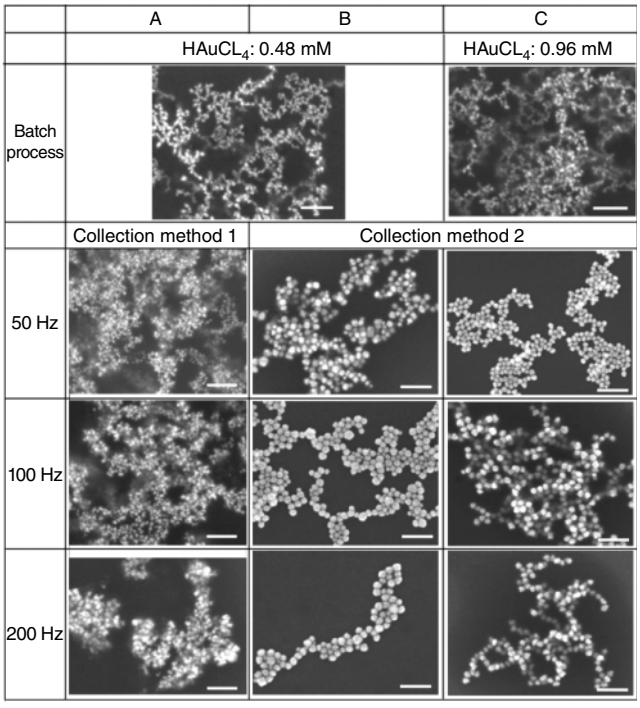


Figure 14.8 Wide-viewed TEM image (a), HR-TEM image (b), and distribution histograms of diameter and length (c) of FeSn core–shell nanorods synthesized at 30 °C; widely viewed TEM image (d), HR-TEM image (e), and distribution histogram of diameter (f) of FeSn core–shell nanospheres synthesized at 90 °C. (Ma *et al*. 2016 [24]. Reproduced with permission of Royal Society of Chemistry.)



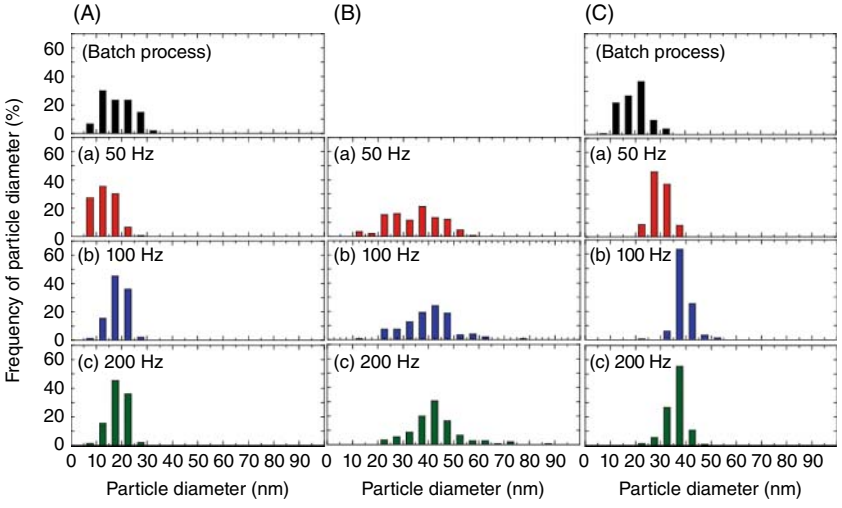


Figure 14.9 SEM images of gold nanocrystals synthesized by batch process and pulsed mixing at switching frequencies of 50 (A), 100 (B), and 200 Hz (C). Scale bars indicate 200 nm. Particle diameter distributions for gold nanocrystals synthesized by the batch process and the pulsed mixing method at switching frequencies of (a) 50 Hz, (b) 100 Hz, and (c) 200 Hz. (A) Collection method 1 with a $HAuCl_4$ concentration of 0.48 mM. (B) Collection method 2 with a $HAuCl_4$ concentration of 0.48 mM. (C) collection method 2 with a $HAuCl_4$ concentration of 0.96 mM. (Sugano *et al*. 2010 [37]. Reproduced with permission of Springer.)

www.ebook3000.com

solutions subsequently inter-diffuse at their common interfaces in the expanded microchannel. This mixing method can be expected to tune the mixing rate by only changing the switching frequency of two solutions. Therefore, it is more suitable than other passive micromixers (e.g., splitting-and-recombination micromixer) to achieve significantly rapid mixing and to decrease the diffusion length of two solutions by stacking of fluid lamellas. Gold nanocrystals with a narrow size distribution have been synthesized via this pulsed mixing method in microfluidics (Figure 14.9). The results show that the different switching frequencies have a significant influence on size distribution due to rapid mixing. At a higher switching frequency (200 Hz), the mean diameter of the gold nanocrystals increased with a narrow size distribution. It is also demonstrated that the pulsed mixing method decreases the coefficient of variation of particle diameters due to rapid mixing.

Experimental studies and simulations have given an amazing image that the size and shape of NPs have great effects on the catalysis and sensing performance, biomedical functions, and optoelectronic properties [38, 39]. It has also been demonstrated that NPs with different shapes, facets, and orientations preserve different catalytic activities and selectivities. Many studies indicate that noble metals (e.g., Au, Pd, Pt, or Ag) are easier to form unique and neat shapes. Lots of noble-metal nanocrystals with desired shapes (spheres, rods, cuboctahedra, cubes, bars, octahedra, tetrahedra, decahedra, icosahedra, bipyramids, plates, and wires) have been successfully synthesized via microfluidic processes, and they possess unique size- and shape-dependent properties that cannot be observed in their bulk counterparts [10, 25, 40, 41]. As a key factor in the NP formation process, orientation can be tuned through the carrier gases and capping agents in gas–liquid dual-phased microfluidic systems. Three carrier phases in the segment microfluidics were compared in Figure 14.10. The TEM images show that the shape of Pd nanocrystals can be controlled by different carrier phases: oxygen (O_2), nitrogen (N_2), and carbon monoxide (CO). The neat Pd nanorods can be obtained by using O_2 as the carrier gas (Figure 14.10a), and their aspect ratio can be tuned by the flow rate of oxygen and reactants. The anisotropic growth can be inhibited in oxygen atmosphere since oxidative atmosphere can etch nanorods into nanocube-like nanocrystals (less aspect ratio). When O_2 was replaced by N_2, Pd NPs of irregular shape and varieties of sizes can be obtained (Figure 14.10b). Without O_2, the system will be free from the oxidative etching, and the anisotropic growth will be terminated, leading to a wider distribution of sizes. If using CO as the carrier phase, thin Pd nanosheets with narrow size distribution (Figure 14.10c) can be synthesized. This relative weak reducing agent can be selectively chemisorbed at different facets and active sites and further leads to the obvious anisotropic growth [43].

Further study suggests that the influence of coupling of CO can be selectively chemisorbed according to the thermodynamic status of reaction systems. Pd nanosheets with multifarious nanostructures (Figure 14.10e–h) can be obtained by just tuning the fluid temperature using CO as the carrier phase since the binding energy between CO and Pd will be changed at different temperatures. Shapes of Pd NPs can change from sharp triangular nanosheets with a mean edge length of 41 ± 12.8 nm (Figure 14.10e), to triangular nanosheets with a mean

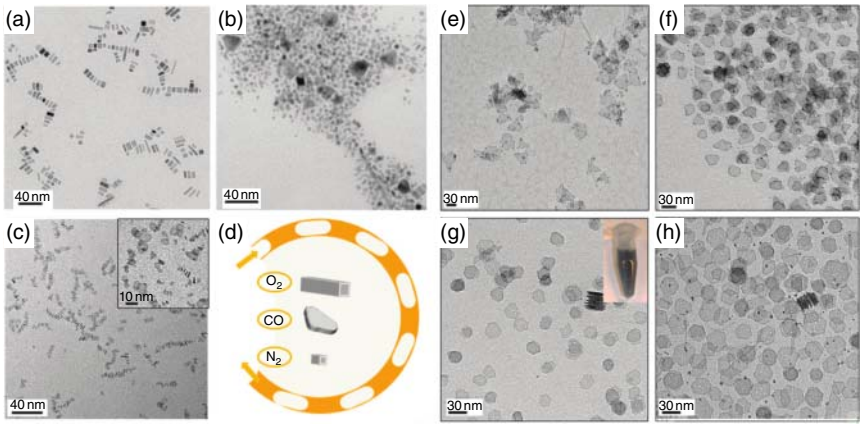


Figure 14.10 TEM images of the Pd nanostructures obtained with segmented flow at 160 °C, 120 s residence time, and $L_2/L_1 = 1.8$: (a) O_2/liquid = 0.8, (b) N_2/liquid = 3.5, and (c) CO/liquid = 3.5. (d) Scheme of palladium nanostructures obtained with the different segmentation gases: oxygen, carbon monoxide, and nitrogen. Temperature 160 °C and residence time of 120 s. TEM images of palladium nanosheets obtained with carbon monoxide segmentation and liquid segments containing dimethyl formamide (DMF) and TTABr: (e) 35 °C, (f) 50 °C, (g) 90 °C (the inset is a detail of a vial with the Pd nanosheets collected at the outlet), and (h) 130 °C. (Sebastian *et al*. 2016 [42] http://pubs.rsc.org/-/content/articlehtml/2016/nr/c5nr08531d. Used under CC BY 3.0 https://creativecommons.org/licenses/by/3.0/.)

edge length of 23 ± 7.0 nm mixed with a trace of other shape nanosheets (e.g., triangle and hexagon) (Figure 14.10f), to majority of homogenous hexagonal nanosheets (Figure 14.10g), and then to polyhedrons (Figure 14.10h) as the system temperatures were increased from 35 to 50 °C, to 90 °C, and then to 130 °C, respectively. Other shapes of Pd nanostructures can be obtained as a consequence of the weak adsorption of CO on the basal planes of Pd crystals when the temperature is increased higher than 170 °C.

Effects of carrier phase on the shape control of nanocrystals have further been confirmed by a series of control experiments [44–46]. In Zhang's work [47], Pd and Ag nanocrystals with different shapes are obtained through changing the carrier phase (air or oil), which also demonstrates the significant effect and necessity of oxidative etching and multiphase mass transfer on the shape and size control in the segment microfluidic processes.

Figure 14.11 shows that the capping agent can be used to induce the growth of crystal anisotropy, forming different shapes of nanocrystals. Pd cuboctahedra (Figure 14.11a) and cube (Figure 14.11b) were prepared by using KCl and KBr as the capping agent, respectively. The seed growth can be further used to tailor the size of Pd nanocubes using KBr as the capping agent (Figure 14.11c,d) and further tailor their shapes using different reducing agents. For an instance, even in the absence of KBr as the capping agent, NPs can grow up to 37 nm octahedra or 21 nm concave cubes from the 18 nm nanocubes as seeds by changing reducing agents to formaldehyde (HCHO) or L-AA, respectively, whose TEM images were shown in Figure 14.10e (using HCHO) and Figure 14.10f (using AA). These results indicate that the influence of capping agents on crystal growth in microfluidic

www.ebook3000.com

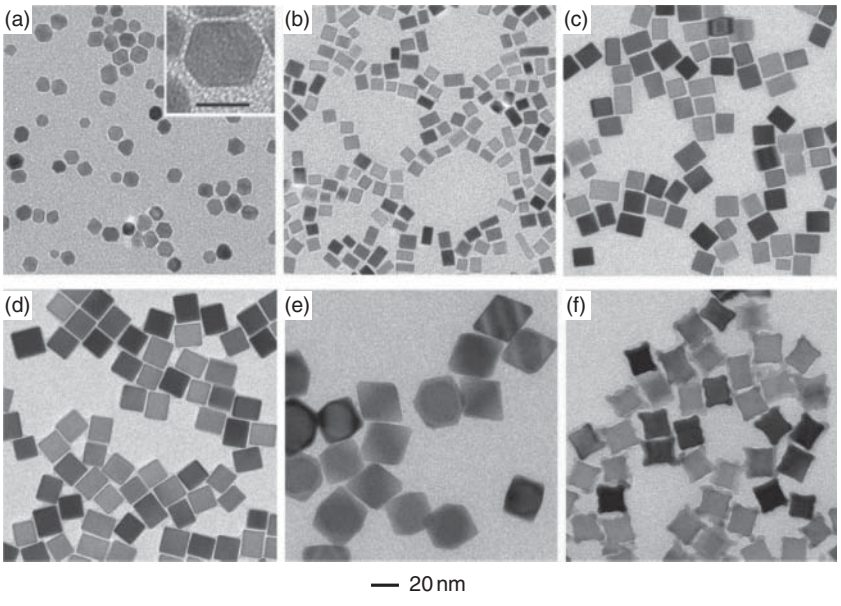


Figure 14.11 TEM images of Pd nanocrystals with well-controlled sizes and shapes: (a, b) 9 nm Pd cuboctahedra and 10 nm Pd cubes prepared using AA as a reductant and (a) KCl and (b) KBr as capping agents, respectively; (c) 14 nm Pd cubes prepared using seeded growth on the 10 nm Pd cubes with AA as a reductant in the presence of KBr; (d) 18 nm Pd cubes obtained via further growth of the 14 nm Pd cubes with AA as a reductant in the presence of KBr; (e) 37 nm Pd octahedra grown from 18 nm Pd cubes using HCHO as a reductant in the absence of KBr, and (f) 21 nm Pd concave cubes grown from the 18 nm Pd cubes with AA as a reductant in the absence of KBr. (Zhang *et al*. 2014 [47]. Reproduced with permission of American Chemical Society.)

is similar to the batch reactors, but microfluidics can facilitate the scale-up in precise synthesis.

Complex shapes of nanostructures increased their dimension parameters that makes NPs difficult to be synthesized in the traditional methods. Due to the advantages of flow orientation and wall shear effects, more complex and delicate nanostructures can be synthesized successfully via microfluidic [12]. Worm- and chain-like nanostructures doped with some short rodlike, spherical, or ellipsoidal NPs were synthesized by a microfluidic reactor process by our group. Figure 14.12 shows the TEM images and SAED patterns of Pd (a), Pt (c), and Ru (e), respectively. These chain-like NPs with high aspect ratio are in metastable states, which will be further transformed to ellipsoidal, spherical, or short rodlike species with enhanced crystallinity after sonicating for more than half an hour or stirring for hours. Through counting the sizes and statistical ratios of wormlike and chain-like shapes to spherical and ellipsoidal shapes, we found that these three metals have roughly the same shape, which can be attributed to the same formation process of NPs in microfluidic systems. In the formation process, spherical or ellipsoidal precursors (small nanoclusters) are formed in the microchannels and then some rod-shaped NPs will attach to each

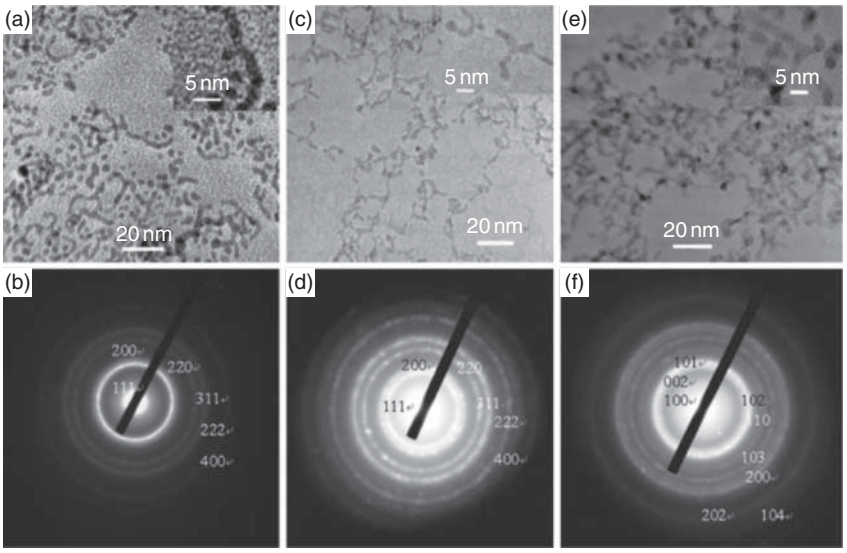


Figure 14.12 The as-synthesized worm-/chain-like NPs by the microfluidic reactor: (a, c, and e) TEM images of the as-synthesized Pd NPs, Pt NPs, and Ru NPs, respectively; (b, d, and f) SAED patterns of the as-synthesized Pd NPs, Pt NPs, and Ru NPs, respectively. (Song *et al*. 2010 [48]. Reproduced with permission of Springer.)

other to form wormlike-shaped nano-chains due to the flow orientation effect and/or wall shear effects.

14.5 Multi-Hierarchical Microstructure- and Composition-Controlled Synthesis of Metallic Nanocrystals

The controlled microstructure and composition of metal nanocrystals have attracted considerable attention in recent years due to the precisely tuned electronic, optical, and catalytic properties [49–52]. Multi-hierarchical structure formation is based on a more refined control of shapes and sizes, while the metallic alloy gives a more diverse electron orbits and atom arrangement in NPs. Therefore, it is still difficult to synthesize metallic nanocrystals of multi-hierarchical microstructures up to now. The traditional batch mean by adding the gold precursors dropwise or all at once often leads to a cluster system that further leads to the uneven particle size distributions [53]. Due to the efficient time and spatial resolution and the precise kinetic and thermodynamic parameter control, microfluidics has to be considered as a good way to synthesize these kinds of nanomaterials.

To investigate the relationship between the physiochemical properties and the compositions or microstructures, Song's group synthesized Co@Au NPs of different thickness by combining the displacement process and the reduction–deposition process in a microfluidic reactor. As shown in Figure 14.13, NPs

www.ebook3000.com

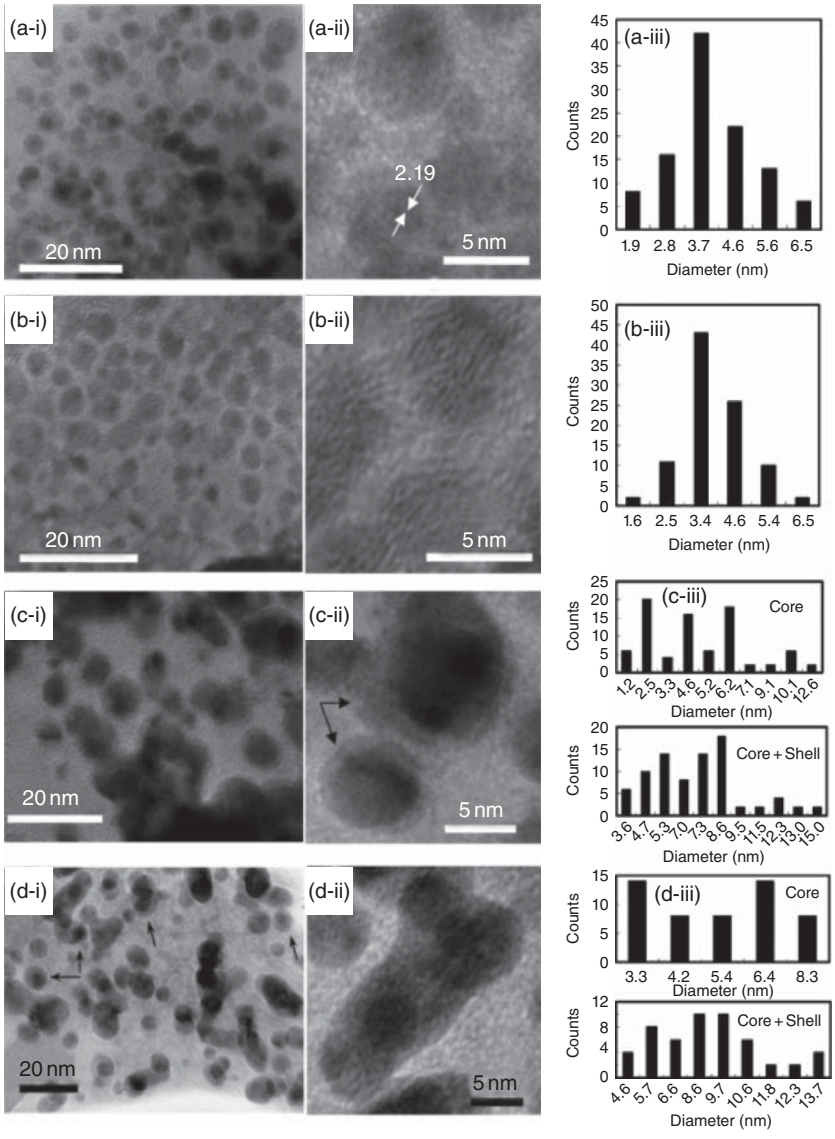


Figure 14.13 The wide view of the TEM image (i), the magnified TEM images (ii), and the histogram of the size distribution (iii) of Co nanocrystals (a), the Co@Au nanocrystals formed by the displacement process (b), the Co@Au nanocrystals formed by the displacement and the first reduction–deposition process (c), and the Co@Au nanocrystals formed by the second reduction–deposition process (d). (Song *et al*. 2012 [54]. Reproduced with permission of American Chemical Society.)

changed from Co (Figure 14.13a) to Co@Au with slightly brighter shells and darker cores (Figure 14.13b), to clearly brighter thick shells and darker cores (Figure 14.13c), and then to distinct brighter and thicker shells and darker cores (Figure 14.13d), which can be successfully synthesized.

The results indicate that shell thickness has significant effects on the fine structure of the core materials. The hybrid structure with magnetic Co as cores and optical Au as shell shows unique magneto-optical properties. Due to the enhanced Co–Au interfacial pinning effects with the shell evolution from the partial coverage to full coverage and the potential atom rearrangement in the interface, the coercivity of Co@Au NPs changed with shell thickness. Besides, the LSPR peak intensity of the core–shell Co@Au NPs can be significantly enhanced with a line width broadening and an increased line shape variation with the shell thickness increasing due to the core–shell electronic and magnetic interaction when irradiated by electromagnetic fields.

Furthermore, take hollow gold nanoparticles (HGNPs) as an example [53]. Large-scaled online synthesis can be realized by two stages, the preparation of the sacrificial Co templates and then growth of gold shell on Co templates in a microfluidic platform. Co templates with desired sizes and narrow size distribution can be obtained by changing the concentration of reducing agents (e.g., $NaBH_4$) and the flow rate of reagents. Hydrolysis of $NaBH_4$ produces the gas slugs in the process of reaction that corresponds to the segment flow in the microchannel and provides a sufficient mixing intensity. Two-key reaction conditions of the residence time and Co/polyvinyl pyrrolidone (PVP) and Co–Au molar ratios were optimized in the second stage to obtain hollow gold nanocrystals of high quality and properties in the shortest time. It also realized the scaling up about 10 times in microfluidic with a longer tubing, which reveals itself, has the ability to overcome the production rate limitations and the potential of industrialization.

This approach of galvanic replacement and seed or templates also have been used for synthesizing multi-hierarchical Au–Ag NPs in microfluidic system. As shown in Figure 14.14, Au–Ag nanocups, nanocages, and nanoboxes were obtained as the concentration of $HAuCl_4$ increased, respectively. Compared with the absence of Triton X-100 (a nonionic surfactant), the structure integrity of NPs has been improved. In the presence of Triton X-100, interfacial adsorption of nanocrystals could be effectively mitigated, which makes sure the growth of microstructure can be stable and continuous. Because of the increasing of Au content, their optical properties show the obvious redshift.

The flow rate, as an easily tuned condition, can be used to control the microstructure. By varying the flow rate in the microfluidic device, a series of Au nanoplates with controlled thickness and multi-hierarchical microstructures (rolled and rigid) can be synthesized [56]. The folded or rolled gold nanoplates were obtained at a high flow rate of 70 μl min^{-1}. The folded or rolled structure can be formed to reduce the surface energy. On the contrary, the rigid, flat nanoplates can be obtained at a low flow rate; they were thin that the surface stress was not strong enough to roll the nanoplates. Additionally, the rolled ones show considerable high catalytic activity in glucose oxidation, which has a higher specific surface area relying on the morphology of nanoplates.

www.ebook3000.com

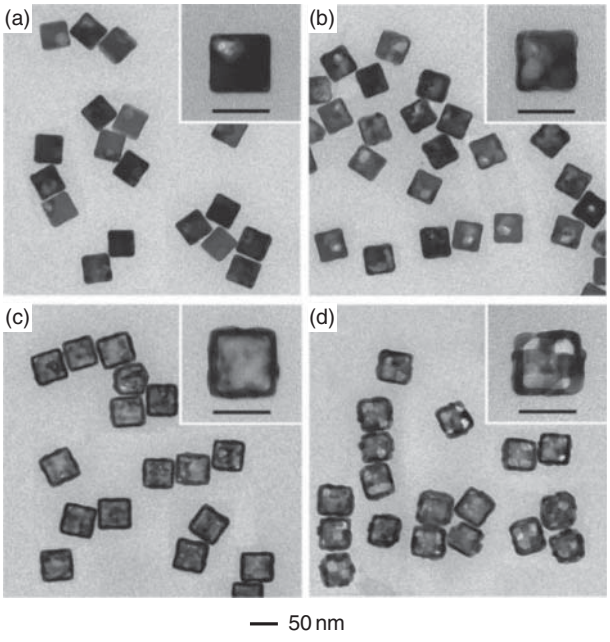


Figure 14.14 TEM images show the structural evolution of 40 nm Ag cubs into Au–Ag nanoboxes and nanocages in different concentrations of $HAuCl_4$ in the presence of Trion X-100. The scale bars in the insets correspond to 40 nm. (Zhang *et al*. 2014 [55]. Reproduced with permission of American Chemical Society.)

In the above review, we successively discussed their synthesis features and structures and analyzed the factors influencing the formation of the NPs. Some typical metallic nanomaterials synthesized by microfluidics were summarized in Table 14.1, which gave the detailed microchannel materials and parameters of tuning reaction.

14.6 Summary and Outlook

Different kinds of metallic nanocrystals have been successfully prepared using microfluidic reactors fabricated by varieties of constructed materials (e.g., polymers, glass). Their sizes, shapes, crystal structures, compositions, and components can be controlled by regulating the kinetic parameters, such as concentrations and flow rates of the reagents, residence times and reaction temperatures at each stage of NP formation, product collection methods, and surface capping agents on NPs. Examples of metallic NPs synthesized by microfluidic processes are summarized in Table 14.1, giving the constructed materials, channel sizes, and kinetic parameters during NP formations. With synthesis conditions with low thermodynamic energy (low concentration, low flow rate, low temperature), the main growth trend of the nanocrystal will show atoms stacking freely along the low-index facet, leading to large nanocrystals of low crystalline quantity or different shapes. Otherwise, reagents in microchannels

Table 14.1 A summary of metallic nanomaterials synthesized using microfluidic devices.

Microfluidic devices	Channel dimension	Flow rate	Composition	Shape	Size	Reaction and conditions	References
Polytetrafluoro-ethylene (PTFE) tube, silica capillaries	Diameter of 0.5 mm	2.6×10^{-4} ml droplets; 0.6–2.0 ml min^{-1} carrier phase	Pd, Ag	Nanocube	15–22 nm	Oil or air phase/80 °C	[10]
Fluorinated-ethylene–propylene (FEP) tube	Diameter of 1 mm	8 ml min^{-1}	Ni	Sphere	~80 nm	70 °C	[25]
Teflon/polyethere-therketone (PEEK)	150–400 μm wide, 300–700 μm deep, 48 cm long	0.08–0.9 ml min^{-1}	Co	Sphere (fcc, hcp, ε)	1.6–6.8 nm	20–40 °C	[34]
SU-8	60 μm wide, 30 cm long	10 ml min^{-1}	CoSm	Ellipsoidal or sphere	~5 nm	Cold quenched/RT/50 °C	[35]
SU-8 (an epoxy photosensitive resin)	300 μm wide, 155 μm deep, 0.45 m long	2.6 μl to 20 μl min^{-1}	Au	Sphere and rod	~20 nm	Ag^{+} as ancillary reagent/RT	[36]
Pyrex glass	Inlet: 25 μm wide, 25 μm deep and 25 μm long; Outlet: 3 μm wide, 25 μm deep and 440 μm long	40 nl s^{-1}	Au	Sphere	~40 nm	Pulsed mixing	[37]
PTFE tube	Diameter of 5.8 mm	30.0 and 50 ml min^{-1}	Pd	Cuboctahedra, cubes, octahedron, concave cubes	9–37 nm	Capping agent 22–80 °C	[47]
SU-8	60 μm wide, 600 μm deep, 30 cm long	80 μl min^{-1}	Pd, Pt, and Ru	Worm/chain like	*D*: 2.5 nm; *L*: ~6 nm	Quenched	[48]
SU-8	60 μm wide, 30 cm long	0.08 ml min^{-1}	Co@Au	Core–Shell	3–15 nm	Displacement method/50 °C	[54]
PTFE tube	Diameter of 0.8 mm, ~300 cm long	15 ml h^{-1}; 25 ml h^{-1}	Au	Hollow sphere	45 nm	Co template/RT	[53]
PTFE tube	Inner diameter of 0.5 mm, 6 m long	120, 20, and 10 μl min^{-1} in different tubes	Au–Ag	Nanocups, nanocages, nanoboxes	~40 nm	Displacement method/RT	[55]
SU8-2100	3 cm long	5–70 μl min^{-1}	Au	Folded and rigid nanoplate	~50 nm; 1–5 nm thick	Collected in ice water	[56]
Tygon polyvinyl tubing	Diameter of 2.79 mm 540.0 cm long	50.0 ml min^{-1}	Au	Rod	Diameter: ~12.0 nm; Length: 28.0–50.0 nm	Overgrowth/RT	[57]

www.ebook3000.com

will be consumed rapidly to cause rapid nucleation and non-oriented growth, usually leading to sphere-shaped nanocrystals. Utilizing time–temperature equivalence principle during the NP growth, we can realize the high throughput reaction and further scale-up of yield.

Lab-on-a-chip process can achieve less resource consumption and less waste output for high throughput testing of NP at low cost. However, the miniaturization of microfluidics brings not only opportunities but also challenges, such as microfluidic design. Blockage often occurs in the process of metallic nanomaterial synthesis because of deposition or adsorption to the interior surface of microchannel. This needs us to find a more efficient way (optimizing microchannel wall materials and device microstructure and increasing flow velocity or the internal pressure) to ensure the continuity and completeness of the experiment. It can also be resolved by redesigning the reaction processes, such as using short reaction channel at high temperature, and terminating the growth of NPs rapidly in a sudden temperature reduce [34, 35].

Nowadays, some traditional interdisciplinary technologies, such as online monitoring or analysis, have been coupled with microfluidic processes to achieve the enhanced functions [58]. UV–Vis absorbance spectroscopy [59], resonant light-scattering spectroscopy [60], and time-resolved *in situ* X-ray scattering spectra [61] equipped with the microfluidics process hold great promise for *in situ* studying of supersaturated solute formation, nucleation, growth, and aggregation under supercritical conditions. Synchrotron neutron imaging and diffraction have also been used to *in situ* analyze NP formation mechanism in each stage [61]. Monitoring of the reaction of each stage would provide precise time-resolved description of nanocrystal formation in microscale, which is usually difficult by conventional methods. Up to now, microfluidic processes have shown not only great abilities in biochemical analysis, clinical diagnose, and *in vitro* bionic model but also great progress in the controlled synthesis of metallic nanomaterials. We expect that progress will be achieved in the precise size-, shape-, and microstructure-controlled synthesis of varieties of metal or alloy NPs and their application extended. Since microfluidic processes also preserve the high throughput ability in the synthesis at low cost, they can be an efficient alternative to build up the gene data base in the metallic NPs by precisely correlating these microstructures with their physicochemical properties.

Acknowledgments

This work was supported by National S&T Major Project (pre-approved No. SQ2018ZX100301), NSFC (Grant No. 51371018 & 81372425) and the Fundamental Research Funds for the Central University of China (FRF-BR-14-001B).

References

1 Nel, A.E., Maedler, L., Velegol, D., Xia, T., Hoek, E.M.V., Somasundaran, P. *et al.* (2009) Understanding biophysicochemical interactions at the nano-bio interface. *Nat. Mater.*, **8**, 543–557.

2 Wu, Z.-S., Ren, W., Wen, L., Gao, L., Zhao, J., Chen, Z. *et al.* (2010) Graphene anchored with Co_3O_4 nanoparticles as anode of lithium Ion batteries with enhanced reversible capacity and cyclic performance. *Acs Nano*, **4**, 3187–3194.
3 Kim, J.E., Choi, J.H., Colas, M., Kim, D.H., and Lee, H. (2016) Gold-based hybrid nanomaterials for biosensing and molecular diagnostic applications. *Biosens. Bioelectron.*, **80**, 543–559.
4 Perezjuste, J., Pastorizasantos, I., Lizmarzan, L., and Mulvaney, P. (2005) Gold nanorods: synthesis, characterization and applications. *Coord. Chem. Rev.*, **249**, 1870–1901.
5 Long, N.V., Yang, Y., Minh Thi, C., Minh, N.V., Cao, Y., and Nogami, M. (2013) The development of mixture, alloy, and core–shell nanocatalysts with nanomaterial supports for energy conversion in low-temperature fuel cells. *Nano Energy*, **2**, 636–676.
6 Li, L., Fan, M., Brown, R.C., Van Leeuwen, J., Wang, J., Wang, W. *et al.* (2006) Synthesis, properties, and environmental applications of nanoscale iron-based materials: a review. *Crit. Rev. Env. Sci. Technol.*, **36**, 405–431.
7 Song, Y., Wang, R., Rong, R., Ding, J., Liu, J., Li, R. *et al.* (2011) Synthesis of well-dispersed aqueous-phase magnetite nanoparticles and their metabolism as an MRI contrast agent for the reticuloendothelial system. *Eur. J. Inorg. Chem.*, **2011**, 3303–3313.
8 Song, Y., Yin, W., Fernandes, C., and Ruda, H.E. (2013) Fabrication of one-dimension ZnSe and ZnO nanostructures via anodic alumina template assisted vapor–liquid–solid growth process. *Thin Solid Films*, **548**, 130–137.
9 Shen, X., Song, Y., Li, S., Li, R., Ji, S., Li, Q. *et al.* (2014) Spatiotemporal-resolved nanoparticle synthesis via simple programmed microfluidic processes. *RSC Adv.*, **4**, 34179.
10 Zhang, L. and Xia, Y. (2014) Scaling up the production of colloidal nanocrystals: should we increase or decrease the reaction volume? *Adv. Mater.*, **26**, 2600–2606.
11 Marre, S. and Jensen, K.F. (2010) Synthesis of micro and nanostructures in microfluidic systems. *Chem. Soc. Rev.*, **39**, 1183–1202.
12 Song, Y., Hormes, J., and Kumar, C.S. (2008) Microfluidic synthesis of nanomaterials. *Small*, **4**, 698–711.
13 Krishna, K.S., Li, Y., Li, S., and Kumar, C.S. (2013) Lab-on-a-chip synthesis of inorganic nanomaterials and quantum dots for biomedical applications. *Adv. Drug Delivery Rev.*, **65**, 1470–1495.
14 Elvira, K.S., Casadevall i Solvas, X., Wootton, R.C., and deMello, A.J. (2013) The past, present and potential for microfluidic reactor technology in chemical synthesis. *Nat. Chem.*, **5**, 905–915.
15 Martinez, A.W., Phillips, S.T., Whitesides, G.M., and Carrilho, E. (2010) Diagnostics for the developing world: microfluidic paper-based analytical devices. *Anal. Chem.*, **82**, 3–10.
16 Gutmann, B., Cantillo, D., and Kappe, C.O. (2015) Continuous-flow technology-a tool for the safe manufacturing of active pharmaceutical ingredients. *Angew. Chem.*, **54**, 6688–6728.

www.ebook3000.com

17 Zhao, Y., Cheng, Y., Shang, L., Wang, J., Xie, Z., and Gu, Z. (2015) Microfluidic synthesis of barcode particles for multiplex assays. *Small*, **11**, 151–174.

18 Liu, Y., Du, J., Choi, J.S., Chen, K.J., Hou, S., Yan, M. *et al.* (2016) A high-throughput platform for formulating and screening multifunctional nanoparticles capable of simultaneous delivery of genes and transcription factors. *Angew. Chem.*, **55**, 169–173.

19 Song, Y., Ji, S., Song, Y.-J., Li, R., Ding, J., Shen, X. *et al.* (2013) In situ redox microfluidic synthesis of core–shell nanoparticles and their long-term stability. *J. Phys. Chem. C*, **117**, 17274–17284.

20 Song, Y., Wang, Y., Li, B.B., Fernandes, C., and Ruda, H.E. (2013) Interface interaction induced ultra-dense nanoparticles assemblies. *Nanoscale*, **5**, 6779–6789.

21 Li, S., Zhong, X., Song, Y., Shen, X., Sun, J., Song, Y. *et al.* (2014) Controlled hybridization of Sn–SnO_2 nanoparticles via simple-programmed microfluidic processes for tunable ultraviolet and blue emissions. *J. Phys. Chem. C*, **2**, 7687.

22 Song, Y., Yin, W., Wang, Y.-H., Zhang, J.-P., Wang, Y., Wang, R. *et al.* (2014) Magneto-plasmons in periodic nanoporous structures. *Sci. Rep.*, **4**. doi: 10.1038/srep04991

23 Wang, J., Zhao, K., Shen, X., Zhang, W., Ji, S., Song, Y. *et al.* (2015) Microfluidic synthesis of ultra-small magnetic nanohybrids for enhanced magnetic resonance imaging. *J. Phys. Chem. C*, **3**, 12418–12429.

24 Ma, J., Wang, J., Zhong, X., Li, G., and Song, Y. (2016) Synthesis of $Sn(1-x)Fex@FeySn(1-y)O$znanohybrids via a simple programmed microfluidic process. *RSC Adv.*, **6**, 84255–84261.

25 Zeng, C.F., Wang, C.Q., Wang, F., Zhang, Y., and Zhang, L.X. (2012) A novel vapor–liquid segmented flow based on solvent partial vaporization in microstructured reactor for continuous synthesis of nickel nanoparticles. *Chem. Eng. J.*, **204**, 48–53.

26 Knauer, A. and Koehler, J.M. (2014) Screening of nanoparticle properties in microfluidic syntheses. *Nanotechnol. Rev.*, **3**, 5–26.

27 Karim, A.M., Al Hasan, N., Ivanov, S., Siefert, S., Kelly, R.T., Hallfors, N.G. *et al.* (2015) Synthesis of 1 nm Pd nanoparticles in a microfluidic reactor: insights from *in situ* X-ray absorption fine structure spectroscopy and small-angle X-ray scattering. *J. Phys. Chem. C*, **119**, 13257–13267.

28 Xu, L., Peng, J.H., Yan, M., Zhang, D., and Shen, A.Q. (2016) Droplet synthesis of silver nanoparticles by a microfluidic device. *Chem. Eng. Proc.*, **102**, 186–193.

29 Thorsen, T., Roberts, R.W., Arnold, F.H., and Quake, S.R. (2001) Dynamic pattern formation in a vesicle-generating microfluidic device. *Phys. Rev. Lett.*, **86**, 4163–4166.

30 Choi, S.B., Barron, R.F., and Warrington, R.O. (1991) Fluid flow and heat transfer in microtubes. Micromechanical Sensors, Actuators and Systems: Proceedings of 1991 ASME Winter Annual Meeting, vol. 32, pp. 123–134.

31 Song, Y., Li, R., Sun, Q., and Jin, P. (2011) Controlled growth of Cu nanoparticles by a tubular microfluidic reactor. *Chem. Eng. J.*, **168**, 477–484.

32 Cabeza, V.S., Kuhn, S., Kulkarni, A.A., and Jensen, K.F. (2012) Size-controlled flow synthesis of gold nanoparticles using a segmented flow microfluidic platform. *Langmuir*, **28**, 7007–7013.

33 Shviro, M. and Zitoun, D. (2013) Nickel nanocrystals: fast synthesis of cubes, pyramids and tetrapods. *RSC Adv.*, **3**, 1380–1387.

34 Liu, H., Song, C., Zhang, L., Zhang, J., Wang, H., and Wilkinson, D.P. (2006) A review of anode catalysis in the direct methanol fuel cell. *J. Power Sources*, **155**, 95–110.

35 Song, Y. and Henry, L.L. (2009) Nearly monodispersion CoSm alloy nanoparticles formed by an *in-situ* rapid cooling and passivating microfluidic process. *Nanoscale Res. Lett.*, **4**, 1130–1134.

36 Duraiswamy, S. and Khan, S.A. (2009) Droplet-based microfluidic synthesis of anisotropic metal nanocrystals. *Small*, **5**, 2828–2834.

37 Sugano, K., Uchida, Y., Ichihashi, O., Yamada, H., Tsuchiya, T., and Tabata, O. (2010) Mixing speed-controlled gold nanoparticle synthesis with pulsed mixing microfluidic system. *Microfluid. Nanofluid.*, **9**, 1165–1174.

38 Wheeler, D.A. and Zhang, J.Z. (2013) Exciton dynamics in semiconductor nanocrystals. *Adv. Mater.*, **25**, 2878–2896.

39 Wang, G., Huang, B., Xiao, L., Ren, Z., Chen, H., Wang, D. *et al.* (2014) Pt skin on AuCu intermetallic substrate: a strategy to maximize Pt utilization for fuel cells. *J. Am. Chem. Soc.*, **136**, 9643–9649.

40 Mettela, G., Siddhanta, S., Narayana, C., and Kulkarni, G.U. (2014) Nanocrystalline Ag microflowers as a versatile SERS platform. *Nanoscale*, **6**, 7480–7488.

41 Kumar, D.V.R., Kasture, M., Prabhune, A.A., Ramana, C.V., Prasad, B.L.V., and Kulkarni, A.A. (2010) Continuous flow synthesis of functionalized silver nanoparticles using bifunctional biosurfactants. *Green Chem.*, **12**, 609.

42 Sebastian, V., Smith, C.D., and Jensen, K.F. (2016) Shape-controlled continuous synthesis of metal nanostructures. *Nanoscale*, **8**, 7534–7543.

43 Kondoh, H., Toyoshima, R., Monya, Y., Yoshida, M., Mase, K., Amemiya, K. *et al.* (2016) In situ analysis of catalytically active Pd surfaces for CO oxidation with near ambient pressure XPS. *Catal. Today*, **260**, 14–20.

44 Cabrera, F.C., Melo, A., de Souza, J.C.P., Job, A.E., and Crespilho, F.N. (2015) A flexible lab-on-a-chip for the synthesis and magnetic separation of magnetite decorated with gold nanoparticles. *Lab Chip*, **15**, 1835–1841.

45 Zhang, L., Wang, Y., Tong, L.M., and Xia, Y.N. (2013) Seed-mediated synthesis of silver nanocrystals with controlled sizes and shapes in droplet microreactors separated by Air. *Langmuir*, **29**, 15719–15725.

46 Sebastian, V., Basak, S., and Jensen, K.F. (2016) Continuous synthesis of palladium nanorods in oxidative segmented flow. *AlChE J.*, **62**, 373–380.

47 Zhang, L., Niu, G., Lu, N., Wang, J., Tong, L., Wang, L. *et al.* (2014) Continuous and scalable production of well-controlled noble-metal nanocrystals in milliliter-sized droplet reactors. *Nano Lett.*, **14**, 6626–6631.

48 Song, Y., Sun, Q., Zhang, T., Jin, P., and Han, L. (2010) Synthesis of worm and chain-like nanoparticles by a microfluidic reactor process. *J. Nanopart. Res.*, **12**, 2689–2697.

www.ebook3000.com

49 Tao, A.R., Habas, S., and Yang, P. (2008) Shape control of colloidal metal nanocrystals. *Small*, **4**, 310–325.

50 Lim, B., Jiang, M., Camargo, P.H., Cho, E.C., Tao, J., Lu, X. *et al.* (2009) Pd-Pt bimetallic nanodendrites with high activity for oxygen reduction. *Science*, **324**, 1302–1305.

51 Jiang, R., Li, B., Fang, C., and Wang, J. (2014) Metal/Semiconductor hybrid nanostructures for plasmon-enhanced applications. *Adv. Mater.*, **26**, 5274–5309.

52 Li, Y. and Shi, J. (2014) Hollow-structured mesoporous materials: chemical synthesis, functionalization and applications. *Adv. Mater.*, **26**, 3176–3205.

53 Gomez, L., Sebastian, V., Irusta, S., Ibarra, A., Arruebo, M., and Santamaria, J. (2014) Scaled-up production of plasmonic nanoparticles using microfluidics: from metal precursors to functionalized and sterilized nanoparticles. *Lab Chip*, **14**, 325–332.

54 Song, Y., Ding, J., and Wang, Y. (2012) Shell-dependent evolution of optical and magnetic properties of Co@Au core–shell nanoparticles. *J. Phys. Chem. C*, **116**, 11343–11350.

55 Zhang, L., Wang, Y., Tong, L., and Xia, Y. (2014) Synthesis of colloidal metal nanocrystals in droplet reactors: the pros and cons of interfacial adsorption. *Nano Lett.*, **14**, 4189–4194.

56 Fu, Q., Ran, G., and Xu, W. (2015) A microfluidic-based controllable synthesis of rolled or rigid ultrathin gold nanoplates. *RSC Adv.*, **5**, 37512–37516.

57 Lohse, S.E., Eller, J.R., Sivapalan, S.T., Plews, M.R., and Murphy, C.J. (2013) A simple millifluidic benchtop reactor system for the high-throughput synthesis and functionalization of gold nanoparticles with different sizes and shapes. *Acs Nano*, **7**, 4135–4150.

58 Salmon, A.R., Esteban, R., Taylor, R.W., Hugall, J.T., Smith, C.A., Whyte, G. *et al.* (2016) Monitoring early-stage nanoparticle assembly in microdroplets by optical spectroscopy and SERS. *Small*, **12**, 1788–1796.

59 Watt, J., Hance, B.G., Anderson, R.S., and Huber, D.L. (2015) Effect of seed Age on gold nanorod formation: a microfluidic, real-time investigation. *Chem. Mater.*, **27**, 6442–6449.

60 Navarro, J.R. and Werts, M.H. (2013) Resonant light scattering spectroscopy of gold, silver and gold-silver alloy nanoparticles and optical detection in microfluidic channels. *Analyst*, **138**, 583–592.

61 Bremholm, M., Jensen, H., Iversen, S.B., and Iversen, B.B. (2008) Reactor design for *in situ* X-ray scattering studies of nanoparticle formation in supercritical water syntheses. *J. Supercrit. Fluids*, **44**, 385–390.

15

Microfluidic Synthesis of Composites

Junmei Wang and Yujun Song

University of Science and Technology Beijing, Beijing Key Laboratory for Magneto- Photoelectric Composite and Interface Science, Centre for Modern Physics Technology, Applied Physics Department, 30 Xueyuan Road, Haidian District, Beijing 100083, PR China

15.1 Introduction

Composites are those materials composed of two or more materials or components with distinctly different properties. Based on the four main types of conventional materials (metals, nonmetal inorganics, polymers, and small molecule organics), varieties of composites can be constructed, for example, those composed of two nonmetal inorganics, metals and nonmetal inorganics, polymers and metals, two metals or alloys, two or more polymers, polymers and biomolecules, etc. Besides, many composites are constructed and widely used but cannot be classified under the above categories due to their special microstructures and components, such as metal–organic frameworks (MOFs).

The small size effect, quantum confinement effect, surface and interface effect, and microstructures of composites can be designed according to their functional requirements for desired applications. When considering the formation of composites, the morphologies and compositional features of each component become increasingly important. Therefore, it is very crucial to control the conditions to synthesize composites with desired morphologies, configurations, and compositions and thus desired functions. Processes such as epitaxial growth [1], displacement [2], and direct deposition [3–5] have been used for large-scale synthesis of various composites by tuning the thermodynamic (e.g., reduction potential, activation energy, electronegativity, and compatibility) and kinetic (e.g., temperature, time, concentration, solvent, and diffusion coefficient) parameters [6–8]. However, it is extremely difficult for the epitaxial growth and displacement processes to address both the lattice mismatch among components and the interfacial stress caused by the large curvature ratio in nanoscale. It is also a significant challenge to control the shell thickness uniform through direct deposition process. For the preparation of complex composites, both solvothermal methods and hydrothermal methods have to be used in conjunction, or complicated sol–gel phase transition methods have to be coupled into the *in situ* reduction process [8]. Therefore, developing new methods for surface- and interface-controlled synthesis of composites is still in its infancy [6, 8].

Microfluidics: Fundamentals, Devices and Applications, First Edition.
Edited by Yujun Song, Daojian Cheng, and Liang Zhao.
© 2018 Wiley-VCH Verlag GmbH & Co. KGaA. Published 2018 by Wiley-VCH Verlag GmbH & Co. KGaA.

www.ebook3000.com

To date, some new methods, such as anion coordination and reduction methods [9], nonepitaxial growth methods [10], multistep liquid precipitation–reduction methods [11], atom-layer deposition and coating methods [12], and high-temperature reduction–oxidization processes [13], have been developed to resolve these issues, which have been partially addressed. Through an in-depth analysis of the key steps in the aforementioned methods, there is no doubt that a regulation of the thermodynamic parameters in each stage of the nanoparticle (NP) formation is very important for optimizing their surface morphologies and interfacial structures. It is also a required step to realize their industrial applications. Usually, it is difficult for conventional bottle batch processes to control the spatiotemporal kinetic parameters of each formation stage of composites, particularly in the scaling-up process. The large-scale surface morphology and interfacial structure-controlled synthesis of composites still faces significant challenges.

Table 15.1 Types of composites synthesized via microfluidic processes.

Composites classified by component types	Composites	References
Composites composed of nonmetal inorganics	γ-Fe_2O_3@SiO_2	[19]
	SiO_2@γ-Fe_2O_3	[18]
	SiO_2@TiO_2	[20]
	CdSe–ZnS	[21, 22]
	CdS/ZnS	[22, 23]
Composites composed of metals and nonmetal inorganics	SiO_2–Au	[24, 25]
	Ag/ZnO	[26]
	PtSn/C	[27]
	Fe@Fe_3O_4	[7]
	FeAl@$Al_{(1-x)}Fe_xO_y$	[28]
	AgAl@$Al_{(1-x)}Ag_xO_y$	
	AuZn@$Zn_{(1-x)}Au_xO_y$	
	CoZn@$Zn_{(1-x)}Co_xO_y$	
Composites composed of polymers and metals	Polyacrylamide/silver	[29]
Composites composed of metal or metal alloy materials	Pt–Pb core–shell composites	[30]
	Co@Au core–shell composites	[31, 32]
Composites composed of polymers and biomolecules or small molecule organics	Lipid–polymer composites	[33–35]
Composites composed of two or more polymers	Janus composites	[36]
Other special types of composites	MOF-5[a]; IRMOF-3[b]; UiO-66[c]; Fe_3O_4@ZIF-8[d] core–shell structure	[37]

a) MOF-5 comprises Zn^{2+} and benzenedicarboxylate (BDC^{2-}).
b) IRMOF-3 comprises Zn^{2+} and 2-aminobenzenedicarboxylate (BDC-$NH_2{}^{2-}$) ligand.
c) UiO-66 comprises Zr^{4+} and benzenedicarboxylate (BDC^{2-}).
d) ZIF-8 is zeolitic imidazolate framework-8.

From all the previous studies, we notice that microfluidic systems have been used in the controllable synthesis of many types of materials (e.g., organics, inorganics, polymers, and metallic materials) due to their advantages related to precise reaction control (e.g., temperature and flow rates), high efficient mixing, high heat and mass transfer, high surface-to-volume ratio, low reagent consumption, and continuous production [14, 15]. One can regulate the residence times within these systems by varying the reactant flow rates and/or design the dimensions of the flow channel [16, 17]. Furthermore, these systems are also capable of automating multistep processes. The combination of analysis, reactions, and purification in a single microfluidic system can be realized. Reagents can be added successively to the desired reacting phase in a simple and flexible manner at precise time intervals in a microfluidic system [18]. Some *in situ* detection and abduction can be realized through the integrated microfluidic systems. All these advantages promote the use of microfluidic systems in the synthesis of composites.

In this chapter, we will illustrate some typical kinds of composites and the widely used composites (MOFs) synthesized in microfluidic systems. Table 15.1 summarizes the material components and properties of these composites that are discussed in this chapter. In the following, several widely used microfluidic systems and their design principles are illustrated firstly. Then, the synthesis features, structures, properties, and applications of various composites are discussed successively. At last, conclusions and perspectives on the composite synthesis by microfluidic systems are presented.

15.2 Microfluidic Synthesis Systems and the Design Principles

Microfluidics is a system that handles small volumes (from microliters to picoliters or less) of fluids or possesses small structure sizes (at least one dimension at microscale). An obvious characteristic is that the fluid in the microchannels is mainly dominated by the viscous forces rather than the inertial forces. In other words, a microfluidic reactor is one that operates at the Reynolds and thermal Péclet numbers below 250 and 1000, respectively [17]. So far, many chapters have been presented to address the applications of microfluidics in composite synthesis due to their advantages [16, 38–42], which we conclude here simply by comparing with the conventional batch methods. Compared with microfluidic processes, the conventional batch method as shown in Figure 15.1a has high concentration gradient and low mass/heat transfer efficiency and finds it difficult to control the reducing agents into bulk solutions, usually resulting in the composites with nonuniform sizes. The synthesis is easily affected due to the stepwise scaling-up process, which makes it difficult to achieve a mass of composites with the same structures or properties. However, the typical microfluidic method as shown in Figure 15.1b has a low concentration gradient and high mass/heat transfer efficiencies due to the microscale heat/mass transfer. The reaction kinetic parameters of each stage during the composite formation can be precisely controlled. Scale-out synthesis of composites with uniform sizes can be achieved

www.ebook3000.com

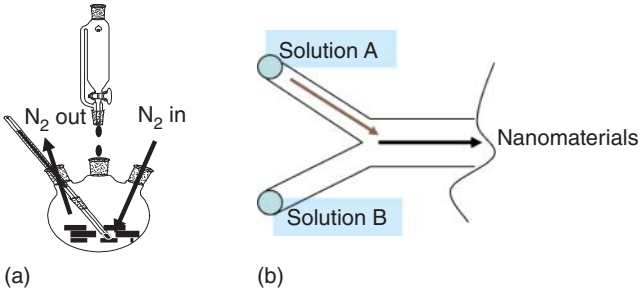


Figure 15.1 (a) The conventional batch process and (b) the typical microfluidic process.

using parallel rather than stepwise scaling-up process. Besides, the small devices will produce wastes as few as possible.

Considering their varieties, microfluidic systems have some advantages and disadvantages for the synthesis of composites as summarized in Table 15.2. In the following part, we will simply introduce several typical microfluidic systems used in composite synthesis based on the classification.

Among all the microfluidic systems, the most widely used is the single-phase flow microfluidic system using either single or multiple miscible solvents, with the reagents mixed through diffusion in laminar flow streams [39]. As shown in Figure 15.2a, the system can realize the slow mixing and high dispersion at desired reaction steps and the spatiotemporal splitting of composite formation stages. It is simple and flexible to control reaction parameters such as flow rate, temperature, and residence time. The process of mixing/reaction, nucleation, growth, and termination during composite formation can be well separated and observed by the changes of some phenomena (e.g., flow colors [28], UV–vis spectra [47] along the microchannels) [48]. However, the single-phase flow microfluidic systems also face some problems. The flow speed along the channel will be different from that of the fluid in the center as the liquid drags along its walls [38]. Therefore, the channel wall will be fouled easily by the reactants or composites formed in the reaction process. Besides, the diffusion rate is slow and the mixing efficiency is low. To overcome these problems, multiphase flow microfluidic systems have been proposed. The design strategy is to prevent direct contact between the reaction liquid and the channel walls. By this way, the contamination of the wall or the clog of the channel can be avoided and the size distribution can be narrowed. In addition, the basic concept is to make the reaction liquid into small volumes or droplets. Different from the diffusion process occurring in the single-phase flow microfluidic systems, two-regime processes are dominated first by convection and then by diffusion in the multiphase flow microfluidic systems. The mixing rate and the heat/mass transfer efficiency can be improved due to the small volumes, individual droplets, and convection process [49–52]. The multiphase flow microfluidic systems can be categorized as gas–liquid and liquid–liquid systems, both of which will be often used in this chapter. Figure 15.2b shows a gas–liquid droplet system in which liquid is segmented by a regular stream of gas bubbles. Figure 15.2c shows a simple liquid–liquid system in which one continuous liquid phase is split into micro-/nano-droplets by another immiscible liquid phase. Even

Table 15.2 Pros and cons of microfluidic synthesis systems for composites.

Microfluidic systems		Pros	Cons
Single-phase flow		Small capillary dimension Large surface-to-volume ratio Precise control of reaction parameters Realize the spatiotemporally splitting Reduced chemical consumption Realize the scale-up synthesis	Slow mixing rates Large residence time distribution Large particle size distribution Contamination of channel walls
Multiphase flow	Gas–liquid	All the above advantages Increased mixing rates and sufficient mixing Manipulation of liquids at small length scales Reduced residence time distribution; High reproducibility Improved heat and mass transfer Narrow particle size distribution	Contamination of channel walls
	Liquid–liquid	All the above advantages Prevent the direct contact of reaction solution with microchannels	Subsequent addition of reagents is difficult
Integrated microfluidic systems		All the above advantages *In situ* reaction induction, detection, and monitoring Enable execution and automation of complicated chemical reactions	Some disadvantages depend on the flow type

though there are many advantages in multiphase flow microfluidic systems, there are still some challenges. For instance, it is difficult to add a reaction solution subsequently or at desired steps [53]. Also, the gas–liquid systems face the problem of the fluid drag along the channel wall just as what occurs in the single-phase flow microfluidic systems.

With the development of microfluidic systems, more functions and complicated chemical reactions can be executed automatically in single assembled devices. Integrated microfluidic systems that coupled a microchannel network with functional microfluidic modules have been considered to be a good method to realize these functions. As shown in Figure 15.2d, shape-based separation of composites can be realized when combining with uniform magnetic field [45]. Additionally, composites with different shapes or properties can be synthesized through the microfluidic systems integrated with lights or other devices [54, 55]. It is a versatile method where reactions can be manipulated without leaving the microchannels. When detection devices are integrated with the microfluidic systems, some *in situ* analysis or monitoring can be realized. Figure 15.2e shows a standard microfluidic platform integrated with online absorbance

www.ebook3000.com

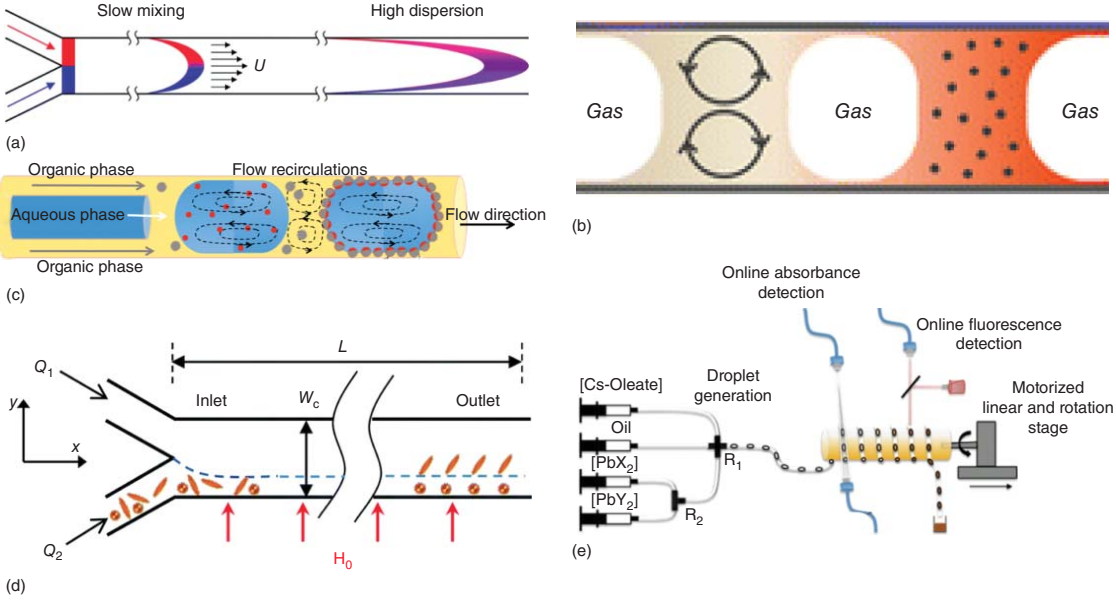


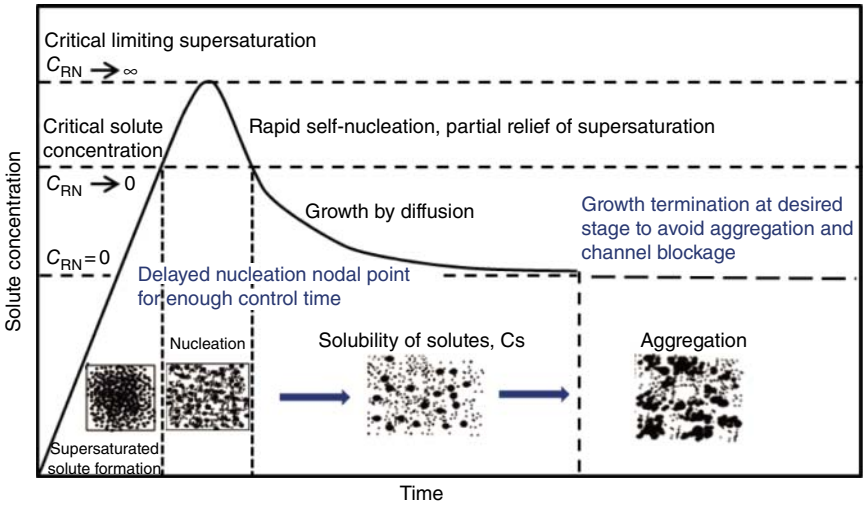
Figure 15.2 Schematic of the microfluidic systems to synthesize composites (a) through single-phase flow microfluidic system. (Niu *et al*. 2015 [38]. Reproducd with permission of Royal Society of Chemistry.) (b) The multiphase flow microfluidic system of gas–liquid system. (Kim *et al*. 2014 [43]. Reproduced with permission of American Chemical Society.) (c) The multiphase flow microfluidic system of liquid–liquid system. (Hassan *et al*. 2015 [44]. Reproduced with permission of American Chemical Society.) (d) The microfluidic system applied with a uniform perpendicular magnetic field. (Zhou *et al*. 2016 [45]. Reproducd with permission of Royal Society of Chemistry.) (e) The microfluidic platform integrated with online absorbance and fluorescence detection. (Lignos *et al*. 2016 [46]. Reproducd with permission of American Chemcical Society.)

and fluorescence detection for the synthesis of composites. These setups have enormous savings in reagent usage and screening times when compared with analogous batch synthetic approaches [46].

15.3 The Formation Mechanism of Composites

Before performing the synthesis of composites, the formation mechanism has to be considered for possible precise morphology and structure control of materials thermodynamically. Lamer and Dinegar demonstrated the particle formation mechanism using a wet chemistry method [56]. It reveals that there are four steps in the formation of supersaturated solutes (e.g., atoms, ions, molecules): formation, nucleation, growth, and agglomeration as shown in Scheme 15.1. As the solute concentration reaches a certain degree of saturation, the nucleation process will occur in a transient time. Subsequently, the growth continues by the solution diffusion. The first two steps result in a decreased concentration of the solutes, which is lower than the critical nucleation concentration. In order to reduce the free energy of the system, growth process proceeds until all the reactants are consumed. Besides, a certain extent of aggregation will also occur to reduce the surface free energy. Based on this theory, it can be realized that the precise control of each step during the formation of composites is critical. The nucleation process should be controlled in a sharp time, and the growth should be terminated at the desired stage to ensure products with controlled sizes, shapes, and structures.

Our group has developed this formation mechanism according to our reaction systems via metal salt reduction to synthesize NPs [7, 28, 31, 32, 57–61]. Then, we invented a simple-programmed microfluidic process to control each stage according to the modified formation mechanism of NPs. Visible chip-based



Scheme 15.1 Particle formation mechanism in the wet chemical method.

www.ebook3000.com

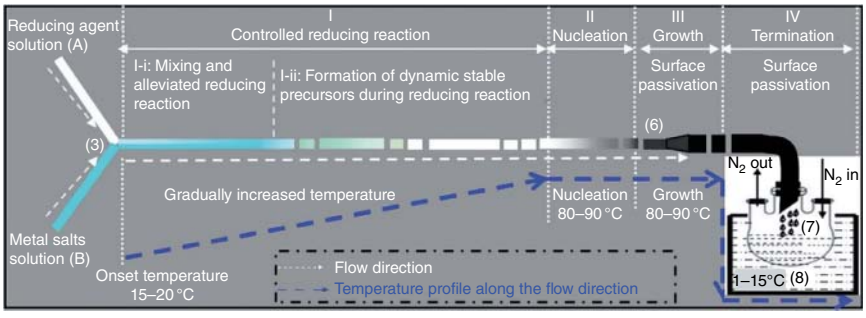


Figure 15.3 Principle of the proposed four-section formation mechanism of nanoparticles via the simple-programmed microfluidic process. (Shen *et al*. 2014 [48]. Reproduced with permission of Royal Society of Chemistry.)

simple-programmed microfluidic processes (C-SPMPs) and sequentially developed microtubing-based simple-programmed microfluidic processes (MT-SPMPs) were used to develop methods for the large-scale continuous production of composites with defined sizes, shapes, structures, and properties. Four stages including mixing/reaction, nucleation, growth, and termination during the formation of NPs could be well separated and observed for the first time based on the changes of the flow color along the microchannels as shown in Figure 15.3 [48]. The nucleation nodal point can be delayed even though the nucleation process is completed instantly, and, thus, the online control and monitoring in the microchannel can be facilitated. Also, the rapid nucleation and delayed nucleation nodal point prevent the subsequent nucleation and ensure composites with good crystallinity and narrow size distribution. Moreover, the growth can be terminated at a desired stage to prevent aggregation due to the spatiotemporal stage separation feature.

15.4 Microfluidic Synthesis of Composites

In the following section, we will illustrate several typical composites synthesized in microfluidics. The first six types of composites discussed in this chapter are classified based on the four main types of materials (polymers and metals, nonmetal inorganics, small organic molecules, and bio-organics). Then, a type of composites (MOFs) that cannot be included in the above classifications but has been widely investigated currently will be presented. Their synthesis features, structures, properties, and applications will be elaborated as follows.

15.4.1 Composites Composed of Nonmetal Inorganics

Nonmetal inorganics refer to the materials consisting of oxides, sulfide, selenide, carbides, nitrides, halogen compounds, borides of some elements and silicate, aluminate, phosphate, borate, and other materials. They all possess unique properties and can form composites with multifunctions. In this section, we mainly discuss several microfluidic-synthesized composites composed of oxides,

sulfide, or selenide of some elements. They were divided into two subsections to be expatiated based on their components or properties.

15.4.1.1 Microfluidic Synthesis of Oxide-Coated Multifunctional Composites

Due to the specific properties that arise from their small dimensions, composites are used in various applications, such as catalysis, optics, electronics, and biomedical diagnosis or nanomedicine. To further extend the range of properties and applications of composites, several materials can be combined into a single composite. The assembled composites preserve the properties of each material. Oxide coating composites described here is a main type of multifunctional composites that are composed of nonmetal inorganics. These coating layers can not only protect the cores but also modify the surface and interface properties of composites. To date, finding a facile method to synthesize these kinds of materials with tailored magnetic, photometric, and chemical characteristics is very important. Microfluidic processes are considered to be a good method compared with the conventional methods.

In 2009, Abou-Hassan *et al.* reported a continuous multistep synthesis of core–shell γ-Fe_2O_3@SiO_2 NPs for the elaboration of an NP lab-on-a-chip platform [19]. They realized the continuous multistep coupling of several chemical reactions in different microreactors and enabled sequential reactions without the NPs leaving the microreactor environment. All the micro-operations (grafting, mixing, and coating) were performed inside an optimized three-dimensional (3D) coaxial flow microreactor. The most important advantage is that it not only realizes desired shapes and dimensions of NPs but also meets the scale-up requirements. Due to the small dimensions of the microfluidic reactors and the direct coupling of different operations, magnetic NPs can be efficiently coated. The core–shell NPs can be produced in a few minutes (~7 min) compared with the several hours that elapse in the bottle batch process. Coating magnetic iron oxide NPs with silica shells can increase the chemical stability of NPs, narrow the size distribution, and obtain good dispersions in the liquid medium. Furthermore, any unspecific aggregation can be prevented. Besides, the formed protective, biocompatible, inert, and hydrophilic surface can be used as an excellent anchoring point for derivatizing molecules. Most importantly, the combination of magnetic and dielectric materials provides composites with both magnetic and luminescent properties, which can extend their applications.

Subsequently, Ferraro *et al.* further developed an automated microfluidic platform that is capable of manipulating nanoliter droplets [18]. Rhodamine B isothiocyanate (RITC)–SiO_2@γ–Fe_2O_3 composites were successfully synthesized through multistep and automated sequential operations. As shown in Figure 15.4a, this microfluidic platform enables the implementation of different chemical operations (mixing, flocculation, magnetic decantation, colloidal re-dispersion, washing, surface functionalization, heating, and colloidal assembly) in a nanoliter droplet, starting from a colloidal suspension of magnetic iron oxide (γ-Fe_2O_3) NPs. A syringe pump equipped with a 250 ml syringe and coupled with a pipetting robot can generate trains of droplets, starting from solutions collected in a standard microtiter plate. A polytetrafluoroethylene (PTFE) capillary is used as a pipetting needle to alternately aspirate different

www.ebook3000.com

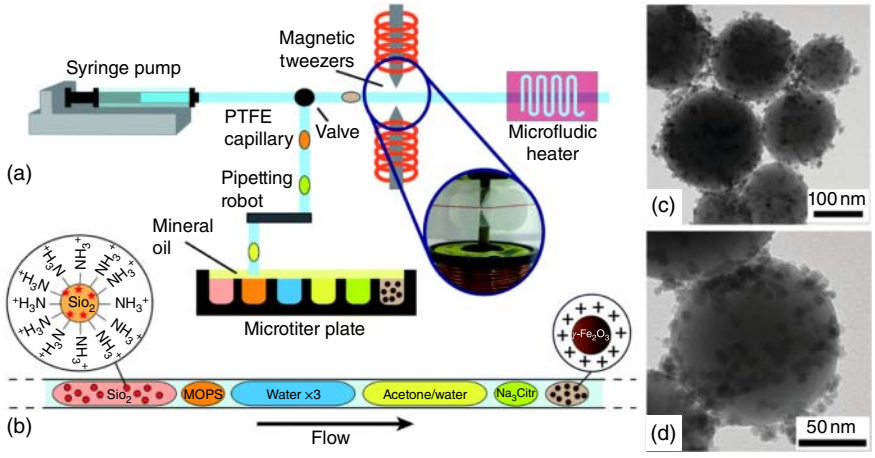


Figure 15.4 (a) Microfluidic setup for the generation of deterministic trains of droplets. (b) Train of droplets for nanoassembly production: droplets from right to left are 50 nl of γ-Fe_2O_3 solution, 50 nl of sodium citrate solution, 200 nl of acetone/water solution, two 200 nl droplets of MilliQ water, 50 nl of 3-(*N*-morpholino) propanesulfonic acid (MOPS), and 200 nl of fluorescent silica NPs, respectively. (c) and (d) TEM images of RITC-SiO_2@γ-Fe_2O_3 composites. (Ferraro *et al*. 2015 [18]. Reproduced with permission of Royal Society of Chemistry.)

reagent solutions and fluorinated oil, which is used as a continuous phase. Droplets of 50–300 nl can be formed in the channel, as shown in Figure 15.4b. Each droplet can be driven between the magnetic tweezers to manipulate the magnetic NPs that pass through a heater, which can control the droplet temperature. The magnetic field can be optimized by the current in the coil. In this process, the biggest innovation is the coupling of magnetic tweezers technology with the advantages of microfluidic systems. The transmission electronic microscope (TEM) images of the spherical core–shell structure RITC–SiO_2@γ–Fe_2O_3 composites with a surface coverage of ~30% synthesized by this setup are shown in Figure 15.4c,d.

One of the advantages of the microfluidic-based synthesis is that the synthesis process can be combined with the continuous and multistep addition of sol–gel reagents and the rapid mixing of small amounts of coating reactants. However, the batch-to-batch process will adversely affect the reproducibility of composites. Therefore, metal oxide-coated composites were considered to be synthesized by a continuous and multistep system. Khan and Jensen used a multistep addition microfluidic system (Figure 15.5a) to synthesize SiO_2–TiO_2 composites with well-defined TiO_2 or SiO_2 shells [20]. This method eliminated the complications of secondary nucleation in bottle batch processes. The microreactor was constructed by combining photolithography-based microfabrication and microscale segmented gas–liquid flow. The utility of this microreactor was demonstrated in the coating of colloidal silica particles with a tunable titania layer thickness through an easy, one-step microfluidic process. In addition, the microreactor design is also inherently scaled out through the parallel operation of multiple microreactors. The synthesized composites show good dispersity. The coating

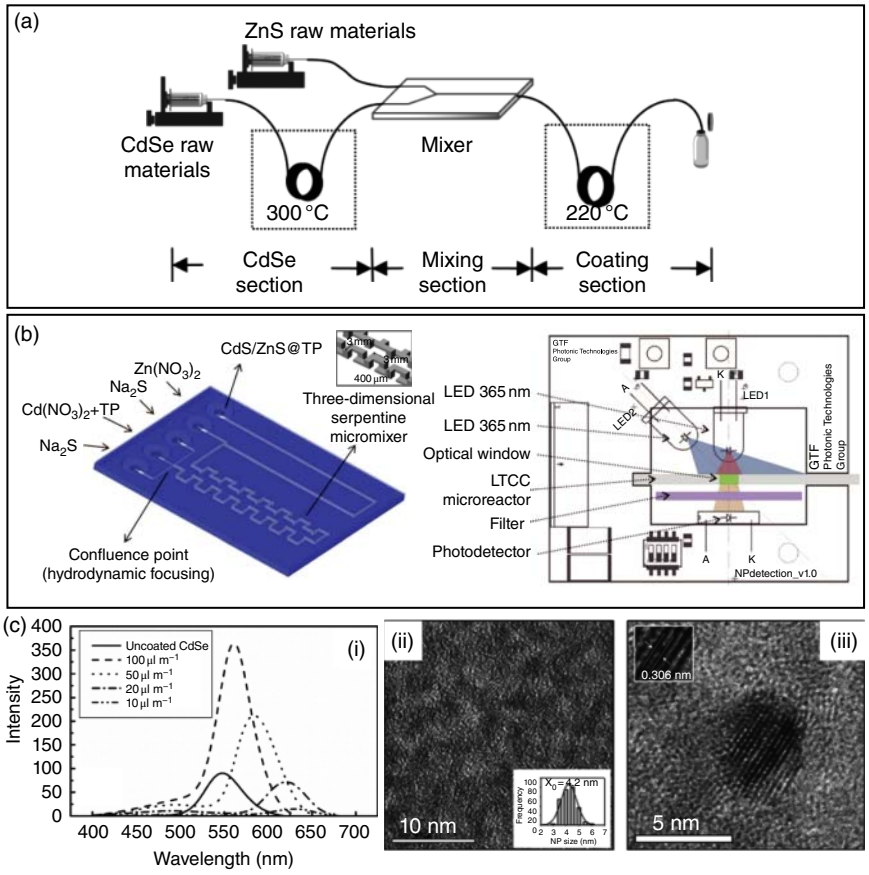


Figure 15.5 (a) Examples of microfluidic processes for generating semiconductor core–shell composites. (b) The ceramic microreactor and the setup of the coupled optical and microreactor system. (c) Luminescence spectra of uncoated CdSe obtained after CdSe synthesis and coated composites obtained from the outlet at different flow volumes (i). TEM image of the quantum dots obtained using the ceramic microreactor (ii) and an HRTEM image with the lattice fringes highlighted (iii). (Adapted from Wang *et al*. 2004 [21] and Gomez-de Pedro *et al*. 2012 [23].)

appears to be composed of compact titania NPs (<5 nm) on the surfaces of large silica spheres. The sizes of composites can be flexibly tuned by changing the addition rate of titanium tetraethoxide (TEOT) in microchannels.

15.4.1.2 Microfluidic Synthesis of Semiconductor–Semiconductor Composites

Nanocrystalline semiconductors demonstrate salient optical properties and excellent chemical processability, and these properties make them good candidates for applications in various fields, such as light-emitting diode (LED) displays, biological labels, and solar cells [62–66]. The key factors that govern the use of luminescent composites (NCs) in the biological and LED fields include their high luminescence quantum yields (QYs), stable luminescent properties under real-field operation conditions, and good solubility in desired solvents.

www.ebook3000.com

All of these require the proper passivation of dangling bonds that are present on the surfaces of the NPs. Organic ligands can endow NPs with high QY of photoluminescence (PL) and good solubility in various solvents. However, these organic ligands are sensitive to the chemical environment, and the degradation of PL can occur during surface modifications. Conversely, growing a thin shell of a higher bandgap inorganic material on the outside of the plain NPs enables substantial improvements of the QY and promotes PL stability. Currently many methods have been used in the synthesis of semiconductor core–shell composites. However, most of the reports are discrete or semi-discrete batch methods, which require tedious purifications of the core NPs to eliminate the cross-contamination of unreacted precursors in each reaction step. Furthermore, the growth of the shells is highly sensitive to the changes in the reaction conditions, including changes in the temperature and the increased concentration gradient. These changes are intrinsic to the bottle-batch reactor but are barriers for the controlled large-scale production.

Among many types of new synthesis methods, continuous-flow microfluidic reactors have been confirmed as an effective and alternative strategy to conventional batch methods due to the precise controllability of the reaction conditions. Over the past years, different types of semiconductor composites, such as CdSe/ZnS [21, 22], CdS/ZnS [22, 23], ZnSe/ZnS [67], and InP/ZnS [68], have been synthesized through this method.

In 2004, Wang *et al.* [21] synthesized semiconductor composites with different sizes and coating thickness in a multistep microfluidic reactor by controlling the residence time and realized large-scale continuous synthesis. The simple setup is shown in Figure 15.5a. The synthesis includes three steps: the CdSe seed synthesis, mixing with ZnS raw materials, and ZnS coating. The reactant solution flows in the microchannel supplied by a microcapillary and a ceramic micromixer, which is used to add the ZnS raw materials into the CdSe seed solution. Two oil baths can supply different temperatures for the nucleation and growth of the CdSe and ZnS. In this system, the microcapillary shows more flexibility in distributing the reactant residence time in the three sections and providing different temperatures. The luminescence spectra of uncoated CdSe obtained after the CdSe synthesis and the coated particles obtained from the outlet at different flow volumes are shown in Figure 15.5c-i. This result confirms that the particles synthesized in the microreactor not only display the same tendency in the luminescence spectra as those synthesized using the conventional flask method but also exhibit the obvious advantage of conveniently controlled structures and properties. Subsequently, some new microreactor systems, such as those shown in Figure 15.5b, have also been developed [23]. It shows a ceramic microreactor integrated with an optical detection system for online absorbance and fluorescence measurements using commercial-miniaturized optical components. The microfluidic device was based on the hydrodynamic focusing of the reagents coupled with a 3D micromixer. Therefore, a simple, economic, robust, and portable microreaction system for the well-controlled synthesis of CdS/ZnS composites was demonstrated. The high resolution transmission electron microscopy (HRTEM) images in Figure 15.5c-ii,iii show homogeneous composites with small sizes and good crystallinity, which were synthesized by

this microfluidic process. Additionally, there is no need to perform tedious purifications of the core NPs to eliminate the cross-contamination of unreacted precursors in each reaction step compared with the discrete or semi-discrete batch methods.

15.4.2 Composites Composed of Metal and Nonmetal Inorganics

It is well known that composites will exhibit more properties if they are composed of two or more components of sharply different properties. In this section, we will state the micro-synthesized composites composed of metal and nonmetal inorganic materials based on their different properties firstly. As a special nonmetal inorganic material, carbon is used to be a support in many composites to improve their physicochemical properties. Therefore, carbon-supported composites synthesized by microfluidics will be discussed in this section. At last, some composites composed of metal and nonmetal inorganic materials synthesized by our group will be exhibited.

15.4.2.1 Microfluidic Synthesis of Dielectric–Plasmonic Composites

Due to the strong dependence of the plasmon frequency of NPs on the dielectric properties of their surroundings, plasmonic NPs coated by/attached to dielectric materials (or dielectric–plasmonic composites) for desired and tunable optical properties have been widely researched [24, 25, 69]. Using SiO_2@Au core–shell composites as a model, the surface plasmon (SP) resonance frequency can be tuned by controlling the ratio of the shell thickness to the particle diameter. The SP properties of nanoshells are extremely sensitive to variations of the shell morphology. Dielectric NPs decorated with small metallic islands ("nanoislands") have attracted considerable interests as substrates for a wide range of biosensor applications. The optical properties of such composites depend on the size and spacing of the metallic islands. Interactions between SPs of neighboring islands can strongly affect the positions of the optical resonances. However, it is very difficult to obtain the same products if the following separated batch processes are performed: the silica cores are first synthesized and surface functionalized, then the preformed gold seeds are supported to attach the core surfaces, and then these seeds will grow on the core surfaces to form a continuous layer.

Due to the flexible kinetic controllability of microfluidic reactors, different reagents can be conveniently added along with the microchannels. One flow can be introduced into another to combine multiple synthetic steps into a continuous process. Thus, the abovementioned issues can be solved easily. Duraiswamy and Khan presented a continuous-flow process to synthesize thin gold "nanoshells" and "nanoislands" on colloidal silica surfaces, as shown in Figure 15.6a,b [25]. "S" stands for the aqueous mixture of gold-seeded silica particles in gold-plating solution, and "R" stands for the aqueous reducing agent solution. These two reaction agents and nitrogen gas are delivered continuously to a T-shaped micro-junction, where the reagents are dispensed as aqueous cells within a composite foam lattice. The flowing foam cells finally enter a collection vial, where the gas escapes, and the aqueous and oil phases spontaneously form two immiscible fluid layers. Then, an ordered, flowing composite foam lattice is

www.ebook3000.com

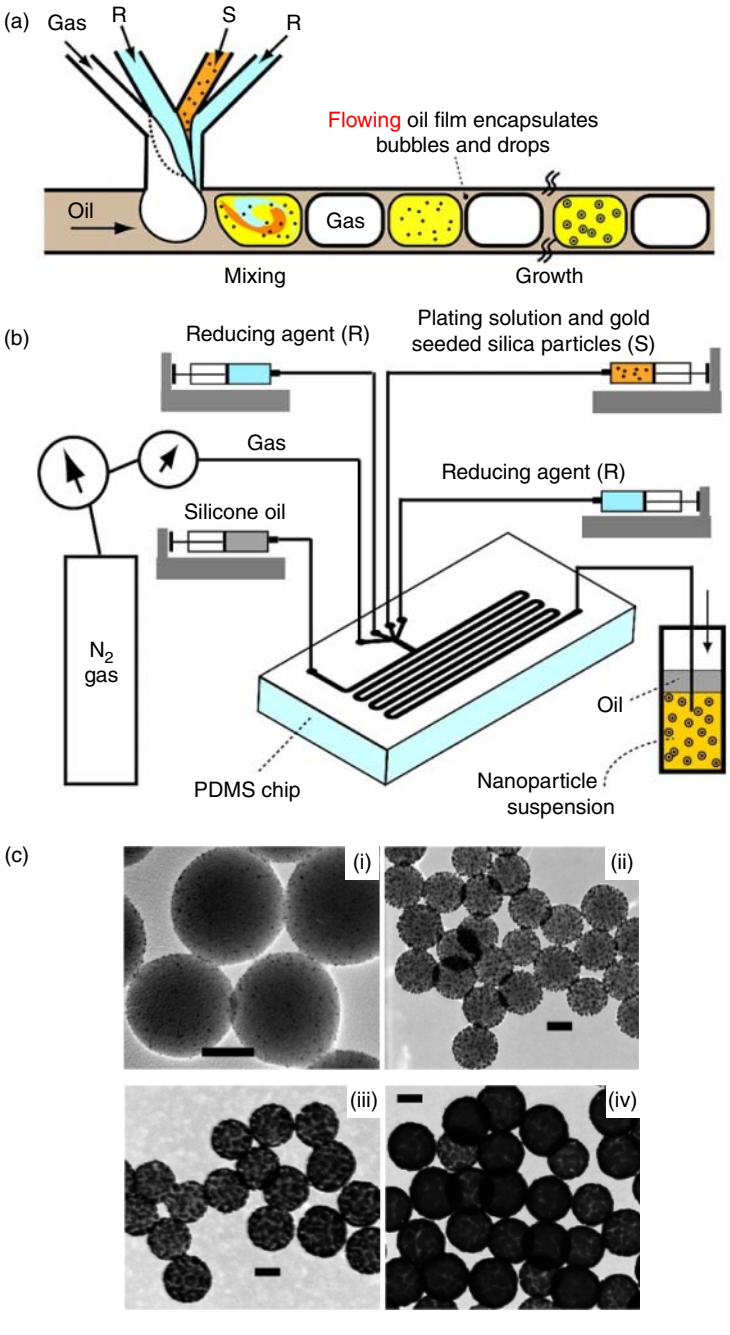


Figure 15.6 (a) The schematic for generating core–shell plasmonic structure composites; (b) the experimental setup of the microfluidic processes; (c) TEM images of gold-seeded silica particles of gold seeds grown from ~3 nm (i) to ~10 nm (ii), ~35 nm (iii), and nearly coalesced islands (iv). All scale bars are 100 nm. (Duraiswamy and Khan 2010 [25]. Reproduced with permission of American Chemical Society.)

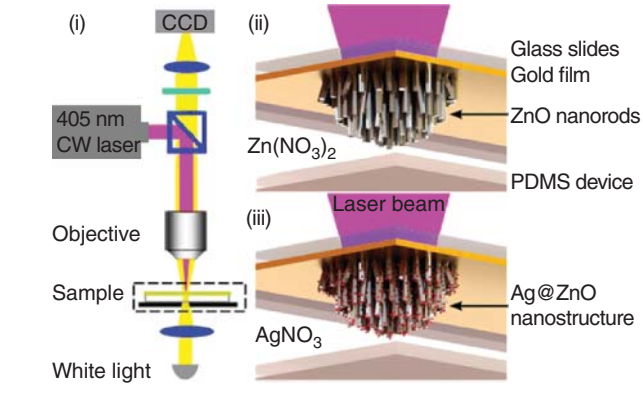
assembled via a simple microfluidic device. This enables the precisely controlled reagent dispensing and mixing and facilitates the splitting of the NP growth. Uniformly sized SiO_2–Au core–shell composites with different contents of Au seeds grown on SiO_2 surfaces can be obtained by using the three-phased arrangement and adjusting both the volume fraction of gold-seeded silica particles (%) and the ionic gold concentration [Au^{3+}] (mM) delivered into the aqueous cells of the foam lattice, as shown in Figure 15.6c. This microfluidic process is simple to implement, which takes less time and consumes a lower amount of reactants compared with the batch reactor process. Reagent dispensing and rapid mixing are accomplished in a robust, automated fashion without operator intervention. Composites with uniform sizes and little particle aggregation can be obtained without post-synthesis treatments. The composites synthesized using this method exhibit suitable SP properties and good reproducibility.

15.4.2.2 Microfluidic Synthesis of Plasmonic–Semiconductor Composites

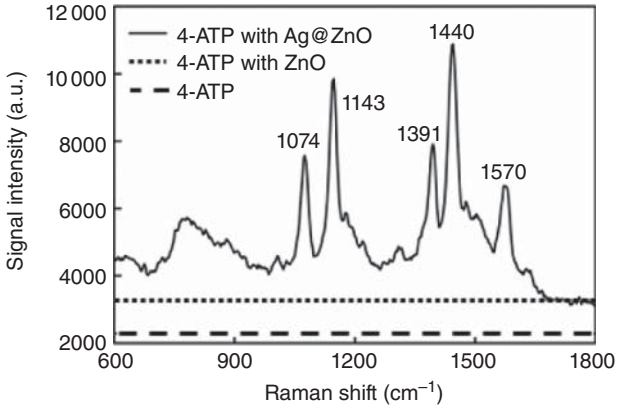
Semiconductor NPs have many applications in energy conversion and storage, environmental remediation, optoelectronics, optical memory, light emission, and so on. However, some special applications are usually affected due to the high charge-carrier recombination rate and limited light absorption of these NPs [70]. Plasmonic noble metals can concentrate and scatter visible light, which plays a key role in the harvesting and conversion of solar energy. Upon combining a semiconductor and noble metal with distinct plasmonic resonances, the interaction with light near the metal surface is enhanced due to the significantly increased local fields that are associated with the SP. This will undeniably affect the forbidden band and conduction band of semiconductors. Thereby, the fluorescence of semiconductors will be significantly affected. In addition, the nonradiative dumping either from energy transfer between semiconductors and metals or from electron transfer from semiconductors to metals will endow the composites with unique physicochemical properties and functionalities, which are far beyond those of the individual components. Over the past years, many methods have been used to synthesize plasmonic–semiconductor composites [71–78], such as solvothermal or hydrothermal methods. Considering the structural and compositional complexity of the plasmonic–semiconductor, particularly in the nanoscale, both the solvothermal and hydrothermal methods have to be combined, or the tedious sol–gel phase transition process and *in situ* reduction have to be used simultaneously. Therefore, a new facile methodology is still needed for the controlled synthesis of these types of composites.

In 2014, Xie *et al.* developed an *in situ* method to grow highly controllable and sensitive 3D surface-enhanced Raman scattering (SERS) composites within microfluidic devices via an optothermal effect [26]. They fabricated SERS composites composed of Ag@ZnO composites, which were formed inside microfluidic channels. As shown in Figure 15.7a-i, a continuous laser, which served as a localized heat source to initially catalyze the formation of ZnO nanorods, was focused onto a gold-coated glass slide, which was used to support the microfluidic channel that contains zinc nitrate ($Zn(NO_3)_2$) and hexamethylenetetramine (HMTA) precursor solutions. The gold film absorbed energy from the laser and heated the surrounding precursor solution. This

www.ebook3000.com



(a)



(b)

Figure 15.7 (a) Optical setups for fabricating Ag@ZnO nanostructures in a microfluidic channel (i); schematic illustration of on-chip, *in situ* creation of (ii) ZnO nanorods and (iii) Ag@ZnO nanostructures by optothermal effects. (b) SERS spectra of 4-aminothiophenol (4-ATP) using the Ag@ZnO nanostructures as SERS substrates (solid line), ZnO nanorods as SERS substrates (dotted line, up-shifted 3000), and with no SERS substrate (dashed line, up-shifted 2000). (Xie *et al*. 2014 [26]. Reproduced with permission of American Chemical Society.)

process resulted in the formation of ZnO nanorods on the gold film as shown in Figure 15.7a-ii. The position of the ZnO nanorod formation was entirely determined by the position of the focused laser spot, which can be controlled by the movement of a programmable motorized stage on which the microfluidic channel was prefixed. After the ZnO nanorods were prepared, the precursor solution was drained. Subsequently, silver nitrate ($AgNO_3$) solution can be injected into the same microfluidic channel. Then, the laser beam was focused onto the preformed ZnO nanorods solution, which led to the formation of Ag NPs on the ZnO nanorods by the optical decomposition of $AgNO_3$ to Ag atoms. The formed Ag atoms can rapidly nucleate into nanoclusters as seeds around which the preformed ZnO rods grow. The Ag@ZnO composites will eventually

form at the position of the laser-focusing spot area as shown in Figure 15.7a-iii. This method can significantly improve the precise control over the synthesis location compared with the conventional ZnO nanorod synthesis process, in which the precursor solutions are heated in bulk reactors. It can resolve the issues associated with the oriented fabrication of SERS substrates in microfluidic channels, and it can be used to incorporate ZnO nanorods inside any position of the microfluidic device. The SERS of 4-aminothiophenol (4-ATP) can be seen clearly using the micro-synthesized Ag@ZnO as substrates when comparing with other substrates (Figure 15.7b).

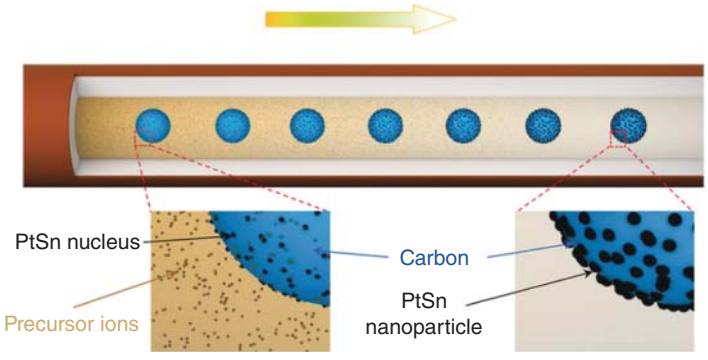
15.4.2.3 Microfluidic Synthesis of Carbon-Supported Composites

It has been demonstrated that composites with ultrasmall sizes and strong nanocrystal–support interface interactions between NPs and carbon-based supports are vital to achieve dramatically increased physicochemical properties (e.g., catalysis) because more metal–carbon binding will result in an accelerated charge transfer between carbon and the active sites of NPs (NC) [79, 80]. The NC–support interaction not only determines the charge transfer rates, the stability, and the active site density but also can govern the particle sizes [79–81]. However, current synthesis methods usually lead to the growth of composites to large sphere species. The extended potential cycling during testing often reduces the active site density. It is always difficult to achieve as small as desired particles and to grow the particles uniformly on support surfaces. Thus far, optimization of the NC–support interaction remains an open issue. Therefore, the development of facile methods to obtain the above features in one nanocatalyst is still in the rudimentary stages. It is necessary to find new methodologies to synthesize these types of composites.

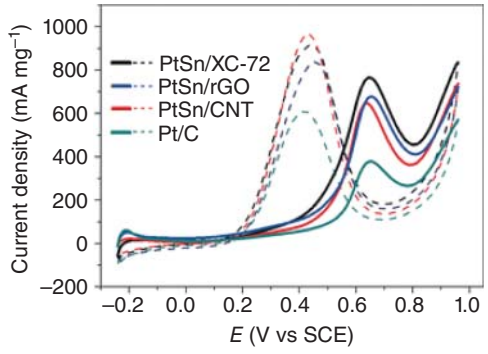
Wu *et al.* developed a capillary tube reactor to synthesize carbon-supported PtSn composites. The carbon supports are commercial XC-72 carbon black particles, carbon nanotubes (CNTs), and reduction graphene oxide (rGO) sheets. Figure 15.8a displays the formation mechanism of the direct growth of ultrafine PtSn NPs on carbon spheres in a capillary microfluidic system [27]. The reaction solution containing carbon black and metal ions is pushed into a chamber using pressure-regulated nitrogen gas and then into the capillary tube reactor. Rapid reduction of H_2PtCl_6 and $SnCl_4$ occurs with an extremely increased temperature. Then supersaturated Pt and Sn atoms will nucleate on the surface of the carbon black spheres. Finally, PtSn NPs are grown uniformly on the surfaces of carbon black spheres with controlled sizes. The loading amount can be as high as 33%. These composites possess significantly enhanced mass catalytic activity and improved stability. Their mass catalytic activities are shown in Figure 15.8b.

Through the microfluidic process, other NCs (e.g., FePt and Pt [82]) can also be loaded directly on these carbon supports to synthesize carbon-supported composites for enhanced catalysis performance. Recently, a methodology by coupling a microfluidic-batch process with *in situ* carbon-black mixing, successive annealing, and dealloying posttreatment was developed for engineering surface and interface microstructures of FePt/C nanocomposites by our group [83]. Ultrasmall angular FePt nanocrystals can directly grow on carbon black with enhanced nanocrystal–carbon interface interaction. After controlled

www.ebook3000.com



(a)



(b)

Figure 15.8 (a) Examples of the formation of ultrafine PtSn NPs on a carbon sphere with uniform loading in a microfluidic reactor; (b) cyclic voltammetry curves recorded from electrodes coated with synthesized PtSn/XC-72, PtSn/rGO, PtSn/CNT and commercial Pt/C in an aqueous solution of H_2SO_4 (0.5 M) and C_2H_5OH (1 M) at room temperature. (Wu *et al*. 2016 [27]. Reproduced with permission of John Wiley & Sons.)

dealloying of Fe in annealed nanocrystals with a Fe/Pt ratio of 2/1, the finally formed nanocatalysts exhibit excellent electrochemical catalytic performance using the methanol oxidation reaction as a model, preserving an activity of 1610 mA mg^{-1} Pt^{-1} (12 times the commercial Pt/C catalysts). Moreover, precise control over the temperature in different zones along the capillary tube microreactors, coupled with continuous-flow reaction processes, indicates that the techniques described here can offer improved control in large-scale synthesis.

In the past years, our group also synthesized some other composites that are composed of metal and nonmetal inorganic materials with microfluidic systems. An *in situ* redox reaction was first conducted to synthesize composites with amorphous metallic cores and uniform metal oxide shells embedded with nanocrystallites in microfluidic systems. The synthesized composites show unique magnetic properties by regulating the interface interaction among the constructed parts. Particularly, the synthesized Fe(B)@iron oxide composites preserve permanent ferromagnetic properties at room temperature due to the

strong magnetic coupling between the different parts and the nanocrystalline pinning effect. This provides an alternative design of nanostructures to overcome the superparamagnetic limit in ultratiny particles. The NPs with amorphous metallic cores and uniform metal oxide shells can be well maintained over 4–5 months [7].

To determine the formation mechanism and optimize the experimental conditions to acquire the highest performing composites, we recently developed a new methodology based on core alloying and shell gradient doping to synthesize a variety of gradient core–shell composites that are composed of metal and nonmetal inorganic materials (e.g., FeAl@$Al_{(1-x)}Fe_xO_y$, CoZn@$Zn_{(1-x)}Co_xO_y$, AgAl@$Al_{(1-x)}Ag_xO_y$, and AuZn@$Zn_{(1-x)}Au_xO_y$). This was realized by coupled competitive reactions or sequenced reducing-nucleation and co-precipitation reaction of mixed metal salts in the invented microfluidic and batch-cooling process. The experimental setup is shown in Figure 15.9a. The composites synthesized by this strategy possess small uniform sizes and good solubility, as shown in Figure 15.9b–e, which enables their extensive application in magnetic resonance imaging, energy storage, or optoelectronic devices. The most important advantage is that this method makes it convenient to investigate the formation mechanism of composites since we can obtain the NPs at any desired reaction stage in time and study their microstructures and properties precisely.

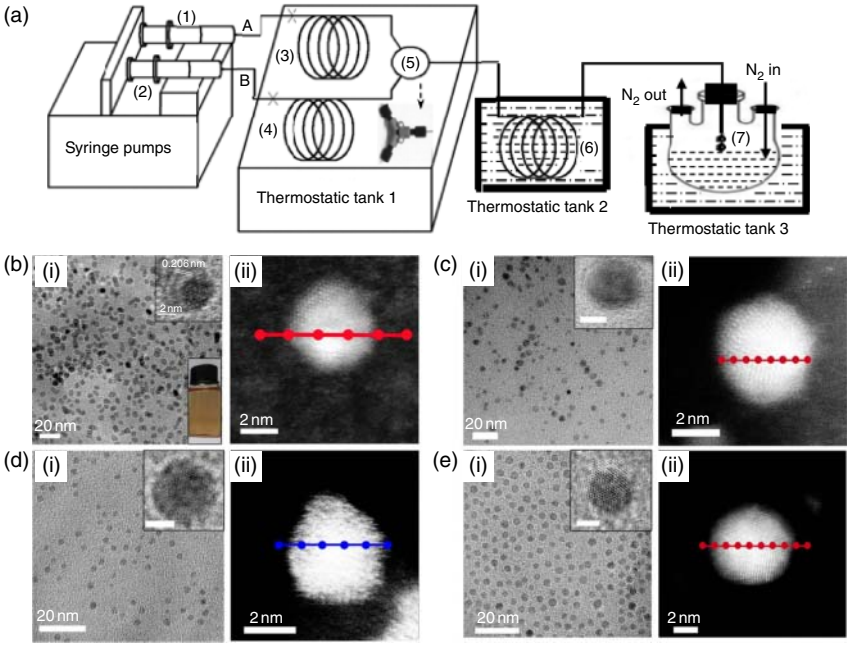


Figure 15.9 (a) Examples of microfluidic processes for generating metal–metal oxide composites. (b–e) Wide-view TEM image (i) and HR-TEM image of a single particle (i: inset); High Angle Annular Dark Field Scanning Transmission Electron Microscopy (HAADF-STEM) image of a single particle of (ii) FeAl@$Al_{(1-x)}Fe_xO_y$ composites (b), AgAl@$Al_{(1-x)}Ag_xO_y$ composites (c), AuZn@$Zn_{(1-x)}Au_xO_y$ composites, and (d) CoZn@$Zn_{(1-x)}Co_xO_y$ composites (e). (Reprinted with permission from Ref. [28] Copyright 2015 Nature.)

www.ebook3000.com

15.4.3 Composites Composed of Polymers and Metals

As two different types of materials, polymers and metal materials possess different physical and chemical properties, for example, light absorbance and permeability. By combining them, some unique properties can be tuned or obtained. The metal content and the internal geometry in composites directly influence their physical and chemical properties. The transport of charge, light, elasticity, and permeability with local homogeneity are crucial to these properties. They can be obtained when one component is homogeneously distributed in the other components. Up to now, various polymerization methods, including microemulsion and suspension polymerization, have been established and used to synthesize both polymeric and metal composites. However, it is difficult for conventional bottle batch methods to control the particle morphology and to achieve a uniform size distribution of metal inclusions in the polymer matrix, especially for magnetic particles. Therefore, inventing a suitable method to synthesize polymer/metal or polymer/metal compound composites with desired contents and geometries has become urgently desired. Microfluidic devices provide an alternative technique for the generation of monodisperse droplets by co-flowing two immiscible fluids to induce droplet formation, and many metal/polymer composites have been successfully synthesized in microfluidic systems [29, 84–87].

The following is a micro-continuous-flow process developed by Köhler *et al.* to synthesize nanoporous composites. The process chain involves a two-step continuous-micro-flow synthesis of silver NPs using the micro-segmented flow process (Figure 15.10a-i), the synthesis of polymer composite particles in a co-flow device (Figure 15.10a-ii), and the silver enforcement (Figure 15.10a-iii). The polyacrylamide particles that incorporate silver NPs can be obtained through the first two steps. Then a type of nanoporous composites with a high content of plasmonic silver nanocrystals can be synthesized through a chemical silver enhancement on the pre-synthesized composites. The microfluidic processes for both the synthesis of seed NPs and porous composites lead to a highly homogeneous particle size at nanoscale (seeds) and microscale (polymer particles), or forming one kind of mesomaterials. This enables a highly homogeneous distribution of silver NPs inside the polymer matrix that is difficult to achieve by conventional synthesis methods. The optical image of the synthesized polymer/Ag composites is shown in Figure 15.10b-i, while their scanning electron microscopy (SEM) image is shown in Figure 15.10b-ii. These composites are porous structure and opaque and their surface is very rough. This kind of mesostructures leads to the direct contact of analytic molecules with the silver surface and thus a strong SERS signal. The structural features of these homogeneous porous composites can be used in optical readout, molecular sensors, and other optical devices. In this synthesis process, the microfluidic system helps to realize the high reproducibility in the transport processes during silver enforcement as well as in the analytical application during the SERS measurements.

15.4.4 Composites Composed of Metal or Metal Alloy Materials

Composites composed of metal materials are also a type of important materials that possess many electronic, optical, and medical applications. Up to now,

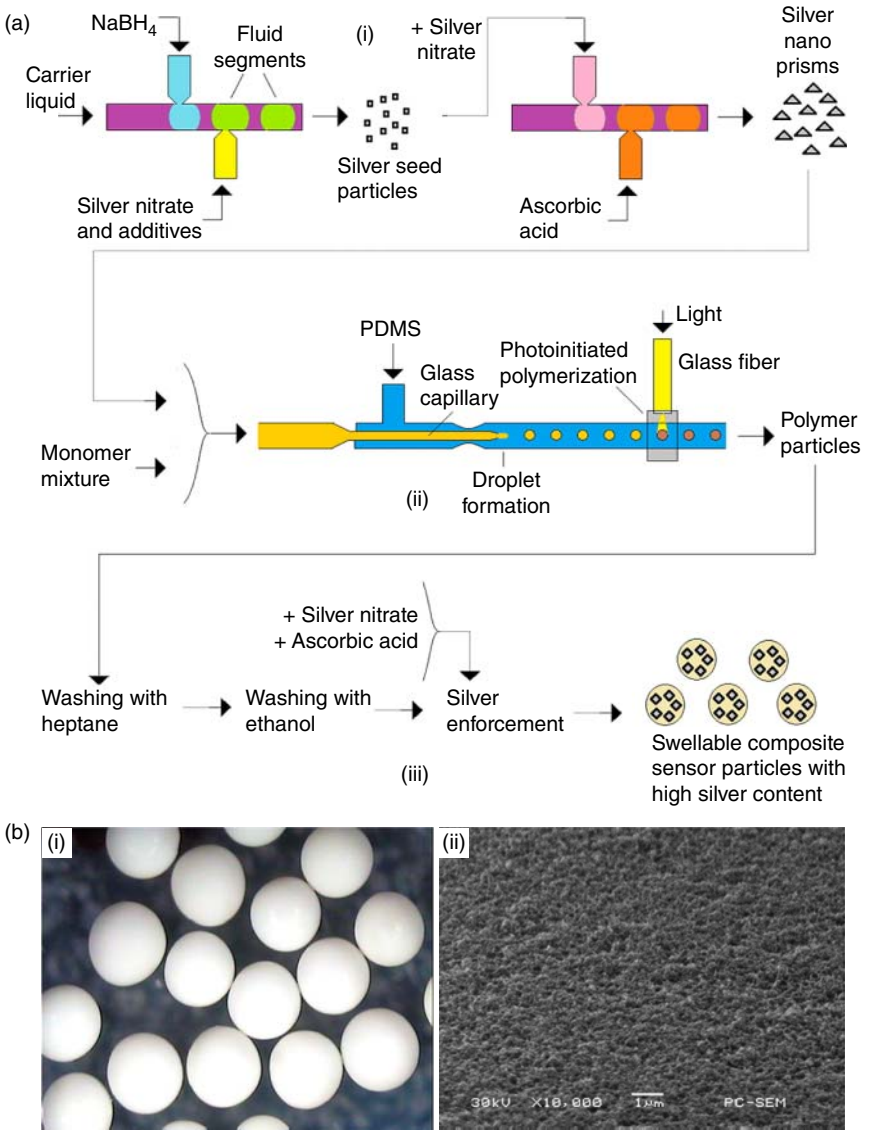


Figure 15.10 (a) Examples of microfluidic processes for generating polymer/metal composites; (b) optical images of a group of particles (i) and SEM image of the particle surface (ii). (Kohler *et al*. 2013 [29]. Reproduced with permission of American Chemical Society.)

synthesis of many monometallic NPs with microfluidic systems has been reported [88–92]. Now it is urgent to synthesize composites composed of two or more different metals to achieve more functions and the enhanced physical and chemical properties.

Sebastian *et al.* reported the synthesis of Pt–Pd core–shell heterostructure at 130 °C with residence time as short as 5 s [30]. The most important novelty of this process lays on the design of the microfluidic system used in the synthesis process

www.ebook3000.com

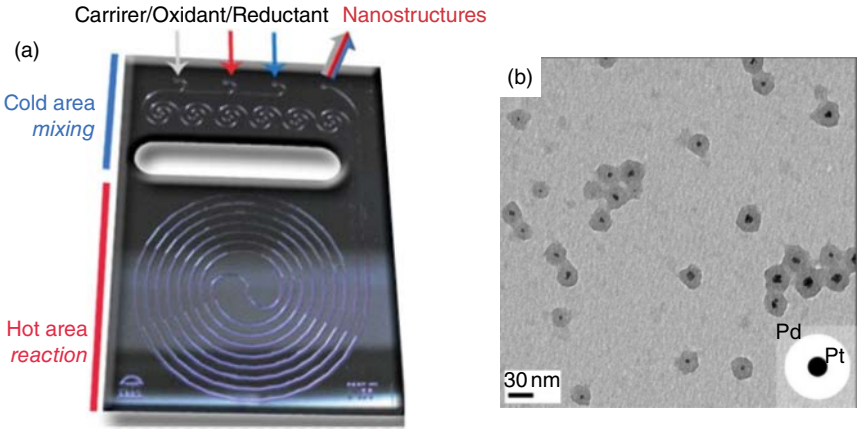


Figure 15.11 (a) The silicon–Pyrex microfluidic reactor device used to synthesize the composites composed of metal materials. (b) TEM images of Pt–Pd core–shell composites synthesized in microfluidic systems. (Reprinted with permission from Ref. [30] Copyright 2016 Royal Society of Chemistry.)

as shown in Figure 15.11a, where the nucleation proceeds in a cold inlet/outlet mixing zone and the growth stage carries out in a hot reaction area. This separation process provides the possibility of sufficient mixing and prevents the nonuniformity of nucleation. The growth will be terminated at the outlet as the solution passes through the cold zone again. The above process enables us to obtain composites with excellent monodispersity as shown in Figure 15.11b. Meanwhile, a rapid multi-fluid lamination caused by high speed flows is required to form the core–shell structure. To obtain composites with different shell thickness and size distributions, the Pt–Pd precursor flow ratios can be tuned accordingly. Many other metal composites such as Ag@Pd core–shell composites have also been synthesized in this microfluidic system.

Co@Au core–shell magnetic–plasmonic composites of different shell thicknesses were fabricated by our group using a combination of the displacement process (Figure 15.12a) and the reduction–deposition process (Figure 15.12b) in a microfluidic reactor [31, 32]. Effects of the shell thickness and the size change on the Co–Au interface pinning effects and the interparticle interaction were further analyzed and correlated to their magnetic properties and the localized surface plasmon resonance (LSPR). The characterization results indicate that the shell thickness has a significant effect on the fine structure of the core materials. Tuning of the optical and magnetic properties of the core–shell NPs via controlling the shell thickness through a microfluidic process provides an efficient and flexible method to obtain desired magnetic and optical properties for multimode sensing technologies and high-efficiency solar cells.

15.4.5 Composites Composed of Polymer and Organic Molecular

With the miniaturization of biological and medical systems, biomaterials with small sizes and monodispersion have attracted great attention [39, 93–98]. Composites composed of polymer and organic molecular are one of the most

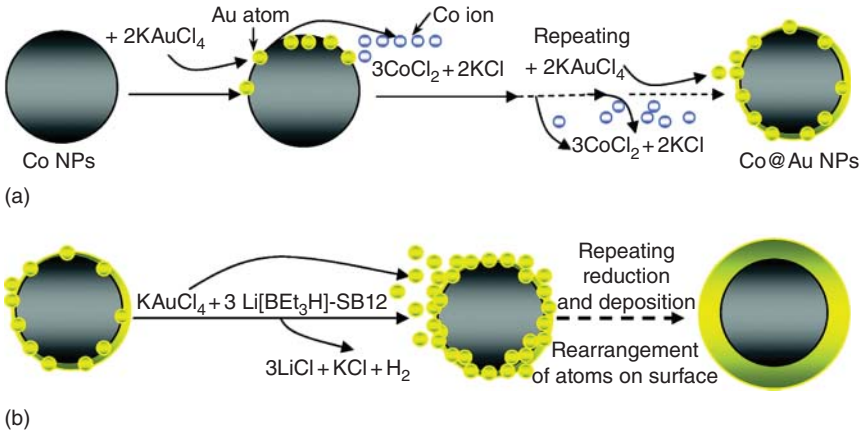


Figure 15.12 (a) Co@Au nanoparticle formation by displacement process; (b) shell thickness increase by the reduction–deposition process. (Song *et al*. 2012 [32]. Reproduced with permission of American Chemical Society.)

important biomaterials. In this section, we will take lipid–polymer as an example to illustrate the properties and the microfluidic synthesis of these kinds of composites. Lipid–polymer composites, that is, composites possessing both the properties of liposomes and polymeric NPs, can deliver a wide range of therapeutic compounds in a controlled manner and have great potential in disease diagnosis and therapy. As a main kind of biomaterials, they are of considerable interest due to their high stability, biocompatibility, and controlled release properties. All these properties of the lipid–polymer composites are strongly related to their size distribution, their effects on cellular uptake, and biological effects. The conventional method in lipid–polymer synthesis always contains two steps of development of polymeric NPs and encapsulation of polymeric NPs within liposomes. The complicated process results in the composites with poor size distribution, low drug recovery rate, and unclear nanostructure. A key challenge to synthesize these kinds of composites with excellent biological properties is obtaining reproducible monodisperse composites with a minimum number of preparation steps. To achieve this goal, methods for controlled synthesis of monodispersion composites are highly required.

Microfluidic systems have been used in the synthesis of lipid–polymer composites [33–35, 99]. Homogeneous composites with relatively narrow size distribution were obtained, owing to the rapid mixing in microfluidic systems during the formation process. Considering the sizes and structures of these lipid–polymer composites that can be precisely controlled by simply tuning the flow rate ratio and the ratio of the lipids to polymeric NPs, Feng *et al.* [35] developed a two-stage microfluidic platform for the size-controlled synthesis of core–shell lipid–polymer composites with lipid–shell and poly(lactic-*co*-glycolic acid) (PLGA)–core (Figure 15.13a). The diameter of the synthesized composites can be regulated by changing the total flow rate in microchannels. The sizes of the synthesized composites at a low flow rate of 41 ml h^{-1} and a high flow rate of 246 ml h^{-1} can be seen clearly through the TEM images in Figure 15.13b,c.

www.ebook3000.com

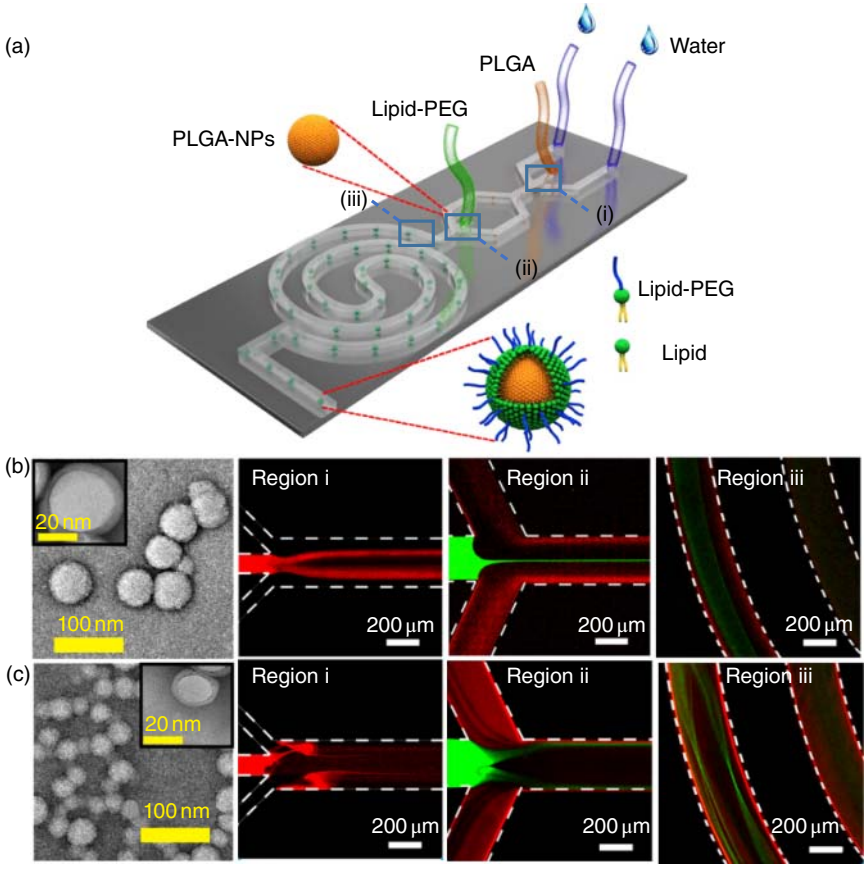


Figure 15.13 (a) Schematic of the two-stage microfluidic chip for synthesizing the lipid–PLGA composites. (b) TEM images of lipid–PLGA composites synthesized at low (41 ml h^{-1}) flow rates and the confocal images of fluidic mixing at different regions of two-stage microfluidic chip under low (41 ml h^{-1}) flow rates. (c) TEM images of lipid–PLGA composites synthesized at high (246 ml h^{-1}) flow rates and the confocal images of fluidic mixing at different regions of two-stage microfluidic chip under high (246 ml h^{-1}) flow rates. Rhodamine B solution (fluorescent red) is introduced into the first stage from the middle inlet, and calcein solution (fluorescent green) is injected into the second stage from the center inlet. The flow rate ratio of two side water sheaths to Rhodamine B solution is 80 at the first stage. The flow rate of Rhodamine B (or calcein) is 0.5 ml h^{-1} when the total flow rate is 41 ml h^{-1}, and 3 ml h^{-1} when the total flow rate is 246 ml h^{-1}. (Reprinted with permission from Ref. [35] Copyright 2015 AIP Publishing.)

The TEM results indicate that composites with uniform and small sizes can be produced at the high flow rate. As a key factor, which determines the size distributions of composites, the mixing processes inside the microfluidic chip at flow rates of 41 and 246 ml h^{-1} can be clearly observed by confocal microscope. The confocal laser scanning microscopy images are shown in Figure 15.13b,c. It is visualized that the mixing is in a chaos state at a high flow rate and thus an efficient and rapid interfacial deposition occurs. Therefore, small-sized and

monodispersed lipid–polymer composites will be obtained at a high flow rate. The obtained small lipid–polymer composites exhibit enhanced stability and cellular uptake efficiencies.

15.4.6 Composites Composed of Two or More Polymers

A composite composed of two or more polymers is another typical material. Different shapes can be formed to realize different properties. Here we take Janus composite as an example. Janus particles that consist of two parts of approximately equal surface areas but different chemistries, polarities, functionalization, and/or other properties have been used in many fields, such as biomedical engineering, catalysis, and optics [100–102]. However, high-throughput, low-cost techniques are still required to synthesize these particles with a precise control of the various structural/physical/chemical properties for advanced applications. Microfluidics provides a unique platform to fabricate Janus particles by carefully controlling the liquid flow in microfluidic channels to form Janus droplets and then solidifying the droplets into Janus particles. Figure 15.14a shows a setup of the Janus droplets formation process [36]. It can be observed that two liquid monomers (M1 and M2) (mixed with a photoinitiator) are introduced into two central channels, with side channels containing sodium dodecylsulfate (SDS) aqueous solution, which acts as sheath flows. Then, Janus droplets are

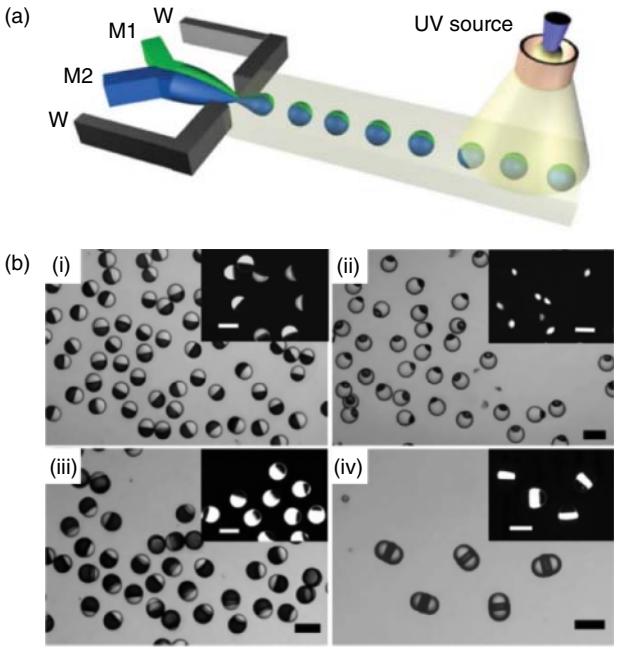


Figure 15.14 (a) Examples of microfluidic processes for Janus nanocomposites synthesis. (b) Optical microscopy images of Janus particles with binary structures (i–iii) and Janus particles with ternary structures (iv). (Nie *et al*. 2006 [36]. Reproduced with permission of American Chemical Society.)

www.ebook3000.com

produced and released at the exit of the central channels. Meanwhile, a sharp interface within the Janus droplet between M1 and M2 can be formed by the photoinitiated polymerization process. The TEM images of the Janus particles synthesized by two polymer phases are shown in Figure 15.14b(i–iii), which demonstrate that the phase ratio between M1 and M2 in the Janus particles can be conveniently adjusted by varying the flow rate of M1 and M2 during the fast photopolymerization process. Janus particles with ternary structures can also be synthesized by the same setup, and the morphologies of these particles are shown in Figure 15.14b-iv.

15.4.7 Microfluidic Synthesis of Metal–Organic Frameworks (MOFs)

As a kind of porous organic–inorganic materials that consist of metal clusters or ions, MOFs have attracted immense attention because of their potential for extremely diverse structural topologies and tunable chemical functionalities. They can be widely used in hydrogen storage [103], gas adsorption and separation [104], drug delivery and magnetic resonance imaging contrast agent [105, 106], bio- and chemical sensors [107], and catalysis [108]. However, these applications always face challenges regarding large-scale synthesis, stability, and controllable shapes and sizes. It is urgent to find methods to overcome these problems. Microfluidics has been considered to be a potential method for this goal, and some MOFs (individual MOFs and integrated MOFs) have been synthesized via microfluidic processes. The scheme of a general setup for droplet-based microfluidic synthesis of MOFs is presented by Faustini *et al.*, as shown in Figure 15.15a [37]. In this process, both organic and metal precursors are dissolved in a polar medium and then encapsulated in nanoliter droplets, which are transported by the nonpolar carrier. Ultrafast mixing and continuous synthesis can be realized in the microchannel. Representative MOF-5, IRMOF-3, and UiO-66 structures have been successfully synthesized.

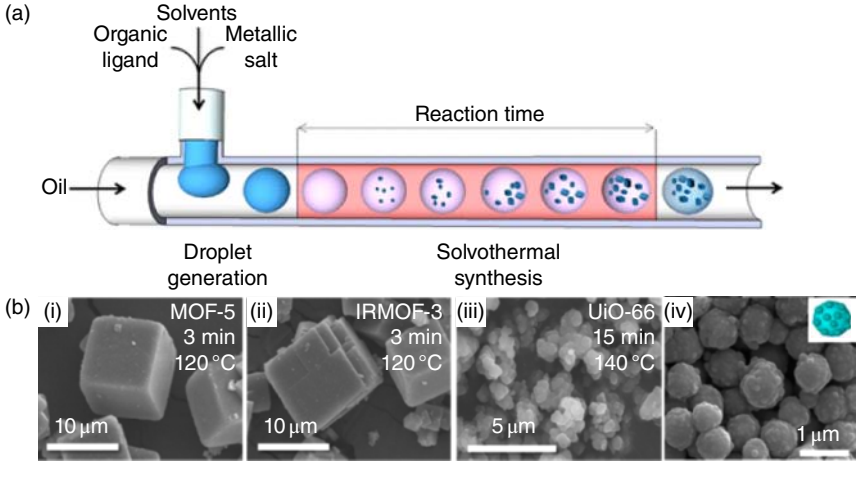


Figure 15.15 (a) Schematic representation of the general microchemical process. (b) SEM micrographs of MOF-5 (i), IRMOF-3 (ii), UiO-66 (iii), and Fe_3O_4@ZIF-8 particles (iv). (Faustini *et al*. 2013 [37]. Reproduced with permission of American Chemical Society.)

In addition, heterostructured core–shell MOFs (e.g., Co_3BTC_2@Ni_3BTC_2, Fe_3O_4@ZIF-8 (zeolitic imidazolate framework-8)) with enhanced structural stability, improved catalytic activity, and excellent adsorption properties have been synthesized. Some TEM images of MOFs with unique morphologies and high crystalline qualities are shown in Figure 15.15b.

Subsequently, more and more complicated MOFs, such as 3D MOF architectures [109], Zn-based MOFs [110], and hollow sphere bio-MOFs [111] have been synthesized and exhibited many interesting applications. Considering so many advantages of microfluidic processes [112–114], it shall be an efficient method to realize these desired morphologies and functions.

More details on microfluidic synthesis of MOFs will be discussed in Chapter 16 of this book.

15.5 Summary and Perspectives

In conclusion, different types of composites have been successfully synthesized via microfluidic processes or hybrid microfluidic batch processes [115–118]. The synthesis of composites using microfluidic-based processes can fulfill many challenges present in conventional bottle batch methods. The regulation of the kinetic parameters in each stage of composite formation can be spatiotemporally realized along microfluidic channels. In the process, the integration of multiple microfluidic systems plays an important role in the optimization of the microstructures and properties of the composites. Coupling of microfluidic systems with some special analysis devices aids online microstructure and performance observation or detection during the composite formation. Moreover, the sequential synthesis and automation of the microfluidics during the entire procedure can provide a general low-cost and scale-out approach in the composition-, component-, and microstructure-controlled synthesis of composites with defined properties for advanced applications.

Although the abovementioned advantages, some challenges still exist. We can illustrate them as follows.

It is obvious that good designed microfluidic reactors are necessary to synthesize composites. Now, it is still challenging to fabricate the microstructures of reactors and conducting the process optimization for the long-term synthesis of composites, especially magnetic composites without channel blockage and clogging in the current microfluidic reactors. In addition, it is still difficult to set up an ideal environment for the synthesis of composites (e.g., biomaterials) that need a desired biocompatible environment. Even though the multiphase microfluidic systems are adopted to solve the above issues, some other problems may still exist. For example, it may be possible for us to synthesize composites without channel clogging using a multiphase microfluidic system (e.g., droplet processes), but it is difficult to add reagents subsequently after the droplets are formed. Moreover, it is still difficult for us to design a general microfluidic reactor system to synthesize composites with desired morphologies and microstructures because of their complexity for different applications. Sometimes the process is usually tedious to synthesize composites with complex constructions that may not be

www.ebook3000.com

desired for practical applications. So far, most microfluidic reactors can only be used at a relatively low temperature and low pressure. However, some synthesis processes need to be performed at very high temperature and pressure (e.g., petroleum refinery or syngas reforming). A high growth temperature is also conducive for semiconductor composites with defect and/or doping control for good crystalline and excellent properties.

Nowadays, composites have been widely used in many fields. The application of information storage due to the magnetic and optical properties of composites is gradually developed with the rapid development of information technology. The use of composites in fuel cells provides possibility to use sustainable and clean fuels and reduce energy consumption and pollution. The small sizes and biocompatible properties of composites make them popular in biomedical engineering. Considering all these applications, it is still difficult to meet the requirement of different applications only by focusing in high flow rates and multiple parallel microfluidic lines or exquisite microstructures. A better way may be to do the system engineering based on microfluidic device (e.g., microreactors, micro-separators, micro-heat exchangers, micro-monitors), assembly, and simulation to achieve these goals. Besides, low-cost and -efficiency synthesis processes for long-term operation should be considered simultaneously.

So far, it is easy for us to synthesize lots of composites with two components but still difficult to synthesize composites of multi-hierarchical microstructures or mesostructures. The relationship between the surface and interface of different components and their interaction with their properties are still difficult to regulate even using multistep microfluidic processes. It is difficult for magnetic, optical, and electrical properties to be integrated in single composites. Though online or *in situ* detection has been realized through the integrated microfluidics, some operations are still inconvenient, such as *in situ* engineering surface and the interface of composites. Therefore, many challenges have to be addressed to achieve a flexible and automated operation to control composition and components and their surface and interface engineering. Besides, the integrated microfluidic devices are far from enough and limited currently [119]. We believe that these integrated microfluidic systems will be more widely used in the sophisticated materials synthesis for advanced applications when overcoming these problems.

Acknowledgments

This work was supported by National S&T Major Project (pre-approved No. SQ2018ZX100301), NSFC (Grant No. 51371018 & 81372425) and the Fundamental Research Funds for the Central University of China (FRF-BR-14-001B).

References

1 Kim, H., Achermann, M., Balet, L.P., Hollingsworth, J.A., and Klimov, V.I. (2005) *J. Am. Chem. Soc.*, **127** (2), 544–546. doi: 10.1021/ja047107x

2 Gaur, S., Wu, H., Stanley, G.G., More, K., Kumar, C.S.S.R., and Spivey, J.J. (2013) *Catal. Today*, **208**, 72–81. doi: 10.1016/j.cattod.2012.10.029

3 Carroll, K.J., Hudgins, D.M., Spurgeon, S., Kemner, K.M., Mishra, B., Boyanov, M.I., Brown, L.W., Taheri, M.L., and Carpenter, E.E. (2010) *Chem. Mater.*, **22** (23), 6291–6296. doi: 10.1021/cm101996u

4 Cho, S.J., Idrobo, J.C., Olamit, J., Liu, K., Browning, N.D., and Kauzlarich, S.M. (2005) *Chem. Mater.*, **17** (12), 3181–3186. doi: 10.1021/cm0500713

5 Levin, C.S., Hofmann, C., Ali, T.A., Kelly, A.T., Morosan, E., Nordlander, P., Whitmire, K.H., and Halas, N.J. (2009) *ACS Nano*, **3** (6), 1379–1388. doi: 10.1021/nn900118a

6 Zhang, Z.C., Xu, B., and Wang, X. (2014) *Chem. Soc. Rev.*, **43** (22), 7870–7886. doi: 10.1039/c3cs60389j

7 Song, Y., Ji, S., Song, Y.-J., Li, R., Ding, J., Shen, X., Wang, R., Xu, R., and Gu, X. (2013) *J. Phys. Chem. C*, **117** (33), 17274–17284. doi: 10.1021/jp404402g

8 Jiang, R., Li, B., Fang, C., and Wang, J. (2014) *Adv. Mater.*, **26** (31), 5274–5309. doi: 10.1002/adma.201400203

9 Serpell, C.J., Cookson, J., Ozkaya, D., and Beer, P.D. (2011) *Nat. Chem.*, **3** (6), 478–483. doi: 10.1038/nchem.1030

10 Zhang, J.T., Tang, Y., Lee, K., and Min, O.Y. (2010) *Science*, **327** (5973), 1634–1638. doi: 10.1126/science.1184769

11 Xu, Z.C., Hou, Y.L., and Sun, S.H. (2007) *J. Am. Chem. Soc.*, **129** (28), 8698–8699. doi: 10.1021/ja073057v

12 Li, J.F., Huang, Y.F., Ding, Y., Yang, Z.L., Li, S.B., Zhou, X.S., Fan, F.R., Zhang, W., Zhou, Z.Y., Wu, D.Y., Ren, B., Wang, Z.L., and Tian, Z.Q. (2010) *Nature*, **464** (7287), 392–395. doi: 10.1038/nature08907

13 Chen, G.X., Zhao, Y., Fu, G., Duchesne, P.N., Gu, L., Zheng, Y.P., Weng, X.F., Chen, M.S., Zhang, P., Pao, C.W., Lee, J.F., and Zheng, N.F. (2014) *Science*, **344** (6183), 495–499. doi: 10.1126/science.1252553

14 Marre, S. and Jensen, K.F. (2010) *Chem. Soc. Rev.*, **39** (3), 1183–1202. doi: 10.1039/b821324k

15 Song, Y., Hormes, J., and Kumar, C.S. (2008) *Small*, **4** (6), 698–711. doi: 10.1002/smll.200701029

16 Krishna, K.S., Li, Y., Li, S., and Kumar, C.S. (2013) *Adv. Drug Delivery Rev.*, **65** (11–12), 1470–1495. doi: 10.1016/j.addr.2013.05.006

17 Elvira, K.S., Casadevall i Solvas, X., Wootton, R.C., and de Mello, A.J. (2013) *Nat. Chem.*, **5** (11), 905–915. doi: 10.1038/nchem.1753

18 Ferraro, D., Lin, Y., Teste, B., Talbot, D., Malaquin, L., Descroix, S., and Abou-Hassan, A. (2015) *Chem. Commun.*, **51** (95), 16904–16907. doi: 10.1039/c5cc07044a

19 Abou-Hassan, A., Bazzi, R., and Cabuil, V. (2009) *Angew. Chem.*, **48** (39), 7180–7183. doi: 10.1002/anie.200902181

20 Khan, S.A. and Jensen, K.F. (2007) *Adv. Mater.*, **19** (18), 2556–2560. doi: 10.1002/adma.200700127

21 Wang, H., Li, X., Uehara, M., Yamaguchi, Y., Nakamura, H., Miyazaki, M., Shimizu, H., and Maeda, H. (2004) *Chem. Commun.*, (1), 48–49. doi: 10.1039/b310644f

www.ebook3000.com

22 Yang, H., Luan, W., Wan, Z., Tu, S.-T., Yuan, W.-K., and Wang, Z.M. (2009) *Cryst. Growth Des.*, **9** (11), 4807–4813. doi: 10.1021/cg900652y

23 Gomez-de Pedro, S., Puyol, M., Izquierdo, D., Salinas, I., de la Fuente, J.M., and Alonso-Chamarro, J. (2012) *Nanoscale*, **4** (4), 1328–1335. doi: 10.1039/c2nr11525e

24 Gomez, L., Arruebo, M., Sebastian, V., Gutierrez, L., and Santamaria, J. (2012) *J. Mater. Chem.*, **22** (40), 21420. doi: 10.1039/c2jm34206e

25 Duraiswamy, S. and Khan, S.A. (2010) *Nano Lett.*, **10** (9), 3757–3763. doi: 10.1021/nl102478q

26 Xie, Y.L., Yang, S.K., Mao, Z.M., Li, P., Zhao, C.L., Cohick, Z., Huang, P.H., and Huang, T.J. (2014) *ACS Nano*, **8** (12), 12175–12184. doi: 10.1021/nn503826r

27 Wu, F., Zhang, D., Peng, M., Yu, Z., Wang, X., Guo, G., and Sun, Y. (2016) *Angew. Chem.*, **55** (16), 4952–4956. doi: 10.1002/anie.201600081

28 Wang, R., Yang, W., Song, Y., Shen, X., Wang, J., Zhong, X., Li, S., and Song, Y. (2015) *Sci. Rep.*, **5**, 9189. doi: 10.1038/srep09189

29 Kohler, J.M., Marz, A., Popp, J., Knauer, A., Kraus, I., Faerber, J., and Serra, C. (2013) *Anal. Chem.*, **85** (1), 313–318. doi: 10.1021/ac302751t

30 Sebastian, V. and Jensen, K.F. (2016) *Nanoscale*, **8** (33), 15288–15295. doi: 10.1039/c6nr04104c

31 Song, Y.J., Wang, Y.H., Ji, S.X., and Ding, J. (2012) *Nano-Micro Lett.*, **4** (4), 235–242. doi: 10.3786/nml.v4i4.p235-242

32 Song, Y., Ding, J., and Wang, Y. (2012) *J. Phys. Chem. C*, **116** (20), 11343–11350. doi: 10.1021/jp300118z

33 Li, Y., Huang, X., Lee, R.J., Qi, Y., Wang, K., Hao, F., Zhang, Y., Lu, J., Meng, Q., Li, S., Xie, J., and Teng, L. (2016) *Molecules*, **21** (10). doi: 10.3390/molecules21101314

34 Valencia, P.M., Basto, P.A., Zhang, L., Rhee, M., Langer, R., Farokhzad, O.C., and Karnik, R. (2010) *ACS Nano*, **4** (3), 1671–1679. doi: 10.1021/nn901433u

35 Feng, Q., Zhang, L., Liu, C., Li, X., Hu, G., Sun, J., and Jiang, X. (2015) *Biomicrofluidics*, **9** (5), 052604. doi: 10.1063/1.4922957

36 Nie, Z., Li, W., Seo, M., Xu, S., and Kumacheva, E. (2006) *J. Am. Chem. Soc.*, **128** (29), 9408–9412. doi: 10.1021/ja060882n

37 Faustini, M., Kim, J., Jeong, G.Y., Kim, J.Y., Moon, H.R., Ahn, W.S., and Kim, D.P. (2013) *J. Am. Chem. Soc.*, **135** (39), 14619–14626. doi: 10.1021/ja4039642

38 Niu, G., Ruditskiy, A., Vara, M., and Xia, Y. (2015) *Chem. Soc. Rev.*, **44** (16), 5806–5820. doi: 10.1039/c5cs00049a

39 Ma, J., Lee, S.M., Yi, C., and Li, C.W. (2016) *Lab Chip*. doi: 10.1039/c6lc01049k

40 Lin, W.Y., Wang, Y., Wang, S., and Tseng, H.R. (2009) *Nano Today*, **4** (6), 470–481. doi: 10.1016/j.nantod.2009.10.007

41 DeMello, A.J. (2006) *Nature*, **442** (7101), 394–402. doi: 10.1038/nature05062

42 Karle, M., Vashist, S.K., Zengerle, R., and von Stetten, F. (2016) *Anal. Chim. Acta*, **929**, 1–22. doi: 10.1016/j.aca.2016.04.055

43 Kim, K.-J., Oleksak, R.P., Hostetler, E.B., Peterson, D.A., Chandran, P., Schut, D.M., Paul, B.K., Herman, G.S., and Chang, C.-H. (2014) *Cryst. Growth Des.*, **14** (11), 5349–5355. doi: 10.1021/cg500959m

44 Hassan, N., Stocco, A., and Abou-Hassan, A. (2015) *J. Phys. Chem. C*, **119** (19), 10758–10765. doi: 10.1021/acs.jpcc.5b02527

45 Zhou, R., Bai, F., and Wang, C. (2016) *Lab Chip*. doi: 10.1039/c6lc01382a

46 Lignos, I., Stavrakis, S., Nedelcu, G., Protesescu, L., de Mello, A.J., and Kovalenko, M.V. (2016) *Nano Lett.*, **16** (3), 1869–1877. doi: 10.1021/acs.nanolett.5b04981

47 Nightingale, A.M., Bannock, J.H., Krishnadasan, S.H., O'Mahony, F.T.F., Haque, S.A., Sloan, J., Drury, C., McIntyre, R., and de Mello, J.C. (2013) *J. Mater. Chem. A*, **1** (12), 4067. doi: 10.1039/c3ta10458c

48 Shen, X., Song, Y., Li, S., Li, R., Ji, S., Li, Q., Duan, H., Xu, R., Yang, W., Zhao, K., Rong, R., and Wang, X. (2014) *RSC Adv.*, **4** (64), 34179–34188. doi: 10.1039/c4ra04168b

49 Yang, L., Nieves-Remacha, M.J., and Jensen, K.F. (2016) *Chem. Eng. Sci.* doi: 10.1016/j.ces.2016.12.003

50 Wang, C.W., Bains, A., Sinton, D., and Moffitt, M.G. (2013) *Langmuir*, **29** (26), 8385–8394. doi: 10.1021/la400011n

51 Mashaghi, S., Abbaspourrad, A., Weitz, D.A., and van Oijen, A.M. (2016) *TrAC, Trends Anal. Chem.*, **82**, 118–125. doi: 10.1016/j.trac.2016.05.019

52 Yao, C., Dong, Z., Zhao, Y., and Chen, G. (2015) *Chem. Eng. Sci.*, **123**, 137–145. doi: 10.1016/j.ces.2014.11.005

53 Nightingale, A.M., Phillips, T.W., Bannock, J.H., and de Mello, J.C. (2014) *Nat. Commun.*, **5**, 3777. doi: 10.1038/ncomms4777

54 Hessberger, T., Braun, L.B., Henrich, F., Müller, C., Gießelmann, F., Serra, C., and Zentel, R. (2016) *J. Mater. Chem. C*, **4** (37), 8778–8786. doi: 10.1039/c6tc03378d

55 Liu, P., Zhao, Y., Qin, R., Mo, S., Chen, G., Gu, L., Chevrier, D.M., Zhang, P., Guo, Q., Zang, D., Wu, B., Fu, G., and Zheng, N. (2016) *Science*, **352** (6287), 797–801. doi: 10.1126/science.aaf5251

56 Lamer, V.K. and Dinegar, R.H. (1950) *J. Am. Chem. Soc.*, **72** (11), 4847–4854.

57 Li, S., Zhong, X.D., Song, Y.J., Shen, X.M., Sun, J.G., Song, Y.J., Wang, R.M., Zhu, M., Zhong, H.Z., and Zheng, A.G. (2014) *J. Mater. Chem. C*, **2** (36), 7687–7694. doi: 10.1039/c4tc00842a

58 Wang, J.M., Zhao, K., Shen, X.M., Zhang, W.W., Ji, S.X., Song, Y.J., Zhang, X.D., Rong, R., and Wang, X.Y. (2015) *J. Mater. Chem. C*, **3** (48), 12418–12429. doi: 10.1039/c5tc02279g

59 Song, Y.J., Jin, P.Y., and Zhang, T. (2010) *Mater. Lett.*, **64** (16), 1789–1792. doi: 10.1016/j.matlet.2010.05.025

60 Song, Y.J., Wang, R.X., Rong, R., Ding, J., Liu, J., Li, R.S., Liu, Z.H., Li, H., Wang, X.Y., Zhang, J., and Fang, J. (2011) *Eur. J. Inorg. Chem.*, (22), 3303–3313. doi: 10.1002/ejic.201100017

61 Ma, J.G., Wang, J.M., Zhong, X.D., Li, G.T., and Song, Y.J. (2016) *RSC Adv.*, **6** (87), 84255–84261. doi: 10.1039/c6ra17768a

www.ebook3000.com

62 Wang, A., Shen, H., Zang, S., Lin, Q., Wang, H., Qian, L., Niu, J., and Song Li, L. (2015) *Nanoscale*, **7** (7), 2951–2959. doi: 10.1039/c4nr06593j

63 Lim, S.J., Ma, L., Schleife, A., and Smith, A.M. (2016) *Coord. Chem. Rev.*, **320–321**, 216–237. doi: 10.1016/j.ccr.2016.03.012

64 Lim, J., Jeong, B.G., Park, M., Kim, J.K., Pietryga, J.M., Park, Y.-S., Klimov, V.I., Lee, C., Lee, D.C., and Bae, W.K. (2014) *Adv. Mater.*, **26** (47), 8034–8040. doi: 10.1002/adma.201403620

65 Nasr, A. (2016) *J. Energy Eng.*, **142** (1), 9. doi: 10.1061/(asce)ey.1943-7897.0000262

66 Hu, S., Zeng, S., Zhang, B., Yang, C., Song, P., Hang Danny, T.J., Lin, G., Wang, Y., Anderson, T., Coquet, P., Liu, L., Zhang, X., and Yong, K.T. (2014) *Analyst*, **139** (18), 4681–4690. doi: 10.1039/c4an00773e

67 Kwon, B.H., Lee, K.G., Park, T.J., Kim, H., Lee, T.J., Lee, S.J., and Jeon, D.Y. (2012) *Small*, **8** (21), 3257–3262. doi: 10.1002/smll.201200773

68 Kim, K., Jeong, S., Woo, J.Y., and Han, C.S. (2012) *Nanotechnology*, **23** (6), 065602. doi: 10.1088/0957-4484/23/6/065602

69 Masse, P., Mornet, S., Duguet, E., Treguer-Delapierre, M., Ravaine, S., Iazzolino, A., Salmon, J.B., and Leng, J. (2013) *Langmuir*, **29** (6), 1790–1795. doi: 10.1021/la3039335

70 Kochuveedu, S.T., Jang, Y.H., and Kim, D.H. (2013) *Chem. Soc. Rev.*, **42** (21), 8467–8493. doi: 10.1039/c3cs60043b

71 Wang, S., Yu, Y., Zuo, Y., Li, C., Yang, J., and Lu, C. (2012) *Nanoscale*, **4** (19), 5895–5901. doi: 10.1039/c2nr31316b

72 Haldar, K.K., Sinha, G., Lahtinen, J., and Patra, A. (2012) *ACS Appl. Mater. Interfaces*, **4** (11), 6266–6272. doi: 10.1021/am301859b

73 Karan, N.S., Keller, A.M., Sampat, S., Roslyak, O., Arefin, A., Hanson, C.J., Casson, J.L., Desireddy, A., Ghosh, Y., Piryatinski, A., Iyer, R., Htoon, H., Malko, A.V., and Hollingsworth, J.A. (2015) *Chem. Sci.*, **6** (4), 2224–2236. doi: 10.1039/c5sc00020c

74 Li, M., Yu, X.-F., Liang, S., Peng, X.-N., Yang, Z.-J., Wang, Y.-L., and Wang, Q.-Q. (2011) *Adv. Funct. Mater.*, **21** (10), 1788–1794. doi: 10.1002/adfm.201002233

75 Sheldon, M.T., Trudeau, P.E., Mokari, T., Wang, L.W., and Alivisatos, A.P. (2009) *Nano Lett.*, **9** (11), 3676–3682. doi: 10.1021/nl902186v

76 Haridas, M., Tripathi, L.N., and Basu, J.K. (2011) *Appl. Phys. Lett.*, **98** (6), 063305. doi: 10.1063/1.3553766

77 Hsieh, Y.-P., Liang, C.-T., Chen, Y.-F., Lai, C.-W., and Chou, P.-T. (2007) *Nanotechnology*, **18** (41), 415707. doi: 10.1088/0957-4484/18/41/415707

78 AbouZeid, K.M., Mohamed, M.B., and El-Shall, M.S. (2011) *Small*, **7** (23), 3299–3307. doi: 10.1002/smll.201100688

79 Cargnello, M., Doan-Nguyen, V.V.T., Gordon, T.R., Diaz, R.E., Stach, E.A., Gorte, R.J., Fornasiero, P., and Murray, C.B. (2013) *Science*, **341** (6147), 771–773. doi: 10.1126/science.1240148

80 Farmer, J.A. and Campbell, C.T. (2010) *Science*, **329** (5994), 933–936. doi: 10.1126/science.1191778

81 Campbell, C.T. and Sellers, J.R.V. (2013) *Faraday Discuss.*, **162**, 9–30.

82 Ran, G., Fu, Q., and Xu, W. (2015) *RSC Adv.*, **5** (19), 14740–14746. doi: 10.1039/c4ra12145g

83 Wang, J., Wang, Z., Li, S., Wang, R., and Song, Y. (2017) *Nanoscale*. doi: 10.1039/c6nr09122a

84 Chen, C.-H., Abate, A.R., Lee, D., Terentjev, E.M., and Weitz, D.A. (2009) *Adv. Mater.*, **21** (31), 3201–3204. doi: 10.1002/adma.200900499

85 Zhou, F., Lu, M., Wang, W., Bian, Z.P., Zhang, J.R., and Zhu, J.J. (2010) *Clin. Chem.*, **56** (11), 1701–1707. doi: 10.1373/clinchem.2010.147256

86 Nunes, J., Herlihy, K.P., Mair, L., Superfine, R., and DeSimone, J.M. (2010) *Nano Lett.*, **10** (4), 1113–1119. doi: 10.1021/nl904152e

87 Fang, C., Shao, L., Zhao, Y., Wang, J., and Wu, H. (2012) *Adv. Mater.*, **24** (1), 94–98. doi: 10.1002/adma.201103517

88 Xu, L., Peng, J., Yan, M., Zhang, D., and Shen, A.Q. (2016) *Chem. Eng. Process. Process Intensif.*, **102**, 186–193. doi: 10.1016/j.cep.2016.01.017

89 Song, Y., Sun, Q., Zhang, T., Jin, P., and Han, L. (2010) *J. Nanopart. Res.*, **12** (7), 2689–2697. doi: 10.1007/s11051-010-0012-5

90 Zeng, C., Wang, C., Wang, F., Zhang, Y., and Zhang, L. (2012) *Chem. Eng. J.*, **204–206**, 48–53. doi: 10.1016/j.cej.2012.07.096

91 Song, Y.J., Modrow, H., Henry, L.L., Saw, C.K., Doomes, E.E., Palshin, V., Hormes, J., and Kumar, C. (2006) *Chem. Mater.*, **18** (12), 2817–2827. doi: 10.1021/cm052811d

92 Lohse, S.E., Eller, J.R., Sivapalan, S.T., Plews, M.R., and Murphy, C.J. (2013) *ACS Nano*, **7** (5), 4135–4150. doi: 10.1021/nn4005022

93 Ran, R., Middelberg, A.P., and Zhao, C.X. (2016) *Colloids Surf., B*, **148**, 402–410. doi: 10.1016/j.colsurfb.2016.09.016

94 Herranz-Blanco, B., Arriaga, L.R., Makila, E., Correia, A., Shrestha, N., Mirza, S., Weitz, D.A., Salonen, J., Hirvonen, J., and Santos, H.A. (2014) *Lab Chip*, **14** (6), 1083–1086. doi: 10.1039/c3lc51260f

95 Li, Y., Lee, R.J., Huang, X., Li, Y., Lv, B., Wang, T., Qi, Y., Hao, F., Lu, J., Meng, Q., Teng, L., Zhou, Y., Xie, J., and Teng, L. (2016) *Nanomed. Nanotechnol. Biol. Med.* doi: 10.1016/j.nano.2016.09.014

96 Liu, D., Cito, S., Zhang, Y., Wang, C.F., Sikanen, T.M., and Santos, H.A. (2015) *Adv. Mater.*, **27** (14), 2298–2304. doi: 10.1002/adma.201405408

97 Herranz-Blanco, B., Liu, D., Mäkilä, E., Shahbazi, M.-A., Ginestar, E., Zhang, H., Aseyev, V., Balasubramanian, V., Salonen, J., Hirvonen, J., and Santos, H.A. (2015) *Adv. Funct. Mater.*, **25** (10), 1488–1497. doi: 10.1002/adfm.201404122

98 Hung, L. and Lee, A.P. (2007) *J. Med. Biol. Eng.*, **27** (1), 1–6.

99 Kim, Y., Lee Chung, B., Ma, M., Mulder, W.J., Fayad, Z.A., Farokhzad, O.C., and Langer, R. (2012) *Nano Lett.*, **12** (7), 3587–3591. doi: 10.1021/nl301253v

100 Yang, S., Guo, F., Kiraly, B., Mao, X., Lu, M., Leong, K.W., and Huang, T.J. (2012) *Lab Chip*, **12** (12), 2097–2102. doi: 10.1039/c2lc90046g

101 Lone, S., Kim, S.H., Nam, S.W., Park, S., Joo, J., and Cheong, I.W. (2011) *Chem. Commun.*, **47** (9), 2634–2636. doi: 10.1039/c0cc04517a

102 Dendukuri, D. and Doyle, P.S. (2009) *Adv. Mater.*, **21** (41), 4071–4086. doi: 10.1002/adma.200803386

www.ebook3000.com

103 Gygi, D., Bloch, E.D., Mason, J.A., Hudson, M.R., Gonzalez, M.I., Siegelman, R.L., Darwish, T.A., Queen, W.L., Brown, C.M., and Long, J.R. (2016) *Chem. Mater.*, **28** (4), 1128–1138. doi: 10.1021/acs.chemmater.5b04538

104 Banerjee, D., Simon, C.M., Plonka, A.M., Motkuri, R.K., Liu, J., Chen, X., Smit, B., Parise, J.B., Haranczyk, M., and Thallapally, P.K. (2016) *Nat. Commun.*, **7**, ncomms11831. doi: 10.1038/ncomms11831

105 Bag, P.P., Wang, D., Chen, Z., and Cao, R. (2016) *Chem. Commun.*, **52** (18), 3669–3672. doi: 10.1039/c5cc09925k

106 Ray Chowdhuri, A., Bhattacharya, D., and Sahu, S.K. (2016) *Dalton Trans.*, **45** (7), 2963–2973. doi: 10.1039/c5dt03736k

107 Lian, X. and Yan, B. (2016) *Inorg. Chem.*, **55** (22), 11831–11838. doi: 10.1021/acs.inorgchem.6b01928

108 Genna, D.T., Pfund, L.Y., Samblanet, D.C., Wong-Foy, A.G., Matzger, A.J., and Sanford, M.S. (2016) *ACS Catal.*, **6** (6), 3569–3574. doi: 10.1021/acscatal.6b00404

109 Doherty, C.M., Buso, D., Hill, A.J., Furukawa, S., Kitagawa, S., and Falcaro, P. (2014) *Acc. Chem. Res.*, **47** (2), 396–405. doi: 10.1021/ar400130a

110 Zanchetta, E., Malfatti, L., Ricco, R., Styles, M.J., Lisi, F., Coghlan, C.J., Doonan, C.J., Hill, A.J., Brusatin, G., and Falcaro, P. (2015) *Chem. Mater.*, **27** (3), 690–699. doi: 10.1021/cm502882a

111 Jeong, G.-Y., Ricco, R., Liang, K., Ludwig, J., Kim, J.-O., Falcaro, P., and Kim, D.-P. (2015) *Chem. Mater.*, **27** (23), 7903–7909. doi: 10.1021/acs.chemmater.5b02847

112 Tai, S., Zhang, W., Zhang, J., Luo, G., Jia, Y., Deng, M., and Ling, Y. (2016) *Microporous Mesoporous Mater.*, **220**, 148–154. doi: 10.1016/j.micromeso.2015.08.037

113 Rodriguez-San-Miguel, D., Abrishamkar, A., Navarro, J.A., Rodriguez-Trujillo, R., Amabilino, D.B., Mas-Balleste, R., Zamora, F., and Puigmarti-Luis, J. (2016) *Chem. Commun.*, **52** (59), 9212–9215. doi: 10.1039/c6cc04013f

114 Polyzoidis, A., Altenburg, T., Schwarzer, M., Loebbecke, S., and Kaskel, S. (2016) *Chem. Eng. J.*, **283**, 971–977. doi: 10.1016/j.cej.2015.08.071

115 Wang, J.M., Zhao, H.F., Zhu, Y.C., and Song, Y.J. (2017) *J. Phys. Chem. C.*, **121** (6), 3567–3572. doi: 10.1021/acs.jpcc.6b10901

116 Wang, J.M., and Song, Y.J. (2017) *Small*, **13** (18), 1604084. doi: 10.1002/smll.201604084

117 Wang, Z.L., Fan, H.S., Liang, H.X., Li, S., Song, Y.J., and Wang, R.M. (2017) *Electrochim. Acta.*, **230**, 245–254. doi: 10.1016/j.electacta.2017.01.159

118 Liang, H.X., Wang, Z.L., Wang, J.M., Huang, D.Y., Zhu, Y.C., and Song, Y.J. (2017) *Mater. Chem. Phys.*, **201C**, 156–164. doi: 10.1016/j.matchemphys.2017.08.005

119 Adamo, A., Beingessner, R.L., Behnam, M., Chen, J., Jamison, T.F., Jensen, K.F., Monbaliu, J.-C.M., Myerson, A.S., Revalor, E.M., Snead, D.R., Stelzer, T., Weeranoppanant, N., Wong, S.Y., and Zhang, P. (2016) *Science*, **352** (6281), 61–67. doi: 10.1126/science.aaf1337

16

Microfluidic Synthesis of MOFs and MOF-Based Membranes

Fernando Cacho-Bailo, Carlos Téllez, and Joaquin Coronas

Universidad de Zaragoza, Nanoscience Institute of Aragon (INA), Chemical & Environmental Engineering Department, Mariano Esquillor, s/n., 50018 Zaragoza, Spain

16.1 Microfluidic Synthesis of Metal–Organic Frameworks (MOFs)

Continuous synthesis of microporous crystalline powders by means of microfluidics has attracted researcher's attention in recent years versus the traditional discontinuous batch reactions. This approach allows not only the continuous production but also an accurate reaction parameter control in the synthesis, giving a step toward intensification, versatility, and scalability in the fabrication of varieties of useful materials [1]. Along with microfluidics, other techniques such as microwave-assisted [2], ionic liquid-based, and high pressure solventless syntheses [3] and mechanochemistry [4] have been investigated.

In the review about microfluidics [1], the ETH Zurich workgroup thoroughly described the state of the art and the potential challenges in microfluidics. Main advantages were pointed out, whereas reactor dimensions and Reynolds and Péclet numbers were delimited to fall in the microfluidic regime. The proposed future challenges in the microfluidic field are mainly the processing of solids and polymer surface modification related to the fabrication of microfluidic devices where metal–organic framework (MOF) powders and MOF-supported membranes stand out as the very promising areas to be synthesized by microfluidic processes. In the last few years, worldwide researchers have made important advances in these two areas [5, 6], which are currently moving toward the upscaling of the developed methods [7, 8]. In this sense, at least two patents have been filed [9, 10]. The most significant works in the microfluidic synthesis of MOFs and MOF-supported membranes will be briefly reviewed in this chapter.

16.1.1 Zeolite Background

Generally zeolite (porous crystalline aluminosilicates) formation conventionally requires hydrothermal synthesis at relatively high temperatures and the resulting autogeneous pressures that make the extrapolation to a microfluidic continuous crystallization system extremely arduous. In fact, nowadays zeolite powders are

Microfluidics: Fundamentals, Devices and Applications, First Edition.
Edited by Yujun Song, Daojian Cheng, and Liang Zhao.
© 2018 Wiley-VCH Verlag GmbH & Co. KGaA. Published 2018 by Wiley-VCH Verlag GmbH & Co. KGaA.

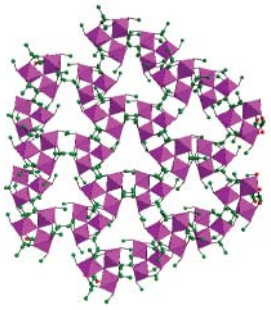
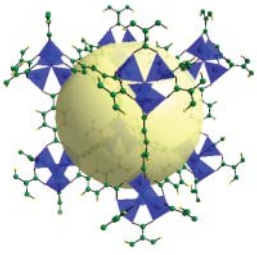
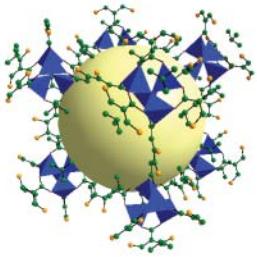
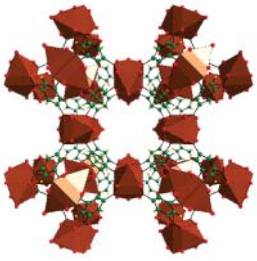
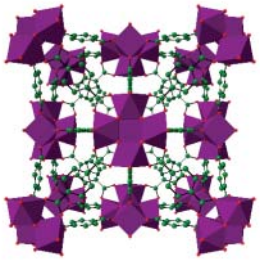
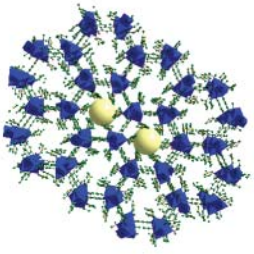
www.ebook3000.com

industrially in batch discontinuously fabricated: gel formation premixer and a crystallization reactor are used in series. A limited number of works have been published on this topic. In 2006, using a single-phase microfluidic system to synthesize zeolite NaA, Ju *et al*. obtained smaller mean particle size and narrower particle size distribution (PSD) within shorter times than using a batch reactor [11]. However, still some improvements have to be done by avoiding some problems, such as clogged channels and control of the PSD. In 2009, Pan *et al*. controlled a very narrow PSD of an ultrafine 4A Linde type A (LTA)-type zeolite by varying the outer size of the microfluidic tube and the gel solution aging at 80–100 °C or above. They took advantage of using two segmented immiscible phases creating confined droplet microreactors where mass and heat transfer were enhanced, leading to shorter reaction times and homogeneity in the final product properties [12]. Using droplet and ionic liquid-assisted microfluidic (DIM) synthesis method, nanoscale-sized ZMS-5 crystals were rapidly and continuously synthesized at 150 °C by Hoang *et al*., having a uniform morphology and a homogeneous particle size [13]. In this case, precursors were dissolved in an ionic liquid, producing a synergistic combination of ionic liquid and droplet microfluidics. In addition, taking advantage of the segmented flow, Hoang *et al*. synthesized zeolite-A nanocrystals with a narrow PSD and a hierarchical meso-microporous structure derived from the introduction of a water-soluble alginate polymer within the gel [14]. In these approaches, the gel was previously formed before entering the reactor. Later, Yu *et al*. developed the process featured by one-step gel formation and crystallization of zeolites in a two-phase segmented microfluidic reactor [15]. Moreover, an aluminophosphate material ($AlPO_4$-5) was also synthesized in a continuous flow system in 2014, but flow reactor dimensions (several millimeters) and flows make this approach to fall in mesofluidics [16]. However, zeolites require hydrothermal conditions with relatively high temperature and pressure. This may have limited the development of microfluidics into the field of zeolites and related inorganic materials. As shown next, porous organic–inorganic materials having most of the important properties of zeolites and some new functions, particularly the so-called MOFs, are suitable to elucidate the benefits from the microfluidic synthetic approach.

16.1.2 Microfluidic MOF Synthesis

MOFs are microporous hybrid materials that have recently been paid great attention because of their applications in catalysis [17, 18], drug encapsulation and delivery [19], gas separation and storage [20, 21], and membrane technology [22–24] and as chemical sensors [25]. They are a subclass of porous coordination polymers (PCPs) consisting of metal clusters covalently connected with organic ligands of different compositions, mostly carboxylates and imidazolates. The latter are typically known as "zeolitic imidazolate frameworks" (ZIFs) [26]. They offer chemical versatility in their crystals, acting as discrete molecules together with unprecedented and tunable porosities [27]. New MOF structures and topologies are still in development, while many research efforts are focused on modifying and adjusting the textural properties of those existing MOFs. The crystalline structures of some of the most commonly microfluidics-synthesized MOF materials are shown in Table 16.1, which will be discussed along this section.

Table 16.1 Structures of those common carboxylate-based MOFs synthesized by microfluidics.

		
MIL-88A(Fe) $Fe(OH)(O_2C–C_2H_2–CO_2)$ CSD[a] refcode FAVKAP [28]	MOF-5 $Zn_4O(BDC)_3$[b] CSD[a] refcode SAHYIK [29]	IRMOF-3 $Zn_4O(NH_2\text{-}BDC)_3$[b] CSD[a] refcode EDUSUR [30]
		
HKUST-1 $Cu_3(BTC)_2$[b] CSD[a] refcode FIQCEN [31]	UiO-66(Zr) $Zr_6O_4(OH)_4(BDC)_6$[b] CSD[a] refcode RUBTAK [32]	MOF-74 $Zn_2(DO\text{-}BDC)$[b] CSD[a] refcode FIJDOS [33]

a) CSD (Cambridge Structural Database) refcodes of each structure are shown.
b) Abbreviations stand for: BDC (benzenedicarboxylate), NH_2- (amino-), DO- (dihydroxy-), and BTC (benzenetricarboxylate).
Structures are drawn on its most representative projection using Diamond Crystal Impact software. Color caption: Metal polyhedra (Fe, pink; Zn, blue; Cu, brown; Zr, purple); O, red; C, green; N, orange. H atoms are hidden for clarity.

The potential application of MOFs in new technologies should be determined by the scalability and sustainability of their synthesis for defined sizes and shapes (preferably based on eco-friendly solvents) and the single crystal morphology and functionalization control in a determined location, among other awaiting tasks [34]. Microfluidic processes have emerged in this field as a promising MOF fabrication technique. A scheme of a general setup for microfluidic oil-segmented droplet-confined MOF synthesis is shown in Figure 16.1.

www.ebook3000.com

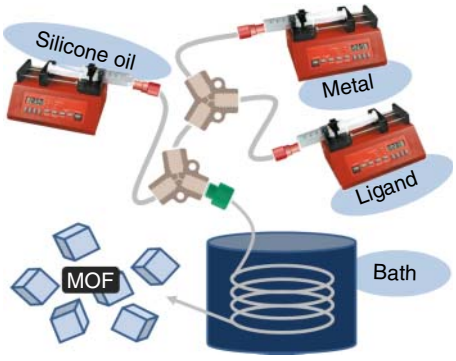


Figure 16.1 General scheme of a microfluidic oil-segmented droplet confined MOF synthesis. Different residence times of the crystallization solutions can be achieved by varying the reactor length.

The microfluidic strategy based on segmented flow synthesis, similar to those above described for zeolites [11–15], was used by Paseta *et al*. in 2013 for accelerating the dicarboxylate MIL-88B(Fe) (Matériaux de l'Institut Lavoisier-88B) crystallization [35]. A segmented flow was created by the interleaving of silicone oil in the H_2O/DMF (Dimethylformamide) reaction solution by means of micropumping from a syringe inside a polytetrafluoroethylene (PTFE) tubing reactor. Three different MOFs starting from benzene-1,4-dicarboxylic (BDC) acid ligands and their functionalized forms (NH_2- and Br-) were crystallized in this system. This approach gave rise to nanoreactors with volumes as small as 100 nl. The noticeable advantages of these segmented flows could be then demonstrated.

Much faster reaction rates were obtained compared with those from the traditional solvothermal syntheses. Shorter times at 95 °C were needed to obtain the corresponding nanoscale-sized powders (see Figure 16.2), with 20 s for NH_2-MIL-88B(Fe) and 4–6 min for MIL-88B(Fe) and Br-MIL-88B(Fe), respectively, while 12–24 h durations had been used as previously reported for a solvothermal crystallization of the same MOFs if using bottle-batch reactors [36, 37]. Not only an acceleration of the reaction was observed, but also, after the proper washing, the collected powders showed controlled PSD and crystal morphology.

Microfluidic parameters enabled to flexibly control the PSDs of powders. For example, longer residence times in the PTFE tubing (varied from 20 to 600 s) led not only to larger and more angular shaped NH_2-MIL-88B(Fe) particles (from 180 to 900 nm; see Figure 16.3) but also to a broader crystal size distribution. The slug volume of each nanoreactor created by the segmented plug flow was increased proportionally with the residence time. The advantages of this synthesis strategy came from an improved mass and heat transfer inside each of these nanoreactors (with volumes as small as 100 nl), which can flow under a laminar regime. The immiscible liquid interphases delimiting the slugs inhibited the temperature and concentration of axial gradients and created an internal recirculation inside every nanoreactor that enhances the mixing [38]. The vorticity in the interphase region (related with this recirculation inside the slug) increased with decreasing residence time and increasing slug area-to-volume ratio and therefore was related with the PSDs of the collected MOFs. Furthermore, the temperature effect was

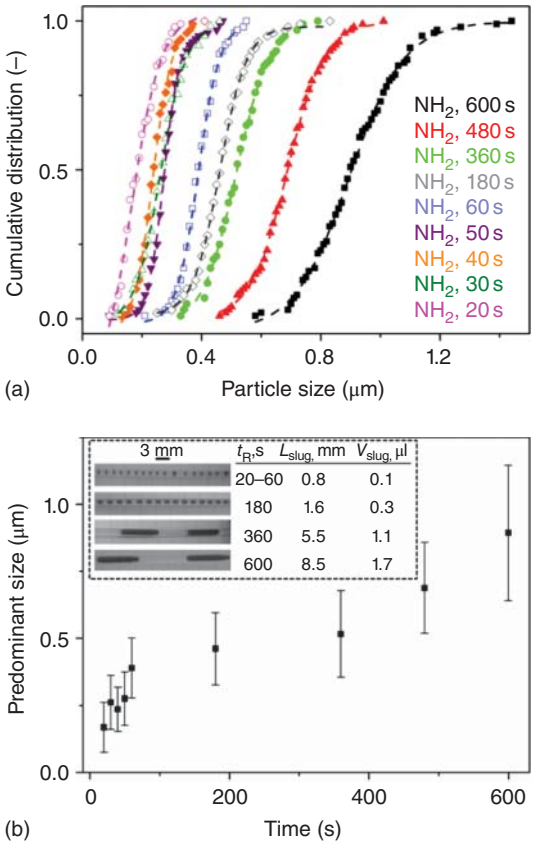


Figure 16.2 Particle size distributions (PSDs) of the powdered NH_2-MIL-88B(Fe) products obtained at 95 °C as a function of the residence time in the oil-segmented nanoliter reactor (a). Mean particle size of the powdered NH_2-MIL-88B(Fe) products obtained at 95 °C at different residence times (b). More heterogeneous and larger MOF crystals are obtained when the residence time, and therefore the slug-reactor volume, was increased. Inset shows images of the oil-segmented slugged flow. (Paseta *et al*. 2013 [35]. Reproduced with permission of American Chemical Society.)

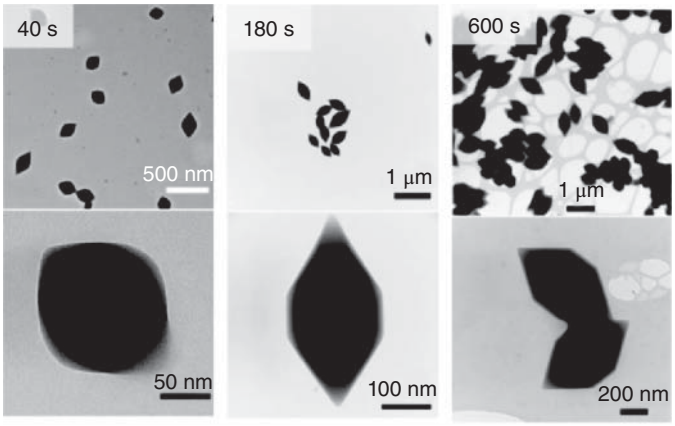


Figure 16.3 TEM images of the NH_2-MIL-88B(Fe) crystalsobtained at different residence times at 95 °C with the oil-segmented flow approach. Sharper and larger crystals are obtained with longer residence times. (Paseta *et al*. 2013 [35]. Reproduced with permission of American Chemical Society.)

www.ebook3000.com

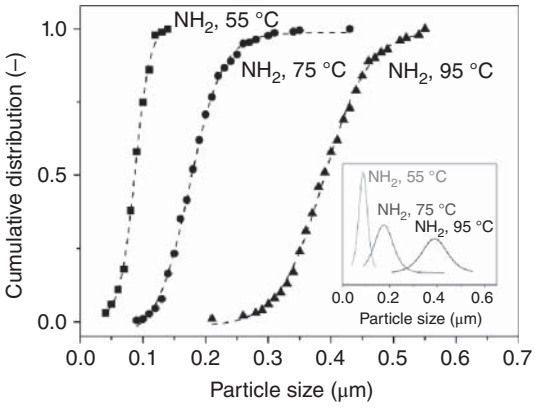


Figure 16.4 PSD dependence with temperature of the NH_2-MIL-88B(Fe) powders obtained with a 60 s residence time using the nanoliter oil-segmented flow approach. Low temperatures led to highly homogenous and small MOF PSDs, owing to a more reduced mass and heat transfer inside the nanoliter slug reactors. (Paseta *et al*. 2013 [35]. Reproduced with permission of American Chemical Society.)

investigated. Low temperatures (55 and 75 vs 95 °C) decreased the molecular mobility and diffusion and gave rise to narrow PSDs and small average crystal sizes (Figure 16.4).

In the same manner, Faustini *et al*. reported the syntheses of high-quality MOFs and core–shell MOF composites using a nanoliter microfluidic approach [39]. Prototypical MOFs such as HKUST-1 (Hong Kong University of Science and Technology-1), MOF-5, IRMOF-3 (Iso-Reticular Metal–Organic Framework-3), and UiO-66(Zr) (Universitetet i Oslo-1; see Table 16.1) were fabricated in a reduced time-consuming manner (from 1 to 15 min) inside nanoliter droplets confined and transported by immiscible oil. The MOF synthesis requiring harsher conditions, as, for instance, Ru_3BTC_2 that needs 160 °C and hydrothermal high pressure, was tackled. The most important novelty here lays on the preparation of hetero-structure core–shell materials combining different metal clusters (Co@Ni-BTC), surface functionalization (MOF-5@CH_3-MOF-5), or magnetic core MOFs (Fe_3O_4@ZIF-8). Shell precursors were injected to merge with the MOF droplets before the entrance in a second capillary reactor, which was serially located. The introduction of surface functionalities and/or hetero-structure shells in MOF crystals taking advantage of microfluidics was herein demonstrated.

As described in the latter work [39], microfluidics permits versatile actions and modifications in the MOF synthesis in order to obtain complex MOF superstructures, which are hard to accomplish by other techniques. Thereby, Jeong *et al*. reported in 2015 a very interesting work in the fabrication of hollow MIL-88A(Fe) spheres by interfacial reactions (being the metal precursor in the aqueous phase and the organic linker in the oil phase) carried out by microfluidics [40]. Single- and double-shelled particles with controlled sizes were achieved (with diameters in the 35–2000 μm range, typically 450 μm with a shell thickness of 2 μm), as well as the *in situ* encapsulation of previously fabricated nanoparticles such as magnetic cobalt, silica, and UiO-66(Zr) MOFs. The catalytic activities of three different encapsulated enzymes were also evaluated, these bio-MOF capsules having a great potential application in biotechnology. The fabrication of biocompatible spheres with a microfluidic approach provides a number of significant advantages over previous techniques. Biomacromolecules could be put inside the MOF

shell using a simple one-step continuous method, which ensures a size and shape control, versus discontinuous and time-consuming bottle-batched approaches. Furthermore, the utilization of aqueous solutions warranted the enzyme stability during the MOF formation.

Henceforth, other works before these articles of Paseta *et al*. and Faustini *et al*. regarding strategies of MOF synthesis by microfluidics, published from 2011 to 2013, are described. The benefits of the interfacial synthesis of MOFs using immiscible liquids were anticipated by Ameloot *et al*. in 2011 and demonstrated by the $Cu_3(BTC)_2$ (HKUST-1) crystallization on the surface of emulsified aqueous slugs inside an 1-octanol continuous flow (see Figure 16.5) [41]. This highly concentrated biphasic inorganic/organic mixture driven by a hollow-needle microfluidic setup led to the formation of hollow MOF spheres that were collected in an alcohol (e.g., ethanol). Interfacial growth ensured a defect-free self-completing MOF layers with a uniform thickness. A relationship between the delineation of the biphasic interface and the thickness and compactness of the MOF suggested that thick and asymmetrically HKUST-1 layers were formed when small ethanol quantities were added to the 1-octanol organic phase.

On the other hand, the automation of microfluidics also enabled the process development of the growth of other MOFs and their precise deposition. By means of a digitally controlled delivering of very small precursor droplets on appropriately modified hydrophilic surfaces in desired locations, arrays patterned with discrete single microscale-sized MOF crystals could be fabricated [42, 43]. Precursor droplet size showed a clear influence on the final MOF crystal size, growing during the latter solvent evaporation [43]. In 2012, Witters *et al*. extended their digital microfluidics (the so-called DMF) setup to obtain a 550 nm thick HKUST-1 coating grown layer by layer (LBL) in 40 cycles [44]. Alternative

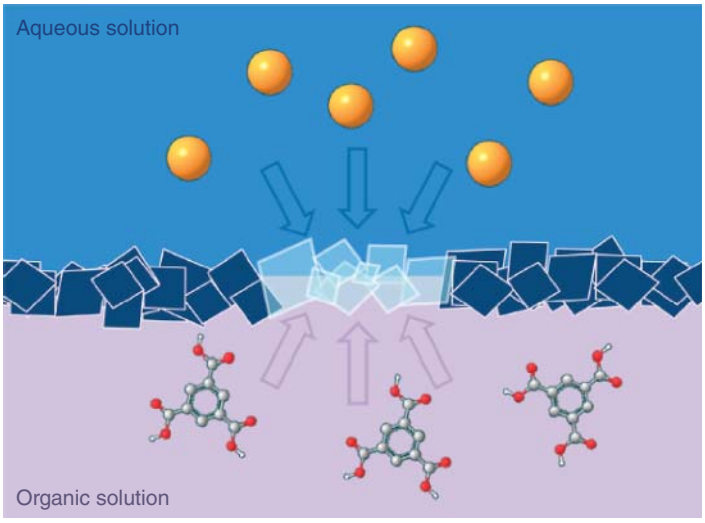


Figure 16.5 Biphasic interfacial MOF synthesis takes advantage of the self-healing crystallization in the pinholes and defects to give rise to compact hollow MOF spheres. (Ameloot *et al*. 2011 [41]. Reproduced with permission of Nature Publishing Group.)

www.ebook3000.com

passing of precursor and pure solvent droplets enabled an automated stepwise washing process. These works demonstrated the versatility and suitability of the digitally controlled microfluidic setups on the formation of MOFs. Automated microfluidic control on MOF size and location extends the potential application of MOF-based electronic devices, selective sensors, and drug delivery systems.

In 2013, Maspoch workgroup took another step toward the scalable continuous MOF fabrication leaning on microfluidics [8, 9]. They reported the massive and fast production of a wide variety of MOFs in a spray-drier. The solutions containing the MOF precursor in a stoichiometric ratio were atomized from a micro-nozzle at a 4.5 ml min^{-1} rate and encountered a heated gas flow (air or nitrogen at a certain temperature) that gave rise to hollow polycrystalline MOF spheres smaller than 5 μm (see Figure 16.6). Each droplet acted as a microreactor where a confined synthesis occurred: the fast evaporation of the solvent made the precursor concentration increase on the surface. When oversaturation was reached, MOF started to crystallize in a well-packed manner, owing to the limited mobility of the formed crystals. HKUST-1, MOF-74, MIL-88A, B(Fe), UiO-66(Zr) and MOF-5, or other types of nanocrystals were crystallized in a short time into the 30–300 nm range. Various guest species were entrapped inside these hollow sphere cavities. For instance, sodium chloride, fluorescein, or magnetic iron oxide, which were dissolved or emulsified in the precursor

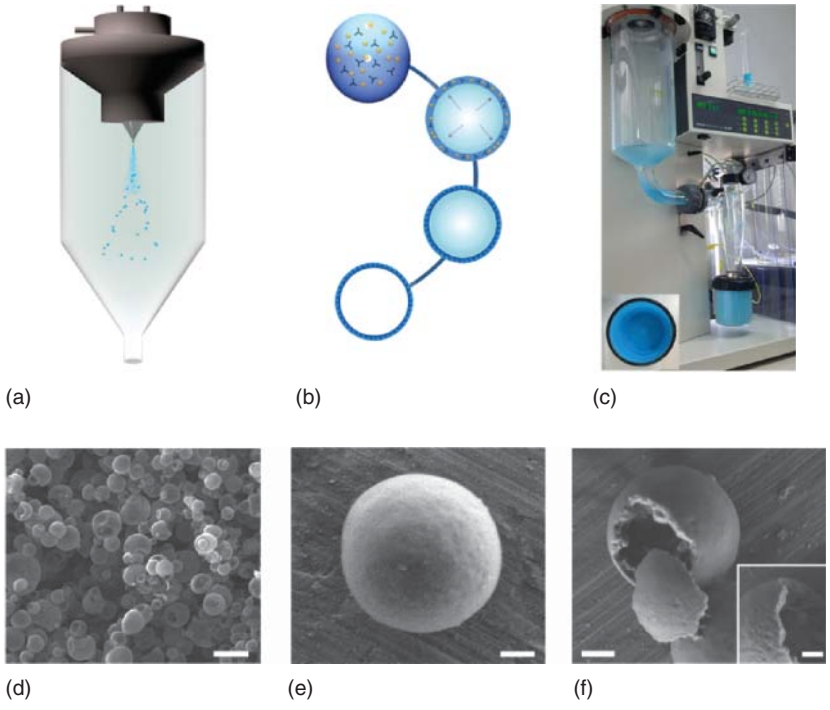


Figure 16.6 Hollow polycrystalline MOF spheres were fabricated making use of a spray-drier. This approach demonstrated the scalability of the microfluidics-based MOF synthesis procedures and the important cutting costs therefore. (Carné-Sánchez *et al*. 2013 [8]. Reproduced with permission of Nature Publishing Group.)

solutions, are present inside the cavity of the spray-dried sphere being evidenced afterward. The authors underlined a very interesting idea: the entrapment of catalysts should give rise to highly selective, discrete membrane reactors where reactant and product diffusivity would be controlled by the MOF porosity.

Various tubing and nozzle conformations were tested to provide different mixing protocols. Reactants were put in contact before the atomizing using a T-connector or were separately sprayed. Independent reactant feeding seemed to be particularly useful in post-addition of additives or deprotonator bases and also in precursor solutions where an amorphous product precipitates immediately after the mixture, which are difficult to be pumped and micronized. Thus the droplets containing the reactants are limited to coalesce inside the heating chamber. In such conditions, high yield (40% vs 10%) and purity (79% vs 8%) in MIL-88A(Fe) formation were only achieved when precursors were separately injected in comparison with a premixed solution spraying. This situation actually reveals a widespread concern in microfluidics (dealing with turbid solutions that have an instantaneous precipitation after mixing), and how versatile solutions can be easily implemented in the microfluidic setups to overcome certain difficulties.

These works showed prototypical examples of versatile and feasible industrial-scalable strategies for the continuous fabrication of a wide range of MOFs taking advantage of microfluidics [8, 42–44]. At the same time, an important eco-friendly and process-intensifying function was involved in the latter. The reagent cutting cost (precursors and solvents) together with a production time reduction with respect to previous approaches was achieved [8].

Analogous to the above spray-drying upscaling, other interesting approaches include the crystallization of MOF powders in the so-called microfluidic reactors. Recent advances in microreaction technology comprise the syntheses of archetypical ZIF-8 [45, 46] and HKUST-1 [47] using micro-mixers with characteristic dimensions between 330 and 750 μm. Tai *et al*. prepared UiO-66 nanoparticles with tunable sizes in a continuous flow microreactor with an inner diameter (ID) of 0.8 mm by controlling the residence time, falling in the so-called mesofluidics [48]. The system was also used to amino-functionalize the UiO-66 nanoparticles intended for drug delivery. UiO-66, HKUST-1, and NOTT-400 (University of Nottingham-400) were also prepared in the mesoscale range by Rubio-Martinez *et al*., making use of a continuous 1 mm-diameter flow reactor [49]. However, high-speed flow rates were typically employed herein (several $ml\,min^{-1}$) looking for high turbulence in mixing and high product yield, giving rise to extremely small residence times in the microfluidic reactors. Meanwhile, D'Arras *et al*. crystallized a Ce-BDC MOF using a coaxial flowing microsystem at high temperature and pressure. Coaxial microfluidic reactors are indicated for the inhibition of heterogeneous nucleation and therefore the creation of nanostructures in a continuous way [50].

To conclude this section, in the sight of the hereby detailed MOF synthesis, microfluidics appears to be a technique with a promising future in the field. A fine-tuning of crystal sizes and morphologies together with noticeable reaction speedups is achieved when working in microfluidic conditions. Operation parameters, such as residence time and reactant contact and mixture, can be

www.ebook3000.com

easily tuned to obtain a product with a narrow PSD and homogeneous textural properties, a key point in a wider MOF application as sensors, catalysts, and contrast agents. Furthermore, post-synthetic modifications in MOF particle design can be easily stepwise implemented in the microfluidic reaction setups in order to either suitably change the product features and surface character or create complex core–shell heterostructures. Looking for sustainable MOF fabrication at industrial scale, microfluidic syntheses offer advantages in effluent control and footprint reduction, so long as it reduces the amount of solvents and reactants and takes a step in reaction versatility. Nevertheless, the efforts of research must be focused on an increase of the yields achieved, for example, by means of recirculation of mother liquor solutions and the development of new particle design for specific purposes (encapsulation and controlled delivery of drugs, biocompatibility, etc.). Besides the MOF fabrication, microfluidics has been recently extended to covalent organic frameworks (COFs) (another type of PCPs together with MOFs) synthesis. Rodríguez-San-Miguel *et al*. made use of a microfluidic chip reactor to produce highly crystalline fiber-shaped COF-1 [51].

16.2 Microfluidic Synthesis of MOF-Based Membranes

16.2.1 Context

Pure polymeric membranes are nowadays applied in the most important and worldwide strategic separations of mixtures, such as those related to H_2 and natural gas purification and air separation. The appearance of novel membrane materials in the last decade paved the way to the rapid development of industrial upscaling of membrane-based separations in the near future, awaiting for a cost reduction in material fabrication [52]. Implementing membrane unit modules as alternatives to heat-based distillation processes would lead to a noteworthy 90% energy reduction, representing the 7% of the US total energy consumption [53].

De Jong *et al*. anticipated in 2006 a promising future for the coupling of membranes and microfluidic fields [54], their applications being as essential as biotechnology or medicine, comprising tissue engineering [55]. They proposed a remarkable scheme for helping in the selection choice of the membrane material, type, and fabrication method. In the same manner as in such review, an outlook on the number of citations in the worldwide research concerning the terms "membranes" and "microfluidics" has been carried out for the 2005–2015 period (see Figure 16.7). However, among those thousands of citations increasing every year (11 080 in 2015), the term "MOF" is only present since 2014 (7 citations), increasing up to 64 citations in 2015, when the inclusion of these novel porous materials in the membrane field was produced [5–7].

The usage of MOFs in membranes by microfluidics has been carried out through a new strategy based on the application of hollow fiber (HF) porous supports for MOF continuous layers acting as selective membranes. This strategy takes advantage of the laminar flow regime for the crystallization of MOFs in a very controllable set of conditions and methods [1] in combination with the high surface-to-volume ratio offered by these HF supports (more

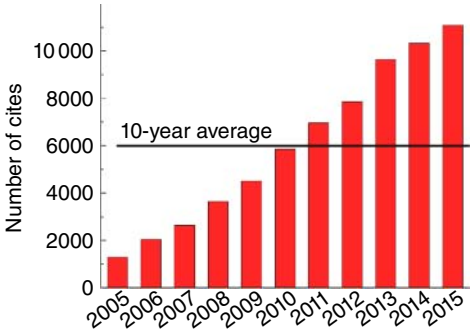


Figure 16.7 Number of cites concerning the terms "microfluidics" and "membrane" in the 2005–2015 period, according to the Web of Knowledge (WOK) database (see also [56]).

than 1000 $m^2 m^{-3}$ are considered attractive for upscaling) [57, 58]. This work focuses on the development of greener separation methods, where polymeric membranes are an ideal alternative to traditional procedures because of their low costs and ease of forming. Polymeric membranes, in contrast with those based on inorganic supports, are considered the only feasible to be used for cost-affordable, large-scale operations [59]. Microfluidic MOF HF-supported membranes would also take a step into the process of intensification of the membrane fabrication at industrial scale [60, 61]. A great reduction of expenses derived from the disposal of effluent streams for membrane fabrication could be achieved, as will be shown below [5]. Table 16.2 summarizes the main advantages of the combination of MOFs and HF membranes by microfluidics that will be widely described in this section.

16.2.2 MOF Membranes by Microfluidics

The starting milestone was reached by Brown *et al*. in Georgia Institute of Technology with the publication of the article "Interfacial microfluidic processing of metal–organic framework hollow fiber membranes" in 2014 [6], being their invention legally protected with a patent file [10]. In their foregoing work in 2012 [62], Nair's workgroup already had solvothermally synthesized a ZIF-90 (Zn-imidazol-2-carboxaldehyde) layer on the outer surface of a TORLON® (polyamide-imide (PAI)) HF support using a secondary seeded growth method. Gas and liquid permeation rates were measured with the resulting MOF-supported HF membrane. This work was pioneer in the development of facile, low-temperature, and technologically scalable methods for MOF membrane fabrication using HF polymeric supports. Before this work, these researchers had also grown mesoporous silica on the surface of a polymeric HF [63]. MOFs are considered the appropriate materials to complement polymers and synergistically form high-performance membranes, owing to their hybrid organic–inorganic character that provides a proper MOF–polymer adhesion. Subsequently, the authors implemented microfluidics to develop the interfacial microfluidic membrane processing (IMMP) approach for the HF membrane fabrication [6].

Herein ZIF-8 layers were supported on either the inner or the outer surfaces of TORLON® HFs by IMMP, depending on the ligand and metal solution placement

www.ebook3000.com

Table 16.2 Summary of the main advantages arising from the combination of MOFs and hollow fiber membranes by a microfluidic approach, to be deeper extended in this section.

Simple and versatile MOF synthesis with alternating reactants and subsequent easy washing out of reactants excess and also possible *in situ* MOF activation	*Ease of upscaling*. MOF-supported HF membranes, chiefly those inner-located, display a high ease to be industrially produced. Cheap and shapeable polymers are nowadays used in compact modules containing thousands of HFs. Implementation of its MOF coating by microfluidics would upgrade their performance and attractiveness for further applications
Reagent and solvent cutting costs. Microfluidic preparation of MOF hollow fiber (HF) membranes derives in small footprints in terms of reagents and solvents. HF lumen volumes are almost negligible in comparison with foregoing membrane preparation strategies	*Enhanced MOF–polymer affinity*. Owing to their hybrid metallic–organic character, the layer-support materials have an enhanced adhesion that improves the stability and durability of the final composite membrane
Versatility in synthesis step sequencing. Serial membrane post-functionalization or encapsulation can be easily accomplished by microfluidics, thus minimizing damage risks from handling	*Increased performance efficiency*. HF-shaped membranes offer extremely high area-to-volume ratios. Pressurizing costs are minimized in gas and liquid separation systems. Also feed–membrane contact and therefore surface effects are enhanced
HF support runs both as a reactor and a support for the MOF synthesis, providing a singular chemical engineering and materials science system	*MOF layer features control*. The easy-tunable microfluidic synthesis parameters determine the MOF layer features: positioning, thickness, interface extent, and so on. Inner-located MOF layers become shielded from mechanical, physical, and chemical damage, and also they minimize the creation of pinholes or defects
Microfluidics offers a high grade of control in the MOF synthesis. Several strategies depending on the MOF type to be crystallized and the initial porosity of the support are available. Those working in continuous offer an easy control on the synthesis parameters: flow regime (Reynolds number), reagent replenishment, and so on, which give rise to highly homogeneous membranes	

during the interfacial syntheses. This MOF was selected as prototypical for the testing of the approach due to its intrinsic molecular sieving properties in H_2 purification and hydrocarbon selective separation [64–66]. Immiscible water and 1-octanol were used to dissolve the organic 2-methylimidazolate ligand and the zinc salt as metal source, respectively, at the ligand/metal ratio of 75 in all the studied cases, thus creating an interphase for the ZIF-8 to grow (see Figure 16.8). The authors designed a stainless steel module to be used for both synthesis and permeation testing. Thus, the potential failure risks in membrane handling were reduced at minimum. At least three high permeable TORLON® HFs (53 000 gas permeation unit (GPU) at their initial state, used as membrane supports) could be sealed, MOF-coated, and tested in the module at the same time, as a probe to the easy scalability of this method.

One of the synthesis solutions was poured to fill the shell volume surrounding the fibers, whereas the other reagent solution was pumped through the bore volume by microfluidics. Control of microfluidic parameters determined the thickness, continuity, and possible presence of defects of the MOF layers during their growth. Flows as low as 10–60 $\mu l\, h^{-1}$ (Zn salt solution in the general event)

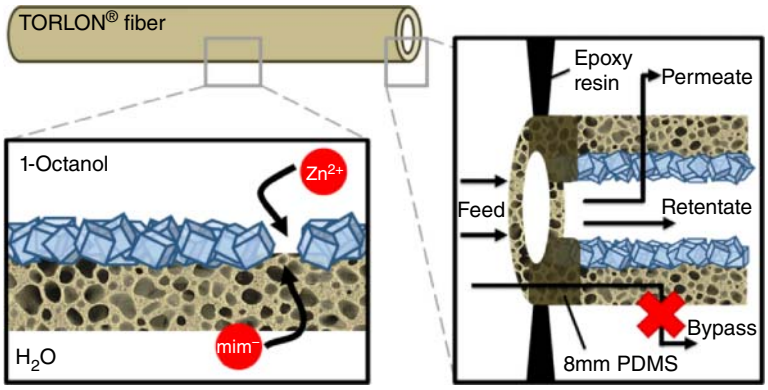


Figure 16.8 Operating scheme of the IMMP technique (see also [6]) from Brown *et al*. showing interfacial MOF synthesis (former) and permeation testing (latter). IMMP approach enables the MOF layer positioning control. An interfacial ZIF-8 crystallization takes place on the TORLON® supports. MOF layer grew on the inner support surface owing to a higher ligand diffusion rate. Inner-supported MOF membranes fabricated with the IMMP pure interfacial procedure revealed an inconvenience: HF membrane ends must be sealed (i.e., with a PDMS rubber) to avoid unselective gas bypassing and take full advantage of the MOF microporosity in the separation.

were pumped through the fiber bore lumen in three different regimes: static, mixed, and continuous regimes. The static conditions gave rise to a thick but noncontinuous ZIF-8 layer due to the depletion of the Zn ions during the MOF crystallization. The reagent replenish was achieved with a continuous bore microflow. The inner volume of the fiber, as small as 1.5 µl, allowed the solution short residence inside the fiber and therefore a constant reagent concentration with negligible depletion all along it. A thin ZIF-8 layer (only 2 µm thick) grew alongside the fiber within this flow regime, as proven by the SEM measurements carried out in several membrane cross sections along a determined length. Mixed flow regime (static flow followed by intermittent specie replenishment) led to 9 µm thick MOF layers with a positive intergrowth grade. The interfacial crystallization of this approach favored the selective ZIF-8 growing in the defects and pinholes, easily accessible and through which the species moved faster.

Moreover, an interesting control in the location of the ZIF-8 layer was achieved, in agreement with that obtained by Yao *et al*. in 2011 [67]. Regardless of the solvent in which it was dissolved (water or long-chain alcohol), ZIF-8 layer was always located on the surface in contact with the metal salt solution (in the same manner as shown in Figure 16.8). According to authors of this article, this evidence is related to the different species concentration (75 times higher for the organic ligand than that for the Zn salt, i.e., 1.37 vs 0.02 mol l^{-1}, respectively). This created a high gradient for the ligand and determined the diffusion rate of the species toward the interphase. Also in the cases where a unique solvent was used, either water or 1-octanol, MOF growth took place inside the pores of the bulk HF, but at a short distance (10 µm) from the Zn metal source location related to a rapid 2-methylimidazolate diffusion as expected. The miscibility of the metal

www.ebook3000.com

and ligand solution solvents therefore determines the interphase and the MOF layer location in this approach.

A later article from Nair's workgroup in 2016 [68] deeply described the mechanisms of the fluidic processing of these HF membranes. Changes observed in the continuity and density of the ZIF-8 layer in the bore side during the mixed static/continuous flow profile followed for the synthesis and their relation with the permeances and C_3H_6/C_3H_8 separation performance at each arrest point were shown. The continuous flow gave rise to a defective ZIF-8 layer, owing to the resistance created by an initial dense layer, which was then healed during the static flow regime. Moreover, the authors achieved an increase in the membrane throughput (selectivity was maintained) by thinning the ZIF-8 layer down to 5 μm using non-isothermal synthesis conditions and some modifications in the HF spinning procedure with respect to the IMMP original method. An initial heating at 40 °C provided an increase in the formation rate of the former ZIF-8 layer, leading to a thinner final MOF layer. With this work, the versatility of the IMMP method in the fabrication of MOF-supported HF membranes was demonstrated.

The importance of gas bypassing through the fiber ends (see Figure 16.8) was also studied by modeling the flow diffusion of the as-fabricated membrane test data [6]. This kind of modeling is a general routine in supported membranes. However, flow passing through the HF ends is an intrinsic inconvenience arising from the MOF layer positioned on the inner surface of the support. A polydimethylsiloxane (PDMS) sealing step is then integrated to the membrane fabrication process. This silicone sealing, penetrated in the fiber by capillarity, blocked the TORLON®-supported pores and thus suppressed the gas bypass. EDX analysis showed PDMS covering the whole cross-sectional surface and its presence up to 8 mm deep from the fiber ends.

Up to 60% of the C_3H_8 flow was then estimated to bypass the MOF membrane through the fiber ends in the as-synthesized membranes, which was almost completely blocked after the PDMS sealing. Consequently, the tests after the capping revealed a 10-fold decrease not only in C_3H_8 gas permeation but also in C_3H_6 and H_2 permeation, giving rise to important enhancements in both mixture separation factors, which were evaluated at four different temperatures. H_2/C_3H_8 separation showed an interesting activation with temperature change (around 250 at 35 °C to 370 at 120 °C), exhibiting a separation mechanism controlled by molecular sieving through the ZIF-8 micropores. Meanwhile, C_3H_6 permeation rate and C_3H_6/C_3H_8 separation factor (12 at 35 °C and 8 at 120 °C, respectively) diminished at high temperature because of a reduced adsorption on ZIF-8. It thereby suggests that these MOF HF membranes obtained by microfluidics only revealed their real potential application in gas separation once the gas bypassing was inhibited and the majority of the flow was forced to pass through the micropores of ZIF-8.

The durability and the stability of the membranes fabricated by IMMP were evaluated in a 35-day duration. Moreover, three HF supports were MOF-coated and tested simultaneously in the module showing similar gas separation performance than that obtained with a single membrane. Microfluidic-based IMMP is therefore established as an easily scalable method for supported MOF membrane fabrication with a simply threefold increase of the solution flow

injection. Microfluidics in HF membrane fabrication offers great potential in process scalability and inhibits some common handicaps when an adequate microflow regime is maintained, providing enough reagent replenishment inside the HF support. Hundreds of fibers and even entire HF modules could be simultaneously processed by simply multiplying the total flow appropriately, working in parallel.

The IMMP approach developed by Brown *et al*. [6] further involved an improvement in the eco-friendly fabrication of high-performance and tunable membranes by taking advantage of microfluidics. The fact is that the intensification of chemical processes has become a key topic for the scientific community: sustainable use of resources is mandatory for the chemical industry in the present and the near future [60, 61]. Hence, microfluidics is essential in the development of new green and sustainable methods in the fabrication of membranes.

As in the IMMP work, the positive implementation of microfluidics in the MOF-based membranes fabrication was also highlighted in the recent work of Cacho-Bailo *et al*. [5]. This approach, published just a few months after the article by Brown *et al*. [6], bases on the growth of supported MOF layers in the inner surface of polysulfone (PSf) HF supports by injecting the entire solution volume into the fiber bore lumen by microfluidics. Consequently, just the volume filling into the fiber lumen is required to synthesize the MOF membrane and therefore negligible amounts of reagents and solvents are used. This represents an increase of the usage efficiency of the resource and would save important costs in effluent disposal in the future industrial upscaling of the product. Moreover, PSf is a well-known polymer used to fabricate commercial liquid-phase and gas-phase membranes.

The requirements, normalized by square centimeter of membrane permeable area, for the fabrication of supported MOF membranes with the Cacho-Bailo *et al*. approach were calculated and compared with other techniques of great impact on the preparation of ZIF-8 membranes such as the IMMP method [6], its predecessor [62], and approaches using inorganic supports (pure hydrothermal and liquid-phase epitaxial (LPE) hydrothermal) [69, 70]. Significant savings in reactant and solvent utilization were achieved by this strategy of Cacho-Bailo *et al*., as shown in Figure 16.9, where all the solutions for MOF crystallization and washing are pumped inside the HF support, in comparison with the membranes that need to be submerged into at least one of the reactant solutions. Subsequently, solvent requirements for washing were also much reduced herein. Meanwhile, in the IMMP pure interfacial approach invented by Brown *et al*. (data are not shown in Figure 16.9), Zn metal consumption was greatly reduced because of the mixed continuous/static flow regime through the fiber bore ($0.18\,mmol\,cm^{-2}$). On the contrary, the consumptions of organic ligand and solvent were high because they filled the reaction vessel. Nevertheless, it must be taken into account that not only one single fiber but also a bunch of fibers can be sealed and MOF-coated at the same time using the same ligand solution with the IMMP strategy. In this situation, reagent depletion should be carefully considered. In summary, savings of 48–89%, 61–89%, and 45–78% could be achieved for metal, ligand, and solvent reagents, respectively, by the microfluidic approach when synthesizing ZIF-8 membranes (see Figure 16.9).

www.ebook3000.com

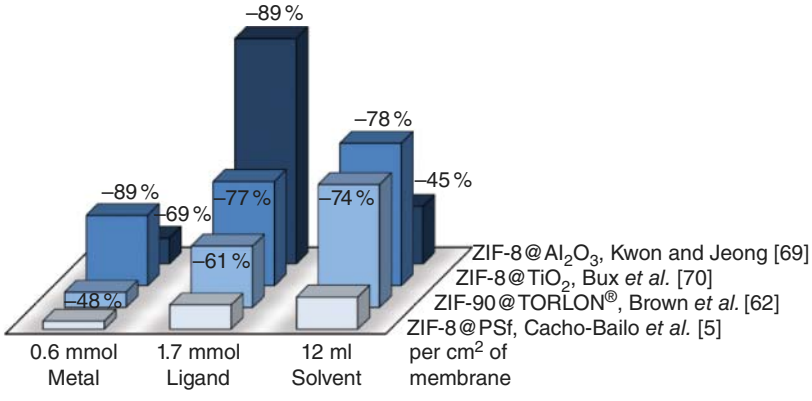


Figure 16.9 Reagent (metal and ligand sources) and solvent costs arising from the Cacho-Bailo *et al*. microfluidic approach for inner HF-supported MOF membrane fabrication [5], normalized per square centimeter of membrane permeable area. Earlier membrane fabrication strategies not based in microfluidics were used for comparison, that is, hydrothermally prepared ZIF-8 membranes supported on inorganic alumina [69] and titania [70] and seeded-assisted ZIF-90 membrane on polymeric TORLON® fibers [62], the corresponding saving being shown. Comparison with Brown *et al*. IMMP approach is described in the text [6].

The use of easily shaped polymeric HFs as membrane supports instead of the inorganic flat disks not only increases the efficiency in gas separation (in terms of surface to volume gas contact) but also facilitates the implementation of microfluidics for its fabrication and modification with MOFs in an eco-friendly way with a sustainable use of oil-based organic solvents. Synthesis procedures for two different ZIFs (ZIF-7 and ZIF-8, composed of zinc clusters and benzimidazolate and 2-methylimidazolate ligands, respectively) were adopted for their application in microfluidics. Both ZIF-7 and ZIF-8 crystallize in the **sod**-structure with 3.0 and 3.4 Å (Angstroms) limiting pore sizes, respectively. Their usefulness in gas separation as molecular sieves has been demonstrated previously in the hydrogen purification and natural gas separation [66, 71]. Hereby, thin continuous ZIF layers with thickness between 2 and 4 μm were crystallized on the inner wall surfaces of PSf HFs with 520/315 μm outer diameter (OD)/IDs.

ZIF synthesis procedures were properly modified to provide an adequate microfluidic flow regime inside the support of such diameters. Solution clearness must be kept along the fiber to prevent from clogging mainly due to the homogenous nucleation in the bulk liquid phase, thus enhancing the heterogeneous crystallization of the MOF on the polymeric inner surfaces. Micropumping is adjusted to a flow rate of 100 μl min^{-1} to ensure a strictly laminar flow regime without back-flush. It therefore gives rise to a regular MOF growth along the fiber. The membrane continuity and density of defects is strongly affected by the microflow regime in microfluidics, as shown above. Reynolds numbers lower than 15 were calculated by considering the flow rate of 100 μl min^{-1}, the HF support diameter, and the solvent viscosity used for the ZIF-7 and ZIF-8 membrane fabrication [1]. The flow velocity can be calculated as 2.14 cm s^{-1} along the fiber (linear velocity) [5].

In the case of ZIF-8, the solid precipitation in the synthesis solution mixture must occur at a time longer than the residence time of the fluid inside the fiber after the mixture, which takes place in a T-junction just at the beginning of the HF support, where both metal and ligand solutions converge. Thereby, the flow rate (100, 50 µl min^{-1} for metal solution and ligand solution, respectively) and the ligand to metal ratio (3 : 1) were adjusted to avoid the solid precipitation in the crystallization solution for a time longer than the residence time of the flow inside the fiber reactor. This residence time (τ) can be calculated as 9.35 s for a 20 cm long membrane and a 100 µl min^{-1} flow rate. Moreover, this ligand to metal ratio provided around 400 nm-sized ZIF-8 crystals, which were trapped or simply grew inside the support pores, thus creating a strongly packed MOF-supported interface and improving the layer adhesion, as shown in Figure 16.10. Sodium formate (NaCOOH) was used as deprotonator to enhance the crystal intergrowth and avoid pinholes [72].

Meanwhile ZIF-7 was grown using a LPE step synthesis. A clear EtOH solution with both reactants (metal and ligand) dissolved was pumped for the PSf fiber to be soaked with it, followed by the injection of a high-concentrated solution containing a strong deprotonator (NH_4OH) that made reactants convert into crystalline ZIF-7 [73, 74]. Pure EtOH was pumped between each step to wash the inner lumen and prevent clogging, thus enhancing the ZIF-7 deposition on the support surface. Nonattached ZIF-7 crystals were pumped outside. It is shown here how different synthesis procedures with multiple steps can be versatilely applied in a very simple way and sequenced with microfluidics, avoiding membrane handling and therefore induced damage.

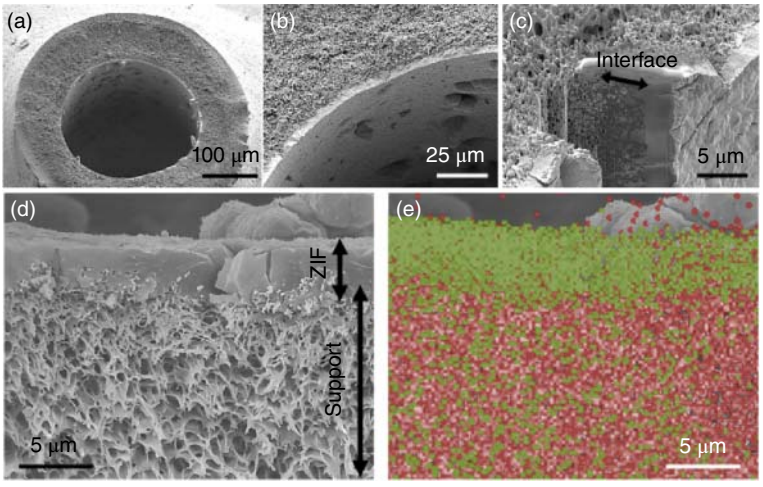


Figure 16.10 Microscopy characterization of the ZIF-8-supported membrane on the inner side of a PSf HF. Membranes were cooled with liquid N_2 and cut blade for the inner HF surface to be observed (a), where a continuous 3.6 µm-thick ZIF layer had been grown (b). Ga-FIB brought to light the MOF–polymer interface, some micrometers thick and related to the enhanced adhesion (c). EDX mapping analyses showed the Zn presence (green) on top of the PSf support (*S* colored in red, d and e). (Cacho-Bailo *et al*. 2015 [5]. Reproduced with permission of Elsevier.)

www.ebook3000.com

The fabricated membranes were characterized in-depth by SEM and EDX [5]. The HF membranes were cut at cryogenic 77 K temperature in order to obtain a clear cross-sectional morphology to be observed. Figure 16.10 shows a cross section of the ZIF-7 and ZIF-8 HF membranes. The 2.4 and 3.6 μm thick layers of ZIF-7 and ZIF-8, respectively, were observed. Both had high crystalline grades, giving rise to a highly continuous and dense MOF coating on the inner surface of the HF. There was a lack of cracks and defects in the observed areas. EDX mapping revealed a great presence of metal Zn from ZIF-8 (green) in the 3.6 μm thick MOF layer in contrast with sulfur (red, coming from PSf support). MOF-supported interface was then placed in the focus spot by the creation of a 150 nm thick lamella fabricated by the Ga-focused ion beam (FIB) technique. The MOF–polymer interface could then be clearly observed, showing a 2 μm thick interpenetration. This wide interface is a positive consequence of the microfluidic synthesis procedure and provides an enhanced ZIF-8 layer adhesion to the support. EDX showed absence of Zn and N at a depth of some micrometers in the pores of the polymeric HF. An interesting explanatory video of the lamella fabrication process is available online in the Elsevier website of *Journal of Membrane Science* [5]. XRD and FTIR patterns of the dissolved ZIF-8 and ZIF-7 HF membranes gave some evidence of the **sod**-structures from the ZIF materials in addition to the PSf spectra. Limited access to a clean view of the MOF layer on the inner surface of the micrometered HF made the characterization much difficult. Finally, MOF contents in the HF membranes were calculated to be around 20 wt% for both ZIF-7 and ZIF-8 by comparing the residues left by the membranes after oxidizing at 750 °C with those residues (considered to be ZnO) of the pure ZIF powders.

In this sense, this method also provides great advantages with respect to that based on a pure interfacial MOF synthesis method [6]. With a microfluidic MOF crystallization that is purely located only inside the HF lumen, the concentration of the species (metal and ligand ratio also) is maintained along all the fiber support during the entire synthesis procedure, preventing reactants from depletion. This results in a continuous MOF layer with good adhesion, constant thickness, and homogeneous properties along the membrane length. MOF layer location is set to be on the inner surface, as long as the static pressure inside the fiber remains at low levels.

Permeation tests carried out with the ZIF membranes fabricated revealed high-performance and very promising separation results. In contrast with the IMMP approach, gas bypassing through the fiber ends of the as-synthesized membranes is supposed to be negligible: Figure 16.11 shows gas permeation (i.e., CO_2 and CH_4) independence with pressure, related with an absence of viscous flow through the highly porous fiber ends. It can be hypothesized that the cross sections of the fiber ends were in contact with the crystallization solution (containing all the reactants) and were also coated with MOF, preventing from nonselective gas bypassing.

Gas permeance:

$$P_i = \frac{\dot{n}_{i,\text{perm}}}{S \cdot \Delta P_{i,\text{MLOG}}} \ (\text{mol s}^{-1}\,\text{m}^{-2}\,\text{Pa}^{-1}) \tag{16.1}$$

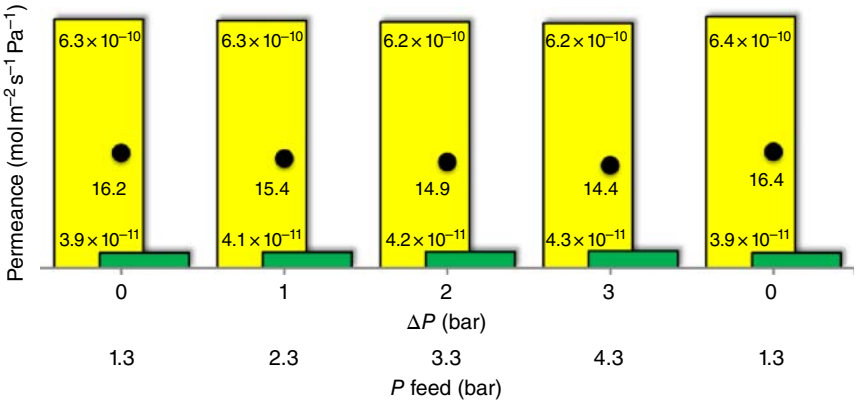


Figure 16.11 CO_2 (yellow) and CH_4 (green) permeance rates of a ZIF-7@PSf HF membrane and the corresponding calculated CO_2/CH_4 selectivities as a function of the total feed pressure. No gas permeance dependence with pressure means the absence of viscous flow through macrodefects, uncovered zones, or bypassing at the fiber ends. (Cacho-Bailo *et al*. 2015 [5]. Reproduced with permission of Elsevier.)

Log-mean partial pressure difference, given the gas depletion in the feed mixture along the HF membrane length during mixture separation:

$$\Delta p_{i,\mathrm{MLOG}} = \frac{(p_{\mathrm{feed}} \cdot x_{i,\mathrm{feed}} - p_{\mathrm{perm}} \cdot x_{i,\mathrm{perm}}) - (p_{\mathrm{ret}} \cdot x_{i,\mathrm{ret}} - p_{\mathrm{sweep}} \cdot x_{i,\mathrm{sweep}})}{\ln \dfrac{p_{\mathrm{feed}} \cdot x_{i,\mathrm{feed}} - p_{\mathrm{perm}} \cdot x_{i,\mathrm{perm}}}{p_{\mathrm{ret}} \cdot x_{i,\mathrm{ret}} - p_{\mathrm{sweep}} \cdot x_{i,\mathrm{sweep}}}} \tag{16.2}$$

Equations (16.1) and (16.2) were used to calculate gas permeances (p_i) of the fabricated membranes. As in any tubular membrane, gas depletion in the feed mixture along with the membrane length must be taken into account, so that the log-mean partial pressure difference is used ($\Delta p_{i,\mathrm{MLOG}}$, Eq. (16.2)) to accurately calculate the permeation driving force of each gas. Permeable areas (S) are calculated from the ID of the corresponding HF support and the membrane length. Figure 16.12 shows the experimental setup for the gas separation testing of the fabricated membranes by the Cacho-Bailo *et al*. approach. The 13 cm long HF membranes were sealed in that module, although longer supports were used during the syntheses (typically 20 cm). Selectivities (or mixture separation factors) are defined just as the ratio of gas permeances. As proven in the IMMP work [6], multiple fiber bunches could be sealed and measured together, a step toward the upscaling gas separation operation with a module containing thousands of these MOF-supported HFs.

As shown in Figure 16.13, promising results in the separation of H_2 and CO_2-containing mixtures were obtained using ZIF-7 and ZIF-8 HF membranes. Separation factors of 35 (H_2/N_2 and H_2/CH_4) and 14 (CO_2/N_2) at 35 °C were calculated by using ZIF-7@PSf membranes, together with a 14 GPU (1 GPU = 3.35×10^{-10} mol m^{-2} s^{-1} Pa^{-1}) H_2 permeation rate. ZIF-8@PSf membranes had worse separation efficiencies because of their wider effective pore

www.ebook3000.com

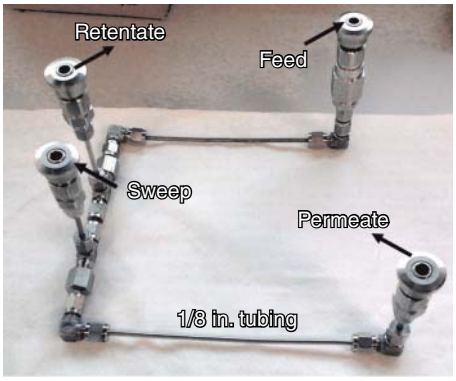


Figure 16.12 Experimental setup for the testing of the MOF inner-supported hollow fiber membranes in mixture gas separation fabricated with the microfluidic Cacho-Bailo *et al*. approach. (Cacho-Bailo *et al*. 2015 [5]. Reproduced with permission of Elsevier.)

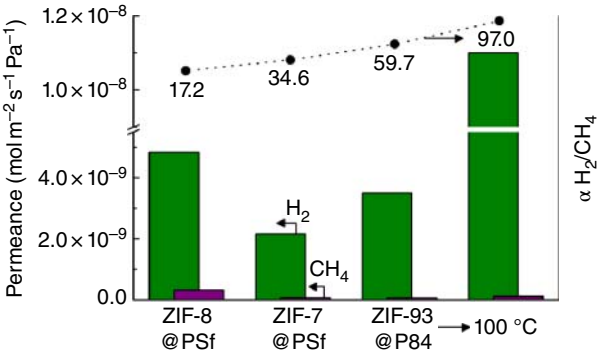


Figure 16.13 Performances of the MOF-supported HF membranes fabricated with the Cacho-Bailo *et al*. approach in the H_2/CH_4 mixture separation. The graph shows gas permeances and selectivities obtained with the ZIF-8, ZIF-7, and ZIF-93 membranes at 35 °C and also those at 100 °C with ZIF-93. (Adapted from Cacho-Bailo *et al*. 2015 [5, 75].)

size (3.4 Å in contrast with 3.0 Å for ZIF-7). Further permeation testing, including other gas mixtures and temperatures, can be examined in the article by Cacho-Bailo *et al*. [5]. Measurements at elevated temperatures showed an activation of the gas permeation and the molecular sieving effect through the MOF layers. However, the total permeances (gas flow rate per square meter, too low even in the bare PSf HF) are low and should be enhanced to achieve attractive membrane performances.

The Cacho-Bailo *et al*. [5] approach gave rise to other remarkable works based on co-polyimide P84® (BTDA–80%TDI/20%MDI) in 2015 [75]. P84® HF supports were intentionally fabricated by Tecnalia© to be defective, highly porous, and permeable. MOF ZIF-93 (zinc-4,5-methylimidazolcarboxaldehyde) layers were synthesized inside those. Its aldehyde-functionalized imidazolate ligand makes ZIF-93 attractive for post-functionalization strategies, that is, a reduction with $NaBH_4$ or an imine condensation with an aliphatic chain [76–78]. As in the case of ZIF-7 and ZIF-8 [5], ZIF-93 synthesis procedure was modified to make it suitable with microfluidic processes. Metal and ligand were dissolved in miscible water and methanol, respectively, in a 1 : 2 ratio, and

injected together just after mixing them at room temperature. Fifty microliter per minute (25 µl min^{-1} for metal solution and ligand solution, respectively) provided a laminar regime flow inside the HF, regarding the P84® HF support dimensions. The residence time (7.7 s) was intentionally shorter than the first crystallization of solids within the liquid fluid. The ZIF-93 membranes, once washed and dried, gave rise to an interesting gas separation performance, as shown in Figure 16.13, with a 97 separation factor for the H_2/CH_4 mixture and a H_2 permeance of 33 GPU at 100 °C.

ZIF-93@P84® membranes, this MOF crystallizing in a **rho**-structure [79], are another example of how microfluidics can be versatilely modified to the MOF synthesis procedures for the fabrication of high-performance continuous crystalline layers inside HFs. This approach also produced important savings in reagent and solvent since all the solutions were injected inside the fiber lumen, following the trend of the previous microfluidic approaches for membrane fabrication.

Using the same co-polyimide P84® supports, Cacho-Bailo *et al*. designed an innovative sequential microfluidic procedure to fabricate ZIF-8/ZIF-9 and ZIF-67/ZIF-9 two-layered membranes [80]. Versatility in the microfluidic step synthesis led to the growth of methylimidazolate and benzimidazolate MOFs in different confined layers in a desired order within the same membrane. Molecular simulation in combination with experimental permeation tests revealed an enhancement in the precombustion gas separation derived from a reduced CO_2 adsorption on the membrane surface.

Likewise there is an additional interesting example of supported MOF membranes applied on the separation in the liquid phase. In 2015, Maya *et al*. published their work on automated growth of MOF coatings on flow through functional supports [81], based on the construction of ZIF-8 coatings on a planar polymeric support with an automated microfluidic setup. As shown in Figure 16.14, metal and ligand precursors were stepwise pumped from their corresponding syringes with the help of a multiposition valve, with a controlled microflow of 500 µl min^{-1} (so that the authors sorted their approach in the mesofluidics). The ZIF-8 coating is based in a LPE crystallization method where pure solvent volumes were pumped between each injection in order to maximize the MOF growth inside the soaked support pores, as in the case of ZIF-7 growth [5]. In this case, in contrast with the latest examples described above, a flat polymeric support was used, sealed in a filter holder for membrane disks, through which the precursor solutions flow. After a determined number of cycles (190), a continuous ZIF-8 coating was achieved. The ZIF-8 coated membrane was then used *in situ* for the sorption and extraction of traces of a mixture of environmentally organic pollutants.

An additional step in HF membrane upscaling was accomplished by Biswal *et al*. [7]. They reported the entire fabrication of a membrane module containing a bunch of 10 MOF-supported HFs. ZIF-8 and Cu-BTC layers were synthesized on both the inner and the outer support surfaces using an interfacial growth procedure at room temperature. A peristaltic pump continuously injected the solution containing one of the reagents through the lumen of the fibers (780 µm OD), being recirculated during the entire synthesis. The fabricated membrane module

www.ebook3000.com

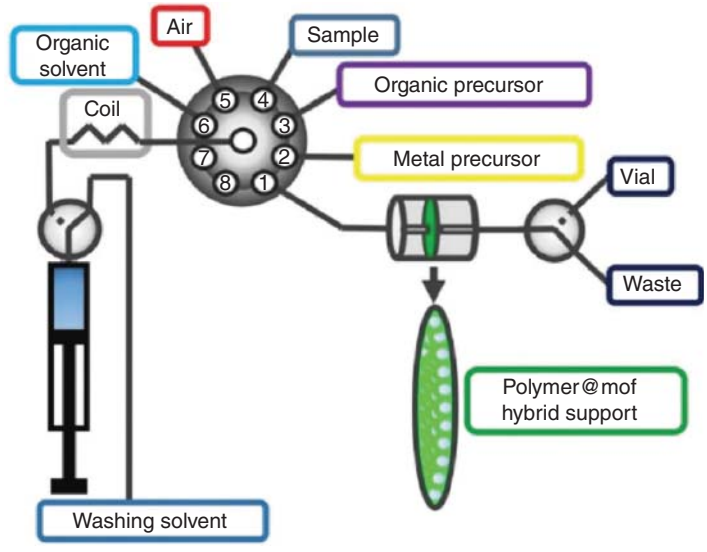


Figure 16.14 Automation of flow sequential for the creation of a ZIF-8 coating on a polymeric substrate by LBL and demonstrates how versatile microfluidics can be in membrane fabrication. This scheme shows the experimental setup developed by Maya *et al*. based on a multiposition valve that sequences the different fluids (i.e., metal and ligand solutions and pure solvent) injection. (Maya *et al*. 2015 [81]. Reproduced with permission of Royal Society of Chemistry.)

exhibited helium sieving separation performance with selectivities of 12 (He/N_2) and 17 (He/C_3H_8) together with a He permeance value of 1.3 GPU. About 64 cm^2 of permeable membrane area were available from the 26 cm long 10-fiber bunch, sealed in a ½-in. diameter module.

16.2.3 Inorganic versus Polymeric Supports: Intensification of Processes

Apart from the eco-friendly reagent saving described above, the use of cheap, easily tailored, and shaped HFs implies other important advantages in terms of intensification of processes, improvement of the efficiency, and feasibility of upscaling implementation. In fact, polymeric membranes shaped as HFs have also been successfully commercialized for separations at the large scale.

Layered ZIF (and generally MOF)-supported polymeric HF membranes display a positive equilibrium between scalability and performance, as claimed by Zhang and Koros [59]. In their opinion, the highest degree of scalability would be achieved with the mixed-matrix MOF HFs. This kind of membranes are formed by a thin mixed-matrix membrane (MMM), where the ZIF or MOF is dispersed, coating the HF support surface. Accordingly, Zhang *et al*. fabricated dual-layer ZIF-8/6FDA-DAM HF MMMs with different ZIF-8 loadings, that is, 17 and 30 wt% [82]. Combining MOFs and HF supports with the microfluidic setups described above, the promising molecular sieving separation effects and an excellent scalability give rise to membranes with expectable outstanding performances. Moreover, MOF and polymeric materials had demonstrated an excellent compatibility [83–85]. Table 16.3 summarizes some of the examples of combinations of ZIF materials and HF-shaped polymers in membranes fabricated by microfluidics, described in Section 16.2.2.

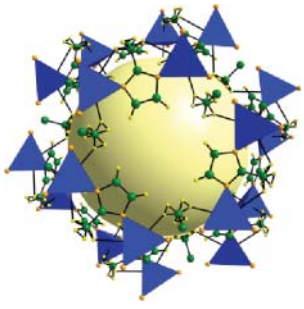
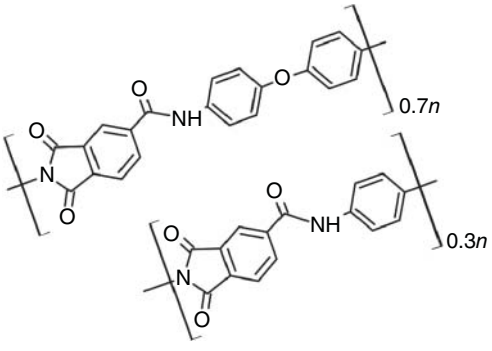
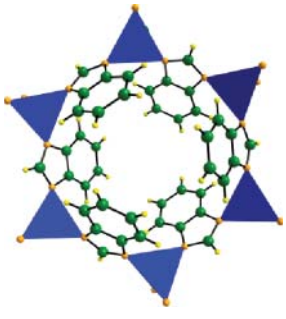
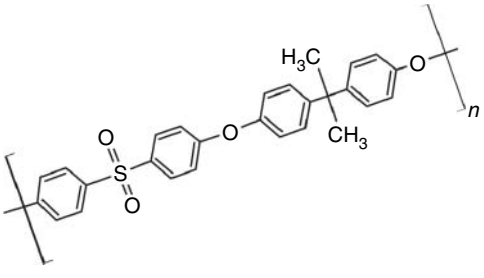
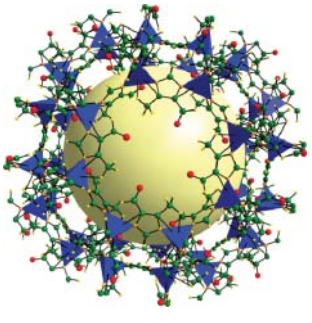
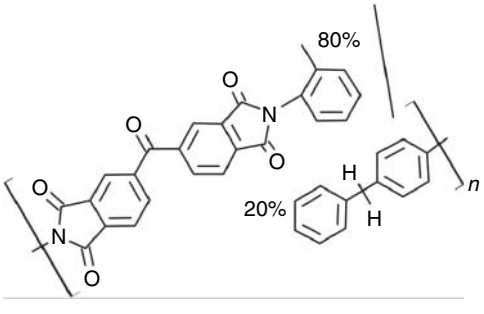
The described examples had demonstrated that how microfluidics can be adapted depends on the dimensions of the HF used as membrane support. Thereby, the overall size of the HF is intimately related with the efficiency, compactness, and how much improvement in the intensification of the separation processes that they can achieve in comparison with the traditional inorganic supports.

In general, the inorganic alumina or silica tubular supports were fabricated with at least 1 cm in diameter. Research in membrane technology is focused using them as supports for zeolites and early MOF membranes [87, 88]. In 2001, the first industrial pervaporation plant exploiting 4A membranes on 12 mm tubular supports was put in operation for dehydration of alcohols [89]. However, the industrial implementation of inorganic-supported membranes still remains nowadays as a challenge because of their brittleness and low efficiency [57, 59]. Otherwise, the benefits of microfluidics are not profitable on supports of such dimensions; the Reynolds number increases directly with the diameter, giving rise to non-applicable flow regimes for MOF crystallization by microfluidics inside them [1].

Polymeric HFs, which are usually extruded in diameters from 50 to 500 μm, take a step in efficiency and intensification of the separation processes with membranes. The smaller the diameter of the HF, the greater the available surface for gas permeation per unit volume. Also the greater savings will be obtained during the microfluidic MOF coating (reagents and solvents and effluent disposal costs, as seen above) and the lower the Reynolds number inside, giving rise to more homogeneous growth of the MOF layer. In addition, narrow HF diameters give rise to high overall efficiencies and compactness of the HF membrane modules.

www.ebook3000.com

Table 16.3 ZIF and polymeric HF combinations used in the fabrication of membranes by microfluidics, that is, ZIF-8@TORLON® [6], ZIF-7@PSf [5], and ZIF-93@P84® [75].

 ZIF-8, sod $Zn(2\text{-mim})_2$ CSD refcodeVELVOY [26]	 TORLON® Polyamide-imide
 ZIF-7, sod $Zn(bim)_2$ CSD refcode VELVIS [26]	 Polysulfone Udel® P-3500 Polysulfone
 ZIF-93, rho $Zn(4\text{-mim-5-CA})_2$ Reference [86]	 P84® Co-polyimide

Further details on the gas separation performance achieved with the resulting membranes are described elsewhere [83]. Imidazolate-based ZIF structure projections (rendered using Diamond Crystal Impact software) are shown together with the chemical formulas of the polymers forming the hollow fiber supports. Color caption: Zn metal polyhedra, blue; O, red; C, green; N, orange.

Thousands of HFs may fit in every membrane module, and each of them provides several square meters available for gas to permeate. Therefore, applying microfluidics during the MOF growth inside small HF supports makes the whole gas or liquid separation process intensified in comparison with the traditional technologies based on a heat-driven phase change.

Figure 16.15 shows the area-to-volume ratio that provides an HF membrane as a function of its OD. Area-to-volume ratios higher than 1000 $m^2\ m^{-3}$ could be considered attractive and profitable to be upscaled [60, 90]. The MOF membranes fabricated with the microfluidic approaches mentioned in this chapter are typical examples for a high intensification/space efficiency. PSf and P84® HF membranes (with diameters of 520 and 356 µm, respectively) used to support ZIF-7, ZIF-8, and ZIF-93 with the Cacho-Bailo *et al.* setup [5, 75], as well as the TORLON® HF supports used by Brown *et al.* (around 250 µm in diameter) [6], can provide an area-to-volume ratio up to 16 000 $m^2\ m^{-3}$ (see Figure 16.15).

Independently from its dimensions, the porosity and therefore the permeance of the polymeric HF are inherent from its fabrication method (i.e., set of experimental parameters of the phase-inversion fabrication procedure) [91, 92]. The fabrication of polymeric HF to be used as MOF membrane supports must lead to high permeable supports of small diameters, in order to provide elevated gas flows in a very compact way.

Some of the examples described in this section would fall partially outside the strictly microfluidic regime regarding the characteristic dimensions (OD) of the HFs, herein used as reactors and supports for MOF growth. For instance, PSf HF supports used for ZIF-8 and ZIF-7 by Cacho-Bailo *et al.* [5] were 520 µm wide. However, according to Elvira *et al.* [1], reactors with a characteristic dimension between 500 and 1000 µm may be also considered in the microfluidic regime,

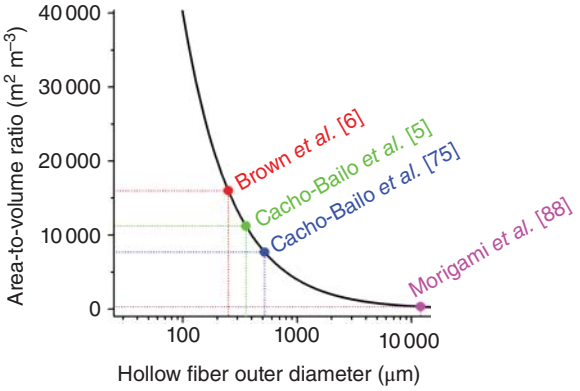


Figure 16.15 Area-to-volume ratio provided by a hollow fiber as a function of its outer diameter (OD), related with its efficiency in the separation processes. Those corresponding to some inner-supported MOF polymeric HF membranes fabricated with microfluidics are shown, being in the high-efficiency 7500–16 000 $m^2\ m^{-3}$ range [5, 6, 75]. In contrast, less than 400 $m^2\ m^{-3}$ are usually provided with inorganic tubular supports. In the Morigami *et al.* work, 4A zeolite layers were supported on inorganic supports with a diameter of 12 mm [89]. It must be taken into account that only area-to-volume ratios greater than 1000 $m^2\ m^{-3}$ would be considered attractive for industrialization.

www.ebook3000.com

depending on the flow characteristics. Generally, reactors with characteristic dimensions between 500 and a few millimeters were considered to be in the "mesofluidics" regime [1]. Thus, Reynolds number and therefore the flow regime were maintained strictly laminar in the case of PSf HF supports. A Reynolds number of 9.0 was actually calculated for the ZIF-8 synthesis [5], operations with Reynolds numbers below 250 considered to be in microfluidics.

16.2.4 Support Influence on MOF Synthesis Method

Figure 16.16 shows the most important synthesis methods for MOF-based membranes, as summarized by Li *et al*. [93]. Linked with how the different reactants are supplied to the substrate, solvothermal (both metal and ligand source dissolved in the same solution and supplied at the same time), LPE (where the reactants are supplied in different steps, with appropriate soaking and rinsing between them), and interfacial syntheses (reactants supplied from separated solutions that encounters within the substrate) are defined. As shown above, these techniques can be applied to microfluidics for the MOF growth, the polymeric HF acting as substrate. They can also provide a control on the MOF layer position in the membrane.

The choice of the synthesis method is related to the support void fraction/porosity and the MOF that is desired to be grown. Solvothermal syntheses are restricted to MOFs starting from clear solutions (both ligand and metal sources must be soluble in the reaction media) with a delayed precipitation, using low-rate deprotonators (sodium formate or acetate, e.g., ZIF-8 on PSf or ZIF-93 on P84® HF) [5, 75]. Otherwise, clogging phenomena could occur, thus invalidating the microfluidic approach. High-speed crystallization of MOFs,

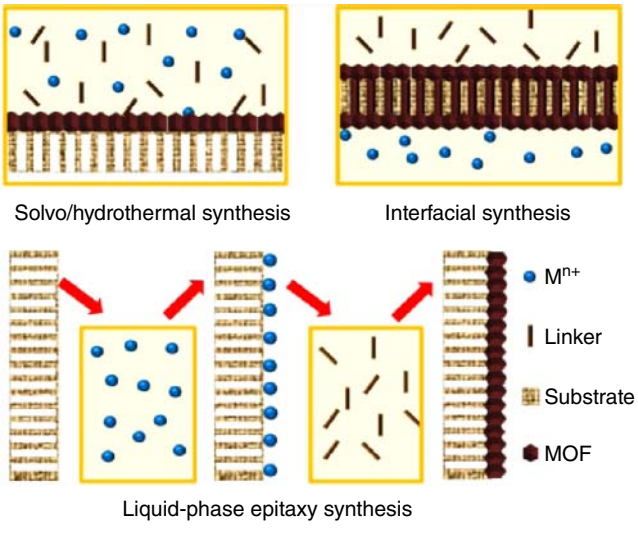


Figure 16.16 Schemes of the synthesis methods for MOF-based continuous membranes, all of them fully transposable to microfluidic preparation of MOF-supported HF membranes, that is, solvothermal (seeded or *in situ* growth), interfacial, and liquid-phase epitaxy (LPE). (Li *et al*. 2015 [93]. Reproduced with permission of Elsevier.)

whose solutions become turbid just after the mixing or making use of strong deprotonators such as ammonium hydroxide, should be formed using LPE and interfacial syntheses. Thereby, considering an appropriate rinsing step in the LPE case, crystallization in the bulk solution is inhibited hence preventing from clogging. ZIF-7@PSf HF membranes represent a clear example on the application of these concepts about the fabrication method [5].

HF support intrinsic porosity is also decisive in the process for the MOF growth. Highly porous HF supports are preferred in membrane technology to decrease the mass transfer resistance to gas or liquid pass-through/throughput [59, 94]. However, the use of solvothermal MOF crystallization methods by microfluidics are restricted to relatively low permeable HF supports, preventing radial flow from leaking outside the fiber. On the contrary, highly porous HF supports are suggested for interfacial synthesis methods, thus favoring to the reactant diffusion toward the interphase.

Moreover, a recent study on the performance of MOF-supported polymeric HF membranes when submitted to an annealing procedure below the glass transition temperature of the polymer revealed that the initial roughness of the surface had a great influence on the MOF adhesion [83]. The annealing of pure P84® HF supports (175 °C for 24 h) led to a polymer chain rearrangement and a surface smoothing, as proven by different techniques such as SEM, atomic force microscopy (AFM), and X-ray photoelectron spectroscopy (XPS), which later produced a worsened ZIF-8 and ZIF-93 bonding during the microfluidic synthesis. Only the use of as-synthesized HF supports with a rougher surface could produce high-quality membranes with a dense MOF–polymer interface that enhanced their performance after the annealing process.

Moreover, each one of the here-described microfluidic methods has advantages when applied for the fabrication of MOF-supported membranes. Solvothermal methods keep a constant reactant concentration along all the fiber (reactor/membrane) during the whole synthesis procedure, giving rise to a more homogenous growth of MOF layers, as in ZIF-8@PSf HF membranes [5]. Besides, solvothermal syntheses, together with the LPE, offer the highest eco-friendly reagent and solvent savings, as shown in Figure 16.9. On the other hand, interfacial synthesis (as ZIF-8@TORLON® membranes) [6], although gives rise to low savings since the HF support must be submerged into either the metal solution or the ligand solution, minimizes defects and uncovered zones on the substrate surface. High reactant diffusion through the cracks causes an auto-healing effect of the MOF layer on the interphase. Absence of precipitation in the bulk liquid phase allows the reactant solution recirculation. However, species depletion must be always taken into account in the interfacial syntheses. LPE synthesis (e.g., ZIF-7@PSf membranes) [5] offers an interesting balance/edge/optimization between efficiency in reactant utilization and MOF membrane final performance (homogeneity, absence of defects, etc.) among all the possibilities arising from the microfluidic application on MOF-based membranes. Above all, always low Reynolds numbers (depending from the HF size) must be kept extremely low for a pure laminar flow regime during the MOF growth.

The previously described examples are a typical evidence of how traditional developed MOF-supported membrane fabrication methods can be extended to

www.ebook3000.com

a microfluidic approach, giving rise to more homogeneous MOF layers, owing to the controlled laminar regime present in the confined bore volume inside the HFs.

16.2.5 Advantages of Inner MOF Growth

First IMMP and then the work from the University of Zaragoza (through the works done by Cacho-Bailo *et al*. [5, 75, 80, 83]) highlighted the advantages of coating the inner surface of the HF support with continuous polycrystalline layers of MOFs, a task where microfluidics play an important role. In comparison with the growth on the outer HF surfaces, the advantages can be condensed in the following:

- The MOF layer is shielded by the polymeric HF surrounding, preventing from mechanical and physical damage, and also from adsorption phenomena from the atmosphere (moisture). It must be noticed that some MOFs reveal instability when subjected under steam conditions and/or high temperatures. Interesting studies were carried out in this aspect [26, 95].
- The inner growing avoids contact points between membranes during synthesis that would lead to defects or uncovered zones, resulting in a worse overall performance of membranes [6].
- The bore fiber volume, which must be filled with the crystallization solutions (by microfluidics), decreases to microscopic dimensions. This reduction leads to an important saving in solvents and reagents, as well as saving in cleaning and disposal requirements [5]. A comparison between different methods and normalized cuttings achieved are shown in Figure 16.9.
- The MOF layer on the inner HF surface provides an intimate contact with the mixture to be separated. This would maximize the selective separation carried out by the crystalline porous MOF structure and the surface adsorption mechanisms on the MOF crystals. However, Mao *et al*. obtained the similar gas permeance values with their HKUST-1 outer-supported HF membrane when feeding the gas mixture from both the lumen and the shell side of the membrane [96]. As a rule of thumb, gas mixtures are fed inside the HF lumen when its diameter is higher than 200 μm.

Moreover, as described above, an easy scalability is expected from this membrane configuration and its microfluidic fabrication procedure. Nevertheless, as pointed out by Zhang and Koros [59], stability of MOF-supported membranes must be verified under realistic feed pressure conditions that are related to the mixtures to be separated, for example, pre- and post-combustion streams. MOF layers previously led to a bad adhesion on flat flexible supports when submitted to pressure or elongation stress. Some attempts have been developed to overcome, or at least partially overcome, this issue when using HF supports [97–101]. They consist of the functionalization of the polyvinylidene fluoride (PVDF) HF surfaces with (3-aminopropyl)triethoxysilane (APTES) and TiO_2 before the MOF growth [85], among others. In that sense, inner surface MOF-supported HF membranes were tested at pressures up to 4.3 bar (see Figure 16.11) [5], showing an enhanced resistance with respect to that expected with outer-supported MOF layers.

16.3 Conclusions and Outlook

All the unprecedented approaches presented herein have set the stage for the development of technology for MOF material fabrication and MOF-based membranes by microfluidics. This flourishing field takes advantage of a high degree of control on the synthetic parameters at the low scale but at the same time is suitable for upscaling through parallelization.

MOFs are promising materials used in a wide variety of areas (i.e., encapsulation, drug delivery, sensing, coating, gas storage, etc.), also including their application as add-ons in membranes for a gas separation performance enhancement. As detailed along this chapter, microfluidics has emerged as a very favorable technique for the fabrication of MOF materials in any forms: powdered, taking part of complex structures, or forming continuous layers in membranes.

First, microfluidics offers a high grade of control when applied to the synthesis of MOF powders. The confinement of the crystallization of precursor solutions in nanoliter-sized droplet reactors flowing through with a laminar flow regime gives rise to extremely narrow PSDs and a control of the final crystal shape together with high reaction rates. This chapter highlights the microfluidic fabrication of MOFs with high crystalline grade in shorter reaction times in comparison with predecessor techniques. Moreover, some other examples described herein took a step into the synthesis of complex heterostructures involving MOFs. The resulting core–shell crystals, *in situ* encapsulation of magnetic or catalyst particles (to be potentially used as nano-membrane reactors), or the stepwise surface functionalization, difficult to be accomplished by other previous techniques, were obtained with the versatile microfluidic-based setups. It has also demonstrated the suitability of the microfluidic preparation of MOF powders for upscaling. In this sense, different MOFs were rapidly crystallized in the form of hollow spheres or powders using a spray-drier.

Furthermore, the use of microfluidics in the crystallization of MOF powders implies a significant cutting of costs in terms of reagents and solvents. The chemical industry focuses on the intensification of any of its basic operations (i.e., crystallization, separation, washing, etc.). Microfluidic MOF preparation has been not only demonstrated to be highly efficient in these terms but also much more emphasized in the preparation of MOF membranes.

MOF-based membranes using polymeric HFs as supports take advantage of the most efficient polymeric membrane shaping, as well as cheap, easy to conform, and already commercially deployed forming modules containing thousands of these HFs. The creation of a continuous MOF layer by microfluidics in a very sustainable way would improve the membrane performance in gas or liquid mixture separation and put it in an attractive situation. Membrane technologies are nowadays the eco-friendly and efficient alternatives to the traditional separation processes that imply a phase change and play a very important role in strategic tasks in the energy field such as the H_2 and natural gas purification and the CO_2 capture.

However, the use of MOF-based HF-supported membranes must not imply a drastic increment of costs; otherwise they would not be suitable for upscaling. The use of microfluidics, as described in this chapter, involves a high eco-friendly

www.ebook3000.com

reagent and solvent savings, especially those supported in the inner surface. Some ZIFs, a subclass of MOF with restrictive small pore sizes, can grow inside TORLON®, PSf, and P84® HFs in the form of continuous layers.

The MOF inner-supported HF membranes are very promising in scalability and performance, in comparison with MMMs or flat-supported membranes. The use of HF-shaped polymers drastically increases the efficiency in terms of MOF synthesis (allows the use of microfluidics) and gas separation (reduces costs of pressurization owing to their high surface to volume ratios) in comparison with the traditional inorganic flat disks or tubular supports.

Microfluidics in the preparation of MOF-supported membranes also provides a great degree of control on the MOF layer positioning (either inner or outer sited), intergrowth, and thickness. The approaches described in this chapter provide interesting examples of the responsible use of oil-based organic solvents and precursors in the preparation of MOF membranes. Moreover, they implicitly involve other advantages: post-functionalization or surface reaction in the *as-synthesized* membrane can be stepwise implemented, avoiding the handling damage. Some examples have been reported on the partial upscaling of the MOF-based HF membrane fabrication, taking advantage of the already deployed technology for HF module manufacturing.

Taking advantage of the high degree of scalability and versatility of the synthesis of MOF materials and MOF-based HF membranes by means of microfluidics, new developments in polymer technology and further screening in possible candidate MOF materials for strategic separations anticipate a promising future in their application at large scale, without excluding other PCPs such as COFs. From now on, efforts may focus in the combination of microfluidics with other techniques of located action such as microwaving for the creation of high-performance fuel cells, controlled-delivery systems, biological sensors, and so on.

Acknowledgments

Financial support (MAT2013-40556-R, MAT2016-77290-R) from the Spanish MINECO, the Aragón Government (DGA, T05), the European Social Fund, and FEDER is gratefully acknowledged. F.C.-B. acknowledges his DGA predoctoral fellowship.

References

1 Elvira, K.S., Casadevall i Solvas, X., Wootton, R.C.R., and deMello, A.J. (2013) The past, present and potential for microfluidic reactor technology in chemical synthesis. *Nat. Chem.*, **5** (11), 905–915.

2 Gordon, J., Kazemian, H., and Rohani, S. (2012) Rapid and efficient crystallization of MIL-53(Fe) by ultrasound and microwave irradiation. *Microporous Mesoporous Mater.*, **162**, 36–43.

3 Paseta, L., Potier, G., Sorribas, S., and Coronas, J. (2016) Solventless synthesis of MOFs at high pressure. *ACS Sustainable Chem. Eng.*, **4** (7), 3780–3785.
4 Klimakow, M., Klobes, P., Thünemann, A.F., Rademann, K., and Emmerling, F. (2010) Mechanochemical synthesis of metal – organic frameworks: a fast and facile approach toward quantitative yields and high specific surface areas. *Chem. Mater.*, **22** (18), 5216–5221.
5 Cacho-Bailo, F., Catalán-Aguirre, S., Etxeberría-Benavides, M., Karvan, O., Sebastian, V., Téllez, C., and Coronas, J. (2015) Metal-organic framework membranes on the inner-side of a polymeric hollow fiber by microfluidic synthesis. *J. Membr. Sci.*, **476**, 277–285.
6 Brown, A.J., Brunelli, N.A., Eum, K., Rashidi, F., Johnson, J.R., Koros, W.J., Jones, C.W., and Nair, S. (2014) Interfacial microfluidic processing of metal-organic framework hollow fiber membranes. *Science*, **345** (6192), 72–75.
7 Biswal, B.P., Bhaskar, A., Banerjee, R., and Kharul, U.K. (2015) Selective interfacial synthesis of metal-organic frameworks on a polybenzimidazole hollow fiber membrane for gas separation. *Nanoscale*, **7** (16), 7291–7298.
8 Carné-Sánchez, A., Imaz, I., Cano-Sarabia, M., and Maspoch, D. (2013) A spray-drying strategy for synthesis of nanoscale metal-organic frameworks and their assembly into hollow superstructures. *Nat. Chem.*, **5** (3), 203–211.
9 Maspoch Comamala, D., Imaz, I., Carné-Sánchez, A., and Cano-Sarabia, A.M. (2013) Method for the preparation of metal organic frameworks. Patent WO2013050402, Abr. 11, 2013.
10 Nair, S., Brown, A.J., Brunelli, N.A., and Jones, C.W. (2014) Flow processing and characterization of metal-organic framework (MOF) membranes in hollow fiber and tubular modules. Patent WO2014200613, Dec. 18, 2014.
11 Ju, J., Zeng, C., Zhang, L., and Xu, N. (2006) Continuous synthesis of zeolite NaA in a microchannel reactor. *Chem. Eng. J.*, **116** (2), 115–121.
12 Pan, Y., Yao, J., Zhang, L., and Xu, N. (2009) Preparation of ultrafine zeolite a crystals with narrow particle size distribution using a two-phase liquid segmented microfluidic reactor. *Ind. Eng. Chem. Res.*, **48** (18), 8471–8477.
13 Hoang, P.H., Park, H., and Kim, D.P. (2011) Ultrafast and continuous synthesis of unaccommodating inorganic nanomaterials in droplet- and ionic liquid-assisted microfluidic system. *J. Am. Chem. Soc.*, **133** (37), 14765–14770.
14 Hoang, P.H., Yoon, K.B., and Kim, D.-P. (2012) Synthesis of hierarchically porous zeolite a crystals with uniform particle size in a droplet microreactor. *RSC Adv.*, **2** (12), 5323–5328.
15 Yu, L., Pan, Y., Wang, C., and Zhang, L. (2013) A two-phase segmented microfluidic technique for one-step continuous versatile preparation of zeolites. *Chem. Eng. J.*, **219**, 78–85.
16 Liu, Z., Wakihara, T., Nishioka, D., Oshima, K., Takewaki, T., and Okubo, T. (2014) Ultrafast continuous-flow synthesis of crystalline microporous aluminophosphate $AlPO_4$-5. *Chem. Mater.*, **26** (7), 2327–2331.
17 Farrusseng, D., Aguado, S., and Pinel, C. (2009) Metal-organic frameworks: opportunities for catalysis. *Angew. Chem. Int. Ed.*, **48** (41), 7502–7513.

www.ebook3000.com

18 Corma, A., Garcia, H., and Llabrés i Xamena, F.X. (2010) Engineering metal organic frameworks for heterogeneous catalysis. *Chem. Rev.*, **110** (8), 4606–4655.

19 Horcajada, P., Chalati, T., Serre, C., Gillet, B., Sebrie, C., Baati, T., Eubank, J.F., Heurtaux, D., Clayette, P., Kreuz, C., Chang, J.S., Hwang, Y.K., Marsaud, V., Bories, P.N., Cynober, L., Gil, S., Ferey, G., Couvreur, P., and Gref, R. (2010) Porous metal-organic-framework nanoscale carriers as a potential platform for drug delivery and imaging. *Nat. Mater.*, **9** (2), 172–178.

20 Sumida, K., Rogow, D.L., Mason, J.A., McDonald, T.M., Bloch, E.D., Herm, Z.R., Bae, T.H., and Long, J.R. (2012) Carbon dioxide capture in metal–organic frameworks. *Chem. Rev.*, **112** (2), 724–781.

21 Liu, J., Thallapally, P.K., McGrail, B.P., Brown, D.R., and Liu, J. (2012) Progress in adsorption-based CO_2 capture by metal-organic frameworks. *Chem. Soc. Rev.*, **41** (6), 2308–2322.

22 Adatoz, E., Avci, A.K., and Keskin, S. (2015) Opportunities and challenges of MOF-based membranes in gas separations. *Sep. Purif. Technol.*, **152**, 207–237.

23 Qiu, S., Xue, M., and Zhu, G. (2014) Metal-organic framework membranes: from synthesis to separation application. *Chem. Soc. Rev.*, **43** (16), 6116–6140.

24 Shah, M., McCarthy, M.C., Sachdeva, S., Lee, A.K., and Jeong, H.K. (2012) Current status of metal–organic framework membranes for gas separations: promises and challenges. *Ind. Eng. Chem. Res.*, **51** (5), 2179–2199.

25 Takashima, Y., Martinez, V.M., Furukawa, S., Kondo, M., Shimomura, S., Uehara, H., Nakahama, M., Sugimoto, K., and Kitagawa, S. (2011) Molecular decoding using luminescence from an entangled porous framework. *Nat. Commun.*, **2**, 1–8.

26 Park, K.S., Ni, Z., Cote, A.P., Choi, J.Y., Huang, R.D., Uribe-Romo, F.J., Chae, H.K., O'Keeffe, M., and Yaghi, O.M. (2006) Exceptional chemical and thermal stability of zeolitic imidazolate frameworks. *Proc. Natl. Acad. Sci. U.S.A.*, **103** (27), 10186–10191.

27 Jiang, J., Zhao, Y., and Yaghi, O.M. (2016) Covalent chemistry beyond molecules. *J. Am. Chem. Soc.*, **138** (10), 3255–3265.

28 Serre, C., Millange, F., Surblé, S., and Férey, G. (2004) A route to the synthesis of trivalent transition-metal porous carboxylates with trimeric secondary building units. *Angew. Chem. Int. Ed.*, **43** (46), 6285–6289.

29 Li, H., Eddaoudi, M., O'Keeffe, M., and Yaghi, O.M. (1999) Design and synthesis of an exceptionally stable and highly porous metal-organic framework. *Nature*, **402** (6759), 276–279.

30 Eddaoudi, M., Kim, J., Rosi, N., Vodak, D., Wachter, J., O'Keeffe, M., and Yaghi, O.M. (2002) Systematic design of pore size and functionality in isoreticular MOFs and their application in methane storage. *Science*, **295** (5554), 469–472.

31 Chui, S.S.Y., Lo, S.M.F., Charmant, J.P.H., Orpen, A.G., and Williams, I.D. (1999) A chemically functionalizable nanoporous material $(Cu_3(TMA)_2(H_2O)_3)_n$. *Science*, **283** (5405), 1148–1150.

32 Cavka, J.H., Jakobsen, S., Olsbye, U., Guillou, N., Lamberti, C., Bordiga, S., and Lillerud, K.P. (2008) A new zirconium inorganic building brick forming metal organic frameworks with exceptional stability. *J. Am. Chem. Soc.*, **130** (42), 13850–13851.

33 Rosi, N.L., Kim, J., Eddaoudi, M., Chen, B., O'Keeffe, M., and Yaghi, O.M. (2005) Rod packings and metal – organic frameworks constructed from rod-shaped secondary building units. *J. Am. Chem. Soc.*, **127** (5), 1504–1518.

34 Flugel, E.A., Ranft, A., Haase, F., and Lotsch, B.V. (2012) Synthetic routes toward MOF nanomorphologies. *J. Mater. Chem.*, **22** (20), 10119–10133.

35 Paseta, L., Seoane, B., Julve, D., Sebastián, V., Téllez, C., and Coronas, J. (2013) Accelerating the controlled synthesis of metal–organic frameworks by a microfluidic approach: a nanoliter continuous reactor. *ACS Appl. Mater. Interfaces*, **5** (19), 9405–9410.

36 Pham, M.H., Vuong, G.T., Vu, A.T., and Do, T.O. (2011) Novel route to size-controlled Fe–MIL-88B–NH_2 metal–organic framework nanocrystals. *Langmuir*, **27** (24), 15261–15267.

37 Horcajada, P., Salles, F., Wuttke, S., Devic, T., Heurtaux, D., Maurin, G., Vimont, A., Daturi, M., David, O., Magnier, E., Stock, N., Filinchuk, Y., Popov, D., Riekel, C., Férey, G., and Serre, C. (2011) How Linker's modification controls swelling properties of highly flexible iron(III) dicarboxylates MIL-88. *J. Am. Chem. Soc.*, **133** (44), 17839–17847.

38 Sebastian Cabeza, V., Kuhn, S., Kulkarni, A.A., and Jensen, K.F. (2012) Size-controlled flow synthesis of gold nanoparticles using a segmented flow microfluidic platform. *Langmuir*, **28** (17), 7007–7013.

39 Faustini, M., Kim, J., Jeong, G.Y., Kim, J.Y., Moon, H.R., Ahn, W.S., and Kim, D.P. (2013) Microfluidic approach toward continuous and ultrafast synthesis of metal–organic framework crystals and hetero structures in confined microdroplets. *J. Am. Chem. Soc.*, **135** (39), 14619–14626.

40 Jeong, G.Y., Ricco, R., Liang, K., Ludwig, J., Kim, J.O., Falcaro, P., and Kim, D.P. (2015) Bioactive MIL-88A framework hollow spheres via interfacial reaction in-droplet microfluidics for enzyme and nanoparticle encapsulation. *Chem. Mater.*, **27** (23), 7903–7909.

41 Ameloot, R., Vermoortele, F., Vanhove, W., Roeffaers, M.B.J., Sels, B.F., and De Vos, D.E. (2011) Interfacial synthesis of hollow metal–organic framework capsules demonstrating selective permeability. *Nat. Chem.*, **3** (5), 382–387.

42 Carbonell, C., Imaz, I., and Maspoch, D. (2011) Single-crystal metal – organic framework arrays. *J. Am. Chem. Soc.*, **133** (7), 2144–2147.

43 Witters, D., Vergauwe, N., Ameloot, R., Vermeir, S., De Vos, D., Puers, R., Sels, B., and Lammertyn, J. (2012) Digital microfluidic high-throughput printing of single metal-organic framework crystals. *Adv. Mater.*, **24** (10), 1316–1320.

44 Witters, D., Vermeir, S., Puers, R., Sels, B.F., De Vos, D.E., Lammertyn, J., and Ameloot, R. (2013) Miniaturized layer-by-layer deposition of metal–organic framework coatings through digital microfluidics. *Chem. Mater.*, **25** (7), 1021–1023.

www.ebook3000.com

45 Polyzoidis, A., Altenburg, T., Schwarzer, M., Loebbecke, S., and Kaskel, S. (2016) Continuous microreactor synthesis of ZIF-8 with high space–time-yield and tunable particle size. *Chem. Eng. J.*, **283**, 971–977.

46 Yamamoto, D., Maki, T., Watanabe, S., Tanaka, H., Miyahara, M.T., and Mae, K. (2013) Synthesis and adsorption properties of ZIF-8 nanoparticles using a micromixer. *Chem. Eng. J.*, **227**, 145–150.

47 Kim, K.J., Li, Y.J., Kreider, P.B., Chang, C.H., Wannenmacher, N., Thallapally, P.K., and Ahn, H.G. (2013) High-rate synthesis of Cu-BTC metal-organic frameworks. *Chem. Commun.*, **49** (98), 11518–11520.

48 Tai, S., Zhang, W., Zhang, J., Luo, G., Jia, Y., Deng, M., and Ling, Y. (2016) Facile preparation of UiO-66 nanoparticles with tunable sizes in a continuous flow microreactor and its application in drug delivery. *Microporous Mesoporous Mater.*, **220**, 148–154.

49 Rubio-Martinez, M., Batten, M.P., Polyzos, A., Carey, K.C., Mardel, J.I., Lim, K.S., and Hill, M.R. (2014) Versatile, high quality and scalable continuous flow production of metal-organic frameworks. *Sci. Rep.*, **4**, 5443.

50 D'Arras, L., Sassoye, C., Rozes, L., Sanchez, C., Marrot, J., Marre, S., and Aymonier, C. (2014) Fast and continuous processing of a new sub-micronic lanthanide-based metal-organic framework. *New J. Chem.*, **38** (4), 1477–1483.

51 Rodríguez-San-Miguel, D., Abrishamkar, A., Navarro, J.A.R., Rodriguez-Trujillo, R., Amabilino, D.B., Mas-Balleste, R., Zamora, F., and Puigmarti-Luis, J. (2016) Crystalline fibres of a covalent organic framework through bottom-up microfluidic synthesis. *Chem. Commun.*, **52**, 9212–9215.

52 Yampolskii, Y. (2012) Polymeric gas separation membranes. *Macromolecules*, **45** (8), 3298–3311.

53 Sholl, D.S. and Lively, R.P. (2016) Seven chemical separations to change the world. *Nature*, **532**, 435–437.

54 De Jong, J., Lammertink, R.G.H., and Wessling, M. (2006) Membranes and microfluidics: a review. *Lab Chip*, **6** (9), 1125–1139.

55 Stamatialis, D.F., Papenburg, B.J., Gironés, M., Saiful, S., Bettahalli, S.N.M., Schmitmeier, S., and Wessling, M. (2008) Medical applications of membranes: drug delivery, artificial organs and tissue engineering. *J. Membr. Sci.*, **308** (1–2), 1–34.

56 Web of Science™ http://webofknowledge.com (accessed 25 May 2016).

57 Baker, R.W. (2002) Future directions of membrane gas separation technology. *Ind. Eng. Chem. Res.*, **41** (6), 1393–1411.

58 Koros, W.J. and Mahajan, R. (2000) Pushing the limits on possibilities for large scale gas separation: which strategies? *J. Membr. Sci.*, **175** (2), 181–196.

59 Zhang, C. and Koros, W.J. (2015) Zeolitic imidazolate framework-enabled membranes: challenges and opportunities. *J. Phys. Chem. Lett.*, **6** (19), 3841–3849.

60 Bernardo, P., Drioli, E., and Golemme, G. (2009) Membrane gas separation: a review/state of the art. *Ind. Eng. Chem. Res.*, **48** (10), 4638–4663.

61 Stankiewicz, A.I. and Moulijn, J.A. (2000) Process intensification: transforming chemical engineering. *Chem. Eng. Prog.*, **96** (1), 22–33.

62 Brown, A.J., Johnson, J.R., Lydon, M.E., Koros, W.J., Jones, C.W., and Nair, S. (2012) Continuous polycrystalline zeolitic imidazolate framework-90 membranes on polymeric hollow fibers. *Angew. Chem. Int. Ed.*, **51** (42), 10615–10618.

63 Jang, K.S., Kim, H.J., Johnson, J.R., Kim, W.g., Koros, W.J., Jones, C.W., and Nair, S. (2011) Modified mesoporous silica Gas separation membranes on polymeric hollow fibers. *Chem. Mater.*, **23** (12), 3025–3028.

64 Pan, Y. and Lai, Z. (2011) Sharp separation of C2/C3 hydrocarbon mixtures by zeolitic imidazolate framework-8 (ZIF-8) membranes synthesized in aqueous solutions. *Chem. Commun.*, **47** (37), 10275–10277.

65 Zhang, C., Lively, R.P., Zhang, K., Johnson, J.R., Karvan, O., and Koros, W.J. (2012) Unexpected molecular sieving properties of zeolitic imidazolate framework-8. *J. Phys. Chem. Lett.*, **3** (16), 2130–2134.

66 Kwon, H.T. and Jeong, H.K. (2013) Highly propylene-selective supported zeolite-imidazolate framework (ZIF-8) membranes synthesized by rapid microwave-assisted seeding and secondary growth. *Chem. Commun.*, **49** (37), 3854–3856.

67 Yao, J., Dong, D., Li, D., He, L., Xu, G., and Wang, H. (2011) Contra-diffusion synthesis of ZIF-8 films on a polymer substrate. *Chem. Commun.*, **47** (9), 2559–2561.

68 Eum, K., Rownaghi, A., Choi, D., Bhave, R.R., Jones, C.W., and Nair, S. (2016) Fluidic processing of high-performance ZIF-8 membranes on polymeric hollow fibers: mechanistic insights and microstructure control. *Adv. Funct. Mater.*, **26** (28), 5011–5018.

69 Kwon, H.T. and Jeong, H.K. (2013) In situ synthesis of thin zeolitic-imidazolate framework ZIF-8 membranes exhibiting exceptionally high propylene/propane separation. *J. Am. Chem. Soc.*, **135** (29), 10763–10768.

70 Bux, H., Liang, F.Y., Li, Y.S., Cravillon, J., Wiebcke, M., and Caro, J. (2009) Zeolitic imidazolate framework membrane with molecular sieving properties by microwave-assisted solvothermal synthesis. *J. Am. Chem. Soc.*, **131** (44), 16000–16001.

71 Li, Y.S., Liang, F.Y., Bux, H., Yang, W., and Caro, J. (2010) Zeolitic imidazolate framework ZIF-7 based molecular sieve membrane for hydrogen separation. *J. Membr. Sci.*, **354** (1–2), 48–54.

72 Shah, M., Kwon, H.T., Tran, V., Sachdeva, S., and Jeong, H.K. (2013) One step *in situ* synthesis of supported zeolitic imidazolate framework ZIF-8 membranes: role of sodium formate. *Microporous Mesoporous Mater.*, **165**, 63–69.

73 He, M., Yao, J., Li, L., Wang, K., Chen, F., and Wang, H. (2013) Synthesis of zeolitic imidazolate framework-7 in a water/ethanol mixture and its ethanol-induced reversible phase transition. *ChemPlusChem*, **78** (10), 1222–1225.

74 He, M., Yao, J., Liu, Q., Zhong, Z., and Wang, H. (2013) Toluene-assisted synthesis of RHO-type zeolitic imidazolate frameworks: synthesis and formation mechanism of ZIF-11 and ZIF-12. *Dalton Trans.*, **42** (47), 16608–16613.

www.ebook3000.com

75 Cacho-Bailo, F., Caro, G., Etxeberría-Benavides, M., Karvan, O., Tellez, C., and Coronas, J. (2015) High selectivity ZIF-93 hollow fiber membranes for gas separation. *Chem. Commun.*, **51**, 11283–11285.

76 Xi, F.G., Liu, H., Yang, N.N., and Gao, E.Q. (2016) Aldehyde-tagged zirconium metal-organic frameworks: a versatile platform for postsynthetic modification. *Inorg. Chem.*, **55** (10), 4701–4703.

77 Morris, W., Doonan, C.J., Furukawa, H., Banerjee, R., and Yaghi, O.M. (2008) Crystals as molecules: postsynthesis covalent functionalization of zeolitic imidazolate frameworks. *J. Am. Chem. Soc.*, **130** (38), 12626–12627.

78 Huang, A.S. and Caro, J. (2011) Covalent post-functionalization of zeolitic imidazolate framework ZIF-90 membrane for enhanced hydrogen selectivity. *Angew. Chem. Int. Ed.*, **50** (21), 4979–4982.

79 Morris, W., Leung, B., Furukawa, H., Yaghi, O.K., He, N., Hayashi, H., Houndonougbo, Y., Asta, M., Laird, B.B., and Yaghi, O.M. (2010) A combined experimental-computational investigation of carbon dioxide capture in a series of isoreticular zeolitic imidazolate frameworks. *J. Am. Chem. Soc.*, **132** (32), 11006–11008.

80 Cacho-Bailo, F., Matito-Martos, I., Perez-Carbajo, J., Etxeberria-Benavides, M., Karvan, O., Sebastian, V., Calero, S., Tellez, C., and Coronas, J. (2017) On the molecular mechanisms for the H_2/CO_2 separation performance of zeolite imidazolate framework two-layered membranes. *Chem. Sci.*, **8**, 325–333.

81 Maya, F., Palomino Cabello, C., Clavijo, S., Estela, J.M., Cerda, V., and Turnes Palomino, G. (2015) Automated growth of metal-organic framework coatings on flow-through functional supports. *Chem. Commun.*, **51** (38), 8169–8172.

82 Zhang, C., Zhang, K., Xu, L., Labreche, Y., Kraftschik, B., and Koros, W.J. (2014) Highly scalable ZIF-based mixed-matrix hollow fiber membranes for advanced hydrocarbon separations. *AIChE J.*, **60** (7), 2625–2635.

83 Cacho-Bailo, F., Caro, G., Etxeberria, M., Karvan, O., Tellez, C., and Coronas, J. (2016) MOF–polymer enhanced compatibility: post-annealed zeolite imidazolate framework membranes inside polyimide hollow fibers. *RSC Adv.*, **6**, 5881–5889.

84 Cacho-Bailo, F., Tellez, C., and Coronas, J. (2016) Interactive thermal effects on metal-organic framework polymer composite membranes. *Chem. Eur. J.*, **22** (28), 9533–9536.

85 Hou, J., Sutrisna, P.D., Zhang, Y., and Chen, V. (2016) Formation of ultrathin, continuous metal–organic framework membranes on flexible polymer substrates. *Angew. Chem. Int. Ed.*, **55** (12), 3947–3951.

86 Biswal, B.P., Panda, T., and Banerjee, R. (2012) Solution mediated phase transformation (RHO to SOD) in porous Co-imidazolate based zeolitic frameworks with high water stability. *Chem. Commun.*, **48** (97), 11868–11870.

87 Bernal, M.P., Coronas, J., Menéndez, M., and Santamaría, J. (2001) Characterization of zeolite membranes by temperature programmed permeation and step desorption. *J. Membr. Sci.*, **195** (1), 125–138.

88 Lai, Z.P., Bonilla, G., Diaz, I., Nery, J.G., Sujaoti, K., Amat, M.A., Kokkoli, E., Terasaki, O., Thompson, R.W., Tsapatsis, M., and Vlachos, D.G. (2003) Microstructural optimization of a zeolite membrane for organic vapor separation. *Science*, **300** (5618), 456–460.

89 Morigami, Y., Kondo, M., Abe, J., Kita, H., and Okamoto, K. (2001) The first large-scale pervaporation plant using tubular-type module with zeolite NaA membrane. *Sep. Purif. Technol.*, **25** (1–3), 251–260.

90 Strathmann, H. (2001) Membrane separation processes: current relevance and future opportunities. *AIChE J.*, **47** (5), 1077–1087.

91 Karvan, O., Johnson, J.R., Williams, P.J., and Koros, W.J. (2013) A pilot-scale system for carbon molecular sieve hollow fiber membrane manufacturing. *Chem. Eng. Technol.*, **36** (1), 53–61.

92 Clausi, D.T. and Koros, W.J. (2000) Formation of defect-free polyimide hollow fiber membranes for gas separations. *J. Membr. Sci.*, **167** (1), 79–89.

93 Li, W., Zhang, Y., Li, Q., and Zhang, G. (2015) Metal – organic framework composite membranes: synthesis and separation applications. *Chem. Eng. Sci.*, **135**, 232–257.

94 Feng, C.Y., Khulbe, K.C., Matsuura, T., and Ismail, A.F. (2013) Recent progresses in polymeric hollow fiber membrane preparation, characterization and applications. *Sep. Purif. Technol.*, **111**, 43–71.

95 Low, J.J., Benin, A.I., Jakubczak, P., Abrahamian, J.F., Faheem, S.A., and Willis, R.R. (2009) Virtual high throughput screening confirmed experimentally: porous coordination polymer hydration. *J. Am. Chem. Soc.*, **131** (43), 15834–15842.

96 Mao, Y., Li, J., Cao, W., Ying, Y., Sun, L., and Peng, X. (2014) Pressure-assisted synthesis of HKUST-1 thin film on polymer hollow fiber at room temperature toward gas separation. *ACS Appl. Mater. Interfaces*, **6** (6), 4473–4479.

97 Su, P., Li, W., Zhang, C., Meng, Q., Shen, C., and Zhang, G. (2015) Metal based gels as versatile precursors to synthesize stiff and integrated MOF/polymer composite membranes. *J. Mater. Chem. A*, **3** (40), 20345–20351.

98 Li, W., Su, P., Zhang, G., Shen, C., and Meng, Q. (2015) Preparation of continuous NH_2-MIL-53 membrane on ammoniated polyvinylidene fluoride hollow fiber for efficient H_2 purification. *J. Membr. Sci.*, **495**, 384–391.

99 Li, W., Meng, Q., Zhang, C., and Zhang, G. (2015) Metal–organic framework/PVDF composite membranes with high H_2 permselectivity synthesized by ammoniation. *Chem. Eur. J.*, **21** (19), 7224–7230.

100 Li, W., Meng, Q., Li, X., Zhang, C., Fan, Z., and Zhang, G. (2014) Non-activation ZnO array as a buffering layer to fabricate strongly adhesive metal-organic framework/PVDF hollow fiber membranes. *Chem. Commun.*, **50** (68), 9711–9713.

101 Li, W., Yang, Z., Zhang, G., Fan, Z., Meng, Q., Shen, C., and Gao, C. (2014) Stiff metal-organic framework-polyacrylonitrile hollow fiber composite membranes with high gas permeability. *J. Mater. Chem. A*, **2** (7), 2110–2118.

www.ebook3000.com

17

Perspective for Microfluidics

Yujun Song[1] *and Daojian Cheng*[2]

[1] *University of Science and Technology Beijing, Centre for Modern Physics Technology, Applied Physics Department, Beijing Key Laboratory for Magneto-Photoelectric Composite and Interface Science, 30 Xueyuan Road, Haidian District, Beijing 100083, PR China*
[2] *Beijing University of Chemical Technology, College of Chemical Engineering, State Key Laboratory of Organic-Inorganic Composites, No. 15 Beisanhuan East Road, Chaoyang District, Beijing 100029, PR China*

As one of the main fields in the miniaturization of systems and instrument assembly, microfluidic technology preserves small device scale, low driving power and flexible driving types, small operation volume, ultrafast response, and high efficiency [1–4]. Current focuses include the interconnection of microfabrication and nanotechnologies and their further interfusing with fundamental chemistry, physics, and biology and varieties of engineering fields [5–18]. Recent development and applications of microfluidic technology have been discussed in the previous chapters and demonstrated a great deal of potentials and abilities in chemical/bioanalysis [4, 19–21], biomedical engineering [4, 5, 22–24], controlled synthesis of chemical/pharmacy/materials [6, 11, 25–31], and miniaturization of other systems [6, 32]. Different from over decades before, lots of breakthroughs in theory and experiments have been achieved in this sprouting field and currently lead to many commercialization of microfluidic devices and assembles, bringing about a paradigm shifting from its infant to one fast-growing field [3, 6, 21, 24, 33–35]. Simultaneously, more requirements and challenges have been proposed for more advanced and extended applications of microfluidic technology, endowing more opportunities to scientists and engineers in this blooming field due to its intensive and intrinsic interdisciplinary features. Therefore, more rooms are constantly emerging for current researchers and the new comers, particularly in the basic micro-/nanofabrication, the related fluid physics, the surface/interface science from microscale to nanoscale, and the interdisciplinary fields with nanotechnology [2, 8, 36, 37], sensing technology [4, 19, 38], biology [5, 22–24], chemistry, chemical engineering [6, 25, 33], new pharmacy discovery and manufacture [6, 14, 39], new materials and energy technology [15, 27, 40, 41], and even astronautic and aeronautic theory development (e.g., microturbines with the thrust–weight ratio of up to 100 : 1; enhanced laminar to turbulence transition by patterned microscale or nanoscale surfaces) [42–45].

Microfluidics: Fundamentals, Devices and Applications, First Edition.
Edited by Yujun Song, Daojian Cheng, and Liang Zhao.
© 2018 Wiley-VCH Verlag GmbH & Co. KGaA. Published 2018 by Wiley-VCH Verlag GmbH & Co. KGaA.

17.1 Design, Fabrication, and Assemble of Microfluidic Systems

The design of various microfluidic devices for desired miniaturization systems is a fundamental issue based on the combined consideration of the current micro/nanofabrication technology for smart microdevices, the constructed materials, and the requirement for analysis, detection, and synthesis of various chemicals or materials. Flow types and power-driving systems are the two preliminary cornerstones in the design of microfluidic devices according to their applications.

Flow types are usually determined and optimized according to the functions of microfluidic systems and also the fundamental in the design of microstructures of microdevices. Currently, there are four types of flows – continuous flow, droplet flow, segment flow, and spray flow – whether they are realized in chip-based or capillary- and tubing-based microfluidic devices [1–3, 15, 25, 46, 47]. Simplicity in microfluidic design and fabrication of capillary tubing-based devices leads to easy scaling-out of the process, albeit compromising on the analysis precision and/or the product quality as shown decades ago, which has achieved great progress recently [6, 15, 48, 49]. On the other hand, microfluidic devices with more complicated structure for other types of flow are required even though droplet flow or segmented flow can offer digital potential control of detection and synthesis [24, 50–52]. Overall, segmented flow or droplet flow microdevices are likely to be useful and flexible for the synthesis of a broad spectrum of chemicals and materials, and the spray flow can have the potential to scale up similar to the continuous phase flow for rapid synthesis of materials with relatively high reaction rates [3, 46, 53–56]. However, if the scale-up of the process is the key issue, the capillary tubing-based operating in a continuous flow mode is preferred, especially for the synthesis of chemicals or materials that are relatively less sensitive to change under the reaction conditions [6, 15, 40, 48, 49, 57].

The driving forces are the power to transport the fluids in the microfluidic devices. To date, they have expanded from the conventional body forces (e.g., centrifugal forces [23, 58], gravity forces [59, 60], and electrostatic forces [17, 61]) and electrokinetically driving forces (e.g., electroosmosis, electrophoresis, and dielectophoresis) [62] to many other new forces, such as magnetic field driving forces [16, 63–65], optical driving forces (radiation pressure and optical tweezers) [66, 67], light-induced capillary forces [68–70], surface tension forces [50, 71], and optical-induced mechanical forces (e.g., photoinduced asymmetric deformation of tubular microactuators) [7] and coupling forces (e.g., opto-thermocapillary effects [68–70, 72], light modulation of electrical actuation: optoelectrowetting and photocontrol of electroosmotic forces [13, 17, 73–75]).

With the vivid and rapid progress of new materials, the construction materials for microstructures have been expanded from traditional Si/SiO_2 wafers, polymers, ceramics, or metals to more varieties of new photoresists (e.g., fluorinated ethylene propylene (FEP)) [76–78], cross-linked, or linear liquid-crystal polymers (e.g., a long alkyl backbone containing double bonds and azobenzene moieties in side chains) [7], ceramics [79, 80], and composites [6, 81, 82]. They provide us the

www.ebook3000.com

material basis to design and fabricate the desired microstructures for microfluidic systems. Up to now, many microdevices have been developed as the basic configuration parts for microfluidic systems in analysis and/or synthesis of chemicals, biomolecules, and materials based on these materials [6, 48, 83]. They usually include micro-motors/pumps, micro-mixers, micro-separators, or extractors, micro-controllers, micro-sensors or detectors and/or connecting microchannels, and so on [5–7, 26, 84]. With the development of construction materials and the driving motors, the precision flow rates of the driving fluids have been increasing from microliters to picoliters or high precision [7, 17, 20, 65, 85].

Fabrication of Si/SiO_2 wafer or newly developed ceramic-based microfluidic devices could be straightforward made at very high space resolution by the well-established and continuous improvement of microelectromechanical systems (MEMS) technology, such as deep reactive ion etching (DRIE), anodic bonding, thin-film metallization, and surface modification [86, 87]. To address the increasing demand of disposable applications such as *in vitro* diagnostic devices and health screening kits, microfabrication technologies for polymer still need to be developed specifically to meet the requirement of microfluidic devices for high machining precision (e.g., sub-microscale structures or sub-nanometer surface patterns) because the traditional thermal casting, hot embossing, milling, and injection molding extremely depend on the precision and complication of molds and tools [88]. The geometrical accuracy of the features could be critical to the device functions such as concentration measurement, which implies a lot of challenges to the polymer fabrication process including mold insert fabrication, process control of injection molding, and lamination [81, 89]. In general, there are lots of room to develop the fabrication method (e.g., X-ray lithography, electroplating, and molding (LIGA), laser fabrication, surface plasmon-enhanced LIGA) [90–93] and molding materials (e.g., amorphous metallic glass) to improve the polymer microfluidic device fabrication [94, 95], especially about the component and material integration and the accurate dimensional control after lamination and bonding [82, 96–99]. Nontraditional fabrication platforms, for example, the roll-to-roll manufacturing, 3D imprinting, and paper imprinting, may find their wonderful future applications in the precise fabrication of microfluidic devices [81, 89, 97, 98, 100–102].

Contrary to the microfluidic devices for chemical analysis or biomedical engineering (diagnosis and therapy), robust and reusable microfluidic devices for long-term operation may be the first consideration in the chemical or materials synthesis, which have to overcome the wall fouling of microfluidic channels or to find a simple and reliable means to clean microchannels without damaging the inner parts and channel walls too much [2, 6, 15, 48]. Subversive high efficient fabrication methods and advanced engineering materials are still required besides the exquisite and practical structure design, particularly for those microfluidic devices operated in extremely demanding environments (e.g., high temperature more than 300 °C; high pressure, such more than hundreds of atmosphere; high concentrated base or acidic solution; high reducing or oxidizing solution; caustic or solvents; or combination of them) [2, 6, 15, 25, 27, 49, 103, 104]. In the fabrication of microfluidic devices, bonding or sealing methods of these microstructures to form an integrated lab-on-chip microfluidic

devices are still the key technology because the bonding interfaces can become the weakest part of the microdevices [80, 86, 99, 105, 106]. If not, capillary- or micro-tubing-based continuous microreactors or spray flow-type microreactors may be good alternatives [3, 6, 25, 48].

Recent progresses in 3D printing technologies have provided us a deserved alternative for microfluidic device prototyping and large-volume production, which would play more significant roles in the future along with the improving of material properties and tools [79, 80, 97, 98]. The development of 3D printing technologies for the future fabrication of microfluidic devices is extremely demanded for various materials whether they are polymers, metals or alloys, ceramics, or composites at high space precision (e.g., sub-microscale) or surface pattern resolution (e.g., sub-nanometers) [81, 90, 97, 98, 102].

Surface properties of microfluidic devices are critical for their applications [2]. Surface microstructures (patterns and roughness) and properties (hydrophilic lipophilic balance and ligands) intensively affect the fluid resistance and state, antifouling capacity or self-cleaning ability, mass and thermal transport, surface reaction rates and the whole reaction routes, surface tension, or shear-induced micro/nanoscale effects [2, 17, 26, 28, 44, 48, 107–115]. Therefore, surface modification of inner walls of microfluidic devices is also one of the important considerations in the design of microfluidic devices, and lots of methods have been developed for this goal [2, 116]. Surface properties of microfluidic devices especially polymer-based materials are extremely critical to certain applications such as point-of-care devices [2, 20, 116–120]. Plasma treatment provided a simple and fast method to generate hydrophilic surfaces for various materials at relatively low cost [119, 120]. However, the short duration of hydrophilic effect is the major drawback of this approach. On the other hand, physical coating systems such as using surfactant to treat polymer channels are easy to carry out, but suffer from poor durability. Surface grafting methods including photo-initiated surface grafting polymerization and surface-initiated atom transfer radical polymerization provide chemical bonding between coating layer and substrates, which can offer almost permanent effects such as hydrophilic, hydrophobic, and biological functionalization [116–118]. For mass production of surface modification of microfluidics, surface grafting techniques and control plasmon treatment still need more research in order to lower the cost and reduce process complexity.

In addition, scaling and assembly of these microdevices together to form active and miniaturized systems is an enduring work in this field for the breakthrough in the future microfluidic applications even though lots of progresses have been achieved in recent years [3, 4, 36, 49, 121]. Standardization of functional parts may be one of the key and challenging steps that have to be well addressed for the reconfiguration of microfluidic system, which requires lots of collaborated work and overcoming many difficulties in the future of this field [6, 36, 121]. Coupling microfluidics with external devices (e.g., sensor, heater, cooler, separator) and the related new or conventional technology (e.g., digitization, nebulator, spray nozzle, light–thermal transfer, magnetic–acoustic transfer, electrochemical technology, nanotechnology, etc.) and their essential miniaturization are still required to construct the practical significance of microfluidic systems [1, 3, 4, 11, 12, 24, 121, 122]. Another point deserved to be mentioned is that the coupling of the bionics

www.ebook3000.com

and the design of microfluidic devices are also interesting and important areas in the development of new microfluidic materials and microstructures in the future research since *Nature* is full of microfluidic systems, particularly in the tissues and organs of animals and plants [7, 107]. For an instance, the simulation of aerosol dynamics in the human respiratory systems and particle thermodynamics in the human vasculatures and also tissue heat and mass transfer as well as aspects of pharmacokinetics may enlighten the reasonable design of pulmonary and arterial drug delivery [14, 39]. Thus, the invention of advanced fabrication and synthesis methods will be definitely another essential and vivid field for the desired new materials and microstructures, and even some subversive design and fabrication technology progress can be achieved simultaneously.

17.2 Precise Control of Critical Device Features for Chemical Analysis and Biomedical Engineering

The development of microfluidic devices for various miniaturized and portable biomedical engineering (i.e., diagnosis, therapy, drug discovery, and delivery) and chemical analysis systems is one of the most infinite creative fields in microfluidic technology [4, 122–125]. In this field, one key aspect is the design and miniaturization of traditional huge bulky analysis instruments to portable and fast detectors operated at low feed usage and low power consumption, but having high detection resolution and reliability (e.g., micro gas chromatography, μ-GC; micro-plate spectrophotometer, μ-PSP) [5, 19, 22, 93]. Another key aspect is to develop the novel prototype devices for quantitative analysis that can be undertaken and tested at low cost by application of appropriate analytical theory [126] or numerical analysis [38, 127], particularly for those expensive and low concentrated biochemical reagents and/or those bulky detectors constructed by expensive materials [22, 24, 128]. These prototype micro-instruments can be expected to be commercialized in the near future.

In the microfluidic systems for the precise analysis, the key technology may be the high-throughput screening of the target fluids with mass or volume as small as possible [123, 125, 129]. Continuous flow methods usually depend on the precision of the flow controller or the smallest volume of pumping. The trend is to develop high resolution pumping technology as it can now reach nanoliters and picoliters or high precision [17, 20, 21, 51]. In order to realize more precision analysis, microfluidic devices with droplet flows or digital flows have been developed and shown good results in volume control and automatization. Microfluidic devices have been showing great commercialization perspectives in potable *in situ* chemical detectors by integrating with lots of advanced detecting techniques (e.g., electrochemical detector, surface plasmon-enhanced Raman spectroscopy, photoluminescence spectroscopy, GC, mass spectroscopy–GC (MS–GC), or even micro inductively coupled plasma-atomic emission spectrometry (μ-ICP-AES)) [61, 93, 129, 130].

Lots of excellent work have shown the mature progress of microfluidic techniques in academic research, and some of them have been turned into

commercialized products, such as the portable user-friendly blood diagnostic instrument (Abbott-i-STAT analyzer) and the digital microfluidic-based Advanced Liquid Logic for gene and protein analyses and the BIA-core microfluidic platform [21, 24, 33–35]. These platforms are designed for the use of life science research and can provide cost-effective automation solutions for complex bioassay workflows. For microfluidic cell-based assays, benchtop equipment for real-time quantitative monitoring of cellular response has also been commercialized for high-throughput drug screening applications, such as xCELLigence system, that can provide quantitative indexes to describe cellular responses during the culture course [123, 128]. To date, microfluidic formats have been used as a powerful tool, which is extremely helpful on probing gene expression at multiple cellular levels, including DNA genotyping, RNA detection, protein imaging, and even for next-generation sequencing due to the advantages of microfluidic platforms (i.e., easy in handling tiny liquid volume and their inherent integration feasibility) [21, 22, 69, 123].

However, these excellent products have not made great impact on the market. Most of the assays in clinical and research laboratories still rely on conventional equipment. One of the possible reasons is these newly developed microfluidic products need to take time to compete with the existing equipment that has been perfected over decades. But it is still expected that more commercial microfluidic products will be launched in the near future to replace the traditional platforms. Additionally, one thing has to be pointed out that, up to now, microfluidic systems are just one in a number of available methods to do chemical analysis (e.g., all of organics and elements) and biomedical engineering (e.g., the complicated gene express, disease-related biomarkers (DNA, RNA, and proteins) analysis and therapy, circulating tumor cell (CTC) detection, targeting drug delivery to any organs, or tissues) [19, 24, 123, 131, 132]. Lots of works have to be done to realize microfluidics' versatility as a dreamful "golden key" that is expected to solve all the current and future problems in chemical analysis and biomedical engineering [19, 24, 123, 133]. If they can be coupled with the optical driving (e.g., opto-capillary, laser tweezer) or opto-electric operation systems [7, 134], device commercialization for superfine liquid transport with a volume of 10^{-18} l or less and single molecule (e.g., single DNA or RNA) may be realized soon with the development of large-scale fabrication technology for microfluidic devices with featured dimension scale down to nanoscale [7, 122]. These progresses may be integrated with the varieties of gene shearing technology, leading to the revolutionary progress of biology and biomedical engineering, particularly in cancer therapy and regulation of life time and characteristics of humans.

17.3 Control of Critical Kinetic Parameters for Chemical and Materials Synthesis

Besides the great success of microfluidic platforms in chemical analysis and biomedical engineering applications, microfluidic methods have been regarded as suitable alternative protocols with a high probability of continuously gaining

www.ebook3000.com

large quantities of chemicals and materials of desired properties with precisely controlled microstructures and compositions at mesoscale [6, 11, 25–31, 37, 50, 53, 135–138]. Microfluidic reactors offer many intrinsic and potential advantages in the chemical industry and material synthesis due to superior reaction kinetic parameter control, high-throughput and safe operational environment, operation safety, low cost in optimization of reaction conditions, and scale-out features [2, 3, 6, 15, 25, 40, 137, 139]. Generally, there are five main advantages of microfluidic systems.

First of all, high efficiency in mass, thermal, and momentum transfer can be easily realized in microfluidic devices due to their high aspect ratio at microscale structures and the ultrasmall handling feed volume (nl–pl or less) [17, 37, 65, 85], leading to uniform mass mixing and thermal exchanging, and the desired uniform/oriented reaction route control. Secondly, the benefit from the progress and of micro/nanotechnology, the related mixers, reactors, separators, sensors, and other essential operating units can be conveniently designed into single microstructures with complicated multi-inlet structures and precise spatial location, in which multiphase fluid mixing and reaction can be realized, such as the appearance of droplet, digital, and spray-like microfluidic reactors [3, 50, 52, 140, 141]. Thirdly, thanks to their continuous operation features in microchannels, microfluidic processes preserve the continuous multistage operation feature with precise and separated reaction condition control to realize a high compact precise synthesis process, which is much suitable for the organic and medicine manufactures with lots of sequenced and complicated reactions [6, 48, 57, 142]. Particularly and most importantly, the reaction stages of composition-designed chemicals and the formation stages of materials with special microstructures can be separated successively along one single microchannel, leading to spatiotemporal regulation of thermodynamic parameters independently for each stage of desired composition and oriented microstructure, avoiding the interference before and after operation [15, 103, 106, 140, 143–146]. This feature is much suitable for the synthesis of special polymers (e.g., Janus particles), drugs, nanohybrids, metal–organic frameworks (MOFs), and other nanoscale and microscale composite materials [15, 27, 40, 49, 123, 135, 137, 147]. The fourth advantage may be that microfluidic devices can be conveniently coupled with necessary external devices (e.g., sensing devices, fluid driving devices), which should be consummated to realize more functions [106, 148, 149]. These couplings help realizing online analysis abilities of the products for *in situ* regulation of the reaction parameters, alleviating the unnecessary experimental variances for high quality control and fundamental mechanism study [106, 145, 150–152]. The typical couplings of microfluidic systems are the optical property regulation of semiconductors by coupling the microfluidic reactors with UV–Vis spectroscopy or photoluminescence spectroscopy [144, 145]. This feature favors developing the *in situ* or *ex situ* online monitoring techniques to investigate the reaction or formation mechanism of chemicals or materials [106, 145, 149, 150]. The Fourier transform infrared (FT-IR) spectroscopy, UV–Vis spectroscopy, fluorescence and absorption spectroscopy, and X-ray absorption fine structure (XAFS) spectroscopy using synchrotron sources can be coupled into the microfluidic systems for analyzing mechanism

in every reaction stage *in situ*, and monitoring of these reactions would provide many answers to questions of nanoparticle formation in microfluidic reactors [26, 106, 142, 150–154]. As a distinct interdisciplinary field, the microfluidic approaches have the infinite potential to marry to the basic material design and microstructure control [3, 15, 27, 54, 103] and other operation or fabrication techniques, such as photo driving forces [7, 9, 17, 62], electric driving forces [17, 155], magnetic driving forces [12, 51, 64], microwave-assisted fabrication [156], ionic liquid-based synthesis [157], and solvent-less high pressure synthesis [147]. These couplings have been creating some subversive fabrication techniques and may be more in the near future [3, 6, 7, 25, 27, 139, 147]. The resulted achievements allow not only the large-scale continuous production but also an accurate synthesis parameter control, giving a step toward intensification, versatility, and scalability in the fabrication of the chemicals and materials [3, 6, 15, 25, 37, 135, 147]. Progress in the recent decades suggests that, in the near future, many large-scale batch processes, where thousands of kilograms of potentially corrosive, toxic, or explosive chemicals have to be mixed and stirred for a long period of time, can be replaced by these kinds of microfluidic processes [6, 28, 47, 104, 158]. Overcoming such challenges and further innovation in the required infrastructure to operate microfluidic chemical reaction system for long term will enable application to address future synthesis problems to satisfy our societal requirements. The fifth main advantage may be their high-throughput screening features since thousands of microfluidic devices of different but coherent functions can be fabricated in one single chip to realize one goal or the lab-on-chip features. This feature is much suitable in the rapid optimization of reaction conditions for medicine selectivity and drug discovery and single-cell/molecule treatment at low cost [22, 24, 84, 123].

Additionally, complications in traditional batch processes associated with large-scale transport and storage as well as safety and health issues (such as explosion and leakage of toxic and flammable solvents) can be alleviated by microfluidic approaches [28, 104, 158–160]. Process scale-up, based on the concept of parallel processing, with a precise control of the synthetic aspects of the final product to produce chemicals and materials with well-defined and predetermined properties in higher yields, have been well demonstrated in Chapters 11–16. The option of manipulating and controlling additional reaction parameters, compared with traditional batch processes, such as flow rates and the ability to cease the reaction as soon as the product is formed in a microliter or even to a picoliter volume, offers even more possibilities for product control [6, 25, 48, 161]. With the development of microfabrication technology, constructed materials, and fundamental fluid and reaction theory at micro- and nanoscale, various materials and chemicals have been successfully synthesized by the related microfluidic reactors, ranging from organics/medicines [3, 6], polymers [40, 41, 54, 139, 146, 162], metals [15, 27, 40, 49, 109, 141, 154, 163–166], ceramics [31, 162, 167–169], semiconductors [52, 53, 103], composites/hybrids [15, 27, 49, 169–171], and MOF [29, 30, 135, 172–174]. Details on the devices and synthesis processes can be referred to the corresponding chapters of this book.

Although there are so many advantages, it should be mentioned that the throughput of microfluidic synthetic method is somewhat limited. There are

www.ebook3000.com

still many challenges in microfluidic technology for the controlled synthesis of chemicals and materials for us to consider. Firstly, for the scale-up of microfluidic reaction systems, not only their parallel scale-out feature has to be utilized, but also designing high flows and/or more complicated microstructures for rapid and efficient mixing and reactions have to be considered intensively to meet future industrial and commercial requirements [6, 48]. Secondly, more researches should be invested in the marriage of the microfluidic systems to other detection or reaction devices to realize more functions that cannot be overcome by traditional synthesis methods. Only by this, microfluidic processes can play an important role to replace not only the traditional synthesis methods but also the key role that the conventional methods cannot fulfill in the industrial applications. Thirdly, there are still existing great challenges in the cost of fabricating thousands of microfluidic reactors with identical features, the uniform flow rate control in each channel from a single source, and the efficient strategy development to address the blockage and self-cleaning of microfluidic channels during long-term operation [2, 49]. Therefore, direct translation of normal batch process into a microfluidic reactor process is still not a trivial issue [2, 6, 48, 49, 153]. Overcoming such challenges and further innovation in the required infrastructure to operate microfluidic chemical reaction system for long term will enable application to address future synthesis problems to satisfy our societal requirements. Fourthly, although microfluidic processes are very suitable for the investigation of the reaction and formation mechanism of the chemicals and materials, there are not so intensive studies in this aspect for the process control [49, 106, 153, 175]. The last one may be the great challenge in the standardization in microfluidic systems (including the operation units of various microdevices and the work safety standardization), which are greatly desired in the configuration of varieties of microfluidic devices for targeting functions. This is more urgent in the microfluidic systems to replace the traditional synthetic methods in the near future. Based on this standard, platform will be very useful in the simulation and optimization of microdevice design, selectivity, assembly, and control of operation conditions based on the current experimental data and other chemical and material databases.

17.4 Development of Fundamental Theory at Micro-/Nanoscale and Fluid Mechanism at Nanoliter–Picoliter for Microfluidic Systems

Recent development of microfluidic techniques and their coupling with other subjects intrinsically depend on the progress in the fundamental mass, thermal, and momentum transfer (3-T) mechanism from molecule size to nanoscale dimension (i.e., mesoscale physics) and in the fluid thermodynamic mechanism from microliter to picoliter or high precision for analysis, and controlled and enforced high flow rates for synthesis [17, 176, 177]. With the rapid development of microfluidic technique and their application, the flow characteristics and the related mass, thermal, and momentum transfer mechanism in microchannels

have become one dominant research area of fluid physics and chemistry. The main goals of these studies are (i) to design and optimize the microfluidic systems to obtain efficient mass, thermal, and momentum transfer at the lowest pressure drop and (ii) more precise reaction kinetic control and (iii) to discover novel methods and build-up theory to handle smaller volume of fluid more precisely. In realizing these goals, the methodology development in microfluidic techniques is definitely featured by disciplinary crossing and integration.

The theoretical investigation in microfluidics is mainly focusing on the size effects due to the reduced dimension in microfluidic devices, including the surface and interface effects on the mass, thermal, and momentum transfer, the related reaction characteristics, the fluid driving mechanism, and the design principle and fabrication technology of microdevices for targeting applications [17, 177, 178]. Even though most of the fundamentals in fluid mechanism with the governing equation for a bulk fluid can be used in microfluidics, such as Pascal's law, Laplace's law, Bernoulli's and Poiseuille's laws, Navier–Stokes Fourier fluid dynamic models, there are lots of new phenomena that cannot be elucidated by the classic fluid mechanism waiting for us to discover as the feature scale in microfluidic devices down to micrometer or even nanometer and the volume down to nanoliters and picoliters or less [17, 44, 177]. These studies provide us some fundamental consideration in the design and optimization of microfluidic devices and also the requirement for the new construction materials for microdevices (e.g., the materials and fabrication technique for microfluidic channels for high pressure and high temperature, the materials and microstructure with highly efficient heat transfer rate at micrometer- or nanometer-thick films).

Particularly, it is more important to find the critical sizes below which the basic principles for bulky fluids based on the continuous media assumption will not be suitable [110, 179]. Therefore, the related viscosity, thermal conductivity, and surface tension have to be reconsidered using the newly developed fluid mechanism and physics principles since the key structure and composition parameters of materials dominating these fluid constants will be changed significantly, leading to the variance in the flow status and mass/heat transfer mechanism, and these fluid laws will not be correct [17, 176, 177, 179]. For an instance, the *Re* ranges indicating the shift from laminar flow to turbulence flow can be reduced significantly in the microchannels, about 300–1500 [176, 178, 180], which is usually in 2000 for the fluid flow in bulky tube. The Nusselt number (*Nu*: representing the dimensionless temperature gradient at the solid surface) of turbulence flow in microchannels is about 5–7 times of that for the bulky fluids [176, 181–185]. Optimization the roughness and shapes of surface patterns can affect the fluid resistance dramatically, leading to a much rapid transition from laminar to turbulence in micro-fluids at a much reduced *Re* [44, 176, 186]. The coefficient of heat transfer can be greatly increased if the surfaces of metal films are micro-patterned. As one consequence, the coefficient of heat transfer can be increased about 4–9 times for the copper films patterned with lots of 270 μm wide and 1000 μm deep grooves by comparing with the copper films of smooth surfaces [176, 181, 182]. Even though the inertia force is inversely proportional to the characteristic length and the viscous force to the square of the characteristic length, the ratio between the inertia force and the viscous force will become

www.ebook3000.com

smaller with the size decrease of devices [42]. As a result, the ratio between the inertia force and the viscous force will be proportional to the Grashof number (*Gr*) in the natural convection, which is different from the result for the macro fluid (it is proportional to the square root of *Gr* (or $Gr^{1/2}$)) [42, 179]. In addition, *Nu* is about equal to $(GrPr)^{1/2}$ at the microscale, and *Nu* is about equal to $(GrPr)^{1/4}$ at the macroscale (*Pr*: Prandtl number, the ratio between the momentum diffusivity and the thermal diffusivity). Therefore, the relative importance criterion for the natural convection and the forced convection will be *Gr*/*Re* for the fluid flow at microscale, but not be *Gr*/*Re* [2] for the fluid flow at the macroscale [42, 179].

Another example is the size-dependent thermal conductivity, which is the heat transfer property of materials and independent of materials sizes. However, as the thickness of thin films is reduced to a critical scale, the thermal conductivity can be reduced with the film thickness. The film thickness-dependent heat conductivity of the commonly used silica for microfluidic devices can refer to Table 2.9 in Chapter 2. As typical materials for heat exchange in microfluidic reactors, or copper films, the thermal conductivity can be reduced from 586 J (m K s)$^{-1}$ for the bulky copper films to 251 J (m K s)$^{-1}$ for the film with thickness of 0.12 μm [179, 182]. The thermal conductivity for the 5 μm thick diamond film can be even reduced to about 1/4 of that for the 30 μm thick film [179, 182]. Theoretical study indicates that the film thickness-dependent thermal conductivity is related to two factors or the characteristic length in the heat transfer and the grain sizes in the films [110, 187]. There are two characteristic lengths: one is the mean free path of particles (λ: depending on the scattering of phonon, electron, impurity, or defect) and the other is the wavelength of the thermal carriers (λ_c). Usually, the thermal transfer complies with the Fourier heat transfer law as the thickness of films (*L*) is far more than λ, where the fluid status is in the macro fluid flow range. As the device length (*L*) is no more than λ, size effects will reduce the phonon transport capacity and the Fourier heat transfer law will be invalid, leading to the micro fluid flow range. As *L* is further reduced less than λ_c, quantum effects have to be considered in the study of the thermal transfer. At the same time, the grain sizes of the films are reduced during the material processing, and the interface among the grains will be increased dramatically, leading to the greatly reduced thermal transport coefficient.

These fundamental progresses sometimes not only boost the design and fabrication of new microfluidic systems and their applications but also promote the progress of the fields related to microfluidics. For example, the reduced *Re* range from laminar flow to turbulence flow transition by the micro-patterned surfaces enlightened the potholed surface pattern design for golf balls to increase their flying speed [181]. The size-dependent law deduced from the study on the convection at microscale, which indicates that the air flow rate and the engine thrust are proportional to the square of the characteristic length, leads to the design and invention of the micro engine with size about 1 mm, which has a thrust–weight ratio of up to 100 : 1, far higher than the traditional engine for airplanes (only about 10 for F119 engine) [42, 179]. This breakthrough theory may favor to supporting the design of the mini type of unmanned aerial vehicle (UAV) of high performance engines in the future. Clearly, theoretical studies in mass, thermal, and momentum and reaction at microscale and nanoscale related

to the microfluidic technology have become important academic and industrial fields to accelerate the technology improvement in electromechanical industry, leisure industry, national defense industry, aeronautic and astronautic industry, and national energy safety.

However, the theory development usually cannot be tested or obtained directly by experiments, whose progress is far less than the experiments decades ago. Direct measurement of fluid status and reaction mechanism at microscale and nanoscale can be done successfully only in some special cases [185, 188]. Thus, most progresses rely on the simulation of the fluid behavior and the performance of microdevices at microscale and/or nanoscale [185, 189]. In particular the use of numerical modeling via, for example, finite difference [6], finite element [9–14], and boundary element methods [15–18] have proved highly successful and then the fluid dynamics theory at micro- and nanoscale develops rapidly in the past decade [43, 178, 183–185, 189, 190].

Microfluidic numerical simulation offers the possibility of solving some system issues for chemistry because the underlying physical properties of microfluidic numerical simulation have led to new chemistry insights. With the development of microfluidic numerical software, the chemistry behavior in microfluidics can be stimulated, which has not been possible with experiment methods [191]. During the last decades, the numerical simulation models adopted for microfluidic investigations have led to a clearer understanding of both the physical and chemical characteristics of the chemistry system. For example, microfluidic numerical simulation has been used to answer fundamental questions in physics including the behavior of single molecules or particles in microreactors used for chemical reaction [192]. In addition, microfluidic numerical simulation is becoming more important for biological applications. Biological researchers were making use of the microfluidic physical phenomena from simulation. As is known to us, the human body is a complex network of molecules, organelles, cells, tissues, and organs: an uncountable number of interactions and transformation center connect all the system's components. In addition to these biological components, the biophysical ones, such as pressure, flow, and morphology, and the location of all of these interactions play an important role in the human body. Technical difficulties have frequently limited researchers from observing cellular biology as it occurs within the human body, but some state-of-the-art microfluidic numerical simulations have revealed distinct cellular behaviors that occur only in the context of the interactions. These types of findings have inspired bioanalytical chemists to provide new tools to better understand these cellular behaviors and interactions. Microfluidics offers an opportunity to understand these insights, and they can control the complexity so researchers can examine critical factors of interest carefully and quantitatively. For example, computational microfluidics plays a vital role in the understanding of drug delivery processes, development of direct drug delivery methods with associated devices, and evaluation of drug delivery efficiency [5]. Moreover, a microfluidic numerical simulation can also be performed to optimize a microfluidic device for DNA isolation [193]. Microfluidic numerical simulations have also been shown to have potential in cell adhesion and detachment [194]. Moreover, microfluidic numerical simulation has been devoted to characterizing and optimizing the microfluidics for biosensors [38] and biosynthesis [195]. Therefore, biological scientists are actively

www.ebook3000.com

adopting and adapting microfluidic numerical simulation. As the numerical simulation matures and becomes more robust, microfluidic numerical simulation that address open needs is progressively being applied to biological questions.

While much work has been done in microfluidic numerical simulation and its biochemistry applications, some challenges still exist on this field [32, 196]. For example, how to accurately deliver drugs to these sites inside the human body while avoiding systemic clearance is still ignored or inadequately addressed. One of the most promising methodologies is the direct drug delivery approach, which target the drugs to the diseased location via a computationally determined patient-specific drug release map. This methodology is applicable to both pulmonary and arterial drug deliveries, which has been numerically simulated and experimentally validated. Nevertheless, some of the challenges need to be addressed in future studies. Moreover, there are gaps in expertise between microfluidic simulations and experiments. The operation and assay design of microfluidic systems might require some understanding of the underlying fundamental physics of mass transport and fluid mechanics from simulation, thus limiting access. At last, not all (or perhaps even many) biological lines of inquiry require microfluidic simulation, and thus biologists will generally prefer to use conventional macroscale tools even though these may be less convenient than to learn and invest in a new method. Given these hurdles, we emphatically acknowledge that widespread dissemination of these microfluidic numerical simulation software will require time, maturation, and commercial availability of the underlying technologies.

Acknowledgments

This work was supported by National S&T Major Project (pre-approved No. SQ2018ZX100301), NSFC (Grant No. 51371018 & 81372425) and the Fundamental Research Funds for the Central University of China (FRF-BR-14-001B).

References

1 deMello, A.J. (2006) Control and detection of chemical reactions in microfluidic systems. *Nature*, **442**, 394–402.
2 Song, Y., Kumar, C.S.S.R., and Hormes, J. (2008) Microfluidic Synthesis of Nanomaterials. *Small*, **4**, 698–711; Wang, J., Song, J. (2017) Microfluidic Synthesis of Nanohybrids. *Small*, **13** (18), 1604084.
3 Amstad, E. *et al.* (2015) Production of amorphous nanoparticles by supersonic spray-drying with a microfluidic nebulator. *Science*, **349**, 956–960.
4 Janasek, D., Franzke, J., and Manz, A. (2006) Scaling and the design of miniaturized chemical-analysis systems. *Nature*, **442**, 374–380.
5 Sackmann, E.K., Fulton, A.L., and Beebe, D.J. (2014) The present and future role of microfluidics in biomedical research. *Nature*, **507**, 181–189.
6 Adamo, A. *et al.* (2016) On-demand continuous-flow production of pharmaceuticals in a compact, reconfigurable system. *Science*, **352**, 61–67.

7 Lv, J.-A. *et al.* (2016) Photocontrol of fluid slugs in liquid crystal polymer microactuators. *Nature*, **537**, 179–185.

8 He, Y., Tsutsui, M., Fan, C., Taniguchi, M., and Kawai, T. (2011) Gate manipulation of DNA capture into nanopores. *ACS Nano*, **5**, 8391–8397.

9 Psaltis, D., Quake, S.R., and Yang, C. (2006) Developing optofluidic technology through the fusion of microfluidics and optics. *Nature*, **442**, 381–386.

10 Campbell, K. *et al.* (2004) A microfluidic 2×2 optical switch. *Appl. Phys. Lett.*, **85**, 6119–6121.

11 deMello, A.J. and Wootton, R.C.R. (2009) Chemistry at the crossroads. *Nat. Chem.*, **1**, 28–29.

12 Utz, M. and Landers, J. (2010) Magnetic resonance and microfluidics. *Science*, **330**, 1056–1058.

13 Fan, X. and Yun, S.-H. (2014) Optofluidic bio-lasers: concept and applications. *Nat. Methods*, **11**, 141–147.

14 Feng, Y., Kleinstreuer, C., Castro, N., and Rostami, A. (2016) Computational transport, phase change and deposition analysis of inhaled multicomponent droplet-vapor mixtures in an idealized human upper lung model. *J. Aerosol Sci.*, **96**, 96–123.

15 Wang, J., Wang, Z., Li, S., Wang, R., and Song, Y. (2017) Surface and interface engineering of FePt/C nanocatalysts for electro-catalytic methanol oxidation: enhanced activity and durability. *Nanoscale*, **9**, 4066–4075.

16 Wen, C.Y., Liang, K.P., Chen, H., and Fu, L.M. (2011) Numerical analysis of a rapid magnetic microfluidic mixer. *Electrophoresis*, **32**, 3268–3276.

17 Squires, T.M. and Quake, S.R. (2005) Microfluidics: fluid physics at the nanoliter scale. *Rev. Mod. Phys.*, **77**, 977–1026.

18 Bazant, M.Z. and Squires, T.M. (2004) Induced-charge electrokinetic phenomena: theory and microfluidic applications. *Phys. Rev. Lett.*, **92**, 066101.

19 Nahavandi, S. *et al.* (2014) Microfluidic platforms for biomarker analysis. *Lab Chip*, **14**, 1496–1514.

20 Zhao, Z., Yang, Y., Zeng, Y., and He, M. (2016) A microfluidic ExoSearch chip for multiplexed exosome detection towards blood-based ovarian cancer diagnosis. *Lab Chip*, **16**, 489–496.

21 Piraino, F., Volpetti, F., Watson, C., and Maerkl, S.J. (2016) A digital-analog microfluidic platform for patient-centric multiplexed biomarker diagnostics of ultralow volume samples. *ACS Nano*, **10**, 1699–1710.

22 Streets, A.M. *et al.* (2015) Microfluidic single-cell whole-transcriptome sequencing. *Proc. Natl. Acad. Sci. U.S.A.*, **111**, 7048–7053.

23 Ibrahim, F., Nozari, A.A., Jahanshahi, P., and Soin, N. (2010) Analysis and experiment of centrifugal force for microfluidic ELISA CD platform. *Biomed. Eng. Sci.*, 466–470.

24 Ottesen, E.A., Hong, J.W., Quake, S.R., and Leadbetter, J.R. (2006) Microfluidic digital PCR enables multigene analysis of individual environmental bacteria. *Science*, **314**, 1464–1467.

25 Elvira, K.S., Casadevall i Solvas, X., Wootton, R.C.R., and deMello, A.J. (2013) The past, present and potential for microfluidic reactor technology in chemical synthesis. *Nat. Chem.*, **5**, 905–915. doi: 10.1038/nchem.1753

www.ebook3000.com

26 Carter, C.F., Baxendale, I.R., O'Brien, M., Pavey, J.B.J., and Ley, S.V. (2009) Synthesis of acetal protected building blocks using flow chemistry with flow IR analysis: preparation of butane-2,3-diacetal tartrates. *Org. Biomol. Chem.*, **7**, 4594–4597. doi: 10.1039/b917289k

27 Wang, Z. *et al.* (2017) Microfluidic synthesis and characterization of FePtSn/C catalysts with enhanced electro-catalytic performance for direct methanol fuel cells. *Electrochim. Acta.*, **230**, 245–254.

28 Gutmann, B., Cantillo, D., and Kappe, C.O. (2015) Continuous-flow technology a tool for the safe manufacturing of active pharmaceutical ingredients. *Angew. Chem. Int. Ed.*, **54**, 6688–6728. doi: 10.1002/anie.201409318

29 Carné-Sánchez, A., Imaz, I., Cano-Sarabia, M., and Maspoch, D. (2013) A spray-drying strategy for synthesis of nanoscale metal-organic frameworks and their assembly into hollow superstructures. *Nat. Chem.*, **5**, 203–211.

30 Brown, A.J. *et al.* (2014) Interfacial microfluidic processing of metal-organic framework hollow fiber membranes. *Science*, **345**, 72–75. doi: 10.1126/science.1251181

31 Ding, X.Q., Zhang, C., Dong, L.M., Wang, C., and Liang, T.X. (2015) Synthesis of TiO_2 nanoparticles using hydrogel as template and TiO_2 microspheres using microfluidic. *J. Inorg. Mater.*, **30**, 605–609.

32 Su, F., Chakrabarty, K., and Fair, R.B. (2006) Microfluidics-based biochips: technology issues, implementation platforms, and design-automation challenges. *IEEE Trans. Comput. Aided Des. Integr. Circuits Syst.*, **25**, 211–223.

33 Haber, C. (2006) Microfluidics in commercial applications: an industry perspectives. *Lab Chip*, **6**, 1118–1121.

34 Point of Care Testing Ltd (2017) Product brochures of the i-STAT®1 blood gas analyser, available at: http://www.poct.co.uk/product.cfm/pID/169 (accessed 16 June 2017).

35 GE Healthcare Life Science (2017) Surface Plasmon Resonance - BiaCore Biosensor., available at: https://proteins.gelifesciences.com/products-for-proteins/spr-systems/

36 Sebastian, V., Arruebo, M., and Santamaria, J. (2014) Reaction engineering strategies for the production of inorganic nanomaterials. *Small*, **10**, 835–853.

37 Paseta, L. *et al.* (2013) Accelerating the controlled synthesis of metal-organic frameworks by a microfluidic approach: a nanoliter continuous reactor. *ACS Appl. Mater. Interfaces*, **5**, 9405–9410.

38 Kim, D.R. and Zheng, X. (2008) Numerical characterization and optimization of the microfluidics for nanowire biosensors. *Nano Lett.*, **8**, 3233–3237.

39 Basciano, C.A., Kleinstreuer, C., Hyun, S., and Finol, E.A. (2011) A relation between near-wall particle-hemodynamics and onset of thrombus formation in abdominal aortic aneurysms. *Ann. Biomed. Eng.*, **39**, 2010–2026.

40 Park, J.I., Saffari, A., Kumar, S., Gunther, A., and Kumacheva, E. (2010) Microfluidic synthesis of polymer and inorganic particulate materials. *Annu. Rev. Mater. Res.*, **40**, 415–443.

41 Tonhauser, C., Natalello, A., Löwe, H., and Frey, H. (2012) Microflow technology in polymer synthesis. *Macromolecules*, **45**, 9551–9570.

42 Ashley, S. (1997) Turbines on a dime. *Mech. Eng.*, **119**, 78–81.

43 Sharp, K.V. and Adrian, R.J. (2004) Transition from laminar to turbulent flow in liquid filled microtubes. *Exp. Fluids*, **36**, 741–747. doi: 10.1007/s00348-003-0753-3

44 Noorian, H., Toghraie, D., and ZAzimian, A.R. (2014) The effects of surface roughness geometry of flow undergoing Poiseuille flow by molecular dynamics simulation. *Heat Mass Transfer*, **50**, 95–104. doi: 10.1007/s00231-013-1231-y

45 Morini, G.L., Lorenzini, M., Salvigni, S., and Spiga, M. (2009) Analysis of laminar-to-turbulent transition for isothermal gas flows in microchannels. *Microfluid. Nanofluid.*, **7**, 181–190.

46 Nightingale, A.M. and deMello, J.C. (2013) Segmented flow reactors for nanocrystal synthesis. *Adv. Mater.*, **25**, 1813–1821.

47 Hartman, R.L., Sahoo, H.R., Yen, B.C., and Jensen, K.F. (2009) Distillation in microchemical systems using capillary forces and segmented flow. *Lab Chip*, **9**, 1843–1849. doi: 10.1039/b901790a

48 Hartman, R.L. and Jensen, K.F. (2009) Microchemical systems for continuous-flow synthesis. *Lab Chip*, **9**, 2495–2507. doi: 10.1039/b906343a

49 Wang, R. *et al.* (2015) A general strategy for nanohybrids synthesis via coupled competitive reactions controlled in a hybrid process. *Sci. Rep.*, **5**, 9189.

50 Venancio-Marques, A. and Baigl, D. (2014) Digital optofluidics: LED-gated transport and fusion of microliter-sized organic droplets for chemical synthesis. *Langmuir*, **30**, 4207–4212.

51 Seemann, R., Brinkmann, M., Pfohl, T., and Herminghaus, S. (2012) Droplet based microfluidics. *Rep. Prog. Phys.*, **75**, 016601.

52 Nightingale, A.M. *et al.* (2013) Large-scale synthesis of nanocrystals in a multichannel droplet reactor. *J. Mater. Chem. A*, **1**, 4067–4076.

53 Lignos, I. *et al.* (2014) Facile droplet-based microfluidic synthesis of monodisperse IV-VI semiconductor nanocrystals with coupled in-line NIR fluorescence detection. *Chem. Mater.*, **26**, 2975–2982.

54 Choi, C.-H., Weitz, D.A., and Lee, C.-S. (2013) One step formation of controllable complex emulsions: from functional particles to simultaneous encapsulation of hydrophilic and hydrophobic agents into desired position. *Adv. Mater.*, **25**, 2536–2541.

55 Tumarkin, E. and Kumacheva, E. (2009) ChemInform abstract: microfluidic generation of microgels from synthetic and natural polymers. *Chem. Soc. Rev.*, **38**, 2161–2168.

56 Haase, M.F. and Brujic, J. (2014) Tailoring of high-order multiple emulsions by the liquid–liquid phase separation of ternary mixtures. *Angew. Chem. Int. Ed.*, **53**, 11793–11797.

57 Sahoo, H.R., Kralj, J.G., and Jensen, K.F. (2007) Multistep continuous-flow microchemical synthesis involving multiple reactions and separations. *Angew. Chem. Int. Ed.*, **46**, 5704–5708.

58 Garcia-Cordero, J.L., Basabe-Desmonts, L., Ducrée, J., and Ricco, A.J. (2010) Liquid recirculation in microfluidic channels by the interplay of capillary and centrifugal forces. *Microfluid. Nanofluid.*, **2010** (4).

www.ebook3000.com

59 Lee, K. *et al.* (2012) Gravity-oriented microfluidic device for cell spheroid formation. *Biomicrofluidics*, **6**, 14114–141147.
60 Yamada, H. *et al.* (2008) Fabrication of gravity-driven microfluidic device. *Rev. Sci. Instrum.*, **79**, 124301.
61 Yao, B. *et al.* (2004) A microfluidic device based on gravity and electric force driving for flow cytometry and fluorescence activated cell sorting. *Lab Chip*, **4**, 603–607.
62 Wu, Z. and Li, D. (2008) Micromixing using induced-charge electrokinetic flow. *Electrochim. Acta*, **53**, 5827–5835.
63 Liang, H., Junmei, W., and Song, Y. (2017) Magnetic field controlled microfluidic synthesis of magnetic and optical nanocrystals, unpublished data.
64 Shikida, M., Takayanagi, K., Inouchi, K., Honda, H., and Sato, K. (2006) Using wettability and interfacial tension to handle droplets of magnetic beads in a micro-chemical-analysis system. *Sens. Actuators, B*, **113**, 563–569.
65 Zhang, K. *et al.* (2009) On-chip manipulation of continuous picoliter-volume superparamagnetic droplets using a magnetic force. *Lab Chip*, **9**, 2992–2999.
66 Ashkin, A. and Dziedzic, J.M. (1973) Radiation pressure on a free liquid surface. *Phys. Rev. Lett.*, **30**, 139–142.
67 Ashkin, A. (1997) Optical trapping and manipulation of neutral particles using lasers. *Proc. Natl. Acad. Sci. U.S.A.*, **94**, 4853–4860.
68 Ichimura, K., Oh, S.-K., and Nakagawa, M. (2000) Light-driven motion of liquids on a photoresponsive surface. *Science*, **288**, 1624–1626.
69 Kotz, K.T., Gu, Y., and Faris, G.W. (2005) Optically addressed droplet-based protein assay. *J. Am. Chem. Soc.*, **127**, 5736–5737.
70 Diguet, A. *et al.* (2009) Photomanipulation of a droplet by the chromocapillary effect. *Angew. Chem. Int. Ed.*, **48**, 9281–9284.
71 Mitani, S. and Sakai, K. (2005) Observation of interfacial tension minima in oil-water-surfactant systems with laser manipulation technique. *Faraday Discuss.*, **129**, 141–153.
72 Yang, D. *et al.* (2007) Photon control of liquid motion on reversibly photoresponsive surfaces. *Langmuir*, **23**, 10864–10872.
73 Chiou, P.Y., Moon, H., Toshiyoshi, H., Kim, C.-J., and Wu, M.C. (2003) Light actuation of liquid by optoelectrowetting. *Sens. Actuators, A*, **104**, 222–228.
74 Park, S.-Y., Teitell, M.A., and Chiou, E.P.Y. (2010) Single-sided continuous optoelectrowetting (SCOEW) for droplet manipulation with light patterns. *Lab Chip*, **10**, 1655–1661.
75 Oroszi, L., Dér, A., Kirei, H., Ormos, P., and Rakovics, V. (2006) Control of electro-osmotic flow by light. *Appl. Phys. Lett.*, **89**, 263508.
76 Lee, J.N., Park, C., and Whitesides, G.M. (2003) Solvent compatibility of poly(dimethylsiloxane)-based microfluidic devices. *Anal. Chem.*, **75**, 6544–6554. doi: 10.1021/ac0346712
77 Willis, P.A. *et al.* (2007) Monolithic Teflon (R) membrane valves and pumps for harsh chemical and low-temperature use. *Lab Chip*, **7**, 1469–1474. doi: 10.1039/b707892g
78 Song, Y. and Henry, L.L. (2009) Nearly monodispersion CoSm nanoparticles synthesized by a microfluidic reactor. *Nanoscale Res. Lett.*, **4**, 1130–1134.

79 Eckel, Z.C. *et al.* (2016) Additive manufacturing of polymer-derived ceramics. *Science*, **351**, 58–62.

80 Zanchetta, E. *et al.* (2015) Stereolithography of SiOC ceramic microcomponents. *Adv. Mater.*, **28**, 370–376.

81 Ren, K., Zhou, J., and Wu, H. (2013) Materials for microfluidic chip fabrication. *Acc. Chem. Res.*, **46**, 2396–2406.

82 Santaniello, T. *et al*. A room-temperature bonding technique for the packaging of hydrogel-based hybrid microfluidic devices. *Microfluid. Nanofluid.* **19**, 31-41, doi:10.1007/s10404-015-1544-x.

83 Marre, S. and Jensen, K.F. (2010) Synthesis of micro and nanostructures in microfluidic systems. *Chem. Soc. Rev.*, **39**, 1183–1202.

84 Whitesides, G.M. (2006) The origins and the future of microfluidics. *Nature*, **442**, 368–373.

85 Chiou, P.Y., Park, S.-Y., and Wu, M.C. (2008) Continuous optoelectrowetting for picoliter droplet manipulation. *Appl. Phys. Lett.*, **93**, 221110.

86 Jensen, K.F. (2006) Silicon-based microchemical systems: characteristics and applications. *MRS Bull.*, **31**, 101–107.

87 Gravesen, P., Branebjerg, J., and Jensen, O.S. (1993) Microfluidics-a review. *J. Micromech. Microeng.*, **3**, 168–182.

88 Narasimhan, J. and Papautsky, I. (2004) Polymer embossing tools for rapid prototyping of plastic microfluidic devices. *J. Micromech. Microeng.*, **14**, 96–103.

89 Miserere, S. *et al.* (2012) Fabrication of thermoplastics chips through lamination based techniques. *Lab Chip*, **12**, 1849–1856.

90 Misawa, H.E. and Juodkazis, S.E. (2006) *3D Laser Microfabrication: Principles and Applications*, John Wiley & Sons, Inc., p. 403.

91 Sugioka, K., Meunier, M., and Piqué, A. (2010) *Laser Precision Microfabrication*, vol. **135**, Springer, Berlin Heidelberg.

92 Ozbay, E. (2006) Plasmonics: merging photonics and electronics at nanoscale dimensions. *Science*, **311**, 189–193.

93 Wang, L. *et al.* (2006) A large format membrane-based x-ray mask for microfluidic chip fabrication. *J. Micromech. Microeng.*, **16**, 402–406.

94 Kumar, G., Tang, H.X., and Schroers, J. (2009) Nanomoulding with amorphous metals. *Nature*, **457**, 868–872.

95 Li, J., Zhang, W., Song, Y., Yin, W., and Zhang, T. (2016) Template transfer nanoimprint for uniform nanopores and nanopoles. *J. Nanomater.*, **2016**, Article ID 9354364.

96 Tsao, C.W. and DeVoe, D.L. (2009) Bonding of thermoplastic polymer microfluidics. *Microfluid. Nanofluid.*, **6**, 1–16.

97 Waheed, S. *et al.* (2016) 3D printed microfluidic devices: enablers and barriers. *Lab Chip*, **16**, 1993–2013.

98 Parekh, D.P., Ladd, C., Panich, L., Moussa, K., and Dickey, M.D. (2016) 3D printing of liquid metals as fugitive inks for fabrication of 3D microfluidic channels. *Lab Chip*, **16**, 1812–1820.

99 Lima, R.S. *et al.* (2015) Sacrificial adhesive bonding: a powerful method for fabrication of glass microchips. *Sci. Rep.*, **5**, 13276.

www.ebook3000.com

100 Lee, C.-Y., Lei, K.F., Tsai, S.-W., and Tsang, N.-M. (2016) Development of graphene-based sensors on paper substrate for the measurement of pH value of analyte. *Biochip J.*, **10**, 182–188.

101 Bhattacharjee, N., Urrios, A., Kang, S., and Folch, A. (2016) The upcoming 3D-printing revolution in microfluidics. *Lab Chip*, **16**, 1720–1742.

102 Ho, C.M.B., Ng, S.H., Li, K.H.H., and Yoon, Y.-J. (2015) 3D printed microfluidics for biological applications. *Lab Chip*, **15**, 3627–3637.

103 Wang, J., Zhao, H., Zhu, Y., and Song, Y. (2017) Shape-controlled synthesis of CdSe nanocrystals via a programmed microfluidic process. *J. Phys. Chem. C*. doi: 10.1021/acs.jpcc.6b10901

104 Cantillo, D., Sheibani, H., and Kappe, C.O. (2012) Flash flow pyrolysis: mimicking flash vacuum pyrolysis in a high-temperature/high-pressure liquid-phase microreactor environment. *J. Org. Chem.*, **77**, 2463–2473.

105 Song, Y., Kumar, C.S.S.R., and Hormes, J. (2004) Fabrication of SU-8 based microfluidic reactor on a PEEK substrate sealed by a 'flexible semi-solid transfer'(FST) process. *J. Micromech. Microeng.*, **14**, 932–940.

106 Shen, X. *et al.* (2014) Spatiotemporal-resolved nanoparticle synthesis via simple programmed microfluidic processes. *RSC Adv.*, **4**, 34179–34188. doi: 10.1039/C4RA04168B

107 Lin, F. *et al.* (2008) Petal effect: a superhydrophobic state with high adhesive force. *Langmuir*, **24**, 4114–4119.

108 Giacomello, A., Chinappi, M., Meloni, S., and Casciola, C.M. (2012) Metastable wetting on superhydrophobic surfaces: continuum and atomistic views of the Cassie-Baxter-Wenzel transition. *Phys. Rev. Lett.*, **109**, 765–781.

109 Song, Y., Sun, S., Zhang, T., Jin, P., and Han, L. (2010) Synthesis of worm and chain-like nanoparticles by a microfluidic reactor process. *J. Nanopart. Res.*, **12**, 2689–2697.

110 Tien, C.L., Majumdar, A., and Gemer, F.M. (1998) *Microscale Energy Transport*, 1st edn, CRC Press, Taylor & Francis, p. 400.

111 Hartman, R.L., McMullen, J.P., and Jensen, K.F. (2011) Deciding whether to go with the flow: evaluating the merits of flow reactors for synthesis. *Angew. Chem. Int. Ed.*, **50**, 7502–7519. doi: 10.1002/anie.201004637

112 Wakami, H. and Yoshida, J. (2005) Grignard exchange reaction using a microflow system: from bench to pilot plant. *Org. Process Res. Dev.*, **9**, 787–791. doi: 10.1021/op0501500

113 Song, Y.J., Sun, Q.Q., Zhang, T., Jin, P.Y., and Han, L. (2010) Synthesis of boron nitride nanotubes by an oxide-assisted chemical method. *J. Nanopart. Res.*, **12**, 2689–2697. doi: 10.1007/s11051-010-0012-5

114 Mason, B.P., Price, K.E., Steinbacher, J.L., Bogdan, A.R., and McQuade, D.T. (2007) Greener approaches to organic synthesis using microreactor technology. *Chem. Rev.*, **107**, 2300–2318. doi: 10.1021/cr050944c

115 Schubert, K. *et al.* (2001) Microstructure devices for applications in thermal and chemical process engineering. *Microscale Thermophys. Eng.*, **5**, 17–39.

116 Tugulu, S. and Klok, H.-A. (2008) Stability and nonfouling properties of poly(poly(ethylene glycol) methacrylate) brushes under cell culture conditions. *Biomacromolecules*, **9**, 906–991.

117 Barbey, R. and Klok, H.-A. (2010) Room temperature, aqueous post-polymerization modification of glycidyl methacrylate-containing polymer brushes prepared via surface-initiated atom transfer radical polymerization. *Langmuir*, **26**, 18219–18230.

118 Barbey, R., Kauffmann, E., Ehrat, M., and Klok, H.-A. (2010) Protein microarrays based on polymer brushes prepared via surface-initiated atom transfer radical polymerization. *Biomacromolecules*, **11**, 3467–3479.

119 Jucius, D. *et al.* (2015) Highly hydrophilic poly(ethylene terephthalate) films prepared by combined hot embossing and plasma treatment techniques. *Appl. Surf. Sci.*, **349**, 200–210. doi: 10.1016/j.apsusc.2015.04.221

120 Bu, X. *et al.* (2016) Surface Modification of C_3N_4 through oxygen-plasma treatment: a simple way toward excellent hydrophilicity. *ACS Appl. Mater. Interfaces*, **8**, 31419–31425.

121 Blow, N. (2009) Microfluidics: the great divide. *Nat. Methods*, **6**, 684–686.

122 Craighead, H. (2006) Future lab-on-a-chip technologies for interrogating individual molecules. *Nature*, **442**, 387–393.

123 Shembekar, N., Chaipan, C., Utharala, R., and Merten, C.A. (2016) Droplet-based microfluidics in drug discovery, transcriptomics and high-throughput molecular genetics. *Lab Chip*, **16**, 1314–1331. doi: 10.1039/c6lc00249h

124 Chen, J., Li, J., and Sun, Y. (2012) Microfluidic approaches for cancer cell detection, characterization, and separation. *Lab Chip*, **12**, 1753–1767.

125 Xu, B.-Y., Hu, S.-W., Qian, G.-S., Xu, J.-J., and Chen, H.-Y. (2013) A novel microfluidic platform with stable concentration gradient for on chip cell culture and screening assays. *Lab Chip*, **13**, 3714–3720.

126 Matsuda, H. (1967) Theory of the steady-state current potentials curves of redox electrodes reactions in hydrodynamic voltametry II laminar pipe-and channel-flows. *J. Electroanal. Chem.*, **15**, 325–336.

127 Compton, R.G., Pilkington, M.B., and Stearn, G.M. (1988) Mass transport in channel electrodes. The application of the backwards implicit method to electrode reactions (EC, ECE and DISP) involving coupled homogeneous kinetics. *J. Chem. Soc., Faraday Trans. 1 F*, **84**, 2155–2171.

128 Ke, N., Wang, X., Xu, X., and Abassi, Y.A. (2011) *The xCELLigence System for Real-Time and Label-Free Monitoring of Cell Viability*, vol. **740**, Humana Press.

129 Tang, C.K., Vaze, A., Shen, M., and Rusling, J.F. (2016) High-throughput electrochemical microfluidic immunoarray for multiplexed detection of cancer biomarker proteins. *ACS Sens.*, **1**, 1036–1043.

130 Castano-Álvarez, M. *et al.* (2009) Fabrication of SU-8 based microchip electrophoresis with integrated electrochemical detection for neurotransmitters. *Talanta*, **80**, 24–30.

131 Warkiani, M.E. *et al.* (2014) Slanted spiral microfluidics for the ultra-fast, label-free isolation of circulating tumor cell. *Lab Chip*, **14**, 128–137.

132 Saylor, R.A. and Lunte, S.M. (2015) A review of microdialysis coupled to microchip electrophoresis for monitoring biological events. *J. Chromatogr. A*, **1382**, 48–64. doi: 10.1016/j.chroma.2014.12.086

www.ebook3000.com

133 Kuhlmann, E. *et al.* (2011) Medicine and management in European health-care systems: how do they matter in the control of clinical practice? *Int. J. Clin. Pract.*, **65**, 722–724.

134 Delville, J.-P. *et al.* (2009) Laser microfluidics: fluid actuation by light. *J. Opt. A: Pure Appl. Opt.*, **11**, 034015.

135 Cacho-Bailo, F. *et al.* (2015) Metal-organic framework membranes on the inner-side of a polymeric hollow fiber by microfluidic synthesis. *J. Membr. Sci.*, **476**, 277–285. doi: 10.1016/j.memsci.2014.11.016

136 Khan, S.A. and Duraiswamy, S. (2012) Controlling bubbles using bubbles-microfluidic synthesis of ultra-small gold nanocrystals with gas-evolving reducing agents. *Lab Chip*, **12**, 1807–1812.

137 Nie, Z., Li, W., Seo, M., Xu, S., and Kumacheva, E. (2006) Janus and Ternary particles generated by microfluidic synthesis: design, synthesis, and self-assembly. *J. Am. Chem. Soc.*, **128**, 9408–9412.

138 Phillips, T.W., Lignos, I.G., Maceiczyk, R.M., deMello, A.J., and deMello, J.C. (2014) Nanocrystal synthesis in microfluidic reactors: where next? *Lab Chip*, **14**, 3172–3180. doi: 10.1039/C4LC00429A

139 Choi, C.-H. *et al.* (2016) Triple emulsion drops with an ultrathin water layer: high encapsulation efficiency and enhanced cargo retention in microcapsules. *Adv. Mater.*, **28**, 3340–3344.

140 Erdem, E.Y., Cheng, J.C., Doyle, F.M., and Pisano, A.P. (2014) Multi-temperature zone, droplet-based microreactor for increased temperature control in nanoparticle synthesis. *Small*, **10**, 1076–1080.

141 Duraiswamy, S. and Khan, S.A. (2009) Droplet-based microfluidic synthesis of anisotropic metal nanocrystals. *Small*, **5**, 2828–2834.

142 Abou-Hassan, A., Bazzi, R., and Cabuil, V. (2009) Multistep continuous-flow microsynthesis of magnetic and fluorescent g-Fe_2O_3@SiO_2 core/shell nanoparticles. *Angew. Chem. Int. Ed.*, **48**, 7180–7183.

143 Chan, E.M., Alivisatos, A.P., and Mathies, R.A. (2006) High-temperature microfluidic synthesis of CdSe nanocrystals in nanoliter droplets. *J. Am. Chem. Soc.*, **127**, 13854–13861.

144 Nakamura, H. *et al.* (2004) Application of a microfluidic reaction system for CdSe nanocrystal preparation: their growth kinetics and photoluminescence analysis. *Chem. Commun.*, 48–49.

145 Krishnadasan, S., Tovilla, J., Vilar, R., deMello, A.J., and deMello, J.C. (2004) On-line analysis of CdSe nanoparticle formation in a continuous flow chip-based microreactor. *J. Mater. Chem.*, **14**, 2655–2660.

146 Ohm, C. *et al.* (2011) Microfluidic synthesis of highly shape-anisotropic particles from liquid crystalline elastomers with defined director field configurations. *J. Am. Chem. Soc.*, **133**, 5305–5311.

147 Paseta, L., Potier, G., Sorribas, S., and Coronas, J. (2016) Solventless synthesis of MOFs at high pressure. *ACS Sustainable Chem. Eng.*, **4**, 3780–3785.

148 Wang, H. *et al.* (2005) Highly luminescent CdSe/ZnS nanocrystals synthesized by a single molecular ZnS source in a microfluidic reactor. *Adv. Funct. Mater.*, **15**, 603–608.

149 Zheng, B., Roach, L.S., and Ismagilov, R.F. (2003) Screening of protein crystallization conditions on a microfluidic chip using nanoliter-size droplet. *J. Am. Chem. Soc.*, **125**, 11170–11171.

150 Bremholm, M., Jensen, H., Iversen, S.B., and Iversen, B.B. (2008) Reactor design for *in situ* X-ray scattering studies of nanoparticle formation in supercritical water syntheses. *J. Supercrit. Fluids*, **44**, 385–390. doi: 10.1016/j.supflu.2007.09.029

151 Bøjesen, E.D. *et al.* (2014) In situ powder diffraction study of the hydrothermal synthesis of ZnO nanoparticles. *Cryst. Growth Des.*, **14**, 2803–2810. doi: 10.1021/cg5000606

152 Chan, K.L. and Kazarian, S.G. (2012) FT-IR spectroscopic imaging of reactions in multiphase flow in microfluidic channels. *Anal. Chem.*, **84**, 4052–4056. doi: 10.1021/ac300019m

153 Song, Y. *et al.* (2005) Investigations into sulfobetaine-stabilized Cu nanoparticle formation: toward development of a microfluidic synthesis. *J. Phys. Chem. B*, **109**, 9330–9338.

154 Song, Y. *et al.* (2006) Microfluidic synthesis of cobalt nanoparticles. *Chem. Mater.*, **18**, 2817–2827.

155 Squires, T.M. and Bazant, M.Z. (2004) Induced-charge electro-osmosis. *J. Fluid Mech.*, **509**, 217–252.

156 Gordon, J., Kazemian, H., and Rohani, S. (2012) Rapid and efficient crystallization of MIL-53(Fe) by ultrasound and microwave irradiation. *Microporous Mesoporous Mater.*, **162**, 36–43.

157 Cybinska, J., Lorbeer, C., Zych, E., and Mudring, A.-V. (2011) Ionic liquid-based synthesis – a low-temperature route to nanophosphates. *ChemSusChem*, **4**, 595–598.

158 Cantillo, D. *et al.* (2014) Sequential nitration/hydrogenation protocol for the synthesis of triaminophloroglucinol: safe generation and use of an explosive intermediate under continuous-flow conditions. *Org. Process Res. Dev.*, **18**, 1360–1366.

159 Acke, D.R.J. and Stevens, C.V. (2007) A HCN-based reaction under microreactor conditions: industrially feasible and continuous synthesis of 3,4-diamino-1H-isochromen-1-ones. *Green Chem.*, **9**, 386–390.

160 Baumann, M., Baxendale, I.R., Martin, L.J., and Ley, S.V. (2009) Development of fluorination methods using continuous-flow microreactors. *Tetrahedron*, **65**, 6611–6612.

161 Marcus, J.S., Anderson, W.F., and Quake, S.R. (2006) Parallel picoliter RT-PCR assays using microfluidics. *Anal. Chem.*, **78**, 956–958.

162 Larrea, A., Sebastian, V., Ibarra, A., Arruebo, M., and Santamaria, J. (2015) Gas slug microfluidics: a unique tool for ultrafast, highly controlled growth of iron oxide nanostructures. *Chem. Mater.*, **27**, 4254–4260.

163 Song, Y., Li, R., Sun, Q., and Jin, P. (2011) Controlled growth of Cu nanoparticles by a tubular microfluidic reactor. *Chem. Eng. J.*, **168**, 477–484.

164 Song, Y., Ding, J., and Wang, Y. (2012) Shell dependent evolution of optical and magnetic properties of Co@Au core–shell nanoparticles. *J. Phys. Chem. C*, **116**, 11343–11350.

www.ebook3000.com

165 He, S. *et al.* (2005) Effects of interior wall on continuous fabrication of silver nanoparticles in microcapillary reactor. *Chem. Lett.*, **34**, 748–749.

166 Wang, J. *et al.* (2015) Microfluidic synthesis of ultra-small magnetic nanohybrids for enhanced magnetic resonance imaging. *J. Mater. Chem. C*, **3**, 12418–12429.

167 Ye, B. *et al.* (2013) Fabrication of size-controlled CeO_2 microparticles by a microfluidic sol–gel process as an analog preparation of ceramic nuclear fuel particles. *J. Nucl. Sci. Technol.*, **50**, 774–780.

168 Khan, S.A., Günthe, A., Schmidt, M.A., and Jensen, K.F. (2004) Microfluidic synthesis of colloidal silica. *Langmuir*, **20**, 8604–8611.

169 Wyżkiewicz, I. *et al.* (2007) A new technology for microfluidic structures preparation based on a photoimageable ceramic. *Microsyst. Technol.*, **13**, 657–661.

170 Kong, T., Liu, Z., Song, Y., Wang, L., and Shum, H.C. (2013) Engineering polymeric composite particles by emulsion-templating: thermodynamics versus kinetics. *Soft Matter*, **9**, 9780–9784.

171 Khaled, S.M., Sui, R., Charpentier, P.A., and Rizkalla, A.S. (2007) Synthesis of TiO_2 -PMMA nanocomposite: using methacrylic acid as a coupling agent. *Langmuir*, **23**, 3988–3995.

172 Biswal, B.P., Bhaskar, A., Banerjee, R., and Kharul, U.K. (2015) Selective interfacial synthesis of metal-organic frameworks on a polybenzimidazole hollow fiber membrane for gas separation. *Nanoscale*, **7**, 7291–7298. doi: 10.1039/c5nr00299k

173 Maspoch Comamala, D., Imaz, I., Carné-Sánchez, A., and Cano-Sarabia, A.M. (2013) *Method for the preparation of metal organic frameworks.*

174 Nair, S., Brown, A.J., Brunelli, N.A., and Jones, C. (2014) Flow processing and characterization of metal-organic framework (MOF) membranes in hollow fiber and tubular modules. US Patent US2014336435

175 Yin, Y. and Alivisatos, A.P. (2006) Colloidal nanocrystal synthesis and the organic-inorganic interface. *Nature*, **437**, 664–670.

176 Jiang, J., Hao, Y., and SHi, M. (2006) Experimental study on flow and heat transfer characteristics in rectangular microchannel (in Chinese). *J. Therm. Sci. Technol.*, **5**, 189–194.

177 Pethig, R.R. and Smith, S. (2013) *Introductory Bioelectronics: For Engineers and Physical Scientists*, John Wiley and Sons, Ltd, p. 462.

178 Jayaraj, S., Kang, S., and Suh, Y.K. (2007) *J. Mech. Sci. Technol.*, **21**, 536–548. doi: 10.1007/BF02916316

179 Guo, Z. (2000) Frontier of heat transfer-microscale heat transfer (in Chinese). *Adv. Mech.*, **30**, 1–6.

180 Harm, T.M. *et al.* (1997) Experimental investigation of heat transfer and pressure drop through deep microchannels in A (110) silicon substrate. Proceedings of the ASME Heat Transfer Division, New York ASME, Vol. 1, pp. 347-357.

181 Ravigururajan, T.S., Cuta, J., McDonald, C.E., and Drost, M.K. (1996) Single-phase Flow Thermal Performance Characteristics of a Parallel MicroChannel Heat Exchanger. *J. Enhanc. Heat Transf.*, **6**, 383–393.

182 Duncan, B. and Peterson, G.P. (1994) Review of microscale heat transfer. *Appl. Mech. Rev.*, **47**, 397–427.

183 Gholami, H., Banaei, M., and Eskandari, A. (2013) Investigation of effect of triangular rib in heat transfer of finned rectangular microchannel with extended surfaces. *Life Sci. J.*, **10**, 206–211.

184 Yadav, V., Baghel, K., Kumar, R., and Kadam, S.T. (2016) Numerical investigation of heat transfer in extended surface microchannels. *Int. J. Heat Mass Transfer*, **93**, 612–622.

185 Deng, D., Wan, W., Tang, Y., Shao, H., and Huang, Y. (2015) Experimental and numerical study of thermal enhancement in reentrant copper microchannels. *Int. J. Heat Mass Transfer*, **91**, 656–670.

186 Pfahler, J., Harlay, J., and Bau, H. (1991) Gas and liquid flow in small channels in microtubes. ASME DSC: Microstructures, Sensors and Actuators. New York ASME, Vol. 32, pp. 123-134.

187 Chen, Y.-F., Liu, Y., and Wang, P.-J. (2008) Research progress of micro-scale heat transfer theory. *J. Univ. Jinan (Sci. Tech., in Chinese)*, **22**, 102–106.

188 Xu, S., Yue, X., and Hou, J. (2007) Experimental investigation on flow characteristics of deionized water in microtubes. *Chin. Sci. Bull.*, **52**, 849–854. doi: 10.1007/s11434-007-0118-z

189 Chai, L., Xia, G.D., and Wang, H.S. (2016) Numerical study of laminar flow and heat transfer in microchannel heat sink with offset ribs on sidewalls. *Appl. Therm. Eng.*, **92**, 32–41.

190 Gong, S. and Cheng, P. (2014) Numerical investigation of saturated flow boiling in microchannels by the lattice Boltzmann method. *Numer. Heat Transfer, Part A*, **65**, 644–661.

191 Hinsmann, P., Frank, J., Svasek, P., Harasek, M., and Lendl, B. (2001) Design, simulation and application of a new micromixing device for time resolved infrared spectroscopy of chemical reactions in solution. *Lab Chip*, **1**, 16–21.

192 Ehrfeld, W., Hessel, V., and Löwe, H. (2005) *Microreactors: New Technology for Modern Chemistry*, Wiley-VCH Verlag GmbH & Co. KGaA, Weinheim.

193 Hale, C. and Darabi, J. (2014) Magnetophoretic-based microfluidic device for DNA isolation. *Biomicrofluidics*, **8**, 044118.

194 Bai, B., Luo, Z., Lu, T., and Xu, F. (2013) Numerical simulation of cell adhesion and detachment in microfluidics. *J. Mech. Med. Biol.*, **13**, 155–167.

195 Huang, H. and Densmore, D. (2014) Integration of microfluidics into the synthetic biology design flow. *Lab Chip*, **14**, 3459–3474.

196 Huang, Y., Williams, J.C., and Johnson, S.M. (2012) Brain slice on a chip: opportunities and challenges of applying microfluidic technology to intact tissues. *Lab Chip*, **12**, 2103–2117.

www.ebook3000.com

Index

a

Abbott i-STAT analyzer 14
acid-nitrile exchange reaction 356, 357
adaptive packed-bed microfluidic process optimization 364
adhesive bonding 127
affinity-based CTC enrichment
  CTC-Chip 243
  CTC-iChip 244–245
  CTC subpopulation sorting 247
  GEDI 243–244
  GO chip 246–247
  HB-chip 244
  HTMSU 245–246
  NanoVelcro rare cell assays 246
  OncoBean Chip 246
Ag@ZnO composites 459, 460
alternating current (AC) voltammetry 213
aluminophosphate material 480
amino acids 273
amperometric protocol 216–219
anisotropic microparticle formation 397
anodic bonding 119
ApoStream (ApoCell) 252
Applied Biosystems SOLiDTM system 301
aptamer 266
Archimedes number 50
ascaridole synthesis 362
atto594-labeled 20-oligmer nucleotide 289
Atwood number 51
Au core–shell composites 457, 459
Au core–shell magnetic-plasmonic composites 466
Auto ChIP platform 284

b

Bernoulli's equation 44
β-galactosidase (β-gal) 289
BIA-core microfluidic platform 522
bio-MOF capsules 484
biomarker proteins 261
Biot number 54
biphasic interfacial MOF synthesis 485
blood 313
Blue Gene/L system 166
B220 marker 291
Bond number/Eötvös number 51
bonding process 117–119
Brinkman number 55
Brownian diffusion 314

c

capacitive sensing 195
capillary effects 63
capillary electrochromatography (μ-CEC) 223
capillary number (Ca) 50, 377
capped gold nano-slit surface plasmonic resonance (SPR) sensor 267
carbon monoxide (CO) 367
carbon paste electrode (CPE) 218
carbon supported composite synthesis 461–463
carbonylation Sonogashira reaction 367

Microfluidics: Fundamentals, Devices and Applications, First Edition.
Edited by Yujun Song, Daojian Cheng, and Liang Zhao.
© 2018 Wiley-VCH Verlag GmbH & Co. KGaA. Published 2018 by Wiley-VCH Verlag GmbH & Co. KGaA.

carboxylate-based MOFs 481
casein kinase I 353
catalytic hydrogenation 366
catechol 213
catheter-based intravascular drug delivery
  particle hemodynamics 331–332
  tissue heat and mass transfer 332–333
CD31 protein 287
CdSe/ZnS composite synthesis 456
Ce-BDC MOF 487
cell-based assays 11–14
cell detection 269–272
centrifuge number 51
ceramic based microfluidic devices 519
CFD-ACE+ software 162
CFX Expression Language (CEL) 162
CFX software 162–164
Chapman–Enskog theory 30
chip-based microfluidic reactor
  advantages 363
  for organic synthesis 360–363
chip-based simple programmed microfluidic processes (C-SPMPs) 412, 452
chromatin immunoprecipitation (ChIP) 283
circle-to-circle amplification (C2CA) 281
circulating tumor cells (CTCs)
  CellSearch platform 238
  CTC-chip 243
  CTC-iChip 244–245
  CTC subpopulation sorting 247
  deterministic lateral displacement 250
  dielectrophoresis and acoustophoresis 251–252
  epithelial to mesenchymal transition 241
  GEDI 243–244
  GO chip 246–247
  herringbone chip 244
  HTMSU 245–246
  isolation by size of epithelial tumor cells (ISET) 238
  limitations 253
  microfluidic devices 239
  microfluidic filtration 249–250
  microfluidic spiral separation 250–251
  multiorifice flow fractionation 251
  NanoVelcro rare cell assays 246
  OncoBean Chip 246
  polydimethylsiloxane 238
  screening for early cancer detection 238
  (SWOG) S0500 clinical trial 239
  synthetic DNA/RNA oligonucleotide ligands 241
  vortex platform 251
closed DMF systems 179
clotrimazole amorphous drug 356
Co@Au nanoparticles 434, 436
coaxial microfluidic reactors 487
cobalt (Co) nanocrystal synthesis 422, 423
coflowing microfluidics 379
coiled tubing microreactor, for organic synthesis 356–360
color function volume-of-fluid (CF-VOF) method 156
compact disc (CD)-based microfluidic device 10
complex microparticle formation 380
composites
  description 445
  formation mechanism 445, 451–452
  preparation, *see* microfluidic process
composites computational fluid-particle dynamics (CF-PD) 319
computational fluid dynamics (CFD) 160–161
computational microfluidics 528
  ferrofluid dynamics 315
  flow through porous media 316–317
  fluid–particle dynamics modeling 313–315
  fluid–structure interaction 317–318
  governing equations 312

www.ebook3000.com

intravascular drug delivery, *see* intravascular drug delivery
model closure 312–313
nonspherical particle dynamics 316
pulmonary drug delivery, *see* pulmonary drug delivery
turbulence modeling 313
ComsolMultiphysics 229
conductivity protocol 221–223
conservative level set (C-LS) method 156
contact angle saturation 183
continuous flow reactors 405
continuous/laminar flow 421
continuum method (CM) 155–158
coprecipitation method 406
core alloying and shell gradient doping strategy 414
core–shell magnetic nanomaterial, synthesis of 414–415
CoSm alloy nanocrystals, IRCPM process 423
Couette flow 22
C-reactive protein (CRP) 218
CTC-chip 243
CTC-iChip 244–245
cytochrome P450 gene 283

d

D-amino acids 273
Damköhler number (Da) 49
Deborah number 52
de Broglie thermal wavelength 150
dense discrete phase model (DDPM) 314
DEP field-flow fractionation (DEPFFF) device 252
deterministic lateral displacement (DLD) 250
dextran-coated superparamagnetic iron oxide (SPIO) NPs 409
diamond-shaped microfluidic aggregation chamber 155
dicarboxylate MIL-88B(Fe) crystallization, segmented flow synthesis 482
dielectric–plasmonic composites, synthesis of 457–459
dielectrophoresis (DEP) 183
dielectrophoresis and acoustophoresis 251–252
diethy-laminosulfur trifluorid (DAST) 360
digital microfluidic (DMF) system 5
approach 213
analytical models 184
chemical and biological applications 199–201
chip fabrication techniques 179–181
controlling and addressing the signals 197–198
different electrode configurations 181–183
droplet metering and dispensing techniques 188–189
droplet routing algorithms 195
droplet sensing techniques 195, 196
effect of the gap height 189–190
electrical signals 185–188
electromechanical and energy based models 183
feedback control 192–195
numerical models 184
prospects of portability 199, 200
types 177–179
digital polymerase chain reaction (digital-PCR) 296
2,3-dihydroxybenzoic acid 219
2,5-dihydroxybenzoic acid 219
dimensionless numbers 377
dimethylitaconate hydrogenation 364
dinitro-herbicide, synthesis of 362
direct drug delivery 335–338, 529
direct simulation Monte Carlo method (DSMC) 151–153
direct tumor-targeting methodology 332
discrete element method (DEM) 314
dissipative particle dynamics (DPD) 153–155
macroscopic hydrodynamic equations 154

d-leucine (d-Leu) 273, 275
d-methionine (d-Met) 273, 275
DNA assays 6–9
dried blood spot analysis 201
dripping 378
DropBot 195
droplet and ionic liquid assisted microfluidic (DIM) synthesis method 480
droplet based microreactors, magnetic iron oxide based nanomaterial synthesis 408
droplet metering and dispensing techniques 188–189
droplet routing algorithms 195
droplet sensing techniques 195, 196
drug–aerosol dynamics 322–323
dry etching method 117
dry powder inhaler (DPI) 319

e

Eckert number 55
E. coli lac-Z gene expression pattern 289
Ekman number 52
electrical signals, DMF
  effect of changing frequency 187–188
  types of signals 185–186
electrochemical analysis
  amperometric protocol 216–219
  conductivity protocol 221–223
  microjet electrode 224–225
  multiplexed microchannels 225
  numerical models 226–229
  potentiometric protocol 219–220
  rotating microdroplet 223–224
  voltammetric analysis 212–215
electrode design 181
electrokinetic methods
  electroosmosis flows 76
  external-operated electric field 79
  Helmholtz–Smoluchowski formula 79
  induced-charge electrokinetic (ICEK) flows 80
  solid–fluid interface 77, 79
  time scale 80
  water and aqueous electrolytic solution 78
electromechanical and energy-based models 183
electrowetting manipulation 11
electrowetting-on-dielectric (EWOD) principle 5
enhanced condensational growth (ECG) aerosol delivery method 326
enhanced deeper lung delivery of drug aerosols via condensational growth 326
Entamoeba histolytica antigen EHI_115350 262
enzyme immunoassays 214
enzyme-linked immunosorbent assay (ELISA) platform 261
epidermal growth factor receptor (EGFR) 286
Euler–Euler approach 314
Euler–Lagrange approach 314
Euler number 52

f

fabrication process techniques
  3D printing technology 114
  semiconductor integrated circuits (IC)/MEMS fabrication 113
FactChecker CTC capture system (Circulogix) 249
Faradaic and non-Faradaic current 212
(FDA)-approved clinical microdialysis probes 272
ferrofluid dynamics 315
FeSn NPs 429
Fick's laws 29
field-programmable gate array (FPGA) 193
flash vacuum pyrolysis (FVP) protocols 357
flow regime, in microfluidics
  coflowing microfluidics 379
  dimensionless numbers 377

www.ebook3000.com

flow-focusing microfluidics 378–379
T-junction microfluidics 377–378
flow through porous media 316–317
FLOW-3D software 165–166, 184
flow-focusing microfluidics 378
FLOW-VU 164
fluctuation–dissipation theorem 154
Fluidigm dynamic arrays 300, 301
fluid particles (FP) 153
fluid–particle dynamics modeling 313–315
fluid–structure interaction 317–318
fluorescent enzymatic assay 11
formyl-tetrahydrofolatesynthetase (FTHFS) 296
Fourier number 55
Fourier transform (FT) algorithm 213
front-tracking (FT) method 156
Froude number 50

g

Galileo number 52
γ-Fe_2O_3 composites 453, 454
gas–liquid reaction 365
gas separation testing 497
Gauss divergence theorem 156
gene expression analysis
individual cell levels 280
merits 305
microfluidic circuits 280
nucleic acid analysis 281–283
protein level analysis 283–288
single cell, *see* single cell gene expression analysis
small cell populations 280
gene shearing technology 522
Gene-Z 281
Geometrically enhanced differential immunocapture (GEDI) 243–244
GO chip 246–247
gold nanocrystals
shape anisotropy 426
sharp-edged 427
optical absorbance spectra 427
Graetz number 52
graft polymers
biofunctional coatings 140
grafting-to technique 142
SI-ATRP 137–142
surface photo-grafting polymerization 135–137
graphene-polyaniline (G-PANI) nanocomposite solution 218
Grashof number (Gr) 52
green fluorescent protein (GFP) reporter 284
Gr-1 marker 291

h

Hagen number 53
Hagen–Poiseuille relationship 45
Hall effect 38
haplotyping 293
herringbone (HB)-chip 244
high resolution pumping technology 521
high throughput ChIP (HTChIP) device 284
high-throughput microsampling unit (HTMSU) 245–246
high-T/p aminolysis reactions, for medicine synthesis 361
hollow gold nanoparticles (HGNPs) 436
hollow polycrystalline MOF sphere fabrication 486
hot embossing 124
human embryonic stem cells (hESCs) 286
human leukocyte antigen (HLA) 296
hydrodynamic voltammetry measurements 212
hydrophilic pore network models (PNMs) 166
hydrophobic organic drug fenofibrate 356
hyperthermia 333

i

IL-8 263
Illumina HiSeq series 301
IMMP approach, *see* interfacial microfluidic membrane processing (IMMP), approach
immunoassays 9–11
immunocytochemistry 286
induced-charge electrokinetic (ICEK) flows 80
inhalers and drug–aerosol transport 319–322
injection molding process 122–124
inner MOF growth, advantages of 506
inorganic alumina 501
inorganic *versus* polymeric supports intensification 501–504
in situ rapid cooling and passivating microfluidic (IRCPM)
  cobalt nanoparticle synthesis 412
  process 423
integrated microfluidic systems 449
interface reconstruction volume-of-fluid (IR-VOF) method 156
interfacial microfluidic membrane processing (IMMP)
  approach 489
  durability and stability of membrane 492
  MOF hollow fiber supported membranes 489
  operating scheme 491
integrated tubular microfluidic reactor, experimental setup 415
interleukin-6 (IL-6) 11
intravascular drug delivery
  direct 335–338
  magnetic 333–335
  nanoparticle-based targeted drug delivery 329–330
ion-selective electrodes (ISEs) 220
ion-sensing electrochemical paper-based analytical devices (EPADs) 220
IonTorrent^{TM} system 301, 303
Ip-Do assay 292, 293
IRCPM, *see in situ* rapid cooling and passivating microfluidic (IRCPM), process
isolation by size of epithelial tumor cells (ISET) 238

j

Jakob number 55
Janus nanocomposite 469

k

kinematic viscosity 23
Knudsen number (Kn) 48

l

lab-on-a-chip (LC) 19
  microfluidic reactors 360, 361
  silicon-based microfluidic reactors 362
Laplace number 53
Laplace's law 42–44
large amplitude AC voltammetry approach 213
Large-scale Atomic/Molecular Massively Parallel Simulator (LAMMPS) 162
large-scale Scalable Parallel Short-range Molecular (SPASM) dynamics software 166
laser ablation 124–125
laser bonding 126–127
laser heating 88
lattice Boltzmann method (LBM) 158–160
level set (LS) method 13
Lewis number 55
lipid-polymer composites 466, 468
liquid-phase high-T/p continuous-flow pyrolysis 357
liquid–solid interface 63
liquid–solid wetting 64
liquids and gases, concepts of
  mean free path (λ) 21–22
  viscosity (μ) fluids
    Couette flow 22

www.ebook3000.com

eddy viscosity 29
in industries/engineering 23
kinetic theory of gases 24
laminar shear of fluid 23
macroscale Couette flow device 23
mass and heat transport analysis 22
Newtonian fluid 27
Newton's law of viscosity 27
non-Newtonian fluids 27
parallel flow 23
round-shaped microfluidic channels 23
shear strain rate and shear stress 28
Sutherland's constant, reference values and ξ values 25
viscoelastic fluids 27
viscosity of slurry 28
zero viscosity 22
loop-mediated isothermal amplification (LAMP) method 281
lotus effect 64
lysosomal-associated membrane protein 1 (LAMP1) 288
lysosomal storage disorders (LSDs) 287

m

Mach number (Ma) 50
Mac-1 marker 291
magnetic drug delivery 333–335
magnetic fields 81
magnetic iron oxide-based nanomaterial synthesis
continuous flow synthesis 411
coprecipitation method 406–411
droplet-based microreactors 408
electron microdiffraction pattern 408
fast solvent extraction 408
laminar flow technique 408
polyol process 411
transmission electron microscopy 408
magnetic nanomaterials 412, 414
Marangoni effect 87
Marangoni number 55
mass conservation principle 44
Maxwell–Stefan diffusion model 34
Meldrum's acid 357
membrane protein 264–266
mesofluidics 487
metal/metal alloy materials 464–466
metal-organic framework (MOF) 407, 480
automated microfluidic control 486
based membrane synthesis 504
IMMP approach 489
inorganic *versus* polymeric supports: intensification 501–504
support influence 504–505
description 480
inner MOF growth, advantages of 506
interfacial synthesis 485
HF support intrinsic porosity 505
post-synthetic modifications 488
surface functionalities and/or hetero-structure shells 484
metallic nanocrystals, microfluidic process
composition controlled synthesis 434–437
crystal structure controlled synthesis 422–426
multi-hierarchical structure formation 434–437
size and shape controlled synthesis 426–434
metallic nanomaterial 419
continuous/laminar flow 421
segmented flow 421
metallic NPs 412, 414
metallization 117, 128
methylation, of 1-pentanol 364
metoprolol 361
microjet electrode 224–225
micro milling 125

microelectromechanical systems (MEMS)
  microfabrication 117
  technology 1
microfluidic(s) 405
  biomedical and chemical applications 1
  bulk micromachining processes and substrate bonding techniques 1
  cell-based assays 11–14
  complex microfluidic systems
    digital microfluidics 5
    electrolytic droplets 4
  construction materials considerations 94–95
  DNA assays 6–9
  electrokinetic methods 76–81
  fabricating microfluidic devices 2
  fabrication, *see* fabrication process techniques
  heat (thermal) capacity
    Brillouin scattering experiments 36
    Dulong–Petit law 35
    electron transportation/phonon (lattice vibrations) status 36
    hydrogen-containing polar molecules 36
    in metals 36
    quantum theory 35
    and temperature 35
    thermal conductivity 36, 39, 41
    thermal diffusivity 41
    thermodynamic energy state 34
  immunoassays 9–11
  lab-on-a-chip (LC) 19
  liquids and gases, concepts of
    individual molecular collisions 21
    mean free path (λ) 21–22
    viscosity (μ) fluids 22–29
  magnetic fields 81
  mass and heat transfer principles
    conservation of energy equation 62
    conservation of mass equation 60–61
    conservation of momentum equation 61–62
    diffusion laws 56–59
    dimensionless numbers 47–56
    energy conservation (Bernoulli's Equation) 44–45
    laminar flow, in circular tube 46–47
    mass conservation principle (Continuity Equation) 44
    Pascal's and Laplace's law 42–44
    Poiseuille's Law 45–46
mass diffusivity (D)
  binary gas system 32
  biomass in water 33
  diffusion coefficient 30
  Fick's laws 29
  gas-gas diffusivity 31
  of solvents 32
  value of constrictivity 30
MEMS technology 1
mesoscopic features 20
micro total-analysis systems (μ-TAS) 19
mixing fluids 20
numerical simulation 528
optofluidic process
  deformation of interface 87
  laser heating 88
  laser intensity 87
  light-driven manipulation, of liquid 89
  light-induced Marangoni effect 89
  light momentum 84
  linear liquid crystal polymer (LLCP) 89
  liquid-crystal polymer microstructures 93
  liquid jets 87
  Marangoni effect 87
  optical manipulation devices 83
  radiation pressure 87
  thermocapillary forcing 88
  TMA 91, 92
PDMS 2
quantum dynamical principles 20

www.ebook3000.com

surface and interface
bubble formation 66–68
capillary effects 70–71
Cassie–Baxter model 64
droplet formation 71–74
effect of surfactants 68–69
energy 62
features 69–70
solid/liquid and liquid/liquid interaction 63
types 63
surface micromachining processes 1
microfluidic approach
hydrodynamic parameters, control of 380–393
phase separation 393–396
spreading coefficient 397–398
microfluidic-based protein quantitation 261
microfluidic cell culture system 12
microfluidic cell-patterning assay 292
microfluidic circuits 280
microfluidic components 3–4
microfluidic devices
advantages 523
biomedical engineering 521
bonding/sealing methods 519
challenges 525
chemical analysis 521
design 274, 518–521
flow types 518
metallic nanomaterials 438
potable *in situ* chemical detectors 521
power-driving systems 518
reduced dimension 526
scaling and assembly 520
surface properties 520
microfluidic devices fabrication
high density micro pillar array 114
material property 114
nanomaterials, bulk modification of polymers 142–143
polymer fabrication process
adhesive bonding 127
hot embossing 124
injection molding process 122–124
laser ablation 124–125
laser bonding 126–127
metallization 128
micro milling 125
mold fabrication 122
PDMS casting 122
polymer patterning 119–125
surface treatment 129
3D printing 128–129
thermal bonding 125
ultrasonic bonding 127
silicon and glass fabrication process
bonding process 117–119
etching 117
metallization 117
photolithography 117
surface modification
grafting polymers 135–142
plasma treatment 132–134
surfactant 134–135
microfluidic filtration 249–250
microfluidic immunoassays 9
microfluidic methods 292–301
microfluidic MOF hollow fiber supported membranes
advantages 489, 490
interfacial microfluidic membrane processing 489
microfluidic nebulator, for organic synthesis 355–356
microfluidic oil-segmented droplet confined MOF synthesis 481, 482
microfluidic paper-based analytical device (μPAD) 272
microfluidic process
advantages 420
composite synthesis
pros and cons 449
advantages 447
Janus nanocomposite synthesis 469
lipid-polymer composite 466, 468
metal and nonmetal inorganics
carbon-supported composite 461–463

microfluidic process (*contd.*)
dielectric–plasmonic composites 457–459
plasmonic–semiconductor composite 459–461
metallic nanocrystals
composition controlled synthesis 434–437
crystal structure controlled synthesis 422–426
multi-hierarchical structure formation 434–437
size and shape controlled synthesis 426–434
metal/metal alloy materials 464–466
MOF 470–471
MOF-based membranes synthesis, *see* MOF-based membrane synthesis
nonmetal inorganics
oxide coated multifunctional composite 453–455
semiconductor-semiconductor composite synthesis 455–457
polymers/metal composite synthesis 464, 465
spatiotemporal kinetic parameters 420
microfluidic reactors
advantage 362
applicability 354
description 351
fine chemical and medicine synthesis 353
flow chemistry 352
high heat-exchanging efficiency 352
hydrodynamic flow 353
mass transfer 351
mixing times 351
microfluidic scalability 293
microfluidic spiral separation 250–251
micro total analysis systems (μ-TAS) 19
microtubing-based simple programmed microfluidic processes (MT-SPMPs) 412, 452
microtubule-associated protein 1 light chain 3 (LC3) 288
MOF, *see* metal-organic framework (MOF)
MOF-supported polymeric HF membranes 505
mold fabrication 122
molecular dynamics (MD) 148–149
momentum diffusivity 23
Morton number 51
moving mesh (MM) method 156
computational fluid dynamics (CFD) 160–161
continuum method (CM) 155–158
direct simulation Monte Carlo (DSMC) method 151–153
dissipative particle dynamics (DPD) 153–155
lattice Boltzmann method (LBM) 158–160
multidrug efflux pump protein P-gp 292
multifunctional microparticles, design of, *see* microfluidic approach
multifunctional nanoparticles 327–328
multiorifice flow fractionation (MOFF) 251
multiphase flow microfluidic systems 448, 449
multiphase microfluidic reactors 405
multiplexed microchannels 225
multipurpose batch/semi-batch reactors 351
multistage multiorifice flow fractionation (MS-MOFF) 251

n

nanoliter microfluidic approach 484
nanoparticle-based targeted drug delivery 329–330
NanoVelcro Rare Cell Assays 246
nanoyeast single-chain variable fragments (NYscFv) 262
nebulizers 319, 321
Newtonian fluid 23

www.ebook3000.com

next-generation sequencing technologies 301–305
NH_2-MIL-88B(Fe)
particle size distributions 483
PSD dependence with temperature 484
TEM images 483
nicking enzyme assisted signal amplification assay 266
96-channel microfluidic array 289
nitriles, preparation of 356
N,*N*,*N*′,*N*′ tetramethyl-1,4-phenylene diamine 213
noble-metal nanocrystals 431
nonaffinity-based CTC enrichment
deterministic lateral displacement 250
dielectrophoresis and acoustophoresis 251–252
microfluidic filtration 249–250
microfluidic spiral separation 250–251
multiorifice flow fractionation 251
vortex platform 251
nonspherical particle dynamics 316
nucleic acid analysis 267–269, 281–283
numerical simulation
CFD-ACE+ software 162
CFX software 163–164
FLOW-3D software 164–166
LAMMPS 162
large-scale Scalable Parallel Short-range Molecular dynamics software 166
models, MD 148–150
Nusselt number 56, 526

o

off-the-shelf Arduino microcontrollers 199
Ohnesorge number 53
OncoBean Chip 246
one silicon based lab-on-chip microfluidic reactor, metoprolol preparation 361
open DMF systems 177
oral squamous cell carcinomas (OSCC) 286
organic synthesis
chip-based microfluidic reactor for 360
coiled tubing micro-reactor for 356
microfluidic nebulator for 355–356
packed-bed micro-reactors for 363–356
ring-shape (tube-in-tube) microfluidic reactor for 365–368
oriented attachment (OA) process 423
orthoester formation 363
oxide coated multifunctional composite synthesis 453–455
ozonolysis 367

p

packed-bed micro-reactors, for organic synthesis 363–365
parallel microchip capillary zone electrophoresis (μ-CZE) 223
particle absorption and translocation 328
particle hemodynamics 331–332
parylene 117
parylene C deposited with chemical vapor deposition system 179
Pascal's law 42–44
Pd nanocrystals 431
Péclet number (Pe) 49, 479
permeation tests 496
petal effect 64
phase-field (PF) method 156
pH-sensitive single-walled carbon nanotube (SWCNT) material 219
photolithography 117, 179
physical coating systems 520
plasma treatment 520
plasmonic–semiconductor composite synthesis 459–461
platelet factor-4 (PF-4) 263
Poiseuille's law 45–46

polyadenosine (5′-AAAAAAAAAA-3′) 268
polycytosine (5′-CCCCCCCCCC-3′) 268
polydimethylsiloxane (PDMS) 2, 238, 407
  casting 122
  microchannel 214
  sealing 492
  substrates 175
polymer fabrication process
  adhesive bonding 127
  hot embossing 124
  injection molding process 122–124
  laser ablation 124–125
  laser bonding 126–127
  metallization 128
  micro milling 125
  mold fabrication 122
  PDMS casting 122
  polymer patterning 119–125
  surface treatment 129
  3D printing 128–129
  thermal bonding 125
  ultrasonic bonding 127
polymeric hollow fibers 501
polymeric microparticles
  emulsion polymerization 375
  functions 375
polymer patterning 119–125
polymers/metal composite synthesis 464, 465
polymethylmethacrylate (PMMA) chip 221
polyol process 411
polysulfone (PSf) hollow fiber, MOF layers in 493
porous coordination polymers (PCPs) 480
porous crystalline aluminosilicates, *see* zeolites
portable microplasma generation device (MGD) 272
potentiometric protocol 219–220
Prandtl number (Pr) 48
precursor droplet size 485
pressurized metered-dose inhaler(pMDIs) 319
printed circuit board (PCB) layers 197
prostate specific antigen (PSA) 263
prostate specific membrane antigen (PSMA) 263
protein analysis
  membrane protein 264–266
  secreted proteins 261–264
protein interleukin 6 (IL-6) 263
protein level analysis 283–288
pseudorabies virus (PRV) gene 281
PSf HF membranes 505
  permeance rates of 497
Pt nanoparticles 433
Pt–Pd core-shell heterostructure synthesis 465
pulmonary drug delivery
  drug–aerosol dynamics 322–323
  enhanced deeper lung delivery of drug-aerosols via condensational growth 326
  inhalers and drug–aerosol transport 319–322
  multifunctional nanoparticles 327–328
  particle absorption and translocation 328
  shape engineering 326–327
  smart inhaler system methodology 325
pulsed mixing method 429
pure polymeric membranes 488

q

Quantum theory 20, 35
quorum sensing (QS) 290

r

racemic sertraline imine hydrogenation 365
rapid prototyping techniques 180
Rayleigh number 56
Rayleigh–Plateau instability 379
rechargeable 3.7 V lithium ion batteries 199

www.ebook3000.com

Reynolds number (Re) 48, 377, 479, 504
Richardson number 53
Richtmyer–Meshkov instability 151
Righi–Leduc effect 38
ring-shape (tube-in-tube) microfluidic reactor, for organic synthesis 365–368
Roche/454 FLX 301
Roche 454 pyrosequencing 301
rolling circle amplification (RCA) 281
Rossby number 51
rotating Froude number 53
rotating microdroplet 223–224
Ru nanoparticles 433

S

Sandwich heterogeneous immunoassays 11
scalable continuous MOF fabrication 486
Schmidt number (Sc) 48
secreted proteins 261–264
secreted proteins 264
segmented flow 421
  synthesis, for dicarboxylate MIL-88B(Fe) crystallization 482
semi batch reactors 351
semiconductor-semiconductor composite synthesis 455
shape engineering 326–327
Sherwood number 53
silica tubular supports 501
silicon and glass fabrication process
  bonding process 117
  etching 117
  metallization 117
silicon-based microfluidic reactor layout 360
Si/SiO_2 wafer fabrication 519
simple microparticle formation 380
simple reduction/thermal decomposition process 411
single cell gene expression analysis
  flow cytometry 288
  fluorescence activated cell sorting 288
  flurescent *in situ* hybrization 288
  imaging 289–292
  microfluidic methods 292–301
  next generation sequencing technique 288
  next-generation of sequencing technologies 301–305
single phase continuous flow 405
single-phase flow microfluidic system 448, 449
SiO_2-TiO_2 composite synthesis 454
sixteen-channel microchip electrophoresis 223
size dependent thermal conductivity 527
slicon and glass fabrication process, photolithography 117
smart inhaler system methodology 325
solvothermal method 505
solvothermal synthesis 504
spin coating 179
spreading coefficient 397–398
squeezing 378
Stanton number 56
Stefan number 56
Stokes number 53
Strouhal number (for oscillatory flow) 54
surface grafting methods 520
surface treatment 129
surface-initiated atom transfer radical polymerization (SI-ATRP) 137–142
SWOG 0500 clinical trial 239

t

Taylor–Aris's dispersion effect 405
Taylor number 54
terminal phosphate-labeled fluorogenic nucleotides (TPLFNs) 303
tetrahydrocarbazole synthesis 360
3D coaxial flow microreactor 407
3D printing, 128–129 520
thermal bonding 125

time-dependent Schrödinger equation (TDSE) 150
tissue heat and mass transfer 332–333
T-junction microfluidics 377
TM7 16S rRNA genes 292
2,4,6-trinitrotoluene (TNT) 213
tubular microactuators (TMA) 92
tumour-necrosis factor (TNF-α) 291
turbulence modeling 313

u

UiO-66 nanoparticles 487
ultrafine PtSn nanoparticle formation 461, 462
ultrasonic bonding 127
UV lithography process 122

v

vascular endothelial growth factor (VEGF) 263
vascular endothelial growth factor A (VEGFA) 286
voltammetric analysis 212–215
volume-of-fluid method (VOF) 160
volume-of-fluid technique 184
vortex platform 251
vortex shedding 151

w

Weber number (We) 49, 377
wet chemistry method 451
wet etching method 117
wetting 63
whole-genome amplification (WGA) 269
Wiedemann–Franz law 36
Womersley number 55

x

xCELLigence system 522

y

yellow fluorescent protein (YFP) 289

z

zeolites 479–480
zeolitic imidazolate frameworks (ZIF) 480
  synthesis procedures 494
zero viscosity 22
ZIF-7 layers
  EDX mapping 496
  liquid-phase epitaxial step-synthesis 495
ZIF-8 coating, on polymeric substrate 500
ZIF-8 layers 489, 491, 492
  EDX mapping 496
  solid precipitation 495
ZIF-8 supported membrane, microscopy characterization of 495
ZIF-93 membranes 499
zinc oxide nanoparticles covered by polyvinyl alcohol (ZnONPs-PVA) 264

www.ebook3000.com